MARTIN MARIETTA ENERGY SYSTEMS LIBRARIES
3 4456 0139118 2

ORNL/Sub/79-21453/21

FINAL REPORT

60 GHz GYROTRON DEVELOPMENT PROGRAM

APRIL 1979 THROUGH JUNE 1984

J.F. Shively, R.E. Bier, M. Caplan, M.K. Cheng, E. Choi, C.C. Conner, L.J. Craig
S.J. Evans, S.J. Evers, K.L. Felch, L.J. Fox, F.I. Friedlander, E. Galli, T.J. Grant
G. Hu, H.E. Huey, H.R. Jory, N. Lopez, J. Manca, J.K. Mann, R.C. Morwood,
A. Salop, S.T. Spang, D. Stone, R.S. Symons, G. Thomas and G.E. Wendell

LIBRARY LOAN COPY
DO NOT TRANSFER TO ANOTHER PERSON
OAK RIDGE NATIONAL LABORATORY
CENTRAL RESEARCH LIBRARY
CIRCULATION SECTION
4500N ROOM 175

Prepared by
VARIAN ASSOCIATES, INC.
611 HANSEN WAY
PALO ALTO, CA 94303

Under
Subcontract Purchase Order No. 53Y-21453C

for
OAK RIDGE NATIONAL LABORATORY
OAK RIDGE, TENNESSEE 37830

Operated by
MARTIN MARIETTA ENERGY SYSTEMS, INC.
FOR THE
U.S. DEPARTMENT OF ENERGY
UNDER CONTRACT NO. DE-AC05-840R21400

Printed in the United States of America. Available from:
National Technical Information Service
U.S. Department of Commerce
5255 Port Royal Road, Springfield, Virginia 22161
NTIS price codes — Printed Copy: A99 Microfiche A01

This report was prepared as an account of work sponsored by an agency of the United States Government. Neither the United States Government nor any agency thereof, nor any of their employees, makes any warranty, express or implied, or assumes any legal liability or responsibility for the accuracy, completeness, or usefulness of any information, apparatus, product, or process disclosed, or represents that its use would not infringe privately owned rights. Reference herein to any specific commercial product, process, or service by trade name, trademark, manufacturer, or otherwise, does not necessarily constitute or imply its endorsement, recommendation, or favoring by the United States Government or any agency thereof. The views and opinions of authors expressed herein do not necessarily state or reflect those of the United States Government or any agency thereof.

FINAL REPORT

60 GHz GYROTRON DEVELOPMENT PROGRAM

APRIL 1979 THROUGH JUNE 1984

J.F. Shively, R.E. Bier, M. Caplan, M.K. Cheng, E. Choi, C.C. Conner, L.J. Craig, S.J. Evans, S.J. Evers, K.L. Felch, L.J. Fox, F.I. Friedlander, E. Galli, T.J. Grant, G. Hu, H.E. Huey, H.R. Jory, N. Lopez, J. Manca, J.K. Mann, R.C. Morwood, A. Salop, S.T. Spang, D. Stone, R.S. Symons, G. Thomas and G.E. Wendell

Prepared by
Varian Associates, Inc.
611 Hansen Way
Palo Alto, CA 94303

Under
Subcontract Purchase Order No. 53Y-21453C

for
Oak Ridge National Laboratory
Oak Ridge, Tennessee 37830

Operated by
Martin Marietta Energy Systems, Inc.
for the
U.S. Department of Energy
Under Contract No. DE-AC05-84OR21400

MARTIN MARIETTA ENERGY SYSTEMS LIBRARIES
3 4456 0139118 2

TABLE OF CONTENTS

Section		Page
I.	INTRODUCTION	1
II.	SUPERCONDUCTING SOLENOID MAGNET	7
	A. Design	7
	B. Transverse Field Measurements	12
	C. Spare System	17
III.	110 GHz 200 kW CW OSCILLATOR	23
	A. Electron Gun Computer Design	23
	B. Interaction Circuit	42
	C. Output/Collector	47
	D. Output Window	53
IV.	TEST FACILITY	54
V.	WAVEGUIDE COMPONENTS	56
	A. Waterload	56
	B. Frequency Samplers and Arc Detectors	73
	C. Mode Filters	73
	D. Miter Bend	81
	E. Flange Adapters	81
	F. Attenuators	81
VI.	60 GHz 200 kw PEAK OSCILLATOR DESIGN	84
	A. Electron Gun	84
	B. Anode	100
	C. Interaction Circuit	109
	D. Output/Collector	158
	E. Window	278
	F. Mechanical Design	288
VII.	GYROTRON BEHAVIOR STUDY	294
	A. Arcing and Crowbar Investigation	294
	B. Voltage Gradients and Trapped Electrons Computer Investigation	300
	C. Process and Bakeout	300
	D. RF Behavior	301
	E. Cavity and Output Taper	311
	F. Maximum Power Limitations	324
	G. Cathode Investigation	326

TABLE OF CONTENTS (Cont'd)

VIII. 60 GHz 200 kW CW OSCILLATOR DESIGN 328

A. Collector Mode Conversion 328
B. Window 344

IX. TEST RESULTS 452

A. First Experimental Tube 452
B. Second Experimental Tube 473
C. Third Experimental Tube 476
D. Fourth Experimental Tube (First CW Tube) 490
E. Fifth Experimental Tube (Second CW Tube) 502
F. VGE-8060 S/N P-1R3 527
G. Sixth Experimental Tube (Third CW Tube) 529
H. VGE-8006A S/N 101 559
I. VGE-8006A S/N 102 571
J. Seventh Experimental Tube 581

X. 56 GHz GYROTRON DEVELOPMENT 603

A. Gun 603
B. Anode Section 603
C. Cavity Assembly 603
D. Output Taper and Collector 606
E. Window 606
F. Test Results 606

XI. SUMMARY 626

XII. REFERENCES 630

APPENDICES

Appendix A - Dielectric Properties of Water 634
Appendix B - Mode Conversion in Overmoded Circular Waveguides at Conical Cylindrical Junctions 642
Appendix C - Voltage Traveling Wave Ratio Measurements 665

LIST OF ILLUSTRATIONS

Figure		Page
1.	Outline VYW-8060 Coil and Dewar Assembly	10
2.	B_t vs z for 60 GHz Magnet	13
3.	B_x and B_y with Dewar in Normal Position	14
4.	B_x and B_y with Dewar Rotated 90°	15
5.	B_x and B_y with Dewar Rotated 180°	16
6.	Transverse to Axial Magnetic Field Ratio with Respect to Split Coil Center	19
7.	B_t/B_z vs Position for VYW-8060	21
8.	Electron Trajectories for a 10° Cathode Angle	26
9.	Transverse Energy Profile for 10° Cathode with 5 A/cm^2 Loading	27
10.	Electron Trajectories for a 23° Cathode Angle with a Short Front-Focus Electrode	29
11.	Electron Trajectories for a 23° Cathode Angle with a Medium Front-Focus Electrode	29
12.	Electron Trajectories for a 23° Cathode Angle with a Long Front-Focus Electrode	29
13.	Variation of Transverse Energy Profile with Length of Front-Focus Electrode	31
14.	Electron Trajectories for a 5 A/cm^2 Cathode Loading Design	32
15.	Transverse Energy Profile for 23° Cathode with 5 A/cm^2 Loading	33
16.	Transverse Energy Profile for the Best 25° Cathode Design	34
17.	110 GHz Gun Trajectory Plot	35
18.	Transverse Energy Profile as a Function of 1st Anode Voltage	37
19.	Variation of Transverse Energy Profile with 1st Anode Angle (Curved Back-Focus Electrode)	38

LIST OF ILLUSTRATIONS (Cont'd)

20. Transverse Energy Profile as a Function of Bucking Coil Ampere-Turns 39

21. Beam Radius at Circuit as a Function of Change in Bucking Coil Ampere-Turns 40

22. Transverse Energy Profile as a Function of Distance from Center of Cathode to Tip of First Anode 41

23. Variation of Transverse Energy Profile with Beam Current 43

24. Figure of Merit for Circular Electric Modes 44

25. Transmission of TE_{11} Mode Through Anode Load vs Load Gap and Frequency 46

26. Effective Interaction Cavity Length 48

27. Output Coupling Options Considered 49

28. Mode Conversion as a Function of Taper Angle 51

29. Waveguide Probe 52

30. Outline VLA-8000 CW Waterload 57

31. Pulsed Waterload 58

32. Outline CW Load Assembly, VLE-8006A2 59

33. Response of TE_{02} Cavity Launcher to CW Load with DC-200 (50 centistokes) Fluid 64

34. Jet Load 66

35. Electromagnetic Radial Diverter 68

36. CW Load 69

37. Redesigned ERD Waterload 72

38. Outline VCE-8006-A2 Frequency Sampler and Arc Detector 74

39. Water Wall Mode Filter 76

40. VFE-8006-A3, S/N 001, TE_{11} Transmission 77

41. VFE-8006-A3, S/N 001, TE_{01} Transmission 78

42. VFE-8006-A3, S/N 001, Response to Cavity Excitation . 79

LIST OF ILLUSTRATIONS (Cont'd)

43. VFE-8006-A2, Outline Elbow 82

44. Electron Trajectory Plot for 60 GHz Gun 85

45. Transverse Energy Profile for 42.5° Slope Rear-Focus Electrode (60 GHz)..... 86

46. Transverse Energy Profile for 40° Rear-Focus Electrode (60 GHz) 87

47. Transverse Energy Profile for 45° Slope Rear-Focus Electrode (60 GHz) 88

48. Normalized Transverse Velocity Profile (60 GHz) 89

49. Transverse Energy Profile as a Function of Longitudinal Displacement of Gyrotron with Respect to Magnetic Field 90

50. Effect of the Difference Between Two Methods of Calculating Off-Axis Magnetic Fields on the Transverse Energy Profile 92

51. Variation of Transverse Energy Profile vs Beam Current 93

52. Gradients for Original Gun Pulsed On 94

53. Magnified View of the Gradient for the Original Gun 96

54. Gradients for Modified Gun 97

55. Power Sensitivity to Gun Anode Voltage for VGE-8060, S/N 004 99

56. Calculations for Gun with Recessed Cathode 101

57. Anode 102

58. Load Ring Assembly 104

59. Cross Section of Brazed Assembly 105

60. Cracked Surfaces After Thermal Cycling 107

61. Normalized Pumping Speed vs Normalized Channel Diameter at Fixed RF Isolation 110

62. Mode Density 111

LIST OF ILLUSTRATIONS (Cont'd)

63. Azimuthal Electric Field Squared for the TE_{021} Oscillator Cavity in Arbitrary Units vs Normalized Axial Position, Z/a, at the Fixed Radius Corresponding to the First Radial Maximum of the Electric Field 114

64. Efficiency vs Normalized Magnetic Field 118

65. Optimized Efficiency vs Output Power 120

66. Output Power vs Beam Current (Magnetic Field Optimized) 121

67. Efficiency vs Normalized Magnetic Field 123

68. Efficiency vs Cavity Length 125

69. Transverse Electric Field Profile for 60 GHz TE_{021} Cavity 126

70. Starting Currents: Varian 60 GHz Gyrotron 128

71. Efficiency vs Beam Current for Optimum Magnetic Field 132

72. Efficiency vs Beam Current for Various Values of Cavity Magnetic Field 133

73. Output Power vs Gun Anode Voltage (related to α) for Two Values of Cavity Magnetic Field 134

74. Schematic Diagram of the Geometry of the Present Cavity and of a Cavity Modified to Lengthen the Pre-bunching Region and Shorten the Interaction Section 137

75. Plot of Efficiency vs Beam Current for Various Magnetic Fields for Cavity with Modified Electric Field Profile 138

76. Plot of Efficiency vs Beam Current for the Original and Modified 60 GHz Cavity Designs for Optimum Magnetic Field 139

77. Plot of Output Power vs Magnetic Field for the Original and Modified 60 GHz Cavity 140

78. Starting Current vs α ($\equiv \beta_\perp/\beta_\parallel$) for Two Values of Magnetic Field for the Original and Modified 60 GHz Cavity Designs 141

LIST OF ILLUSTRATIONS (Cont'd)

79. Example of a TE_{011}/TE_{021} Step Cavity 143

80. Example of a TE_{011}/TE_{021} Step Cavity as Simulated on a Computer Code Which can Handle Open Step Cavities 145

81. Efficiency vs Beam Current for Various Magnetic Fields for Step Cavity #1 146

82. Efficiency vs Beam Current for Various Magnetic Fields for Step Cavity #3 147

83. Efficiency vs Beam Current for Various Magnetic Fields for Step Cavity #3 with an Increasing Magnetic Field Taper of 12% 148

84. Open Cavity SUPERFISH plot of Step Cavity Design No. 3 150

85. SUPERFISH Resonance Curve for Step Cavity with Iris 151

86. Q_L and f_o as Functions of the Ratio of Iris Diameter to Diameter of Iris Used in Step Cavity Design #3 152

87. Example of a Complex Cavity with a Tapered Wall in the TE_{02} Section to Profile the Axial Dependence of the rf Electric Field 154

88. Efficiency Calculations for Several Values of Magnetic Field for a TE_{01}/TE_{02} Complex Cavity Design with a Tapered Wall in the TE_{02} Section 155

89. Example of a TE_{01}/TE_{02} Step Cavity with Modified Cavity Lengths 156

90. Efficiency Calculations for Several Values of Magnetic Field for a TE_{01}/TE_{02} Step Cavity Design with Modified Cavity Lengths 157

91. Comparision of Mode Content of the X-6 Step Cavity with that of the Standard Tapered Cavity Used on X-5 159

92. Taper to Cylinder Waveguide Junction 160

LIST OF ILLUSTRATIONS (Cont'd)

93. Mode Conversion 163

94. Mode Conversion as a Function of Taper Angle 164

95. Infinitely Thick Slab 167

96. Slab of Finite Thickness 169

97. Roots of cot y = y/B 171

98. Transient Temperature Profiles in Collector Wall 173

99. Pulse Duration Regimes for Gyrotron Collectors 174

100. VGE-8060 Collector, Steady-State (1 kW/cm^2), 20 ft/sec Flow Rate Mesh Plot 177

101. Mesh Plot 178

102. Heat Transfer Coefficient at 20 ft/s, 100 psig, 35^oC 180

103. VGE-8060 Collector, 2.0 sec Pulse, 20 ft/sec Flow Rate 182

104. VGE-8060 Collector, Steady-State (1 kW/cm^2), 20 ft/sec Flow Rate Isoplot 183

105. VGE-8060 Collector, Decay After 2.0 sec Pulse, 20 ft/sec 184

106. Time to Burnout, VGE-8060 Collector, Calculation on TACO 187

107. VGE-8060 Collector, Transient-State (2 kW/cm^2) - 50 ft/sec Flow 188

108. VGE-8060 Collector, Steady-State, 40 ft/sec Flow Isoplot 189

109. VGE-8060 Collector, Three 1 kW/cm^2 Pulse Cycles, 40 ft/sec Flow Temperature History 190

110. VGE-8060 - 3 sec Pulse, 3 sec Decay, 1 kW/cm^2 40 ft/sec 191

111. Axial Magnetic Field Curves for 60 GHz Gyrotron 193

112. Current Distribution 60 GHz Gyrotron Collector 194

LIST OF ILLUSTRATIONS (Cont'd)

113. Smoothed Current Distribution 60 GHz Gyrotron Collector 196

114. Collector Power Density 60 GHz Gyrotron 197

115. Elevated Temperature Tensile Properties of Annealed OFHC Copper Plate 200

116. Elevated Temperature Tensile Properties of Hard Drawn OFHC Copper Rod 202

117. Increase of Electrical Resistivity of Copper with Admixtures of Various Elements 203

118. Room Temperature Fatigue Strength of AMAX-MZC in Various Conditions 203

119. Tensile Strength vs Temperature for NARLOY Z 204

120. Typical Stress-Strain Curves for NARLOY Z 205

121. 810.9°K (1000°F) Cycle Stress-Strain Curves for NARLOY Z 206

122. Typical Low-Cycle Fatigue Life of NARLOY Z 208

123. Tensile Strength vs Temperature for OFHC Copper Annealed Condition 209

124. Typical Stress-Strain Curves for OFHC Copper Annealed Condition 210

125. Typical Low-Cycle Fatigue Life of OFHC Copper Annealed 211

126. Glidden AL-15 (oxygen free) After 1000°C Dry Hydrogen Firing/100 X Magnification 212

127. Glidden AL-15 (oxygen free) After 1000°C Dry Hydrogen Firing/400 X Magnification 212

128. Glidden AL-20 (oxygen bearing) Unfired 400X Magnification 214

129. Glidden AL-20 (oxygen bearing) After Dry Hydrogen Firing at 1000°C at 400X Magnification 214

130. Effect of Cold Work on the Room Temperature Mechanical Properties of AL-20 GLIDCOP Rod 215

LIST OF ILLUSTRATIONS (Cont'd)

131. Effect of One Hour Elevated Temperature Exposure on the Room Temperature Mechanical Properties of AL-20 GLIDCOP Strip 216

132. Elevated Temperature Stress Rupture Properties of AL-20 GLIDCOP 217

133. Inner Wall Temperature for 2 kW/cm^2 221

134. Outer Wall Temperature for a 250 ms Pulse 222

135. Calculated Collector Wall Temperature Rise 224

136. Schematic of Computer Data Acquisition System 225

137. Measured Collector Power Density in X-8: 2 Coils with rf 226

138. Measured Power Density in X-8: 2 Coils, no rf 227

139. Measured Power Density in X-8: 3 Coils, with rf 228

140. Measured Power Density in X-8: 3 Coils, no rf 229

141. Collector Magnetic Field with 2 and 3 Coils 233

142. Measured Power Density in X-8: 3 Coils, with rf; Cylindrical Coordinate Heat Transfer Analysis 230

143. Measured Power Density in X-8: 3 Coils, no rf; Cylindrical Coordinate Heat Transfer Analysis 232

144. Simulated Electron Trajectories 235

145. Power Density Distribution for S/N 104, no rf, 2 Small Coils 237

146. Power Density Distribution for S/N 104, no rf, Two Small Coils, with Superconducting Solenoid Magnet Rotated 180° 238

147. Power Density Distribution for S/N 104, no rf, no Coils, with Superconducting Solenoid Magnet Rotated 180° 239

148. Power Density Distribution Calculations 241

149. A Partial Cross Section View of the Current Collector Cooling Channel Geometry Showing the Location of the Finite Element Map 242

LIST OF ILLUSTRATIONS (Cont'd)

150. Finite Element Map Used for Calculating Temperature-Time Relationship for Existing Cooling Channel Geometry 242

151. Transient Temperature for Two Critical Nodes for the Current Collector Cooling Channel Geometry 243

152. A Partial Cross Section View of a Proposed Collector Cooling Channel Geometry with the Channels 0.100 Inch Closer to the beam 245

153. Finite Element Map Used for Calculating Temperature-Time Relationship for the Proposed Cooling Channel Geometry 245

154. Transient Temperature for the Two Critical Nodes for the Proposed Collector Cooling Channel Geometry 246

155. Electron Trajectories from a Modified Production Gun 251

156. Measured and Calculated Electron Density as a Function of Beam Radius 252

157. Internal Configuration of Beam Analyzer 254

158. A Typical Electron Gun Showing the Hollow Beam and Density Profile Variations as a Function of Distance from the Cathode 255

159. Comparison of Beam Current Density Profiles for the Standard and Modified Guns 256

160. Maximum Space Charge Limited Emission Curve 257

161. Anode Assembly Showing Coolant Channels 258

162. Sectional View of the Complete Diode Assembly 259

163. Schematic of the Cooling System Controls 261

164. OFHC Copper after 38,000 Cycles, 3X, Power Density = 1.0 kW/cm^2 262

165. OFHC Copper after 38,000 Cycles, 12X, Power Density = 1.0 kW/cm^2 263

166. OFHC, 0.200" Wall, 38,000 Cycles at 1.6 kW/cm^2, 3X ... 264

LIST OF ILLUSTRATIONS (Cont'd)

167. OFHC, 0.200" Wall, 38,000 Cycles at 1.6 kW/cm^2, 18X .. 265

168. OFHC, 0.200" Wall, 38,000 Cycles at 1.6 kW/cm^2, 25X .. 266

169. OFHC, 0.200" Wall, 38,000 Cycles at 2.0 kW/cm^2, 3X ... 268

170. OFHC, 0.200" Wall, 38,000 Cycles at 2.0 kW/cm^2, 12X .. 269

171. OFHC, 0.200" Wall, 38,000 Cycles at 2.0 kW/cm^2, 25X .. 270

172. OFHC, 0.200" Wall, 1.0 kW/cm^2, 38,000 Cycles, 50X 271

173. OFHC, 0.200" Wall, 1.6 kW/cm^2, 38,000 Cycles, 50X 272

174. OFHC, 0.200" Wall, 2.0 kW/cm^2, 70,000 Cycles, View of Beam Center, 50X 273

175. OFHC, 0.200" Wall, 1.6 kW/cm^2, Beam On 274

176. OFHC, 0.200" Wall, 1.6 kW/cm^2, Beam Off 275

177. Computed VSWR for a Single-Disc Beryllia Window 279

178. Window Cold Test Arrangements 280

179. Ceramic Disc 282

180. Single-Disc Window 284

181. Temperature Distribution in the Disc Window 285

182. Tangential Stress in the Disc 286

183. Radial Stress in the Disc 287

184. Steady-State Temperature Distribution of 60 GHz Single-Disc BeO Window 289

185. Steady-State Stress Distribution of the 60 GHz Single-Disc BeO Window 290

186. Upper Seal Arc 296

187. Lower Seal Arc 297

188. Cathode Arc to Ground 298

189. Optimized Power vs Gun Anode Voltage 302

190. Power vs Main Magnet Current 303

LIST OF ILLUSTRATIONS (Cont'd)

191. Power vs Gun Coil #1 Current 304

192. Parameter Space - VGA-8000, S/N 11 CW 305

193. Parameter Space - VGA-8050, S/N 9 - Pulsed 2.4% Duty 306

194. Power and Frequency Sensitivity to Main Magnet No. 3 Current 308

195. VGA-8000, S/N 11 Pulsed Oscillation Map 309

196. VGA-8000, S/N 11 CW Oscillation Map 310

197. VGA-8000, S/N 8 Power vs Beam Current 314

198. VGA-8000, S/N 8B Peak Output Power Sensitivity to Main Solenoid Magnet Coil #3 Current 315

199. VGA-8000, S/N 8B Peak Output Power vs Main Magnet Coil #3 Current with Gun Anode Voltage and Gun Coil Current Changed (V_o = 80.8 kV) 316

200. VGA-8000, S/N 8B Peak Output Power vs Main Magnet Coil #3 Current with Beam and Gun Anode Voltages Changed (V_o = 70 kV) 317

201. Peak Output Power vs Main Magnet Coil #3 Current at Lower Gun Anode Voltage and Gun Coil Current 318

202. VGA-8000, S/N 8B Pulsed Oscillation Map with Gun Coil #1 Current = 9A 319

203. VGA-8000, S/N 8B Pulsed Oscillation Map with Gun Coil #1 Current = 10A 320

204. VGA-8000, S/N 8B Pulsed Oscillation Map with Lower Beam Voltage 321

205. VGA-8000, S/N 8B Pulsed Oscillation Map with Higher Gun Coil Current at 70 kV 322

206. VGA-8000, S/N 8B Pulsed Oscillation Map with Higher Gun Coil Current at 80 kV 323

207. Mode Conversion in the X-6 Collector at 60 GHz Calculating Conversion of TE_{02} to TE_{01} using TAPER ... 329

208. Mode Conversion in the X-6 Collector at 60 GHz Calculating Conversion of TE_{02} to TE_{03} Using TAPER ... 330

LIST OF ILLUSTRATIONS (Cont'd)

209. Mode Conversion in 5-inch Diameter Collector with 5° Linear Tapers at 60 GHz Calculating Conversion of TE_{02} to TE_{01} using TAPER 331

210. Mode Conversion in 5-inch Diameter Collector with 5° Linear Tapers at 60 GHz Calculating Conversion of TE_{02} to TE_{03} using TAPER 332

211. Mode Conversion in 4-inch Diameter Collector with Curved Tapers at 60 GHz Calculating Conversion of TE_{02} to TE_{01} using TAPER 334

212. Mode Conversion in 4-inch Diameter Collector with Curved Tapers at 60 GHz Calculating Conversion of TE_{02} to TE_{03} using TAPER 335

213. Mode Conversion Levels of 4" Collector Design #2 337

214. Collector with 2° Linear Up-Taper 339

215. Computed VSWR for an FC-75, Face-Cooled Alumina Double-Disc Window 345

216. Computed VSWR for an FC-75, Face-Cooled Beryllia Double-Disc Window 346

217. Computed VSWR vs Frequency for Beryllia Double-Disc Window Designs 348

218. Computed VSWR vs Frequency for Alumina Double Disc Window Designs 349

219. Temperature Distribution of Double-Disc Window, λ thick, 3" Diameter 354

220. AL-995 Double-Disc Window Stress Distribution of Vacuum Side, λ thick, 3-inch Diameter 355

221. Temperature Distribution, Vacuum-Side, Double-Disc Window, 1.5 λ Thick 356

222. AL-995 Double-Disc Window Stress Distribution 60 GHz, 120 kW CW, 1.5 λ thick 3" Diameter 357

223. Temperature Distribution on Vacuum-Side, Double-Disc Window, 2λ thick 358

224. AL-995 Double-Disc Window Stress Distribution, 2λ thick 359

LIST OF ILLUSTRATIONS (Cont'd)

225. Temperature Distribution on Vacuum-Side, 60 GHz Double-Disc Window, 2.5λ thick, 120 kW CW, α = 0.03175 nepers/cm, Film Coefficient = 2.5 watts/in^2 $^\circ$C 360

226. AL-995 Double-Disc Window Stress Distribution, 2.5λ thick 361

227. AL-995 4-inch Double-Disc Window Temperature Distribution, 60 GHz, 120 kW CW, 1.5λ thick, α = 0.03175 nepers/cm, h = 2.5 W/in^2 $^\circ$C 362

228. AL-995 Double-Disc Window Stress Distribution, 1.5λ thick, 4-inch Diameter 363

229. Grid Geometry 366

230. Calculation of Effective Grid Hole Length 369

231. Calculation of f_H 371

232. Grid Transmittance Along Vertical and Horizontal Diameters versus ϕ 373

233. Thermal Imaging Experimental Arrangement Details 374

234. Photograph of Model Used in Measuring Planar Grid 376

235. Model used in Measuring ϕ 377

236. Angle, ϕ, Between Grid Hole Axis and IR Ray 378

237. Grid Transmittance (%) 379

238. Overview of Thermal Imaging Experimental Arrangement 382

239. Finger Viewed through Grid with IR Camera 383

240. System Resolution Check 383

241. Hot, Black Can Viewed through Grid and Checkerboard Pattern 384

242. 26°C Isotherm on Finger Viewed Through Grid 385

243. 26.4°C Isotherm on Finger Viewed Through Grid 385

244. 34.4°C Isotherm on Finger 387

LIST OF ILLUSTRATIONS (Cont'd)

245. $34^{o}C$ Isotherm on Finger 387

246. Checkerboard Pattern 388

247. Horizontal Field of View Determination at top of Picture 389

248. Horizontal Field of View Determination at Bottom of Picture 389

249. Field of View Looking Closer to Near Wall 391

250. Black Paint at $51.7^{o}C$ through Grid, Isotherm at $36.4^{o}C$ 392

251. Black Paint at $51.7^{o}C$ through Grid, Isotherm at $39.2^{o}C$ 392

252. Black Paint at $53.3^{o}C$ through Grid, Grid Holes Show .. 392

253. IR Optical Path 394

254. $60^{o}C$ Blackbody Calibration of Grid Transmission 396

255. IR Image of Template for Alignment and Calibration of IR System 398

256. IR Image of P-1R3 Window, no rf 399

257. IR Image of P-1R3 Window, 30 ms, 200 kw Pulse 400

258. Improvement of the Thermal Image of a Template with Radial Pattern of Holes, Center Denoted with a "+" 401

259. VGE-8005 S/N 1 Thermal Image at 110 kW Output Power, Window Center Denoted by "+" 402

260. Temperature at Inner Radial Maximum vs Output Power .. 404

261. Radial Temperature Profile, Output Power = 110 kW 405

262. Maximum Window Temperature vs FC-75 flow 406

263. Maximum Window Temperature vs Output Power for Different Water Load Flows 408

264. Thermographs of X-6 Window 409

LIST OF ILLUSTRATIONS (Cont'd)

265. Compilation of all Window Temperature Measurements as a Function of Output Power for the VGE-8006, S/N X-6 During CW Operation 410

266. Peak Window Temperature as a Function of Main Magnet #1 Current for a Constant Output Power for the VGE-8006, S/N X-6 During CW Operation (FC-75 Inlet Temperature 15.6 °C) 412

267. Influence of Window Diameter on Thermal Hoop Stress ... 414

268. Influence of Window Thickness on Thermal Hoop Stress .. 415

269. Temperature Distribution of Double-Disc Window 419

270. Stress Distribution of Double-Disc Window 420

271. Calculated Temperature Profiles 426

272. Calculated Stress Profiles on "Vacuum Side" Disc 427

273. Calculated Stress Profiles on "Vacuum Side" Disc with Various Output Power Levels 428

274. Calculated Displacement of X-6 Window Under 45 psia Static Load 429

275. Calculated Temperature Distribution on a Double-Disc Window 431

276. Calculated Thermal Stress Distribution in a Double-Disc Window for the Temperature Conditions Shown in Figure 275 432

277. Temperature Distribution in Double-Disc Window (reduced pattern) 433

278. Thermal Stress Distribution on a Double-Disc Window (reduced pattern) 434

279. The Schematic Sketch of a Double-Dish Window 436

280. Temperature Distribution of Double-Dish Window 438

281. Stress Distribution of Double-Dish Window 439

282. Cavity Response with Single-Disc Window 440

283. Single-Dish Window TE_{01} Mode Reflection 441

LIST OF ILLUSTRATIONS (Cont'd)

284. Geometry of a Dish Window 442

285. Buckling Pressure Load for a Dish with a Fully Clamped Edge 443

286. Schematic of an Arch Window 445

287. Schematic of a Double-Disc Window with Edge Support ... 447

288. Stress Distribution in 60 GHz, 200 kW CW Vacuum Window 448

289. Stresses Due to Static Load Only 449

290. Window Displacement Due to Static Load 450

291. Operating Frequency vs Top Coil Current for X-1 455

292. Peak Output Power vs Top Coil Current for X-1 456

293. Peak Output Power vs Bucking Coil Current for X-1 457

294. Peak Output Power vs Beam Current for X-1 459

295. Sensitivities of Peak Output Power and Frequency to Top Main Coil Current for the Parameters of Table 42 461

296. Gun Anode Voltage and rf Pulse Shapes 464

297. Body Heating Correlation 465

298. Schematic Layout of VGE-8060 466

299. Comparison of Load Cavity and Drift Tube Resonances ... 468

300. Drift Tube Resonances for Different Boundary Conditions 469

301. Resonance Curve for Modified Drift Tube 471

302. Oscillation Map, VGE-8060, S/N X-2 474

303. Collector Boiling Curves for VGE-8060, S/N X-2 475

304. Oscillation Map for i_o = 6 a, VGE-8060, S/N X-3 477

305. Oscillation Map for i_o = 8 a, VGE-8060, S/N X-3 478

306. Power Sensitivity to Magnet Current 479

LIST OF ILLUSTRATIONS (Cont'd)

307. Densitometer Reading vs Axial Location of X-ray Film .. 480

308. Densitometer Reading vs Axial Location of X-ray Film for VGE-8060, S/N X-3 with Iron Polepieces 481

309. VGE-8060, S/N X-3R Oscillation Map (i_o = 6 a) 483

310. VGE-8060, S/N X-3R Oscillation Map (i_o = 8 a) 484

311. Optimized Microwave Power and Efficiency as a Function of Main Magnet No. 1 Current for X-3R 485

312. Operating Frequency for Fixed Gun Anode Voltage as a Function of Main Magnet No. 1 Current for Three Values of Beam Current for X-3R 486

313. Microwave Power for Fixed Gun Anode Voltage as a Function of Main Magnet #1 Current for Three Values of Beam Current for X-3R 487

314. Microwave Efficiency for Fixed Gun Anode Voltage as a Function of Main Magnet No. 1 Current for Three Values of Beam Current for X-3R 488

315. Oscilloscope Photograph of the rf Pulse During 100 ms, 10% Duty Operation 489

316. Oscilloscope Photograph of the rf Pulse During Short Pulse Operation 491

317. Beam Current as a Function of Input Heater Power for X-3R 492

318. Beam Current as a Function of Gun Anode Voltage for X-3R 493

319. Oscillation Map for the VGE-8006, S/N X-4 under Short Pulse Conditions for 1.8 a Beam Current 494

320. Oscillation Map for the VGE-8006, S/N X-4 under Short Pulse Conditions for 6 a Beam Current 495

321. X-4 Cathode Emission Cooling 497

322. X-4 Oscillation Map, CW Operation, I_o = 3.2 A 499

323. X-4 Oscillation Map, Pulse Operation, i_o = 1.8 a 500

324. X-4 Collector Power Density Distribution 501

LIST OF ILLUSTRATIONS (Cont'd)

325. Oscillation Map for VGE-8006, S/N X-5 for a Beam Current of 8 a, Operating Under Pulse Conditions 504

326. Peak Power as a Function of Main Magnet No. 1 Current for VGE-8006, S/N X-5 Operating Under Pulse Conditions 505

327. Peak Power as a Function of Beam Current for VGE-8006, S/N X-5 Operating Under Pulse Conditions 506

328. Peak Power as a Function of Gun Anode Voltage for VGE-8006, S/N X-5 Operating Under Pulse Conditions 507

329. Peak Power as a Function of Beam Voltage for VGE-8006, S/N X-5 Operating Under Pulse Conditions 508

330. Oscillation map for VGE-8006, S/N X-5 for a Beam Current of 3.0 A, Operating Under CW Conditions 510

331. Threshold Conditions for the TE_{02} Mode with Variation of the Gun Anode Voltage as a Function of Main Magnet No. 1 Current 511

332. Starting Currents for the VGE-8006, S/N X-5 in CW Operation Showing the Effects of Mode Locking 513

333. Output Power vs Gun Anode Voltage for Several Values of Main Magnet No. 1 Current 514

334. Output Power vs Main Magnet No. 1 Current for a Beam Current of 2.0 A for the VGE-8006, S/N X-5 in CW Operation 515

335. Output Power vs Main Magnet No. 1 Current for a Beam Current of 3.0 A for the VGE-8006, S/N X-5 in CW Operation 516

336. Mode Patterns of Competing Modes at 50.08 GHz and 51.8 GHz Obtained using Temperature-Sensitive Paper in the Output Waveguide of the VGE-8006, S/N X-5 in CW Operation 518

337. Collector Power Density Distribution for VGE-8006A, S/N X-5R with no rf and Coil at 8 inches with 0.5 A ... 522

338. Collector Power Density Distribution for VGE-8006A, S/N X-5R with rf Coil at 8 inches with 0.5 A 523

339. Collector Power Density Distribution for VGE-8006A, S/N X-5R in Magnet #1002 with no rf and Coil at 8 inches with 0.5 A 525

LIST OF ILLUSTRATIONS (Cont'd)

340. VGE-8060, S/N P1-R3 Oscillation Map 528

341. VGE-8060, S/N P1-R3, rf Power vs Gun Anode Voltage 530

342. Output Power vs Gun Anode Voltage with a 2% Magnetic Taper Across the Cavity for the VGE-8006, S/N X-6 532

343. Output Power vs Main Magnet #1 Current with a 2% Magnetic Taper Across the Cavity for the VGE-8006, S/N X-6 533

344. Oscillation map with a 2% Magnetic Taper Across the Cavity for the VGE-8006, S/N X-6 534

345. Output Power vs Main Magnet #1 Current with a 3% Magnetic Taper Across the Cavity for Three Values of Beam Current for the VGE-8006, S/N X-6 536

346. Frequency vs Main Magnet #1 Current with a 3% Magnetic Taper Across the Cavity for Three Different Beam Currents for the VGE-8006, S/N X-6 537

347. Output Power vs Main Magnet #1 Current with a 6% Magnetic Taper Across the Cavity for Three Different Beam Currents for the VGE-8006, S/N X-6 538

348. Output Power vs Main Magnet #1 Current with a 9% Magnetic Taper Across the Cavity for Three Values of Beam Current for the VGE-8006, S/N X-6 539

349. Oscillation Map with a 9% Magnetic Taper Across the Cavity for the VGE-8006, S/N X-6 540

350. Output Power vs Gun Anode Voltage for 9% Magnetic Taper Across the Cavity for the VGE-8006, S/N X-6 541

351. Output Power vs Beam Current for 9% Magnetic Taper Across the Cavity for the VGE-8006, S/N X-6 542

352. Output Power vs Main Magnet #1 Current with no Magnetic Taper Across the Cavity for Three Values of Beam Current for the VGE-8006, S/N X-6 544

353. Schematic Diagram Showing the Relative Positions of the Three Magnet Coils and the Step Cavity for X-6, Tapered and Flat Magnetic Field Profiles are Plotted on the Same Axial Scale 545

LIST OF ILLUSTRATIONS (Cont'd)

354. Comparison of Optimum Efficiencies as a Function of Magnetic Field Taper for Different Beam Currents, as Predicted by Theory and Observed on VGE-8006, S/N X-6 546

355. Output Power vs Main Magnet #1 Current with a 3% Magnetic Taper Across the Cavity for Two Values of Beam Current 549

356. Output Power vs Gun Anode Voltage with a Magnetic Taper of 3% Across the Cavity for a Beam Current of 4.9 A 550

357. Output Power vs Beam Voltage with a Cavity Magnetic Taper of 3% for a Beam Current of 5 A 551

358. Output Power vs Beam Current with a 3% Magnetic Taper Across the Cavity for the VGE-8006, S/N X-6 in CW Operation 552

359. Body Power (Cavity and Beam Tunnel Losses) vs Output Power with a Magnetic Taper at 2% for a Beam Current of 3A 553

360. FC-75 ΔT (Outlet Temperature - Inlet Temperature) as a Function of Output Power for the VGE-8006, X/N X-6 During CW Operation 556

361. Schematic of Experimental Set-up for Mode Content Measurements on X-6 using Mode Selective Directional Couplers Furnished by GA Technologies 558

362. Power vs Beam Current for X-6 CW Operation 560

363. Power vs Gun Anode Voltage for X-6 CW Operation 561

364. Temperature vs Time for Two Sensor Positions 564

365. Peak Heat Flux vs Aiding Coil Current 565

366. Incident Heat Flux vs Position VGE-8060A, S/N 101, 5 ms rf Pulse, 640 kw Beam, 200 kw rf 567

367. Incident Heat Flux vs Position, VGE-8006A, S/N 101, 5 ms Pulse 640 kw Beam, no rf 568

368. Oscillation Map 570

369. Peak Power Out vs Gun Anode Voltage 572

LIST OF ILLUSTRATIONS (Cont'd)

370. Peak Power Out vs Magnet No. 3 Current 573

371. Peak Power Out vs Magnet No. 1 Current 574

372. Peak Power Out vs Beam Voltage 575

373. Peak Power Out vs Beam Current 576

374. Peak Window Temperature vs Main Magnet #1 Current 578

375. Peak Power Output vs Gun Anode Voltage for S/N 102 579

376. Peak Power Output vs Magnet #3 Current for S/N 102 580

377. VGE-8006A, S/N X-7 Oscillation Map 583

378. Peak Power Out vs Magnet No. 1 Current 584

379. X-7 Collector Power Density, No Coils, Without rf 586

380. X-7 Collector Power Density, Two Aiding Coils at 0" and 8", 1 A in each Coil Without rf 587

381. X-7 Collector Power Density, Two Aiding Coils at 0" and 8", 1 A in each Coil with rf 588

382. Output Power vs Main Magnet No. 1 Current 590

383. Power Out vs Gun Anode Voltage 591

384. Power Out vs Beam Voltage 592

385. VGE-8006A, S/N X-7 Cavity Power vs Output Power (CW Operation) 594

386. VGE-8006A, S/N X-7 FC-75 Power vs Output Power 595

387. Maximum Window Temperature vs Output Power 597

388. VGE-8006A, X/N X-7 Comparison of CW, Pulsed and 30 s Boost Filament Power 600

389. 30-Second Pulse 602

390. Calculated Output Power for the 56 GHz Cavity for Three Beam Currents at 80 kV 604

391. 56 GHz Cavity Measured Resonances 605

392. Computed VSWR for 56 GHz Double-Disc Window 607

LIST OF ILLUSTRATIONS (Cont'd)

393. Temperature Distribution on Vacuum Side of 60 GHz Double-Disc Window 1.5λ thick, 120 kW CW 608

394. Thermal Stress Distribution for 60 GHz Double-Disc Window 1.5λ thick, 120 kW, CW 609

395. 56 GHz Pulsed Power vs Magnetic Field with Beam Current as a Parameter 610

396. 56 GHz Peak Pulsed Power vs Magnetic Field 611

397. 56 GHz Pulsed Power vs Beam Current 612

398. 56 GHz Optimum Pulsed Power vs Beam Voltage 613

399. 56 GHz Pulsed Power vs Gun Coil Current 615

400. 56 GHz Pulsed Power vs Gun Anode Voltage (Optimized) .. 616

401. 56 GHz Pulsed Power vs Gun Anode Voltage 617

402. 56 GHz Pulsed 8 A Oscillation Map 618

403. 56 GHz Pulsed 3 A Oscillation Map 619

404. 56 GHz CW Power vs Magnet Current 621

405. 56 GHz CW Power vs Gun Anode Voltage 622

406. 56 GHz CW Power vs Beam Voltage 623

407. 56 GHz CW Power vs Beam Voltage 624

408. VGE-8005 Oscillation Map, CW, (3 A) 625

LIST OF TABLES

Table		Page
1.	Typical Superconducting Niobium Titanium Short Sample Characteristics	7
2.	Main Superconducting Solenoid Magnet Specifications	8
3.	Superconducting Solenoid Magnet Dewar Cryogenic Data.	9
4.	Early Cathode Cases Considered	25
5.	Transverse Energy and Velocity Spread for Three Gun Designs	30
6.	Waterload Power Densities	62
7.	Calculated Skin Depth and Measured Load VSWR for Various Liquids	63
8.	Test Results - 6" Water Wall Mode Filter	80
9.	Voltage Gradients	95
10.	Peel Tests	108
11.	Pumping Speed	109
12.	Values of Parameters used in TRAJ Computer Simulations	117
13.	Comparison of TRAJ and NRL Results	122
14.	Parameters for Cooling Calculations	172
15.	Time to Burnout Calculations on TACO	186
16.	Candidate Materials for Improved Collector Fatigue Life	199
17.	Material Hardness Reduction	213
18.	Results of Mechanical Fatigue Test of High Strength Copper Alloys	247
19.	Results of Braze Joint Test as Reported by ORNL	249
20.	OFHC Diode Fatigue Results	278
21.	Three-Inch Diameter Single Disc Window Analysis Conditions	283

LIST OF TABLES (Cont'd)

22. Four-Inch Diameter Single Disc Window Analysis Conditions 288

23. High Performance Data VGA-8000 S/N 11 325

24. Calculated Mode Conversion at Several z Positions in 2.5 Inch Diameter Collector with Linear 2° Taper (Using OPENCAV) 338

25. 60 GHz Gyrotron Mode Content Measurements 340

26. Mode Content of the 5-inch Collector 341

27. Mode Content of the 2-1/2-Inch Collector 342

28. Mode Content of the 4-inch Collector 343

29. 60 GHz Double Disc Window Designs 347

30. Design Trade-offs for 60 GHz CW Window Designs 352

31. Double-Disc Window Calculation Conditions 353

32. Grid Characteristics 368

33. Calculated Value of Transmission of Grid When Viewing a Vertical Line Through the Center of the Window 370

34. Calculated Values of f_H, A_{clear}/A_{holes} and T vs ϕ_H 372

35. Summary of Design Optimization 413

36. Temperature Dependence of Heat Transfer Coefficient . 417

37. Double-Disc Window Design Conditions 418

38. Comparison of Experimental and Analytical Results for a 56 GHz Double-Disc Window 3" Dia x 0.099, AL-995 424

39. Double-Dish Window Design Considerations 437

40. Parameters for Frequency vs Top Coil Current 454

41. Parameters for Power vs Bucking Coil Current 458

42. Operating Parameters 462

LIST OF TABLES (Cont'd)

43. Best Long Pulse Results, VGE-8060 X-1 462

44. TE_{211} Drift Tube Interaction 471

45. X-1 Long Pulse Performance 473

46. 71.5 kW, CW Operating Conditions 498

47. Comparison of X-5 Performance into Water Load and DC-200 rf Load (CW Operation) 519

48. Operating Parameters for X-5 at the Time of the Window Failure 520

49. Operating Parameters for 200 kW CW Operation of VGE-8006, S/N X-6 554

50. Mode Content Measurements on X-7 (Pulsed) 585

51. Operating Conditions for 207 kW CW RF Output Power .. 593

52. 56 GHz Pulsed Data 614

53. 56 GHz CW Operation 620

ABSTRACT

The original objective of this program was to develop a microwave amplifier or oscillator capable of producing 200 kW CW power output at 110 GHz. The use of cyclotron resonance interaction was pursued, and the design phases of this effort are discussed.

Later, however, the program's objective was changed to develop a family of oscillators capable of producing 200 kw of peak output power at 60 GHz and at some higher frequency, possibly 90 or 110 GHz, with pulse durations of 100 ms, 30 s, and CW. The higher frequency objectives were later deleted. To aid in the 60 GHz design, gyrotron behavior studies were performed at 28 GHz to obtain generic design information as quickly as possible.

The first experimental device at 60 GHz produced over 200 kw of peak power at a pulse duration of 20 μs. A body heating problem caused by a drift tube oscillation was identified and a correction designed for a subsequent experimental tube. A collector heating problem above the well-cooled region of the collector was identified. The first tube also suffered from mode interference from undesired cavity and beam tunnel modes.

The second experimental tube incorporated an optimized gun location but also suffered from mode interference.

The third experimental tube included modifications that reduced mode interference. It demonstrated 200 kw of peak output at 100 ms pulse duration. The tube proved to be easier to operate than previous experimental tubes because of the modifications.

The fourth experimental tube, which used an older rf circuit design but in a CW configuration, produced 71.5 kW CW.

The fifth experimental tube incorporated a thinner double-disc output window which improved window bandwidth and reduced window loss. This tube also incorporated modifications to the drift tunnel and cavity coupling,

which had proven successful in the third experimental pulse tube tests. It produced 123 kW of CW output power at 60 GHz before rf load coolant boiling and tube window failure terminated the tests. A new waterload was designed and constructed, and alternative window designs were explored.

At this stage of the development program, the following was also accomplished:

1) In a rebuild of the third experimental pulse tube, a modified cavity was demonstrated to have improved dynamic range.

2) A secondary task of developing a 56 GHz CW tube produced in excess of 100 kW CW at this alternate frequency.

3) A waterload using a larger cone diameter was tested. Results were not satisfactory and indicated a lack of rf beam divergence.

4) An additional task was undertaken to study collector fatigue.

5) Window work stressed the implementation of an FC-75 chilling system and a thermal imaging system for viewing the output window.

Testing of the sixth experimental tube resulted in operation at CW output power in the range of 200 to 206 kW for an hour. This demonstration satisfied one of the program's major milestones and set a new world record for CW power at frequencies above 28 GHz.

Output mode purity of the seventh experimental tube was measured at 95% TE_{02}. The tube was operated for about forty-five minutes with CW power output over 200 kW.

I. INTRODUCTION

The original objective of this program was to develop a microwave amplifier or oscillator capable of producing 200 kW of CW power at 110 GHz. Tunability or bandwidth was not considered an important parameter in the design, but efficiency was important. Mode purity in the output waveguide was not a requirement for the device originally, but the circular electric mode was considered desirable because of its low loss properties.

With these objectives in mind, an approach based on a cyclotron resonance interaction between an electron beam and microwave fields was pursued. The detailed arguments which led to this approach are contained in the final report of a preceding study program.[1] The device configurations of particular interest, called gyrotrons, have been discussed in recent literature.[2-5] They employ a hollow electron beam interacting with cylindrical resonators of the TE_{0m1} class. The experimental gyrotrons described have been of both the amplifier[3] and oscillator[2-5] type. At 28 GHz, an amplifier with 76.0 kw peak output power at 41 dB gain has been reported.[3]

For the amplifier alternative a power gain of 20 dB was chosen as a reasonable goal. Stability of an amplifier is a very important technical consideration. To capitalize fully on the advantages of the cyclotron resonance interaction, diameters large with respect to a wavelength are used. This exposes the device to the effect of microwave coupling between amplifier stages through the beam tunnel. Prevention of this coupling is an important consideration in the design.

The optimum beam for the cyclotron resonance interaction is one in which the electrons have most of their energy in velocities perpendicular to the axial magnetic field. Low axial velocity spread is another requirement. Electrons which have different axial velocities will not interact efficiently.

A magnetron injection gun[6,7] was chosen to generate the beam. A similar gun was used on the 28 GHz gyrotron, also developed for ORNL (Oak

Ridge National Laboratory). With this type of gun, the shaping of the magnetic field in the gun region is quite important.

The early phases of the 200 kW, 110 GHz activity concentrated on the design of a pulsed oscillator including the electron gun, superconducting solenoid magnet, interaction circuit, output coupling schemes, collector, and output window. Most of these elements would be common to both oscillators and amplifiers.

The electron gun design utilized a cathode loading of 4 A/cm^2 and a maximum cold negative electric field gradient of <100 kV/cm.

A TE_{021} oscillator cavity for the pulsed tube was designed and parts were ordered. Cold test hardware for evaluating various output coupling schemes in conjunction with the cold test oscillator cavities was ordered.

A facility was designed to furnish rf drive power for the 110 GHz amplifier. The design was based on a modification of an existing test set to operate a gyrotron oscillator as a drive power source.

In December of 1979 the objective of the program was changed to develop families of microwave oscillators capable of producing 200 kw of peak power output at 60 GHz and some higher frequency, possibly 90 GHz or 110 GHz, with pulse durations of 100 ms, 30 s, and CW.

The 110 GHz gyrotron design work was terminated. Prior to termination, the electron gun computer design was completed and mechanical design started. A drift tube load cavity had been designed. Cold test measurements directed at determining the effective interaction cavity length were completed. A variety of output/collector coupling schemes were considered. A window was designed and ceramics were received. Piece parts for the waterload and frequency sampler and arc detector were received.

A gun with a cathode loading of 3 A/cm^2 was designed for the 60 GHz gyrotron. Modifications to the gun to reduce ion sputtering and improve tube life were studied.

Since we expected to return to a higher frequency later in the program, the ampere-turn locations determined for the 110 GHz gyrotron superconducting solenoid magnet were used to procure the magnet. Identical coil positions with lower currents were used for the 60 GHz gun design. A contract was awarded to Magnetic Corporation of America for the balance of the design and construction of the first magnet. The first superconducting solenoid magnet system was received December 30, 1980. Transverse field measurements demonstrated a need for improved coil alignment. Modifications to the design were made to improve coil alignment, allow more beam steering and reduce the liquid helium boil-off. A specification and acceptance test procedure for the magnet were proposed and a spare magnet system procured.

Techniques for loading the anode drift tube were selected for the first two tubes. Based on test results of the first tube, the drift tube design was modified for the third experimental tube. Further modifications were made on subsequent tubes to lessen the problem of mode competition.

A method of improved cathode pumping was incorporated in the 60 GHz tubes as compared to the 28 GHz design. This involved a change in mechanical design to allow larger vacuum passages leading to the gun region.

Based on tests of the first experimental pulsed tubes, the cavity was modified to improve efficiency and reduce mode competition. The reduced mode competition made the tube less sensitive to power supply variations and increased the available dynamic range. The improved efficiency was achieved by reshaping the cavity. These efforts culminated in the development of the step cavity.

The major effort on collector design concerned four areas: electron trajectories, heat transfer, fatigue life and mode conversion. Computer calculations of magnetic field and electron trajectories were made to adjust the location of the beam landing site. Computer calculations were made of

heat transfer and temperature cycle data, with pulse durations relevant for fusion experiments. Improvements in collector fatigue life through the use of high strength copper alloys, dispersion-strengthened copper or metal matrix composites were studied. Cooling geometries to minimize fatigue effects were also studied.

An edge-cooled, single-disc beryllia window was designed for the 100 ms pulse tube. Several face-cooled, double-disc CW window designs were theoretically evaluated using FC-75^{tm} as a coolant. (FC-75 is a Minnesota Mining and Manufacturing Co. trademark for a fluorocarbon liquid.) Alternate window designs were considered. Window failures and newly available values of dielectric loss, measured at the Massachusetts Institute of Technology under contract with Oak Ridge National Laboratory, indicated a need for improved window designs for both pulsed and CW tubes. Methods for measuring the temperature of the window during operation were studied and found to be feasible. A system using an IR camera for this purpose was implemented. An improved single-disc window design was developed for pulse tubes. The double-disc window design was optimized. A nonlinear analysis of the CW window was performed. An FC-75 chiller was implemented for improved window cooling. A strain gage analysis of the window edge was studied. A new dish window concept was introduced.

Gyrotron behavior studies utilizing 28 GHz test vehicles studied high voltage gun arcing, new cathode materials, rf behavior, and cavity and output taper design.

A variety of waveguide components including waterloads, mode filters, miter bends and flange adapters were designed. These designs were later modified to include Oak Ridge flanges. CW testing indicated that the initial load design could not handle full CW power. Three new loads were developed: a five-inch diameter cone load, a jet load and an electromagnetic radial diverter. The load first used for achieving 200 kW CW was a 2.5 inch diameter ceramic cone load with modified water flow combined with a water wall section of guide used as a pre-attenuator. Work on the electromagnetic radial diverter load continued at low priority and was eventually

terminated. A mode filter for preferentially attenuating noncircular electric modes with respect to circular electric modes was developed.

The flatness and regulation of pulsed voltages available from the test set proved to be inadequate in early testing. Modifications were made to improve the test set performance.

The first experimenal tube yielded promising results in terms of demonstrating the peak output power. A body heating phenomenon was identified as a drift tube oscillation. A collector heating problem beyond the well-cooled portion of the collector was identified.

The second experimental tube incorporated a cathode in an optimized location and a water-cooled anode. Tests on the second tube confirmed the problems with the first tube and provided some useful collector test data.

The third experimental tube incorporated a modified drift tube. 200 kW at 100 ms pulse duration were demonstrated with this tube. Further modifications to the beam tunnel and cavity were made in a rebuild of this tube.

The fourth experimental tube was the first CW version of the 60 GHz gyrotron. This tube produced 71.5 kW of CW rf output power. RF testing was halted by collector melting.

The fifth experimental tube (second CW tube) incorporated the X-3R rf circuit in a CW configuration and a thinner double-disc window. The tube demonstrated 100 kW CW, limited by the waterload. Efficiency hysteresis effects were noted during CW operation. This tube was operated in a new superconducting solenoid magnet. Analysis revealed no collector melting.

The sixth experimental tube (third CW tube) incorporated further design modifications directed toward ease of operation and a wider dynamic range. An improved double-disc window design was incorporated in this tube. A step cavity was incorporated to suppress competing modes and enhance efficiency. The cavity resulted in good mode suppression but no significant change in

efficiency. Testing resulted in operation at CW output power in the range of 200 to 206 kW for one hour. This satisfied one of the program's major milestones and set a new world record in CW power at frequencies above 28 GHz.

Testing of the seventh experimental tube included operation for about forty minutes with CW power output exceeding 200 kW.

A 200 kW CW, 56 GHz gyrotron development task was added to this program. The tube produced 280 kW at 44% efficiency pulsed, and 105 kW CW at 43% efficiency.

II. SUPERCONDUCTING SOLENOID MAGNET

A. DESIGN

A superconducting magnet was designed using a 0.020-inch diameter wire of filamentary niobium-titanium (NbTi) embedded in a copper matrix, with a copper to NbTi ratio of 1.8 to 1. The wire has the typical short sample characteristics shown in Table 1.

Table 1
Typical Superconducting Niobium-Titanium
Short Sample Characteristics

Field	Maximum Current Before Quenching
45 KG	131 Amps
50	119
55	106
60	95
65	85
70	77

The magnet consists of a Helmholtz pair centered at the circuit to give a homogeneous (to $\pm$ 0.5%) field region at 45 KG 2-1/2 inches long. A small bucking coil is included as part of the coil system to give the desired field profile characteristics in the gun region.

The superconducting magnet has the specifications given in Table 2.

Table 2
Main Superconducting Solenoid Magnet Specifications

ID	=	6" (winding)
OD	=	8.25" (winding)
Length	=	3" (per coil of Helmholtz pair)
Central Field	=	45 KG
Peak Field	=	67.6 KG (at winding ID)
Amp Turns	=	315980 x 2
Current	=	81 Amps
Turns	=	3900 x 2
Conductor	=	0.020" Dia Nb-Ti Multifilamentary 1.8:1 Cu Ratio
No. Layers	=	52
Turns/Layer	=	150

The magnet is housed in a superinsulated 4" warm hole dewar.

Both on-axis and off-axis axial and radial components of flux density and vector potential were computed using the Varian magnetostatic program. The magnetostatic program computes the normalized flux array for an iron-free magnet system in a form suitable for use in the Varian gun program.

The diameter of the bucking coil is larger than the main coils to achieve better voltage hold-off characteristics.

The superconducting solenoid magnet design consists of a split pair of coils, for the main magnetic field, and a bucking coil in the gun region, for shaping the magnetic field near the magnetron injection gun. Two pairs of transverse trim coils are available for beam steering. The main coils and bucking coil are wound on the same bobbin to ensure concentricity. The transverse coils are outside the main coils. The entire coil assembly operates in a liquid helium bath. The liquid helium vessel is surrounded by consecutive layers of vacuum, a liquid nitrogen temperature heat shield, vacuum, and the room temperature shell.

The room temperature shell has a flange which mounts on an existing flange in the test set oil tank. The superconducting solenoid magnet has a vertical bore. A socket is attached to the bottom of the dewar to accept the tube gun. Leads and service ports exit the room temperature shell at a

45° angle on the outside diameter of dewar. This arrangement leaves the top surface of the dewar available for any room temperature collector coils and supports which may become necessary.

After topping the liquid helium and liquid nitrogen levels, the initial thermal design allowed for one day's operation. After being shut off for as long as a weekend, the liquid reservoirs merely had to be filled, since they had not warmed to a temperature which required cooling.

The outline drawing of the coil and dewar assembly is shown in Figure 1.

The superconducting solenoid magnet was ordered from Magnetic Corporation of America.

The pertinent cryogenic data for the superconducting solenoid magnet dewar are given in Table 3.

Table 3
Superconducting Solenoid Magnet
Dewar Cryogenic Data

	Guaranteed	Calculated
Liquid Nitrogen Boiloff/Liters per hour	0.17	0.13
Liquid Nitrogen Hold Time/Hours	120	160
Liquid Nitrogen/Total Volume in Liters	21	21
Liquid Helium Boiloff/Liters per hour, Coil on*	0.70	0.56
Liquid Helium Boiloff/Liters per hour, Coil on**	0.42	0.33
Liquid Helium Hold Time/Coil on*	32	41
Liquid Helium Hold Time/Coil off**	135	172
Liquid Helium Volume/Above the Coil/Liters	23	23
Total Helium Volume/Liters	57	57

* Calculated with liquid helium above the coil only.

** Calculated with entire liquid helium volume.

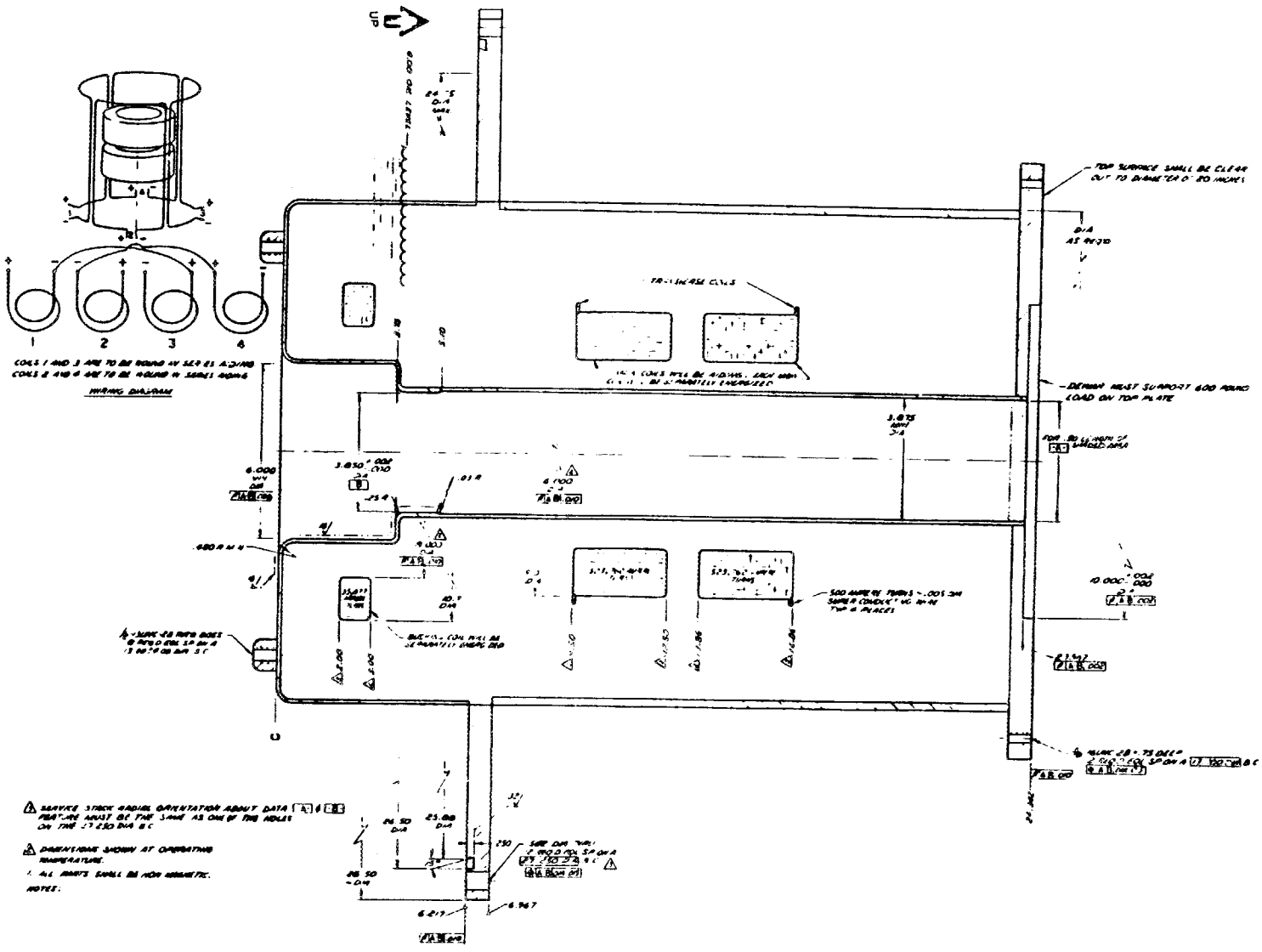

Figure 1. Outline VYW-8060 Coil and Dewar Assembly

Difficulty was encountered in winding the coils. In addition, an accident in magnet operation at Magnetic Corporation of America resulted in a partial short in one of the main coils, requiring coil repair and rewinding. Testing of the superconducting solenoid magnet system was completed at Magnetic Corporation of America in December 1980. The system was received at Varian on December 30.

The superconducting solenoid magnet exhibited some dimensional problems. The short cylindrical section of the bore, which mates with the O-ring at the bottom of the tube body and provides alignment, was undersized, tapered and out of round. This condition likely occurred during welding of the plate and shell dewar assembly. A procedural machine operation was apparently omitted.

This mechanical problem, which prevented inserting the gyrotron completely through the bore of the dewar, was solved at Varian by setting up the entire dewar in a mill and boring out the inside surface to the correct diameter.

After evacuating the vacuum chamber of the dewar, the boil-off of liquid helium and liquid nitrogen was approximately as expected.

An axial magnetic field measurement was made at Varian that agreed with the field measurement at the vendor and with calculations.

The only remarkable electrical problems involved the time required to change the magnetic field. The coils were designed to operate a 110 GHz gyrotron. Consequently, they have more inductance than absolutely necessary to operate a 60 GHz gyrotron. This problem was alleviated by introducing a suitable resistance in series with the power supplies and main coils.

During initial tube operation, it was necessary to trim the mechanical axis of the gyrotron, with respect to the mechanical axis of the dewar, to improve beam transmission.

This discrepancy in the dewar between the mechanical and magnetic axes in the magnetic system is associated with the minimal mechanical support consistent with high performance boil-off characteristics.

B. TRANSVERSE FIELD MEASUREMENTS

Measurements of the transverse fields of the superconducting magnet were conducted to determine the cause of the beam interception problem experienced with tube X-1. A transverse hall effect probe was used in a fixture designed to provide axial movement of the probe along the bore. To minimize errors caused by a misalignment of the probe holder axis and the bore axis, this fixture allows rotation of the probe within a well-aligned cylinder.

The actual tilting of X-1 was 0.0644" at an angle of 3.6°. Tube X-3 was installed and a tilt of 0.099" at an angle of 37.2° was necessary to minimize beam interception. The measured transverse field was strong enough to cause the observed beam deflection, and the direction of this deflection corresponded with the direction in which the tubes were tilted. To correct this problem, the specification for the superconducting magnet was changed to call out more specific transverse field measurements and to include transverse field correction coils ten times as strong as the original ones.

A quadrature method of data analysis was used for measuring transverse field. This involves taking measurements at four angular positions spaced ninety degrees apart. These data are then combined to derive a transverse field vector magnitude and angle. The technique gives an accurate indication of the angle of the transverse field, to aid in tube alignment.

Measurements were made with the dewar at 0°, 90° and 180° with respect to the environment, to determine if the transverse fields were caused by the magnetic environment in which the dewar is situated.

A comparison of measurements is given in Figure 2. The measurements indicate good reproducibility of results. Plots of B_x and B_y with the dewar in the 0°, 90° and 180° positions are given in Figures 3, 4, and 5,

Dwg 82-2182 FED

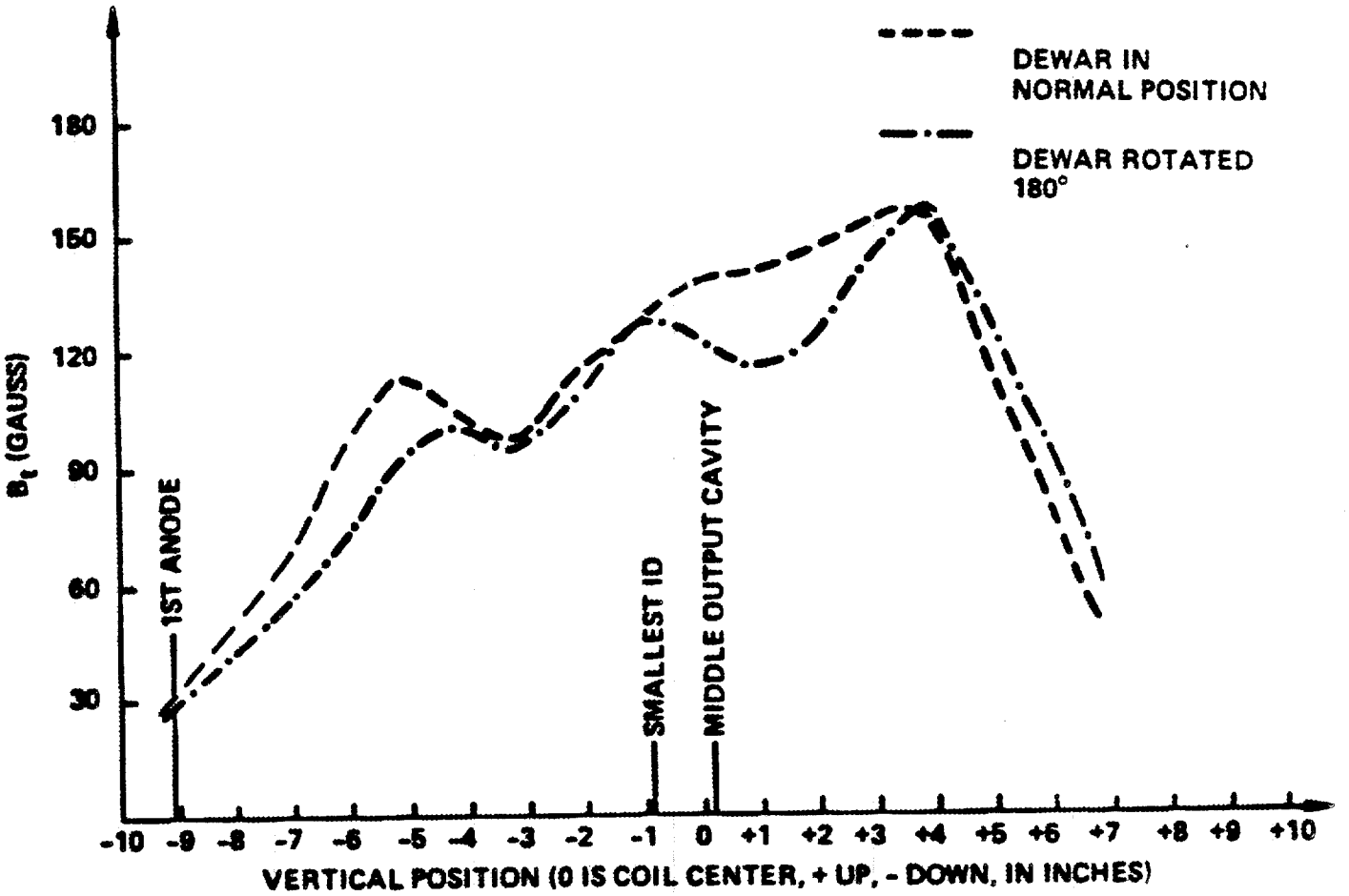

Figure 2. B_t vs Z for 60 GHz Magnet

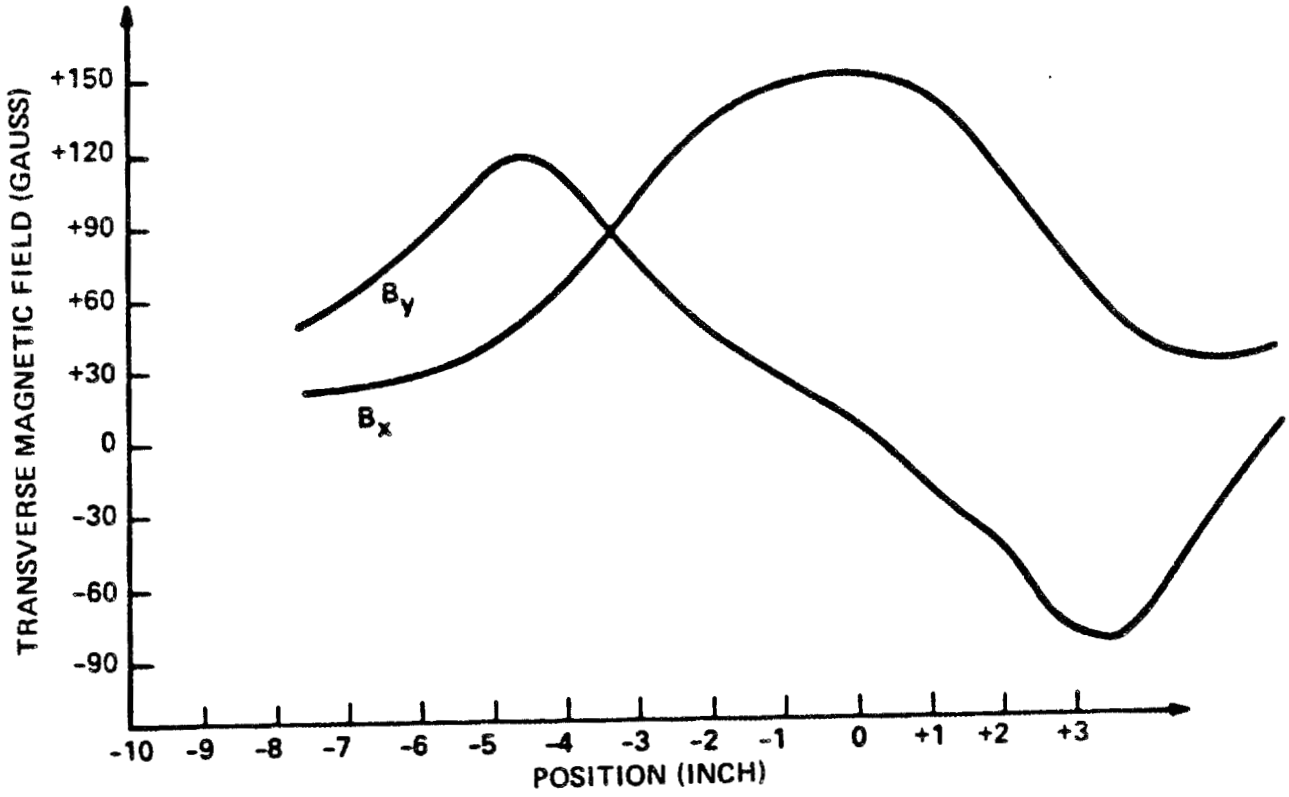

Figure 3. B_x and B_y with Dewar in Normal Position

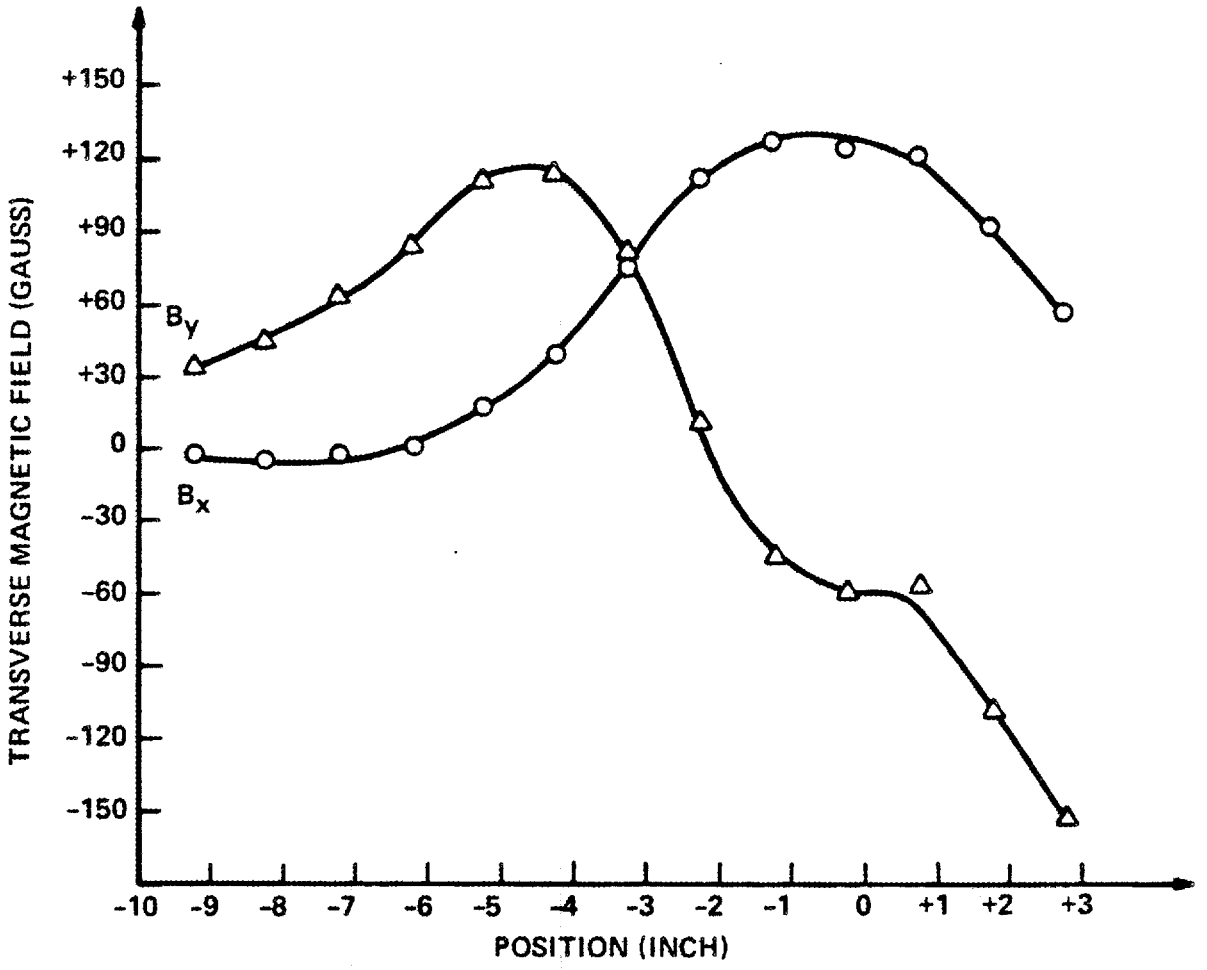

Figure 4. B_x and B_y with Dewar Rotated 90°

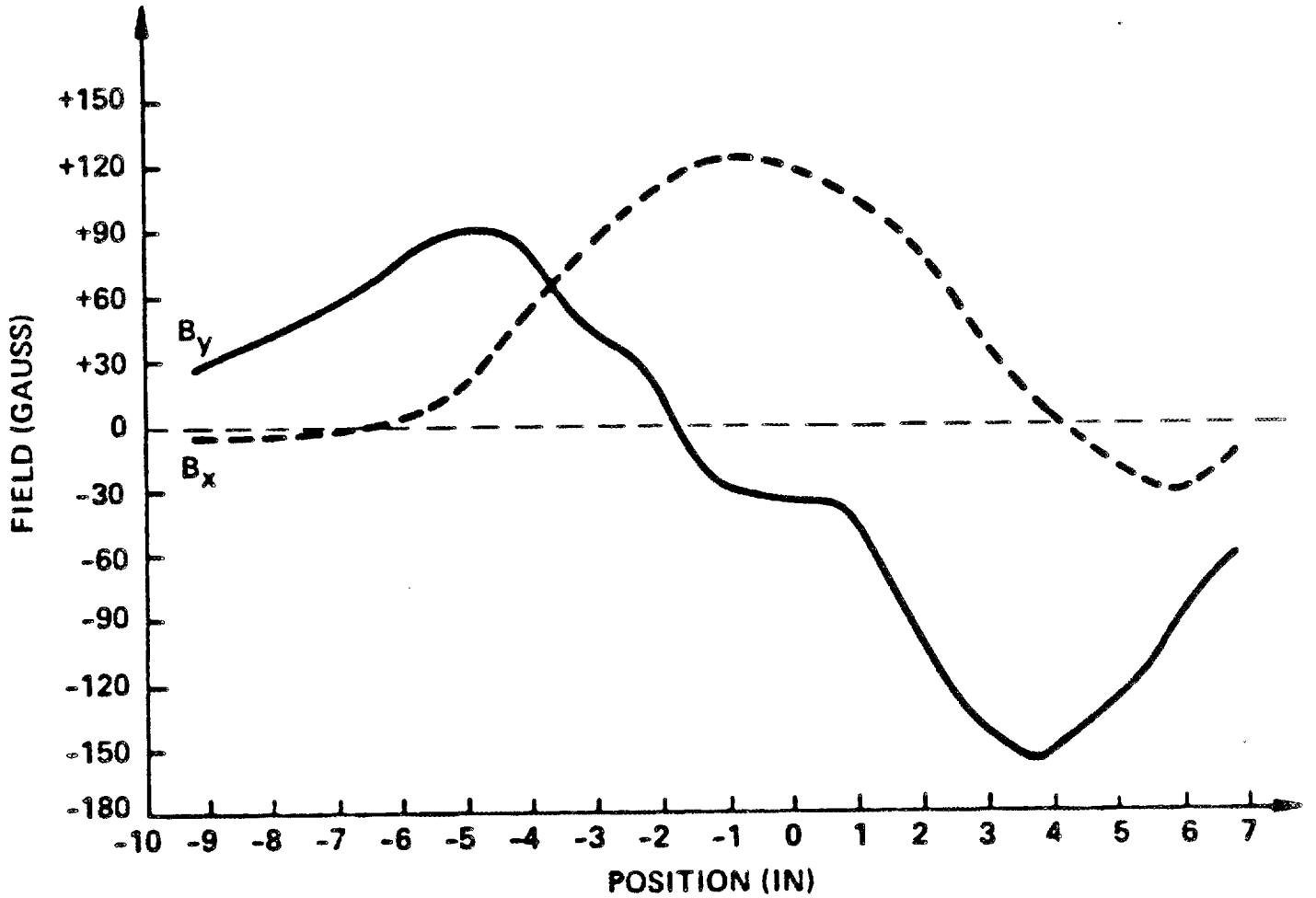

Figure 5. B_x and B_y with Dewar Rotated 180°

respectively. The fact that the direction of the transverse field was relatively independent of the dewar orientation indicated that the major transverse fields were not caused by any asymmetries in the magnetic environment. These tests demonstrated that the tube tilting necessary to obtain beam transmission was mainly due to transverse fields within the solenoids. This transverse field was, in all likelihood, due to a misalignment of the coils within the dewar, or to variations in the windings themselves.

Varian and MCA minimized transverse magnetic fields in subsequent magnets by revising the specification and acceptance test procedure and by patient attention to construction details.

C. SPARE SYSTEM

Because of the lead time required for any potential repair of the superconducting solenoid magnet system, it was deemed prudent to provide for a spare. The spare magnet system was ordered from Magnetic Corporation of America.

Based on the experience of testing X-1 in the first superconducting solenoid magnet system, several changes were suggested. In addition to several minor convenience items, the two major changes were an order of magnitude increase in the capability of the transverse steering coils, and the specification of power supplies with higher dynamic impedance for the main coils. The higher dynamic impedance decreased settling time when changing coil currents.

A new field measuring fixture was developed. Great care was taken to ensure alignment of the probe element with the mechanical axis of the dewar. Provisions were made to provide a continuous recording of magnetic field strength as a function of position.

This field measuring fixture was tested on the spare magnet — which was the first unit of the second-generation magnet system. The second-generation

system differs from the first-generation system in the following ways:

- The dewar was changed to assure proper alignment of the magnetic and mechanical axes, and to reduce the helium boil-off rate.

- The manufacturing procedure was changed to maintain the alignment of magnetic and mechanical axes.

- Interlocks were added to the electronic control system for over-current and to provide a current set point readout.

- The power supplies for the main coils were changed to provide a higher dynamic output resistance, which resulted in a reduced settling time.

- The trim coils were increased from 500 amp-turns to 5000 amp-turns, which eliminated the necessity of physically tilting the tube.

- Polarity switches were added to the trim coils.

- The wire connections to the superconducting coils were changed to further reduce the boil-off rate.

The first system with this configuration was received and tested. An Acceptance Test Plan (ATP) was developed to automatically judge the suitability of a magnet system for gyrotron applications. This was used on the first second-generation unit and the magnet was found to be acceptable. The transverse field was a factor of 3 lower than on the prototype unit, as shown in Figure 6. The new probe fixture gave reproducible results. The alignment of the probe fixture was checked by making a series of field measurements with the fixture rotated to various positions. The offset computed from these data was 0.002". By averaging the data from the various radial positions, the effect of this offset can be eliminated from the measurements. The boil-off rate was reduced from 1.2 ℓ/hr on the prototype

Dwg. No. 82-2206 FED

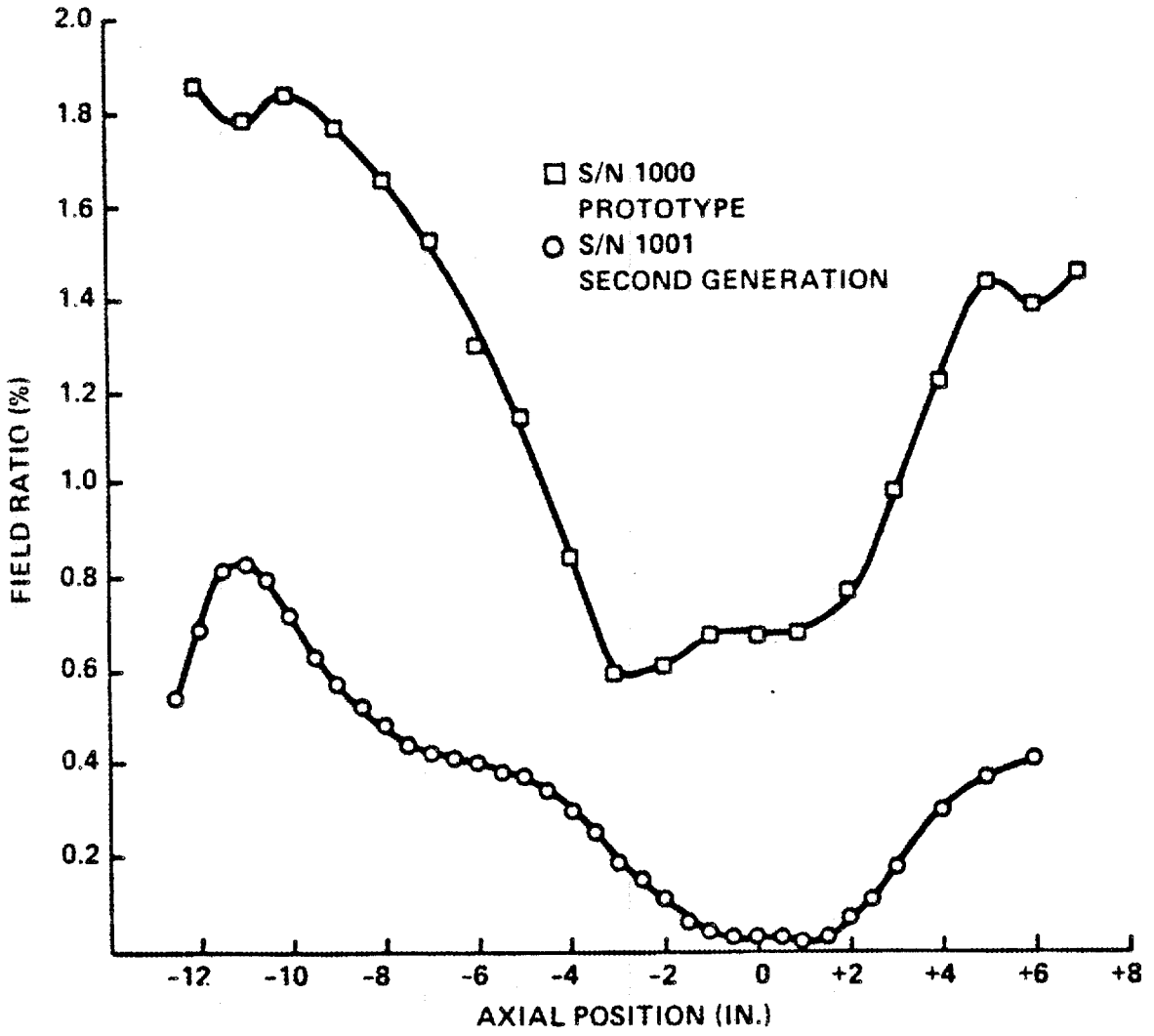

Figure 6. Transverse to Axial Magnetic Field Ratio with Respect to Split Coil Center

unit to 0.6 ℓ/hr on the second-generation unit. The new electronics and power supplies functioned adequately and produced the expected results.

In summmary, there were several accomplishments with respect to superconducting solenoid magnet systems. A technique for measuring transverse fields in solenoid magnets which gave accurate and reproducible results was implemented and tested. The vendor improved the design significantly in response to the feedback from the operation of the prototype unit. The first unit with these design changes was tested and met the criteria for acceptable performance. An ATP and specification were written that enabled the vendor and user to independently determine the acceptability of a gyrotron magnet system.

The question of supplying a reliable magnet system to users for gyrotron operation was then addressed. Several units of the second-generation design were tested and accepted. They confirmed the reduced boil-off rate of approximately 0.5 ℓ/hr seen on the first unit of this design. The significant improvement in transverse field noted previously was substantiated by the test results of three new units. A graph of the ratio of transverse field to axial field (B_t/B_z) as a function of position is given in Figure 7 for the four second-generation units and the prototype unit. It shows consistent improvement has been made.

One of the new magnet systems was installed at the Varian test facility. Gyrotron tests were conducted to determine the effect of the improved design. The installation and initial operation of the system indicated no adverse effects due to shipping. With the tube mechanically centered in the magnet system, tests were conducted with the trim coils to determine beam centering and interception points. The trim coils were found to be unnecessary for full beam transmission. With the beam precisely centered, each trim coil current was increased until the onset of beam interception. Using that current value and the experimentally determined trim coil field profiles, the net flux line deflection required to cause beam interception was computed. This turned out to be 10.7 mils, which was in good agreement with half the difference between the expected beam diameter and the diameter of the tunnel at this point. The maximum

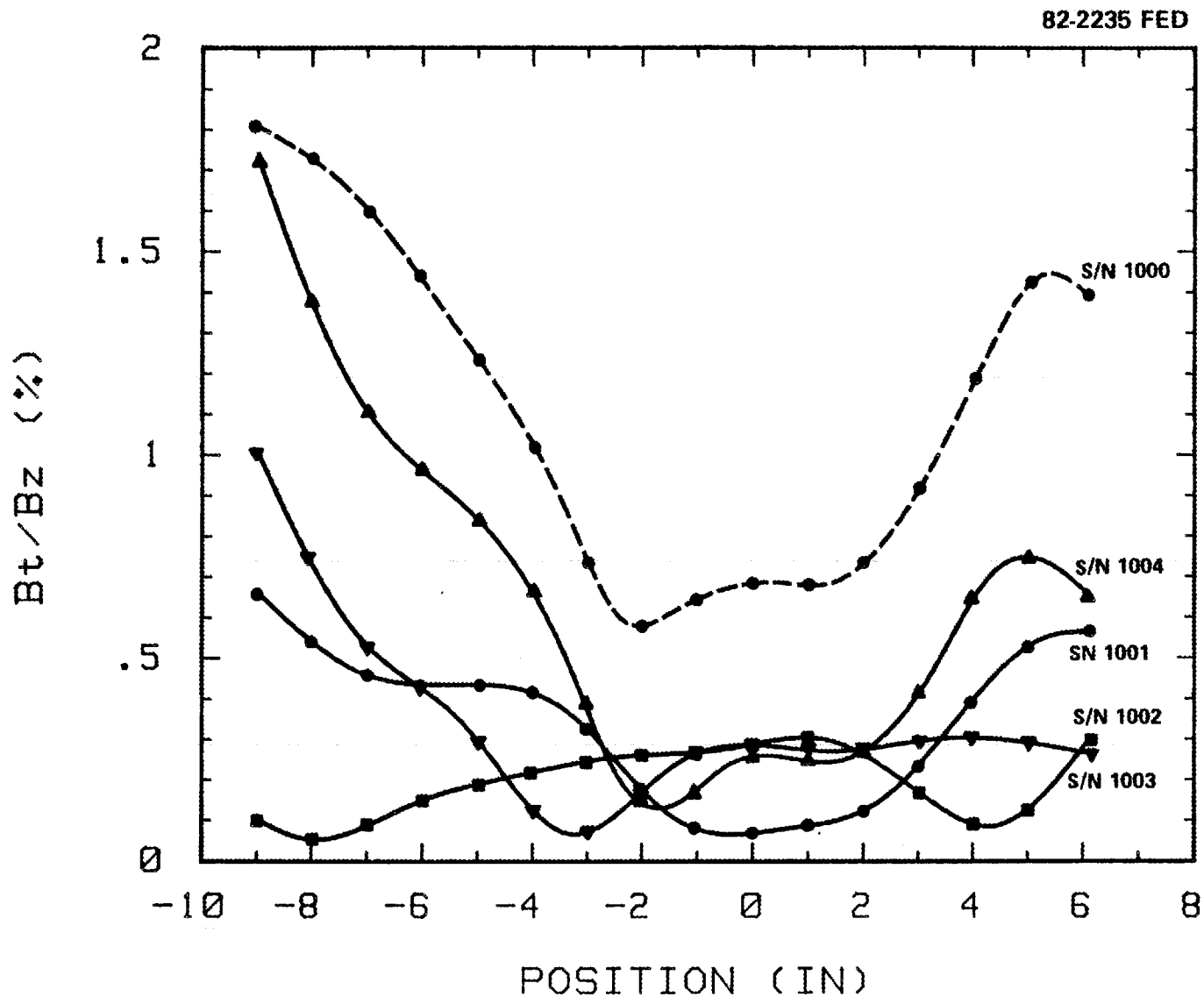

Figure 7. B_t/B_z vs Position for VYW-8060

allowable B_t/B_z ratio determined by this experiment was 0.2% to 0.25%. This assumed the worst case, with the transverse field always pointing in the same direction, which is usually not the case. Further experiments with different tubes and magnet systems verified these figures.

With this in mind, the magnet vendor conducted experiments to demonstrate the feasibility of reducing the transverse fields by mechanical adjustments of the magnet bore. The tests indicated that obtaining a B_t/B_z ratio of about 0.10% does not appear to be difficult using this method of magnet construction. Repetition of this test also validated the results.

These test results showed that a reduced B_t/B_z specification was feasible and attainable. The updated specification for the third-generation units stated that the B_t/B_z ratio would not exceed 0.2%, from the middle of the bucking coil to three inches above the top coil. With this magnitude of transverse field, there will be no magnet-induced problems with beam transmission. Other changes to the specification included a liquid helium boil-off rate of less than 0.75 ℓ/hr and other miscellaneous clarifications. With this specification, it is possible for any gyrotron user to independently obtain a magnet system suitable for Varian gyrotrons. To accompany this specification, a final revision of the Acceptance Test Plan was completed to allow the user to automatically determine the acceptability of a magnet system for gyrotron usage. The first prototype magnet system was rebuilt to the latest specification ($B_t/B_z < 0.2\%$).

An automatic magnet probe was constructed, including a stepping motor-driven probe positioning fixture. The analog output of the gaussmeter is digitized and stored in a desk-top computer. The computer also handles the data analysis and provides plots of transverse and axial fields.

III. 110 GHz 200 kW CW OSCILLATOR

A. ELECTRON GUN COMPUTER DESIGN

The design of the gyrotron gun took into account previous gyrotron gun designs and analyses at Varian and elsewhere. For a cathode sloped 10° with respect to the axis, the effects of varying mean cathode radius and length were estimated to achieve given values of cathode loading (i.e., current density). The constants in the simple planar gun equations were adjusted to fit the results from a representative computer solution for a gyrotron gun. The simple equations used were:

$$h = 2.86 \frac{E_{\perp k}}{\eta B_K^2} \tag{1}$$

$$E_k = \frac{B_K^{3/2} B_o^{-1/2} \nu_{\perp_o}}{1.265} \tag{2}$$

$$d = 1.25h \tag{3}$$

and

$$V_{al} = E_{\perp k} \, d/\cos\theta_k \tag{4}$$

where
- θ_k = slope angle of cathode
- d = spacing along normal from cathode to first anode
- h = maximum spacing of outer beam envelope from cathode
- B_k = magnetic field at cathode = $0.98\sqrt{\frac{r_o}{r_k}}\, B_o$
- B_o = magnetic field in interaction circuit, 45 kGs
- r_o = mean beam radius in interaction circuit, 0.798 mm
- r_k = mean radius of cathode
- $E_{\perp k}$ = electric field component at cathode that is normal to magnetic field

v_{1o} = desired transverse velocity in interaction circuit, 1.35 x 10^8 m/s or 0.449 c (for 64 KeV transverse energy and 80 KeV total energy)

V_{a1} = voltage rise from cathode to first anode

η = charge/mass ratio for electron

Further study verified that for a given cathode length to mean radius ratio, the space charge limited current varies approximately as the inverse third power of the mean radius.

The maximum cathode loading considered was 7.5 A/cm^2 and the minimum was 3.0 A/cm^2. It was assumed desirable to operate as low as possible in this range for stable, reasonably uniform emission, and for the maximum duration of useful cathode life.

It was further assumed that the space charge limited current should be at least three times the operating current, or 24 amperes, to avoid deleterious and severe space charge effects. In particular, this assumption limited the maximum permissible cathode radius.

It was also assumed that the ratio of length to mean radius for the cathode should not be greater than 1.75, to avoid deleterious variations in the beam. This, and the limit assumed for cathode loading, resulted in a lower limit for cathode radius. Another disadvantage of using a small cathode radius is that it requires high electric field gradients in the gun.

This study resulted in four initial cases worthy of further consideration. These are tabulated in Table 4.

Table 4
Early Cathode Cases Considered

Cathode Loading A/cm^2	Mean Cathode Radius Inches	Cathode Length/Radius	Space Charge Limited Current Amps	E_k kV/cm
3.0	0.192	1.76	25.0	21
7.5	0.150	1.15	42.0	44
5.0	0.150	1.73	49.5	44
7.5	0.125	1.66	87.5	76

The high electric field gradient expected necessary for the fourth case led to its elimination. As a reasonable trade off between minimizing cathode loading and maximizing space charge limited current, the third case above was chosen as the initial case for optimization on the computer. The magnetic field shape considered initially had a point of inflection in the flux lines at the plane tangent to the tip of the front focus electrode, and a slope of 6° at that plane for the flux tube threading the center-plane of the cathode at a radius 1% greater than the mean cathode radius. At the cathode end furthest from the circuit, the slope of the flux line was assumed to be zero. Experience has indicated this approximates an optimum field shape for a "short" cathode. For the "long" cathode studied initially, this did not appear to be true. In addition, it was found that this magnetic field shape could not be achieved with the relatively large diameter field coils required for this device.

An "inside-out" gun approach was also considered, for which the first anode would be inside a hollow, conical cathode. However, this approach had no advantage over the conventional gyrotron gun approach which used a cathode of the same mean radius, and, if anything, the "inside-out" gun was more difficult to design.

A number of electrode and magnetic field configurations were simulated by the computer for the 10° cathode case. One of the better cases is shown in Figure 8. The accompanying graph, Figure 9, shows the transverse energy

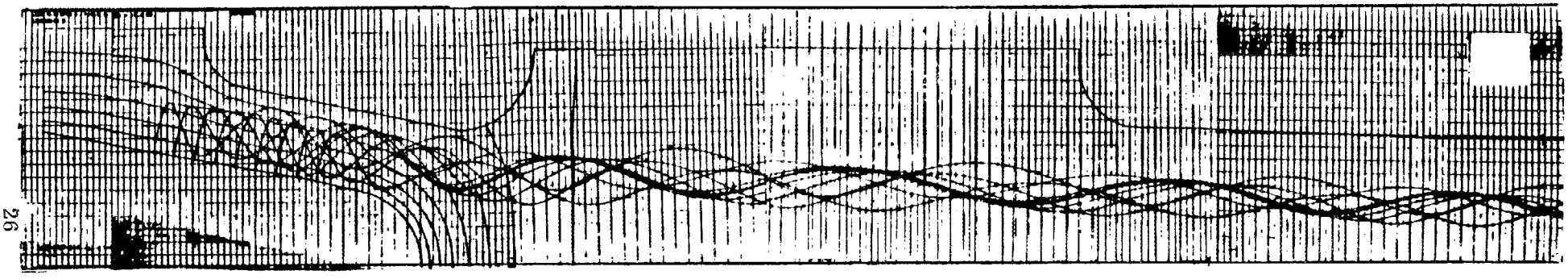

Figure 8. Electron Trajectories for a 10° Cathode Angle

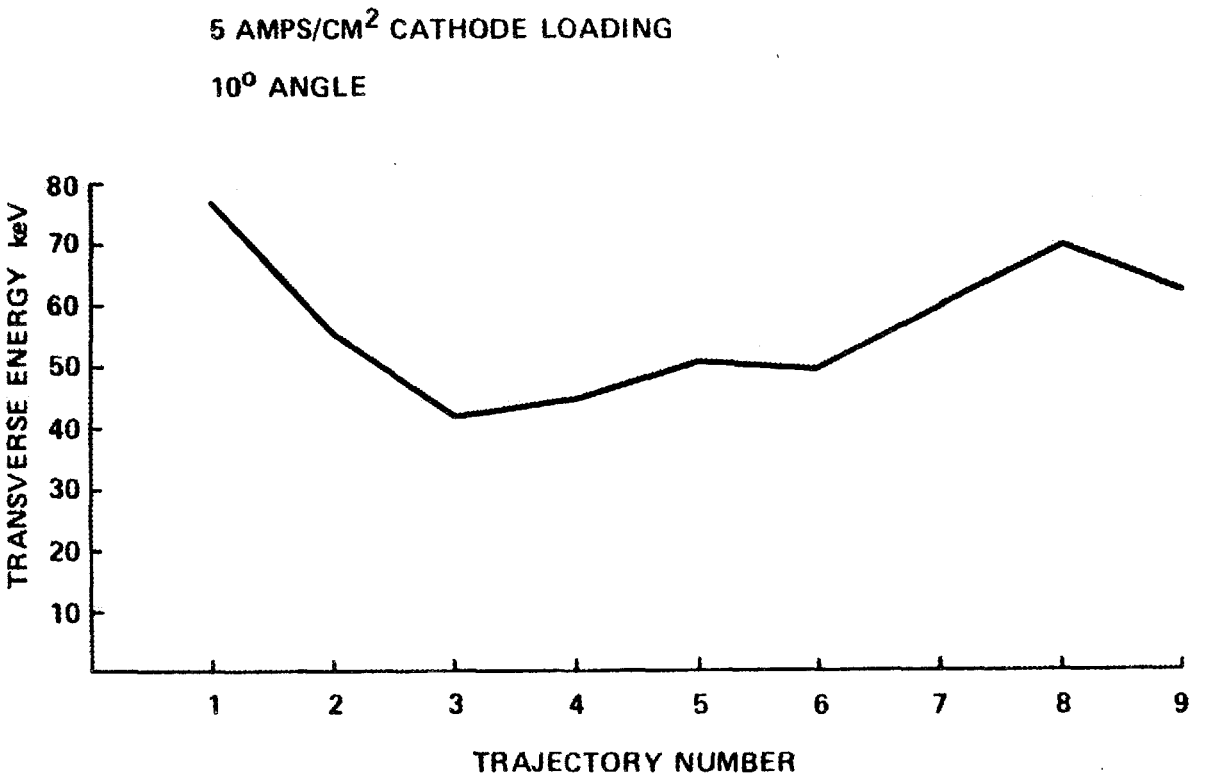

Figure 9. Transverse Energy Profile for 10° Cathode with 5A/cm² Loading

as a function of trajectory number. The numbering starts at the rear of the cathode. The cathode loading for this case was 5.0 A/cm^2. Some trials were made for 7.5 A/cm^2 loading, before it was decided that such a high loading was untenable.

The velocity variation is calculated by scaling the transverse energies of each trajectory up to 45 kG from its value in the uniform field region at the right end of the trajectory plot. The inner trajectories are weighted by a factor of two by finding the statistics of a sample consisting of each inner trajectory counted twice and each outer counted once. The formulas used are:

$$\mu = \frac{1}{N} \sum_{n=1}^{N} E_n \tag{5}$$

$$\sigma = \sqrt{\frac{1}{N-1} \sum_{n=1}^{N} (E_n - \mu)^2} \tag{6}$$

$N = 2\ (N_T - 1)$ where N_T = number of trajectories,
E_n = transverse energy associated with observation n.

The velocity variation is $\pm$ 1/2 σ, or more accurately, $(\sqrt{1 + \sigma} - 1)$, $(\sqrt{1 - \sigma} - 1)$.

Although the velocity variation for the 5 A/cm^2 case is on the order of $\pm$5%, the trajectories are out of phase. Therefore, based on the results described in an article by the Russians[8], simulations were made using a cathode angle of 23°. The Russian results were achieved by assuming a desired flow, and from this, by analytic continuation, determining the necessary electrode boundary parameters. The magnetic field was assumed to be uniform.

Figures 10, 11 and 12 show the trajectories for a 23° cathode with different lengths of front focus electrodes. The shorter the electrode, the

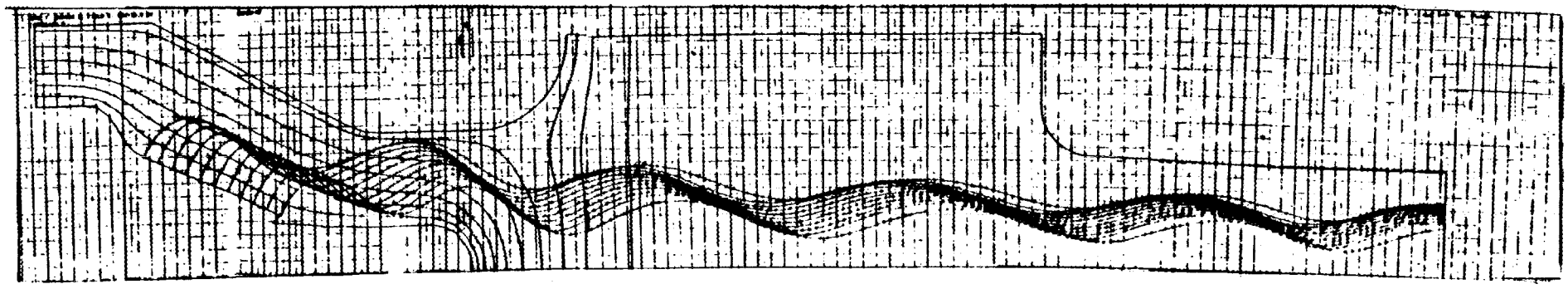

Figure 10. Electron Trajectories for a 23° Cathode Angle with a Short Front Focus Electrode

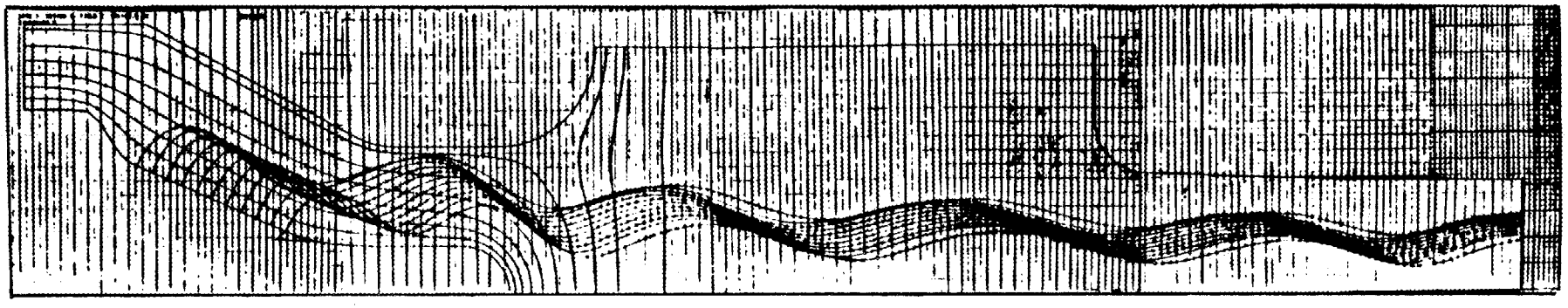

Figure 11. Electron Trajectories for a 23° Cathode Angle with a Medium Front Focus Electrode

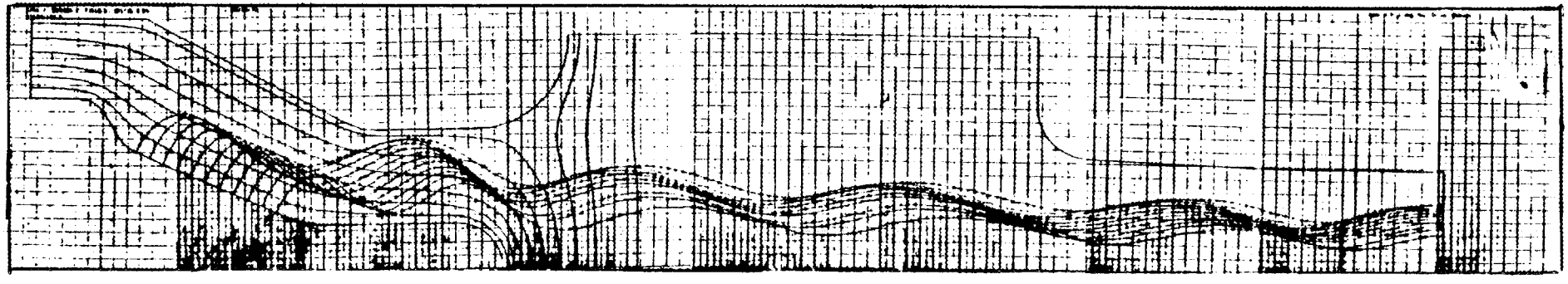

Figure 12. Electron Trajectories for a 23° Cathode Angle with a Long Focus Electrode

higher the transverse energy and the steeper the slope of transverse energy versus trajectory number, as can be seen in the plots in Figure 13.

The mean transverse energy and velocity variation at the magnetic field strength in the interaction circuit for these three cases, with 4 A/cm^2 cathode loading, is given in Table 5.

Table 5
Transverse Energy and Velocity
Spread for Three Gun Designs

Front Focus Electrode	Mean Transverse Energy, eV	Velocity Variation
Short	74349	$\pm$6.80%
Medium	61720	5.40%
Long	47806	3.25%

The trajectories for the best design with 5 A/cm^2 loading are shown in Figure 14. The variation of transverse energy among trajectories is shown in Figure 15.

The mean transverse energy for this case is 64904 eV. The velocity variation is $\pm$ 2.1%.

The optimum cathode angle was determined, but 3 A/cm^2 cathode loading could only be achieved at a 0.168" mean cathode radius by using a compound curvature of the cathode surface, rather than a conical surface. For ease of construction, a loading of 4 A/cm^2 was selected for the 110 GHz gun design.

Various designs using a 25° cathode angle instead of 23° were tried on the computer with good results. The transverse energy profile for the best 25° design is shown in Figure 16. The transverse velocity variation at the interaction circuit for this case is $\pm$2.45%. Nine trajectories were used in the computer simulation. Figure 17 is the plot of these trajectories as computed by the XGUN program. Computer runs were made using this design to determine the sensitivity of the transverse energy profile to various parameters.

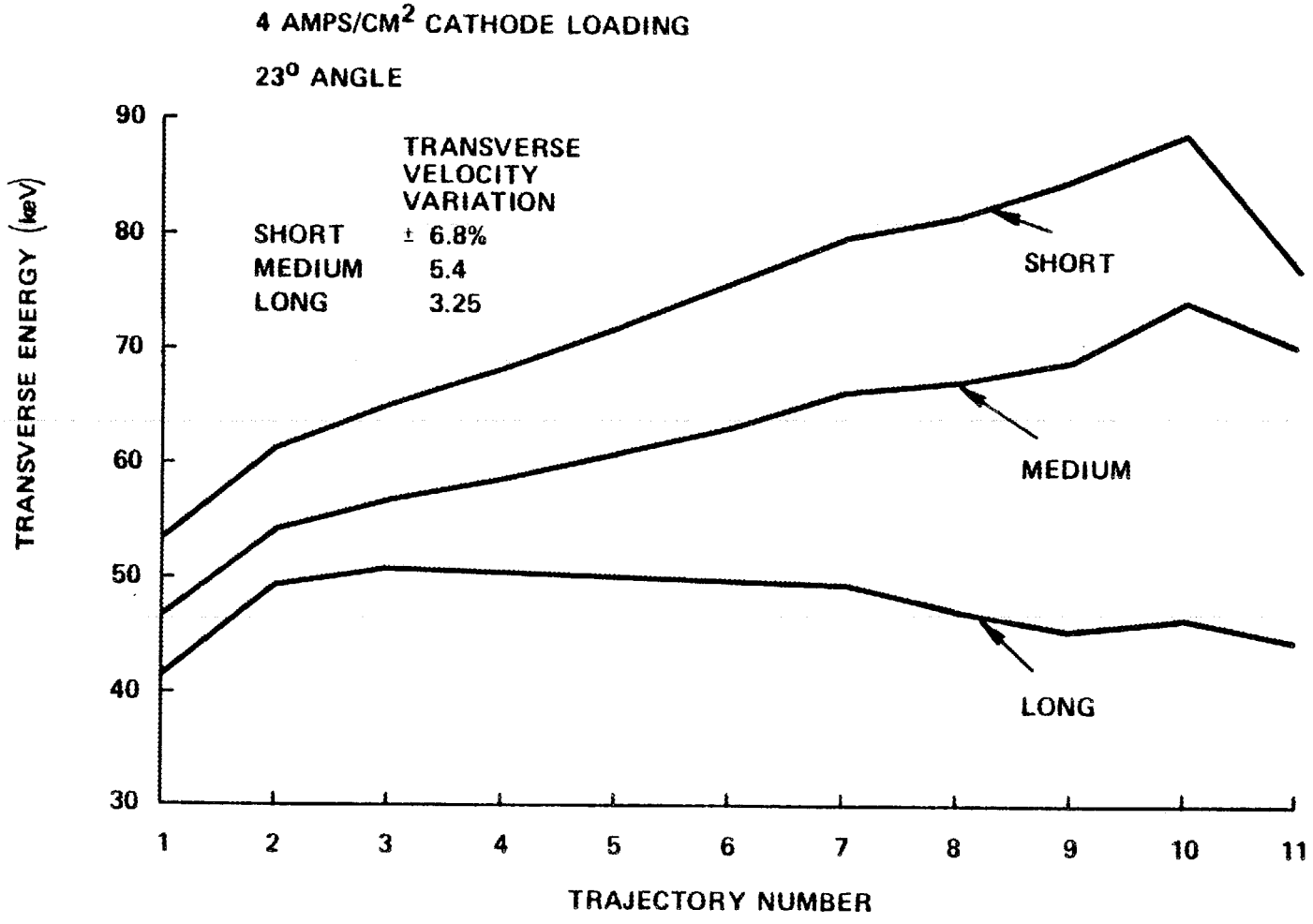

Figure 13. Variation of Transverse Energy Profile with Length of Front Focus Electrode

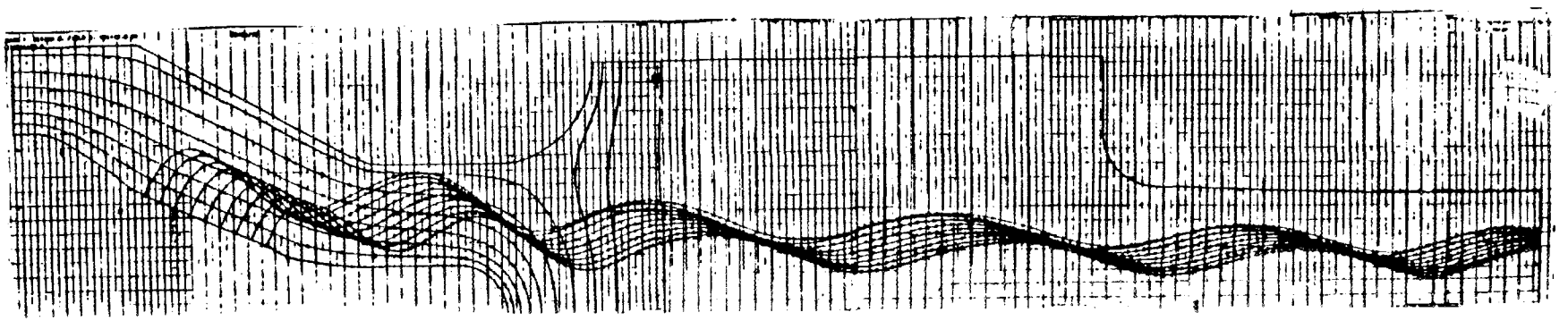

Figure 14. Electron Trajectories for a 5A/cm^2 Cathode Loading Design

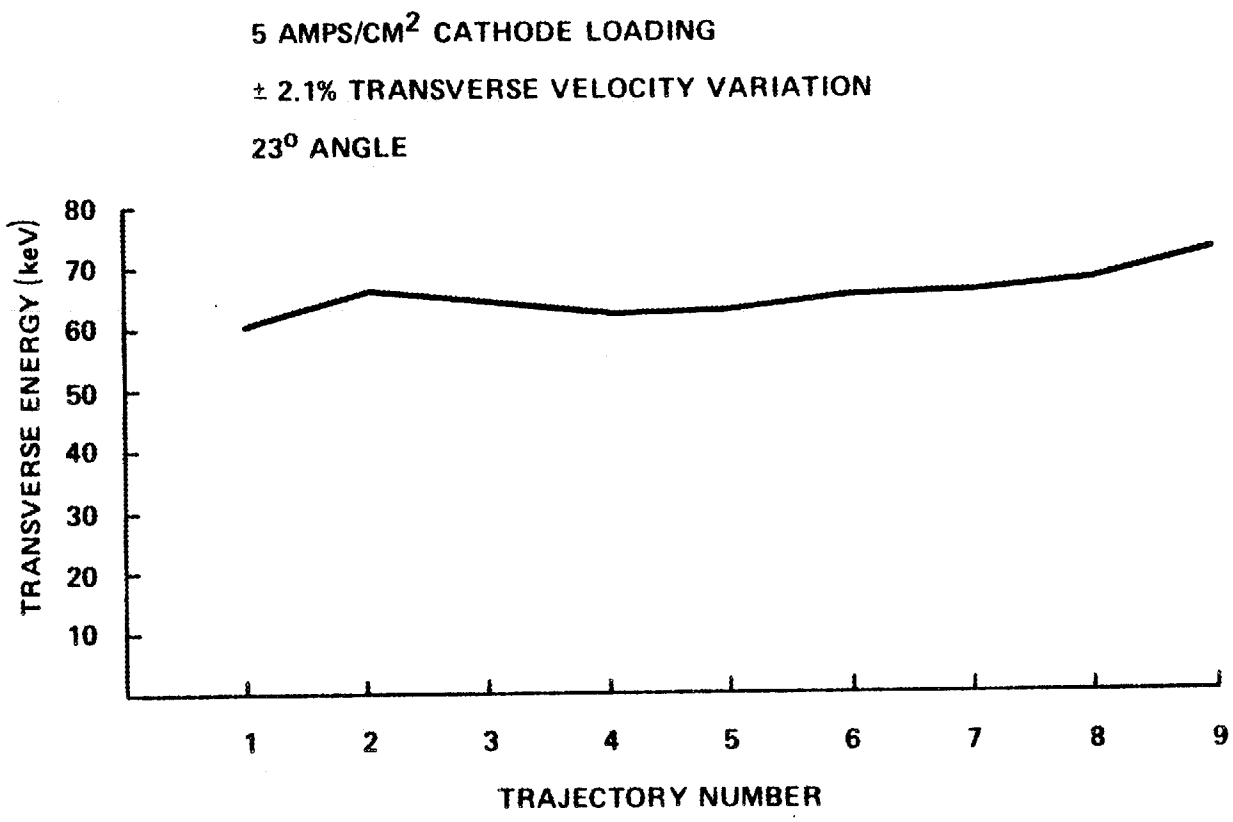

Figure 15. Transverse Energy Profile for 23° Cathode with 5A/cm² Loading

WEIGHTED MEAN TRANSVERSE ENERGY μ = 65820 keV

WEIGHTED STANDARD DEVIATION IN TRANSVERSE ENERGY σ = 3879 keV (5.9%)

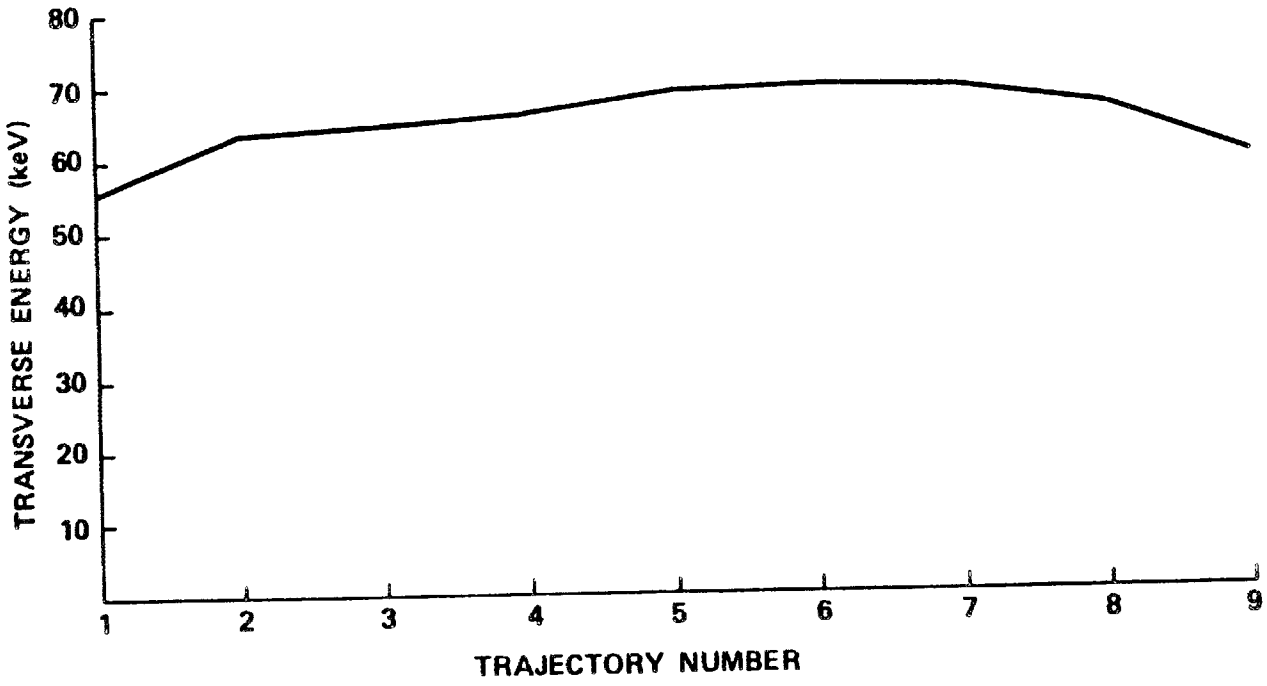

Figure 16. Transverse Energy Profile for the Best 25° Cathode Design

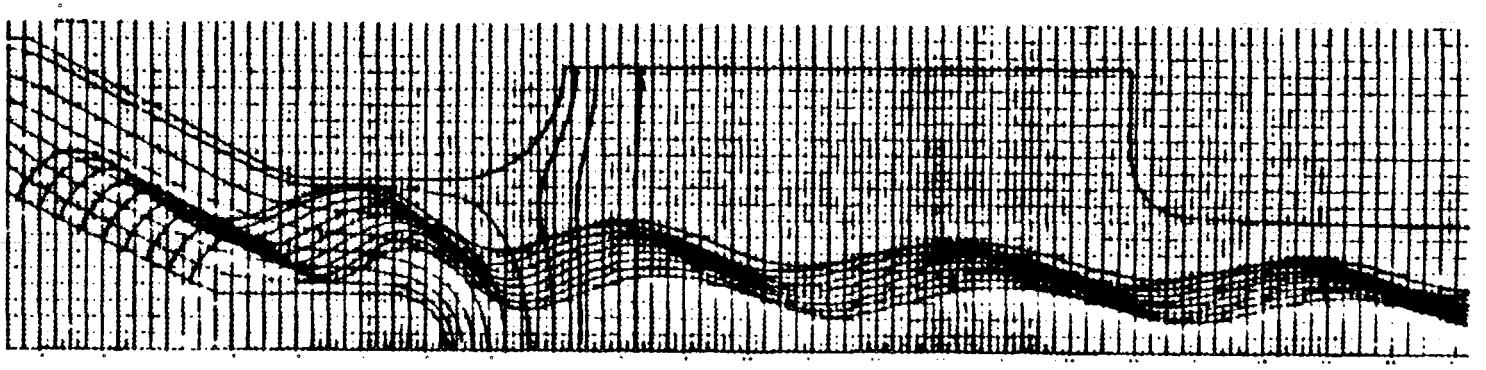

Figure 17. 110 GHz Gun Trajectory Plot

The first anode voltage for this design is 15,800 volts. Two additional computer runs were made — one at 15,500 volts and one at 16,100 volts. The resulting transverse energy profiles are shown in Figure 18.

To determine the effect of changing the angle of the first anode, five computer runs were made with the following angles:

1. 25.590°
2. 26.362°
3. 27.604°
4. 28.724°
5. 29.930°

The results of the runs are plotted in Figure 19. In this case, eight trajectories were used and the graph shows the transverse energy at the interaction circuit for each trajectory and each first anode angle.

Since the current in the bucking coil at the cathode would be trimmed, we wanted to determine the sensitivity of the gun performance to nominal changes in this current. Two additional runs were made by recomputing the input magnetic field profiles for changes in the bucking coil current of -10% and -20%. The effects of these changes on the transverse energy profile are seen in Figure 20. Raising the current in the bucking coil is tantamount to lowering the field at the cathode. This has the same effect as lowering the voltage at the first anode.

From these same computer runs, it was possible to determine the beam radii at the interaction circuit for each of the three cases, assuming adiabatic compression. A graph of these results can be seen in Figure 21.

Figure 22 shows the results of small perturbations in the distance from the center of the cathode to the tip of the first anode.

The nominal beam current is 8 amperes. Since there may be occasions when different beam currents may be used, the effect of changing the beam

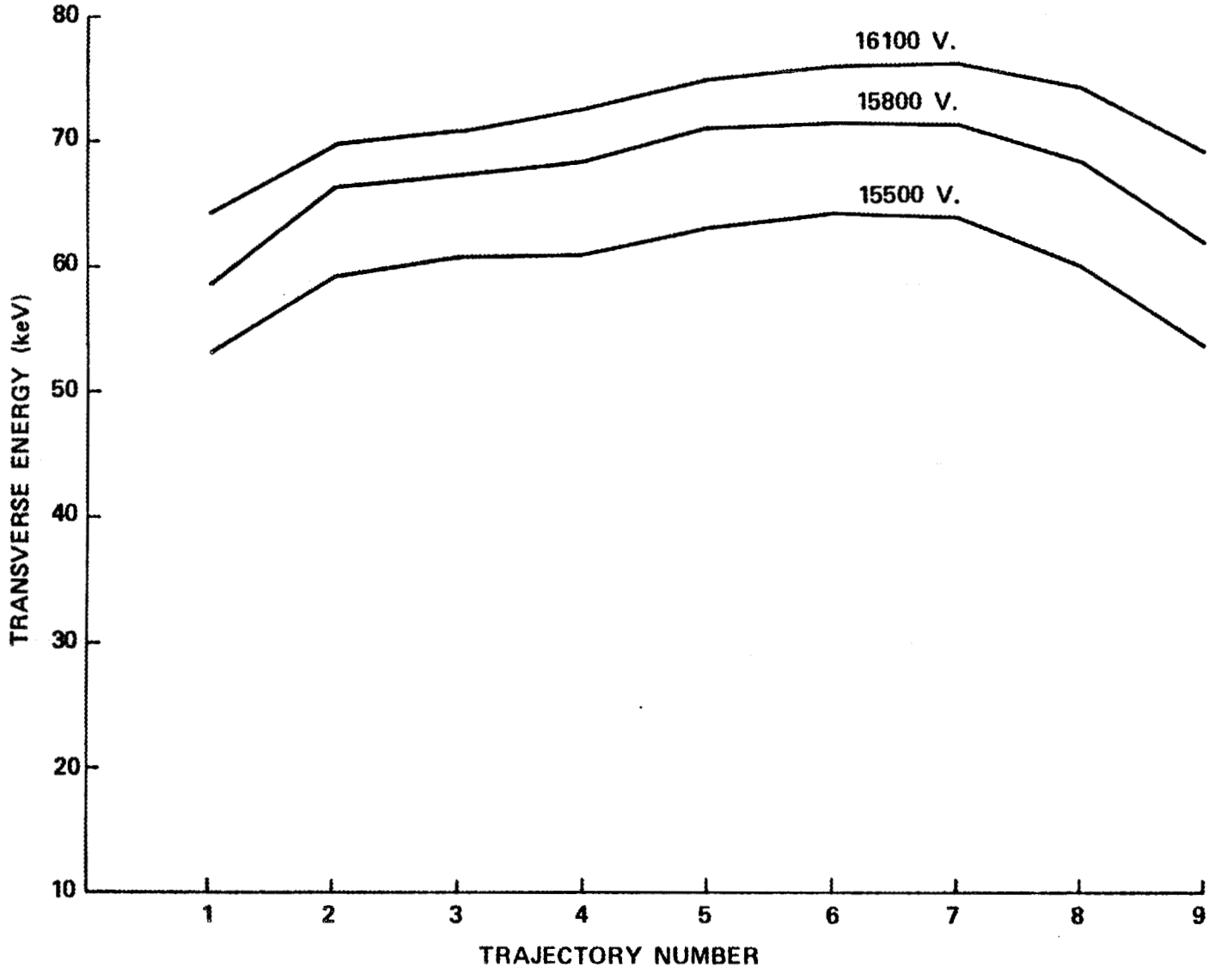

Figure 18. Transverse Energy Profile as a Function of 1st Anode Voltage

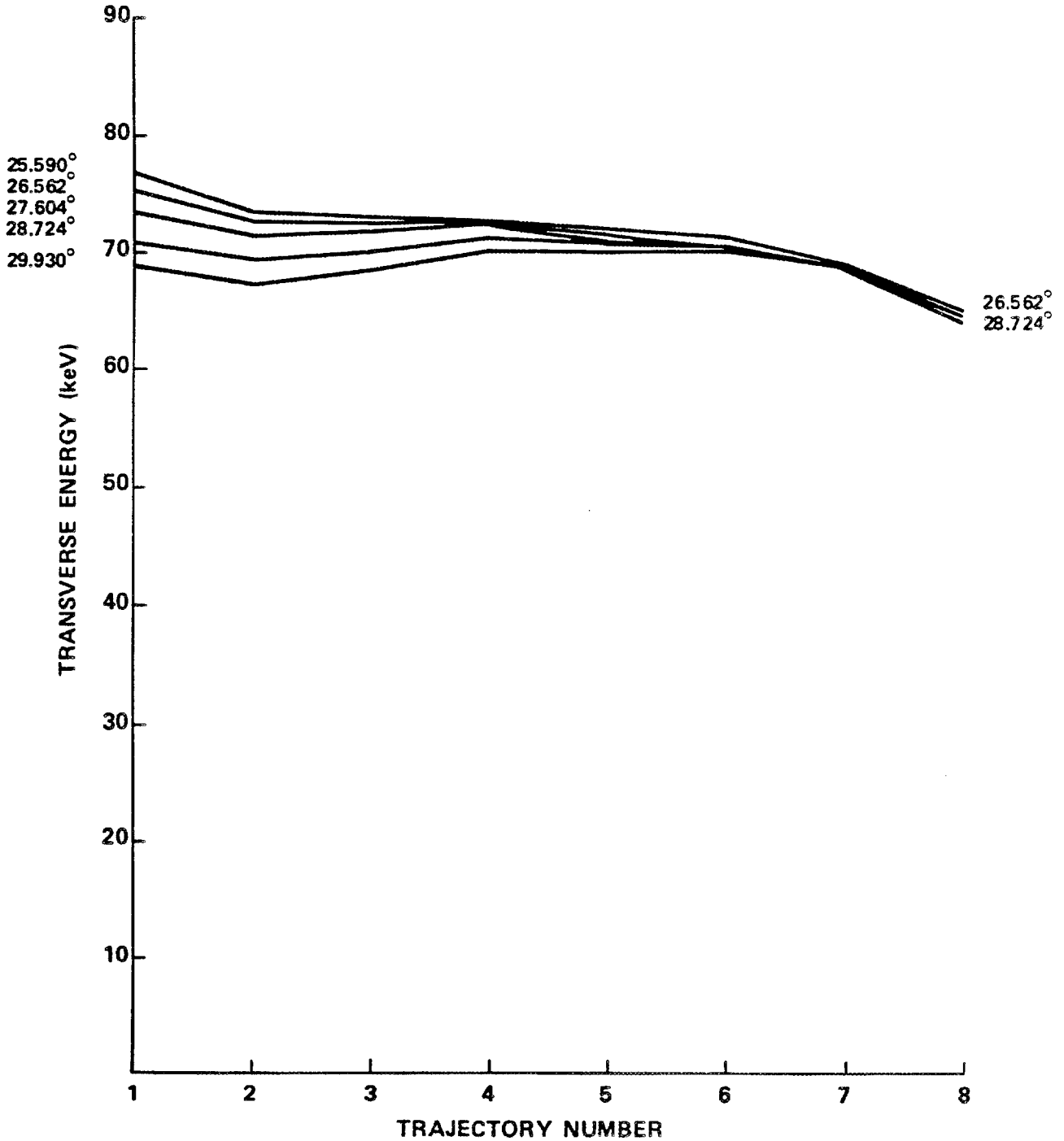

Figure 19. Variation of Transverse Energy Profile with 1st Anode Angle (Curved Back Focus Electrode)

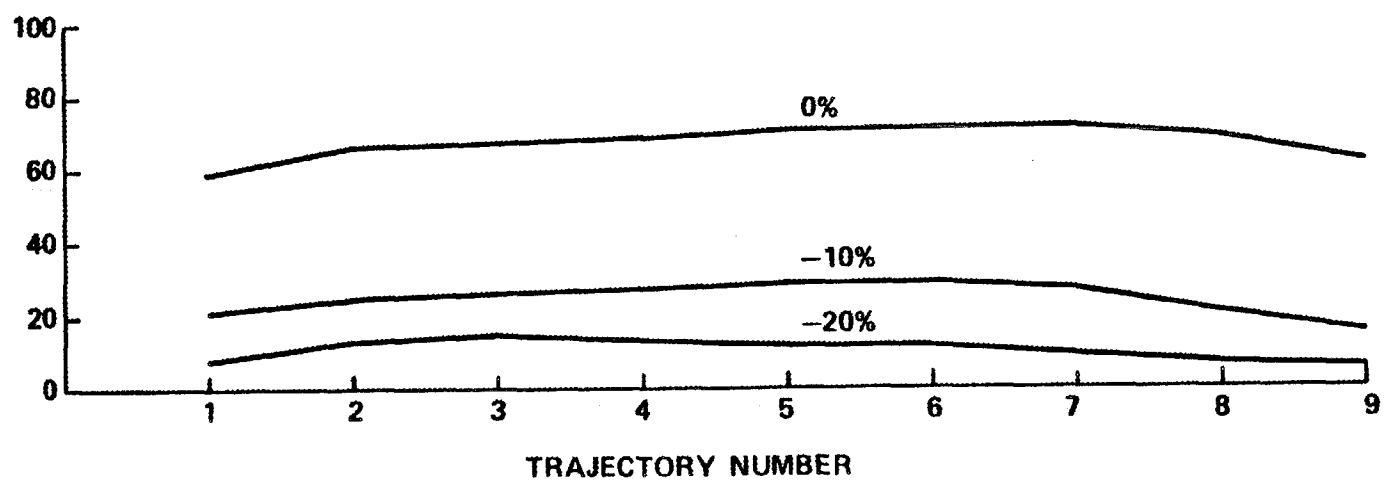

Figure 20. Transverse Energy Profile as a Function of Bucking Coil Ampere-Turns

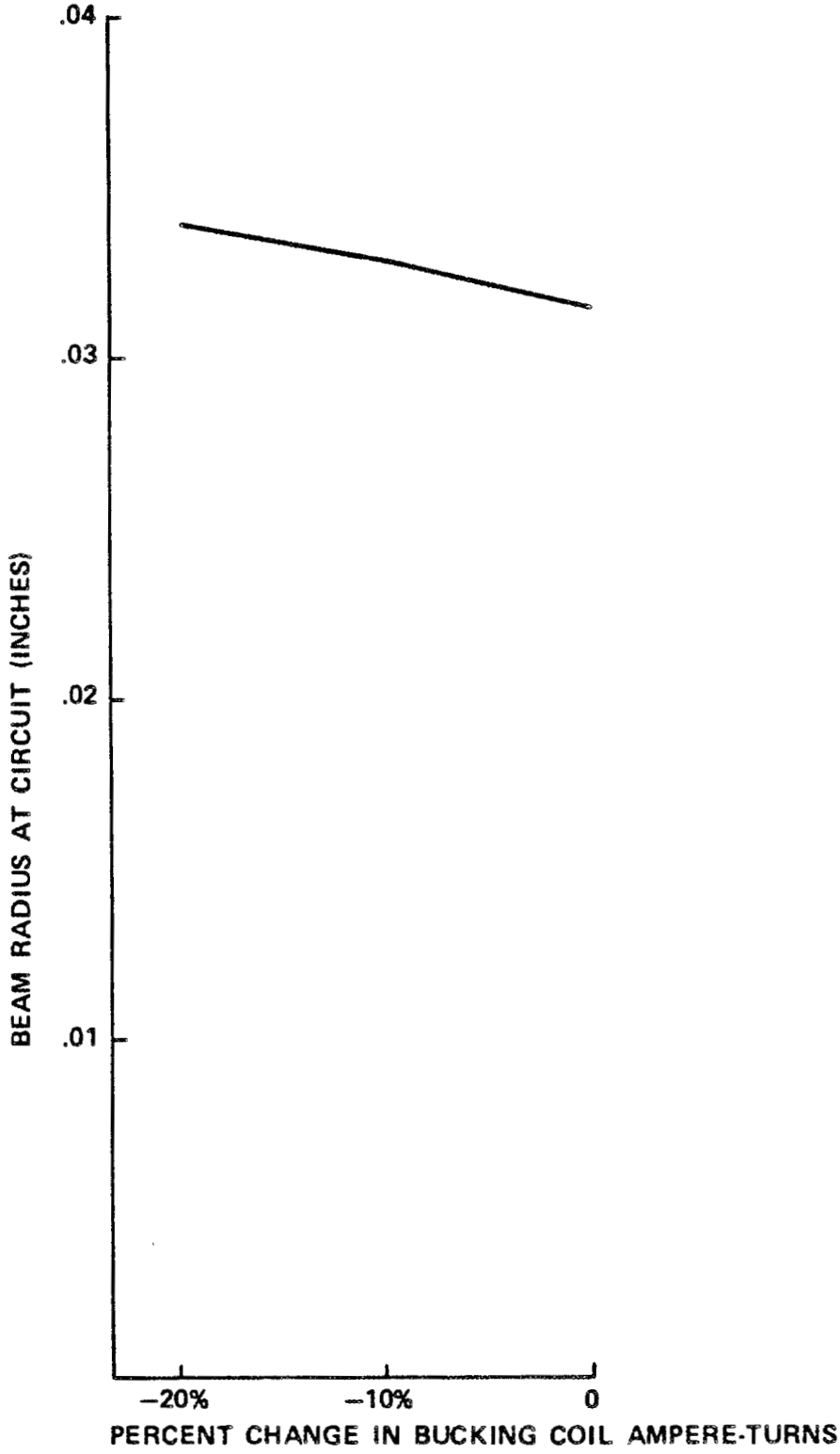

Figure 21. Beam Radius at Circuit as a Function of Change in Bucking Coil Ampere-Turns

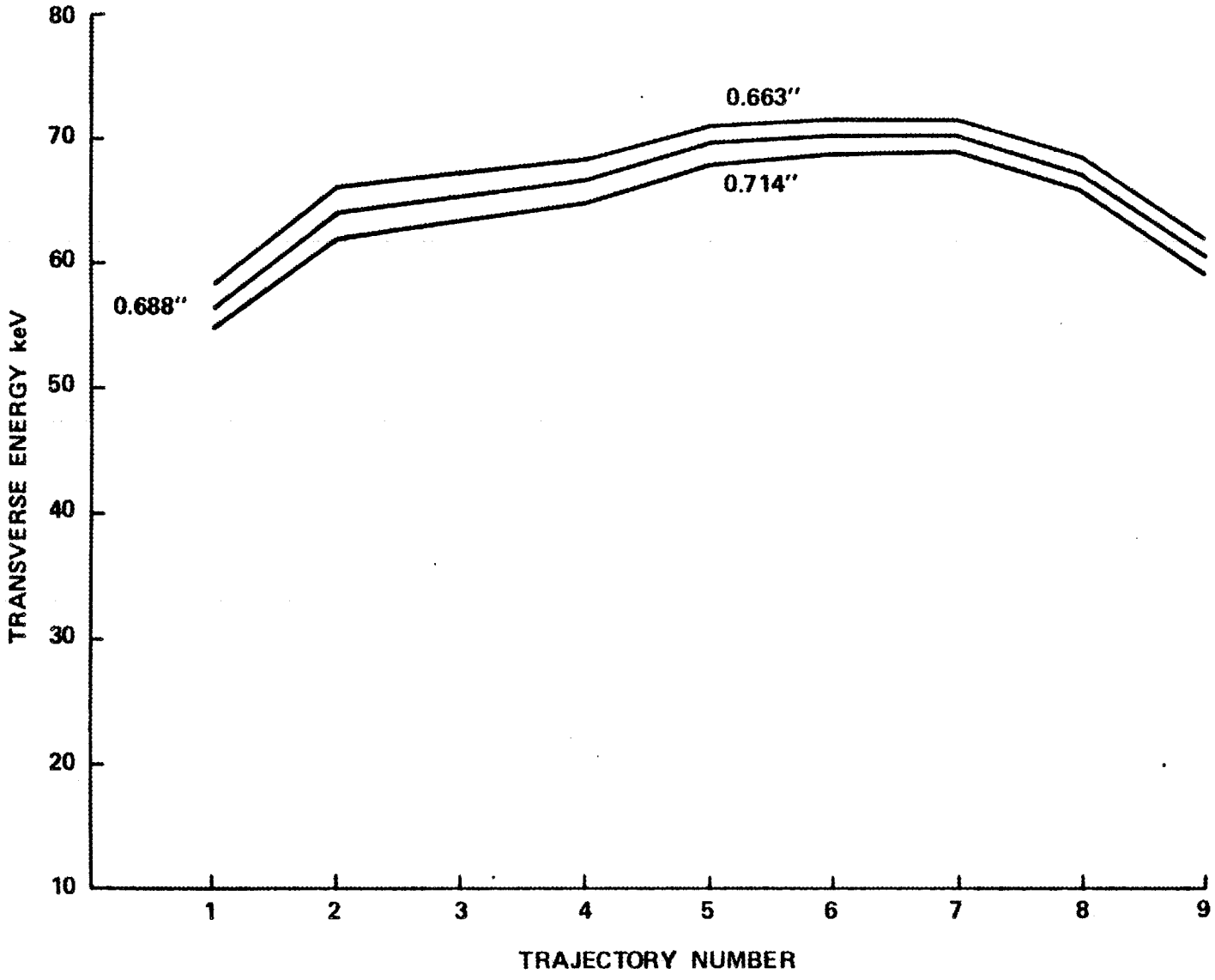

Figure 22. Transverse Energy Profile as a Function of Distance from Center of Cathode to Tip of 1st Anode

current on the transverse energy profile was investigated. Three runs were made on a similar design at 5 A/cm^2 loading. The effects are shown in Figure 23.

B. INTERACTION CIRCUIT

1. TE_{021} Cavity Design

The TE_{021} oscillator cavity dimensions were scaled directly from the 28 GHz cavity. In anticipation of the tighter machining tolerances required at 110 GHz, cold test cavities, as well as actual cavity tube parts, were built to investigate difficulties encountered with the requisite tolerances. Optical techniques for checking the cavity parts after fabrication were explored.

2. TE_{031} Cavity Design

A 110 GHz oscillator cavity operating in the TE_{031} mode was also considered for several reasons. First, the larger radius of a TE_{031} cavity simplifies mechanical design, machining, and allows larger tolerances for the cavity dimensions. Also, as is shown in Figure 24, the figure of merit for the tube operation with a TE_{031} cavity is 50% better than that for the TE_{021} cavity.

Cold test cavities at 28 GHz and 110 GHz and output tapers were fabricated and were tested for resonance characteristics and mode purity.

3. Load Cavity Design

The transmission loss of TE_{11} radiation, launched at the oscillator cavity drift tube through the load cavity designed for the 110 GHz oscillator, was measured. The loss element in the load cavity was a water-cooled lossy, silicon carbide-loaded beryllia ceramic, rather than a water-backed ceramic window, as had been used in the 28 GHz designs. The advantage of this approach is a broader band load cavity. The load cavity transmission coefficient is plotted versus frequency for various load cavity

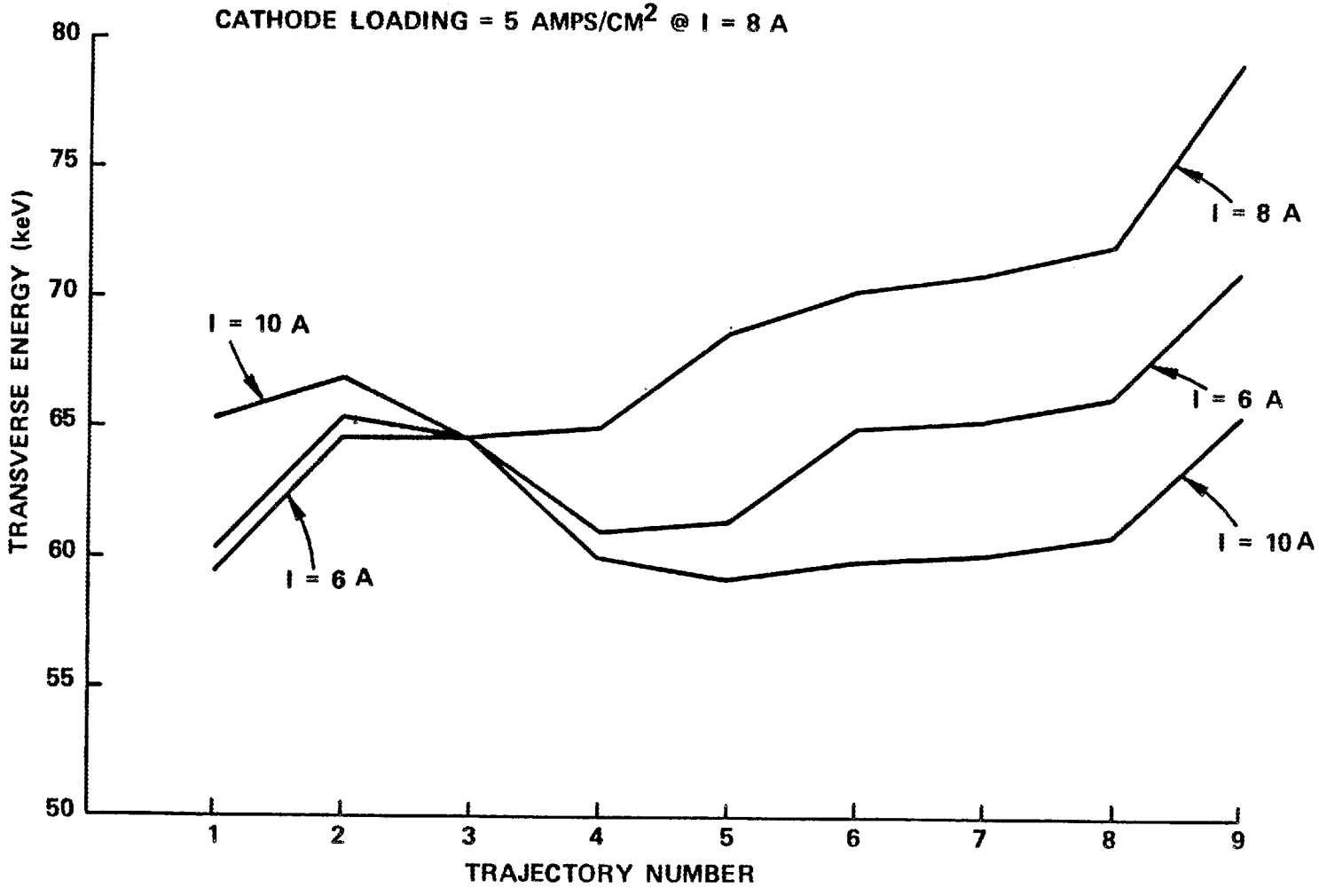

Figure 23. Variation of Transverse Energy Profile with Beam Current

MAXIMUM FIGURE OF MERIT $\left(\frac{R}{Q}\right)\left(Q\frac{\delta}{\lambda}\right)\left(\frac{A}{\lambda^2}\right) = \left(E_\phi^2 \Big/ 2\frac{P_L}{A}\right)\frac{\delta}{\lambda}$

AS A FUNCTION OF MODE INDEX FOR TE_{ON1} MODES

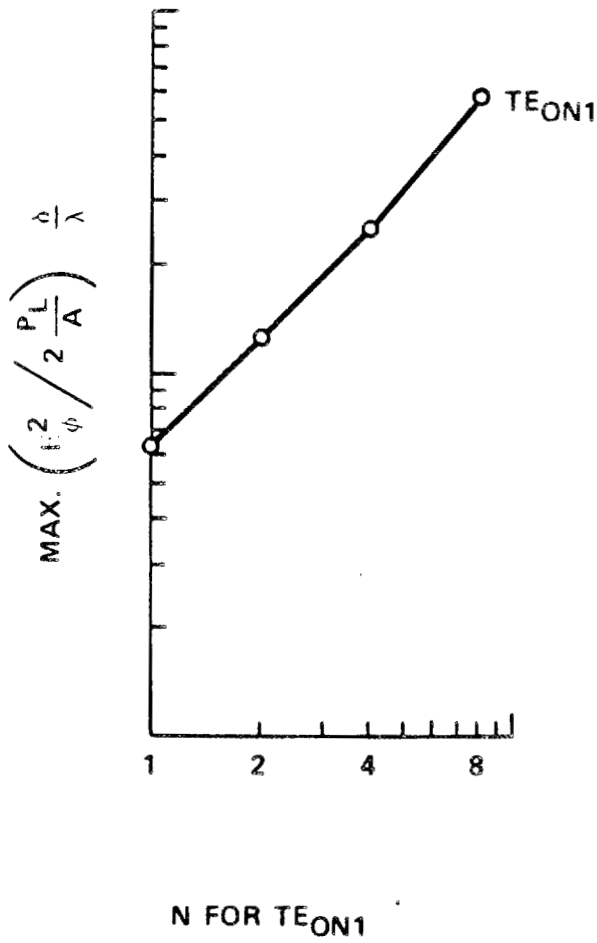

Figure 24. Figure of Merit for Circular Electric Modes

drift tube gap sizes in Figure 25. At larger gap sizes, the loss became less sensitive to frequency. A 1.27 λ gap provided about 7 dB of loss at 110 GHz. These results were encouraging, and mechanical design of a scaled version of this load cavity was later started for the 60 GHz tube.

4. Effective Interaction Cavity Length

The reactive loading properties of a dielectric bead were used to investigate the rf field structure in the interaction circuit. The dielectric bead affects the overmoded cavity transmission resonance signal in two ways. First, there is the familiar dielectric detuning of the resonance frequency, f_o, by some frequency shift, $\Delta f \sim E_\theta^2$ (Z). A second effect dominates when the bead is large (i.e., when (bead size) ÷ (cavity size) << 1 is not satisfied). In this case, the bead imposes boundary conditions which couple the cavity fields to propagating (non-evanescent) waveguide modes. This diminishes Q_{EXT}, the external Q of the cavity, from the value, Q_L, the loaded Q of the cavity, measured when the bead is absent. The resulting reduced cavity, Q_{EXT}, is a function of the axial bead position, z. Using a simple argument, one can show that the fractional change in Q_{EXT} is related to the cavity field amplitude according to: $(1-Q_{EXT}(z)/Q_L \sim E_\theta^2(Z)$, where z is the axial position. This expression is valid only when $z \leq l$ is satisfied, where l is the length of the cavity. For $z \geq l$, the bead partially reflects the cavity output signal. In this region, while the data provide no exact information on electric field amplitudes, local maxima in $Q_{EXT}(z)$ are observed at axial positions where the electric field is at a null.

An experiment was performed to determine the rf field structure within the interaction cavity and the nearby output waveguide structure. A small (0.13 cm x 0.13 cm) cylindrical dielectric bead was drawn through the 110 GHz TE_{02} cavity (cavity radius = 0.31 cm) on a nylon thread along a line parallel to the axis of symmetry and with a radial displacement corresponding to the position of the first electric field maximum in the cavity. The cavity was excited in the TE_{02} mode and the peak height of the transmission resonance signal, which is roughly proportional to the cavity, Q_{EXT}, was observed as a function of bead position. A typical set of data

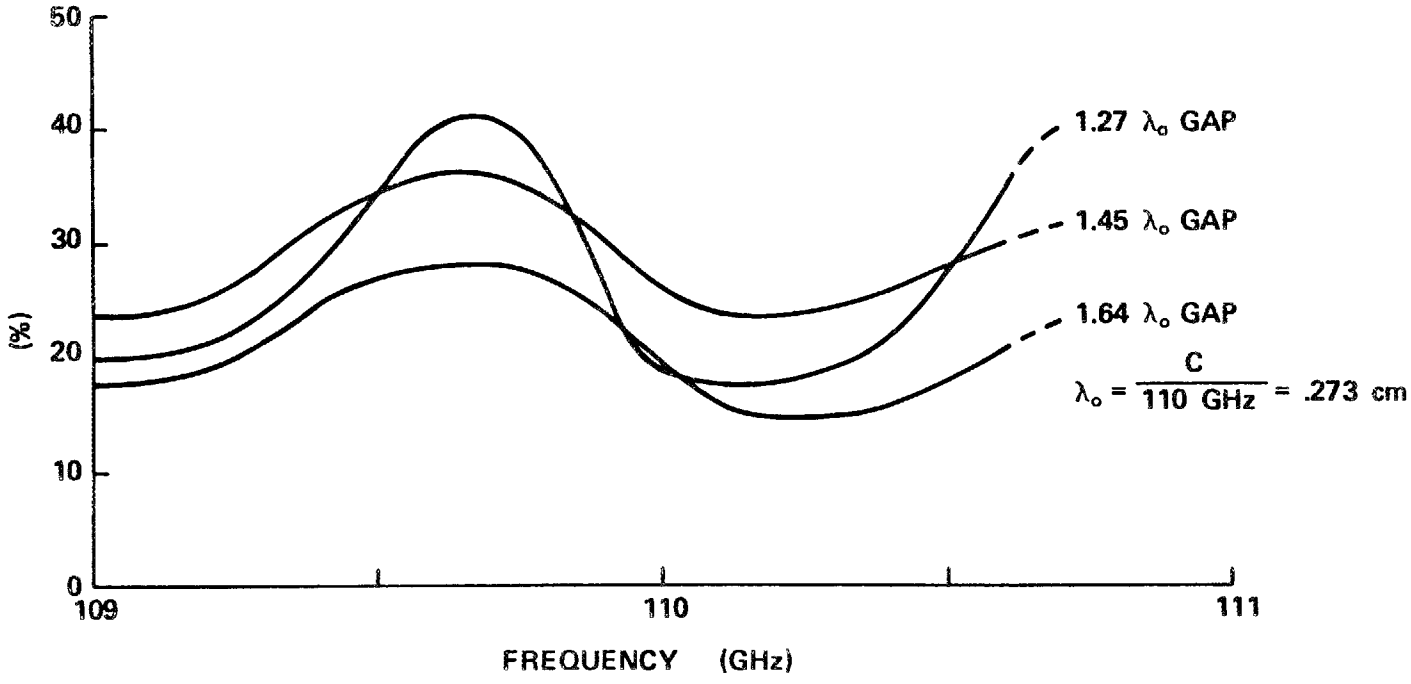

Figure 25. Transmission of TE_{11} Mode Through Anode Load vs Load Gap and Frequency

is shown in Figure 26. The cavity contains a one-half wavelength electric field variation, which extends slightly beyond the cavity structure toward the output waveguide. From there to the collector, the guide wavelength of the rf field decreases, as seen by the decreasing separation between the local maxima in the data. The effective length of the cavity is the distance between the first two local maxima, in this case 1.8 cm or about 6.6 λ.

C. OUTPUT/COLLECTOR

Several different options were considered for the output coupling, as shown in Figure 27, including:

1) a gradual taper to a 2-1/2" cylindrical waveguide,

2) a gradual taper to a two-section compound taper to a 5" waveguide,

3) a single miter bend to a 2-1/2" waveguide, and

4) a triple miter bend to a 2-1/2" waveguide.

Strongest consideration was given to the first two options. The first and second options, the straight-through collectors, offered the best mode purity at the output and allowed less reflection to the oscillator cavity than the third and fourth options, the miter bend outputs. On the other hand, thermal design of the collector was more difficult for options 1 and 2, since these designs required a smaller surface area for electron beam collection.

1. Gradual Taper to 2-1/2" Waveguide

This was the choice for output coupling in the experimental pulsed oscillator, as it provided the best mode purity with the simplest construction and permissible values of average electron beam power density at the collector walls. The problem of mode conversion from the TE_{02} to other TE_{on} modes, which occurred at the junction of the conical taper and

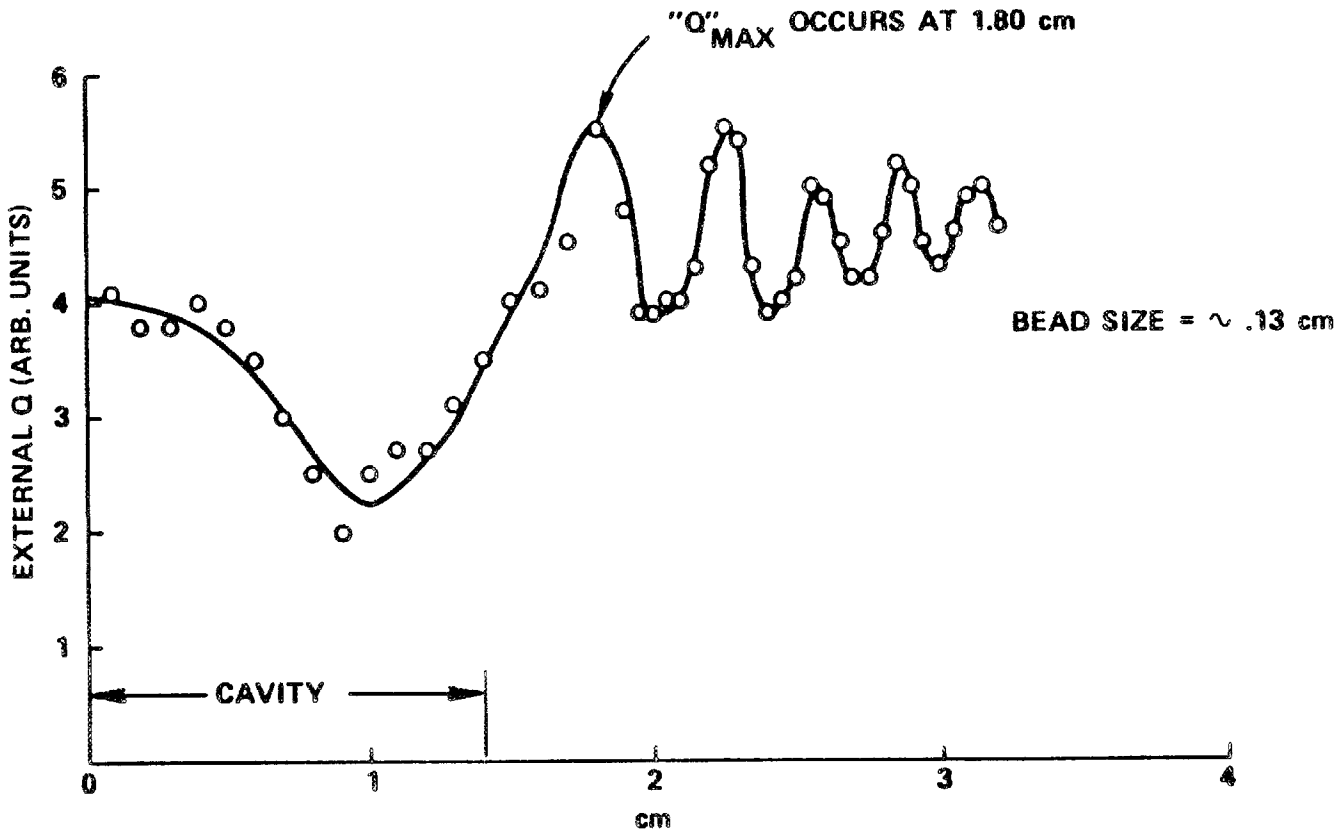

Figure 26. Effective Interaction Cavity Length

A) GRADUAL TAPER TO A 2.5 INCHES DIAMETER CYLINDRICAL WAVEGUIDE

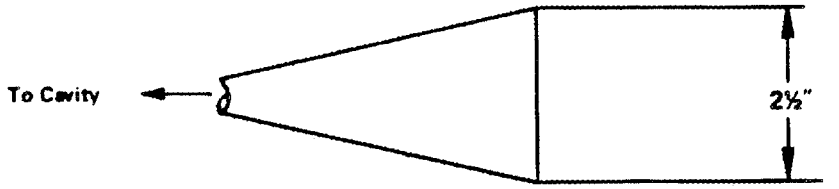

B) GRADUAL TAPER TO A TWO SECTION COMPOUND TAPER TO A FIVE INCH DIAMETER WAVEGUIDE

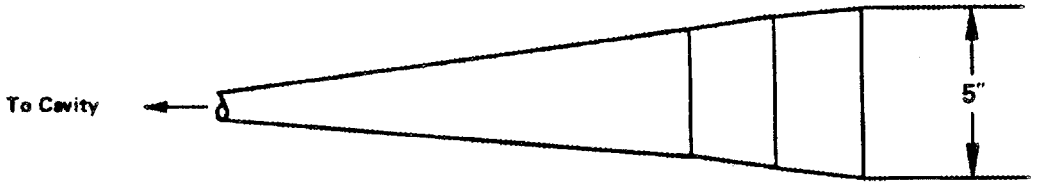

C) SINGLE MITER BEND TO A 2.5 INCHES DIAMETER WAVEGUIDE

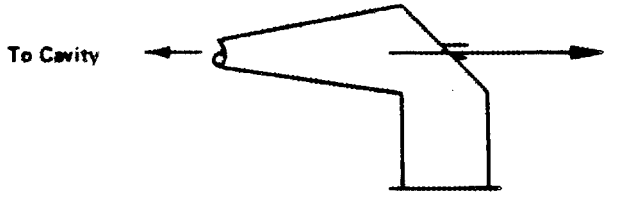

D) TRIPLE MITER BEND TO A 2.5 INCHES DIAMETER WAVEGUIDE

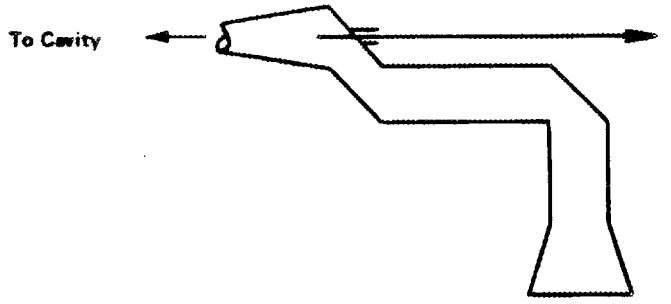

Figure 27. Output Coupling Options Considered

the cylindrical 2-1/2" guide was analyzed. For a 5° taper, roughly 30% of the TE_{02} mode power is converted to both the TE_{01} and TE_{03} modes, with 5% of the power going into the TE_{04} and higher order TE_{on} modes, as shown in Figure 28.[9]

2. Gradual Taper to Compound Taper to 5" Waveguide

This option, more compatible with the high average power collector wall loading in a CW tube, is a solution to the severe mode conversion which occurs when a simple taper is extended to a 5" diameter guide. The fraction of rf power, P_{m2}, converted from the TE_{02} to other TE_{on} modes at a conical-cylindrical junction, scales according to,

$$P_{n2} \sim D^2 f^2 \theta^2 \qquad (7)$$

for small taper angles, θ.[10] The wave frequency is f, and D is the cylindrical waveguide diameter. In going from a 2-1/2" to 5" diameter conical-cylindrical junction, the mode conversion increases by a factor of 4.

To correct the mode conversion, design of a compound taper, shown in Figure 27, was started. One additional taper section was required for cancellation of each unwanted TE_{on} mode. A two-section compound taper was, therefore, necessary in this case, because the simple conical-cylindrical junction tends to convert the TE_{02} mode predominantly into two other unwanted modes, the TE_{01} and TE_{03}. The angles in the compound taper were chosen to create specific mode conversion coefficients for these two unwanted modes. The lengths of these additional taper sections were then chosen so that upon superposition, contributions from the unwanted modes destructively interfere.

3. High Power Mode Probe

Mechanical design of a high power mode probe was completed, as shown in Figure 29. This instrument was intended to provide a complete picture of the gyrotron output rf field pattern. When mounted on a 2-1/2"

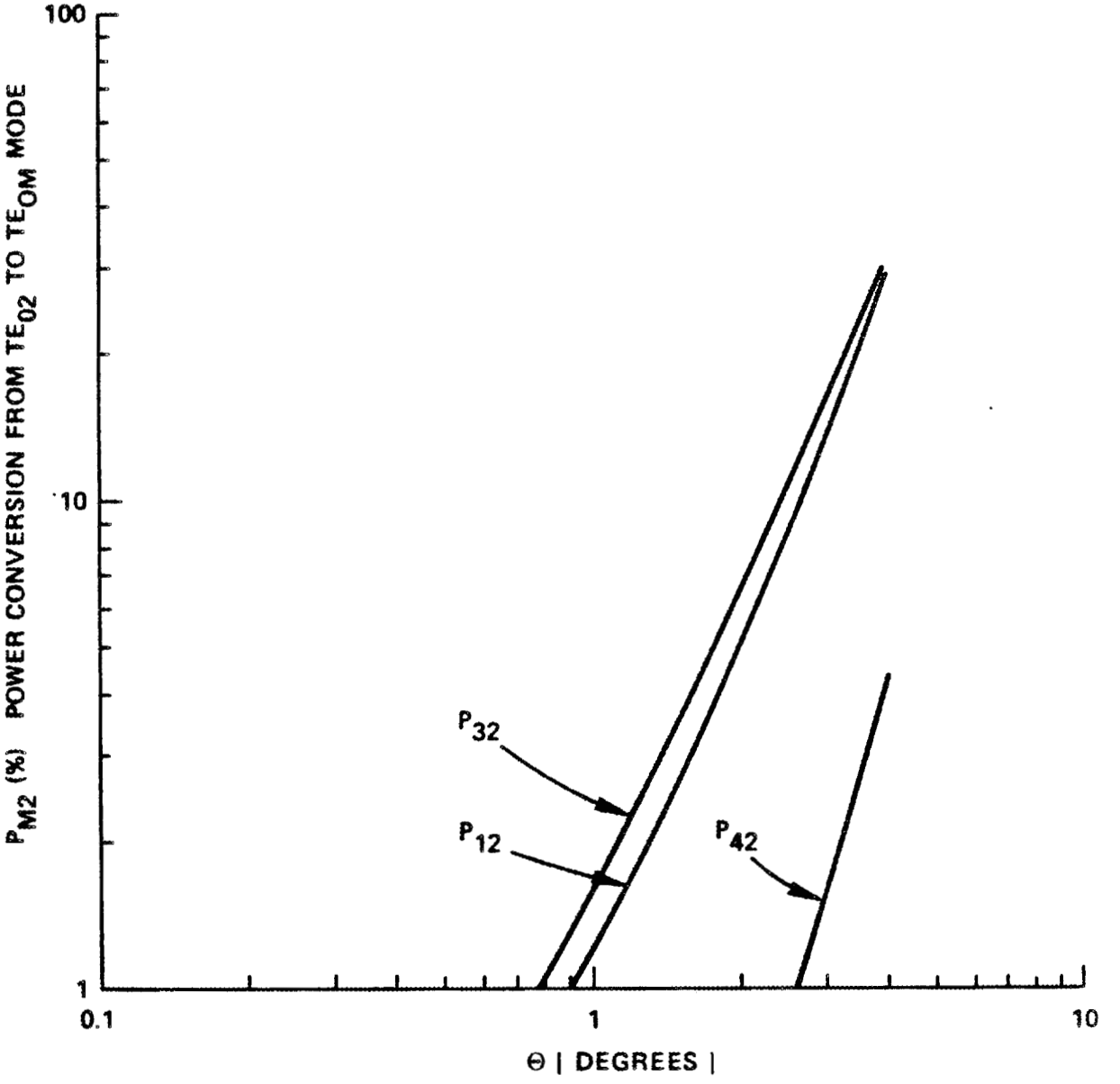

Figure 28. Mode Conversion as a Function of Taper Angle

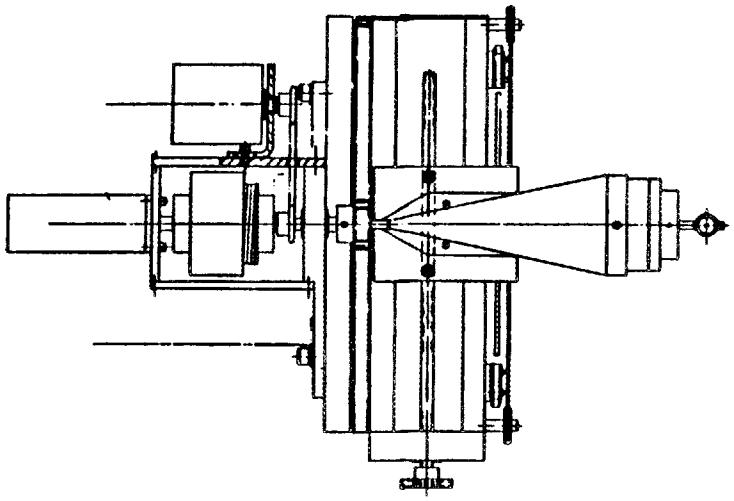

TOP VIEW

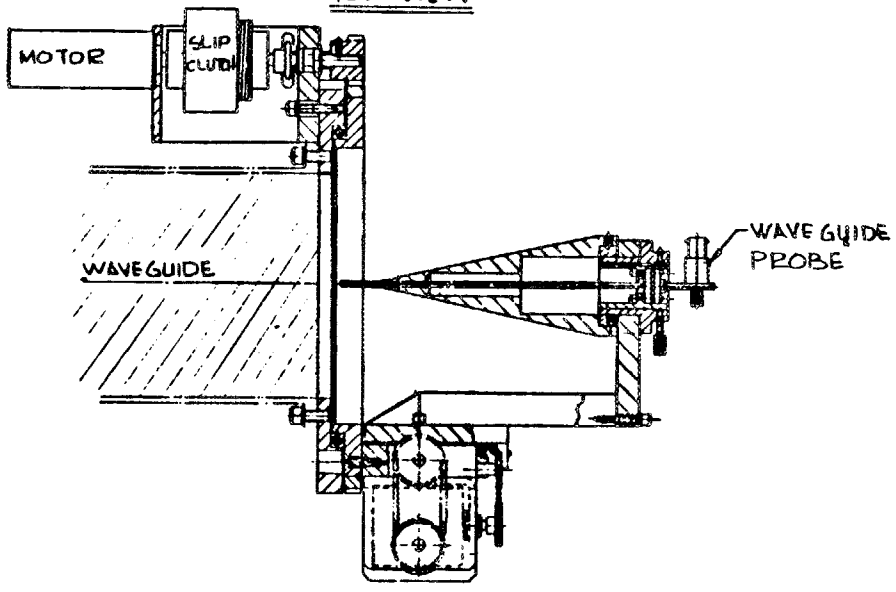

SECTIONED SIDE VIEW

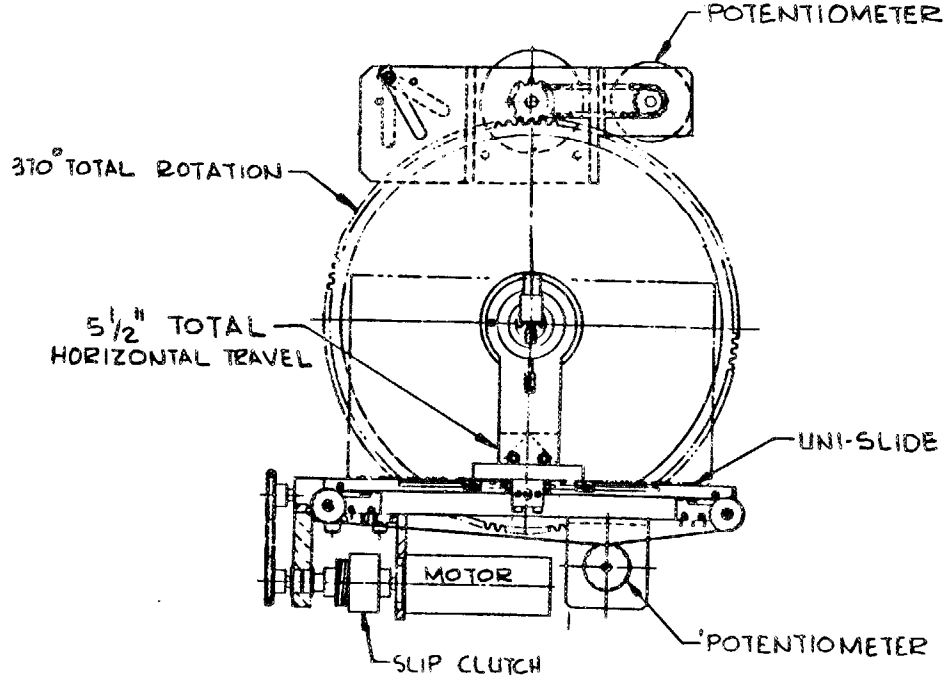

FRONT VIEW

Figure 29. Waveguide Probe

or 5" waveguide, the device would probe the magnitude and direction of the rf field, both radially and azimuthally, across the guide. The probe mount was designed to minimize wave reflection back down the waveguide. A piece of WR-10 guide with a coupling aperture on one end was to be used as the probing element. It would couple the sampled rf power into a broadband crystal detector. The coupling aperture size may be varied, depending on the peak rf power densities expected in the output waveguide of the tube. The instrument was designed to be operated by remote control during tests on live tubes, but of course, may be used in cold test experiments as well. It was anticipated that the tubes would be tested with this device at full peak power and up to 1 to 2 kW average power.

D. OUTPUT WINDOW

Microwave designs for flourocarbon liquid face-cooled, double-disc alumina and beryllia windows were completed.

The design of the alumina window consisted of a $5\lambda_g/2$-thick vacuum window, one-half wavelength of flourocarbon liquid, and a $2\lambda_g$-thick air window.

The design of the beryllia window consisted of two $2\lambda_g$-thick windows separated by one-half wavelength of flourocarbon liquid.

These designs would allow at least sixty pounds per square inch absolute pressure capability for the vacuum windows.

Assuming a loss tangent of 0.006, a loss of 3.7 kilowatts was expected in the flourocarbon liquid. Total loss in the two discs was expected to be 0.5 kilowatts for alumina and 1.0 kilowatt for beryllia.

The long lead time alumina and beryllia discs were received.

Mechanical design of the remaining parts was terminated with the redirection to 60 GHz.

IV. TEST FACILITY

An investigation was initially made to determine which test station would be most suitable for testing a 110 GHz amplifier. This would require two supplies, one for the drive power source and one for the amplifier. The stations having the required capabilities were evaluated, taking into account existing schedules and the amount of floor space available. The drive facility had to be near the amplifier facility. The Super Power Test Set with its nearby driver facility was determined to be the best choice. Plans were made to move the 28 GHz project, which was currently being tested there, to a new location.

Based on the project requirements, modifications and new equipment requirements were outlined to upgrade the existing driver facility to properly operate the 110 GHz gyrotron driver.

The gyrotron driver socket required a high voltage beam power supply source with properly interfaced interlock protection and a multichannel crowbar logic scheme to divert the capacitor bank's stored energy in the event of a load fault. Calibrated instrumentation was also required to measure the beam power supply voltage and load currents.

A new crowbar logic assembly would have been interfaced to the existing power supply, which would have allowed accurate read-out of the fault signal's trip levels in each of three available input channels. The unit would have provided protection against excessive peak pulse or average current levels as monitored by sensors placed in the circuits of concern.

Another power supply would have been retrofitted to provide both the pulse voltage parameters in the first stages of development and later the dc voltages required for the modulating anode of the gyrotron driver device. Calibrated instrumentation for both modes of operation would have been installed to properly evaluate the driver's performance.

The gyrotron socket would have been in an oil filled tank which would have been designed and built to also interface to the superconducting

solenoid magnet dewar. The tank would have also contained the pulse instrumentation components.

A separate water manifold would have been designed and built to properly channel and control the driver's coolant. This would have included flow instrumentation and flow interlock protection. A special heat exchanger, utilizing FC-75, would also have been interfaced into the coolant system to provide coolant to the output windows.

For protection against waveguide arcs, a new arc-detector would have been installed in the drive waveguide and connected to the electronic fault protection.

When the program was redirected to develop a 60 GHz oscillator rather than a 110 GHz amplifier, these plans to modify the Super Power Test Set were dropped. The discussion was made then to test the 60 GHz oscillators in the Nike Zeus Test Set. Considerable modification of the Nike Zeus Test Set was ultimately required to achieve proper gyrotron operation with pulse durations up to 30 seconds.

V. WAVEGUIDE COMPONENTS

A variety of waveguide components was developed for use with the 110 GHz, and later the 60 GHz gyrotron, including both pulsed and CW waterloads, frequency samplers and arc detectors, mode filters, miter bends, flange adapters and attenuators.

A. WATERLOAD

The waterload to be used with the 110 GHz tube was identical to that used with the 28 GHz tube. The waterload is shown in Figure 30. Since the cone load was expected to be broadband, the change to 60 GHz was not expected to change the basic design. However, the flange used on the 28 GHz waterload was modified to prevent flange arcing and heating at high CW powers in multimode waveguide systems. This new flange design utilized a disposable copper gasket captured by stainless steel flanges.

Both a pulsed and CW load were designed and built. The pulsed waterload design allowed more turbulent flow at lower water flow rates and had a smaller thermal mass. The outline of the pulsed waterload is shown in Figure 31.

During the program, Varian was directed to change flange designs and incorporate the Oak Ridge flange. The CW waterload with the Oak Ridge flange is shown in Figure 32.

Work was performed to improve the waterloads after two pulsed rf loads had failed during long pulse operation. Both loads were used with an adjustable baffle at low flow, 3 gpm and 5 gpm. Unfortunately, it was difficult to know precisely where the baffle was located. It was possible that the baffle actually touched the ceramic at a point and cut off the coolant flow and, thereby, cracked the ceramic. The first load was broken at 6% duty, with 60 millisecond pulses of 200 kw at 3 gpm of water flow; the second broke at 1% duty, 100 milliseconds, 150 kw at 5 gpm. These failures prompted the use of an accelerometer to listen for boiling in the waterloads.

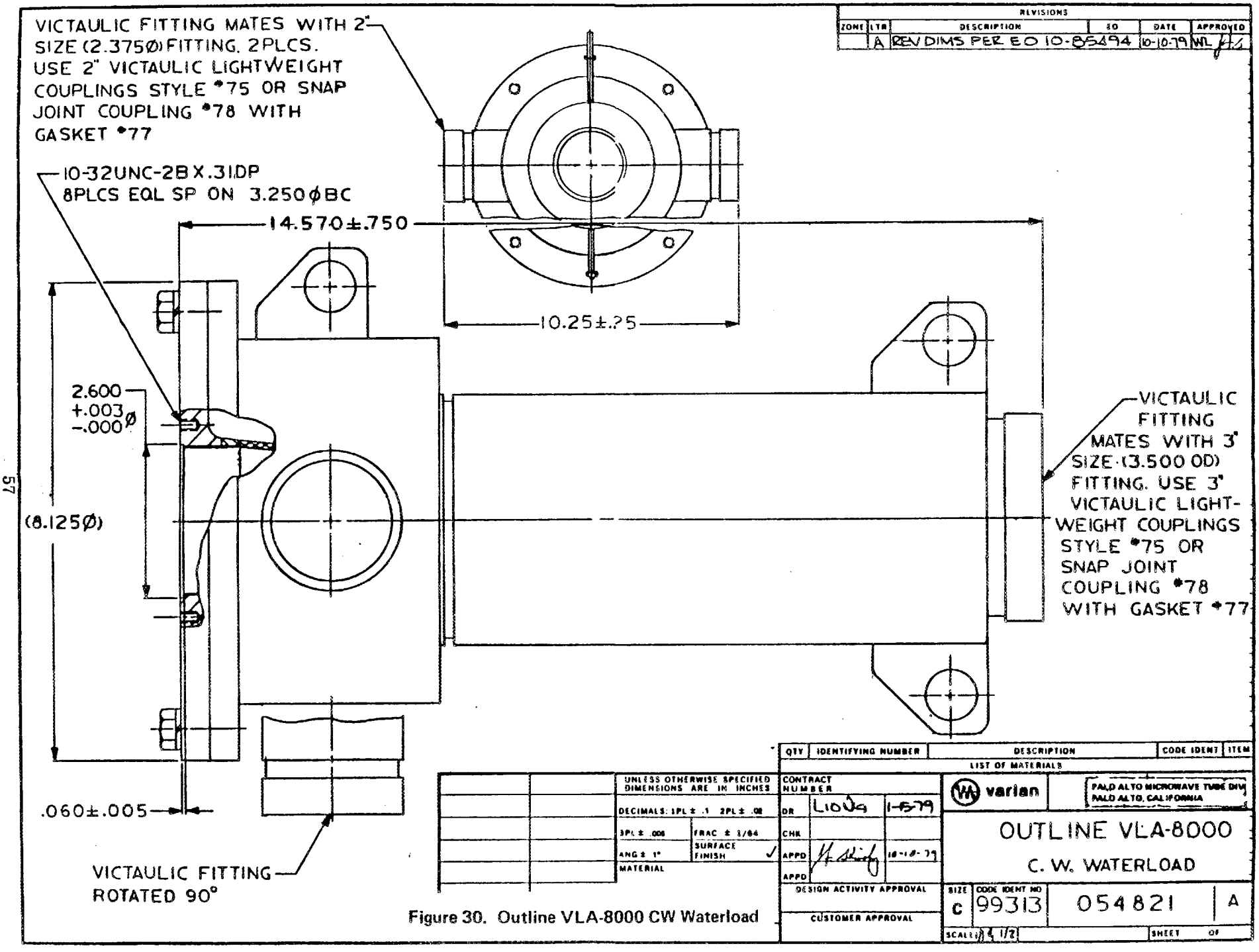

Figure 30. Outline VLA-8000 CW Waterload

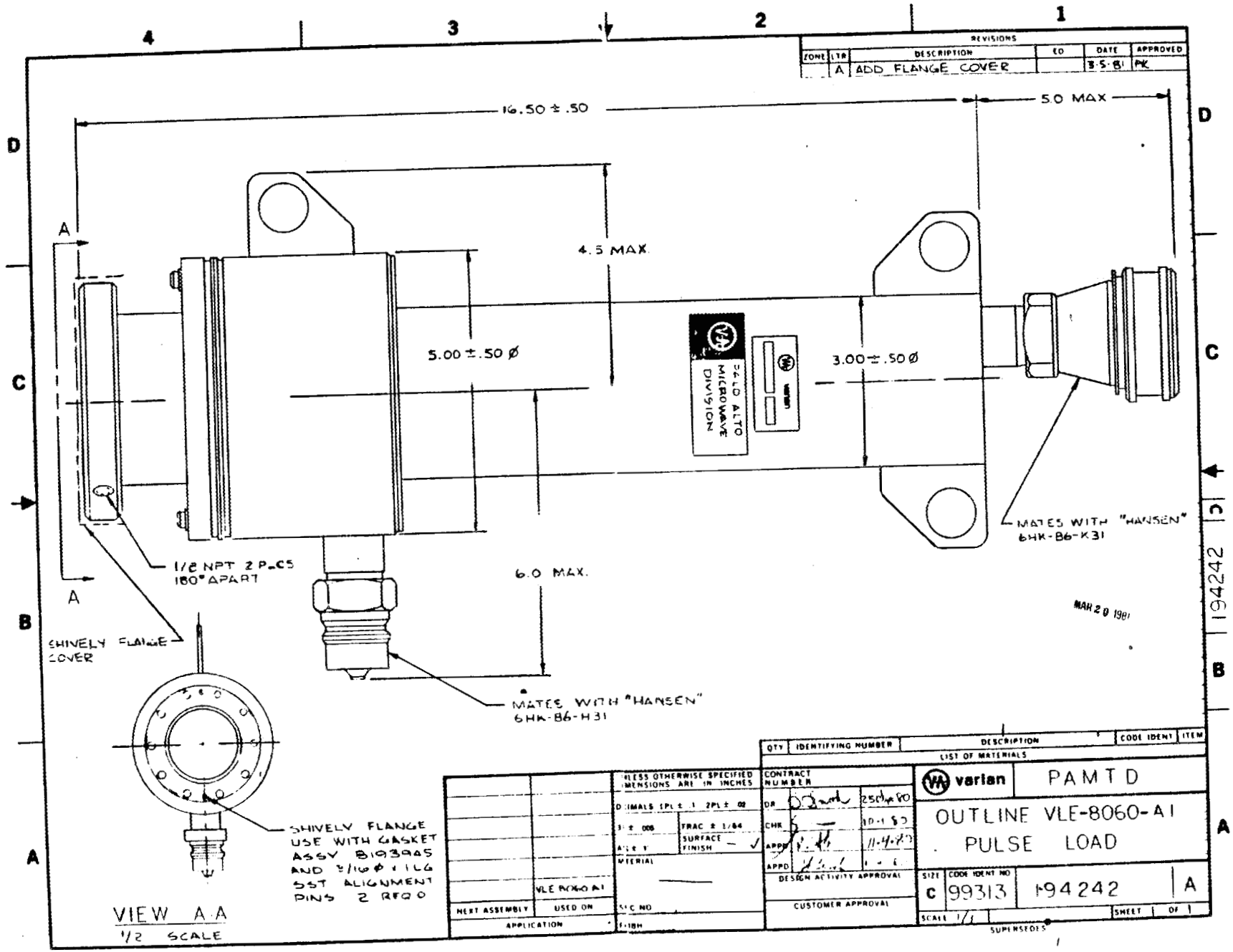

Figure 31. Pulsed Waterload

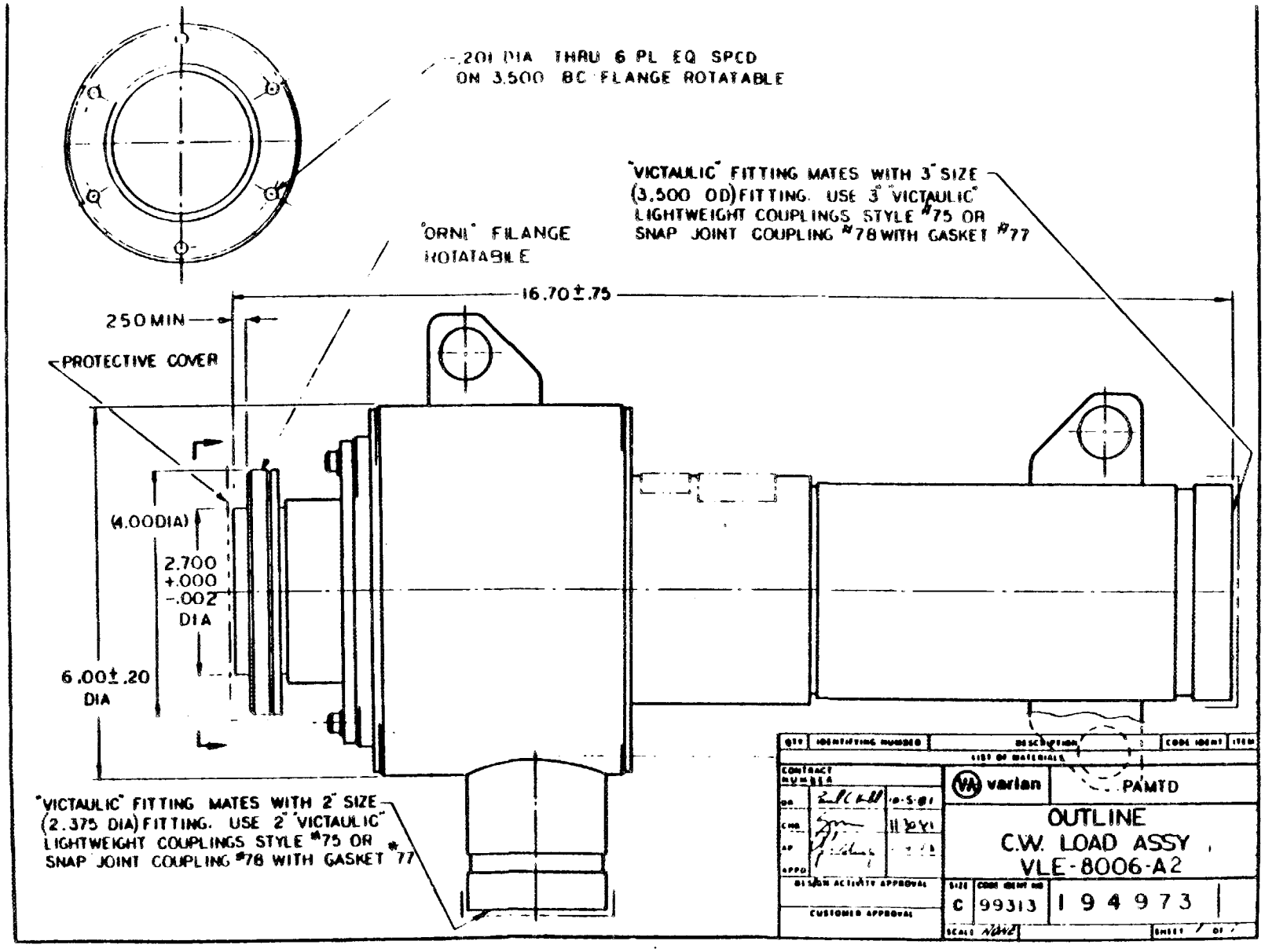

Figure 32. Outline CW Load Assembly, VLE-8006-A2

The first CW tests showed that with the existing waterloads and 136 gpm flow, boiling occurred at 85 kW. This was for a bulk temperature rise of only 2.4°C. A baffle was inserted which increased the flow velocity by a factor of two. This did not decrease the flow from the 136 gpm rate, but raised the power level at which boiling occurred at 110 kW. A second baffle was designed to increase the water velocity at the inner electric field maximum by a factor of seven. However, the second baffle only increased the power level at which boiling occurred from 110 kW to 115 kW. The water velocity was then at 46 ft/second. The problem was the high power density in the 2.5-inch diameter waveguide. Because of its small skin depth at 60 GHz, only a small volume of water was heating.

Boiling in the 2.5-inch diameter waterload was detected both acoustically and by observing the detected rf pulse from the frequency sampler. Cavitation erosion was observed on the cone surface at the location of the inner E-field maximum for the TE_{02} mode in 2.5-inch diameter guide. Attenuation measurements for a 2.5-inch diameter water-backed, ceramic cylinder indicated a loss of only 1 dB/ft. These observations suggested there was neither significant mode conversion nor rf beam divergence in the system. Therefore, one could assume a 2.5-inch diameter TE_{02} mode impinging on the cone. The power density at the inner E-field maximum was calculated as follows:

Let P_d = power density amplitude constant in W/cm^2

P = total rf power

a = radius of cone = 1.25 inch

h = height of cone = 12.5 inches

$P_d J_1^2\left(\frac{\lambda_2 r}{a}\right)$ = power density in W/cm^2

λ_2 = second root of $J_1(x)$

$$P = \int_0^{2\pi} \int_0^{a} \sqrt{\frac{h^2 + a^2}{a}}\, P_d \; r \; J_1^2\left(\frac{\lambda_2 r}{a}\right) dr\, d\phi \qquad (8)$$

where $\sqrt{\frac{h^2 + a^2}{a}}$ is the factor accounting for the grazing incidence on the cone.

$$P = 2\pi \sqrt{\frac{h^2 + a^2}{a}} \; P_d \int_0^a r \, J_1^2 \left(\frac{\lambda^2 r}{a}\right) dr \tag{9}$$

Let $r = a\,x$

$$P = \frac{2\pi\sqrt{h^2 + a^2}}{a} \, Pd \int_0^1 a\,x\,J_1^2\left(\lambda_2 x\right) d\left(a\,x\right) \tag{10}$$

$$P = 2\left[\pi \; a\sqrt{h^2 + a^2}\right] P_d \int_0^1 x\,J_1^2\left(\lambda_2 x\right) d\,x \tag{11}$$

Let $A_c = \pi \; a\sqrt{h^2 + a^2}$ = surface area of cone

$$P = 2\,A_c\,P_d\left[\frac{1}{2}\,J_2^2\left(\lambda_2\right)\right] \tag{12}$$

$$P = A_c\,P_d\left[-J_o\left(\lambda_2\right)\right]^2 = A_c\,P_d\,J_o^2\,\lambda_2 \tag{13}$$

$$P_d = \frac{P}{A_c\,J_o^2\left(\lambda_2\right)} \tag{14}$$

$$P_d = \frac{2 \times 10^5}{\pi\;1.25\sqrt{(12.5)^2 + (1.25)^2}\;(2.54)^2\;(0.3)^2} \tag{15}$$

$$P_d = 6.98 \text{ kW/cm}^2 \tag{16}$$

The power density at the inner E-field maximum is

$$Pd\;J_1^2\,(1.84) = 6.98\;(0.5819)^2 = 2.36 \text{ kW/cm}^2 \tag{17}$$

Because the skin depth of the water is so thin, 0.005 - 0.010 inch, the heating of the water can be likened to heating by a hot cone. A more detailed appreciation of the problem can be gleaned from a perusal of Appendix A, concerning dielectric properties of water. As we know, 2.36 kW/cm^2 is not trival, particularly at the low pressures (< 40 psig) found in the waterload.

By going to a 5-inch diameter cone, this power density would be reduced to 590 W/cm^2, if the TE_{02} mode follows the guide without mixing. If it acts more like a directed energy beam, the power density may be close to 2 kW/cm^2. The perfect mix, though unlikely, would result in uniform power density over the 5-inch diameter cone.

$$\bar{P}_d = \frac{P}{A_c} = 157 \ W/cm^2 \tag{18}$$

Some limits are given in Table 6 for 200 kW.

Table 6
Water Load Power Densities

	Inner E_{max}	Outer E_{max}	Average over cone
2.5 in. cone	2.36 kW/cm^2	836 W/cm^2	628 W/cm^2
5 in. cone	590 W/cm^2	209 W/cm^2	157 W/cm^2

Another approach considered was to a liquid other than water in the rf load. Some of the materials examined were transformer oil, ethylene glycol, FC-75^{tm} (FC-75 is a Minnesota Mining and Manufacturing Co., trademark for an inert electronic flourocarbon fluid), and DC-200^{tm} (DC-200 is a Dow Chemical Company trademark for a silicone fluid). The first qualities examined were skin depth and microwave match. The numbers used for calculating the skin depth were generally 10 GHz values of dielectric constant and loss tangent. The value of the liquids' 60 GHz skin depth was then calculated from

$$\delta \text{ (inches)} = \frac{1}{\sqrt{\pi f \mu \sigma}} = \frac{c(\text{inch/sec})}{\sqrt{2}\ \pi\ f(\text{sec}^{-1})} \frac{1}{\sqrt{\varepsilon_r \tan \delta}} = \frac{2.656}{f(\text{GHz})} \frac{1}{\sqrt{\varepsilon_r \tan \delta}} \quad (19)$$

Table 7 shows the microwave match for the fluids tested. A CW load was filled with the fluid and the cavity launcher technique[11] was used to determine the VSWR (voltage standing wave ratio).

Table 7
Calculated Skin Depth and Measured Load
VSWR for Various Liquids

	Skin Depth (Calculated)	VSWR (Measured at 60 GHz)
Water	0.008"	1.01
100% Ethylene Glycol	0.019"	1.01
FC-75	0.490"	1.02
DC-200 - 50 cs	0.118"	1.06
Transformer Oil	0.683"	1.11

The measured VSWR of the transformer oil was too high for use with the gyrotron. It is assumed that the large skin depth of the oil allowed power to be reflected from the metallic can. The skin depth of ethylene glycol was only a factor of 2 better than that of water. It appeared that either FC-75 or DC-200 would be logical choices for alternative fluids. The FC-75 is about 100 times as expensive as the DC-200, so DC-200 was tried first. Fifty centistoke viscosity DC-200 was selected because it was readily available in the required quantity and delivery time. Figure 33 shows the microwave response of the DC-200 rf load. The DC-200 load was tried on X-5. The tube was operated at 120 kW CW with 100 gpm DC-200 flow. There was some boiling detected at this level. It appeared that a 200 kW solution would require some improvement to the existing DC-200 load.

The next load design tested used a 5-inch diameter cone, as opposed to the standard 2-1/2-inch diameter cone. Additionally, a 12-inch long taper section was installed between the 2-1/2-inch diameter waveguide and the 5-inch diameter waterload. The outer shell of this load was fabricated from

Dwg 82-3604 FED

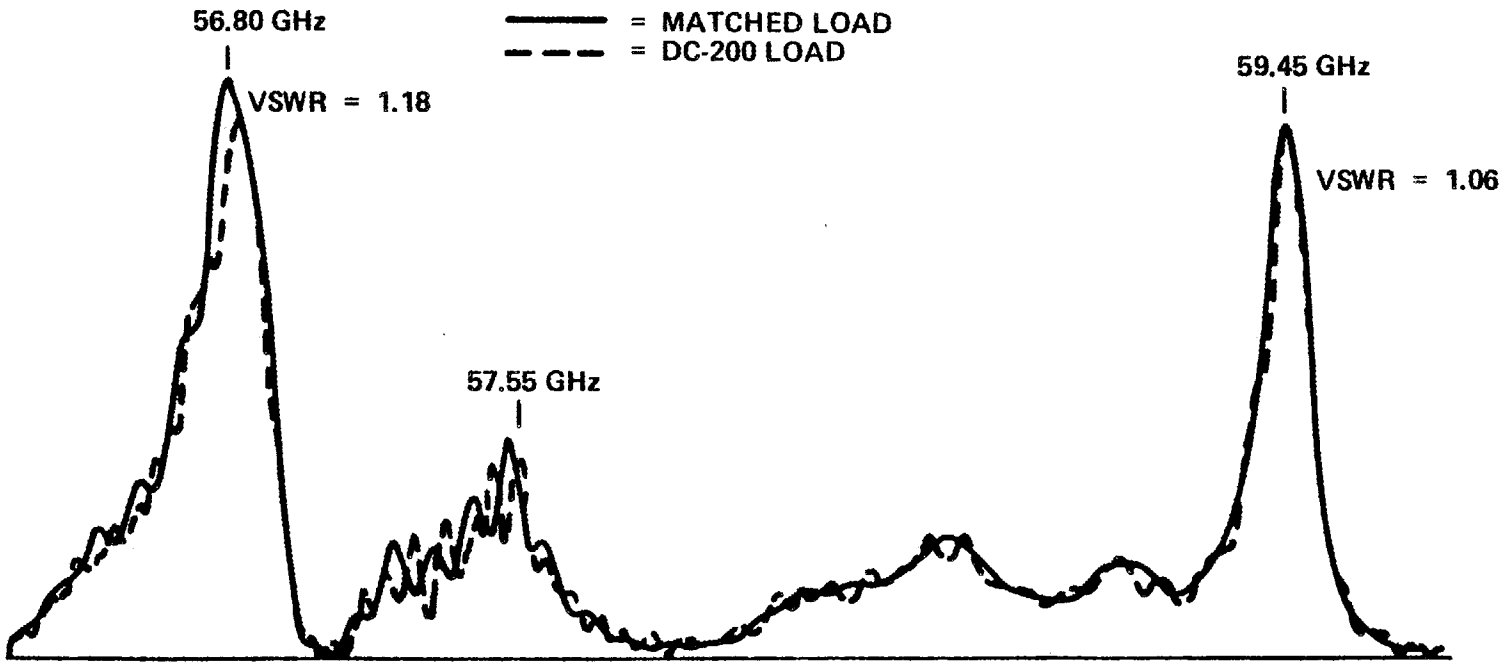

Figure 33. Response of TE_{02} Cavity Launcher to CW Load with DC-200 (50 Centistokes) Fluid

clear plastic, so any boiling which might occur could be observed on a closed-circuit TV system. The 56 GHz CW gyrotron was used to evaluate the load.

This load was designed to reduce the power density in the first radial maximum from:

$$P_d = 2.36 \text{ kW/cm}^2 \tag{20}$$

to

$$P_d = 590 \text{ W/cm}^2 \tag{21}$$

assuming that the rf energy would spread by the square of the ratio of the diameters. Since any boiling could be observed on a real time basis with the TV system, the energy spreading could be determined readily.

During operation, boiling initiated with the 5-inch cone at the same power level as the 2-1/2-inch load, and at the same diameter on the cone as the 2-1/2-inch load. In other words, the rf energy is highly optical and spread very slowly as a function of distance, essentially independent of the waveguide diameter. It was obvious that alternate designs were necessary in order to obtain a reliable 200 kW CW calorimetric load.

Two additional calorimetric load concepts were then evaluated. These were a selective cooling load, referred to as the jet load, and an rf spreading load, referred to as the electromagnetic radial diverter (ERD).[12]

The jet load was tested using a 60 GHz pulsed tube at millisecond pulse durations. The jet load had a clear plastic jacket allowing boiling to be observed visually, by using a closed circuit TV system, and audibly, by using an accelerometer.

In the jet load, the inlet water is split into two paths. One path is designed to cool the end of the cone, while the main path is designed to direct a high velocity jet at a known area of high power density along the ceramic surface, as shown in Figure 34. The jet flow was directed above the high power density area shown by the darkened portion of the ceramic.

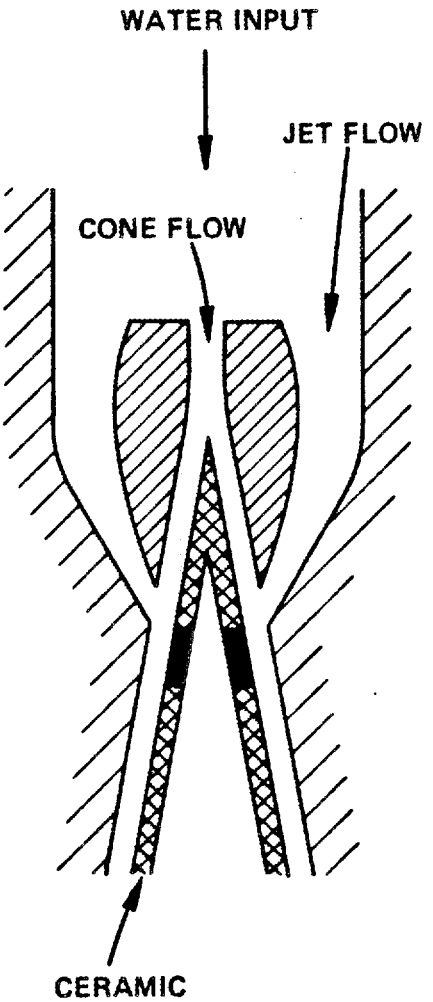

Figure 34. Jet Load

Boiling was detected at a reasonably low power level, about 80 kW pulsed. Visually, it was determined to be boiling just above and just below the point where the jet struck the cone. The area which had previously boiled without the jet, was no longer boiling.

The jet was axially adjusted by putting in some shims. Boiling again occurred in the same positions relative to the jet. This evidenced a very low water velocity in the areas adjacent to the jet, probably no more than a few feet/second. It also pointed out that, although the physical damage to previous loads occurred at the aforementioned hot spot, there is considerable power density throughout the entire top end of the cone and care must be taken to adequately cool this entire area.

In analyzing the waterloads built and tested using the ceramic cone, it was obvious that selective cooling of the cone was not as effective as cooling the entire cone with a baffle which kept the water velocity high over the entire surface. Additionally, it proved very helpful to be able to see the boiling; consequently, subsequent experimental loads were built in this manner.

The next load evaluated was the electromagnetic radial diverter (ERD), shown schematically in Figure 35. In this design, the rf entered the load, was spread by the diverter and collected at a reduced power density at the ceramic cylinder.

One load of this design was built and tested. The 56 GHz CW tube was used as a test vehicle. No boiling was observed up to a power level of 80 kW CW. However, some load arcing was noticed and the tests were terminated. The load was rebuilt with an improved diverter design and an improved termination between the cone and ceramic.

The next waterload designed, built, and tested improved the coolant entrance conditions and kept the water velocity high over the entire ceramic cone, which had proved especially important in the top portion of the cone. This is shown in Figure 36.

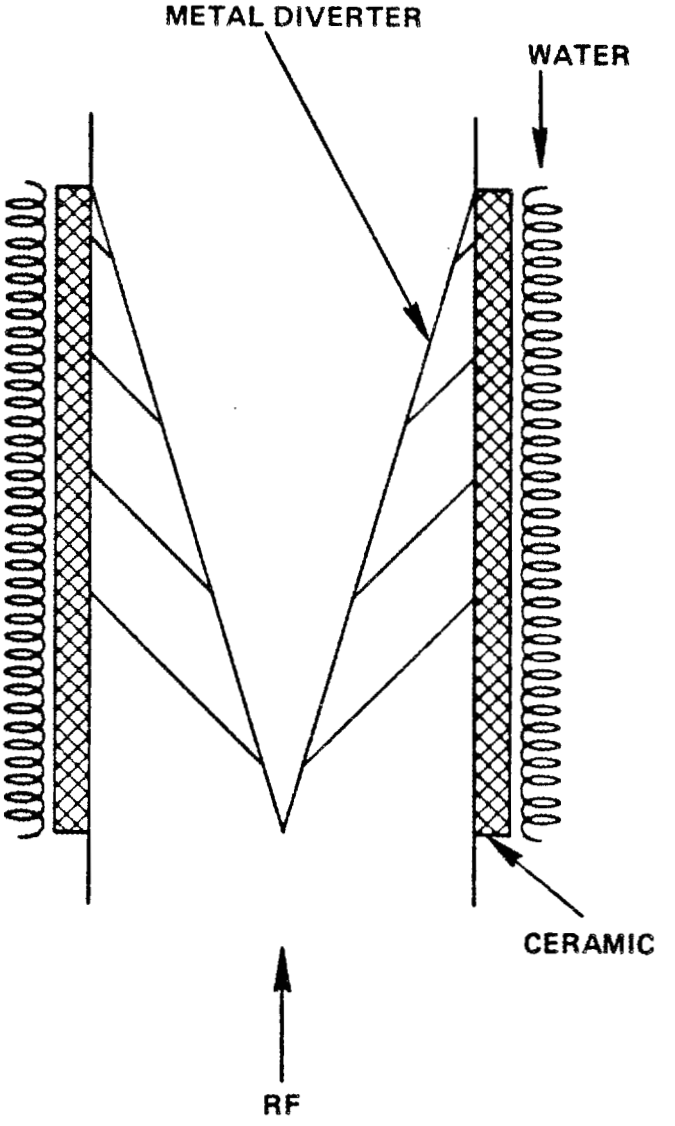

Figure 35. Electromagnetic Radial Diverter

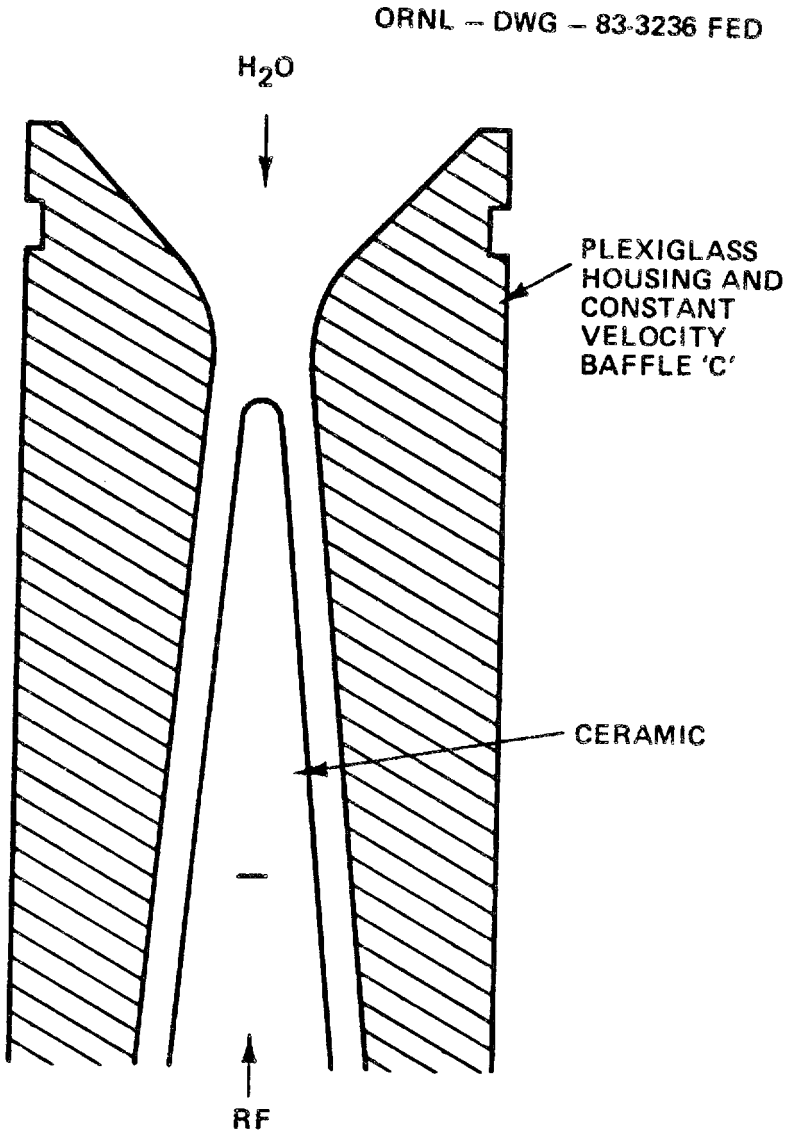

Figure 36. CW Load

The baffle was essentially the same as the one used with the pulsed load, except for the tapering at the top. This design was chosen over previous CW load baffles because previous designs were somewhat selective in increasing the water velocity in specific areas. Tests with the jet load showed conclusively that this is undesirable and that the water velocity must be kept high over the entire surface of the cone, especially the top end.

As can be seen from Figure 36, there is a very smooth, nozzle-like transition from the large 3" diameter Victaulic^{tm} (Victaulic is a trademark of Victaulic Co. of America for pipe couplings and fittings) to the end of the cone where the baffle starts, and the flow is well organized right from the start. Additionally, this load was made from clear plastic, which had two benefits. First, the areas of boiling can be observed using a video camera, and second, because O-rings are used, the baffle can be lined up exactly with the cone, which ensures constant water velocity around the cone. The load was designed to have a constant water velocity of 50 ft/sec at a flow of 100 GPM.

This load was tested using VGE-8006, S/N X-6. It was used both with and without a waveguide attenuator during these tests. With the load by itself, 160 kW CW was obtained with no boiling at 100 GPM water flow. Power was limited to this level during the test, due to the unavailability of the IR camera for monitoring window temperature at the time. The flow was lowered to 60 gpm, 30 ft/sec and boiling still did not occur at 160 kW. At 30 gpm, local boiling was observed at 82 kW CW and at 40 gpm, boiling was observed at 121 kW CW. At the 200 kW CW operating level, a waveguide attenuator was used in front of the load. Completely stable 200 kW operation was obtained with no boiling observed in either the attenuator or the waterload. In another test on a 60 GHz pulsed tube, 234 kW, at 100 ms was dissipated with no detectable boiling at 75 gpm. Although this combination of waterload and attenuator appears to work satisfactorily at the 200 kW CW, 60 GHz level, it is hard to extend the ceramic-cone-load

concept to much higher power and frequency levels. This is due to the high concentration of power, characteristic of the modes of interest. Because of this, work continued on the electromagnetic radial diverter.

For the diverter load, an analysis was carried out using geometrical optics principles to solve the problem of high power at the termination between the ceramic cylinder and the metal diverter which resulted in failure of the first ERD. The analysis showed that by choosing the initial angles of the cone carefully, the power could indeed be spread over a much larger area of the ceramic cylinder and greatly reduced at the termination which had failed previously. This concept is shown in Figure 37.

Two loads were designed using these principles. One was similar to the first ERD load using a 2-1/2" ID ceramic cylinder. The second was a larger, more conservative version. A cold test model of the smaller ERD was constructed and tested using a cavity exciter. It has an excellent match to both the TE_{02} and the TE_{22} cavity modes. Cold test probing of fields also confirmed the geometrical optics analysis relating to power distribution.

One conclusion which came out of the work done is that waveguide attenuators are useful in reducing the power which must be handled by the waterload. This will likely become increasingly important in the future for higher power and frequency requirements.

The work on calorimetric loads was de-emphasized at this point by direction of ORNL. Some construction work was done on the second radial diverter waterload on a low priority basis.

The ceramic cone waterload with improved tapered water flow, shown in Figure 36 was tested using X-6 without the preload attenuator to 198 kW. No boiling was observed; but minor arcing could be seen at the cone tip when this level was reached.

Because of this arcing, the preattenuator-waterload combination was used on subsequent CW testing.

ORNL – DWG – 83-3237 FED

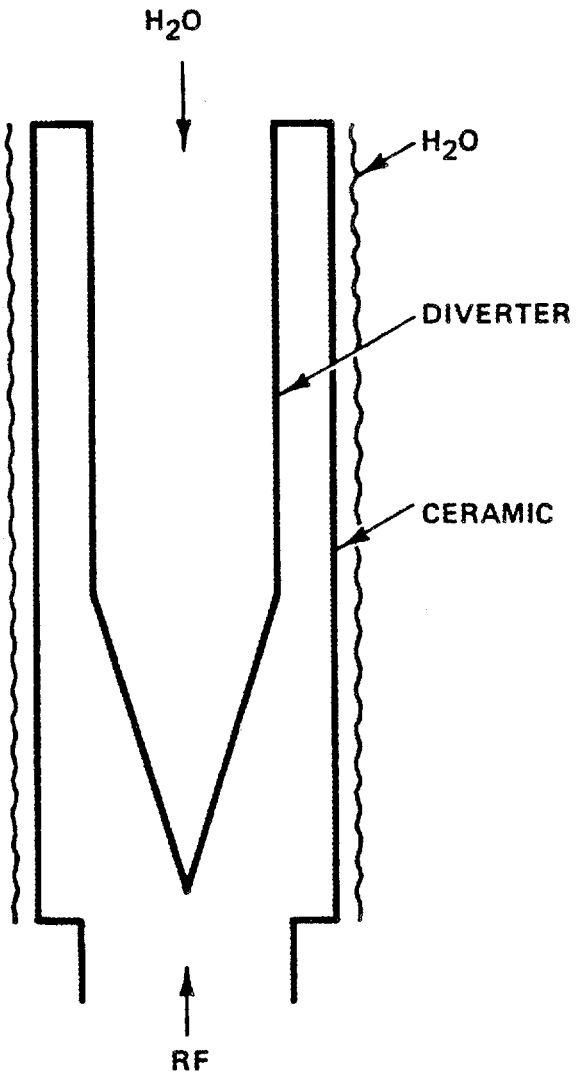

Figure 37. Redesigned ERD Water Load

This combination was used on X-7, which had a relatively pure (~90%) TE_{02} mode. No boiling was observed at 215 kW rf power at 500 ms pulse duration.

This concluded development work on the waterload.

B. FREQUENCY SAMPLERS AND ARC DETECTORS

A combination frequency sampler and arc detector was designed for 110 GHz, and parts were received.

After the program was redirected to 60 GHz, the frequency sampler and arc detector were redesigned. The frequency sampler portion was designed to cutoff up to the third harmonic of the design operating frequency of the gyrotron to prevent rf leakage into the fiber optics light guides. The arc detector included a test lamp for checking the arc detector system. The unit also includes a gas port for introducing dry nitrogen into the waveguide section, intended for applications located in humid climates. The outline is shown in Figure 38.

C. MODE FILTERS

Three types of mode filters were designed. The first was a water-cooled, stainless steel waveguide. The second filter alternated stainless steel rings and gaps, which were backed up by a water-loaded ceramic cylinder. The third consisted of a thin, ceramic cylinder backed by water as a loss material.

The water-cooled, stainless steel waveguide utilized the differential in loss between non-circular and circular electric modes. One of the advantages of rf heating is that the gyrotron can be located at a remote location with respect to the plasma vessel. Long waveguide runs of stainless steel guide would enhance the ratio of circular to noncircular modes.

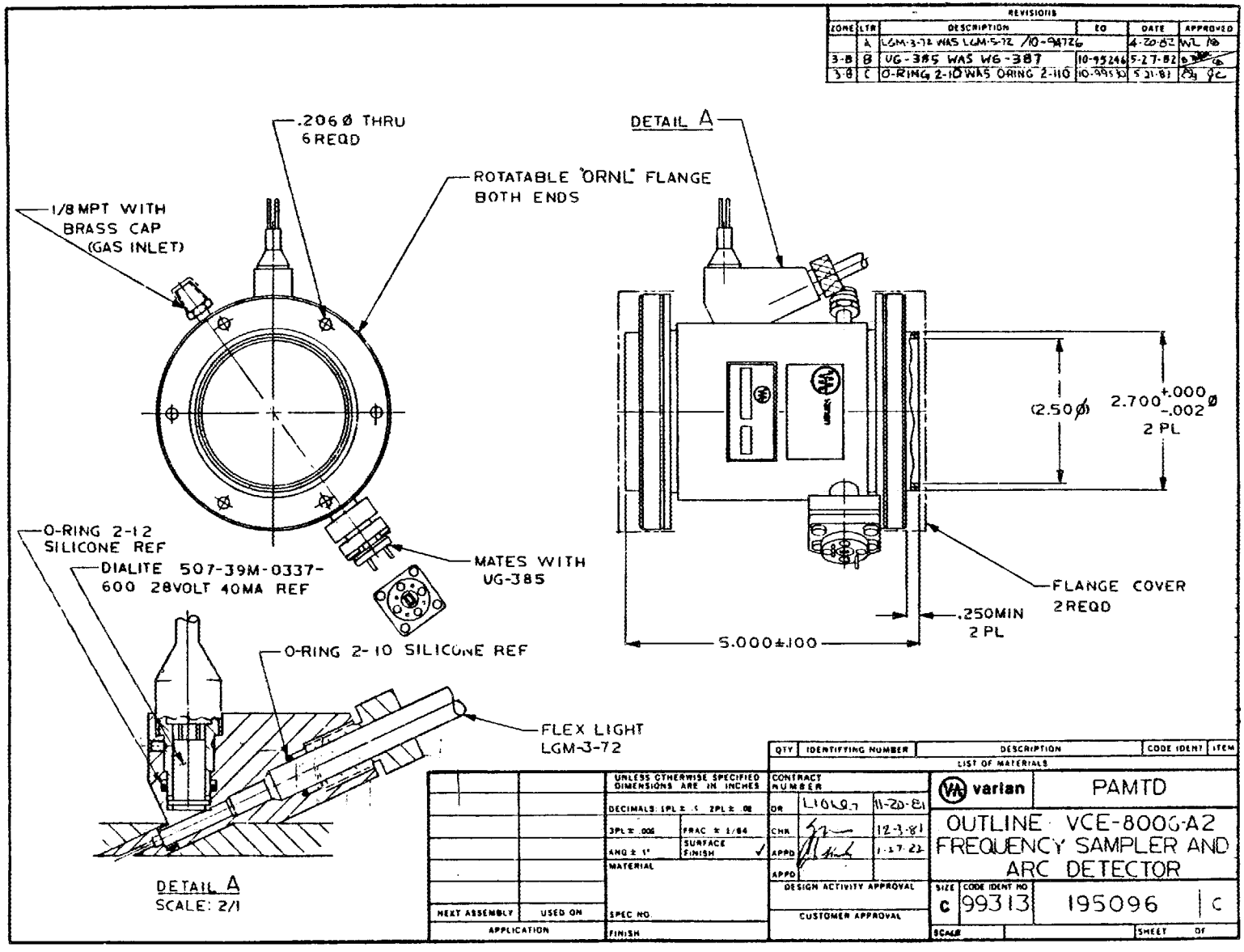

Figure 38. Outline VCE-8006-A2 Frequency Sampler and Arc Detector

In addition to the differential loss mechanism of the stainless steel waveguide, alternating stainless rings and gaps create breaks in the conducting wall for noncircular electric modes, but not for circular electric modes. Measurements, using a cavity launcher, indicated a VSWR of 1.04 or less from 50 - 60 GHz. The insertion loss was 1 dB for the TE_{11} mode, and would be increased if a smaller diameter waveguide were used.

The water-backed, ceramic cylinder mode filter, shown schematically in Figure 39, was both cold and hot tested. Figures 40, 41 and 42 show cold test results for noncircular electric mode transmission, circular electric mode transmission and reaction back on a 60 GHz cavity. In Figures 40 and 41, the heavy curve is the measured transmission in each case. The lighter curves are reference levels. The dotted curves in Figure 40 are the estimated levels obtained by plotting a smooth curve through the peaks of the reference curves. These results were very close to the original cold test setup, giving results of ~4 dB attenuation for the TE_{11} mode, ~ 0.3 to 0.4 dB attenuation for the TE_{01} mode, and a slightly better match for the cavity, due to improved mechanical design.

The filter was hot tested using a 60 GHz pulsed tube. Attenuation for the TE_{02} mode was very close to the cold test results of 0.3 dB, and attenuation for the TE_{22} mode was 3 dB, compared to the cold test of 4 dB. Attenuations for a group of low power modes which were observed between 49 and 51 GHz were 1.2 to 1.4 dB.

Further evaluation of the water wall mode filter is summarized in Table 8. The circular mode attenuation was verified at about 0.35 dB on several tubes at several frequencies, 53, 56 and 60 GHz. Methods of reducing this circular mode attenuation were studied. The best approach still appears to be some kind of helical structure in the water wall waveguide.

The 6" water wall filter appears to be a reasonable compromise between forward power loss, and gyrotron protection from reflection, in operating

ORNL DWG 83-2187

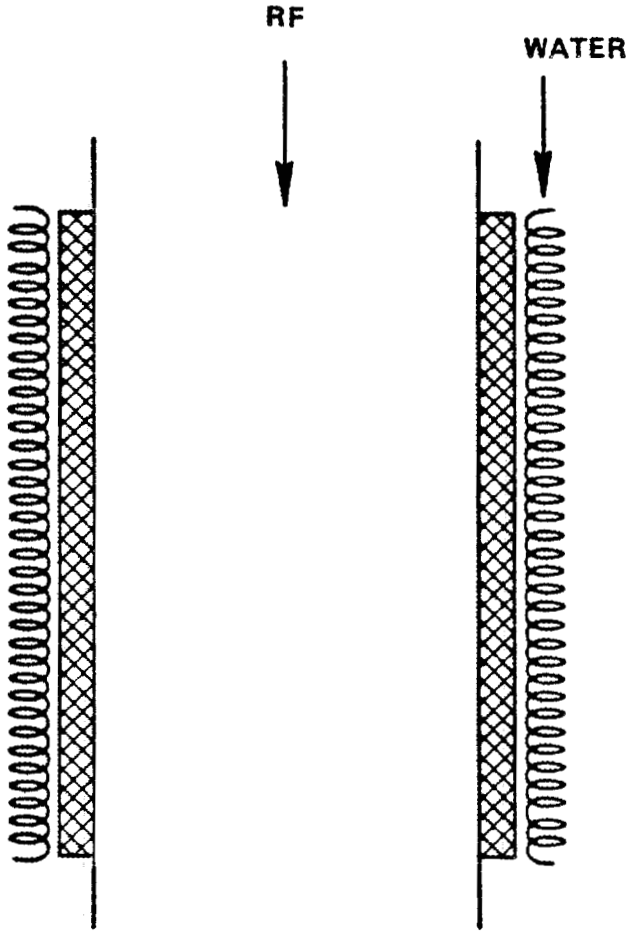

Figure 39. Water Wall Mode Filter

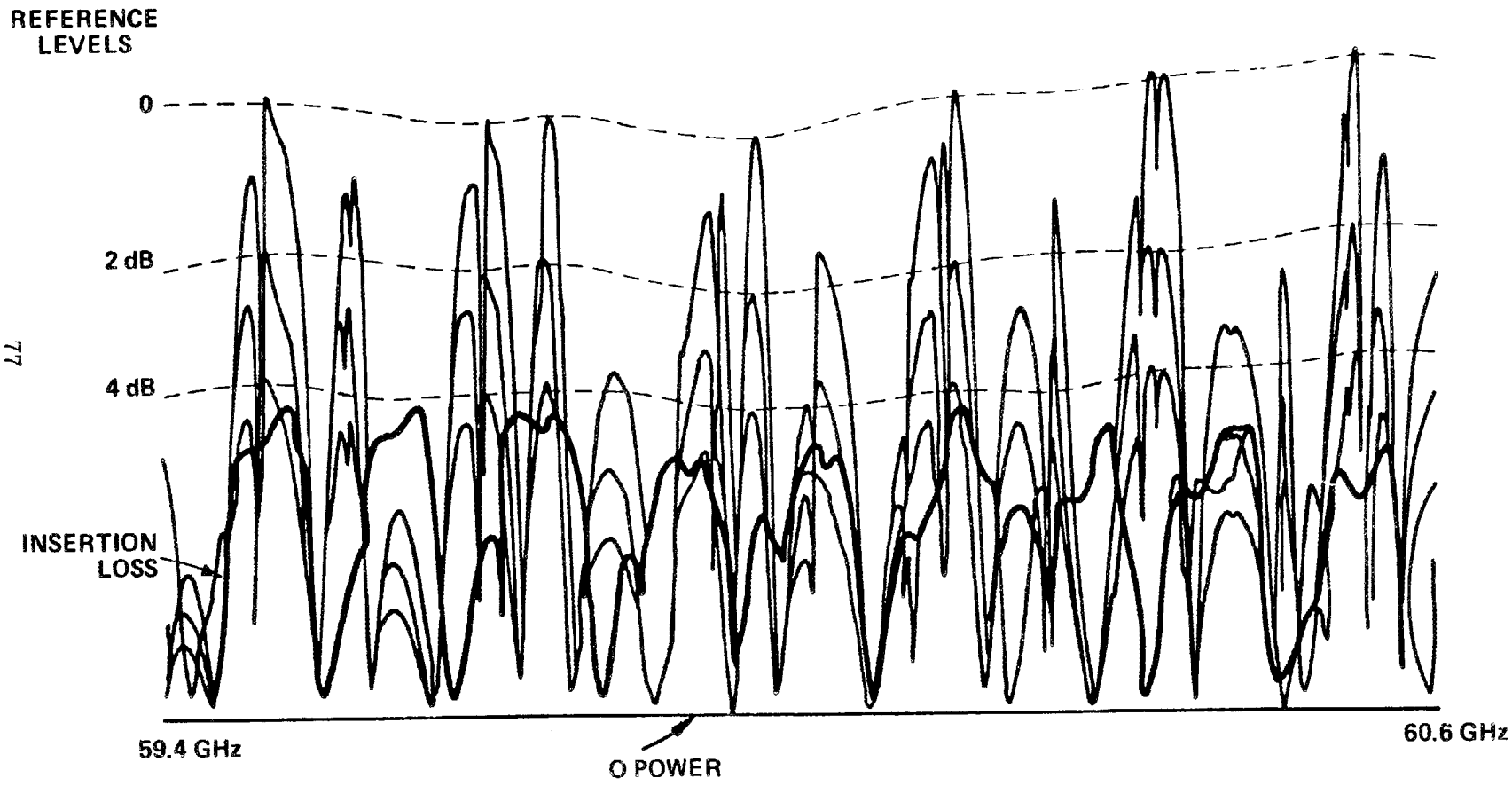

Figure 40. VFE-8006-A3 S/N 001, TE_{11} Transmission

ORNL DWG 83-2189

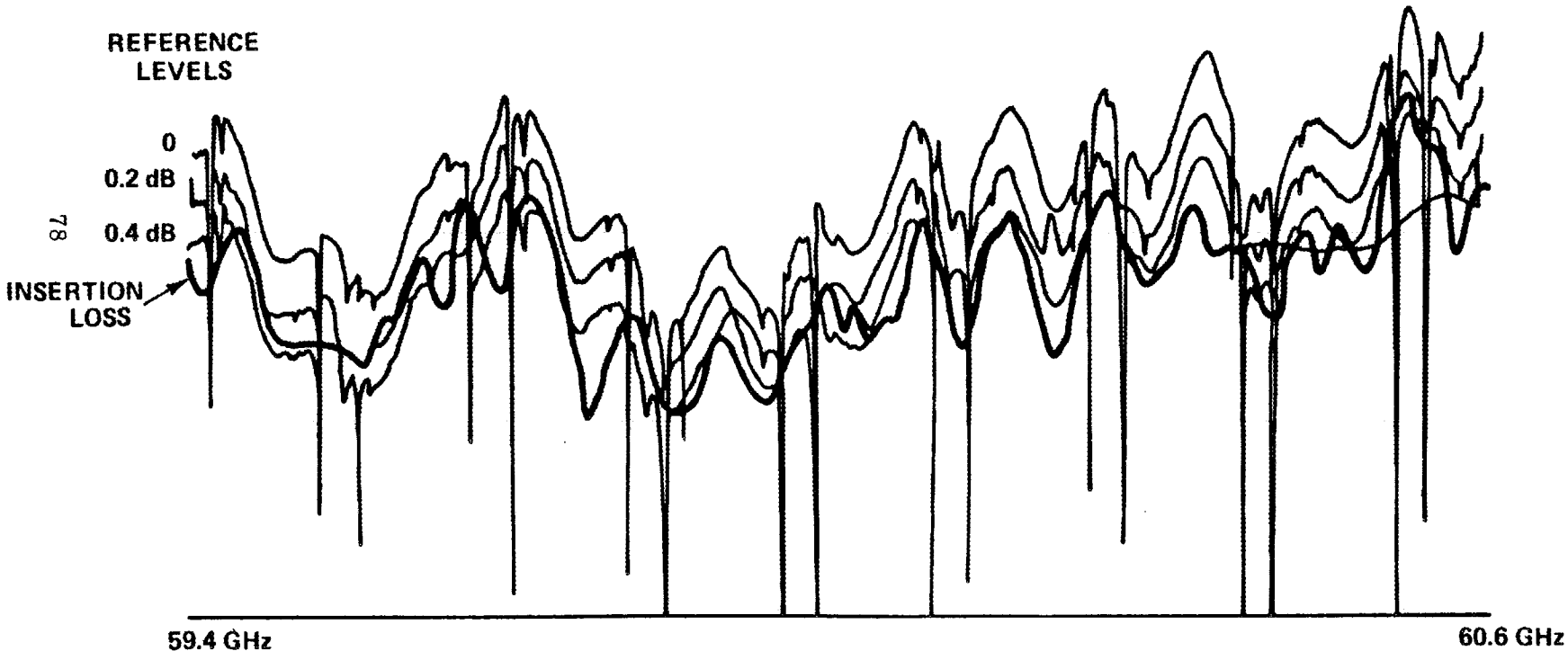

Figure 41. VFE-8006-A3 S/N 001, TE_{01} Transmission

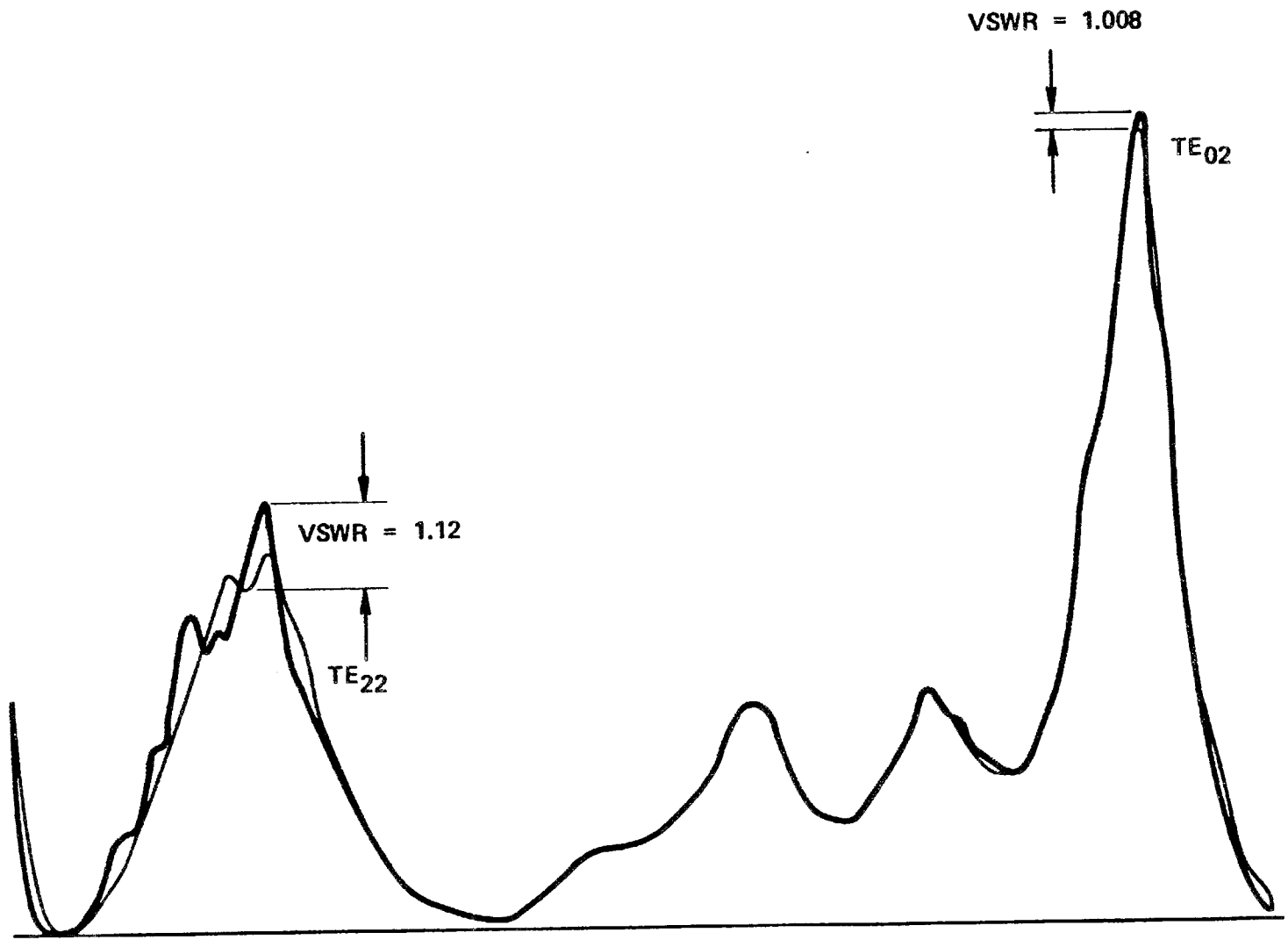

Figure 42. VFE-8006-A3 S/N 001, Response to Cavity Excitation

TABLE 8 TEST RESULTS---6″ WATER WALL MODE FILTER

TEST	CIRCULAR MODES	NONCIRCULAR MODES	
COLD TEST	0.35-0.4 dB TE01	4 TO 4.5 dB TE11	NOTE: 1.2 TO 1.4 dB 50 GHz MODES
HOT TEST	0.4 dB TE02	3-3.2 dB TE22	

COMPARISON OF WATER WALL TO OPEN WAVEGUIDE

CIRCULAR MODES:	MODE FILTER:	=	0.4 dB
	AIR GAP	=	0.7 dB
NONCIRCULAR:	MODE FILTER:	=	3.0 dB
	AIR GAP	=	4.2 dB

systems. Further efforts to improve the discrimination between circular and noncircular modes would be desirable, and will still require much more effort.

D. MITER BEND

A 90° miter bend was designed, built and cold tested. Measurements, using a cavity launcher, indicated a VSWR of 1.06 or less in the frequency range of 59 to 60 GHz. An outline of the elbow is shown in Figure 43.

E. FLANGE ADAPTER

Adapters for male and female 28 GHz flanges, copper-gasketed flanges and Oak Ridge flanges were designed and built to allow use of all waveguide components available. The adapters consisted of short sections of 2-1/2-inch diameter copper waveguide with various flanges mounted on the ends.

F. ATTENUATORS

Two approaches were investigated for attenuators. The first was a lossy metal wall waveguide, and the second was the water wall guide previously described in the mode filter section of this report.

Several lossy waveguide coatings were evaluated at 60 GHz. These included stainless steel, chrome oxide (i.e., wet hydrogen-fired stainless steel), barium titanate, and titanium dioxide. These were all evaluated in a 3/8" circular waveguide. These tests showed that chrome oxide had twice the attenuation of stainless steel, is easy to obtain, and very stable over a wide range of temperatures. Titanium dioxide showed, by far, the most attenuation, but the effect of the relative roughness of the applied plasma spray in the 3/8" guide was not evaluated.

Some interesting observations were made with the 9" long water wall attenuator used in conjunction with the waterload on X-6. There was much

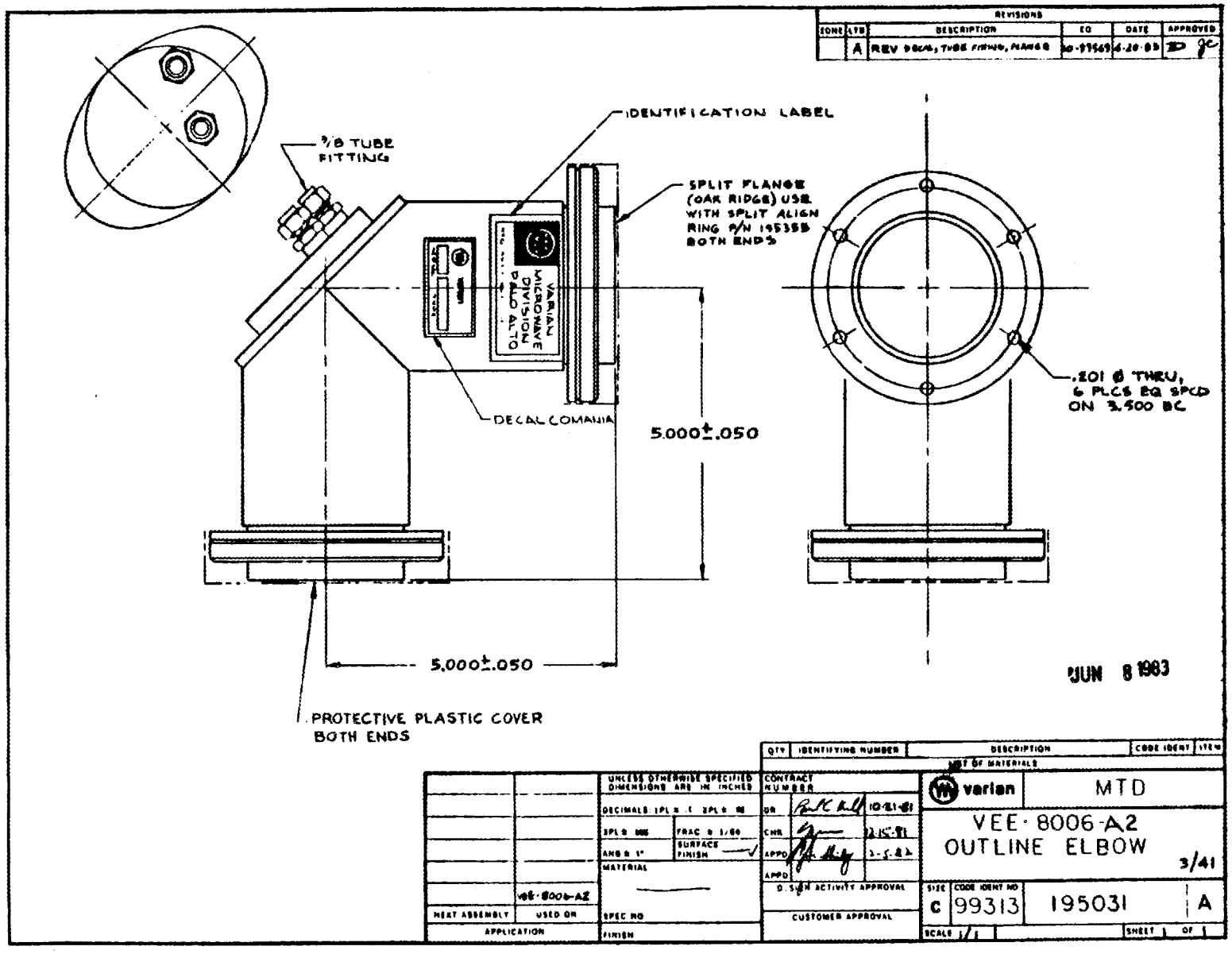

Figure 43. VEE-8006-A2 Outline Elbow

more power dissipated in the attenuator than had been expected on a simple dB/ft extrapolation from the 6" water wall mode filter.

Comparing these results with the air gap measurements showed that, indeed, the dB/ft extrapolation is invalid in highly optical systems past a length of about 6" for 60 GHz TE modes in 2-1/2" waveguide. When the metallic waveguide is severed and the gap reaches a certain value, the attenuation increases more rapidly. This is reasonable because the severed guide should look more like an antenna as the gap is increased. As a result, practical waveguide attenuators can be built for TE modes without requiring mode conversion. For the water wall, for instance, the relation between length and attenuation was 0.4 dB for 6", 1.4 dB for 9", and 3 dB for 12". The attenuation of the attenuator used in X-6 was slightly more than 1.4 dB, but that was probably the result of mode impurity.

VI. 60 GHz 200 kw PEAK OSCILLATOR DESIGN

A. ELECTRON GUN

The gun was designed using a mean cathode radius of 0.22", with a cathode loading of 3 A/cm^2. The cathode angle was 25°. The first anode potential was 22 kV. A 67% filling factor at the gun exit allowed adequate clearance between the beam and the first anode.

A trajectory calculation for this design, using eighteen trajectories, is shown in Figure 44. Assuming adiabatic compression, the mean transverse energy at the circuit was 64,755 volts. The transverse velocity variation was $\pm$ 1.3%. This variation was calculated statistically from the weighted transverse energies of each trajectory.

A plot of the transverse energy profile for a 42.5° slope rear focus electrode is shown in Figure 45. Simulations were also run for 40° and 45° slopes of the rear focus electrode, but 42.5° gave the best results. Plots for 40° and 45° are shown in Figures 46 and 47.

The normalized transverse velocity profile for the final design is shown in Figure 48.

The effect of a longitudinal displacement of the gun, with respect to the magnetic field, was studied during the preliminary design phase. The results of a $\pm$0.015" displacement are shown in Figure 49.

The same superconducting solenoid magnet coil locations as in the 110 GHz design were assumed, though of course, the coils would be run at lower current. The field at the interaction circuit is 25 KG. The field at the cathode is approximately 1300 gauss.

The magnetic field values used in the simulations were computed from the magnet's off-axis vector potentials. These were calculated by means of complete elliptic integrals. The difference between this method and that

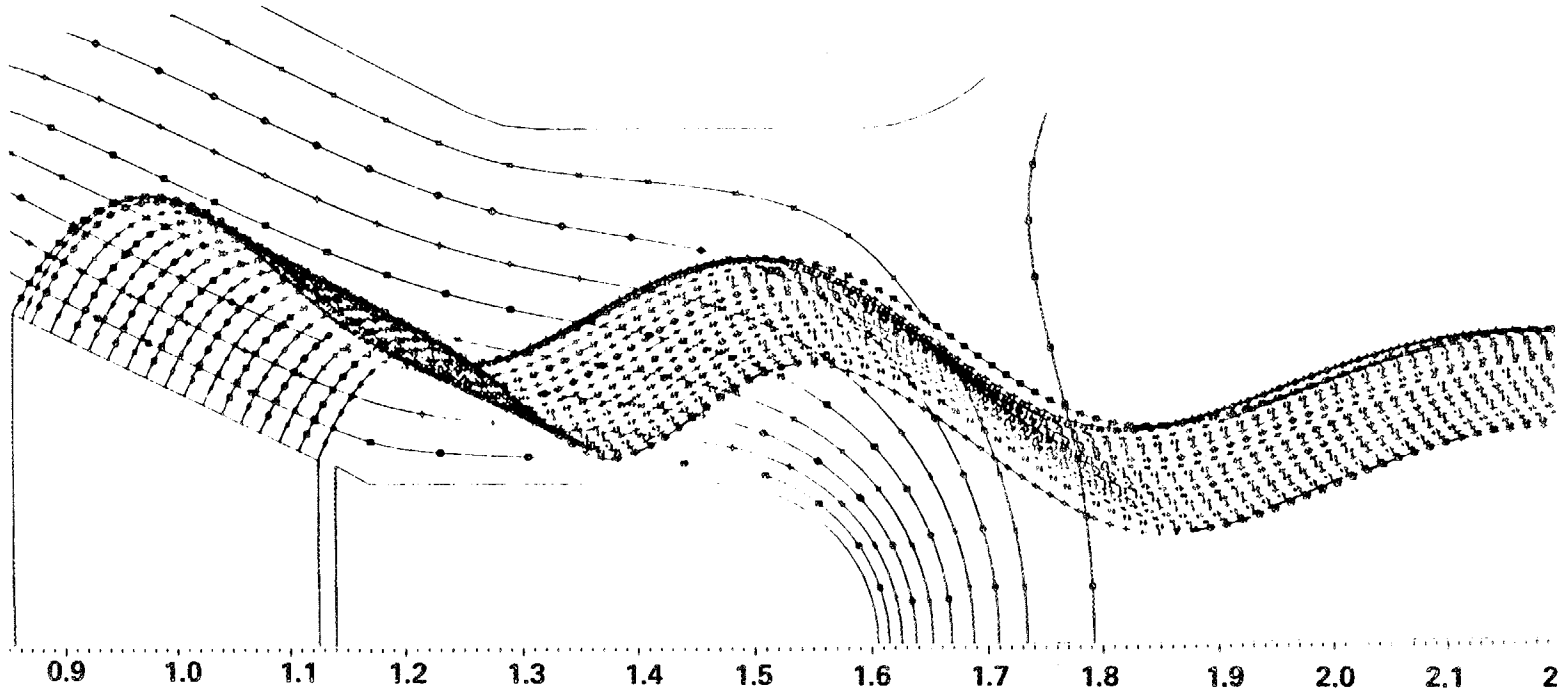

Figure 44. Electron Trajectory Plot for 60 GHz Gun

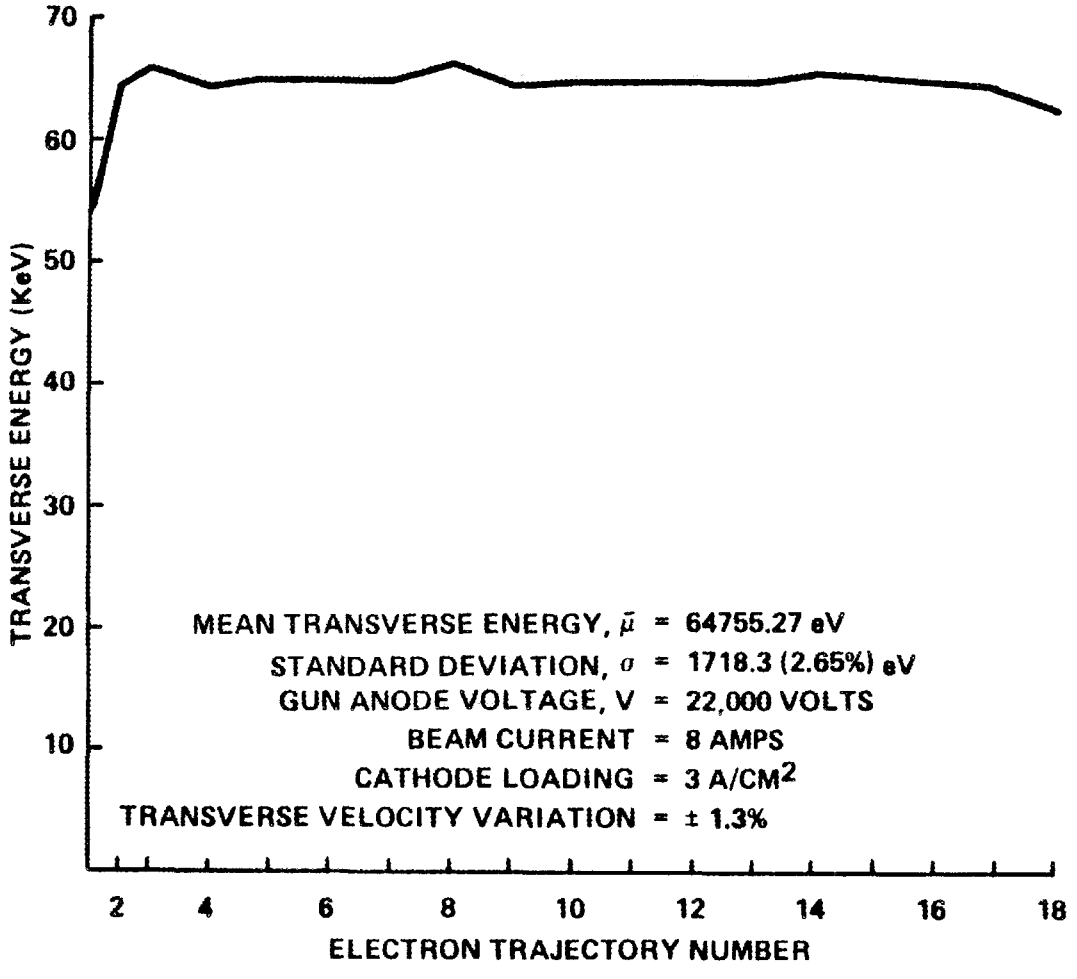

Figure 45. Transverse Energy Profile for 42.5° Slope Rear Focus Electrode (60 GHz)

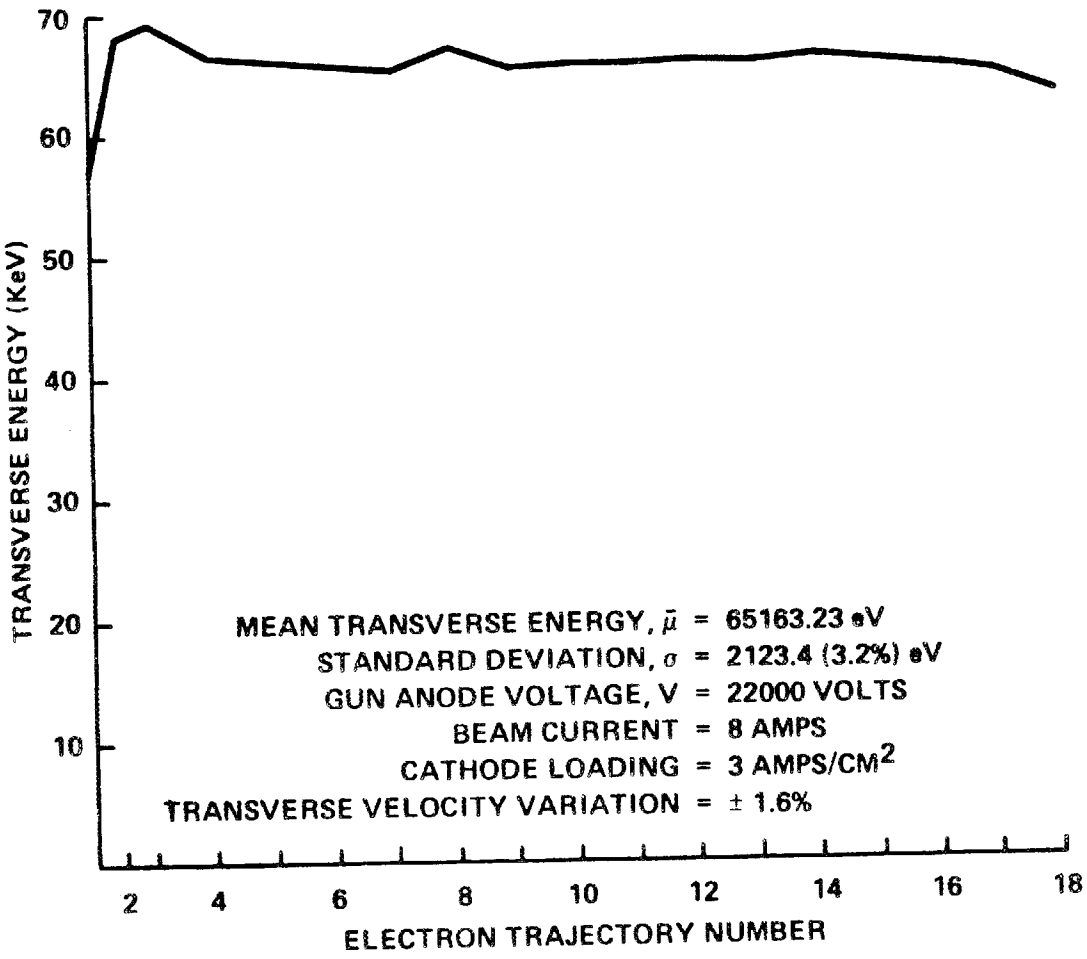

Figure 46. Transverse Energy Profile for 40° Rear Focus Electrode (60 GHz)

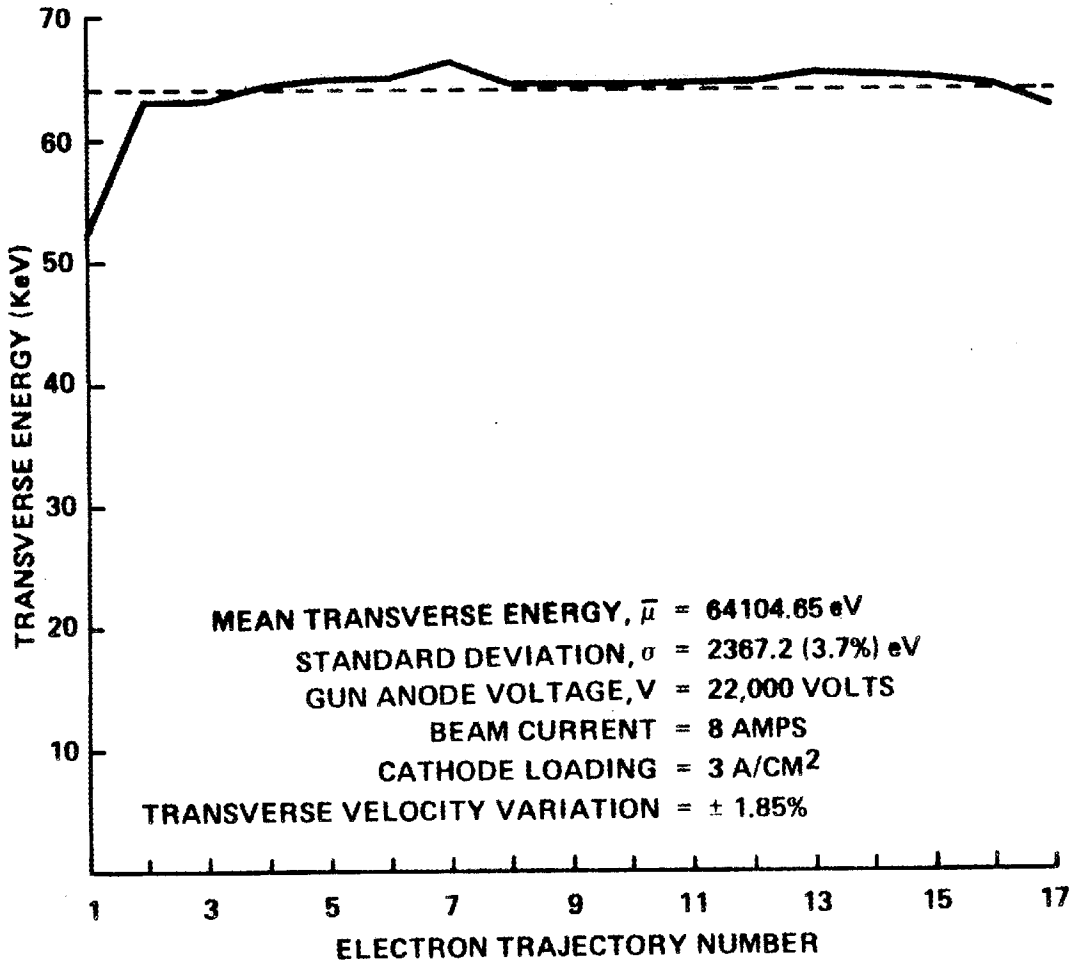

Figure 47. Transverse Energy Profile for 45° Slope Rear Focus Electrode (60 GHz)

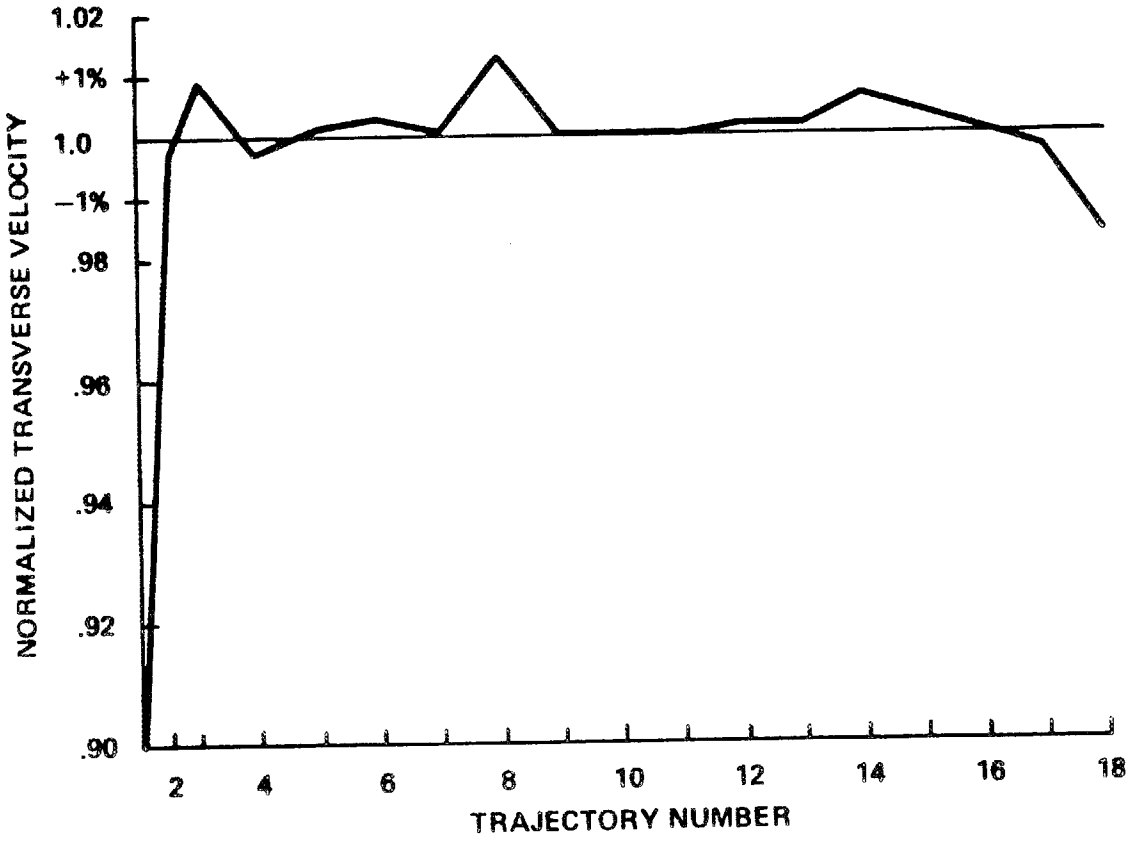

Figure 48. Normalized Transverse Velocity Profile (60 GHz)

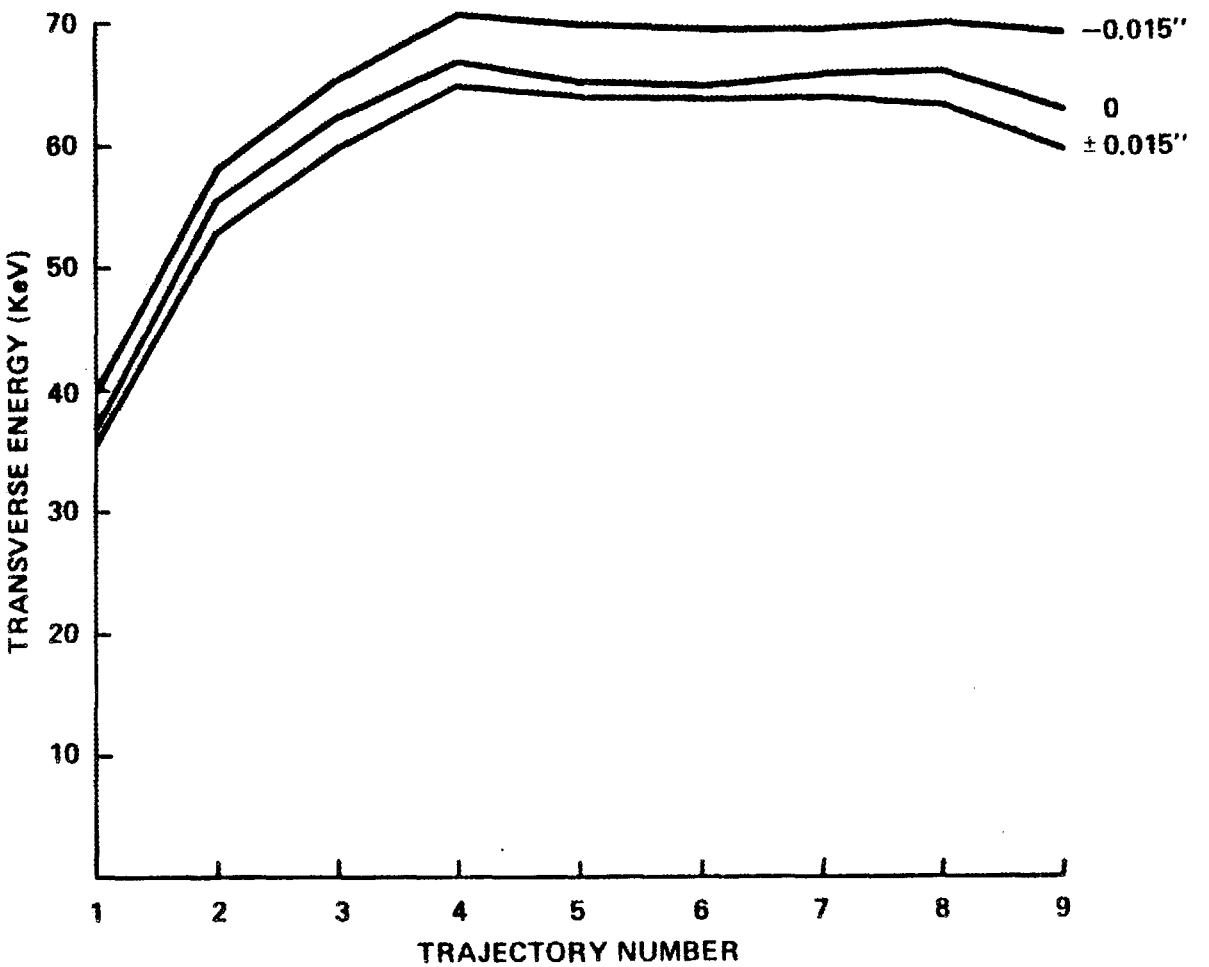

Figure 49. Transverse Energy Profile as a Function of Longitudinal Displacement of Gyrotron with Respect to Magnetic Field

computed by expansion from axial field on the transverse energy profile in a typical case can be seen in Figure 50.

The nominal beam current is 8 amperes. Simulations were made for beam currents of 6 and 10 amperes. These results are shown in Figure 51.

The transverse velocity spread for a 6 ampere beam was $\pm 1.6\%$, and for a 10 ampere beam was $\pm 2.1\%$, compared to the $\pm 1.3\%$ for the design value of 8 amperes.

The 60 GHz gun design was subjected to computer analysis to calculate the magnitudes of the dc electric field normal to the surfaces of the negatively-biased electrodes. This work was done to ensure that surface gradients would contribute minimally to the generation of an arc in the gun region.

The calculations were done using a Varian computer program which solves Laplace's equation in cylindrical coordinates (by finite element methods) for the potential in a given two-dimensional region. The fields were then determined by calculating the gradient of the potential distribution in a desired direction. Surface gradients were then obtained by matching a power dependence on radius of the field to calculated values near the electrode, and extrapolating to the electrode surface.

Figure 52 depicts a computer-generated plot of the electrical geometry in the gun region, showing the cathode support and focusing structure, the gun anode, and the body of the tube. It also shows the gun ceramic and the solenoid dewar. In the computer program, the gun ceramic is modeled as a finite thickness cylinder. The figure shows the potential distribution when the tube is turned on (i.e., with the gun anode at 25 kV and the body at 80 kV, with respect to the cathode potential). The surface gradient was calculated both for this turned-on configuration and for the turned-off case, with the gun anode biased 2 kV below cathode. In general, the surface gradient was higher for the turned-off case at the gun anode surface, and was higher in the turned-on case at the tip of the cathode structure (front focus electrode).

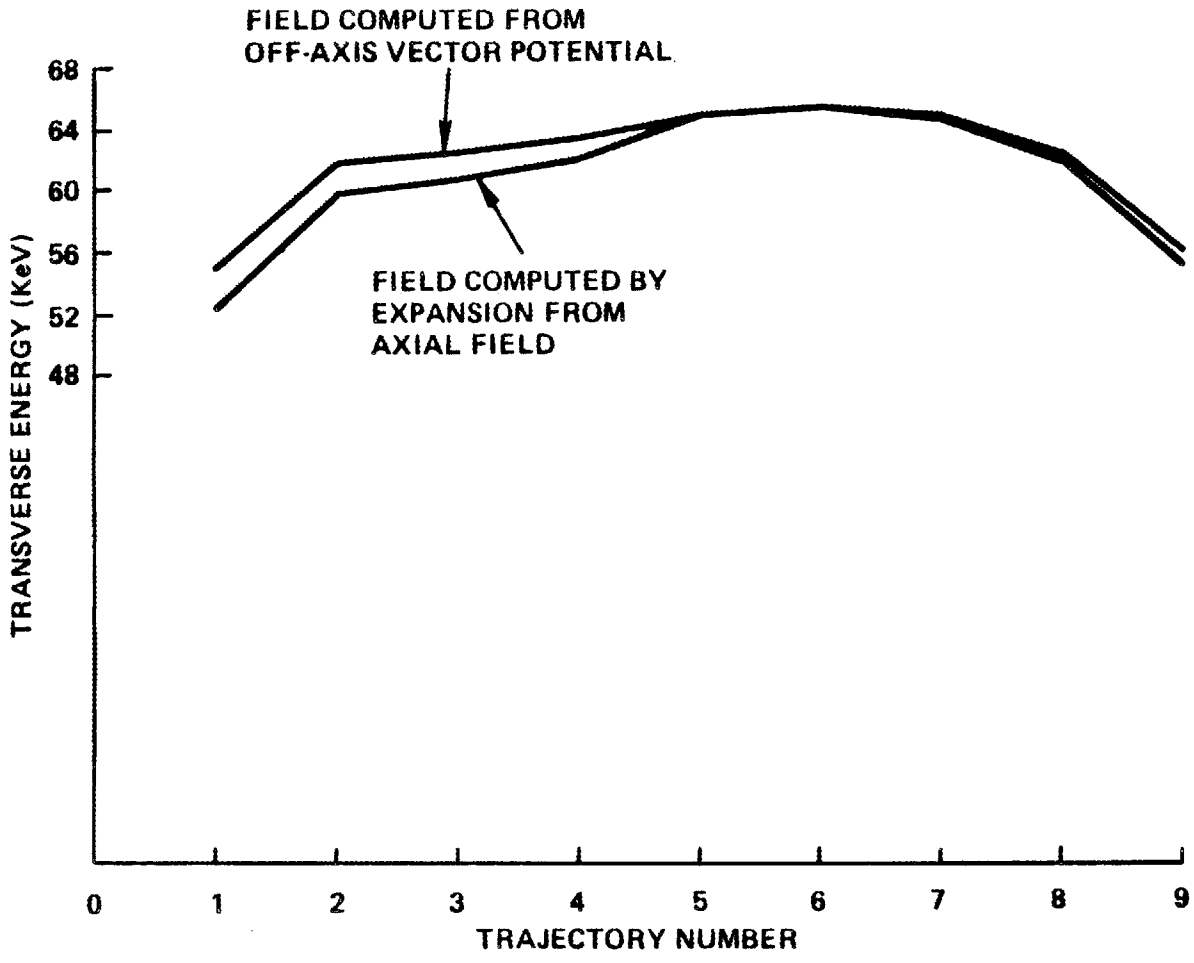

Figure 50. Effect of the Difference Between Two Methods of Calculating Off Axis Magnetic Fields on the Transverse Energy Profile

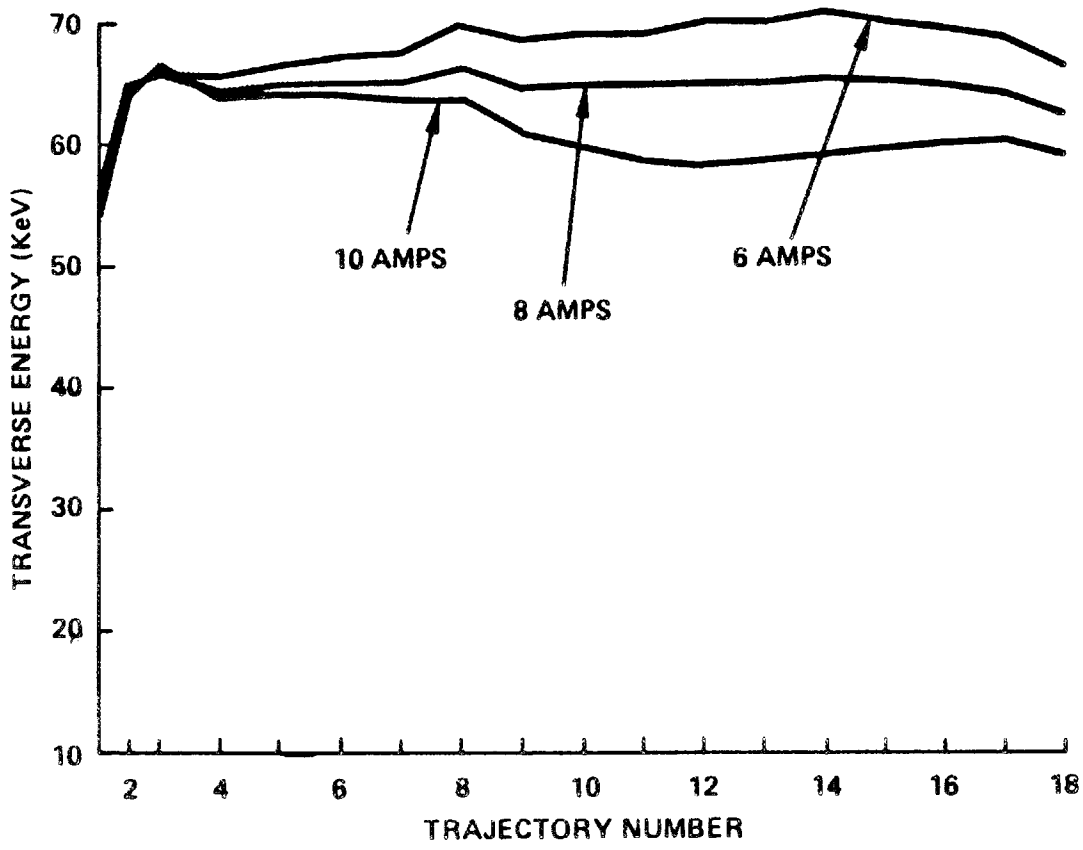

Figure 51. Variation of Transverse Energy Profile vs Beam Current

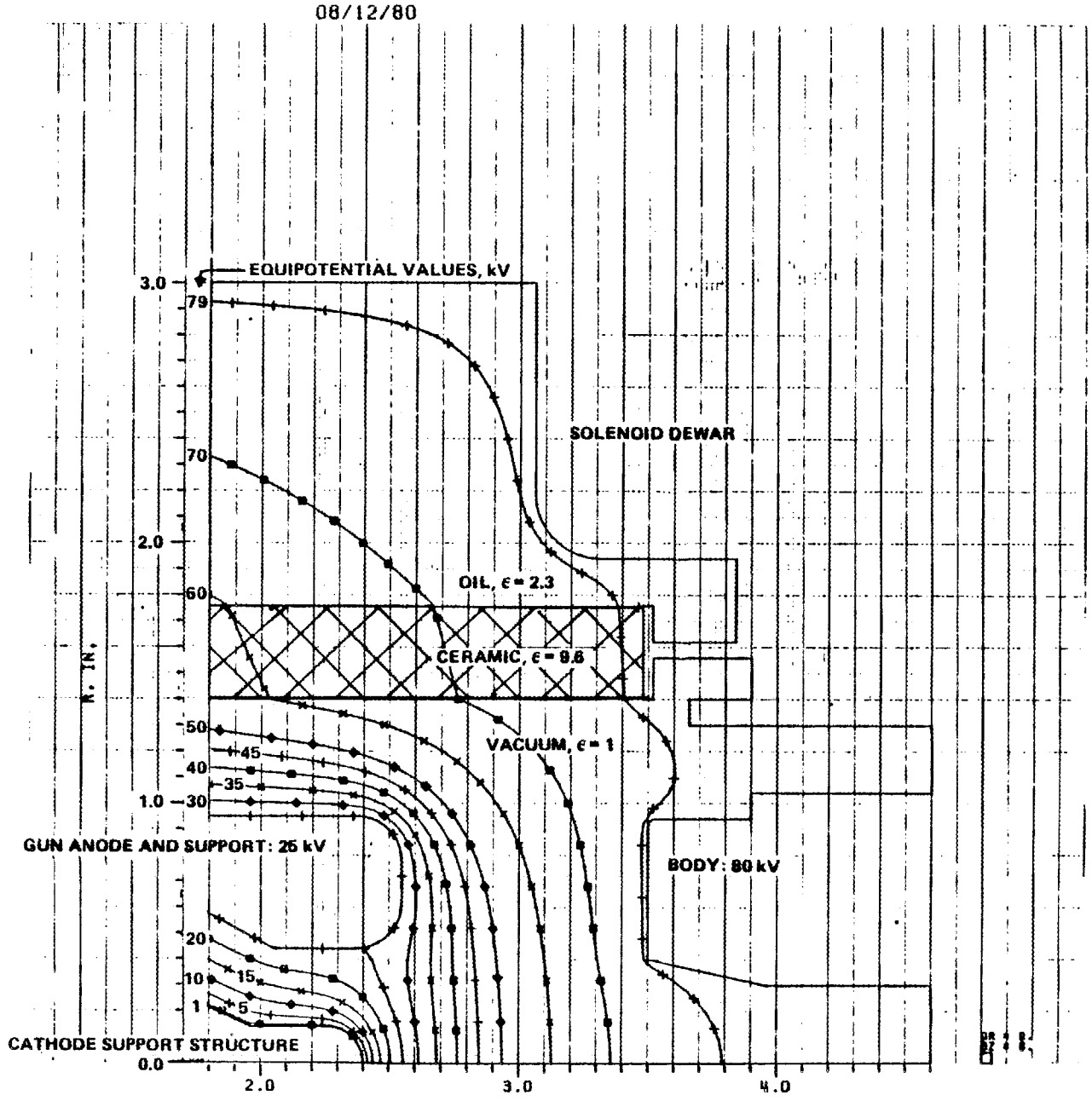

Figure 52. Gradients for Original Gun Pulsed On

Attention was focused on locating the maximum surface gradients of the gun anode and cathode front focus electrode. These two areas are shown in Figure 52. Figure 53 is a magnified view of these two locations, indicating where the surface gradient was calculated to be maximum.

Gun anode voltage gradient reduction was desirable. The most straightforward approach was to increase the radius of curvature of the gun anode piece that had the maximum calculated surface gradient. If the maximum outside diameter and length of the gun anode were to remain constant (to preserve beam optics and ceramic gradients), a larger radius of curvature could easily be accommodated. This change in the shape of the gun anode is shown in the computer-generated plot of Figure 54, which shows the change in potential distribution for the new shape. The calculated maximum surface gradient was in the same direction as for the previous design, but the magnitude of the maximum gradient decreased by 20%. This relatively small change in gun design geometry, accompanied by a very significant decrease in the maximum surface gradient, lessened the chances of arc formation in the gun.

For the case shown in Figure 54, the maximum voltage gradients at the gun anode and the tip of the cathode focus electrode are given in Table 9 for on and off conditions.

Table 9
Voltage Gradients

	ON	OFF
Gun Anode	60 kV/cm	90.5 kV/cm
Cathode Tip	119 kV/cm	42 kV/cm

The heater required 20.5 watts of heater power for 8 A beam current, about 30% of that required for the 28 GHz gyrotron. This is the result of both a smaller cathode button and an improved potted heater design.

The beam quality from this gun is good from the standpoint of obtaining 200 kW rf power from the 60 GHz gyrotron. The main beam parameters which

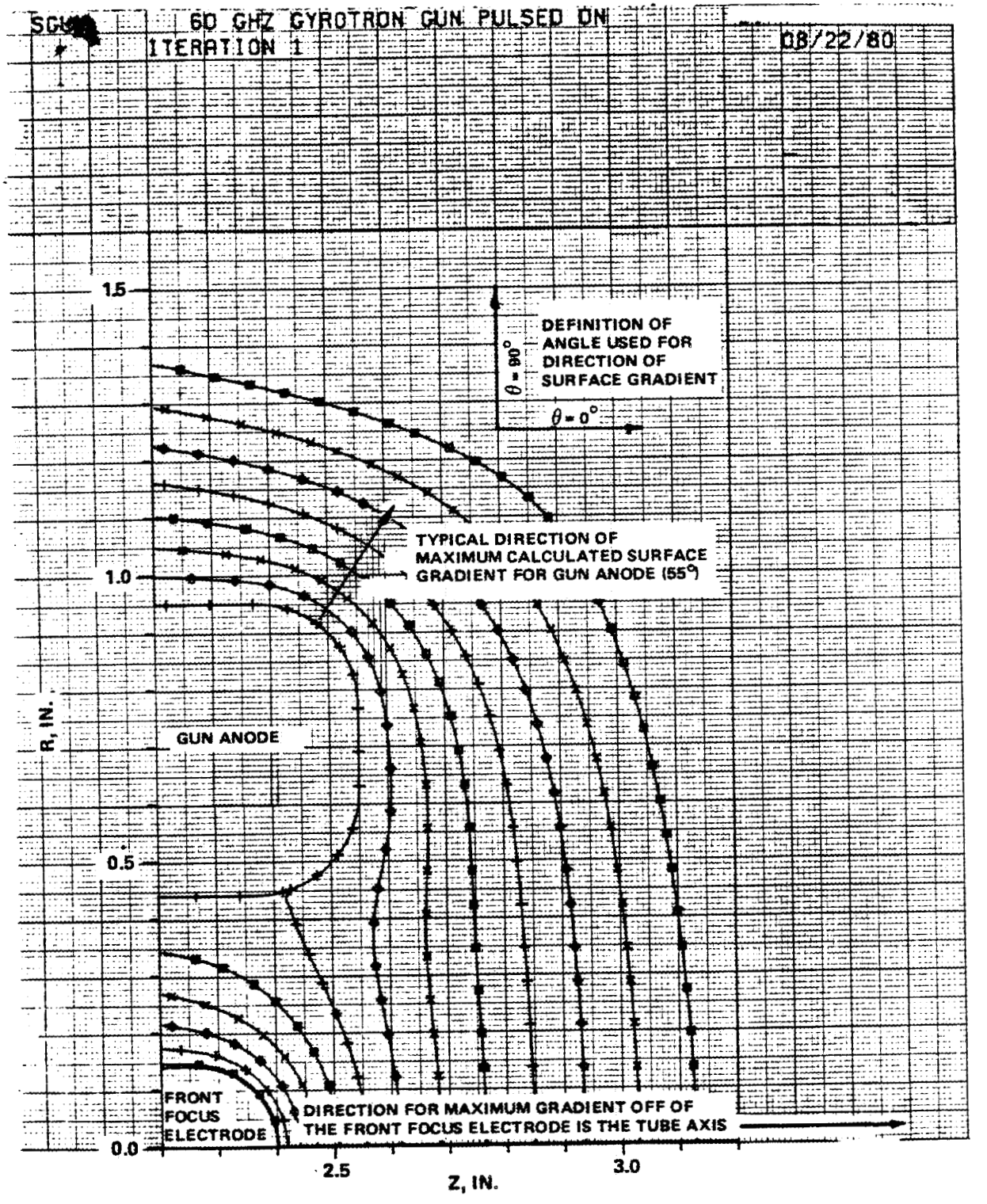

Figure 53. Magnified View of the Gradient for the Original Gun

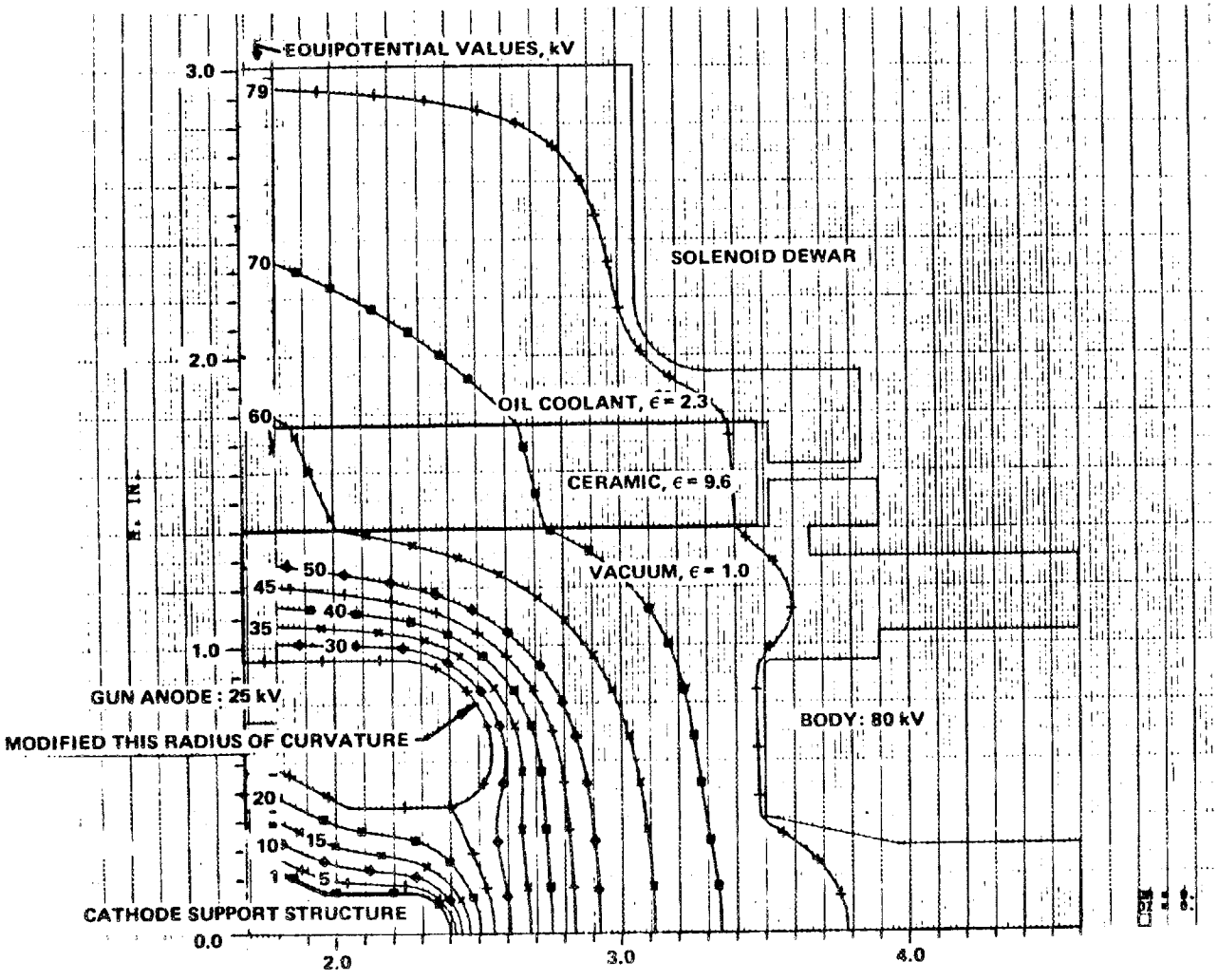

Figure 54. Gradients for Modified Gun

affect rf performance are the transverse velocity ratio ($v_\perp/v_\parallel$) and the velocity spread ($\Delta v_\perp/v_\perp$). These parameters, to some extent, affect the dynamic range of the tube, that is, in the variation of the rf output power using the gun anode voltage.

The principal limit on dynamic range is mode competition, primarily from the TE_{221} mode. Additional restraints are set up by the variation of transverse velocity with gun anode voltage. The variation of output power with gun anode voltage for a typical early 60 GHz gyrotron is shown in Figure 55.

A typical oscillation map shows that TE_{02} power can be obtained over a gun anode voltage range of about 1000 volts at the high efficiency magnetic field setting. However, because of the variation of power shown in Figure 55, 200 kW output power could be achieved over only about 350 volts of this range. While this affected operating stability, it was not the limiting factor in obtaining a large dynamic range. For this, the mode competition problem needed to be resolved.

An area of concern in the present gun is sputtering of material from the front focus electrode when it is bombarded by ions coming down the center of the hollow electron beam. This material ends up on adjacent electrodes, as well as on the high voltage insulator. The sputtering does not appear to affect tube performance over the short term. However, because of the ceramic, it may have an effect on long life and it definitely slows down tube processing.

Design work to decrease or eliminate the sputtering to critical areas was performed. First, consideration was given to making the front focus electrode out of Poco Graphite (A high performance graphite for specialty applications manufactured by Poco Graphite, Inc., affiliated with Union Oil Company of California.) to minimize ion sputtering effects. Second, several computer runs were made on positioning the cathode back far enough to eliminate line of sight sputtering on the ceramics.

Dwg 82-2259 FED

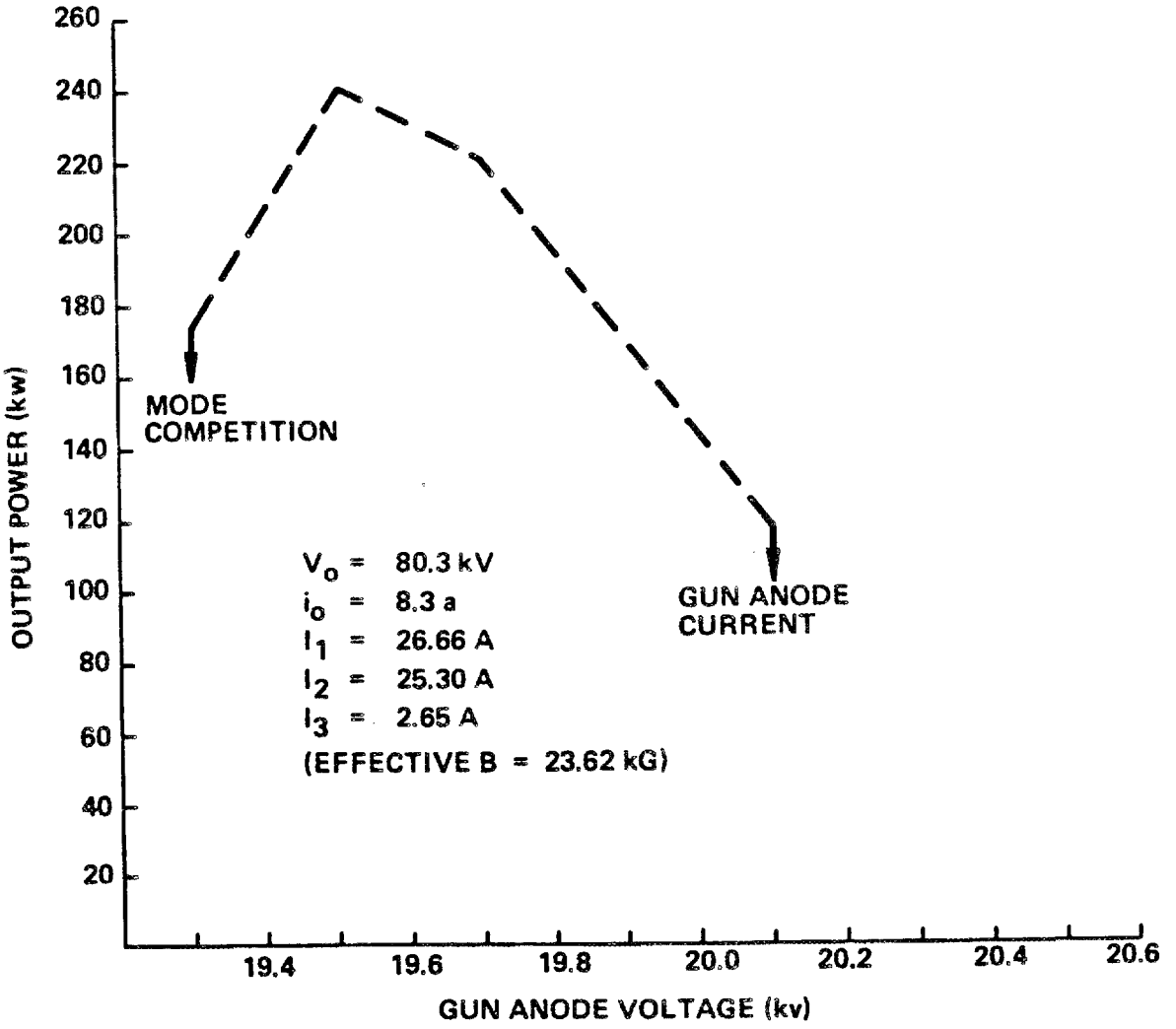

Figure 55. Power Sensitivity to Gun Anode Voltage for VGE-8060 S/N 004

As a fabrication test, Poco graphite was successfully brazed, using a diffusion brazing technique, to molybdenum. High strength diffusion bonds were successfully made through the formation of carbides.

Piece part drawings and fabrication were completed for the gun with a Poco graphite front-focus electrode, and assembly was started. Assembly included additional pinning which had been recommended for this material.

A sample calculation of the recessed cathode design is shown in Figure 56. This can be compared with the original design shown in Figure 44. The important parameters of α (transverse velocity to axial velocity ratio) and velocity spread were preserved from the original design. For example, the calculation of Figure 56 resulted in a beam with $\alpha = 1.6$ and $\Delta v_{\parallel}/v_{\parallel} = 4.8\%$. A slightly higher anode voltage resulted in calculated values of $\alpha = 2$ and $\Delta v_{\parallel}/v_{\parallel} = 5\%$.

Both the Poco graphite and recessed cathode gun efforts were terminated. Some sputtering of molybdenum on the gun electrodes and ceramic is still seen, and some difficulty in initial tube aging continues. These effects are minor enough that further work on the gun was not considered necessary. In addition, the recessed cathode could adversely affect microwave performance, and the present operation of the gun is reasonably satisfactory.

B. ANODE

The beam tunnel design is sketched in Figure 57. This assembly is composed of the second anode electrode face on one end, and the load cavity on the other end. Following the adiabatic compression of the electron beam, the beam tunnel diameter contracts as it extends toward the interaction circuit. To prevent parasitic oscillations in the beam tunnel, this region was designed for high rf loss. SiC-BeO (silicon carbide-loaded beryllia) loss rings were alternated with metal beam shaving rings to provide an axisymmetric loss structure. The SiC-BeO rings are recessed, with a larger inner diameter than the beam shaving rings, to prevent electrostatic charging by stray electrons. To avoid any cylindrical structure which is

ORNL-DWG-83-2157

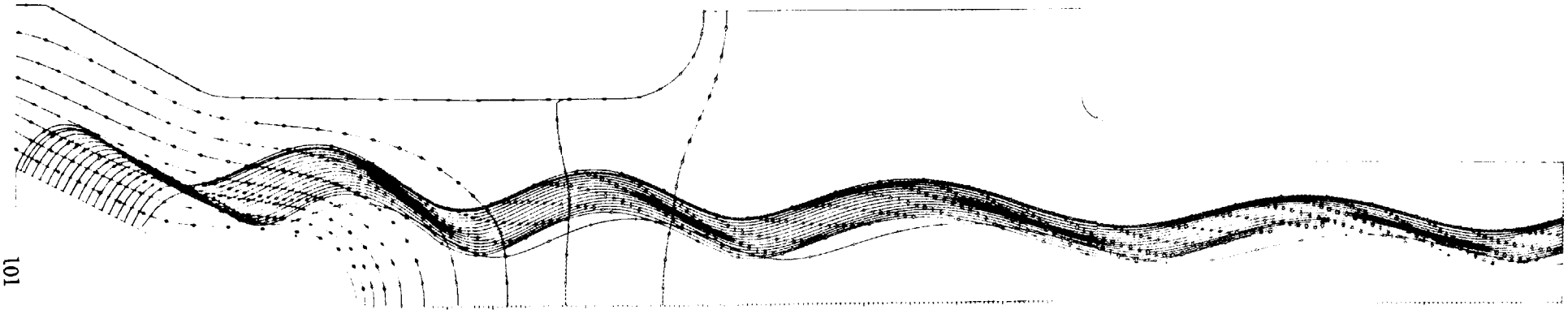

V_o = 80 kV
I_o = 8 A
V_{MA} = 22 kV

Figure 56. Calculation for Gun with Recessed Cathode

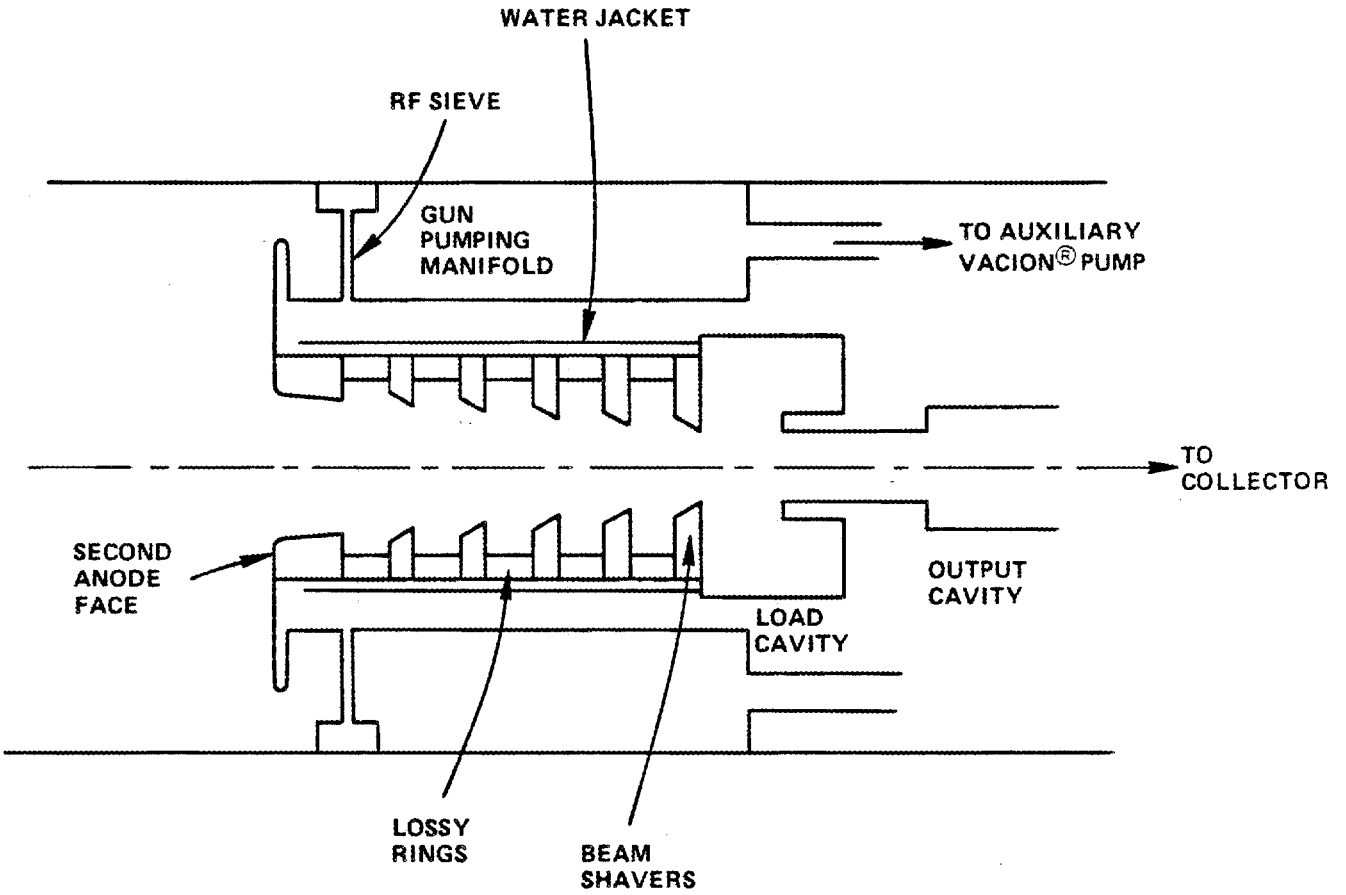

Figure 57. Anode

capable of exciting oscillations, the individual metal beam shavers have conically-tapered beam holes. A variety of braze joints used in the ceramic anode subassemblies were tested for strength, bonding uniformity, and their ability to withstand the thermal cycling of subsequent brazing operations. These subassemblies required a bond between the faces of a silicon carbide-loaded beryllia washer and thin copper caps, as shown in Figure 58. For the fabrication trials, two of the most appropriate Varian active metal braze processes were selected. The active metal braze requires excellent surface contact between the copper caps, the ceramic, and the active metal braze material. The braze fixture is designed to guarantee good surface contact by taking advantage of differential expansion between the jig and the assembly to hold the joint under compression at braze temperature.

The anode subassembly shown in Figure 58 represents a particularly difficult application of this technique because of the large differential radial expansion between the ceramic and the copper. Once the braze joint is formed at high temperature, the differential radial contraction during cooldown (approximately 0.014") tends to shear the joint. If the joint is initially strong, but brittle, then during cooldown either the joint or the ceramic will crack. If, on the other hand, a weaker but more ductile bond is employed, the shear can be relieved by the elasticity of the joint. In spite of its lower strength, the ductile joint was chosen for the anode subassemblies because of its resistance to cracking, even after repeated thermal cycling.

To check the metallurgical quality of the braze joints in the test samples, a cross section of the brazed assembly was examined with the scanning electron microscope for active metal, silicon, and copper. The cross section is shown in Figure 59. No sign of excessive active metal migration into the copper or the ceramic was evident; no diffusion of silicon into the copper cup was found, either. These scans indicated that the assemblies were brazed for the proper time and temperature and that the active metal braze joints were properly formed.

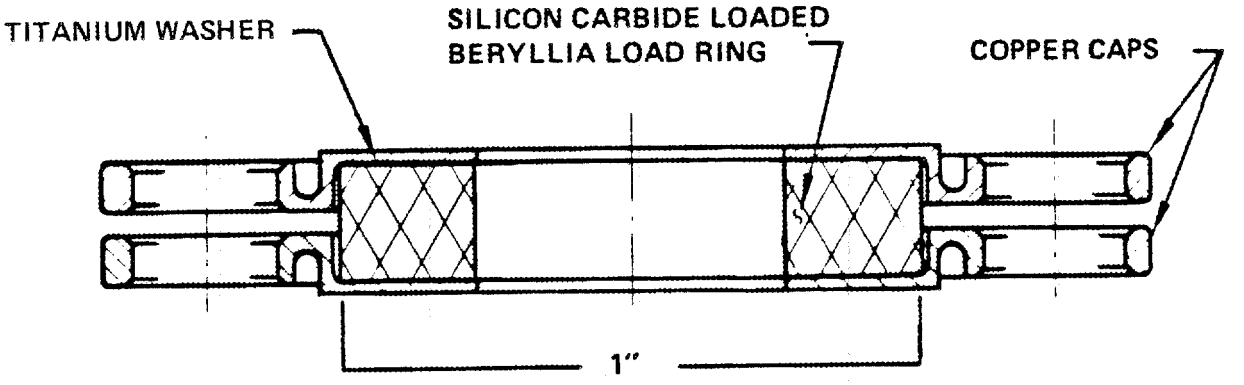

Figure 58. Load Ring Assembly

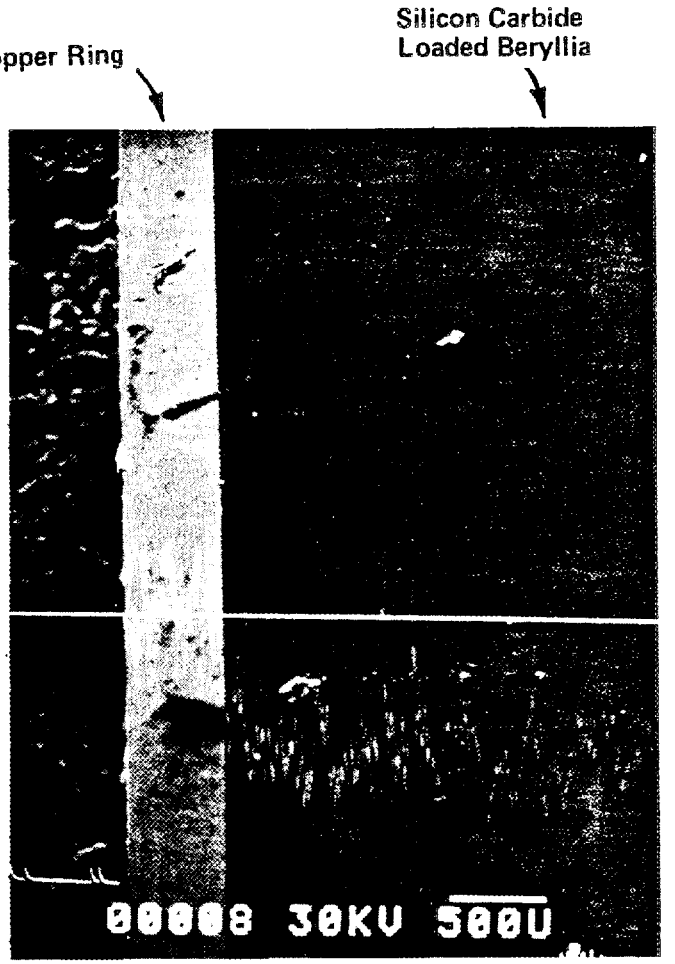

A. Active Metal Line Scan of Braze Joint Cross Section (Copper to Silicon Carbide Loaded Beryllia)

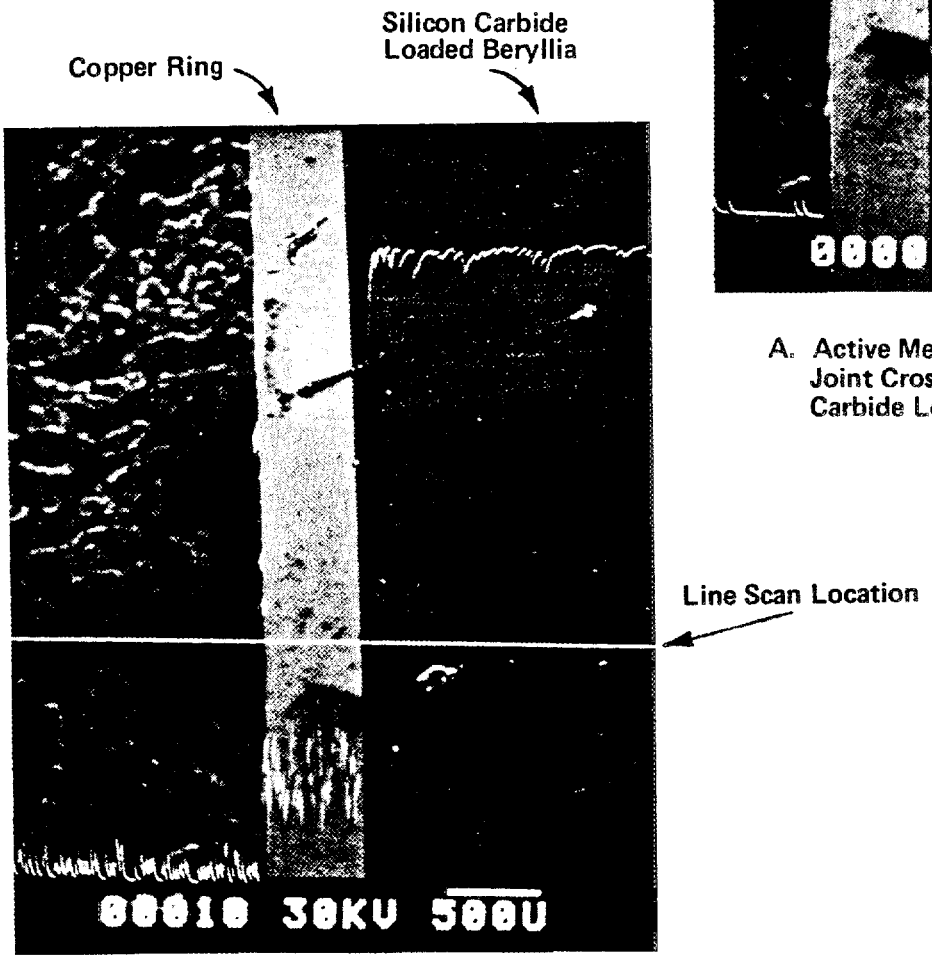

B. Silicon Line Scan of an Active Metal Braze Cross Section

Figure 59. Cross Section of Brazed Assembly

The strength of the braze joints was determined by peel testing. The assemblies were cut into semicircular halves and the copper cups were peeled off. The peel strength was then determined according to

$$\text{Peel strength (lb/in)} = \frac{\text{Peel force (lb)}}{\text{Width of peel strip (in)}}$$

The brazed assemblies were also subjected to thermal cycling on a schedule similar to that which would be required of each subassembly during subsequent brazes of the final anode assembly. The subassemblies were placed in a molybdenum boat, fired in dry hydrogen at 1010°C for 10 minutes and allowed to cool to room temperature. This cycle was repeated twice before peel testing. Six samples were brazed and tested. The results are given in Table 10.

From the six tests, one joint, made of ductile braze alloy, sample 3, demonstrated the highest peel strength, even after thermal cycling. However, samples 5 and 6 showed substantially lower peel strengths. The brittle braze alloy joint, Sample 4, also showed a high bond strength. The break in this sample did not occur in the interface, but in the silicon carbide-loaded beryllia. Figure 60 shows that the break was caused by the thermal expansion differences between the materials. The poor bond strengths of samples 1 and 2 are due to insufficient braze alloy at the interfaces.

Although the number of samples was inadequate to obtain statistically valid measurements of braze joint properties, the qualitative evidence favors the use of the ductile braze joint in the anode subassemblies.

Cracked Silicon Carbide Loaded Beryllia Piece on Copper Ring

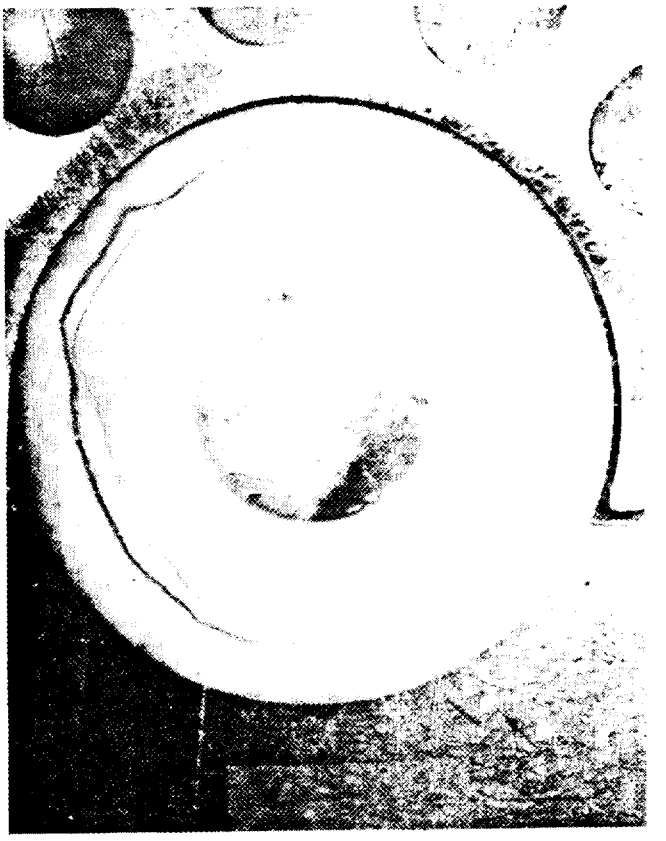

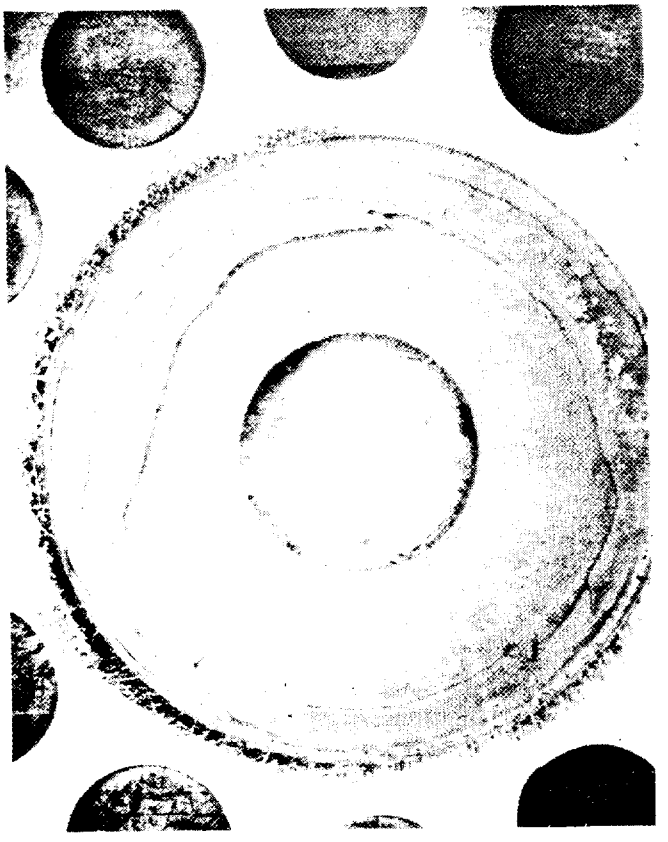

Copper Ring with Pieces of Silicon Carbide Loaded Beryllia Attached

Figure 60. Cracked Surfaces After Thermal Cycling

Table 10
Peel Tests

Sample No.	Braze Joint	Peel Strength (lb/in)	Remarks
1	Brittle	43	No thermal cycle.
2	Brittle	--	Top copper piece fell off of silicon carbide-loaded beryllia ring during thermal cycle. Insufficient braze alloy.
3	Ductile	166	After three thermal cycles at 1010°C.
4	Brittle	(1) 114	Two tests were performed: (1) Peel test before thermal cycle. (2) The remaining parts of the sample were thermal cycled at 1010°C three times. No peel test was done, because the joint failed under the radial shear caused by thermal expansion mismatch between the two materials.
5	Ductile	32	No thermal cycle.
6	Ductile	43	After thermal cycle at 1010°C.

To avoid cathode poisoning during gas bursts in the tube, it is necessary to provide sufficient ($\gtrsim 1$ L/sec) pumping speed at the gun. Unfortunately, because of space restrictions, the gyrotron VacIon^{tm} pumps (VacIon is a Varian Associates, Inc. trademark for an ion pump) must be located at the collector end of the tube. The beam tunnel is then used as the pumping path to the gun. A separate gun pumping manifold has become necessary in high frequency gyrotrons because, as the beam tunnel diameter

is reduced, the pumping speed of the beam tunnel drops sharply, as shown in Table 11.

Table 11
Pumping Speed

Device	Frequency (GHz)	Pumping Speed (ℓ/s)
VGA-8000	28	3.0
VGE-8060	60	0.4
VGT-8010	110	0.05

The gun pumping manifold surrounds the beam tunnel assembly and terminates near the face of the second anode. A separate 8 L/sec VacIon pump connects into the pumping manifold via a long large diameter pumping line, which runs toward the collector end of the tube.

Past experience has shown that the gun end of the pumping manifold must be baffled with an rf sieve to avoid rf heating of the auxiliary VacIon pump. The sieve must attenuate rf without cutting down on the pumping speed. Assuming that the sieve will contain a large number of long, circular cross section holes, the optimum hole size for good pumping speed, combined with good rf attenuation, lies in a narrow range, as shown in Figure 61. With this sieve design, the gun pumping system provides a total pumping speed estimated to be 2 L/sec at the gun.

C. INTERACTION CIRCUIT

Cold test cavities for the 60 GHz oscillator were fabricated, and the TE_{02} cavity, when properly loaded, had an external Q of 520 $\pm$ 50.

Experience with the 28 GHz oscillator indicated that modes other than the desired cavity mode may compete for interaction with the electron beam. Particularly troublesome modes were those with the same radial mode number and roughly the same frequency as the desired mode. The competing mode densities of a 60 GHz TE_{01}, and a 60 GHz TE_{02} cavity, are compared in Figure 62. Sister modes of TE_{011} and TE_{021} with axial mode numbers greater than unity, and all other modes with axial mode numbers greater than six, have

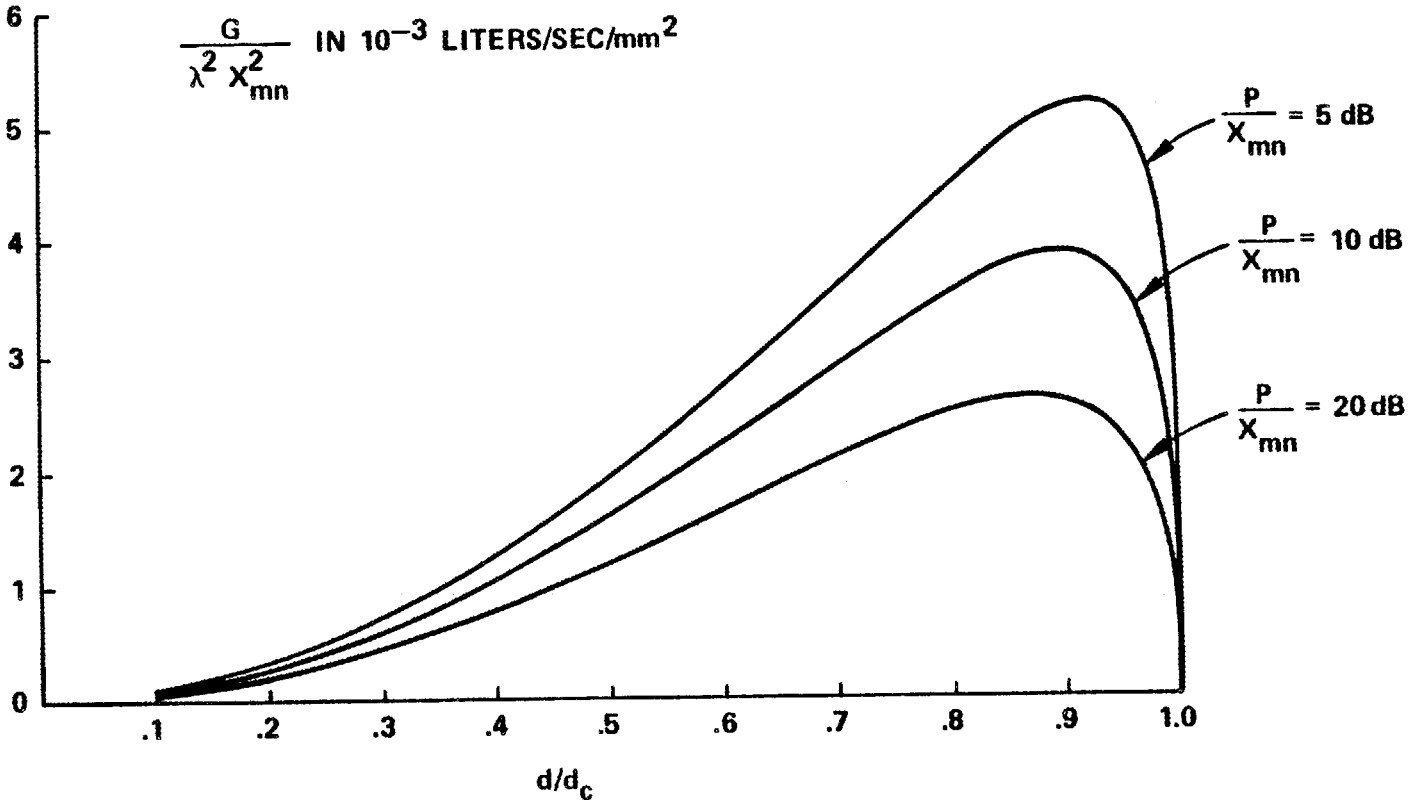

Figure 61. Normalized Pumping Speed vs Normalized Channel Diameter at Fixed rf Isolation

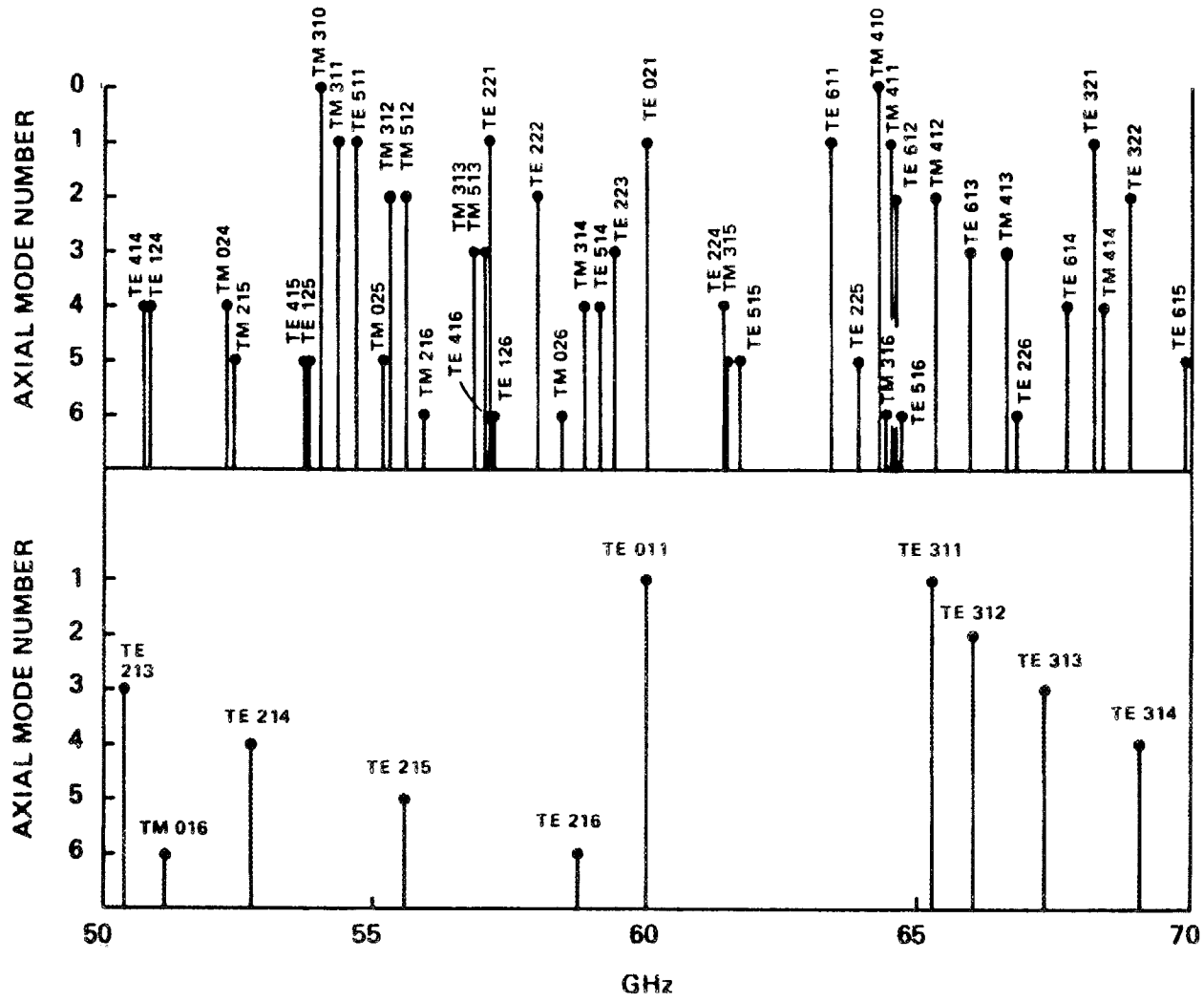

Figure 62. Mode Density

been omitted for clarity. The TE_{22p} mode family have proven to be troublesome in the 28 GHz devices, which operate in the TE_{021} cavity mode. The TE_{32p} mode family may also have been in mode competition in these devices, but these are too far removed from the TE_{021} in frequency to cause significant problems.

As shown in Figure 62, a TE_{011} oscillator would be subject to a far lower competing mode density than a TE_{021} device, although the TE_{216} and the TE_{311} may prove difficult. For this reason, the possibility of using the TE_{011} cavity mode for the 60 GHz oscillator was explored. A TE_{01} cold test cavity was made.

A theoretical model was also developed to investigate, with the aid of a computer code, the vacuum electromagnetic properties of the TE_{on} resonance for the interaction circuit geometry. The model provided excellent agreement with cold test data on cavity Q.

Some of the problems overcome in the gyrotron design included heating of the cathode by rf and undesired interaction in the tunnel between the gun and the cavity. Two precautionary measures included in the design of the beam shaver and output assembly were:

a. a SiC-BeO-loaded cavity preceding the oscillator cavity,

b. a beam shaver tunnel of alternating molybdenum and SiC-BeO washers precede the the SiC-BeO loaded cavity. The SiC-BeO washers are brazed to copper washers, which in turn, are brazed with the copper beam shavers to copper water tubing for cooling.

Further analytical work on the interaction circuit included the mathematical solution for the vacuum electromagnetic fields in a cavity geometry, which was sufficiently arbitrary to obtain any reasonable combination of external Q, resonant frquency, and axial electric field profile by varying the geometric parameters. The solution was obtained in the following manner:

An "initial value" solution for the vacuum fields, E and B, was derived for modes TE_{mn1} from a Debye potential of a form such that,

$$\vec{E} = \vec{e}_z \times \dot{\nabla}\pi \tag{22}$$

$$\vec{B} = \nabla (\vec{e}_z \cdot \nabla\pi) - \frac{\vec{e}_z \ddot{\pi}}{c^2} \tag{23}$$

where $\vec{e}$ is the unit vector in the direction of propagation (along the z axis), c is the speed of light, and π is the Debye potential which satisfies the wave equation,

$$\Box\pi = 0. \tag{24}$$

The boundary conditions on the components of the electromagnetic fields are:

(A) $\vec{E} \cdot \vec{e}_z = 0$ at conducting boundaries, (25)

(B) $\vec{B}(\vec{r} = 0) \cdot \vec{e}_z \Big|_+ = \vec{B}(\vec{r} = o) \cdot \vec{e}_z \Big|_-$ at boundaries $\perp \vec{e}_z$, (26)

while the integrated Poynting flux is also matched at boundaries $\perp \vec{e}_z$:

(C) $\frac{1}{2}\iint(\vec{E} \times \vec{B}^*)_+ \cdot \vec{e}_z \, dA = \frac{1}{2}\iint(\vec{E} \times \vec{B}^*)_- \cdot \vec{e}_z \, dA$, and (27)

(D) the radiative boundary condition is applied for $z \to +\infty$. (28)

The Varian interaction circuit computer code, which was set in this analytical framework, can predict the cavity electric field profile for circular electric cavity modes. Figure 63 shows a plot of the calculated electric field profile at the first radial maximum of the electric field versus axial position for the TE_{021} cavity mode. Some computational difficulties were encountered in extending this work to noncircular electric cavity modes.

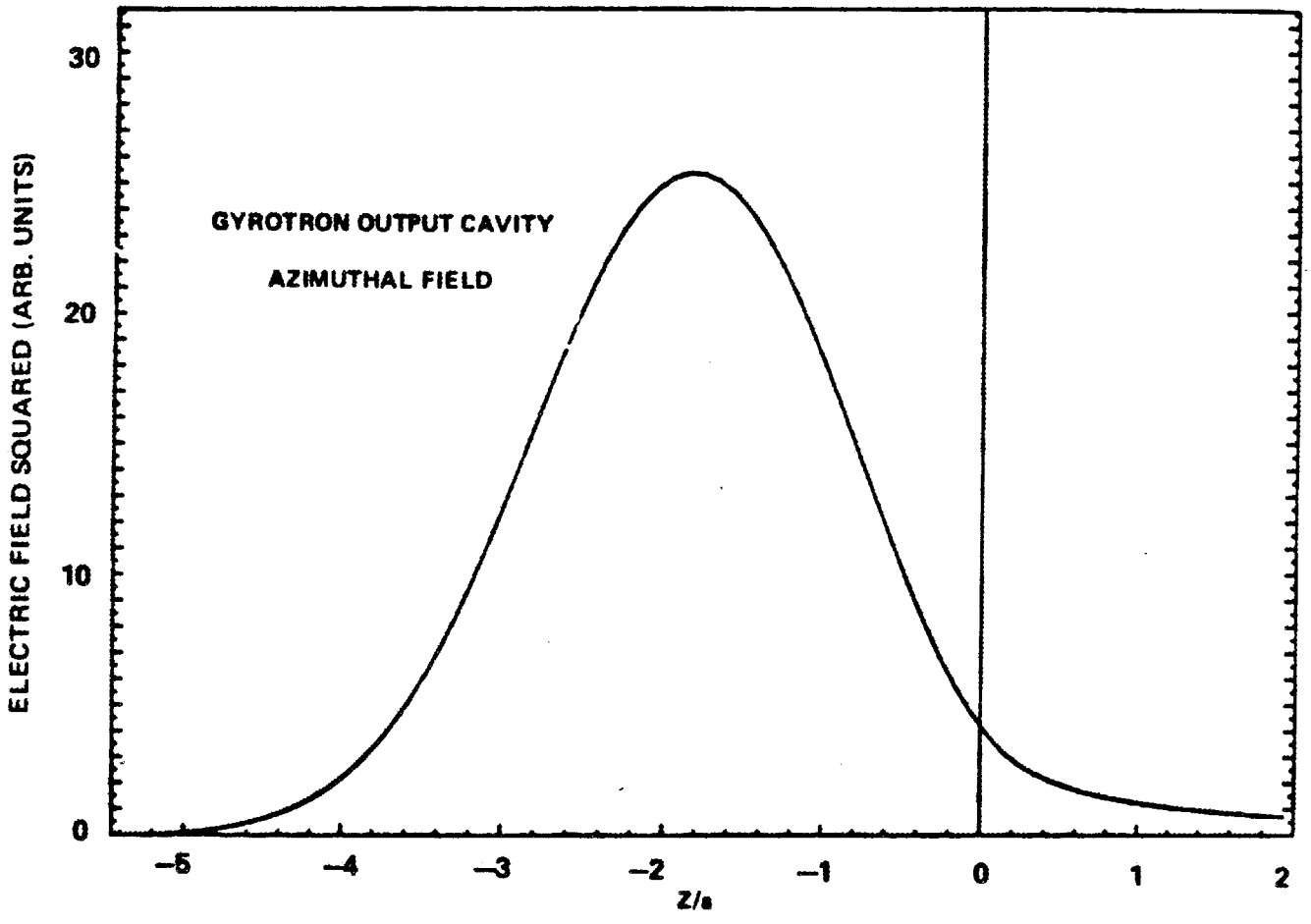

Figure 63. Azimuthal Electric Field Squared for the TE_{021} Oscillator Cavity in Arbitrary Units vs Normalized Axial Position, Z/a, at the Fixed Radius Corresponding to the First Radial Maximum of the Electric Field

A previous calculation of ohmic losses in the gyrotron resonator cavity was modified to show, explicitly, the dependence of cavity power dissipation on the external cavity Q. Several simplifying assumptions, generally valid for gyrotrons, were made:

a. Q_{EXT} is independent of the ohmic losses in the cavity and is, therefore, equal to Q_L;

b. the electric field profile in the cavity has an axial dependence of ~ sin $\pi z/L$ where z is the axial position and L is the cavity length;

c. The cavity length is large compared to its radius, a.

With these approximations, we find the result for the average power dissipation in watts/cm^2 in the cavity walls for a TE_{0n1} cavity:

$$\frac{dP}{dA} = \frac{Q_{EXT}\ P_o\ f^{5/2}}{\sqrt{\sigma}\ c^2\left(\frac{L}{\lambda}\right) x_{1n}^{\ 2}} \quad \text{(cgs)} \tag{29}$$

$$\text{with } Q_{EXT} \cong Q_L, \left(\frac{\pi a}{x_{1n} L}\right)^2 \quad << \quad 1,$$

where P_o is the cavity output power in watts, f is the cavity resonant frequency in hertz, c is the speed of light in cm/sec, L is the cavity length in units of $\lambda = c/f$, x_{1n} is the nth positive root of the equation $J_1(x) = 0$, and σ is the rf conductivity of the cavity walls in cgs units.

For a copper cavity:

$$\frac{dP}{dA}\ (\text{kW/cm}^2) = 4.87 \times 10^{-8} \cdot \frac{Q_{EXT}\ P_o\ (\text{kW})\ f\ (\text{GHz})^{5/2}}{\left(\frac{L}{\lambda}\right) x_{1n}^2} \tag{30}$$

Equations 29 and 30 explicitly include the dependence of dissipation on Q_{EXT} and P_o. The strong frequency dependence of the dissipation $\sim f^{5/2}$ is clearly

evident, as is the advantage of using higher order TE_{on} cavity modes. For the 60 GHz, 200 kW, TE_{02} cavity mode oscillator, Equation 30 gives dP/dA = 440 watts/cm^2 for $L/\lambda = 5$ and $Q_{EXT} = 400$.

1. Large-Signal Calculations

a. 8 λ Cavity Efficiency

To further compare the operation of the 60 GHz tube with theoretical predictions, a series of large-signal computer simulations were carried out using the TRAJ computer code[13]. The code integrates the relativistic equation of motion for an electron injected into the electromagnetic fields appropriate for TE_{mnp} or TM_{mnp} modes in a closed, right-cylindrical cavity. A dc magnetic field guides the electrons through the cavity. To obtain the efficiency for given cavity parameters and rf field amplitude, the final energies of an ensemble of electrons initially equally spaced about 2π of rf phase are calculated. If, for example, eight electrons are used, the efficiency is given by:

$$\eta \equiv \frac{E_i - \frac{\sum_{n=1}^{8} E_f}{8}}{E_i} \tag{31}$$

where E_i and E_f are the initial and final energies, respectively.

There are two main differences between such an efficiency calculation and the actual situation encountered in the tube. First, no space charge effects are included in the program. Second, a gyrotron cavity has open ends and is usually tapered rather than right-cylindrical. Thus, instead of having rf fields with a sinusoidal variation with respect to the axial variable, the fields resemble a skewed Gaussian.[14] It has been previously determined that such field profiles can improve the efficiency of the gyrotron[15]. Since TRAJ cannot handle this geometrical consideration, the sinusoidal variation results serve as a lower limit for the real case.

For the initial calculations, a cavity length of 8λ was chosen as a possible upper limit on the effective length, which is equivalent to the tapered cavity used in the 60 GHz tube. Fixed parameters for this set of runs are given in Table 12. These were chosen to correspond as closely as possible to the design values for the 60 GHz tube.

Table 12

Values of Parameters Used in TRAJ Computer Simulations

Perpendicular Velocity Divided Speed of Light, $\beta_\perp$	0.45
Parallel Velocity Divided by Speed of Light, $\beta_\parallel$	0.225
Relativistic Factor, $\gamma \equiv \frac{1}{\sqrt{1-\beta_\perp^2-\beta_\parallel^2}}$	1.157113 (80.28 kV)
Normal Position of Beam Guiding Center, $R_e \equiv \frac{2\pi r_e}{\lambda_{cutoff}}$	1.84118
Wavelength Divided by Cutoff Wavelength, λ/λ_c	0.99804 for 8λ cavity, for $n\lambda$ $\lambda/\lambda_c = \sqrt{1 - \frac{1}{4n^2}}$
Mode	TE_{021}
Magnetic Field and RF Field Amplitude	Varied in Calculations

For each value of rf field amplitude, A, a series of magnetic field values are input to optimize the efficiency. In such a manner, a curve like that shown in Figure 64 is generated for each value of A. Since the Q of a cavity is defined by:

$$Q = \frac{\omega U}{P_{out}} , \qquad (32)$$

ORNL Dwg. 81-16836FED

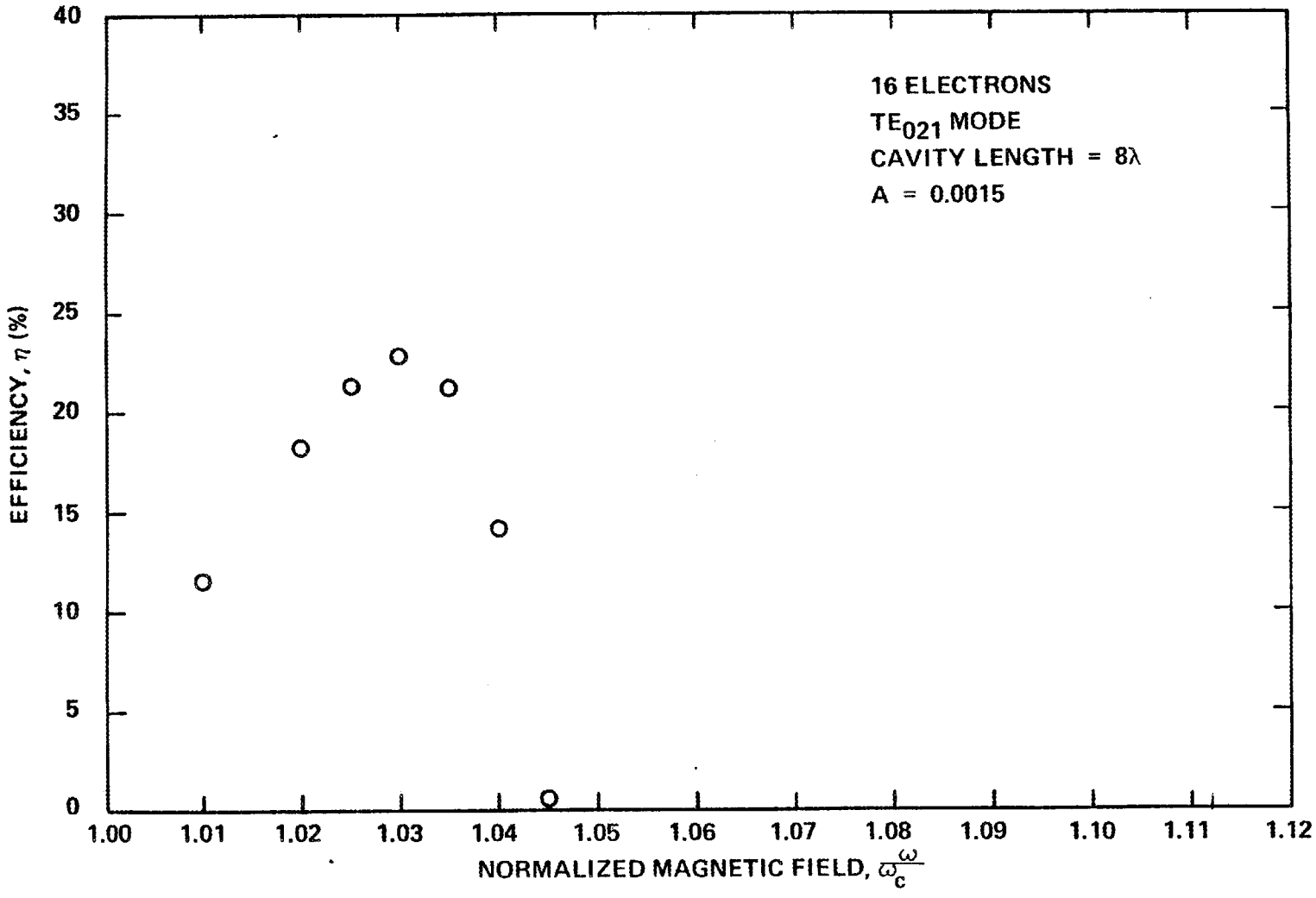

$$\omega_c = \frac{eB}{\gamma mc}$$

Figure 64. Efficiency vs Normalized Magnetic Field

where U is the stored energy, P_{out} the power leaking out of the cavity and ω is the radian rf frequency. The normalized rf field amplitude, A, is related to the quantity P_{out} Q. For TE_{mn1} modes in a closed, right-cylindrical cavity we have:

$$P_{out}\,Q = \frac{\sqrt{\frac{\varepsilon_o}{\mu_o}}\,\pi^2 \left(\frac{x'^2_{mn}}{\pi^2} + \frac{r_o^2}{L^2}\right)^{3/2} \frac{L}{r_o} (8\pi V_N A)^2 \left[x'^2_{mn} - m^2\right] J_m^2\, x'_{mn}}{16\, F\, x'^2_{mn}}, \tag{33}$$

where F = 1 for m = 0 or m ≠ 0 with circular polarization or F = 2 for m ≠ 0 with linear polarization, where ε_o and μ_o are the permittivity and permeability of free space, respectively, where r_o/L is the ratio of the cavity radius to cavity length, V_N is the electron rest energy, 511 kV, J_m is a Bessel function of order m, and x'_{mn} is the nth root of $J'_m(x) = 0$.

The results of the 8λ runs are shown in Figure 65, where efficiency is plotted versus power having used the maximum efficiency (corresponding to optimum magnetic field) for each value of A. A self-consistent beam current for each point as shown in Figure 65 can be calculated since:

$$QP_{out} \equiv \eta\, V_b\, I_b \tag{34}$$

where η is the efficiency defined in Equation 31, and V_b and I_b are the electron beam voltage and current, respectively. The efficiency and power as a function of current are shown in Figure 66.

Figures 65 and 66 show the double-peaked nature of the efficiency as a function of power and current. This behavior has been noticed in previous investigations by K.R. Chu at the Naval Research Lab[16] and G.S. Nusinovich in the U.S.S.R[17,18]. It is believed that such a phenomenon disappears for shorter cavity lengths (i.e. when fewer cyclotron orbits are executed by the electrons while in the cavity).

ORNL Dwg. 81-16837FED

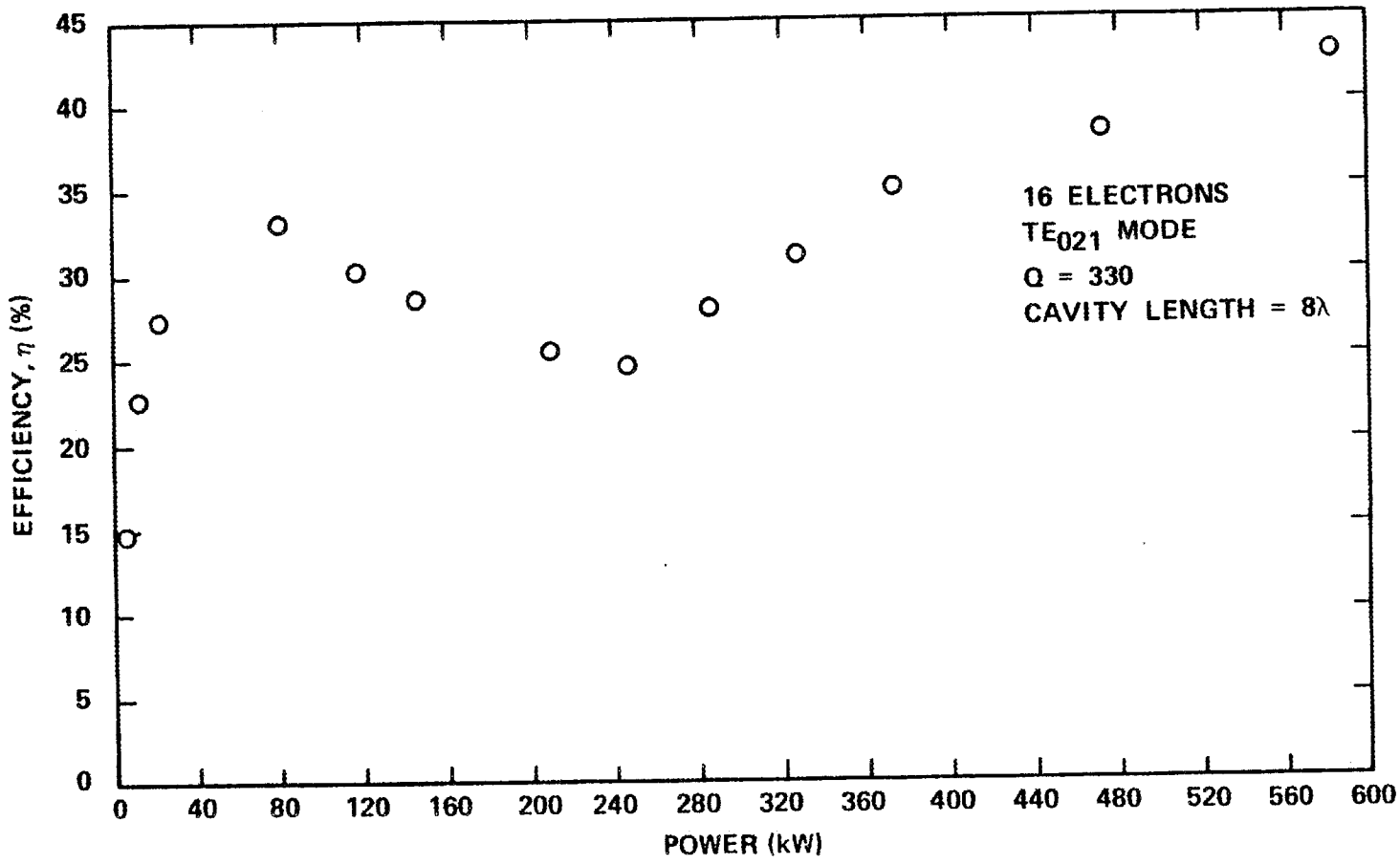

Figure 65. Optimized Efficiency vs Output Power

ORNL Dwg. 81-16838FED

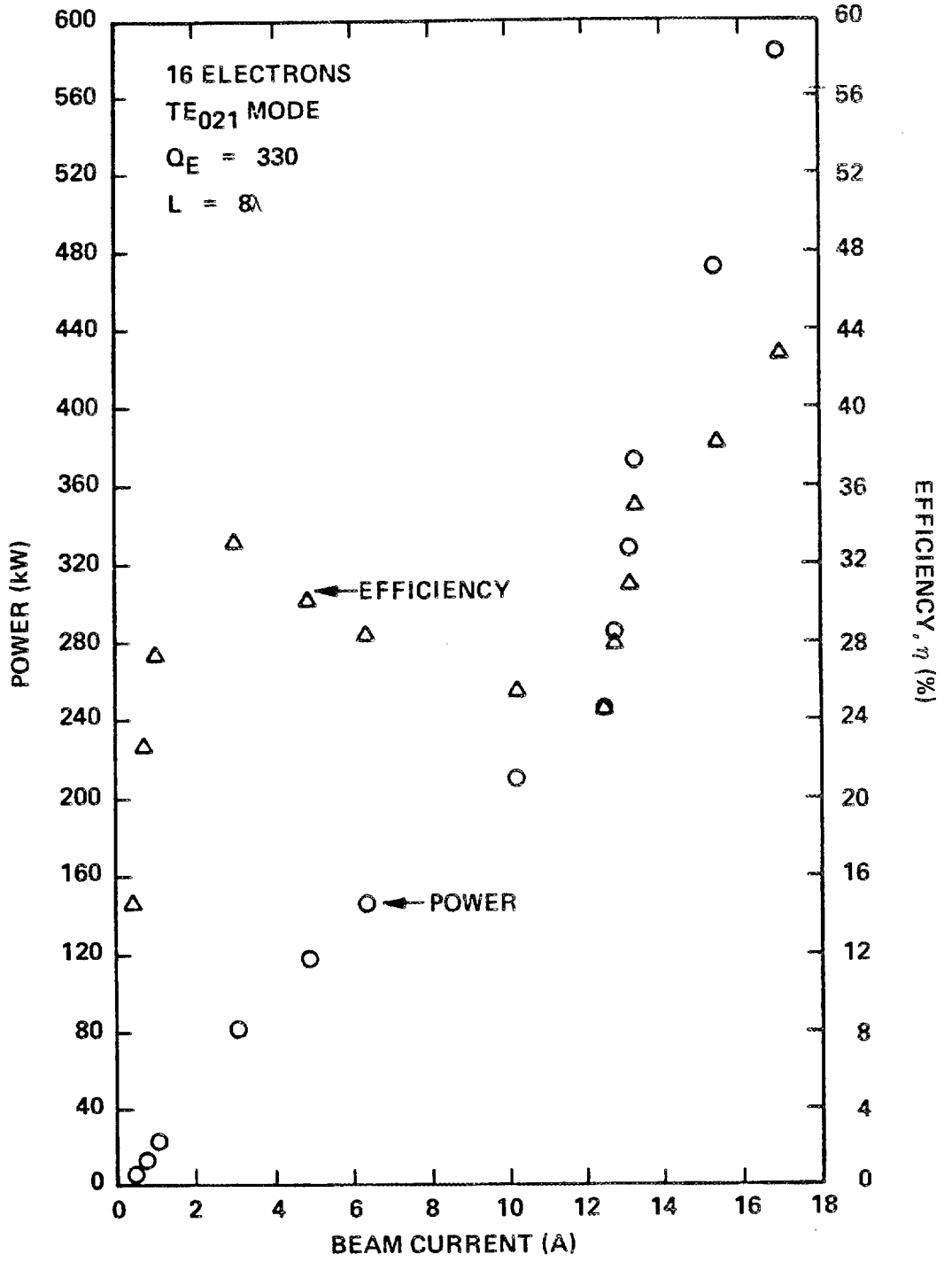

Figure 66. Output Power vs Beam Current (Magnetic Field Optimized)

Another peculiarity of these results was the erratic behavior of the efficiency as a function of magnetic field for large values of the rf amplitude A. This phenomenon is shown in Figure 65 and may be contrasted with the results for lower A shown in Figure 64. The optimum efficiency points shown in Figures 65 and 66 were sometimes difficult to identify because of the jigged nature of curves, like those in Figure 67. Again, this phenomenon is believed to be due to the excessive length of the cavity.

b. Comparison of NRL and Varian Large-Signal Codes

Since the 8λ cavity results were not entirely as expected, the TRAJ code results were compared with those obtained by Chu et al. at NRL (reference 19). Parameters for data points 18-22, as published in an NRL publication[19], were input with TRAJ for comparison. The result of this comparison is shown in Table 13.

Table 13

Comparison of TRAJ and NRL Results

NRL Point #	NRL Result	TRAJ Result	Cavity Length
18	38.5%	40.9%	3.1 λ
19	41.2%	36.7%	4.9 λ
20	40.2%	40.3%	5.6 λ
21	34.1%	18.9% (32.0%)*	8.1 λ
22	29.7%	34.7%	8.9 λ

The efficiency of all the points, except point number 21, were in agreement to within 5% efficiency. This was thought to be acceptable considering the reduced number of significant digits of the parameters quoted in Reference 19, and the possible errors encountered in renormalizing the NRL parameters to TRAJ parameters. NRL point number 21 was for a very long cavity (L ~ 8.1 λ), where the erratic nature of the efficiency as a function of magnetic field had been noted in the previous

ORNL Dwg. 81-16839FED

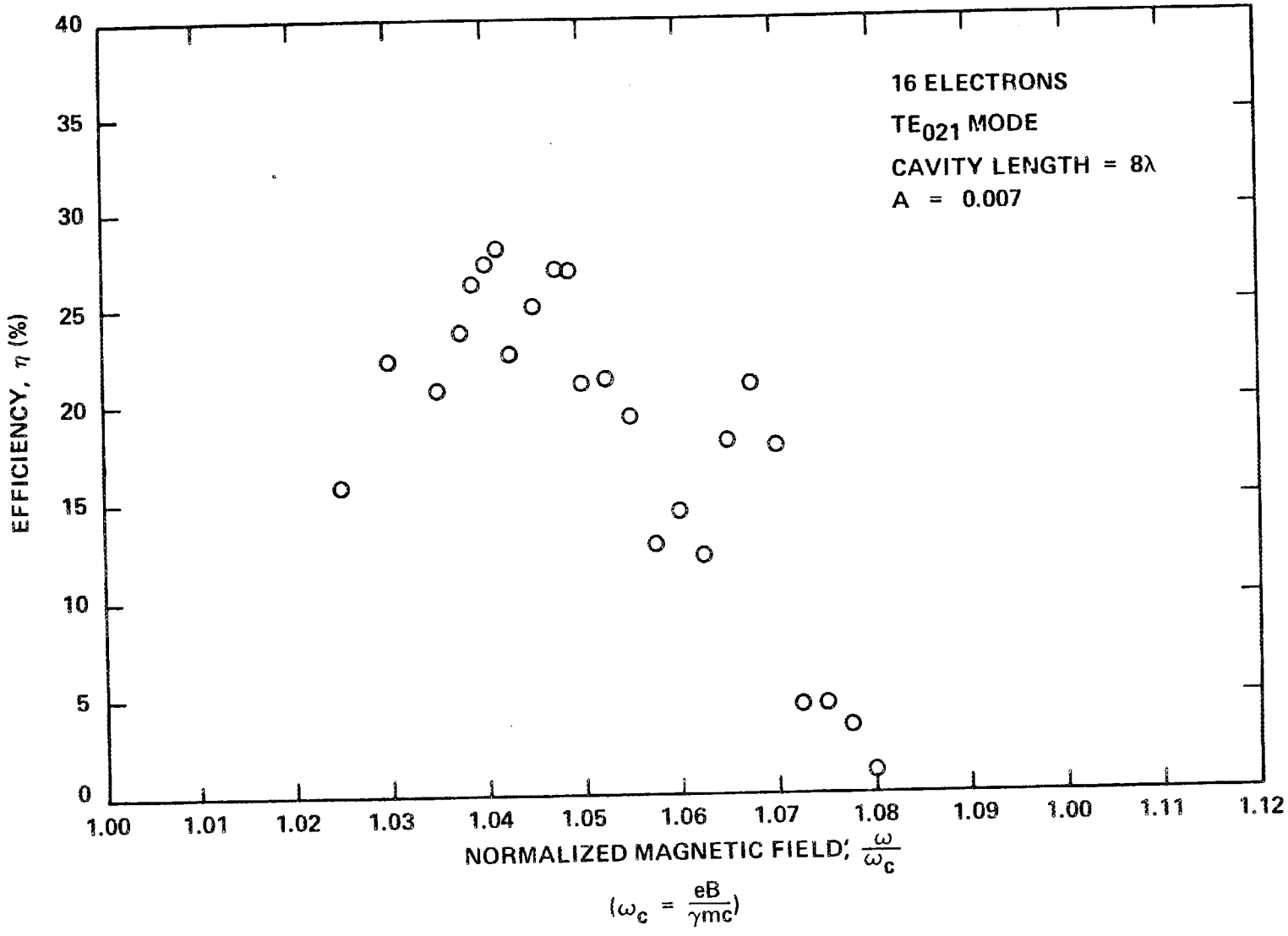

Figure 67. Efficiency vs Normalized Magnetic Field

8 λ study. Upon Chu's suggestion, the magnetic field for point 21 was varied slightly ($B_o = 11.22 \rightarrow B_o = 11.09$), and the results were comparable to those of Chu, as noted by asterisk in Table 13.

c. Efficiency vs Cavity Length

To add further insight into the behavior of efficiency versus cavity length, another set of large-signal calculations was performed. In these runs, two values of P_{out} were examined for constant Q (= 330), 146 kW and 210 kW, leaving all of the parameters, other than cavity length, the same as for the 8 λ case. Runs were performed for 3λ, 4λ, 5λ, 6λ and 7λ cavity lengths. The magnetic field was optimized for maximum efficiency for each power level for each cavity length. The results of these calculations are shown in Figure 68.

As expected, efficiencies were, indeed, higher for shorter cavities, peaking between 4λ and 5λ. In addition, the ragged nature of the curves shown in Figure 67 disappeared as the cavity was shortened.

2. Starting Current Calculations

To better understand the operation of the 60 GHz tube under threshold conditions, that is, in the small signal regime, the starting currents for the operating TE_{021} mode and the neighboring TE_{221} and TE_{611} modes were calculated. The calculations were done using the expression for starting current obtained by Nusinovich and Erm.[18] The calculations assume that the rf field profile with respect to the axial cavity coordinate (z) is a Gaussian with the form:

$$E \propto \exp\left[-\left(\frac{2z}{L}\right)^2\right] \tag{35}$$

To relate the 60 GHz cavity length to that defined by L in Equation 35, the actual rf field profile of the tapered 60 GHz cavity was calculated using the theory of Derfler, et al.[14] This profile is shown in Figure 69, where the square of the rf field is plotted as a function of the

ORNL Dwg. 81-16840FED

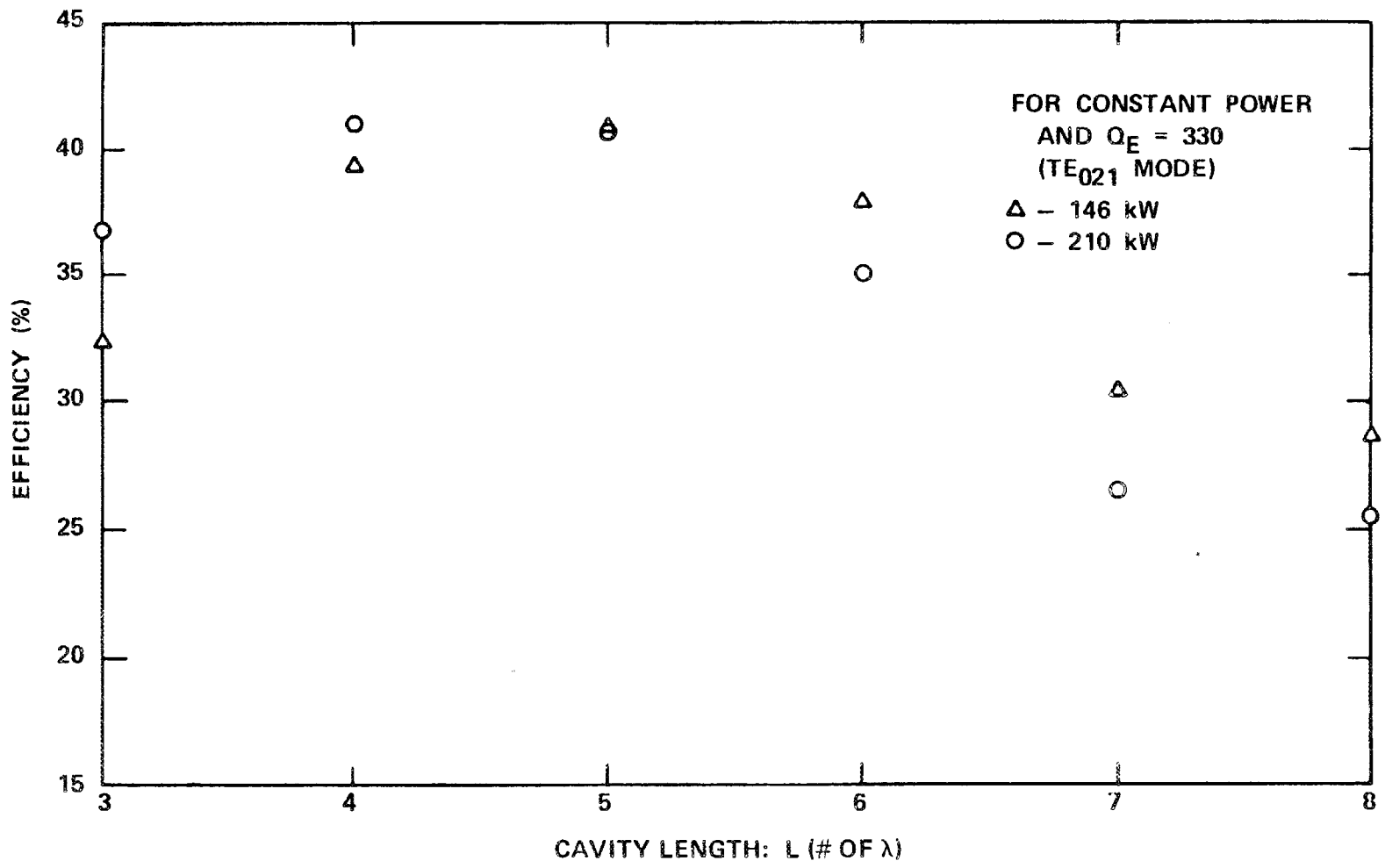

Figure 68. Efficiency vs Cavity Length

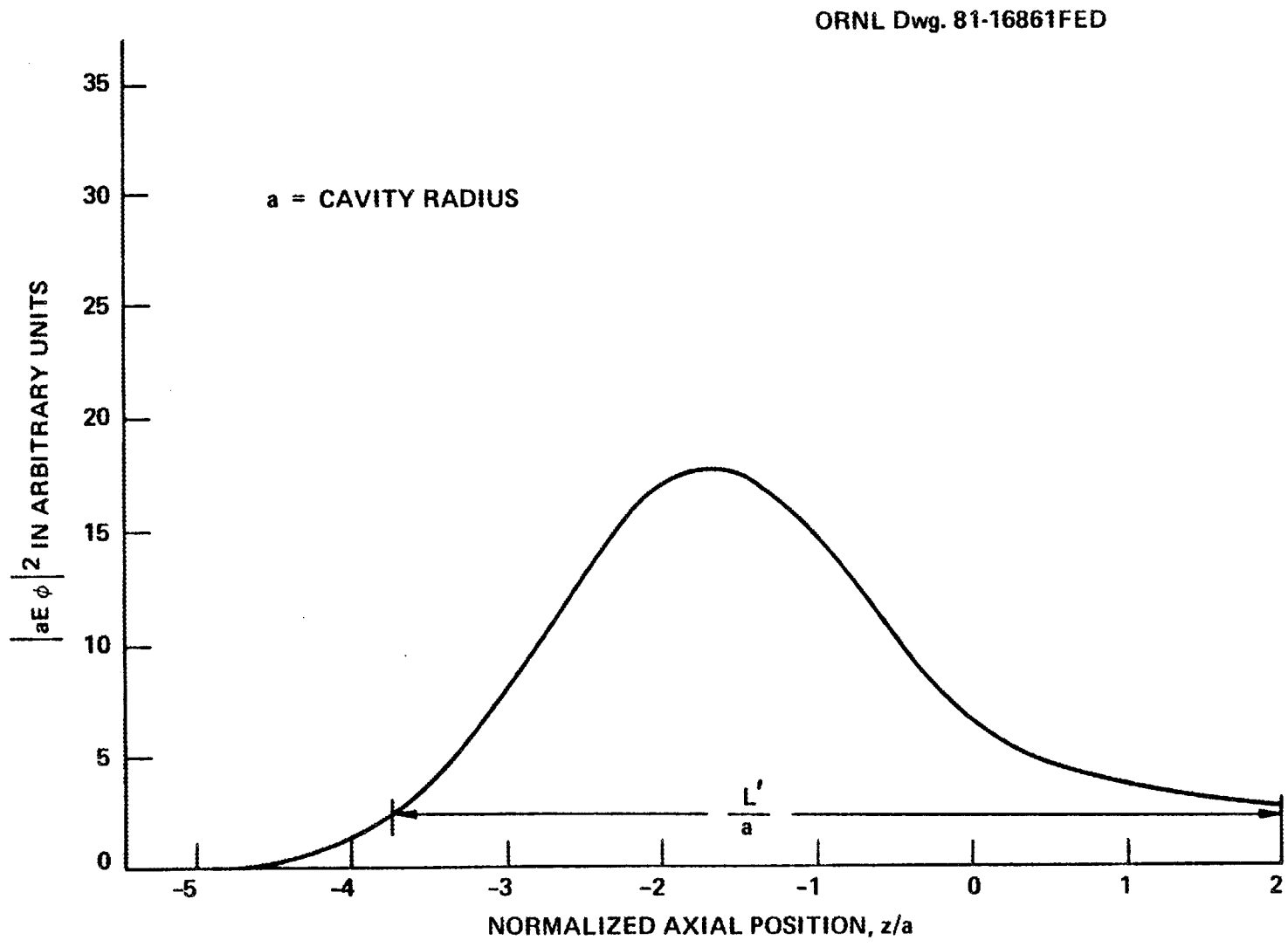

Figure 69. Transverse Electric Field Profile for 60 GHz TE_{021} Cavity

normalized axial variable. An effective length of the cavity can be defined by 1/e points of E field with the result $\frac{L'}{a} \cong 5.75$, where a is the cavity radius. There is some question in doing this because the curve in Figure 69 is not a true Gaussian. In terms of the operating wavelength of the TE_{021} mode, $\frac{L'}{\lambda} \cong 6.4$. Scaling to the TE_{221} and TE_{611} modes, $\frac{L'}{\lambda} \cong 6.12$ and 6.84 are obtained, respectively.

Using these cavity lengths, the starting currents normalized to cavity Q for three modes are plotted in Figure 70 as a function of magnetic field. For each mode, three different values of α, the ratio of perpendicular to parallel velocity, were calculated. The cavity frequency was kept constant for each mode and given by 57.7 GHz, 60.0 GHz, and 64.1 GHz for the TE_{221}, TE_{021}, and TE_{611} modes, respectively. The beam voltage was 80 kV in all cases. In these calculations, the beam is assumed to be infinitesimally thin and located at the inner electric field maximum of the TE_{021} mode. From the plot, it is evident that for $\alpha = 1.0$, the TE_{221} and TE_{021} starting currents are quite closely spaced, but with increasing values of α they tend to separate. The TE_{611} mode has much higher starting currents than the other two modes, since the beam position in the cavity is quite far from being optimized for this mode.

A starting current expression derived by Kreischer and Temkin[20] yields results similar to those of Nusinovich and Erm, where both derivations assume weakly relativistic electrons. However, Kreischer and Temkin have explored the effects of velocity spread on the starting current, as opposed to the cold beam approximation of Nusinovich and Erm. Their results indicate that increasing velocity spread lowers the starting current slightly and shifts the curves to higher magnetic field. A fully relativistic theory for TE_{on} modes has been carried out by Chu,[21] but instead of a Gaussian rf field profile, a sinusoidal profile was employed corresponding to the idealized geometry of a closed, right-cylindrical cavity. Calculations using this theory yield starting currents three to five times greater than those done following Nusinovich and Erm for the TE_{021} mode at 60 GHz. This disagreement was cause for concern and further investigation. Clearly, one problem was the method of defining effective length with various field distributions.

ORNL Dwg. 81-16862 FED

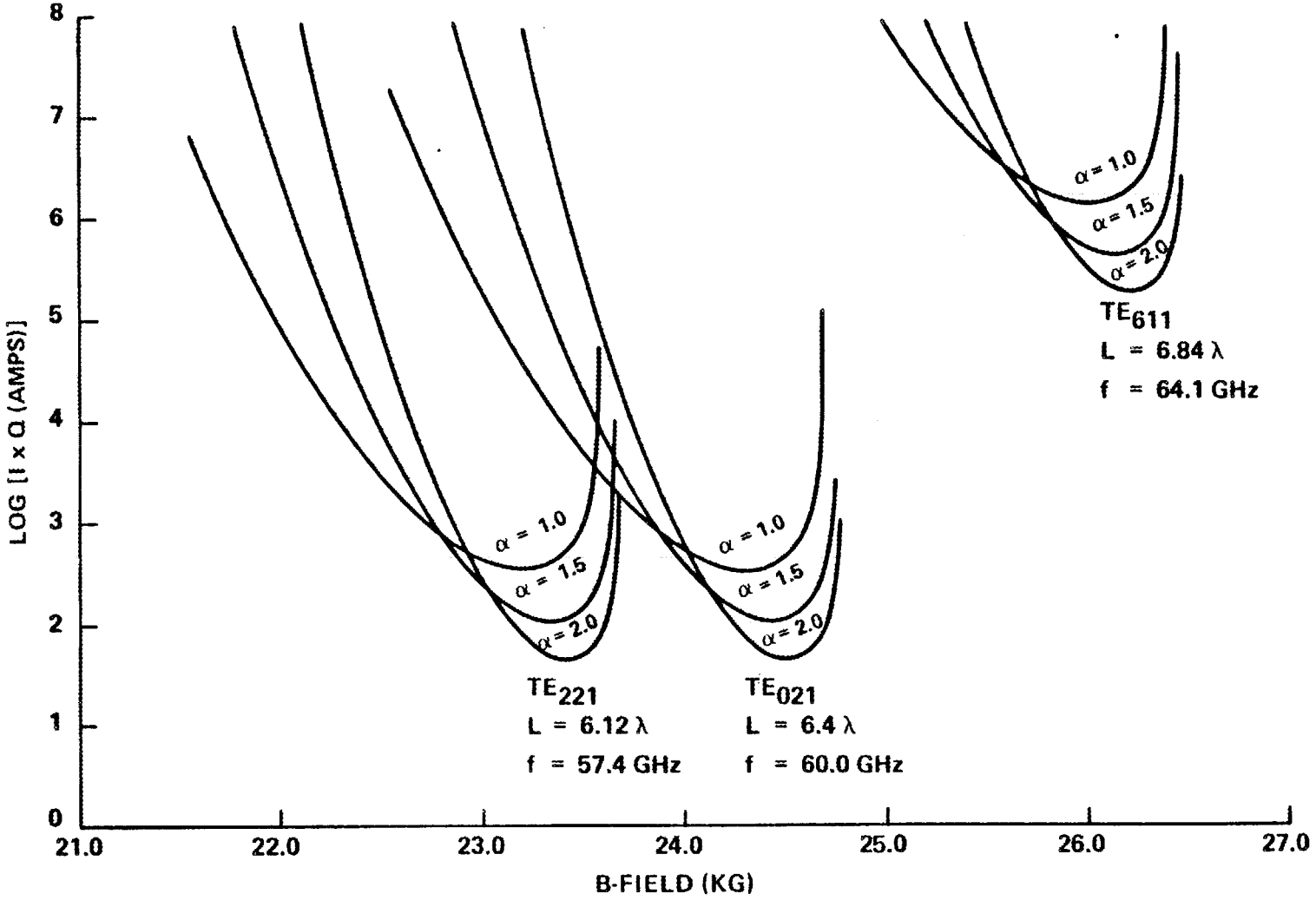

Figure 70. Starting Currents: Varian 60 GHz Gyrotron

3. Cavity Design Modification for X-3R

In light of the test performance of pulsed tube X-3, it was decided that minor changes in the design of the output cavity might improve the dynamic range and efficiency of the desired mode of oscillation, the TE_{021} mode. Specifically, the inability to control the TE_{02} oscillation using the gun anode voltage, except over a very narrow range, indicated that the loaded Q of the TE_{021} mode might be too low. In addition, nonlinear calculations (Section VI.C.1.c) indicated that the effective interaction length of the cavity might be shortened to enhance the efficiency of the tube.

To investigate a cavity change that would, both, raise the loaded Q and shorten the interaction length of the TE_{021} mode, the theory of vacuum electromagnetic properties of tapered cavities of Derfler, et al.[14] was employed. Calculations using the Derfler theory indicated that such a change could be implemented by varying the output taper angle of the cavity.

A design was chosen which would increase the loaded Q by 26%, and shorten the effective interaction length by 25%. Cold tests were performed on the new cavity design and gave results in rough agreement with theoretical predictions for the loaded Q.

The design was then integrated into the output taper section of the existing pulse tube design and incorporated in a rebuild of X-3 (X-3R).

4. Drift Tube Modification

The drift tube section of the tube which precedes the output cavity was previously modified in tube X-3 to combat a spurious oscillation in the drift tube section. The oscillation caused body heating and limited the dynamic range available to the desired TE_{02} mode. Test results on X-3 indicated that the modification had only partially alleviated the problem. Further cold tests were carried out to find a design which would eliminate

the oscillation. A design was chosen and incorporated into a rebuilt tube, X-3R, and was successful in suppressing the unwanted oscillation.

5. Effects of Window Mismatch on Cavity Resonances

Tests were performed to study the effects of the narrow bandwidth of, both, the double-disc and single-disc windows on the various cavity resonances. These tests indicated that at 59.5 GHz, mode competition problems are greatly aggravated by the high VSWR for modes other than the operating TE_{021} mode. Several methods of widening the bandwidth of, both, the pulsed and CW window designs were studied (Sections VI.E and VIII.B).

6. Mode Suppression

To suppress modes competing with the desired TE_{02} mode, various methods of selectively loading the output cavity were considered. Specifically, these approaches took advantage of the longitudinal wall currents that exist in the presence of noncircular modes, but which are absent for circular electric modes, such as the TE_{02} mode. Either conductive or dielectric types of loss near the entrance of the cavity wall, where longitudinal wall currents are maximum, will inhibit the oscillation of noncircular electric modes. Cold tests, performed using a conductive type of loss, indicated that the loaded Q of the TE_{221} mode could be decreased by a factor of two. Cavities using dielectric loss were tested at NRL[22] with some success.

7. Efficiency Enhancement

Methods of increasing the efficiency of the 60 GHz tube include optimizing the electrical length of the cavity, and profiling the cavity field in such a way that some pre-bunching of the electron beam occurs at the front of the cavity. Experimental results from pulsed tube X-3R (Section IX.C.2) and CW tube X-5 (Section IX.E) indicated an anomalous decrease in efficiency as the gun anode voltage was increased past a certain point. One possible explanation for this phenomenon was that the electrical length of the cavity was too long, such that the electrons reaccelerated

near the end of the cavity, reducing the interaction efficiency. Since most of the electron energy is in the transverse direction, the electrical length of the cavity depends critically on the number of cyclotron orbits existing in the cavity. Therefore, variation of the gun anode voltage, or transverse energy, will change the effective interaction length.

In Figure 71, the calculated efficiency versus beam current is shown for a cavity with $L = 6\lambda$, for electron beams with three different perpendicular to parallel velocity ratios, $\alpha = \beta_{\perp}/\beta_{\parallel} = 1.5$, 2.0, and 2.5. The simulations employed an 80 kV electron beam interaction with the TE_{021} cavity mode, assuming a sinusoidal axial dependence of the rf electric field. A loaded Q of 410 was assumed in calculating the self-consistent beam current, and the three curves are optimized with respect to magnetic field.

These results indicated that for beam currents of interest for the 60 GHz tubes, 2-8 A, the maximum efficiency occurred for $\alpha = 1.5$ or 2.0, while $\alpha = 2.5$ yielded a lower efficiency. This phenomenon explained the behavior of the output power as a function of gun anode voltage. The solution to this problem was to shorten the cavity physically, and electrically, to a point where the efficiency was optimized for the range of transverse energies accessible to the electron beam.

The calculations of Figure 71 were extended to model the actual rf fields of the 60 GHz cavity, rather than the fields of a closed right cylindrical cavity. Figure 72 shows the results of efficiency calculations for the 60 GHz cavity for various magnetic fields as a function of beam current. The perpendicular to parallel velocity ratio, α, was set at two for these simulations. Similar calculations were performed for a = 1.5 and 2.5. By linking α to the gun anode voltage in the electron gun, from simulations of the electron gun performance, output power can be related to gun anode voltage. In Figure 73, output power versus gun anode voltage is plotted for different magnetic fields, holding the beam current to 8a. The decrease in output power for increased gun anode voltage, or α, compares

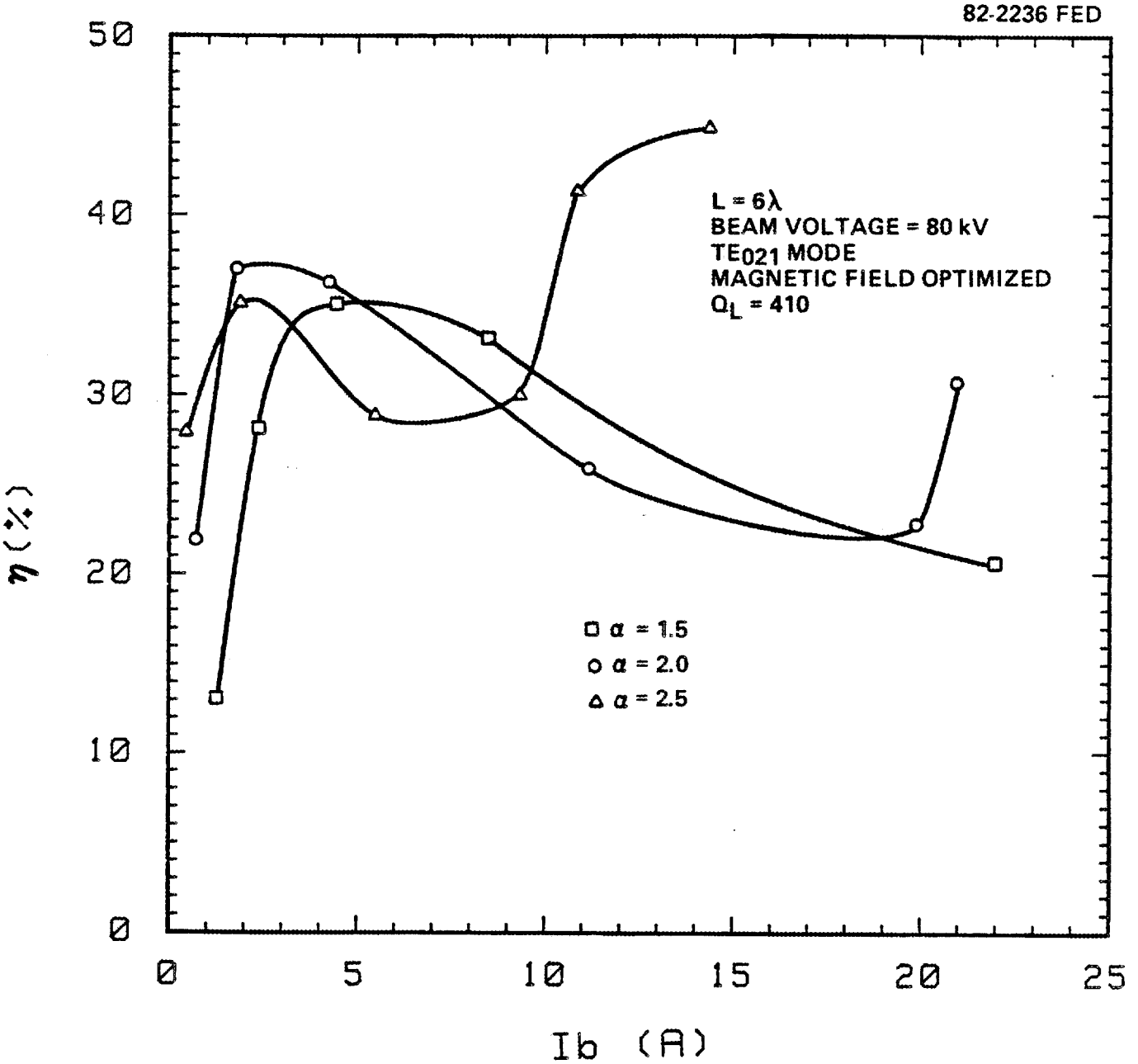

Figure 71. Efficiency vs Beam Current for Optimum Magnetic Field

Dwg 82-2260 FED

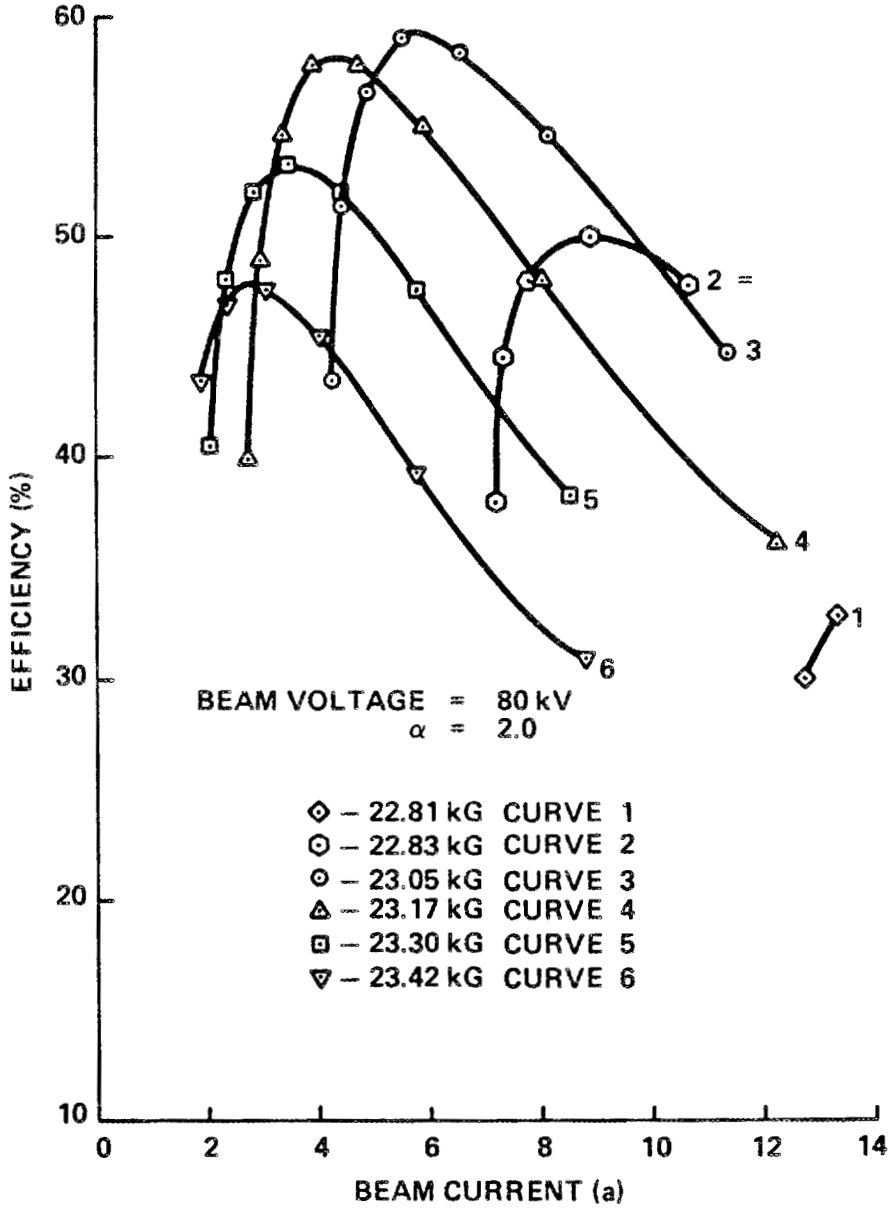

Figure 72. Efficiency vs Beam Current for Various Values of Cavity Magnetic Field

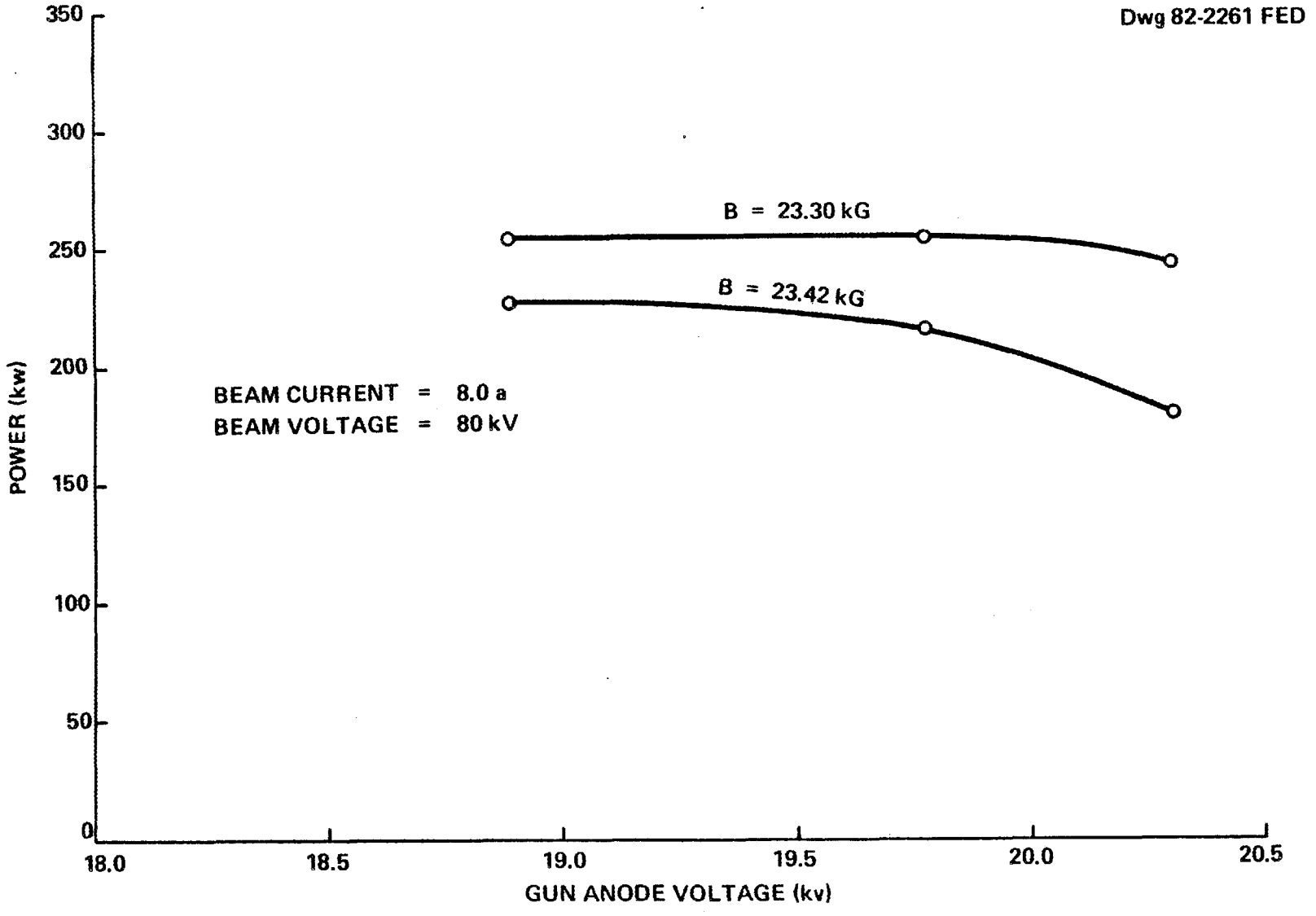

Figure 73. Output Power vs Gun Anode Voltage (Related to α) for Two Values of Cavity Magnetic Field

with experimental observations made on X-5 (Section IX.E), as well as on various pulsed tubes, but the quantitative agreement is not as good as one would hope (cf Figure 55).

As noted previously, the decrease in output power for increased gun anode voltage, present in Figure 73, is due to an excessive interaction length in the cavity . A long pre-bunching region, followed by a short interaction region, gives the most efficient exchange of energy between the electron beam and the rf fields.

8. Resistive-Coated Cavity

Resistive loading was incorporated into the cavity of pulse tube P-1R3. The loading was located in the input taper portion, gun end, of the cavity, where the competing TE_{221} mode has axial wall currents. Cold tests of the cavity indicated that the loaded Q of the TE_{221} mode was lowered by 30% from that of a cavity without the resistive coating, while the TE_{021} mode remained unaffected. Cavity tests were performed to ensure that the coating was still effective after exposure to high temperatures during construction of the tube. No changes in the microwave properties of the cavity were observed during these tests, though some migration of the coating into the copper substrate was noted. A manufacturing procedure was developed for this cavity design. An assembly was fabricated and originally scheduled for X-6, a CW tube. This assembly was subsequently used on P-1R3, a pulsed tube to enable an earlier test.

Tests on tube P-1R3 employing the resistively-coated cavity were performed and indicated that some improvements in the dynamic range of the tube had been made. These results will be discussed in detail in Section IX.F.

9. Modified Electric Field Profile

A cavity was designed with a longer pre-bunching region and shorter interaction section than any previous design. These modifications would enhance the mode selectivity of the cavity and optimize the length of

the cavity over which energy is extracted. To achieve the aforementioned features, the input taper angle was reduced, while the length of the input taper section was lengthened and the straight section was shortened. Figure 74 shows, schematically, the geometric changes involved in making these modifications. When varying the lengths and angles of the cavity, the loaded Q of the cavity must remain approximately constant for optimum gyrotron performance with given beam parameters.

Figure 75 shows the results of large signal computer calculations for the final modified cavity geometry design. This plot of efficiency versus beam current for various magnetic field values may be compared with a similar plot for the original 60 GHz cavity shown, in Figure 72. Figure 76 shows a plot of efficiency versus beam current for the modified and present cavity designs for optimum magnetic field. Some improvements in performance for the modified cavity design can be noted, especially at higher current values. A plot of output power versus magnetic field for a beam current of 8 A for the original and modified cavities is shown in Figure 77. The calculated efficiency for the two cavities is similar. However, the optimum magnetic field is shifted, despite the fact that both designs have the same resonant frequency.

The above calculations indicate that the electric field of the modified cavity may improve efficiency, but since the analysis is for a single cavity mode, the extent to which mode competition with the TE_{221} mode diminishes is not known. Small signal calculations show that the two designs have similar starting conditions, except that the magnetic field for a given starting current is shifted to a higher value for the modified design, as shown in Figure 78.

10. TE_{011}/TE_{021} Step Cavity

Another method of effectively pre-bunching the electron beam to avoid mode competition is to employ an initial pre-bunching cavity, resonant at the desired frequency, 60 GHz, in a lower order mode, where mode competition is absent.[23] The pre-bunched beam then enters the main cavity,

ORNL – DWG-83-2100

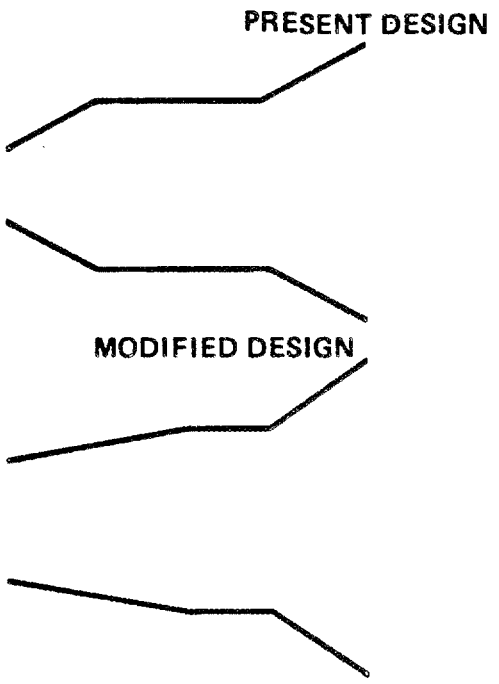

Figure 74. Schematic Diagram of the Geometry of the Present Cavity and of a Cavity Modified to Lengthen the Pre-Bunching Region and Shorten the Interaction Section

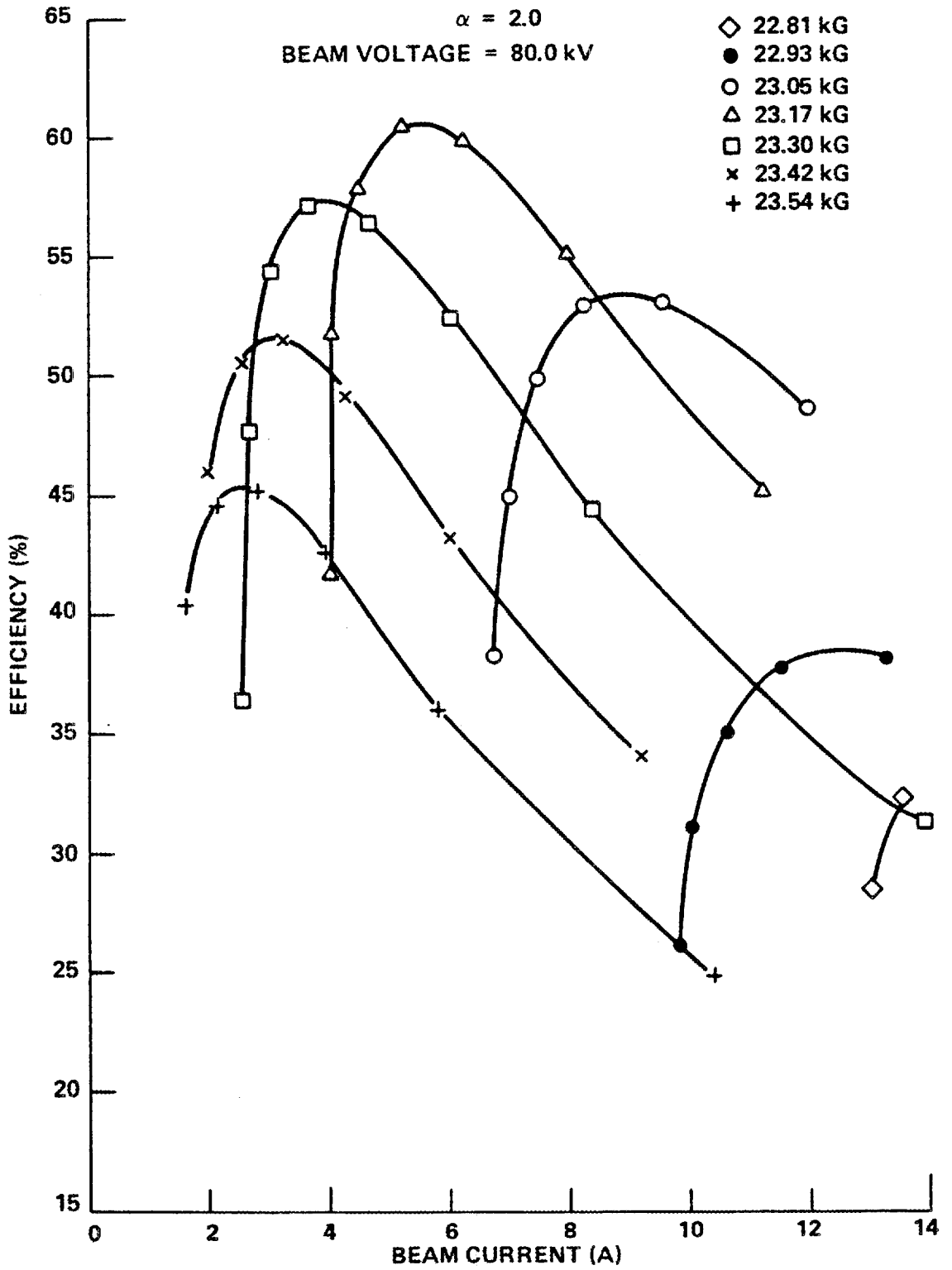

Figure 75. Plot of Efficiency vs Beam Current for Various Magnetic Fields for Cavity with Modified Electric Field Profile

ORNL – DWG-83-2102

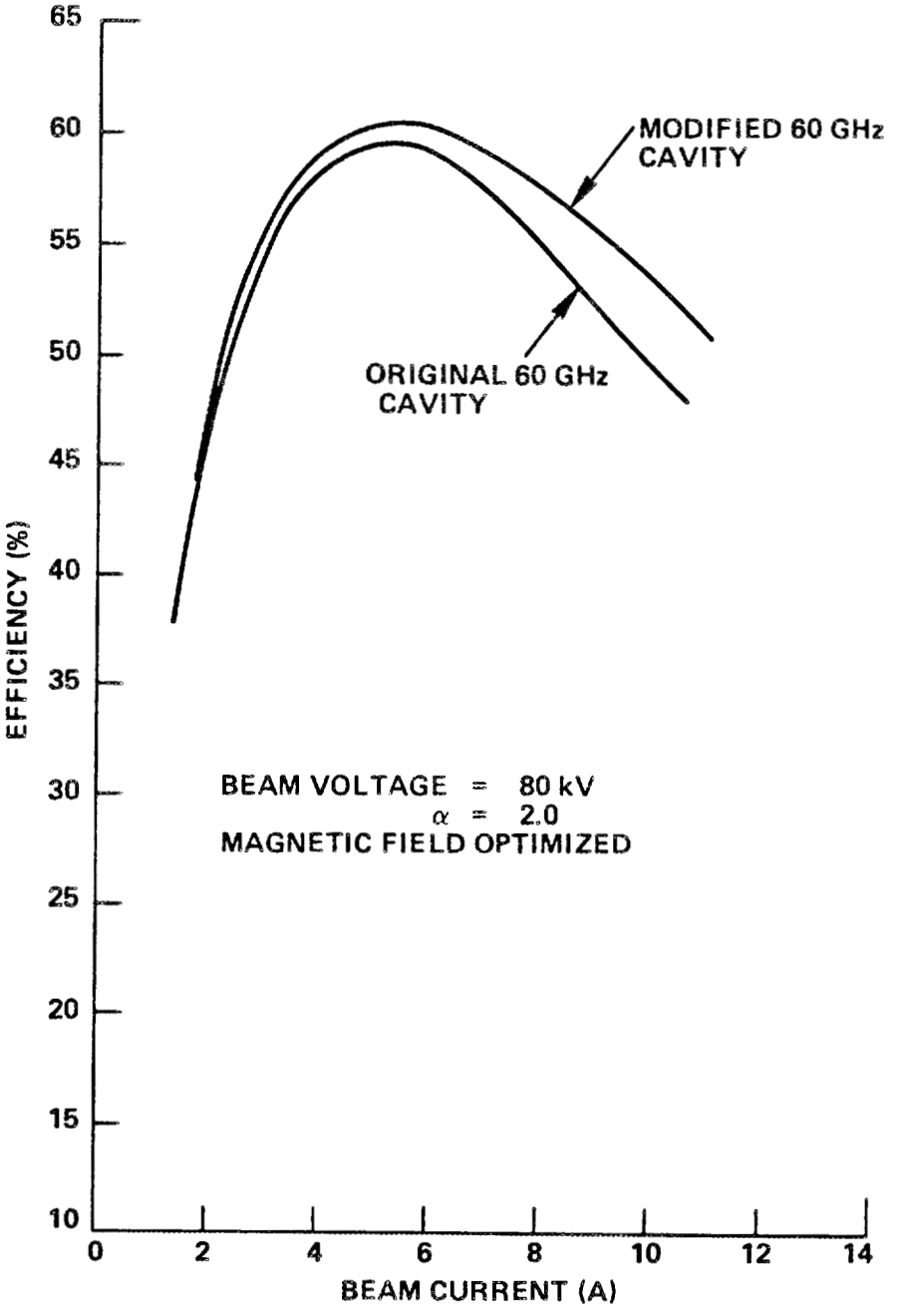

Figure 76. Plot of Efficiency vs Beam Current for the Original and Modified 60 GHz Cavity Designs for Optimum Magnetic Field

ORNL – DWG-83-2103

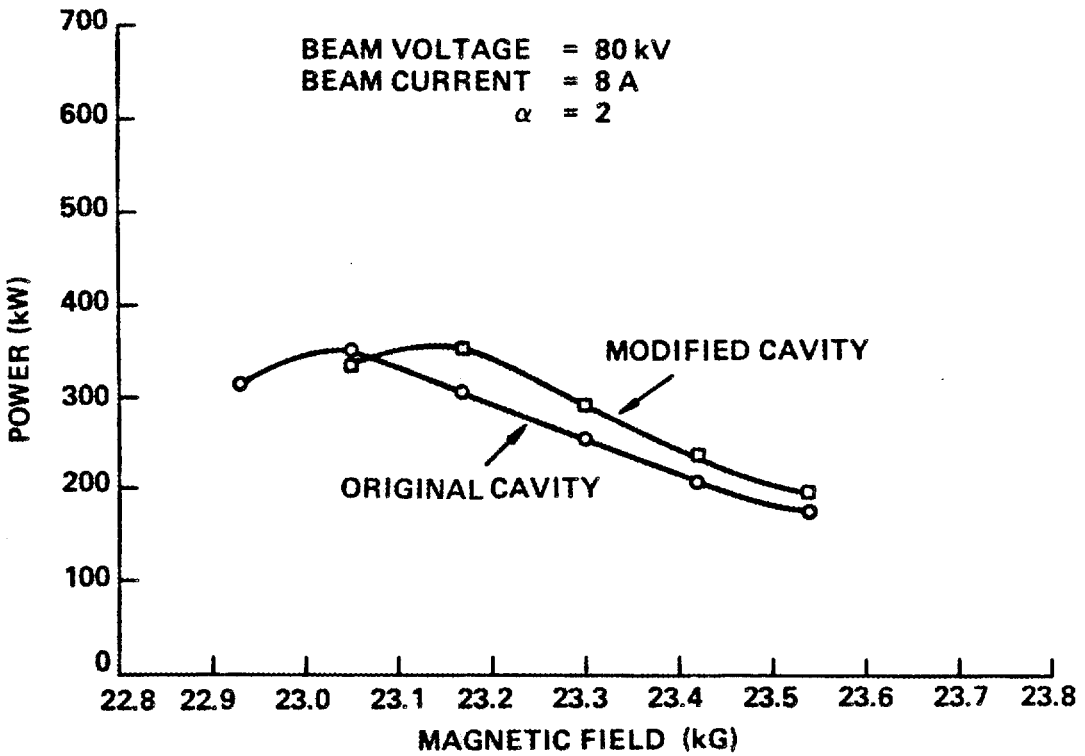

Figure 77. Plot of Output Power vs Magnetic Field for the Original and Modified 60 GHz Cavity

ORNL – DWG-83-2104

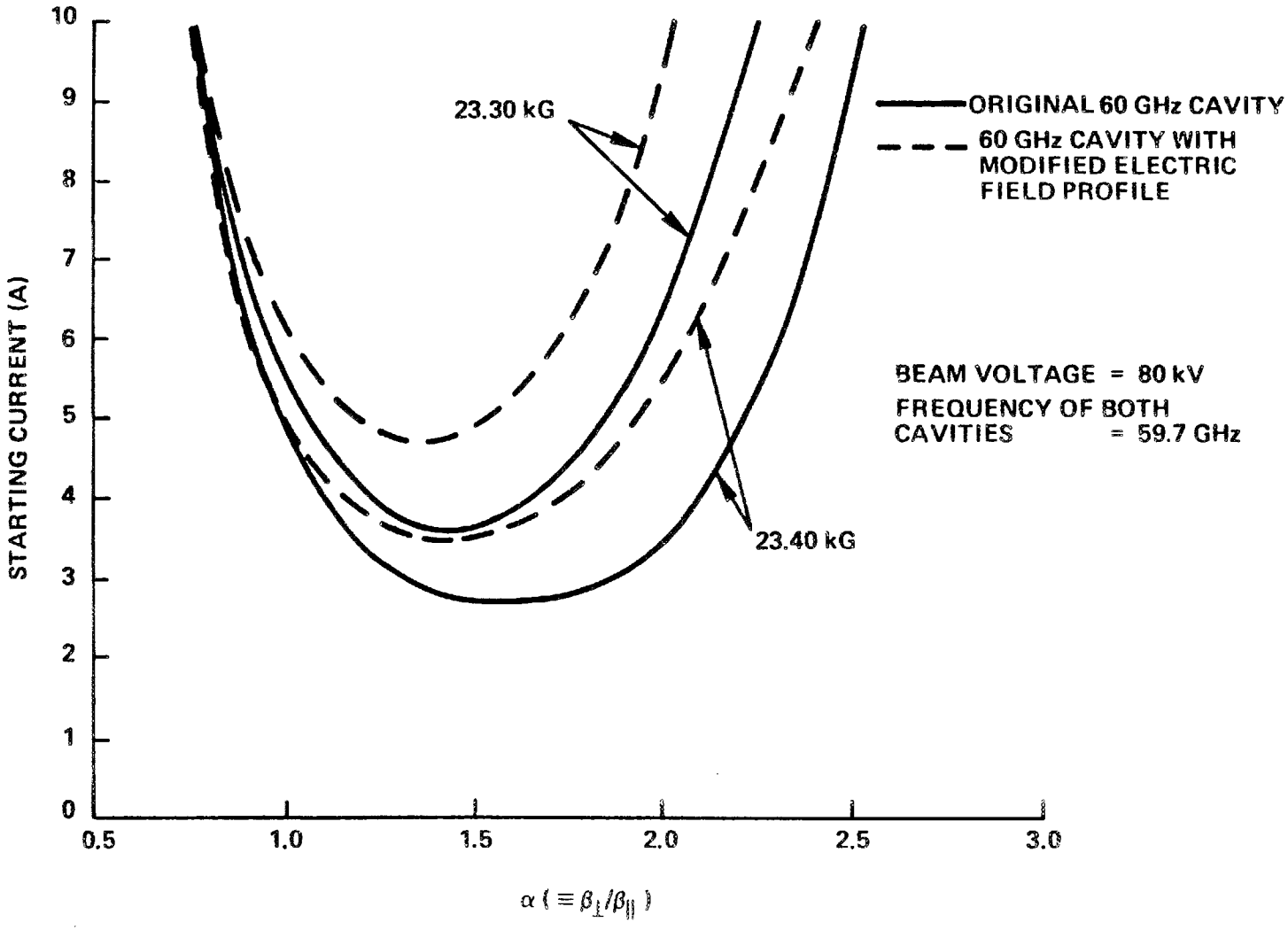

Figure 78. Starting Current Versus α ($\equiv \beta_{\perp}/\beta_{\parallel}$) For Two Values of Magnetic Field For The Present and Modified 60 GHz Cavity Designs

where energy is extracted in the desired operating mode. Since the beam is preferentially bunched for the desired mode, starting conditions for the desired mode should be reduced, and the competing mode should be impeded. More recently, experiments at NRL[24] using a TE_{011}/TE_{041} step cavity at 35 GHz were successful in suppressing mode competition with the competing TE_{241} mode. Work at Varian was aimed at designing a TE_{011}/TE_{021} step cavity for use on the 60 GHz gyrotron.

An example of TE_{011}/TE_{021} step cavity is shown in Figure 79. The lines shown inside the step cavity are magnetic field lines, or lines of constant rE_{ϕ}. The "+" and "-" signs in the two cavity sections indicate that the two sections are 180° out of phase at the position of the inner electric field maximum (the location of the electron beam in the 60 GHz gyrotron).

Numerous cavity geometries similar to those shown in Figure 78 were investigated to obtain cavities with the desired TE_{011}/TE_{021} electromagnetic fields, with varying ratios of the peak electric field of the TE_{021} section to that of the TE_{011} section. Electric field ratios of between 1.5 and 5.0 were obtained. To analyze a given step cavity design, once the electric and magnetic fields in the cavity have been obtained, electrons are injected into the cavity fields with a given energy and perpendicular to parallel velocity ratio, α. The efficiency of the cavity is then determined by the average amount of energy lost by the electrons during their transit through the cavity. To fully analyze a given cavity geometry, calculations must be performed for a range of magnetic fields, and for a range of electric fields corresponding to a range of output power levels.

The loaded Q of the cavity is determined primarily by the TE_{021} section of the step cavity. Since this section is short, loaded Q's of such cavities are quite low when coupled to the output waveguide by a gradual taper as was done with the original type of 60 GHz cavity. To raise the loaded Q, an iris was inserted at the end of the cavity. Using irises of different widths and diameters, one would expect that a wide range of loaded Q's could be obtained. The iris size was determined in cold test by

ORNL – DWG-83-2105

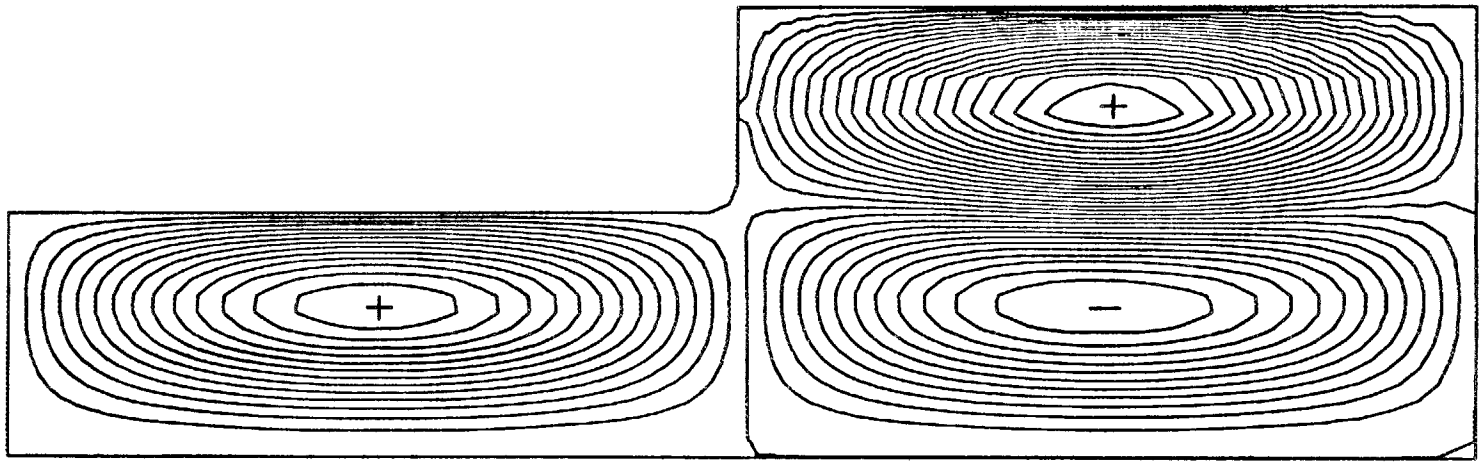

TE_{011} SECTION

TE_{021} SECTION

Figure 79. Example of a TE_{011}/TE_{021} Step Cavity

experimenting with different irises to obtain the desired loaded Q. This was confirmed with a computer code which handles open cavities with abrupt changes in the cavity walls, as is the case when an iris is inserted at the end of a step cavity. An example of the output of the open cavity computer program is shown in Figure 80. Various iris sizes were calculated to determine dimensional tolerances. This program cannot handle the efficiency calculations previously discussed. Efficiency is calculated using the closed cavity program which produced Figure 79. All of the programs discussed here are versions of the well-known SUPERFISH code.

Figure 81 shows efficiency calculations for step cavity #1 for various magnetic fields and no linear magnetic field taper along the cavity. Tapering of the magnetic field had little effect on the efficiency and starting current of this design. Tapers investigated were increasing, linear tapers. Figures 82 and 83 show similar calculations for step cavity #3, for magnetic tapers of 0% and 12%, respectively. In this case, the magnetic taper was very important, allowing much higher efficiencies. In all of the above calculations, a loaded Q of 350, similar to the loaded Q of the original 60 GHz cavity was assumed. The main difference between step cavity #1 and step cavity #3 was that the TE_{021}/TE_{011} ratio of electric fields for the two cavities was much higher in step cavity #1 than it was in step cavity #3. In Figure 83, efficiencies of up to 70% were obtained and efficiencies in excess of 50% were present over a very wide range of beam currents and magnetic fields. These calculations may be compared with those of the modified cavity shown in Figure 75. Magnetic field tapering in conventional cavities is in general not successful because of increased mode competition caused by the low magnetic field at the beginning of the cavity, but in the step cavity, the pre-bunching section makes it possible to use a magnetic taper since mode competition is greatly reduced.

Several additional step cavity designs were investigated, using the open-cavity version of SUPERFISH to predict the loaded Q. Since the present TE_{01}/TE_{02} step cavity designs[2] require the presence of an iris to achieve a sufficient loaded Q, computer codes that are based on weakly

ORNL – DWG-83-2106

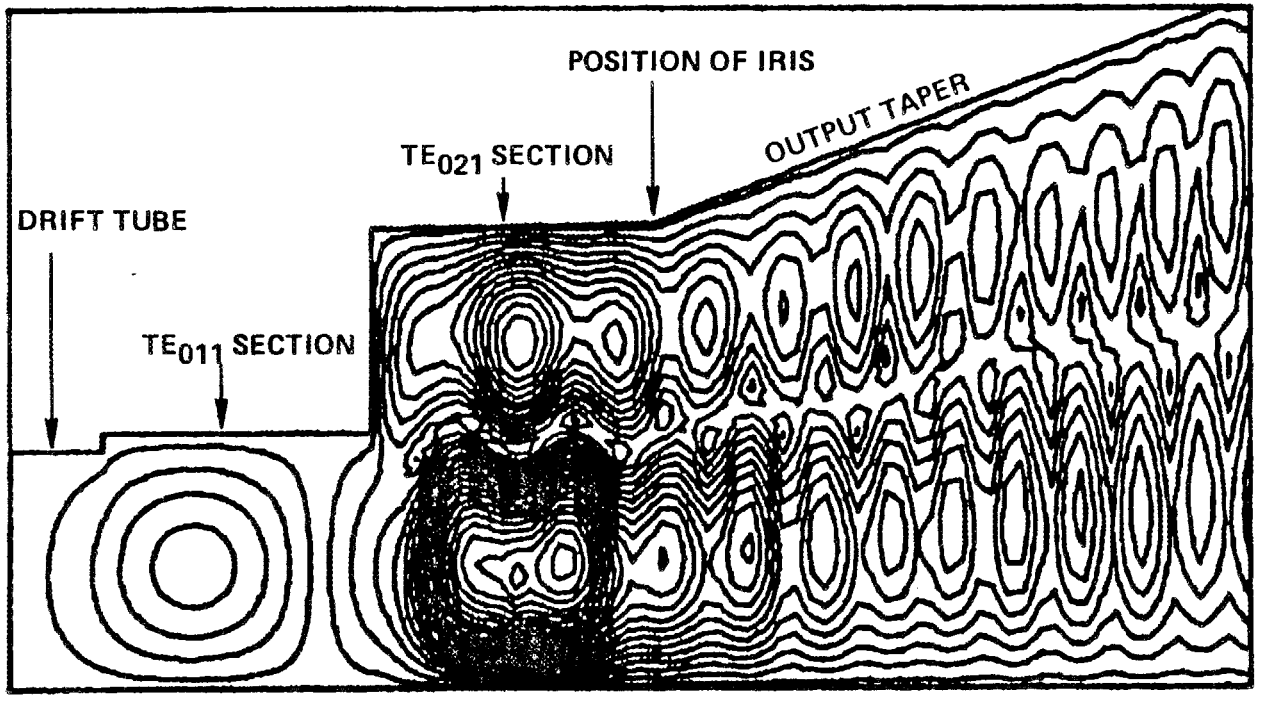

Figure 80. Example of a TE_{011}/TE_{021} Step Cavity as Simulated on a Computer Code Which Can Handle Open Step Cavities

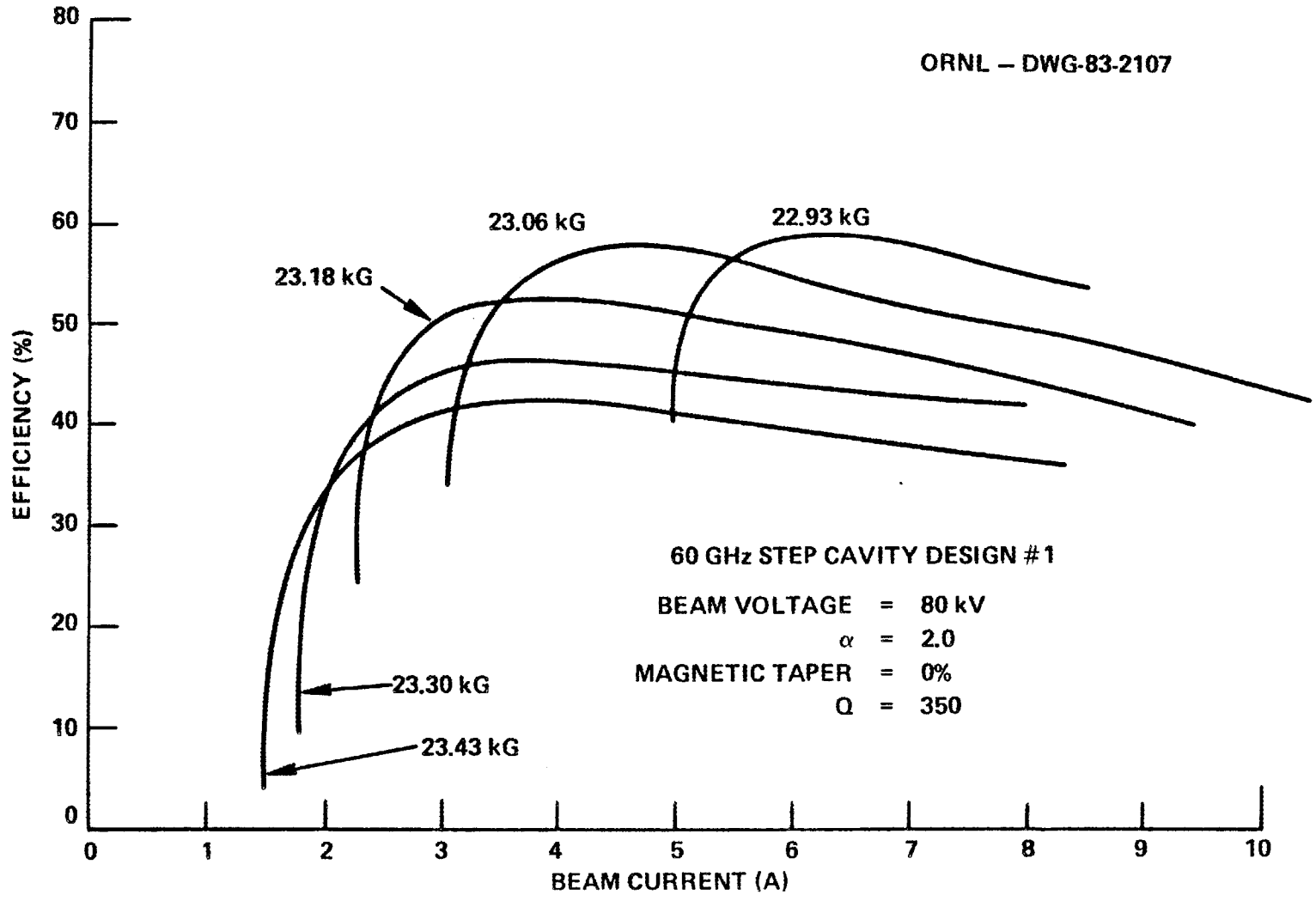

Figure 81. Efficiency vs Beam Current for Various Magnetic Fields for Step Cavity No. 1

ORNL – DWG-83-2108

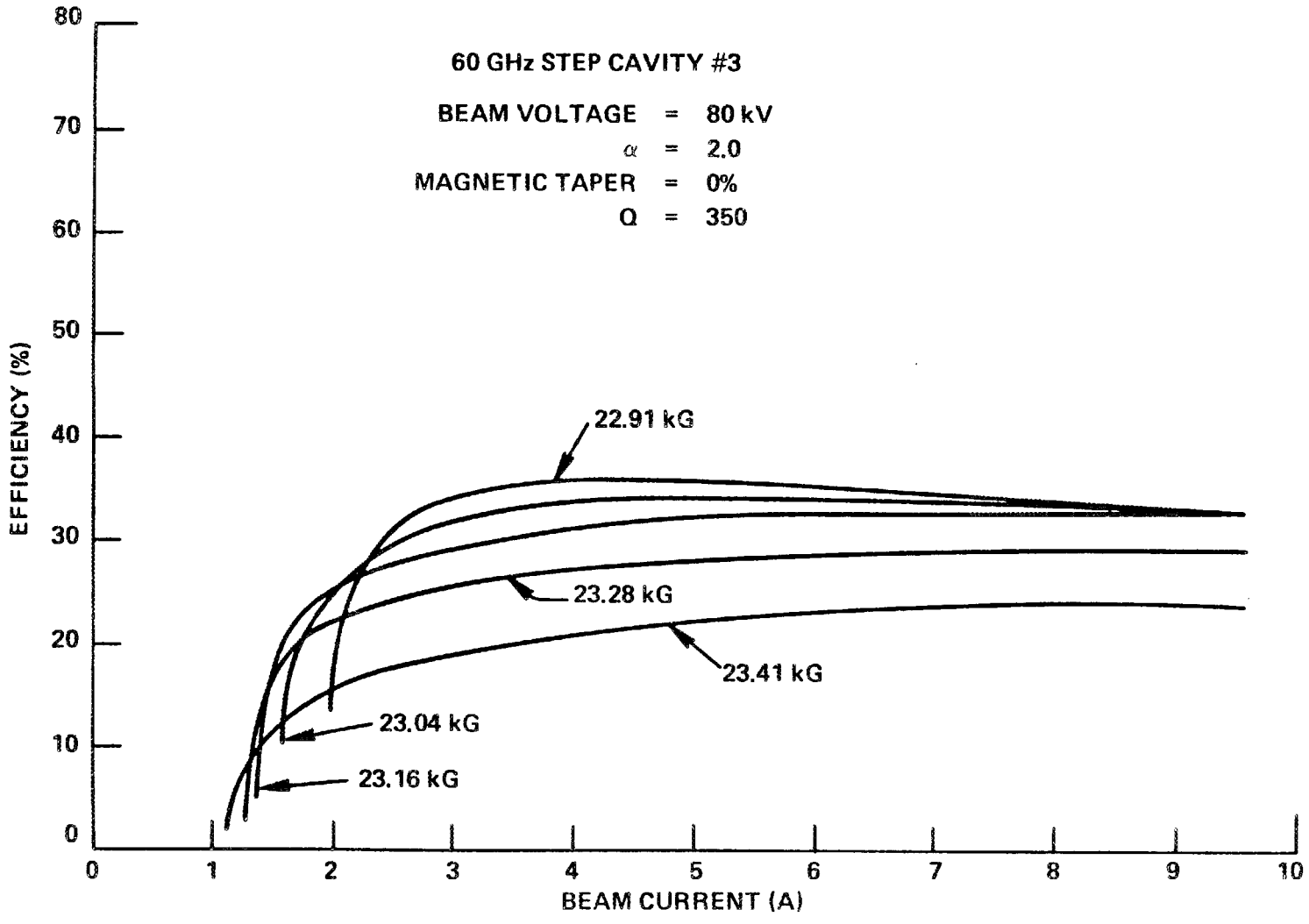

Figure 82. Efficiency vs Beam Current for Various Magnetic Fields for Step Cavity No. 3

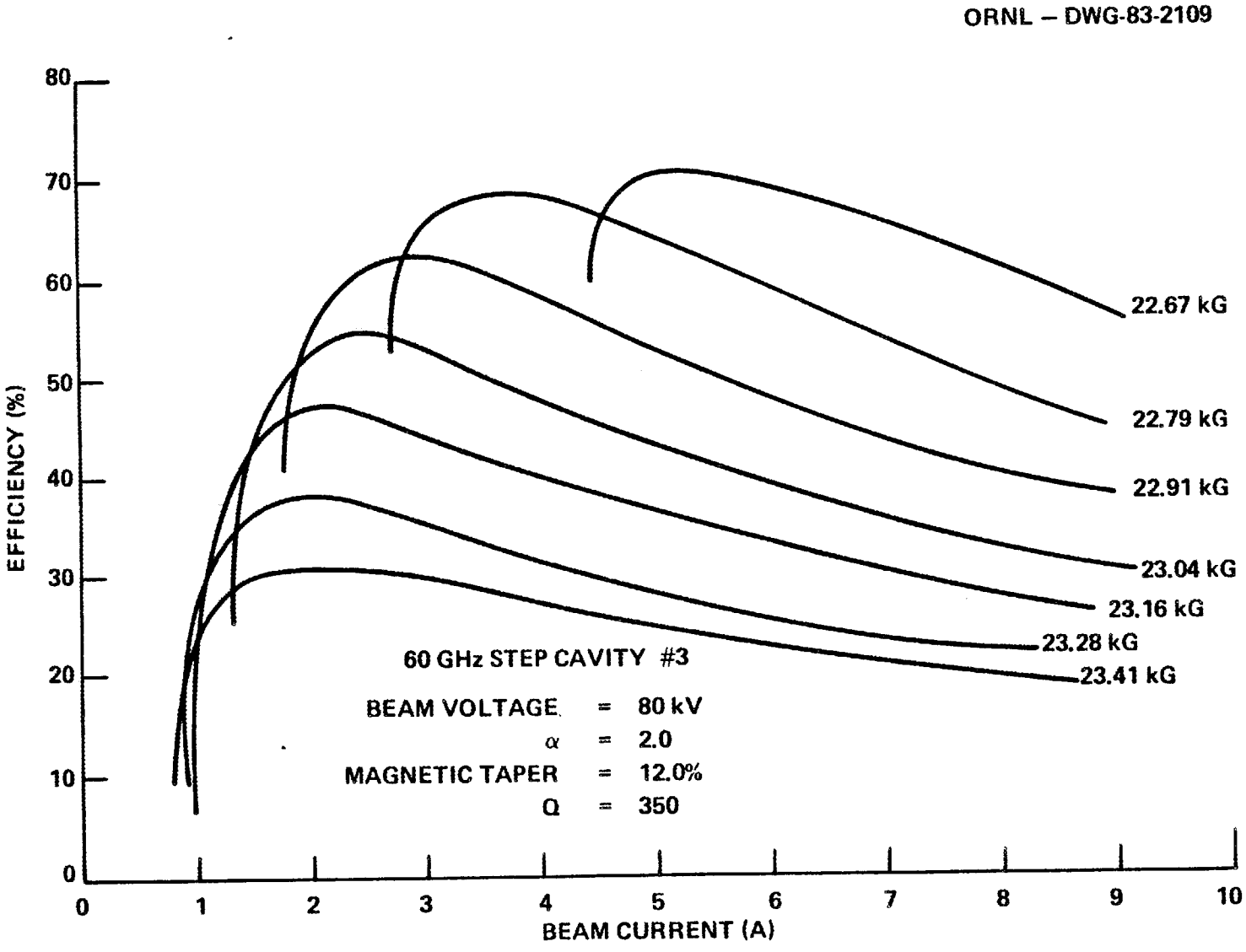

Figure 83. Efficiency vs Beam Current for Various Magnetic Fields for Step Cavity No. 3 With an Increasing Magnetic Field Taper of 12%

varying waveguide theory (i.e. where abrupt steps in the wall are not allowed) are not capable of providing correct values of the loaded Q, and a code like SUPERFISH must be used.

In Figure 84, an open-cavity SUPERFISH plot is shown of step cavity design # 3, excited at the resonant frequency of the cavity. It is easy to observe the effect of the iris in containing the cavity field, thus increasing the loaded Q from that of an open cavity with no iris.

In Figure 85, a typical resonance curve obtained from SUPERFISH for a step cavity with an iris is plotted. In Figure 86, the sensitivity of the loaded Q and resonant frequency to the iris diameter is shown. Iris diameter is referenced to the iris chosen for step cavity design #3. The thickness of the iris was fixed in all of the calculations. There was good agreement between the calculated value of the loaded Q and the cold test value for step cavity design # 3. However, the resonant frequency was somewhat different for the calculations and the cold test measurement, a result which is not yet understood.

The step or complex cavity concept greatly enhanced the stability of the present 60 GHz gyrotron, as evidenced by the success of the TE_{01}/TE_{02} step cavity design in reducing mode competition with the TE_{221} mode in X-6. Comparisons of theoretical predictions of tube efficiency with tube measurements made on X-6 will be discussed in Section IX.G. However, one experimental observation made during the testing of X-6 points toward the possibility of further optimizing the step cavity design. Specifically, large (>6%) magnetic tapers across the cavity, which were required for optimum efficiency, caused electron beam-related problems which affected body current and gun-anode current, and even reduced the perpendicular to parallel velocity ratio. A step or complex cavity design which yields good efficiencies without a magnetic field taper would probably eliminate those problems.

One such design was discussed previously (identified as step cavity design #1) as a possible choice for use in X-6. The reasons that it was not used were: 1) it appeared to have comparatively higher starting

ORNL DWG 83-2159

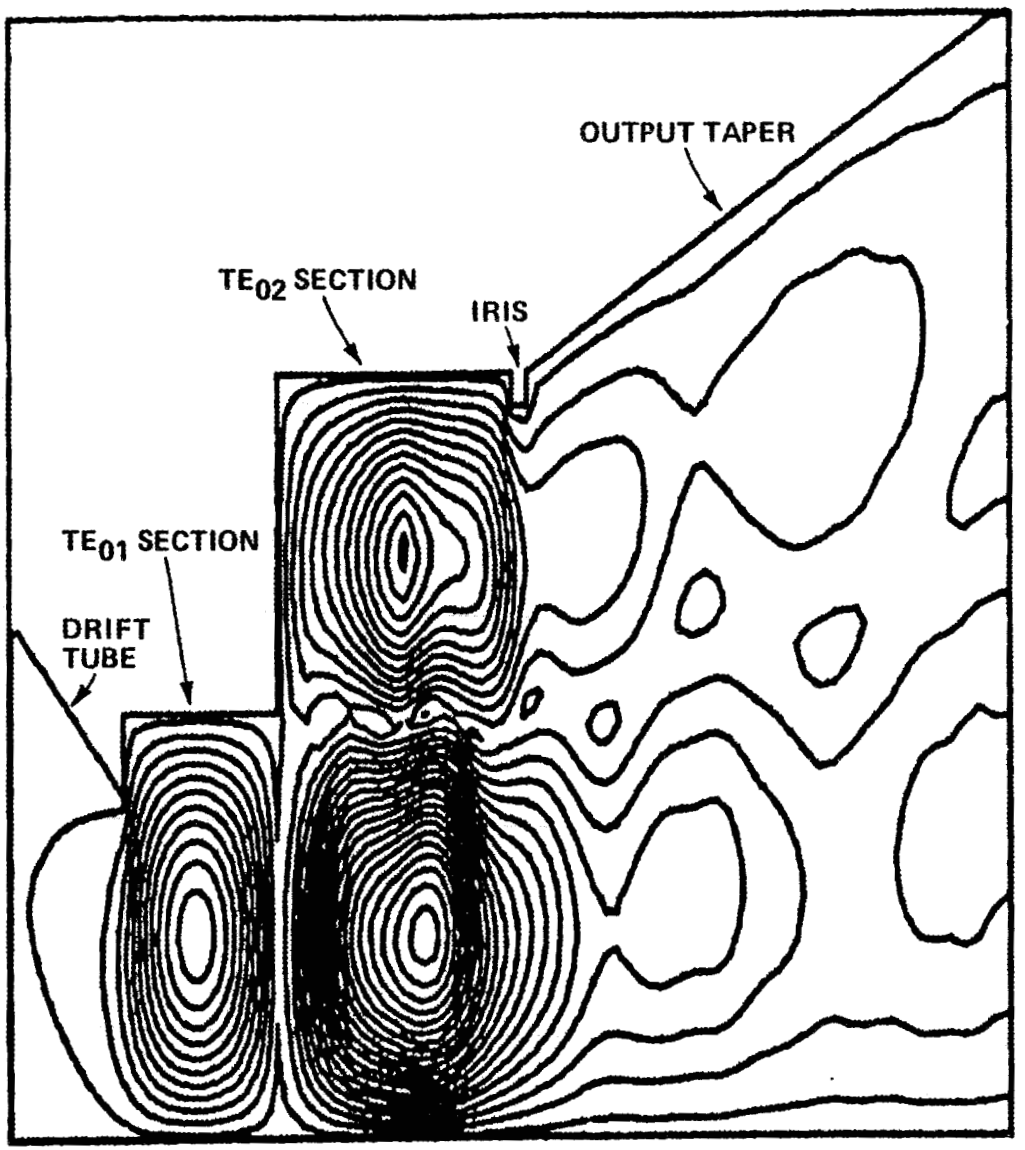

Figure 84. Open Cavity SUPERFISH Plot of Step Cavity Design No. 3

ORNL DWG 83-2160

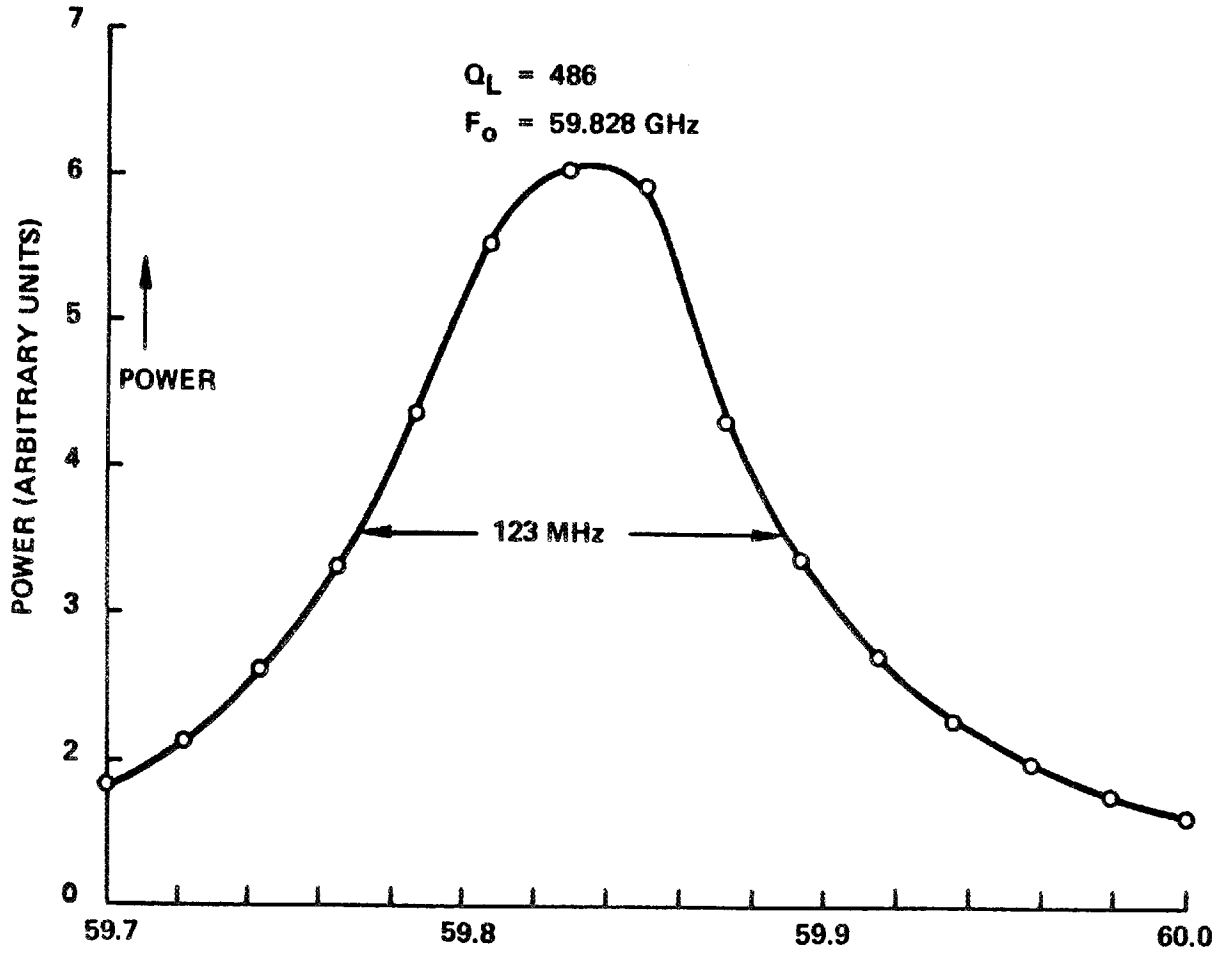

Figure 85. SUPERFISH Resonance Curve for Step Cavity with Iris

ORNL DWG 83-2161

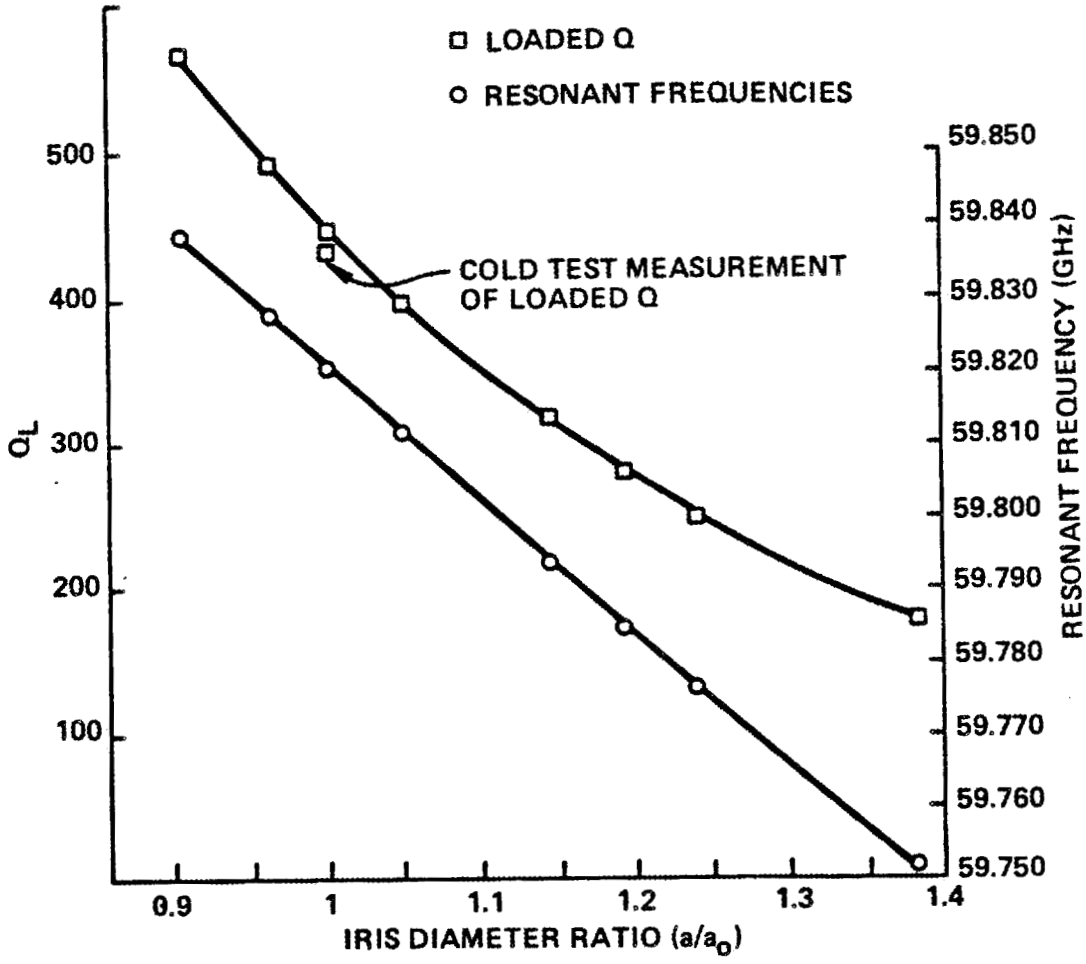

Figure 86. Q_L and f_o as Functions of the Ratio of Iris Diameter-to-Diameter of Iris Used in Step Cavity Design #3

currents (less bunching of the beam in the TE_{01} section) and 2) the highest efficiency achievable with or without a magnetic field taper was 60%; whereas the design chosen for X-6 (denoted step cavity design #3) had a calculated peak efficiency of 70%. However, the 60% value was achievable with no magnetic taper. The amount of suppression of the unwanted TE_{221} mode for a given design is hard to determine from the way starting currents are presently calculated. It is possible that only a small amount of electron bunching in the TE_{01} cavity is enough to inhibit excitation of the TE_{221} mode. Since the cavity used in X-6 had a calculated peak efficiency of 45% for magnetic tapers of 6% and lower, use of step cavity design #1 would improve the efficiency dramatically, were its mode suppression properties adequate.

Other complex cavity designs were investigated in an effort to achieve a design with the mode suppression qualities of design #3 (used in X-6) and capable of retaining a high efficiency without a magnetic field taper, as in design #1. One such design is shown in Figure 87. The wall of the TE_{02} section is tapered to profile the axial dependence of the rf electric field. Efficiency calculations for this cavity are shown in Figure 88. These results can be compared with those of design #1 shown in Figure 81, and design #3 (X-6) shown in Figure 82, for no magnetic field taper. In general, when compared to design #1, the range of starting currents is somewhat narrowed and lowered for a given range of magnetic fields. The starting current range is similar to that of design #3. The peak efficiency of 50% is an improvement over the 35% efficiency of design #3, though not as high as the 60% of design #1. These simple comparisons indicate that refining of the electric field profile may lead to a design with the desired characteristics having little or no magnetic field taper.

A TE_{01}/TE_{02} cavity design where the relative lengths of the two cavity sections were drastically altered is shown in Figure 89. Though the efficiency calculations for this design, shown in Figure 90, show no drastic improvements (again for no magnetic taper), the wide range of geometries that must be considered to arrive at an ideal TE_{01}/TE_{02} complex cavity design is obvious.

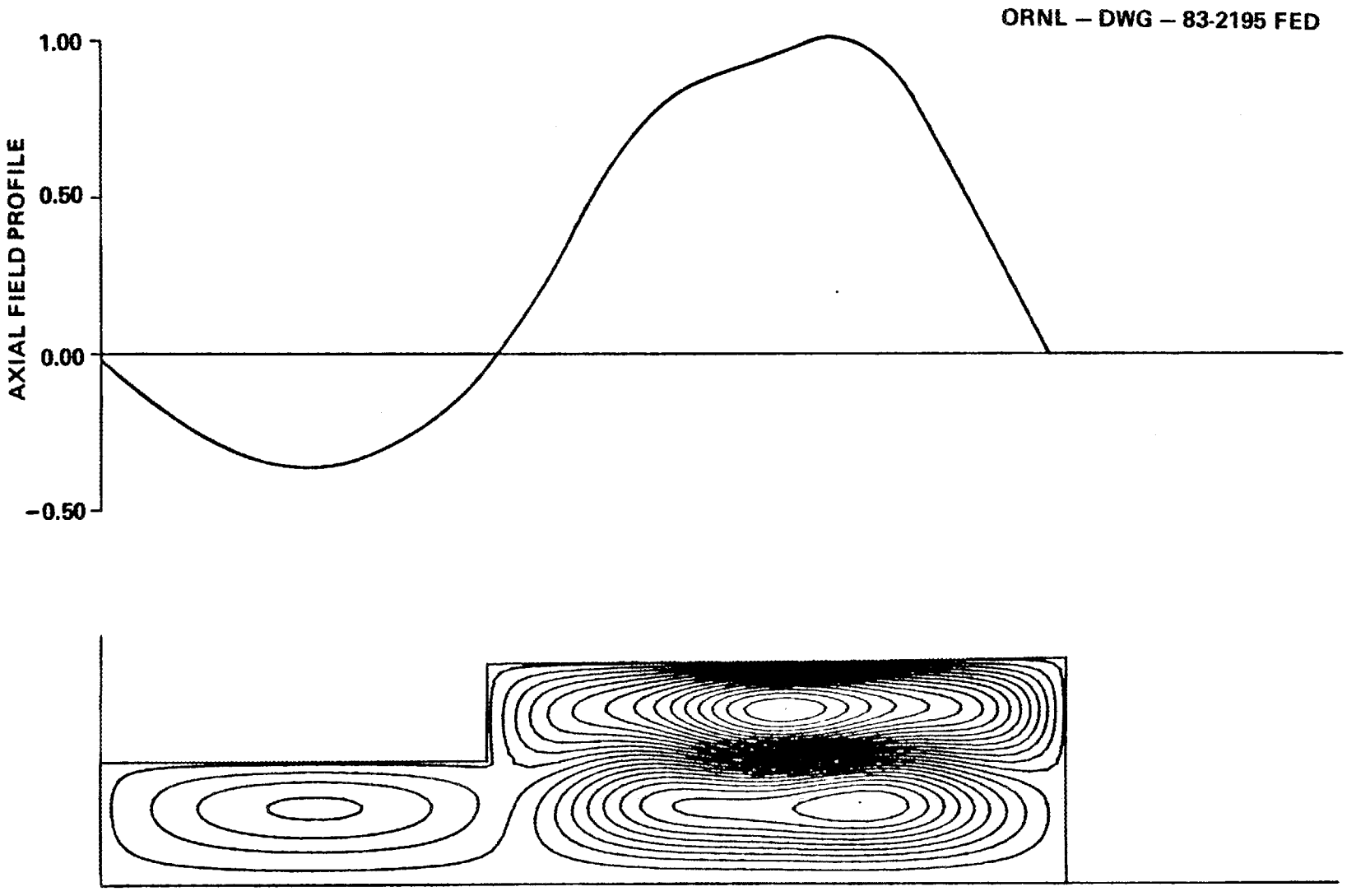

Figure 87. Example of a Complex Cavity with a Tapered Wall in the TE_{02} Section to Profile the Axial Dependence of the rf Electric Field

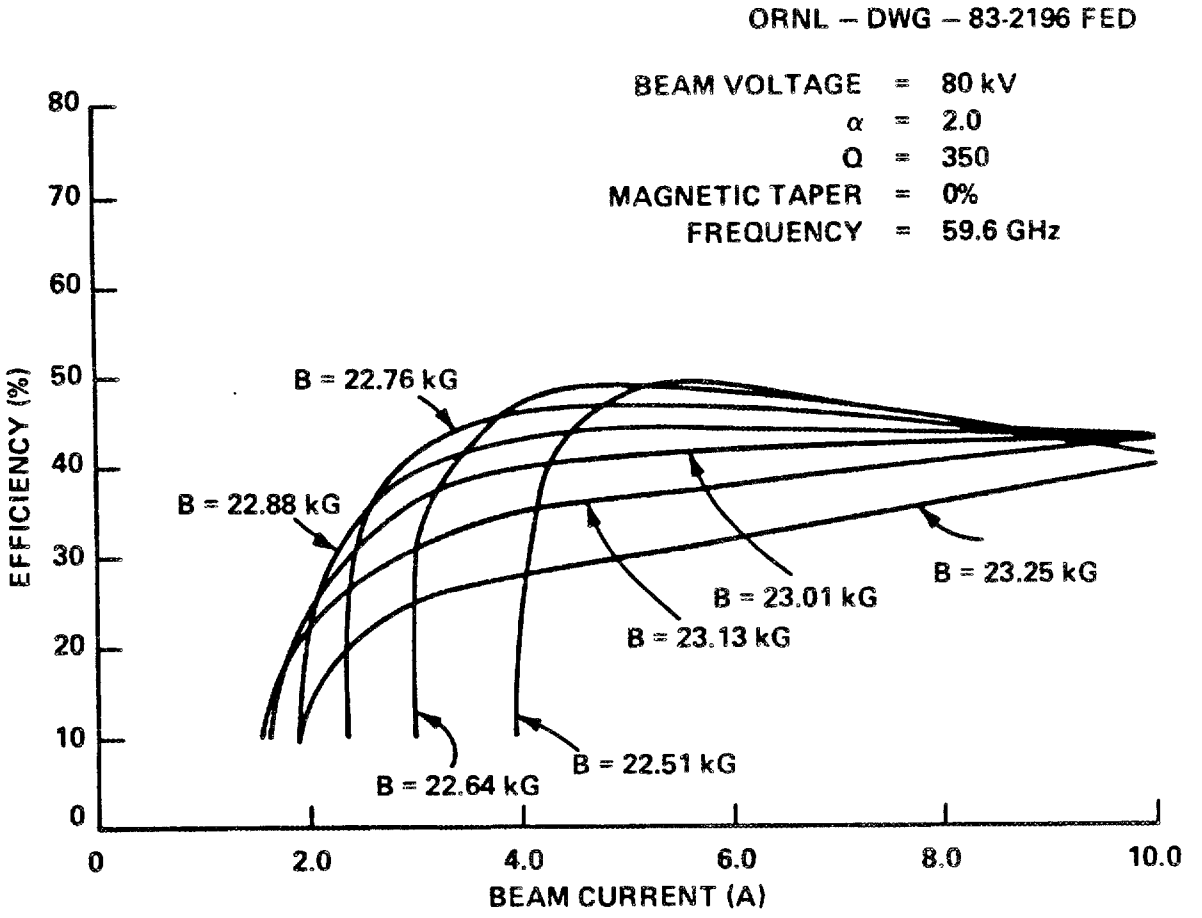

Figure 88. Efficiency Calculations for Several Values of Magnetic Field for a TE_{01}/TE_{02} Complex Cavity Design with a Tapered Wall in the TE_{02} Section

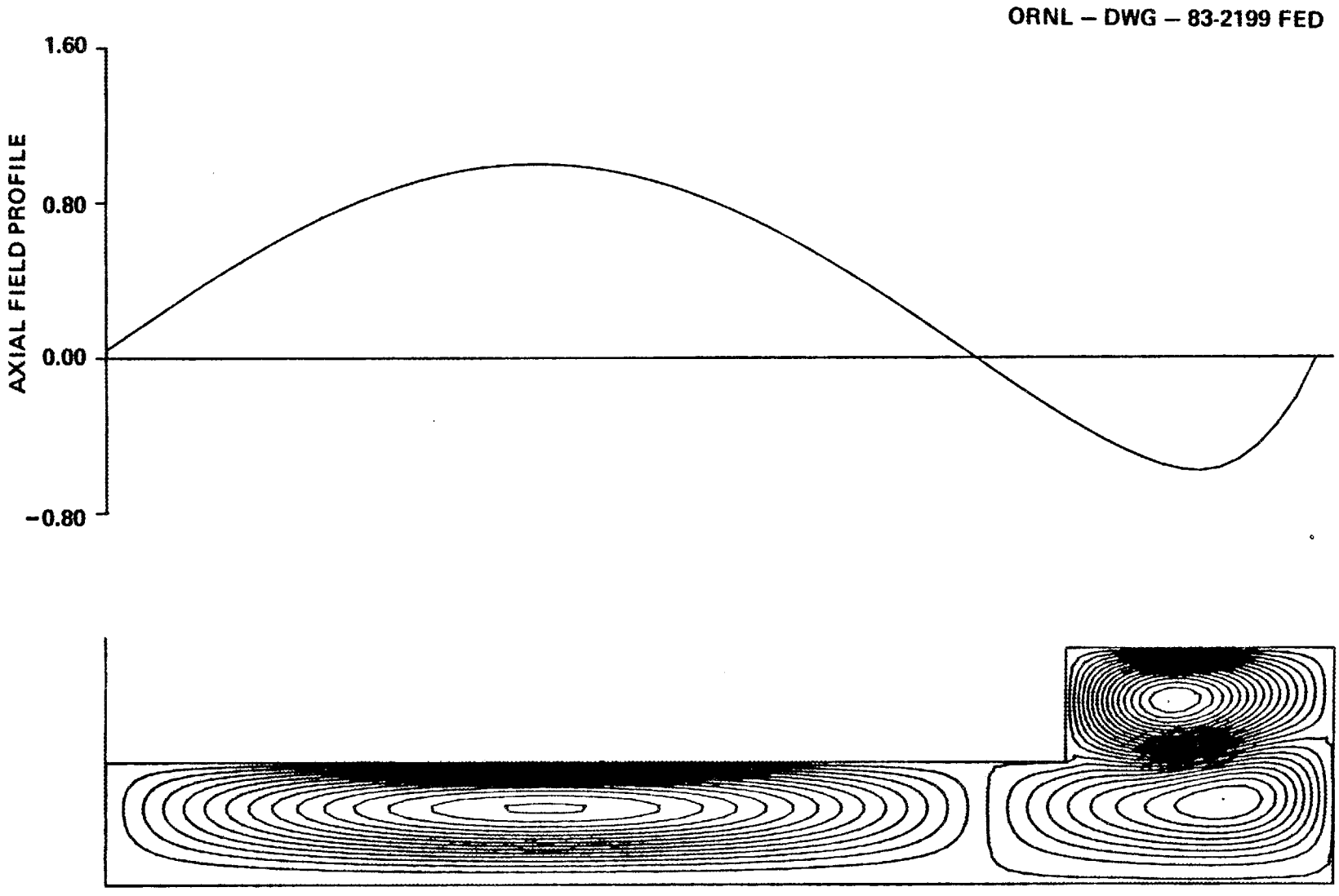

Figure 89. Example of a TE_{01}/TE_{02} Step Cavity with Modified Cavity Lengths

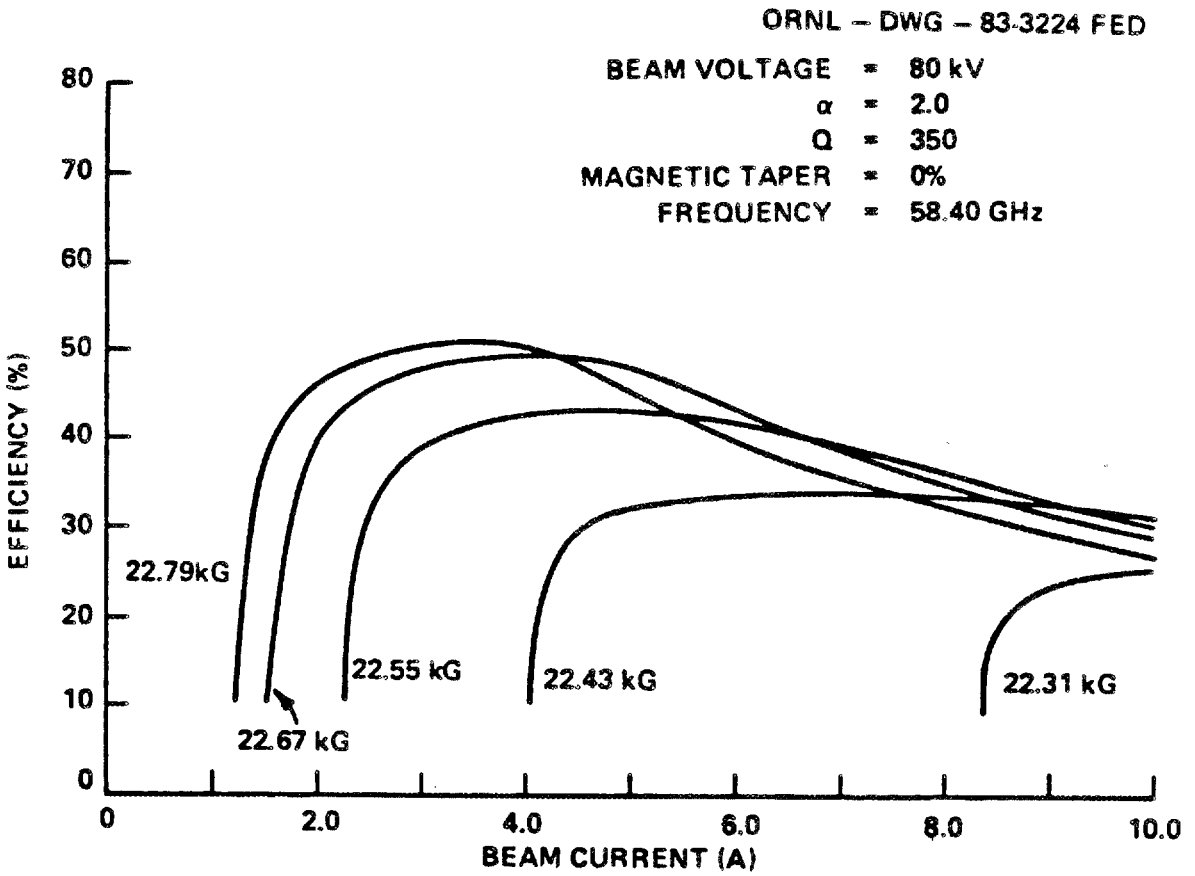

Figure 90. Efficiency Calculations for Several Values of Magnetic Field for a TE_{01}/TE_{02} Step Cavity Design with Modified Cavity Lengths

11. Mode Purity of Cavity Designs

The output mode content of the gyrotron cavity used on X-3R and X-5 and the step cavity used on X-6 (design #3) were calculated and compared. The calculations were performed using the open cavity SUPERFISH code discussed previously. Both cavities were excited at their resonant frequencies, and the output mode, 6 cm from the beginning of the cavities, well into the output taper section, was analyzed by matching the fields of the outgoing wave to the TE_{01}, TE_{02} and TE_{03} modes. The coefficients of each of the modes then gave a measure of the output mode content. The results of these calculations are shown in Figure 91. Both cavities yield TE_{02} modes that are at least 98.5% pure, indicating that the mode purity of the two cavities is similar. Though the effects of the electron beam and small asymmetries in actual tube cavities might alter the results somewhat, these results show that the use of the iris with the step cavity does not appear to degrade the purity of the output mode and that the cavity section, in general, does little to disturb the mode purity of the gyrotron.

D. OUTPUT/COLLECTOR

One problem commonly encountered in gyrotron design is the creation of modes other than the intended mode of oscillation. The unwanted modes are generated at discontinuities such as miter bends, gaps, and conical-cylindrical junctions which occur in the circular cross section output waveguide of the tube. The particular problem of mode conversion at conical-cylindrical junctions, is addressed in detail following the more abridged derivation of Solymar[9]. The derivation given in Appendix B concludes with formulas particularly applicable to gyrotron engineering.

In the assumed problem, a single TE_{on} mode propagates down an expanding linear overmoded waveguide taper, characterized by the half angle, θ_o, in radians. [See Figure 92.] At radius a, the taper is joined to a cylindrical waveguide and, at this junction, the TE_{on} mode is partially converted to other TE_{om} modes. The power conversion coefficient, P_{mn}, the ratio of power converted into the TE_{om} mode to the incident power in the TE_{on} mode, as a function of the taper angle, θ_o, junction radius, a, and

ORNL – DWG – 83-3225 FED

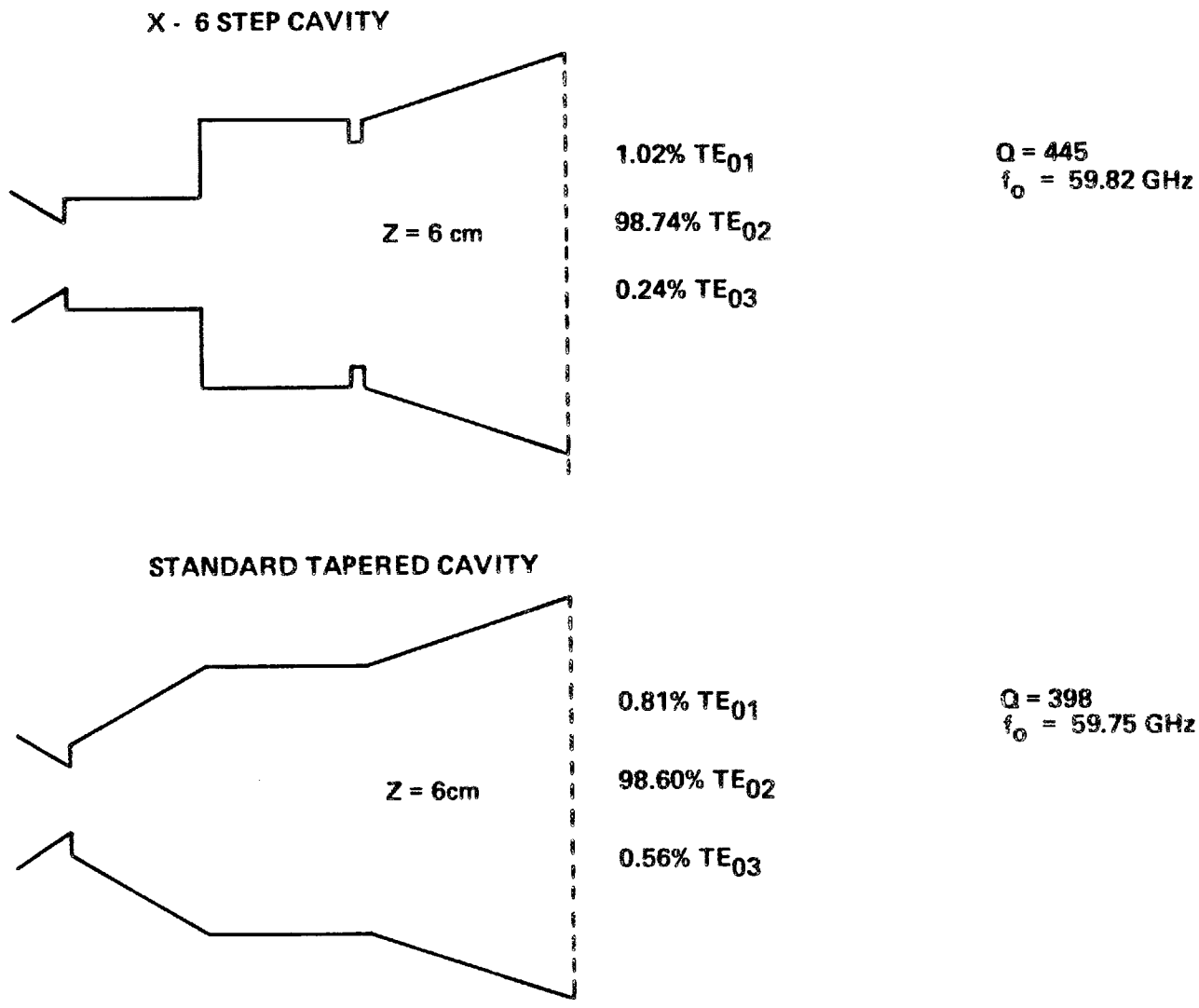

Figure 91. Comparison of Mode Content of the X-6 Step Cavity with that of the Standard Tapered Cavity Used on X-5.

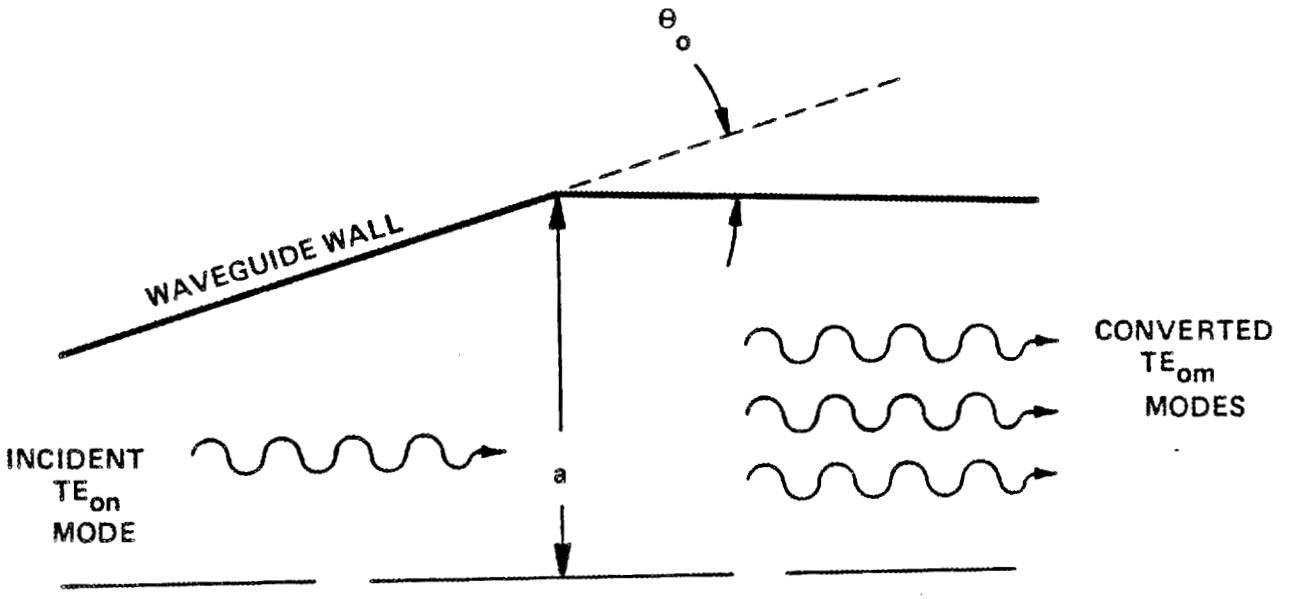

Figure 92. Taper to Cylinder Waveguide Junction

free space radiation wavelength, λ, will be computed. Several simplifying assumptions will be made. The taper angles are assumed to be small ($\theta_o \ll 1$), and the waveguide overmoded ($a/\lambda \gg 1$). The treatment also ignores reflections at the junction, as well as the presence of any non-axisymmetric modes.

It is shown in Appendix B that the complex coefficient, T_{mn}, for determining the power conversion is given by

$$T_{mn} = \frac{2}{J_o^2(X_{1m})} \int_0^1 te^{iKt^2} J_1(X_{1m}t) J_1(X_{1n}t)\,dt \tag{36}$$

where X_{1n} = the nth positive root of the equation $J_1(X) = 0$

$t = \theta_1/\theta_{10}$

θ_1, θ_{10} = as defined in Figure 2 in Appendix B

K = defined in Equation 20 in Appendix B

Consider the case of the large taper angle ($\pi a\theta_o/\lambda > 1$, $\theta_o \ll 1$). The total power in the TE_{om} mode is given by

$$P_m \propto \left|T_{mn}\right|^2 J_o^2(X_{1m}) \quad . \tag{37}$$

Thus, the ratio of $P_m/P_n \equiv P_{mn}$, which is the power conversion from a pure TE_{on} mode at the junction to the TE_{om} mode is

$$P_{mn} \equiv \frac{P_m}{P_n} = \frac{\left|T_{mn}\right|^2}{\left|T_{nn}\right|^2} \frac{J_o^2(X_{1m})}{J_o^2(X_{1n})} \quad . \tag{38}$$

For a small taper angle ($\pi a\theta_o/\lambda < 1$, $\theta_o \ll 1$), Equation (38) reduces to

$$P_{mn} = \frac{a^2\theta_o^2}{\lambda^2} \cdot \frac{64\pi^2 X_{1m}^2 X_{1n}^2}{(X_{1m}^2 - X_{1n}^2)^4} \quad . \tag{39}$$

A physical interpretation of the results can be given. First, in the limits $\pi a\theta_o/\lambda < 1$, $\theta_o << 1$, and $a/\lambda >> 1$, $P_{mn} = P_{nm}$, or mode conversion between two modes is symmetric. Furthermore, P_{mn} scales according to,

$$P_{mn} \sim \frac{x_{1m}^2 \, x_{1n}^2}{(x_{1m}^2 - x_{1n}^2)^4} \quad , \tag{40}$$

which shows that mode conversion is strongest between "nearest neighbor" modes, and falls off rapidly as

$$P_{mn} \sim \frac{1}{m^6} \quad \text{for } n \sim 1,\ m >> 1 \quad , \tag{41}$$

as shown in Figure 93. Finally, P_{mn} also scales as $(a\theta_o/\lambda)^2$. If there is an upper limit on the value of P_{mn} which can be tolerated, P_{mn}^{MAX}, there is an upper bound on θ_o:

$$\theta_o^{MAX} \sim \frac{\lambda}{a} \sqrt{P_{mn}^{MAX}} \tag{42}$$

In Figure 94, the function P_{mn} is plotted versus θ_o for the special case of f = 110 GHz and 2a = 2 1/2". Putting in some numbers for a TE_{02} oscillator at 60 GHz, and looking for a value of $P_{32}^{MAX} = 5\%$ at a 2 1/2" conical-cylindrical junction, we find $\theta_o^{MAX} = 3.3°$.

A mode probe, or traveling wave indicator, was designed and built to aid in cold test analysis of the mode conversion properties of various multimode waveguide structures such as mode filters, waveguide bends, and output/collector assemblies. Tests of the mode probe at 28 GHz showed that the instrument can be used with multimode waveguides for which

$$\frac{d}{L} \lesssim \frac{\lambda}{d} \lesssim 0.2, \tag{43}$$

where d is the waveguide diameter, λ is the free space wavelength, and L ($\sim$ 1 meter) is a length over which it is practical to measure the beat pattern of two waveguide modes. The mode probe was used successfully to

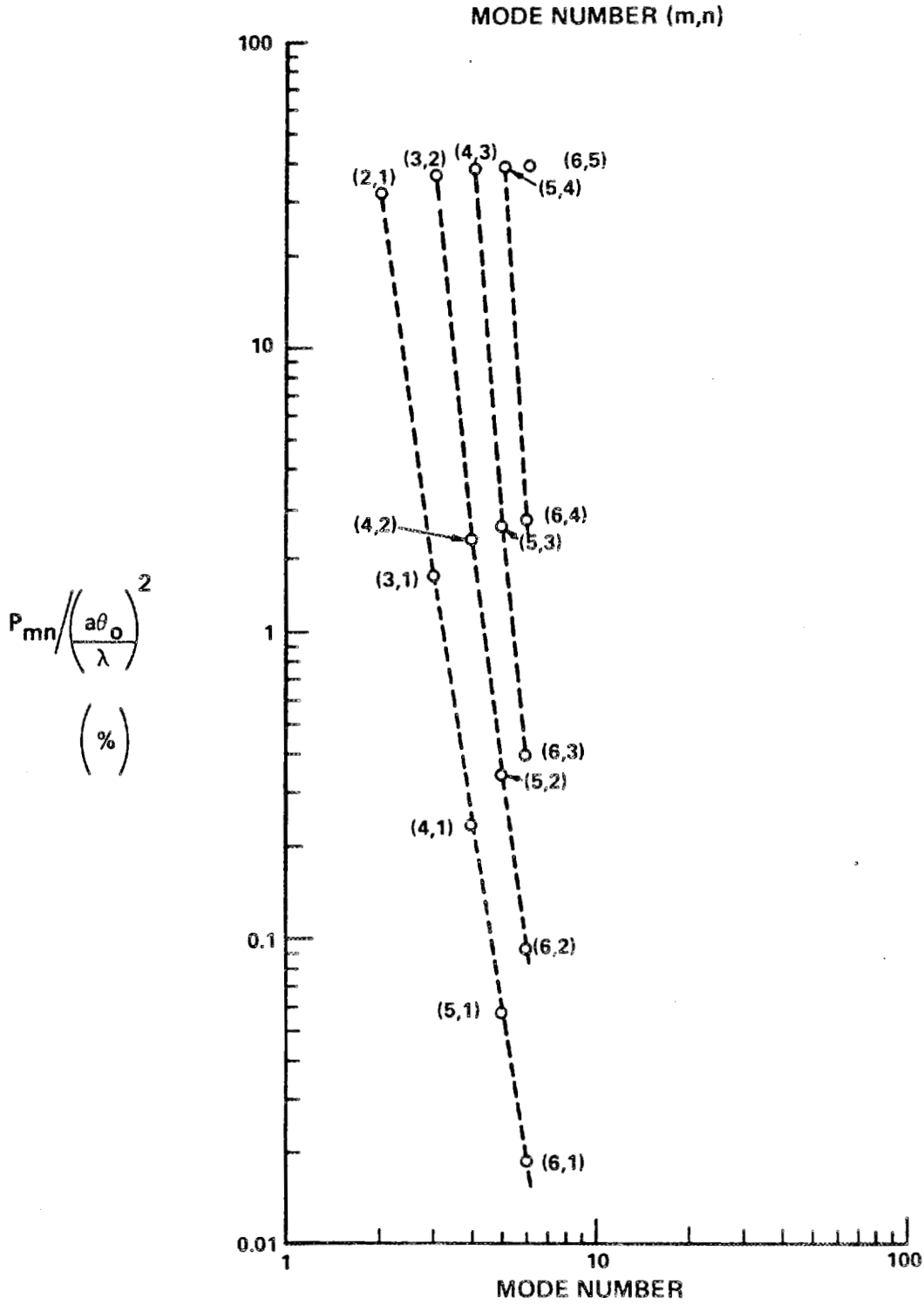

Figure 93. Mode Conversion

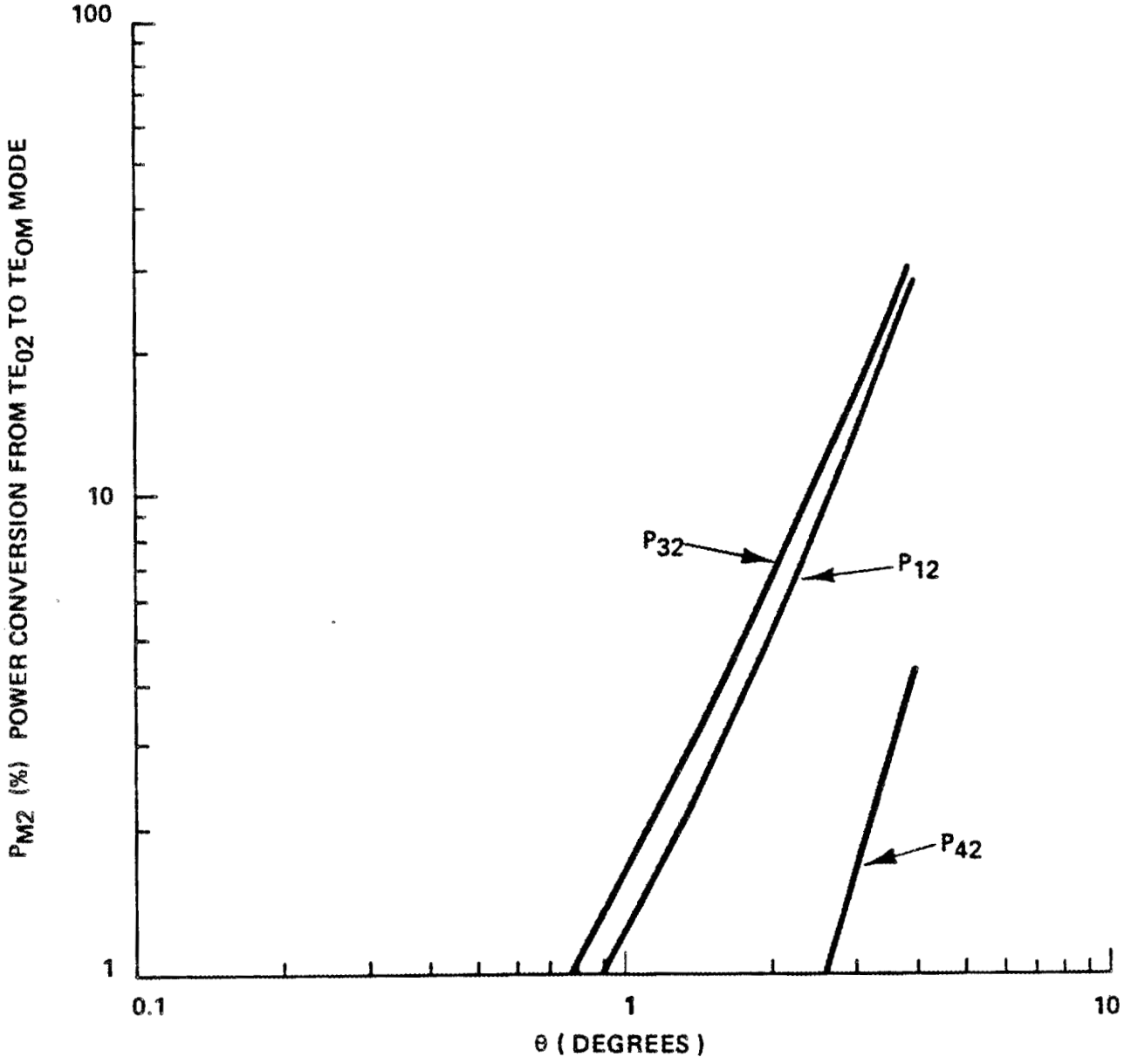

Figure 94. Mode Conversion as a Function of Taper Angle

determine the mode conversion properties of the VGA-8000 SN 6 (28 GHz, 200 kW CW) output/collector assembly on a cold test basis.

An analytic framework was developed for interpreting the traveling wave measurements made with the mode probe. The analysis was intended to be sufficiently general to apply not only to simple mode conversion problems, such as the conversion of a single TE_{on} mode to other $TE_{on'}$ modes, but also to the conversion of a set of modes TE_{mn} and TM_{pg} into a second set of modes $TM_{m'n'}$ and $TM_{p'g'}$. The analysis and experimental considerations are discussed in Appendix C.

1. Thermal Analysis

a. Heat Flow Study

The problem of transient heating in the gyrotron collector was analyzed to determine the effect of hydrodynamic and geometric parameters on heat transport in the long pulse regime. As a first step in the analysis, one dimensional transient heat transport calculations were made. Two dimensional modeling, carried out with the aid of a transient heat transport code, and further work on this topic will be discussed in Section VI.D.1.b-d.

The one dimensional transient heat transport analysis is based on "initial value" calculations. The results are, therefore, valid only for a single heat flux pulse of amplitude $\hat{q}$ (watts/cm^2) and duration τ (sec). In practice, of course, all pulsed devices will be required to withstand finite duty, $\nu \equiv \tau/\Delta$ where Δ is the pulse repetition period. For very low duties, the single pulse analysis is valid, but for $\nu \geq 0.02$, the presence of the residual temperature profile, resulting from an infinite pulse train, must be considered.

The single heat impulse is turned on at the collector wall at time, $t = 0$, and terminated at $t = \tau$. For very short times, the heat pulse will not penetrate the collector wall material to the cooling channels. The

collector wall, then, appears to be semi-infinite as shown in Figure 95. The one dimensional heat diffusion equation,

$$\frac{\partial^2 \Delta T\ (x,t)}{\partial x^2} - \frac{1}{D} \frac{\partial \Delta T(x,t)}{\partial t} = 0 \quad , \tag{44}$$

for the temperature rise, $\Delta T(x,t)$, above the ambient (coolant) temperature, T_c, has been solved. The parameter D is the thermal diffusivity of the collector wall material. The boundary conditions for the semi-infinite slab model are

$$\frac{\partial \Delta T\ (o,t)}{\partial X} = \frac{-q\ (o,t)}{K} \tag{45}$$

with $\quad q(o,t) = \hat{q} \quad o < t < \tau$

$\qquad\qquad\quad = o \quad t > \tau$

and

$$\Delta T\ (\infty,t) = 0 \quad .$$

The solution is [25]

$$\Delta T(x,t) = \frac{2\hat{q}\sqrt{D}}{\sqrt{\pi}\ K}\left[\sqrt{t}\left\{2T\left(\frac{3}{2}\right) \text{ierfc}\left(\frac{x}{2\sqrt{Dt}}\right)\right\}\right] \quad o<t<\tau \tag{46}$$

$$= \frac{2\hat{q}\sqrt{D}}{\sqrt{\pi}\ K}\left[\sqrt{t}\left\{2T\left(\frac{3}{2}\right) \text{ierfc}\ \frac{x}{2\sqrt{Dt}}\right\} - \sqrt{t-\tau}\left\{2T\left(\frac{3}{2}\right) \text{ierfc}\left(\frac{x}{2\sqrt{D\ (t-\tau)}}\right)\right\}\right] t>\tau$$

If we set x = o in Equation 46, we find that the quantities in the curly brackets go to unity. The peak temperature rise at the collector wall is then

$$\Delta T(x=o)\Big|_{max} = \frac{2\ \hat{q}\ \sqrt{D\tau}}{\sqrt{\pi}\ \ K} \tag{47}$$

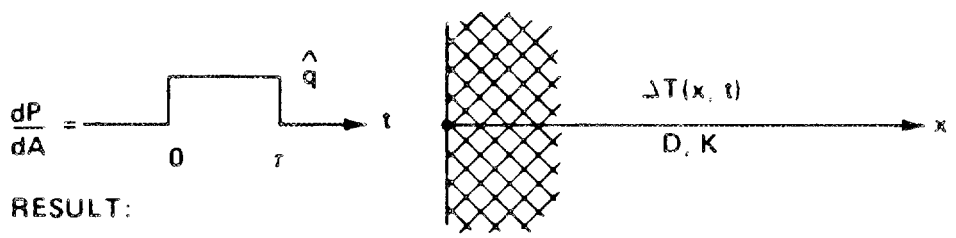

Figure 95. Infinitely Thick Slab

For copper, with an incident heat flux of 1 kW/cm^2, Equation 47 becomes

$$\Delta T(x=o)\Big|_{max} (^{o}C) = 299 \sqrt{\tau(sec)} \tag{48}$$

By inspection of Equation 46, we see that the heat pulse penetrates the collector wall a distance $\hat{L} \sim 2\sqrt{Dt}$. If the water channels are located a distance L from the collector wall, then the heat pulse will reach the water channel in a time $\hat{t} \sim L^2/4D$. For the pulsed collector design, this time is on the order of 50-100 ms. Therefore, for a pulse duration in excess of 50 ms, the analysis must be generalized to consider the heat transfer into the coolant. The generalized, one-dimensional geometric model is shown in Figure 96. The heat diffusion Equation 44 must now be solved subject to a new set of boundary conditions:

$$\frac{\partial \Delta T(o,t)}{\partial x} = \frac{-q(o,t)}{K} \text{, as before} \tag{49}$$

while

$$\frac{\partial \Delta T(L,t)}{\partial x} = - \frac{h(t)\Delta T\ (L,t)}{K} , \tag{50}$$

where h(t) is the heat transfer coefficient of the water channel boundary layer. By invoking Equation 50, the water channel boundary layer is assumed to a) have zero heat capacity b) be spatially much thinner than the wall thickness, L, and c) support heat flow which may always be considered steady state compared to the other thermal time scales in the problem.

The heat transfer coefficient, h, is, in general, a complicated function of the hydrodynamic parameters, as well as the absolute temperature, T, of the water channel wall. Qualitatively, h is roughly independent of T in the "convection cooling" regime ($T \lesssim 100^{o}C$). Once the water channel wall temperature exceeds the boiling point, the boundary layer supports the formation of small bubbles which are continuously reabsorbed in the bulk of the coolant. This regime of operation, "nucleate boiling", improves heat transport, and the heat transfer coefficient is a strongly increasing function of T until the burnout condition occurs[26]. At burnout

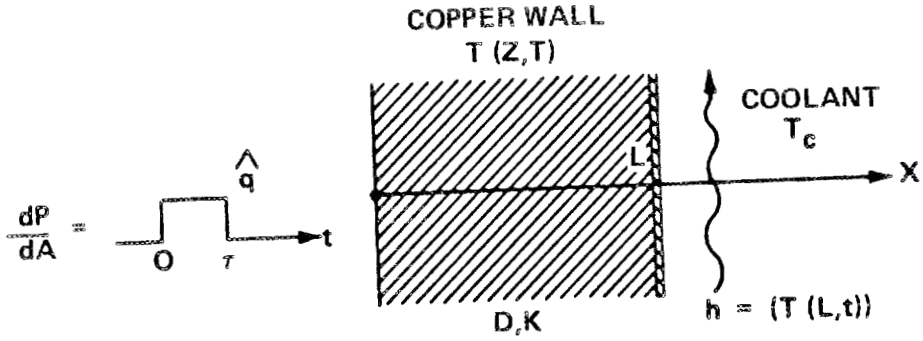

Figure 96. Slab of Finite Thickness

the turbulent fluid boundary layer is replaced by a blanket of superheated steam and the heat transfer coefficient drops radically.

As long as the water channel wall temperature does not exceed $100^{\circ}C$, we may approximate $h(t) = h$ = constant. Then for $t < \tau$, equation 44 can be solved subject to Equations 49 and 50[27].

$$\Delta T(x,t) = \frac{\hat{q}\,L}{K}\left[\frac{1}{B} + \left(1-\frac{x}{L}\right) - 2\sum_i \frac{e^{-Dy_i^2\,t/L^2}\left(\cos\frac{y_i x}{L}\right)\left[y_i^2 + B^2\right]}{y_i^2\left[y_i^2 + B^2 + B\right]}\right]_{o < t < \tau}, \qquad (51)$$

where $B \equiv h\,L/K$ is the thermal conductance of the water channel boundary layer normalized to the thermal conductance of the collector wall, and the y_i's are the positive roots of

$$\cot y = \frac{y}{B} \quad . \qquad (52)$$

The sum $\sum_i$ in Equation 51 represents a spectrum of highly damped "heat waves" with "wavenumbers" which are "resonant" according to Equation 52. The first three roots of Equation 52 are plotted in Figure 97 versus the thermal conductance parameter, B. Typically, only the first and, possibly, the second, roots of Equation 52 are required for appropriate convergence of the sum $\sum_i$ in Equation 51. For times $t > \tau$, Duhamel's theorem can be applied to Equation 51 to obtain

$$\Delta T(x,t) = \frac{\hat{q}\,L}{K}\; 2\sum_i \frac{\left(\cos\frac{y_i x}{L}\right)\left[y_i^2 + B^2\right]\left\{e^{-Dy_i^2\,(t-\tau)/L^2} - e^{-Dy_i^2\,t/L^2}\right\}}{y_i^2\left[y_i^2 + B^2 + B\right]} \quad . \qquad (53)$$

$$t > \tau$$

Equations (51) and (53) were used to calculate the transient temperature profiles for a case of particular interest for the 60 GHz, 100 ms pulsed tube as shown in Table 14.

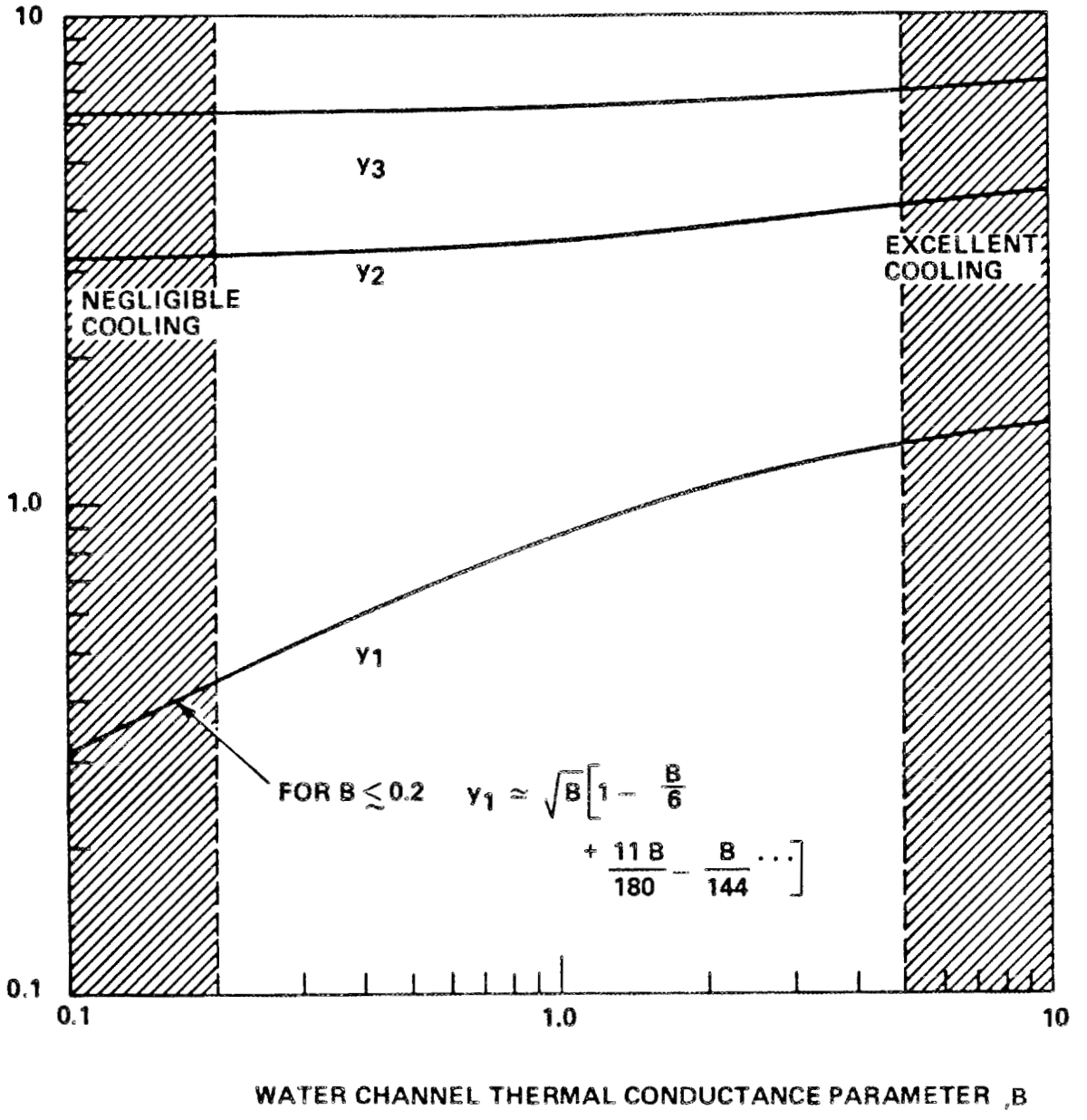

Figure 97. Roots of Cot $y = \frac{y}{B}$

Table 14

Parameters for Cooling Calculations (Figure 98)

coolant temperature	$35^{o}C$
coolant pressure	100 psig
coolant velocity	0.91 ft/sec
coolant flow rate	2 gpm
coolant heat transfer coefficient	0.22 watts/cm^2-^{o}C
incident heat flux	1 kW/cm^2
wall thickness	0.508 cm
wall thermal conductivity	4.0 watts/cm-^{o}C
wall thermal diffusivity	1.12 cm^2/sec
pulse duration	100 msec
duty	10^{-3}

The cooling parameters in Table 14 were chosen to provide sufficient cooling for the average power (1 watt/cm^2). The resulting time history for the temperature profile, as in Figure 98, shows that the cooling parameters are indeed sufficient to hold temperature excursions within the design limits. Note that the thermal conductance of the water channel for this case is very low compared to that of the copper wall; the water channel boundary acts as an insulator during the heat pulse. The assumption, h = constant, which was used in calculating these profiles is, in hindsight, valid because the water channel wall temperature never exceeds the point of transition (~ $100^{o}C$) from convection cooling to nucleate boiling. On a timescale large compared to the pulse duration, the temperature profile labeled as t = 0.2s decays uniformly to the coolant temperature in a time ~ LK/hD ~ 10 seconds. Thus, the peak bulk water temperature excursion is ~ $25^{o}C$, while the average bulk water temperature excursion is ~ $2.5^{o}C$.

From the temperature profiles shown in Figure 98, we expected that for the cooling parameters in Table 14 and pulse durations on the order of several hundred milliseconds, the temperature excursion at the water channel wall would not exceed the burnout temperature. The one-dimensional collector calculations are summarized in Figure 99. These preliminary heat transfer calculations suggested that more detailed, computer calculations be

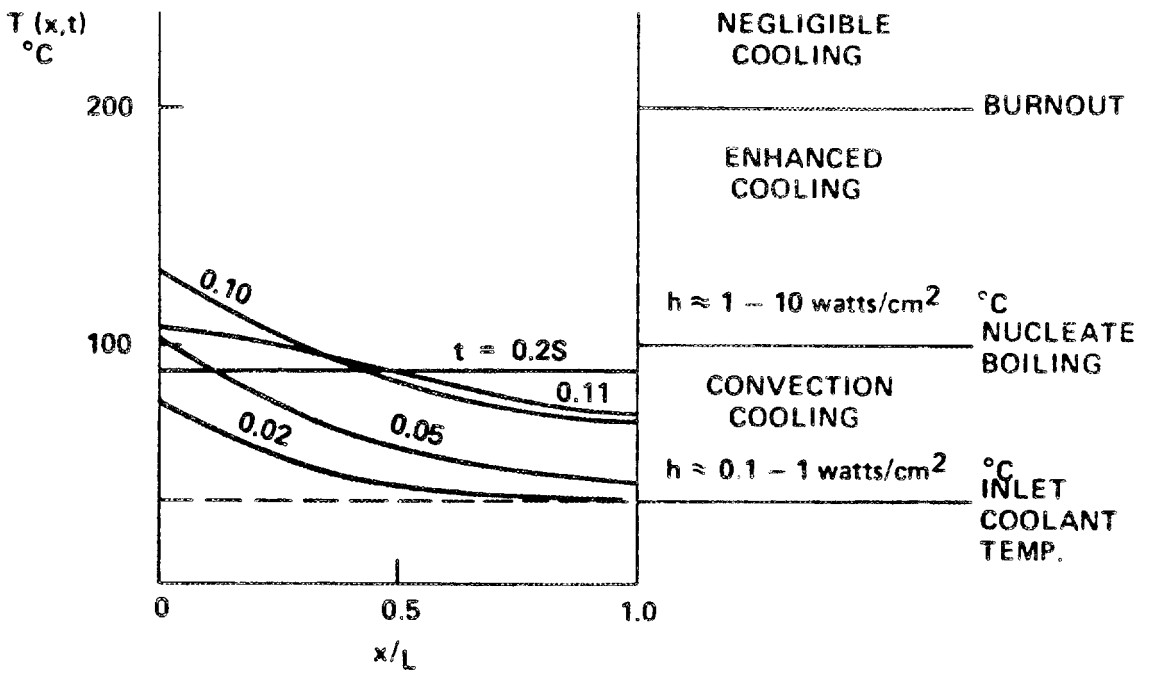

Figure 98. Transient Temperature Profiles in Collector Wall

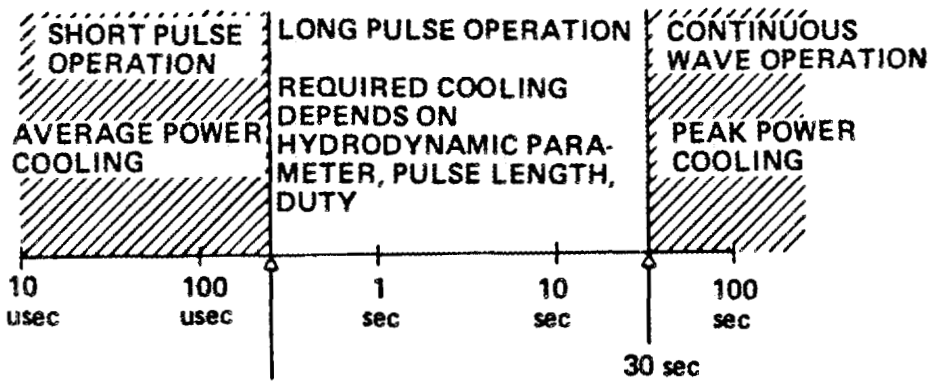

Figure 99. Pulse Duration Regimes for Gyrotron Collectors

performed to determine behavior at the water channel. The temperature as a function of position and time, both during and after a pulse, was required for stress calculations. It was necessary to determine the suitability of the collector for repeated long pulse operation and to determine the collector cooling water flow rates required for less than continuous operation.

Proposals were solicited from outside vendors to perform these calculations. One vendor had been used previously to perform CW burnout calculations during the 28 GHz gyrotron development. Approximately half the cost of the proposed effort was for computer time. The heat flow in the collector was studied by means of mathematical modeling on the TACO computer program at the National Magnetic Fusion Energy Computer Center at Lawrence Livermore National Laboratory in Livermore, California.

TACO[28] is a two-dimensional implicit finite element code for heat transfer analysis. It can perform both linear and nonlinear analyses and can be used to solve either transient or steady-state problems. Either plane or axisymmetric geometries can be analyzed. The collector is a nonlinear case.

TACO is capable of handling time or temperature-dependent material properties, and material may be either isotropic or orthotropic. A variety of time and temperature-dependent loadings and boundary conditions are available, including temperature, flux, convection, and radiation boundary conditions and internal heat generation.

b. The Mesh

In the TACO program, the region to be analyzed for heat transfer is represented by a mesh. Because of collector symmetry, there are a number of identical cross sections and their mirror images. Each section is centered on one of the channels through which cooling water flows. By symmetry, it can be assumed that no heat flows between adjacent cross sections. It was also assumed, for simplicity, that no heat flows across the outer radius of the collector. A further assumption is that heat flows

into a section across the vacuum-copper boundary, which represents the inner radius of the collector, and out of the section across the copper-water boundary, which represents the water channel.

Calculations were performed with a mesh of 174 nodes and 140 elements, including two triangular elements on the water channel surface. Due to the large amount of computing time required for the 174-node mesh, a coarser mesh, with 96 nodes and 72 mesh cells, was calculated. All cells in the coarser mesh are quadrilateral, i.e., there are no triangles.

Each mesh mode represents a point at which the temperature is specified or is to be calculated. Each cell represents a volume of unit depth. Heat flowing across the cell boundaries is specified, or is calculated by the program. The two meshes are shown in the plots in Figures 100 and 101. Dimensions are in centimeters.

c. Boundary Conditions

TACO can operate in either the steady-state or the transient mode. Input heat flow across the inner radius of the collector is specified as a constant heat flux (e.g., 1 kW/cm^2) for the duration of a pulse, or as zero after the pulse is turned off. Output heat flow across the water channel boundary is represented by a temperature-dependent curve approximating normal convection cooling at lower temperatures, as given by the equation[29]

$$\frac{h_L}{c_{pb}G}\left(\frac{c_p\mu}{k}\right)_f^{2/3} = \frac{0.023}{(DG/\mu_f)^{0.2}} \quad , \qquad (54)$$

where h_L = coefficient of heat transfer between fluid and surface based on logarithmic mean Δt, [Btu/hr ft^2 ^oF]

C_{pb} = specific heat at constant pressure for bulk [Btu/lb^oF]

G = mass velocity [lb/hr ft^2 of cross section]

ORNL Dwg. 81-16841FED

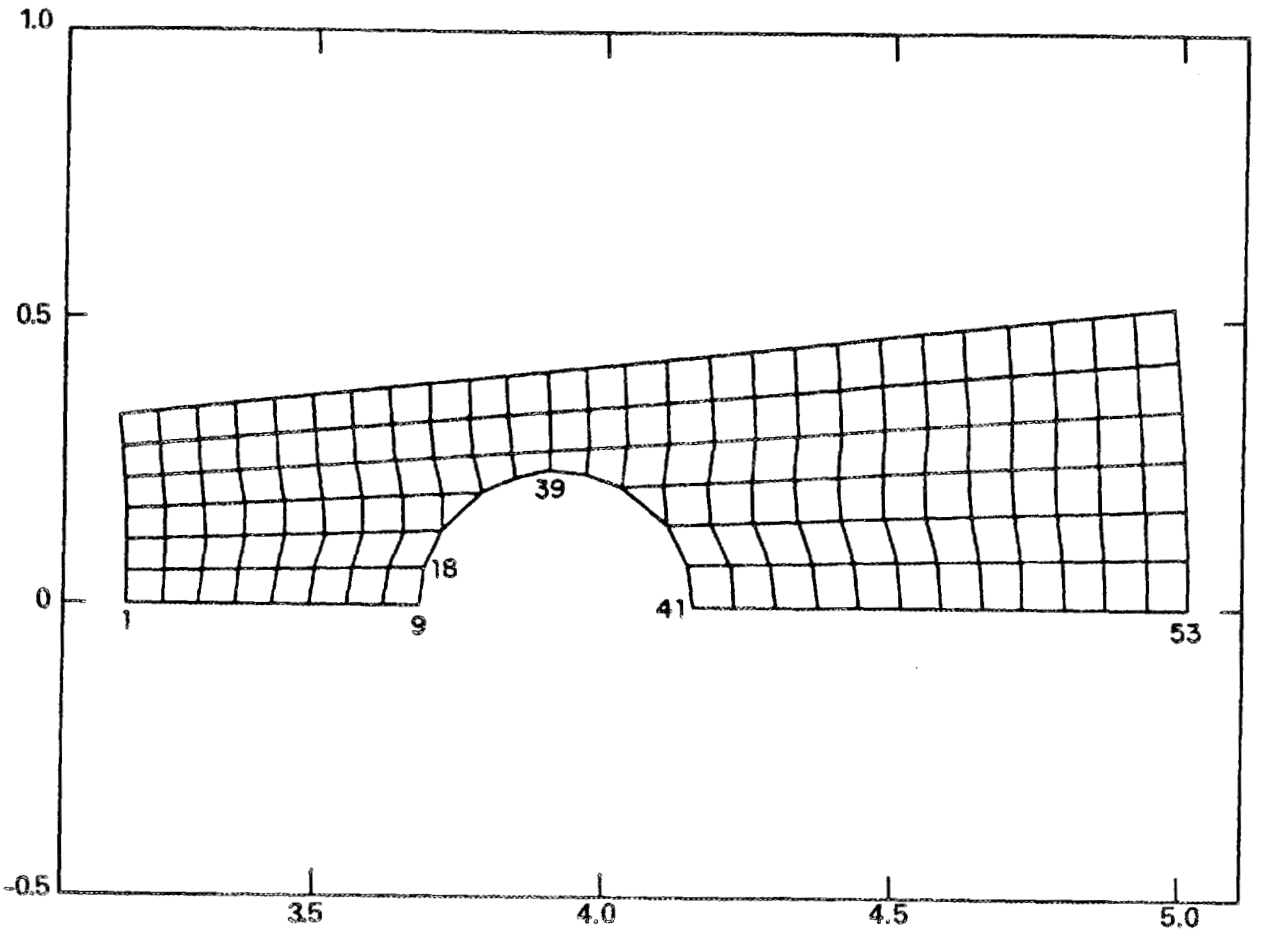

Figure 100. VGE-8060 Collector - Steady State (1 kW/cm^2) - 20 Ft/Sec Flow Rate Mesh Plot

ORNL Dwg. 81-16842FED

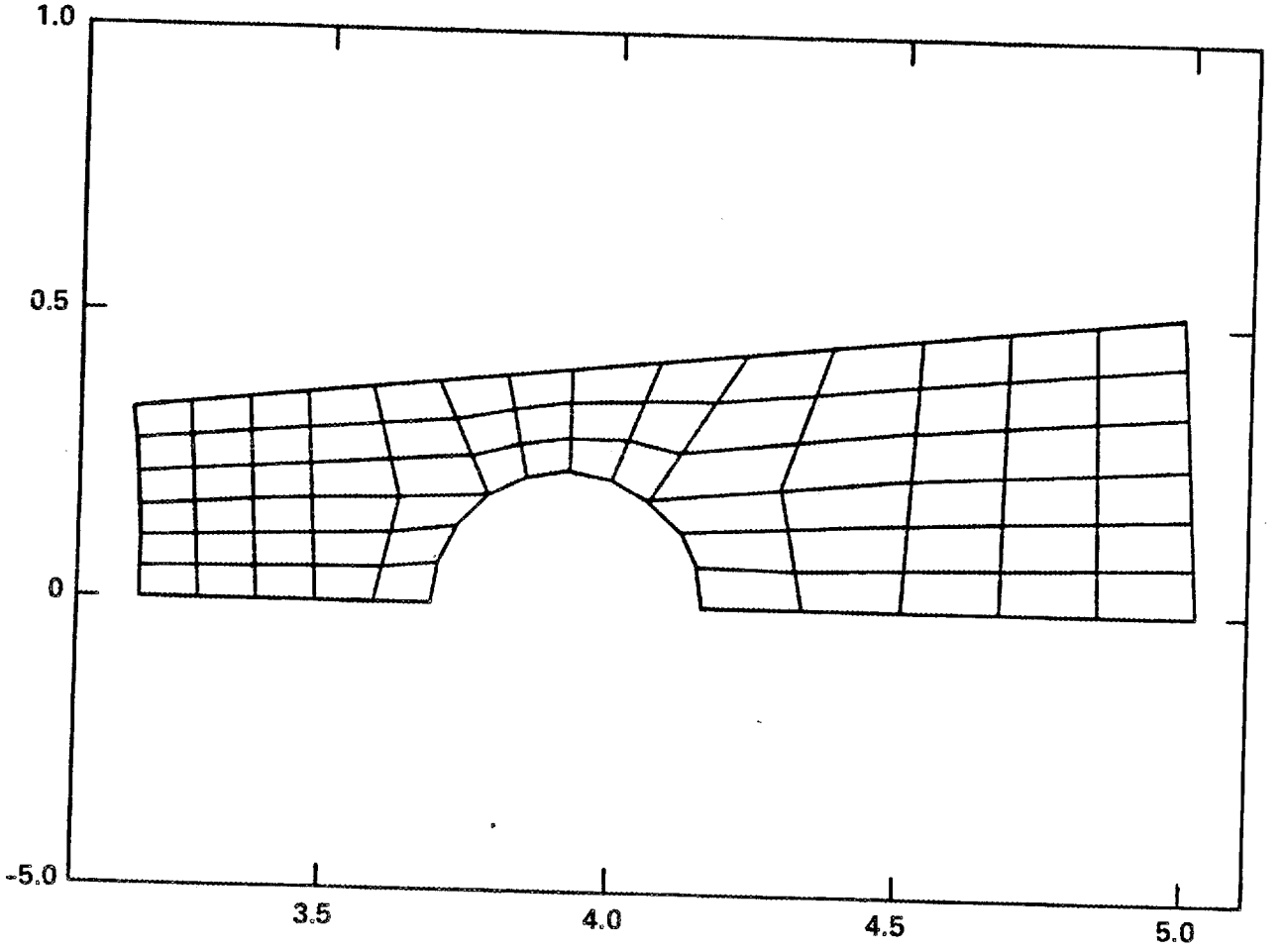

Figure 101. Mesh Plot

D = diameter (ft)

μ = viscosity of fluid [lb/hr ft]

k = thermal conductivity of fluid [Btu/hr ft ^{o}F]

Subscript$_f$ = for film $t_f = [t_b + t_w)/2$

Subscript$_b$ = bulk

Subscript$_w$ = wall

and film boiling at higher temperatures, as given by the equation,[30]

$$t_w - t_{sat} = \frac{1.9\ (q/A)^{1/4}}{e^{\ p/900}} \tag{55}$$

where t_w = surface temperature
t_{sat} = saturation temperature of liquid [^{o}F]
q/A = heat flux [Btu/hr ft^2]
p = pressure [lb/in^2 absolute].

An example of such a curve is shown in Figure 102. When film boiling reaches a critical point, it is no longer an effective cooling mechanism and "burnout" occurs, as given in the equation[31]

$$(q/A)_p = 400{,}000V^{1/3} + 4800\ (t_{sat} - t)\ V^{1/3} \tag{56}$$

where $(q/A)_p$ = peak heat flux in range of nucleate boiling
V = average velocity (ft/sec).

ORNL Dwg. 81-16843FED

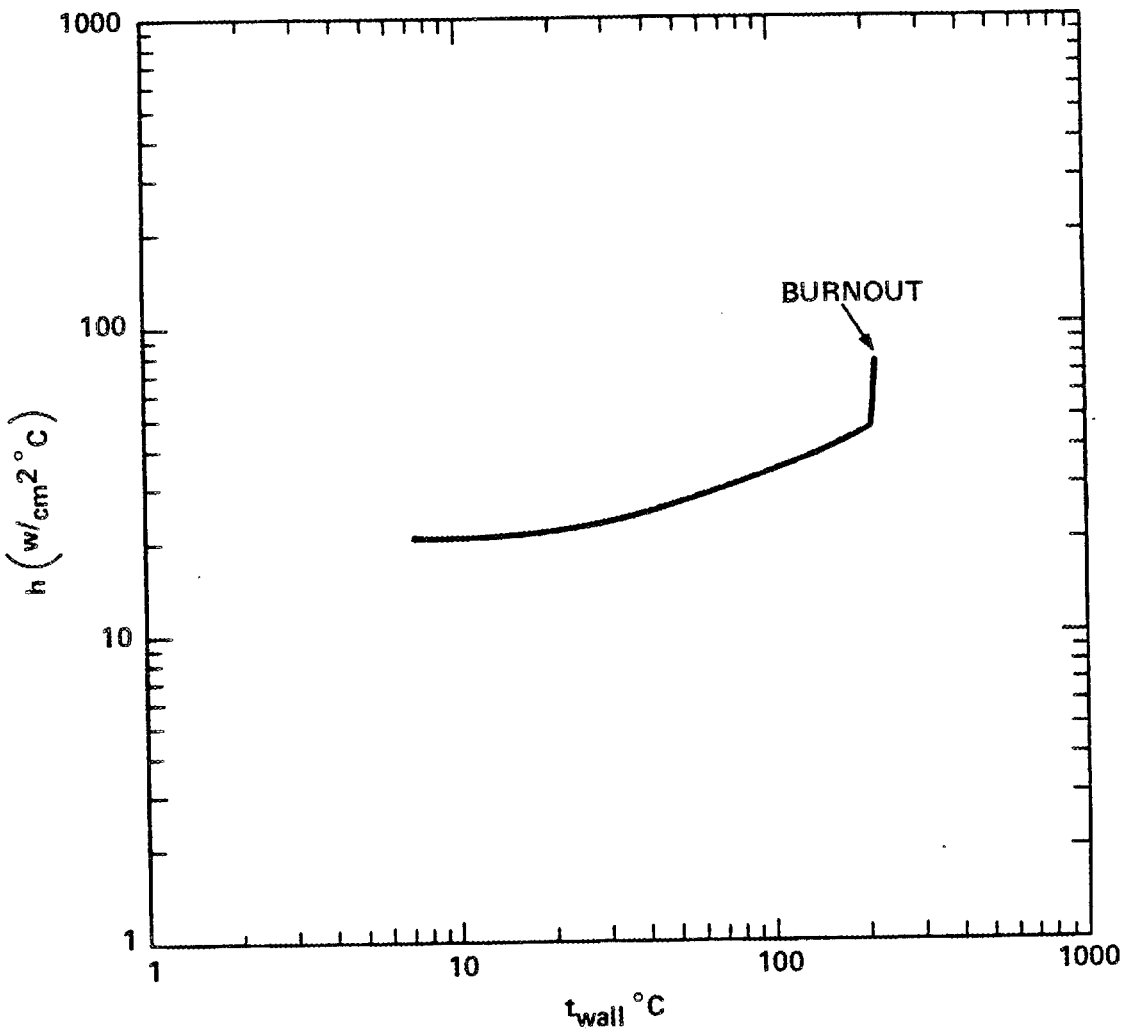

Figure 102. Heat Transfer Coefficient at 20 Ft/Sec, 100 psig, 35°C

The objective of the calculations on TACO was to determine the combinations of heat input flux (collector dissipation), pulse duration, and water pressure and flow rate that can be expected without "burnout".

d. Results

An example of the output from TACO is shown in Figure 103, a plot of temperatures at selected nodes versus time for a 2.0 second pulse. The node numbers are indicated in Figure 100. Initial temperature of the entire collector body was assumed to be 35°C, the same as the bulk water temperature. The maximum temperature reached by any node was 311°C, on the heated wall. The maximum temperature on the water channel was 192°C at node 9. Burnout temperature is 212°C.

A plot of isothermal lines for the steady-state solution with the same flow rate is shown in Figure 104. The highest temperature reached by any node on the water channel is approximately 200°C.

By setting the heat flux across the inner radius to zero, and inserting the initial node temperature obtained at the end of the computer run in Figure 103, it is possible to calculate the temperature decay following a 2-second pulse. The results are shown in Figure 105. Node numbers are the same.

Further work with the TACO computer program included:

1) calculation of time to burnout for several water flow rates at input heat fluxes (dissipations) of 1 kW/cm^2 and 2 kW/cm^2,

2) calculation of pulse decay rates and pulse rise-decay cycles,

3) calculation of temperature rise and fall to be used for stress analysis.

ORNL Dwg. 81-16844FED

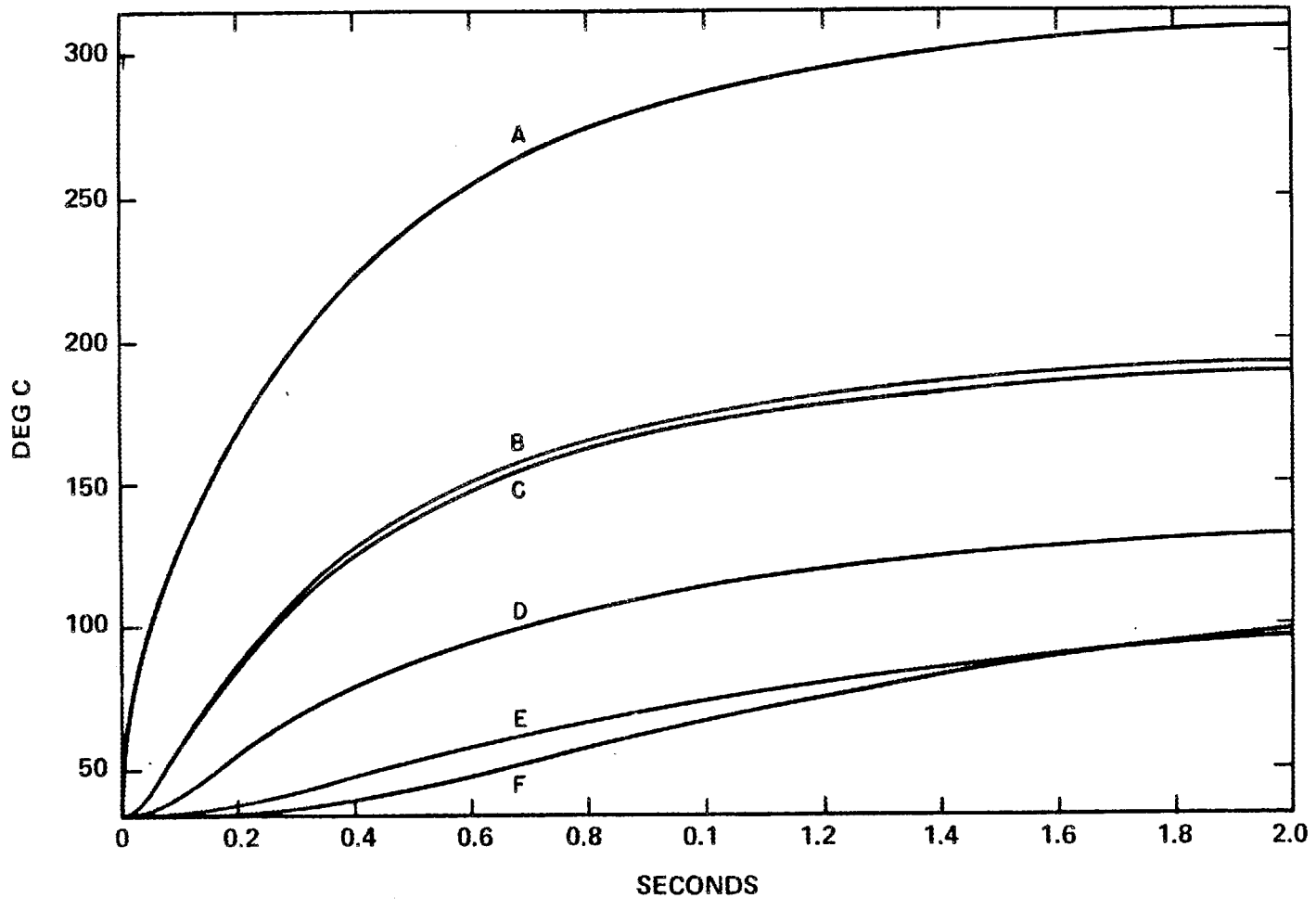

NODES: 1:A 9:B 18:C 39:D
41:E 53:F

Figure 103. VGE-8060 Collector - 2.0 Sec Pulse - 20 Ft/Sec Flow Rate

ORNL Dwg. 81-16845FED

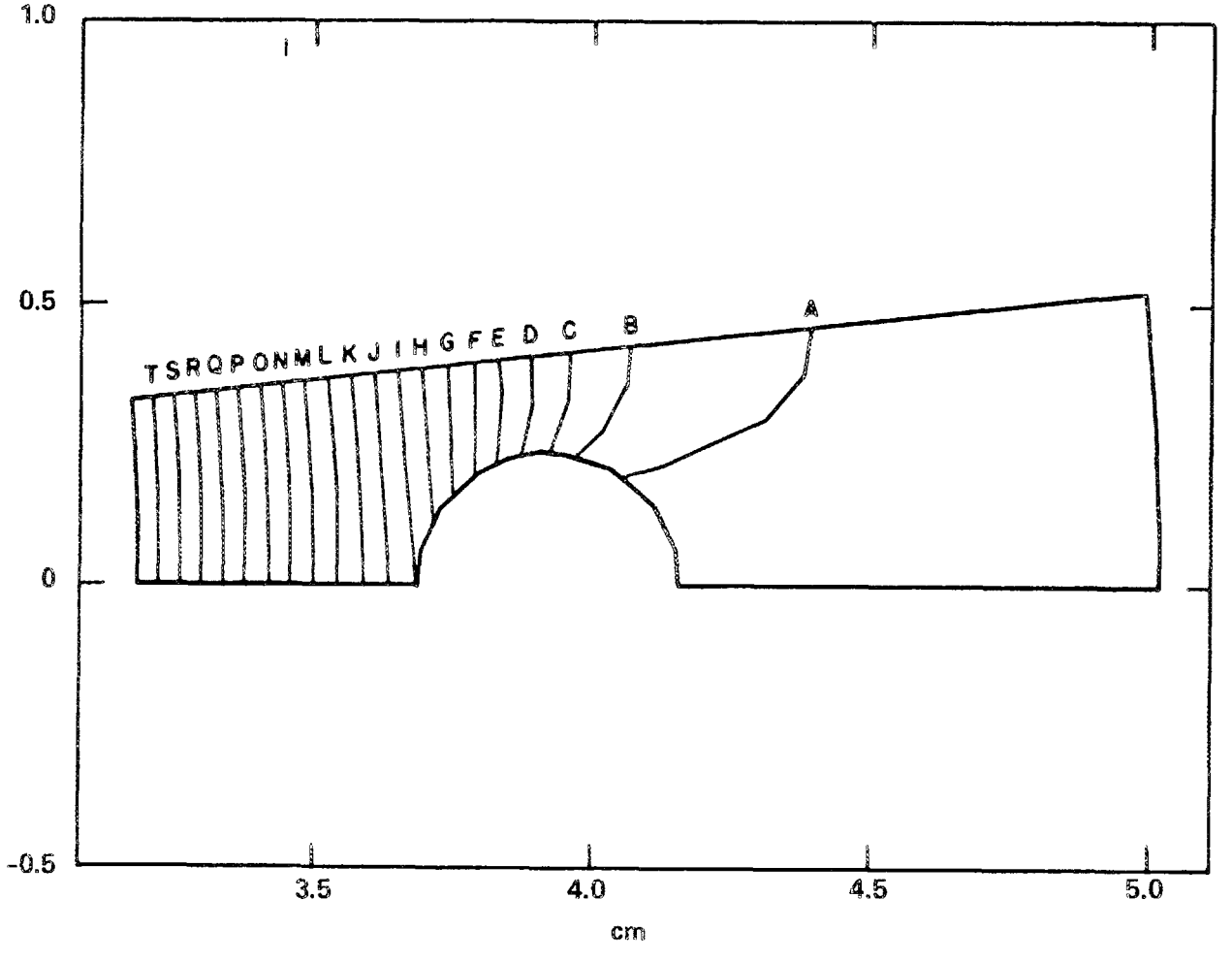

TEMPERATURE CONTOUR LEVELS DEG. C

A	=	1.200E+02
B	=	1.300E+02
C	=	1.400E+02
D	=	1.500E+02
E	=	1.600E+02
F	=	1.700E+02
G	=	1.800E+02
H	=	1.900E+02
I	=	2.000E+02
J	=	2.100E+02
K	=	2.200E+02
L	=	2.300E+02
M	=	2.400E+02
N	=	2.500E+02
O	=	2.600E+02
P	=	2.700E+02
Q	=	2.800E+02
R	=	2.000E+02
S	=	3.000E+02
T	=	3.100E+02

Figure 104. VGE-8060 Collector - Steady State (1 kW/cm^2) - 20 Ft/Sec Flow Rate Isoplot

ORNL Dwg. 81-16846FED

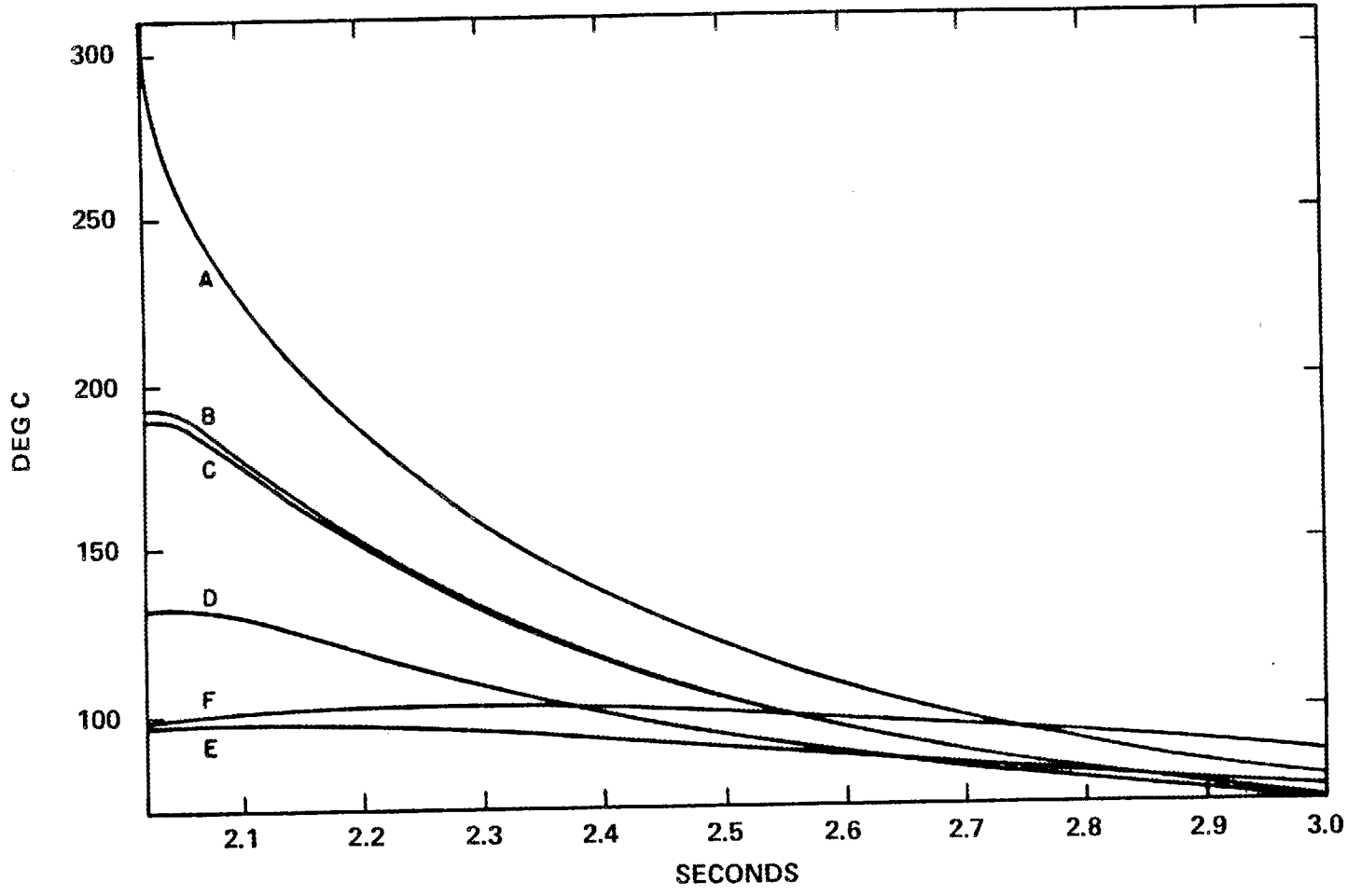

NODES: 1:A 9:B 18:C 39:D
41:E 53:F

Figure 105. VGE-8060 Collector - Decay After 2.0 Sec. Pulse - 20 Ft/Sec

i. Time-to-Burnout

Time-to-burnout was calculated by running TACO in the transient mode until the temperature of the hottest node on the water channel reached burnout temperature. The results of the time-to-burnout calculations with TACO are tabulated in Table 15. The results are plotted in Figure 106. An example of the temperature versus time behavior for 2 kW/cm^2 and 50 ft/sec flow rate is shown in Figure 107. The elapsed time to reach the burnout temperature of 215.46°C is 1.48 seconds. Note that for 1 kW/cm^2 and a flow rate of 20 ft/sec, a steady-state condition was reached. There was no burnout.

Steady-state temperatures are calculated by TACO in the nonlinear, steady-state mode. An example for a 1 kW/cm^2 input flux and 40 ft/sec flow rate is shown in Figure 108. Isothermal lines are plotted.

ii. Pulse Cycling

In the transient pulsed calculations described previously, the input heat flux was entered into the program as a constant over the inner radius surface.

Pulse cycling can be modeled by entering the input heat flux along the inner surface as a piecewise-linear function of time. One calculation was made for a 1 kW/cm^2 pulse and cooling water flow rate of 40 ft/sec. The pulse was on for 3 seconds and off for 3 seconds and the on-off cycle was repeated three times. Results of the cycling calculation are shown in Figure 109. Peak temperatures were 273°C for the heated wall and 152°C for the hot spot on the cooling channel. At the end of the pulse decay, just before restarting the pulse, the temperature on the heated wall had dropped to 36.9°C and the temperature of the hot spot on the cooling channel was 36.7°C. A single cycle of the same pulse train, calculated with a time step of 0.025 seconds, is shown in Figure 110.

TABLE 15 TIME TO BURNOUT—CALCULATIONS ON TACO

Flow Rate Ft/Sec	Burnout Temp °C	Surface Boiling Temp °C	1 kW/sq cm		2 kW/sq cm	
			Seconds to Burnout	Steady-State Temp °C	Seconds to Burnout	Steady-State Temp °C
1	202.80	189.50	0.70	---	0.29	---
2	204.75	192.57	0.78	---	0.31	---
5	207.52	197.43	1.00	---	0.33	---
10	209.75	201.82	2.37	---	0.37	---
20	212.12	206.97	---	197.58	0.44	---
30	213.57	210.38	---	169.46	0.48	---
40	214.63	213.01	---	153.48	0.72	---
50	215.46	215.17	---	139.34	1.48	---

ORNL Dwg. 81-16864FED

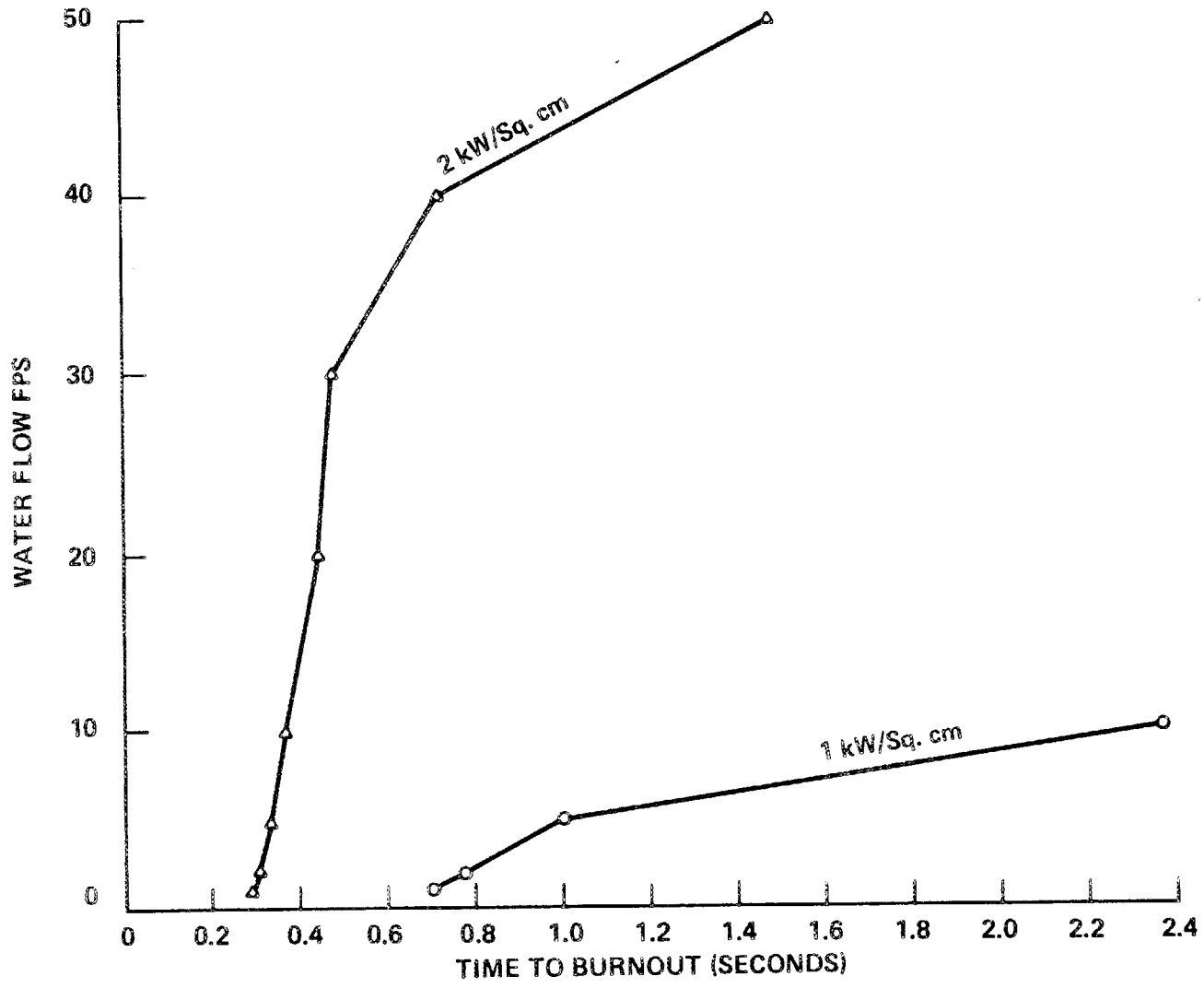

Figure 106. Time to Burnout VGE-8060 Collector Calculation on TACO

ORNL Dwg. 81-16865 FED

NODES: 1:A 36:B 47:C 55:D 90:E

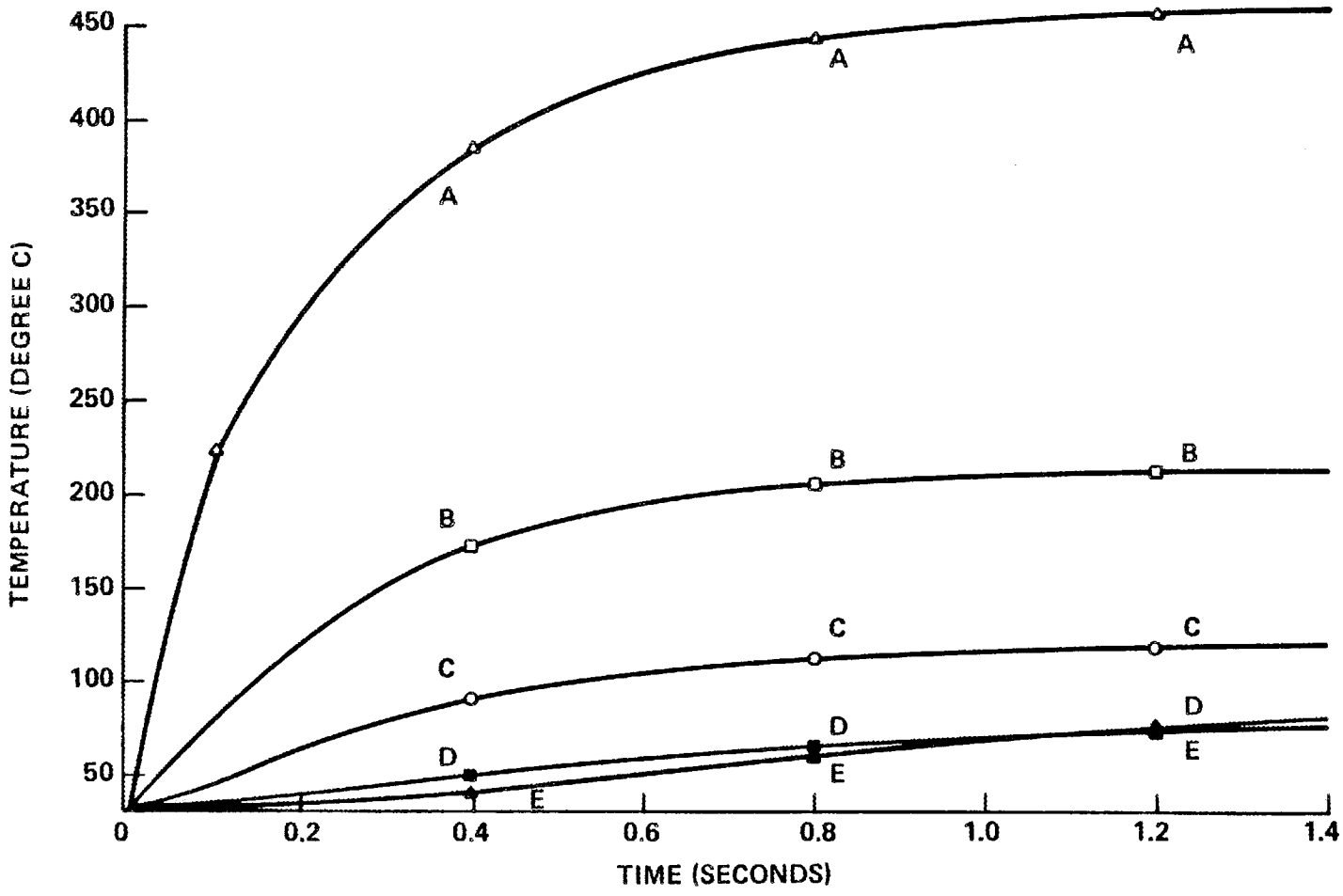

Figure 107. VGE-8060 Collector – Transient State (2 kW/cm^2) – 50 Ft/Sec Flow

ORNL Dwg. 81-16866FED

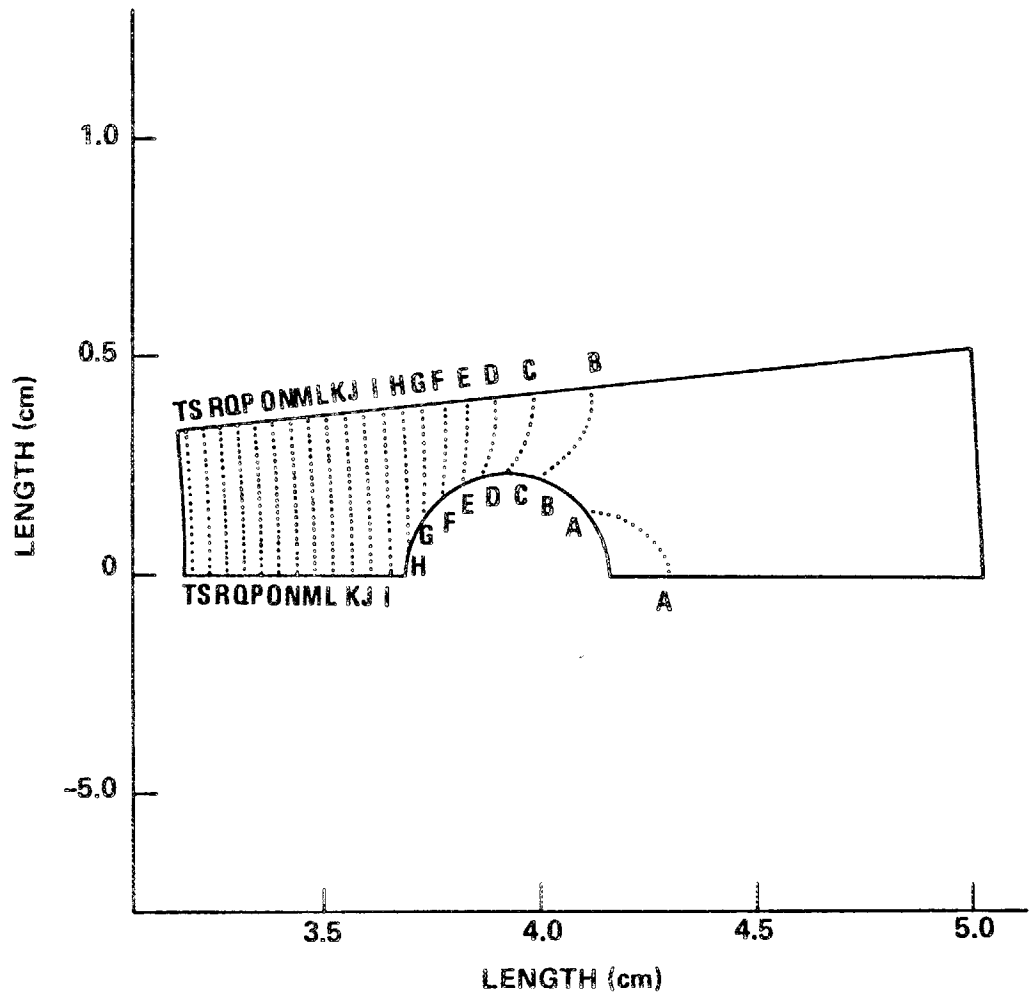

TEMPERATURE
CONTOUR LEVELS °C

A = 8.000E+01
B = 9.000E+01
C = 1.000E+02
D = 1.100E+02
E = 1.200E+02
F = 1.300E+02
G = 1.400E+02
H = 1.500E+02
I = 1.600E+02
J = 1.700E+02
K = 1.800E+02
L = 1.900E+02
M = 2.000E+02
N = 2.100E+02
O = 2.200E+02
P = 2.300E+02
Q = 2.400E+02
R = 2.500E+02
S = 2.600E+02
T = 2.700E+02

Figure 108. VGE-8060 Collector - Steady State 40 Ft/Sec Flow Isoplot

ORNL Dwg. 81-16867FED

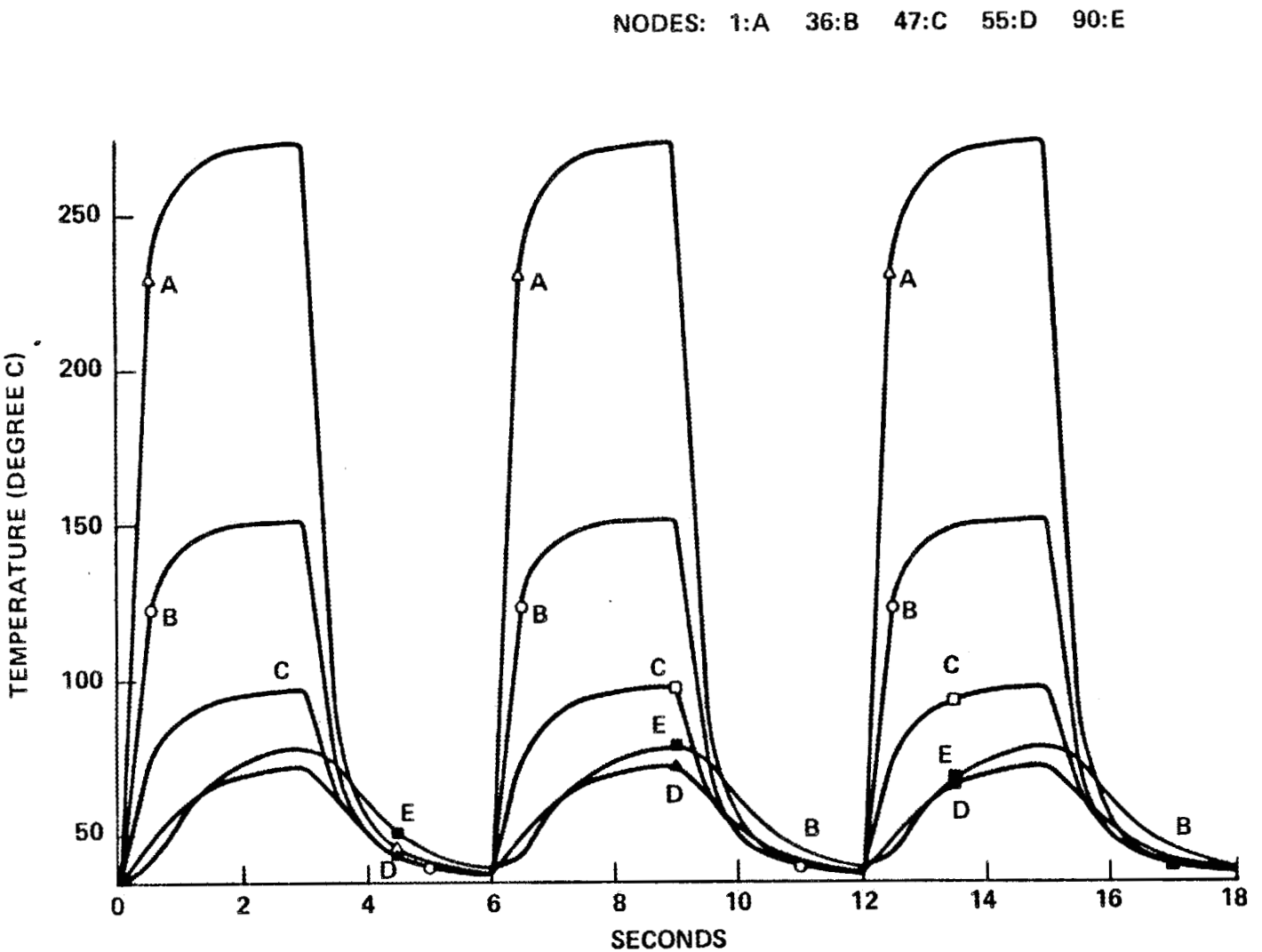

Figure 109. VGE-8060 Collector – Three 1 kW/cm^2 Pulse Cycles – 40 Ft/Sec Flow Temperature History

ORNL Dwg. 81-16868FED

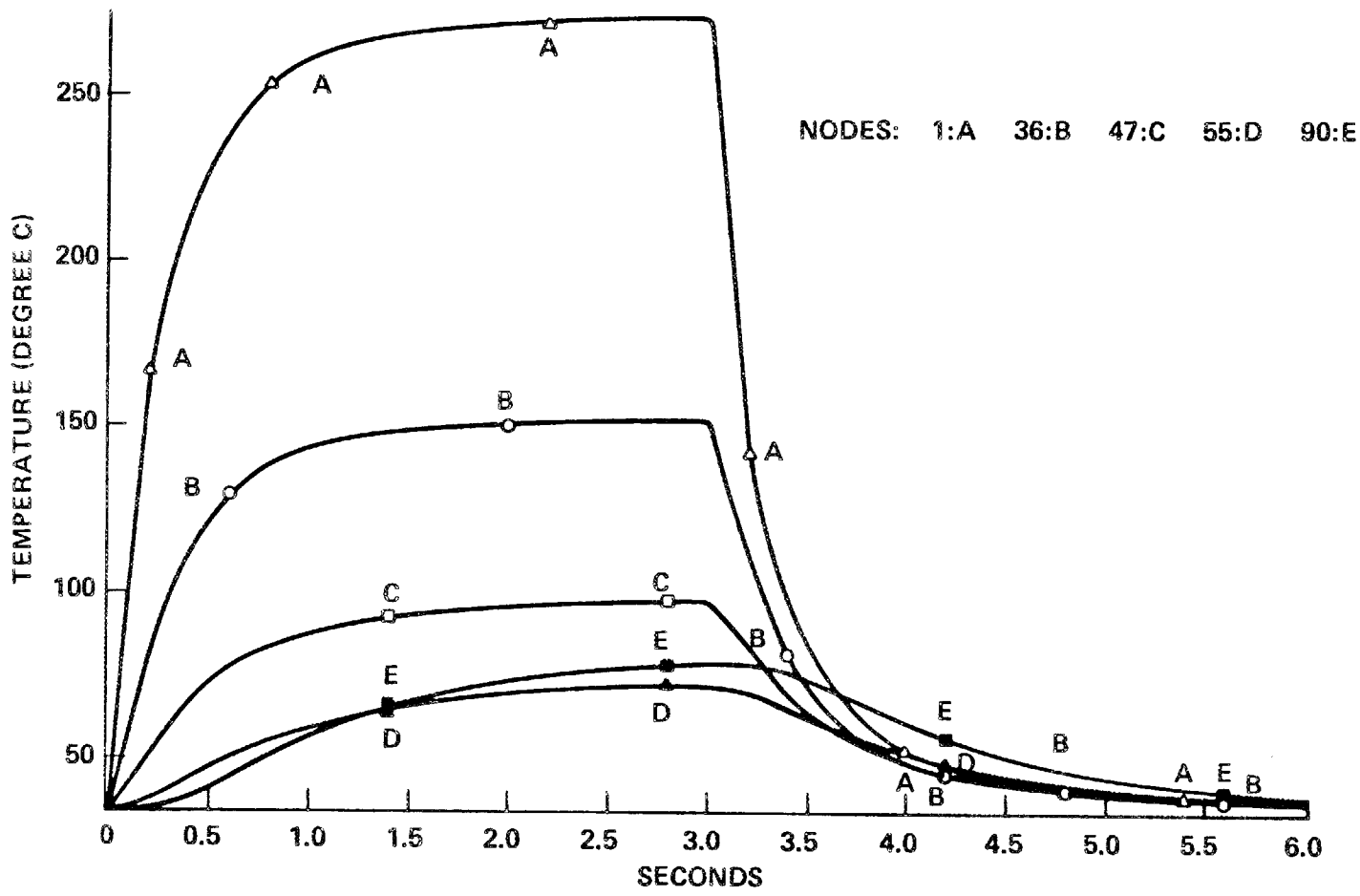

Figure 110. VGE-8060 – 3 Sec Pulse, 3 Sec Decay, 1 kW/cm² – 40 Ft/Sec

iii. Conclusions

At higher cooling water flow rates, the rise of temperature at the cooling channel wall is very gradual and only a slight change in temperature occurs over a relatively long time. It is important to carefully consider the safety factors required to avoid burnout of an actual collector. For example, in the case represented by Figure 107, a "one degree safety factor" in burnout temperature will reduce the time-to-burnout pulse duration from 1.48 seconds to 1.31 seconds. Notice, also, that as the flow rate increases, the temperature spread narrows between the onset of surface boiling and actual burnout.

2. Magnetic Field and Collector Electron Trajectory Calculations

The X-1 collector melted near the top of the cooling channels. The electrons appeared to be landing too high in the collector. Magnetic field calculations and trajectory simulations in the collector region were done to see if "hot spot" problems could be solved by replacing a non-magnetic flange with a polepiece made of magnetic material.

Figure 111 shows the magnetic field on axis in the collector region for three cases:

1. No polepiece
2. 5" ID polepiece
3. 4" ID polepiece

It can be seen from the plot in Figure 111 that the most pronounced effect on the magnetic field occurs at about 11 to 15 inches from the center of the interaction circuit. Using a beam simulated by 24 trajectories computer runs were made for the three cases above.

Figure 112 shows a cumulative current distribution for these three cases. The total current collected is incremented by the amount of current represented by the trajectory at the point where the trajectory impinges on the collector wall. It can be seen that the addition of the polepiece

Dwg 82-2186 FED

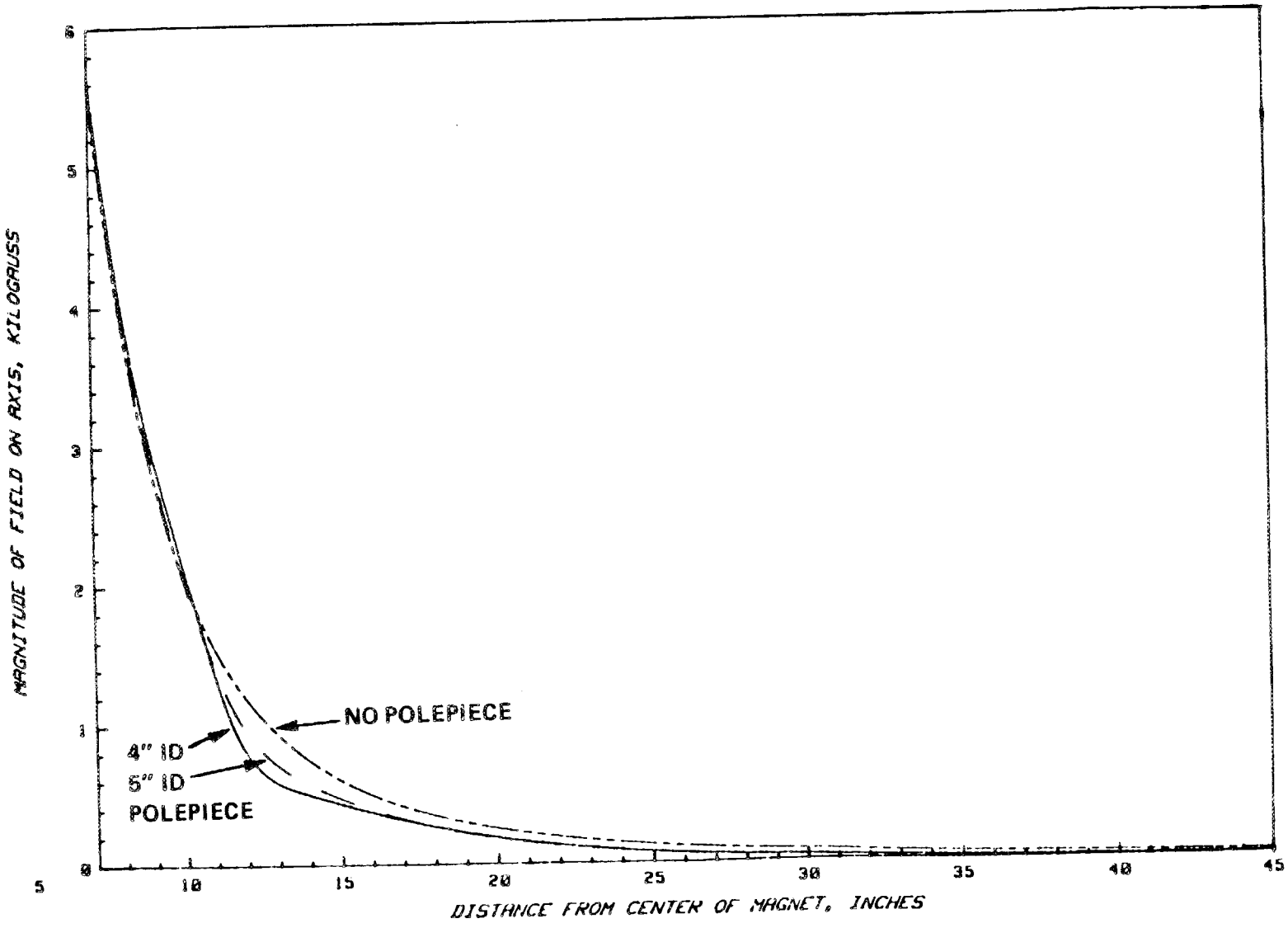

Figure 111. Axial Magnetic Field Curves for 60 GHz Gyrotron

Dwg 82-2187 FED

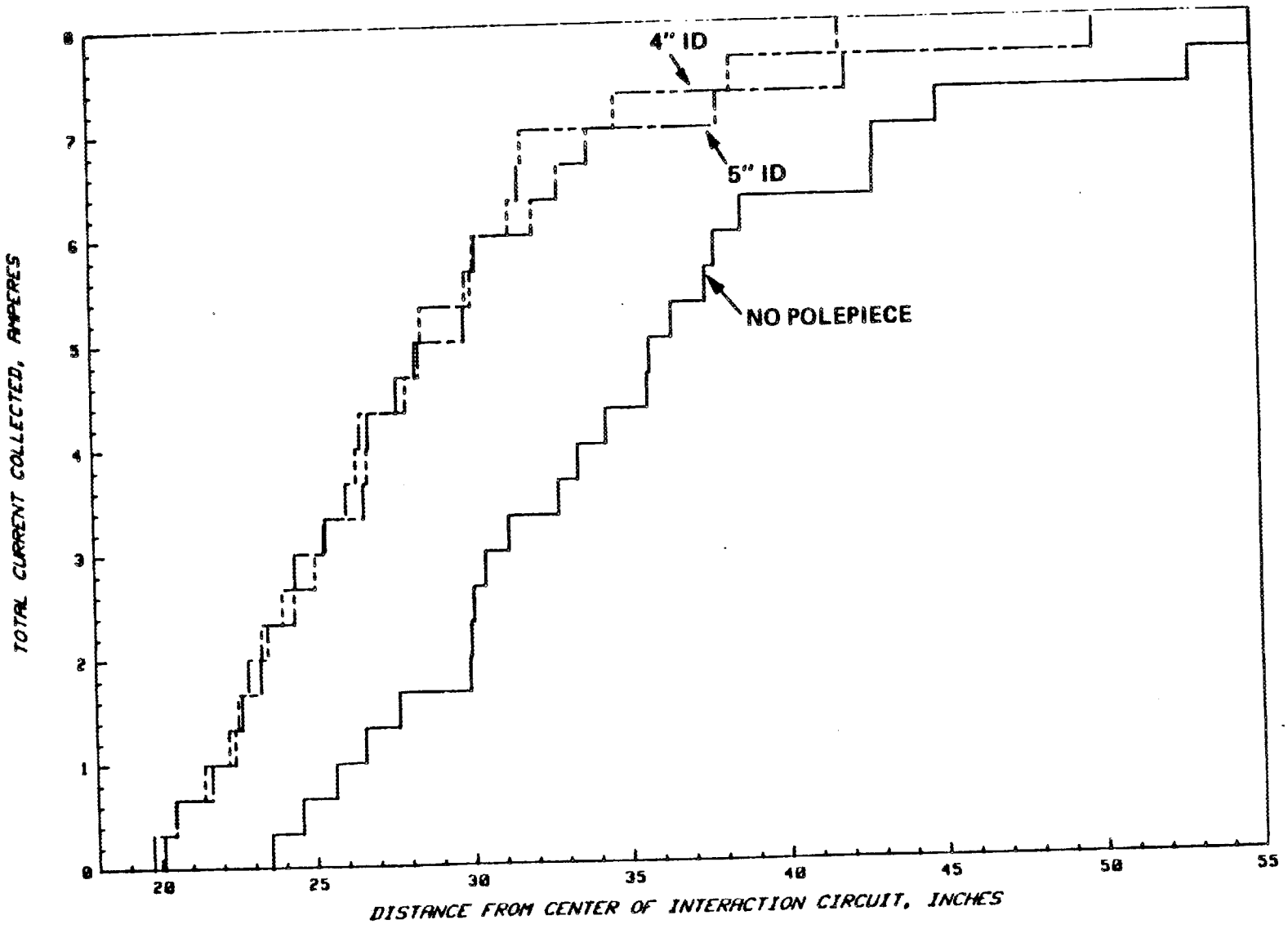

Figure 112. Current Distribution 60 GHz Gyrotron Collector

causes the current to be collected several inches closer to the interaction circuit. For the 4" polepiece case, a least squares fit polynominal was calculated yielding the formula:

$$I_{cum} = -22.15 + 1.44786\ x\ -0.017438x^2, \qquad (57)$$

where x is the distance from the center of the interaction circuit. This smoothed current distribution is shown in Figure 113. The power distribution was derived from the smoothed current distribution and is plotted in Figure 114. The break in the curve at $x \cong 30$ occurs at the transition from conical to cylindrical walls.

3. Improving Collector Fatigue Life

Fusion applications subject the collector to the repeated thermal shock of extended pulse durations and possible fatigue failure. One solution would be to find a construction material better suited to fusion applications. Since fatigue life is difficult to predict analytically, experiments were performed to measure the fatigue life of the present construction material, OFHC copper (OFHC is an AMAX Inc. trademark for high conductivity oxygen-free copper).

The experimental equipment consisted of planar diodes using a standard electron gun from a UHF-TV transmitter tube. The anodes were fabricated from OFHC copper and used cooling channel geometries and cooling fluid parameters identical to those of the collector. The water velocity, pressure, and inlet temperature were controlled during the test. The electron gun was adjusted to produce a beam of uniform electron density, and the density at the anode position was measured in two dimensions, with existing equipment, before the diodes were assembled. By adjusting the anode voltage, the power density could be set at any value. The anode voltage was switched on and off for equal time intervals until the test was completed. The time intervals were set equal to three collector thermal time constants.

Dwg 82-2188 FED

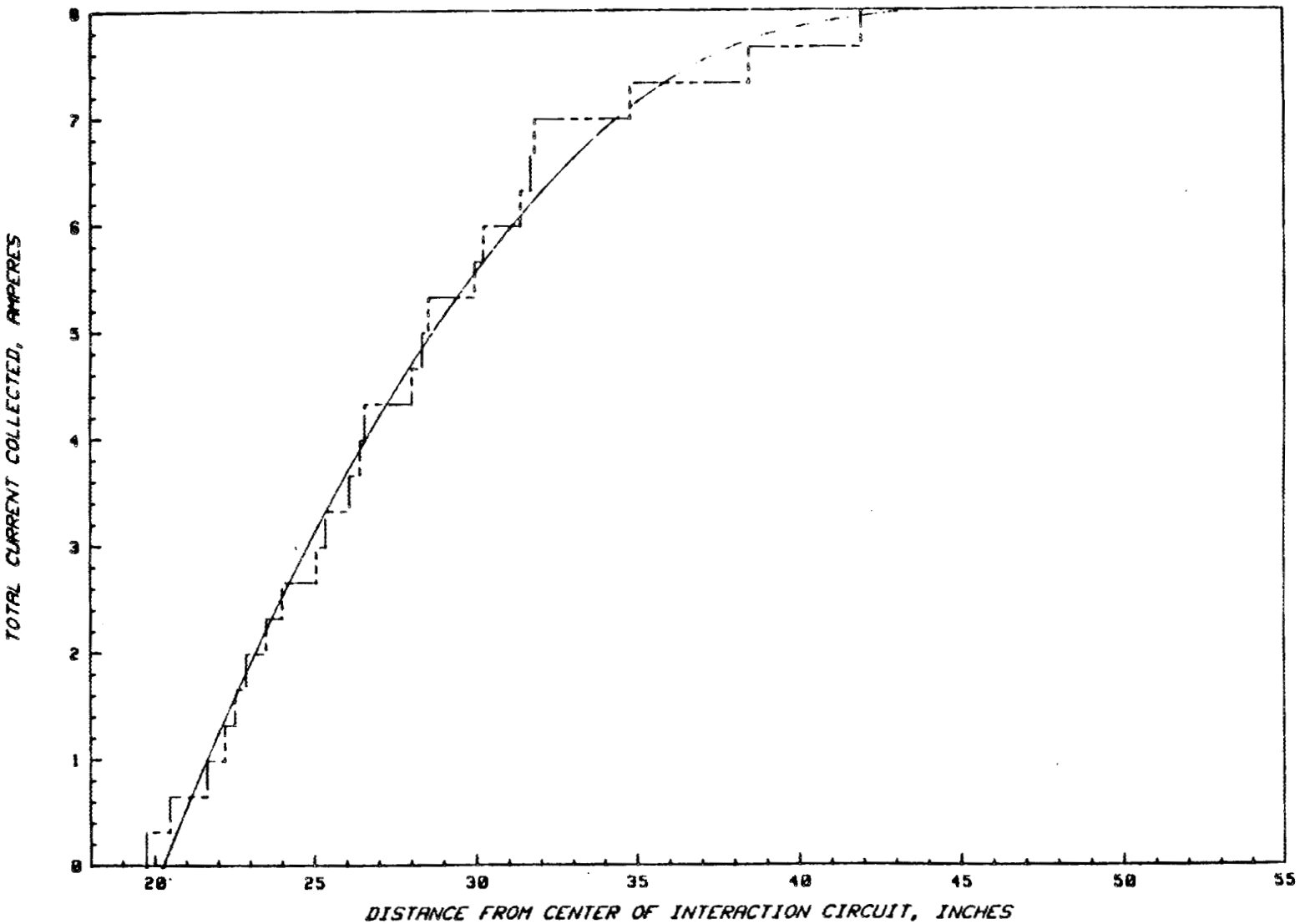

Figure 113. Smoothed Current Distribution 60 GHz Gyrotron Collector

Dwg 82-2189 FED

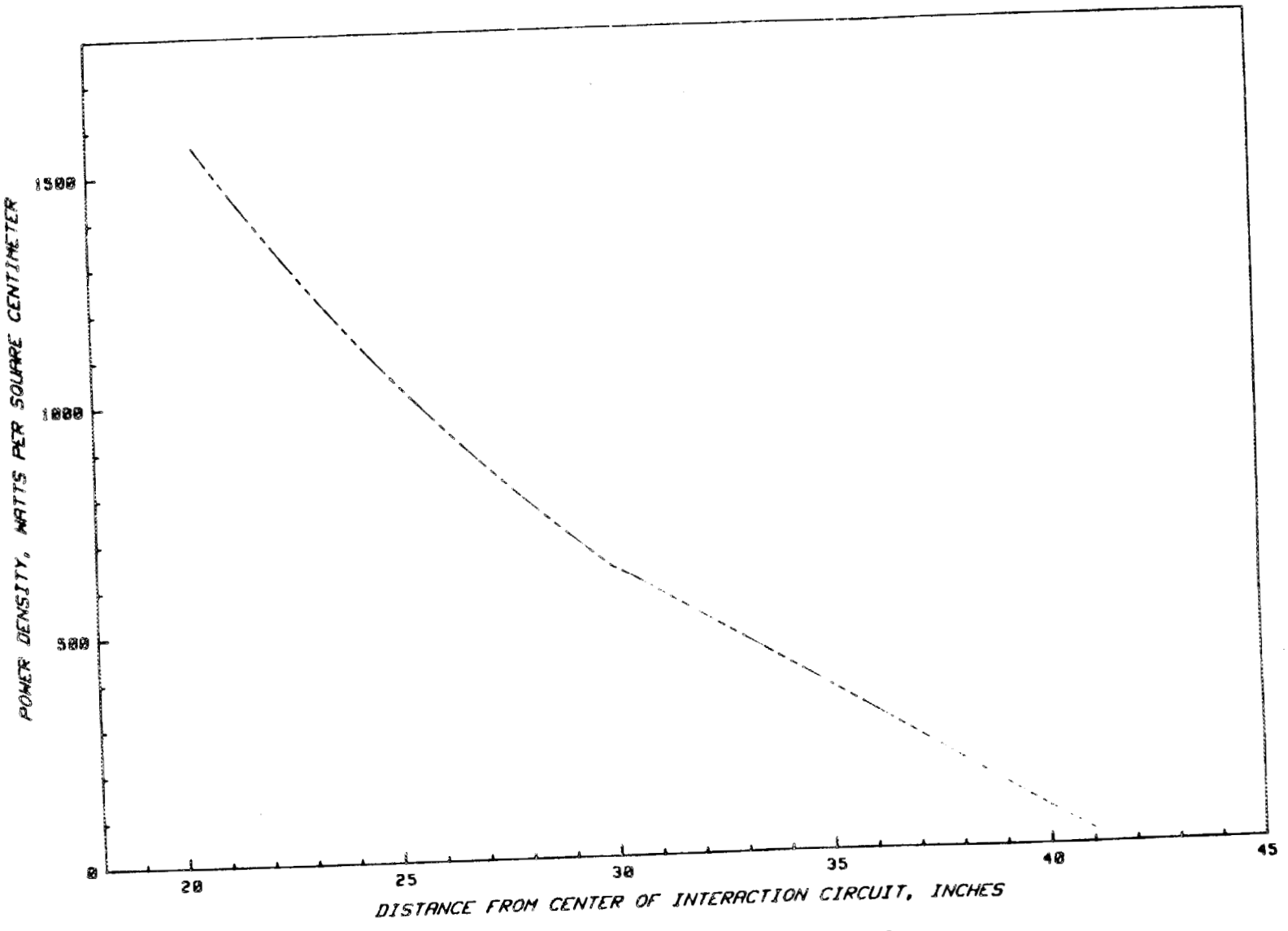

Figure 114. Collector Power Density 60 GHz Gyrotron

4. High Strength Copper Alloys

The collector is manufactured from a copper forging, but a brazing temperature of 1000°C is sufficiently high to completely anneal any of the suitable collector materials, thus removing any strength acquired during the forging operation. Also, after the tube is assembled, it must withstand several hours of bakeout at 500°C.

The ideal material has a melting point above 1000°C, has at least 75% of the thermal conductivity of OFHC^{tm} copper, produces maximum tensile strength by solution heat treatment only, without cold working, and is able to age at the bakeout temperature of 500°C. The aging is necessary to recover the thermal conductivity lost during the quenching cycle.

Since fatigue life is proportional to the ultimate tensile strength, the two most important parameters, tensile strength and thermal conductivity, for a variety of candidates are shown in Table 16. It is expected that the maximum temperature of the collector will not exceed 375°C during normal operation, thus, the strength of all the candidate materials must be tested at that temperature. Most of the material properties are known only at ambient temperatures, which are the values shown in Table 16.

As can be seen from the comments column in Table 16, a large number of these materials have significant disadvantages. Alloy 10 is not commercially available. Numbers 8 and 9 are not acceptable due to the very high vapor pressure of cadimum; silver is not suitable for the same reason. Magnesium has a moderately high vapor pressure, thus, alloy number 6 will not be considered further. However, number 7 is acceptable since the amount of magnesium is only 0.05%. Because of its high conductivity, Number 5 looks attractive, but its high temperature strength is not significantly better than OFCH copper. The remaining candidates 4, 7, 12 and 13 are examined in detail later.

Alloy #2, OFHC copper was tested to establish a base line for the experiment. Figure 115 shows the tensile and yield strength, along with elongation and reduction of area for annealed OFHC copper as a function of

TABLE 16

CANDIDATE MATERIALS FOR IMPROVED COLLECTOR FATIGUE LIFE

ALLOY NUMBER	TRADE NAME	COMPOSITION WEIGHT PERCENT	THERMAL (1) CONDUCTIVITY	TENSILE (2) STRENGTH	COMMENTS AND RESTRICTIONS
1	Silver	100% Ag	4.3		Expensive, high vapor pressure
2	OFHC Copper	100% Cu	3.8	30(85)	
3	AMZIRC*	Cu + 0.10Zr	3.3	52(80)	
4	AMZIRC*	Cu + 0.15Zr	3.3	58(85)	
5	AMSIL**	Cu + 0.092Ag	3.6	40(50)	
6	SSC - 155	Cu + 0.04 Ag + 0.05P + 0.11Mg	3.4	45(0)	Mg has high vapor pressure
7	AMAX - MZC	Cu + 0.06Mg + 0.15Zr + 0.4Cr	3.2	60(40)	
8	CDA - 162	Cu + 0.02 Fe + 1.0Cd	3.4	38(37)	Cd has a very high vapor pressure
9	PD - 135 Phelps Dodge	Cu + XCr + YCd	3.1	50(0)	Cd has a very high vapor pressure
10	B-D Copper Boron Deoxidized	Cu + 0.01B	3.6	30(85)	No longer commercially available
11	CUBE-Alloy***	Cu + 0.5BeO_2	2.1	70(50)	Low Conductivity
12	GLIDCOP AL-15	Cu + 0.2Al_2O_3	3.5	60(55)	May contain oxygen
13	NARLOY - Z Rocketdyne	Cu + XAg + YZr	2.95	56(50)	Not readily available commercially
14	DWA	Cu + Ceramic			Under development
15	DWA	Cu + Graphite			Under development

(1) Thermal Conductivity W/cm/°C
(2) Tensile Strength X 10^3 psi. Numbers in parentheses are % reduction during cold working prior to measuring tensile strength.
* Trademark for oxygen-free copper plus zirconium manufactured by AMAX Inc.
** Trademark for silver-bearing copper manufactured by AMAX Inc.
*** Trademark for dispersion hardened copper manufactured by Handy and Harman.

Dwg 82-2262 FED

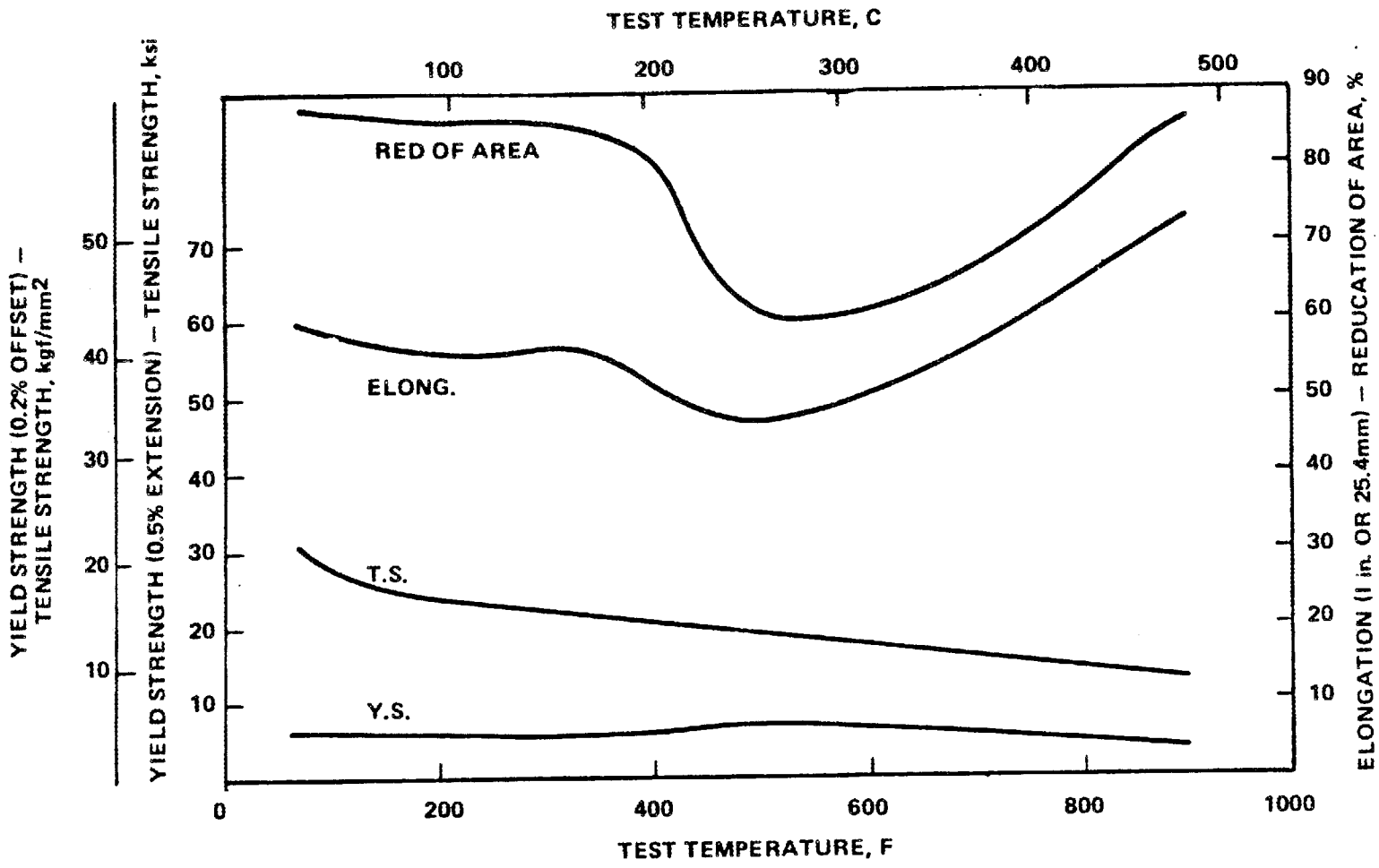

Figure 115. Elevated Temperature Tensile Properties of Annealed OFHC Copper Plate

temperature.[32] The tensile strength at the projected operating temperature of 375°C is approximately 15 ksi. The objective was to find a copper alloy that is significantly stronger than OFHC at 375°C after being subjected to 1000°C brazing temperature.

An example of work-hardened OFHC copper is shown in Figure 116. It is interesting to note that all of the strength due to cold working has been lost at the brazing temperature of 1000°C; the tensile strength is only 2.0 ksi.[33]

Alloys 3, 4 and 7 are all from the same manufacturer, and they recommended number 7 as the best of the three for this application since it has higher tensile strength at elevated temperatures. Thus, alloys 3 and 4, were no longer considered. The slight loss in thermal conductivity of alloy 7 is due primarily to the presence of chromium, as shown by Figure 117.[34]

Alloy number 7 would be particularly well suited if the brazing cycle could be followed by a rapid water quench and then aged at 400 to 500°C, which matches the bakeout cycle. However, a water quench will undoubtably cause dimensional changes, as well as severe oxidation of the surfaces. It is not known whether an inert gas quench will be rapid enough to produce significant improvements in strength. If alloy number 12 cannot be obtained in suitable condition and/or sizes, a preliminary test could be made on alloy number 7 to test its ability to be heat treated without dimensional changes. Figure 118 indicates that a stress level of 25 ksi can be used and still produce 10^6 cycles to failure even without cold working.[35]

Alloy 13 (NARLOY-Z) is a proprietary material containing silver and zirconium as alloying elements. The material was developed by the Rocketdyne Division of Rockwell International Corporation and has been tested for NASA by Boeing Aerospace Company.[36] The Ultimate Tensile Strength (TUS) at 375°C is 33 ksi, which is considerably better than OFHC copper. The tensile strength and the ultimate yield strength (TYS) is shown as a function of temperature in Figure 119. The stress-strain relationship for this alloy is shown in Figures 120 and 121. The low-cycle fatigue failure is given at 537°C, with a strain rate of 0.002 sec^{-1}, as shown in

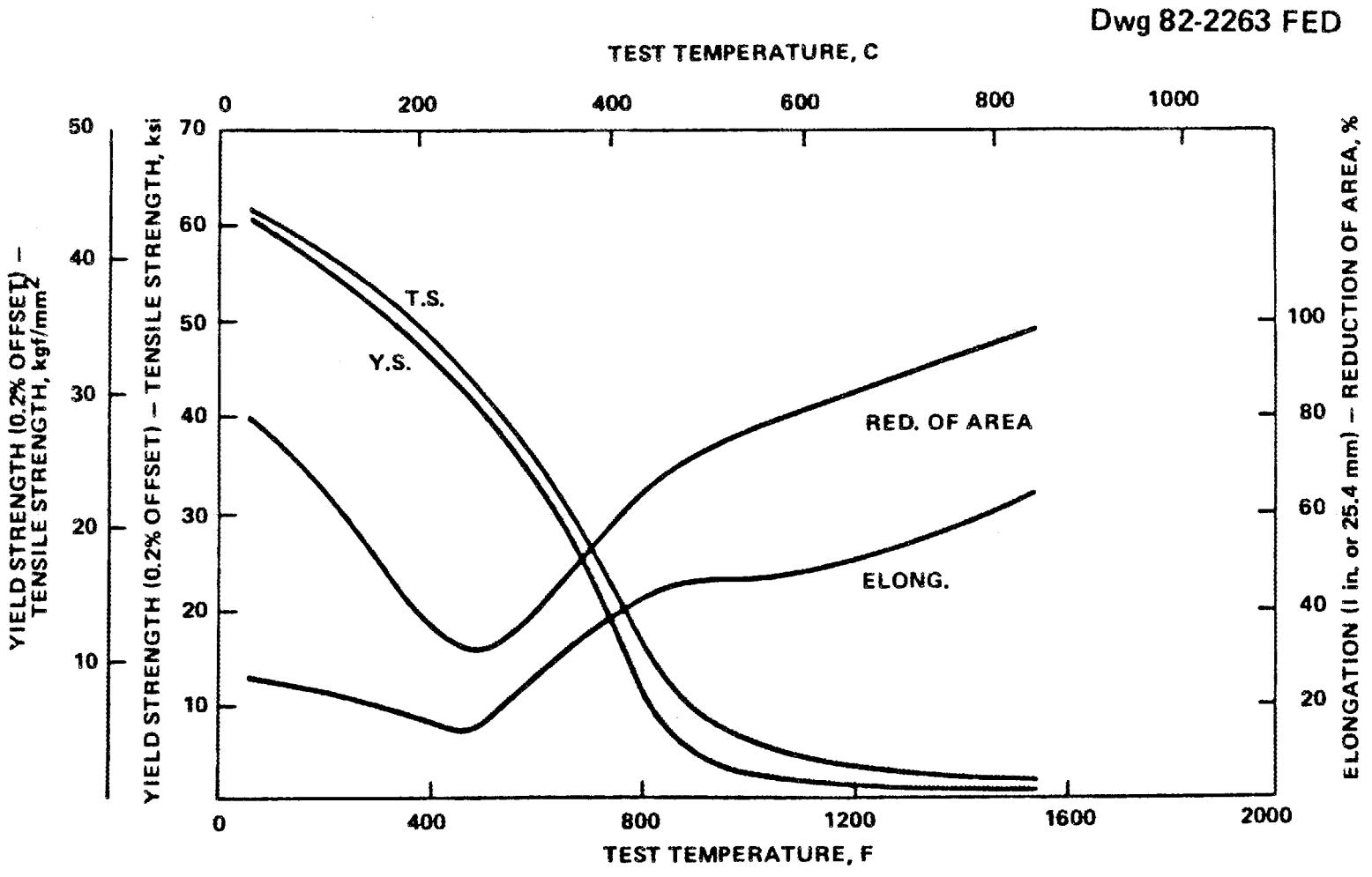

Figure 116. Elevated Temperature Tensile Properties of Hard Drawn OFHC Copper Rod

Dwg 82-2264 FED

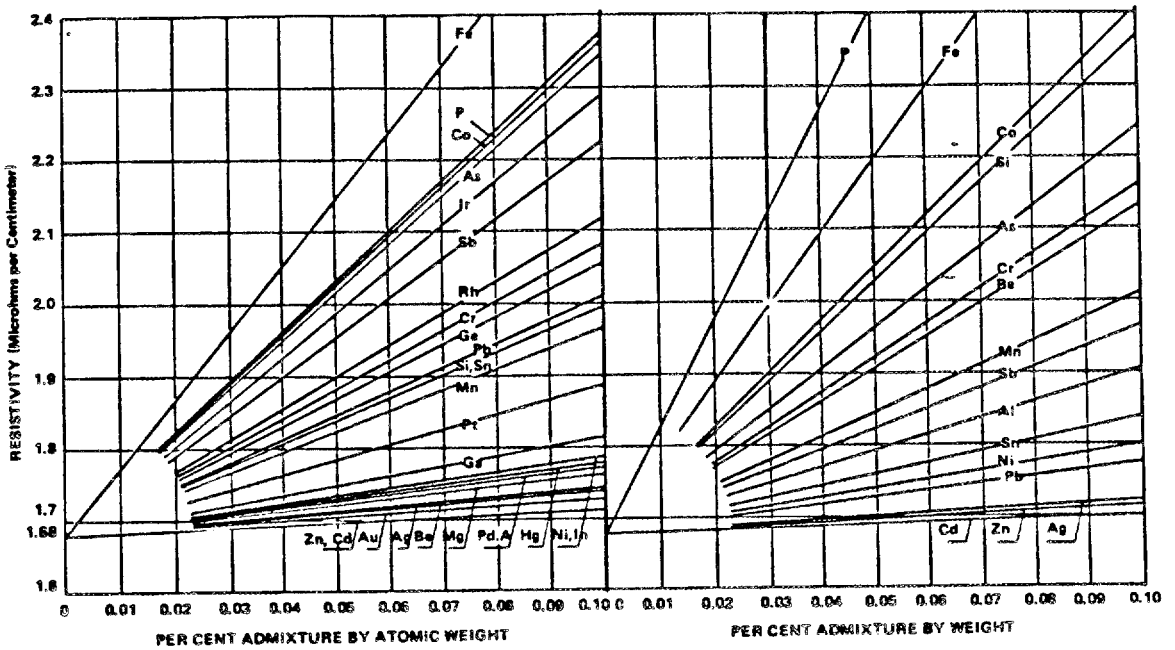

Figure 117. Increase of Electrical Resistivity of Copper with Admixtures of Various Elements

Dwg 82-2265 FED

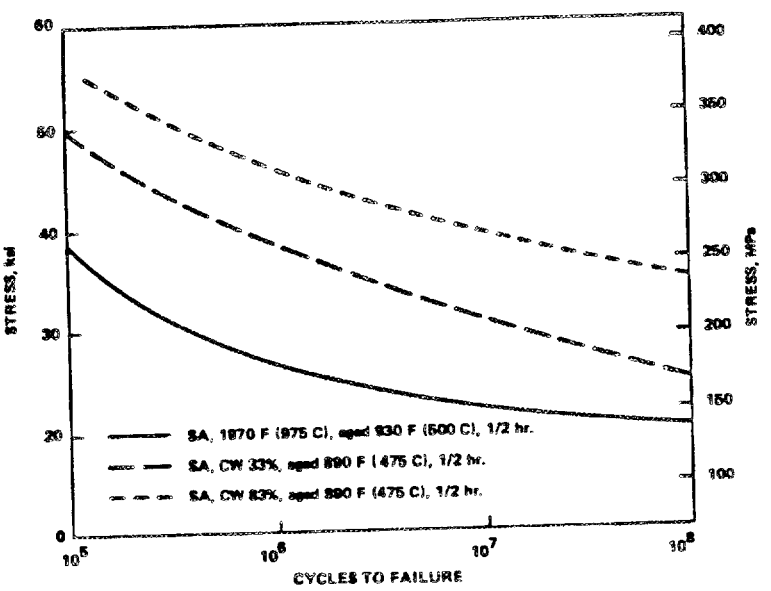

Figure 118. Room Temperature Fatigue Strength of AMAX-MZC in Various Conditions

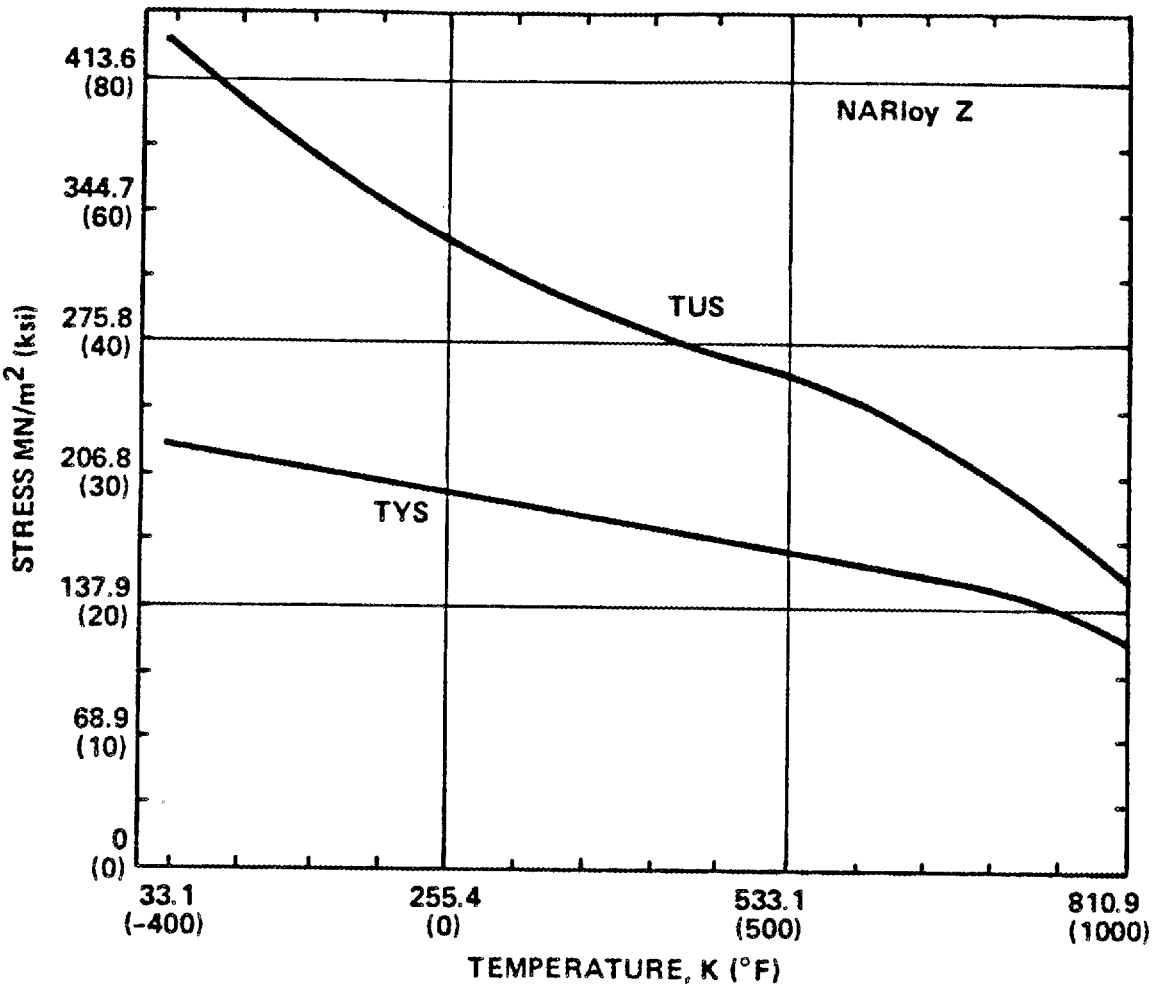

Figure 119. Tensile Strength vs Temperature for NARLOY Z

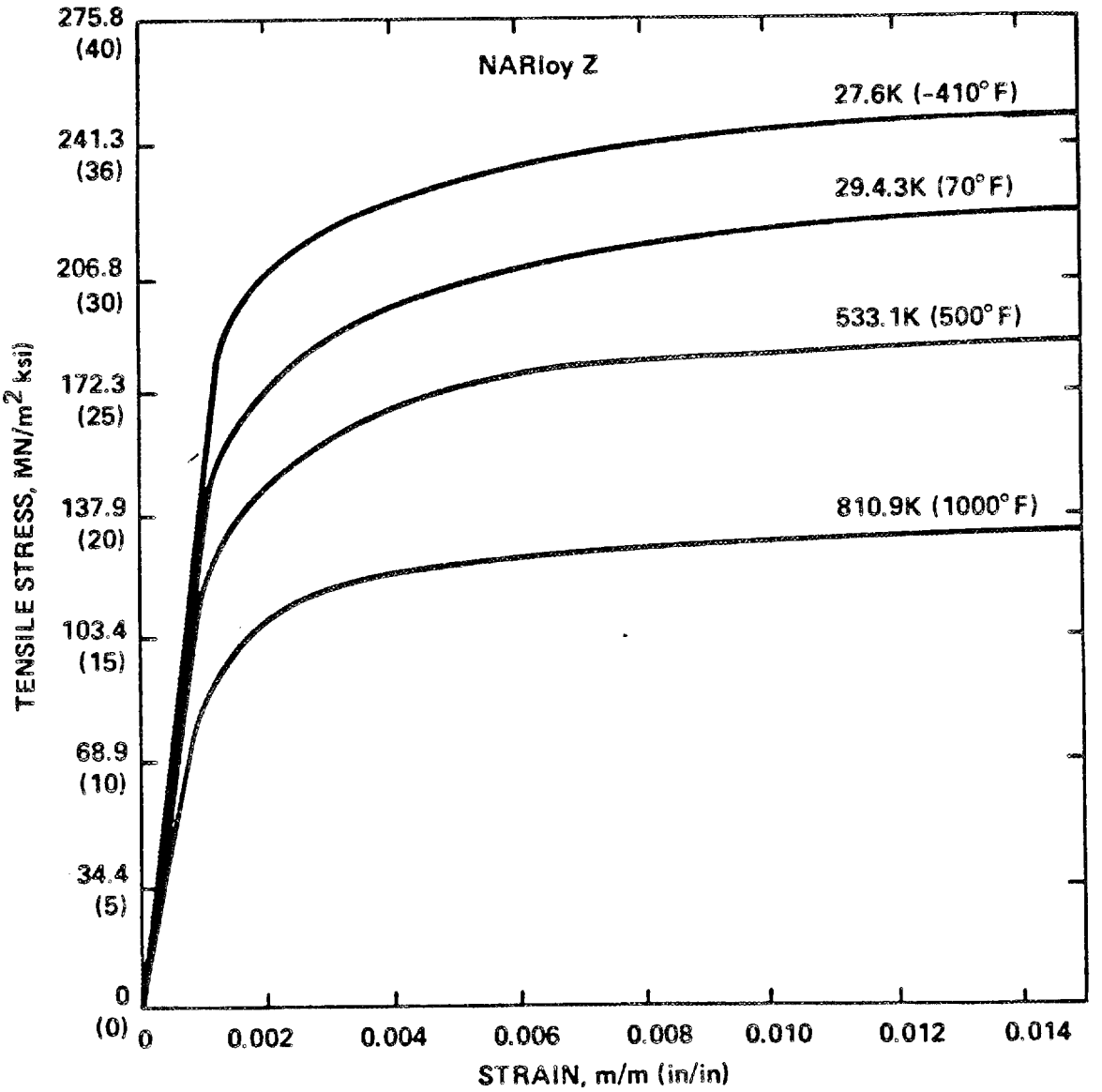

Figure 120. Typical Stress-Strain Curves for NARLOY Z

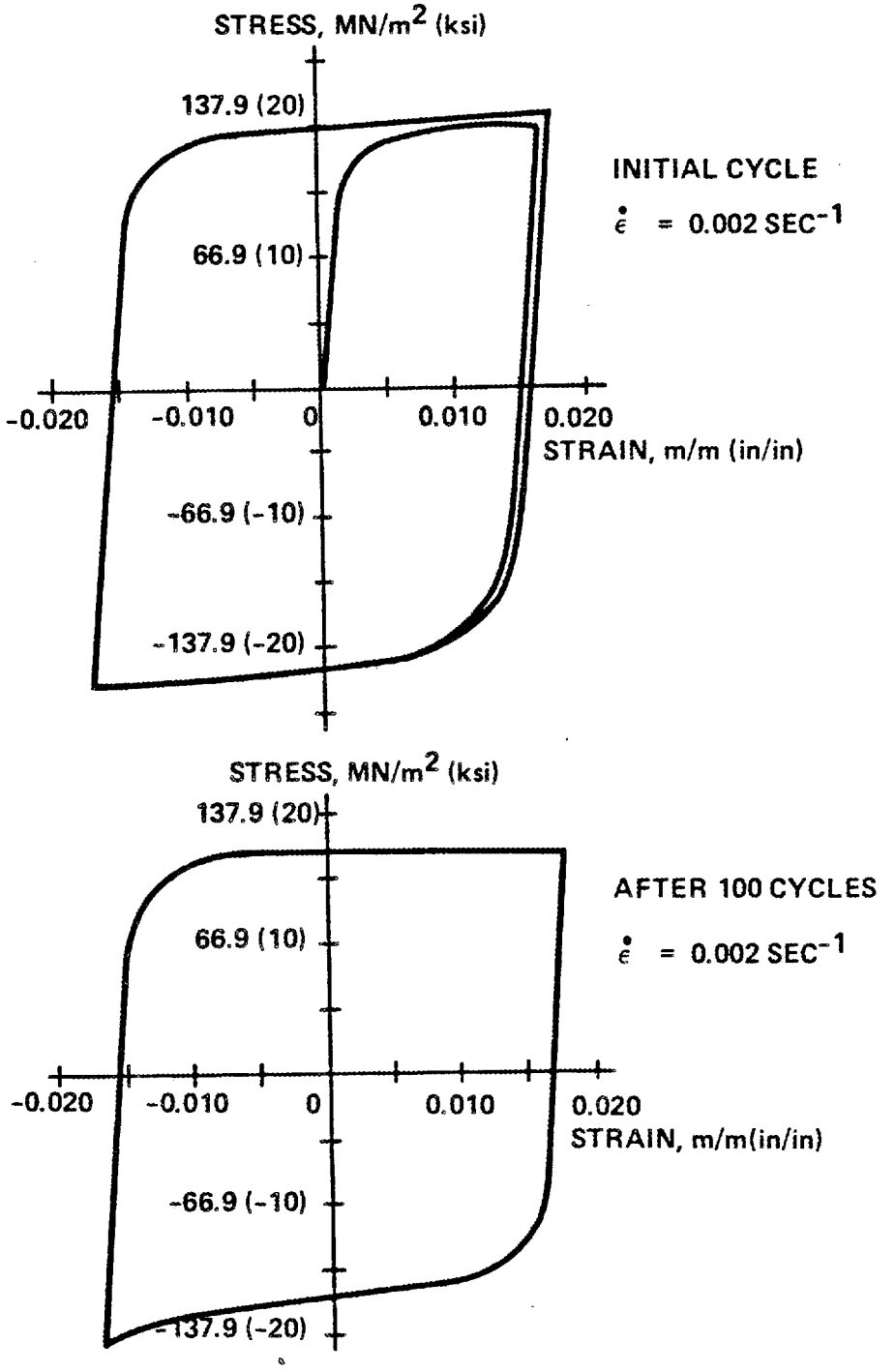

Figure 121. 810.9° K (1000° F) Cycle Stress-Strain Curves for NARLOY Z.

Figure 122. If a linear extrapolation is made to 40,000 cycles, the maximum strain range is 0.35%. Again, doing some interpolating on Figure 120 to obtain the operating temperature of 375°C, the stress level is 20 ksi to produce a strain range of 0.35%.

As a reference, the same information given for Alloy 13 is also shown for Alloy 2 (OFHC copper) in Figures 123, 124 and 125.[35] The ultimate tensile strength (TUS) as shown in Figure 123 is 14 ksi at 375°C. The stress-strain relationship is presented in Figure 124. Extrapolating Figure 125 to 40,000 cycles produces the strain range of 0.35%, which is the same as NARLOY-Z. Again, the low-cycle fatigue data were taken at 537°C, which is above the operating temperature of 375°C. Examining Figure 124 at this strain range, we see that the stress level is limited to 6.5 ksi to produce the same value of 40,000 cycles to failure as NARLOY-Z at 20 ksi.

5. Dispersion Strengthened Copper

The Glidden Metals Division of the SCM Corporation has an experimental material called GLIDCOP AL-15, number 12 in Table 16, which obtains its high temperature strength by the addition of a small, 0.3% by wt., amount of aluminum oxide, Al_2O_3. The manufacturing process is complicated. It involves controlled amounts of oxygen added to a mixture of elemental aluminum and copper in powdered form at elevated temperatures in a controlled atmosphere furnace. The final product must be extruded, or for sizes required for collectors, it must be hot-isostatically-pressed. A sample of this material was supplied by SCM and checked for grain size and oxygen content. The sample was sectioned, fired in dry hydrogen at 1000°C until the part had reached thermal equilibrium, polished, acid-etched and photographed at 100 magnification and 400 magnification, shown respectively, in Figures 126 and 127. This sample was extruded in an OFHC copper cup; therefore, the area at the top is OFHC copper and the area at the bottom is Al_2O_3 dispersion-hardened copper. As can be seen from the photographs, the grain growth in the OFHC copper approached 0.5 mm in diameter, whereas the AL-15 grain size was at least an order of magnitude smaller. There was no evidence of oxygen in the sample material, since hydrogen at this temperature will reduce copper oxide to copper and water vapor. The water

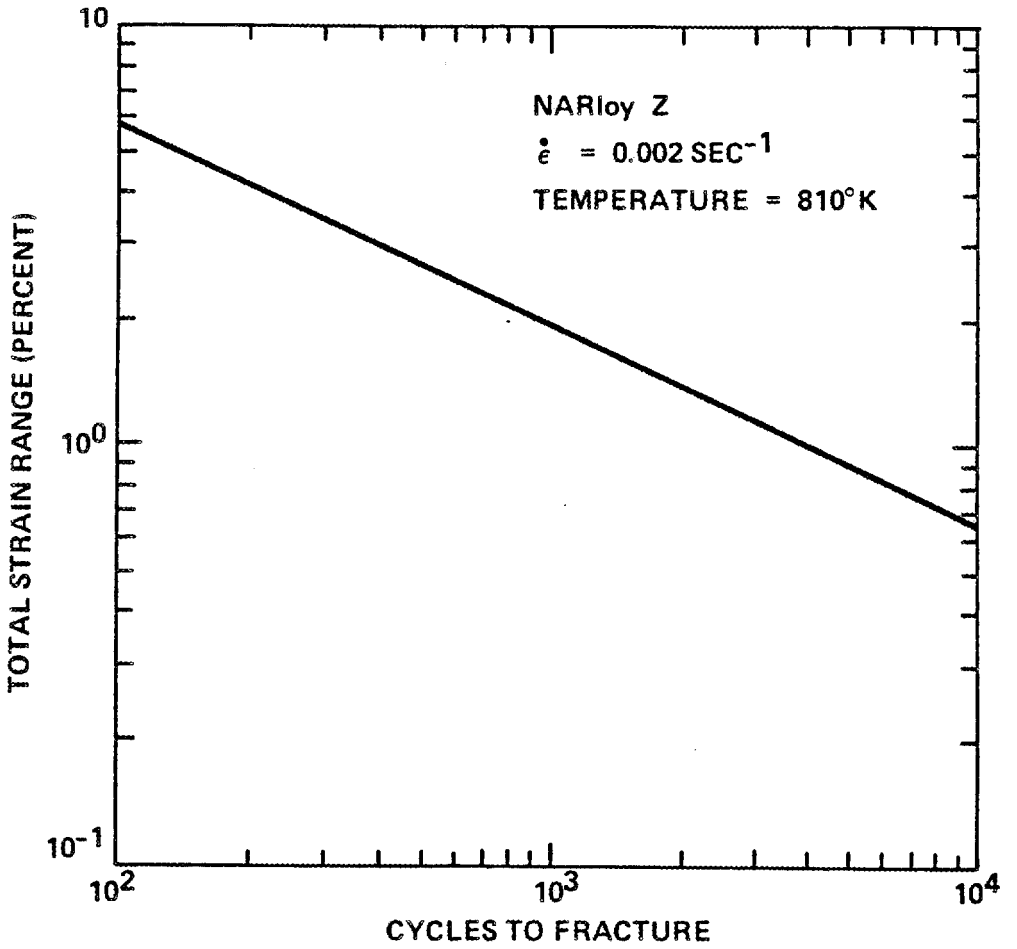

Figure 122. Typical Low-Cycle Fatigue Life of NARLOY Z

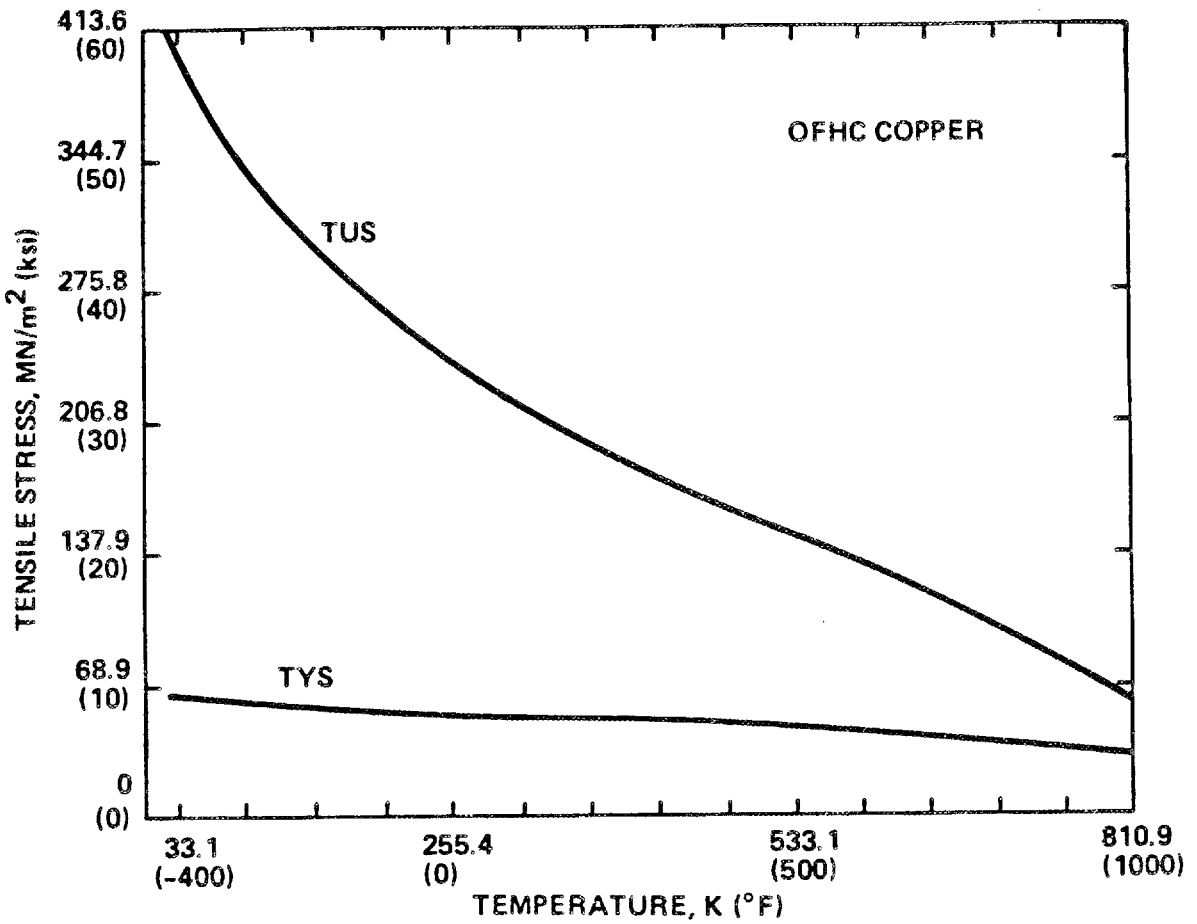

Figure 123. Tensile Strength vs Temperature for OFHC Copper Annealed Condition

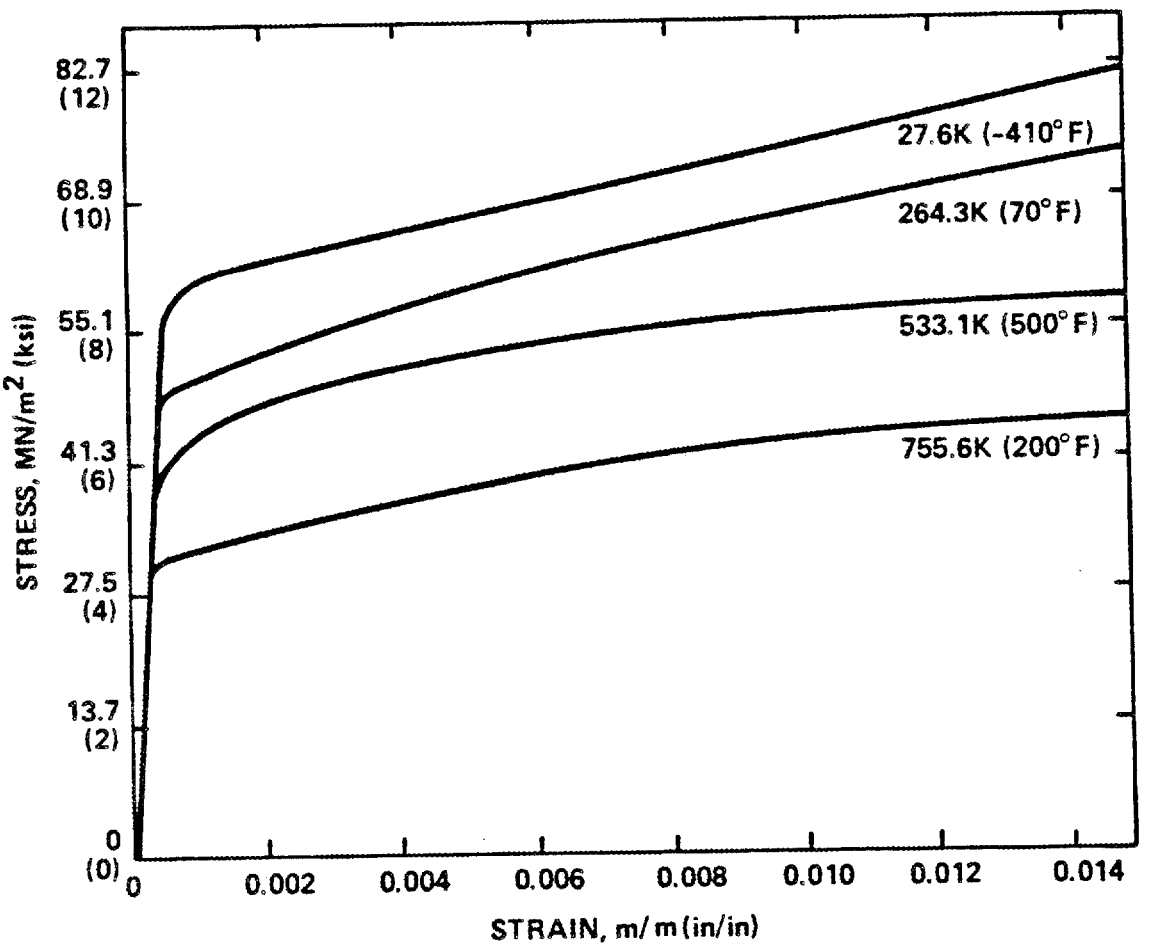

Figure 124. Typical Stress-Strain Curves for OFHC Copper Annealed Condition

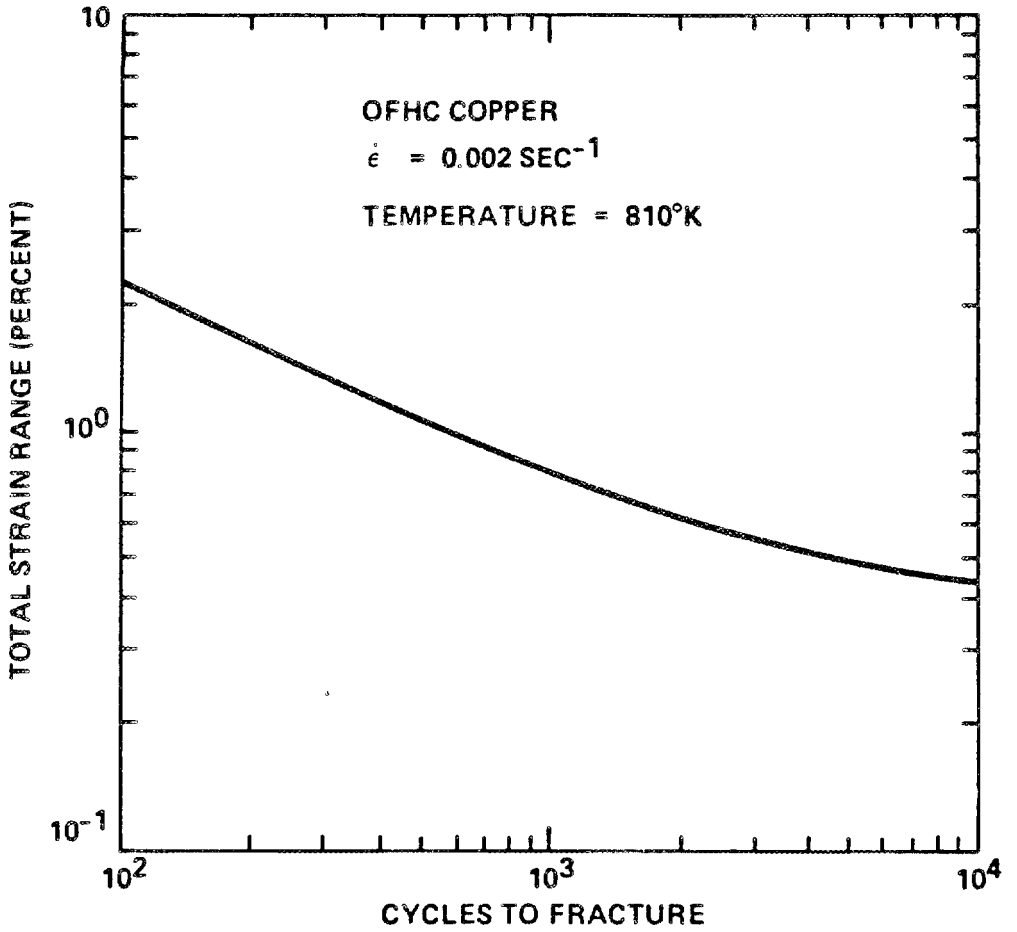

Figure 125. Typical Low-Cycle Fatigue Life of OFHC Copper Annealed

Photo 0681-82

Figure 126. Glidden AL-15 (Oxygen Free) After 1000°C Dry Hydrogen Firing 100X Magnification

Photo 0682-82

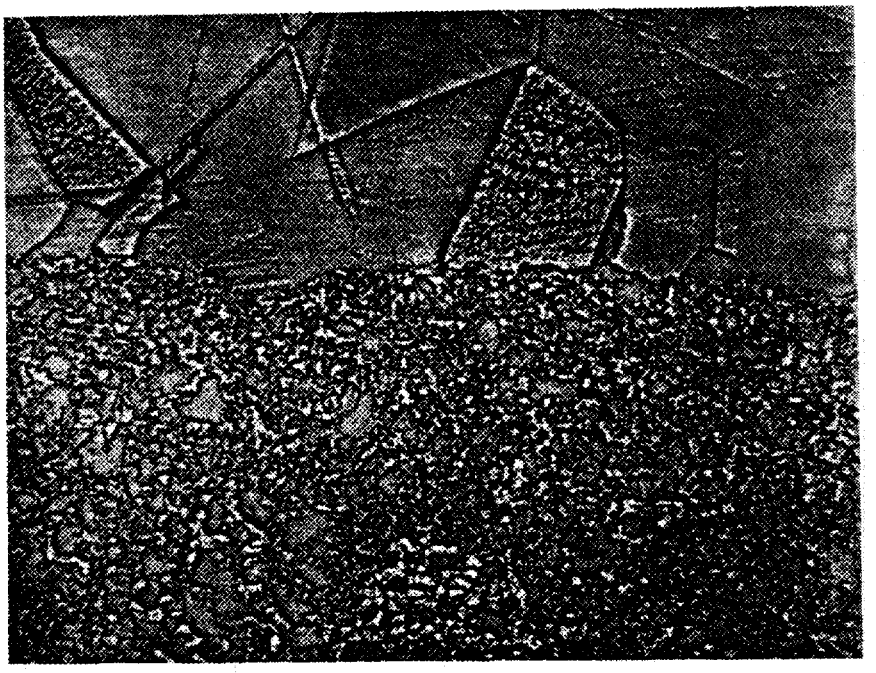

Figure 127. Glidden AL-15 (Oxygen Free) After 1000°C Dry Hydrogen Firing 400X Magnification

vapor becomes steam and ruptures the surface producing visible voids when viewed under sufficient magnification.

An earlier sample received from SCM did contain oxygen in the form of copper oxide, which was readily reduced by the hydrogen during the firing cycle. The black areas, shown in Figures 128 and 129 are voids caused by hydrogen penetration into the material.

Dispersion-hardened copper behaves quite differently from the copper alloys. It does not require heat treatment or aging and maintains its strength at much higher temperatures than the alloys. SCM corporation has not produced full specifications for the AL-15 material. However, they state that it is very similar to AL-20 except for the lack of oxygen.[37] It can be noted from Table 16 that the thermal conductivity of AL-15 is 92% of the value for OFHC copper.

The strength, hardness and elongation is given in Figure 130 as a function of cold work. A typical forging or hot pressing will achieve a 50% reduction in thickness. Therefore, the room temperature tensile strength is approximately 70 ksi, which is superior to all the other materials considered. An indication of its high temperature properties can be seen in Figure 131. The dramatic improvement of AL-20 over OFHC copper in rupture strength at elevated temperature can be seen in Figure 132.

A sample of AL-15 and OFHC was checked for hardness before and after 1000°C hydrogen firing. The results are shown in Table 17.

Table 17
Material Hardness Reduction

	Before Firing	After Firing	% Reduction in Hardness
OFHC	91.6 DPH*	42.1 DPH	54%
AL-15	128 DPH	110 DPH	14%

* DPH = Diamond point hardness numbers, which are the same as Vickers hardness numbers.

Photo 0684-82

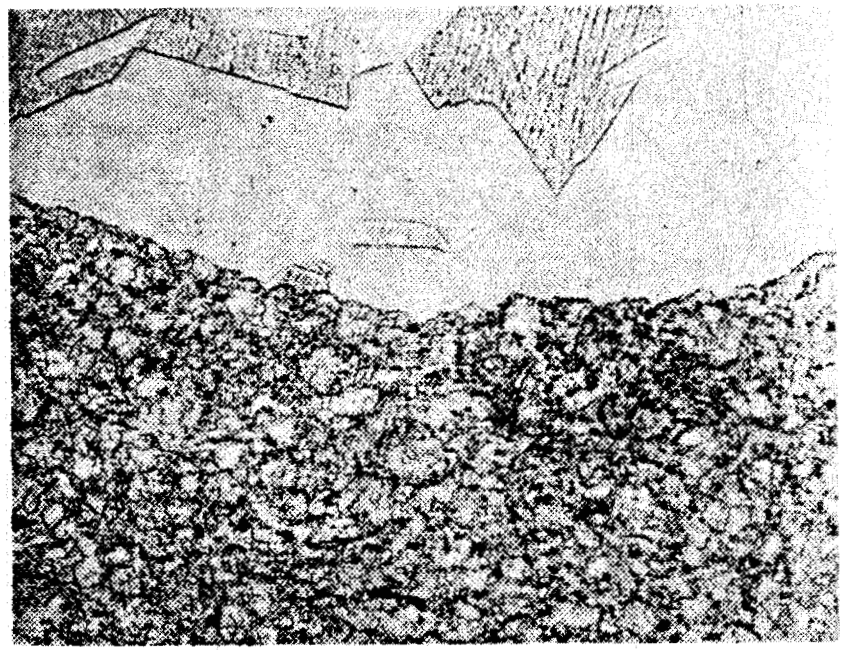

Figure 128. Glidden AL-20 (Oxygen Bearing) Unfired 400X Magnification

Photo 0685-82

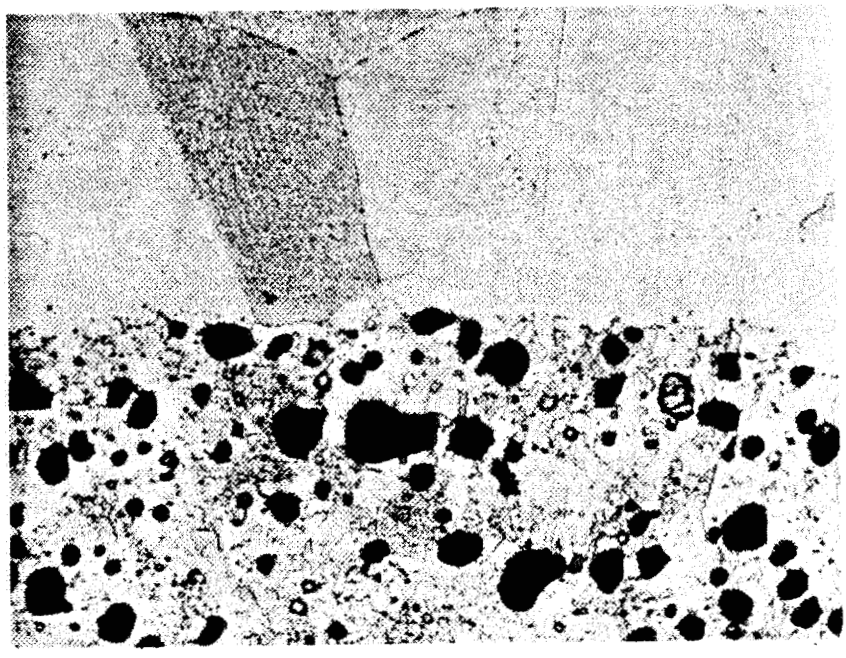

Figure 129. Glidden AL-20 (Oxygen Bearing) After Dry Hydrogen Firing at 1000°C at 400X magnification

Dwg 82-3576 FED

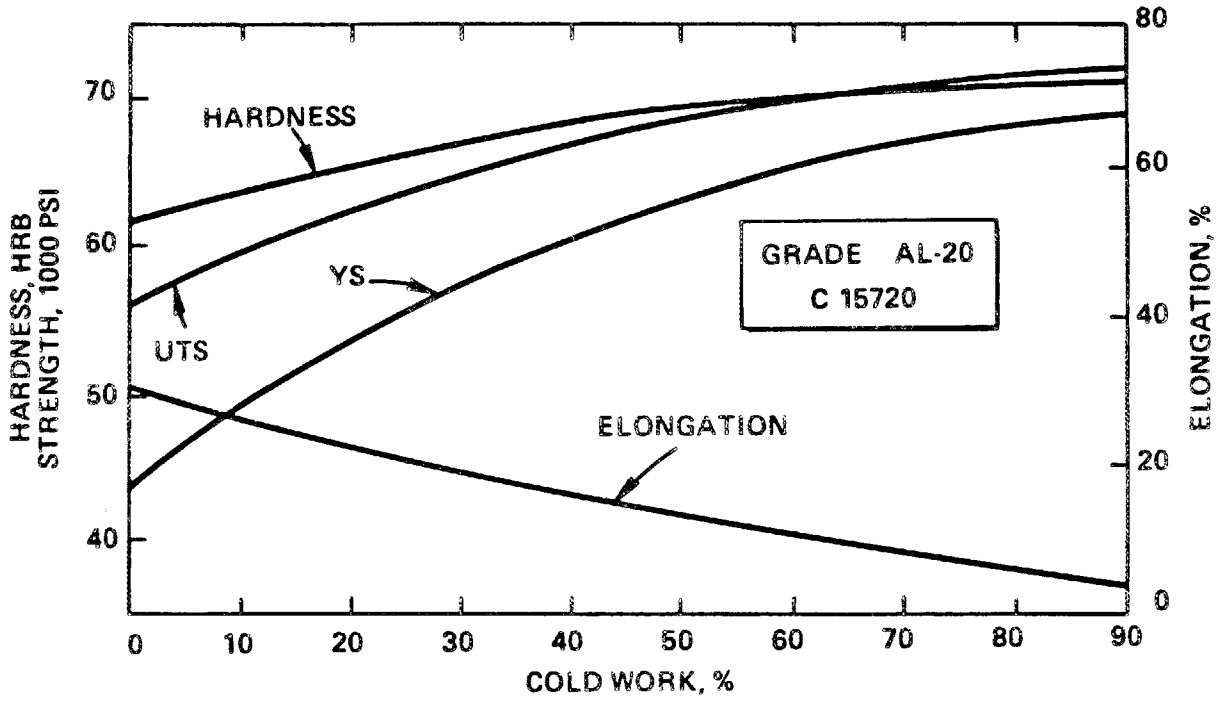

Note: Starting Rod was 0.791" As Extruded Y.S. 0.2% Offset

Figure 130. Effect of Cold Work on the Room Temperature Mechanical Properties of AL-20 GLIDCOP Rod

Dwg 82-3577 FED

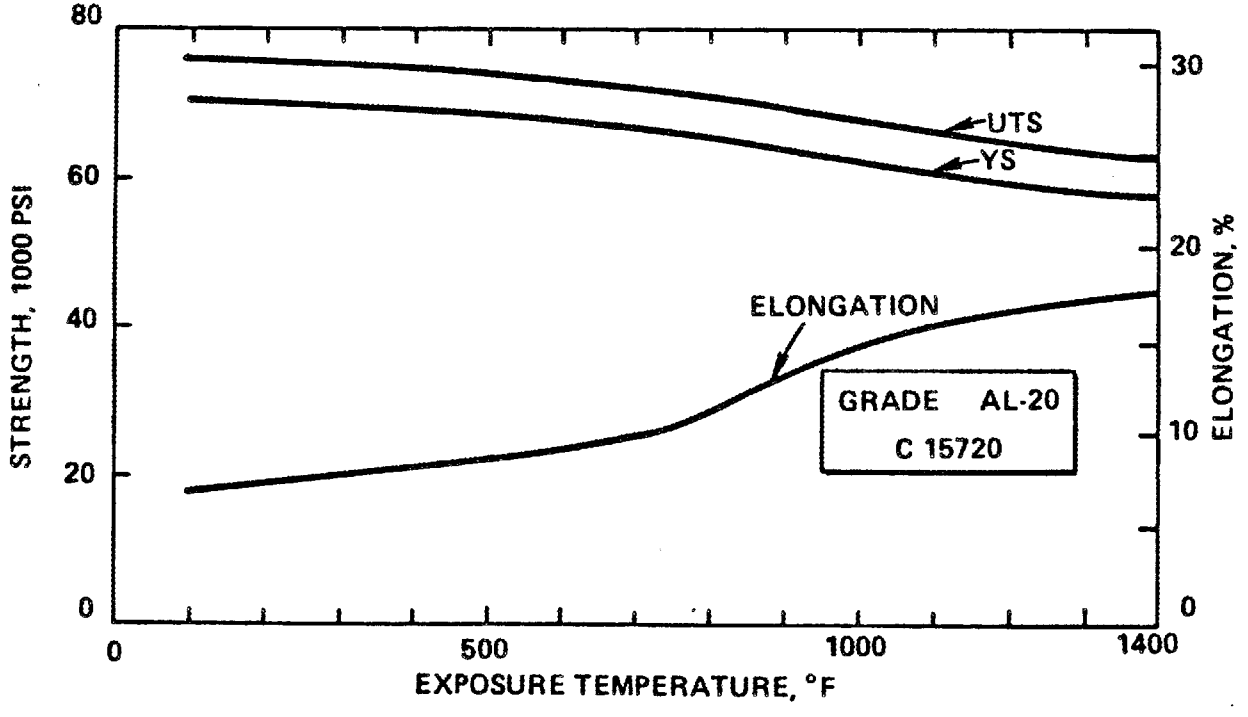

Note: 0.032" Strip Y.S. 0.2% Offset

Figure 131. Effect of One Hour Elevated Temperature Exposure on the Room Temperature Mechanical Properties of AL-20 GLIDCOP Strip

Dwg 82-3578 FED

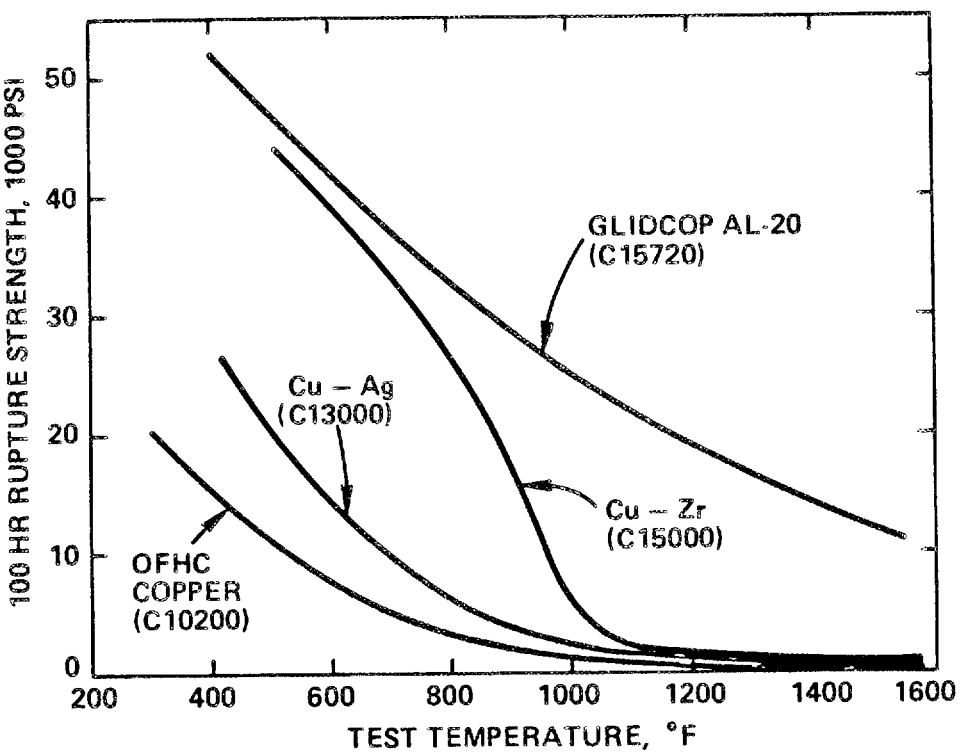

Figure 132. Elevated Temperature Stress Rupture Properties of AL-20 GLIDCOP

Since hardness is proportional to tensile strength, which is a measure of fatigue life, it is apparent that AL-15 is much stronger initially. It also does not lose a significant amount of room temperature strength after being subjected to 1000°C.

If AL-15 can be consistently produced oxygen free, in sizes sufficient for collector fabrication, it clearly is the best material listed in Table 16. Therefore, the alloy numbers of interest are 2, 7, 12 and 13.

6. Metal Matrix Composites

Most of the composites have been developed for aerospace applications, where high strength to weight ratio is paramount. Therefore, most of the matrix materials have been aluminum and magnesium. However, there has been a minor development effort which uses copper as the matrix material. The most promising combination for water-cooled collectors in pulsed applications is OFHC copper strengthened by graphite fibers. Only two companies were located that had worked with this material. Materials Concepts, Inc., in Columbus, Ohio, had coated graphite yarn with copper, but not in an oxygen-free environment. DWA, Inc., in Chatsworth, California, was strengthening copper with continuous filaments of Al_2O_3, supplied by E.I. DuPont de Nemours and Co., Inc., but again, the work was not done in an oxygen-free environment. A significant development program would have to be funded to develop OFHC metal matrix composites.

7. Beam Distribution Measurement

The power distribution inside gyrotron collectors was determined experimentally. When the gyrotron is operating under beam-only conditions the electrons have a small spread of energies. This allows the use of x-ray detection techniques to accurately determine the relative power density. At parameters suitable for 200 kw operation, the electron energy distribution is very broad with a median energy of 55 kV. The collector power distribution was measured under these conditions.

Under beam-only conditions, either film or TLD detectors can be used to determine the relative x-ray density and, directly, the beam current landing in a particular area. With a wide spread of electron energies, and, therefore, a wide spread of x-ray energies, a means must be provided to differentiate the x-ray energies, as well as determine their density. A scintillation detector can do this, but the correlation between beam current and count rate is not well defined. Another drawback to this method is that x-rays below 60 kV will be attenuated almost entirely by the copper wall of the collector. This is very discouraging, since the majority of the power of the spent beam lies below this level.

A second technique was to measure the temperature differences created on the outside surface of the collector by the incident beam power. In this case, the relationship between the observed change in temperature and the incident beam flux was well defined. To use this technique, the collector cooling water was turned off to prevent the rapid removal of the incident power. There were two experimental options with this method. One was to use an infrared camera to measure the temperature distribution. The other technique was to use an array of surface temperature sensors. The infrared camera approach would have had the advantage of being easy to set up, and the equipment was already on hand. The surface temperature sensors were more accurate and did not suffer from problems with background temperatures. Both of these approaches were investigated.

The relationship between incident power flux and outside surface temperature is easy to specify for a one-dimensional model. For a slab of finite thickness with constant heat flux, F, at X = L for pulse duration, τ, and no heat flow at X = 0, the temperature is:[38]

For $0 < t < \tau$

$$T = \frac{2\,F\,(\alpha t)^{1/2}}{K} \sum_{n=0}^{\infty} \text{ierfc}\,\frac{(2n+1)\,L - X}{2\,(\alpha t)^{1/2}} + \text{ierfc}\,\frac{(2n+1)\,L + X}{2\,(\alpha t)^{1/2}} \qquad (58)$$

For $t > \tau$

$$T = \frac{2F}{K} \sum_{n=o}^{\infty} (\alpha t)^{1/2} \; \text{ierfc}\left(\frac{(2n+1)L - X}{2(\alpha t)^{1/2}} + \text{ierfc}\,\frac{(2n+1)L + X}{2(\alpha t)^{1/2}}\right)$$

$$-(\alpha(t-\tau))^{1/2} \; \text{ierfc}\left(\frac{(2n+1)L - X}{2(\alpha(t-\tau))^{1/2}} + \text{ierfc}\,\frac{(2n+1)L + X}{2(\alpha(t-\tau))^{1/2}}\right) \tag{59}$$

where $\text{ierfc}\, X = \frac{1}{\sqrt{\pi}} e^{-X^2} - X \,\text{erfc}\, X$

$$\text{erfc}\, X = \frac{2}{\sqrt{\pi}} \int_X^{\infty} e^{-t^2} dt \quad ,$$

where α is the thermal diffusivity and k is the thermal conductivity.

Using these equations, the inner wall temperature at $X = L$ as a function of time for different pulse durations was determined and is shown in Figure 133. A maximum incident power flux of 2 kW/cm^2 was assumed to give at least a factor of two safety margin. As can be seen, a pulse duration of 0.250 second gives a tolerable temperature rise. With the pulse duration fixed, we plotted the outer wall temperature at $X = 0$ as a function of time for various incident power flux levels, as shown in Figure 134. A power flux level as low as 100 W/cm^2 still causes a detectable temperature rise.

The spatial resolution of the experiment was limited by the transverse diffusion of the heat. The collector was operated uncooled for a single pulse of 5 to 20 ms. The pulse caused a small, but detectable, temperature rise which could be compared to theoretical correlations between incident power flux and temperature rise. Temperatures were recorded at four azimuthal positions (called north, south, east and west) to check for asymmetries.

ORNL – DWG-83-2110

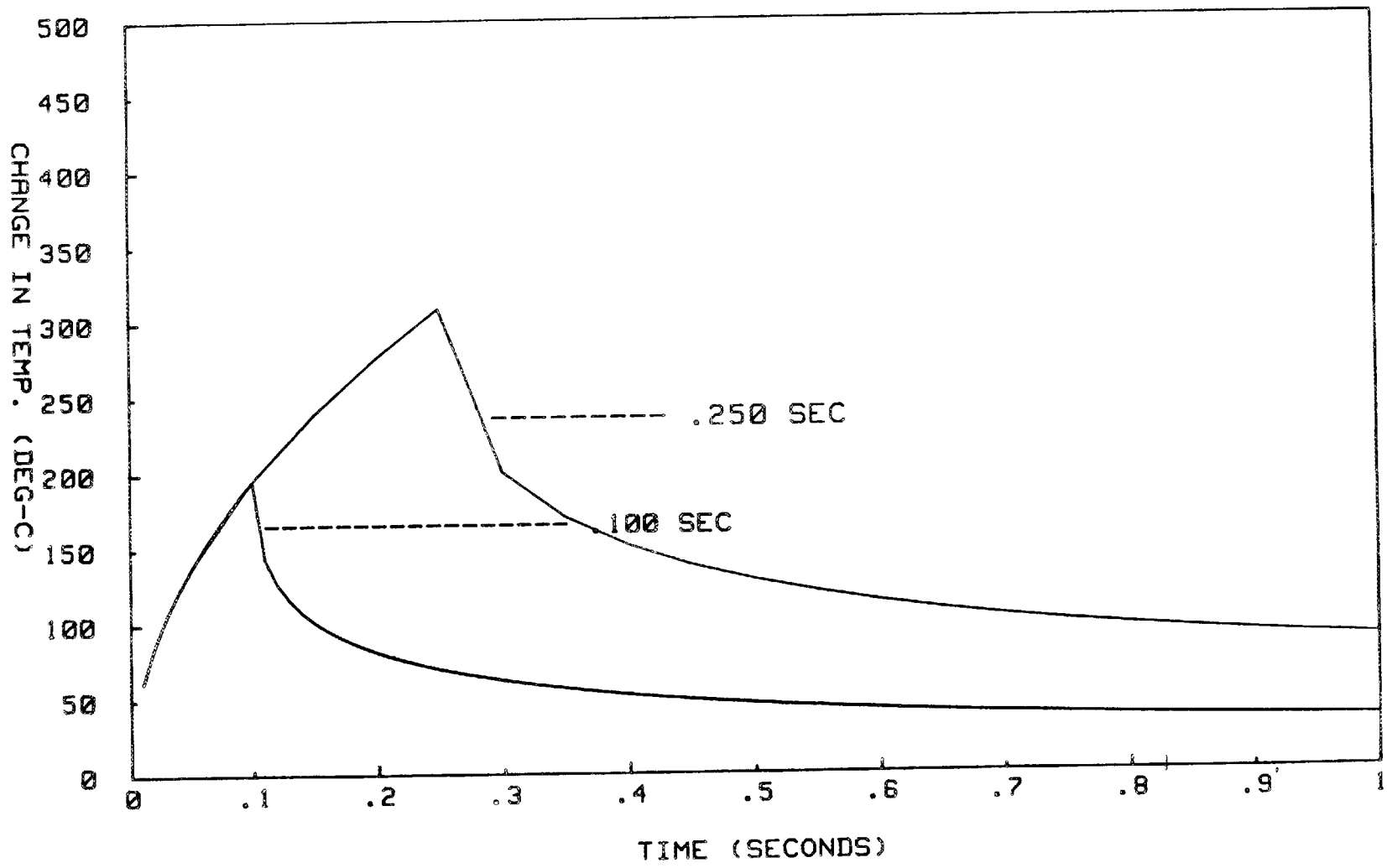

Figure 133. Inner Wall Temperature for 2 kW/cm^2

ORNL – DWG-83-2111

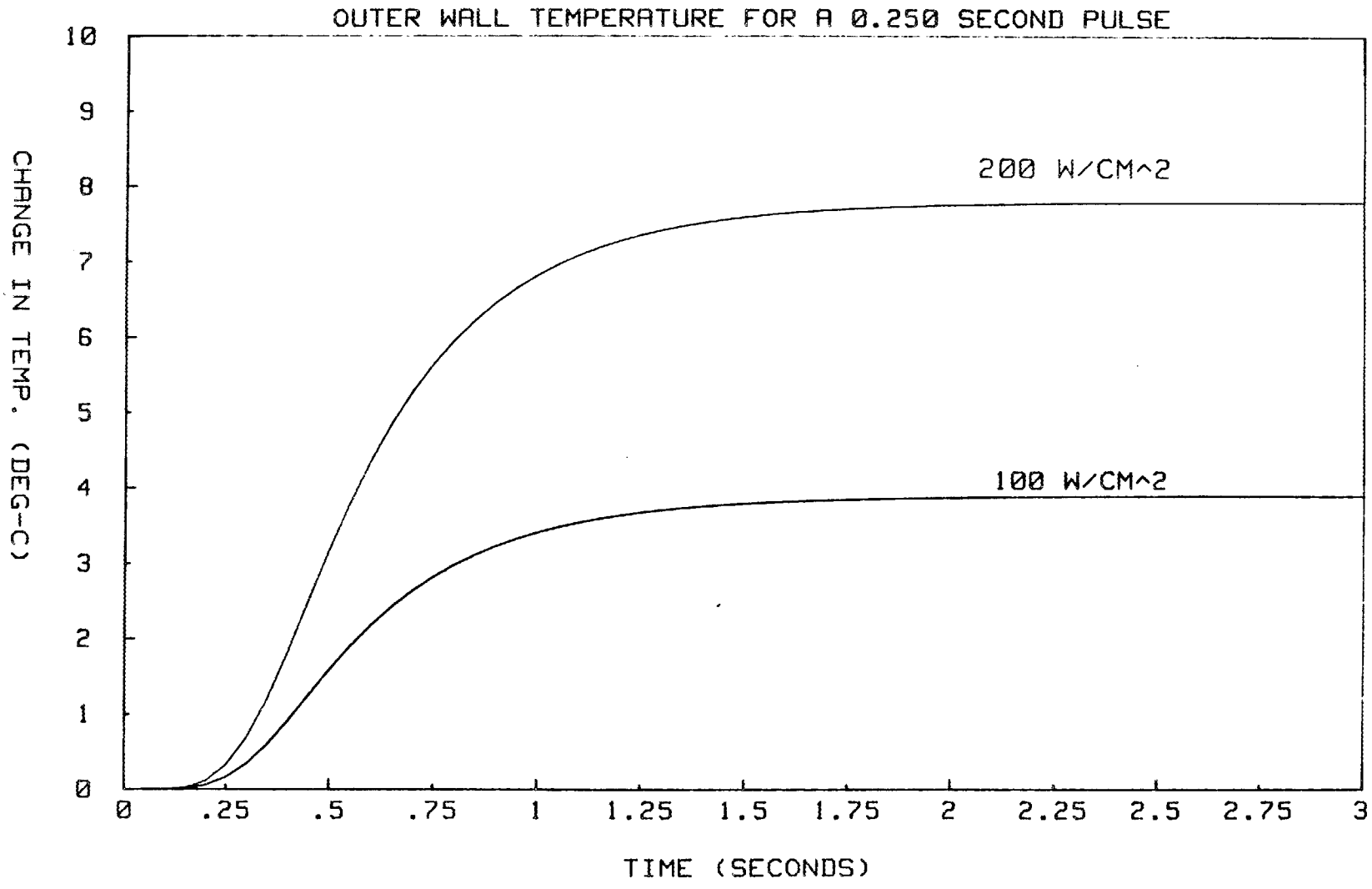

Figure 134. Outer Wall Temperature for a 250 ms Pulse

The theoretical model is a two-dimensional, rectangular, cylindrical model computed on a finite element code known as MARC analysis. Figure 135 gives the calculated temperature rise as a function of time and position for a 1 kW/cm^2 input heat flux over one square centimeter, with no heat flux over the rest of the surface. The peak temperature rise is about $0.14^{\circ}C$. If the heat flux is a constant 1 kW/cm^2 over the entire surface, then the peak temperature rise is about $0.6^{\circ}C$. The actual effect of diffusion away from small areas of high power density in the tube probably results in temperature rises between these two values. In calibrating the measurements, no azimuthal heat flow away from hot spots was assumed; i.e., the $0.6^{\circ}C$ case. Indicated densities, by doing this, were actually somewhat lower than the true values.

Early temperature readings were made on an oscilloscope, limited to viewing two sensors at a time. Later, a computer-based data acquisition system, capable of recording 16 readings simultaneously was developed. The computer also automatically converted temperature rise to incident heat fluxes. This system allowed quick and reliable exploration of many more magnet coil configurations. A schematic of the system is shown in Figure 136.

The collector section of X-8 was made 12 inches longer than that of X-7, to allow a bucking coil to be moved higher and to provide more room at the bottom of the collector for different coil configurations.

Two coil configurations were tried. The first was identical to that used on X-7: a bucking coil near the top, and an aiding coil just above the main magnet dewar. The power-density measurements are summarized in Figures 137 and 138.

The second configuration had an extra aiding coil at the bottom of the collector, and the bucking coil was moved six inches higher. Results are shown in Figures 139 and 140. The magnetic fields for the two configurations are shown in Figure 141.

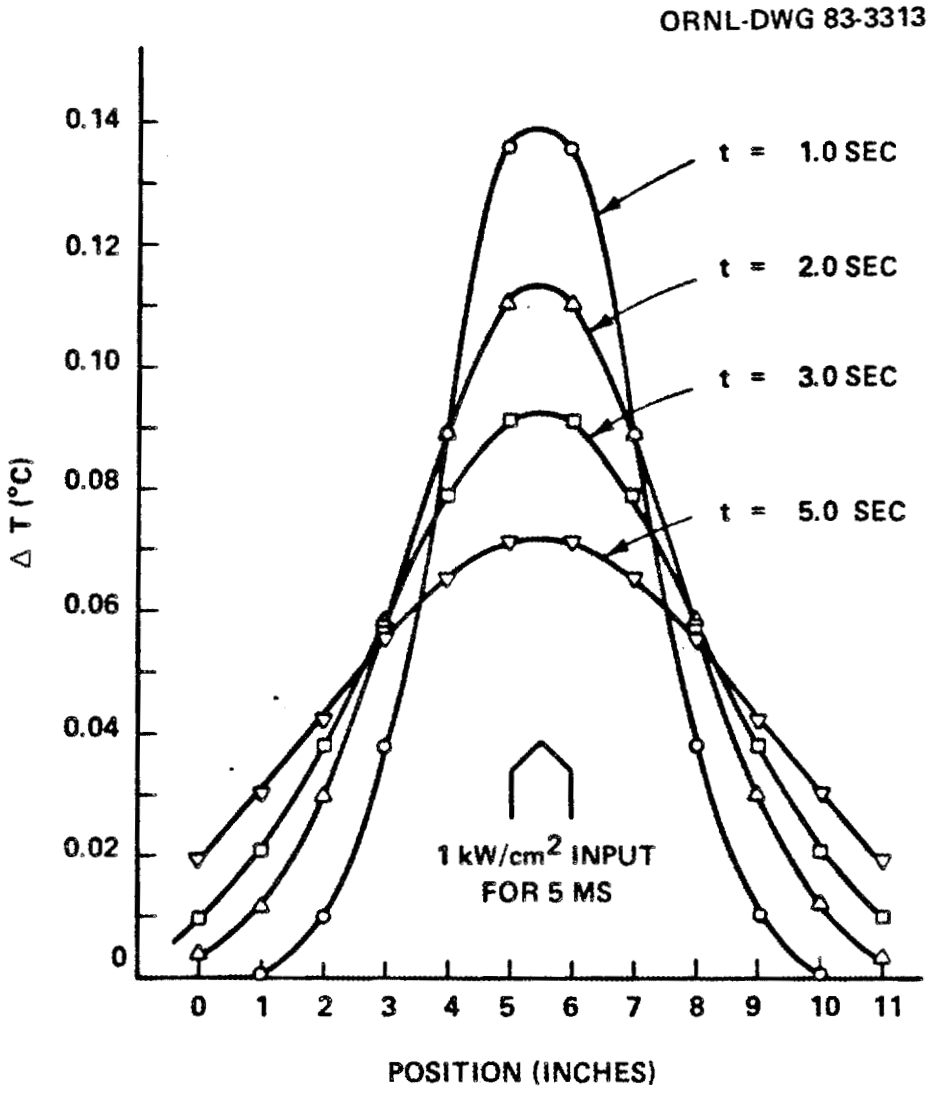

Figure 135. Calculated Collector Wall Temperature Rise

ORNL-DWG 83-3314

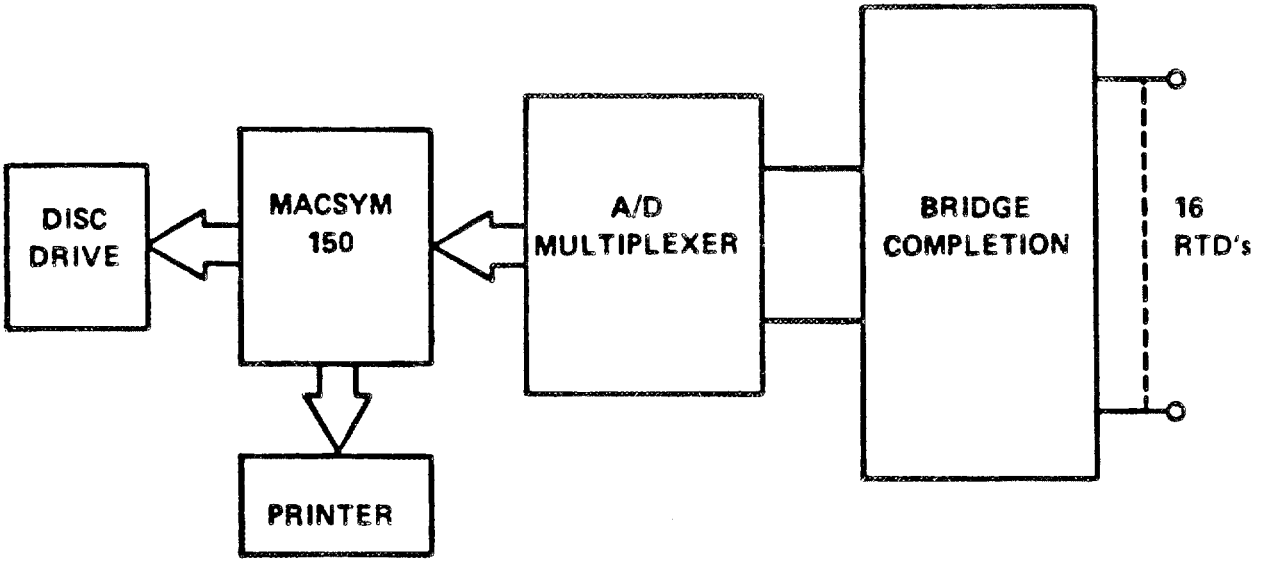

Figure 136. Schematic of Computer Data Acquisition System

ORNL-DWG 83-3315

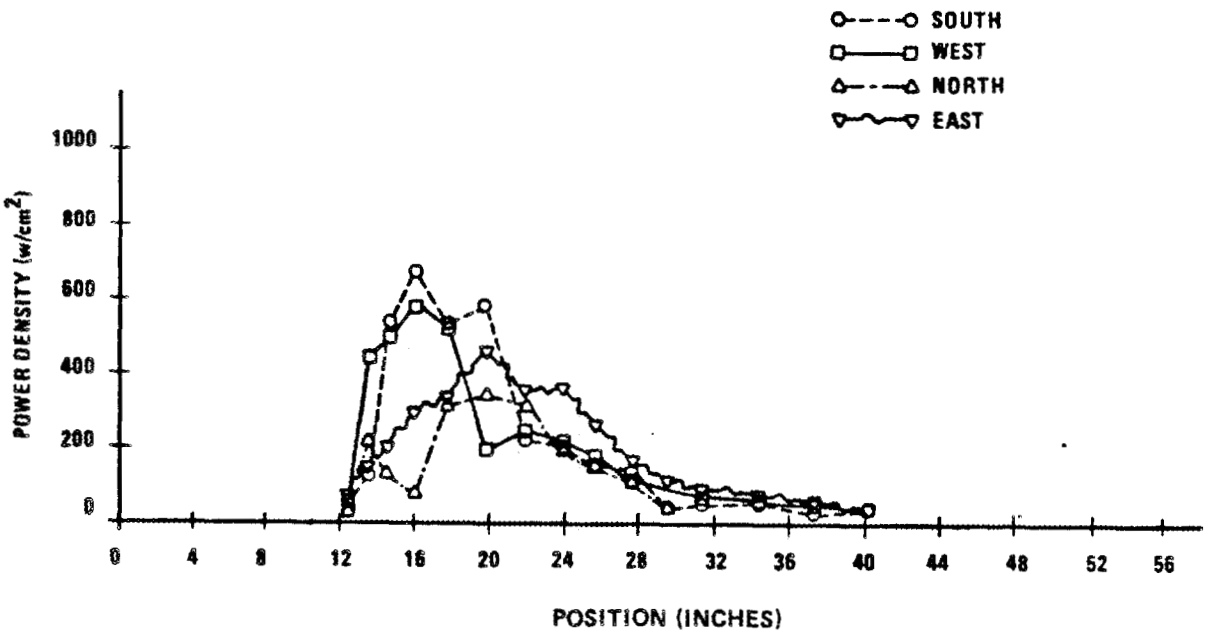

Figure 137. Measured Collector Power Density in X-8: 2 coils with rf

ORNL-DWG 83-3316

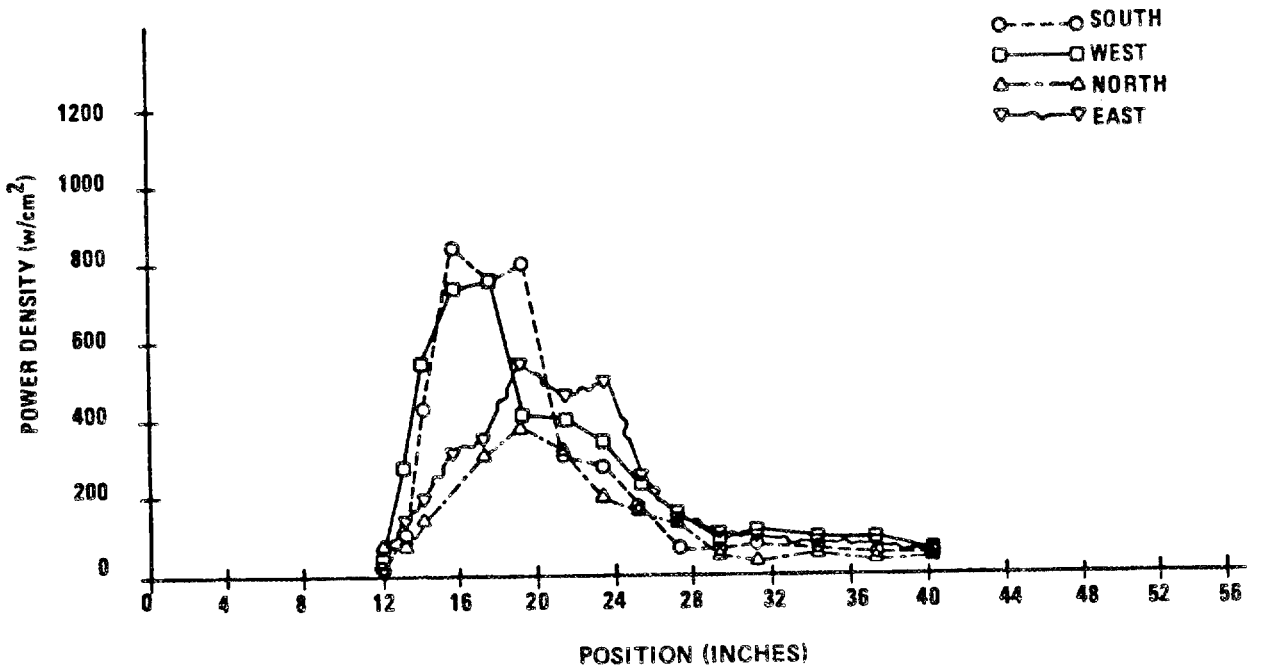

Figure 138. Measured Power Density in X-8, 2 Coils, No RF

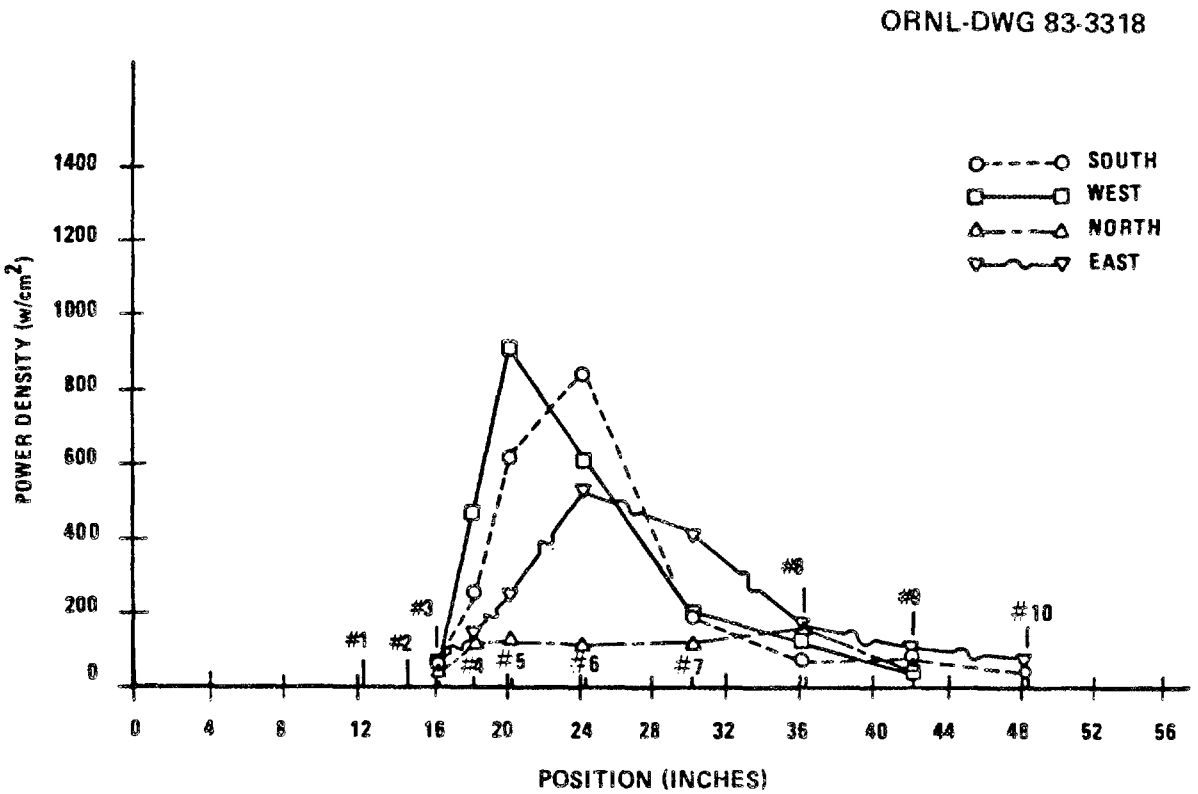

Figure 140. Measured Power Density in X-8: 3 Coils no rf

ORNL-DWG 83-3319

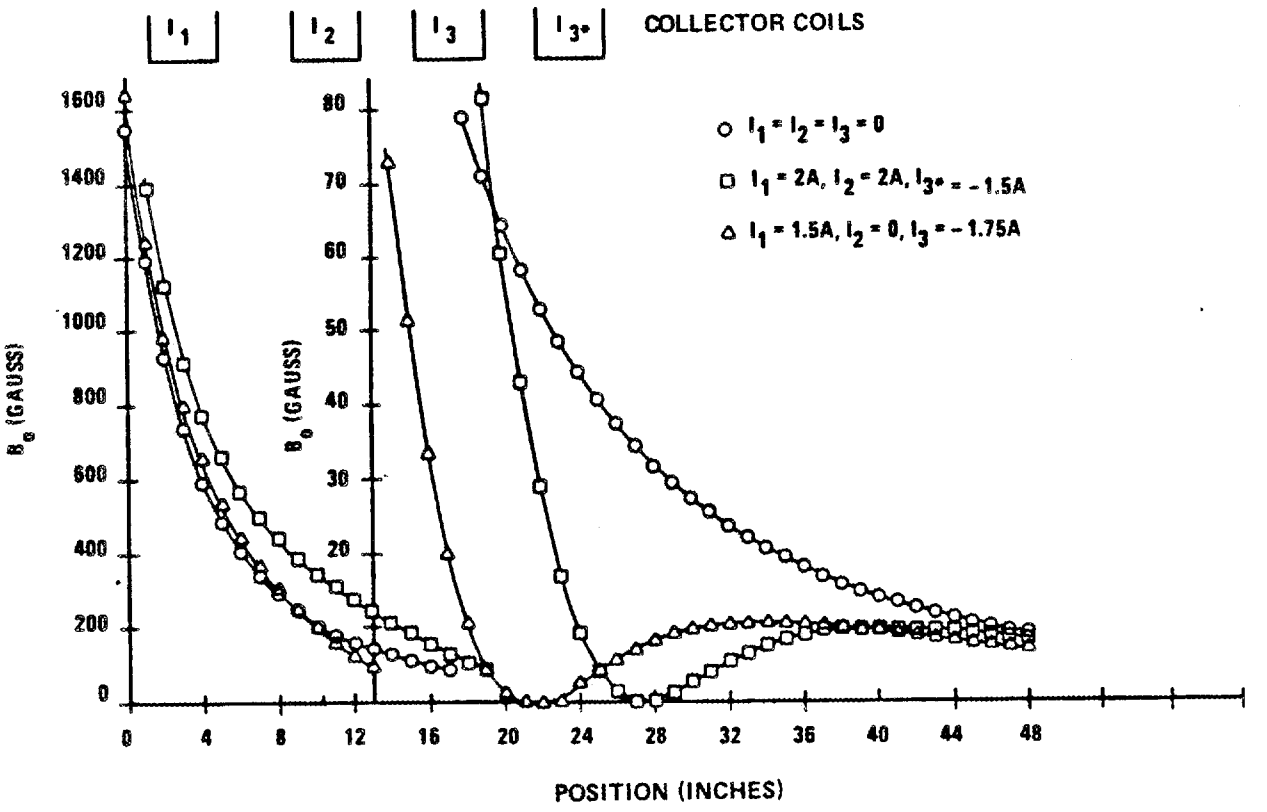

Figure 141. Collector Magnetic Field with 2 and 3 Coils

The data indicate peak power densities of about 700 W/cm^2 with rf, and 900 W/cm^2 without rf, for both coil configurations. However, integration of the power density curves to yield total power deposited, fell short of the actual beam power by 33% with rf, and 45% without. Therefore, the power densities were scaled up to correct the total power deposited, giving peak incident fluxes of 1.0 kW/cm^2 with rf, and 1.6 kW/cm^2 for the beam-only case.

Figures 137 through 140 assumed a rectangular coordinate model. When the model was improved to use cylindrical coordinates, the incident power fluxes increase slightly.

Results for the three-coil configuration, without correction for total power deposited, are shown in Figures 142 and 143. Now, with rf, the peak flux is 900 W/cm^2, and without rf, it is 1.2 kW/cm^2. After correcting for the total power deposited, these values increase to 1.0 kW/cm^2 and 1.7 kW/cm^2, respectively. Such power densities are clearly too high for reliable CW operation, particularly when we consider that the measurement method may not give true peak values because of transverse heat diffusion in the thick copper collector.

The shape of the power density profiles for the two coil configurations is essentially the same. The main difference is that the pattern has shifted upward about six inches. Figure 141 reveals that the null in the magnetic field has also shifted upward about six inches. The bucking coil causes this null and essentially determines where the beam lands.

From these data, two conclusions were drawn. First, the large diameter coils used in this experiment did not provide enough sensitivity and control to properly spread the beam out along the collector. Second, an alternate means of protecting the top of the collector needed to be found, because the bucking coils bunched the beam at the bottom of the collector.

Calculations were performed using a computer code, COLECT, to model the particle trajectories in the collector. This code is an extension

ORNL-DWG 83-3317

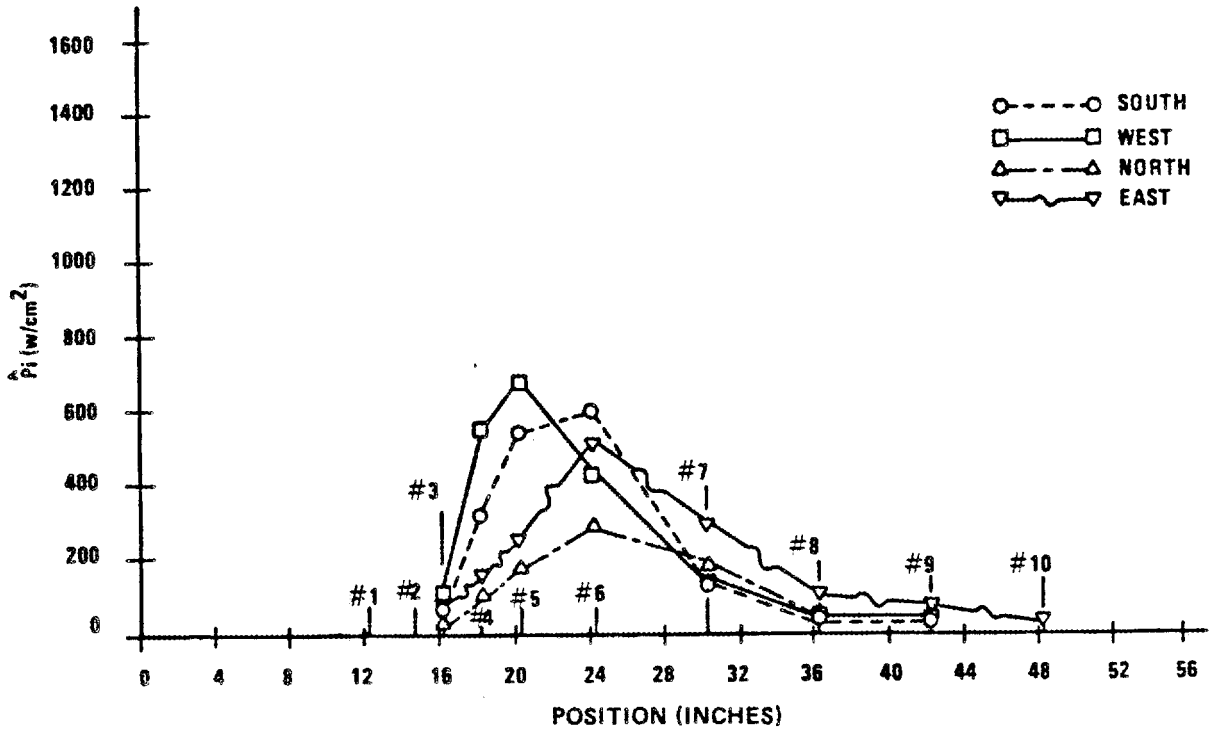

Figure 139. Measured Power Density in X-8: 3 Coils with rf

ORNL-DWG 83-3320

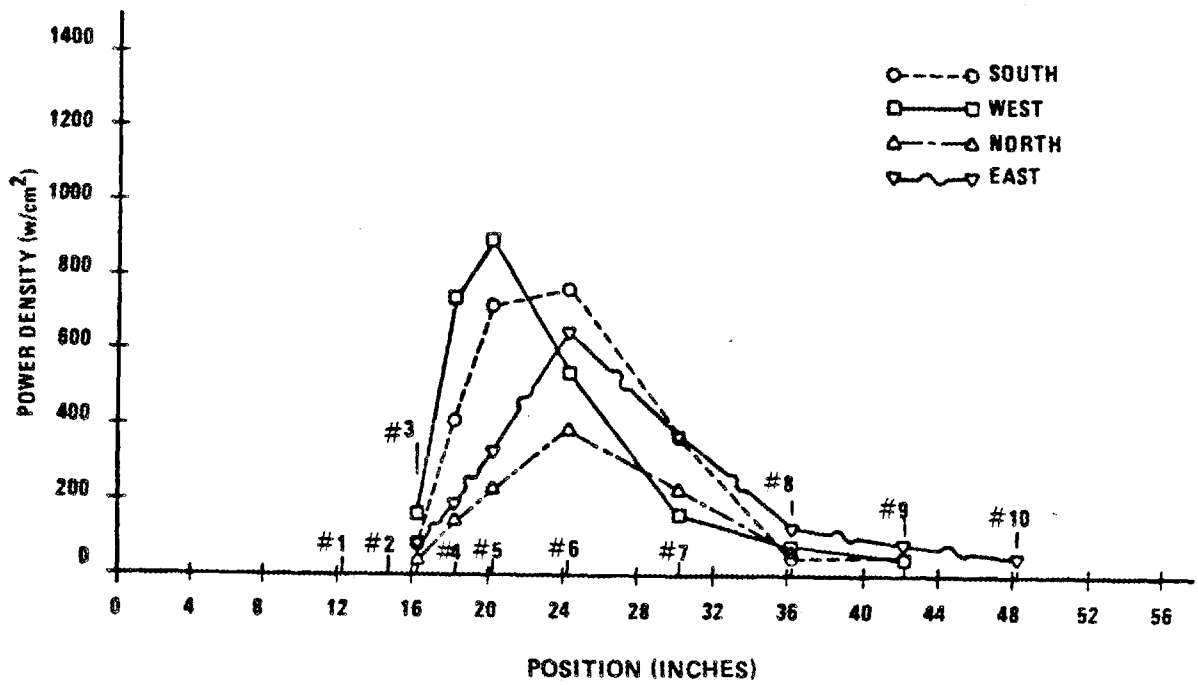

Figure 142. Measured Power Density in X-8: 3 Coils with rf; Cylindrical Coordinate Heat Transfer Analysis

ORNL-DWG 83-3321

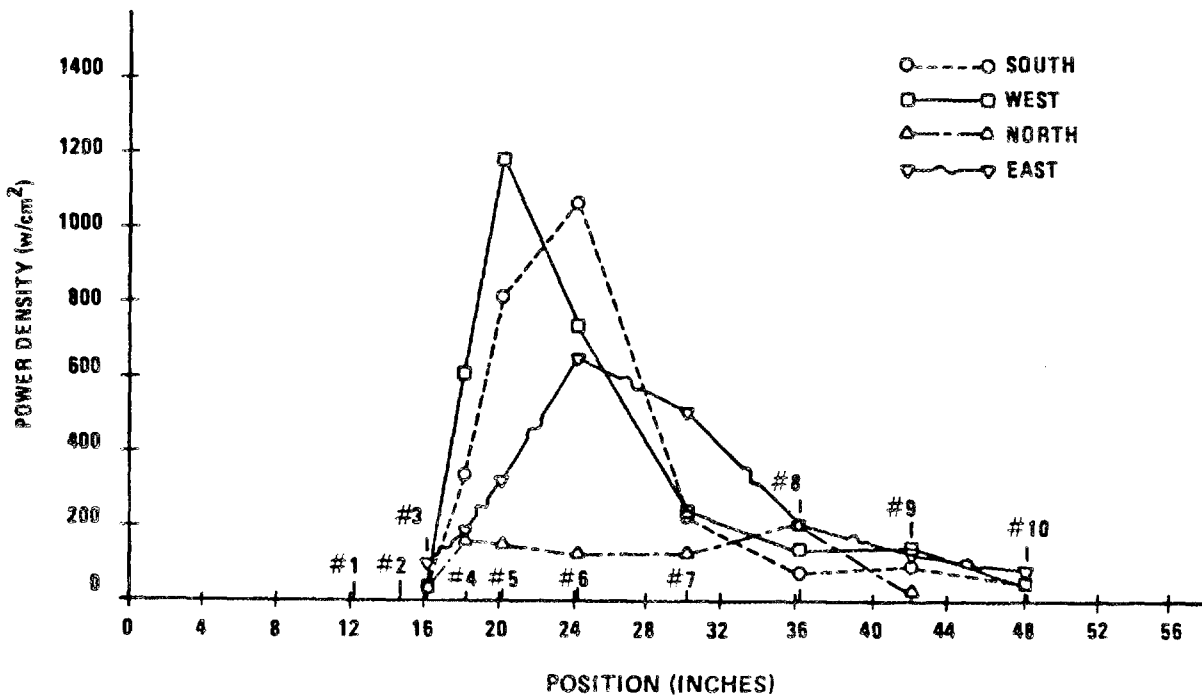

Figure 143. Measured Power Density in X-8: 3 Coils no rf; Cylindrical Coordinate Heat Transfer Analysis

of the code used for large-signal efficiency calculations. As a result, the code allows the rf to be switched off and on to check the effect of rf on the power density distribution. A sample of a trajectory plot using the code is shown in Figure 144.

COLECT has only radial space charge, which saves substantial computer time compared to the fully two-dimensional space charge model. The savings in computer time allows more particles to be used, which gives greater accuracy in determining power density. Up to 200 particles have been used.

One of the problems in calculating the power density in the gyrotron collector is properly accounting for the radial thickness of the beam, as well as the angular phase distribution of electrons around each orbit center. If one uses too few orbit centers or too few electrons distributed in phase around each orbit center, then the calculated power densities tend to be quite lumpy. By randomly selecting phases and guiding centers of the particles, a smooth, realistic power density curve was obtained.

VGE-8006A S/N 104 was identical in structure to X-8. Both of these tubes used the extended length collector to provide more room for profiling the spent beam. A series of measurements was performed on S/N 104 using the computerized measurement system and various configurations of small collector coils. The small collector coils were wrapped directly on the tube and fit underneath the collector support bars.

Previously, a large diameter bucking coil had been used to protect the top of the tube from melting. This arrangement caused the beam to bunch at the bottom of the collector, resulting in excessively high power densities. The small diameter coils were necessary to help spread the beam before too much current reached the top of the collector where otherwise it would be diverted by the transverse magnets that protect the window from stray electrons. The resulting power densities in the transverse magnet area would cause collector melting if CW operation were attempted.

ORNL-DWG 83-3322

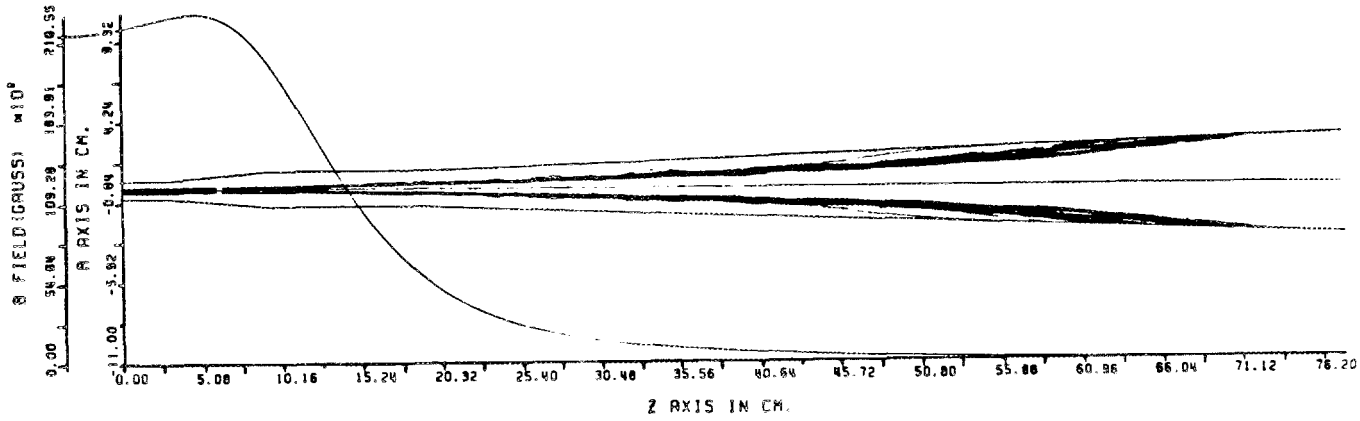

Figure 144. Simulated Electron Trajectories

The power densities in the collector were measured with various combinations of small diameter coils. The final configuration used two aiding coils. The resulting power densities are given in Figure 145. The indicated (uncorrected) peak power density was 550 watts/cm^2. The current reaching the window protection transverse magnet region was found to be negligible. The integrated power for this measurement was 40% below the actual beam power. Applying the error as a correction term to the measured power densities resulted in a peak power density of 910 watts/cm^2. This level of power density is within the cooling capacity of the collector and indicated that CW operation should be possible.

Analysis of the power density data indicated that two-thirds of the beam power was deposited on one side of the collector. The asymmetrical beam collection could be caused by either tube misalignment, magnet misalignment, or environmental asymmetries. Tube misalignment was ruled out because the asymmetrical collection was the same from tube to tube. To investigate whether the magnet or the environment was the cause of the asymmetries, a power density measurement was made with the magnet rotated 180 degrees. If the magnet was the primary cause of the asymmetries, then the pattern of power density inside the collector should also rotate 180 degress. The results of the power density measurements are given in Figure 146. The pattern of power density was nearly the same as when the magnet was in its proper orientation. The test results indicated that the magnet was not the cause of the asymmetrical beam collection. This left only the environment as the possible cause of the asymmetries. The asymmetries produced by the environment in the Nike Zeus Test Set are not of a degree to preclude CW operation. However, to provide consistent, reliable CW operation in any tube socket, it may be necessary to require the installation of extensive magnetic shielding.

To provide a complete picture of the collector power density on S/N 104, measurements were made with the collector coils turned off. The results of these measurements are given in Figure 147. The peak power density was 1050 watts/cm^2. The total integrated power was 33% less than the actual beam power. Applying this as a correction factor resulted in a

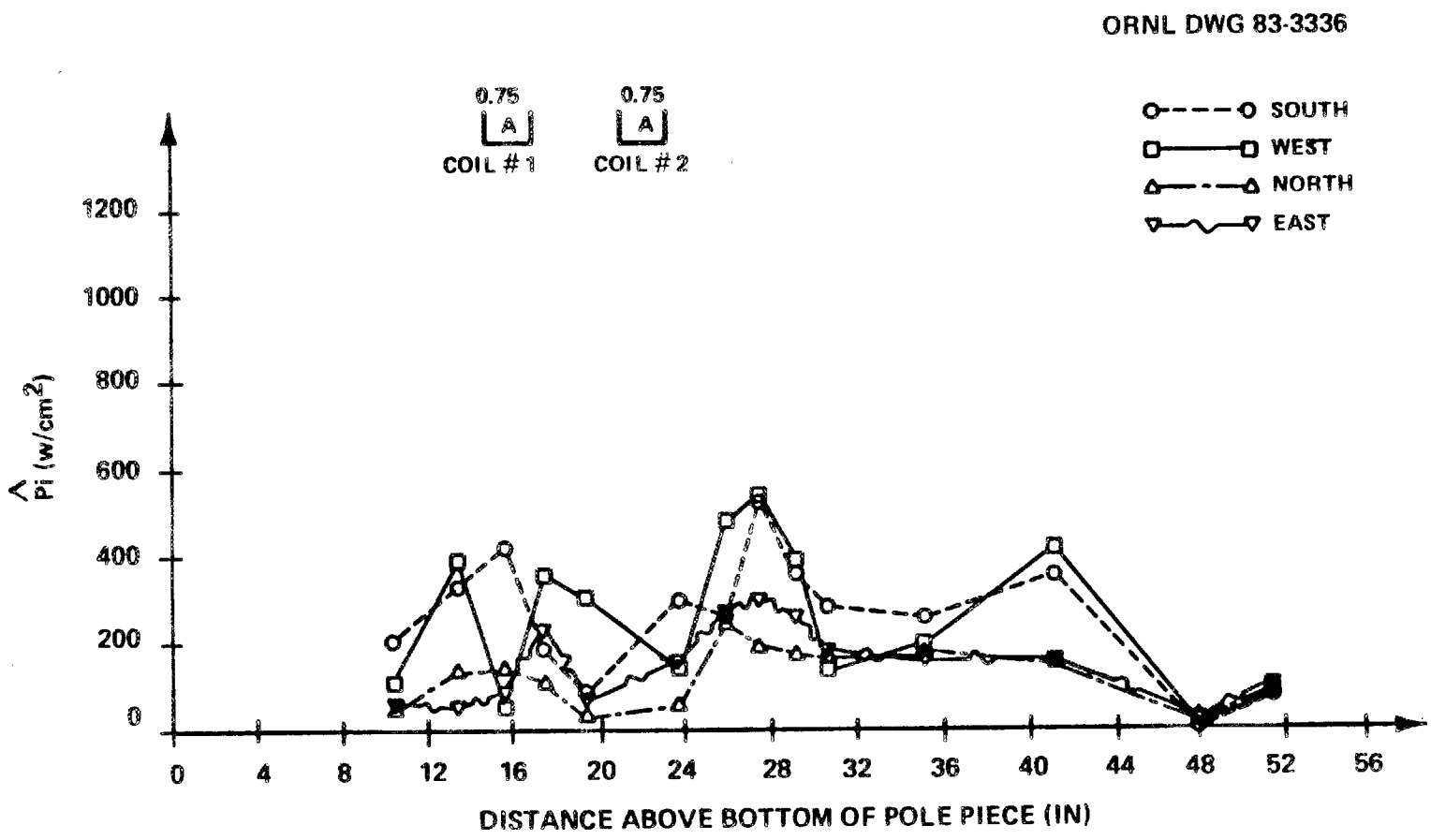

Figure 145. Power Density Distribution for S/N 104, No rf, 2 Small Coils

ORNL DWG 83-3337

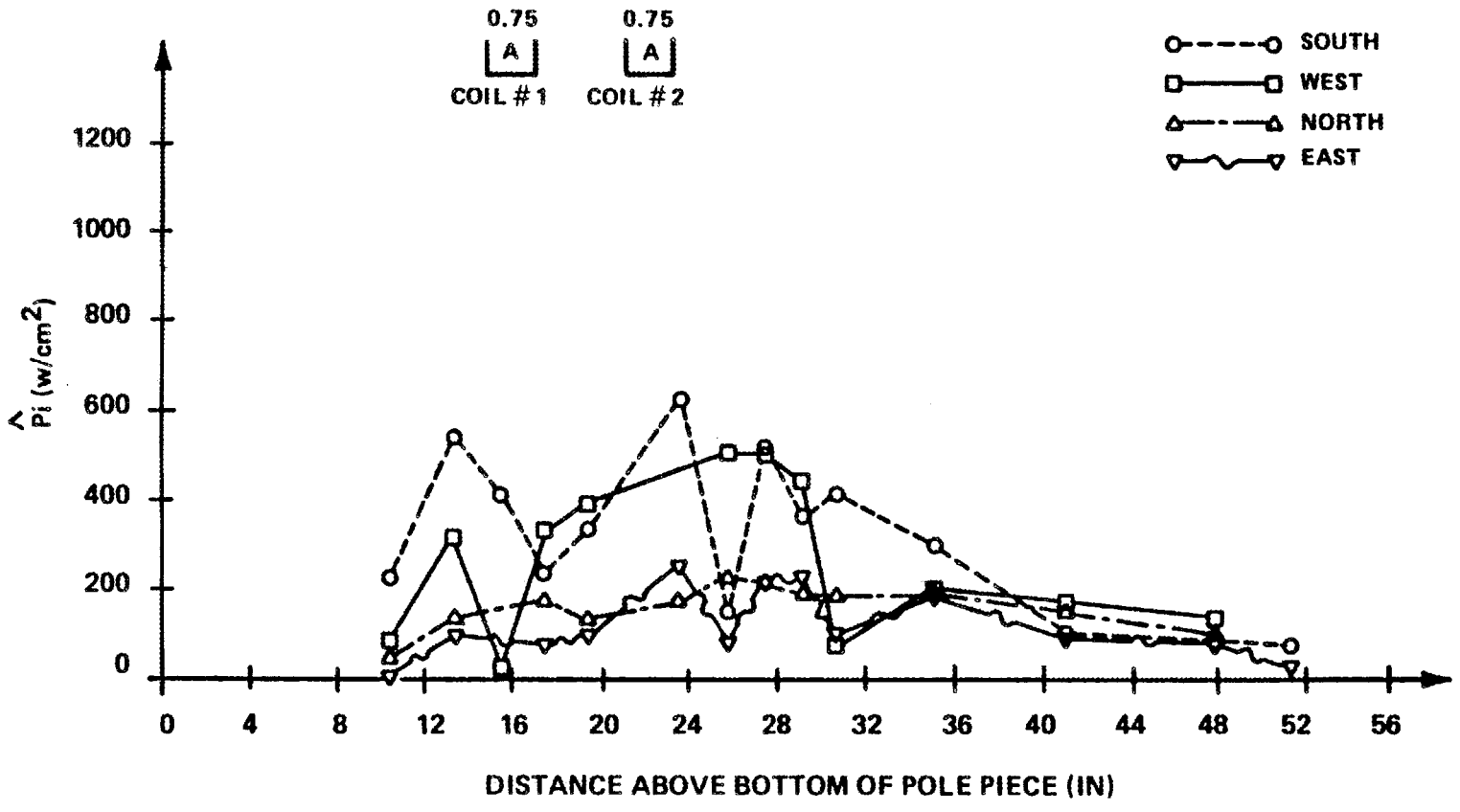

Figure 146. Power Density Distribution for S/N 104, No rf, Two Small Coils, with Superconducting Solenoid Magnet Rotated 180°

ORNL DWG 83-3338

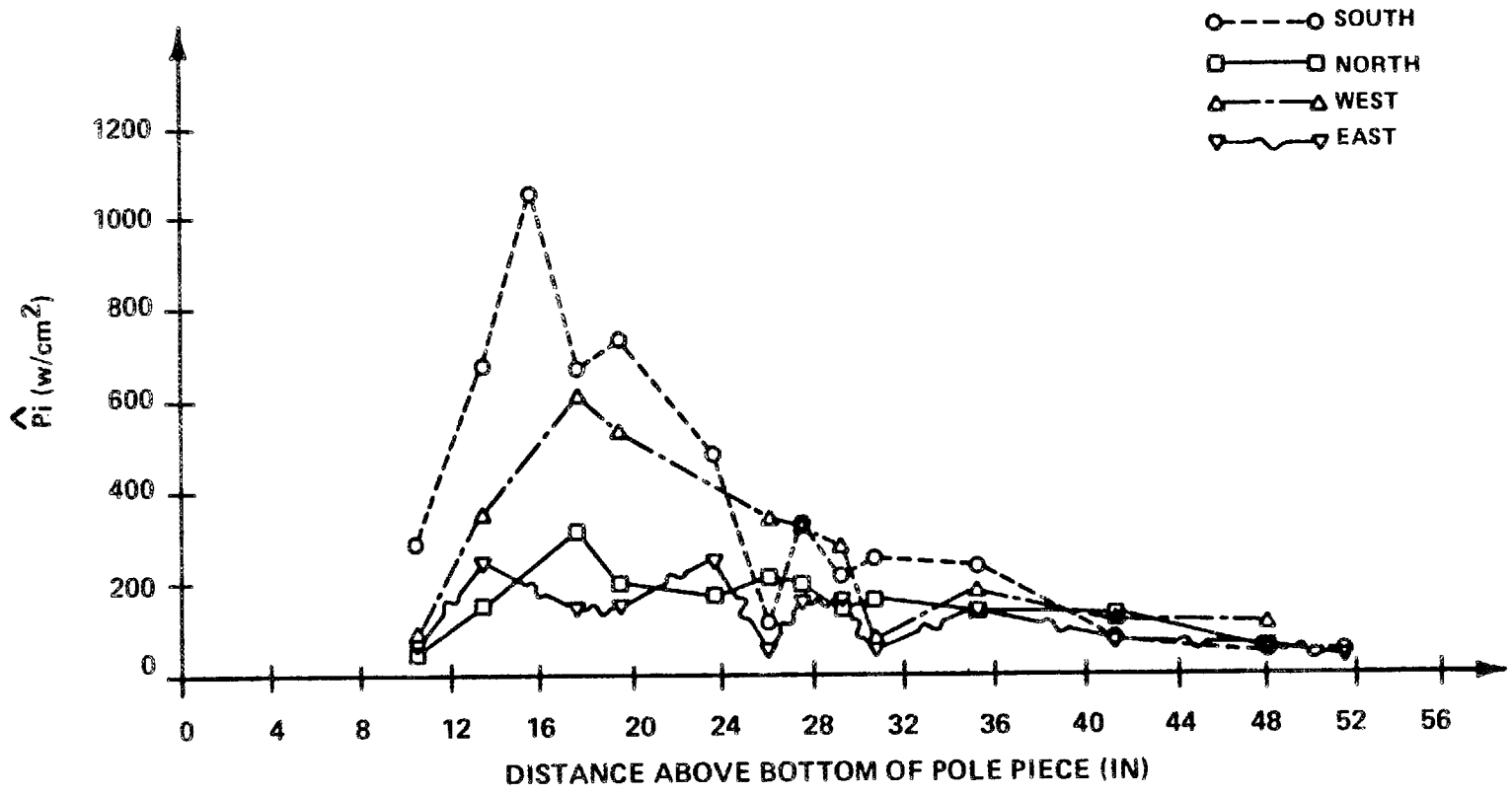

Figure 147. Power Density Distribution for S/N 104, No rf, No Coils, with Superconducting Solenoid Magnet Rotated 180°

peak power density of 1500 watts/cm^2. Clearly, the collector coils are necessary to provide for safe CW operation.

Calculations to compare the theoretical model with experimental measurements were made. The results of these measurements are given in Figure 148. For each calculation 200 particles were used. The curves labeled "three large coils" and "two large coils" refer to two configurations of large diameter collector coils. The experimental measurements corresponding to these two cases are shown in Figures 138, 140 and 142. The curves for two small coils and no collector coils correspond to the measurements shown in Figures 146 and 147, respectively. There was excellent agreement between the calculated results and the experimental results.

8. Cooling Improvements

In addition to material changes to improve collector fatigue life, a change in the cooling channel geometry was also considered. A geometry change would reduce the temperature differential in the material.

The current collector cooling channel geometry is shown in Figure 149, along with the location of the finite element map used for calculating the transient temperature distribution.

The details of the finite element map are shown in Figure 150. Node seven is the highest temperature point on the collector since it is the greatest distance from a cooling channel. The nodes in contact with the coolant are all very near the same temperature, therefore the maximum temperature differential will be between nodes 7 and 43.

The temperature as a function of time is shown in Figure 151. The temperature differential between node 7 and node 43 is 127°C. The stress is proportional to this number. Note that temperature equilibrium is reached in 1.5 seconds. Therefore, any pulse duration greater than this value will produce maximum thermal stress. Also, the maximum temperature of node 43 is 180°C, 10°C above the saturation temperature of the coolant at

ORNL DWG 83-3339

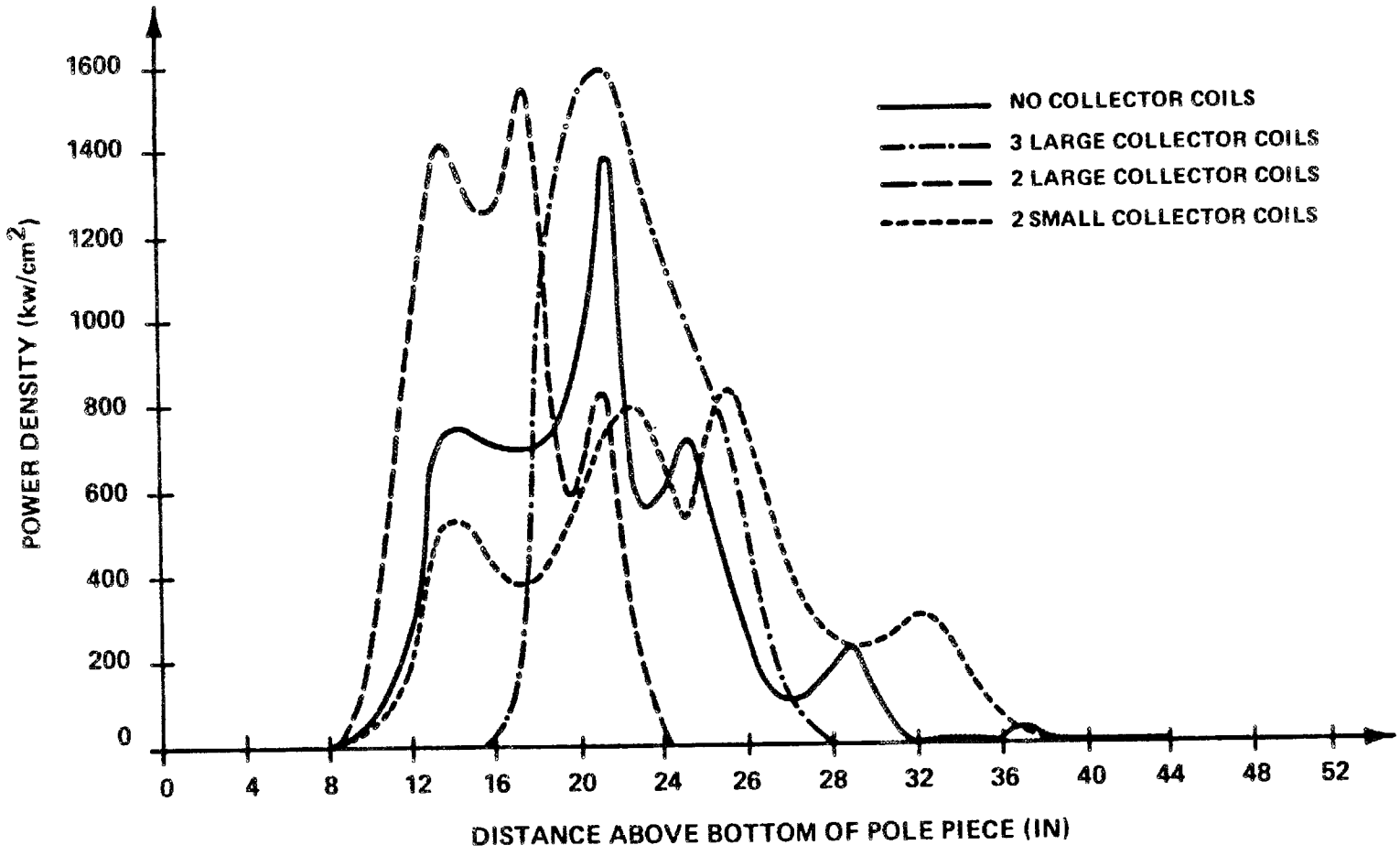

Figure 148. Power Density Distribution Calculations

ORNL – DWG-83-2112

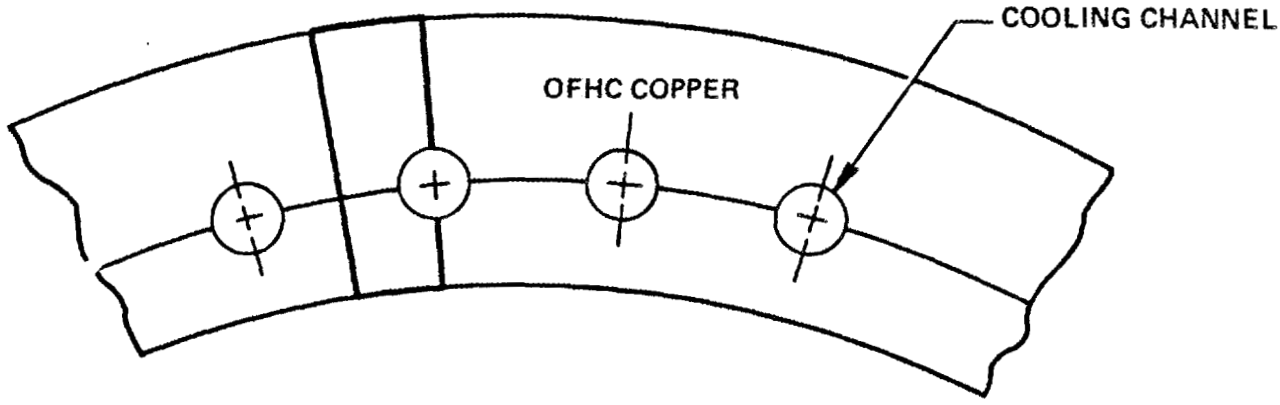

Figure 149. A Partial Cross Section View of the Current Collector Cooling Channel Geometry Showing the Location of the Finite Element Map

ORNL – DWG-83-2113

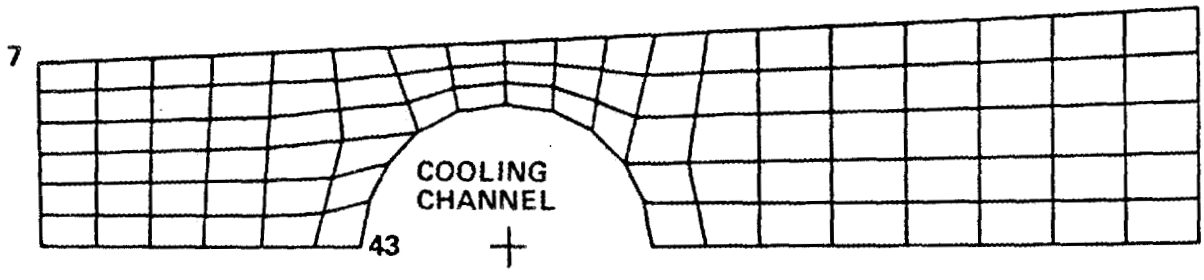

Figure 150. Finite Element Map Used for Calculating Temperature - Time Relationship for Existing Cooling Channel Geometry

ORNL – DWG-83-2114

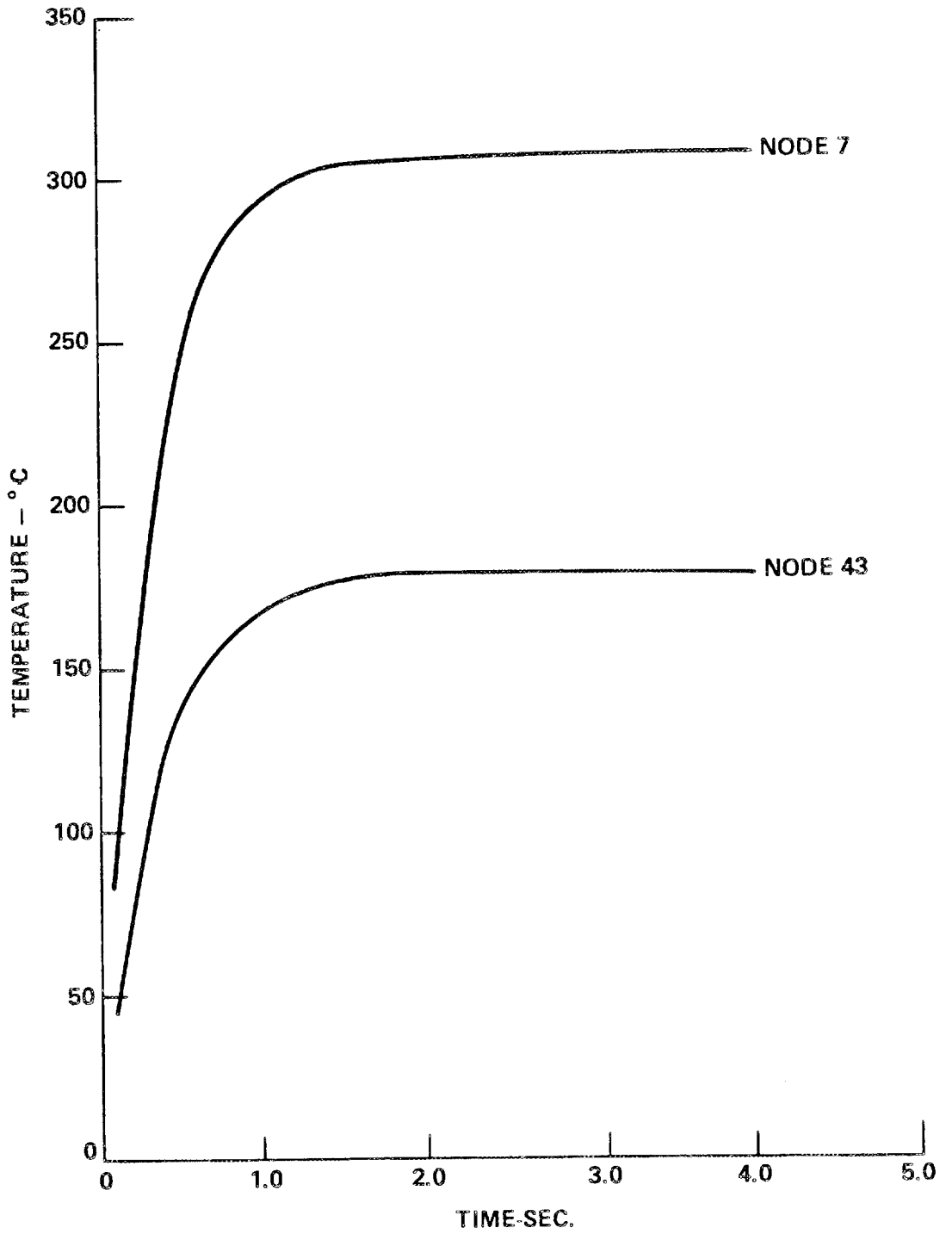

Figure 151. Transient Temperature for Two Critical Nodes for the Current Collector Cooling Channel Geometry

100 psig, which is the operating pressure at the center of the collector. Thus, at maximum power density, the coolant will be operating in the nucleate boiling regime. However, the improved heat transfer coefficient will more than compensate for the 10°C of superheat.

The new cooling channel geometry is shown in Figure 152. The only change is the movement of the channels 0.100 inch closer to the source of heat. The finite element map used to calculate the temperature profile is shown in Figure 153. Again, as shown in Figure 154, the maximum temperature differential is between nodes 7 and 36. The temperature differential with this geometry is 67°C; a reduction of 60°C over the current geometry. Since the stress is proportional to the temperature differential per unit length, the reduction in stress will not be significant. However, the temperature reduction will reduce the possibility of melting. The coolant will be in the nucleate boiling regime since there will be 13°C of superheat.

With proper beam distribution, the fatigue life test requirements of 35,000 cycles of full power pulses at 50% duty cycle will be met, if not with the present collector, then with the use of stronger materials and the reduction in temperature due to improved cooling.

9. Mechanical Fatigue Life Tests

The three most promising candidate materials for improving the collector fatigue life were dispersion-hardened copper from SCM Metals Products, designated AL-15, and two alloys from Amax, Inc., called MZC and AMZIRC. The complete specifications for these materials were shown in Table 16.

Varian provided samples of these three materials to Oak Ridge National Laboratory for testing, using their mechanical fatigue testing facilities. All of the samples went through a dummy braze cycle identical to the brazing technique used for collectors at Varian. The fatigue tests were performed under vacuum at 300°C, which is the same environment in which the material will be subjected in the actual tube. The test results noted

ORNL – DWG-83-2115

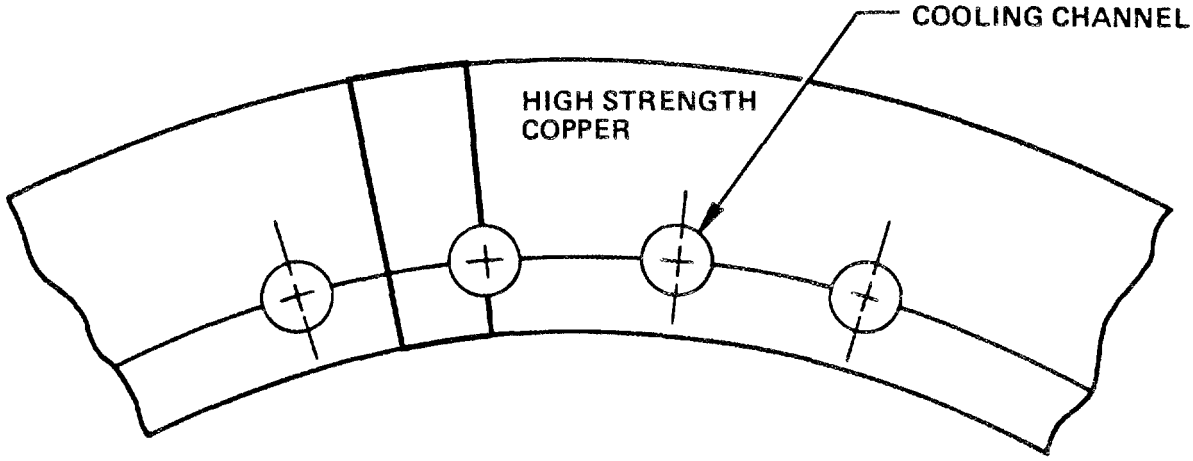

Figure 152. A Partial Cross Section View of a Proposed Collector Cooling Channel Geometry with the Channels 0.100" Closer to the Beam. Also the Finite Element Map Location is Indicated.

ORNL – DWG-83-2116

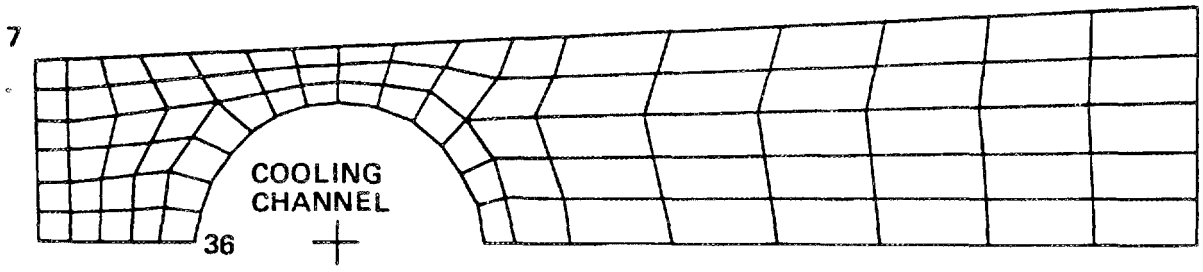

Figure 153. Finite Element Map Used for Calculating Temperature - Time Relationship for the Proposed Cooling Channel Geometry

ORNL – DWG-83-2117

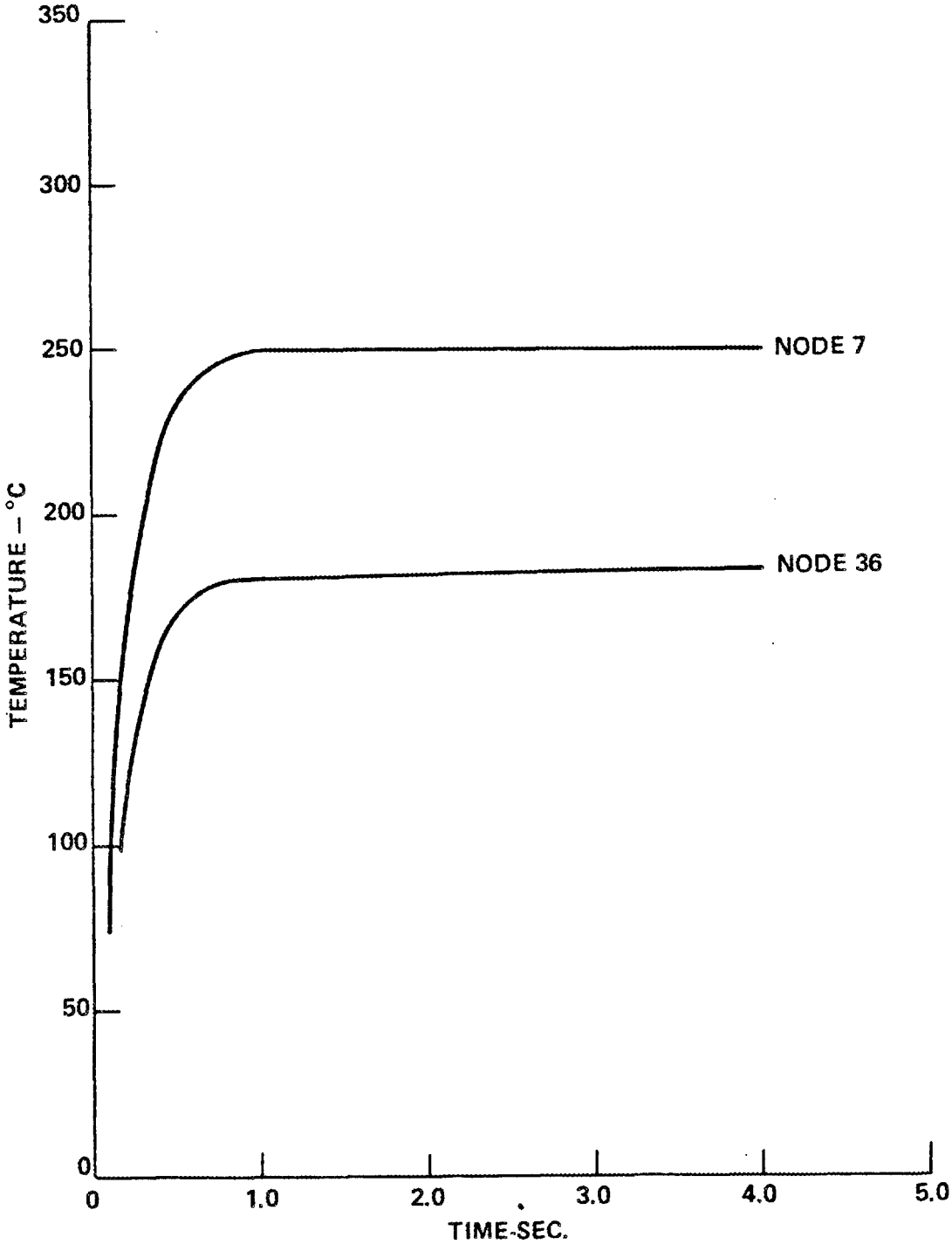

Figure 154. Transient Temperature for the Two Critical Nodes for the Proposed Collector Cooling Channel Geometry

in Table 18 indicate the superiority of dispersion hardened copper and an apparent problem with AMZIRC.

With OFCH copper, according to a single test run at ORNL, the addition of gold plating strengthens the copper well beyond the strength of the parent material, as shown in Table 18. However, the alloys and the dispersion-hardened copper would probably not profit from gold plating to the same degree, due to their own inherent strengthening elements which are already present.

Table 18

Results of Mechanical Fatigue Test of High Strength Copper Alloys[39]

Material[(3)]	% Strain	Cycles to Failure	Comments
OFHC	0.3	17,000	
OFHC	0.3	170,000 [(1)]	Gold Plated
AMZIRC	0.3	9,000 [(2)]	Aborted
MZC	0.3	214,000	
AL-15	0.3	800,000 No failure	Test Stopped
AL-15	0.4	400,000	100,000 psi[(4)]
AL-15	0.6	17,000	

(1) Only one sample plated with 300Å of gold plating by sputtering, then fired in vacuum at 1000°C before tests were started.

(2) This material softened during test and excessive elongation caused the samples to exceed the range of the fatigue machine. Test aborted after 9000 cycles.

(3) All samples subjected to 2 hours at 880°C and then 2 minutes at 915°C under vacuum. All data were taken at 300°C under vacuum strain rate, one cycle per second.

(4) Stress level peak-to-peak, fired at 1025°C in vacuum.

Table 19 summarizes the results of mechanical fatigue tests run at Oak Ridge National Laboratory on brazed samples using the candidate materials brazed with two different alloys.

10. Thermal Fatigue Diode Life Test Results

To adequately test candidate materials for improved collector fatigue life, it is imperative that the material be stressed in the same manner and in the same environment as the actual gyrotron collector. This requirement implies thermally induced stresses in a water-cooled sample material with the same coolant velocity, the same saturation pressure and the same power density as expected in the gyrotron. The test also must be performed under vacuum and, ideally, the power density should be provided by energetic electrons, again, simulating actual tube operation. A planar diode was chosen as the best geometry to fulfill these requirements.

11. Diode Description

The advantage of a planar diode as a test vehicle is the low total power required for a given power density, making this geometry more attractive than a conventional cylindrical diode. The availability of a production electron gun which could be easily modified to produce an electron beam large enough to bridge several water channels and maintain a uniform power density across its area is another economic advantage. The diode is comprised of the electron gun, the anode and the cooling system.

12. Electron Gun

The electron gun must be able to provide a uniform density electron beam with sufficient diameter to bridge at least three coolant channels, and be capable of producing a power density of 1 kW/cm^2. A standard production gun was modified by changing a few dimensions to produce a more uniform density over an area of 0.700 inch in diameter.

TABLE 19 RESULTS OF BRAZE JOINT TEST AS REPORTED BY ORNL

MATERIAL	BRAZE MATERIAL	BRAZE TEMP.	CYCLES TO FAILURE	COMMENTS
AL-15	40Au/60Cu	1010°C	200,000	FAILED IN COPPER
AMZIRC	40Au/60Cu	1010°C	2,000	FAILED IN BRAZE JOINT
AMZIRC	27Cu/68Ag/5Pd	825°C	2,000	FAILED IN BRAZE JOINT
AMZIRC	40Au/60Cu	1010°C	90,000	FAILED IN COPPER
MZC	40Au/60Cu	1010°C	100,000	FAILED IN COPPER
MZC	27Cu/68Ag/5Pd	825°C	120,000	FAILED IN COPPER

ALL DATA TAKEN AT 0.4% STRAIN
AL-15 HYDROGEN BRAZED, ALL OTHERS VACUUM BRAZED

The electron trajectories were calculated using an existing computer code, and the plotted results are shown in Figure 155. Successive calculations were made while altering the dimensions of the focus electrode, gun anode and the cathode radius to optimize the electron density across the beam. The density is inversely proportional to the spacing of the electron trajectories. It was necessary to change the cathode radius, make a new gun anode, and slightly alter the focus electrode to obtain the desired results shown in Figure 156. The electron density is uniform to within $\pm 20\%$ over a beam diameter of 1.78 cm, which will bridge three cooling channels with a uniform power density.

Since the current density is uniform to within $\pm 20\%$ over a diameter of 0.70 inch or 1.78 cm, and the desired power density is 1.0 kW/cm^2, the area is

$$A = \frac{\pi D^2}{4} = \frac{\pi}{4} (1.78)^2 = 2.48 \text{ cm}^2 \quad , \tag{60}$$

thus, the power required is

$$P = IE = 2.48 \text{ kw} \ . \tag{61}$$

Since the measured perveance is 1.63×10^{-6},

$$\frac{I}{E^{3/2}} = 1.63 \times 10^{-6} \quad , \tag{62}$$

combining Equations 61 and 62,

$$E = 4.71 \text{ kV} \tag{63}$$

the current will be

$$I = \frac{2.48}{4.71} = 0.527 \text{ A} \quad . \tag{64}$$

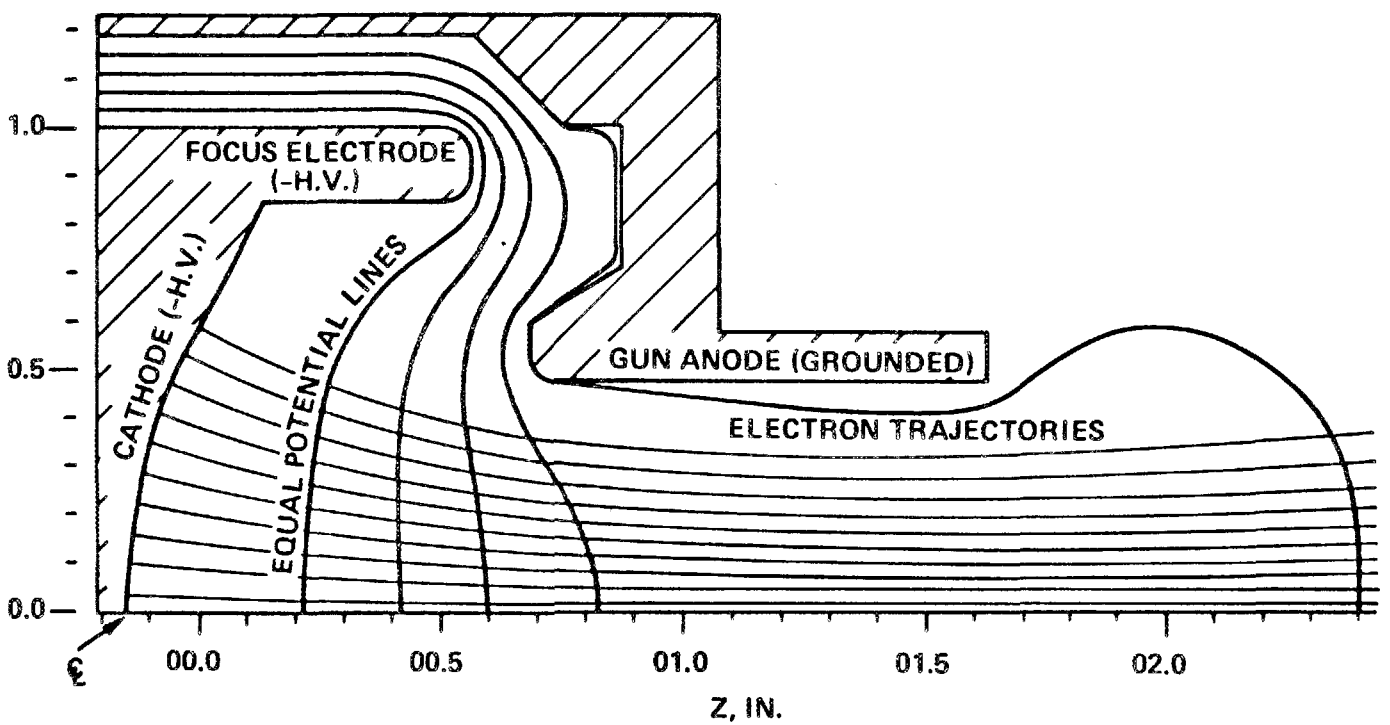

Figure 155. Electron Trajectories from a Modified Production Gun

ORNL DWG 83-2163

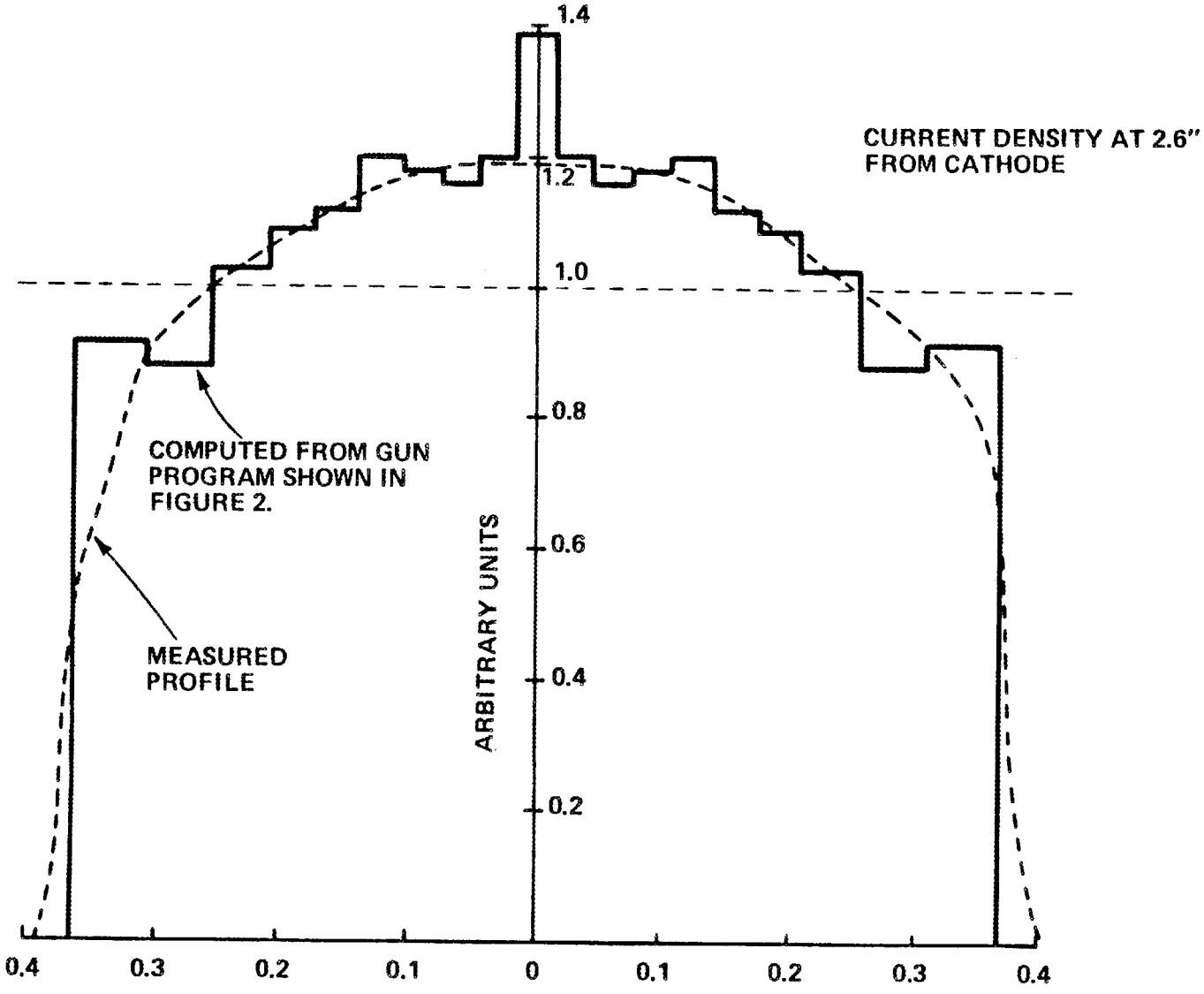

Figure 156. Measured and Calculated Electron Density as a Function of Beam Radius

The peak power in the center of the beam will be 20% higher than the average, or 1.2 kW/cm^2. This will be the level used during the fatigue tests.

The electron density profile, shown in Figure 156, was measured with a Faraday cup which can be moved in known increments in two directions. The configuration is shown in Figure 157. The reason for the split collector is to more easily detect the minimum electron density when measuring production guns. A typical production gun, with beam density profiles, is shown in Figure 158. The change in electron density across the beam is plotted in Figure 159 for the standard design and a modified version. A slight modification was made to obtain the final beam profile taken at the location of the diode anode as shown in Figure 156. The cathode current versus heater power curve, as shown in Figure 160, was measured to determine the sensitivity of the cathode current to changes in heater voltage. The operating point selected is 6.0 volts at 16.0 amps.

13. Anode Description

The diode anode has the same coolant channel geometry as the gyrotron collector, except the channels have been moved closer to the source of heat. In the current collector design, the distance from the edge of the channels to the front surface is 0.200 inch and one sample with this geometry was tested. The distance was reduced to 0.100 inch on another fatigue test sample. According to calculations, this change should have little effect on fatigue life, but produce a 70°C reduction in front surface temperature, a significant improvement with respect to collector melting. The diode anode has been designed to simulate the collector as nearly as possible. The anode is restrained around the edges by a stainless steel flange, as shown in Figure 161, backed by a relatively rigid stainless steel plate to simulate the thick copper collector. The constraints imposed on the diode anode are somewhat more severe than in the actual collector, thus, the fatigue life in the diode tests will be conservative relative to the gyrotron. A sectional view of the diode is shown in Figure 162.

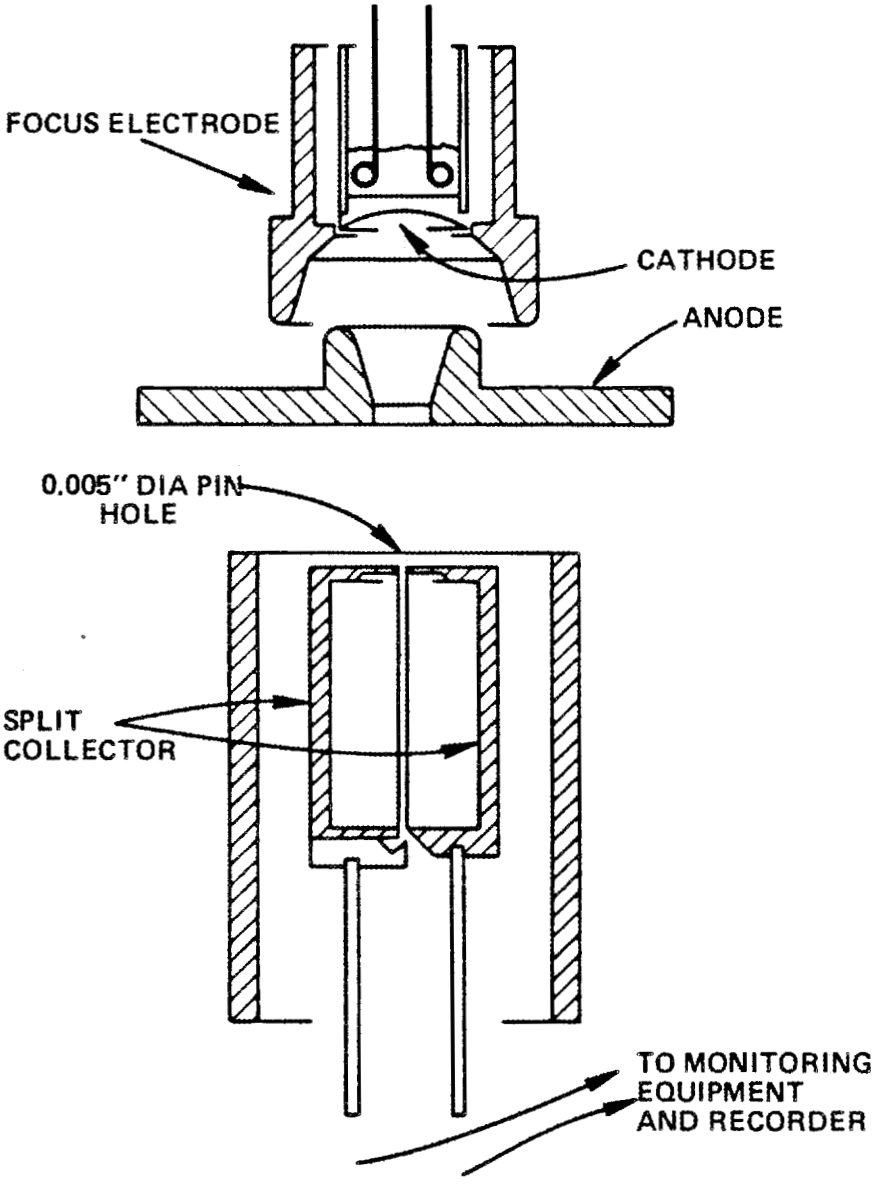

Figure 157. Internal Configuration of Beam Analyzer

ORNL DWG 83-2165

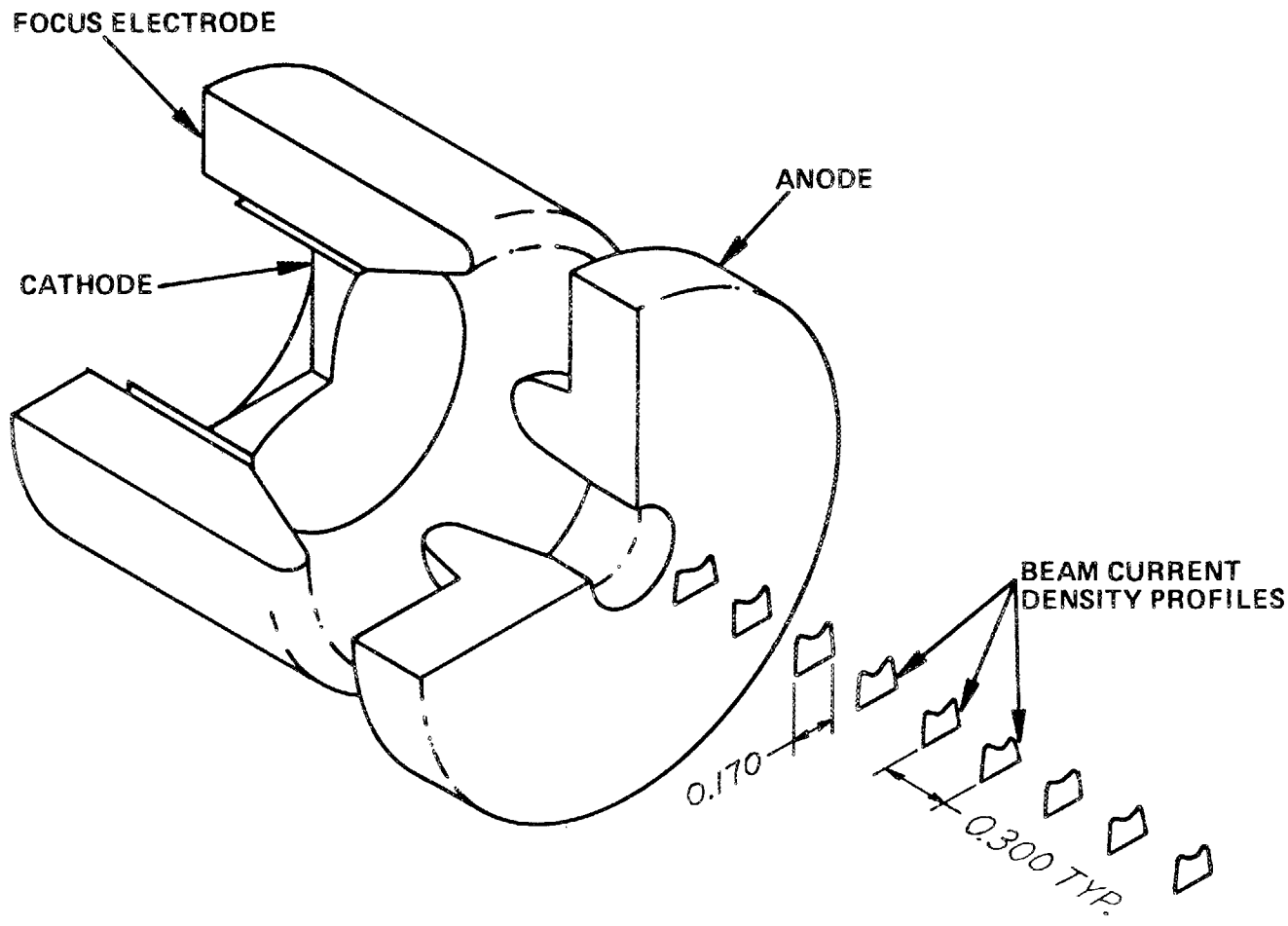

Figure 158. A Typical Electron Gun Showing the Hollow Beam and Density Profile Variations as a Function of Distance from the Cathode

ORNL DWG 83-2166

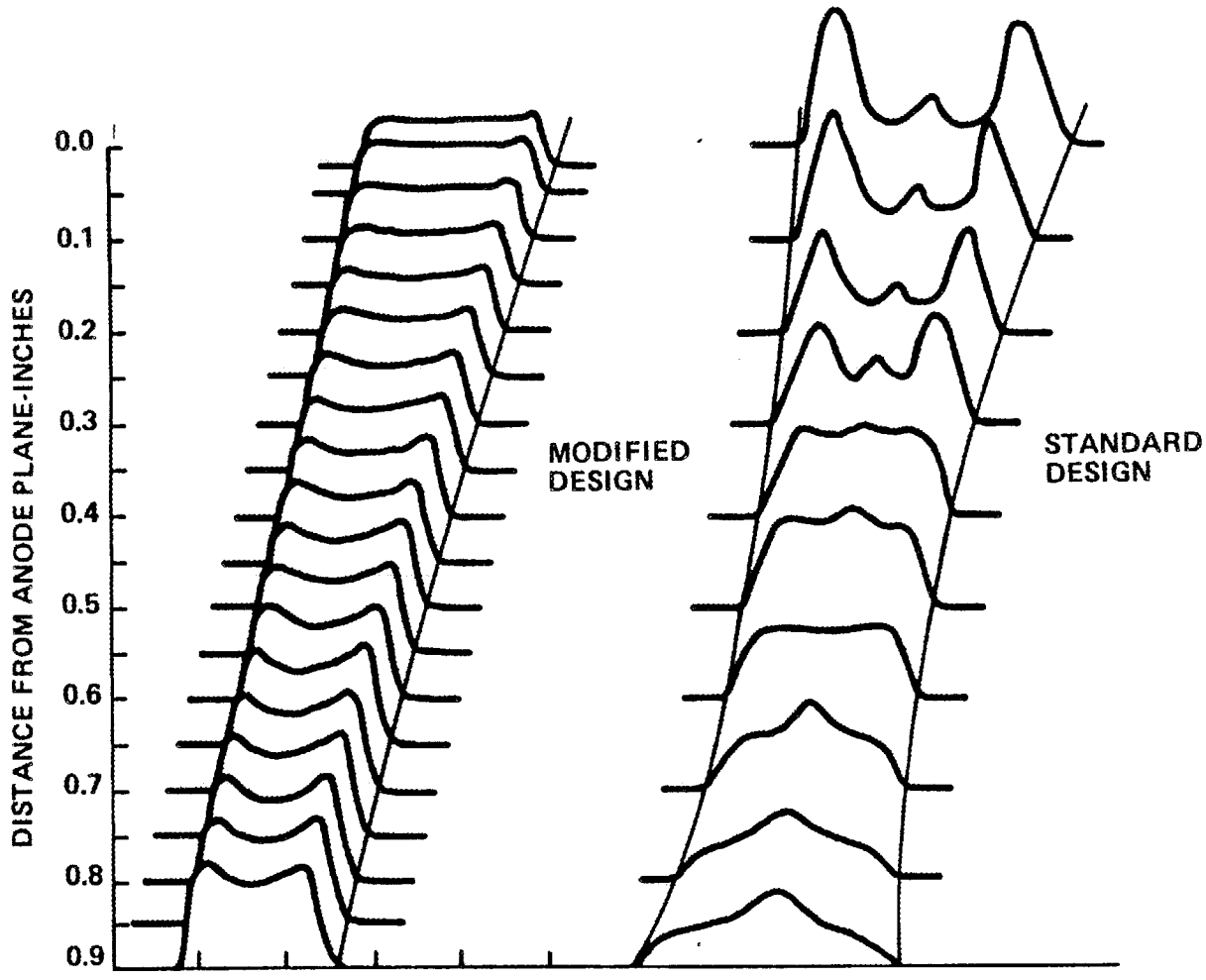

Figure 159. Comparison of Beam Current Density Profiles for the Standard and Modified Guns

ORNL DWG 83-2167

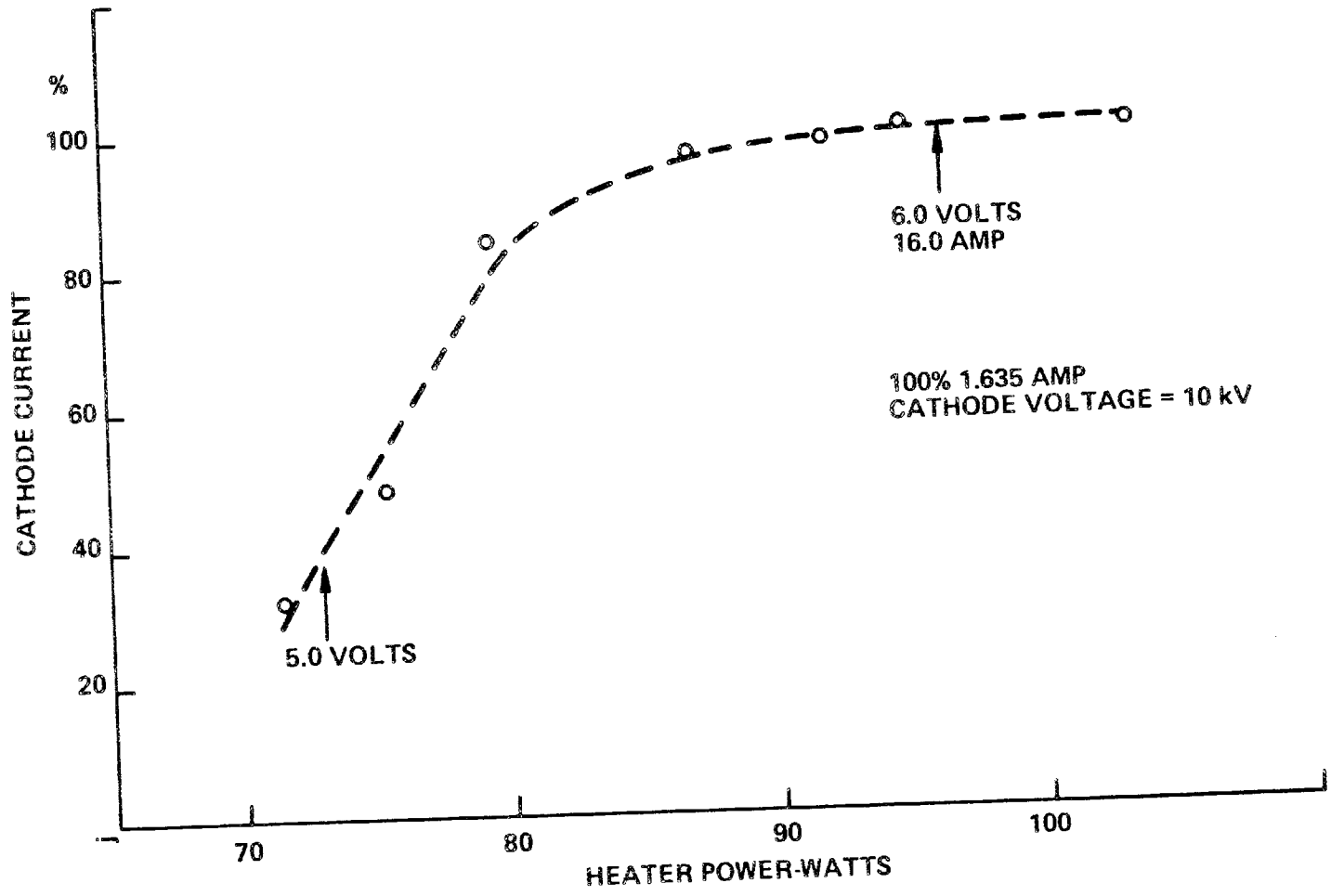

Figure 160. Maximum Space Charge Limited Emission Curve

ORNL DWG 83-2168

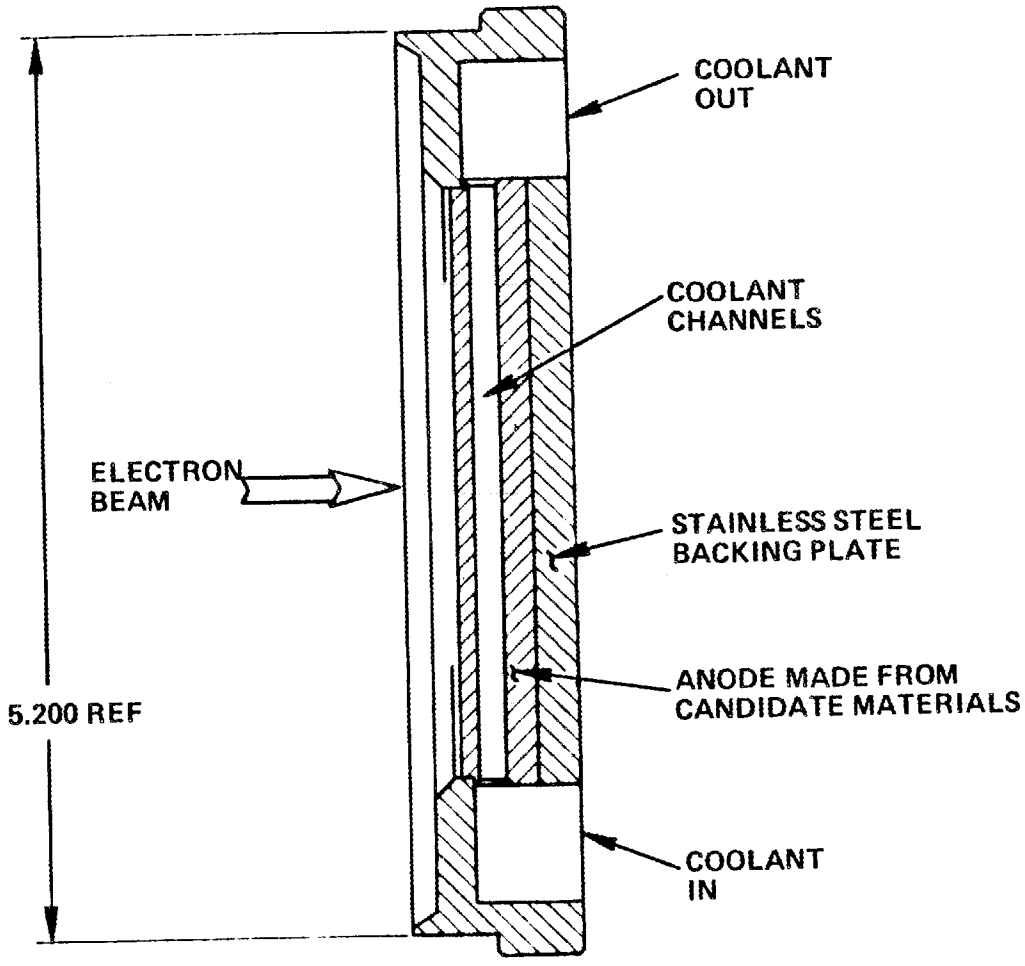

Figure 161. Anode Assembly Showing Coolant Channels

ORNL DWG 83-2169

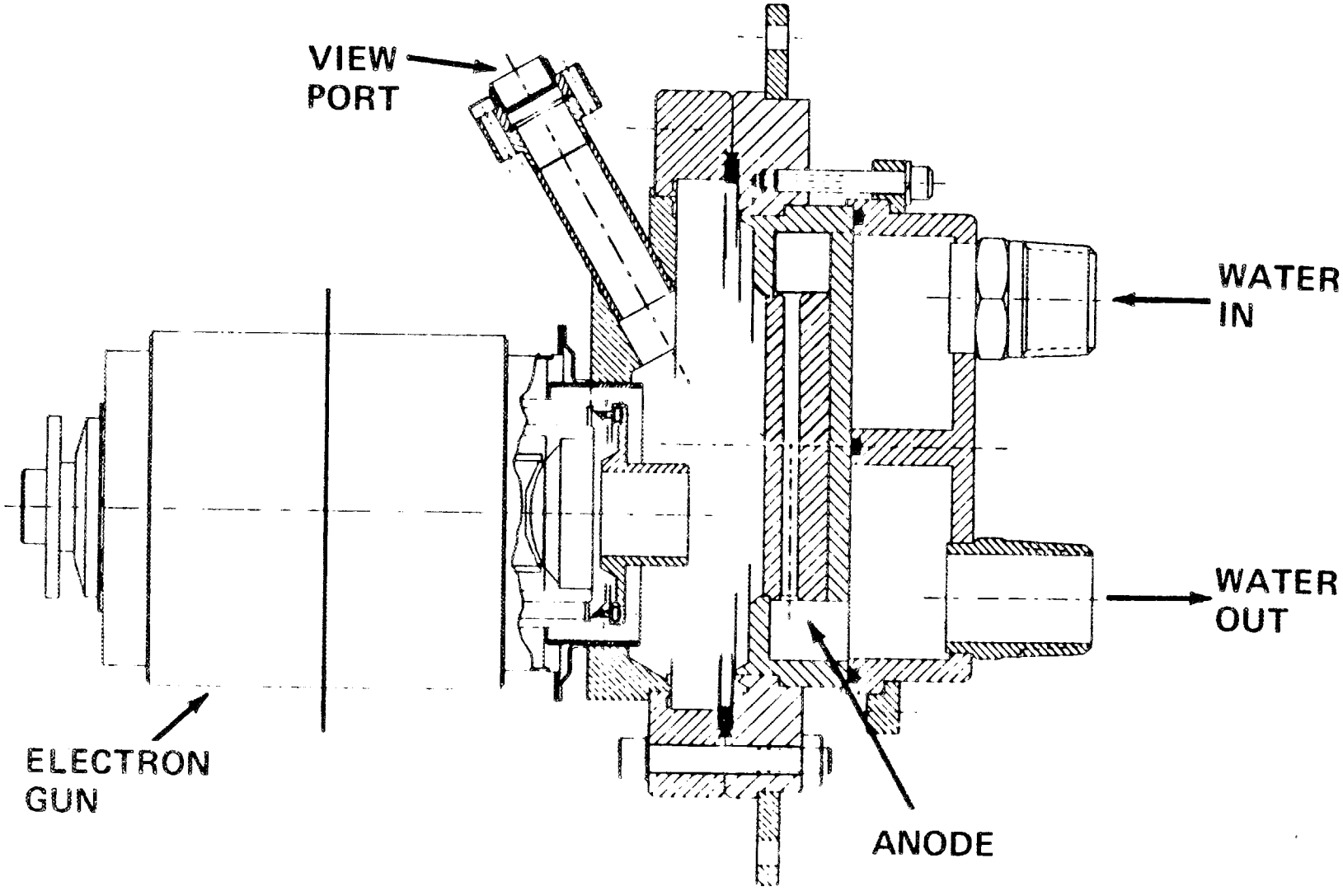

Figure 162. Sectional View of the Complete Diode Assembly

14. Cooling System

The cooling system was designed to maintain the coolant velocity at 27 ft/sec, which was the same value as in the collector, and at the same time, maintain the pressure in the center of the anode at 100 psig, which was also the same value as in the collector. The total coolant flow required to produce the above velocity was 40 GPM. In order to maintain both the velocity and pressure constant with changing input pressure, it was necessary to have a flow and pressure regulator as indciated in Figure 163. There are two motor-operated valves, which are interlocked with the pressure sensors such that when a water leak occurs, indicating a failure, the inlet and return water are blocked and the system drained. The inlet and outlet water temperature were monitored to correlate the temperature differential with calculations.

A series regulator was added to an existing 20 kV, 4 A power supply to maintain the output voltage within $\pm 1\%$ with a $\pm 10\%$ change in line voltage and with a 0 - 0.5 A load change.

The first diode fatigue test had an OFHC copper anode with a wall thickness of 0.200 inch between the heater surface and the water channel, similar to that used in the CW gyrotrons. Figure 164 shows the surface after 38,000 cycles of 2.5 sec on 50% duty and a power density of 1.0 kW/cm^2. The white dots are foreign material embedded in the soft copper. They glow white hot when the beam is on. One of the hot spots can be seen at higher magnification in Figure 165, and it is apparent that a fatigue crack has started under the hot spot.

The diode was reassembled with a new area of the anode exposed to the electron beam. An additional 38,000 cycles were run at a higher power density of 1.6 kW/cm^2. The results are shown in Figure 166. Notice the large grain structure and local melting near the center. Figure 167 is the same view at higher magnification. Notice the fatigue crack which has started near the center. Figure 168 shows another hot spot with a fatigue crack which has started directly under the spot.

ORNL DWG 83-2170

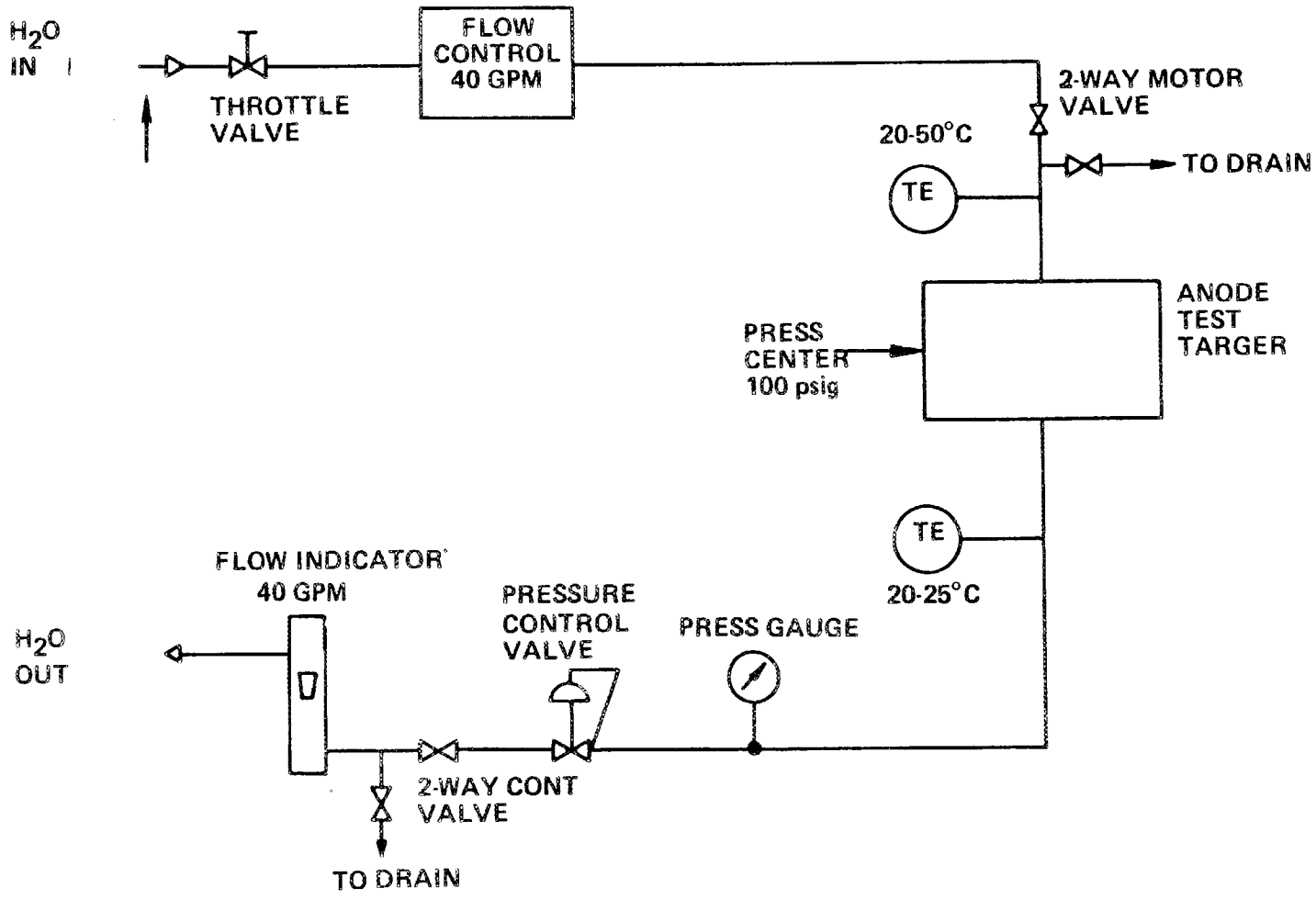

Figure 163. Schematic of the Cooling System Controls

ORNL – PHOTO – 0083-83

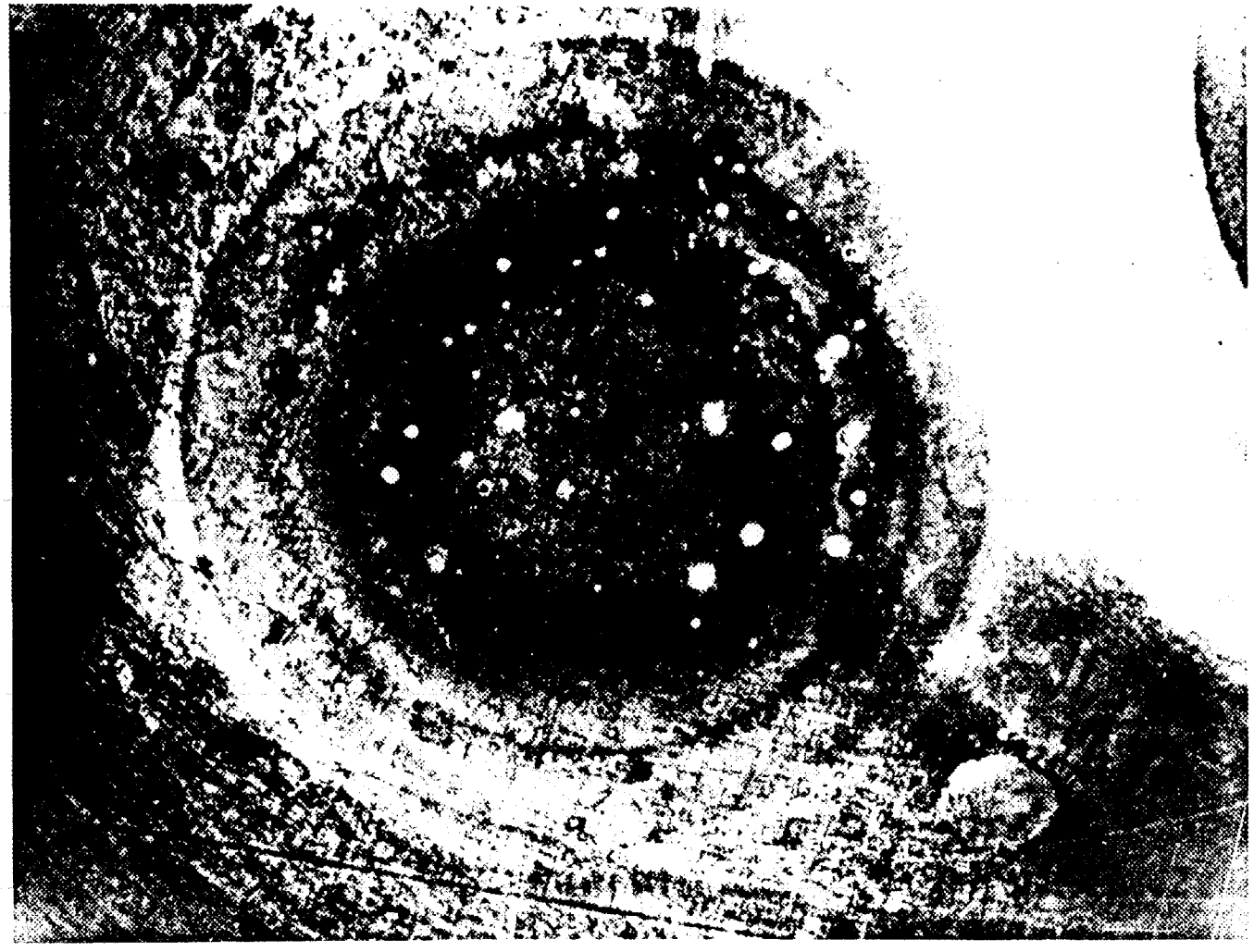

FIGURE 164. OFHC COPPER AFTER 38,000 CYCLES, 3X, POWER DENSITY = 1.0 kW/cm^2

ORNL – PHOTO – 0084-83

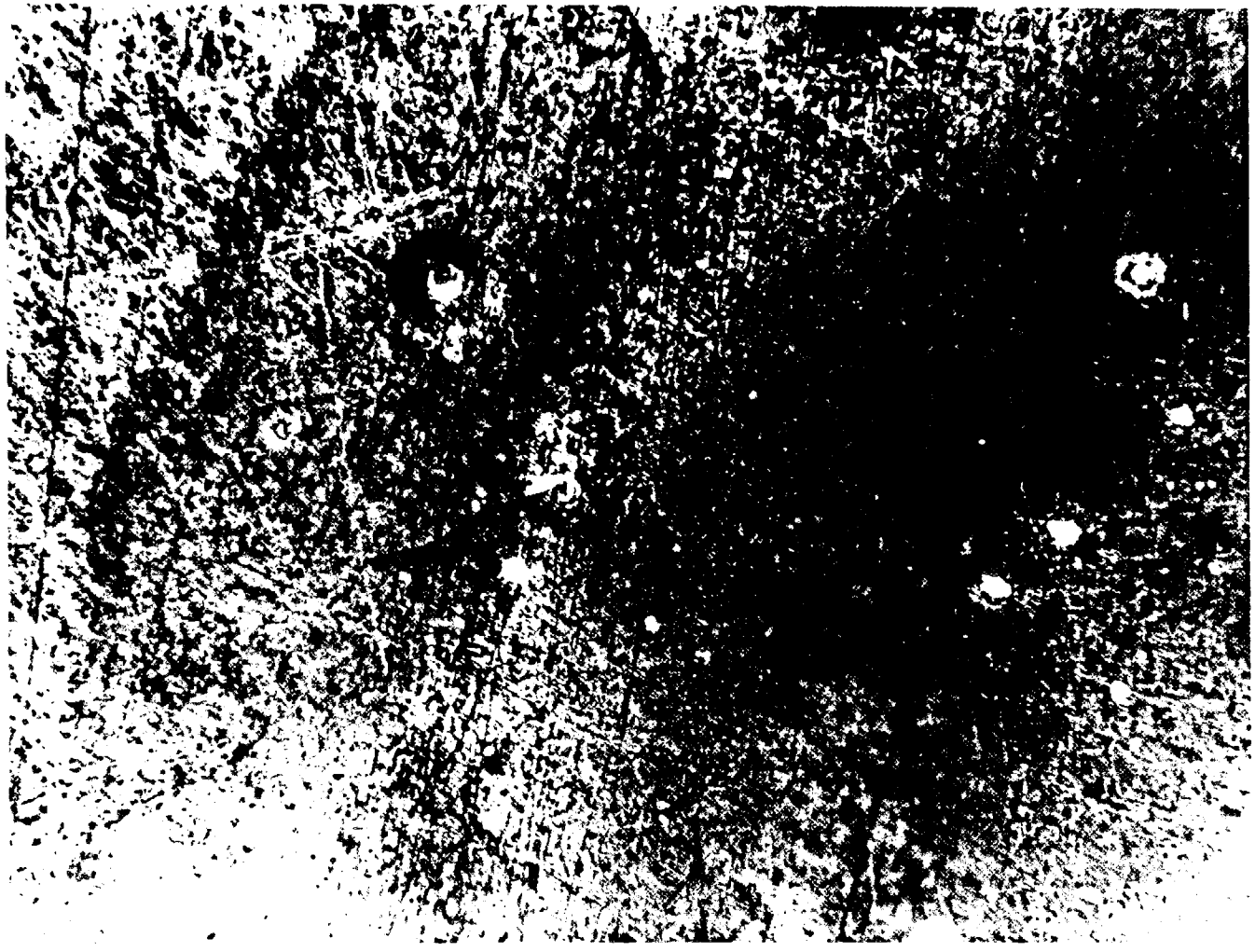

FIGURE 165. OFHC COPPER AFTER 38,000 CYCLES, 12X, POWER DENSITY = 1.0 kW/cm^2

ORNL – PHOTO – 0085-83

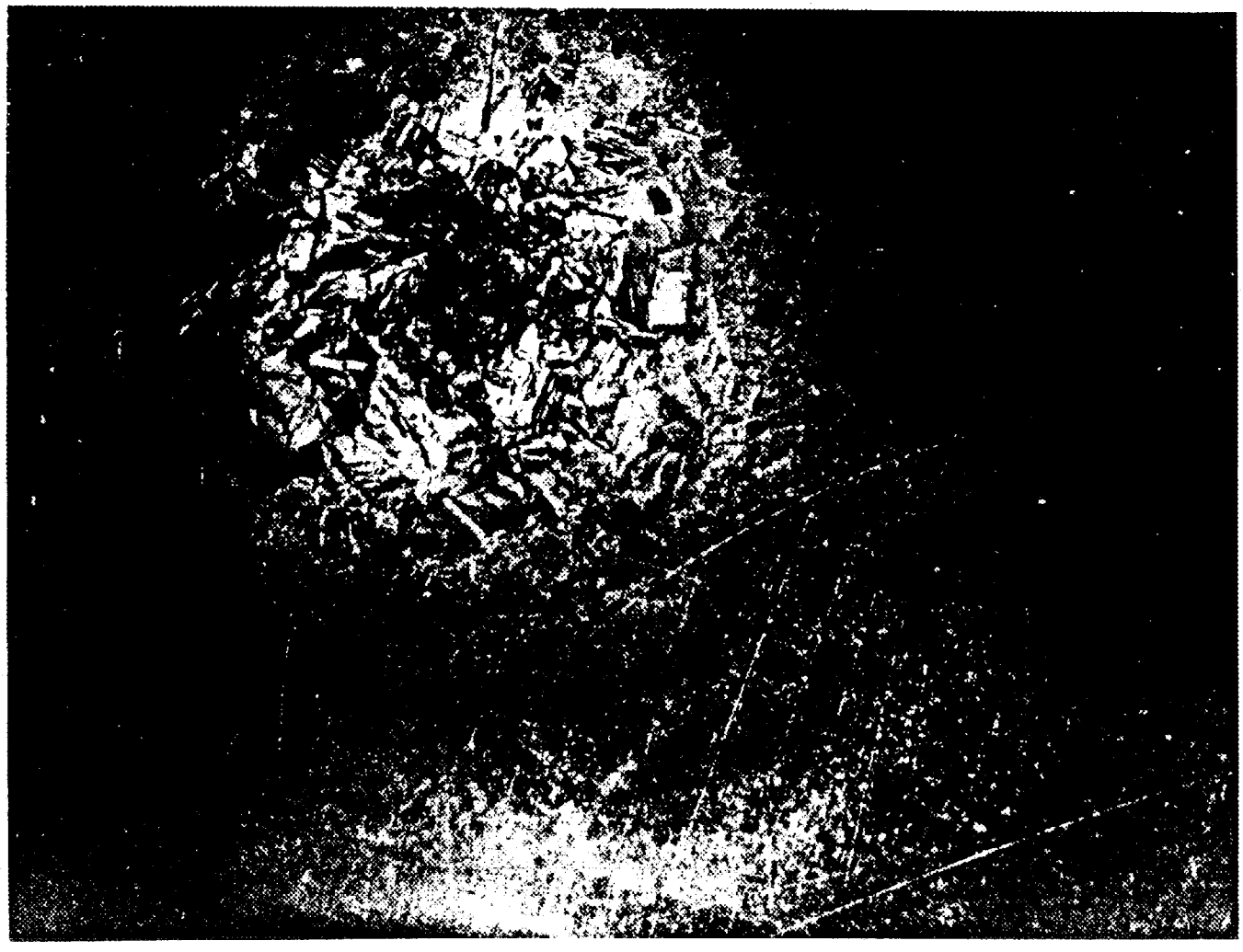

FIGURE 166. OFHC, 0.200" WALL, 38,000 CYCLES AT 1.6 kW/cm^2, 3X

ORNL – PHOTO – 0086-83

FIGURE 167. OFHC, 0.200" WALL, 38,000 CYCLES AT 1.6 kW/cm^2, 18X

ORNL – PHOTO – 0087-83

FIGURE 168. OFHC, 0.200" WALL, 38,000 CYCLES AT 1.6 kW/cm^2, 25X

Again, the diode was reassembled with a new area of the anode exposed to the beam and 38,000 cycles were run at a power density of 2.0 kW/cm^2. The results are shown in Figure 169. Figure 170 is the same view at higher magnification. Notice the numerous cracks which have formed and the rather severe melting in the center. Figure 171 is a view off-center showing fatigue cracks forming under a hot spot.

Next, the diode was reassembled with the beam in the same location and an additional 32,000 cycles were accumulated making a total of 70,000 cycles at 2.0 kW/cm^2 power density without a fatigue failure.

The anode was removed, sectioned through the center of the three test areas, polished and photographed at various magnifications. The 1.0 kW/cm^2 area is shown in Figure 172 with the heated surface at the top. Notice the very large grain size, but very little distortion of the heated surface and no fatigue cracks visible. The area tested at 1.6 kW/cm^2 is shown in Figure 173. Again the grain size is quite large, but no cracks are seen; however, the heated surface is irregular due to local melting. Figure 174 shows the area bombarded at 2.0 kW/cm^2. The grain size at the surface is small due to complete melting of the surface copper. Toward the bottom of the picture, near the water cooling channels, the grain size is large due to high temperatures, but without melting.

It is apparent that fatigue cracks are forming, but before they can propagate to the cooling channels, the copper partially melts at the heated surface, sealing the cracks and eliminating them. It may be impractical to operate a gyrotron at these extreme power densities because vaporization and ionization of the copper may transport material through the gyrotron and create problems, for example, in the gun region.

Figures 175 and 176 are photographs of the anode taken through the view port with the beam on and off, respectively. The bright spots when the beam is on are caused by impurities embedded in the copper anode. The anode as seen through the viewport has a reddish color when the beam is off. This is the result of a reflection from the cathode, and not an indication of anode temperature.

ORNL – PHOTO – 0088-83

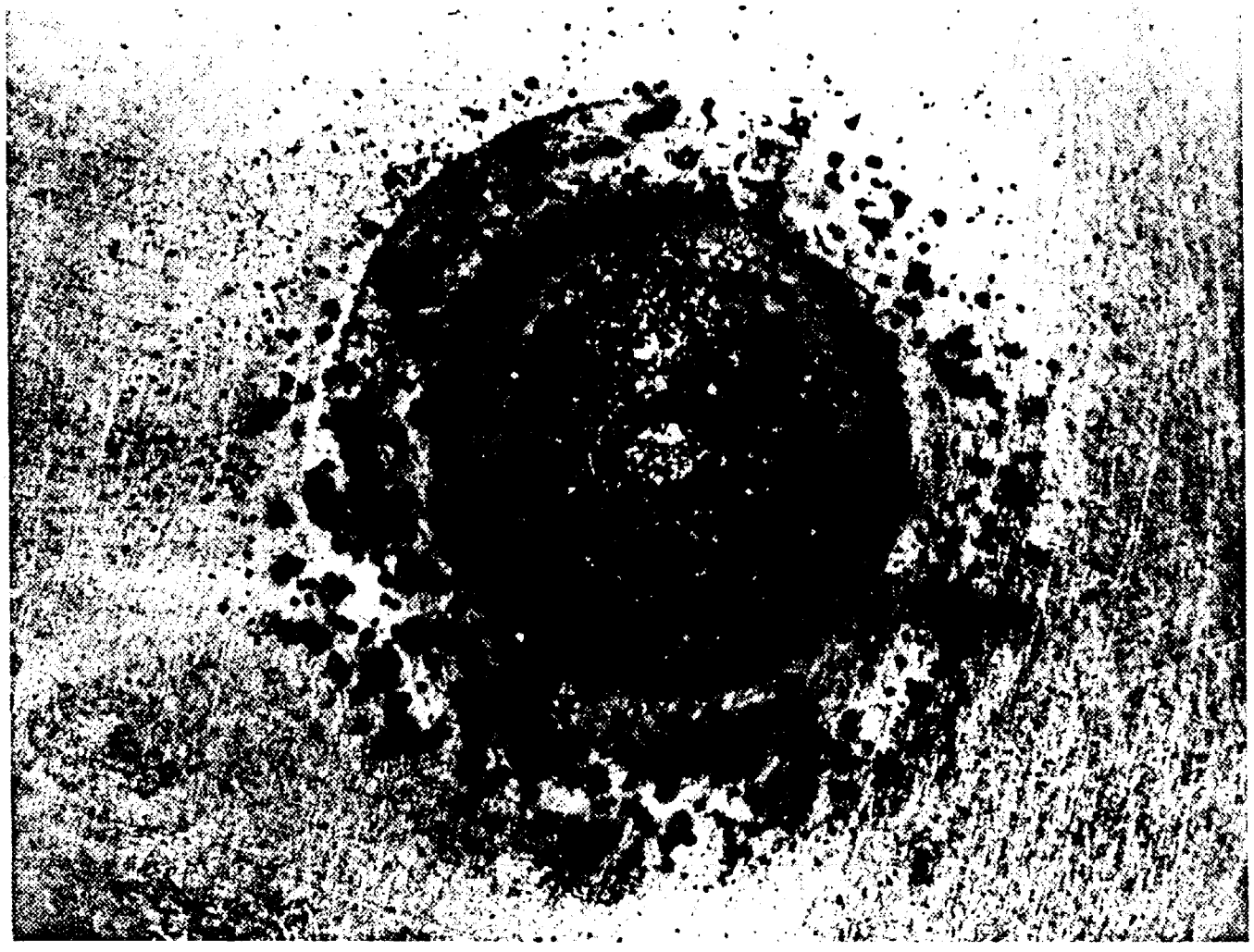

FIGURE 169. OFHC, 0.200" WALL, 38,000 CYCLES AT 2.0 kW/cm^2, 3X

ORNL – PHOTO – 0089-83

FIGURE 170. OFHC, 0.200" WALL, 38,000 CYCLES AT 2.0 kW/cm^2, 12X

ORNL – PHOTO – 0090-83

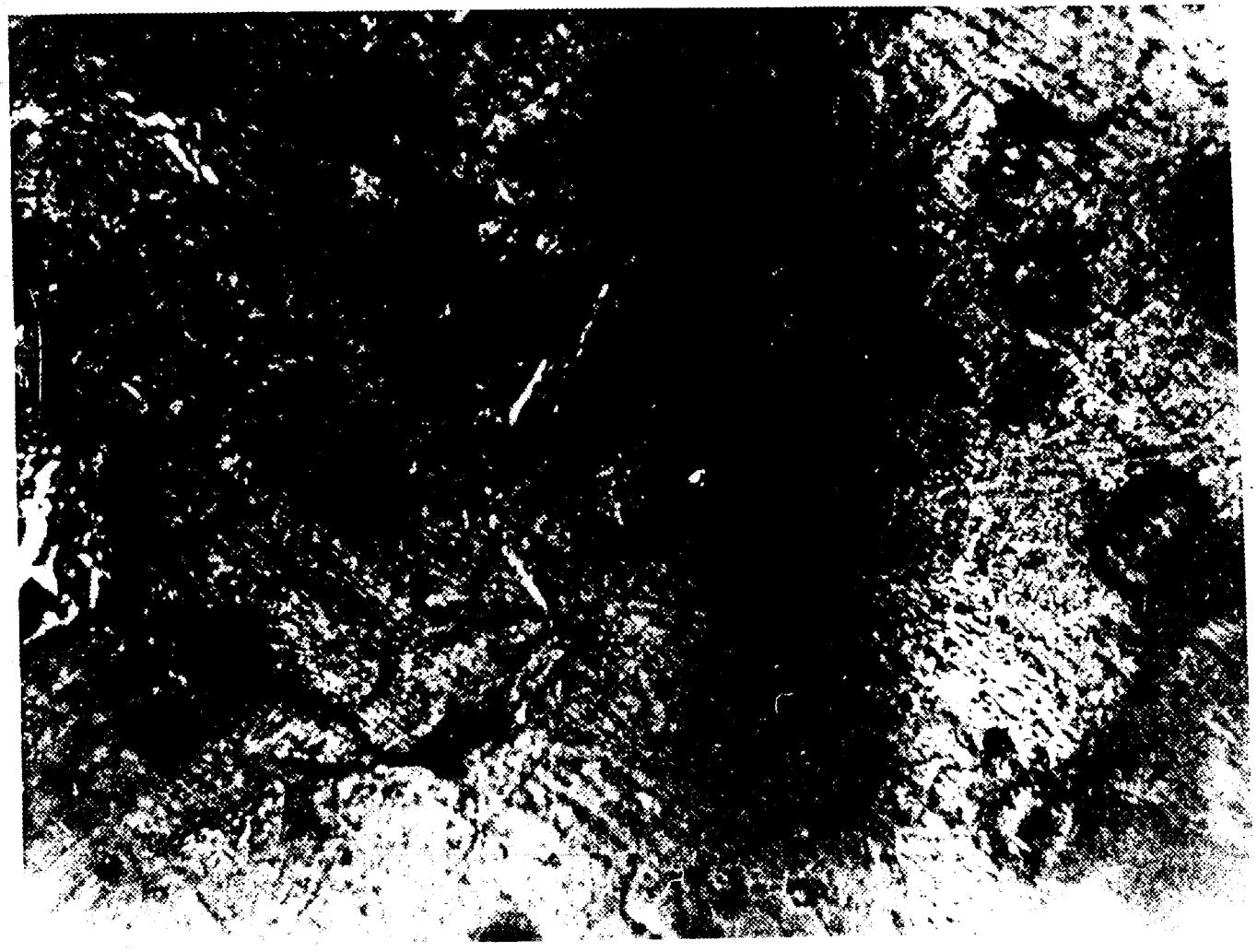

FIGURE 171. OFHC, 0.200" WALL, 38,000 CYCLES AT 2.0 kW/cm^2, 25X

ORNL – PHOTO – 0091-83

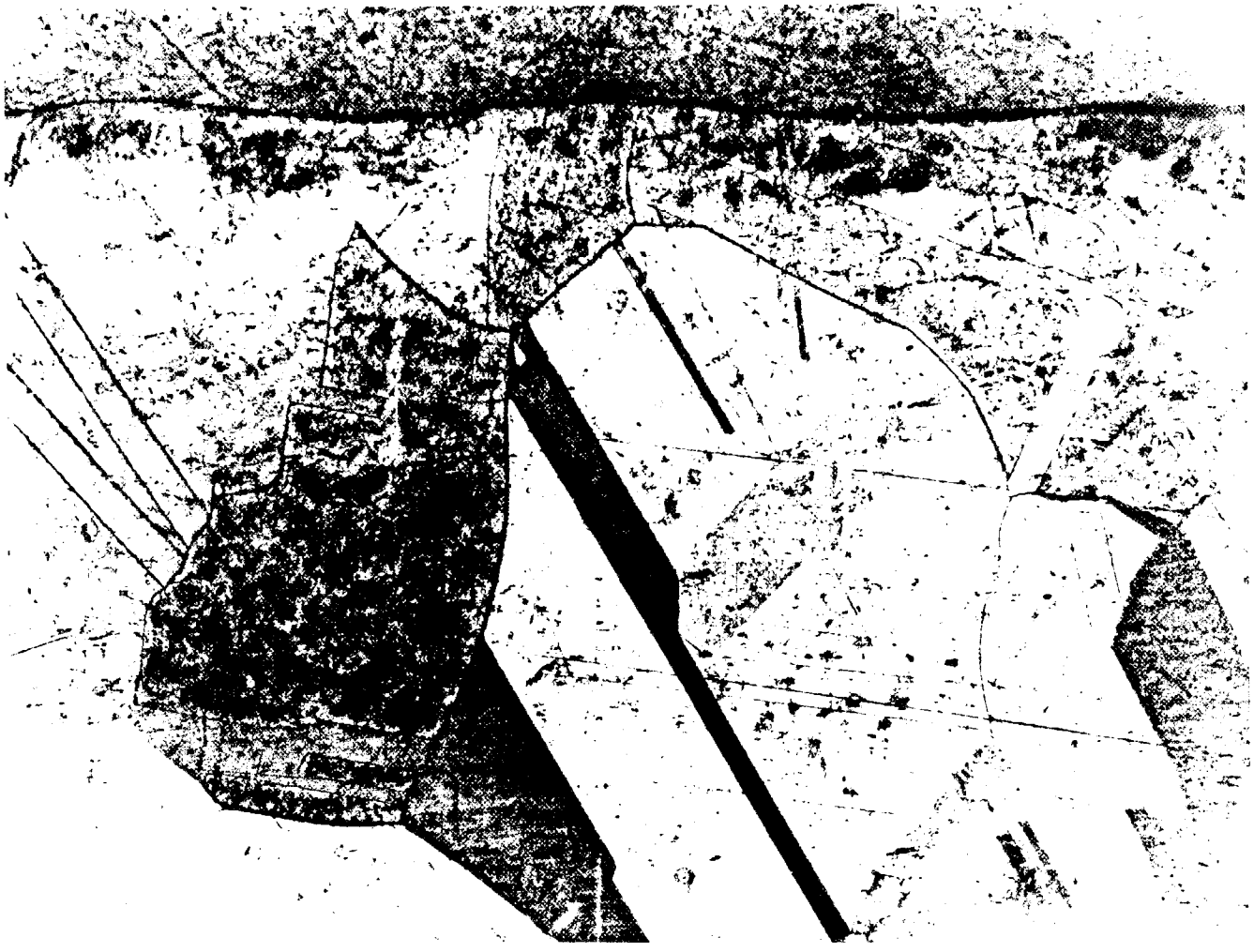

FIGURE 172. OFHC, 0.200" WALL, 1.0 kW/cm^2, 38,000 CYCLES, 50X

ORNL – PHOTO – 0092-83

FIGURE 173. OFHC, 0.200″ WALL, 1.6 kW/cm^2, 38,000 CYCLES, 50X

ORNL – PHOTO – 0093-83

FIGURE 174. OFHC, 0.200" WALL, 2.0 kW/cm^2, 70,000 CYCLES, VIEW OF BEAM CENTER, 50X

ORNL – PHOTO – 0094-83

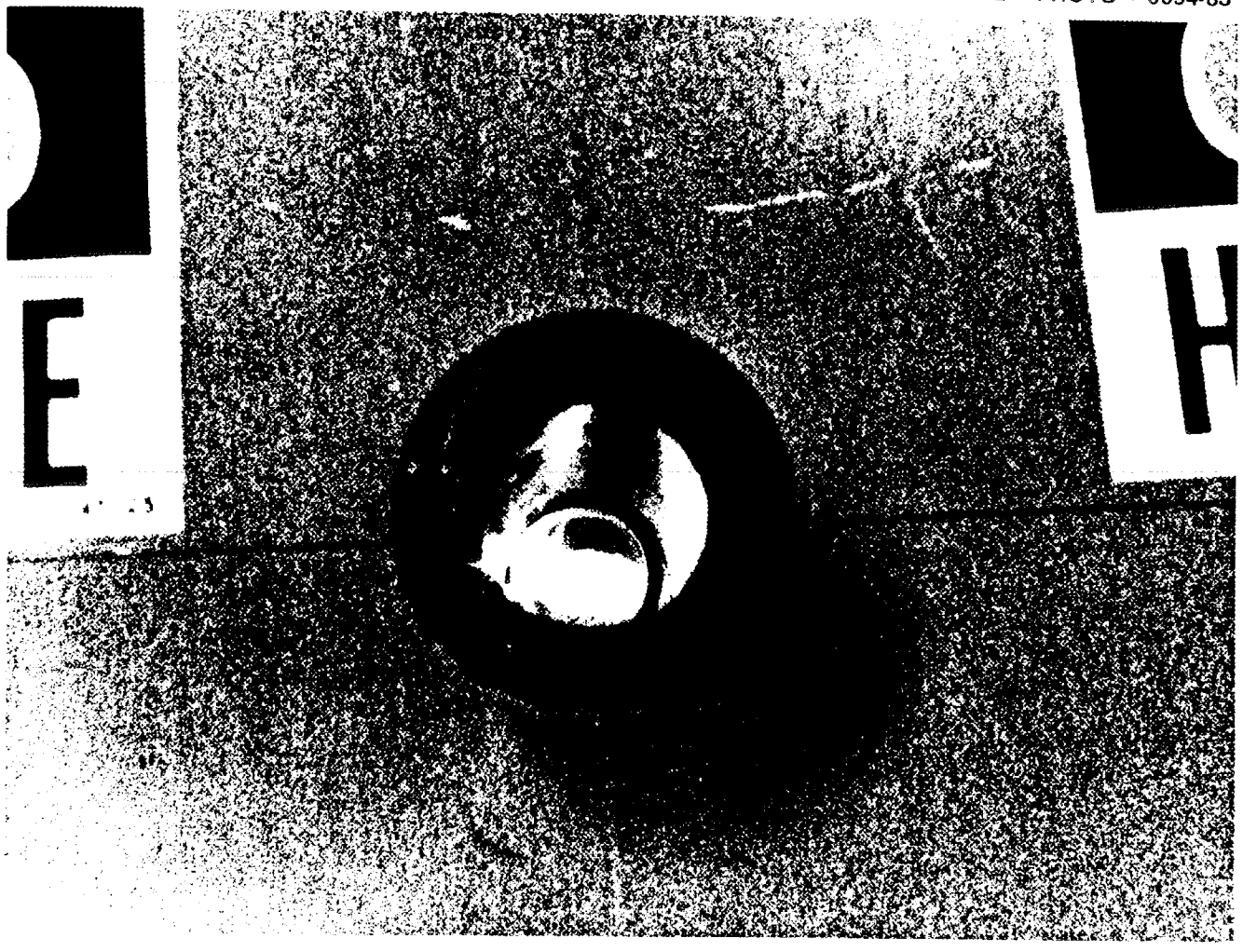

FIGURE 175. OFHC, 0.200" WALL, 1.6 kW/cm^2, BEAM ON

ORNL – PHOTO – 0095-83

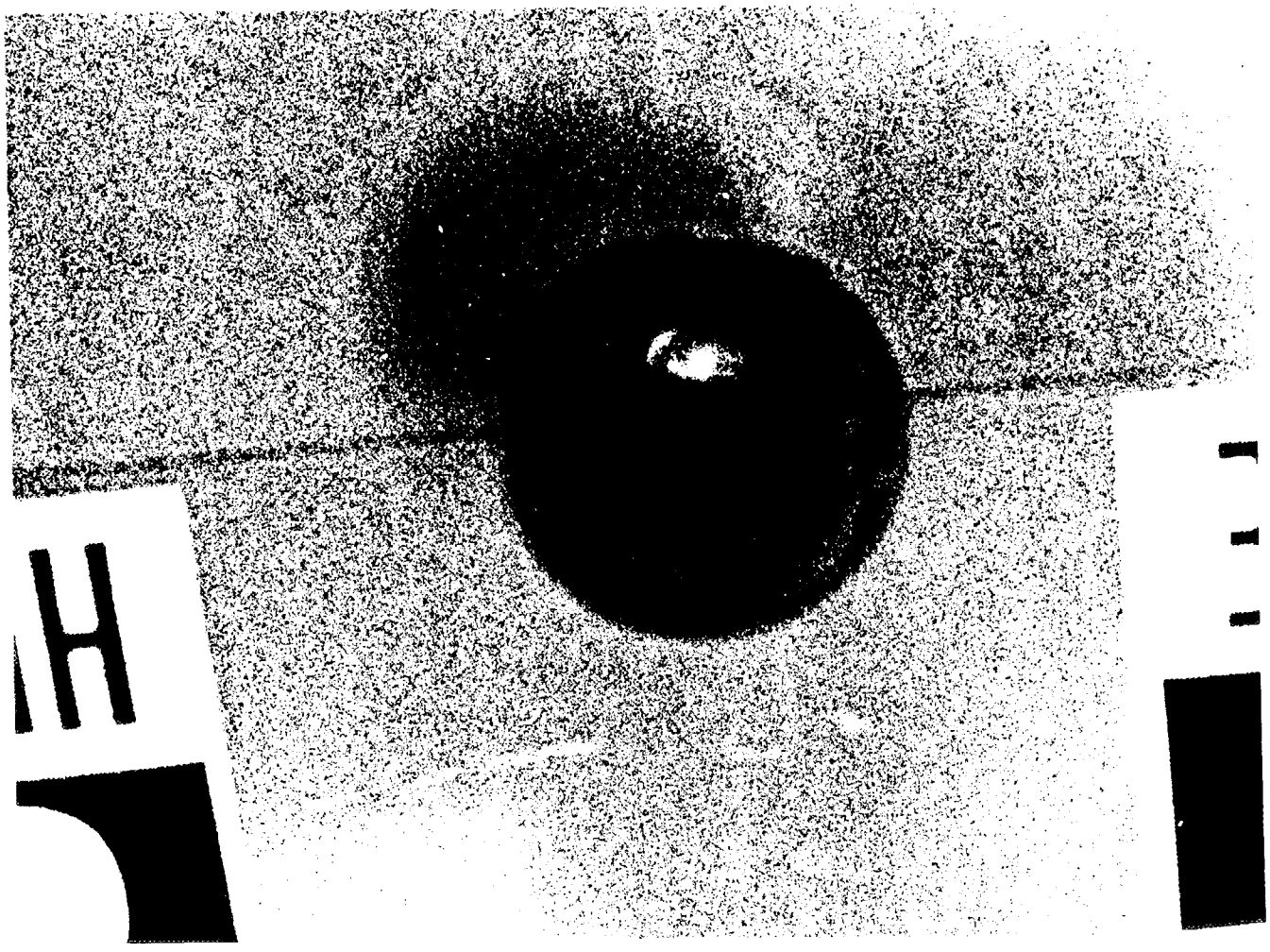

FIGURE 176. OFHC, 0.200" WALL, 1.6 kW/cm^2, BEAM OFF

Four thin wall (0.100 inch wall thickness) diodes were run at 50% duty cycle, 2.5 second pulse duration until thermal fatigue failure. The first diode anode was made of pure OFHC copper, typical of that used in gyrotron collectors. This material failed at 52,000 cycles. The second and third anodes were originally like the first, but were then sputter-plated with 500 Å of gold, then fired at 1090°C in a hydrogen braze furnace. This caused the gold to migrate into the immediate subsurface of the anode face. These anodes were cycled until failure at 61,000 and 73,000 cycles. This improvement over pure OFHC may be due to the gold's fluid properties during grain reformation. A fourth anode was prepared with 10 microns of gold sputtered onto the surface, then braze fired at 1090°C. This anode failed prematurely at 38,000 cycles. The gold layer had flaked off under electron bombardment, leaving behind a rough OFHC surface. Although the gold-plated sample had a longer fatigue lifetime than the plain OFHC samples, the tests done to date are not sufficient to draw firm conclusions.

An interesting result of this testing was observed by varying the wall thickness. In the diode experiment completed in June 1983, the thick-walled (0.200") OFHC anode was tested to 70,000 cycles without significant fatigue (the experiment was halted to allow disassembly and pre-failure inspection of the anode). Thin-walled (0.100") anodes were then tested to observe the tradeoffs between the improved cooling and decreased mechanical strength. Although only one directly comparable test was run at each thickness, it was apparent that the effects of the improved cooling did not sufficiently offset the decreased mechanical strength. This caused the thin-walled samples to fail well before the thick sample had shown significant fatigue.

Two other interesting phenomena were observed at high power densities: small grain formation and healing. Small grain formation occurs as a result of strain hardening due to repeated thermal expansion and contraction cycles. Crack healing occurs when localized copper temperatures are sufficiently high to cause annealing and molten flow of the copper into the cracks.

A thick-walled OFHC anode was then tested at 1.5 kW/cm^2 beam loading for 110,000 cycles without failure. The duty cycle was 5%; the cycle time five seconds. After disassembly, extensive surface cracking was observed, but none of the cracks had propagated to the water jacket.

The collector fatigue test diode is a nearly complete thermal model of the gyrotron collector. Although minor factors, such as rf heating, asymmetric heat distribution, and slight surface curvature are not considered. The effects of differential temperature expansion, boundary constraint stress and wall thickness were well modeled in these tests. The repeated ability of the OFHC diode model to survive over 100,000 thermal cycles enhances confidence in the ability of the OFHC to survive the specification requirement of 35,000 cycles in the gyrotron collector. The final and most applicable tests were on collector model anodes with 0.200" wall thickness (to water channel) and an average power density of 1.5 kW/cm^2.

These tests cannot make determinations beyond the fatigue lifetime to vacuum integrity failure. This would become a concern if the collector surface had prematurely roughened enough to cause excessive mode conversion and/or rf loss.

OFHC has been determined to be a sufficiently strong collector material for all forseeable operating conditions. This study confirmed the collector cooling geometry design and maximum incident power change that will ensure future tube life. The experimental data shown in Table 20 are sufficient to make certain general conclusions about the thermal behavior of OFHC gyrotron collectors.

Table 20
OFHC Diode Fatigue Results

Using
- 0.200" Wall Thickness
- 50% Duty Cycle, 12 PPM

Beam Power (Avg)	Test Length	Results
1.6 KW/cm^2	38,000	Slight Surface Melting No Failure Test Halted for Sectioning
1.6 KW/cm^2	70,000	Slight Surface Melting No Failure Test Halted for Sectioning
1.5 KW/cm^2	110,000	No Surface Melting Onset of Cracking No Failure Test Halted for Sectioning
1.5 KW/cm^2	102,000	No Surface Melting Onset of Cracking Test Halted Due to Power Supply Failure

E. WINDOW

A single-disc beryllia window was designed for the experimental pulsed oscillators. To ensure mechanical integrity, the window thickness was chosen as 1.5 λ_g or 0.117".

The computed VSWR for a 1.5λ-thick beryllia window is shown by the dashed curve in Figure 177. It was recognized that the limited bandwidth of the window may prove to be a problem by raising the Q of adjacent tube resonances. Work was done to broaden the bandwidth of the window using sophisticated techniques. The computed VSWR for a simulated improved window is shown by the solid curve in Figure 177.

Cold testing of 60 GHz single-disc beryllia windows was undertaken using two different techniques as shown in Figure 178. A conventional

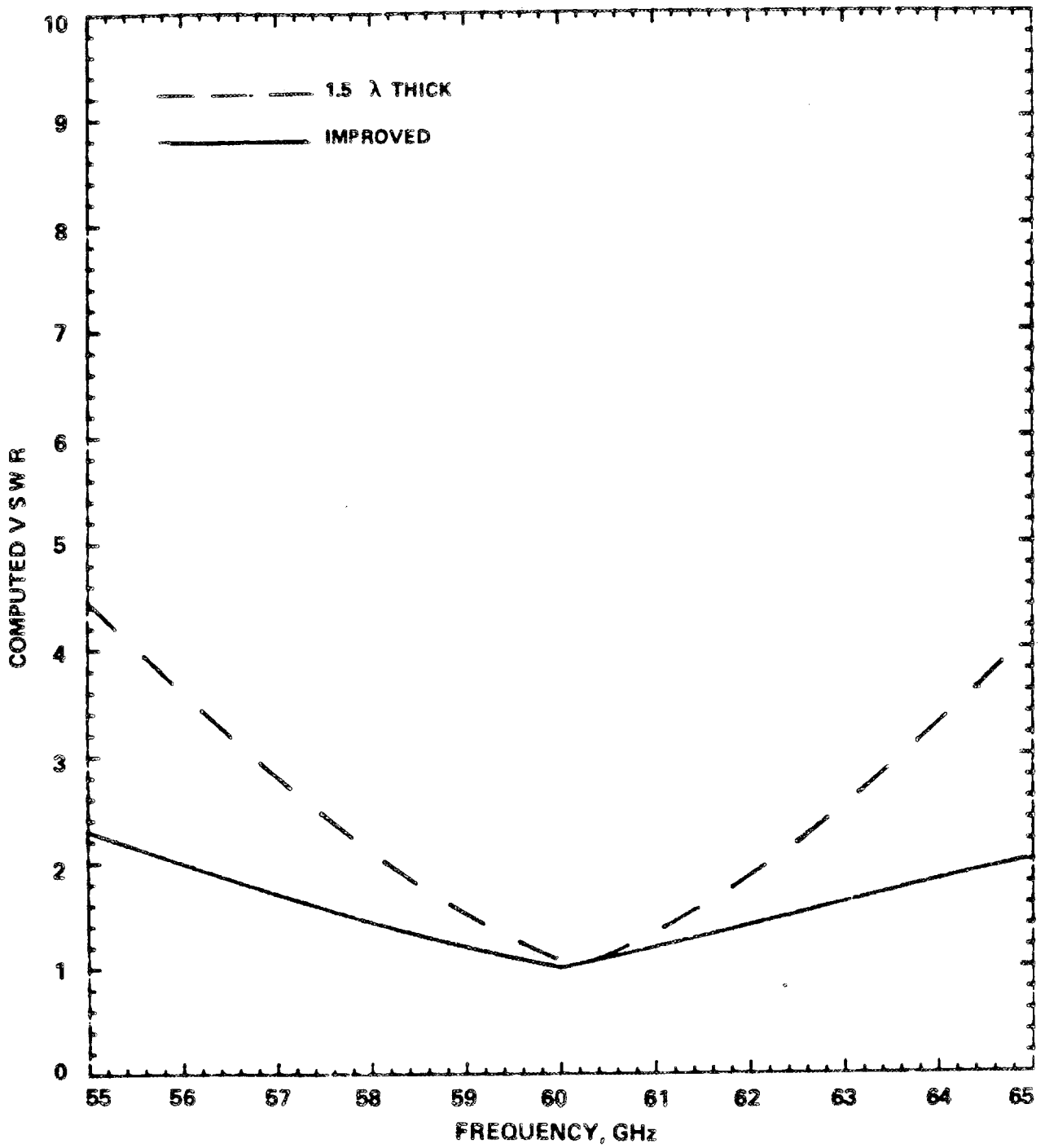

Figure 177. Computed VSWR For A Single Disc Beryllia Window

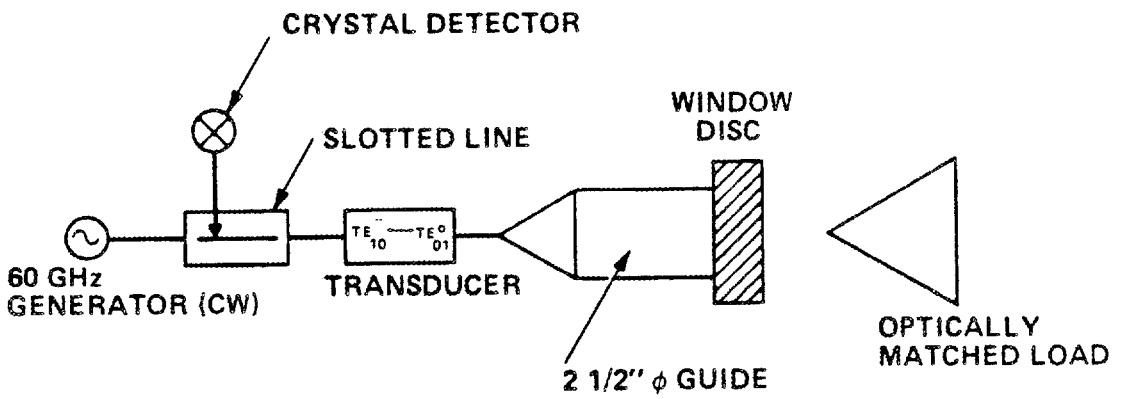

a. SLOTTED LINE TECHNIQUE

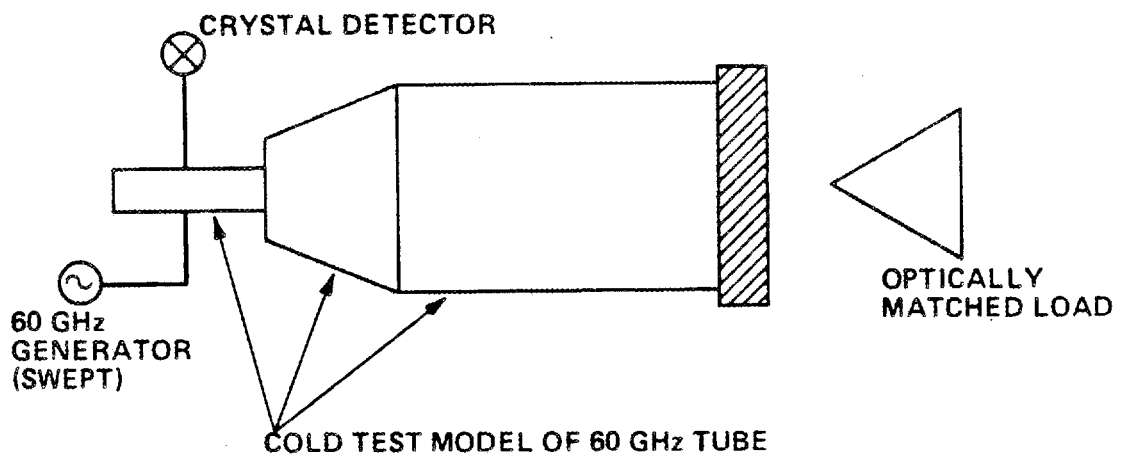

b. RESONANT CAVITY TECHNIQUE

Figure 178. Window Cold Test Arrangements

measurement of the standing wave ratio of the window discs was performed using the set-up shown in Figure 178a. A transducer (TRG model #V330) was used to launch a TE^{o}_{01} wave toward the window and the standing wave ratio was measured with a slotted line in the TE_{10} portion of the transmission line. This technique has several disadvantages. First, circular electric mode transducers are characteristically narrow band and poorly matched, even at their center frequency; this prevents an accurate broadband measurement of window VSWR. Second, the actual mode of interest for the window cold test is the TE_{02} mode. The match of the window for the TE^{o}_{02} mode must be simulated measuring VSWR versus frequency for the TE^{o}_{01} mode and then scaling the abscissa of the resulting VSWR curve by the ratio of the guide wavelengths for the TE^{o}_{01} and the TE^{o}_{02} modes.

The cold test arrangement shown in Figure 178b was also used to study the window match. For this setup, a cold test model of the actual 60 GHz tube was built to simulate the rf properties of the region from the cavity to the end of the collector. This structure was terminated with various window discs and the effect on the cavity resonance curve was observed. The thickness of each window disc was adjusted until the window mismatch did not cause an appreciable change in the loaded cavity Q. The disc thickness necessary to provide an acceptable match was found to be critical, since the bandwidth for a $3\lambda/2$ window is only a few times larger than the cavity resonance bandwidth.

A procedure was developed for fabricating single-disc window assemblies which ensured the proper disc thickness. The early unmetalized discs were fabricated to the specification shown in Figure 179. Note that the tolerances on parallelism and flatness are stringent. The former was required to maintain a uniform reflection coefficient across the window face while the latter was needed to allow subsequent grinding operations which can maintain the requisite parallelism. After the mismatches of the unmetalized dics were measured, each individual disc was ground down by an appropriate amount and cold tested again. This process was repeated as necessary until each disc was matched. The discs were then metalized and

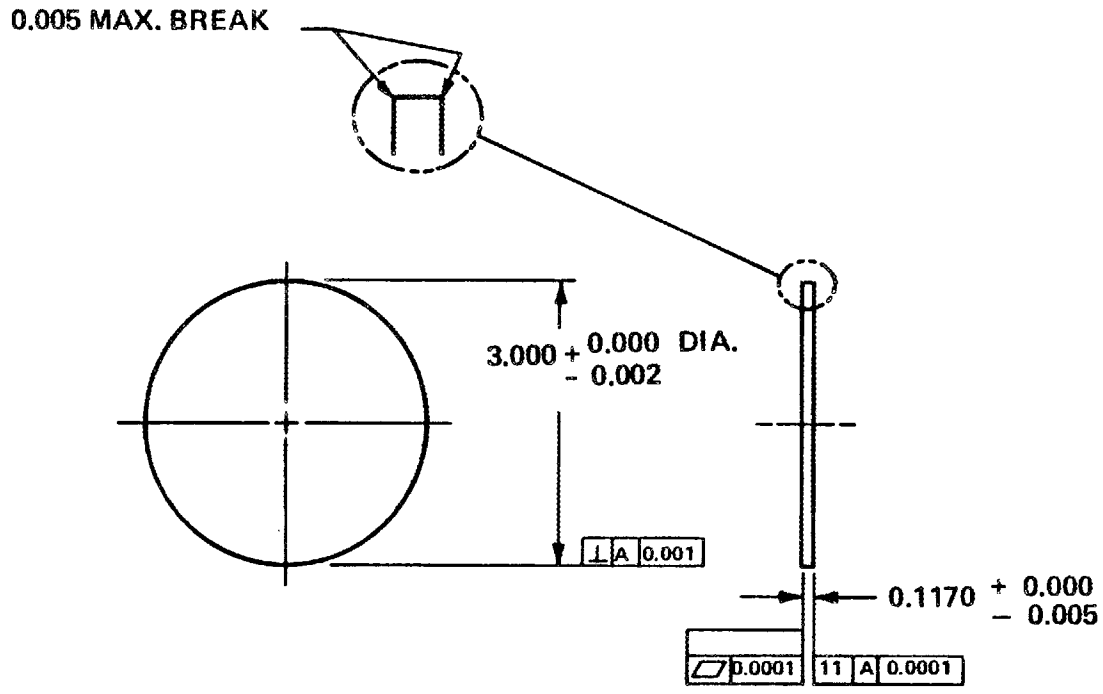

Figure 179. Ceramic Disc

brazed into the window assembly. In early batches, within a single batch there was a variation in dielectric constant of ~0.5%, while an ~1.0% variation from batch to batch was observed.

A thermal analysis of the early 60 GHz single disc window revealed that the cooling water reached the boiling point at the edge with 10% duty operation due to the small flow velocity (0.33 ft/sec) and limited area for heat transfer.

The overall geometry and loading conditions for the window are shown in Figure 180. Specific design parameters are shown in Table 21.

Table 21
Three-Inch Diameter Single Disc Window Analysis Conditions

Window Material	Beryllia 99.5%
Frequency	60 GHz, TE_{02} mode
Power Transmitted	200 kW, 100 msec pulse at repetition rate of 1 Hz
Attenuation Constant	0.04 Nepers/cm at 25°C
Calculated Heat Transfer Coefficient (before boiling)	22.3 Watts/in^2-°C

Temperature distribution, based on the pre-boiling heat transfer coefficient, was calculated by the Varian computer code VULCAN and the results are shown in Figure 181. The thermal stresses corresponding to the temperature distribution were calculated by SAPIV finite element code. The results are shown in Figures 182 and 183.

It can be seen that the tangential tensile stress is the highest at the edge of the disc. Judging from the magnitude, failure probably starts there. It is noteworthy that the stress distribution is disturbed near the braze ring. The thermal stress is expected to be more severe if the loss as a function of local temperature is considered.

82-2237 FED

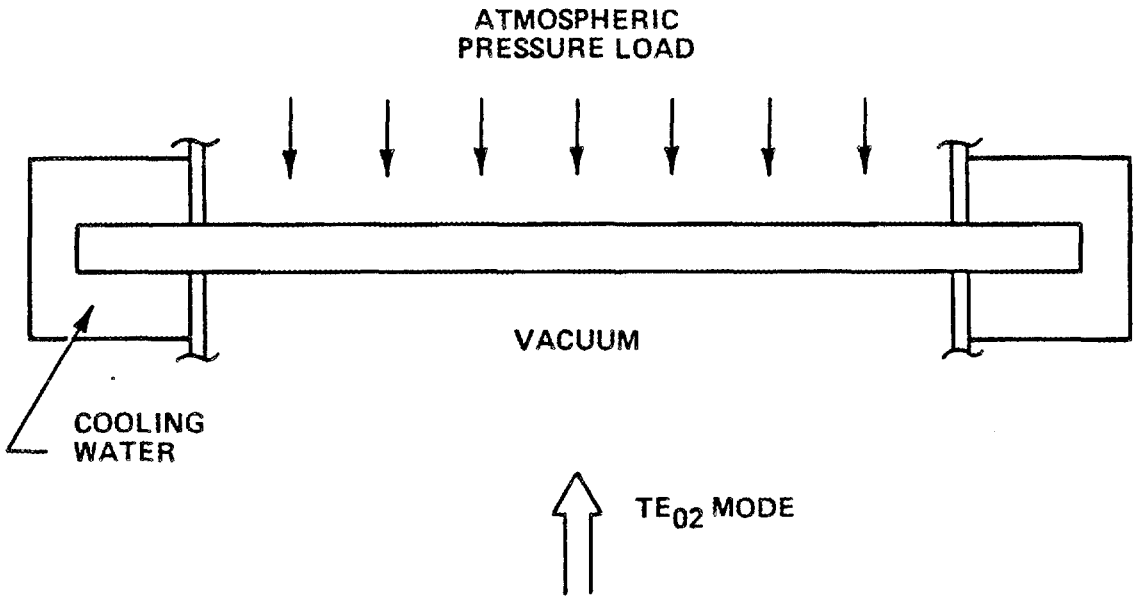

Figure 180. Single Disc Window

82-2238 FED

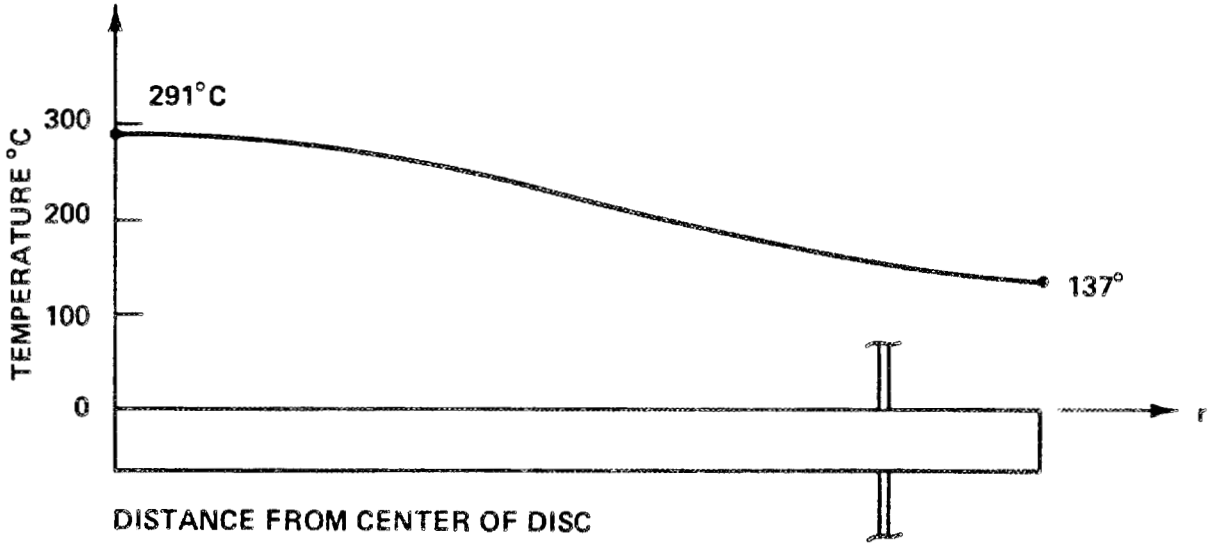

Figure 181. Temperature Distribution in the Disc Window

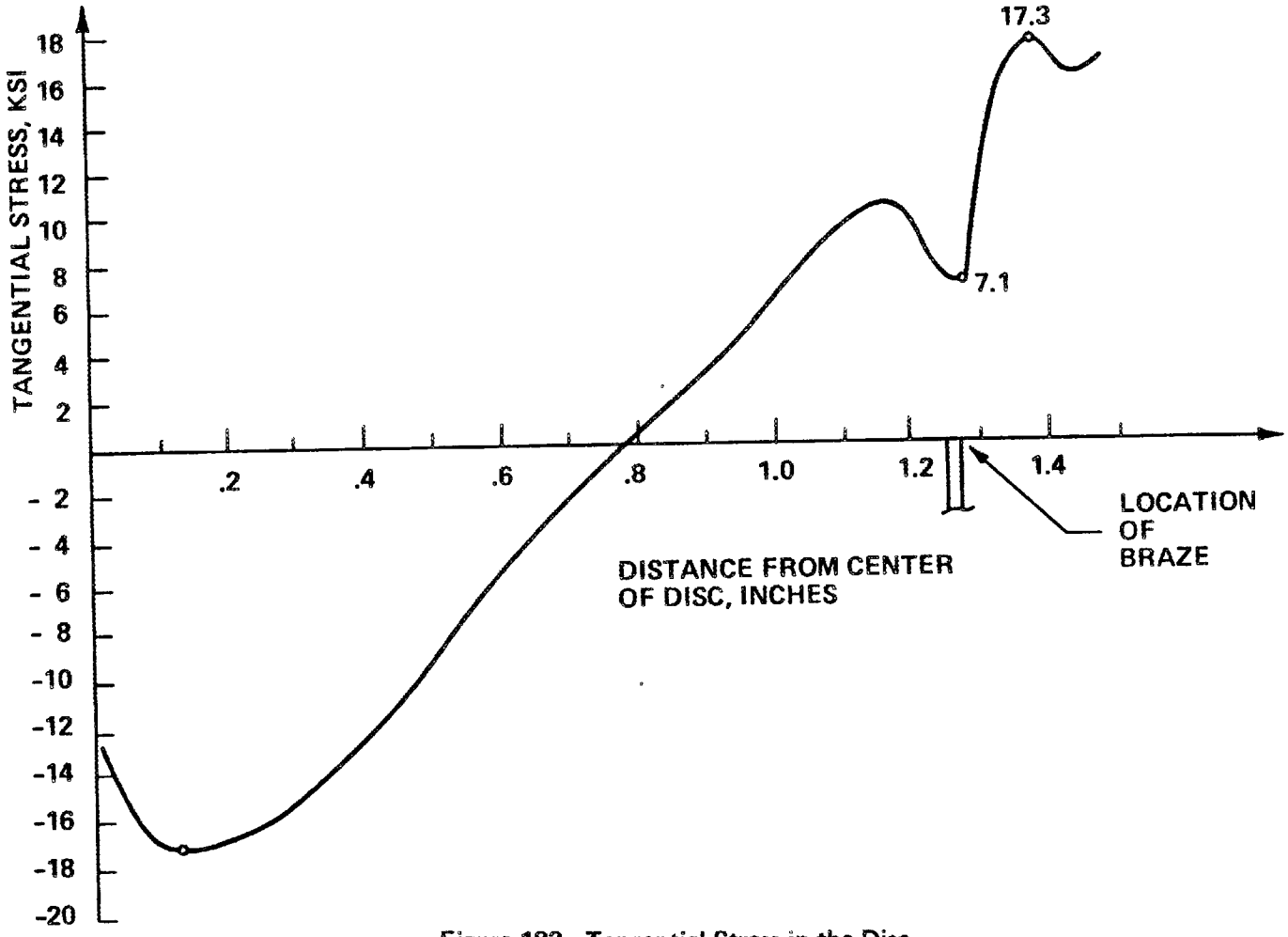

Figure 182. Tangential Stress in the Disc

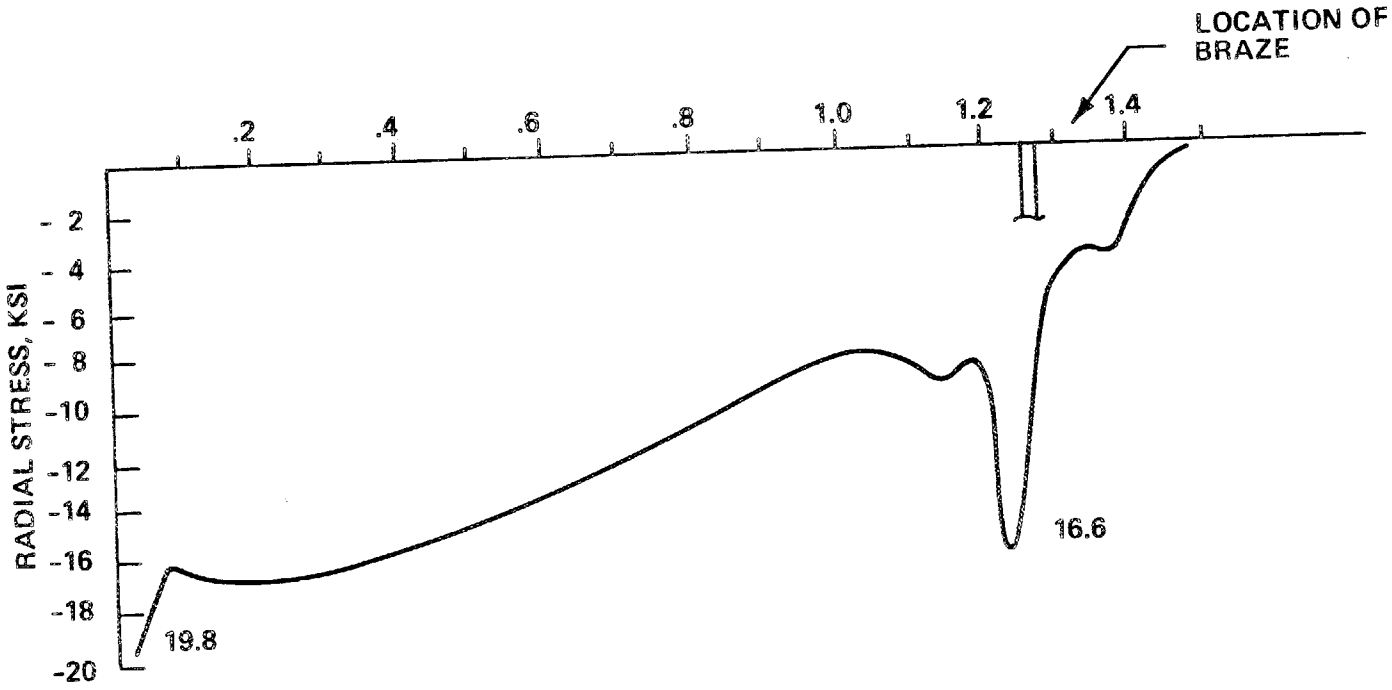

Figure 183. Radial Stress in the Disc

Two areas of the hardware design were significantly improved. First, the coolant passage around the edge of the disc was narrowed to increase flow velocity; second, the diameter of the disc was increased to provide a larger heat transfer area. An added advantage of a large diameter disc is the reduction of thermal hoop stress at the edge due to the restraining effect of the colder mass at the outer rim.

Figures 184 and 185 show the calculated temperature distribution and the corresponding thermal stresses for the analysis conditions shown in Table 22.

Table 22
Four Inch Diameter Single-Disc Window
Analysis Conditions

Window Material	Beryllia 99.5%
Operating Frequency	60 GHz, TE_{02} Mode
Power Transmitted	200 kW, 100 ms pulses at 1 pulse per second (10% duty)
Attenuation Constant	0.073 Nepers/cm
Coolant Type	Water
Coolant Surface Velocity	3 ft/sec
Calculated Heat Transfer Coefficient	5.86 $W/in^2 {}^oC$

Compared to the analysis for the old design as presented in Figures 182 and 183, it can be seen that the maximum hoop stress has been reduced from 17.3 kpsi to 7.0 kpsi. Furthermore, the temperature at the edge of the disc is reduced to merely 27^oC.

F. MECHANICAL DESIGN

The experimental gyrotron consisted of several major subassemblies:

Dwg 82-3579 FED

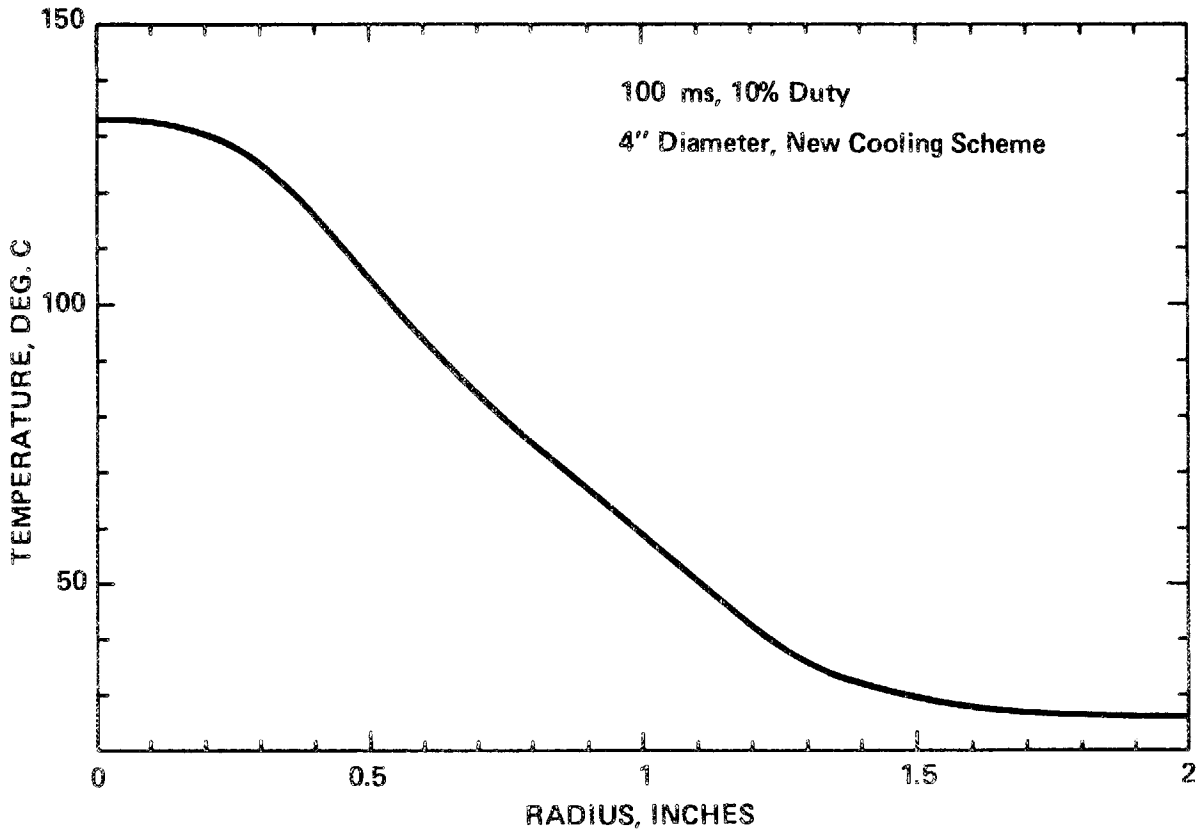

Figure 184. Steady State Temperature Distribution of 60 GHz Single Disc BeO Window

Dwg 82-3580 FED

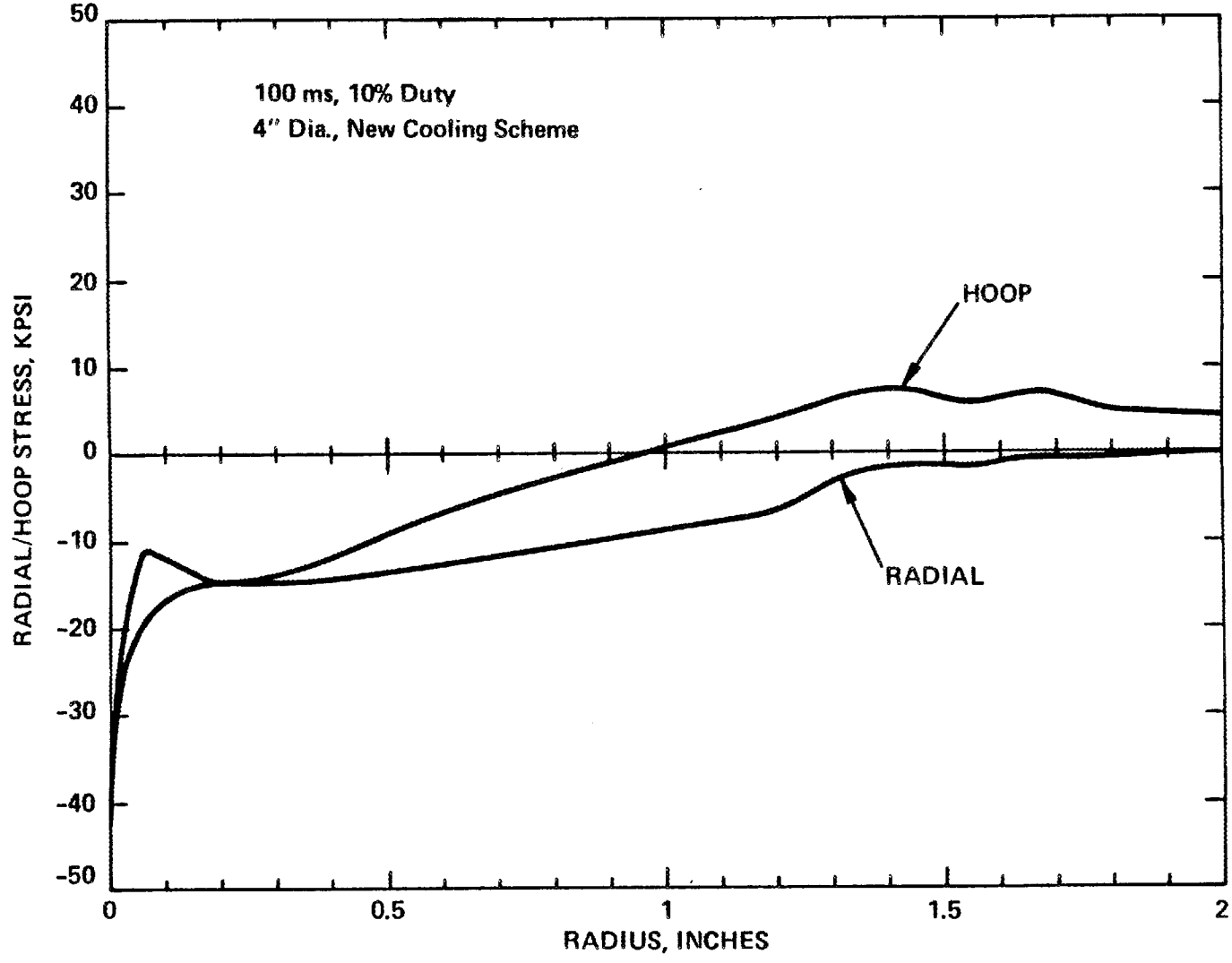

Figure 185. Steady State Stress Distribution of the 60 GHz Single Disc BeO Window

1. Single-disc window assembly
2. Collector extension assembly
3. Two collector ceramic assemblies
4. Tubulation assembly
5. Collector assembly
6. VacIon pump assembly
7. Output taper assembly
8. Three elbow assemblies
9. Body cylinder assembly
10. Beam shaver and output assembly
11. Anode shroud assembly
12. K-8060 final cathode assembly

These major subassembiles are joined to one another with tungsten inert gas-welded joints. This modular construction allows ease of modification and rebuilding. This type of construction is also necessary to reduce the number of braze cycles and to accommodate construction of assemblies too large to fit in the hydrogen braze furnaces.

The K-8060 final cathode assembly is composed of two assemblies, the final cathode stem assembly and the high voltage seal assembly, which are joined at the base of the tube by a tungsten inert gas weld. Radial alignment is accomplished by mating cylinders at the base. Axial alignment is assured by a machined step.

The anode shroud assembly comprises several stainless steel body shrouds and a weld ring. It forms the lower portion of the vacuum envelope surrounding the anode and provides structural support between the K-8060 final cathode assembly and the body cylinder assembly.

The beam shaver and output assembly, which is housed within the anode shroud assembly and the body cylinder assembly, includes a hydrogen furnace-brazed collection of rf load ring assemblies, the output cavity, the anode assembly and water cooling tubing.

The body cylinder assembly is a welded stainless steel plate and shell assembly which forms the vacuum envelope surrounding the upper portion of the beam shaver and output assembly and the lower portion of the output taper assembly. It also provides structural support between the anode shroud assembly and the output taper assembly.

Three elbow assemblies consisting of a coolant tube brazed to weld adapters provide cooling water to the beam shaver and output assembly and to the lower end of the output taper assembly, all of which are inside the body cylinder assembly.

The output taper assembly is composed of a tapered copper waveguide. It is surrounded by a stainless steel water jacket and a stainless steel plate and shell section at the top, which provides structural support between the body cylinder assembly and the lower collector ceramic assembly. The assembly also provides a water pipe for the top of the taper assembly and an elbow to connect to the VacIon pump assembly.

The VacIon pump assembly is comprised of two stainless steel tubulations, a stainless steel manifold and an eight-liter-per-second VacIon pump. The tubulation of this assembly connects to an elbow on the output taper assembly. The purpose of this pumping channel is to pump the cathode region of the tube through the anode shroud, body cylinder and output taper assemblies, independent of the beam tunnel.

The collector assembly includes a stack of water-cooled, cylindrical copper sections with stainless steel plate and shell water manifolds at the top and bottom. Four stainless steel stiffening bars provide structural support between the tube lifting eyes, welded to the top water manifold, and the lower water manifold. The collector assembly provides structural support between the upper and lower collector ceramic assemblies.

The collector ceramic assemblies which are metal and ceramic assemblies are used to electrically isolate the collector, which enables monitoring of body, collector and window current. The collector ceramic assemblies provide compressive support between the output taper assembly and collector

assembly, and also between the collector assembly and collector extension assembly. Tensile support is provided by insulated bolts.

The collector extension assembly consists of a 2.5" inside diameter copper waveguide, water cooled by a stainless steel plate and shell water jacket. The assembly also includes a stainless steel plate and shell vacuum pumping manifold for evacuation and pumping through the gap between the collector and collector extension assemblies. The plate and shell sections provide structural support between the upper collector ceramic and single-disc window assemblies.

The tubulation assembly includes two sealing rings and a piece of tubulation. The assembly goes between the collector extension assembly and the pumping station during bakeout. After bakeout, part of this assembly is pinched off.

The single-disc window assembly is composed of:

1. The beryllia window disc;
2. a short waveguide section on the vacuum side, ending in a copper cup for the window braze;
3. a short waveguide section on the air side with a copper cup on one end for the window braze;
4. a stainless steel waveguide flange, terminating the tube, and
5. a plate and shell water jacket providing structural support for the window waveguide.

VII. GYROTRON BEHAVIOR STUDY

A gyrotron behavior study was undertaken using the 28 GHz CW gyrotron, the VGA-8000, as a test vehicle to investigate arcing, crowbars, voltage gradients, trapped electrons, tube processing and bakeout, rf behavior, cavity and output taper design, and maximum power limitations.

A. ARCING AND CROWBAR INVESTIGATION

Time was spent working with various tubes to find a cause for the frequent crowbars in the VGA-8000 and VGA-8050 tubes. The purpose of this work was to eliminate some of the design problems in gyrotrons and to hasten development work at higher frequencies.

A table was formulated of events which would probably occur with different types of faults. This enabled specific faults to be identified. To help in this matter, a capacitive divider was placed between cathode and ground to monitor cathode voltage fluctuations around the time of a crowbar.

Different types of oscilloscopes were used to determine the timing between events, such as changes in magnitude of gun anode current and cathode current. The timing difference between these two currents at crowbar is usually undetectable. Many crowbars were observed, and in 98% of the cases the crowbar occurred during the pulse. Only a few interpulse crowbars were observed. It was also noted that the crowbars occurred only when there was some amount of beam current. Most of the crowbars were very similar in their characteristics. The timing of various current increases and voltage decreases were the same time after time and the amplitudes of current were always about the same. Most of the fault current is seen in the collector and not in the body. This would seem to indicate an upper seal arc.

Data taken did not show any correlation between the cathode temperature and the frequency of crowbars.

Four antennas were placed in the oil tank near the gyrotron gun to look for rf in the gun region. Investigation, using a digital storage scope with 50 nanoseconds-per-point speed, showed that the rf followed the gun anode arc by 100-200 nanoseconds. This rf could be due to the high beam current drawn when the gun anode voltage approaches ground potential.

Using the table of probable events that would occur with various tube faults, all types of faults were seen. Observed were the following:

1. gun anode arc to ground (Figure 186);
2. gun anode arc to cathode (Figure 187);
3. cathode arcs to ground with the gun anode following (Figure 188)

These three figures were taken with the digital storage scope during the CW operation of the VGA-8000 S/N 11. Figure 186 shows the mod anode voltage going quickly towards ground potential, while at the same instant the gun-anode current goes in the direction of discharging the capacitance in the modulator between gun-anode and anode. As can be seen in Figure 186, the time constant for the discharging of that capacitance is quite long. Figure 187 shows a lower seal arc. This seems to be much less frequent than an upper seal arc. In Figure 187, the gun-anode voltage tries to go more negative, and at the same instant, the current goes for a short time in the direction of charging the capacitance in the modulator from gun-anode to anode. The crowbar then fires and the voltages go to zero. Figure 188 shows an arc from cathode to ground. This is very seldom seen. The gun-anode voltage goes towards the cathode voltage, and yet the mod-anode current is going in the direction of discharging the mod-anode to anode capacitance in the modulator.

In the event shown in Figure 187, the beam should shut off without a crowbar, but this doesn't seem to be the case. During pulse operation, the gun anode voltage tends to go more negative, rather than more positive, with the start of the crowbar. While in CW operation, the failure mode seems to be the gun anode voltage going more positive, indicating an arc from gun anode to ground.

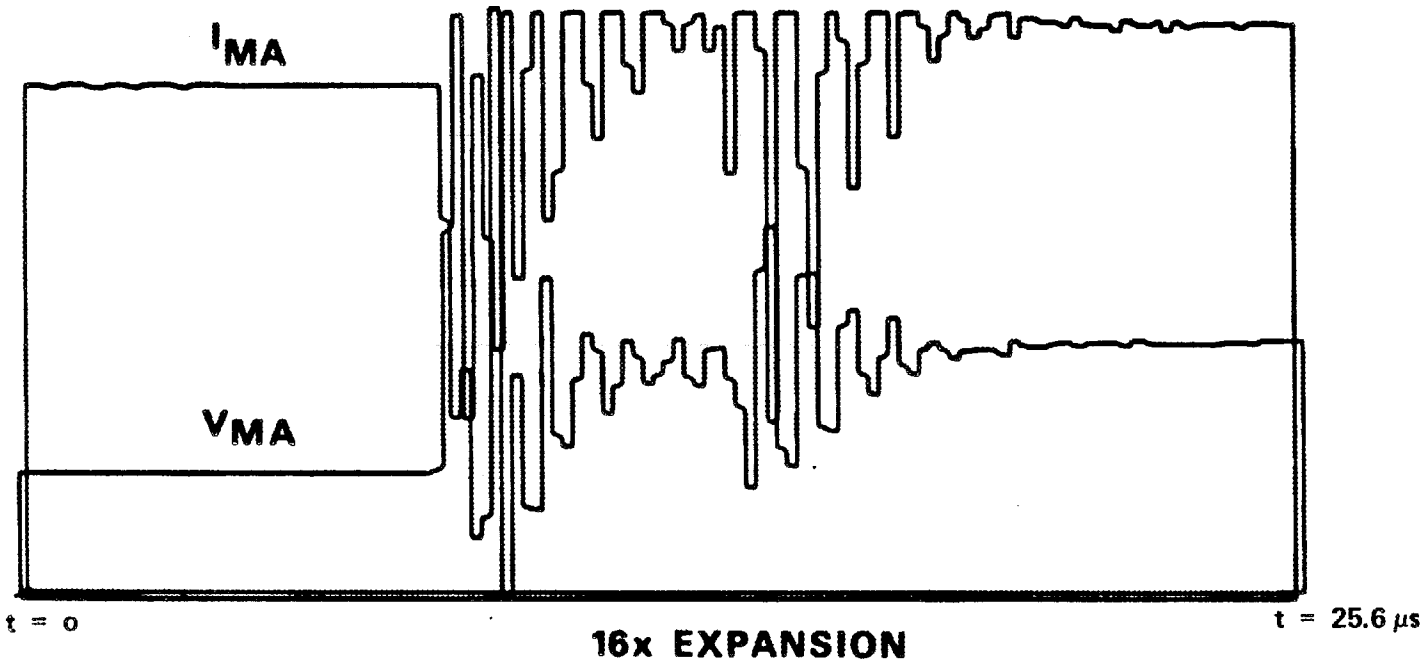

Figure 186. Upper Seal Arc

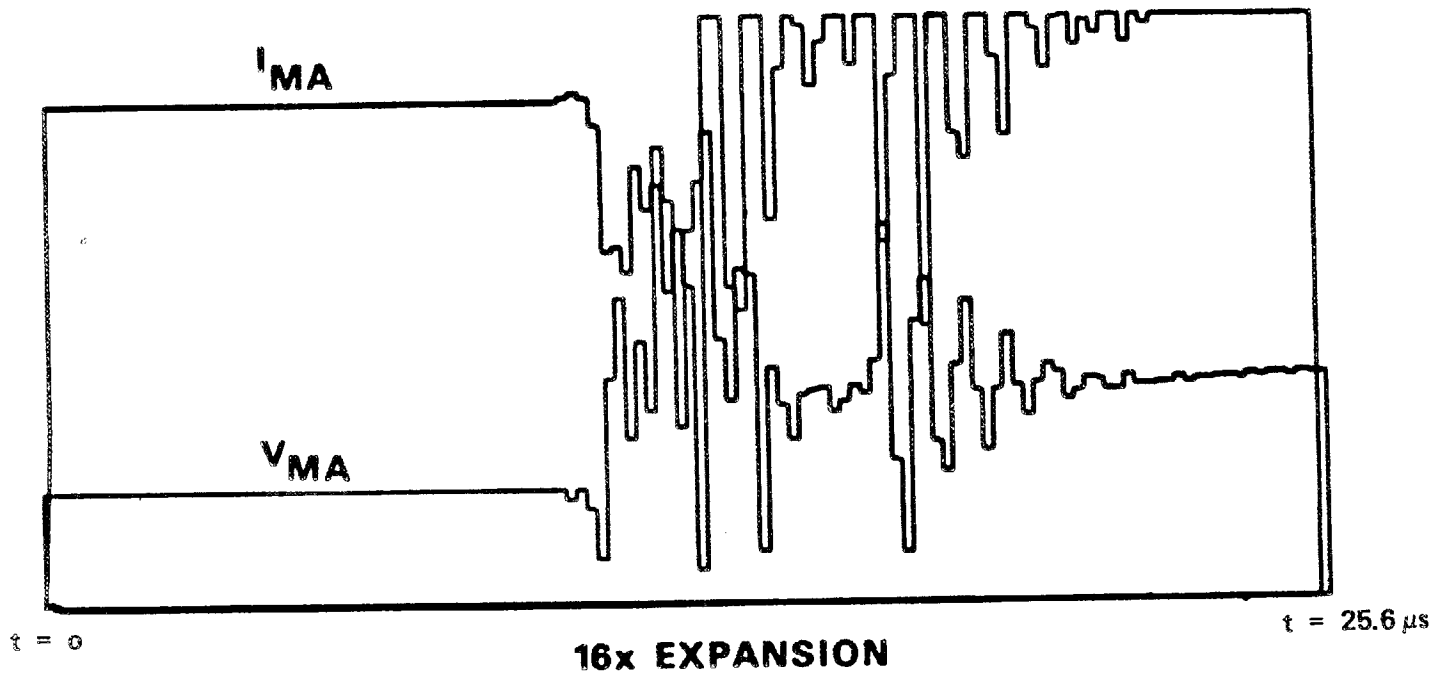

Figure 187. Lower Seal Arc

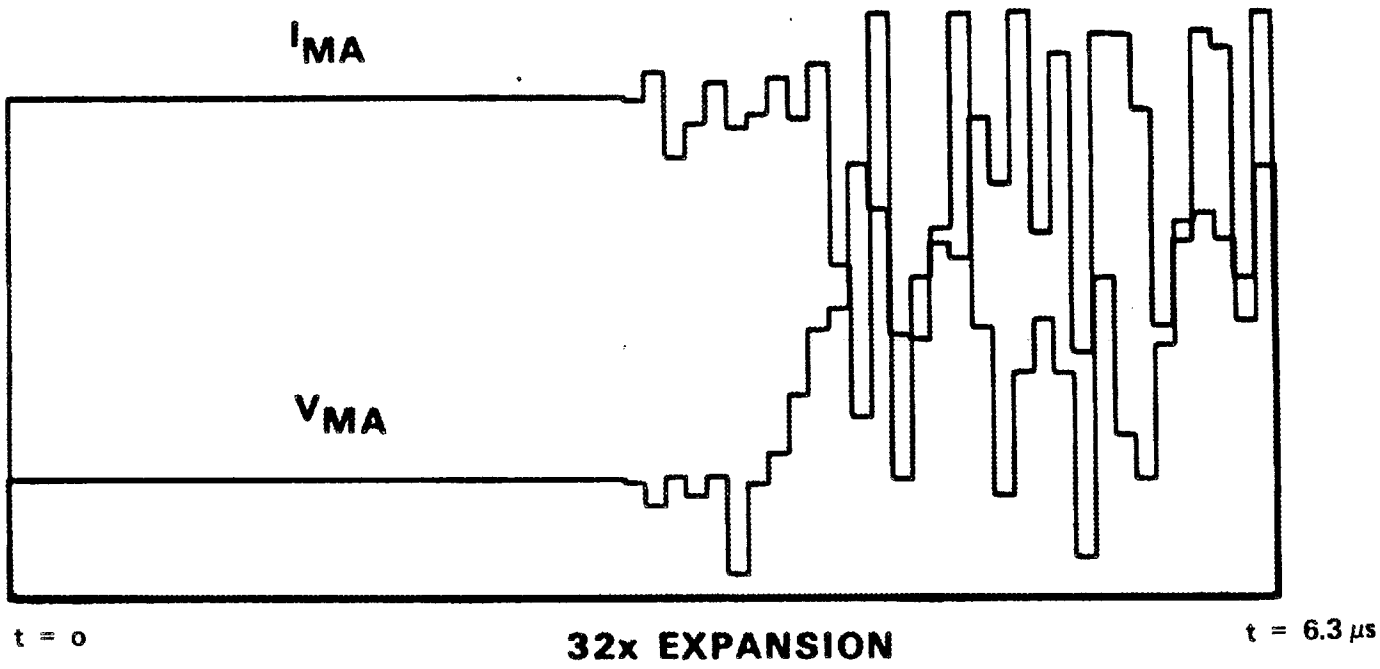

Figure 188. Cathode Arc to Ground

Different types of faults were catalogued to differentiate between tube related and power supply related problems. Using the VGA-8050 S/N 7, it was observed that 90% of the arcs occurred during the pulse and 85% occurred in the first half of the pulse.

It appears that the 28 GHz design does not have a dc gradient problem. The tubes that tend to arc from gun anode to ground, do so only with the beam present.

Experiments were done with an antenna in the oil tank to observe any oscillations in the gun region of the tube. With a CW tube, no gun oscillations were observed until after the tube fault. Using a pulse tube, VGA-8050 S/N 7, oscillations were observed in the gun region whenever there was rf in the tube's output. There were no conditions where rf was observed in the gun region without the same rf frequency being detected at the tube output. The difference between the CW and pulse tube in the gun region was that the CW tube had a lossy coating on the anode and the pulse tube did not.

While testing VGA-8000 S/N 8B, it was observed that when the 100Ω resistance was added in series with the cathode, the tube gas pressure at crowbar rose to 1×10^{-7} torr. While without the 100Ω, the pressure in the gun rose to 5×10^{-7} torr. The pressure in the collector without the 100Ω resistance was 1.8×10^{-7} torr at crowbar. With the 100Ω resistance, the gun pressure was generally the same as the collector pressure. This indicates that the power supplied to an arc becomes excessive without the 100Ω resistor in the line. Because of power dissipation, the particular 100Ω resistor used could not remain in the line for CW operation. The gun anode current at crowbar with the 100Ω resistor was about 300 amperes, whereas it was 600 amperes without the 100Ω resistor in the line. Also, the amount of gas liberated from the arcing indicates that the gas is being freed from a volume, and not just a surface, condition.

B. VOLTAGE GRADIENTS AND TRAPPED ELECTRONS - COMPUTER INVESTIGATION

Voltage gradients in the gun were investigated. The gradient from the gun anode was found to be 65 kV/cm when the tube is pulsed on and 111 kV/cm when pulsed off. The gradient from the surface of the front focus electrode is 109 kV/cm when the tube is pulsed on and 74 kV/cm when the tube is pulsed off. These gradient values are acceptable but have a minimal safety factor. By moving the gun 0.3 inches away from the body, the gradients at the gun anode could be lowered to 92 kV/cm. Further work would be necessary to see if this movement would be detrimental to beam quality.

Sputtering of metals on the ceramic insulators of the gun led to an investigation of ion bombardment of the tip of the focus electrode. The computer calculations showed that any ions formed in the interaction region of the tube will indeed strike the front focus electrode. The diameter of the ion impact area is dependent on the atomic number of the ions. Chemical analysis of the material sputtered on the ceramics found all materials normally used in vacuum tubes. After exposure to the air, this coating was found to be non-conducting.

Electron trajectory calculations of the focus electrode emission showed that electrons emitted from the front focus electrode and anode will go down the drift tube, while those from the rear focus electrode will split, some striking the anode and the remainder going down the drift tube. None seem to stay for any appreciable time in the region of the gun.

C. PROCESS AND BAKEOUT

The bakeout time for the test vehicle, VGA-8000 S/N 11, was doubled to release and eliminate more gas from the metal walls of the tube. This new bakeout schedule made an improvement in tube processing and was used on subsequent tubes.

The VGA-8000 S/N 8B was baked out at 450°C for 9 hours. The cathode was processed for 4 hours. While in operation, the tube gases were analyzed using a residual gas analyzer (RGA). The analysis showed that there was

still a lot of hydrogen gas, which should have been removed in bakeout and processing. It appeared that the gyrotron should be baked out for a longer period of time, perhaps twice as long at temperature. The heater should be run at rated power for 12 hours before going to test. When applying power to the heater, the hydrogen and carbon monoxide gases evolved are sufficient to slow testing time but are of low 10^{-7} torr pressure. It is difficult for bakeout stations to get the tube pressure below 10^{-7} torr. Therefore, a long processing time with the VacIon pump, which can get the pressure much lower, would be useful. This would not occupy the bakeout station. The 12 hour cathode processing could be done overnight.

D. RF BEHAVIOR

Although VGA-8000 S/N 8 was not operated with high level rf, the tube was found to have a cracked output window. The crack appeared to be from pressure, rather than any thermal or rf induced problem.

VGA-8000 S/N 11 was pulse tested to 200 kw peak power. Curves were taken to show the types of excursion possible in magnet currents and gun anode voltage, Figures 189-191.

Figure 189 shows the optimized power output at a given gun anode voltage. In Figure 189, the magnetic fields were varied to optimize the peak power output. Figure 190 shows the peak output power variation for a given change in main magnetic field. The main magnet current was lowered until the tube oscillated in a mode other than the TE_{021}. Figure 191 shows how the output power varies with gun coil magnet current. The tube is normally operated with no gun anode current being drawn. At 12.1 A of gun coil No. 1 current, the gun anode began drawing current. Above 12.1 A, there is no gun anode current.

Results of an exploration of parameter space are shown in Figure 192. Figure 192 shows that the best way to start the tube oscillating in the correct mode is to begin with a low gun anode voltage and a high magnetic field, then raise the gun anode voltage to the design value and then lower the magnetic field to get the desired output power. Figure 193 shows the

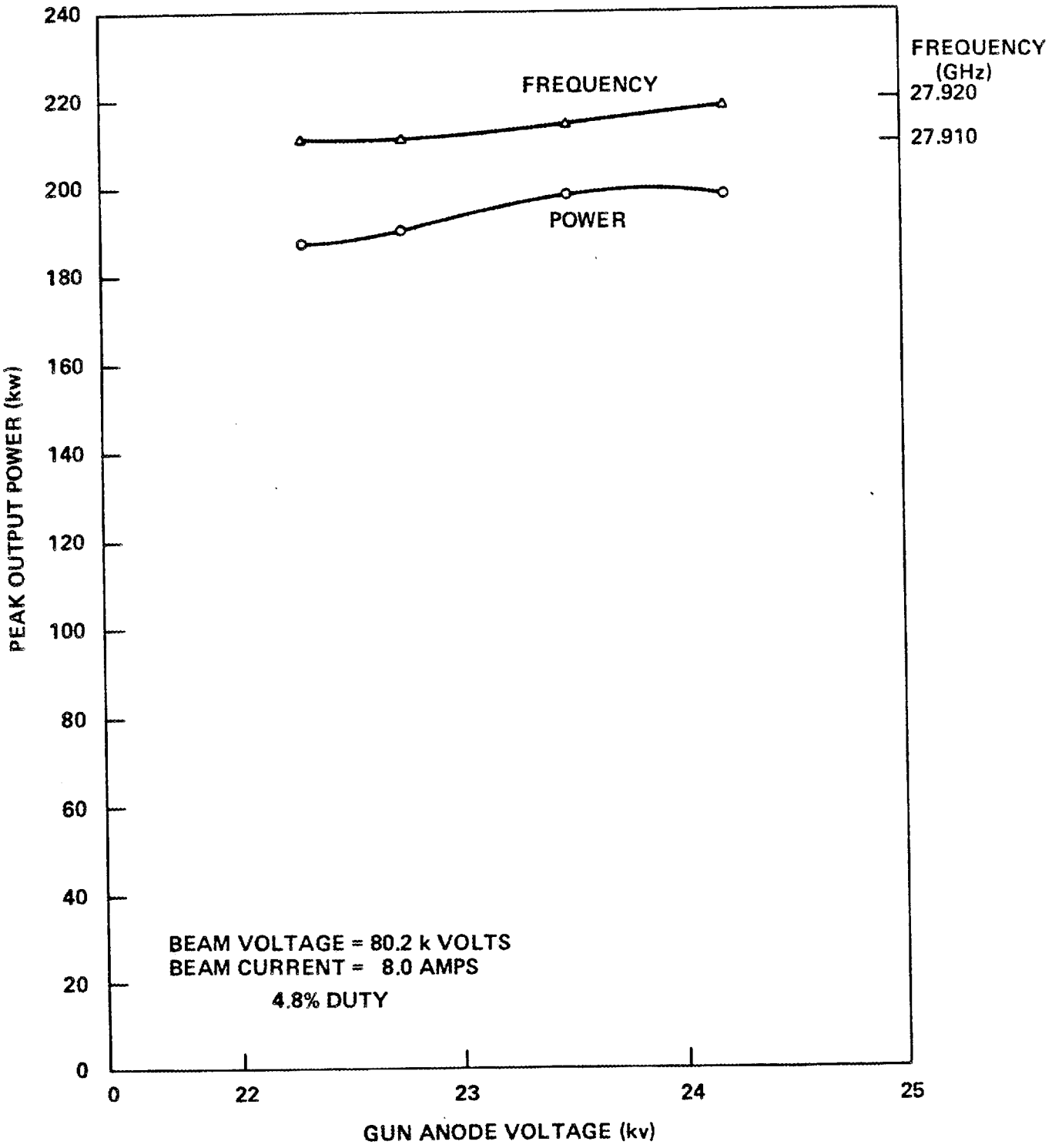

Figure 189. Optimized Power vs Gun Anode Voltage

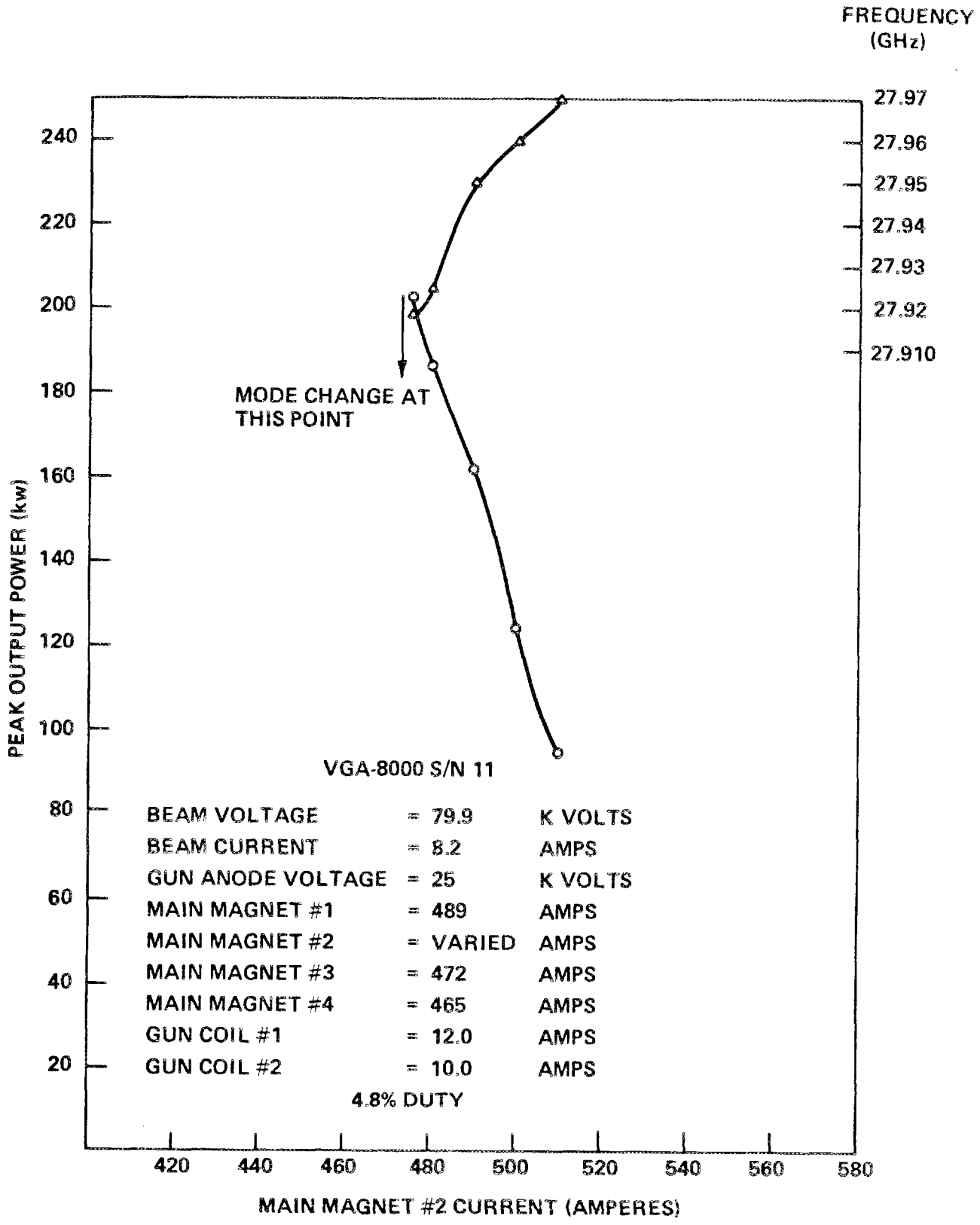

Figure 190. Power vs Main Magnet Current

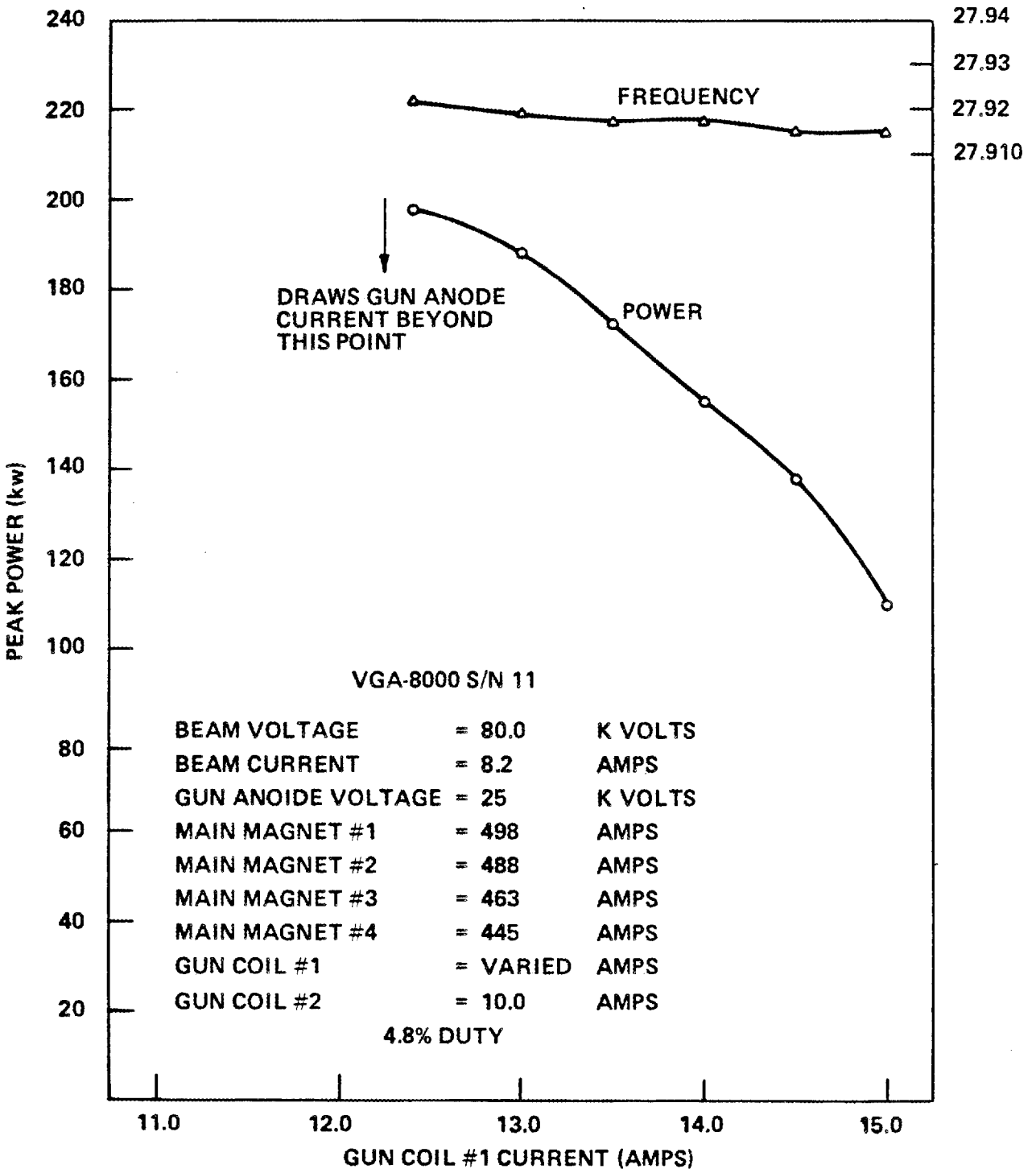

Figure 191. Power vs Gun Coil No. 1 Current

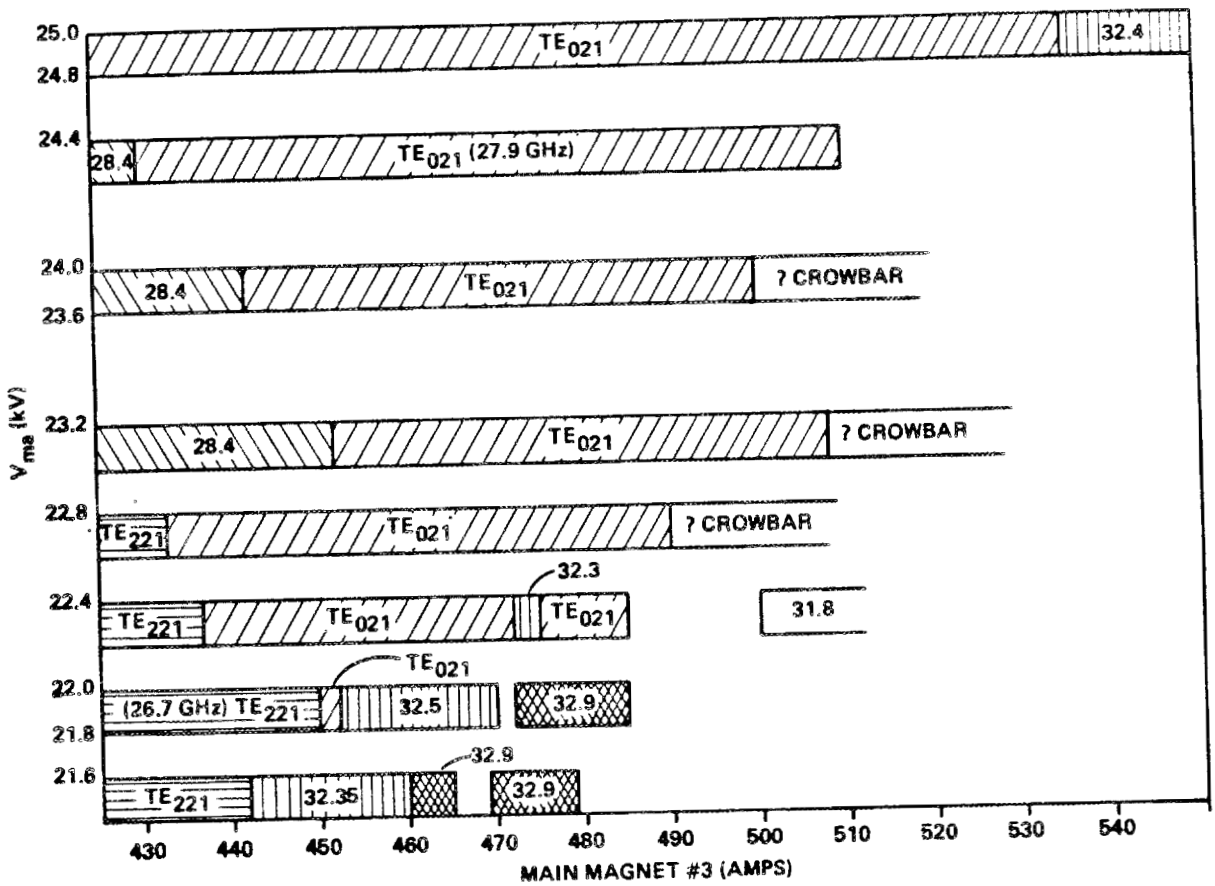

Figure 192. Parameter Space - VGA-8000 S/N 11 CW

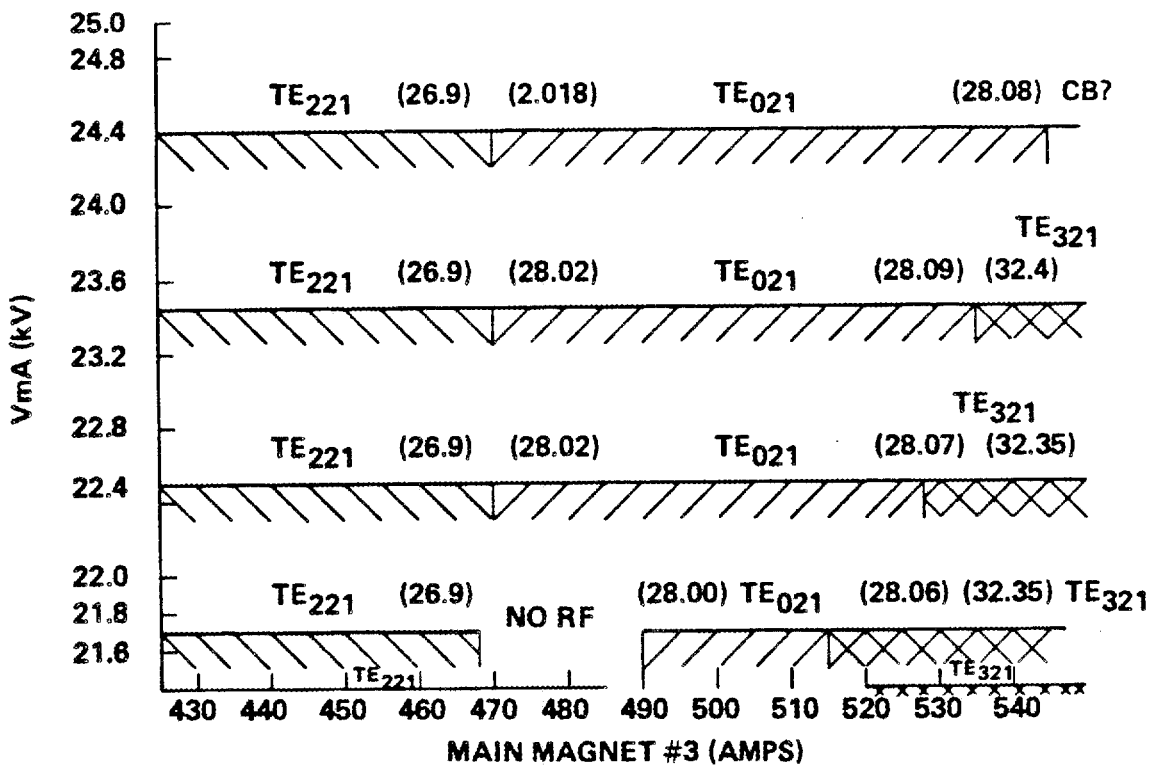

Figure 193. Parameter Space - VGA-8050 S/N 9 - Pulsed 2.4% Duty

data for VGA-8050 S/N 9, a pulse tube. Comparing Figures 192 and 193 illustrates that the operation of the CW and pulse tubes is very similar, except for two apparent differences. First, the CW tube has a 28.4 GHz mode and the pulse tube does not. Further examination will have to be done to identify this mode. Though it is not shown in Figure 192, the TE_{221} mode was at a lower magnetic field than the 28.4 GHz and TE_{021} modes, as it is also at lower field than the TE_{021} mode in the pulse tube. The second difference occurs at the low gun anode voltage levels. It appears more difficult to operate in the correct mode under CW conditions than under pulsed conditions.

At high magnetic fields, the 32.4 GHz mode oscillates with low power. This mode does not seem to be a problem because it can be avoided with the appropriate magnetic field setting. The TE_{221} mode appears to be a more serious problem. As can be seen in Figure 194, to obtain high output power, the main field is lowered and then the TE_{221} mode becomes the lower limit in main magnet field, and the upper limit for power output.

Figure 194 shows the characteristics of the VGA-8000 S/N 11. It was operated for periods of a few hours at the 200 kW CW level. This curve compares well with the previous curves for S/N 5R2 and S/N 6. This tube achieved 40% efficiency.

CW Tube No. 11 was operated both pulsed and CW with the identical load conditions to determine if there were any apparent behavior differences with the two modes of operation. Figures 195 and 196 show that there are differences between pulsed and CW operation. At low transverse energy, the CW operation has more mode competition than the pulsed operation. At moderate gun anode voltages, the tube stays in the correct mode over a wider range with CW than with pulsed operation. This is probably due to the fact that once an oscillation has started, it will dominate as the magnetic field is changed, whereas in pulsed operation, oscillation must restart with every pulse. While taking data, it was discovered that the 27.15 GHz mode had a second harmonic at 55.3 GHz which would give a false wavemeter indication at 32.4 GHz. We now believe the frequency listed as 32.4 in previous mode pictures may actually have been 27.15 GHz. However, as can be seen in

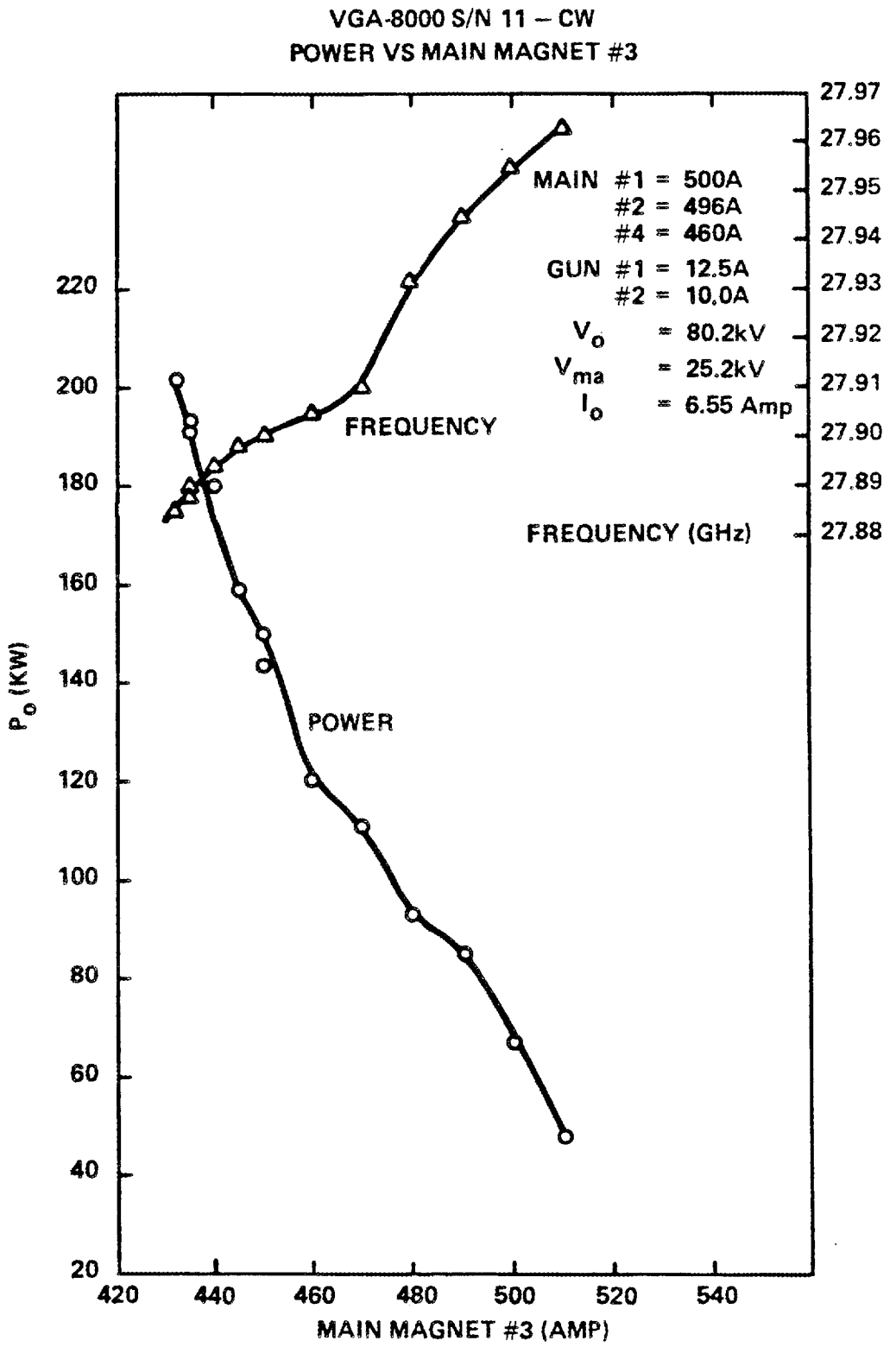

Figure 194. Power and Frequency Sensitivity to Main Magnet No. 3 Current

ORNL Dwg. 81-16834FED

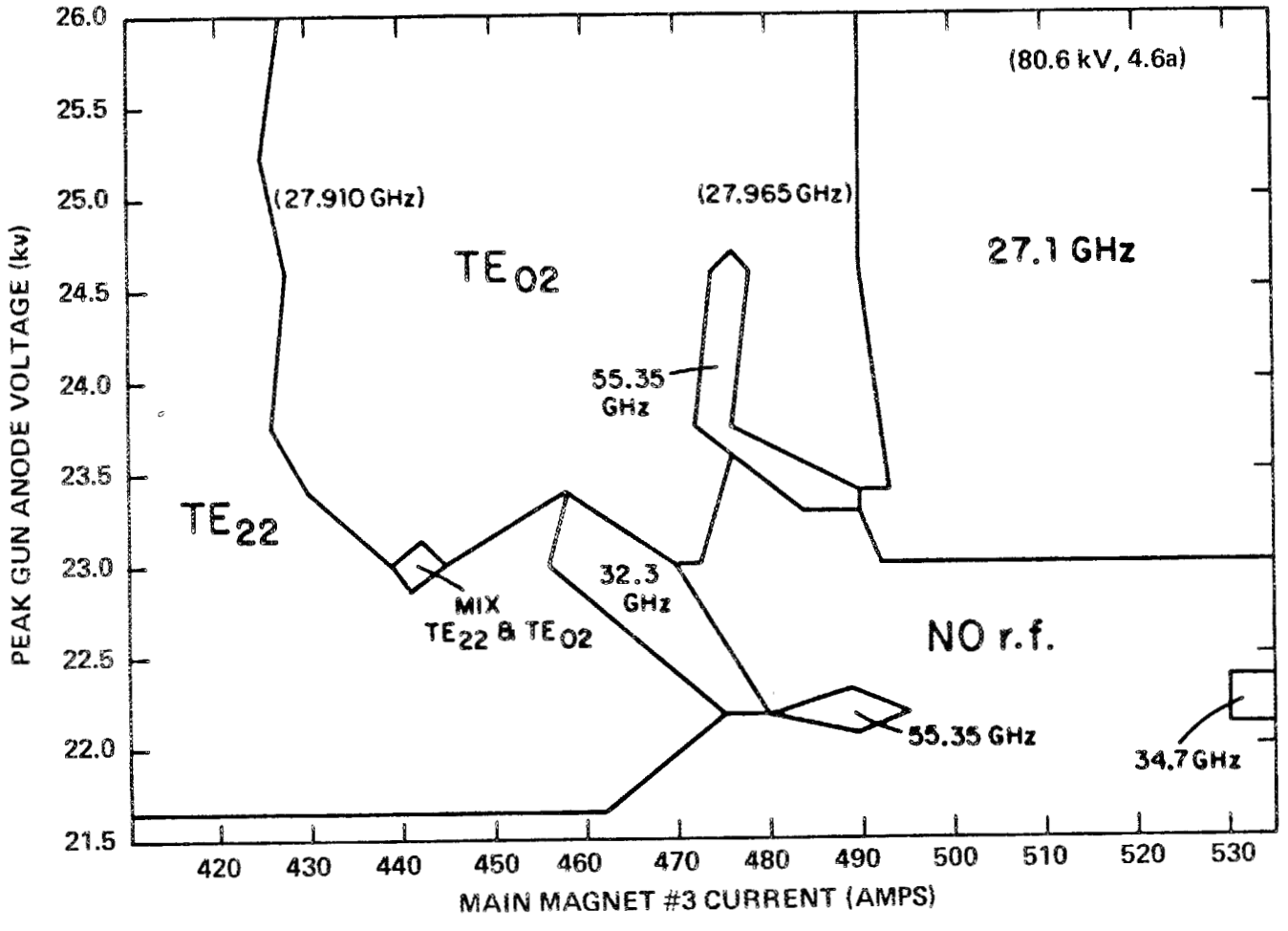

Figure 195. VGA-8000 S/N 11 Pulsed Oscillation Map

ORNL Dwg. 81-16835FED

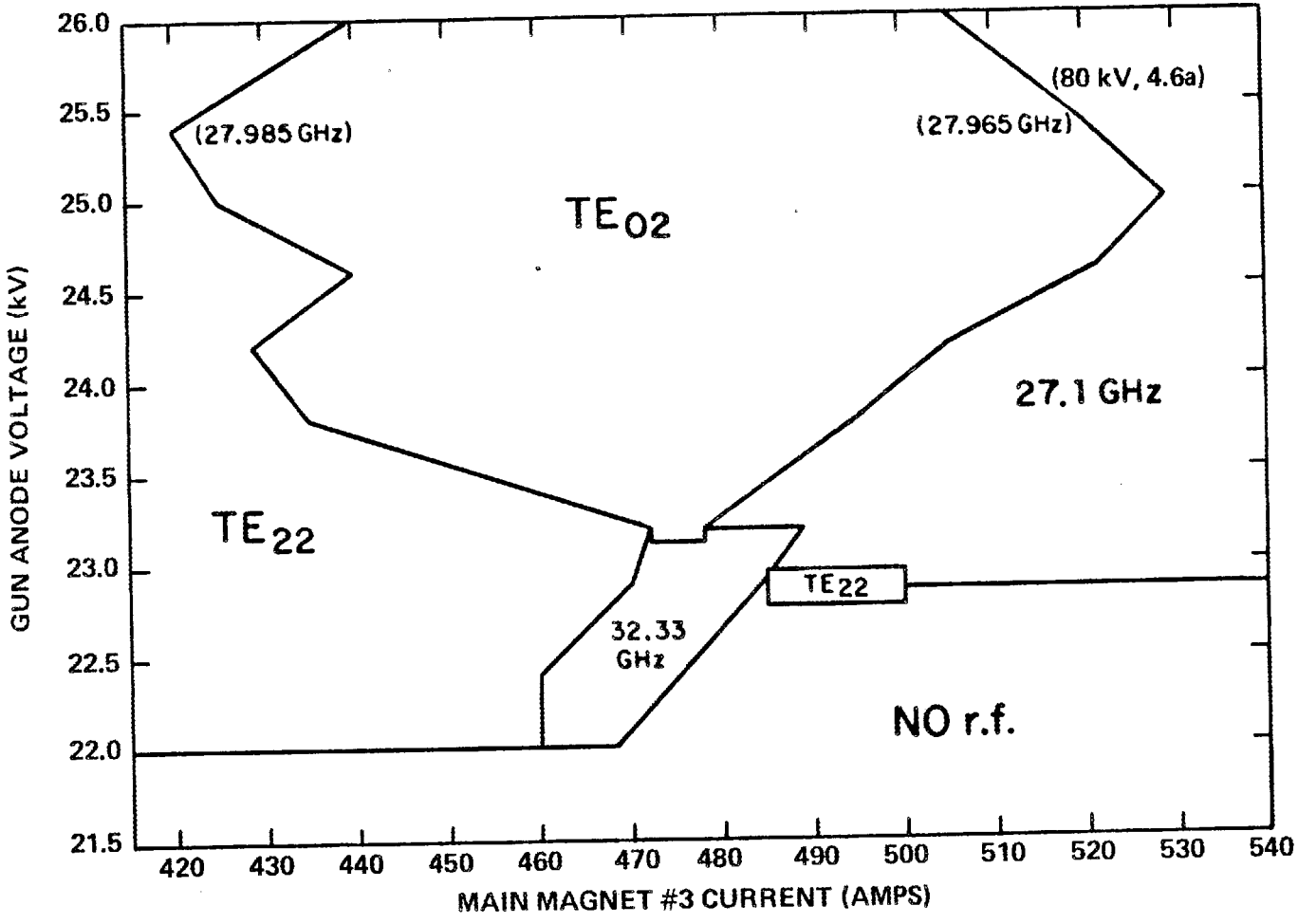

Figure 196. VGA-8000 S/N 11 CW Oscillation Map

Figures 195 and 196, there is a 32.3 GHz mode that is real. Another factor that would explain differences between these parameter space plots and previous ones, is that the output window had to be changed. While previously operating VGA-8000 S/N 11, the output waveguide arced. Normally, the operator has to reset the arc detector before an interlock allows the high voltage to come on again. At the time of the failure, this interlock was apparently not working correctly and the high voltage was allowed to come on without the arc detector being reset. Therefore, the tube was being operated without a functional arc detector. When the waveguide arced again, the arc was not extinguished fast enough, and it cracked the air side of the output window. The crack was due to the extreme heat from the arc. Part of the window was replaced and the tube operated with the results seen in Figures 195 and 196.

In conclusion, the tube operation, pulsed and CW, is very similar. The few differences can be explained by the fact that CW operation will settle into a particular mode and tend to stay there. In fact, there is some hysteresis when going from one mode to the next. However, with pulsed operation, the oscillation shuts off and restarts with every pulse and, therefore, can easily start in any mode where the correct conditions exist.

E. CAVITY AND OUTPUT TAPER

Computer simulation was used to design a new cavity and output taper for low mode conversion. The existing cavity, if used with the new output taper configuration, would have a Q less than 200. The new cavity and taper design has a Q of 430, which was used in the earlier 28 GHz work.

Work was performed on two schemes for a better cavity design. The first idea was a cavity that was already being used, but with pins or vanes added for mode suppression. The second scheme was a two-section cavity which would pre-bunch the beam in the first section and extract energy from the beam in the second. The pinned or vaned cavity idea was not new, but the design method, maintaining the cooling and necessary mechanical features was challenging. Vanes were tested and worked very well, but pins seemed a

simpler solution. This work was directed at reducing the possibility of interference from TE_{221} mode.

Cold tests of the pinned cavity demonstrated the importance of pin diameter. Pins that were 0.080" diameter affected the TE_{021} mode, whereas pins of 0.061" diameter were not detrimental to the TE_{021} mode. The depth of penetration of the 0.061" diameter pins was 1/8". The best locations for the pins were determined by cold tests. With the pins in place, the Q of the TE_{021} mode remains unchanged, whereas the Q of the TE_{221} mode is reduced from 350 to 150. The effective length of the cavity was determined by drawing a dielectric bead through the cavity to measure the electric field of the cavity. A comparison was made of the effective length of the new cavity with pins and without an iris to the effective length of the existing cavity used in the previous 28 GHz gyrotrons. The new cavity length is 0.380" longer. The electrical length in cold tests appeared to be 0.7 λ free-space (f.s.) longer than the 3.1 λ f.s. length of the existing cavities. In this comparison, the lengths are defined using the points where the electric field is 1/e of the peak value.

The following modifications were made on the VGA-8000 S/N 8B.

1. There were 7 posts in the cavity to detune the TE_{22} mode. The posts were 0.061" diameter by 0.12" long.

2. The cavity had no iris: its Q was 420.

3. The cavity was 0.380" longer. In cold tests it appeared to be 3.8 λ f.s. long, as opposed to its previous 3.1 λ f.s. length.

4. It had a new alumina window.

5. There was a 0.2 ℓ/sec pump at the gun end of the tube to monitor the pressure at the gun.

6. There was a vacuum valve for a residual gas analyzer connection.

RF testing of the tube was done in the pulsed mode. Figure 197 shows how the output power varied with the beam current. In this experiment, the gun anode voltage was 24.6 kv and the gun coil 1 and 2 settings were 11.5 A and 10.0 A, respectively. The main magnets were varied to achieve optimum power. This curve is similar to those of previous tubes except that the maximum power achieved was only 146 kw, as opposed to 200 kw. The maximum power achieved with the VGA-8000 S/N 8B was 176 kw. This was at 8.2 a beam current and 11.0 A in gun coil No. 1 with 23.9 kv on the gun anode voltage.

The operation of S/N 8B showed some peculiar results. The following figures point out some unusual behavior patterns. Figure 198 shows that at high power operation the tube efficiency goes towards a peak, but the peak is not defined. Figure 199 shows how a small change in the gun anode voltage and gun coil current affects the output power but does not change the shape of the curve. Figure 200 compares with Figure 201. Only the beam voltage and gun anode voltage were changed. Notice how the curve now goes past the peak efficiency point and defines the peak. One of the major reasons for this tube's cavity modifications was to be able to find this peak in efficiency. Previously, tubes had power versus magnet current curves that looked like Figures 198 and 199. Figure 200 has the peak efficiency point shown but the peak output power is not acceptable. Figure 201 shows that at lower gun anode voltage and lower gun coil current, the power falls very low before changing modes. (This case is still at a high transverse energy but a different diameter beam.) Both Figures 200 and 201 show that the interfering mode is not the TE_{22} mode at 26.8 GHz, but another mode at the low magnetic field values.

Figures 202, 203, and 204 are mode oscillation maps for the VGA-8000 S/N 8B. Figure 202 shows the best TE_{02} operating conditions. The only problem is that the peak power is much too low, as was seen in Figure 201. Figures 203 and 204 depict the results of attempts to get to a higher output power regime. At 80 kV, the mode picture is much more complex than at the 70 kV level. Figures 205 and 206 compare the 80 kV and 70 kV beam voltage oscillation maps. Figure 206 shows the difficulty in operating at the highest power level.

Dwg 82-2172 FED

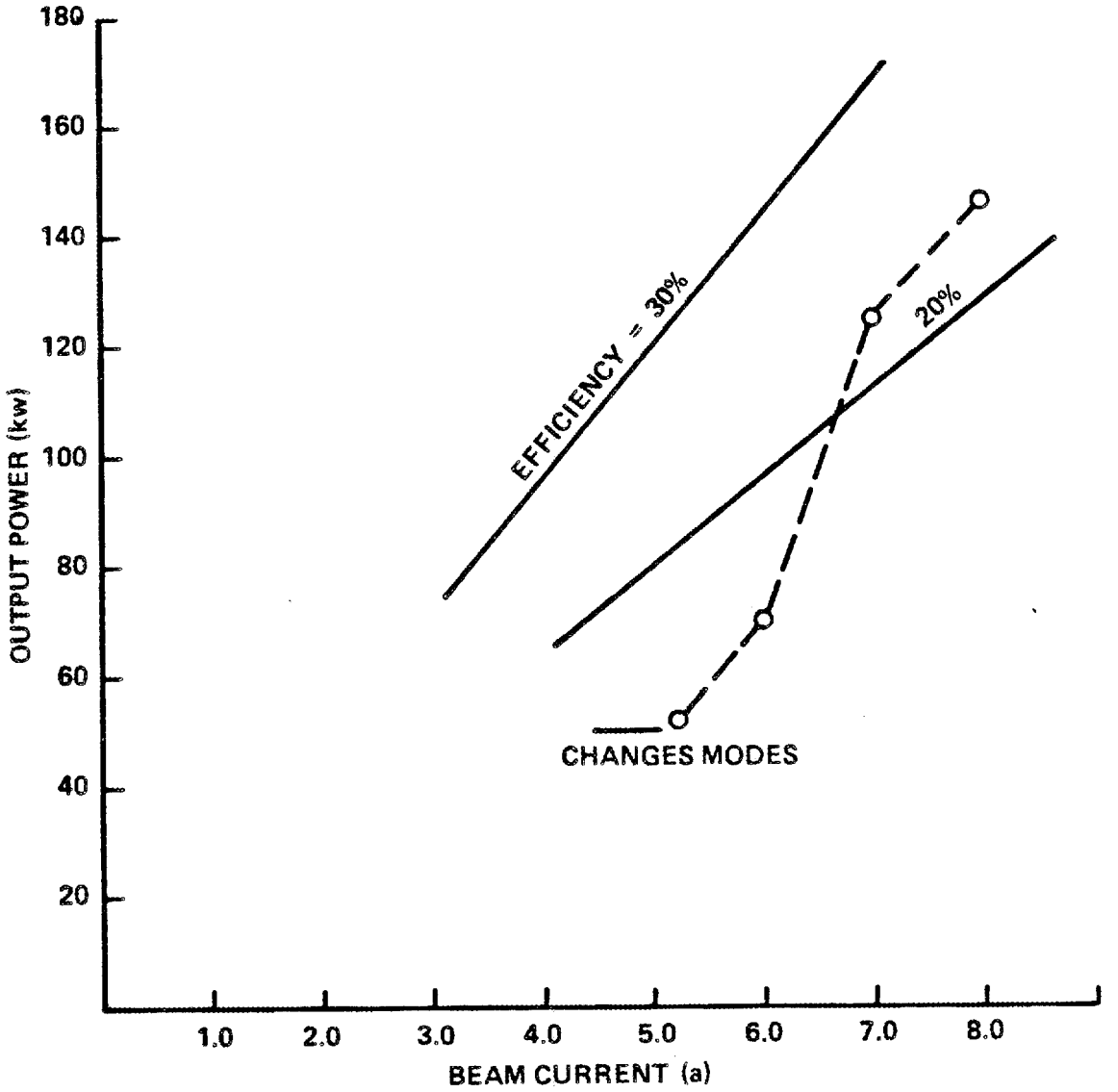

Figure 197. VGA-8000 S/N 8 Power vs Beam Current

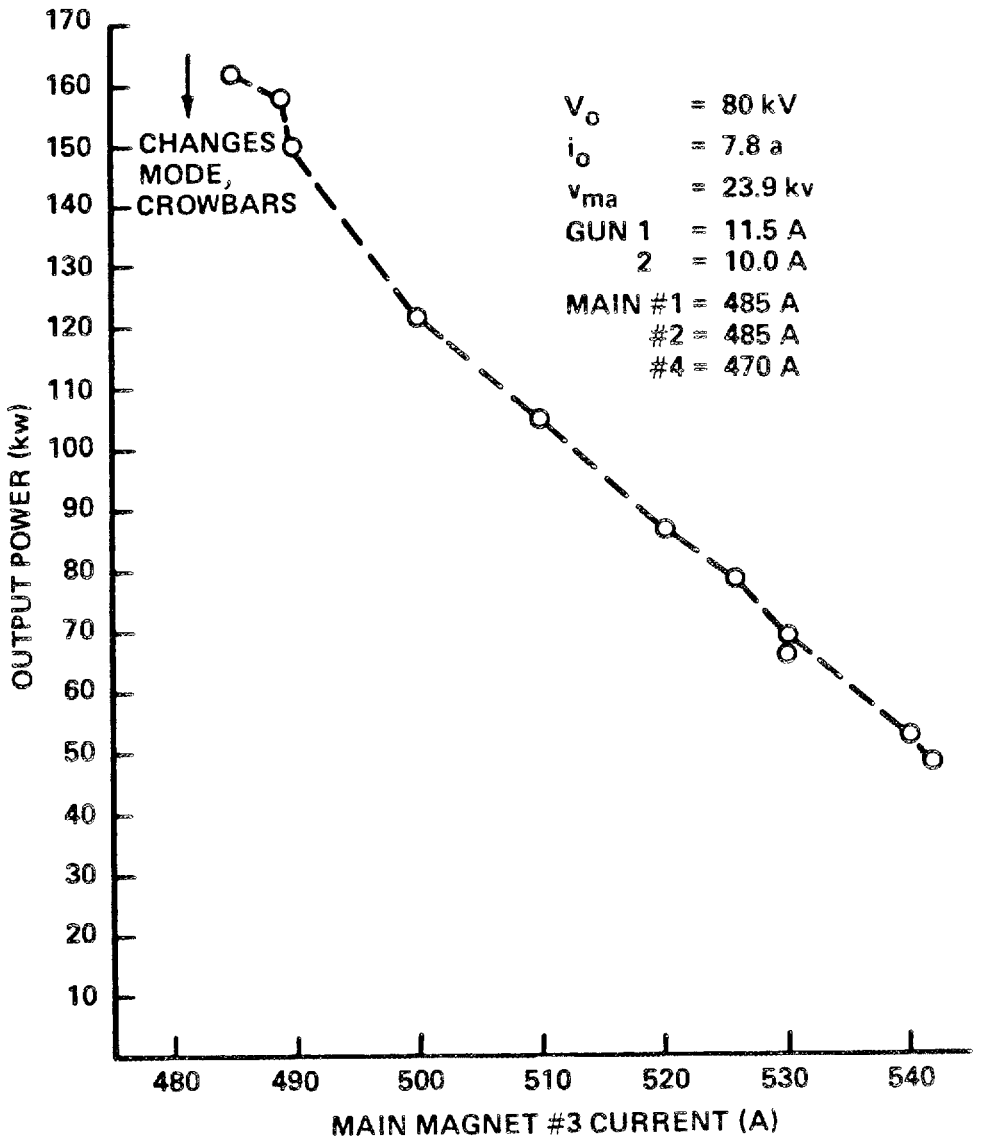

Figure 198. VGA-8000 S/N 8B Peak Output Power Sensitivity to Main Solenoid Magnet Coil No. 3 Current

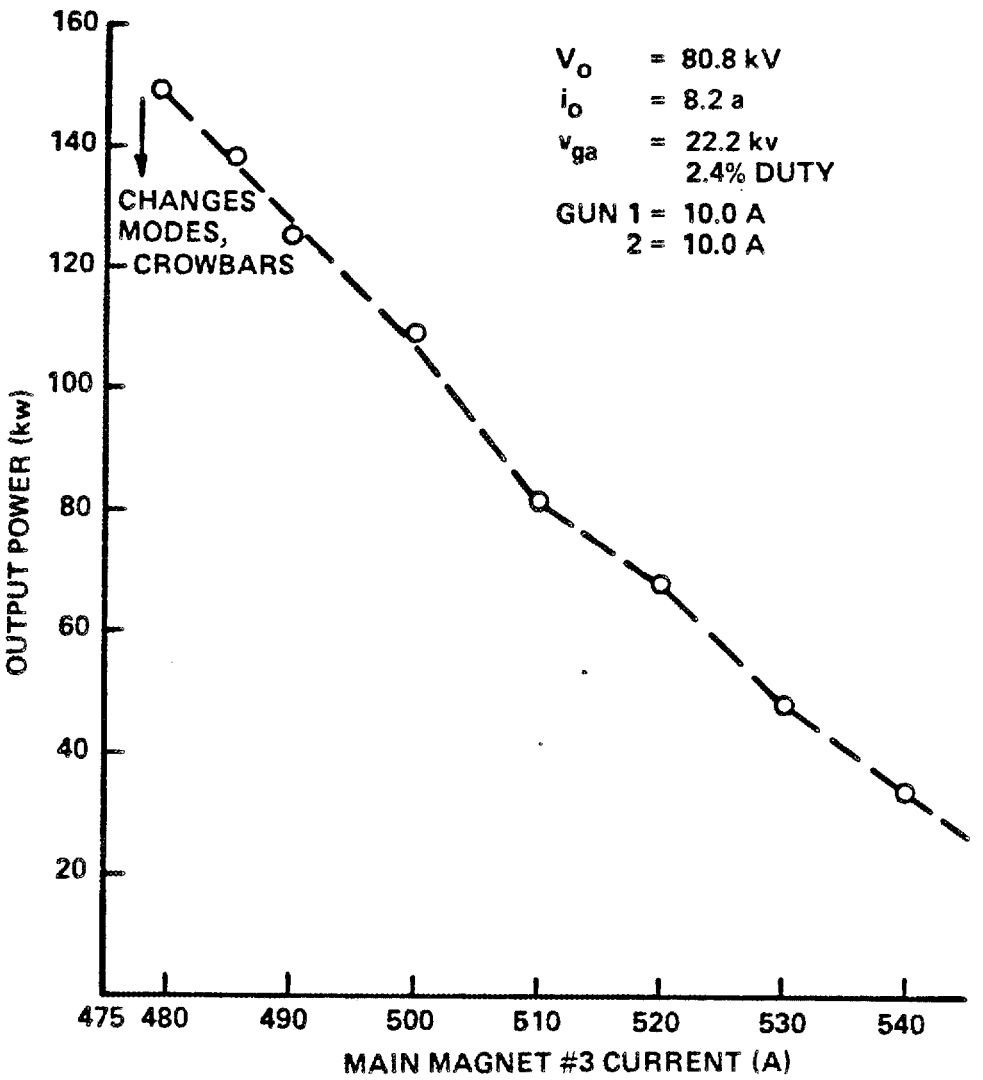

Figure 199. VGA-8000 S/N 8B Peak Output Power vs Main Magnet Coil No. 3 Current with Gun Anode Voltage and Gun Coil Current Changed (V_o = 80.8 kV)

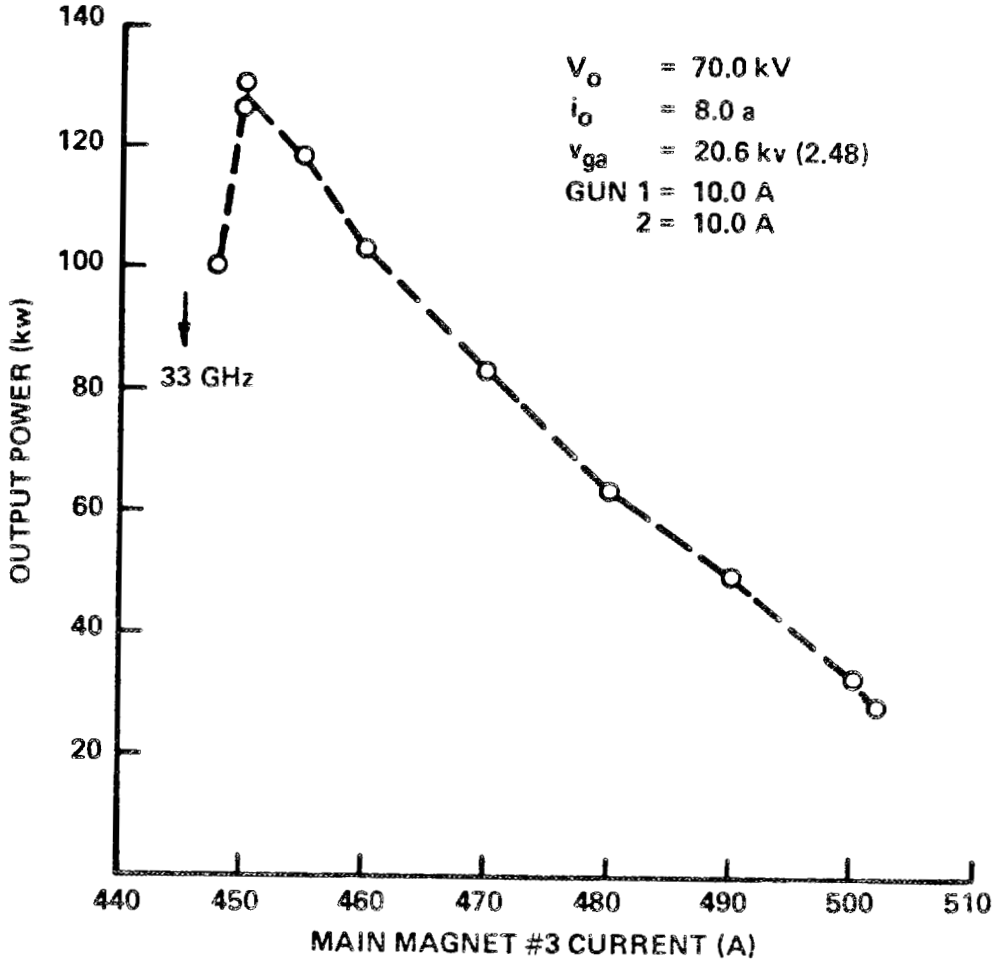

Figure 200. VGA-8000 S/N 8B Peak Output Power vs Main Magnet Coil No. 3 Current with Beam and Gun Anode Voltages Changed (V_o = 70 kV)

Dwg 82-2176 FED

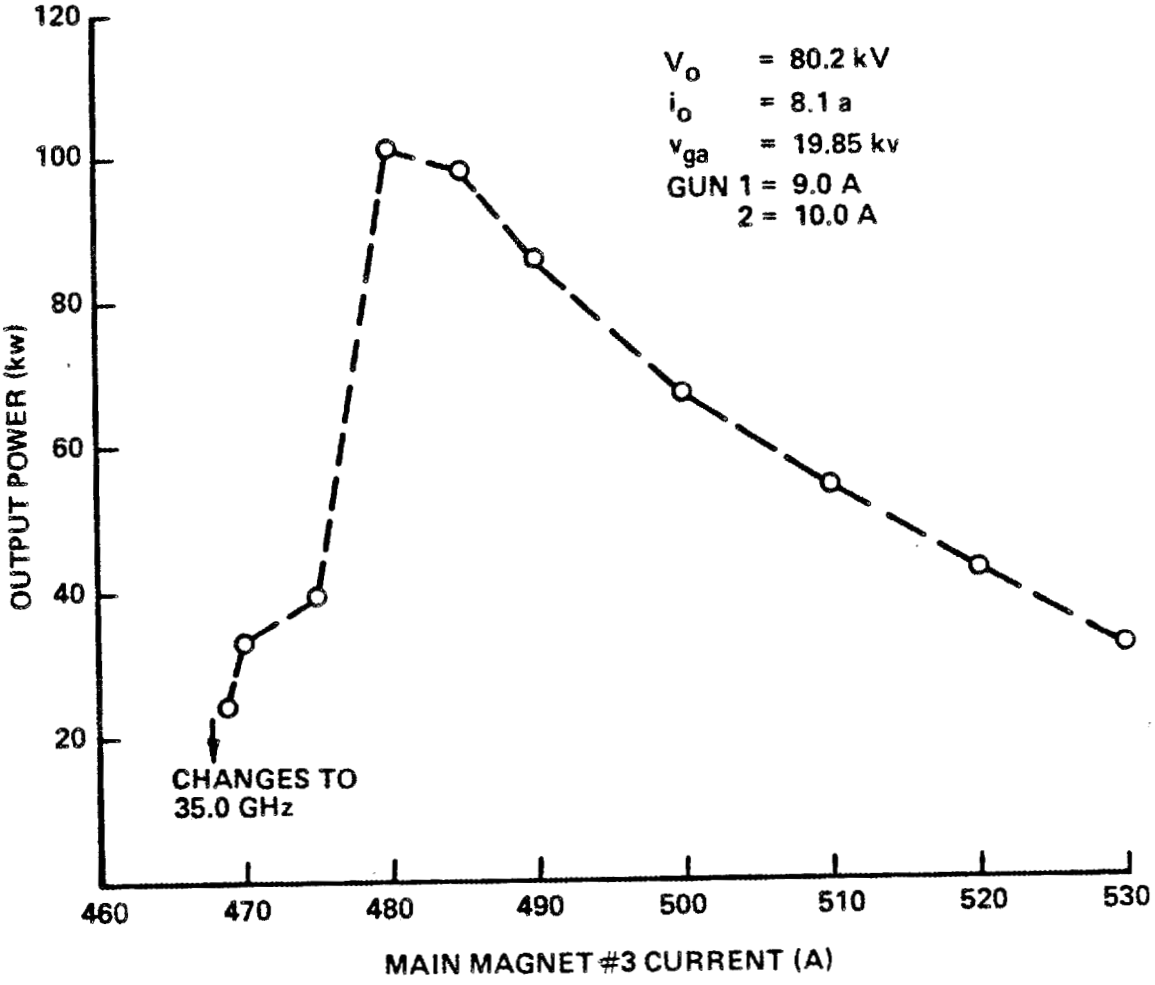

Figure 201. Peak Output Power vs Main Magnet Coil No. 3 Current at Lower Gun Anode Voltage and Gun Coil Current

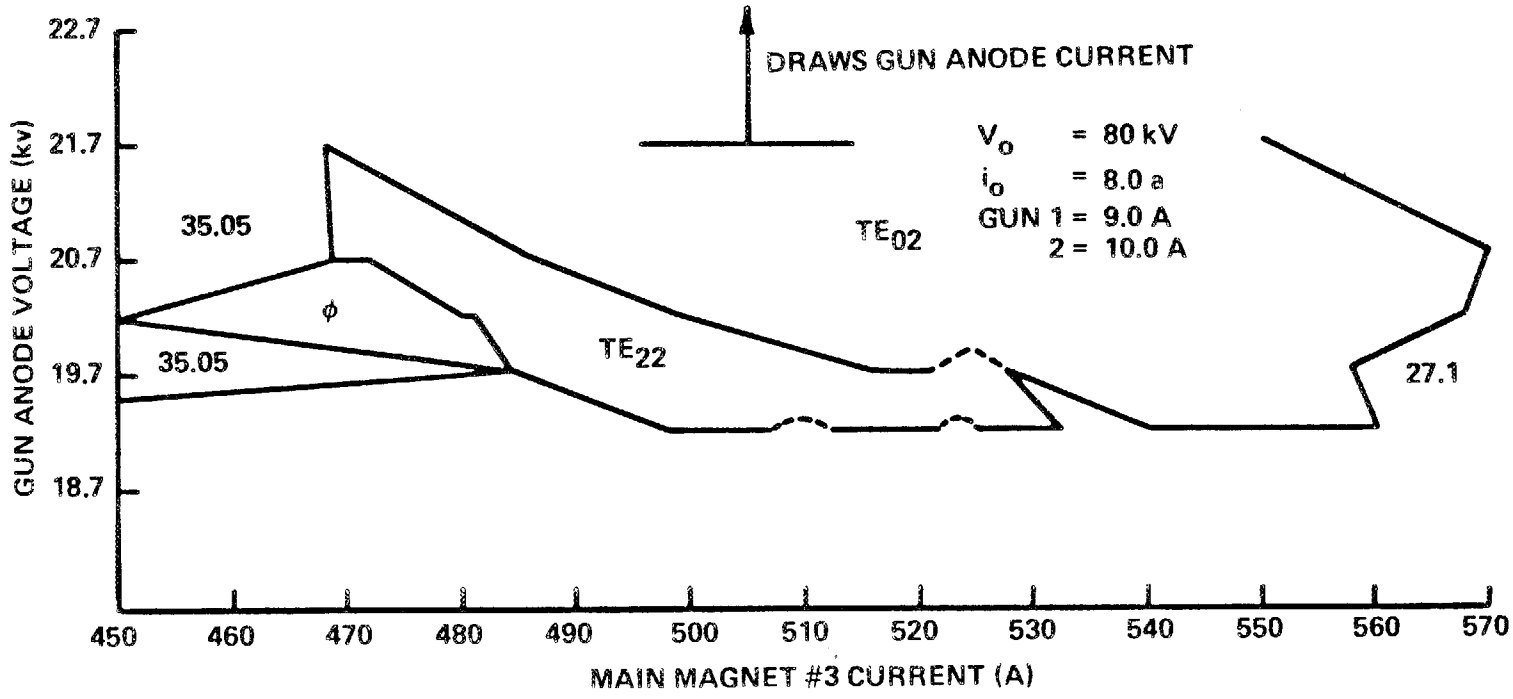

Figure 202. VGA-8000 S/N 8B Pulsed Oscillation Map with Gun Coil No. 1 Current = 9A

Dwg 82-2178 FED

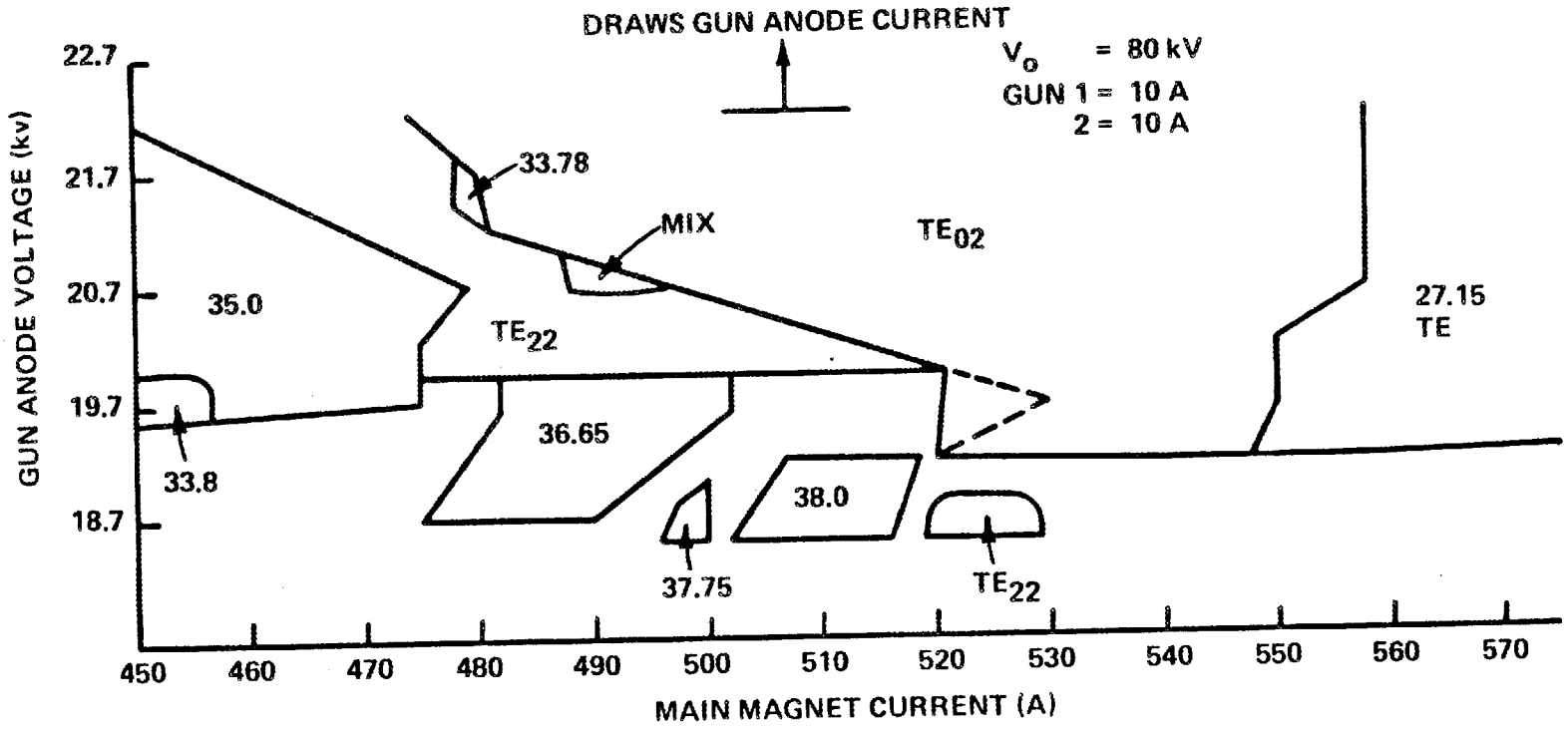

Figure 203. VGA-8000 S/N 8B Pulsed Oscillation Map with Gun Coil No. 1 Current = 10A

These maps point out that the TE_{22} mode has not been eliminated, but that it has been changed. The main difficulty is that in changing the TE_{22} mode, other modes have been introduced or accentuated. It appears that the changes made in this tube have not brought about the desired changes in tube performance.

F. MAXIMUM POWER LIMITATIONS

The VGA-8000 S/N 11 was operated at higher power than any previous gyrotron. A summary of performance data is shown in Table 23. Previous 28 GHz gyrotrons were operated at the 80 kV, 6.25 Amp level with 200 kW output. The beam current was raised to 8 Amps and the output power increased to 260 kW. To get 250 kW output, the beam power was 80.5 kV, 7.4 A with 42% efficiency. Most of the 250-280 kW data were taken at 80.5 - 81.5 kV with 7.4 - 8.25 Amps and efficiencies in the 39% - 42% range. An experiment was performed at this power level to determine the effect of beam voltage versus beam current. The tube was operated at 80 kV, 8.5 Amps and achieved only 272 kW output (40% efficiency). The magnet settings were the same and the tube behaved similarly in both cases. Therefore, with the same beam power, the higher efficiency was seen with higher current and lower voltage.

As seen with earlier tubes, the peak efficiencies of about 50% occurred at 4 to 5 Amps of beam current, but the voltage was always held constant at 80 kV. At 80.5 kV and 7.96 Amps, the output power was 268 kw, which is 41.7% efficient. Table 23 shows the power achieved. All of the high power operation was above 35% efficiency. As can be seen, the ultimate power achieved was 342 kW. This occurred with 84.2 kV, 10.9 Amps input. The operation at this point was not difficult, but at this power level, the air side of the output window broke. The tube operated at 342 kW for 12 minutes before the window broke. The arc detector was tested and found to be working properly. The response time from arc until crowbar was ≤ 6 μs. The tube operated for 1-3/4 hours at 300 kW or greater. At the 309-319 kW level the tube was run for 1 hour without crowbar.

Dwg 82-2179 FED

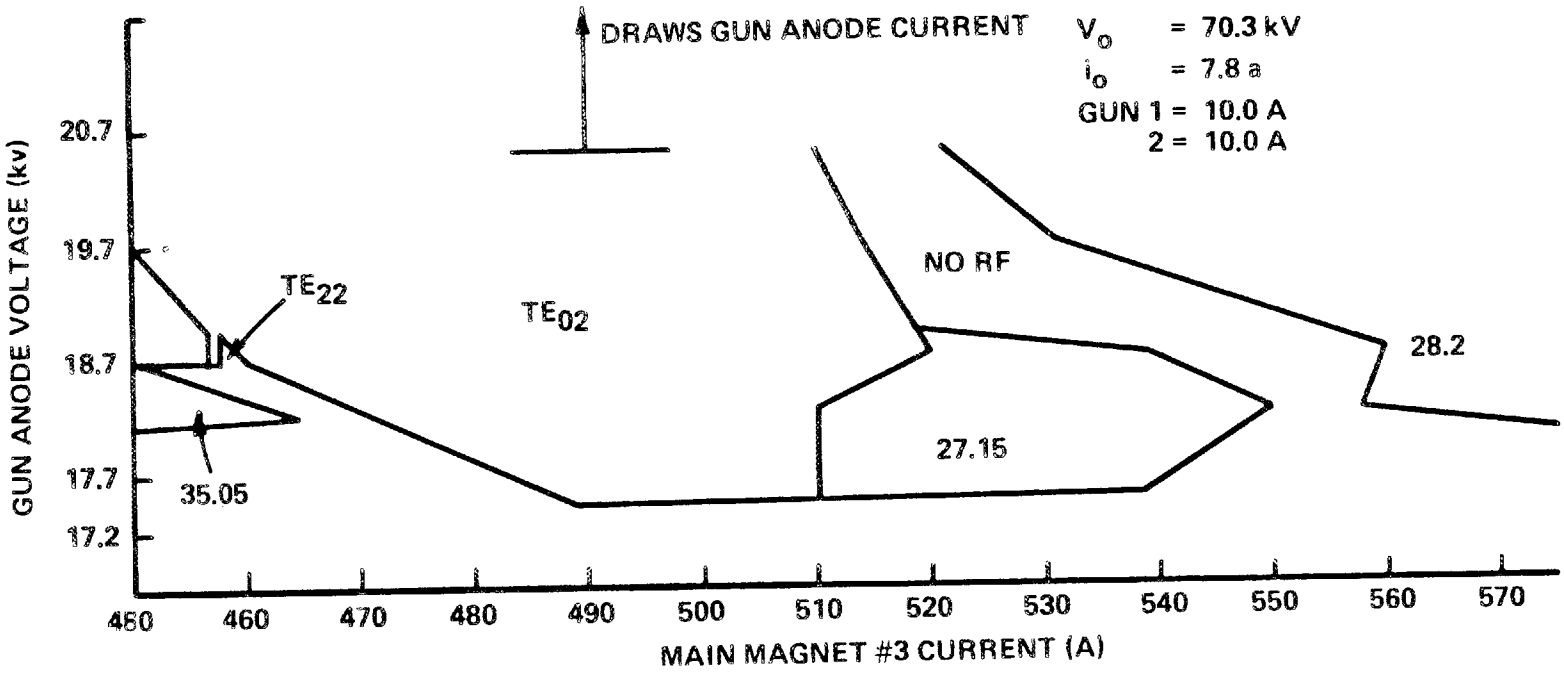

Figure 204. VGA-8000 S/N 8B Pulsed Oscillation Map with Lower Beam Voltage

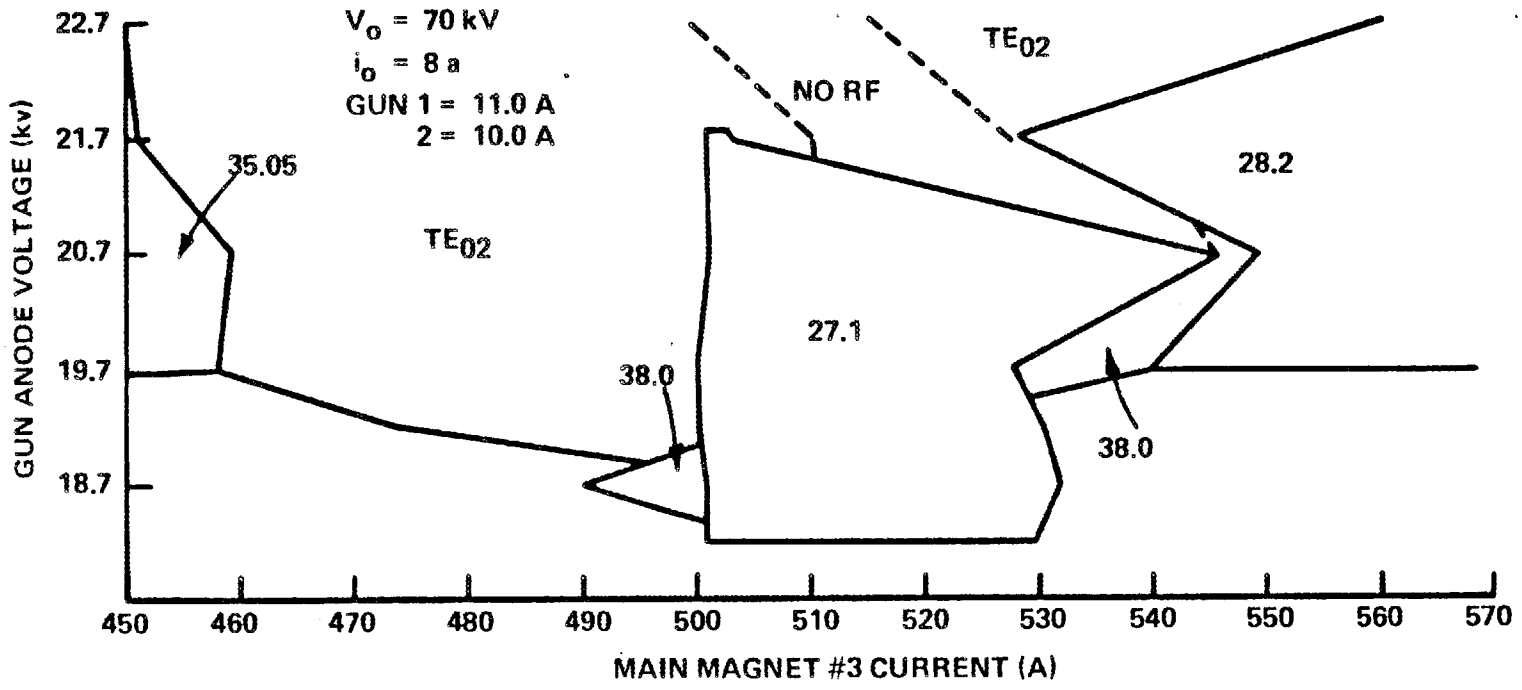

Figure 205. VGA-8000 S/N 8B Pulsed Oscillation Map with Higher Gun Coil Current at 70 kV

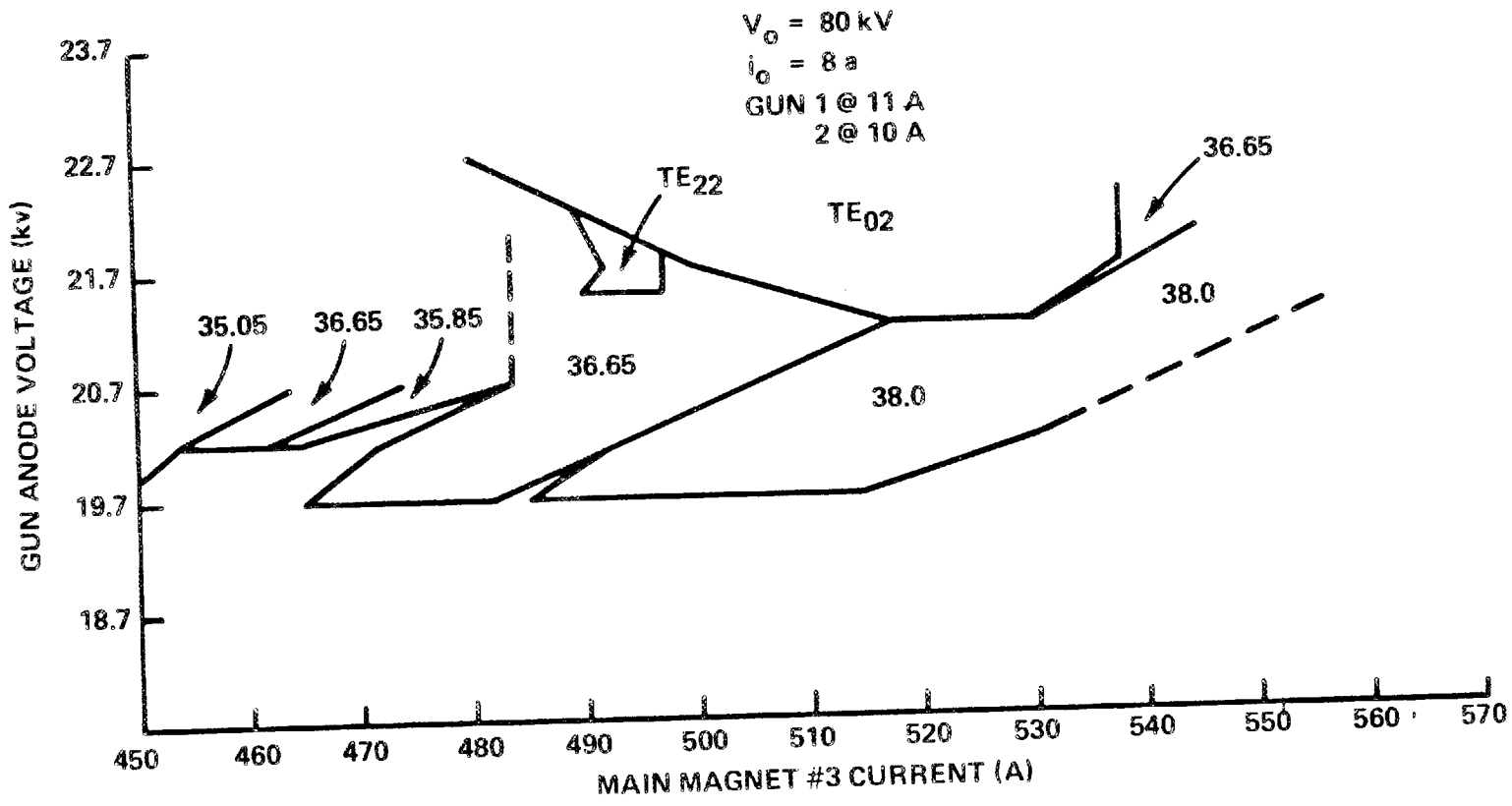

Figure 206. VGA-8000 S/N 8B Pulsed Oscillation Map with Higher Gun Coil Current at 80 kV

TABLE 23 HIGH PERFORMANCE DATA VGA-8000 S/N 11

Output Power [kW]	Beam Voltage [kV]	Beam Current [A]	Efficiency	Gun Anode Voltage [kV]	Power Losses		Frequency [GHz]
					FC-75 [kW]	Collector Seal [kW]	
342	84.2	10.9	37.2%	27.2	1.6	2.5	27.882
322	82.4	11.15	35.0%	25.9	1.6	1.6	27.880
*319	82.0	10.38	37.4%	25.8	1.5	1.6	27.880
*309	82.2	10.2	36.8%	25.8	1.5	1.8	27.880
282	80.7	8.45	41.4%	25.9	1.5	4.3	27.878
268	80.5	7.96	41.7%	25.9	1.4	3.8	27.880

*Ran for one hour without crowbar.

During the high efficiency operation, there was a detectable level of rf in the gun region. This rf was of the same frequency as the output rf. The rf appeared at all voltage and current levels whenever the main magnets were lowered to achieve high efficiency operation. This usually correlated with an increase in the collector seal heating. It appears that in tuning for maximum efficiency there is a greater mismatch in the output, which allows more mode conversion. At the 342 kW level, there was a large amount of rf in the gun region. This would possibly prohibit a large increase in power above the 324 kW level.

The tube was still under vacuum at the end of the behavior study and was available to Department of Energy programs.

G. CATHODE INVESTIGATION

Discussions were held with those involved in cathode design at Varian. Some data were obtained on results from the cathode study programs at Varian and elsewhere. The M-type and mixed-metal matrix cathodes appear to be worthy of investigation. They can have lower work functions than the barium cathodes as well as higher emission density with good life. The M-type cathodes typically seem to have a more uniform surface emission, which is good for lower velocity spread due to surface roughness and spotty emission.

A more thorough study could be made by building an Auger microscope and observing the uniformity of emission. This could be done on a modest budget; but the real question arises in the velocity spread. This measurement would require building a good beam analyzer. At the moment, none exists for magnetron injection guns and construction of a beam analyzer would require a substantially large budget.

Heater temperature data have been taken for the new K-8002 gun. To obtain 1000°C temperature at the cathode, the heater temperature must be 1800°C. This exceeds the temperature considered good for long life cathodes. For this reason, it appears best to use the K-8000 gun, with a potted heater, for the tubes to be used in plasma experiments.

The Behavior Study Investigation was to accomplish four main goals. One goal was to determine the ultimate power capacity of the VGA-8000 tubes. This goal was accomplished when tube No. 11 was successfully operated at 342 kW, CW. A second goal was to improve stability and starting characteristics of gyrotrons. This was partially accomplished with the development of oscillation maps to better control the turn-on procedures of gyrotrons. Work was also done to improve the design of high power windows, as well as to collect a large data base for future gyrotron development. A third goal was to minimize gun arcing and decrease tube processing time. Diagnostics were developed to determine the types of arcs occurring. These arcs were primarily gun anode to ground, during the pulse. The voltage gradients and gun pressure were checked and no problems were found. Using a residual gas analyzer, it was determined that the tube processing time in test could be reduced by better bakeout procedures. This has been shown to be correct in subsequent tubes. The fourth goal was to improve mode purity. Computer analyses and cold tests were done to achieve this goal. In tube tests it was found that the cavity design of tube No. 8 introduced or enhanced other modes than those seen in the regular cavity. Although these tests did not result in significant improvements to mode purity, they did provide useful design information.

VIII. 60 GHz 200 kW CW OSCILLATOR

With the exception of the collector and window, the design of the pulsed oscillator was suitable for CW operation. The design of these two important assemblies for CW operation is discussed in this section.

A. COLLECTOR

1. Mode Conversion

a. Taper Design for 4-Inch Diameter Collectors

Measurements on X-6, which will be described later in this report, indicated that mode conversion to TE_{01} and TE_{03} was unacceptably high in the X-6 design for use in pure mode ECH systems. A comparison with pulsed tube results, which will also be discussed, suggested that a major portion of the mode conversion took place in the collector tapers. A computer code, called TAPER, based on two-mode coupled telegrapher's equations, was used to calculate mode conversion in the X-6 collector. The results in Figures 207 and 208 show that significant mode conversion does indeed occur in the collector taper sections. A redesign of the collector taper was performed to limit the output TE_{01} and TE_{03} mode conversion levels to $\leq$ 16 dB, similar to the levels that might arise from assembly tolerances. Other design criteria included: 1) limit maximum tube length to the present CW tube length, 2) make the collector section as large in diameter as possible, and 3) check the bandwidth to determine sensitivity to frequency scaling.

A mode conversion analysis was performed using TAPER, with the Gaussian up and down taper sections replaced with simple linear 5° tapers. The results, depicted in Figures 209 and 210, showed mode conversion was still severe. A reduction in the angle of the linear taper to about 2° would decrease the mode conversion level to an acceptable value at the expense of greatly increasing the tube length or reducing the diameter of the collector. Thus, a complex nonlinear taper was considered.

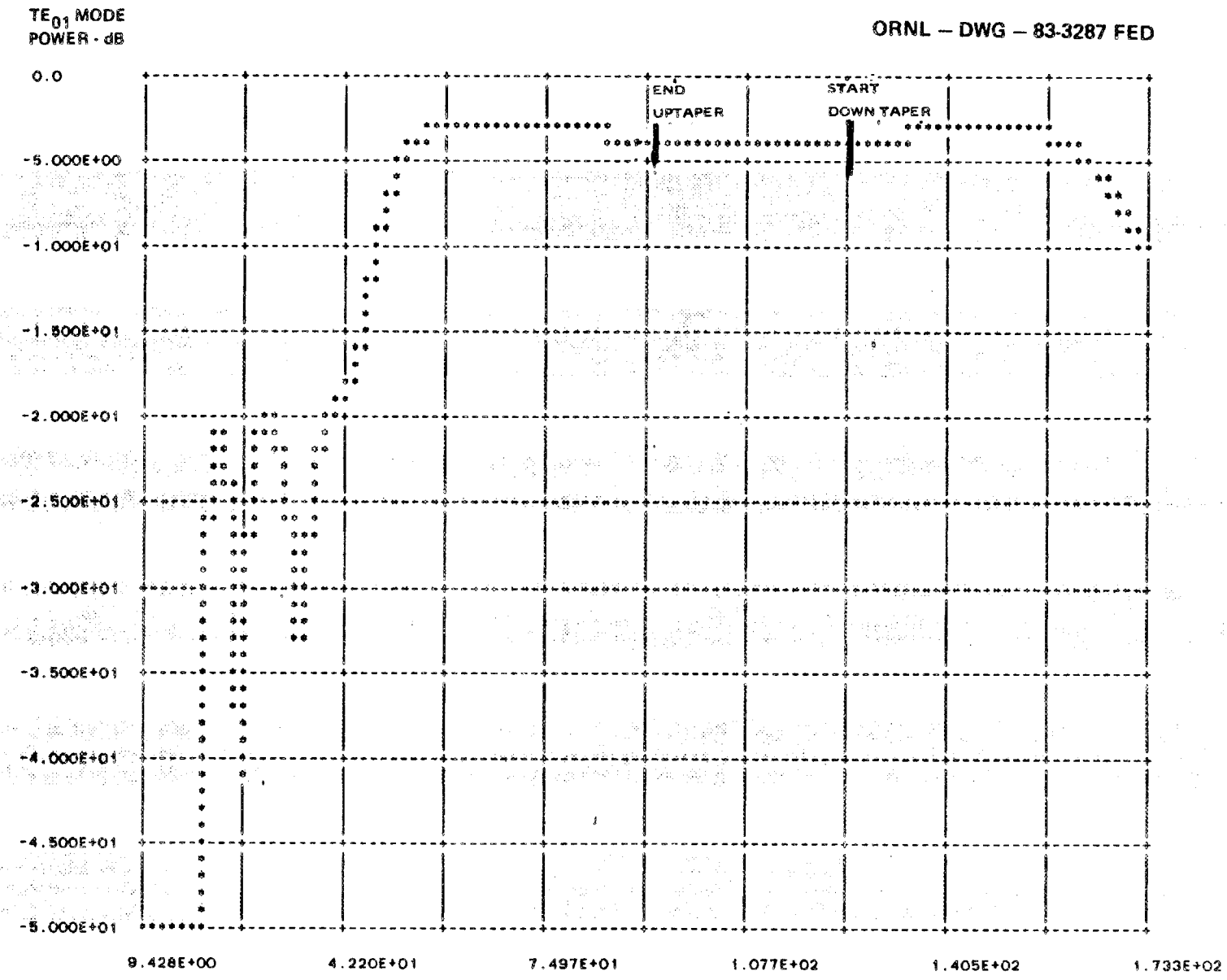

Figure 207. Mode Conversion in the X-6 Collector at 60 GHz Calculating Conversion of TE_{02} to TE_{01} Using TAPER

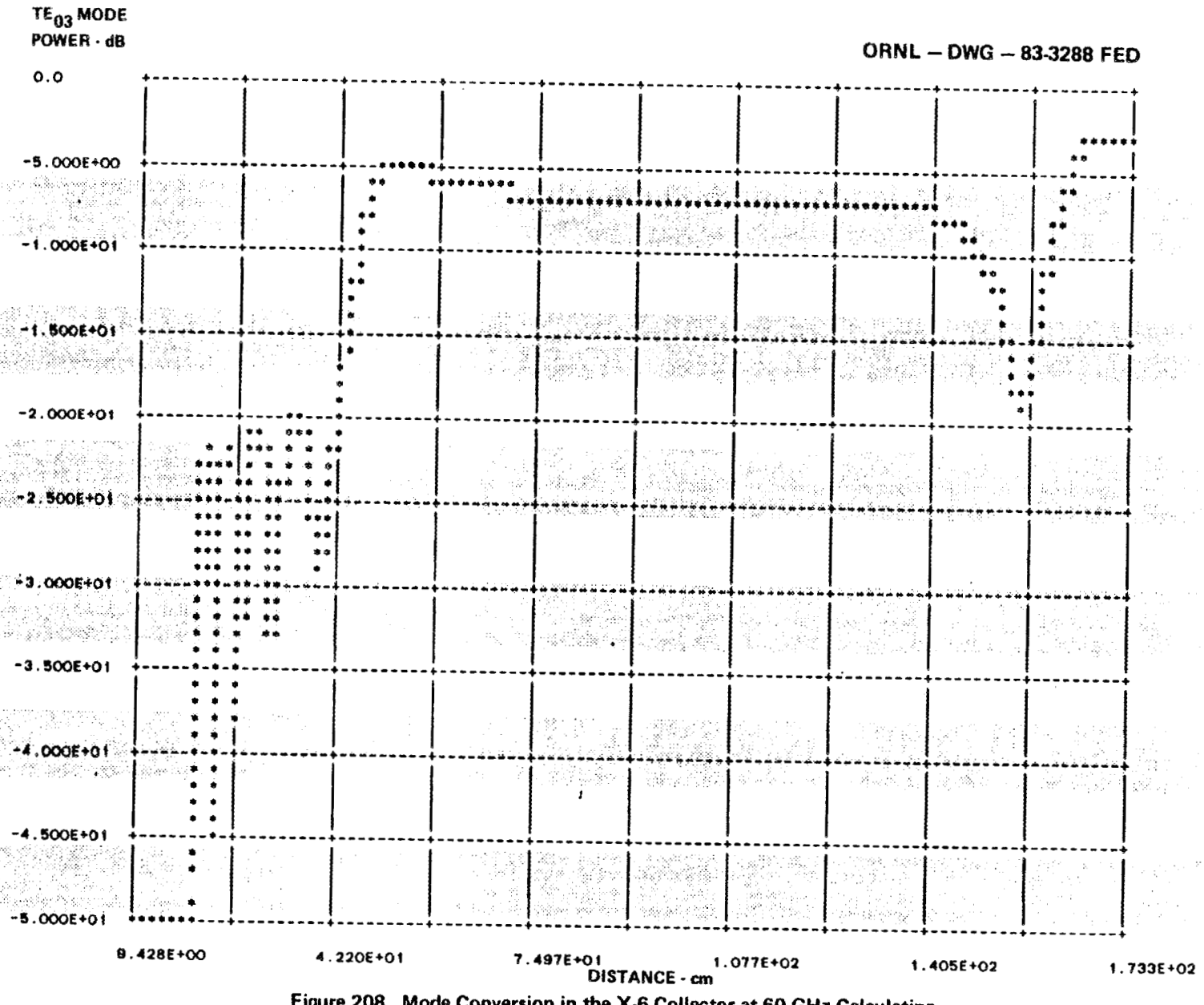

Figure 208. Mode Conversion in the X-6 Collector at 60 GHz Calculating Conversion of TE_{02} to TE_{03} Using Taper

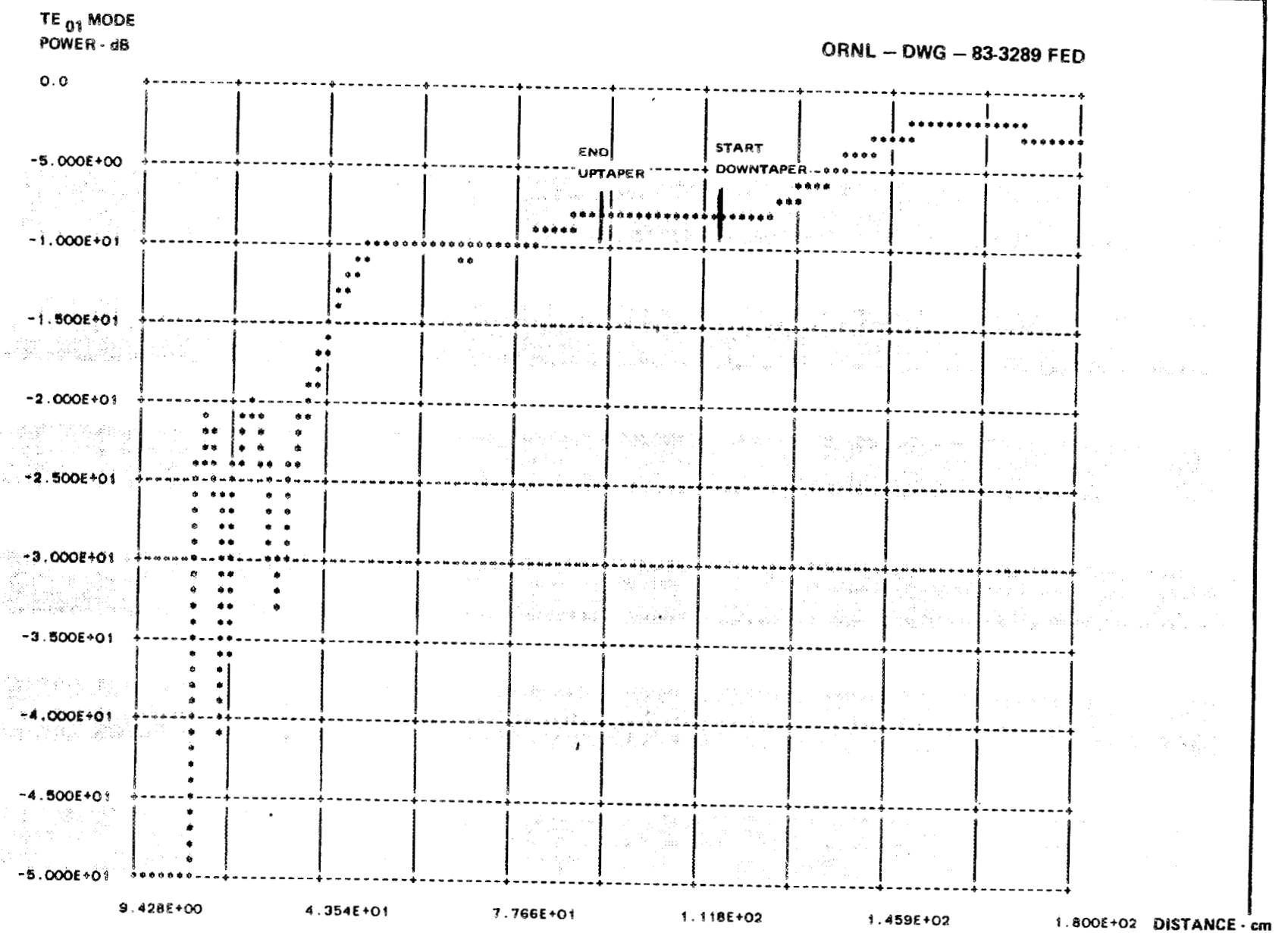

Figure 209. Mode Conversion in 5" Diameter Collector with 5° Linear Tapers at 60 GHz Calculating Conversion of TE_{02} to TE_{01} Using TAPER

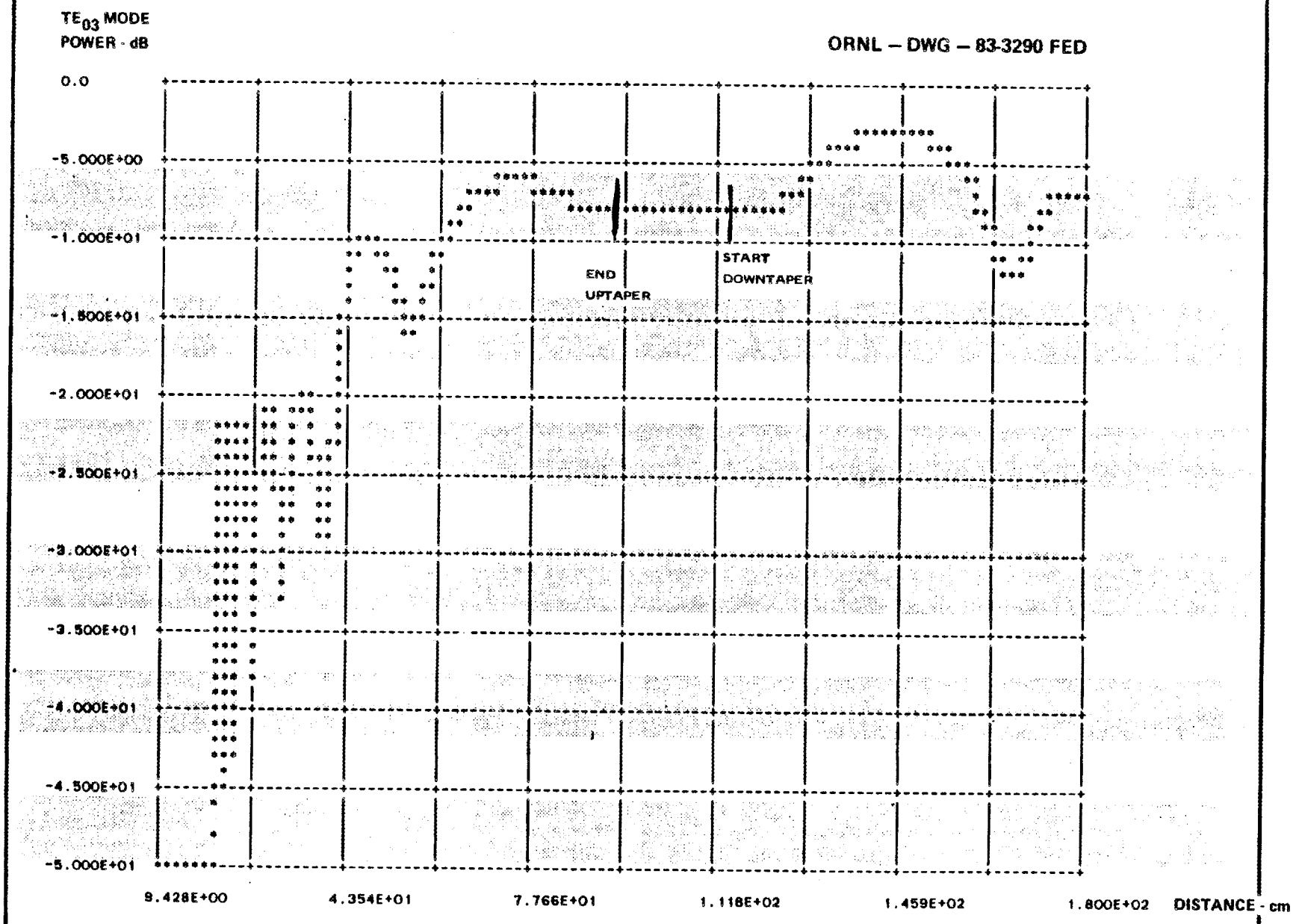

Figure 210. Mode Conversion in 5-Inch Diameter Collector with 5° Linear Tapers at 60 GHz Calculating Conversion of TE_{02} to TE_{03} Using Taper

Based on analyses by Unger[40] and Tang[41], a 4-inch diameter collector design was developed that satisfied the above constraints.

Figures 211 and 212 show the conversion of the TE_{02} mode to TE_{01} and TE_{03}, respectively, for the new 4-inch collector design. Note the single peaks in the up and down tapers that show conversion and reconversion. For the region in which mode conversion is -10 dB or higher, the two-mode assumption made in the analysis may be violated. Since these regions are reasonably short, conversion into modes other than the two considered is probably still low, and the results of the calculation should be reasonably valid. Calculations using the two-mode analysis for TE_{02} to TE_{04} (which show low final conversion levels) are not valid since similar amounts of conversion may develop via the $TE_{02} - TE_{03} - TE_{04}$ route. The bandwidth of the collector is excellent from 50 - 64 GHz for -16 dB TE_{01} or TE_{03} mode conversion levels.

The 4-inch diameter collector has the advantage of having lower power densities than the 2.5-inch diameter collector, assuming proper contouring of the magnetic field. A design refinement was pursued to improve the mode purity of the initial 4-inch design.

The analysis of mode conversion in the 4-inch collector was performed using TAPER. Reflections in the tapers, beam-induced perturbations, and window reflections or mode conversion are not included in the calculations. Also, TAPER calculations assume a pure TE_{02} mode coming out of the cavity. However, previous agreement between TAPER, OPENCAV and actual mode purity measurements gives good confidence in the accuracy of the results when mode purity is high. A new 4-inch design (design II) achieved the following output: 3.5% TE_{01}, 94.4% TE_{02} and 2.0% TE_{03}. To illustrate the bandwidth of the design II, a graph of the mode conversion level of the TE_{01}, TE_{03} and TE_{04} modes as a function of frequency is shown in Figure 213. Note that total mode conversion actually decreases at lower frequencies with a minimum at about 53 GHz.

The physical length of the design II 4-inch diameter collector is a few inches longer than the collector length between the lower

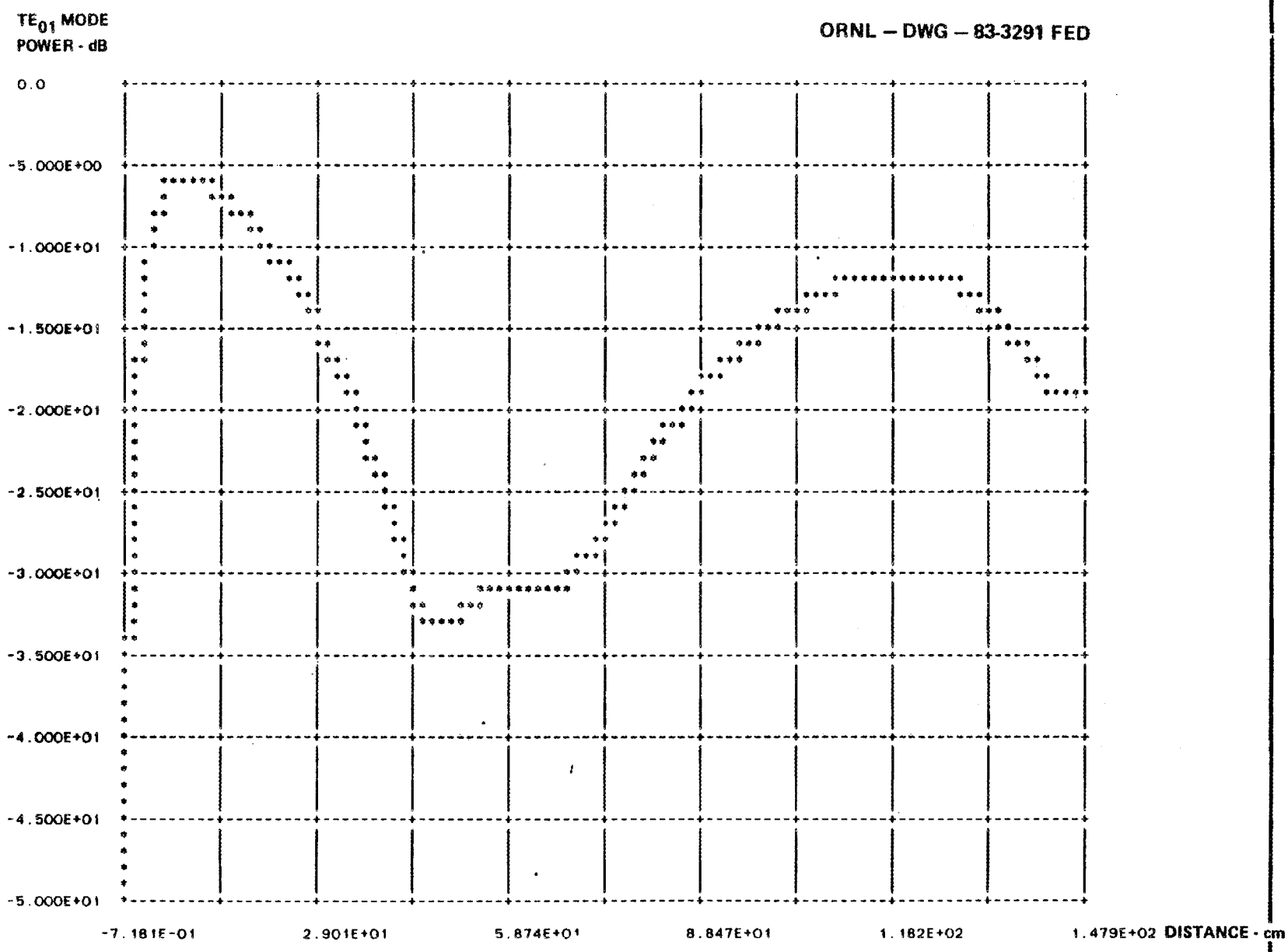

Figure 211. Mode Conversion in 4" Diameter Collector with Curved Tapers at 60 GHz Calculating Conversion of TE_{02} to TE_{01} Using TAPER

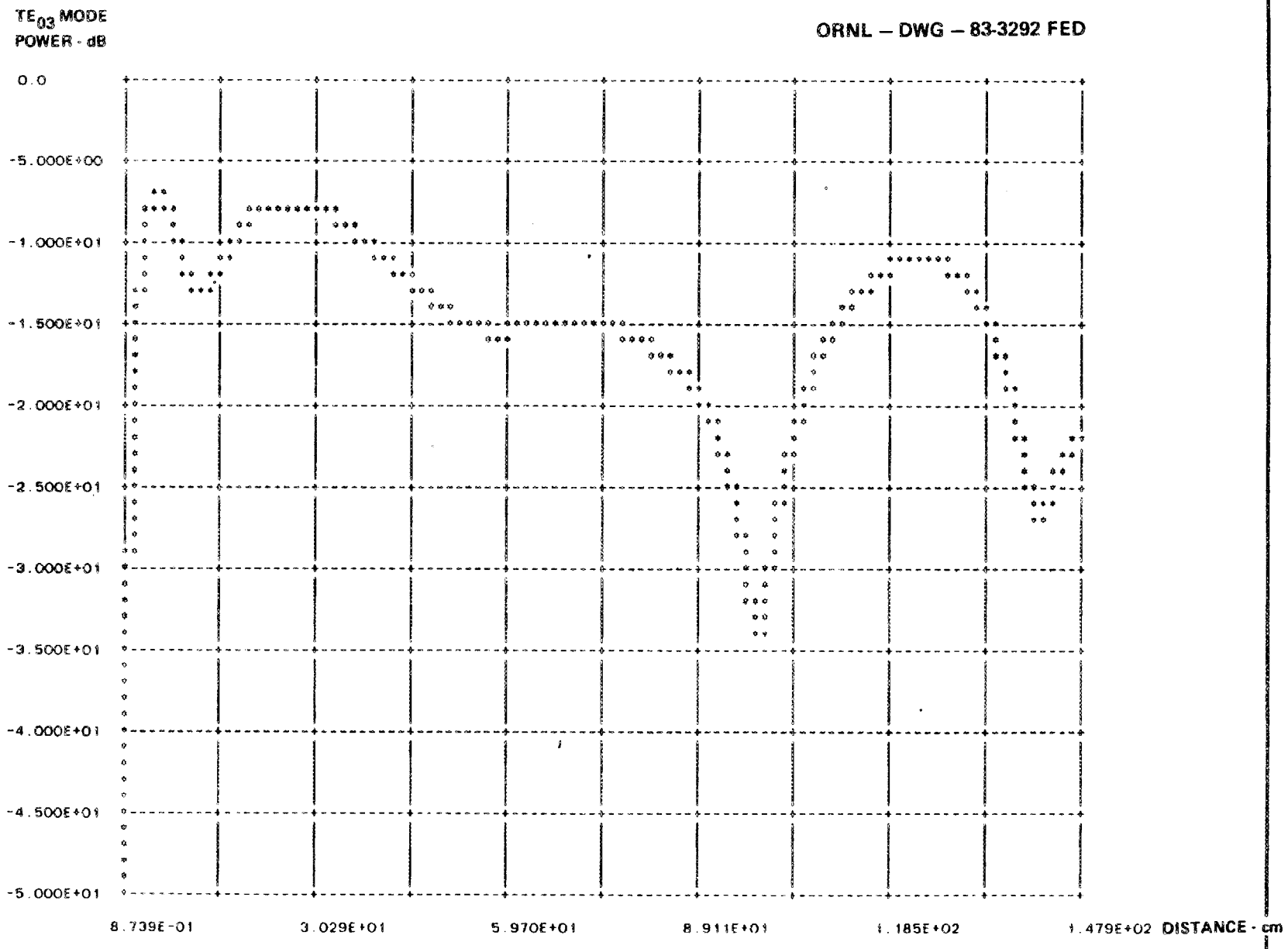

Figure 212. Mode Conversion in 4" Diameter Collector with Curved Tapers at 60 GHz Calculating Conversion of TE_{02} to TE_{03} Using TAPER

and upper seals on X-6. Incorporation of this design would require relocating the upper seal. Alternatively, Figure 213 suggests that one might take advantage of the mode conversion minimum at 53 GHz and shift it in a new design to 60 GHz. Further work to decrease the length of the collector would be required to incorporate the 4-inch design without changes in tube length.

A four-inch collector was designed to match the original lower seal diameter as on X-6. This would facilitate retrofits while maintaining the high mode purity and length requirements. TAPER calculations included the cavity 5° output taper followed by a 2° taper to the lower seal. The nonlinear uptaper was then matched at the lower seal by diameter and slope. This resulted in an excellent mode purity at 60 GHz: 96.8% TE_{02}, 0.8% TE_{01}, 2.1% TE_{03} and 0.3% TE_{04}. Final drawings on the 4-inch collector were halted by agreement with ORNL.

Modifications of the mode probe to minimize reflections and improve resolution have yielded a significant improvement. This work was performed concurrently with the 4-inch diameter collector to permit cold testing of a high mode purity collector.

This work was also halted by agreement with ORNL.

b. <u>2.5-Inch Diameter Collector</u>

Calculations on linear tapers used between the interaction cavity and 2.5-inch diameter collector have been performed using the OPENCAV code. OPENCAV is a finite element code which solves for the complete electric and magnetic fields at every point. Unlike TAPER, OPENCAV is valid with multiple modes and large amounts of mode conversion, but it is a difficult and time-consuming code to use, and until recently was not capable of calculating over large volumes compared to a wavelength. The linear tapers generate less mode conversion; however, their disadvantage is that they are generally longer than tapers having more complex shapes. In the case of the present gyrotrons, a 2° linear taper can satisfy the

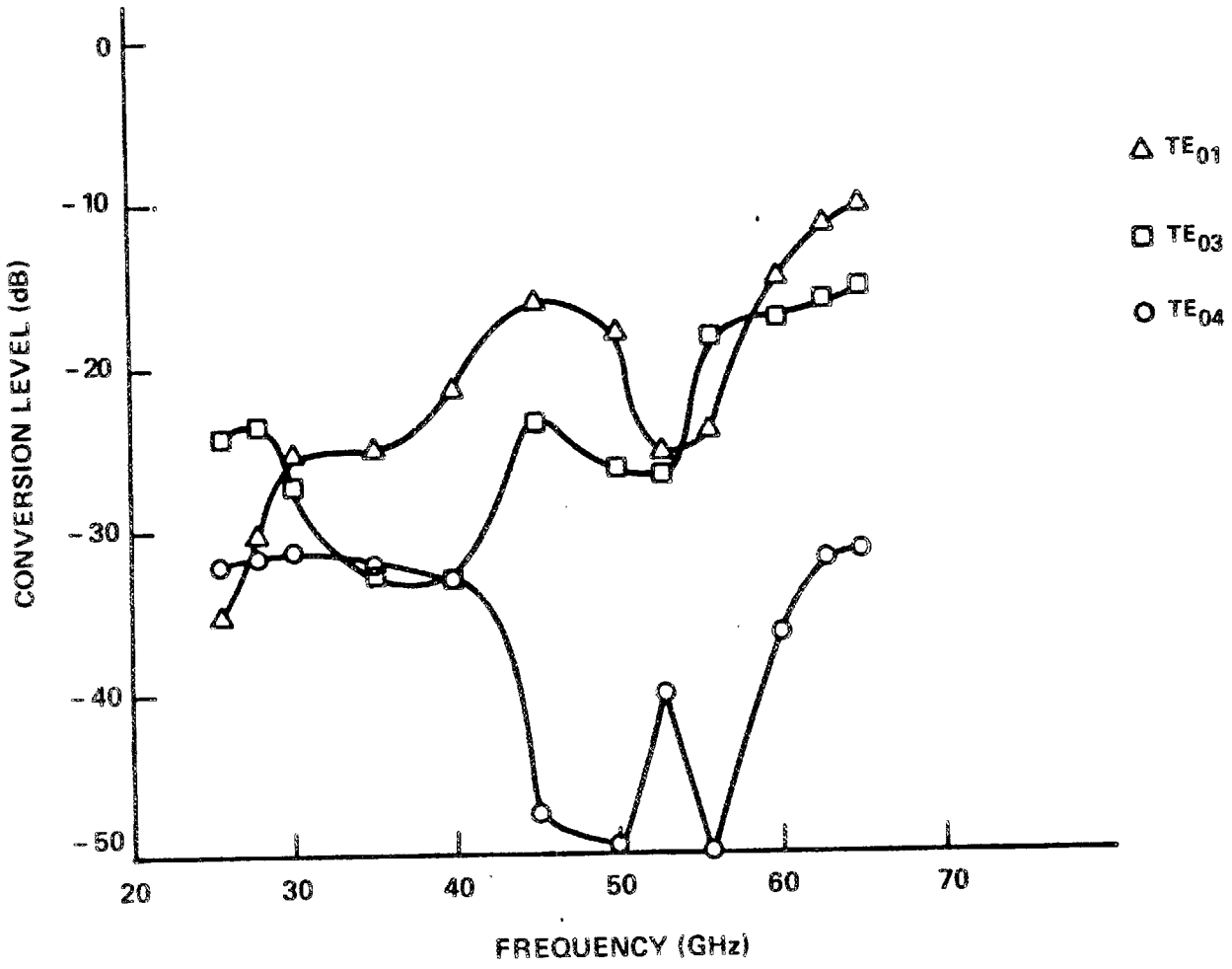

Figure 213. Mode Conversion Levels of 4" Collector Design No. 2

requirements of overall length and low unwanted mode content, provided the collector diameter is not greater than 2.5 inches.

The taper design, which has been analyzed in detail, starts at the radius of the interaction cavity, R = 0.564 cm, shown in Figure 214, and the taper radius increases linearly up to the interaction section, at which point the profile follows a circle section of large radius to blend to the 3.175-cm radius output guide. With the radius of curvature R = ~115 cm, a 4 cm long section makes a smooth transition.

The design in Figure 214 was used for mode conversion calculations up to the total length of 76.81 cm. The results of the calculations are shown in Table 24. The table shows the amount of mode conversion to various TE_{0m} modes with the calculation terminated at several different lengths along the collector in order to determine mode content at various positions. The resonant frequency of the system changes by a very small amount, depending on the length, as noted in the first column in the table.

Table 24
Calculated Mode Conversion at Several Z Positions
in 2.5-Inch Diameter Collector with Linear 2° Taper
(Using OPENCAV)

F (GHz)	TE_{01}	TE_{02}	TE_{03}	TE_{om} (m>3)	Z (cm)	R (cm)
60.085	1.82	98.18	0	0	5.967	0.6786
60.08	1.72	98.28	0	0	9.3457	0.7948
60.0734	3.8	96.03	0.14	0.0044	22.86	1.2614
59.9565	0.98	94.5	3.6	0.92	76.81	3.175

The content of the TE_{01} mode in this design does not exceed 1% at a z position of 76.81 cm (in the output waveguide). The TE_{03} mode and higher order mode content does not exceed 5% of the total power, while the content of the TE_{02} mode is over 94%.

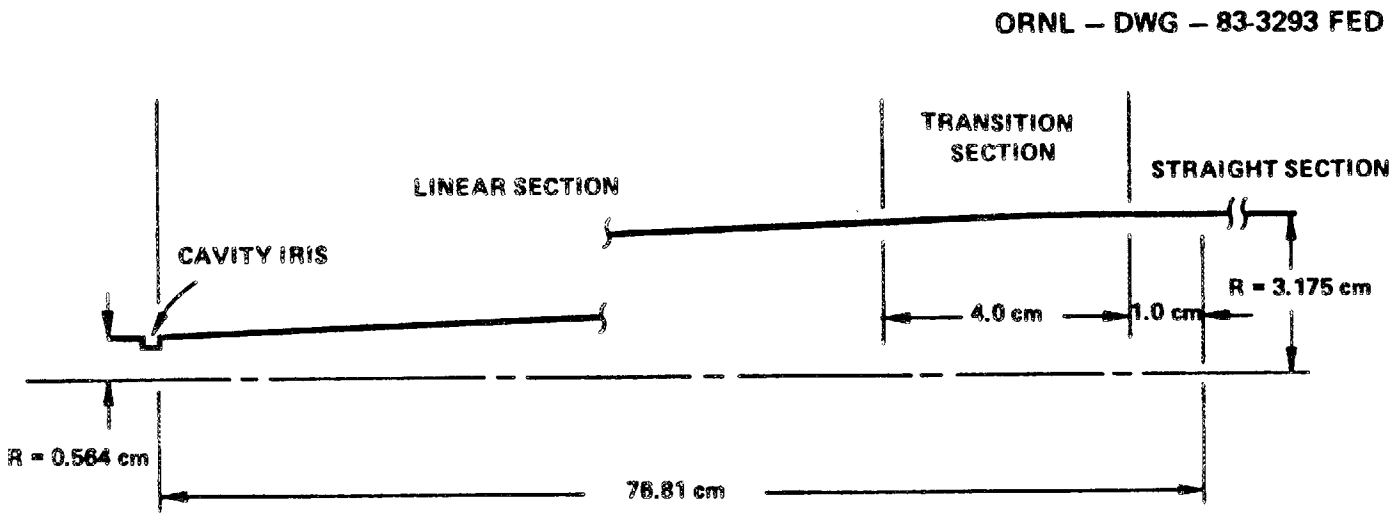

Figure 214. Collector with 2° Linear Up-Taper

The calculations were done for both a tapered and a step cavity followed by a 2° linear taper. There were no substantial differences between the two cases.

If the beam is allowed to follow the natural fringing field of the solenoid, the 2.5-inch diameter collector has a marginal safety factor for beam power dissipation on its wall, with respect to the maximum allowable for CW beams or pulses longer than 100 msec.

Mode content measurements indicated that mode conversion was much more severe in CW tubes with the five-inch diameter than in pulse tubes. The two major differences between these tubes are the collector and window designs.

Table 25 summarizes the mode content measurements taken to date. Comparison of X-6 and X-8 suggests that most of the mode conversion seen in the CW tube X-6 is due to the nonlinear tapers used in the 5-inch collector section. Comparison of X-8 and Culham tubes in Table 28 suggests that the CW double-disc window could be responsible for about 10% mode conversion. However, the number of measurements was too small to draw a firm conclusion.

Table 25
60 GHz Gyrotron Mode Content Measurements

Tube	Duty	Collector Diameter	Cavity	Window	Mode Content %		
					TE_{01}	TE_{02}	TE_{03}
X-6	CW	5"	Complex	Double-Disc	38±3	12±4	50±9
X-8	CW	2.5"	Complex	Double-Disc	12±3	85±5	3
Culham	Pulse	2.5"	Complex	Single-Disc	4	94±1	2
G1/G2	Pulse	2.5"	Tapered	Single-Disc	3	96±1	1

Previous calculations for the complex and tapered cavities showed both had mode purity greater than 98.5% TE_{02}, in good agreement with the results for Culham and G1/G2.

Table 26 shows the calculated mode conversion in the 5-inch collector with non-linear tapers used in X-6. Cases 1, 2 and 6 were done with the computer code TAPER, which solves the telegrapher's equations. This code was recently upgraded to handle 20 modes. TAPER does not account for the presence of the cavity, collector seal gaps, waveguide and window reflections and beam-induced effects. These simplifications are probably the source of the disagreement between cases 2 and 3.

Table 26
Mode Content of the 5-Inch Collector

Case	Technique	Mode Content (%) TE_{01}	TE_{02}	TE_{03}	TE_{04^+}
1	2-Mode TAPER	11	38	50	ϕ
2	20-Mode TAPER	25.6	6.5	43	24.6
3	Measured W/W.G. Couplers	38±13	12±4	50±9	<1
INTERMEDIATE CALCULATIONS					
4	1-Step OPENCAV	37.4	2.1	41.6	18.9
5	4-Step OPENCAV	40.8	9.3	24.4	25.5
6	5-Step OPENCAV	38.6	14.1	20.1	27.1
7	20-Mode TAPER	35.3	19.3	15.0	30.4

Case 3 gives the mode content of X-6 as measured using waveguide couplers borrowed from GA Technologies. The help of Dr. Charles Moeller of GAT is gratefully acknowledged.

Cases 4, 5 and 6 were calculated using the finite-element code OPENCAV. OPENCAV models the cavity and waveguide system, but still does not account for collector seal gaps, window reflections or beam-induced effects. The mesh size necessary to properly run OPENCAV limited the overall size of calculations that could be made; thus, the intermediate calculations only model the tube from the cavity to the end of the collector uptaper. In cases 5 and 6, the solution was divided into several steps.

Reflections from one section back to another were ignored in these calculations. This approach tended to lower the calculated higher-order mode content slightly. The close agreement between cases 6 and 7 gives good confidence that both TAPER and OPENCAV, when used carefully, yield useful and reliable results.

Table 27 summarizes mode conversion data for the 2-1/2 inch collector with 2° linear tapers. Smoothing in the calculation of abrupt waveguide transitions helped to obtain excellent agreement between OPENCAV calculations and experiments. This good correlation implies that the effects of neglecting the window, collector seal gaps and beam-induced effects in the calculations are quite small.

Table 27
Mode Content of the 2-1/2 Inch Collector

Case	Technique	Mode Content (%)			
		TE_{01}	TE_{02}	TE_{03}	TE_{04^+}
1	OPENCAV (sharp transitions)	7	91	2	<1
2	OPENCAV (smooth transitions)	4	94	2	<1
3	10-Mode TAPER	1.5	95.9	2.5	<1
4	2-Mode TAPER	1.1	96.0	2.7	ϕ
5	*Measured W/W.G. Couplers - Step Cavity	4	94±1	2	<1
6	*Measured W/W.G. Couplers - Tapered Cavity	3	96±1	1	<1

* Include Single-Disc Window

TAPER calculations, which neglect cavities as well, are also in excellent agreement with measured mode conversion values.

The additional mode conversion that apparently results from use of a double-disc window, rather than a single-disc, may have several origins. Mode conversion may occur in the window itself or the window may reflect rf, which then converts in the taper sections. Static pressure

loading on double-disc windows causes slight deformations of the ceramics, which may also contribute to mode conversion.

Calculation results of the mode conversion in a preliminary four-inch collector design are summarized in Table 28. The four-inch collector has the advantage of having lower power densities than the 2-1/2 inch. The results again show good agreement between TAPER and OPENCAV.

Table 28
Mode Content of the 4-inch Collector

Case	Technique	Mode Content (%) TE_{01}	TE_{02}	TE_{03}
1	2-Mode TAPER	1.1	98	0.7
2	20-Mode TAPER	9.9	87.4	2.6
INTERMEDIATE CALCULATIONS				
3	1-Step OPENCAV	4.9	87.2	7.9
4	20-Mode TAPER	5.9	88.0	5.9

A cold test using the mode probe modified to minimize reflections and improve resolution and a TE_{01} transducer followed by a filter into a 2° taper to the 2-1/2 inch diameter collector yielded excellent agreement with a TAPER calculation:

	TE_{01}	TE_{02}	TE_{03}
TAPER	97.8%	2.1%	0.1%
Mode Probe	98.3%	1.5%	0.3%

This work was also halted by agreement with ORNL.

B. WINDOW

For CW operation, the original double-disc windows with face cooling (FC-75) were designed with 0.050", FC-75 gaps using both AL-995 and BeO (99.5%) ceramics. A computer program was written and used to determine the ceramic thicknesses needed for a match at 60 GHz. These values were 0.524 λ_g for AL-995 and 0.529 λ_g for BeO (99.5%). In terms of actual dimensions, these translated to 0.0413" and 0.0338", respectively. To ensure that the ceramic could withstand stress due to heating and pressure, BeO ceramics with thicknesses of 1.529 λ_g (0.120") and 2.529 λ_g (0.198"), and AL-995 ceramics with thicknesses of 1.524 λ_g (0.099") and 2.524 λ_g (0.163") were fabricated.

The computed VSWR for an FC-75 face-cooled alumina double-disc window is shown in Figure 215. By comparison, the computed VSWR for an FC-75 face-cooled beryllia double-disc window is shown by the dashed curve in Figure 216. The lower dielectric constant of the beryllia results in a wider bandwidth compared to alumina. The computed VSWR of an improved FC-75 face-cooled beryllia double-disc is shown by the solid curve in Figure 216.

The electrical properties (bandwidth and dielectric loss), as well as the mechanical properties (deflection and thermal stress), of double-disc FC-75 face-cooled window assemblies were investigated. A summary of the design results is given in Table 29 for six different assemblies employing both beryllia and alumina discs.

1. Location of Passbands

For each of the six designs presented in Table 29, the gap size was optimized to provide a perfect match at the operating frequency of the VGE-8060 S/N X-1, namely 59.7 GHz. The experimental tube also tended to jump into an undesired mode, the TE_{221}, at a frequency of 57.7 GHz. For this reason, it was desirable to match the CW window assembly for this frequency as well as the desired frequency. The computer VSWR is plotted versus frequency in Figures 217 and 218 for each of the window designs under consideration. Characteristically, the CW window passband takes a double

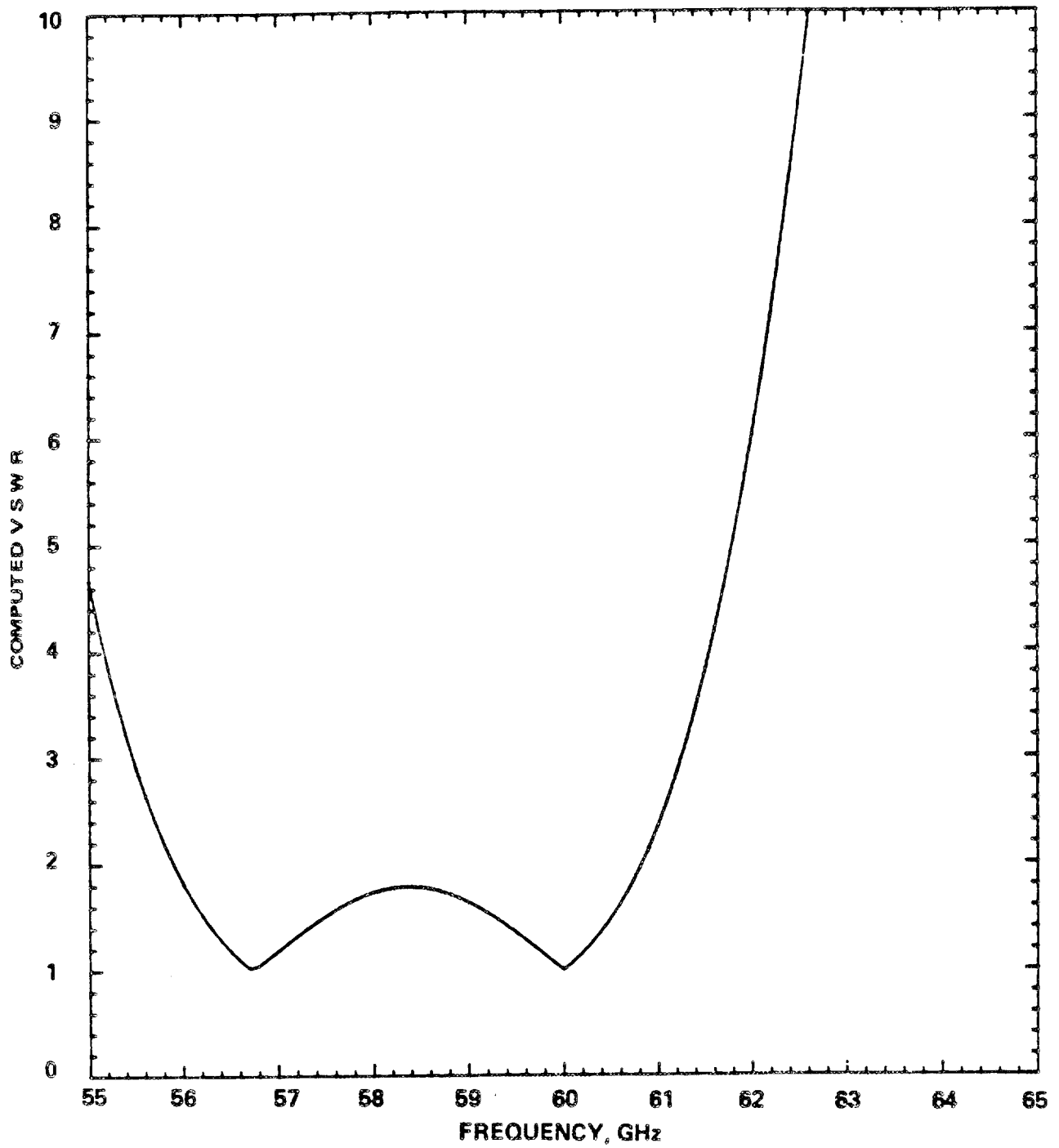

Figure 215. Computed VSWR for an FC-75 Face-Cooled Alumina Double-Disc Window

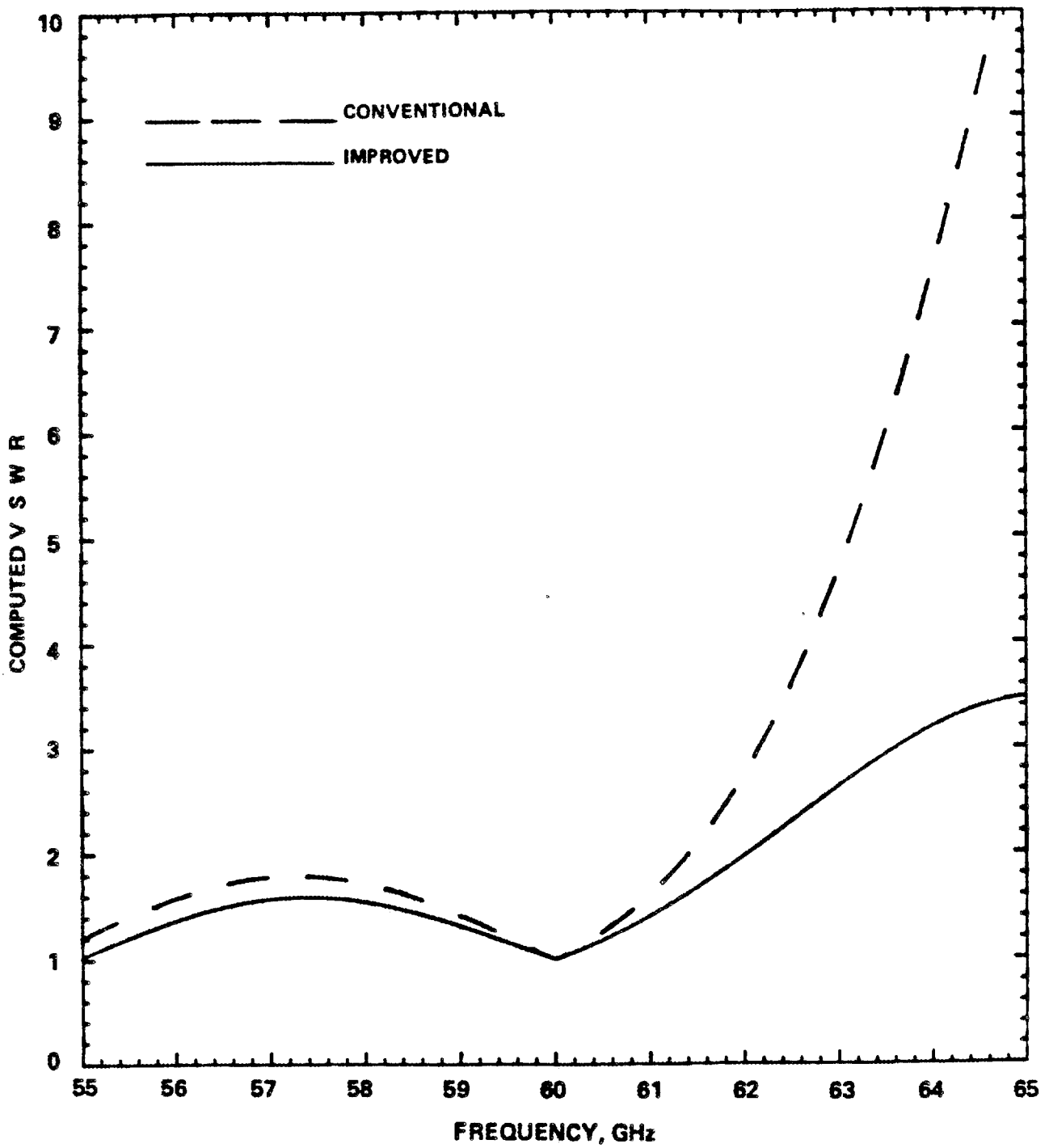

Figure 216. Computed VSWR for an FC-75 Face-Cooled Beryllia Double-Disc Window

Table 29
60 GHz Double Disc Window Designs

Double Disc Configuration			Electrical Properties			Mechanical Properties		
Disc Material	Disc Thickness (Inches)	FC-75 Gap (Inches)	TE_{021} Bandwidth for VSWR = 1.2 (MHz)	TE_{221} VSWR	Window Assembly Loss (kW)	Deflection @ 30 psig (Inches)	Deflection Stress (psi)	Thermal Stress (psi)
Beryllia	2/2 λ 0.083	0.028	760	1.85	2.1	0.0026	12,800	92
Beryllia	3/2 λ 0.120	0.033	570	1.82	2.6	0.0008	6,100	190
Beryllia	4/2 λ 0.157	0.039	470	1.59	3.1	0.0004	3,600	330
Alumina	3/2 λ 0.099	0.036	500	1.71	2.3	0.0017	9,000	740
Alumina	4/2 λ 0.131	0.036	420	1.40	2.4	0.0007	5,100	1,300
Alumina	5/2 λ 0.163	0.036	300	1.10	2.5	0.0004	3,300	2,000

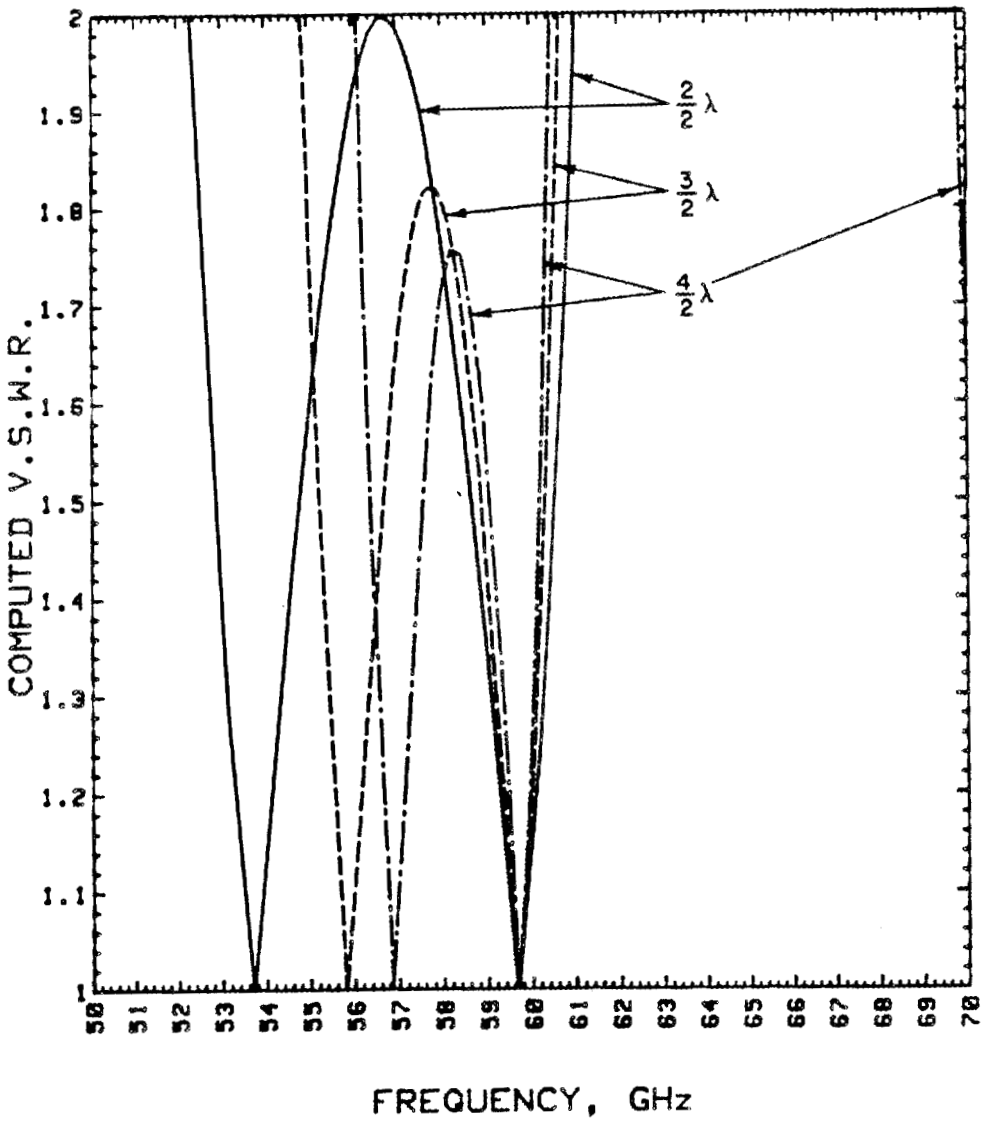

Figure 217. Computed VSWR vs Frequency for Beryllia Double-Disc Window Designs

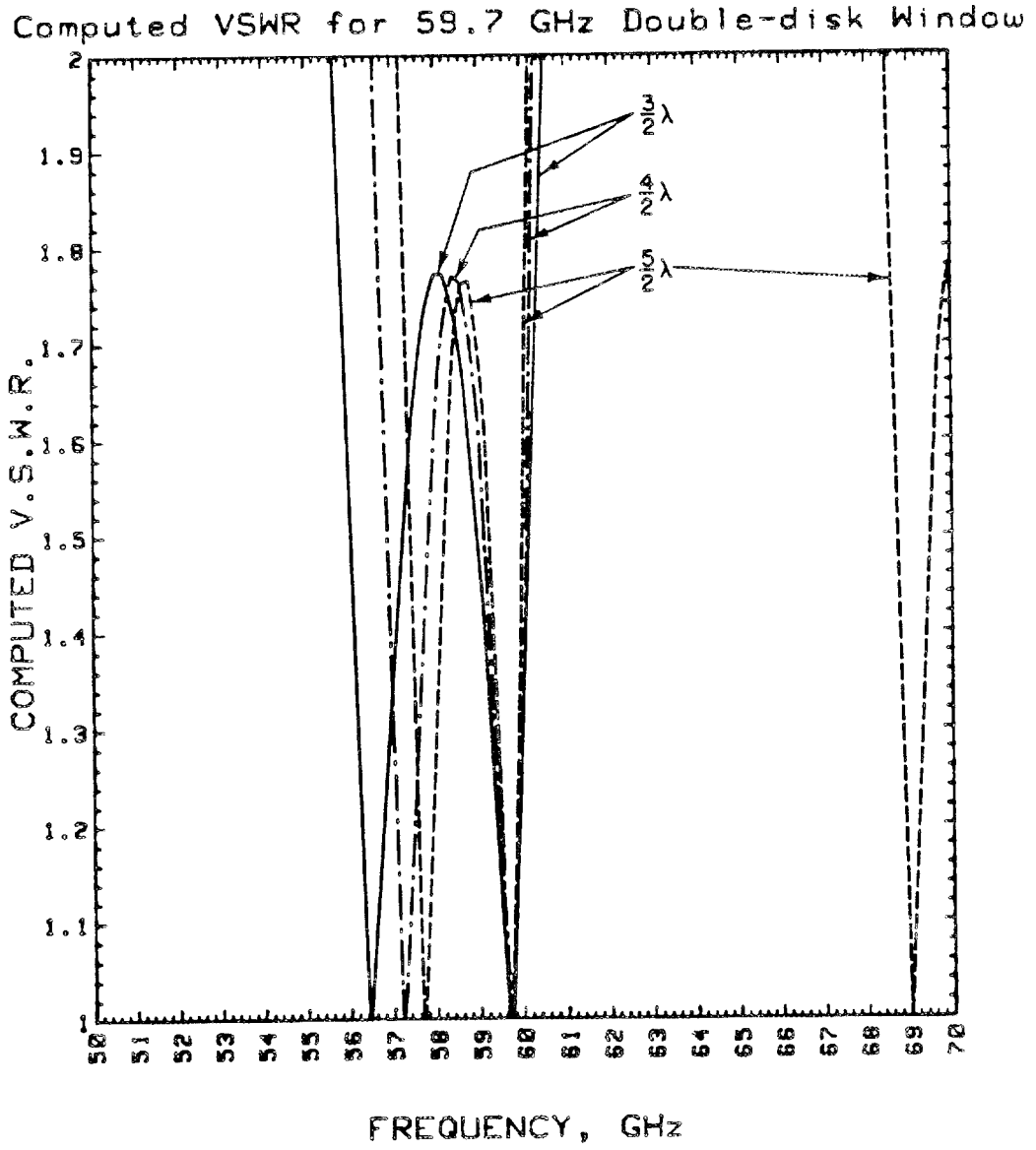

Figure 218. Computed VSWR vs Frequency for Alumina Double-Disc Window Designs

notch form as shown in Figures 217 and 218. It is possible, by choosing an appropriate window thickness, to approximately center one passband on each of the frequencies observed with X-1. The double-disc window with 5/2 λ alumina discs is one such configuration as described in Table 29.

2. Bandwidth

The bandwidth of each passband should be as wide as possible, but in any case, must exceed the oscillator resonance bandwidth, f/Q. This criterion implies an upper limit on the allowable electrical thickness of the CW window assembly. All the designs listed in the table meet this bandwidth criterion. However, the 5/2 λ alumina window assembly appears to have reached the absolute limit in electrical thickness, as it provides a passband for a VSWR of 1.2:1 of only 300 MHz.

3. Dielectric Loss

The power lost in these window assemblies through dielectric dissipation is expected to be higher than that observed at 28 GHz because the windows, in numbers of half wavelengths, are thicker. All the window assemblies considered in Table 29 should exhibit dissipation in the range of 2-3 kW, most of which is due to dielectric loss in the FC-75 coolant itself. As the amount of loss is similar for all the designs considered, this property does not present any strong argument in favor of any particular design. It is noted, however, that because beryllia has a higher loss tangent than alumina, the dissipation in the beryllia assemblies will be slightly higher than in the alumina assemblies.

4. Deflection Stress

There are two major sources of stress on the ceramic discs in these CW window designs. There is a deflection, and therefore, a restoring deflection stress, caused by the load of the pressurized FC-75 distributed across the face of each disc. The disc on the vacuum side must, in addition, withstand the load of atmospheric pressure. When running with an FC-75 pressure of 30 psig, the load on the vacuum-side disc will be 45 psi

absolute load pressure. This leads to a deflection stress at the center of the window, as listed in Table 29. Excessive deflections are encountered when the discs are less than one tenth of an inch in thickness.

5. Thermal Stress

As the heat dissipated in the ceramic diffuses toward the coolant, the temperature difference between the faces of the disc induces a thermal stress in the ceramic. Beryllia, because of its excellent thermal conductivity, is subject to an order of magnitude less thermal stress than alumina. For a given ceramic material, the temperature difference between the disc faces are higher for thicker discs, although the thermal stress remains within safe limits for all of the designs in Table 29. When both thermal and deflection stress are considered together, there is a narrow range of disc thicknesses which simultaneously permit low deflection and low thermal stresses.

6. Comparison of CW Designs

The window designs of Table 29 have been rated against the criteria described above as shown in Table 30. The labels, "unacceptable", "marginal", and "acceptable" are applied to those window properties which differ significantly among the designs under consideration. According to the rating system, the 5/2 λ alumina window was the clear winner for the first 60 GHz CW window design, although it had the disadvantage of a narrow TE_{02} bandwidth for the passband centered at 59.7 GHz. Once the window assembly was completed, it was necessary to retune the window slightly by adjusting the FC-75 gap size to provide a perfect match for the TE_{02} mode at 59.7 GHz.

7. Alumina Double-Disc Window

Several window geometries were investigated to determine the optimal thickness and diameter combination that would yield the lowest thermal hoop stress.

Table 30
Design Trade-offs for 60 GHz CW Window Designs

Property	Beryllia 2/2 λ	Beryllia 3/2 λ	Beryllia 4/2 λ	Alumina 3/2 λ	Alumina 4/2 λ	Alumina 5/2 λ
TE_{021}, Bandwidth	Acceptable	Acceptable	Marginal	Marginal	Marginal	Marginal
TE_{221}, VSWR	Unacceptable	Unacceptable	Unacceptable	Unacceptable	Marginal	Acceptable
Deflection	Unacceptable	Acceptable	Acceptable	Unacceptable	Acceptable	Acceptable
Deflection Stress	Unacceptable	Marginal	Acceptable	Unacceptable	Marginal	Acceptable

The specific calculation conditions used are shown in Table 31.

Table 31
Double-Disc Window Calculation Conditions

Window Material	Alumina 99.5%
Frequency	60 GHz, TE_{02} Mode
Power Transmitted	120 kW CW
Attenuation Constant	0.03175 Nepers/cm
Heat Transfer Coefficient	2.5 W/in2°C
Coolant	FC-75
Fluid Pressure at Surface of Disc	30 psia

Figures 219 through 228 show the temperature distribution and corresponding thermal stresses for each case. It is clear that a 4-inch diameter, $3\lambda/2$-thick disc would be the best choice of those shown because it has the lowest thermal hoop stress, as shown in Figure 228.

8. Thermal Imaging of Gyrotron Windows

An infrared thermal imaging task was undertaken to establish the feasibility of thermal imaging gyrotron windows. The thermal imaging task comprises two parts: 1) an analysis of the effect of viewing the output window through an array of small holes in the waveguide wall using an infrared imaging system and 2) tests with an infrared camera looking at various heated objects through a sample grid of holes.

The transmission through the grid is a function of the point on the gyrotron window being imaged by the infrared camera. In the derivation, the grid is assumed to be large enough that its edges do not limit the field of view. The grid fabricated with holes around the entire circumference of the waveguide would meet this requirement. The transmission as a function of the location of the observed point on the window will be called the Grid Transmission Function.

Dwg 82-3581 FED

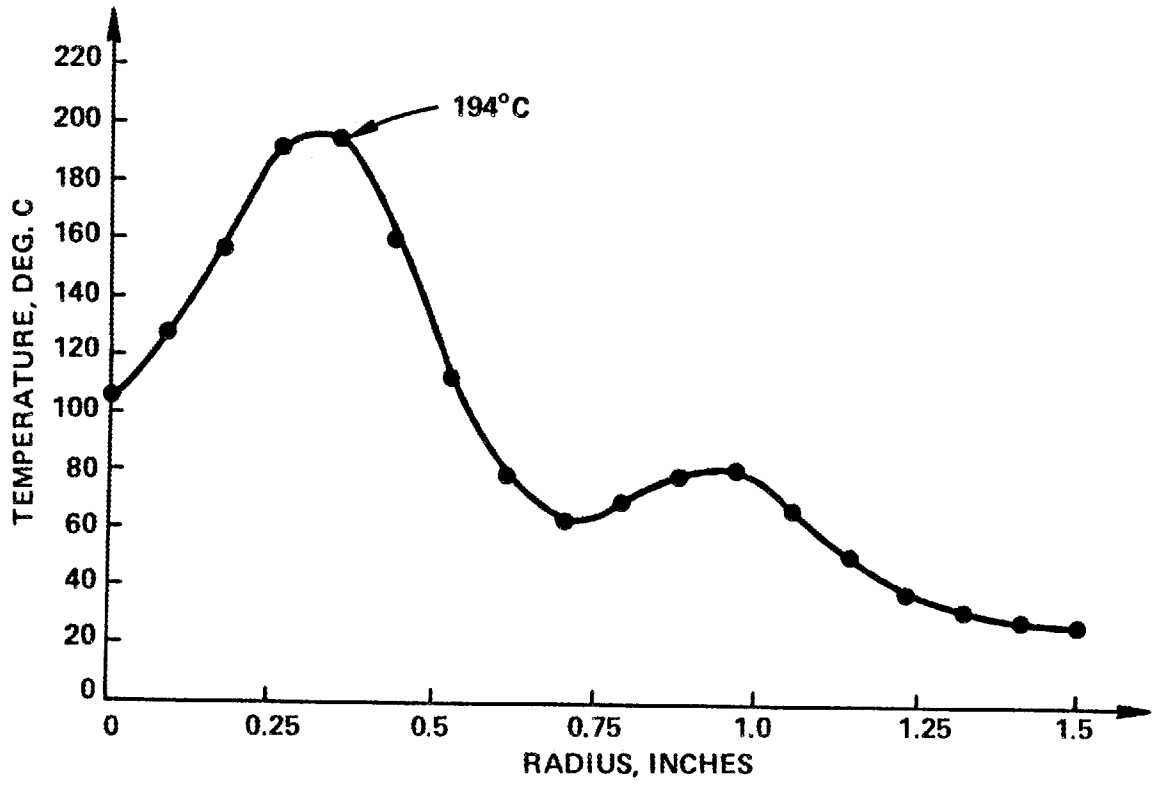

Figure 219. Temperature Distribution of Double Disc Window, λ Thick, 3" Diameter

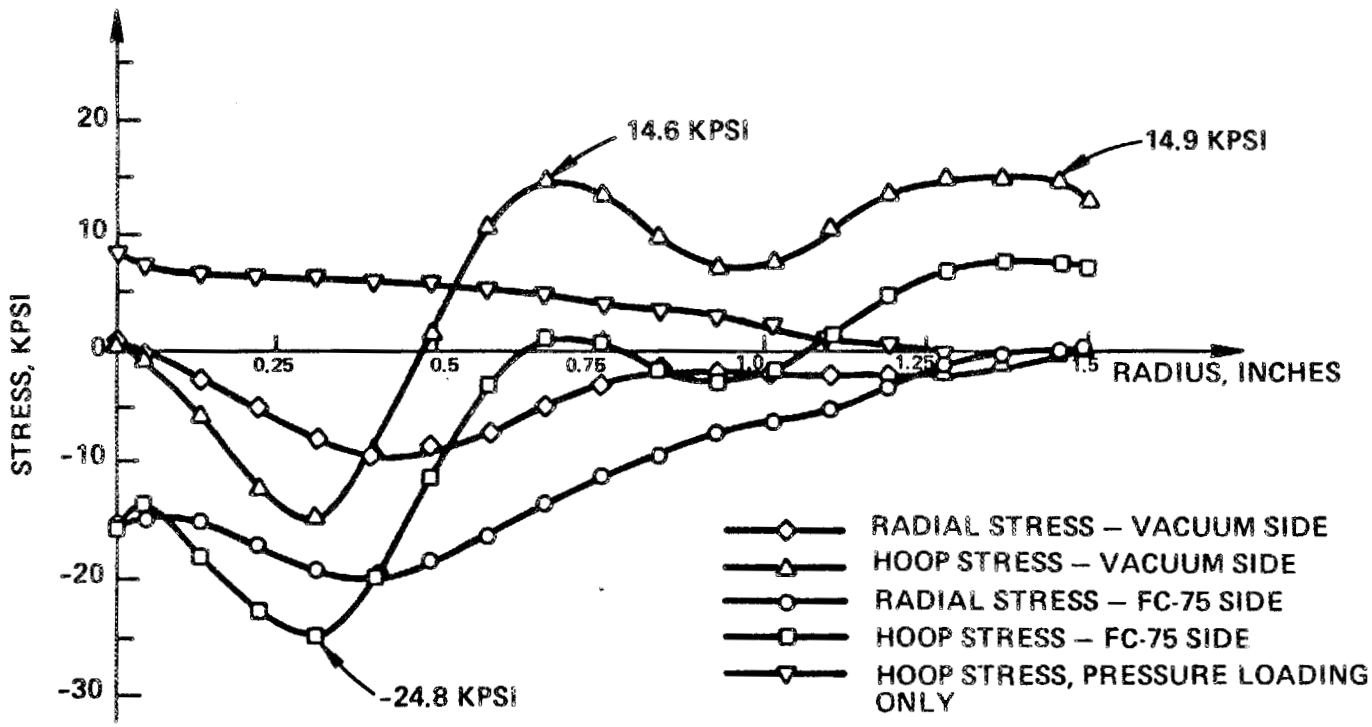

Figure 220. AL-995 Double Disc Window Stress Distribution of Vacuum Side, λ Thick, 3" Diameter

Dwg 82-3583 FED

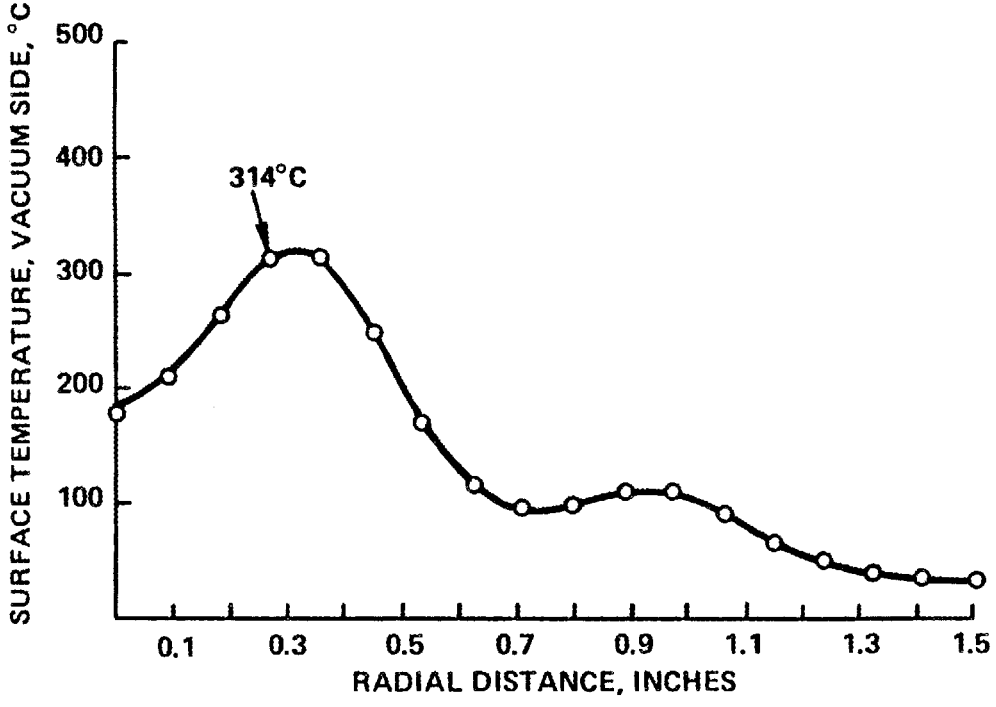

Figure 221. Temperature Distribution Vacuum Side Double-Disc Window, 1.5 λ Thick

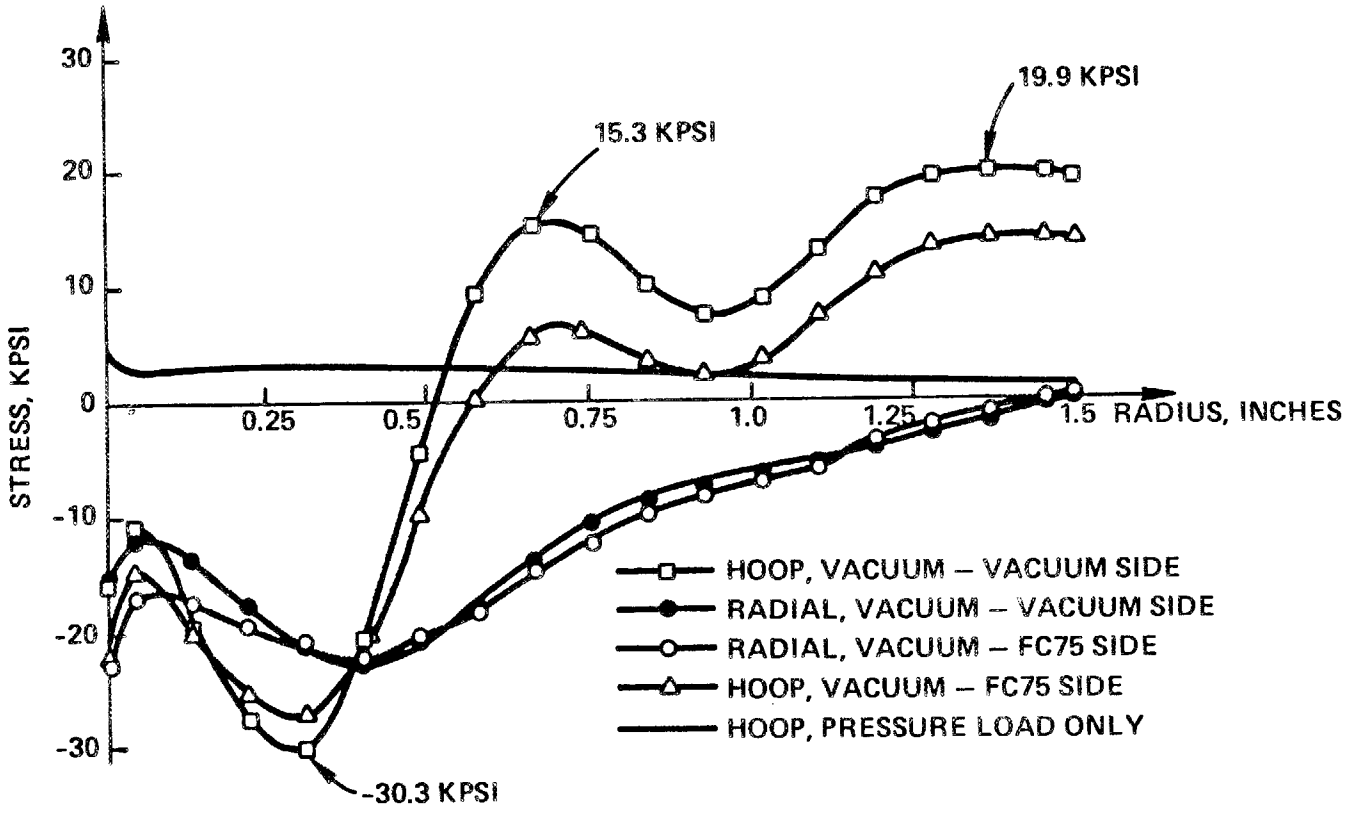

Figure 222. AL-995 Double Disc Window Stress Distribution 60 GHz, 120 kW CW, 1.5 λ Thick, 3" Diameter

Dwg 82-3585 FED

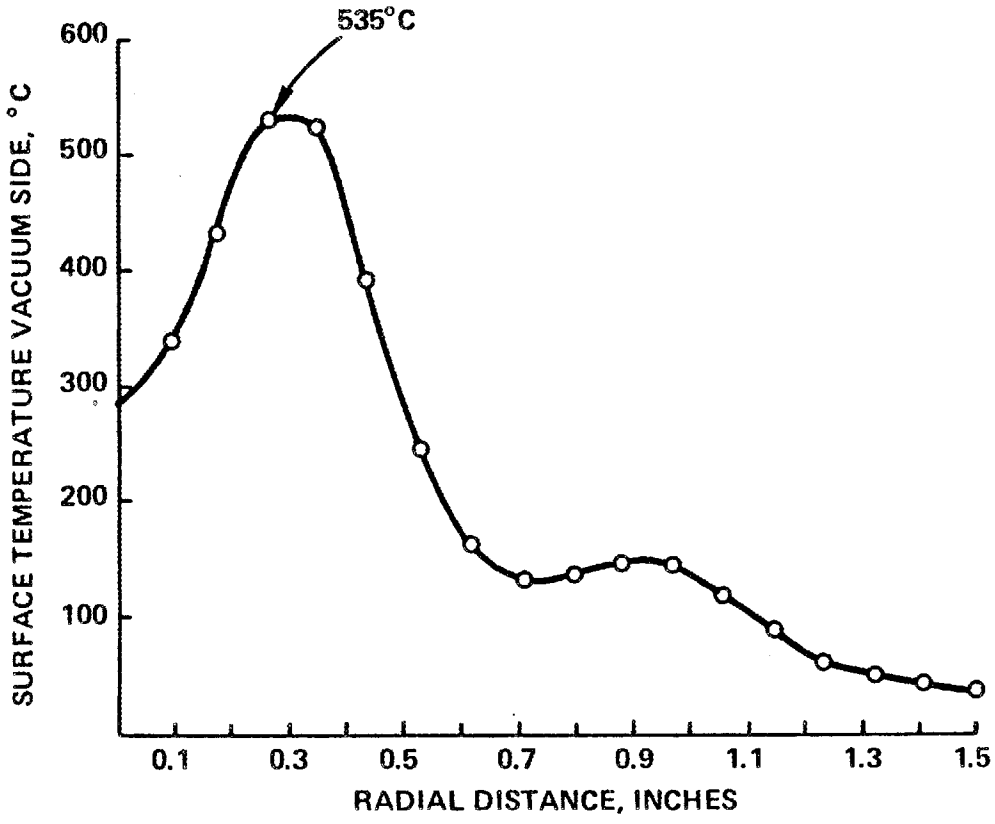

Figure 223. Temperature Distribution on Vacuum Side Double-Disc Window, 2 λ Thick

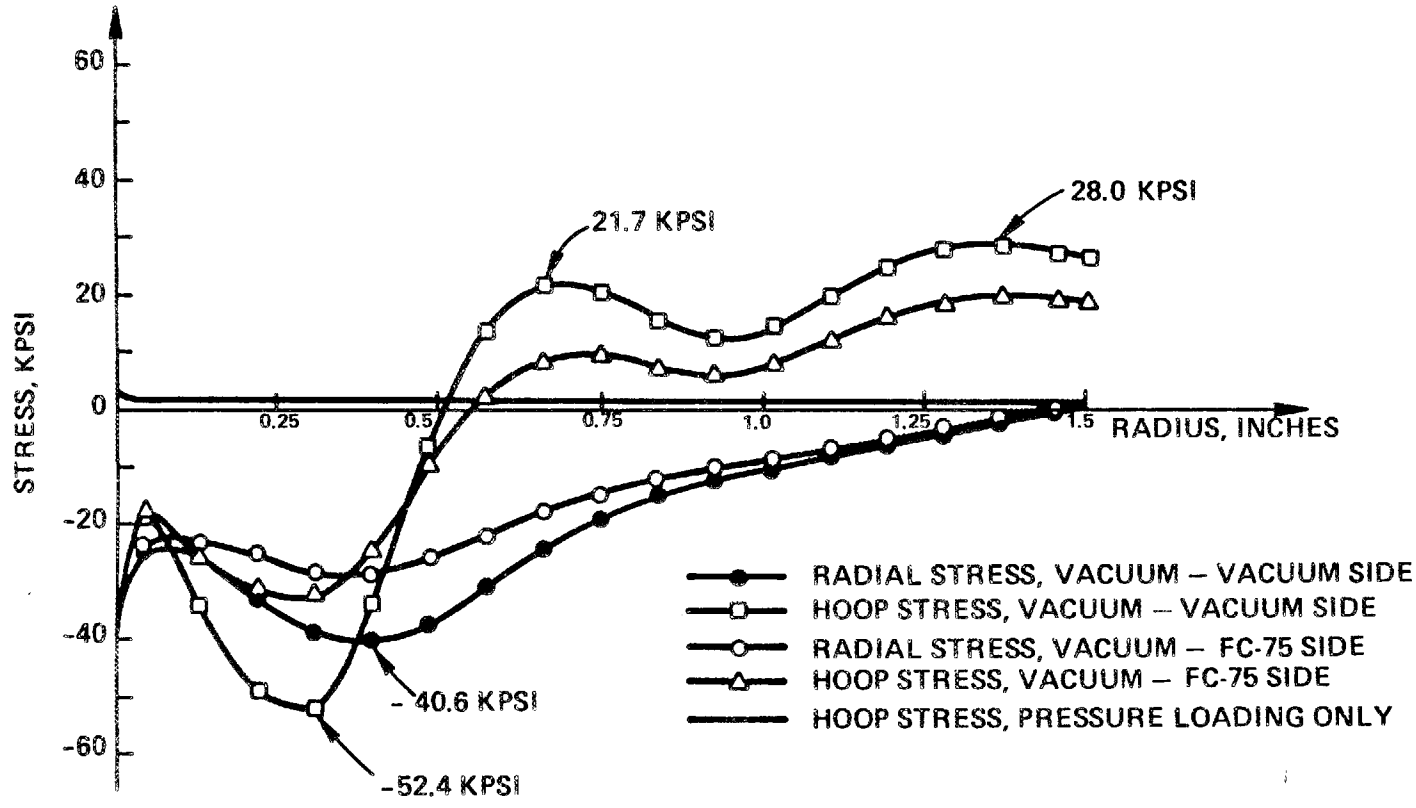

Figure 224. AL-995 Double Disc Window Stress Distribution, 2λ Thick

Dwg 82-3587 FED

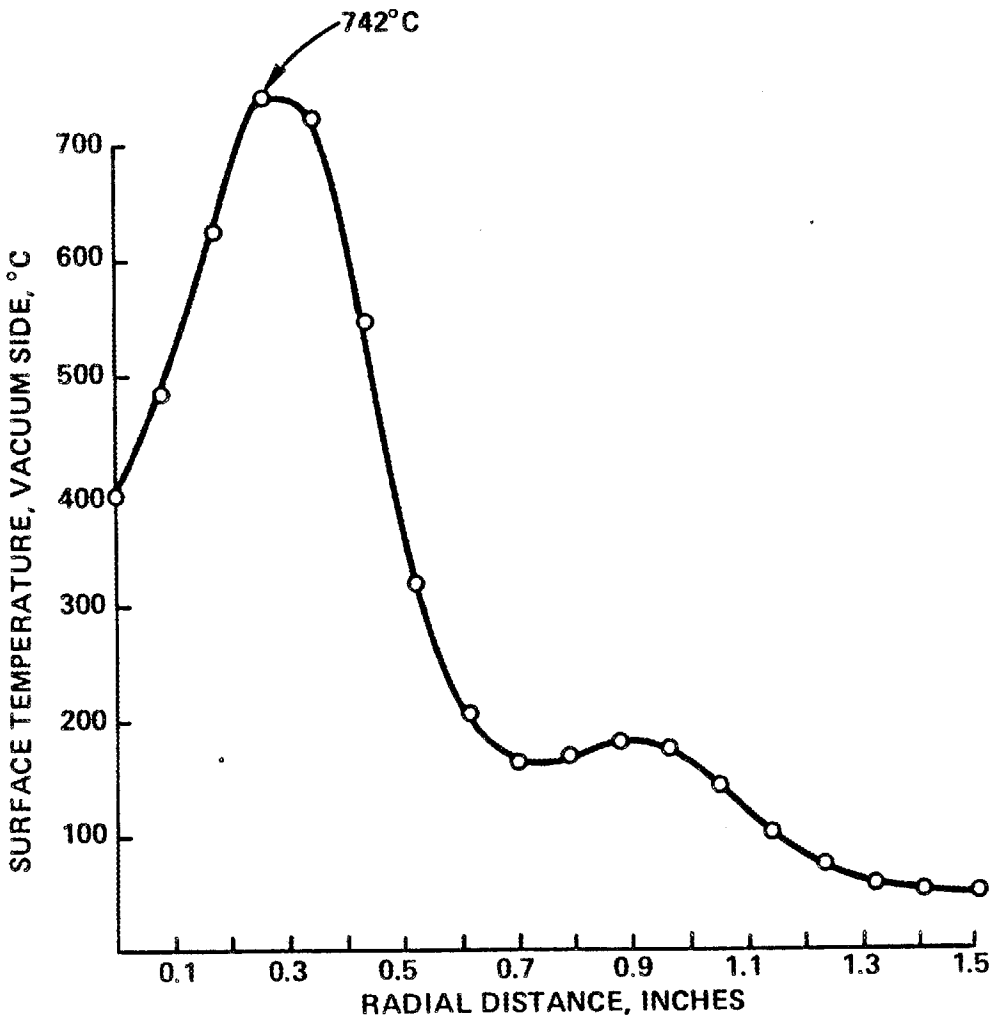

Figure 225. Temperature Distribution on Vacuum Side 60 GHz Double-Disc Window, 2.5 λ Thick, 120 kW CW, α = 0.03175 Nepers/cm, Film Coefficient = 2.5 Watts/in^2 °C

Dwg 82-3588 FED

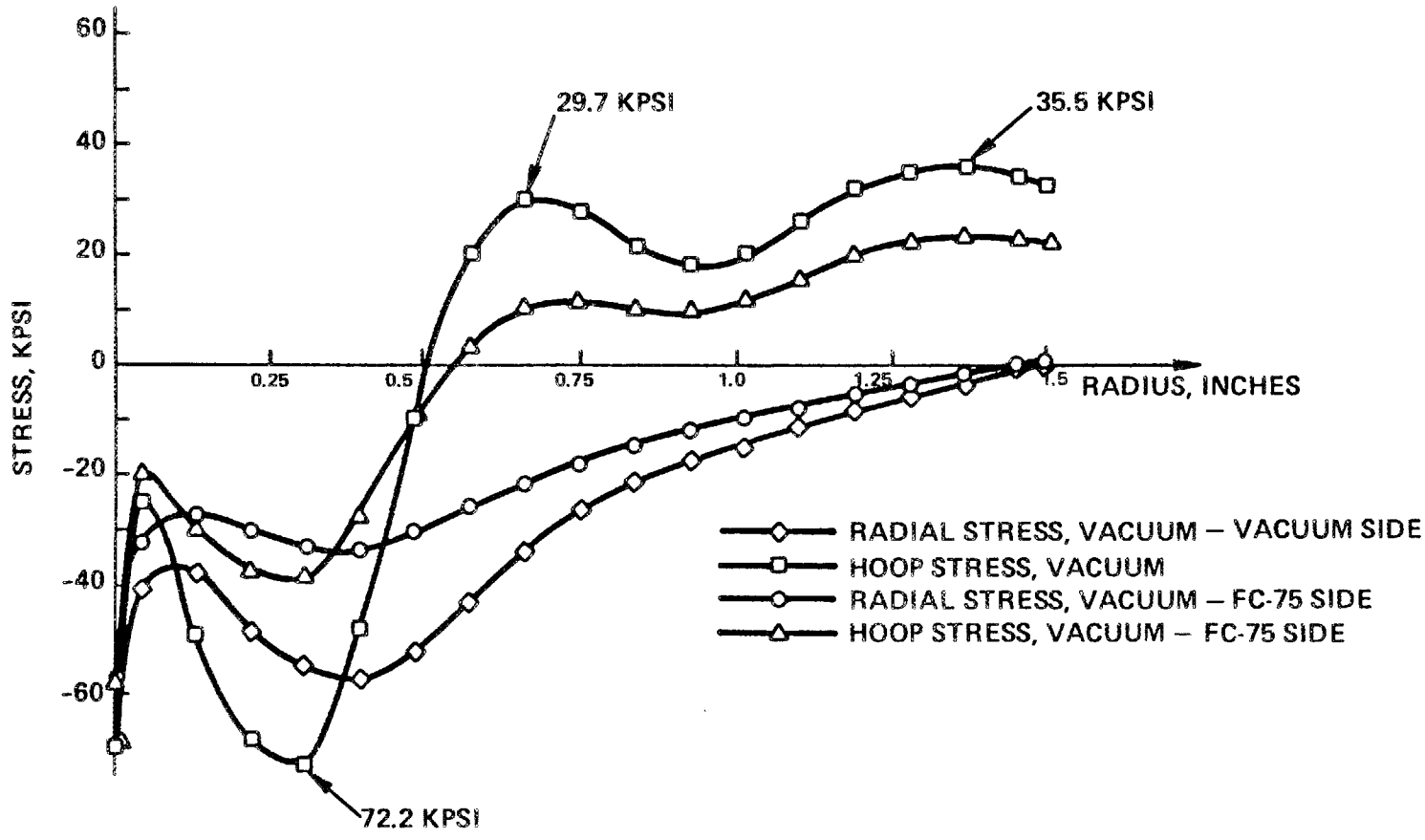

Figure 226. AL-995 Double Disc Window Stress Distribution, 2.5 λ Thick

Dwg 82-3589 FED

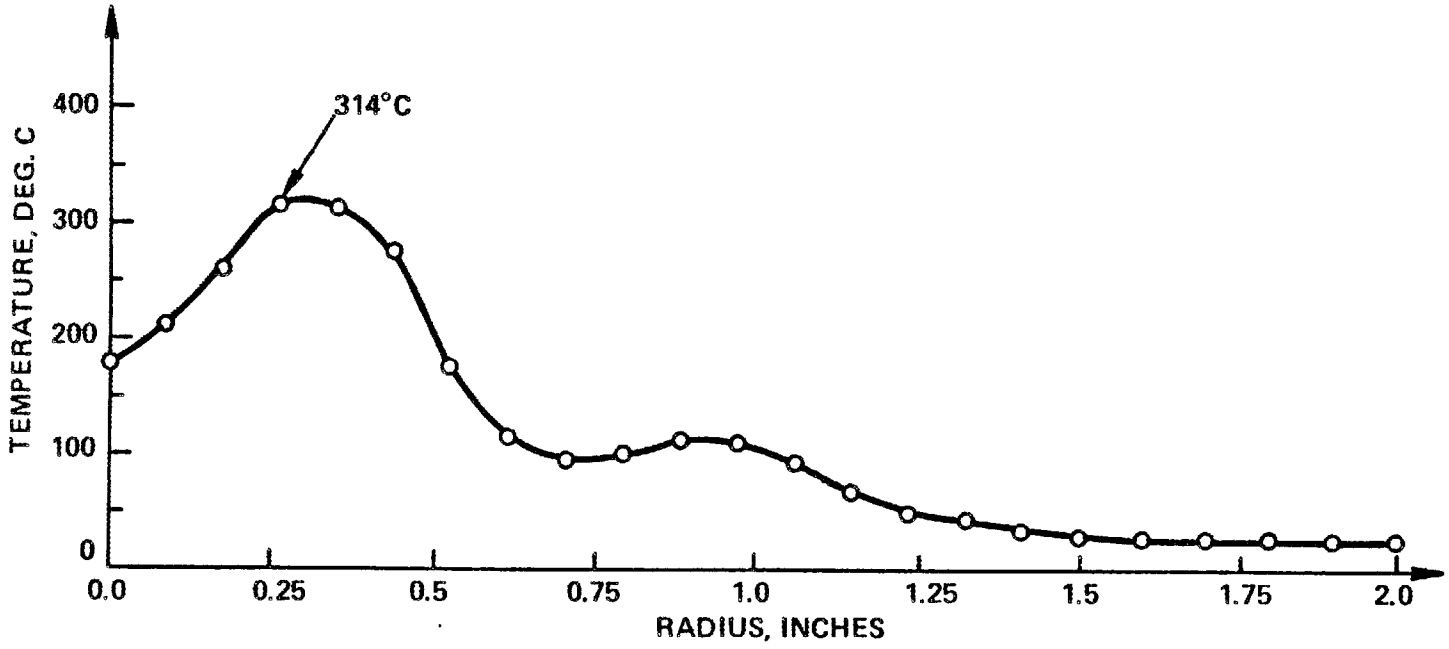

Figure 227. AL-995 4 Inch, Double Disc Window Temperature Distribution 60 GHz, 120 kW CW, 1.5λ Thick, $\alpha = 0.03175$, h = 2.5 W/in² °C

Dwg 82-3590 FED

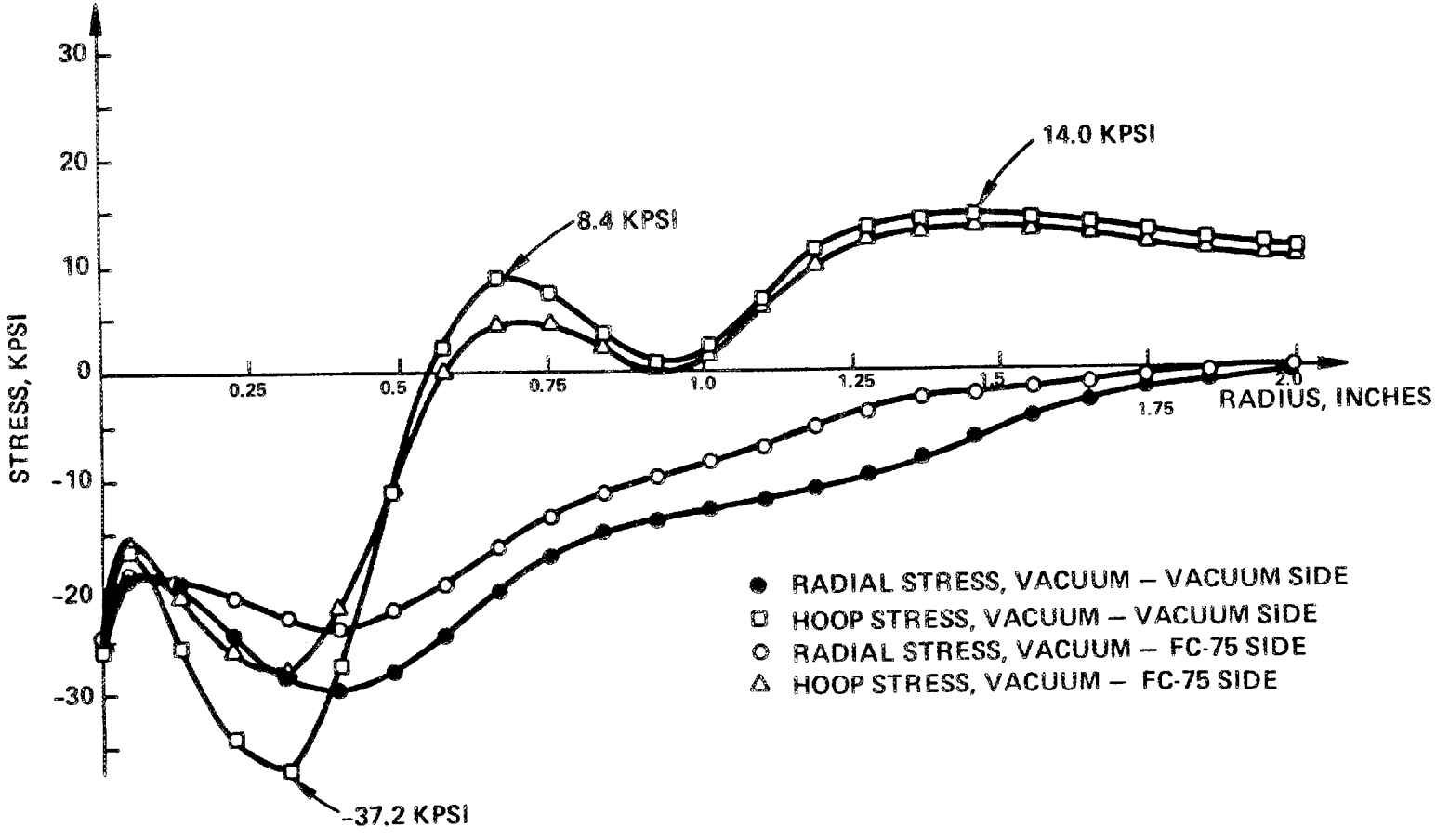

Figure 228. AL-995 Double Disc Window Stress Distribution 1.5 λ Thick, 4" Diameter

a. Determination of the Grid Transmission Function

The grid transmission, T, can be expressed as the product of three factors. The first factor is the effect of a restricting, overall grid area. Since the grid has holes all the way around the perimeter, this factor becomes unity. The second factor, A_{holes}/A_{grid}, is 0.196, since the grid has 1/32" holes on 1/16" centers. The third factor, A_{clear}/A_{holes} is the hole wall blockage factor. This factor is more difficult to estimate, and is the subject of a careful study, as described below.

i. Calculation of the Hole Wall Blockage

Several steps were involved in calculating the hole wall blockage function:

a) An expression was obtained for hole wall blockage when viewing points on the window located on a vertical diameter as a function of θ_v, the angle between the axis of these grid holes and the axis of the waveguide.

b) An expression was derived for θ as a function of x, the position of the observed point on the vertical window diameter.

c) Using the results of a) and b), the hole wall blockage factor for points along the vertical window diameter was calculated.

d) An expression was derived for the hole wall blockage factor for points on the horizontal window diameter (perpendicular to FG in Figure 229) as a function of ϕ_H, the angle between the axis of the holes and the rays traversing them.

e) Except for points on the vertical window diameter, an analytical expression for ϕ, the angle between the hole axis and the traversing ray, is difficult to derive, so a 3-D model was built and used to measure this angle for all locations on the window.

f) The value of ϕ from e) was combined with the results of a) and d) to calculate the hole wall blockage factor for all points on the window.

These steps will now be described in detail.

(a) Calculation of A_{clear}/A_{holes} vs θ_v

The fraction A_{clear}/A_{holes} is given by Equation 65

$$\frac{A_{clear}}{A_{holes}} = 1 - \frac{2}{\pi}\left[(1-f)\ (2f-f^2)^{1/2}\ \sin^{-1}\ (1-f)\right] \qquad (65)$$

where f = fraction of hole diameter which appears unblocked to the camera:

$$f = 1 \pm (t/d)\ (\cos\theta_g - \sin\theta_g \cot\theta_v) \qquad (66)$$

t = waveguide wall thickness where holes drilled

d = hole diameter

θ_g = angle between grid hole axis and axis of waveguide

θ_v = angle between waveguide axis and line of sight to points on the window lying on the line HC in Figure 229.

(b) Calculation of θ_v as a Function of x

A value of θ_v can be determined with reference to Figure 229 as follows: Let h_g be the height (above the window) of the point on the grid joining the center of the window to the center of the camera lens. From triangle DGF it is seen that GD = GF csc θ_g

Where $GF = D_E/2 + 1/8" \times \sec\theta_g$ $\quad GF = D/2 + 1/8" \times \sec\theta_g$

$$\theta_g = \tan^{-1}\ 1.25/h_g \qquad (67)$$

Also, since triangles ACE and GFE are similar:

Dwg 82-3591 FED

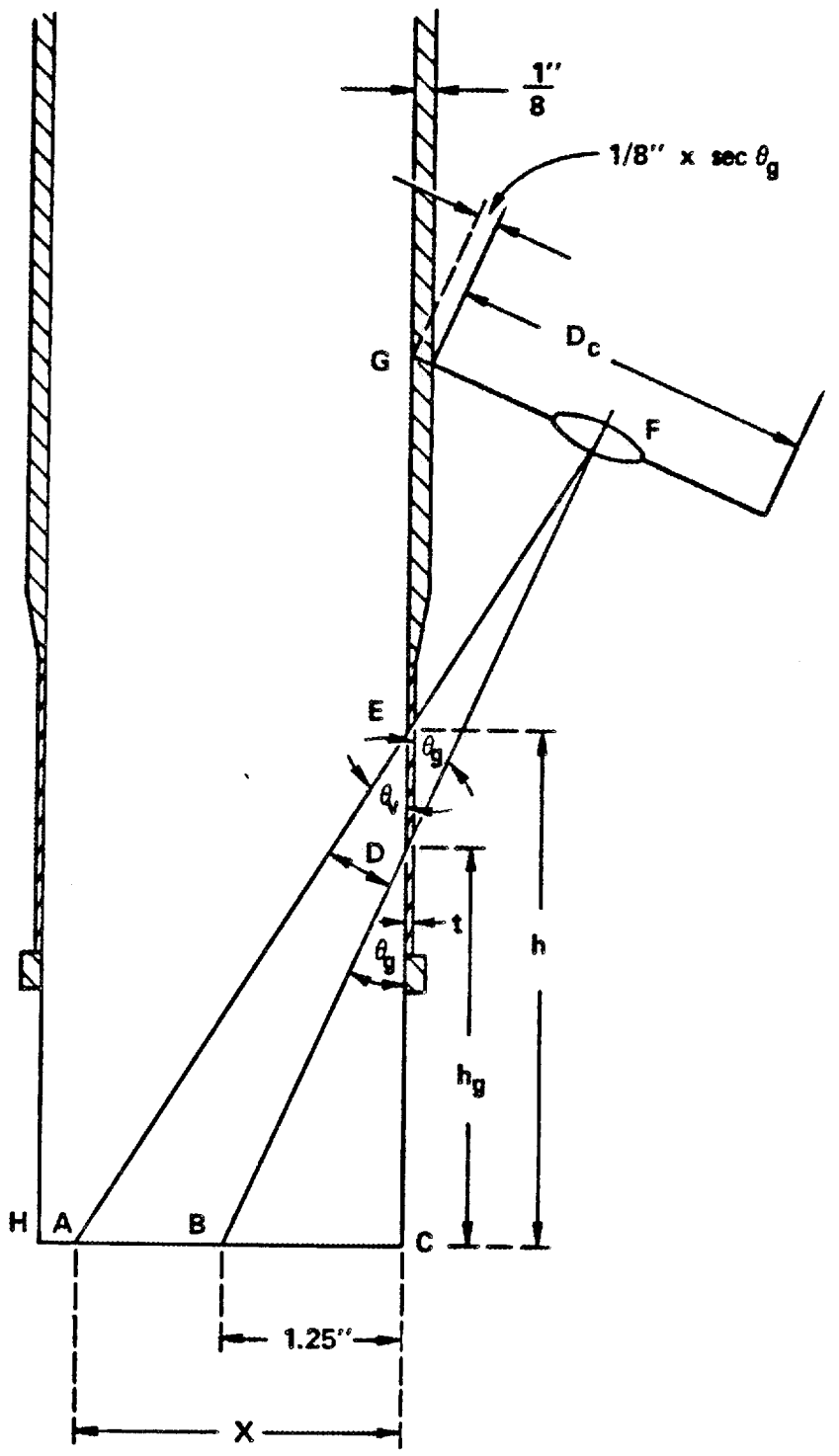

Figure 229. Grid Geometry

$$\frac{x}{GF} = \frac{AE}{EG} = \frac{AE}{GC-EC} = \frac{AE}{h_g+GD-EC} = \frac{x\csc\theta}{h_g+GD-x\cot\theta} \quad . \tag{68}$$

Thus,

$$\frac{x}{(D_c/2 + 1/8''\ x\sec\theta_g)} = \frac{x\csc\theta}{hg + (D_c/2+1/8''\ \sec\theta_g)\csc\theta_g - x\cot\theta_v}$$

$$x = \frac{hg + (D_c/2 + 1/8''\ \sec\theta_g)\csc\theta_g - (D_c/2 + 1/8''\ \sec\theta_g)\csc\theta_v}{\cot\theta_v} \quad . \tag{69}$$

With the present AGA camera lens (no optical relay), $D_c = 2.5''$. In our present arrangement, $h_g = 2.75$ inches, so that

$$\theta_g = \tan^{-1}(1.25/2.75) = 24.44^{\circ}. \tag{70}$$

Inserting these values of D_c and h_g, and θ_g into Equation 69, it reduces to:

$$x = \frac{6.11\sin\theta_v - 1.39}{\cos\theta_v} \quad . \tag{71}$$

Solving for θ:

$$\theta_v = \sin^{-1}\left[\frac{16.98 \pm \sqrt{2.88 - 4(1.93-x^2)\ (37.33+x^2)}}{2(37.33+x^2)}\right] . \tag{72}$$

(c) Calculation of A_{clear}/A_{holes} vs x

Knowing θ from Equation 72, we can use Equations 65 and 66 to calculate A_{clear}/A_{holes} for various values of x, t, d and θ_g.

In calculating microwave leakage through the grid, the effective length, l, of the grid holes must be known. This can be

calculated with the aid of Figure 230. Here the value of l is equal to the length DC, which can be evaluated as follows:

$$l = DC = DB - CB = t \csc \theta_g - d \cot \theta_g \quad . \tag{73}$$

The grid characteristics are given in Table 32.

Table 32

Grid Characteristics

Characteristic	Dimensions
Hole Diameter, d (in)	1/32
Wall thickness, t (in)	3/64
Grid area	2" wide (a)
Angle between hole axis and Waveguide axis, θ_g (deg)	24
Effective hole length, l (in)	0.045
Ratio of l/d	1.44

(a) The grid extends around the entire perimeter of waveguide.

The results of applying Equations 65, 66, 72 and 73 to the grid are presented in Table 33. Note that with increasing θ_v, the value of A_{clear}/A_{holes} falls off. The value of T, grid transmission, obtained by multiplying the ratio A_{clear}/A_{holes} by 0.196 (the value of A_{holes}/A_{grid}), is also included in Table 33.

Dwg 82-3592 FED

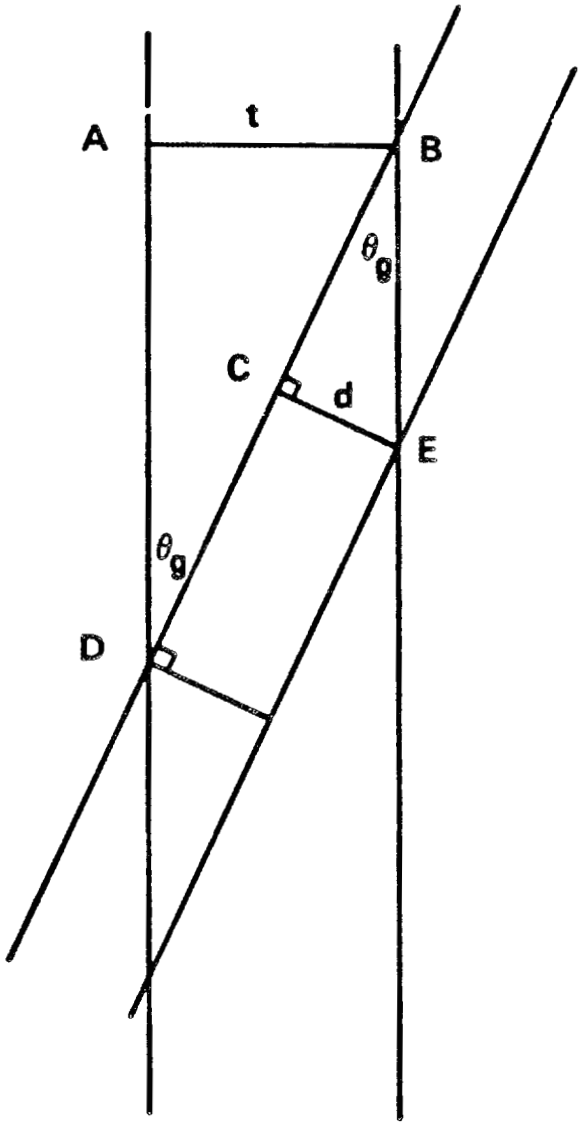

Figure 230. Calculation of Effective Grid Hole Length

Table 33
Calculated Value of Transmission of Grid when Viewing a Vertical Line Through the Center of the Window

x (in)	θ_v (deg)	ϕ_v (deg)	f	$\frac{A_{clear}}{A_{holes}}$	T
0.25	15.4	9.0	0.12	0.049	0.0096
0.5	17.8	6.7	0.43	0.32	0.061
0.75	20.0	4.4	0.66	0.58	0.11
1.0	22.3	1.8	0.85	0.81	0.16
1.25	24.4	0	1.0	1.0	0.20
1.5	26.6	2.1	0.88	0.85	0.17
1.75	28.6	4.2	0.78	0.72	0.14
2.0	30.6	6.2	0.69	0.61	0.12
2.25	32.5	8.1	0.61	0.52	0.10
2.5	34.4	10	0.54	0.44	0.085

The value of θ_v, the angle between the axis of the grid holes and the rays going through them to points on the vertical diameter of the window, is given by

$$\phi_v = \left| \theta_v - \theta_g \right| \tag{74}$$

The values of ϕ_v are included in Table 33.

(d) Calculations of A_{clear}/A_{holes} vs ϕ_H

When a grid hole is viewed "broadside", i.e., normal to its length from a point lying in the plane containing the axis of the grid holes and the waveguide, it appears as shown in Figure 231. In this case, the fraction, f_H, of the diameter of the hole which is not blocked by the hole wall is

$$f_H = \frac{AB}{AC} = \frac{AC-BC}{AC} = \frac{d - t\csc\theta_g \tan\phi_H}{d} \quad . \tag{75}$$

Dwg 82-3593 FED

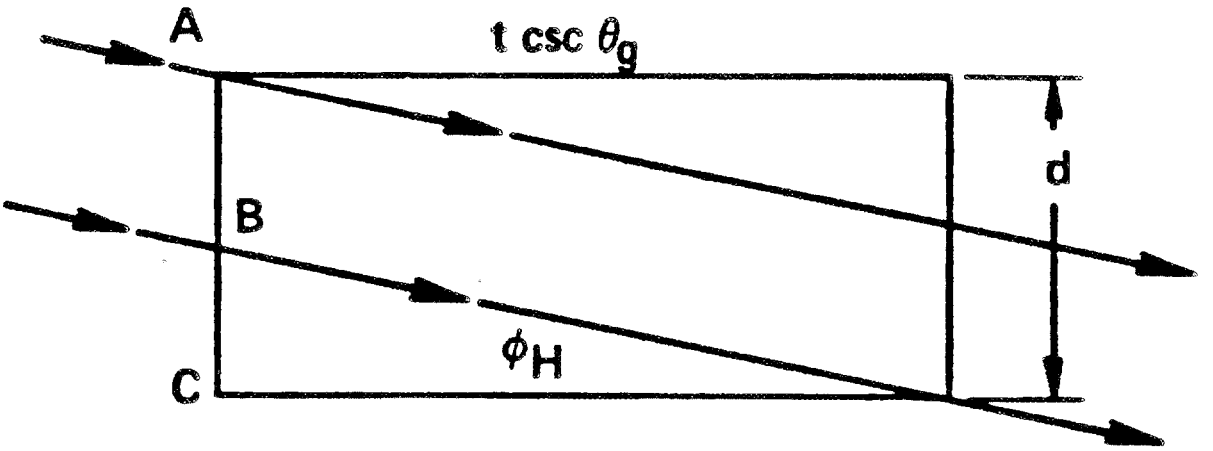

Figure 231. Calculation of f_H

Values of f_H, together with the corresponding values of A_{clear}/A_{holes}, and T are presented in Table 34.

Table 34
Calculated Values of f_H, A_{clear}/A_{holes} and T vs ϕ_H

ϕ_H (deg)	f_H	A_{clear}/A_{holes}	T
0	1	1	0.196
2	0.87	0.84	0.16
4	0.75	0.68	0.13
6	0.62	0.53	0.10
8	0.49	0.38	0.074
10	0.36	0.24	0.048
12	0.23	0.13	0.025
14	0.095	0.035	0.0068
15	0.027	0.0054	0.0011

The values of T from Tables 33 and 34 are plotted as a function of ϕ in Figure 232. Note that the values of T are symmetrical in the horizontal direction, but in the vertical direction the transmission falls off more rapidly when changing the line of sight from the center towards the top than towards the bottom. This is to be expected from an examination of the hole geometry.

(e) Measurement of ϕ in the General Case Using a Mechanical Model

The determination of ϕ, the angle between the grid hole axis and the rays traversing the holes, is straightforward for points lying on a vertical diameter of the window, line FG in Figure 233. In this case, ϕ is found by combining Equation 72 and 74. For any other point on the window, the analytical calculation of ϕ is complex. To avoid this complexity, a model was fabricated which permitted measurement of ϕ for any point on the window.

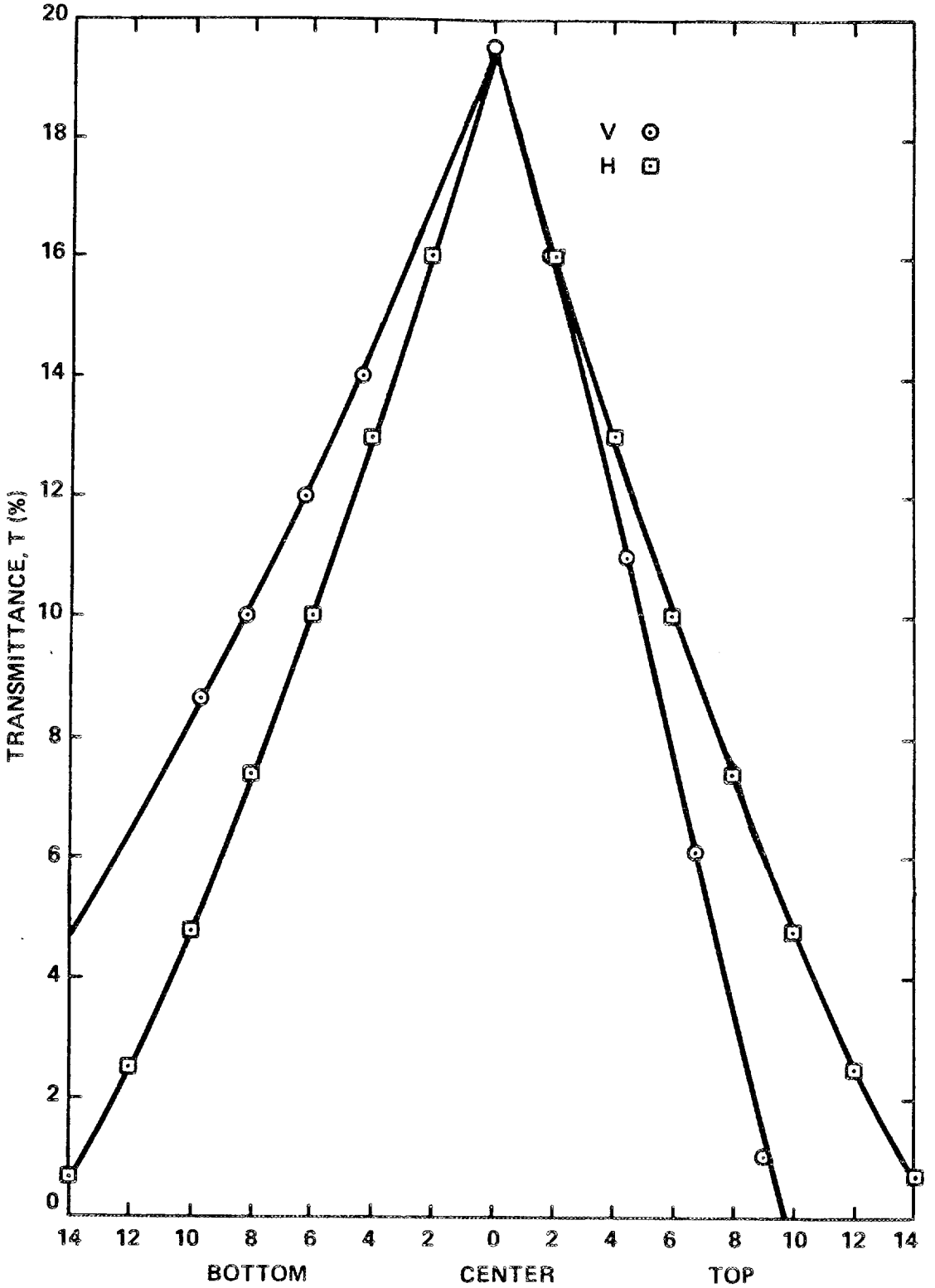

Figure 232. Grid Transmittance Along Vertical and Horizontal Diameters vs ϕ

Dwg 82-3599 FED

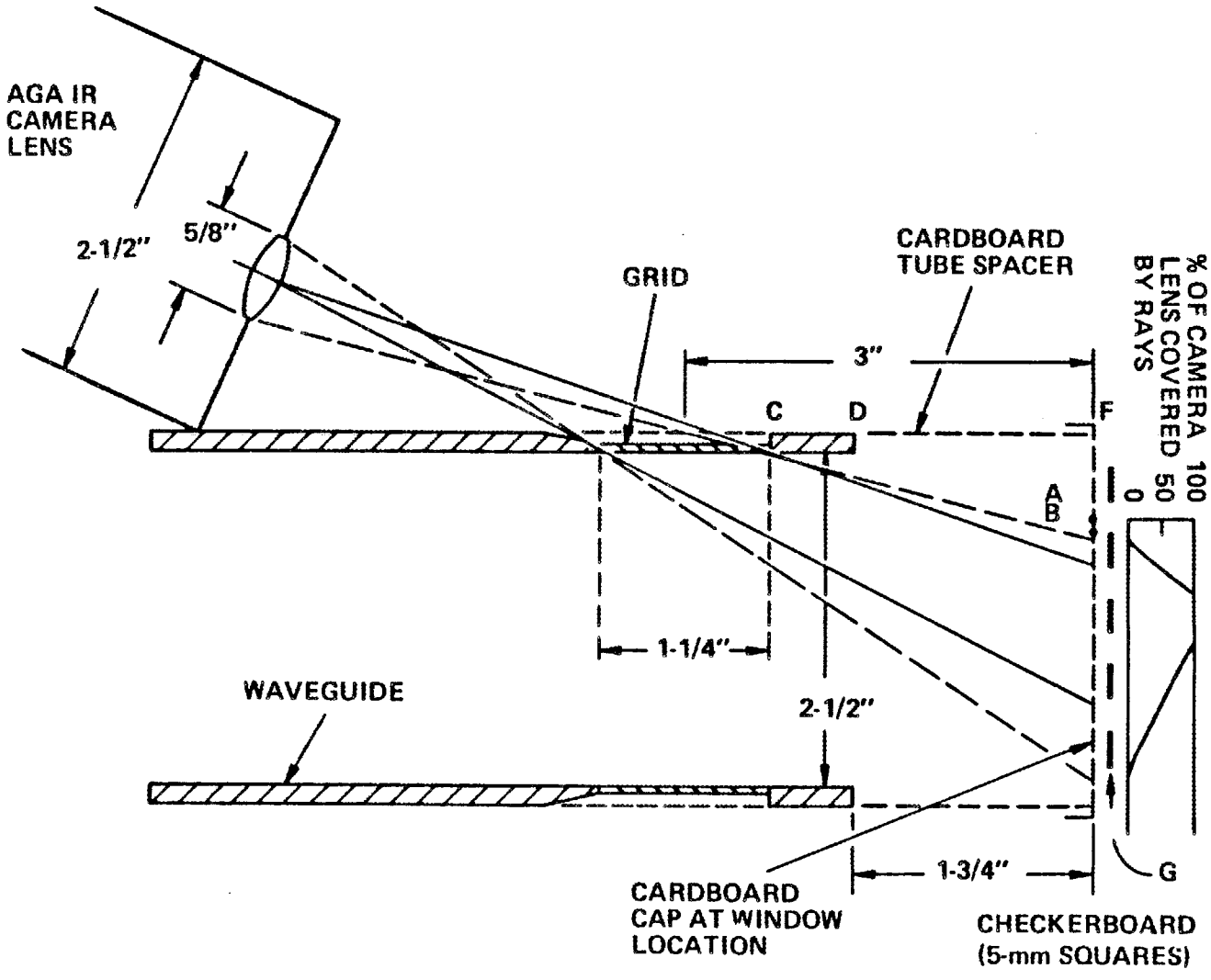

Figure 233. Thermal Imaging Experimental Arrangement Details

Figure 234 is a photograph of the model, while Figure 235 is a sketch of it. The model utilized two stainless steel rods. One of these rods, AB in Figure 235, represents the axis of the waveguide, whose walls are represented by the dashed lines. The other rod, CD, represents an infrared ray traveling from a representative point, E, on the window, FG, to the center, H, of the front surface of the camera lens. The rods were stabilized by passing through H, E, J, and K through cardboard surfaces, LM and NO, which are simply the sides of cardboard boxes. The rod AB carries a vane, PQRS, which slides freely along its length, and rotates freely about the axis AB. The side QS of this vane is 1-1/4" long, so that the point Q always lies on the inner surface of the imaginary waveguide. The side PQ is inclined to AB by the angle θ_g, so that PQ is always parallel to the hole in the waveguide which passes through the point Q.

To measure ϕ, the vane is adjusted until point Q just touches the rod CD. The angle between PQ and the rod CD is then measured. This angle is ϕ, the angle between the waveguide hole and the ray utilized in observing point E. The rod CD is then removed and passed from H through another hole in NO, representing another point on the window, and the measurement is repeated. This process was repeated for the 76 holes covering the area of the window, as shown in Figure 234, with the results shown in Figure 236. The dashed lines in this figure represent lines of constant ϕ, with values of 8, 12 and 16 degrees.

Knowing ϕ as a function of location of the point on the window being viewed, the grid transmission along the vertical diameter of the window can be calculated from Equations 65 and 66, and along the horizontal diameter from Equations 65 and 75, (or in both cases from Figure 232). In the absence of an exact procedure for other points on the window, Equation 66 was assumed to apply to the entire upper and lower quadrants of the window, the positive sign referring to the lower quadrant. Similarly, Equation 75 was assumed to apply to both the right and the left quadrants.

The results of this process are shown in Figure 237. Lines of isotransmittance are again indicated.

Photo 0686-82

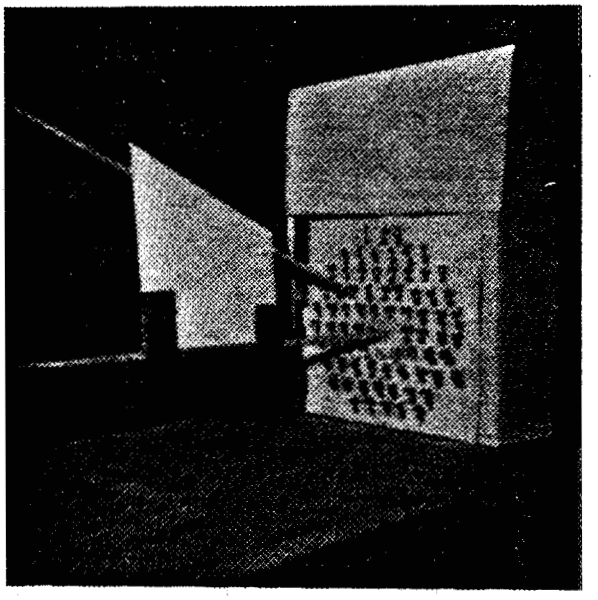

Figure 234. Photograph of Model Used in Measuring Planar Grid

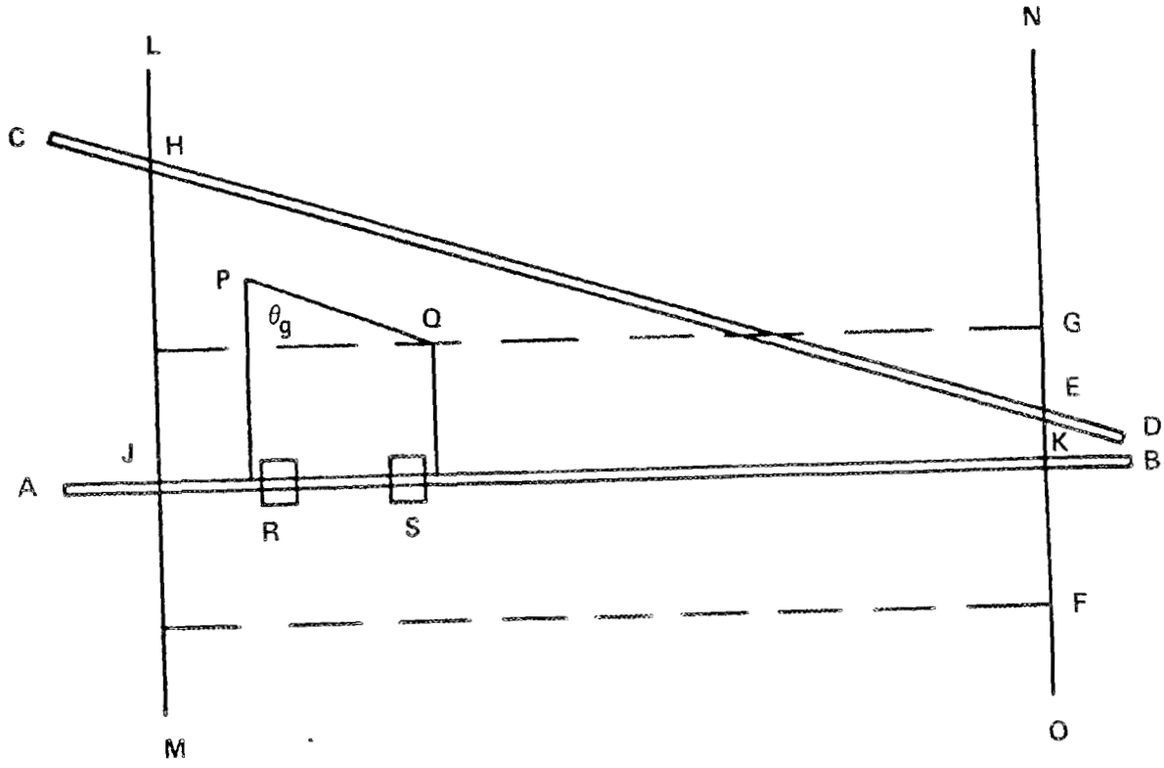

Figure 235. Model Used in Measuring ϕ

GRID (TOP)

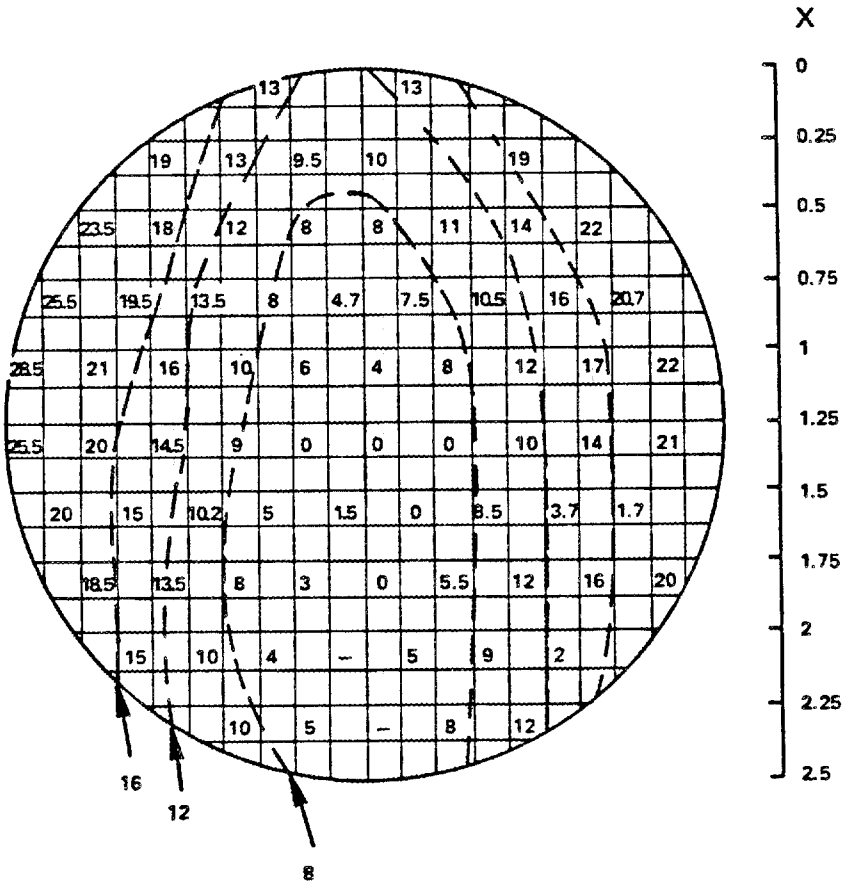

Figure 236. Angle, ϕ, Between Grid Hole Axis and IR Ray

$t = 3/64''$

$d = 1/32''$

$\frac{\ell}{d} = 1.5$

TOP GRID

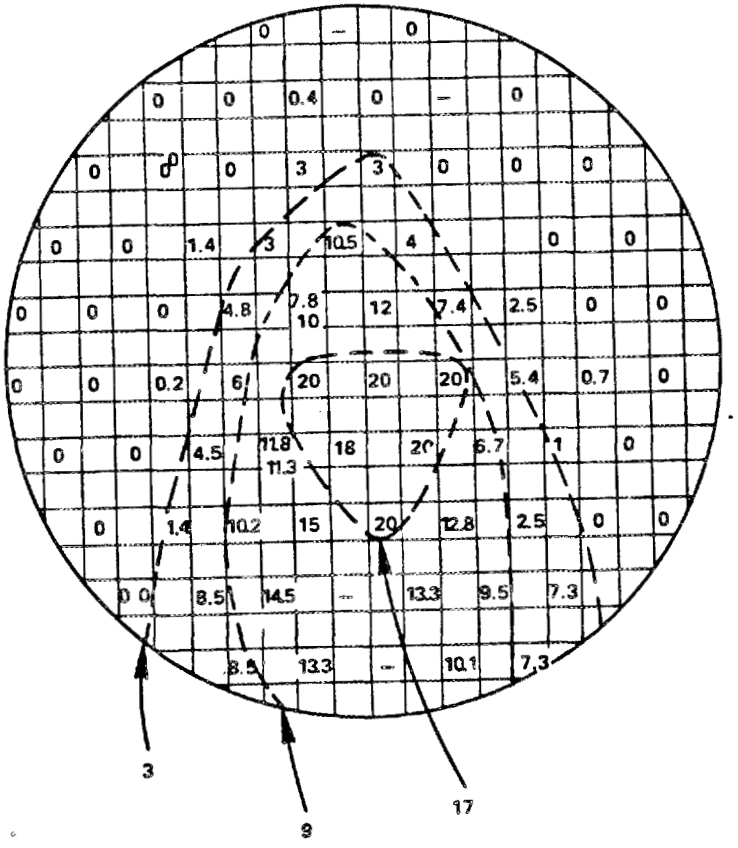

Figure 237. Grid Transmittance (%)

ii. Observance of the Window Through the Grid

A checkerboard pattern was observed through the grid. It was noted that a considerably larger area of the window could be seen through the viewfinder than is indicated in Figure 237. Perhaps the method used to get Figure 237 was too conservative - rays other than the center one considered may provide useable signals in areas labelled "zero" in Figure 237.

b) The Tests

The performance of an AGA 780 camera, including tests through the grid in the 60 GHz waveguide, was demonstrated. The grid was comprised of 1/32" diameter holes through a 1/32" wall. The holes were on 1/16" centers and inclined 22.6° to the wall. The pattern extended over the rather small area of 3/4" x 1-1/4". The sensitivity, resolution, and field of view through the grid were checked, together with the ease of alignment through the grid.

The results and conclusions, described in detail below, can be summarized as follows:

1) The camera worked well, and was convenient to use.

2) Alignment of the camera to see through the grid was easy (not critical).

3) Transmittance of the grid was roughly 15% on axis of holes. Sensitivity through the grid was about 0.7°C at the center of the field of view.

4) The resolution at the window was better than 2 mm.

5) Field of view was limited by the grid. (Changes in shape and size of subsequent grids minimized this limitation.)

6) The camera focal setting needed to be increased to better defocus the grid holes. This effect was not serious.

7) The camera, combined with a new grid, would be suitable for window temperature measurement. Environmental problems could be solved with the aid of an optical relay, if necessary.

Figures 233 and 238 are sketches of the experimental arrangement. In Figure 238 the object mounted in the vise is the waveguide.

Figure 239 shows the remarkable sensitivity obtained with the IR camera through the grid. The grey object in the center is a finger viewed against an ambient background. The white object at the right is the base of the finger viewed directly.

Figure 240 is a resolution check. The arrangement is the same as that in Figure 239 except that two vertical bar charts were interposed between the finger and the grid. The bar charts were actually six slits cut in the cardboard spacer tube, as shown in Figure 233; each slit was 2mm wide, and the opaque region between slits was also 2 mm. The arrangement of slots was like this: ▯▯▯ ▯▯▯. The slits were barely resolved. Also, in Figure 241, the vertical and horizontal resolutions appear about the same, 2 mm.

Figure 242 and 243 represent a demonstration of temperature distribution measurements across the finger through the grid. In Figure 242, the isotherm was set at the edge of the finger. The white square indicator at the left of the scale, combined with lens aperture, thermal level, and thermal range settings (which correspond to "brightness" and "contrast" settings on a TV set) indicated an isotherm of 26°C. In

Dwg. 82-3600 FED

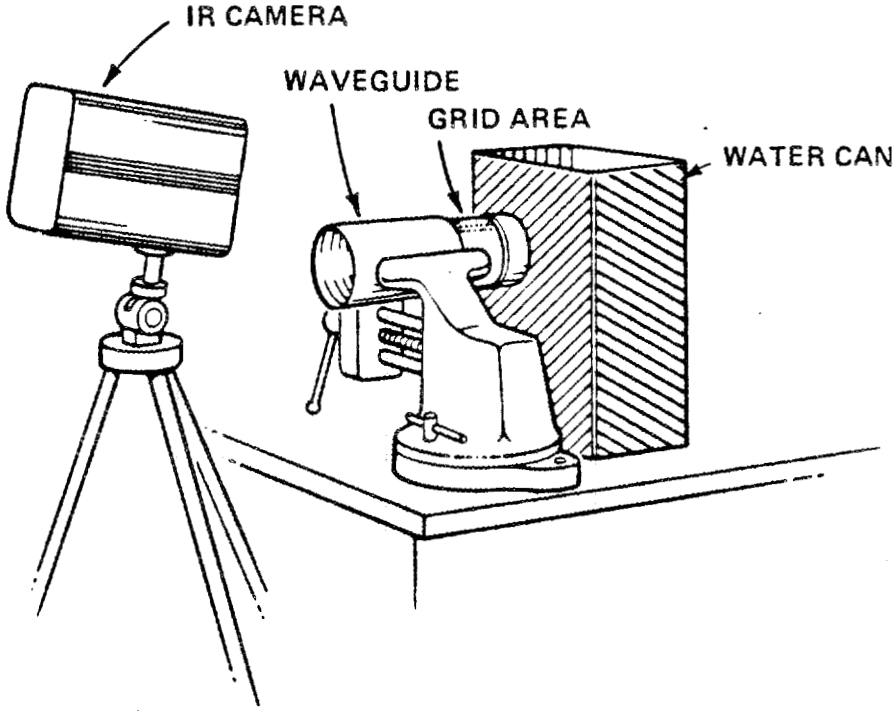

Figure 238. Overview of Thermal Imaging Experimental Arrangement

PHOTO 0687-82

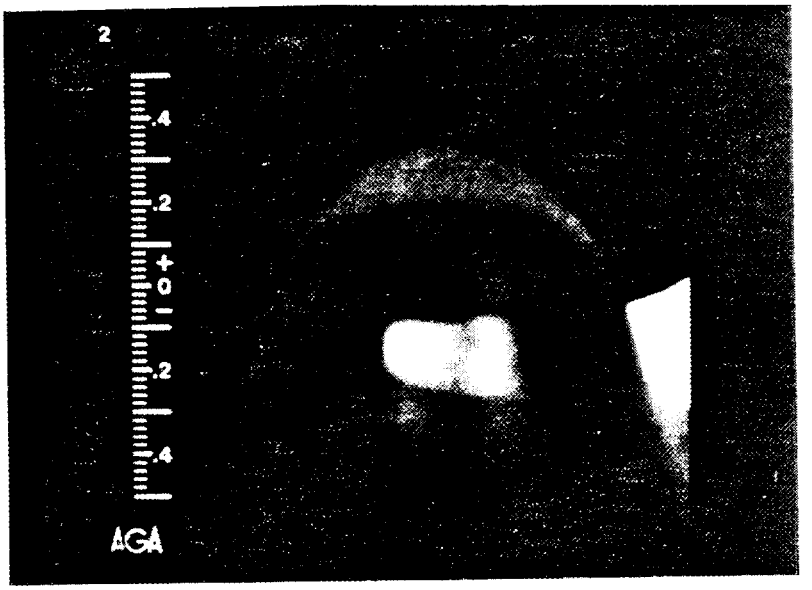

Figure 239. Finger Viewed Through Grid with IR Camera

Photo 0688-82

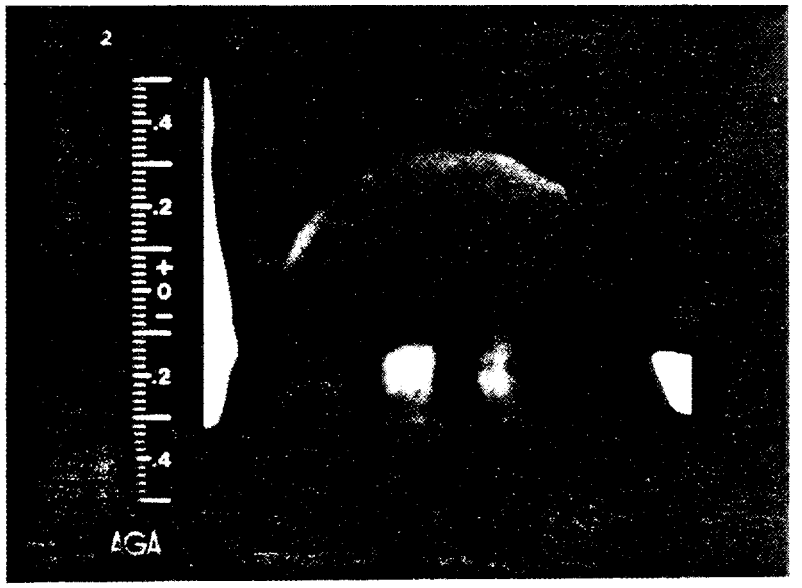

Figure 240. System Resolution Check

Photo 0692-82

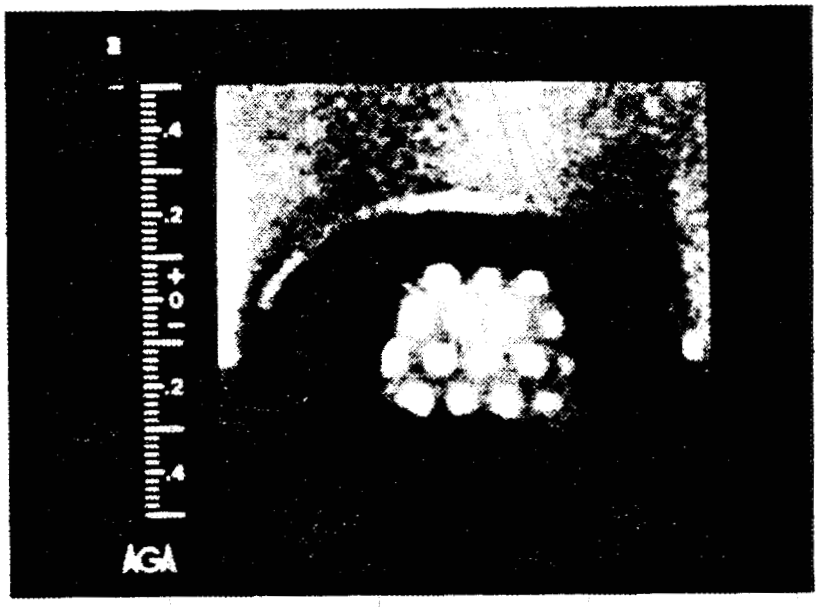

Figure 241. Hot Black Can Viewed Through Grid and Checkerboard Pattern

Photo 0689-82

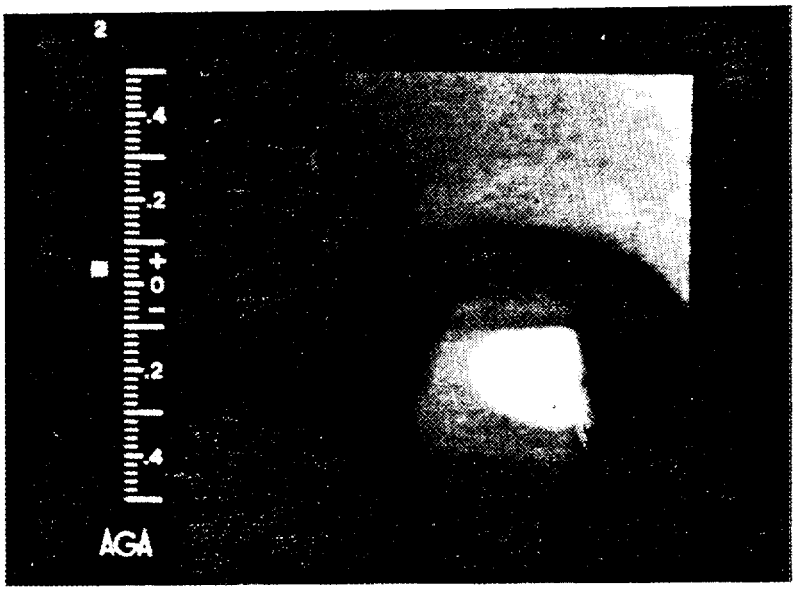

Figure 242. 26°C Isotherm on Finger Viewed Through Grid

Photo 0690-82

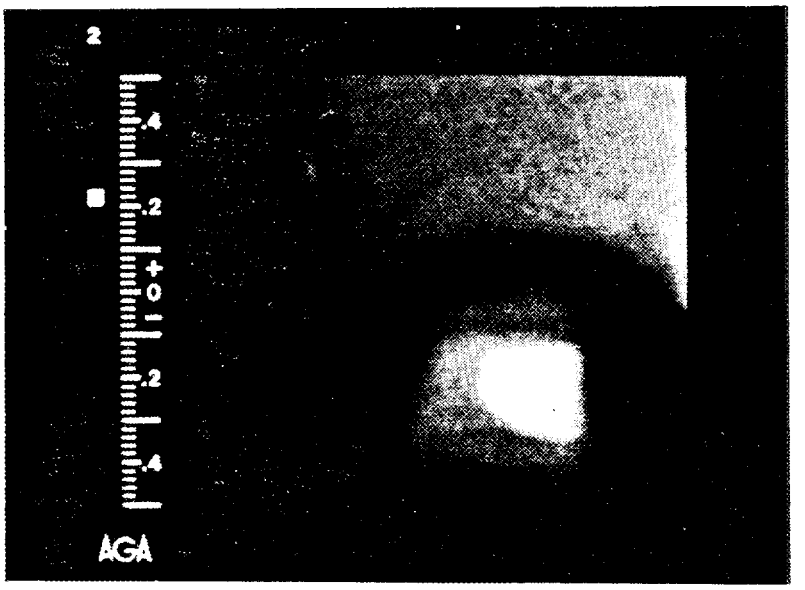

Figure 243. 26.4°C Isotherm on Finger Viewed Through Grid

Figure 243, the isotherm, moved to the center of the finger, is 26.4°C. These figures confirm high sensitivity through the grid. The rectangular outline of the grid can be seen in these photos. Also, the horizontal rows of grid holes can be perceived. This will be discussed later.

Figures 244 and 245 are similar to Figures 242 and 243, but in Figures 244 and 245, the grid was removed, so the camera observed the finger directly. Note the increased sharpness when blurring due to diffraction at the grid is no longer present. The isotherms were at 34.4°C and 34°C, respectively. The equivalence of this 0.4°C difference to the value obtained through the grid is not regarded as especially significant, because in both cases the outside isotherm rides the line between finger and background, and so, its setting may not have been exact.

The previous figures were all made with ambient background. At this point a black-painted, 1-gallon paint thinner can, seen at the center of Figure 238, was filled with hot water to provide an extended hot source for measuring the field of view. To accomplish this, a "checkerboard" cardboard cap was placed over the end of the spacer tube. The checkerboard comprised 5 mm square holes in rows with 10 mm center-to-center spacing, as shown in Figure 246. Adjacent rows were offset by 5 mm. The checkerboard openings are represented, edge-on in Figure 233, by heavy vertical line segments at the right-hand side.

Figure 241 shows the checkerboard pattern through the grid. In Figure 247, a piece of masking tape partially blocked the center hole to identify it. It is the center hole in the top row of Figure 246 and 241 that appears noticeably fainter than the other holes. The field of view, shown in Figures 246 and 241 is indicated by the dashed contour line in Figure 246. Note that the sensitivity is essentially uniform over the observed field of view, and that the walls of the grid holes do not block the view very much. However, the field of view is quite narrow at the top of the field of view. In an effort to determine whether this could be due to blockage by the edge of the grid, Figures 247 and 248 were drawn. These figures are nearly a top view of Figure 233. Figure 247 is a view normal to the plane containing the row of grid holes closest to the window

Photo 0683-82

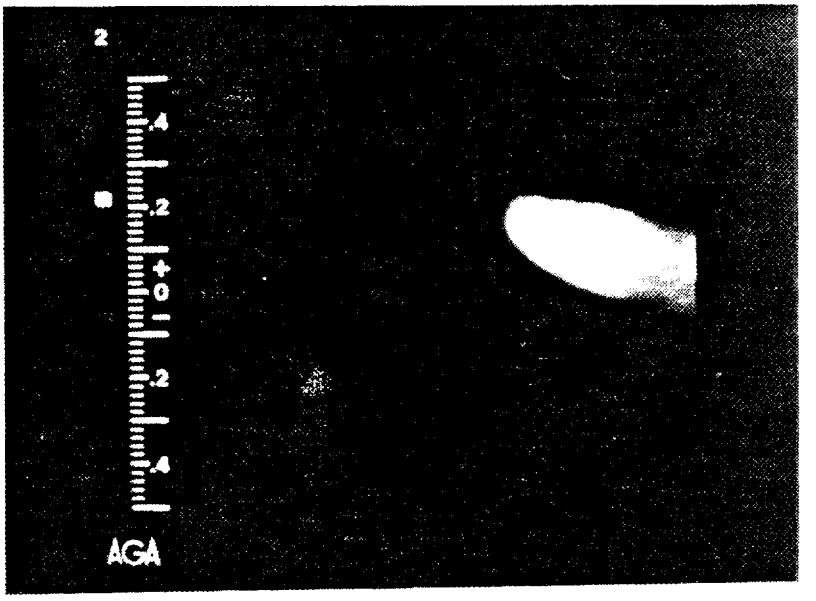

Figure 244. 34.4°C Isotherm on Finger

Photo 0691-82

Figure 245. 34°C Isotherm on Finger

Dwg. 82-3601 FED

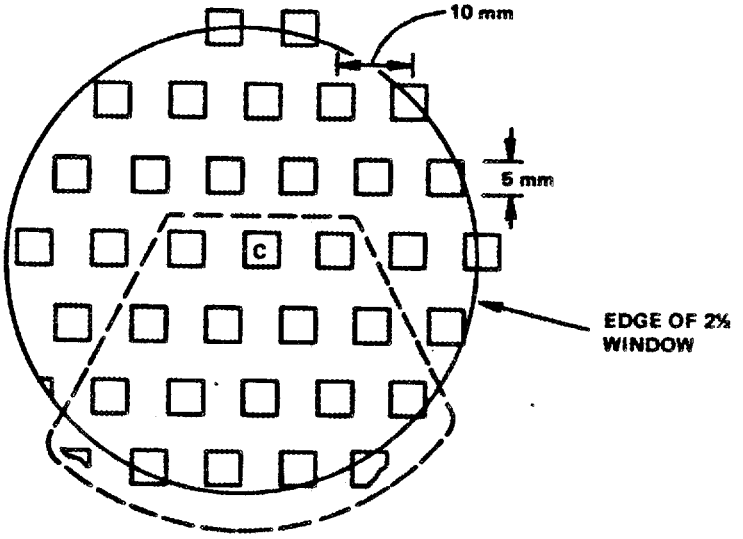

Figure 246. Checkerboard Pattern

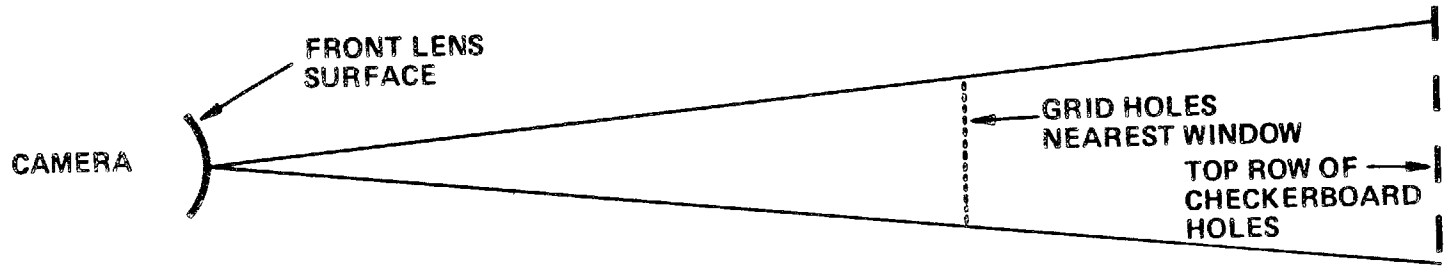

Figure 247. Horizontal Field of View Determination at Top of Picture

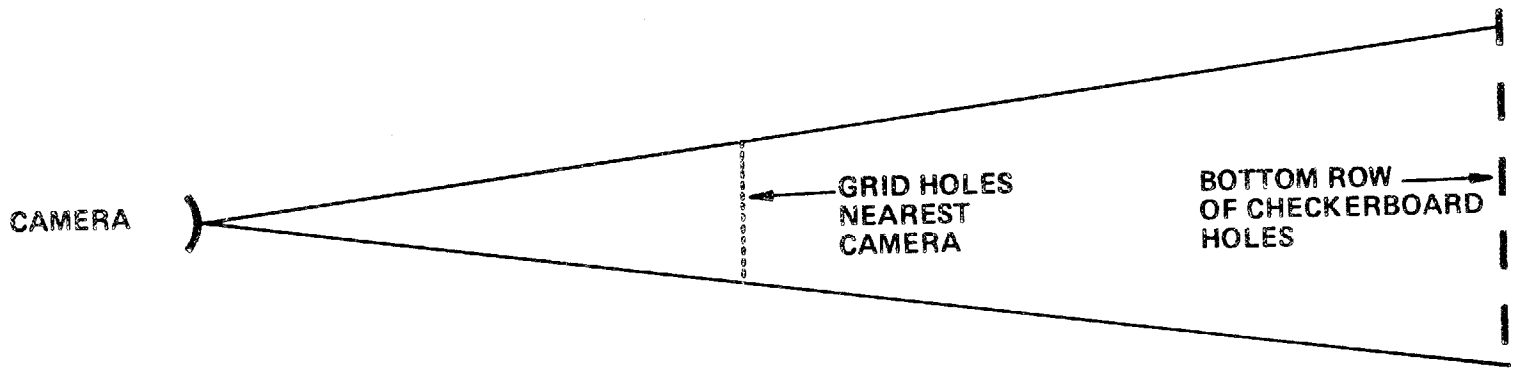

Figure 248. Horizontal Field of View Determination at Bottom of Picture

and the line joining the center of the camera lens to the center member of this row of holes. The checkerboard holes are indicated at the right. Note that 3-1/2 holes represent the extreme range of coverage; this explains why only three holes are visible in the top row of Figure 241. Similarly, Figure 248 indicates why all five holes in the bottom row were observed in Figure 241. The grid appears to limit the horizontal field of view near the center of the window.

Figure 249 represents an effort, by changing the position of the camera, to see areas of the window closer to the near wall. The center hole of the checkerboard is near the center hole in the lower row. Note that only one very short (2 holes) row of holes above center is visible. All other rows are located below the grid (below the line joining the camera lens to the near end of the grid). This is fairly consistent with what one would expect from an examination of Figure 233, but may be due to blockage by the hole walls.

The second grid has holes around the entire circumference, so only blockage by the grid hole walls comes into play. This effect will now be examined in greater detail.

Figures 250 and 251 represent a demonstration of the temperature gradient measurement across the front surface of the water can, through the grid. The isotherms are set at 36.4°C and 39.2°C in Figures 250 and 251, respectively. Again, little significance is attached to the difference, 2.8°C. The water temperature was 51.7°C when these pictures were taken.

Isotherms permit a calculation of the grid transmittance, from the relation:

$$T_a = T_g (1-T) + T_s T = T_g + T (T_s - T_g) \qquad (76)$$

where T_a is the apparent temperature of the source seen through the grid, and T_s and T_g are, respectively, the temperatures of the source and the grid.

Photo 4213-82

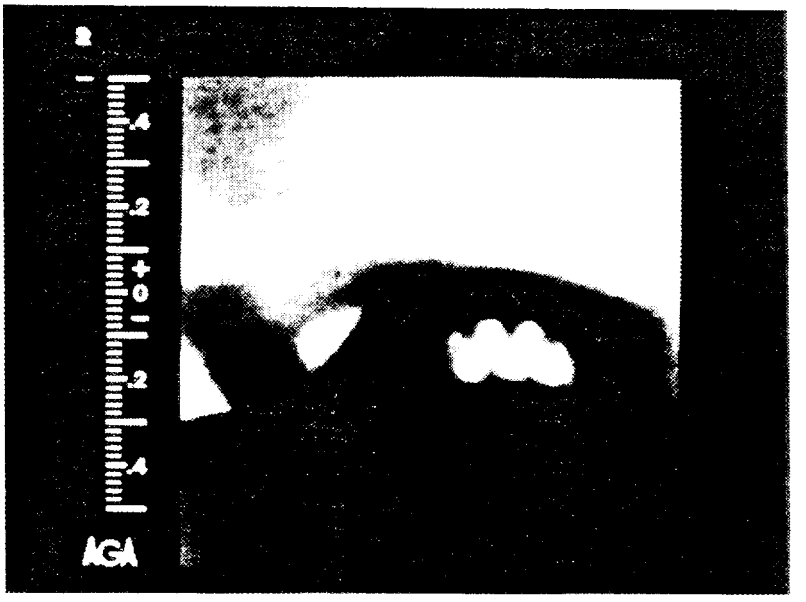

Figure 249. Field of View Looking Closer to Near Wall

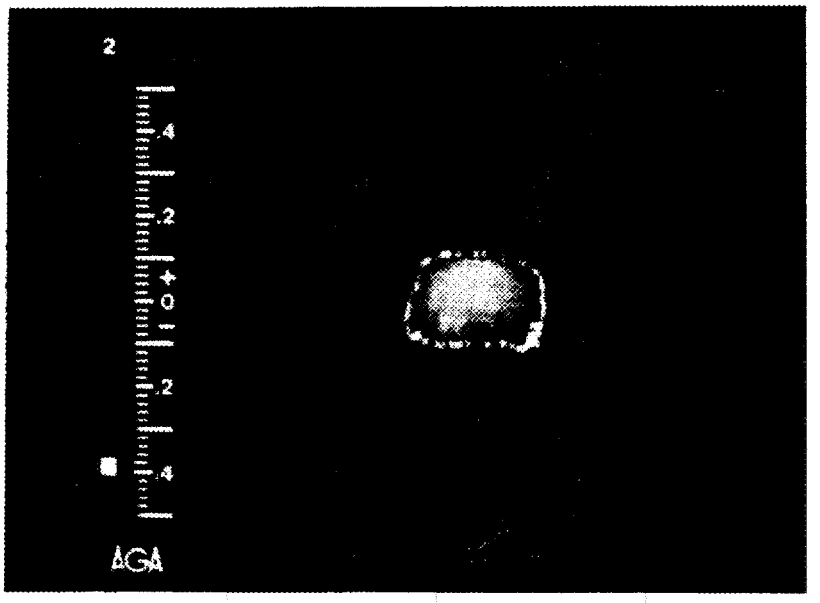

Figure 250. Black Paint at 51.7°C Through Grid, Isotherm at 36.4°C

Photo 4215-82

Figure 251. Black Paint at 51.7°C Through Grid, Isotherm at 39.2°C

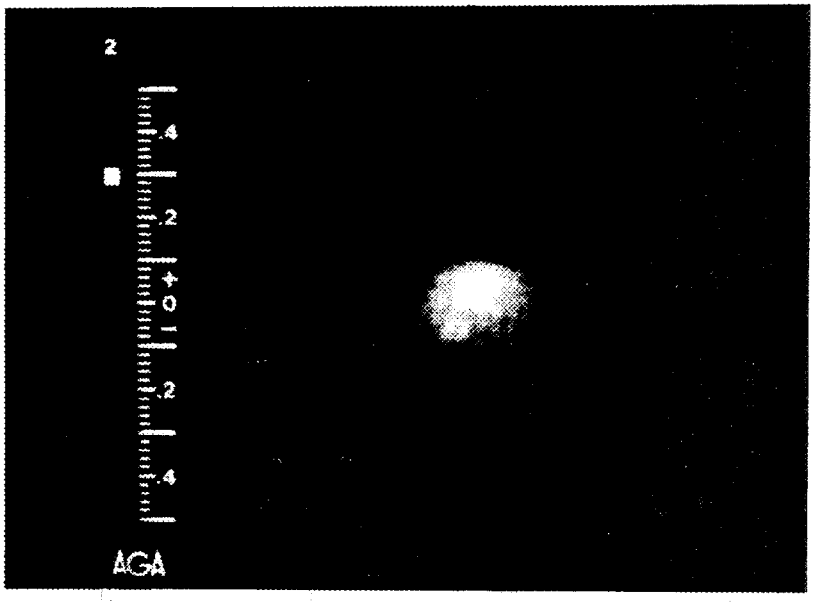

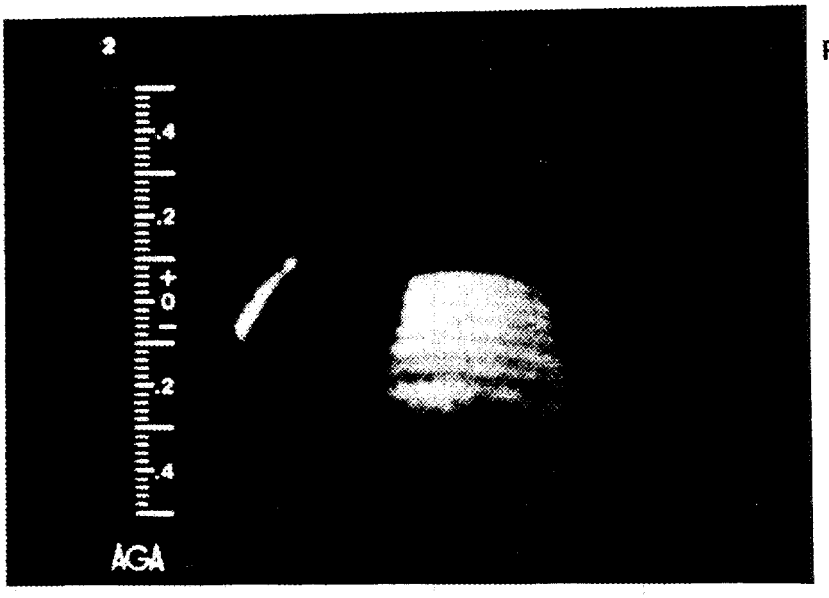

Photo 4216-82

Figure 252. Black Paint at 53.3°C Through Grid. Grid Holes Show.

Figures 252 shows the hot, painted source through the grid. The contrast and brightness adjustments were set to maximize the visibility of the grid elements. The focus may also have favored the grid. The seven rows of grid holes are clearly visible, and individual holes are faintly visible, as they were in Figures 242, 243, 250 and 251. Perhaps the camera should not have been set at its shortest focal distance, which was located 4.9" from the front lens surface. The grid was 3.5" away, and the window was 6.5" away. If the focus were set out farther, just until the window becomes defocussed, the grid would be defocussed, and this structure would vanish. The contrast had to be turned up quite high to get this picture.

The analysis of the effect of viewing the output window through an array of small holes in the waveguide wall using an infrared imaging system was encouraging. Tests with an AGA 780 infrared camera looking at various heated objects through a sample grid of holes demonstrated the potential of such a diagnostic. Next, tests were performed with the IR camera on P-1R3, a pulsed 200 kw, 60 GHz tube (at 1% duty, maximum pulse duration of 30 ms).

The vertical position of the output waveguide necessitated placing a front-silvered mirror in the IR optical path to limit the angle of declination of the camera, as shown in Figure 253. This was done to prolong the LN_2 holding time and facilitate access to the LN_2 dewar in the camera. The attenuation factor of the mirror was negligible, but the length of the optical path was increased slightly. This placed a portion of the grid structure into the field of focus. This effect is seen in Figure 254. A solution to this problem will be discussed later.

Before placing the camera in situ, problems in the gyrotron environment had to be addressed. Potential environmental hazards to the IR camera included:

ORNL – DWG-83-2127

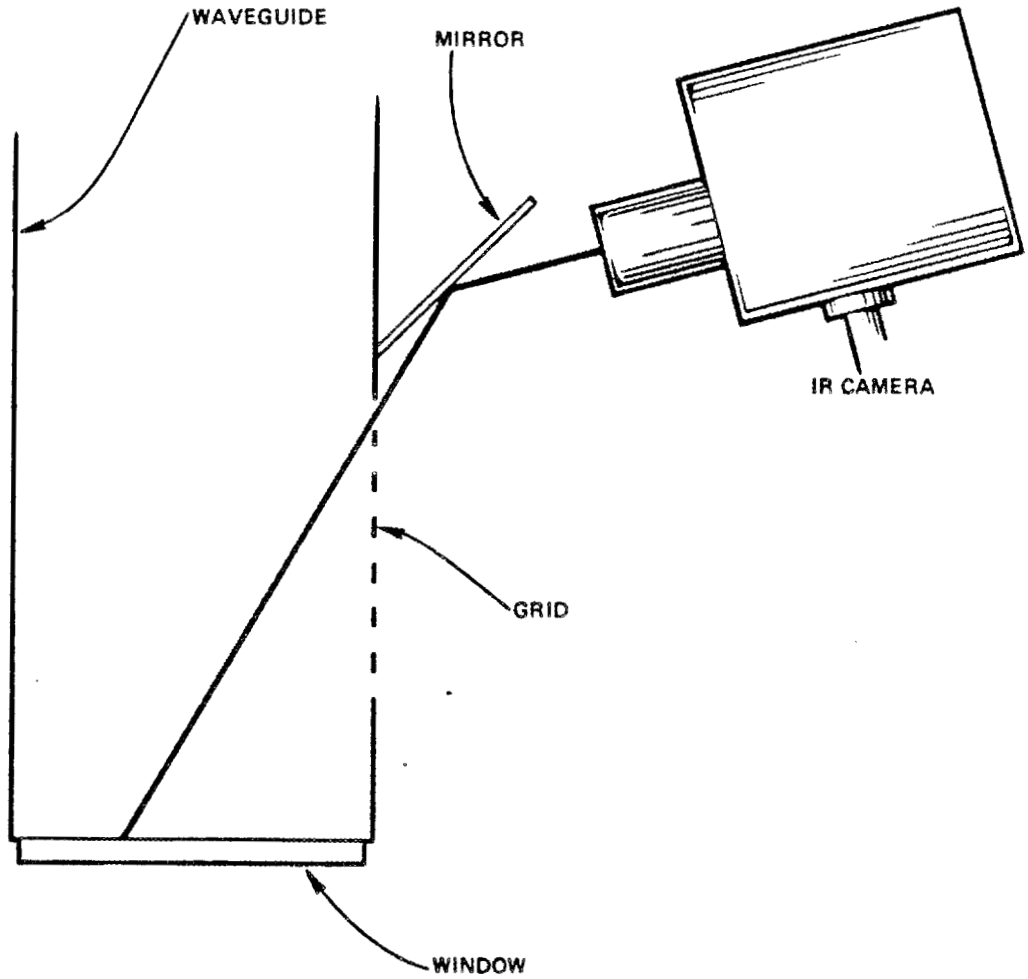

Figure 253. IR Optical Path

1) x-rays
2) microwave leakage, and
3) pickup or ground loops.

These hazards might have contributed to enhanced noise levels in the IR camera, degraded the long term performance of the camera, or even damaged the indium antimonide detector in the camera. Measurements of the x-ray leakage indicated that a lead plate below the camera would suffice. The microwave leakage at the surface of the grid was measured using a calibrated thermistor and a horn antenna. A peak power of 0.1 W total, corresponding to much less than 10 mW/cm^2 at the camera was measured. Pickup problems were minimal.

The thermal emissivity of both alumina and beryllia in the infrared was measured to be $\varepsilon \approx 0.95$. This indicated that an IR measurement of the pulsed or CW window was a surface temperature measurement and that the inner vacuum window in the CW tube cannot be analyzed using this technique. This was confirmed in a test placing a $330^{\circ}C$ soldering iron behind an alumina window at room temperature. Aligning the soldering iron, window and camera along a horizontal axis reduced the convective heating effects on the window. No image of the soldering iron was observed even when it was placed 4" behind the window.

Polished copper and aluminum are excellent reflectors of 3-5 μm light. Tests with a window assembly indicated that reflections might become a problem. This was solved by coating the outside copper waveguide and holes with a fine layer of flat black paint. This then required that the waveguide be kept cool; room temperature was sufficient. Figure 254 shows a measurement of the transmissivity of the grid, using a $60^{\circ}C$ blackbody. The center of the "window" is denoted by a +. The lowest bright arc in the figure is the boundary of the "window". Note the dim region below that arc is due to reflection on the inside copper waveguide wall. The inside wall reflection can be reduced by "painting" the wall black and keeping it cool. The white square boundary in Figure 254 represents the electronic viewing area for calculating the maximum thermal level, as displayed on the lower right.

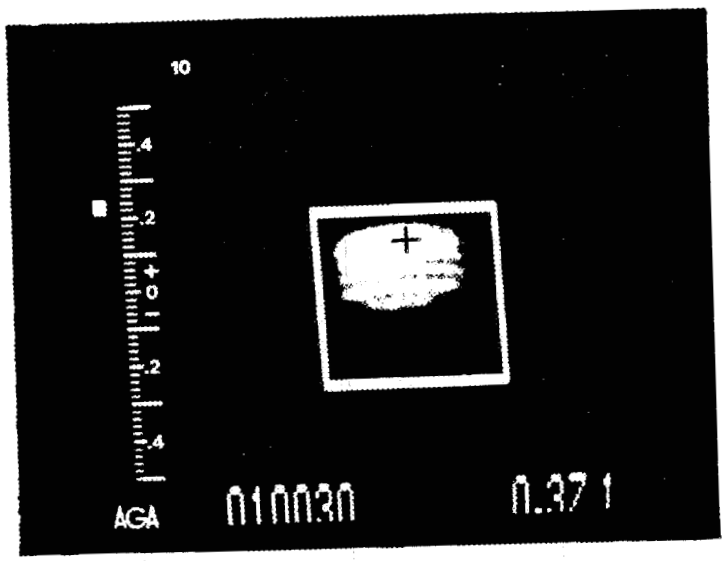

Figure 254. 60°C Blackbody Calibration of Grid Transmission

Figures 255, 256 and 257 are thermal imaging results of the P-1R3 window. Figure 255 shows the IR image of a heated template for alignment and calibration as viewed through the grid in situ. The center of the window is marked with a +. Note reflections of the flanges, etc., at the top of the picture. Figure 256 shows the thermal image of a cold window, no rf, and using the isotherm contour control. Figure 257 shows the resultant thermal pattern of a 30 ms, 200 kw pulse. Note the curved contour. The resultant image is a combination of the grid transmission function and the window thermal profile. The maximum temperature change measured was only $\Delta T \simeq 4\text{-}5^{\circ}C$ at approximately the center of the window. No unusual hot spots were observed. For longer pulses, the temperature rise will be much greater which will improve the thermal image. The use of a larger grid surface would increase the observed window area. A computer analysis of the grid transmission function can improve the thermal image and is highly desirable. These results from P-1R3, a pulsed tube, are highly encouraging.

An improvement in the apparent size of the window area on the IR monitor screen was made by changing to a lens with a narrower field of view. The new system has two advantages: 1) the field of view is decreased, thus increasing the apparent size of the IR monitor, and 2) the focal depth of field is reduced, thus reducing the effect of the grid.

The photos in Figures 258a and 258b show the improved image using a template with holes drilled in radial patterns. The new lens has enabled better viewing of the thermal pattern on the window and helped determine the effects of various operating conditions.

The first opportunity to test the IR system on the 60 GHz family of CW tubes was on VGE-8005 S/N 1 (56 GHz CW). This tube had a double-disc alumina window, 3/2 λ thick.

The photo in Figure 259 is a thermal image of the window at 110 kW CW. The center of the window is denoted by a "+" and the edge of the window was sketched in. The small, bright spot at the upper

ORNL – PHOTO-0077-83

Figure 255. IR Image of Template for Alignment and Calibration of IR System

ORNL – PHOTO-0078-83

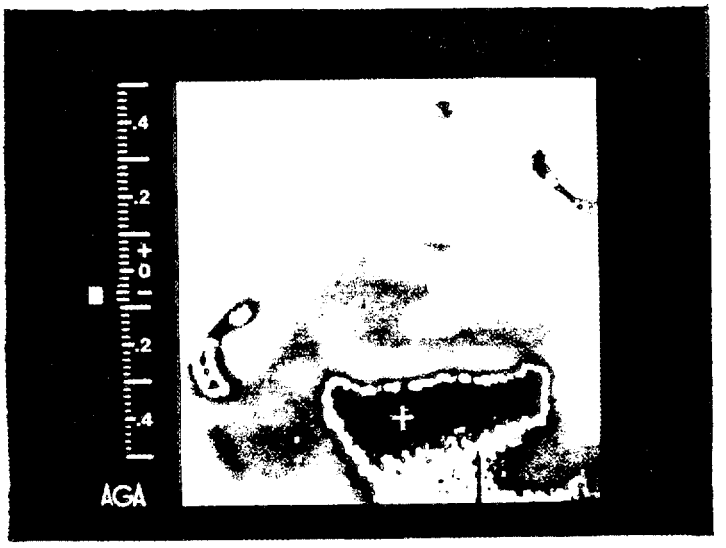

Figure 256. IR Image of P-IR3 Window, no rf

ORNL – PHOTO-0079-83

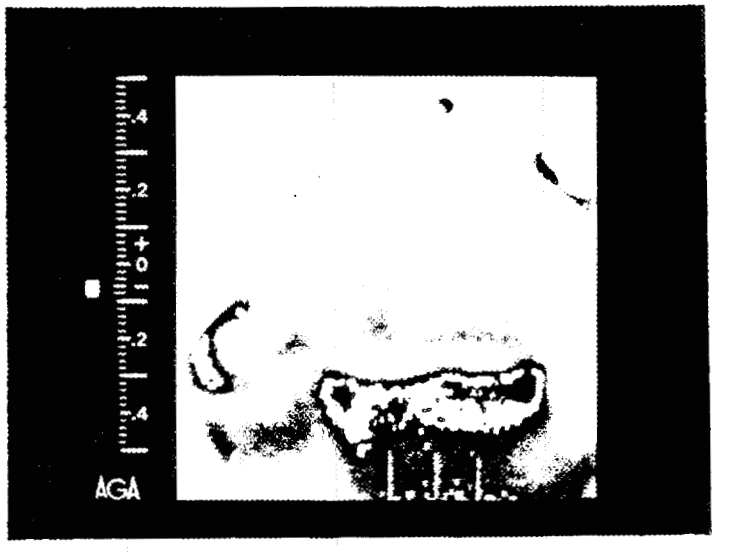

Figure 257. IR Image of P-IR3 Window, 30 ms, 200 kW Pulse

ORNL PHOTO - 0080-83

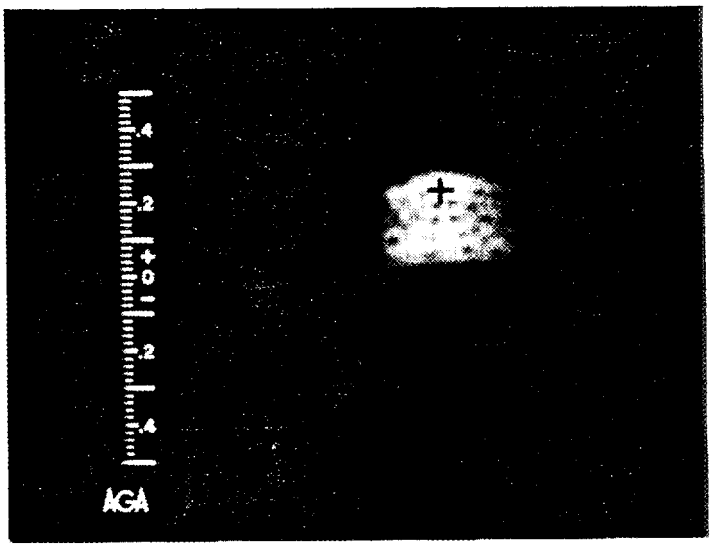

(a) Old Lens

ORNL PHOTO - 0081-83

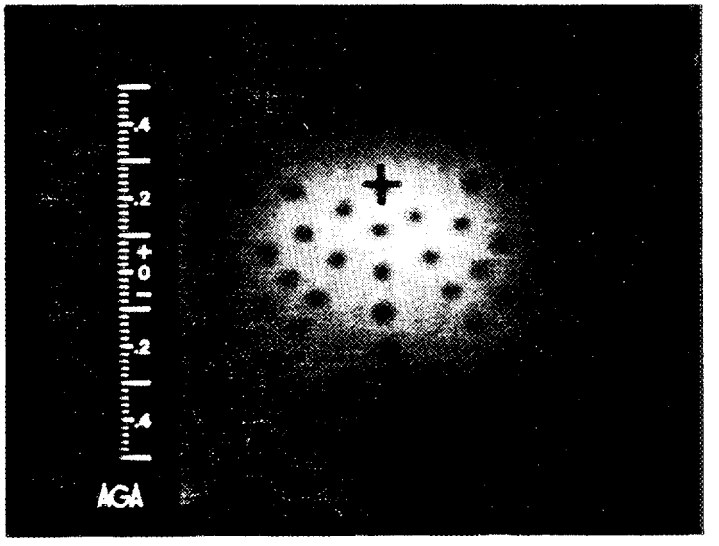

(b) New Lens

Figure 258. Improvement of the Thermal Image of a Template with Radial Pattern of Holes. The Center is Denoted with a "+".

ORNL PHOTO - 0082-83

110 kW

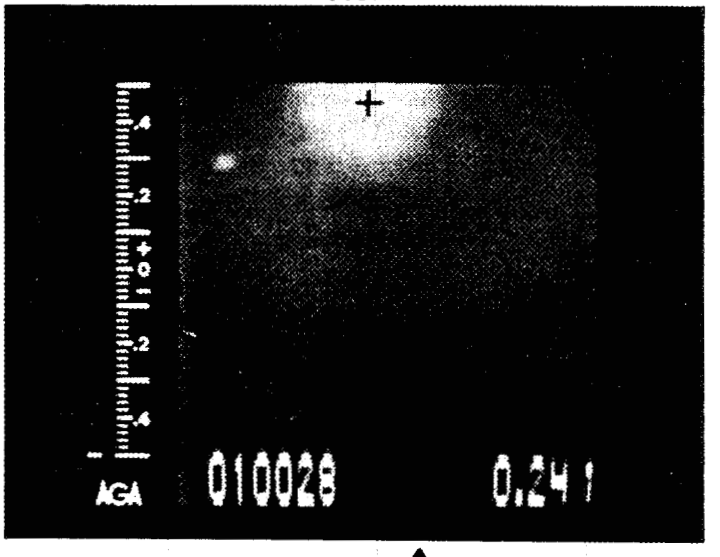

FC-75 FLOW DIRECTION

Figure 259. VGE-8005 S/N 1 Thermal Image at 110 kW Output Power. Center of the Window is Denoted by "+". IR Camera: F/1.8.

left is due to a speck of material that had fallen onto the window surface. The large, white spot at the window center is the "hot" region of the window. FC-75 coolant flow is 7.8 gpm in the direction indicated. Moving the camera to a different position resulted in virtually the same image.

Figure 260 is a graph of the temperature at the first maximum as a function of output power. A linear regression curve fit to the data extrapolates to $90^{\circ}C$ temperature at 200 kW. Error bars on the temperature were determined by varying, within reasonable limits, the ambient (background) temperature and transmission function. Note the error bars are slightly larger at lower temperatures than at higher temperatures. The FC-75 inlet temperature was found to rise $8.5^{\circ}C$ during the course of the measurements. FC-75 flow rate was 7.8 gpm. Slight boiling of the water load was detected at 110 kW. The measured maximum window temperature was much less than $100^{\circ}C$, thus temperature gradients were not expected to cause large thermal stresses.

A radial temperature profile was taken at 110 kW output power, as shown in Figure 261. Both peaks appeared to occur at smaller radii than in an empty waveguide for TE_{02}. The direction of FC-75 flow is $\sim 10^{\circ}$ off from this radial direction. No unusual asymmetries were observed as a function of angle except for the small hot spot mentioned earlier.

A critical dependence of the FC-75 flow on the window temperature at the first maximum is shown in Figure 262. At various output powers, the flow of FC-75 is varied. It appears that at higher powers, the rise in temperature for reduced flow rates is sharper. An extrapolation at 130 kW indicates that boiling of FC-75 might occur near 4 gpm. The boiling point of FC-75 at 25 psi is about $136^{\circ}C$.

There was some concern that boiling in the waterload might cause severe mismatching or mode conversion, which would result in a reflection of power to the window.

ORNL DWG 83-2177

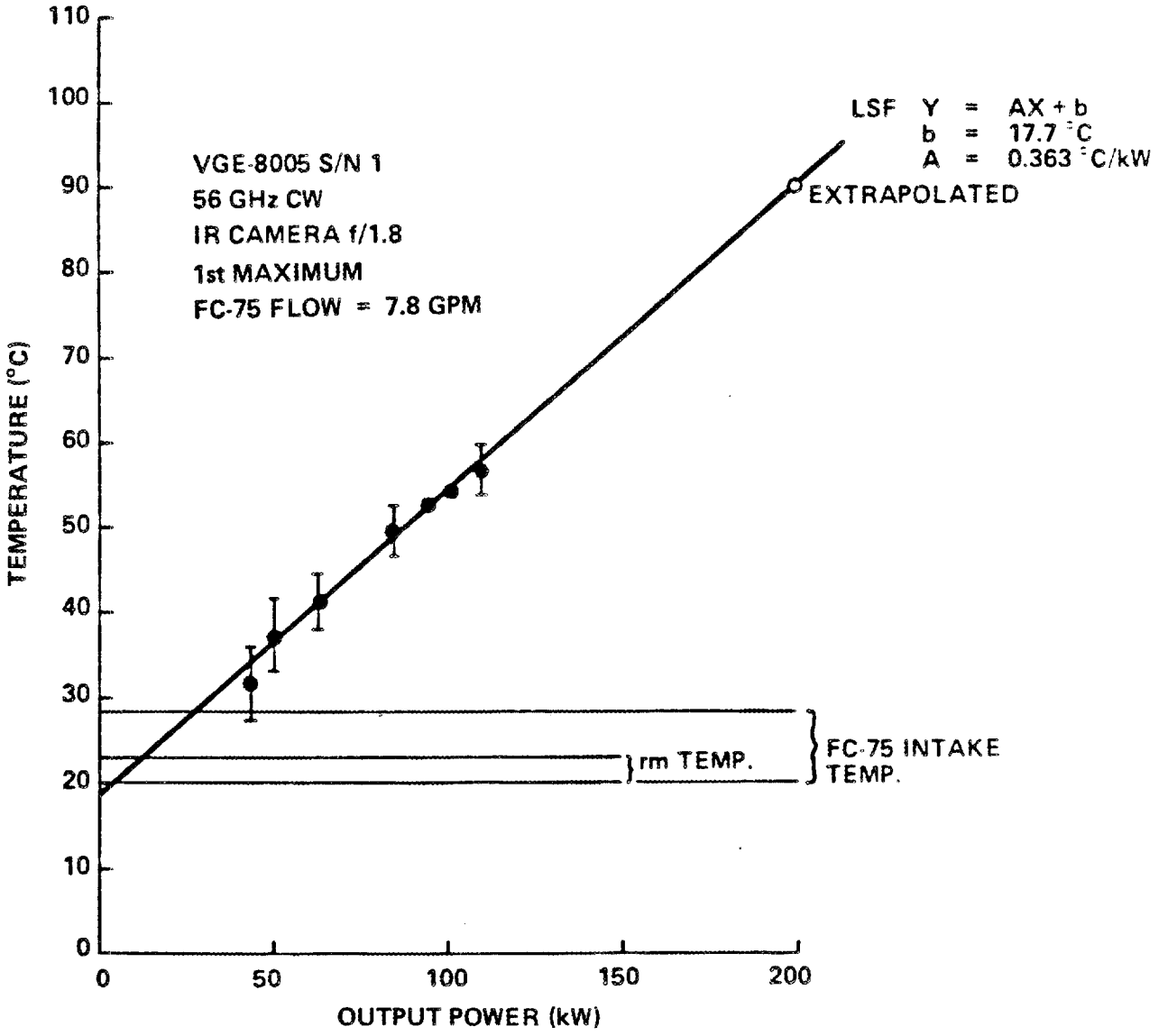

Figure 260. Temperature at Inner Radial Maximum vs Output Power

ORNL DWG 83-2178

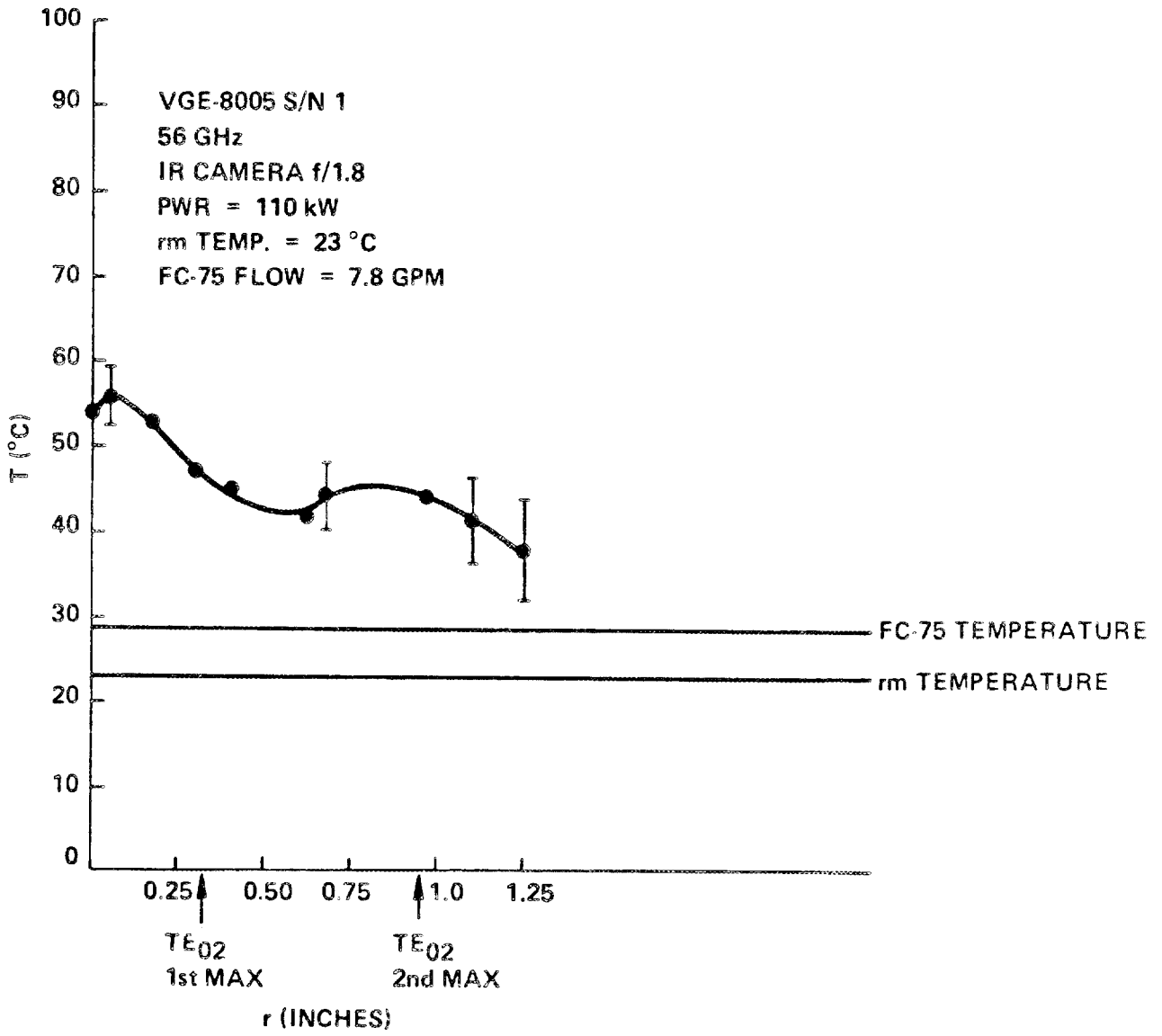

Figure 261. Radial Temperature Profile, Output Power = 110 kW

ORNL DWG 83-2179

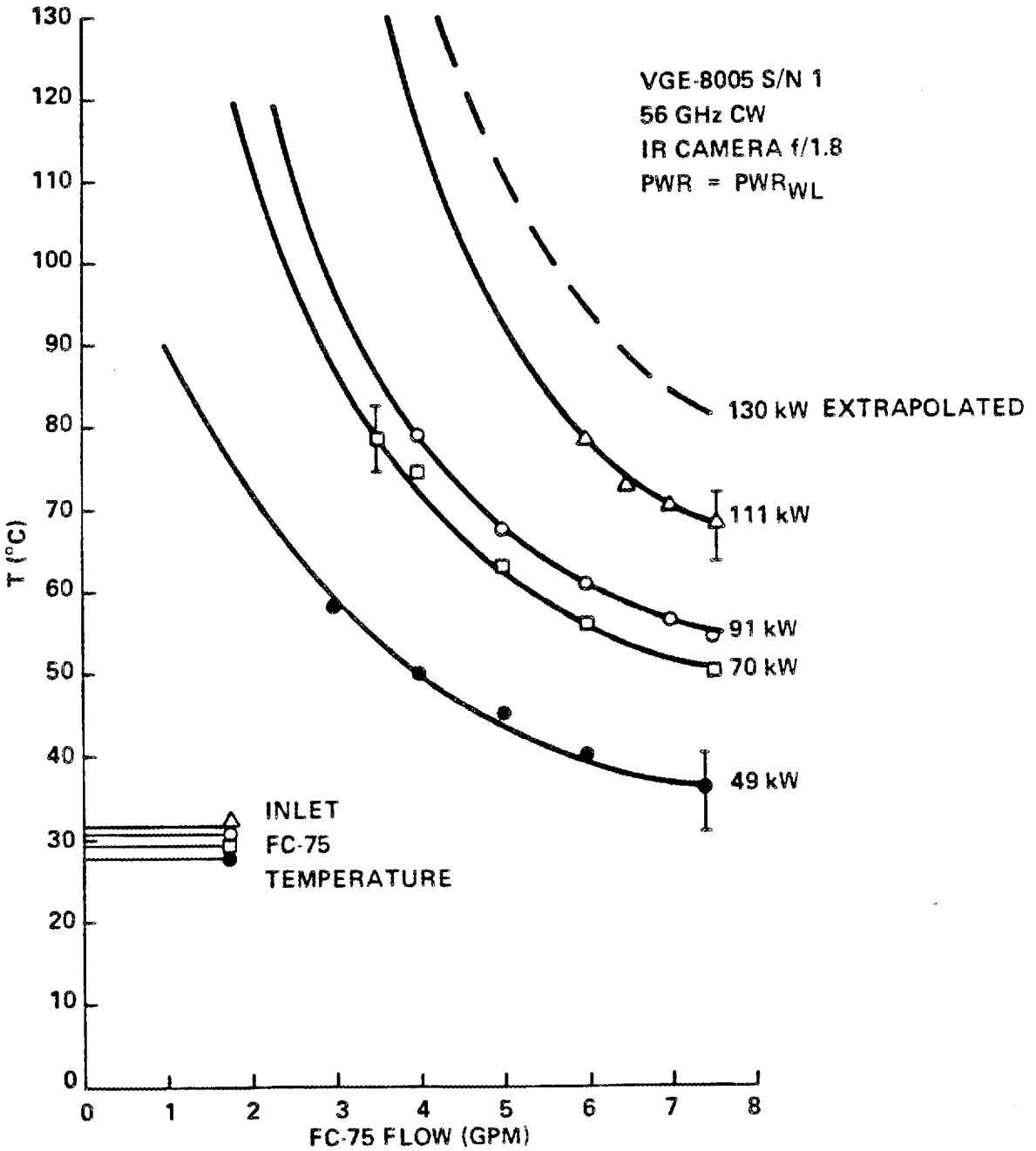

Figure 262. Maximum Window Temperature vs FC-75 Flow

In Figure 263, a comparison of the window temperature versus output power for two different waterload flows are shown. The onset of boiling in the water load is indicated. No sharp deviation in the window temperature occurred even as the boiling in the waterload became violent. The offset in temperature for the two different cases is mostly due to changes in the FC-75 inlet temperature.

One can compare the results shown in Figures 260 and 263, to determine the consistency (reproducibility) of the IR camera measurements. Taking into account slight differences in FC-75 flow and FC-75 inlet temperature, reproducibility is well within error limits.

Measurements with the FC-75 chiller indicate an $8.5^{\circ}C \pm 2^{\circ}C$ reduction of the first maximum for a $13^{\circ}C$ FC-75 inlet temperature reduction operating at 95 kW. At 75 kW, a $13^{\circ}C \pm 2^{\circ}C$ reduction of the window temperature was measured for a $10^{\circ}C$ FC-75 inlet reduction. The measurements were performed by noting the temperature under normal operation, then shutting down to make a plumbing change. Slight variations in the operating parameters may result in different mode mixture or phasing which may account for the larger temperature reduction at 75 kW.

Measurements were made using the IR camera system to view the output window of X-6. Figure 264 is a pair of thermographs (raw data) which were taken at the same output power (143 kW CW) on X-6, but at two slightly different tube operating conditions. The window centers are indicated by a "+", and the waveguide wall edge of the window is sketched in. The whiter portions of the thermographs represent a combination of the hotter parts of the window and the transmission function of the grid. However, the salient features of the window heating patterns can be discerned. In Figure 264a, a distinct ring corresponding to the TE_{01} peak, can be seen. Figure 264b, though, shows patterns similar to the 56 GHz case, where only the center region is hot. The magnetic field at the cavity center for the two cases differs by only 37 G (out of 23 kG).

Figure 265 is a plot of the peak window temperature as a function of output power. In the region between 80 kW and 125 kW, the

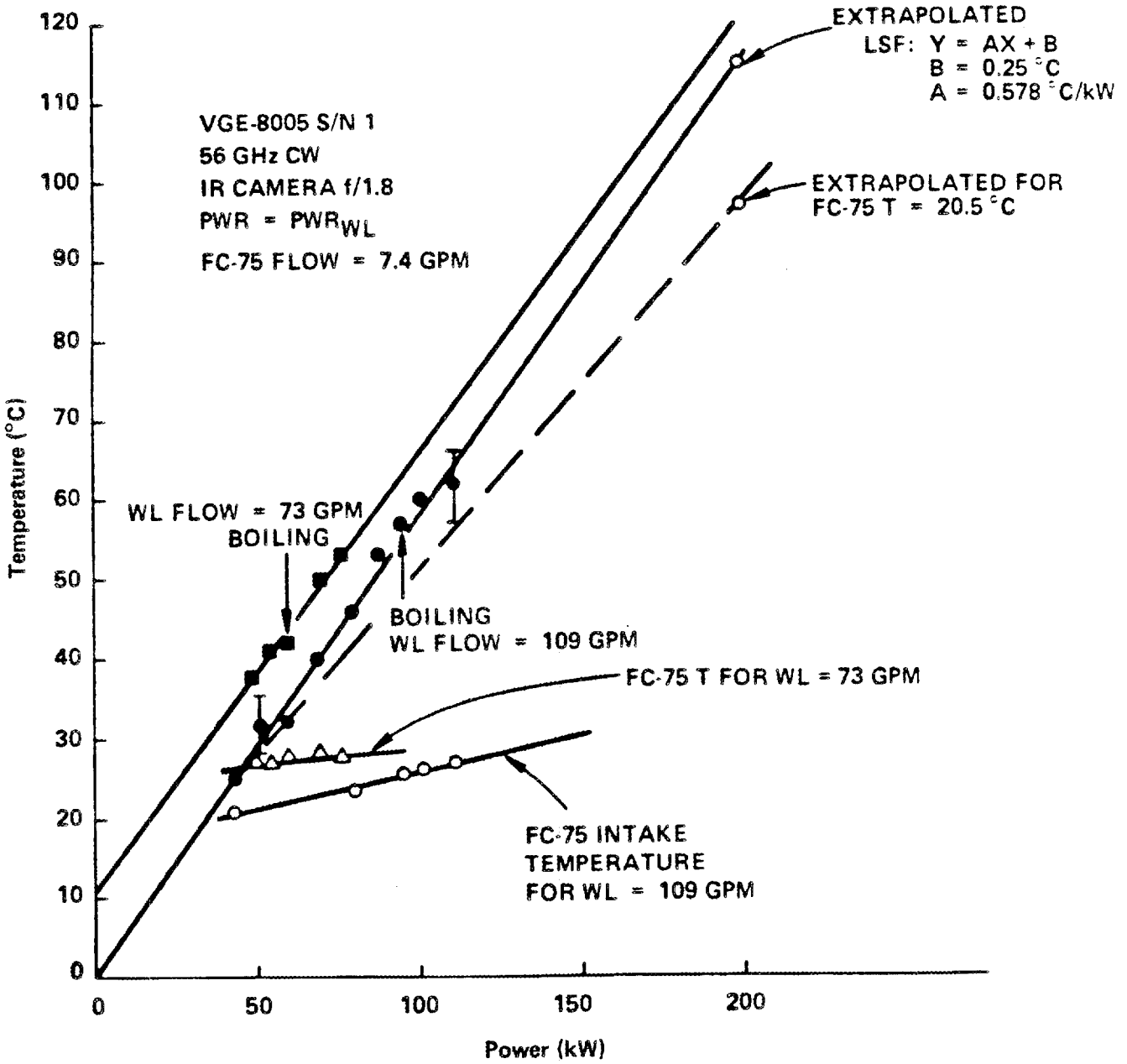

Figure 263. Maximum Window Temperature vs Output Power for Different Water Load Flows

ORNL – PHOTO – 0096-83

143 kW CW

a.

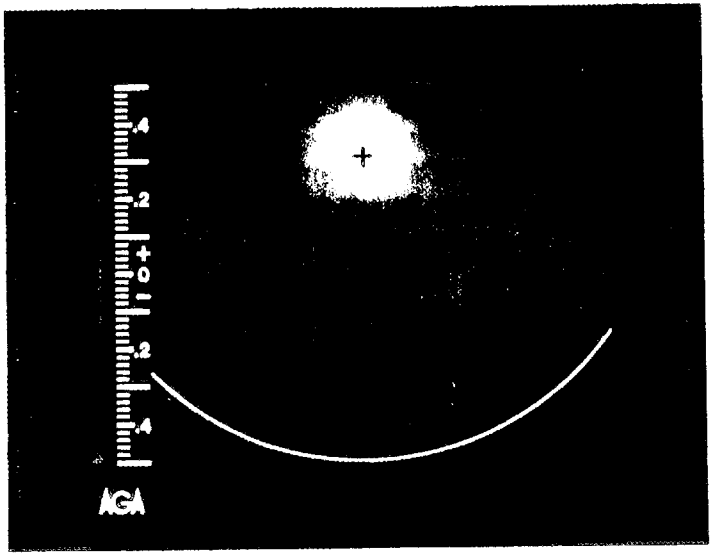

T_{max} = 90°C ± 5°

b.

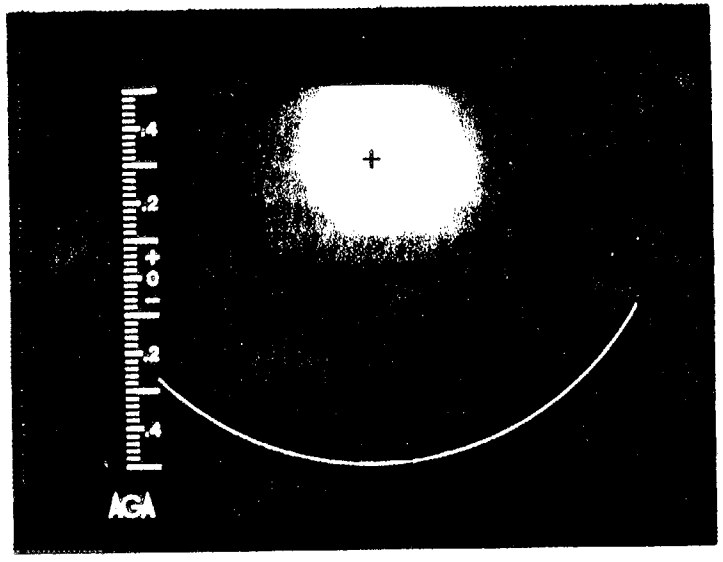

T_{max} = 100°C ± 5°

	I_1 (A)	I_2 (A)	I_3 (A)	V_o (kV)	I_o (A)	V_{MA} (kV)
A)	27.56	23.06	2.15	78.3	4.80	19.3
B)	27.60	23.10	2.13	80.3	4.65	19.0

Figure 264. Thermographs of X-6 Window

ORNL – DWG – 83-3234 FED

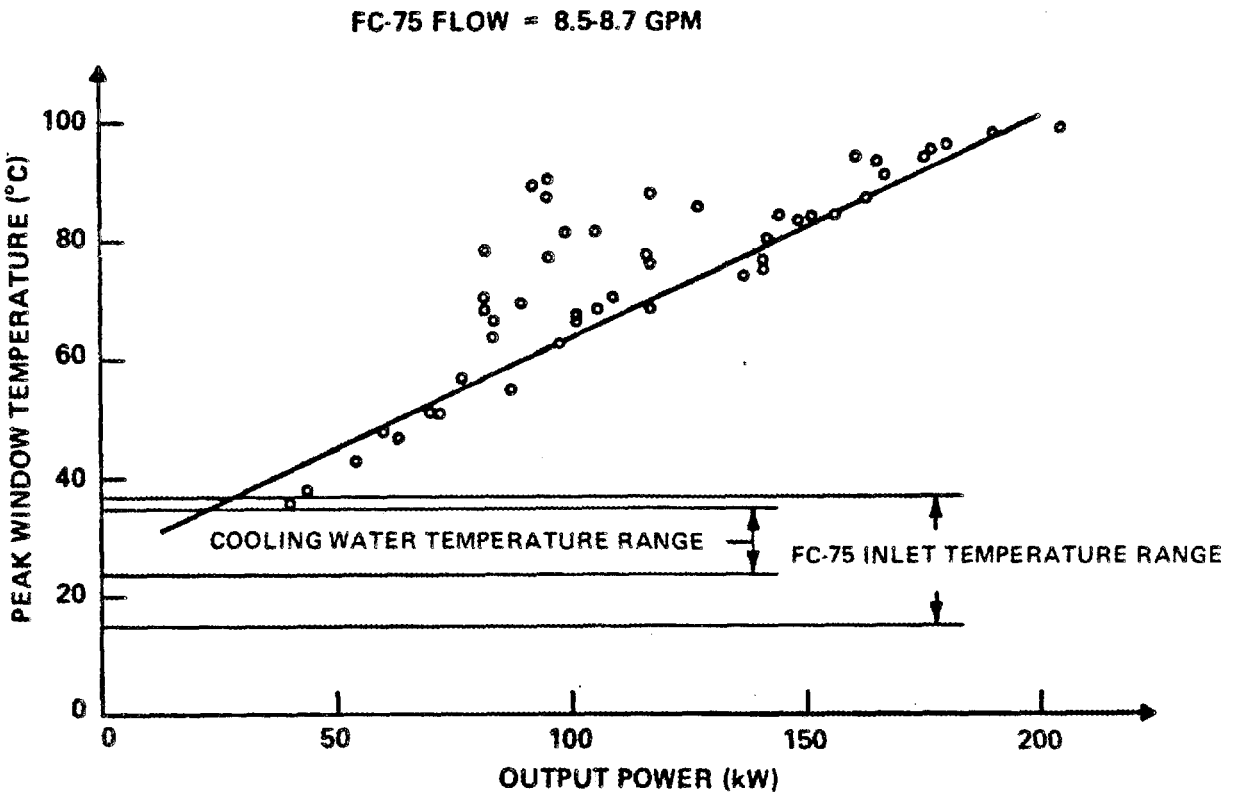

Figure 265. Compilation of All Window Temperature Measurements as a Function of Output Power for the VGE-8006, S/N X-6 During CW Operation. A Number of Tube Parameters and Operating Conditions Changed in the Course of Taking These Measurements.

main magnet #1 current was varied. Operation of X-6 at 200 kW was attained by carefully increasing the output power while maintaining a low ($\leq 100^{\circ}C$) peak window temperature. At 200 kW, the peak window temperature was maintained at $100^{\circ} \pm 5^{\circ}C$ for about an hour.

The range of variation of the peak window temperature is also illustrated in Figure 266, which is a plot of the peak temperature versus main magnet #1. The output power was held constant by adjusting the gun anode voltage. These measurements by the IR camera suggest a number of possible occurrences. Mode conversion in the cavity or at other areas of the tube might be taking place. Load matching and ghost modes in the window are other possibilities. A major difference in the X-6 tube is the use of a step cavity. On the 56 GHz tube (VGE-8005 S/N 1), the low temperature of the window (due to operating at $\leq$ 110 kW), together with the much more limited operating regime of the standard cavity, did not permit us to see much of a window temperature variation.

In summary, the IR camera has provided us with a real time observation of the window temperature to guide X-6 tube operation to 200 kW performance. A large variation in peak window temperature on X-6 has also been noted.

9. Design Optimization of Double-Disc Windows

A parametric study was performed on a series of discs made of different materials and with different diameters and thicknesses for the 60 GHz CW windows. The cases studied are summarized in Table 35. The best geometric and material combination is a 4"-diameter by λ-thick alumina window.

The influence of window diameter on thermal hoop stress is shown in Figure 267. It can be seen that with the same thickness and material, a larger diameter window will have a smaller thermal hoop stress under the same design condition. Similarly, if the diameter, the material and the design conditions are the same, the thinner window has lower temperature and hoop stress. This is shown in Figure 268.

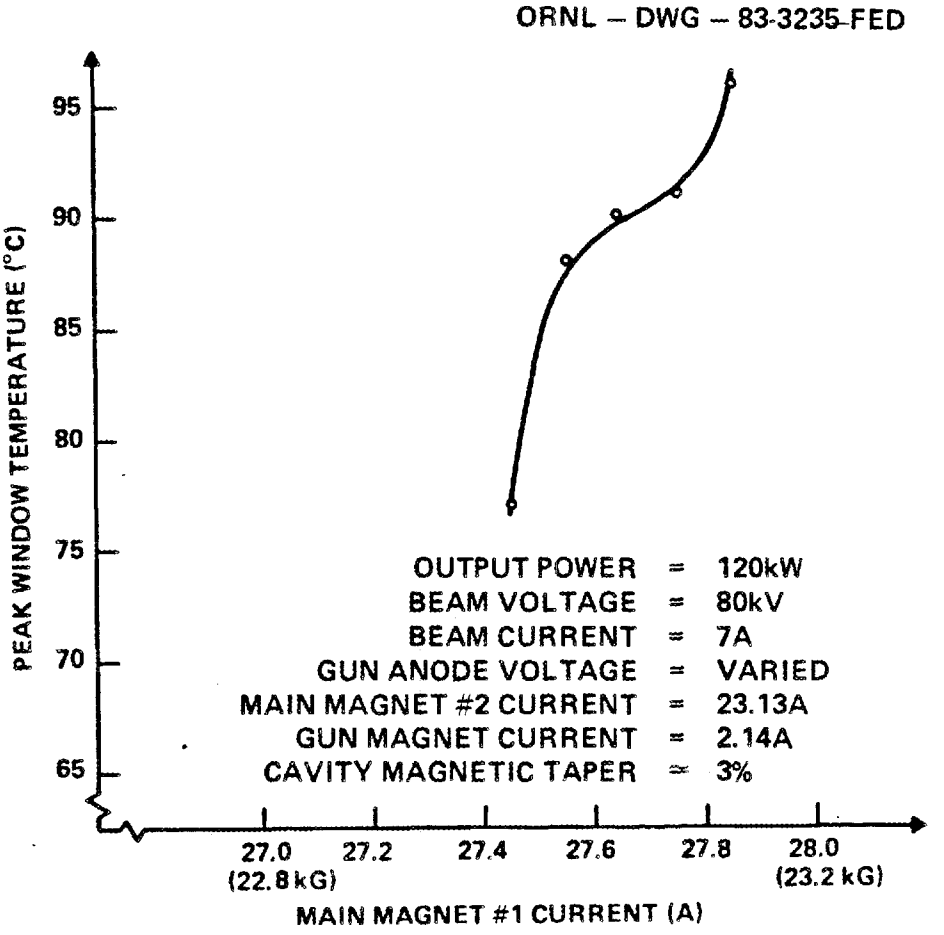

Figure 266. Peak Window Temperature as a Function of Main Magnet No. 1 Current for a Constant Output Power for the VGE-8006, S/N X-6 During CW Operation (FC-75 Inlet Temperature 15.6°C)

TABLE 35 SUMMARY OF DESIGN OPTIMIZATION

THICKNESS / DIAMETER	$2\left(\frac{\lambda}{2}\right)$	$3\left(\frac{\lambda}{2}\right)$	$4\left(\frac{\lambda}{2}\right)$	$5\left(\frac{\lambda}{2}\right)$
3 INCH	ALUMINA 995	ALUMINA 995 BERYLLIA 995 SAPPHIRE	ALUMINA 995	ALUMINA 995
4 INCH	ALUMINA 995 (BEST DESIGN)	ALUMINA 995		

NOTE: THE SAME DESIGN CONDITIONS OF 120 kW CW (TE_{02} MODE) AND HEAT TRANSFER COEFFICIENT OF 2.5 W/IN^2·°C HAVE BEEN APPLIED TO ALL CASES

ORNL – DWG-83-2121

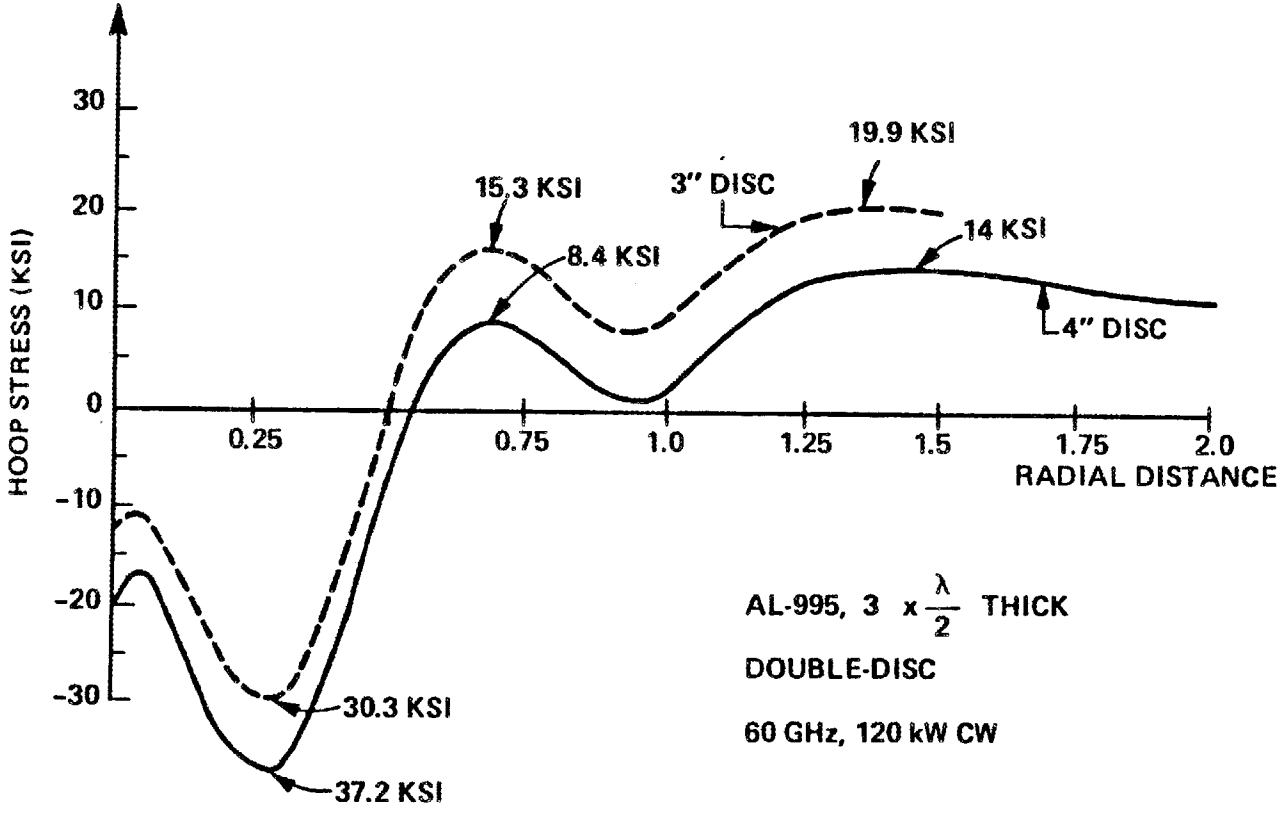

Figure 267. Influence of Window Diameter on Thermal Hoop Stress

ORNL – DWG-83-2122

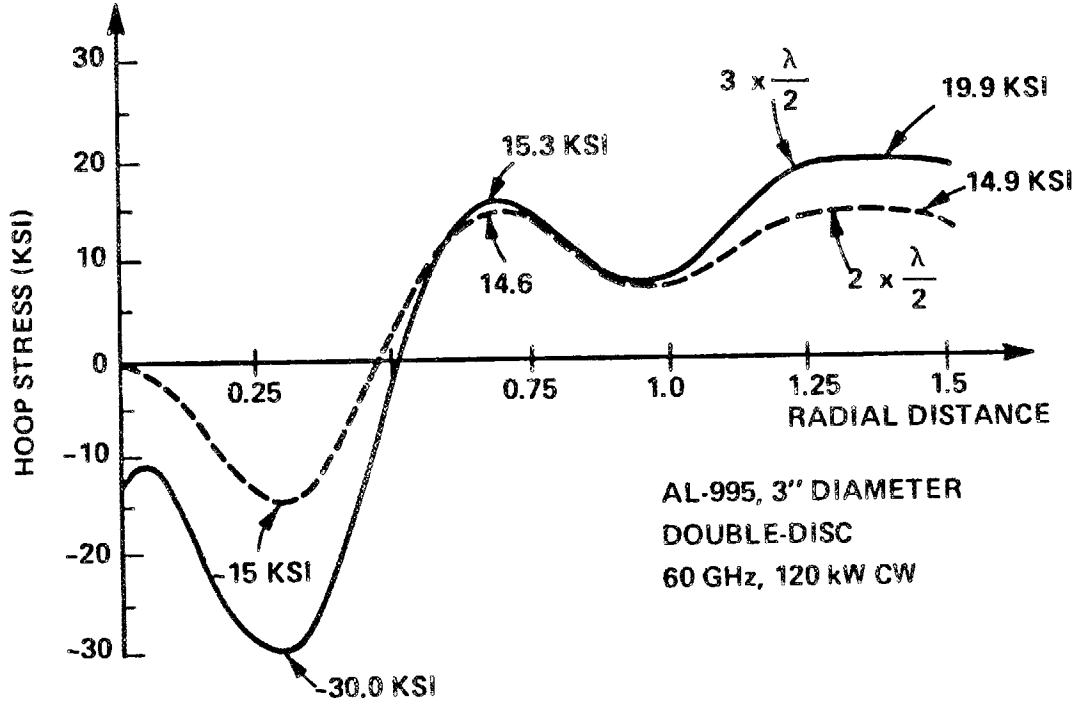

Figure 268. Influence of Window Thickness on Thermal Hoop Stress

10. Nonlinear Analysis of 60 GHz Windows

All previous analyses were performed with the assumption that the attenuation constant and the heat transfer coefficient are independent of temperature. In a more refined analysis, the temperature dependence of both the dielectric loss and the heat transfer coefficient need to be considered.

The power loss in the window was calculated by the formula

$$P_{loss} = P_{output} \left(1 - e^{-\alpha \ell}\right) \quad , \tag{77}$$

where P_{output} is the power output distribution for TE_{02} mode, which is proportional to Bessel function $J_1^2(r)$.

α = effective attenuation constant in Nepers/cm

ℓ = thickness of disc.

(Note that the effective α must account for the internal reflections which occur within the dielectric.) Only α is temperature dependent, and it is calculated by the equation for half-integral wavelength thicknesses

$$\alpha = \frac{2\pi \sqrt{\varepsilon} \tan\delta}{\lambda} \; \frac{1 + |\rho|^2}{1 - |\rho|^2} \quad , \tag{78}$$

where ε is the dielectric constant, tan δ the loss tangent, λ the free space wavelength and

$$|\rho| = \frac{\sqrt{\varepsilon'} - 1}{\sqrt{\varepsilon'} + 1} \tag{79}$$

The formulas for the calculation of the temperature dependent heat transfer coefficient are shown in Table 36. The temperature dependence of the heat transfer coefficient, h, is reflected in the changing values of viscosity and thermal conductivity of the fluid.

TABLE 36 TEMPERATURE DEPENDENCE OF HEAT TRANSFER COEFFICIENT

- HEATER TRANSFER COEFFICIENT: h

$$St \; P_r^{\frac{2}{3}} = \frac{f}{8}, \qquad St = \frac{h}{C_p \rho u}, \qquad P_r = \frac{\mu C_p}{K}$$

$$f = \frac{1}{2 \times \log\left(\frac{\epsilon}{14.8 R_H} + \frac{2.5}{4} \frac{\upsilon}{u R_H \sqrt{f}}\right)}$$

WHERE
- St = STANTON NUMBER
- Pr = PRANDTL NUMBER
- h = HEAT TRANSFER COEFFICIENT
- f = FRICTION FACTOR
- υ = KINEMATIC VISCOSITY
- R_H = HYDRAULIC RADIUS
- ϵ = ABSOLUTE ROUGHNESS
- u = SPEED OF FLOW

The general approach for the nonlinear analysis follows:

1. Assume an arbitrary temperature for dielectric loss calculation.
2. Obtain temperature distribution with thermal code.
3. Use the calculated local temperature to recalculate dielectric loss and heat transfer coefficient.
4. Repeat steps 2 and 3 until temperature distribution converges.

This solution technique was used to analyze the optimized double-disc window design. The results are shown in Table 37 and Figures 269 and 270.

Table 37

Double-Disc Window Design Conditions

Window Material	Alumina 99.5%
Operating Mode	60 GHz TE_{02} at 200 kW CW
Attenuation Constant	Temperature Dependent
Coolant	FC-75, Flow Speed at 61 ft/sec
Heat Transfer Coefficient	Temperature Dependent

A flow speed of 61 ft/sec was assumed, as this is the minimum velocity which prevents boiling of the FC-75. This flow speed corresponds to a flow rate of 20 gpm using previous designs. However, preferential jetting of the FC-75 flow over the heated central region of the window allows the total flow rate to be substantially reduced, while maintaining the necessary velocity in the central region to prevent boiling.

The new design to cool the CW double-disc window incorporates a simple baffle arrangement designed to concentrate the flow over the central region of the window, thus profiting from the effects described above. It

ORNL – DWG-83-2125

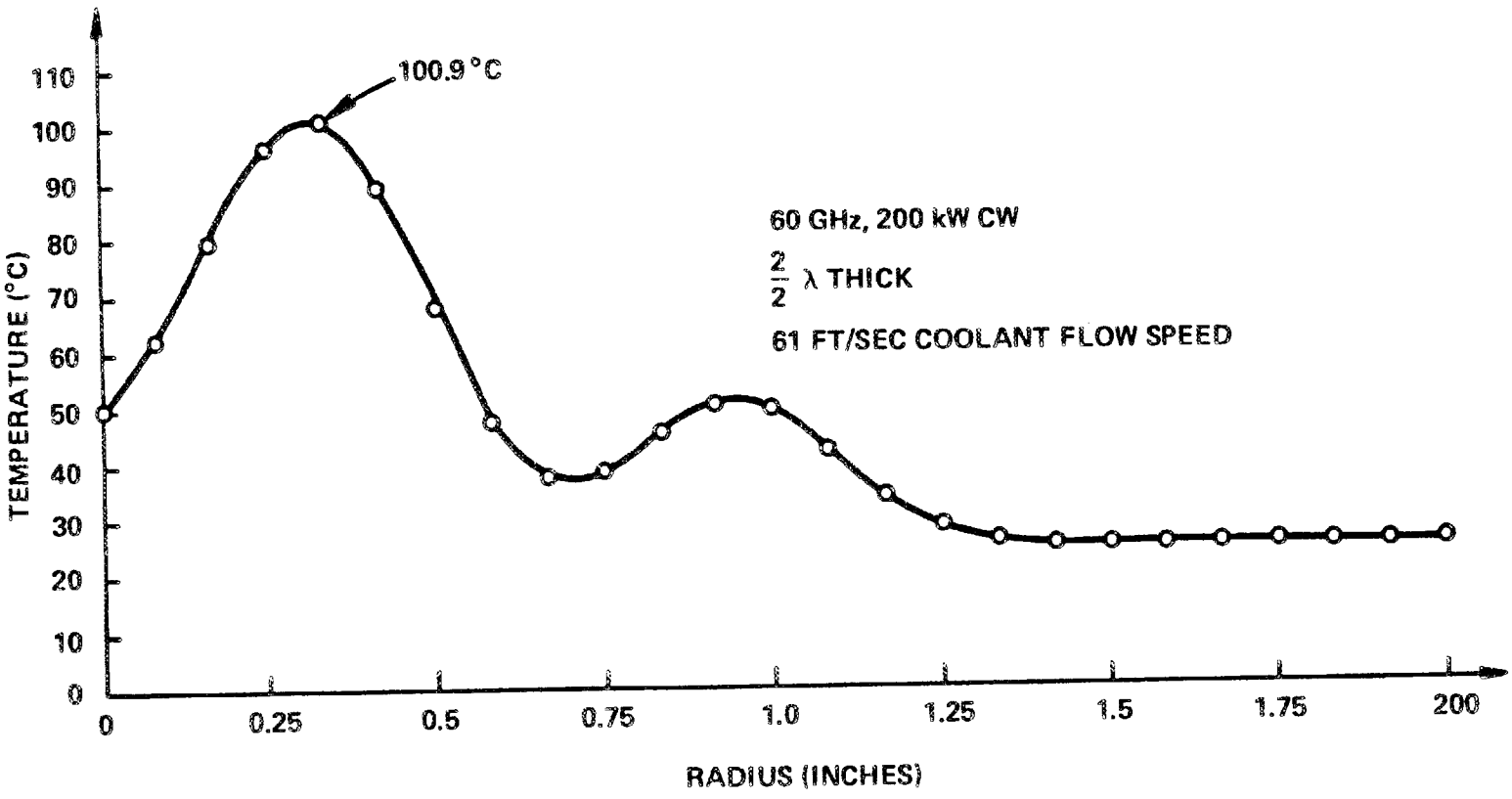

Figure 269. Temperature Distribution of Double Disc Window

ORNL – DWG-83-2126

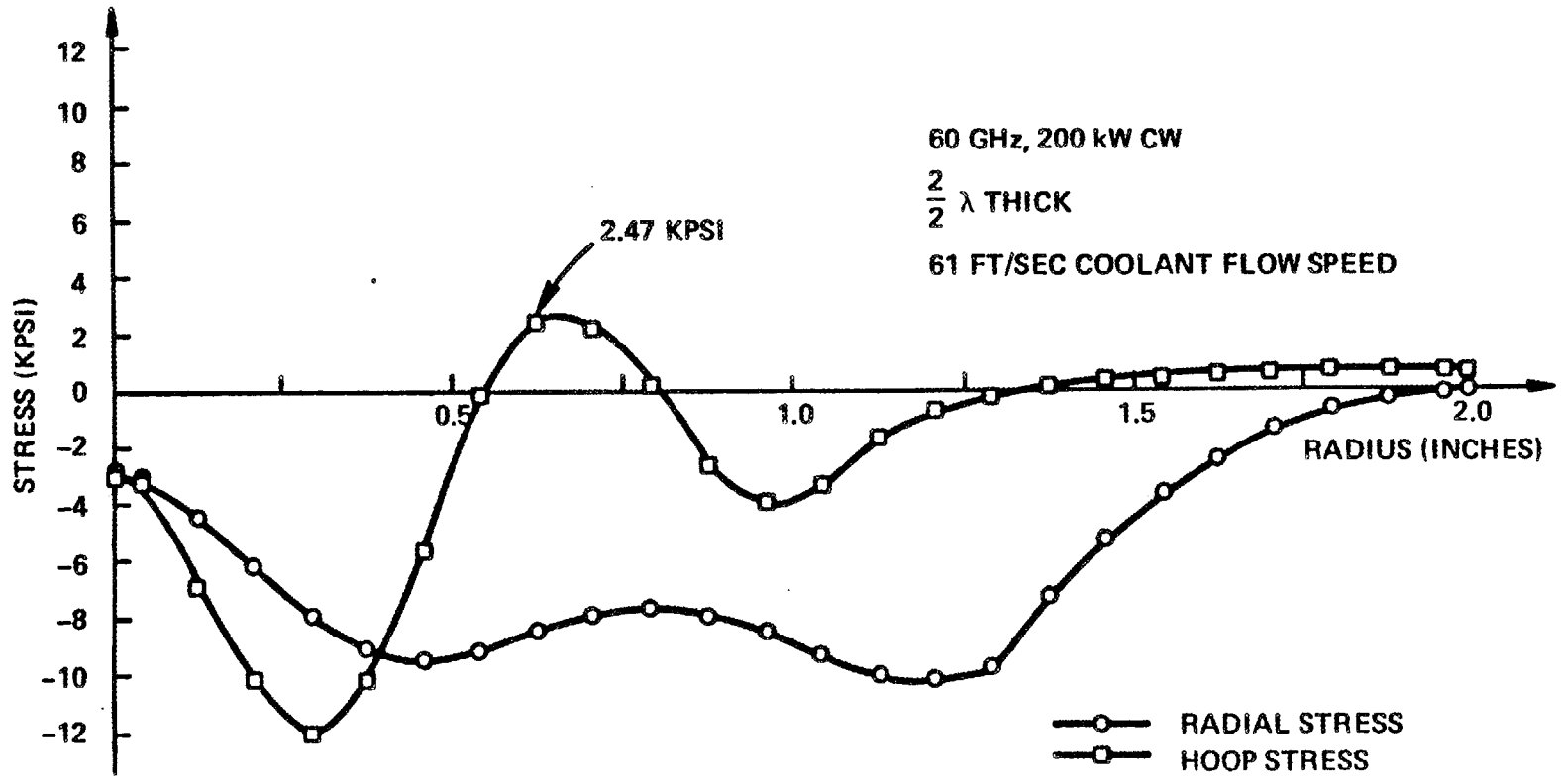

Figure 270. Stress Distribution of Double Disc Window

also allows higher coolant flow rates for a given pump than the previous design. This is accomplished by eliminating complex baffle inserts and flow channels, thus reducing the pressure drop across the window assembly.

11. FC-75 System Chiller

An inexpensive system to chill the FC-75 window coolant was designed and built. It was designed to cool the FC-75 to approximately $0^{\circ}C$. (Previously, the system operated near room temperature.)

The system consisted of a 60-foot coil of thin-walled copper tubing submerged in an ice and saltwater bath. The large diameter (1-1/4") tubing ensured a total pressure drop in the system of less than 8 psi.

The chiller was connected in series after the standard FC-75 pump and heat exchanger, and was first operated in conjunction with the 56 GHz CW tube, VGE-8005 S/N 1.

Chilling the window coolant to below room temperature yields the following benefits:

1. The loss tangent of FC-75 decreases. Thus, less power is lost directly to the FC-75, and the FC-75 heats up less as it flows across the window.

2. The loss tangent of the window ceramic, AL-995, also decreases thus reducing the total power loss and lowering the thermally-induced stresses in the window.

3. The strength of the window ceramic increases with decreasing temperature.

4. The total heat flux, Q, from the window ceramic to the FC-75 is given by the convective heat transfer equation, $Q = hA\,(T_{ceramic} - T_{FC-75})$. Thus, Q increases as T_{FC-75} decreases.

Chilling the FC-75 also has the undesired effect of lowering the total FC-75 flow rate available, due to the increased fluid viscosity and the added pressure drop in the copper tubing.

Results of testing the chiller were promising and were discussed in more detail in Section VII.B.8. They showed a significant drop in window temperature as FC-75 temperature was decreased. Two cases are listed below.

Gyrotron Output Power (kW)	FC-75 Inlet Temperature Drop (^{o}C) Produced by Chilling	Reduction of Peak Window Temperature (As Measured by IR Camera at 1st Radial E-Field Maximum ^{o}C
95	13	8.5 $\pm$ 2
75	10	13 $\pm$ 2

The measurements were performed with an IR camera before and after the shutdown to change the FC-75 plumbing. A slight variation, due to the reproducibility of the operating parameters, may result in a different mode mixture or mode mix phasing. This may account for the larger temperature reduction at 75 kW.

The maximum FC-75 flow rate was reduced from 7.5 gpm to 6.7 gpm by adding the chiller. However, much of this drop is due to extra fittings which were later eliminated.

The icebox FC-75 chiller was used in testing X-6 to achieve the 200 kW CW landmark. Specifically, the chiller lowered the FC-75 temperature from 37°C to 17°C, resulting in an approximately 5°C lower peak window temperature. For a constant peak window temperature, the chiller extends the safe operating range of the gyrotron by about 15 kW. Recent results from the ORNL Metals and Ceramics group show that slow crack growth in polycrystalline ceramics exposed to FC-75 is severely retarded by lowering the FC-75 temperature. This combination of positive results from using the chiller has prompted Varian to install more permanent chilling systems.

In the first new system, $7^{\circ}C$ water, from existing Varian lines, flows through the same FC-75 heat exchanger that previously ran room temperature water. The FC-75 window inlet temperature is typically about $10^{\circ}C$ at full FC-75 flow rate.

12. Stress Measurement of Output Windows

Measurement of stress at the edge of a double-disc CW window with strain gages was considered. Direct measurement of the strain gives the stress via Hooke's law

$$\sigma = E \varepsilon \quad , \tag{80}$$

where σ is the stress, E is the modulus of elasticity, and ε is the dimensionless strain.

The primary difficulty arises from the very low strain (about 0.02%) expected in the CW window. This low value necessitates the use of high-gain, semiconductor-type strain gages, which are generally more temperature sensitive and less accurate than conventional wire gages. Placement of the gage, calibration, and the way in which the gage leads are fed out the window assembly also pose technical difficulties. For these reasons, the investigation of stress measurement was discontinued.

13. Comparison of Experimental and Analytical Results

Using an infrared camera, temperature measurements were made on a 56 GHz CW gyrotron output window at several power levels. These measurements are compared to calculated temperatures in Table 38. The agreement between experimental and analytical results is poor. The two most probable sources of discrepancies are the values of the heat transfer coefficient and attenuation constant assumed in the calculations. To explore the sensitivity of the calculation to the value of h used, a series of calculations were made where h was varied to force agreement between

TABLE 38 COMPARISON OF EXPERIMENTAL AND ANALYTICAL RESULTS FOR A 56 GHz DOUBLE DISC WINDOW 3 DIA X .099, AL-995

OPERATING CONDITION		PEAK TEMP. BY ANALYTIC METHOD		PEAK TEMP. BY ANALYTIC METHOD W/ADJUSTED η		PEAK TEMPERATURE MEASURED BY I.R. CAMERA
Power, kW	Cooling flow, GPM	Attenuation Const. α	film Coeff. h	Attenuation Const. α	film Coeff. h	
111	7.4	0.02184	4.6	0.02184	23.0	68 °C	119.6 °C	68 °C
111	6.0	0.02229	3.85	0.02229	14.0	78.2 °C	134.0 °C	78.5 °C
70	7.4	0.02107	4.6	0.02107	23.0	50.9 °C	81.6 °C	50 °C
70	3.5	0.02162	2.46	0.02162	5.5	78.7 °C	116.9 °C	78.5 °C

calculated and measured temperatures. The results are included as one of the columns in Table 38. They indicate that large deviations in h would be required to obtain agreement in temperature.

Varian introduced a new code for calculating temperature distributions in windows due to rf heating. Previously, VULCAN was used, which required the user to first create an electrical network analogy for the thermal resistances. VULCAN slowed the analysis process and was less accurate than the new code, TACO2D, which uses finite element analysis. TACO2D is available on MFE, is straightforward and yields more accurate results than VULCAN.

Window stress analyses were done on SAP-IV, a finite element code also available on MFE. Results from TACO2D can generally be used directly as input to SAP-IV, thus saving more time. Through experience, confidence in using these codes to accurately predict temperature and stress distributions in windows has greatly increased.

The temperatures, stresses and deflections in the X-6-type window were recalculated using a finer mesh pattern, to see the full effects of static pressure loading (e.g. 30 psi FC-75 and 15 psi atmosphere). The results are shown in Figures 271 through 274. The high tensile stresses associated with the static load created concerns.

14. Transient Analysis of Double Disc Window Under Pulsed Loading

Two thermal transient cases were run for the double-disc, face-cooled window. The design conditions for the first case are:

- Window material: AL-995, 4" diameter by 0.066" thick
- Operating condition: 60 GHz TE_{02}, 200 kw peak power, 0.5 sec pulse at 1% duty
- Attenuation constant: $\alpha = 0.0232$ nepers/cm
- Coolant: 10 gpm flow of FC-75
- Heat transfer coefficient: 2.5 watts/in^2-$^\circ$C

ORNL – DWG – 83-3228 FED

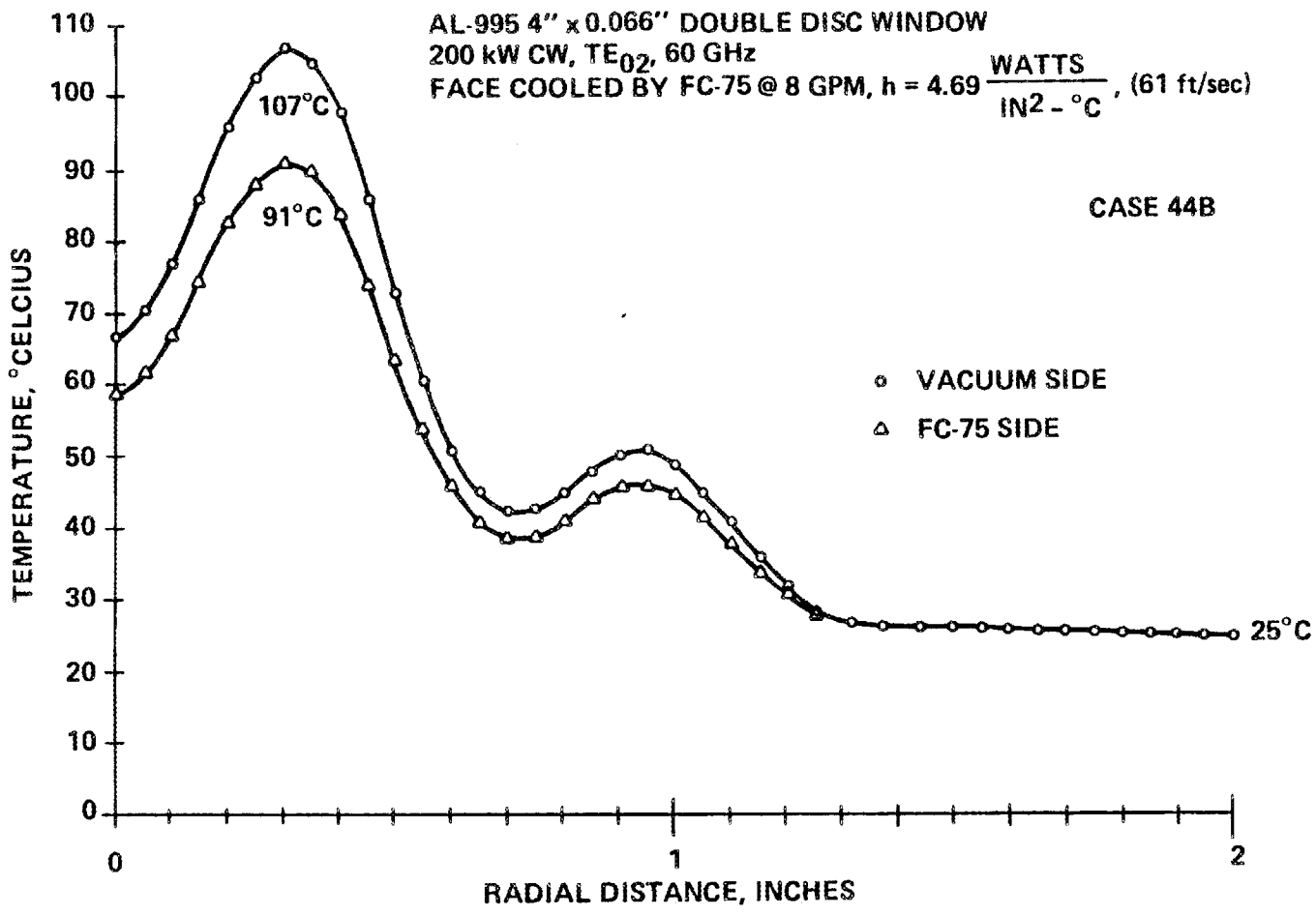

Figure 271. Calculated Temperature Profiles

ORNL – DWG – 83-3229 FED

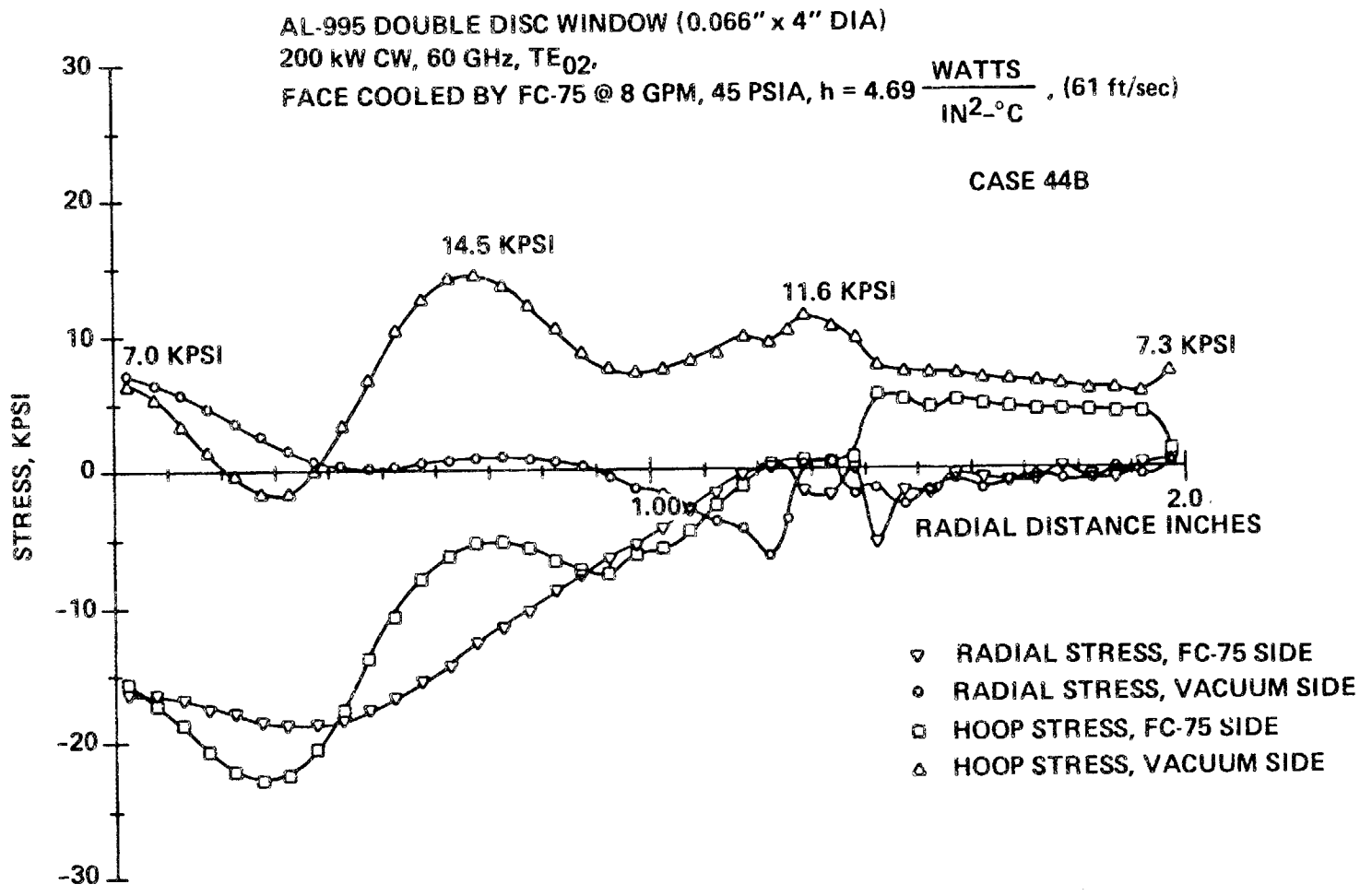

Figure 272. Calculated Stress Profiles on "Vacuum Side" Disc

ORNL – DWG – 83-3230 FED

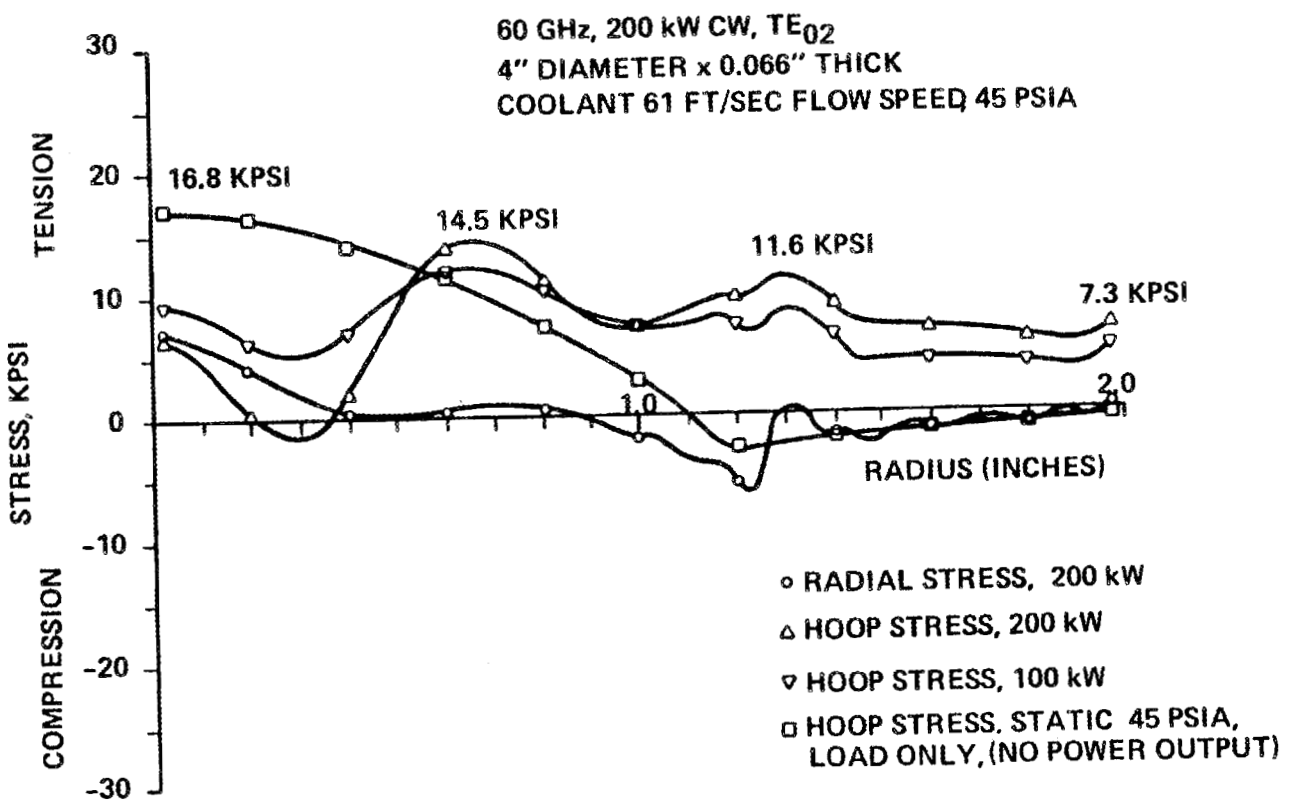

Figure 273. Calculated Stress Profiles on "Vacuum Side" Disc with Various Output Power Levels

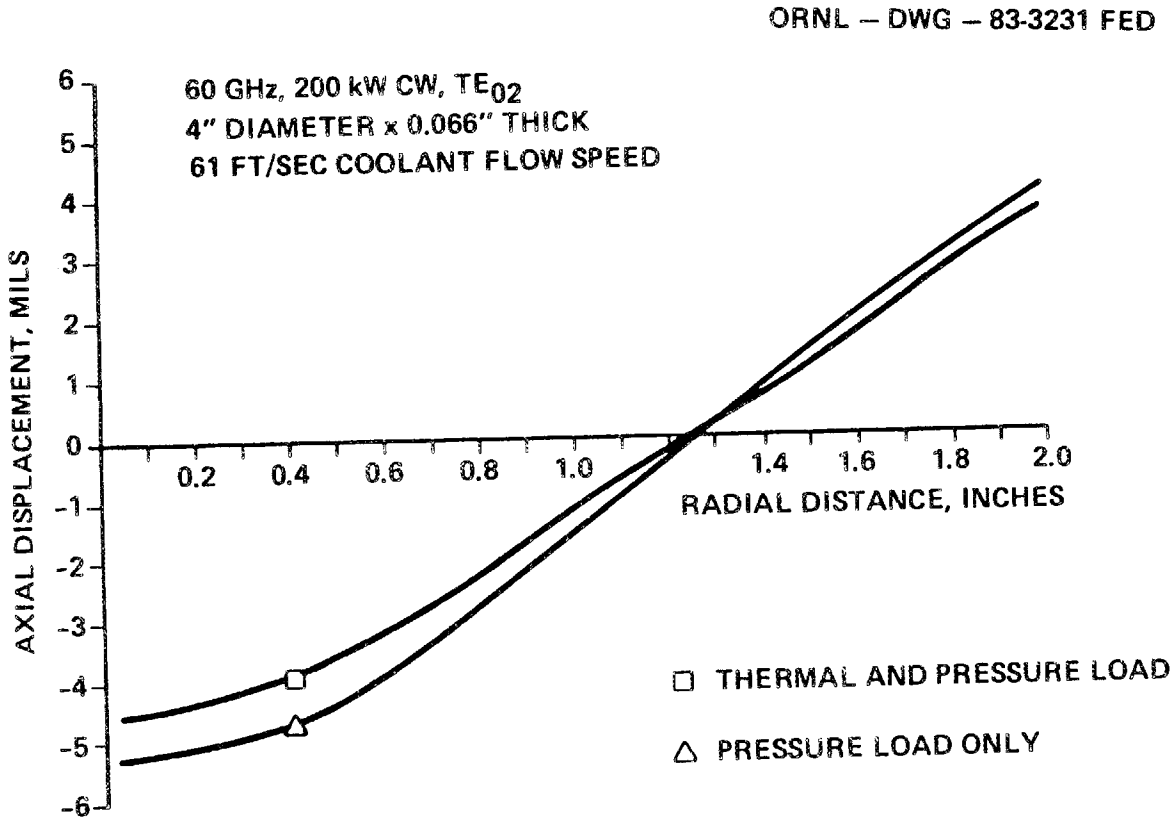

Figure 274. Calculated Displacement of X6 Window Under 45 PSIA Static Load

Because of the low duty cycle, pulses are spaced far apart, so it is sufficient to look at a single pulse. The temperature and the thermal stresses at the end of the pulse are shown in Figures 275 and 276.

An additional thermal analysis was performed to study the effect of a reduced TE_{02} pattern using the identical design conditions for the previous transient analysis, but reducing the TE_{02} pattern by a ratio of 1.7/2.5 (i.e. using a waveguide diameter of 1.7"). As shown in Figures 277 and 278, the increase in peak temperature and thermal stress at the end of a pulse is quite dramatic. This points to the importance of knowing the operating mode shape on the window precisely.

15. X-6 Window

X-6 was the first tube to incorporate all of the following improvements in the window design:

- A λ - thick window (reduced from $3\lambda/2$): This reduced the total power dissipated in the ceramics by 33%.

- A 4"-diameter window (increased from 3"): This lowered the peak tensile stresses in the ceramic and moved them in from the edge.

- A surface finish of 8 microinches or better (improved from 32 microinches): This eliminated many of the pre-existing microcracks in the ceramics that can be initiation sites for slow crack growth, which may lead to catastrophic failure.

- A full radius edge (previously squared off): This also helped to eliminate microcracks on the surface, and prevented further damage during normal handling.

ORNL DWG 83-2171

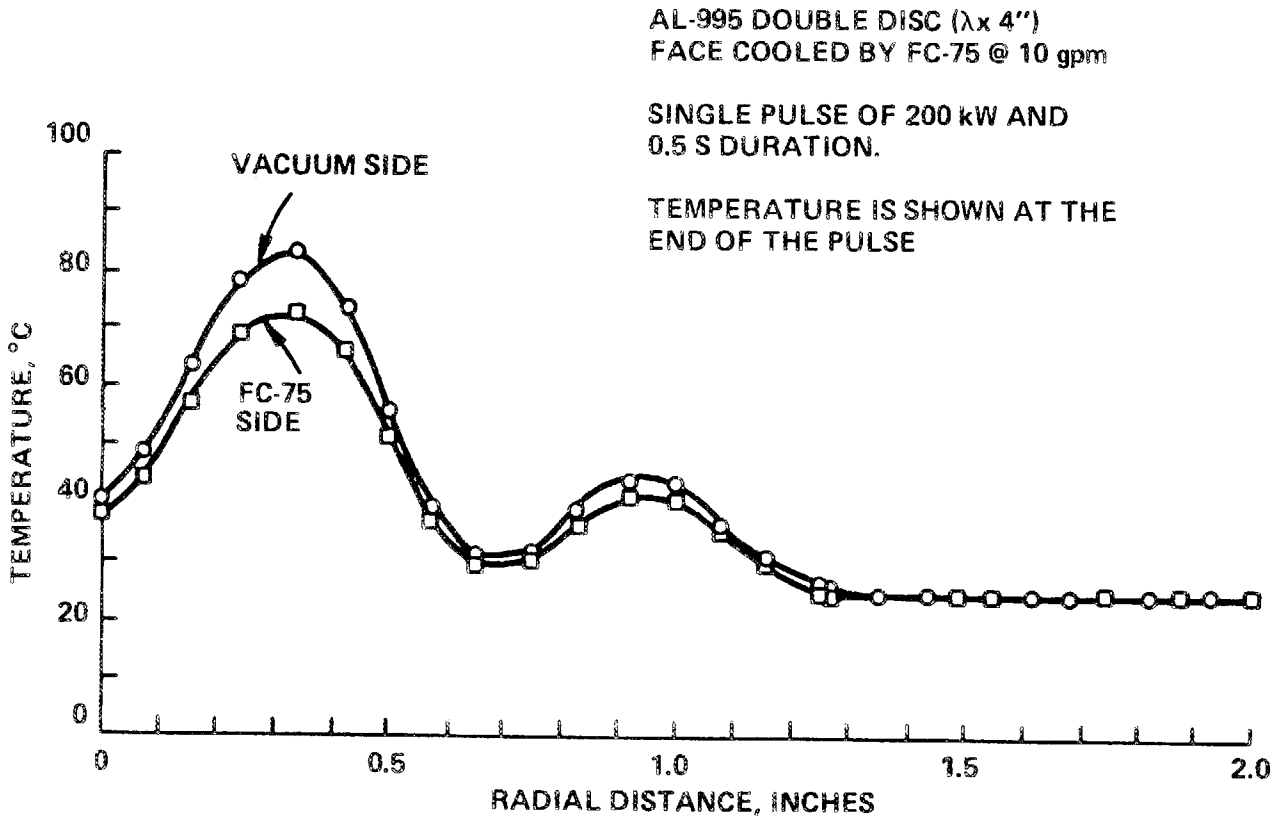

Figure 275. Calculated Temperature Distribution on a Double-Disc Window

ORNL DWG 83-2172

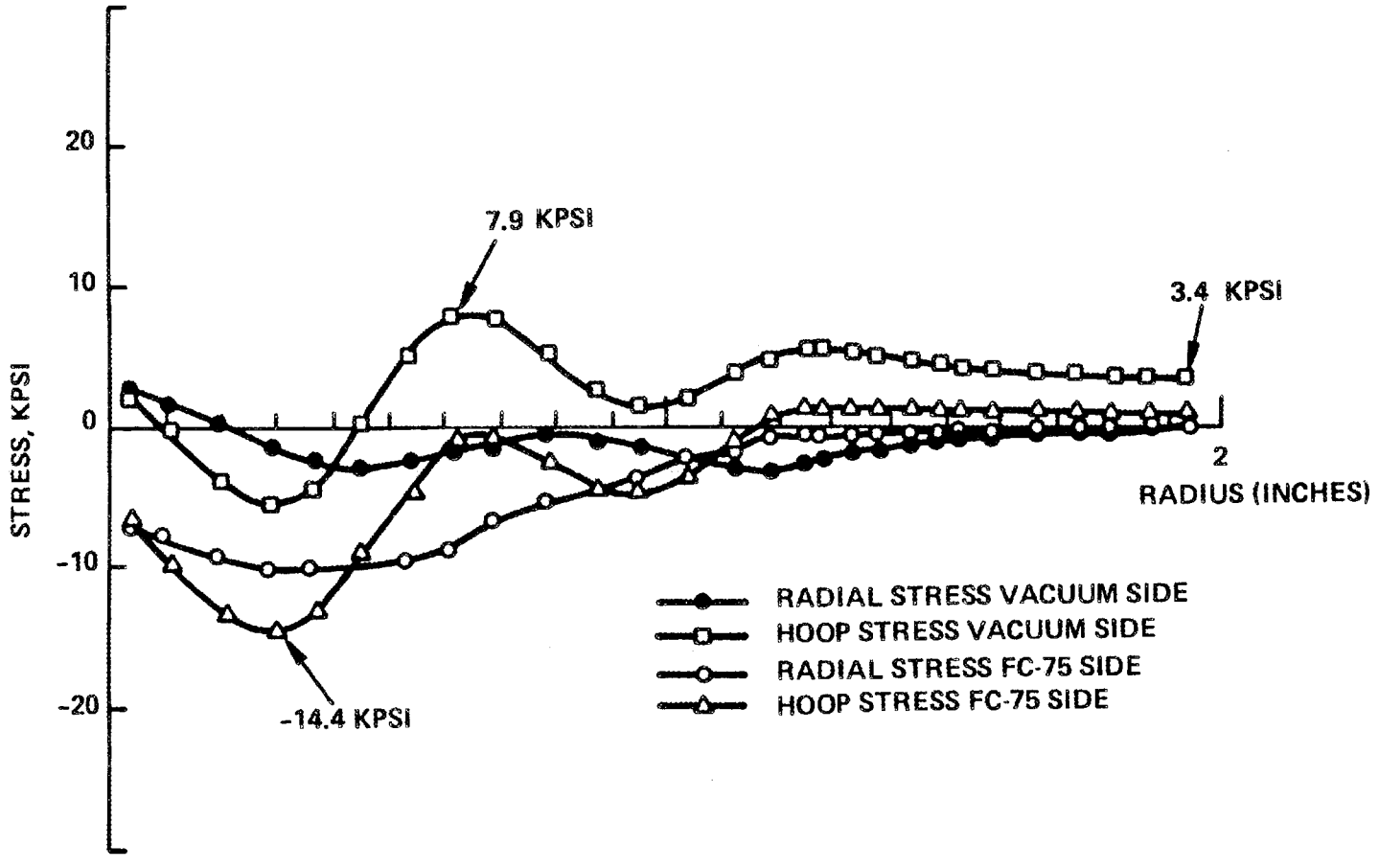

Figure 276. Calculated Thermal Stress Distribution in a Double-Disc Window for the Temperature Conditions Shown in Figure 275

ORNL DWG 83-2173

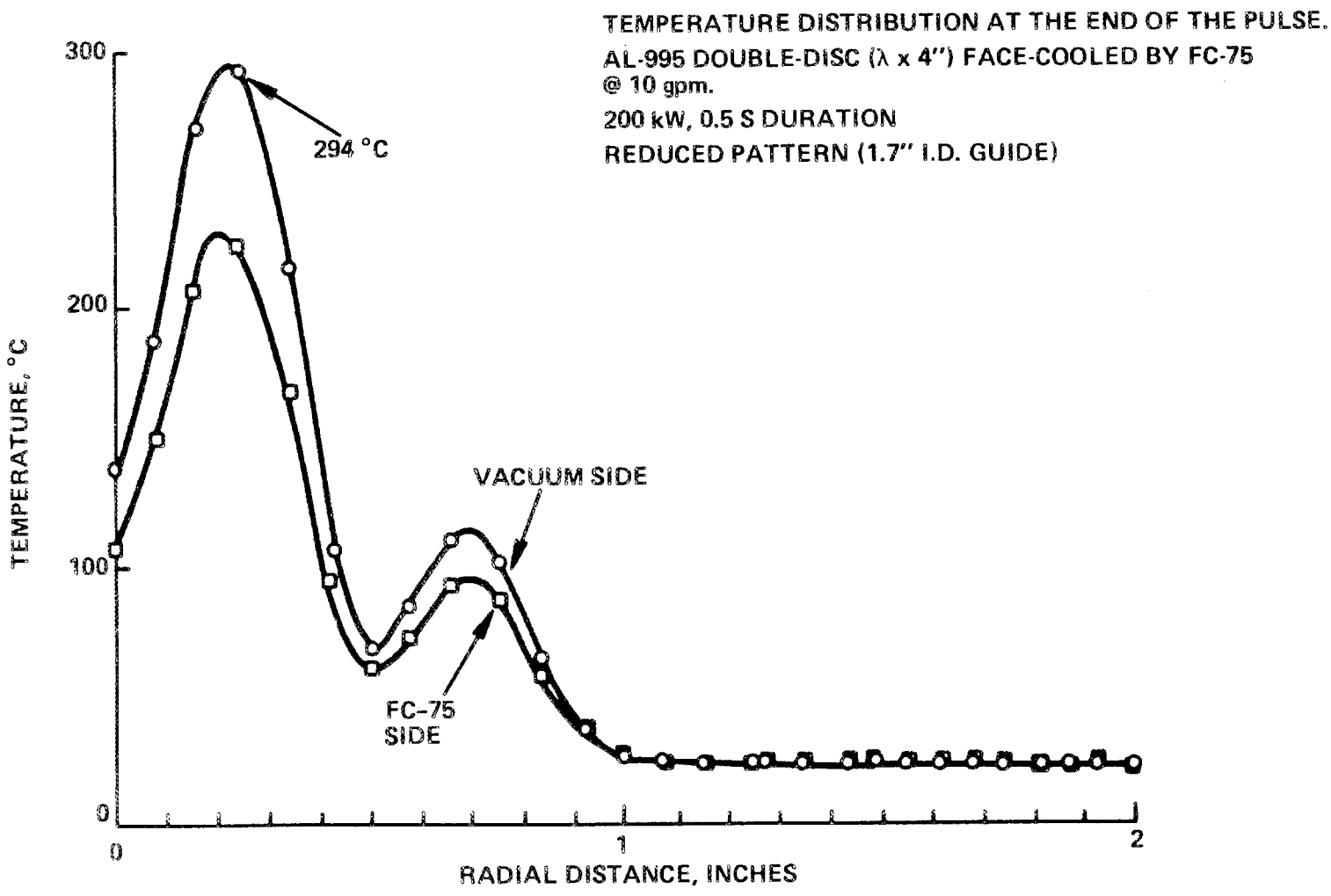

Figure 277. Temperature Distribution in Double-Disc Window (Reduced Pattern)

ORNL DWG 83-2174

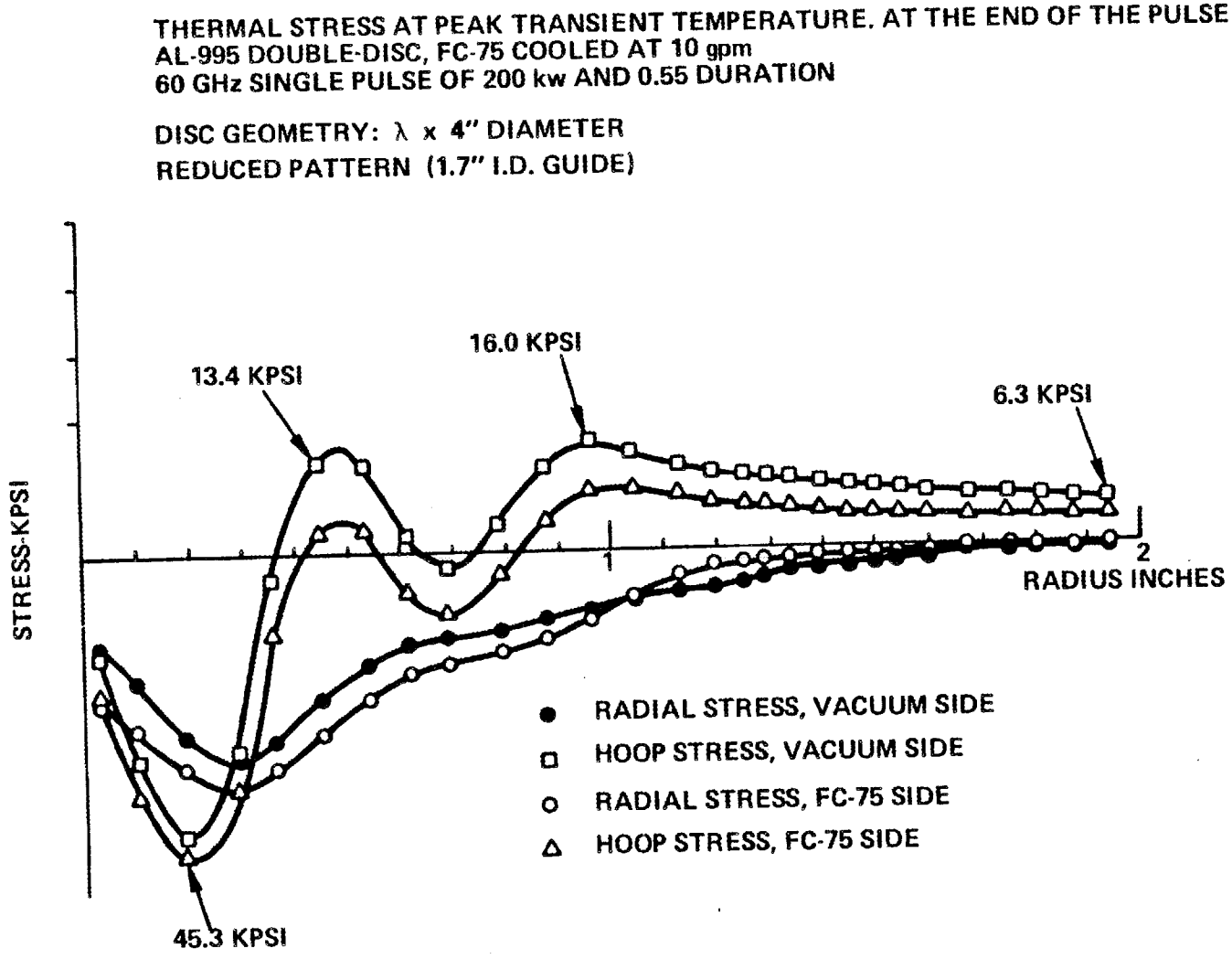

Figure 278. Thermal Stress Distribution on a Double-Disc Window (Reduced Pattern)

- A "jet-flow" cooling design which gave high FC-75 velocities over the heated central region of the window, thus increasing the effective heat transfer coefficient. The new design also increased the total FC-75 flow rate for a given system pressure by minimizing the pressure drop in the window assembly.

These improvements resulted in X-6 successfully operating at over 200 kW CW for one hour, setting a new world record for continuous power at this frequency.

The IR camera successfully guided the operation of X-6 to 214 kW CW. For an FC-75 flow rate of 7.8 gpm and inlet temperature of $14.6^{\circ}C$, the peak window temperature was $115^{\circ}C \pm 5^{\circ}C$. The IR camera was used to adjust the tube operating parameters to minimize the peak window temperature.

Additional experience was gained operating X-6 with the basic double-disc window design at power levels in excess of 200 kW CW. At one point in the testing, when waveguide and load configurations were being changed, a small acoustic probe fell unnoticed onto the window. Installation practices have been improved to prevent a repeat occurence. Subsequent operation of the tube resulted in arcing and eventual failure of the outer disc with no loss of tube vacuum. The outer disc was replaced and the tube was operated satisfactorily again. More details of X-6 operation are included in Section IX.G.

16. Dish Window, A New Concept

A novel design concept, shown in Figure 279, was analyzed. Due to the ability of the dome shape to effectively resist pressure, the thickness of the window can be decreased to merely one-half wavelength. The thinness of the window reduces the power dissipation and, hence, the induced thermal stress.

ORNL DWG 83-2181

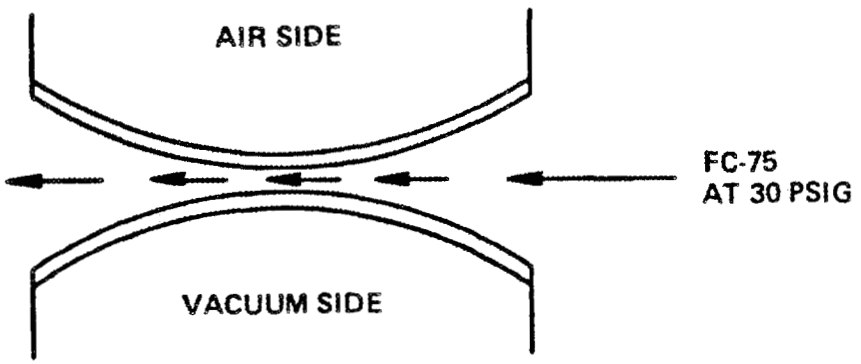

Figure 279. The Schematic Sketch of a Double Dish Window

The analysis was performed with full consideration of temperature dependence of dielectric loss and heat transfer coefficient. The design conditions are summarized in Table 39. The calculated temperature distribution and thermal stresses are shown in Figures 280 and 281. It is significant that the damaging hoop stress has been substantially reduced and pushed toward the center of the disc.

Cold tests of a prototype single-dish made of AL-300 have shown favorable results with respect to broadband VSWR, as can be seen in Figures 282 and 283.

Table 39

Double-Dish Window Design Conditions

Window Material	Alumina 99.5%
Operating Mode	60 GHz, TE_{02}, 200 kW CW
Attenuation Constant	Temperature Dependent
Coolant:	FC-75 at 5 gpm and 15.3 ft/sec Surface Speed
Heat Transfer Coefficient:	Temperature Dependent

The allowable buckling load under static pressure was calculated. Figure 284 shows the geometry of the dish. The buckling pressure load for a dish with a fully clamped edge is a classic case and can be calculated in closed form by the formula[42] shown in Figure 285. Using the material properties for AL-995, λ can be calculated from Equation 1 in the Figure 285. For a given λ, R_{cr} can be obtained from a table[43] and P_{cr} calculated from Equation 2. The calculated critical buckling pressure is 660 psi.

The double-dish window consists of two slightly-rounded ceramics with their convex sides facing together, as shown in Figure 279. The double-dish window functions in essentially the same manner as the standard double-disc window. The dish configuration provides greater strength per unit thickness in withstanding the static pressure load of atmosphere and

ORNL – DWG-83-2130

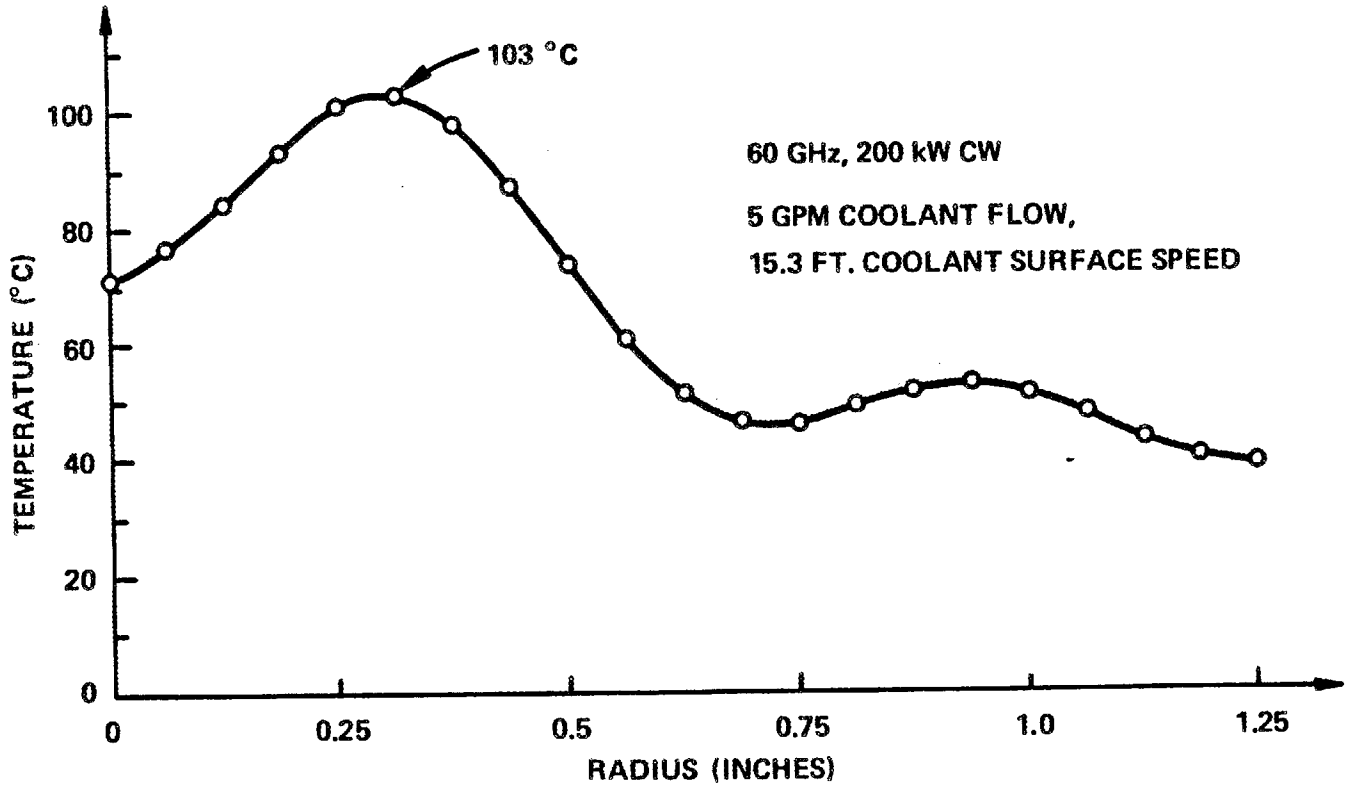

Figure 280. Temperature Distribution of Double-Dish Window

ORNL – DWG-83-2131

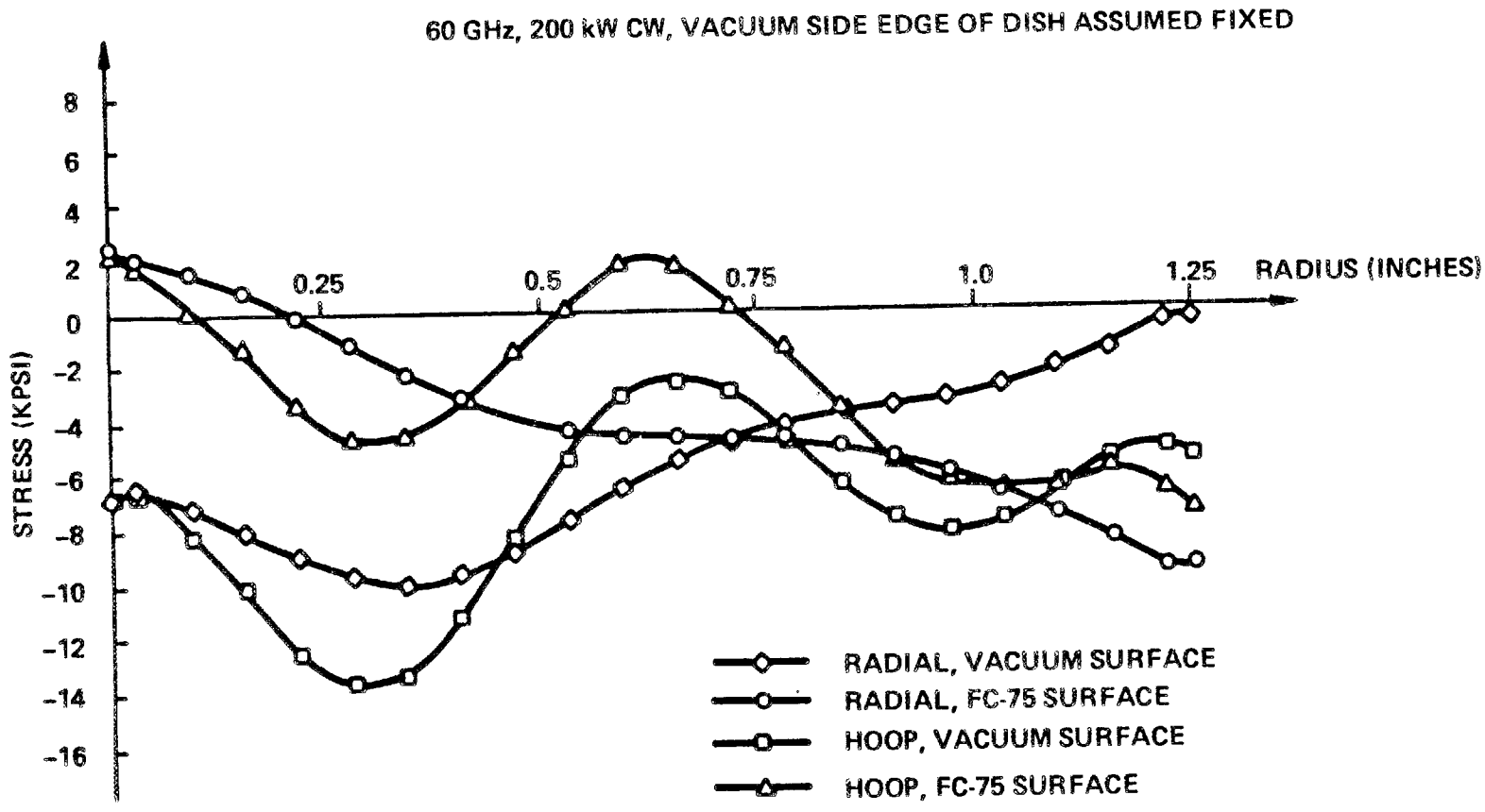

Figure 281. Stress Distribution of Double-Dish Window

ORNL – DWG-83-2132

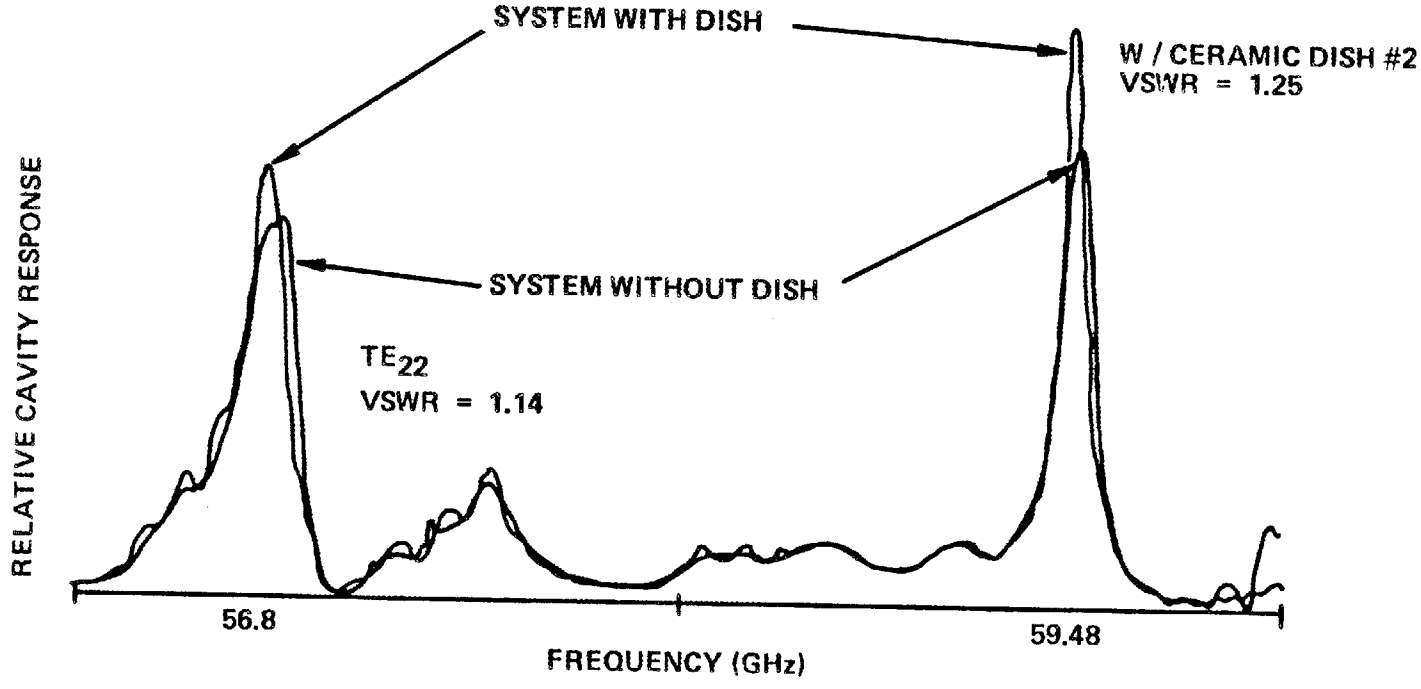

Figure 282. Cavity Response with Single Dish Window

ORNL – DWG-83-2133

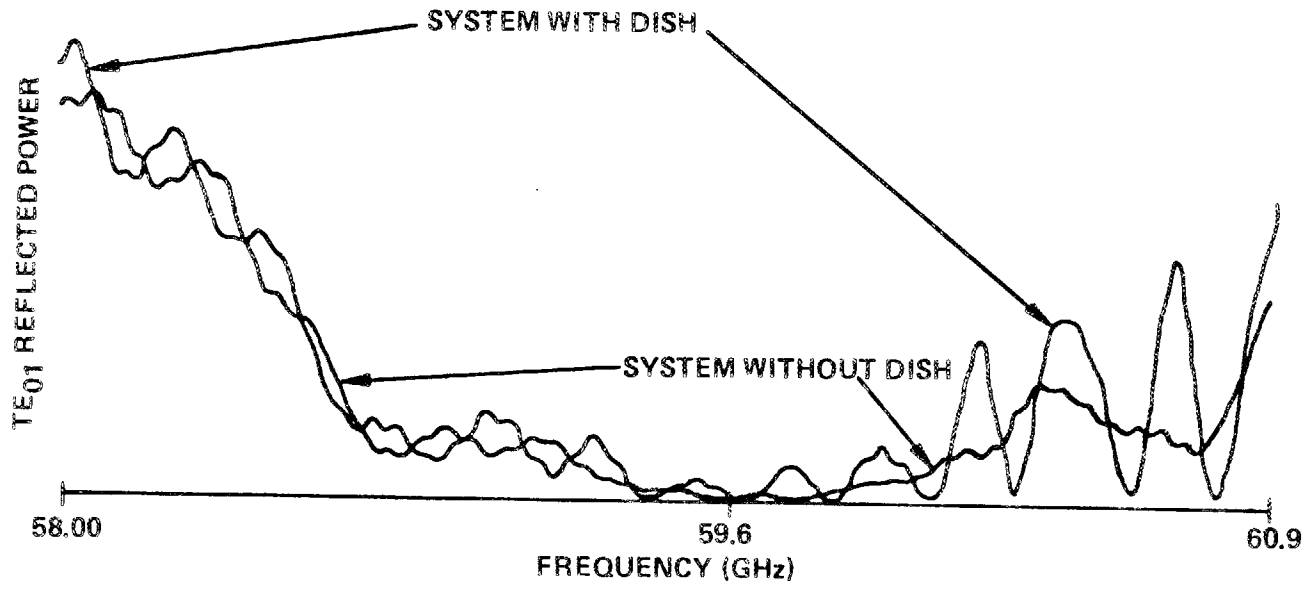

Figure 283. Single Dish Window TE_{01} Mode Reflection

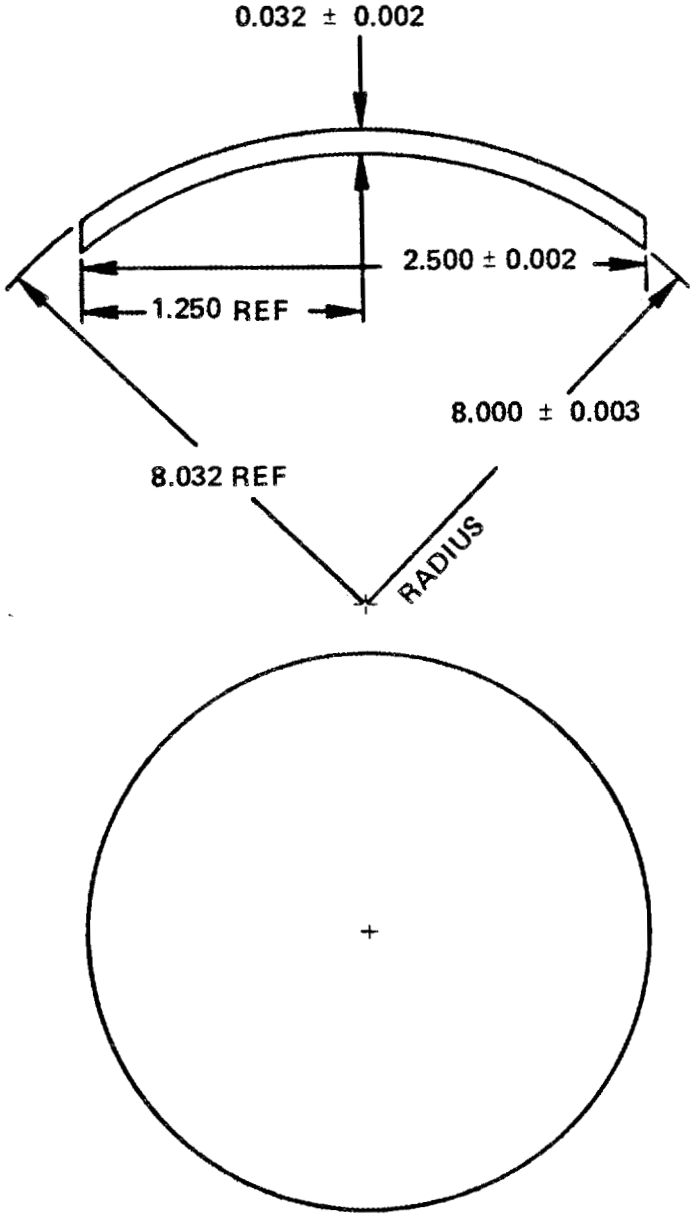

Figure 284. Geometry of a Dish Window

ORNL DWG 83-2176

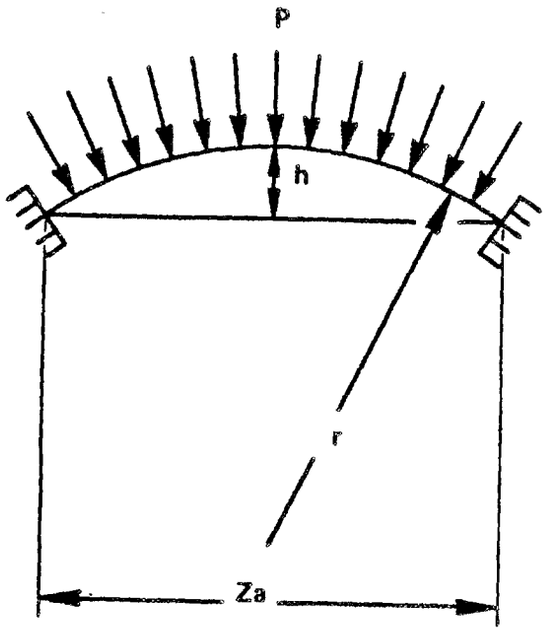

(1) $$\lambda^2 = \frac{a^2}{tr}\sqrt{12\,(1-\upsilon^2)}$$

(2) $$R_{CR} = \frac{P_{CR}}{E}\left(\frac{a}{t}\right)^4\left(1-\upsilon^2\right)$$

WHERE t = DISH THICKNESS, r = RADIUS, υ = POISSON'S RATIO

E = YOUNG'S MODULUS, P_{CR} = CRITICAL PRESSURE

λ = GEOMETRICAL PARAMETER

R_{CR} = LOAD PARAMETER

Figure 285. Buckling Pressure Load for a Dish with a Fully Clamped Edge

FC-75 than the disc. The bottoms of pressurized cans and bottles illustrate this principle nicely.

Cutting the window thickness in half reduces the rf power deposited in the ceramic by a factor of two as well. This allows the tube to be operated at higher power levels while limiting the stresses in the window to acceptable levels. The calculated maximum stress of 1.8 ksi, which is well within the safe operating range of AL-995, is attained with only 5 gpm of FC-75.

However, a variety of technical difficulties have hindered progress on this design. Among the mechanical problems are the warping of the dish during metallizing, and the difficulty of brazing to an edge of only 0.033" thickness. More important, it is likely that the curvature of the ceramics and the variations in thickness of the FC-75 layer across the radius would cause phase shift and mode conversion in the wave. Although many plausible solutions to this problem have been proposed, all were deemed either mechanically infeasible or not apt to fully solve the problem. These problems combined to foreshadow a lengthy and arduous process of design and redesign.

A proposed variation of the dish window is the arch window, shown in Figure 286. This design has a constant thickness of FC-75, and retains the benefits of having a thin ceramic in the center region where the power density is the highest. However, it suffers from the same varying electrical path problem as the disc window, except in this case, it is the ceramic thickness which is not constant. Thus, for the same reasons as with the dish window, the arch window was not pursued.

Another dish window concept pursued was the gas-cooled dish window. Preliminary calculations show that 300 psi of nitrogen could sufficiently cool the dish window shown in Figure 279, while not exceeding the static buckling strength of the window. Furthermore, gas cooling, unlike a boiling fluid, does not cause cavitation erosion. As the dielectric constant of compressed nitrogen is very near unity, mode conversion in the gap region should be less of a problem. Using 300 psi

ORNL DWG 83-2184

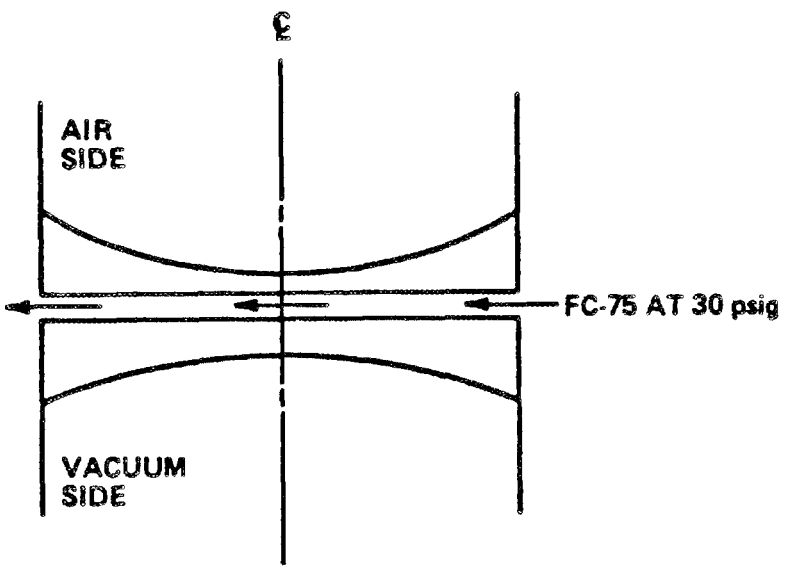

Figure 286. Schematic of an Arch Window

nitrogen, $50^{o}C$, a surface velocity of 300 ft/sec gives a heat transfer coefficient of 3.1 W/in^2-^{o}C, about the same as is achieved with 5 gpm of FC-75. Thus, the temperature distribution ought to look quite similar to that shown in Figure 280. A dish window with an 8" spherical radius has a critical buckling pressure of 660 psi, more than double the applied load. The pressure drop for a typical system should not exceed 50 psi. Cold test work on the double-dish window was not conclusive.

In order to minimize mode conversion, a dish window was designed which has no radial or azimuthal variations in electrical path length. Thus, the emerging rf would be at the same relative phase as the rf incident to the window. This window design was then analyzed for possible mismatches. By setting the nominal matching point of the window to be at the first radial maximum of the TE_{02}, the VSWR at all other radii could be calculated using the computer code VSWR7. At the second radial maximum, the VSWR is 1.5, and at the window center, the VSWR is 1.35. If the window were redesigned to be a better match at other radii, then the electrical path lengths would no longer be constant, which might result in significant mode conversion. By direction of the gyrotron review committee, work on the double-dish window was terminated at this point.

Various alternate materials were scrutinized to determine their applicability to different window designs. Quartz and sapphire both showed some promise as possible future window materials. Work began on developing reliable metalizing procedures for sapphire and Al_2O_3 99.9%.

A complete mechanical analysis of the edge support window design was performed. A schematic of the double-disc window with edge support is shown in Figure 287. Figure 288 shows the stress distribution on the vacuum side of the window, with and without edge support. Figure 289 shows the stress distributions on the window under the static load only, with no rf power. Figure 290 shows the deflection of the window due to the static pressure load. The edge support substantially reduces the peak tensile stresses as well as the peak deflection. Since the deflected window is a

ORNL-DWG 83-3325

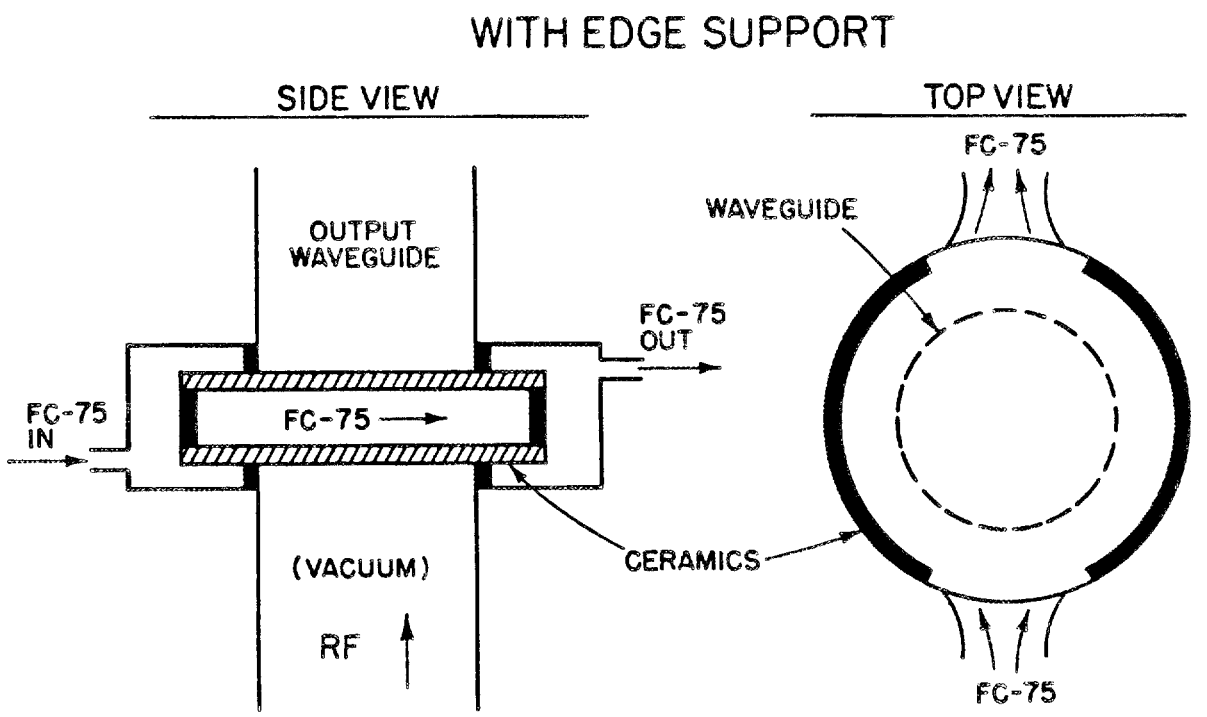

Figure 287. Schematic of a Double-Disc Window with Edge Support

ORNL-DWG 83-3326

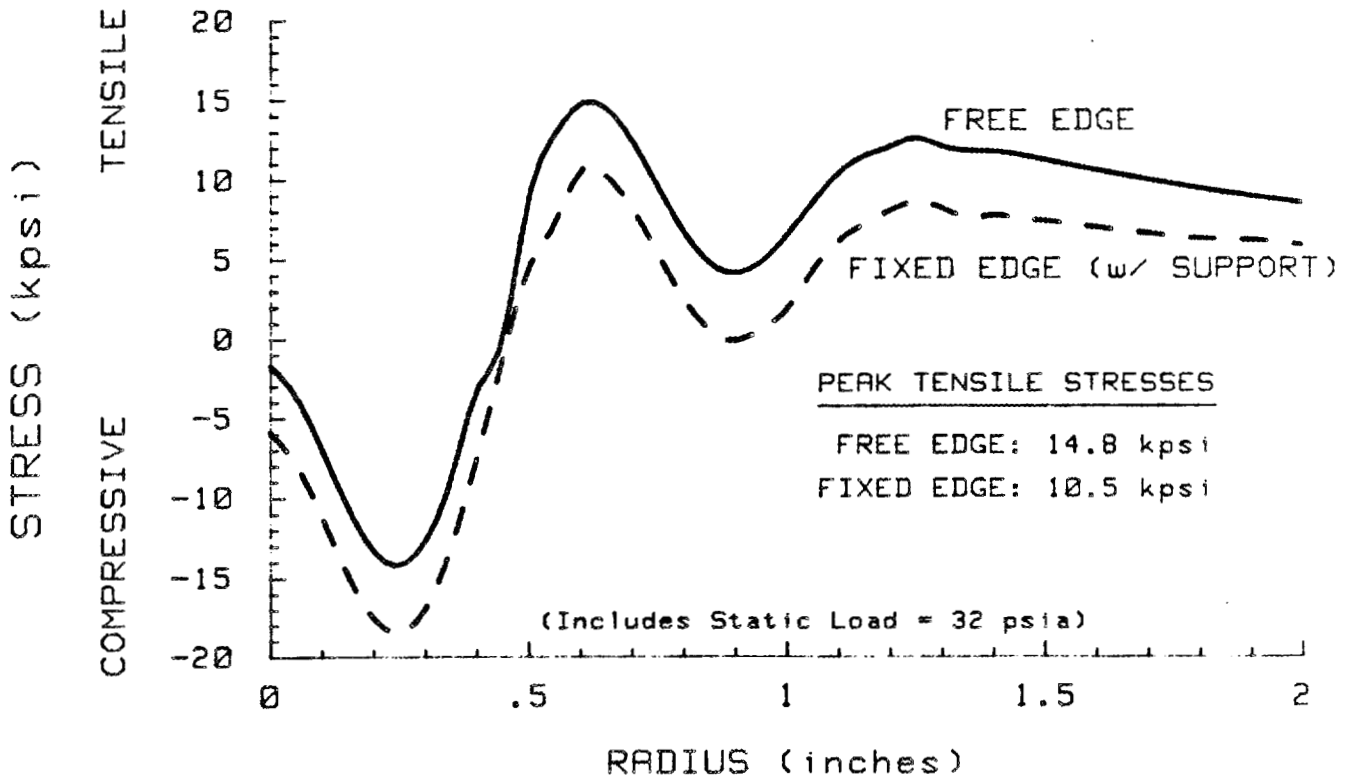

Figure 288. Stress Distribution in 60 GHz 200 kW CW Vacuum Window

ORNL-DWG 83-3327

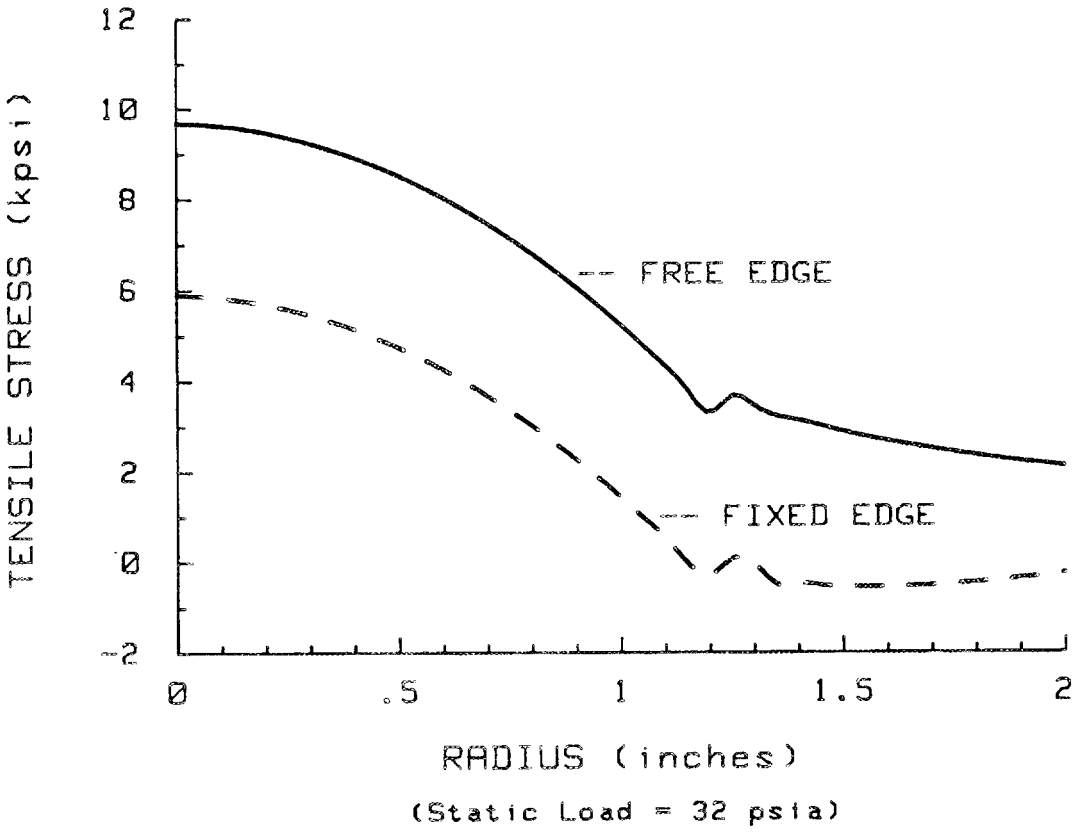

Figure 289. Stresses Due to Static Load Only

ORNL-DWG 83-3328

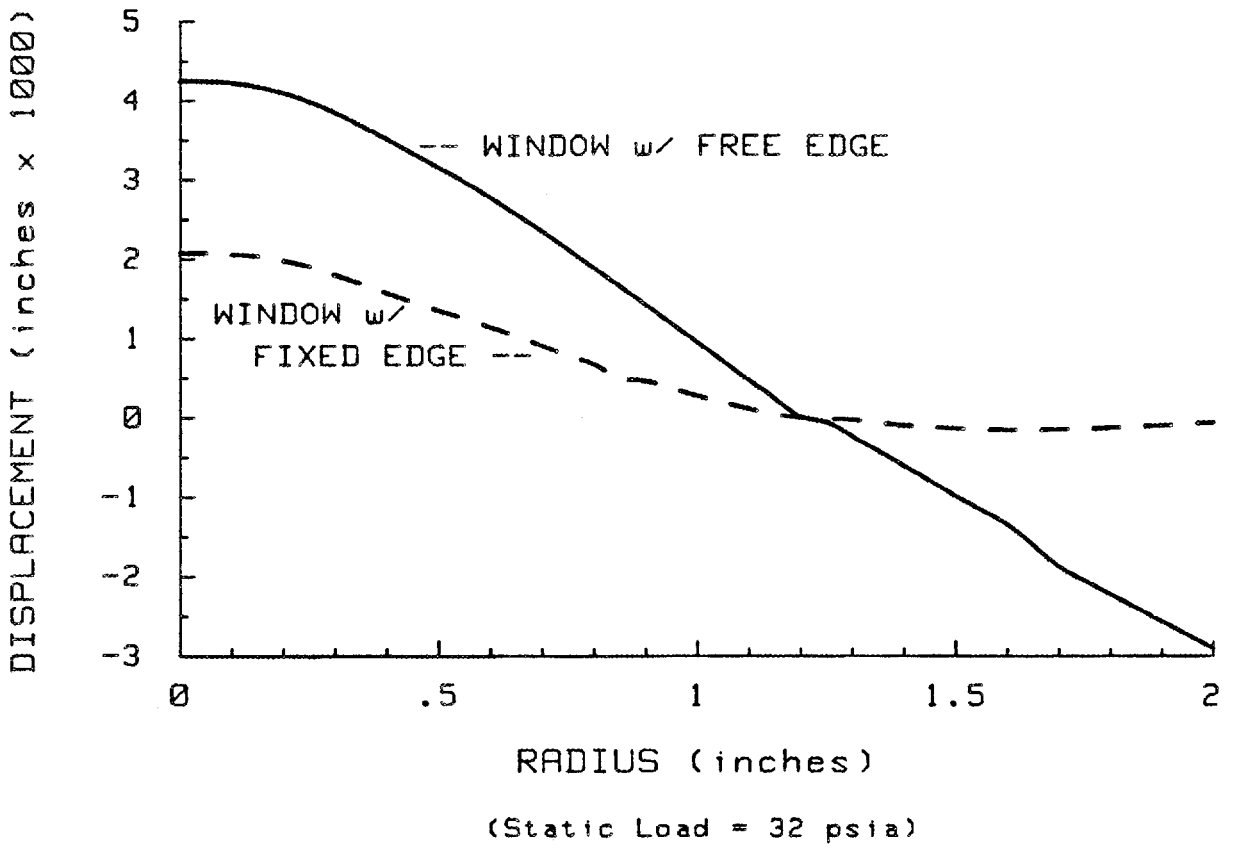

Figure 290. Window Displacement Due to Static Load

probable source of mode conversion, this design should improve mode purity as well as lower window stresses. Work on one edge support design which used ceramic inserts between the two windows was halted due to foreseen difficulties in assembly.

Measurements of the dielectric properties of Crystal Systems HEMLITE, a single-crystal sapphire, were made by Dr. W. W. Ho of Rockwell Science Center. The loss tangent at 60 GHz is substantially lower than that of the best available alumina ceramics. The tensile strength of sapphire is typically quoted to be about twice that of alumina, which makes sapphire promising as a candidate material. Varian odered several sapphire discs from Crystal Systems to be tested as a barrier window. A new infrared temperature monitoring system, suitable for use with sapphire as well as alumina, was ordered. The system consists of a camera at 8 to 12 micron wavelengths and a custom lens and filter, and will employ the existing electronics for data assimilation. This IR system will be used in conjunction with the new 60 GHz socket in the modified Super Power Test Set.

Two local vendors were secured who are capable of providing alumina ceramics with a surface finish of less than 2 microinches. Future double-disc window ceramics will be polished by one of these vendors. Varian has several excellent instruments for inspecting high-quality surface finishes, including a scanning electron microscope, a Numarski-lens microscope, and a state-of-the-art, computer-driven surface profilometer.

The finite element electromagnetic computer code OPENCAV has been successfully used to predict mode conversion in a dielectric material of arbitrary shapes in a waveguide. These added capabilities will be of tremendous value in accurately analyzing the electrical behavior of existing and future window designs.

IX. TEST RESULTS

A. FIRST EXPERIMENTAL TUBE

1. Hipotting

Testing of the first experimental tube was begun during the first week of February 1981. The tube was successfully hipotted to 30 kV across the cathode - gun anode seal and to 100 kV across the gun anode - anode seal. During hipotting, a few mild gas bursts were observed. As the pumps recovered from a gas pressure surge, the pump pressure was two orders of magnitude higher in the gun pump than in the collector pump. This was expected since the low pumping conductance of the beam tunnel effectively isolates one end of the tube from the other.

2. Excessive Body Current

During the second week of February, pulsed beam power was applied and a comparison of body current to beam current showed excessive beam interception in the beam tunnel. While the magnet steering coils did have a slight effect in reducing the body current, their ampere-turns rating was insufficient to steer the beam clearly through the beam tunnel. To correct this problem, iron shields were wrapped around both ends of the magnet dewar to shield the tube from external magnetic perturbations. This had no effect on the excessive beam interception. Finally, by using a mechanical adjustment on the plate which supports the tube at the top of the dewar, the tube was tilted about a pivot point near the gun. A transverse adjustment of the beam tunnel, with respect to the axis of the dewar bore of 0.022" east and 0.015" north, was necessary to send the beam through the beam tunnel with acceptable (~ 5 ma) beam interception at full beam current (8 a).

3. Observation of RF Output

RF output near 60 GHz was first observed on 24 February 1981. It was apparent that the modulator voltage pulse was not sufficiently flat.

The voltage divider in the modulator was adjusted to better compensate the system for running at 8 a, 80 kV. The gun anode voltage pulse was improved enough to observe rf pulses of ~ 20 μsec in duration. However, because this tube appeared to be very sensitive to small changes in gun anode voltage, the rf pulse duration was limited by the slope of the gun anode voltage waveform. Thus, it was not possible to increase the rf pulse duration without first flattening the voltage pulse.

During this portion of the testing, measurements were obtained, indicating a peak output power of ~ 200 kw at ~ 50% efficiency. However, some uncertainty must be attributed to these preliminary data because, while average rf power (~1 kW) was measured calorimetrically, the inferred peak power depended on the less certain measurement of rf pulse duration. When running under such modulator pulse shape conditions, the rf pulse duration was less than the beam pulse duration. This might cause significant error in the peak power measurement if, for example, any unobserved rf was put out by the tube at other times during the beam pulse.

4. Control of Operating Parameters

To improve the accuracy of the rf power measurements, the pulse shape needed improvement. Additional adjustments on the test set improved the flatness of the gun anode pulse to ± 1%. Better control of the voltage pulse amplitude was also necessary to tune the tube to the optimum operating point. Drift in the dc beam voltage also hampered tuning the tube to the optimum operating point, indicating that the beam voltage regulation was inadequate. Finally, the bucking coil current and main solenoid coil currents were subject to long settling times (about 10 seconds and 3 minutes, respectively) because of the high load inductance and low series load resistance in the magnet energizing circuits. These system problems were addressed during the long-pulse upgrade of the test set.

5. RF Data

In spite of the complications mentioned above, sufficient preliminary data were obtained to identify the basic operating

characteristics of this 60 GHz design. The tube was run at 100 μsec pulse durations and somewhat lower peak power levels (~ 150 kW). The data shown in Figures 291 and 292 were obtained with the parameters given in Table 40.

Table 40
Parameters for Frequency vs Top
Coil Current

Beam Voltage	~ 80 kV
Beam Current	~ 6.1 a
Gun Anode Voltage	~ 18 kv
Pulse Duration	~ 100 μsec
Pulse Repetition Rate	120 $(sec)^{-1}$
Bottom Coil	25.51 A
Bucking Coil	2.68 A

Behavior similar to that observed in the 28 GHz experiments was observed here. A decrease in main magnet current detuned the output frequency, while it increased the power output. After a sharp peak in output power, the operating frequency jumped to that of another mode, probably the TE_{221}, at 57.79 GHz. The parameters given in Table 41 accompany the plot of output power versus bucking coil current shown in Figure 293. As expected, an increase in bucking coil current decreased the magnetic field at the cathode, thereby increasing the transverse energy in the beam and raising the rf output power.

ORNL Dwg. 81-16824 FED

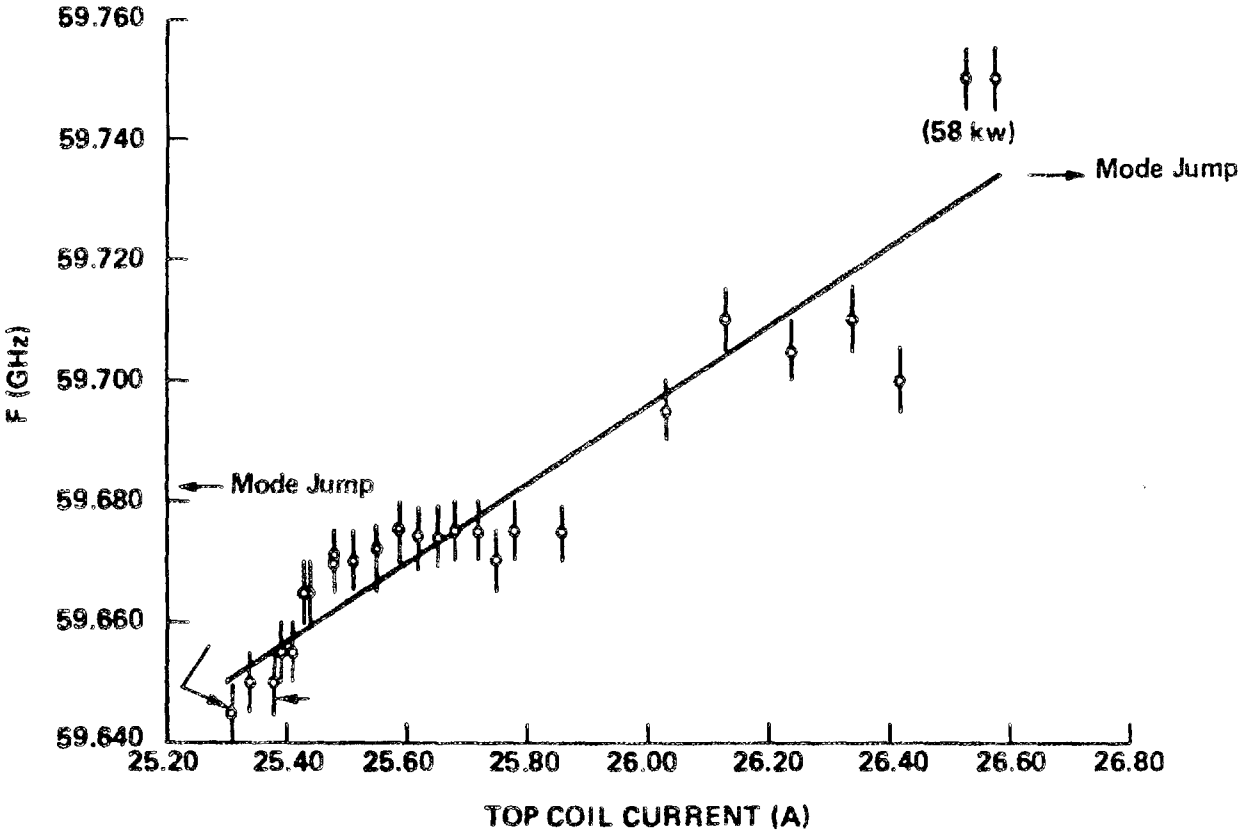

Figure 291. Operating Frequency VS Top Coil Current for X-1

ORNL Dwg. 81-16825 FED

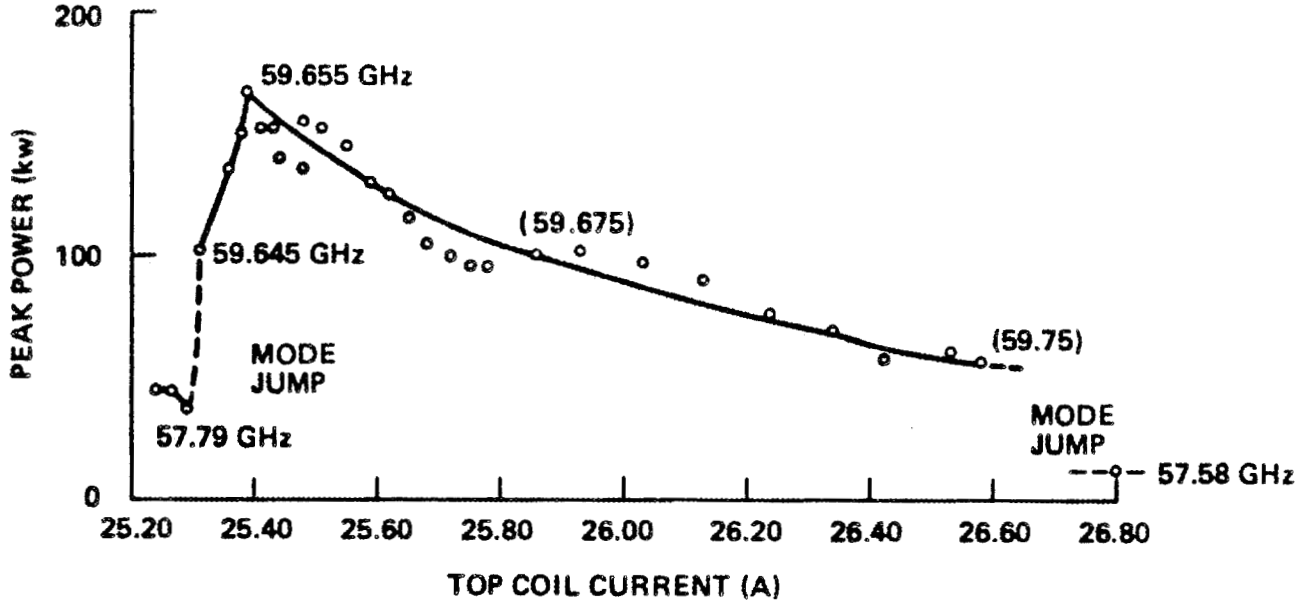

Figure 292. Peak Output Power VS Top Coil Current for X-1

ORNL Dwg. 81-16826 FED

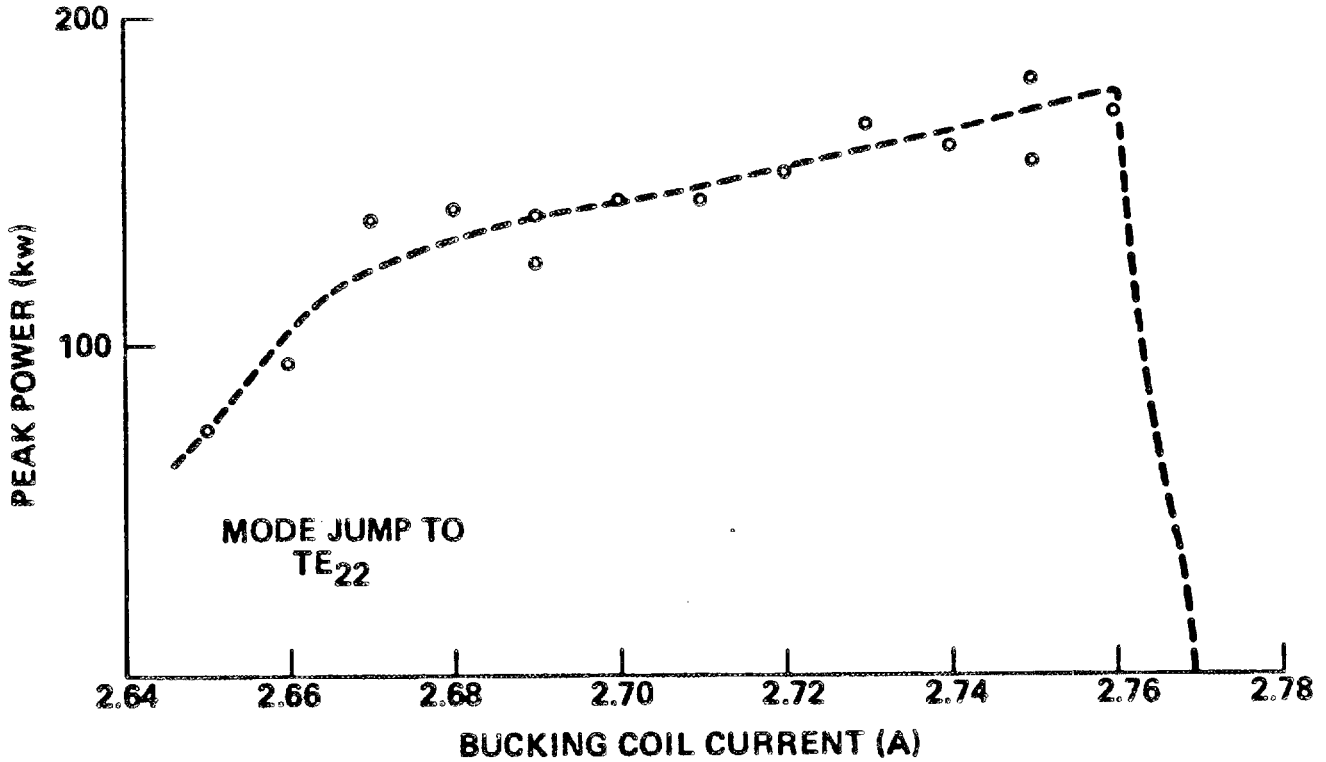

Figure 293. Peak Output Power VS Bucking Coil Current for X-1

Table 41

Parameters for Power vs Bucking Coil Current

Beam Voltage	~ 80 kV
Beam Current	~ 6.4 a
Gun Anode Voltage	~ 17.8 kv
Pulse Length	~ 50 μsec
Repetition Rate	120 s^{-1}
Top Coil	25.45 A
Bottom Coil	25.51 A

A summary of the data obtained for peak output power versus beam current is shown in Figure 294. These points were obtained over a large range of operating parameters, including pulse durations from 20-100 μsec. The data were compared with the performance predicted by Chu[44] for starting current, and by Nusinovich and Erm[45] for large signal interaction efficiency. The curves were calculated using the theoretical results in Reference 45 for cavities with Gaussian electric field profiles of 6λ, 8λ, and 10λ in length. The experimental data fall roughly in the range of 6λ - 10λ indicating that the tapered cavity is comparable to a Gaussian field profile cavity of length ~ 8λ.

A number of qualitative conclusions were also drawn from the preliminary test results of this tube:

1) The sensitivity of the 60 GHz gun performance to variations in gun anode voltage and bucking coil current was more pronounced than that of the 28 GHz guns. This had been anticipated because a long-cathode gun optics design was used which was inherently more sensitive to changes in these parameters than the short cathode design employed in the 28 GHz guns.

2) The mechanical tolerances specified in building the first magnet were not sufficient to prevent beam interception in the beam tunnel. When ordering subsequent solenoid magnets, this problem was corrected by requiring more ampere-turns for the steering coils. It was not within the

ORNL Dwg. 81-16827 FED

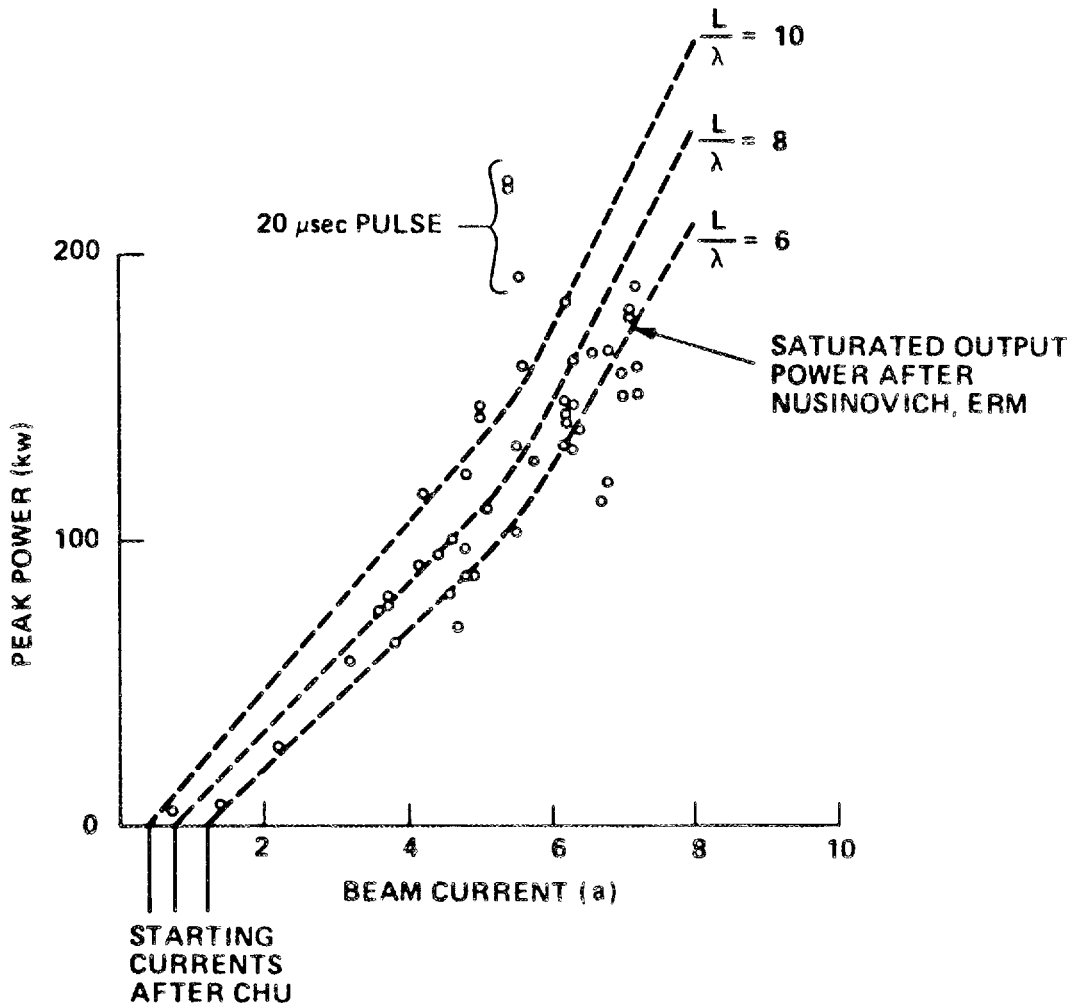

Figure 294. Peak Output Power VS Beam Current for X-1

state-of-the-art to achieve the necessary mechanical tolerances inside the vacuum dewar for alignment of the magnetic field with the mechanical axis of the dewar and still maintain a low liquid helium boil-off rate.

3) A separate vacuum manifold and pump at the gun end of the tube was an important aspect of the 60 GHz tube design. The gun pump provided an interesting diagnostic for the tube during crowbars. Furthermore, although it was too early in the life of the design to draw conclusions about the burn-in behavior of the tube, the gun pump appeared to have decreased tube processing time and permitted operation with fewer crowbars than was possible for the 28 GHz tubes.

4) The magnitudes of gun anode voltage and bucking coil current used to achieve optimum rf performance indicated that the gun sat too low in the dewar bore. After rechecking all of the design data, it was discovered that the tube length between the cavity and the gun was excessive. This error was corrected on X-2. In any event, it appeared that respectable beam quality could be obtained, even when the gun was in the incorrect axial position, by compensating for the error with changes in bucking coil current and gun anode voltage.

Testing of the first experimental tube was resumed in early May 1981 after the beam voltage regulator was incorporated in the Nike-Zeus Test Set power supply. It became immediately apparent that the gun anode voltage pulse had a severe droop (approximately 6.5 volts/μsec). As discovered in March, a droop of this size limited rf pulse durations to ~ 20 μsec. However, the beam voltage itself was extremely stable. These conditions allowed operation with a very stable rf pulse shape. Although the rf pulse duration was limited to 20 μsec, stable average rf power absorption in the waterload was assured. This permitted more accurate rf power measurements.

Operating the test set under these limitations, attempts were made to reproduce the rf data obtained earlier. Sensitivity of peak output power and rf frequency to top main coil current are plotted in Figure 295 for the test parameters given in Table 42. A maximum peak power of 146 kw was obtained at 6 a of beam current. The 200 kw rf result earlier reported

ORNL Dwg. 81-16847FED

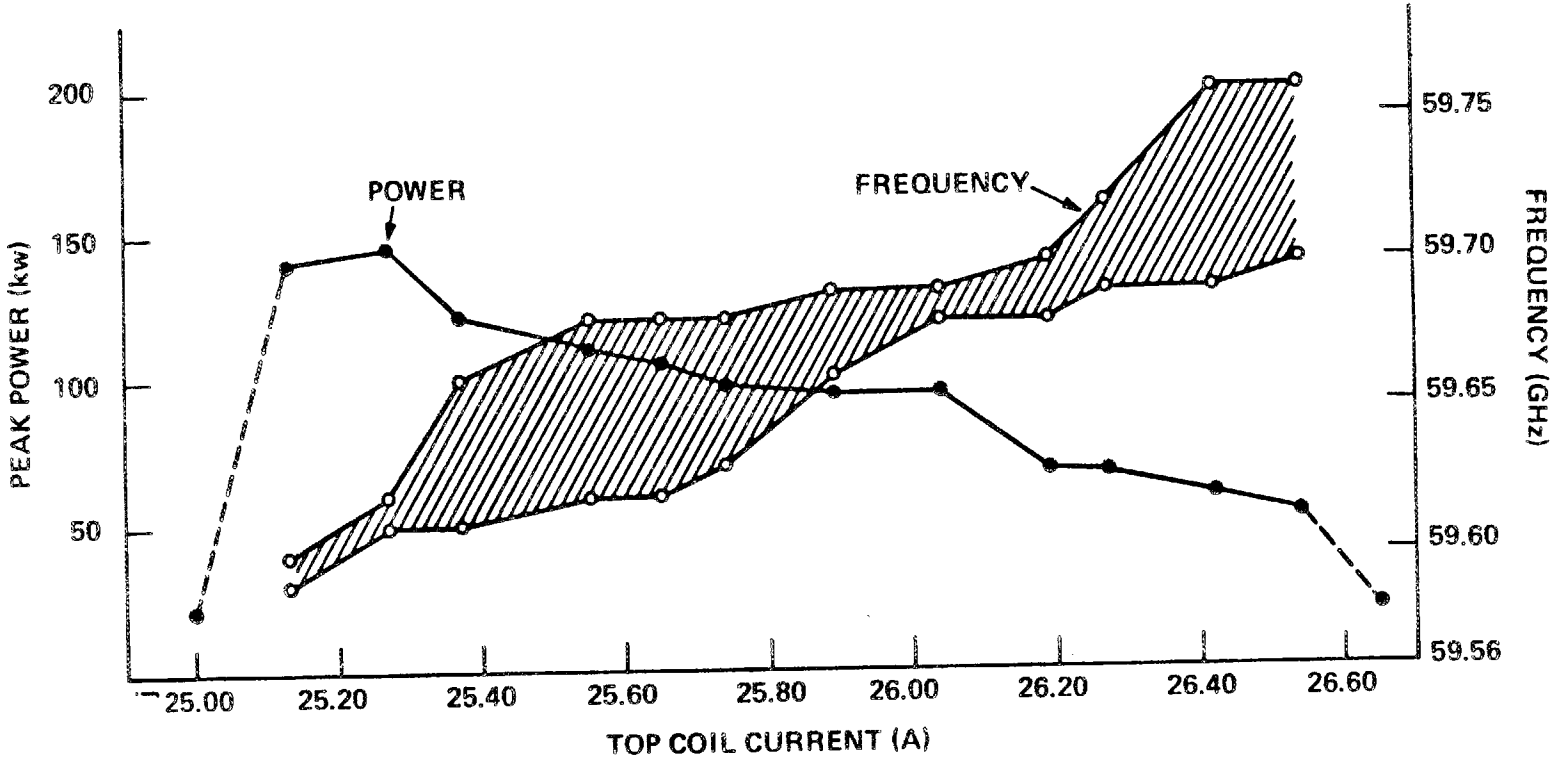

Figure 295. Sensitivities of Peak Output Power and Frequency to Top Main Coil Current for the Parameters of Table 42.

could not be reproduced. Whether this discrepancy was due to error in the previous measurement or change in the voltage pulse shape or other test parameters, was not known.

Table 42

Operating Parameters

Gun Anode Voltage	~ 18.6	kv
Beam Voltage	80.0	kV
Beam Current	6.0	a
Pulse Repetition Rate	60	s^{-1}
Rf Pulse Duration	~ 20	μs
Beam Pulse Duration	~ 80	μs
Bottom Coil Current	25.54	A
Gun Bucking Coil Current	2.83	A

Further attempts to flatten the modulator pulse were moderately successful. The longest rf pulses obtained, shown in Table 43, were achieved in early June 1981, although power supply difficulties required operation at ~ 8 a to obtain these longer pulses.

Table 43

Best Long Pulse Results, VGE-8060 X-1

Beam Voltage	80.2 kV
Beam Current	7.8 a
RF Pulse Duration	265 μsec
Peak RF Power	150 kw

Additional changes in the test set were initiated to correct the gun anode pulse shape.

6. Body Heating

When operating the tube at a stable beam voltage, a peculiar mode of behavior was observed. This behavior was overlooked during previous

tests when the beam voltage varied during the recording of calorimetric data. A rise in the body-cooling water temperature indicated extreme (~ 50 kw peak) heating in the body section of the tube. The onset of this body heating was simultaneous with the upper limit in gun anode voltage where the 60 GHz oscillation was observed.

Figure 296 shows a sketch of the beam pulse, specifying where the 60 GHz oscillation occurred. By adjusting the amplitude of the gun anode pulse, the rf pulse could be effectively adjusted back and forth within the beam pulse. A correlation existed between the body heating and the delay between the start of the beam pulse and the start of the rf pulse. This correlation is described in Figure 297. When the rf pulse and the beam pulse started simultaneously, there was little body heating, several hundred watts of average 60 GHz power at the waterload, and acceptable pressure at both ends of the tube. As the rf pulse was delayed, the body heating rose rapidly, and pressure in the tube increased notably. Finally, for long time delays and excessive gun anode voltage, interception of the beam occurred at the gun anode. No body current was observed during the body heating.

These data suggested that some internal rf oscillation was taking energy out of the beam and depositing it in the body. The body water temperature responded rapidly to any sudden change in gun anode voltage which activated the body heating. This was evidence of a short heat path between the rf dissipation zone in the body and the body water channels. Given the plumbing connections used in tube X-1, this implied that the dissipation was occurring in either the body cavity, the drift tube, or the output cavity. These sections of the tube are represented schematically in Figure 298.

Minimal rf power was coupled into the waterload and very low level rf signals (~ 40 dB below the 60 GHz signal) were coupled out of the tube output waveguide at the power sampler during operation in the body heating mode. As any oscillation in the output cavity would couple strongly to the output waveguide, these results indicated that the body heating oscillation did not originate there. Frequencies of the weak output signals included: 57.21 - 57.25, 57.80, and 57.89 GHz. Rf detectors were also placed in the

ORNL Dwg. 81-16848FED

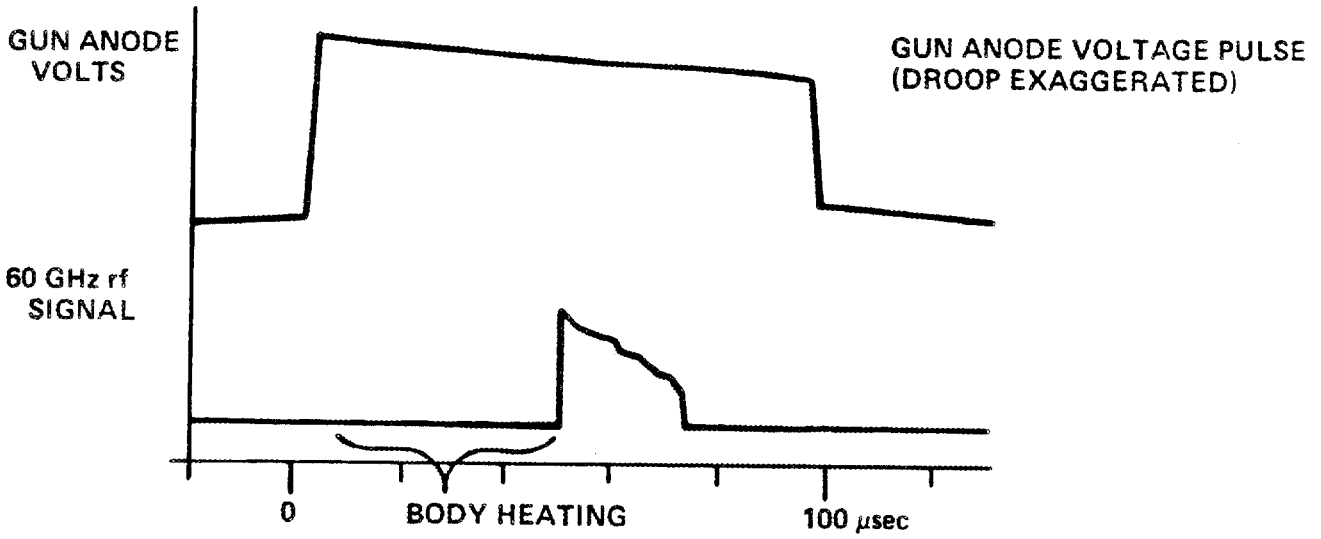

Figure 296. Gun Anode Voltage and RF Pulse Shapes

ORNL Dwg. 81-16849FED

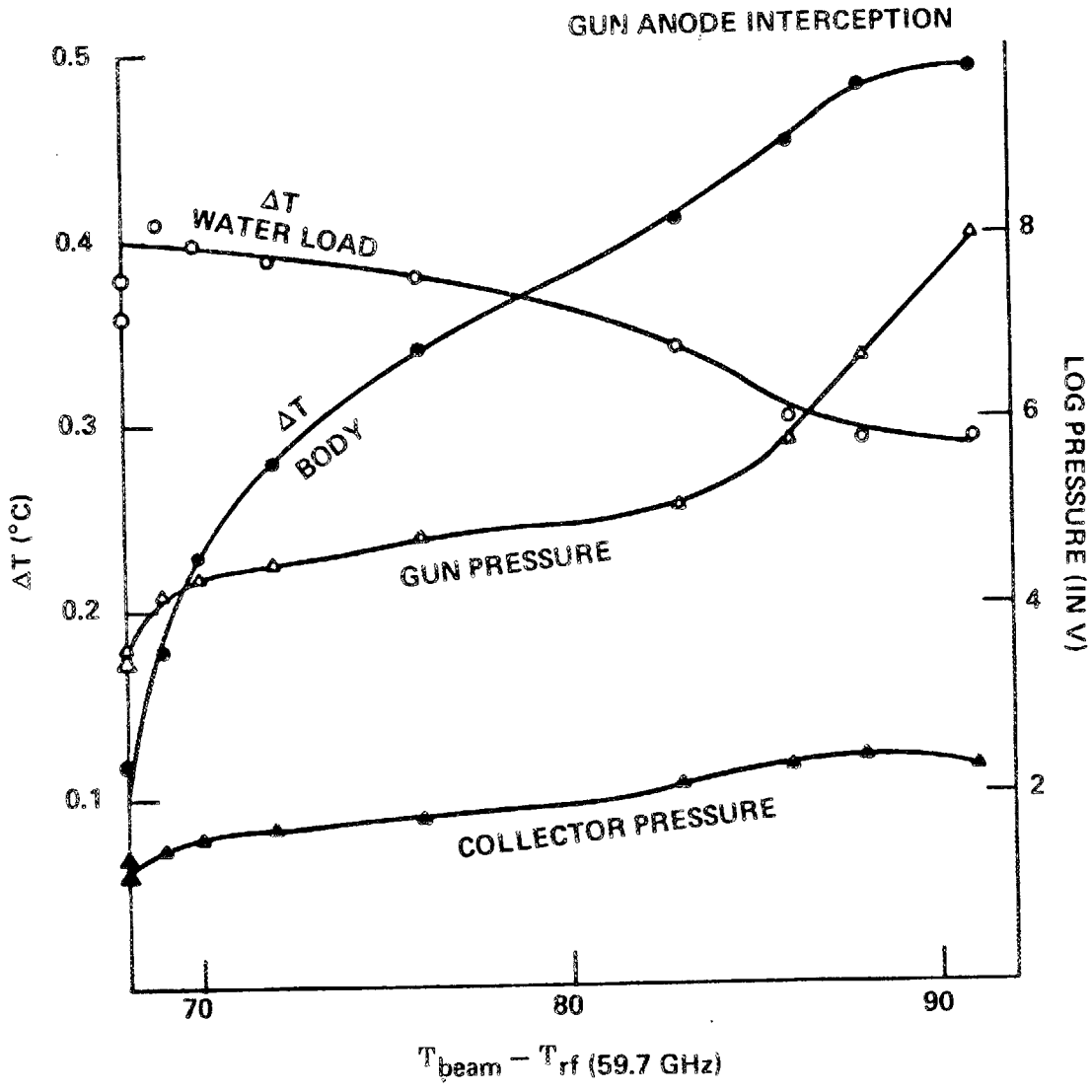

Figure 297. Body Heating Correlation

ORNL Dwg. 81-16850FED

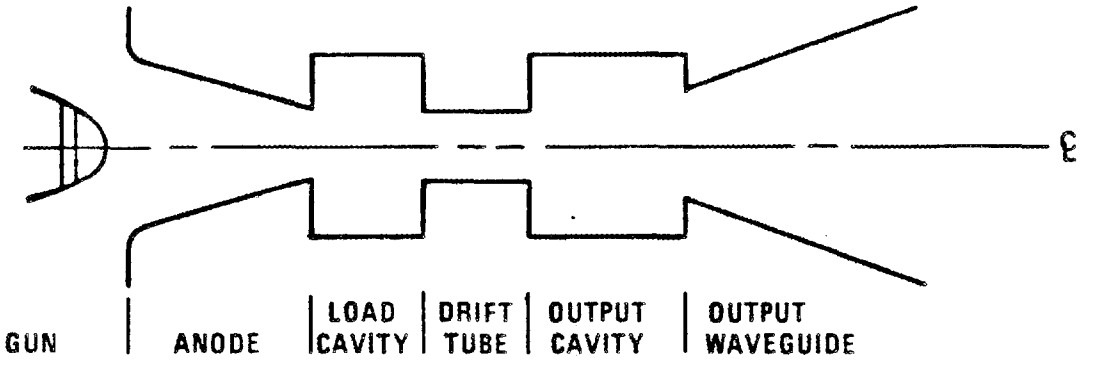

Figure 298. Schematic Layout of VGE-8060

oil tank near the electron gun ceramic seals to determine if any of the rf causing the body heating was transmitted downward into the gun region. No rf signals were exiting the gun end of the tube.

Further investigation of the body heating oscillation was carried out in cold test. Various portions of the body structure of the tube were analyzed for the possibility of resonances near 60 GHz. Transmission resonance characteristics of the load cavity and the drift tube are compared in Figure 299. A suspicious set of drift tube resonances is visible in the band from 57.2 - 58.2 GHz, the same frequencies observed at low levels in the output waveguide.

Figure 300 shows the effect on the Q of the drift tube resonances caused by the presence of a) neither the load cavity nor the output cavity, b) the load cavity only, c) the output cavity only, and d) both the load cavity and the output cavity. The presence of the output cavity increased the Q of the drift tube resonances and suggested that the output loading on the drift tube "cavity" was primarily in the direction of the load cavity. The rf generated in the drift tube was then readily absorbed in the load cavity, as the tube test data suggested. Using perturbing metal probes on the cold test model of the drift tube, it was determined that the drift tube resonance was due to the TE_{211} drift tube mode. As indicated in Figure 300, the Q for this mode is ~ 100 - 200.

A large signal calculation was made of the TE_{211} gyrotron interaction efficiency expected for the drift tube region of the tube. The results are compared with the test data in Table 44.

ORNL Dwg. 81-16851FED

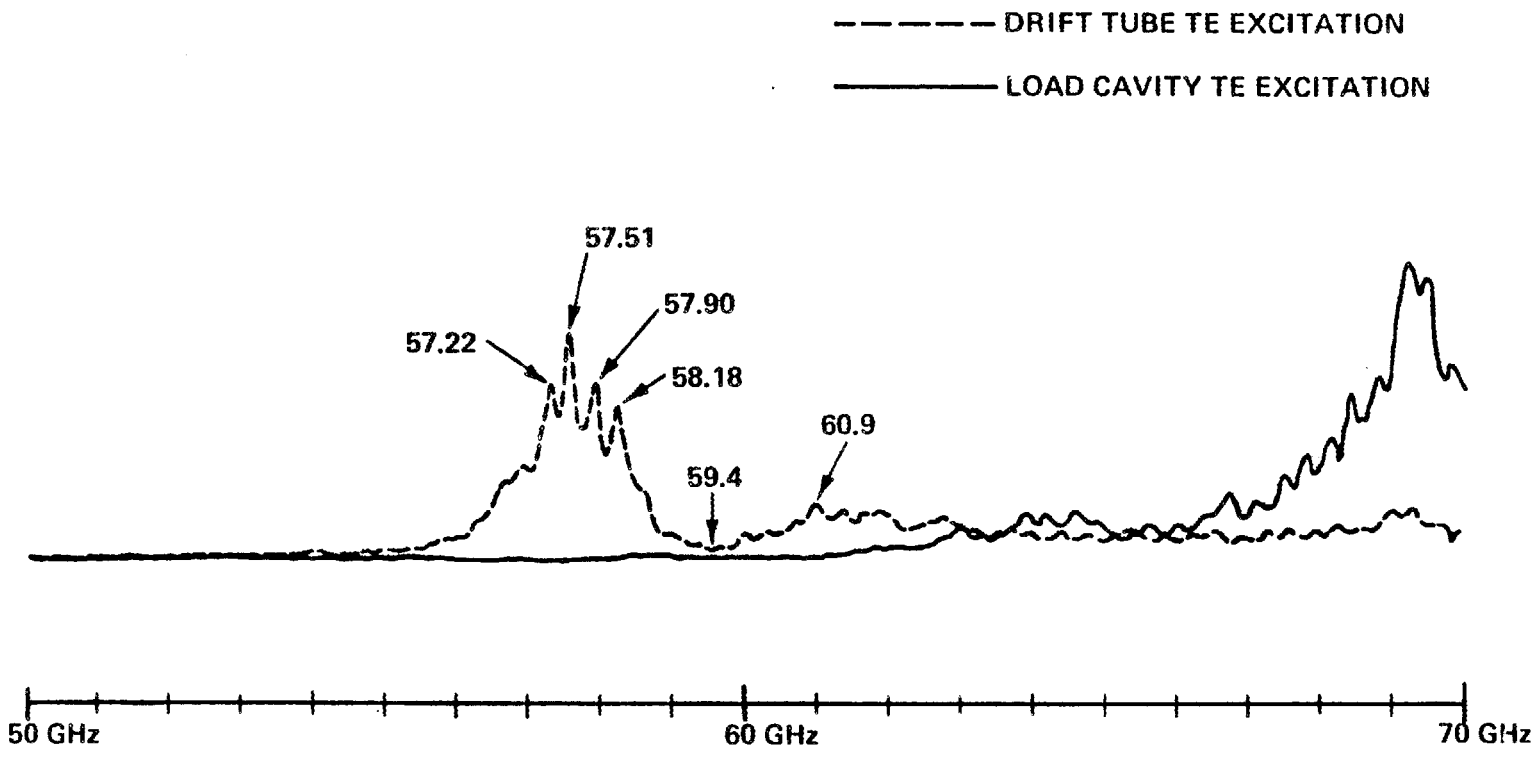

Figure 299. Comparison of Load Cavity and Drift Tube Resonances

ORNL Dwg. 81-16852FED

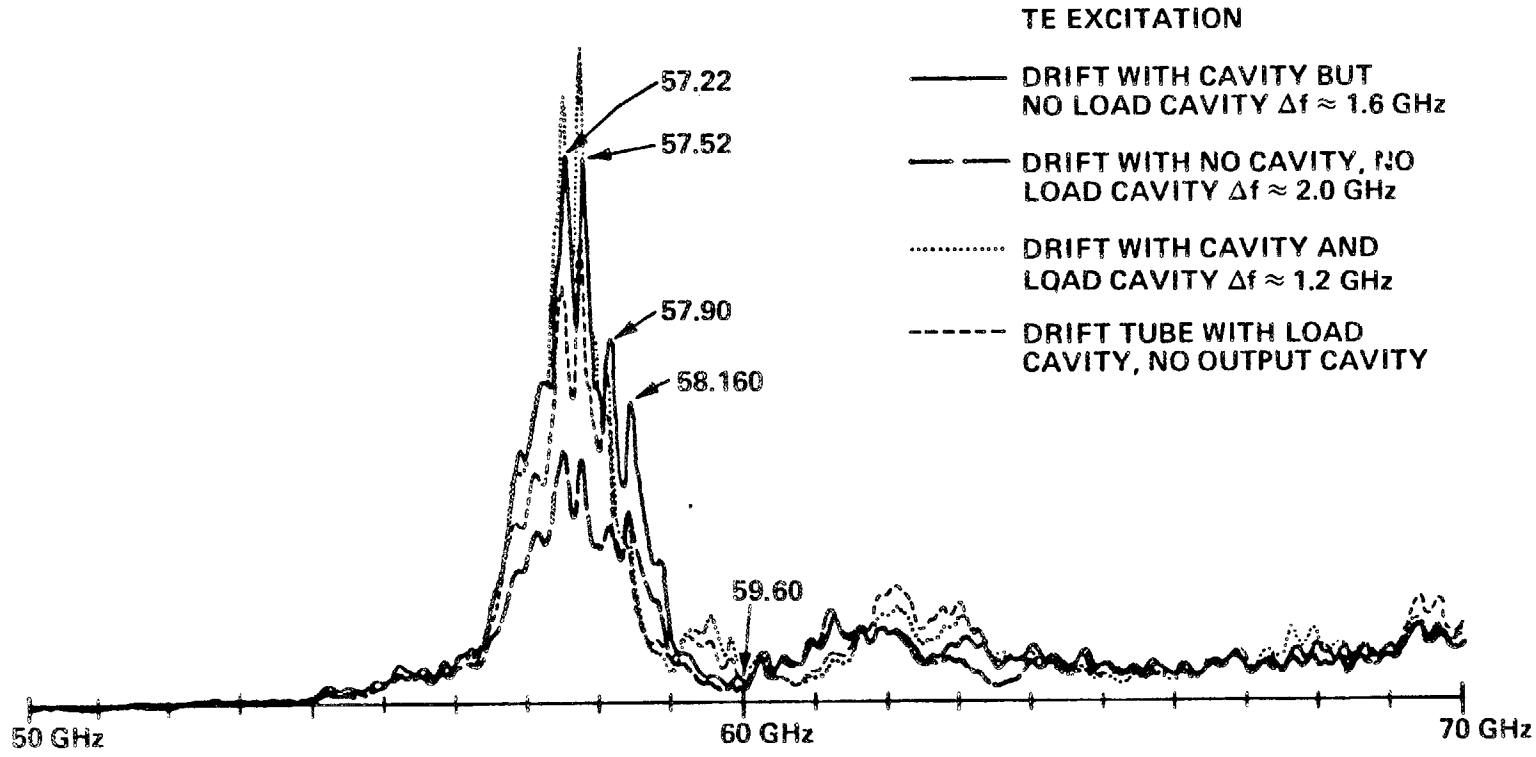

Figure 300. Drift Tube Resonances for Different Boundary Conditions

Table 44

TE_{211} Drift Tube Interaction

	Experiment	Computer Simulation
Beam Voltage	80 kV	80 kV
Beam Current	6 a	2.7 A
*Output Power	50 kw	50 kW
Efficiency	10 %	23 %

(* It should be noted that these results were obtained at 1% duty, demonstrating that the load cavity design was capable of dissipating at least 500 watts average power, or about 100 watts/cm^2 average power density.)

Operation of X-1 at higher beam transverse energies was limited by the onset of a TE_{211} drift tube oscillation. This condition caused extreme body heating in the load cavity section of the tube. The solution to the oscillation problem was to shorten the drift tube, thereby reducing the Q of the resonance, as shown in Figure 301. This raised the starting current for the TE_{211} oscillation above the nominal beam current. The necessary design changes were implemented. Tube X-3 contained a drift tube of the corrected design.

Further testing of X-1 was in support of test set debugging. The rf tests consisted of operating the tube at increasing pulse durations. Two interesting results are shown in Table 45. The ability to adjust parameters to obtain high output power declined with the tube's life.

ORNL Dwg. 81-16853FED

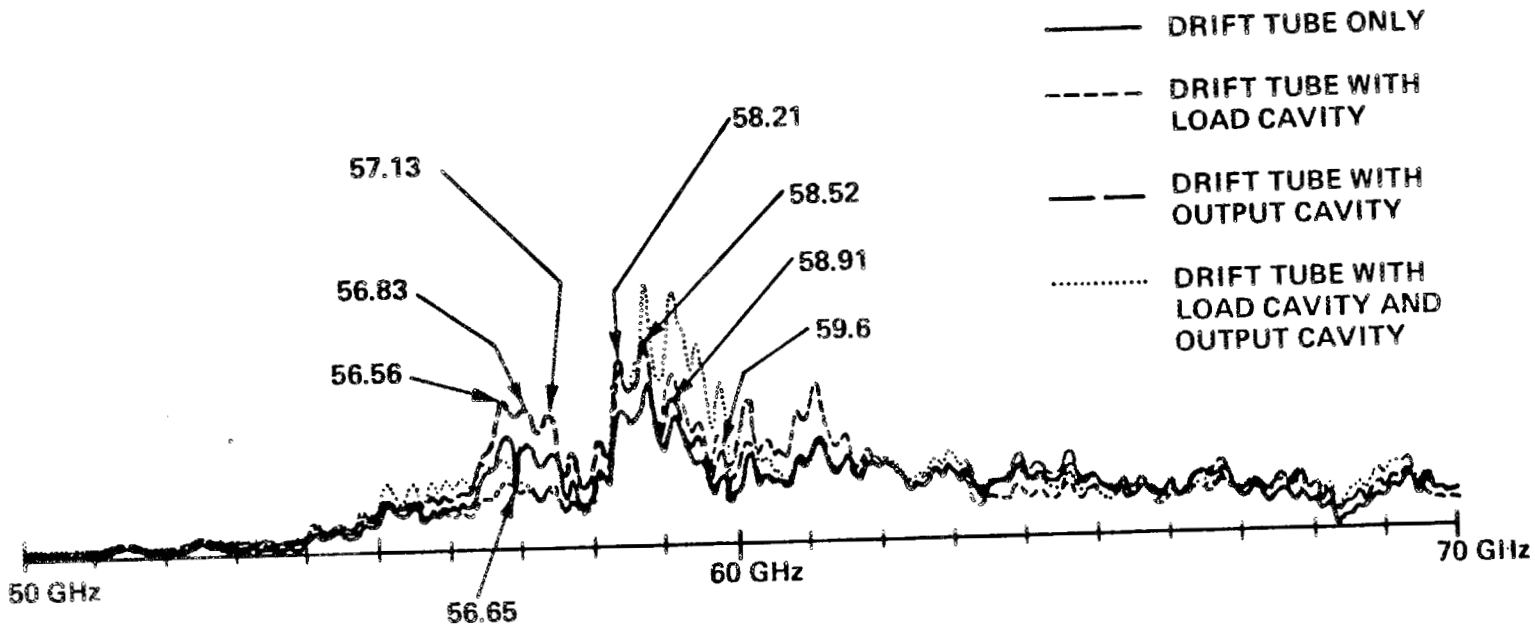

Figure 301. Resonance Curve for Modified Drift Tube

Table 45

X-1 Long Pulse Performance

Top Main Coil Current	[A]	26.0	26.0
Bottom Main Coil Current	[A]	25.5	25.5
Gun Bucking Coil Current	[A]	2.91	2.91
Heater Voltage	[V]	10.1	10.1
Heater Current	[A]	2.0	2.0
Beam Voltage	[kV]	80.0	80.0
Beam Current	[a]	7.0	7.0
RF Pulse Duration	[ms]	50	60
Pulse Repetition Rate	[s^{-1}]	2.5	2
Average Power Output	[kW]	11.3	10.3
Peak Power Output	[kw]	90.3	86.0
Frequency	[GHz]	59.7	59.7

A leak between the collector water channel and the vacuum caused the tube to fail. Disassembly indicated that the inside diameter of the collector was melted on one side at the top of the upper collector water manifold. The tube had been operated at 12.5% duty.

Several options were available to prevent this problem in the future. First, operational limitations on the gun bucking coil current could spread the beam faster. This may be inconsistent with gun parameters desired for optimum rf performance and may be insufficient for beam spreading. Second, the collector could be lengthened. While this could be accomplished at Varian, it is undesirable for the user. Third, a collector bucking coil could be installed to enhance beam spreading. Fourth, the duty cycle could be reduced for pulse tube testing.

Any rebuild effort would require replacing the gun, anode and collector sections. The cathode was destroyed, since the tube went down to water hot. Beam erosion of the molybdenum rings deposited metal on the silicon carbide-loaded, beryllium oxide load ceramics in the anode (beam tunnel) section. It should be noted that the anode assembly in tube X-1 did not have the water cooling of later tubes.

B. SECOND EXPERIMENTAL TUBE

The second experimental tube, X-2, was essentially the same as X-1, except that the cathode was repositioned.

1. Parameter Space

An oscillation map for a beam current of 6 to 6.5 a is given in Figure 302. X-2 showed the same mode competition as X-1. This confirmed that the body heating mode was the primary cause of the limited range of operation of the TE_{02} mode. A relatively straight-forward change in the drift tube would eliminate this problem.

2. Long Pulse Data

The first stage of long pulse testing consisted of beam-only tests to help verify the collector design. Time-to-boiling data for various collector water flows are given in Figure 303. Comparisons with theoretical calculations indicated a maximum power density greater than 2 kW/cm^2. However, the experiment was clouded by the possibility of boiling near the low pressure end of the cooling channels. With a maximum water flow rate of 180 gpm, the collector was able to sustain 560 kw peak beam pulses of three-second duration without boiling.

The final test on X-2 was the taking of long pulse rf data. Because of mode competition, the peak output power was only 125 kw. However, with the tube operating at 100 kw of peak output power, a maximum duty factor of 20% was obtained. This corresponds to an average power output of 20 kW, the highest ever obtained from a 60 GHz gyrotron at that time.

Dwg 82-2195 FED

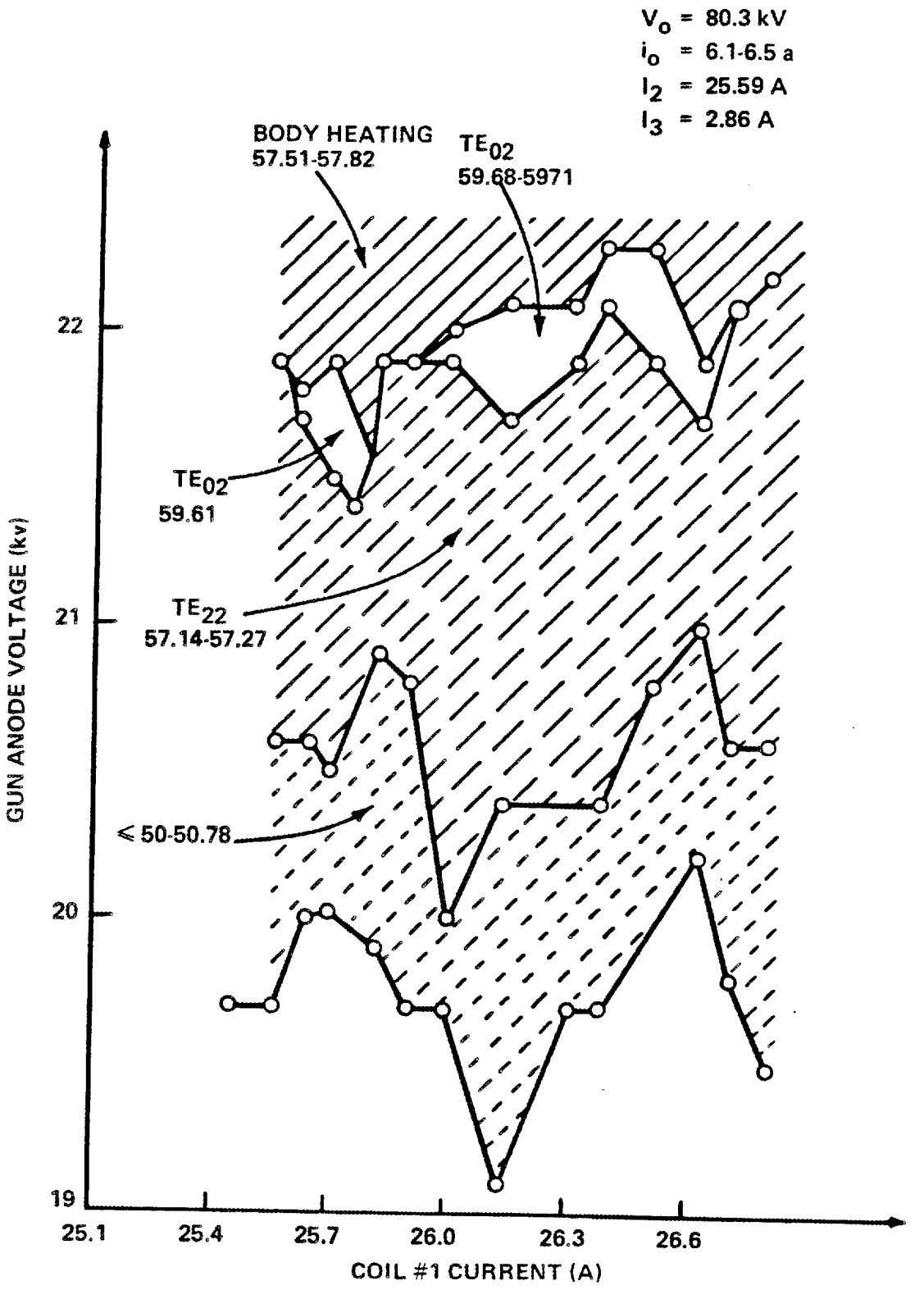

Figure 302. Oscillation Map, VGE-8060 S/N X-2

Dwg 82-2196 FED

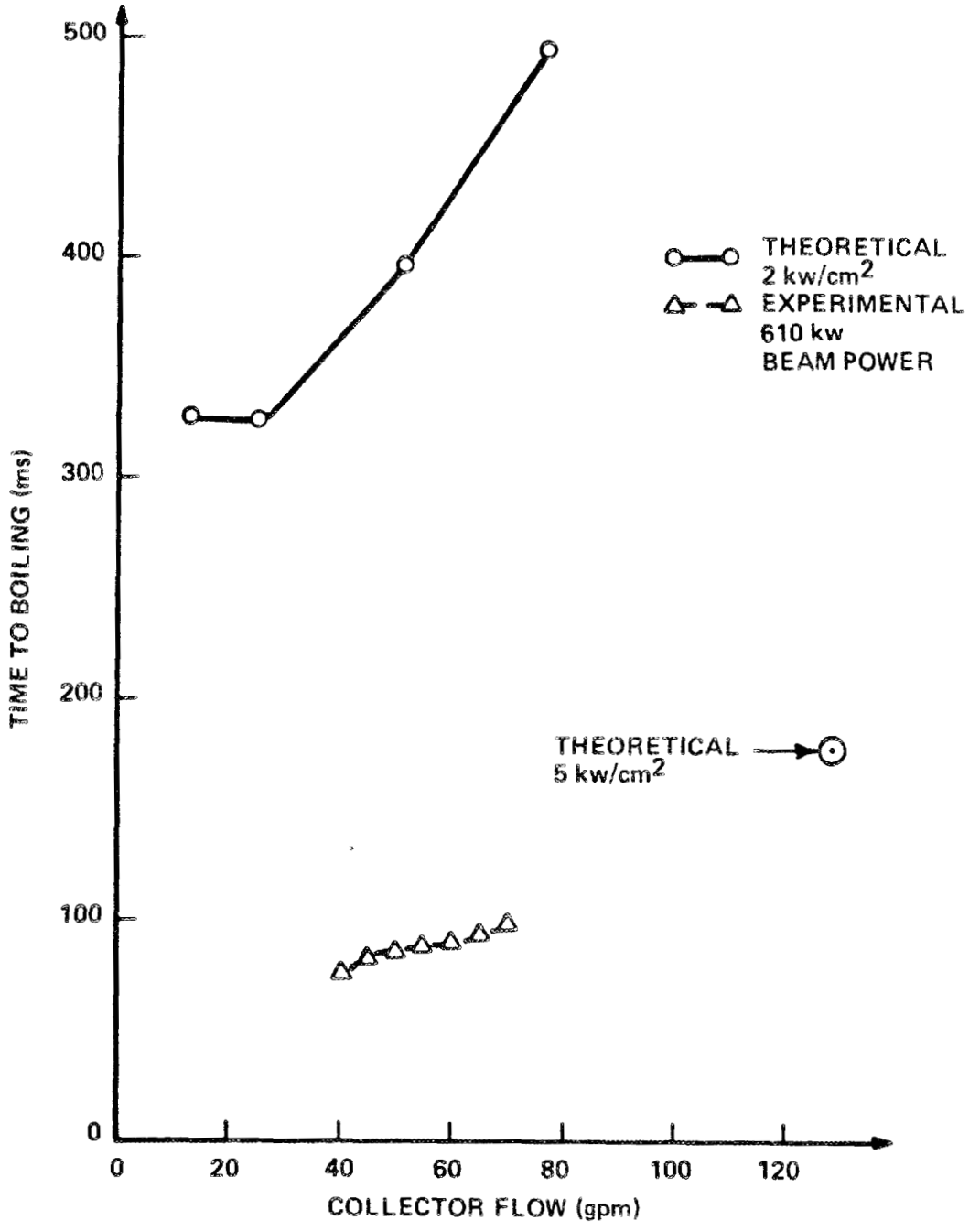

Figure 303. Collector Boiling Curves for VGE-8060 S/N X-2

C. THIRD EXPERIMENTAL TUBE

1. Original Build

Major improvements in the adjustability and flatness of the gun anode voltage pulse allowed the completion of detailed oscillation maps. These are given in Figures 304 and 305 for beam currents of six and eight amps, respectively. Strong competition from the TE_{22} mode and the body heating mode limited the range of operation for the desired TE_{02} mode. From theoretical calculations, competition from the TE_{22} mode was expected, but not to the degree observed in the measurements. The body heating mode appeared to be a TE_{21} oscillation in the drift tube. Design modifications were incorporated in later tubes to eliminate this mode. The 50 to 51 GHz oscillation on the 6 a oscillation map was very low power (<5 kw) and did not appear to present a problem.

The dependence of output power on top coil current, with beam current as a parameter, is given in Figure 306. The peak output power for 8 a of beam current is 215 kw, which corresponds to an efficiency of 33.6%. This occurred at a top coil current of 25.5 A, or a peak magnetic field of 22.9 kG.

The design of the pulsed collector was checked by using x-ray film density as an indication of power density inside the collector. The original result of x-ray density versus axial position is given in Figure 307. It indicated that the beam was landing too high in the collector. This was consistent with the collector failure observed on X-1. Based on theoretical calculations, an iron polepice was installed to lower the beam landing site. Subsequent x-ray tests, shown in Figure 308, indicated that the beam landing site had been lowered.

With the beam landing in a better position in the collector, the way was cleared for increasing the pulse duration to 100 msec. A peak output power of 200 kw at a pulse duration of 100 msec was obtained. A

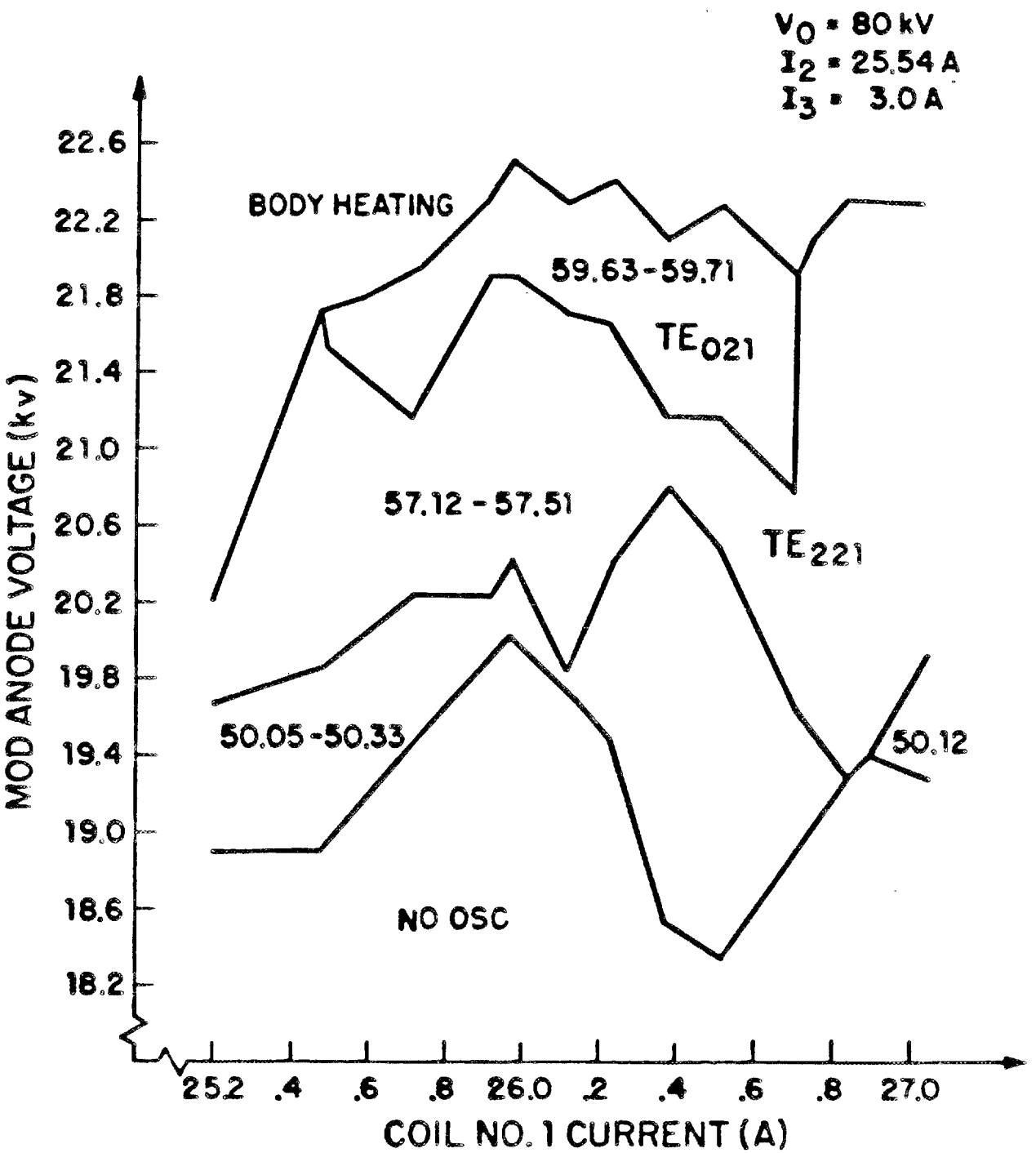

Figure 304. Oscillation Map for i_0 = 6a
VGE-8060 S/N X-3

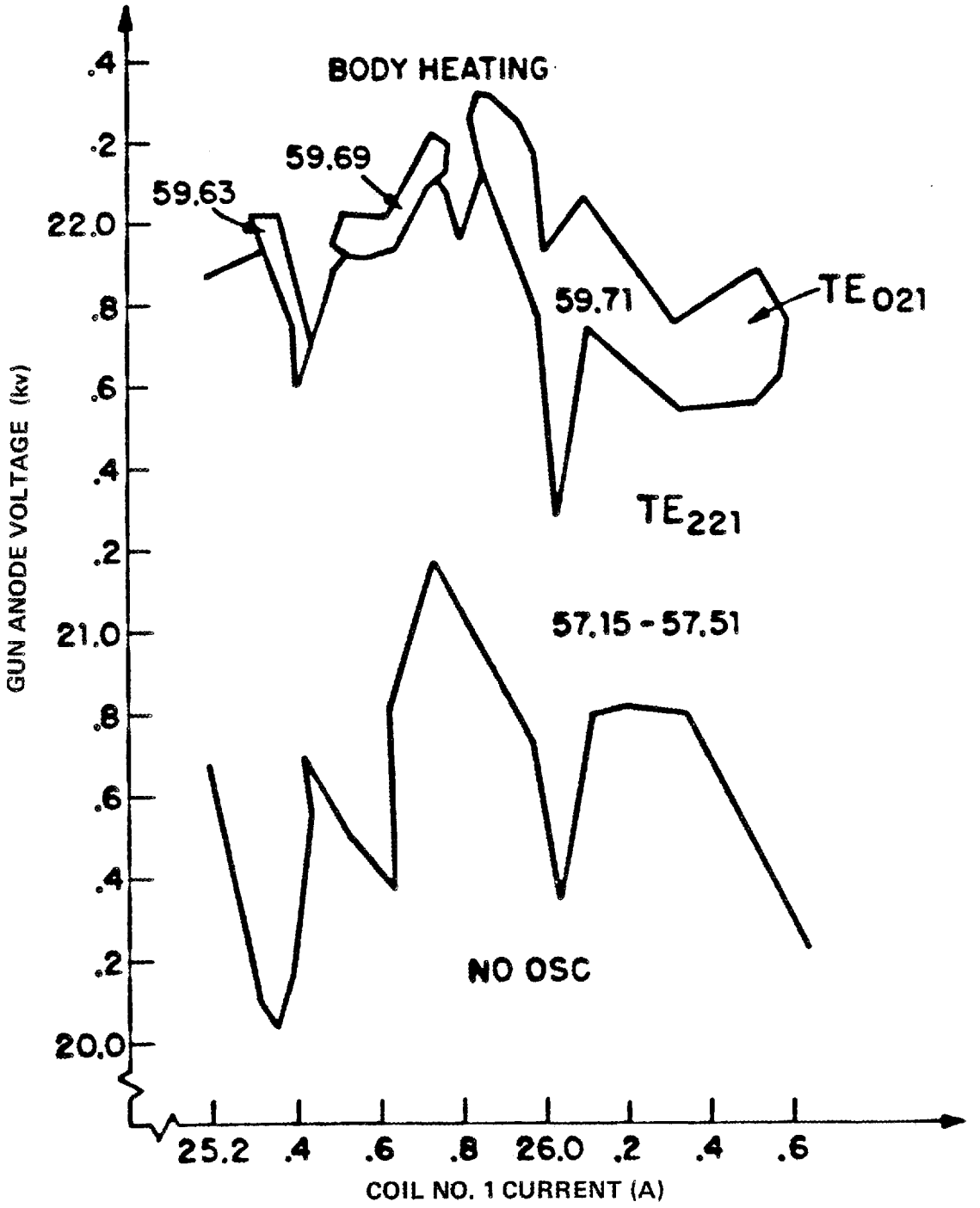

Figure 305. Oscillation Map for i_o =8a
VGE-8060 S/N X-3

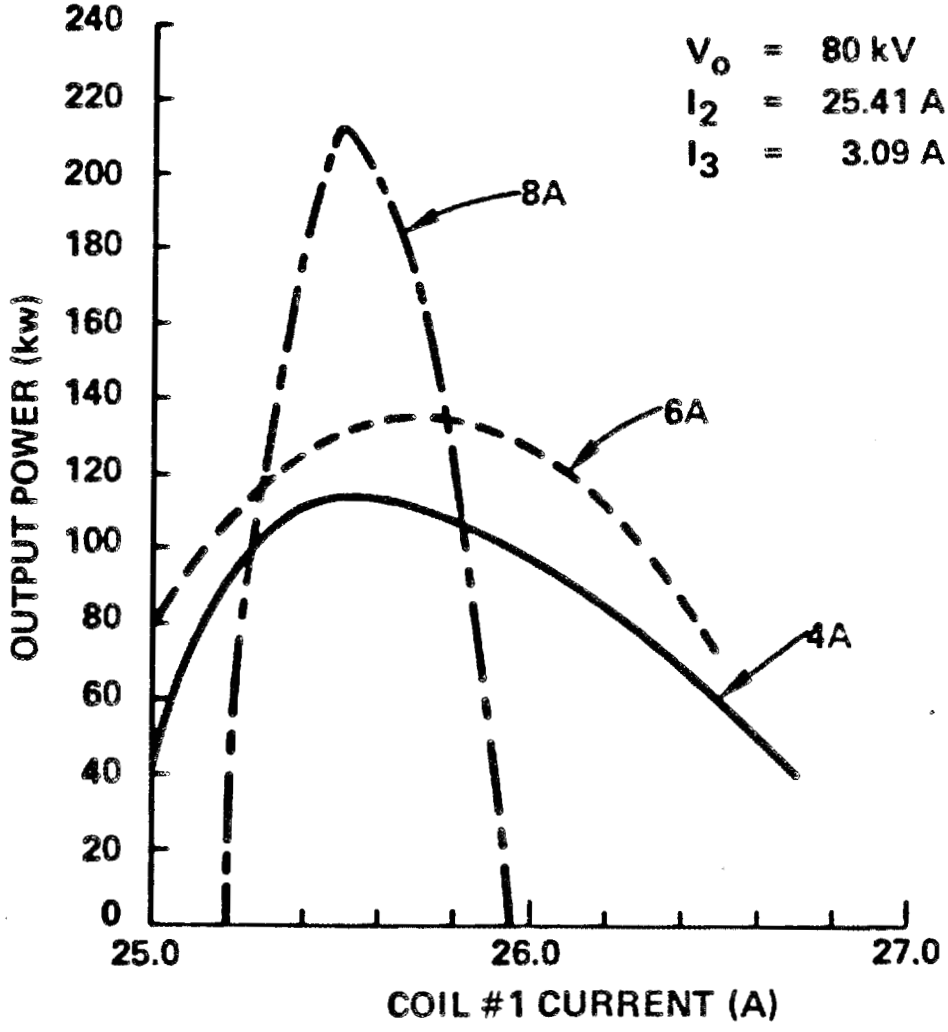

Figure 306. Power Sensitivity to Magnet Current

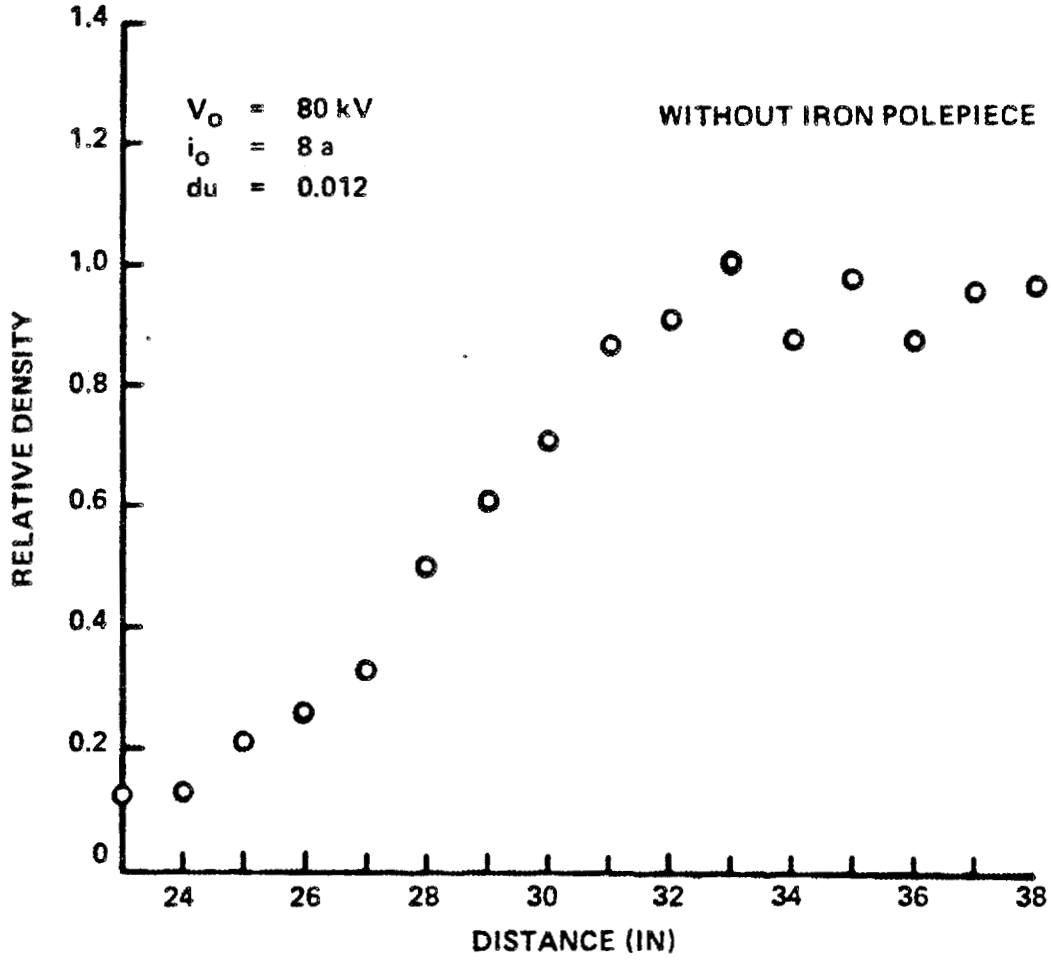

Figure 307. Densitomer Reading VS Axial Location of X-Ray Film, VGE8060 S/N X-3

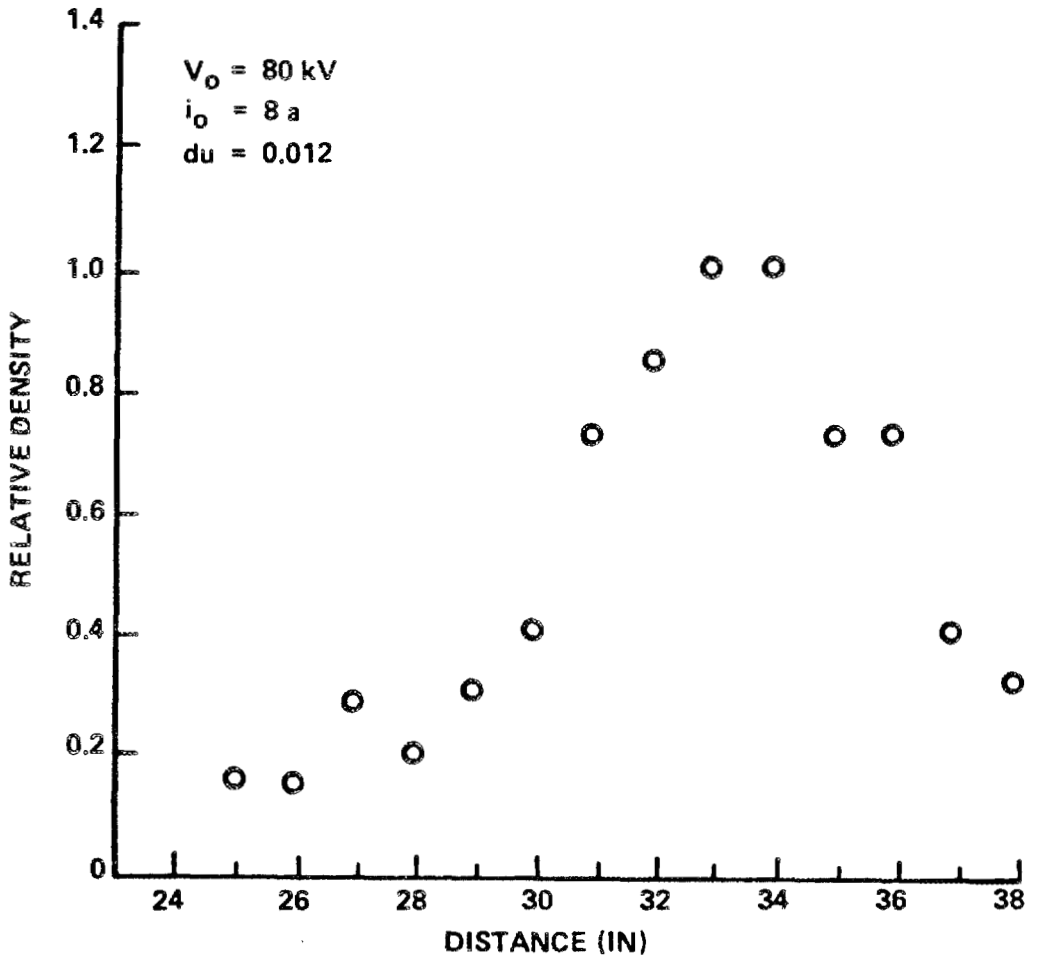

Figure 308. Densitometer Reading VS Axial Location of X-Ray Film VGE-8060 X-3 with Iron Polepiece

malfunction of the pulse repetition rate generator caused the duty factor to increase well above 30%. The excessive average rf power caused a thermal crack in the output window, ending X-3 tests.

2. Rebuild

Performance tests on X-3R, the rebuild of the third experimental tube, are summarized below. Initial tests were performed using 300 μs pulses at a repetition rate of 60 s^{-1}, 1.8% duty. Changes to the output cavity coupling and the drift tube were incorporated for the first time on X-3R. The effect of these changes can be seen in the 6 amp oscillation map of Figure 309 and the 8 amp oscillation map of Figure 310. The region of TE_{02} mode operation is enlarged and continuous in both cases instead of the insular behavior of earlier designs. Figure 311 shows a plot of optimized power and efficiency (gun-anode voltage is varied to obtain optimum results for each setting) as a function of the current in Main Magnet #1. The approximate magnetic field at the cavity is also shown. A maximum peak power of 232 kw at 36% efficiency (79.6 kV, 8.4 a) was achieved. Since the frequency of the gyrotron is based on the electron cyclotron frequency of an electron orbiting in a magnetic field, the output frequency increases slightly with increasing magnetic field, as shown in Figure 312.

In Figure 313 is the plotted output power for a constant gun-anode voltage as a function of Main Magnet #1 current for three different values of beam current. Power varies smoothly over a wide range of magnetic fields for each beam current value, though the maximum efficiency occurs at a higher magnetic field for lower values of current, as shown in Figure 314.

Following the above parameter variation tests, X-3R was operated under 100 ms pulse conditions at one pulse per second, 10% duty. The tube was operated continuously for 1 to 2 hours with a microwave output of 205 kw at an efficiency of 35.5% (80.2 kV, 7.2 a). No deleterious effects were detected under the long pulse conditions during these tests. An oscilloscope photograph of the 100 ms rf pulse is shown in Figure 315. The additional scope traces are the beam current and gun-anode voltage, as

BEAM VOLTAGE	= 79.8 kV
MAIN MAGNET #2 CURRENT	= 25.47 A
GUN MAGNET CURRENT	= 3.55 A
BEAM CURRENT	= 5.2-6.4 a (DEPENDS ON GUN ANODE VOLTAGE)
PULSE DURATION	= 300 μs
PULSE REPETITION	= 60 s^{-1}

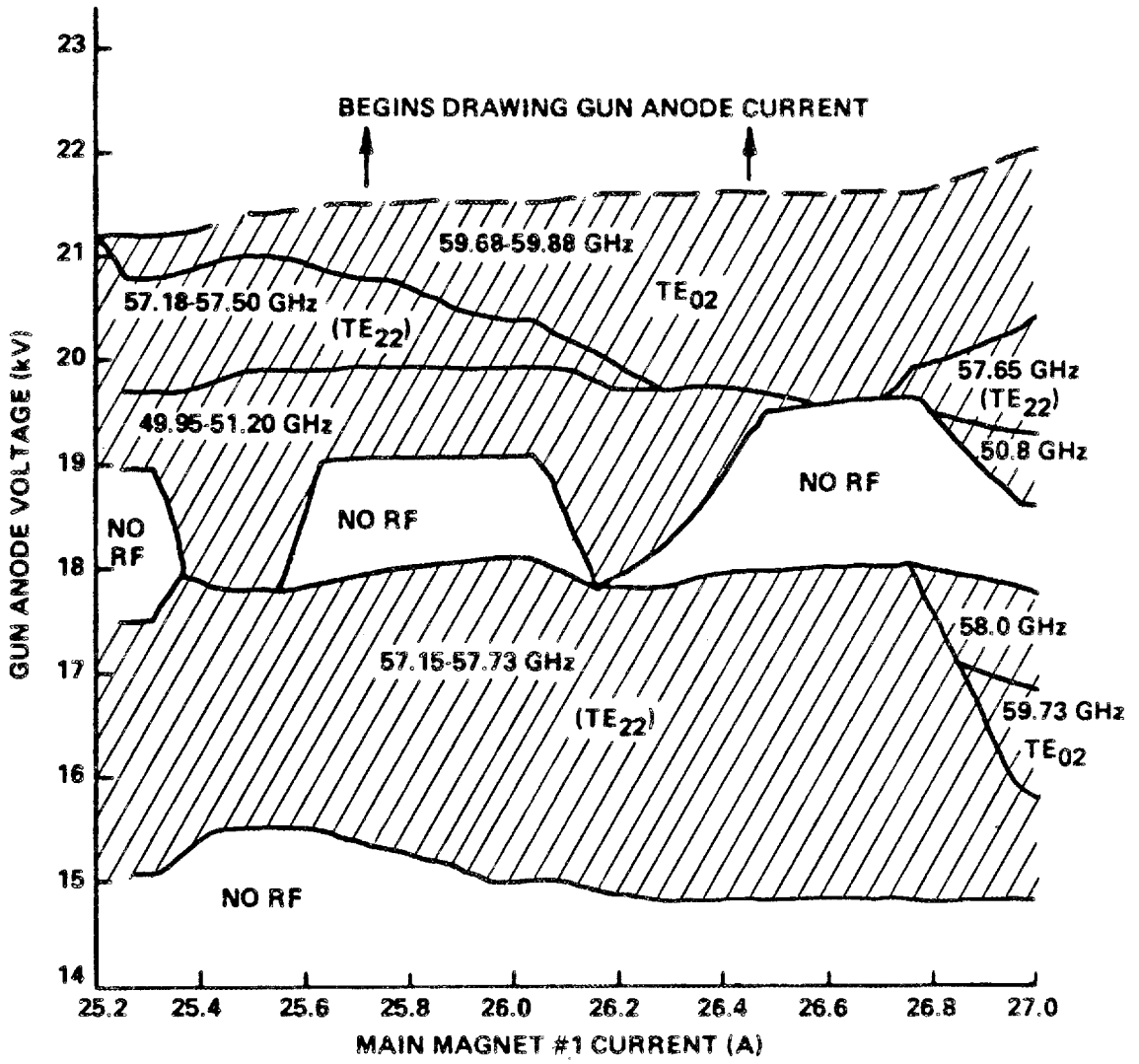

Figure 309. VGE-8060, S/N X-3R, Oscillation Map (I_0 = 6 a)

BEAM VOLTAGE = 79.6 kV
MAIN MAGNET #2 CURRENT = 25.47 A
GUN MAGNET CURRENT = 3.45 A
BEAM CURRENT = 7.3-8.4 a (DEPENDS ON GUN ANODE VOLTAGE)
PULSE DURATION = 300 μs
PULSE REPETITION RATE = 60 s^{-1}

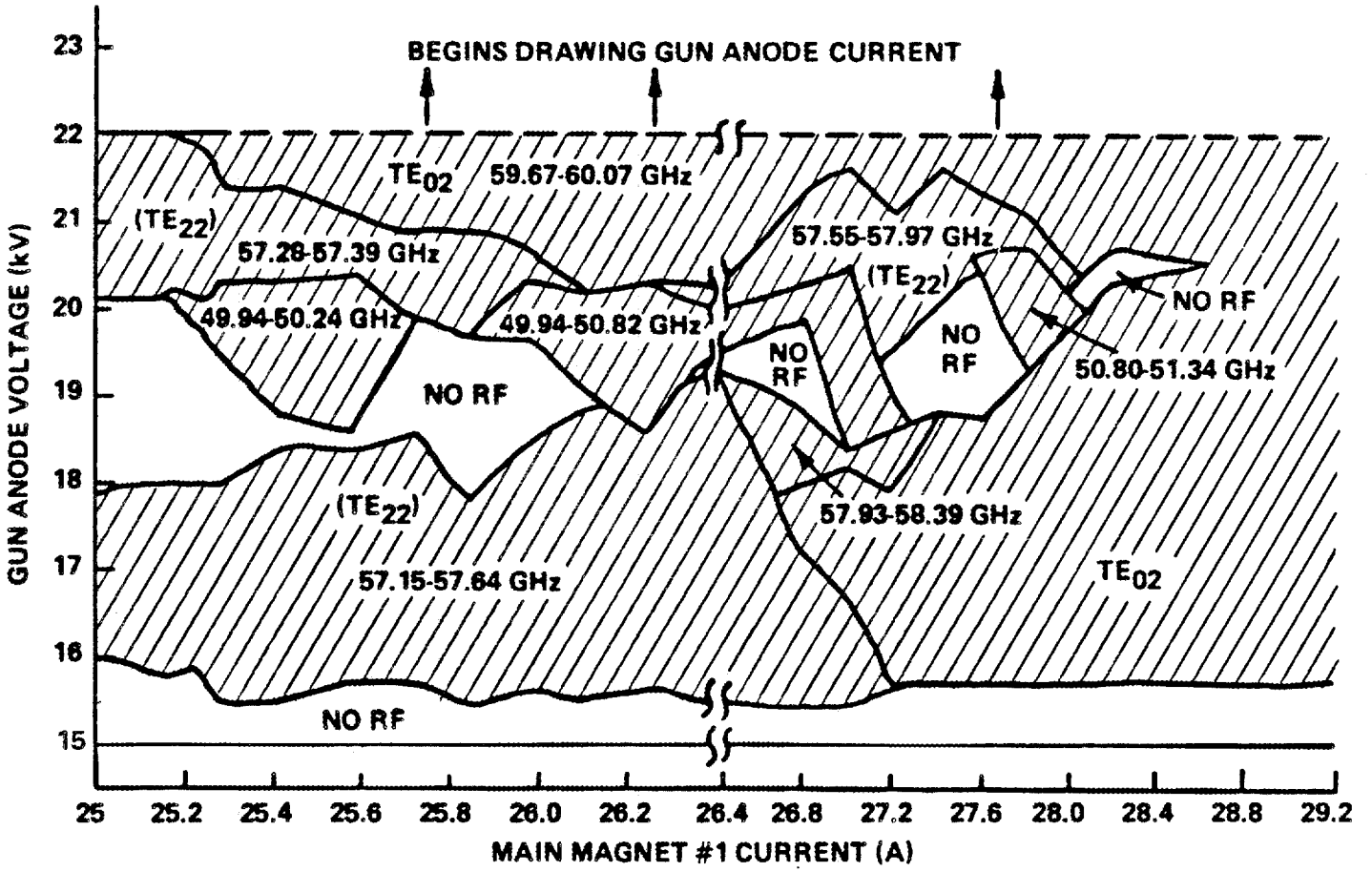

Figure 310. VGE-8060, S/N X-3R, Oscillation Map (I_0 = 8 a)

Dwg. No. 82-2214 FED

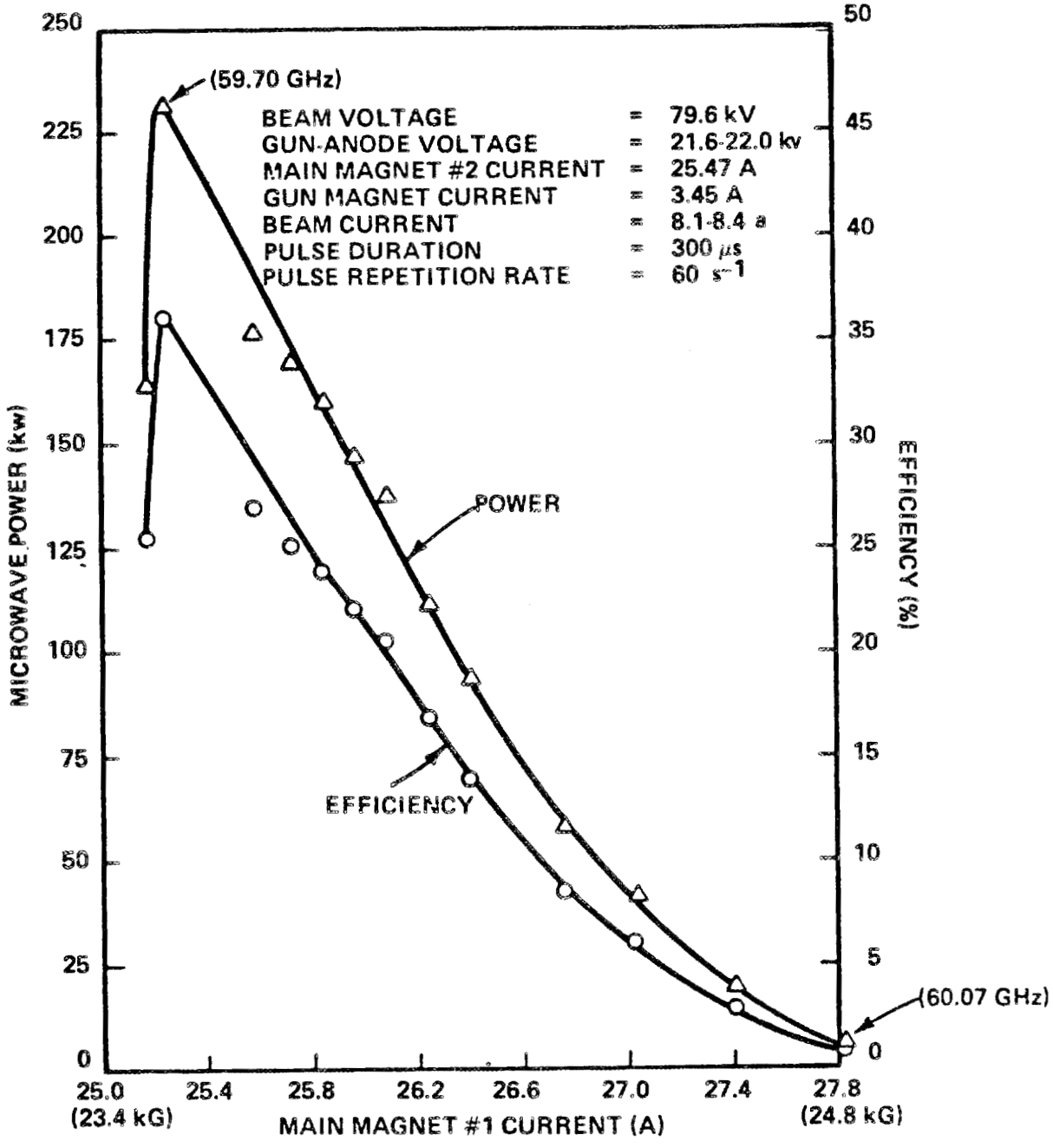

Figure 311. Optimized Microwave Power and Efficiency as a Function of Main Magnet No. 1 Current for X-3R

Dwg. No. 82-2217 FED

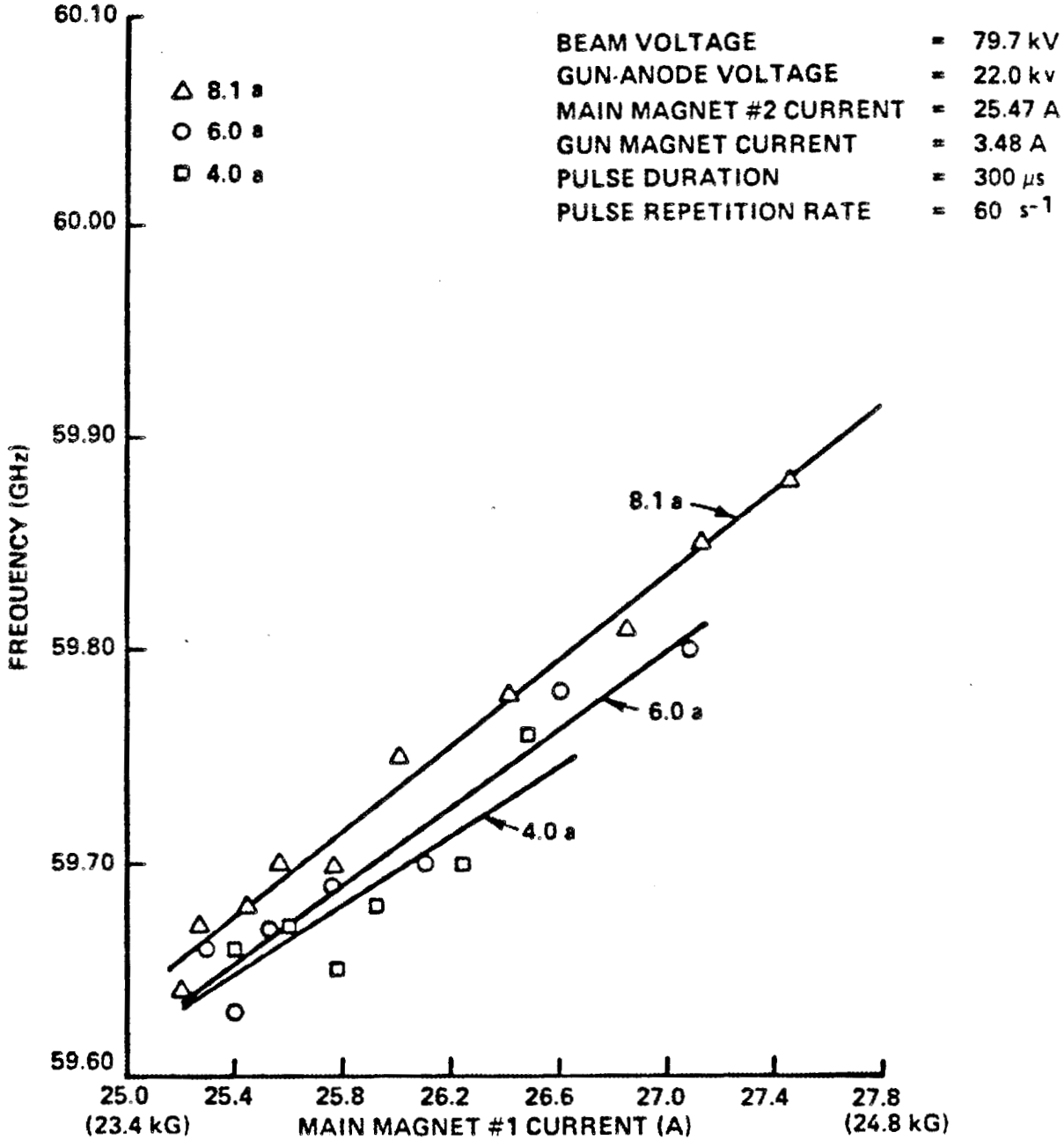

Figure 312. Operating Frequency for Fixed Gun-Anode Voltage as a Function of Main Magnet No. 1 Current for Three Values of Beam Current for X-3R

Dwg. No. 82-2215 FED

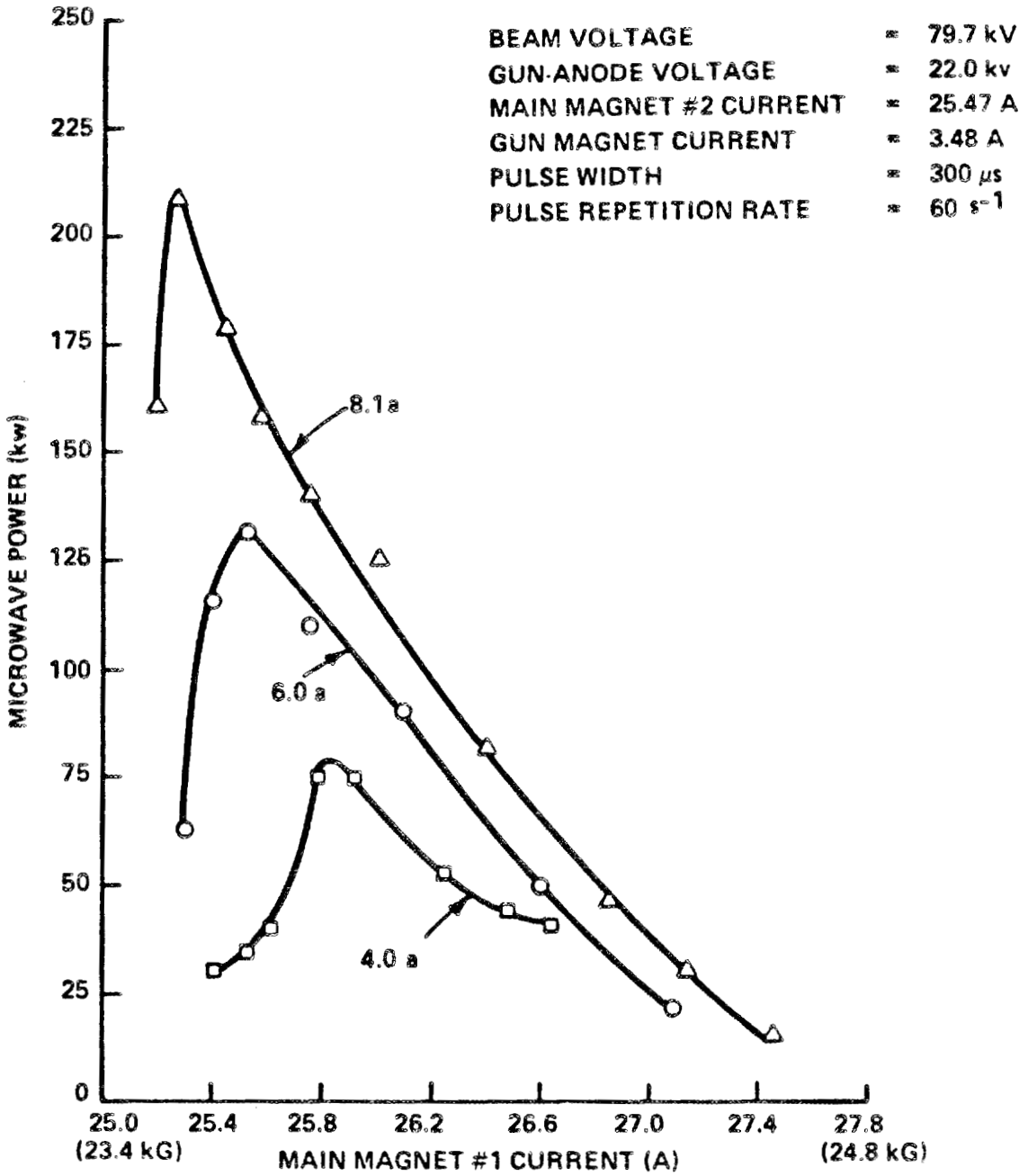

Figure 313. Microwave Power for Fixed Gun-Anode Voltage as a Function of Main Magnet No. 1 Current for Three Values of Beam Current for X-3R

Dwg. No. 82-2216 FED

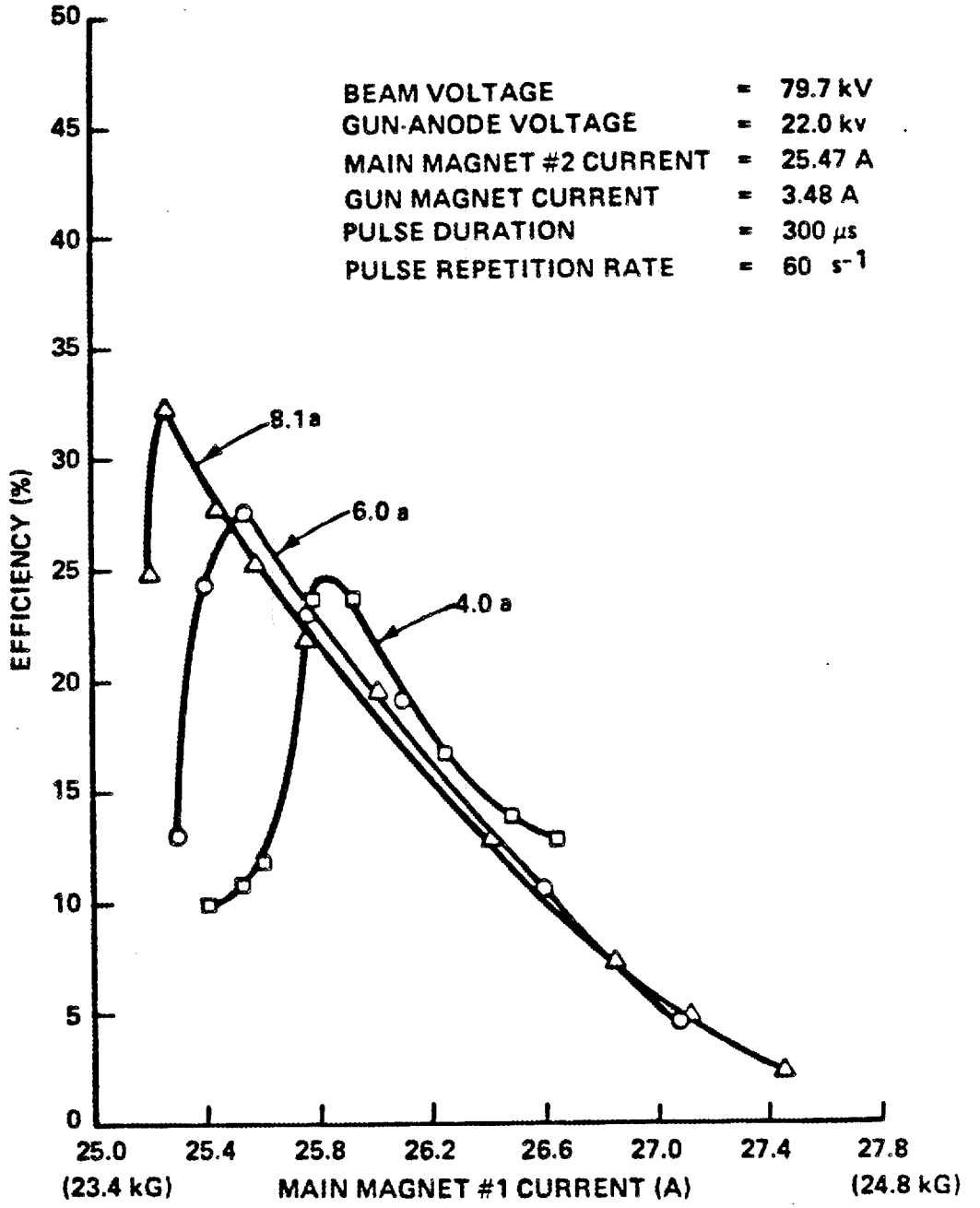

Figure 314. Microwave Efficiency for Fixed Gun-Anode Voltage as a Function of Main Magnet No. 1 Current for Three Values of Beam Current for X-3R

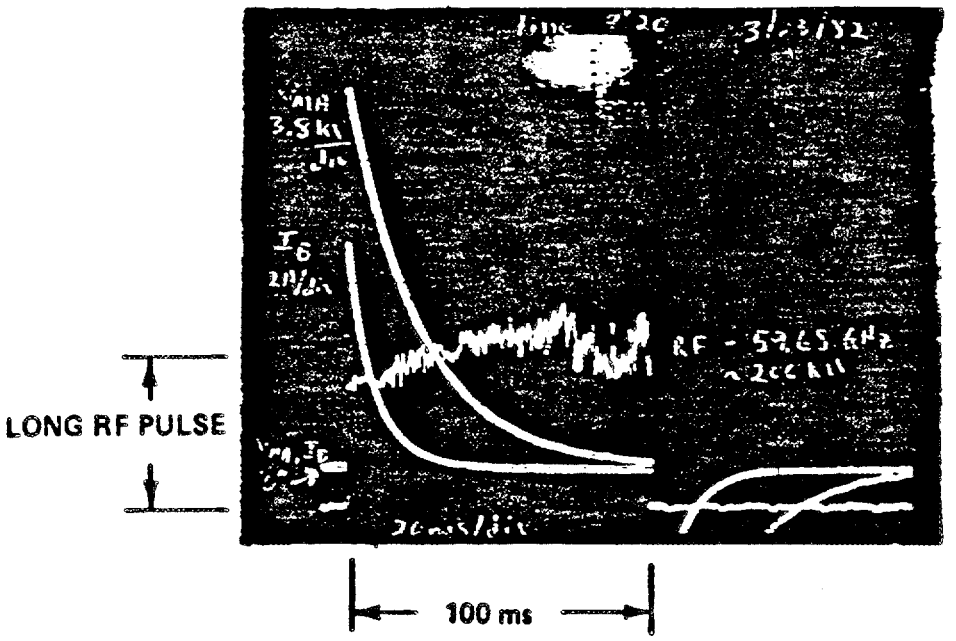

Photo No. 0678 82

Figure 315. Oscilloscope Photograph of the rf Pulse During 100 ms, 10% Duty Operation. The rf Output Power was 205 kw During this Test. The "Hash" for t > 10 ms is Believed Due to Localized Boiling in the Water-Load. The Gun-Anode Voltage ("V_{mA}") and the Electron Beam Current ("I_B") are Shown as Monitored on Short Pulse Measurement Equipment, (Time Constant of Monitors << 100 ms).

described in the figure caption. The "hash" occurring in the rf pulse after 10 ms is due to the local boiling of the water at the surface of the water-cooled cone used as an rf load. For comparison purposes, a typical short pulse oscilloscope trace is shown in Figure 316. Again, the additional electron beam monitoring traces are present and described in the figure caption.

Figure 317 shows the dependence of the beam current on input heater power and Figure 318 plots beam current as a function of gun anode voltage for X-3R. Other operating parameters held constant during the tests are also shown.

With the changes to the drift tube and ouput cavity coupling incorporated for the first time in X-3R, the operation and performance of the 60 GHz gyrotron were improved considerably.

D. FOURTH EXPERIMENTAL TUBE (FIRST CW TUBES)

The first 60 GHz, CW gyrotron (VGE-8006, S/N X-4) was tested during February 1981. During these tests, 70 kW of rf power was observed under CW conditions. The tube was subjected to the full CW beam power of 640 kW during beam-only operation, and a series of tests was performed using pulse durations of 32 seconds, 25% to 50% duty. Cathode emission cooling measurements were taken during a 32-second pulse for 25% and 50% duty. Due to the tube's inability to operate in the correct (TE_{02}) mode, the tube was removed from the socket even though the tube had retained its vacuum integrity throughout all tests. The various tests performed on X-4 are detailed chronologically.

1. Short Pulse Tests

Short pulse tests (50 μs, 0.15-3% duty) were performed on X-4 following hipotting. After exploring regions in parameter space which would be suitable for CW operation in later tests, oscillation maps were drawn. Oscillation maps at 1.8 a and 6 a are shown in Figures 319 and 320, respectively. The 6 a results, when compared to the 6 a results with pulse

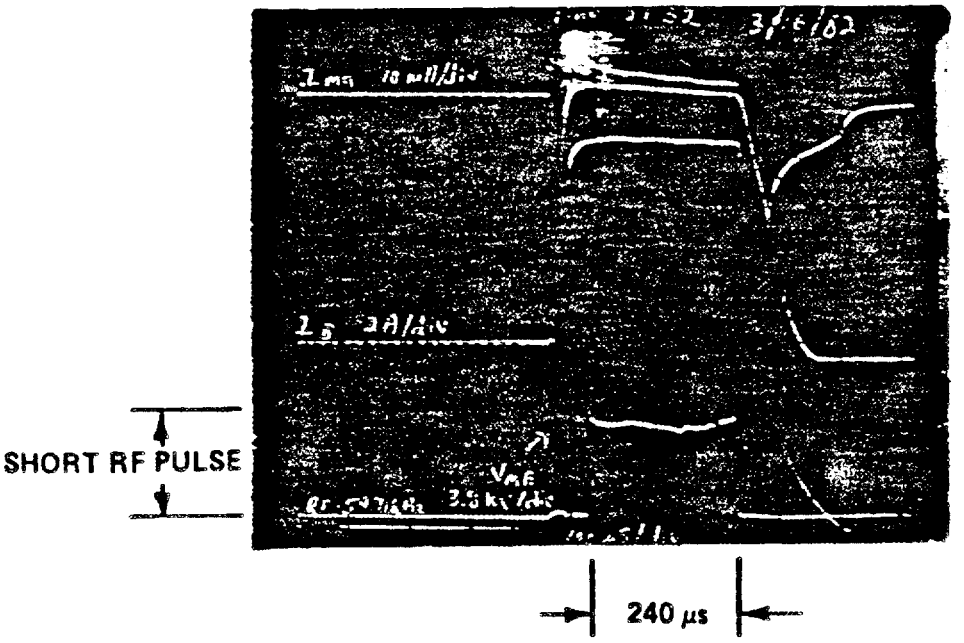

Photo No. 0679 82

Figure 316. Oscilloscope Photograph of the rf Pulse During Short Pulse Operation. Peak rf Power was 216 kw. Gun-Anode Current ("I_{mA}"), Beam Current ("I_B") and Gun-Anode Voltage ("V_{mA}") are also Shown.

Dwg. No. 82-2218 FED

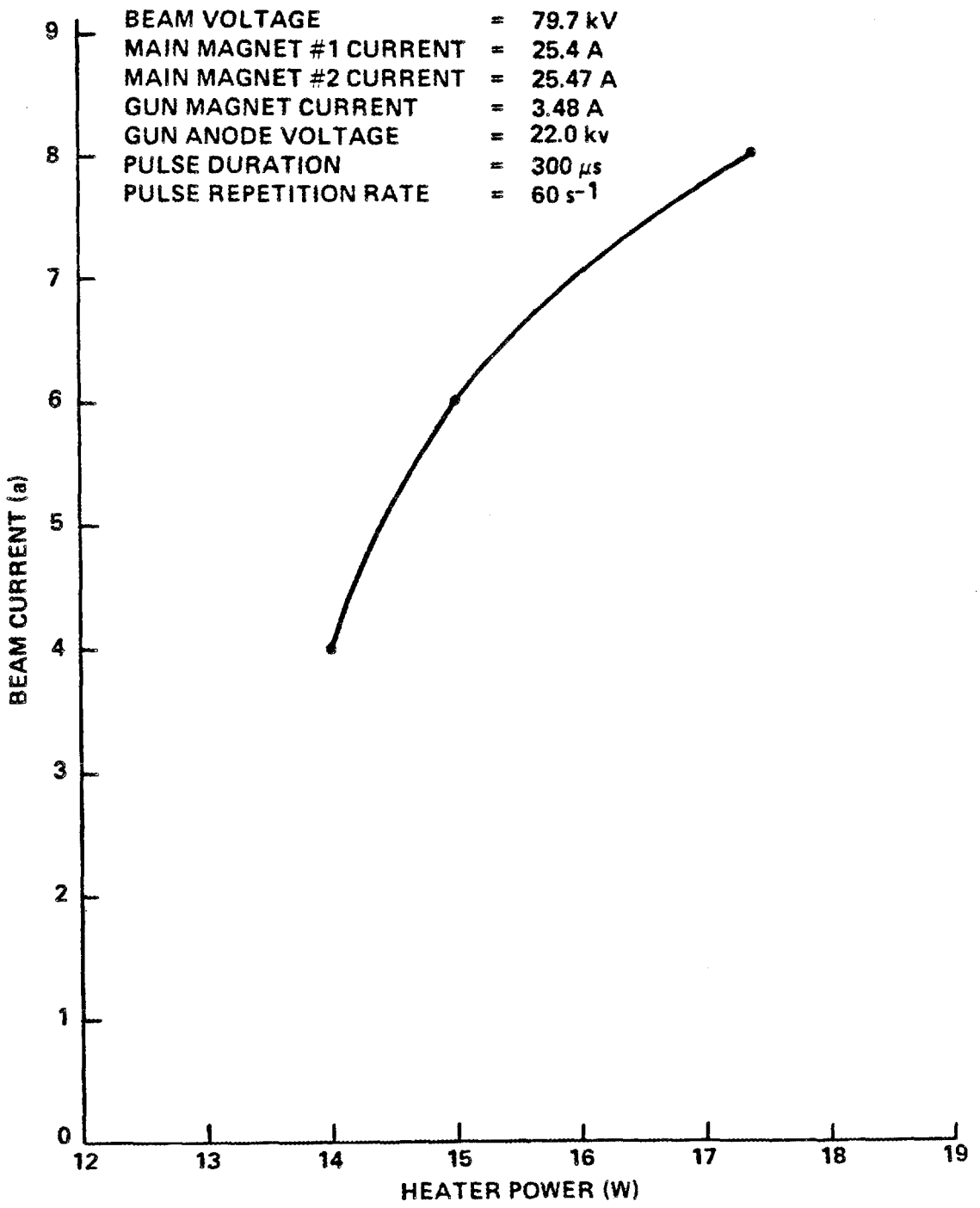

Figure 317. Beam Current as a Function of Input Heater Power for X-3R

Dwg. No. 82-2219 FED

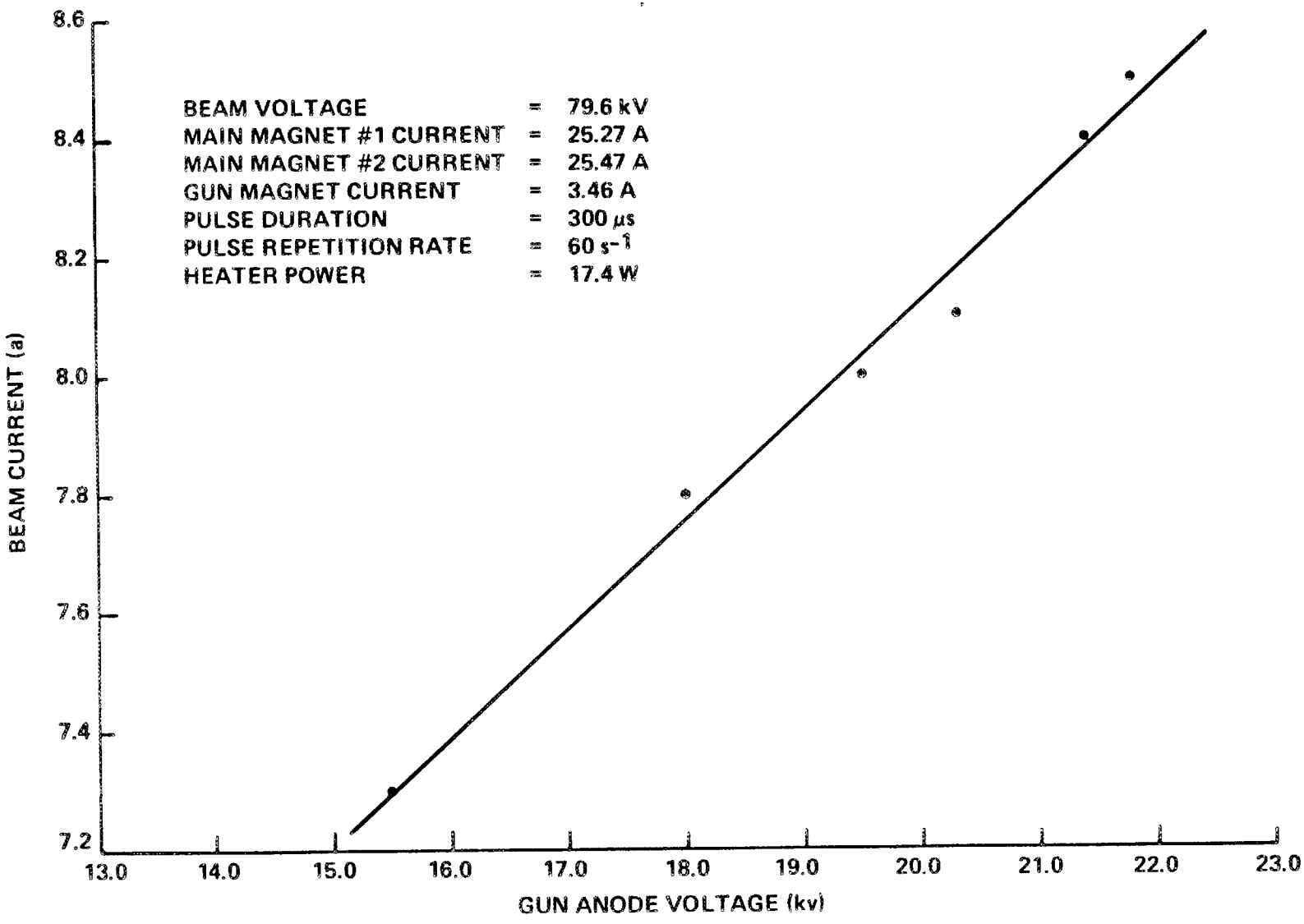

Figure 318. Beam Current as a Function of Gun-Anode Voltage for X-3R

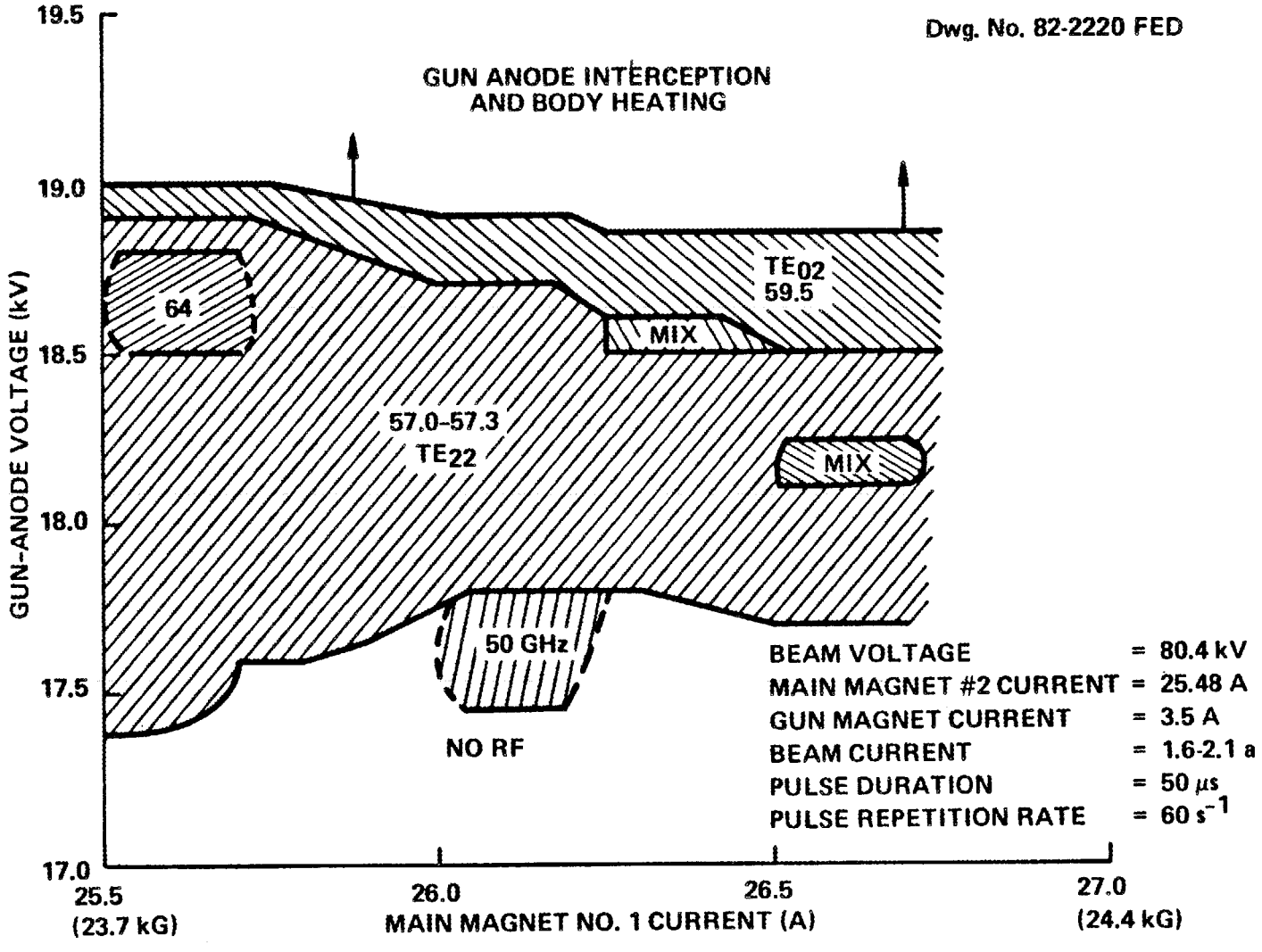

Figure 319. Oscillation Map for the VGE-8006 S/N X-4 Under Short Pulse Conditions for 1.8a Beam Current

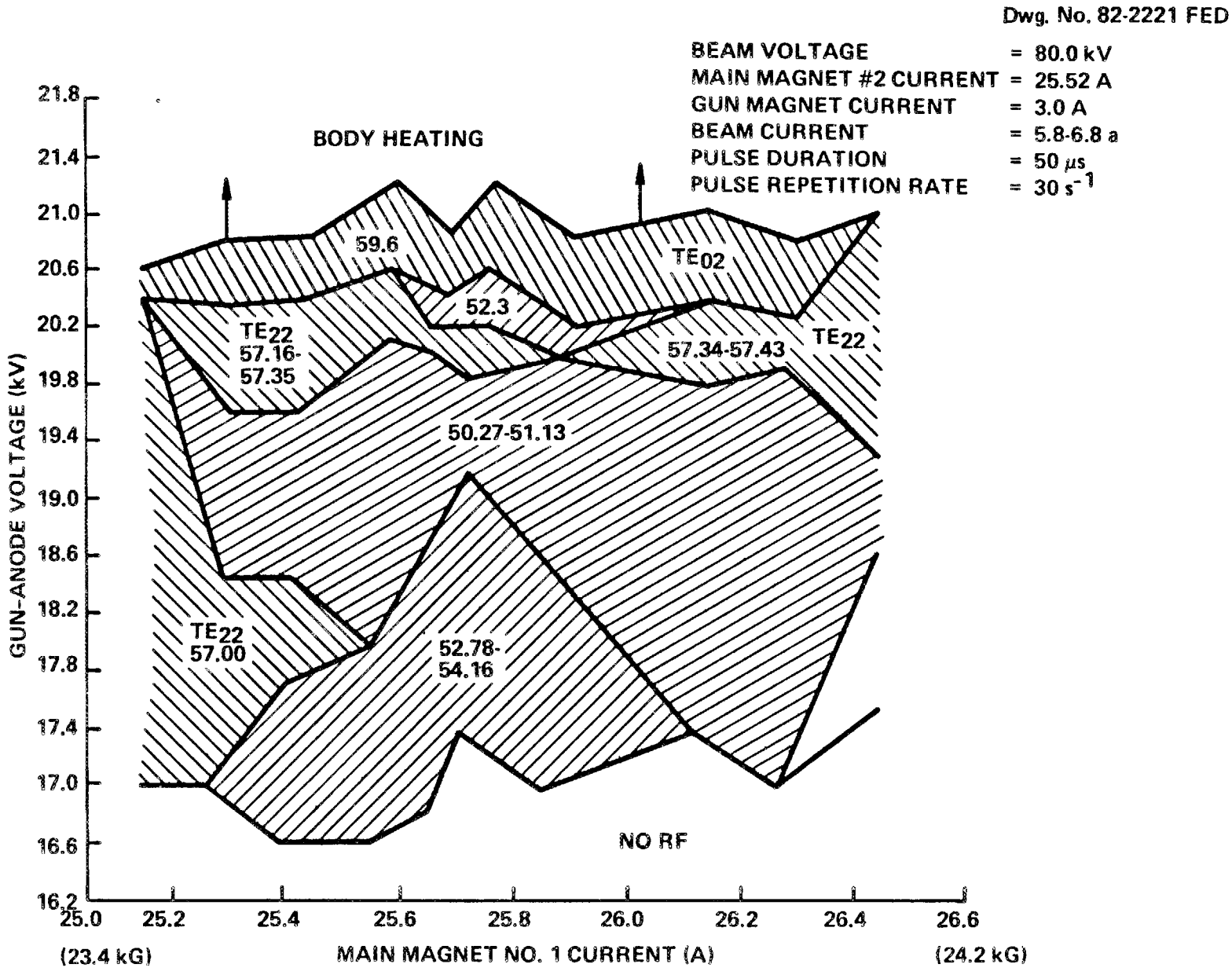

Figure 320. Oscillation Map for the VGE-8006 S/N X-4 Under Short Pulse Conditions for 6.0a Beam Current

tube X-3, indicate that the two tubes behaved similarly. The exception was the TE_{22} region (57.1 to 57.5 GHz), which occurred at gun-anode voltages just below the onset of the TE_{02} mode and was much narrower for X-4 than the 50 to 51 GHz region. The CW tube had a larger diameter collector and a double-disc, rather than a single-disc window. The rest of the design was identical to that of the pulse tube.

The oscillator circuit of X-4 was identical to that used in X-3. Any differences in operation must be attributed to the window or collector. Since X-4 did not have the cavity modifications made in X-3R, the body heating mode observed in X-1, X-2 and X-3 was still present, as indicated on the oscillation maps. A peak power of 190 kw was obtained during these tests.

2. Long Pulse Tests (Beam-Only)

X-4 was operated under long pulse beam-only conditions ($\tau > 3$ sec) for approximately 600 pulses. These tests were performed to measure the emission cooling characteristics of the cathode under long pulse conditions. In Figure 321, the beam current as a function of time during a 32 second beam pulse for 26% and 53% duty operation is shown. Equilibrium is reached by the end of the 32-second pulse for both cases, but the 26% duty pulse (90 seconds between pulses) starts at a much higher initial current value. For a given heater power, a maximum initial current was reached when 90 to 120 seconds separated two 30-second pulses.

3. CW Operation

Rather than perform rf tests for 30 second pulse durations, it was decided to proceed directly into CW testing. By increasing the beam current and beam voltage gradually, a CW rf power of 71.5 kW was reached during the first day of CW testing. Tube parameters for the 71.5 kW measurement are shown in Table 46.

Dwg. No. 82-2222 FED

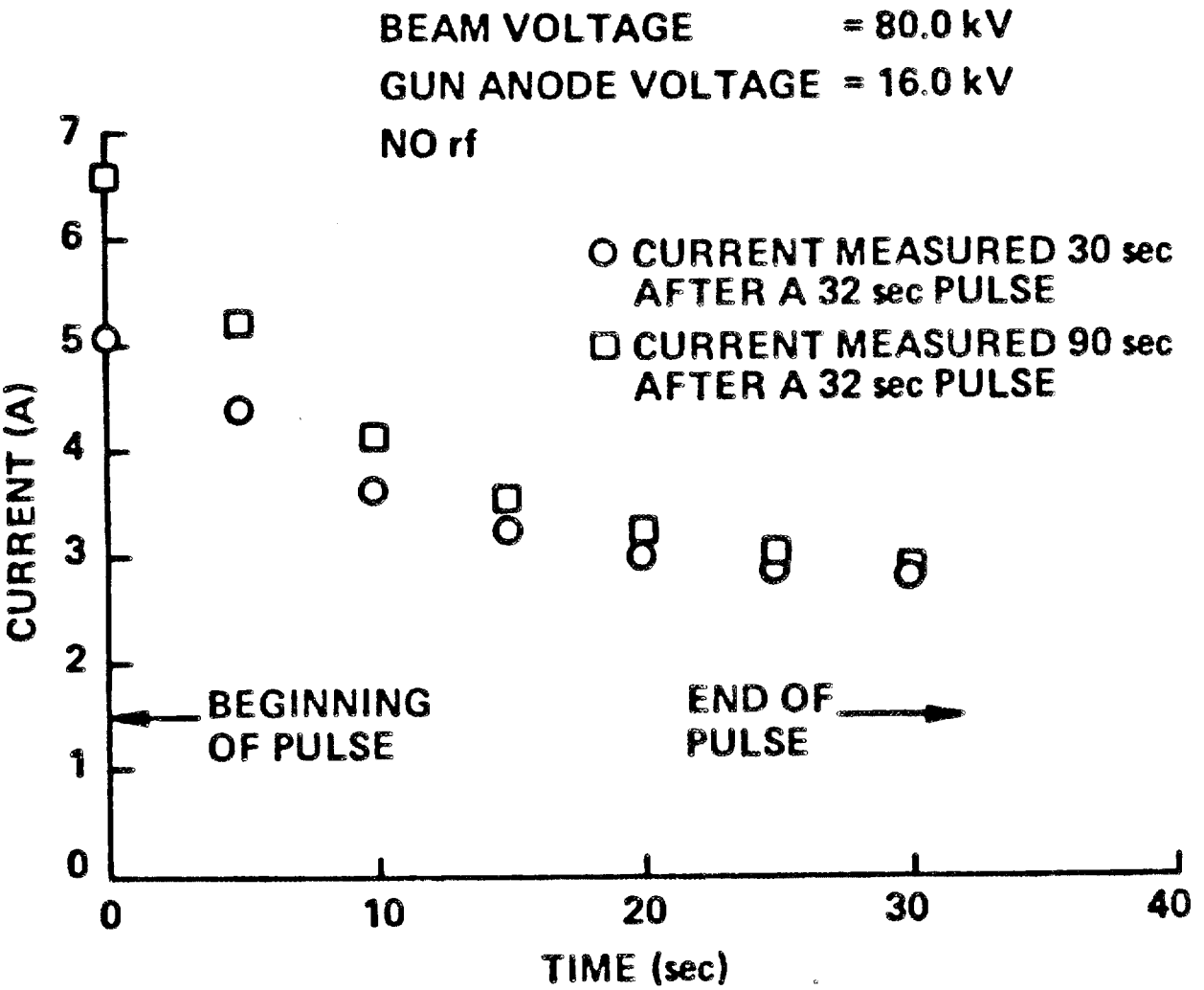

Figure 321. X-4 Cathode Emission Cooling

Table 46
71.5 kW, CW Operating Conditions

Frequency	59.58 GHz
Output CW Power	71.5 kW
Beam Voltage	70.4 kV
Beam Current	4.0A
Efficiency	25%
Gun Anode Voltage	19.0 kV
Main Magnet Current #1	25.43 A
Main Magnet Current #2	25.50 A
Gun Magnet Current	3.22 A
Cavity Magnetic Field	23.7 kG

Following a weekend shutdown, CW tests were resumed, but crowbars prevented the tube from running at currents high enough to repeat the 71.5 kW rf power measurement. Two full days of testing failed to improve the situation; at the end of the second day it was concluded that some internal change in the tube must have occurred. A CW oscillation map is shown in Figure 322. Following the CW tests, the tube was switched to pulsed operation. An oscillation map under conditions identical to those of Figure 322 was prepared, and the result is shown in Figure 323. Comparison of the two parameter space maps confirmed that changes had occurred in the tube during CW operation.

After the above problems were observed, the gun anode voltage was lowered to prohibit any rf oscillation and an X-ray film was attached to the collector to measure the axial distribution of the impinging electron beam. These tests were carried out at 80 kV, 7 A CW and the current was raised briefly to 8 A during these tests without detectable problems. Results of these X-ray measurements are shown in Figure 324. Also shown, are similar measurements taken under short pulse conditions. The pulse tests were performed prior to CW testing. Both tests indicated that the beam distribution was located within the well-cooled portion of the collector. The slight discrepancies between the two may be attributed to different operating parameters during the two tests.

Dwg. No. 82-2223 FED

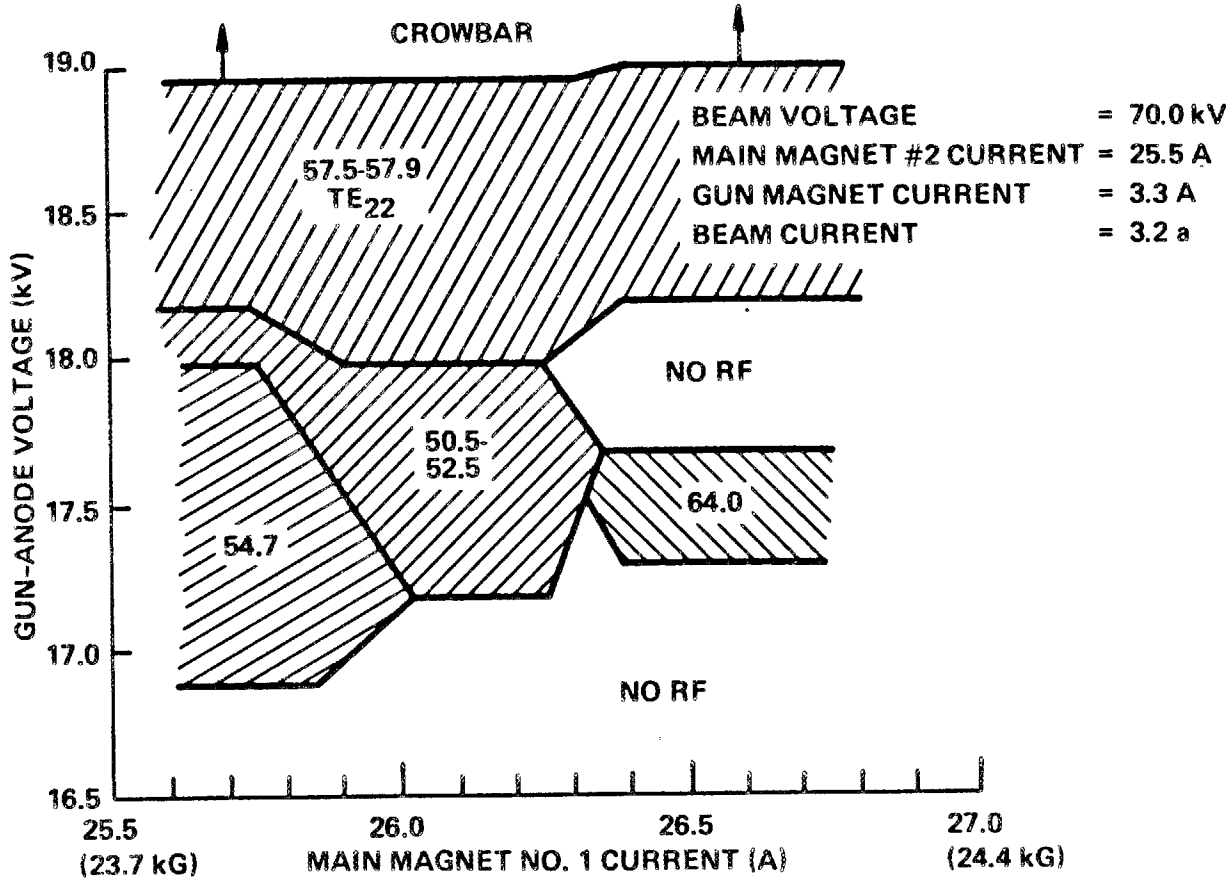

Figure 322. X-4 Oscillation Map, CW Operation I_o = 3.2A

Dwg. No. 82-2224 FED

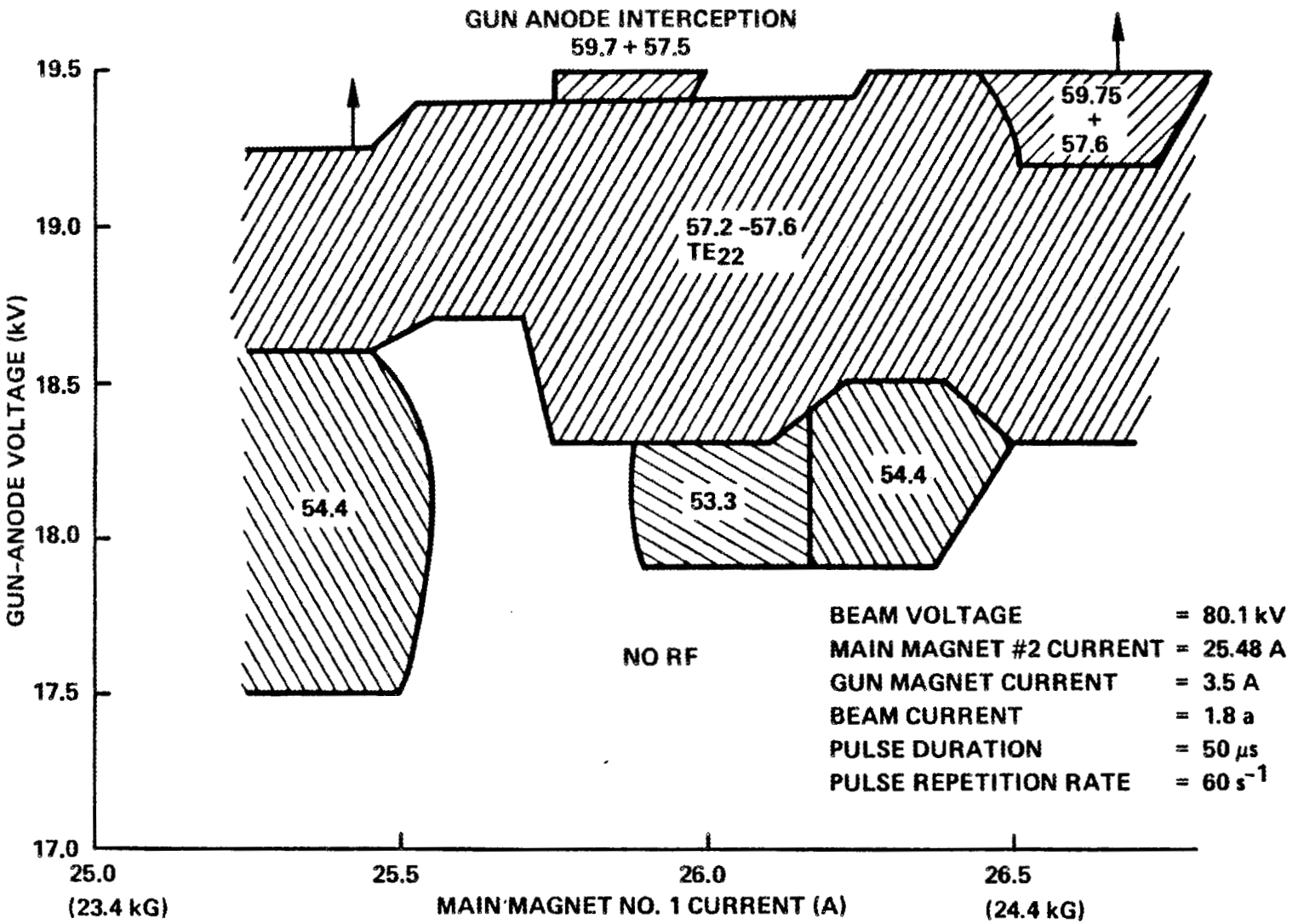

Figure 323. X-4 Oscillation Map, Pulse Operation I_o = 1.8 a

Dwg. No. 82-2225 FED

	PULSED	CW
BEAM VOLTAGE	80.2 kV	80.3 kV
MAIN MAGNET #1 CURRENT	25.47 A	25.53 A
MAIN MAGNET #2 CURRENT	25.49 A	25.51 A
DUTY CYCLE	48 %	100 %
GUN MAGNET CURRENT	3.37 A	3.20 A
BEAM CURRENT	7.0 a	2.2-80 A

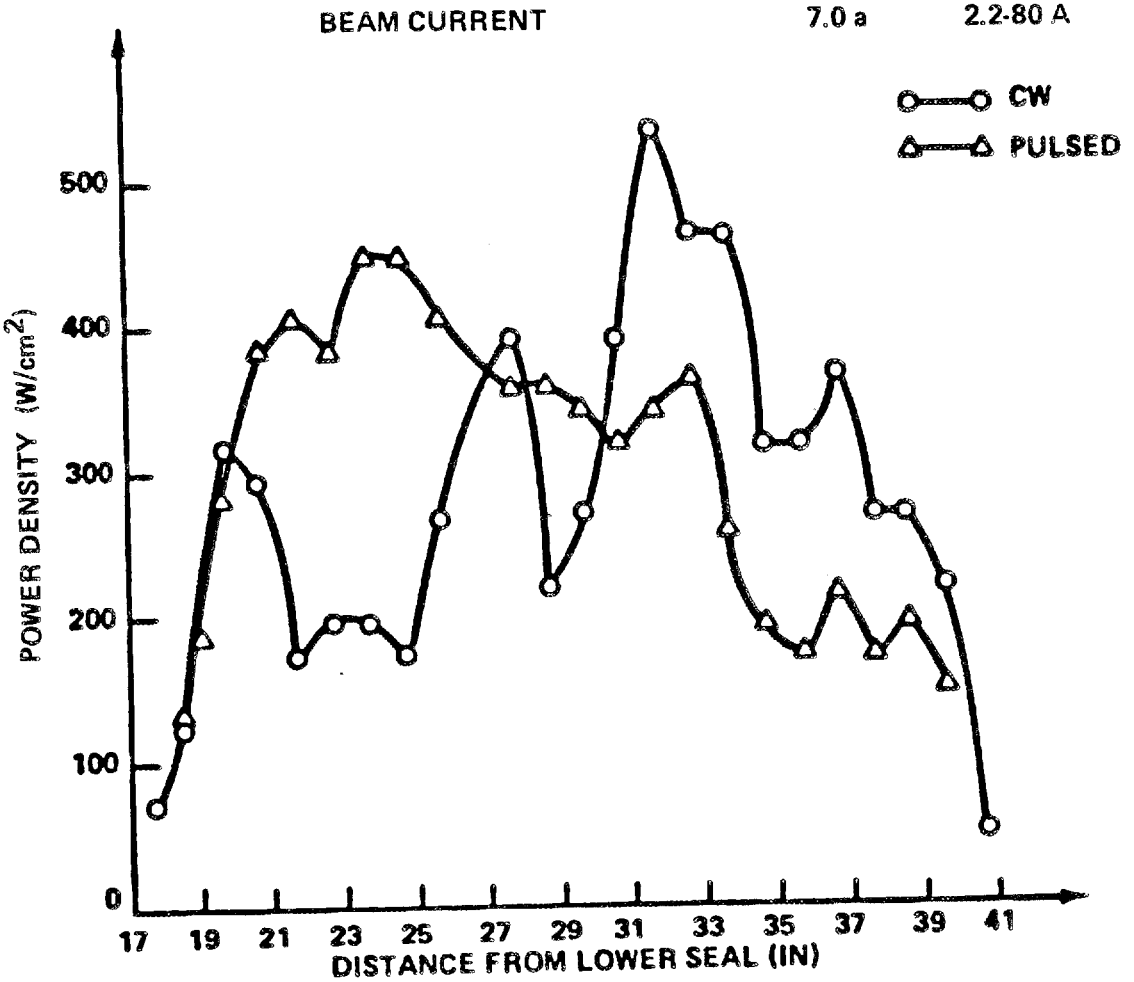

Figure 324. X-4 Collector Power Density Distribution

4. Post Test Examination

Following its removal from the socket, X-4 was disassembled for analysis. Inspection of the collector revealed a melted region at the down transition at the upper end of the collector. This melting resulted in molten copper solidifying in and perturbing the output cavity. Additional damage included beam erosion of the beam tunnel and metallic deposits on the anode and upper high voltage ceramic. Cold tests indicated that the molten copper found in the cavity provided sufficient perturbation to disrupt operation in the TE_{02} mode.

E. FIFTH EXPERIMENTAL TUBE (SECOND CW TUBE)

1. Original Build

a. Salient Features

The fifth experimental tube, X-5, was the second CW tube to be tested. It incorporated four distinct modifications to the design of the first CW tube, X-4.

1) The beam drift tube was changed to the X-3R design.
2) The output cavity was changed to the X-3R design.
3) The double-disc window used thinner ceramic discs than those on X-4.
4) The collector pressure drop was reduced.

In addition, the tube was operated in a new superconducting solenoid magnet with significantly reduced transverse field on the axis, and a collector bucking coil was added to modify the distribution of the spent electron beam in the collector.

b. Pulse Test Results

Pulse testing of X-5 went very well, yielding results similar to those achieved on X-3R concerning output power, efficiency and the

absence of the body heating mode which limited the rf performance of X-4 and pulse tubes X-1, X-2, and X-3. An oscillation map taken at a beam current of 8 a is shown in Figure 325. The notable difference between this map and that of X-3R is the emergence of competing modes around 50 GHz and between 62 and 67 GHz, while the TE_{22} modes at approximately 57 GHz played a lesser role than on X-3R. This behavior was also observed to some extent on X-4. Although exact identification of the modes other than those at 57 GHz has not been made, their presence is generally attributed to the extreme mismatch of the double-disc window at these frequencies in contrast to the more moderate mismatch presented by the single-disc window used on pulse tubes such as X-3R.

In Figure 326 the peak output power as a function of main magnet #1 current, operating at a beam voltage of 80.2 kV and a beam current of 8.0 a, is shown. A peak power of 233 kw was achieved at an efficiency of 36%. These measurements were performed at 1.8% duty with a pulse duration of 300 μsec.

Figures 327 - 329 show variation of the output power with beam current, gun anode voltage, and beam voltage, respectively. Again, the results are very similar to those achieved on pulse tube X-3R. In particular, we again note the decrease in power with increased gun anode voltage, a phenomenon not understood at the time but now known to be due to the length of the cavity.

Before proceeding to CW operation on X-5, a series of x-ray measurements, using, both, x-ray film and survey meters, was performed near the top of the collector to optimize the position and field strength of a collector bucking coil. These tests were carried out with rf, since the beam deposition profile without rf required no bucking coil, as found in previous measurements on X-4. These tests led to the optimum position and current setting for the bucking coil and indicated that the azimuthal variation of the beam deposited at the top of the collector was more uniform than on X-4; additionally, the tests showed that the detected x-rays were of much higher energy with rf than without rf, as evidenced by an approximately 1/200 decrease in the amount of time needed to expose the x-ray film. This

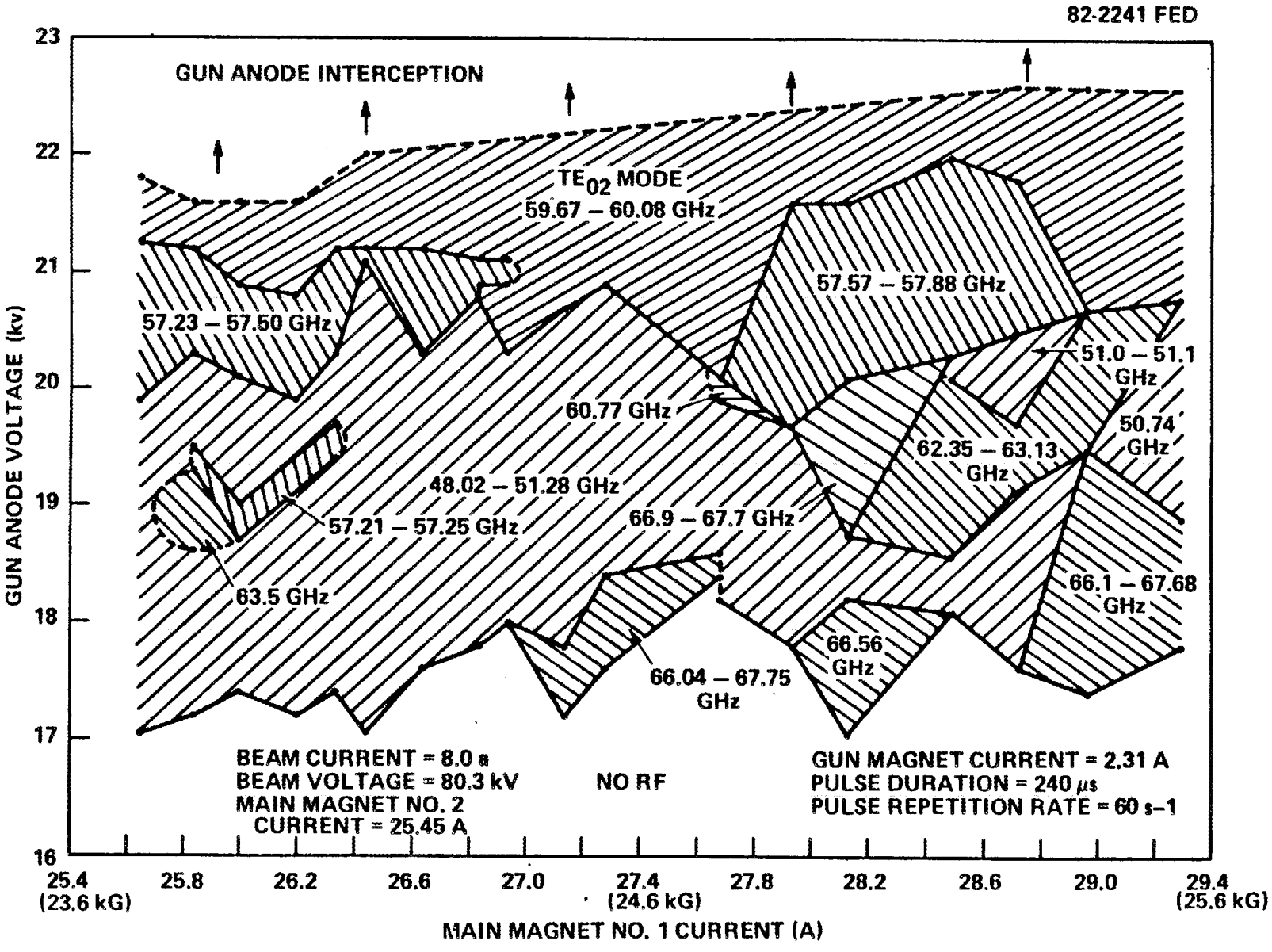

Figure 325. Oscillation Map for VGE-8006 S/N X-5 for a Beam Current of 8a, Operating Under Pulse Conditions

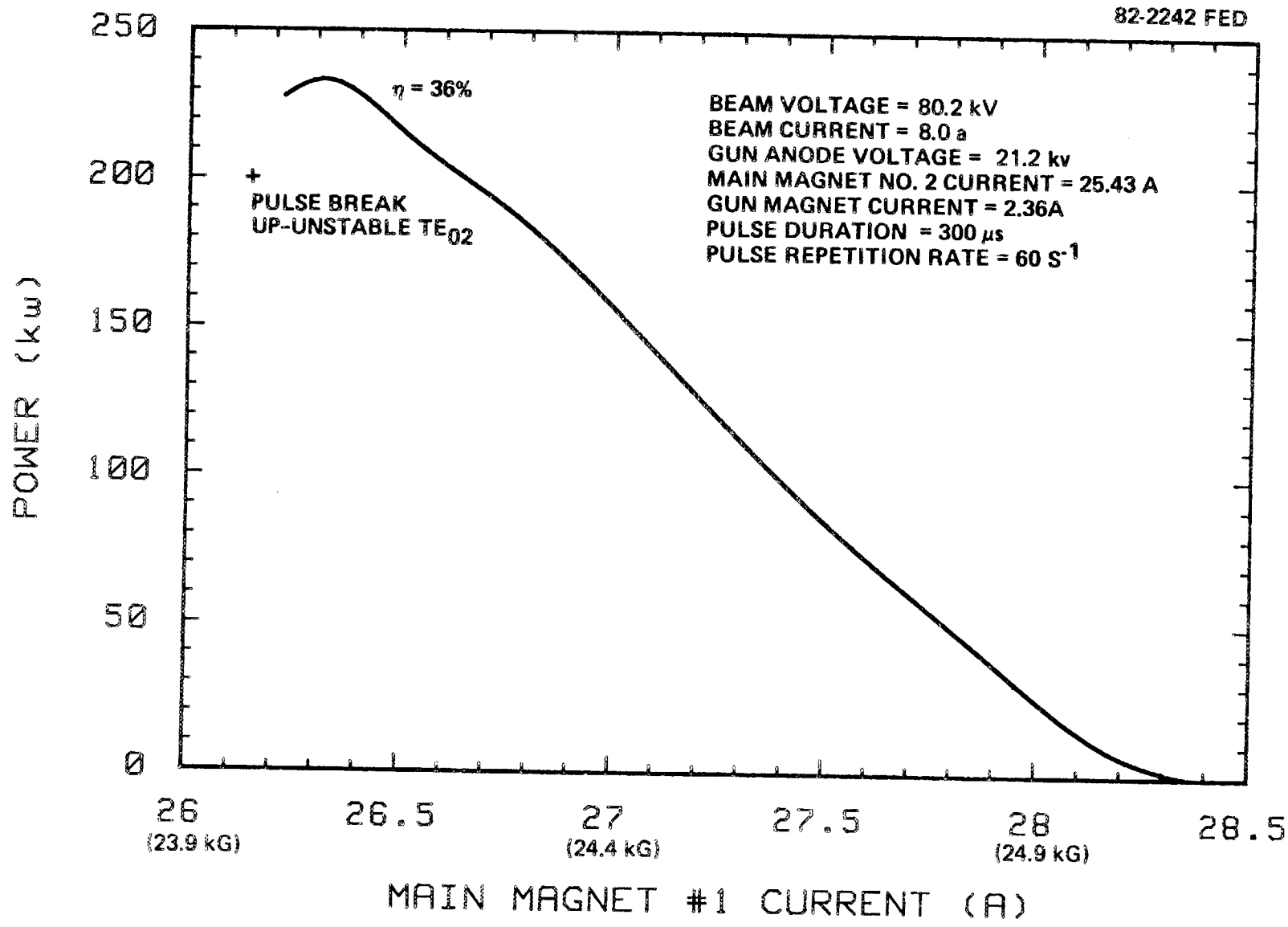

Figure 326. Peak Power as a Function of Main Magnet No. 1 Current for VGE-8006 S/N X-5 Operating Under Pulse Conditions

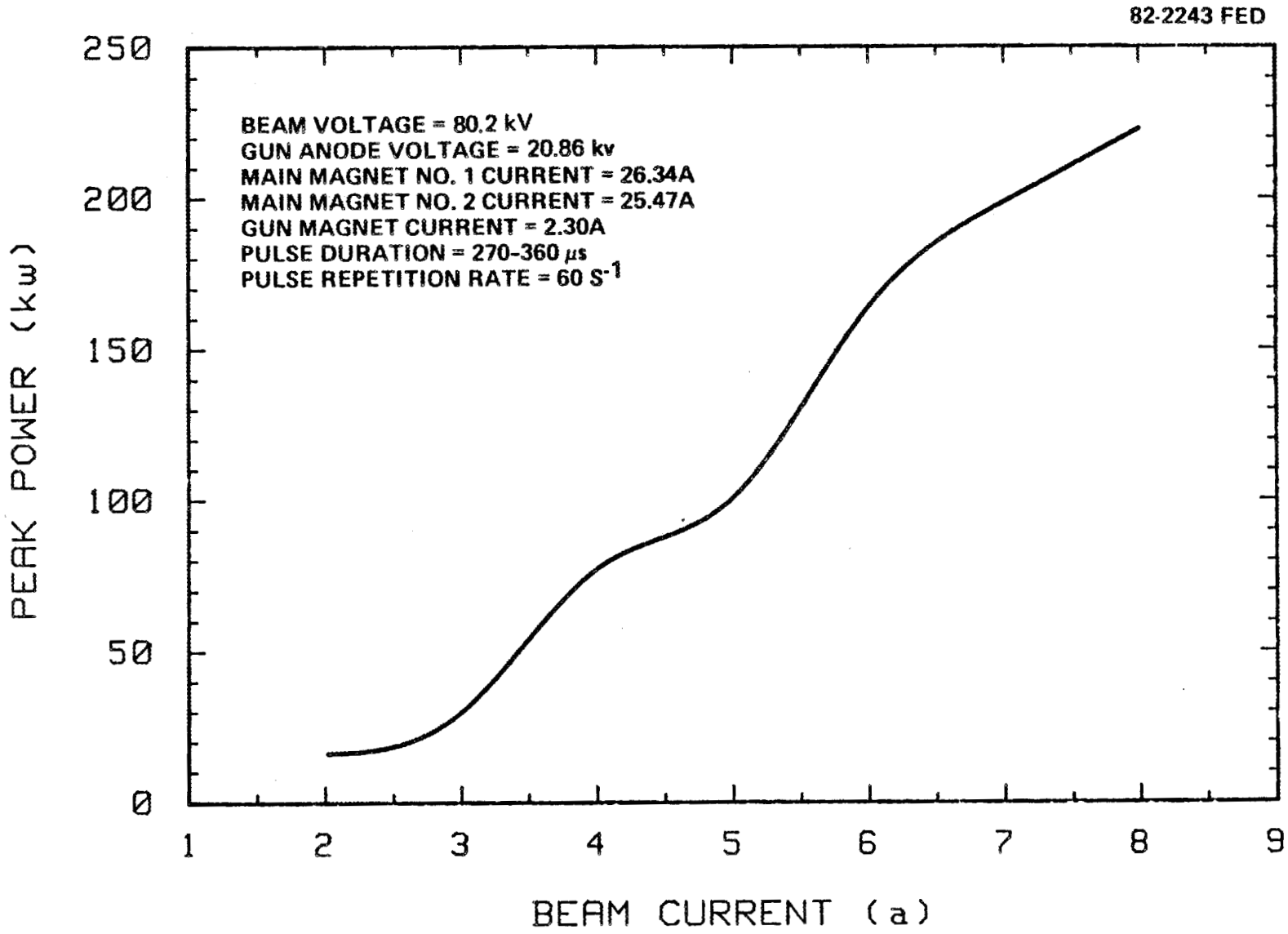

Figure 327. Peak Power as a Function of Beam Current for VGE-8006 S/N X-5 Operating Under Pulse Conditions

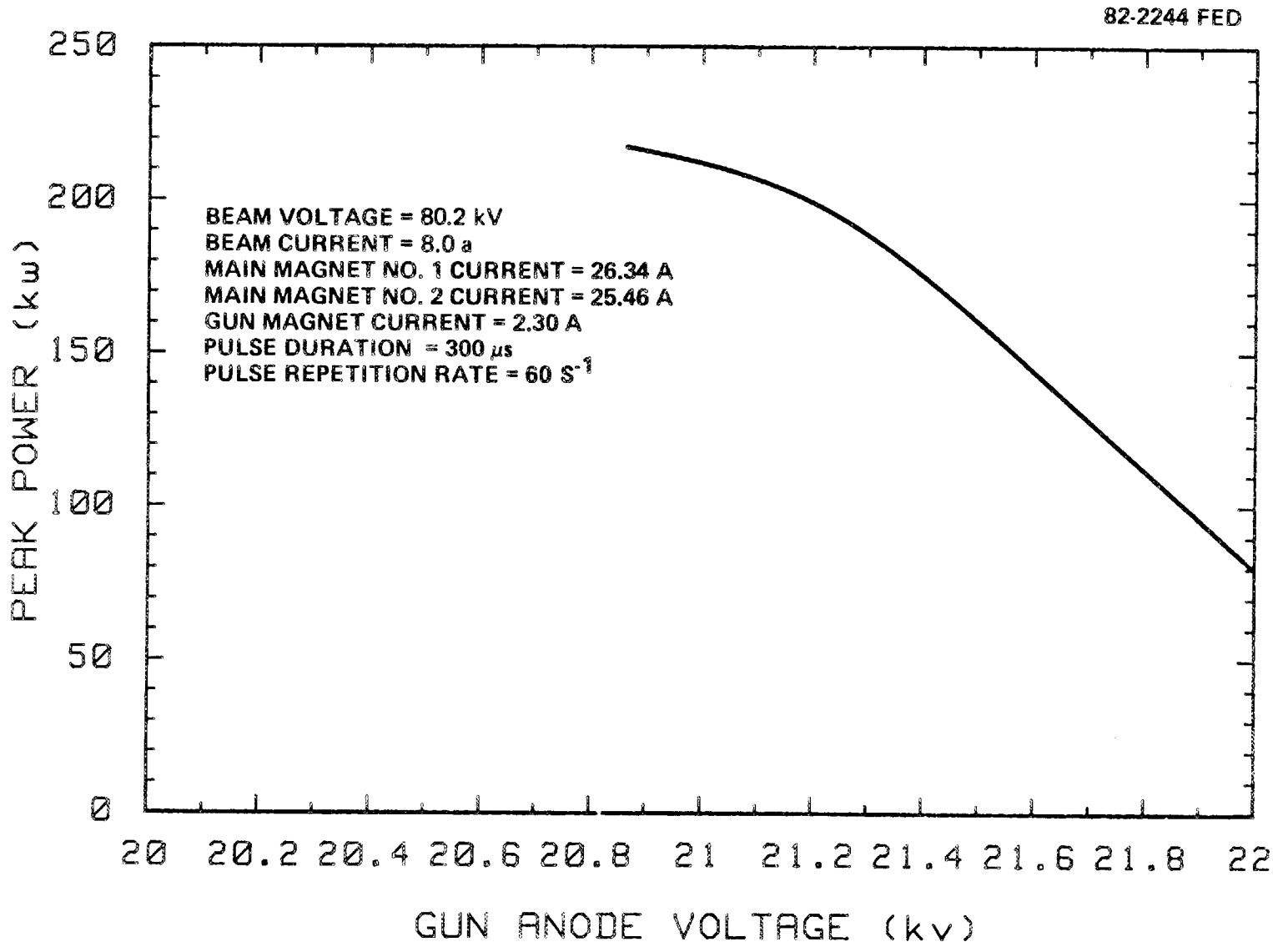

Figure 328. Peak Power as a Function of Gun Anode Voltage for VGE-8006 S/N X-5 Operating Under Pulse Conditions

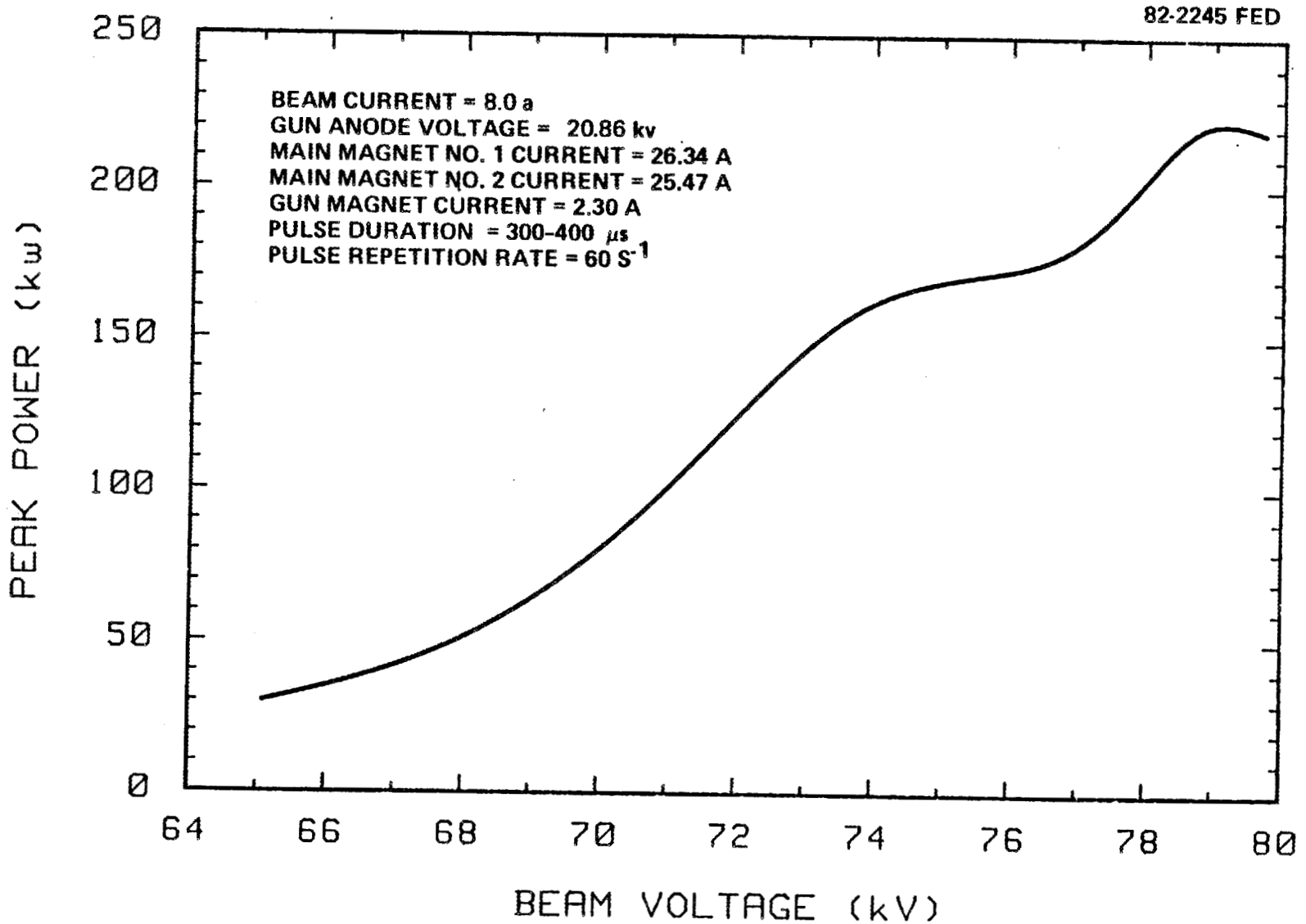

Figure 329. Peak Power as a Function of Beam Voltage for VGE-8006 S/N X-5 Operating Under Pulse Conditions

is due to fast electrons produced in the rf interaction (most electrons lose energy but a small fraction gain energy).

c. CW Test Results

During the first day of CW testing, a power of 103 kW at an efficiency of 36% was achieved. However, at this power level, there was extensive boiling in the rf waterload, as evidenced by jitter on the rf video trace and crackling heard on an accelerometer attached to the waterload. The boiling started at approximately 50 kW of rf power. By modifying the waterload and increasing the water flow over the waterload ceramic cone, a power of 123 kW at 41% efficiency was safely obtained before waterload boiling again made it inadvisable to advance to higher powers. The narrow skin depth of water at 60 GHz caused the waterload boiling. Most of the rf power was deposited in the thin, slowly-moving boundary layer along the ceramic surface. Several approaches were pursued to elimnate the problem, including lowering the power density in the load, increasing the water velocity, and using fluids with lower loss tangents.

Due to the waterload problem it was not possible to take rf data at full beam power, but extensive data, including start oscillations curves, were obtained at lower powers. Figure 330 is an oscillation map taken at a beam current of 3.0 A. Although it cannot be compared directly with the pulse version shown in Figure 325, because the beam current is lower, the behavior is quite similar. The region labeled "mix" simultaneously contains both the TE_{02} mode and the TE_{22} mode at ≈ 57 GHz. In addition, it was noted that the threshold in gun anode voltage for the desired TE_{02} mode depended critically on whether the mode was excited by raising the gun anode voltage, or whether the threshold boundary was determined by lowering the gun anode voltage until oscillation in the TE_{02} mode ceased and a competing mode was excited. This "mode locking" has not been noticed on pulse tubes, probably because the rise and fall of the gun anode voltage prevents the beam from being "locked" in such a manner. In Figure 331 this phenomenon is illustrated. The TE_{02} threshold is

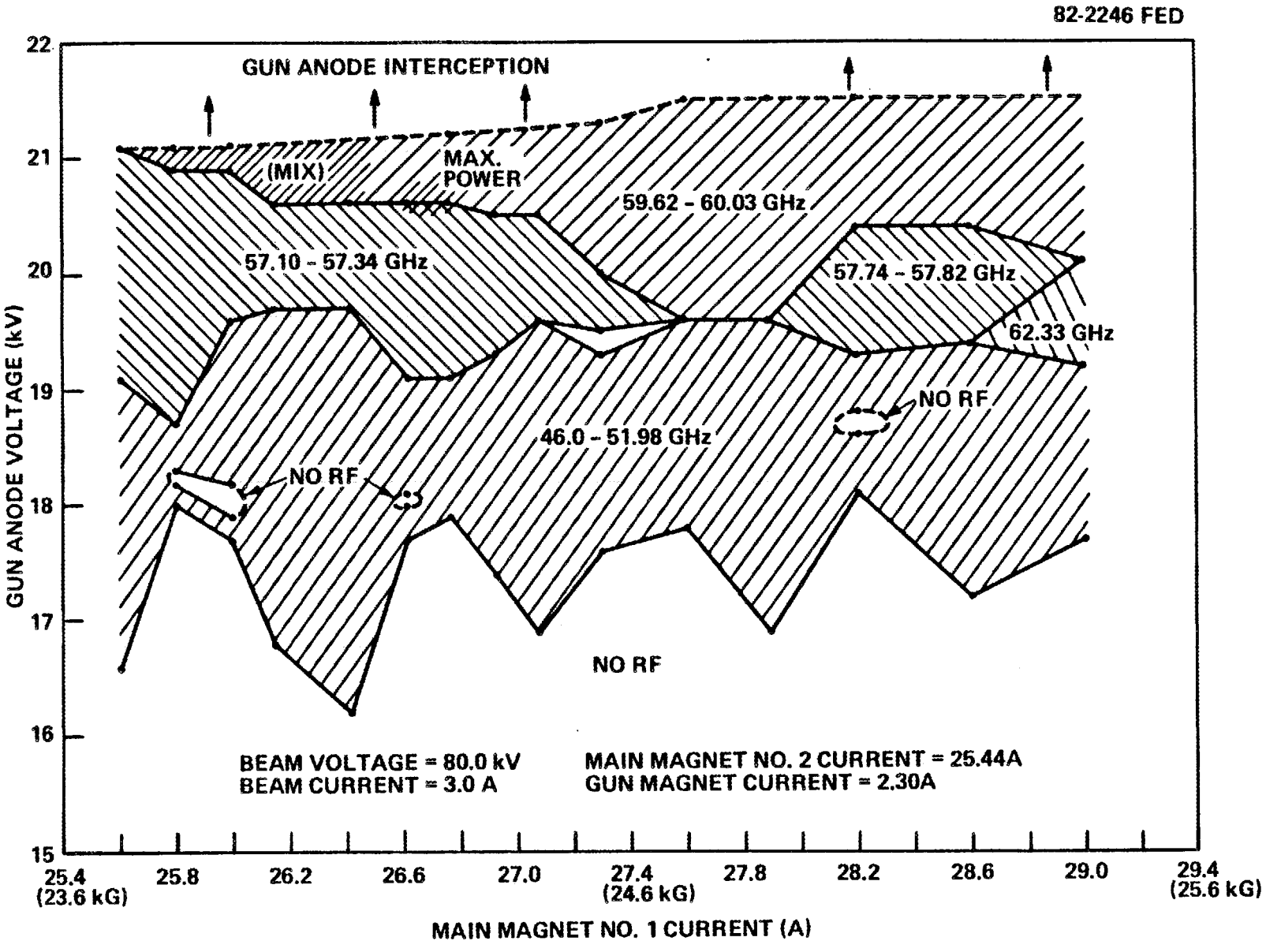

Figure 330. Oscillation Map for VGE-8006 S/N X-5 for a Beam Current of 3.0A, Operating Under CW Conditions

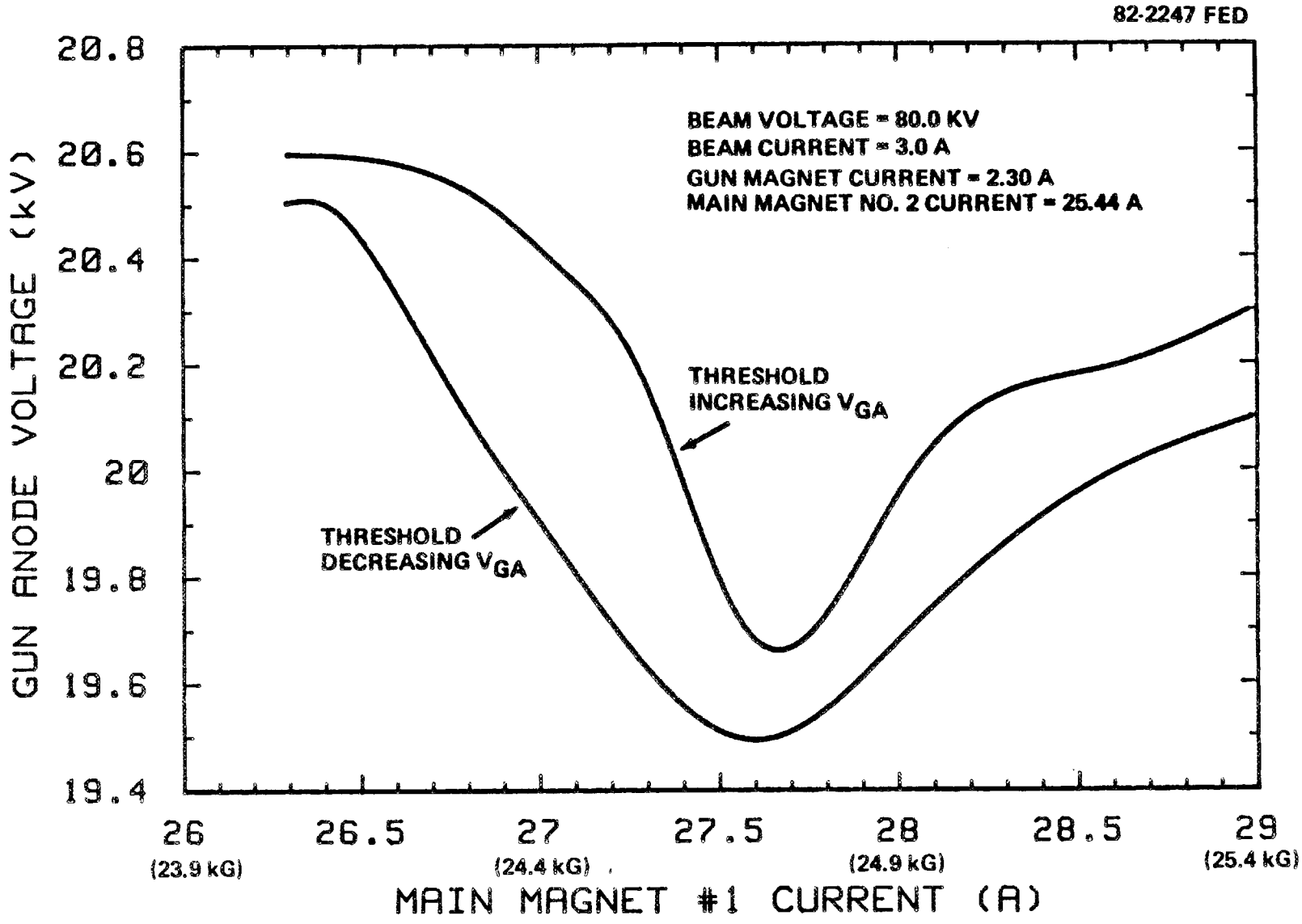

Figure 331. Threshold Conditions for the TE_{02} Mode with Variation of the Gun Anode Voltage as a Function of Main Magnet No. 1 Current. The upper curve represents the threshold boundary obtained by entering the TE_{02} mode (from the TE_{22} or 50 GHz modes) by raising V_{GA}. The lower curve was obtained by lowering V_{GA} while in the TE_{02} mode until the competing TE_{22} or 50 GHz mode is excited. The difference between the two curves shows the effects of mode locking.

"locked" at a constant beam current of 3.0 A by both, raising V_{GA} and entering the TE_{02} mode, and by lowering V_{GA} until a competing mode takes over.

A similar effect was observed when measuring the starting current of the TE_{02} mode for constant gun anode voltage. These data are shown in Figure 332, again, as a function of the current in main magnet coil #1. In this case, the mode locking is most dominant in regions of minimum starting current.

In Figure 333, the variation of output power as a function of gun anode voltage for several values of magnetic field is shown. As was observed under pulse operation, the output power drops at high gun anode voltages; however, possibly because these measurements were made at a lower beam current (3 A rather than 8 a), there is a much wider range over which increased gun anode voltage yields increased output power. The region which is accessible only with mode locking is shown with dashed lines. Additionally, there is a phenomenon that occurs for I_{mag} #1 ≈ 26.76 A. The arrows denote a hysteresis effect that makes it possible to access a high efficiency point by taking advantage of mode locking. To access point 4 in Figure 333, the sequence is as follows: The gun anode voltage is raised until the TE_{02} oscillation turns on at point 1. Next, the gun anode voltage is lowered to point 2 and the power increases abruptly from 57 kW to 75 kW. If V_{GA} is raised to point 4, the same gun anode voltage as point 1, a power of 83 kW is reached. A further increase of V_{GA} brings a significant drop in power at point 5. Point 5 could also have been reached by raising V_{GA} directly from point 1. Point 3 is again the threshold of the TE_{02} oscillation with mode locking. This phenomenon shows that higher efficiencies can be achieved under CW operation where certain regions of parameter space, not available under pulse conditions, can be accessed.

In Figures 334 and 335, the output power as a function of main magnet #1 current for 2.0 A and 3.0 A of beam current, respectively, are plotted. Since these measurements were taken for constant beam current and gun anode voltage in the two cases, it was not possible to determine if operation was in a mode locking regime or not. Further study of mode

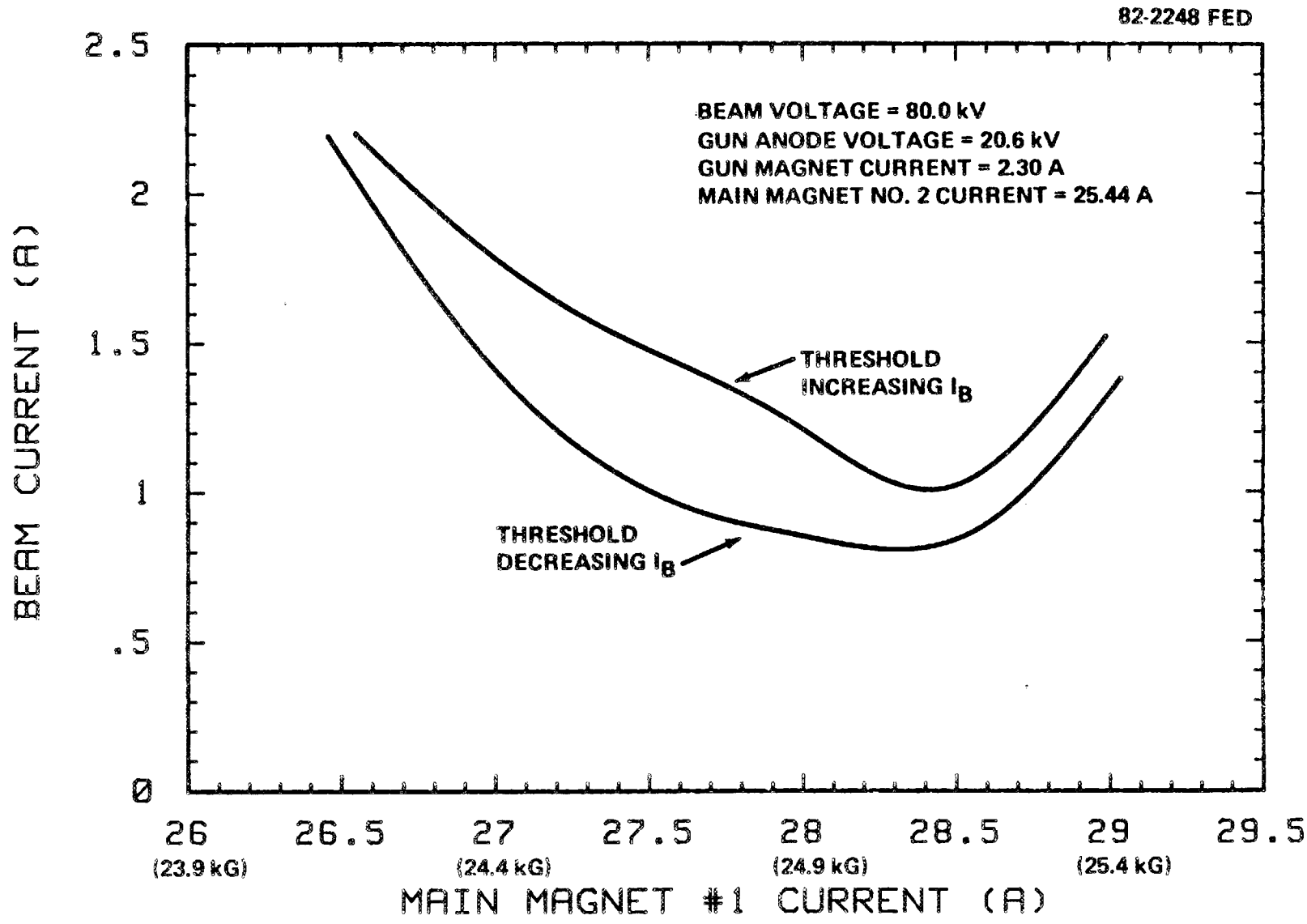

Figure 332. Starting Currents for the VGE-8006 S/N X-5 in CW Operation Showing the Effects of Mode Locking. The upper curve was obtained by raising the beam current until the TE_{02} mode began oscillating (in favor of the competing mode at 57 GHz), and the lower curve was obtained by lowering the beam current until the TE_{02} oscillation disappeared and the competing mode at approximately 57 GHz reappeared.

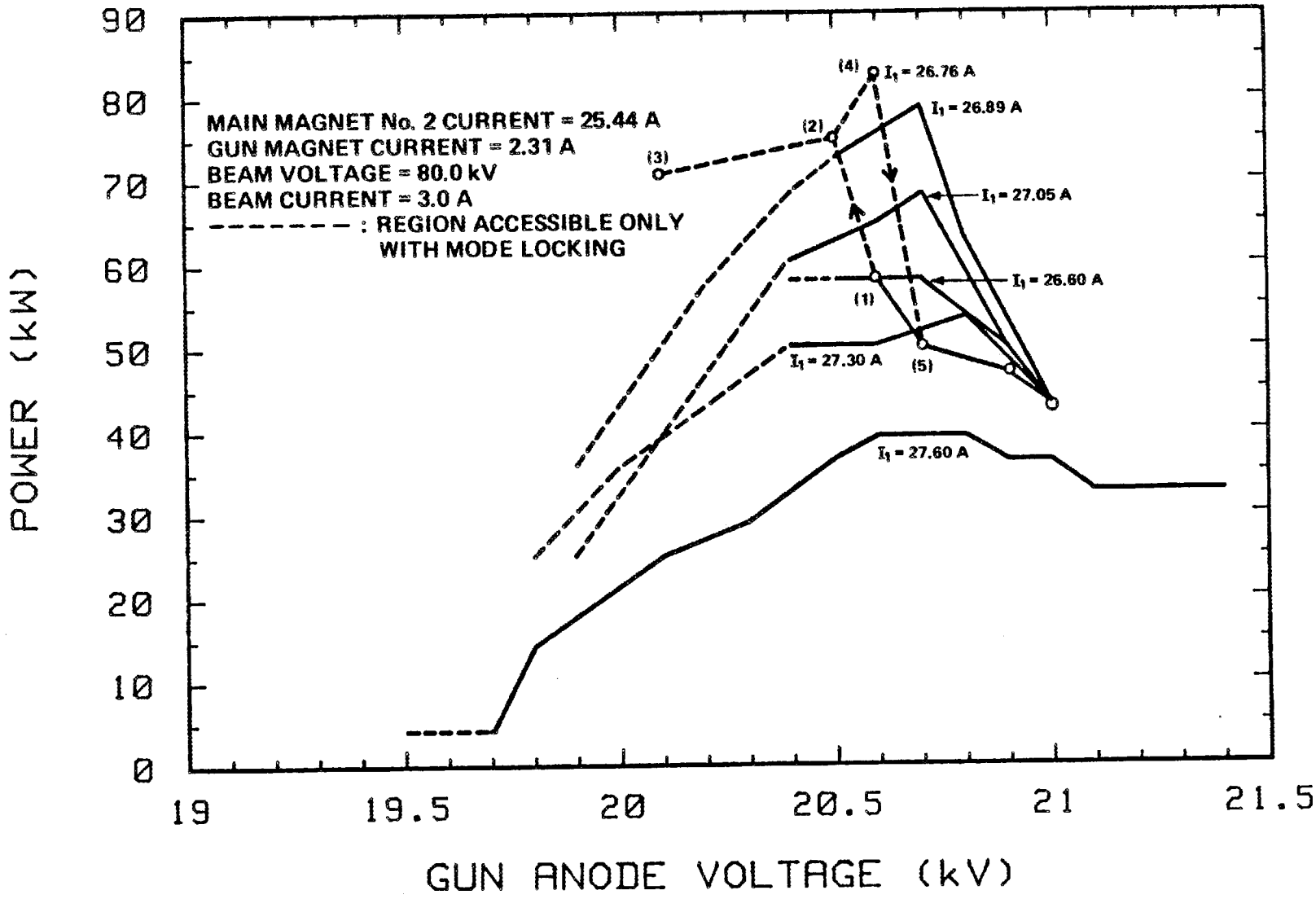

Figure 333. Output Power VS Gun Anode Voltage for Several Valves of Main Magnet No. 1 Current. The dashed lines indicate region available only when mode locking is present (regions accessed while in the desired TE_{02} operating mode). For a main magnet No. 1 current = 26.76 A we have shown a hysteresis effect which allows access for a high efficiency region when in mode locking conditions.

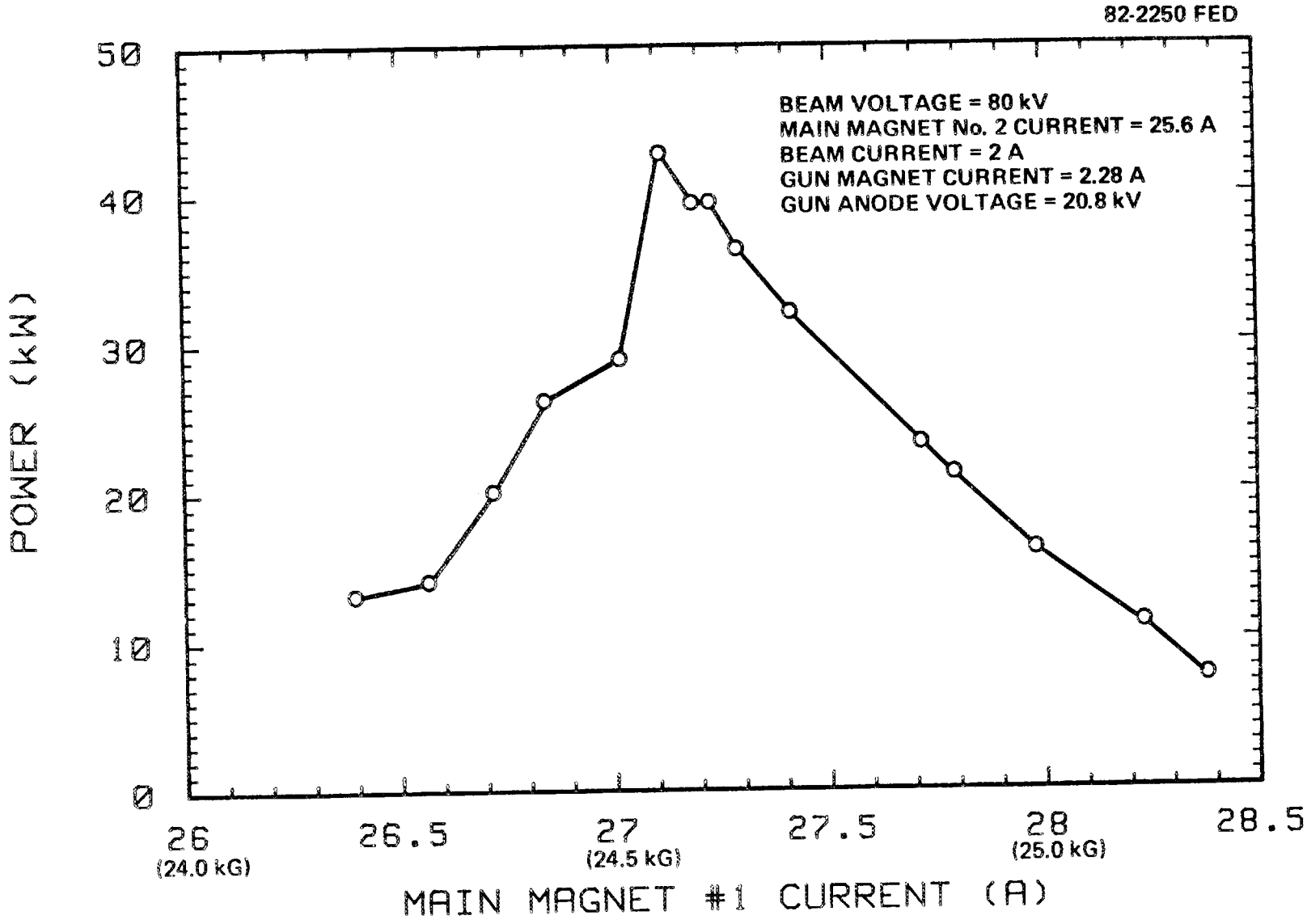

Figure 334. Output Power VS Main Magnet No. 1 Current for a Beam Current of 2.0A for the VGE-8006 S/N X-5 in CW Operation.

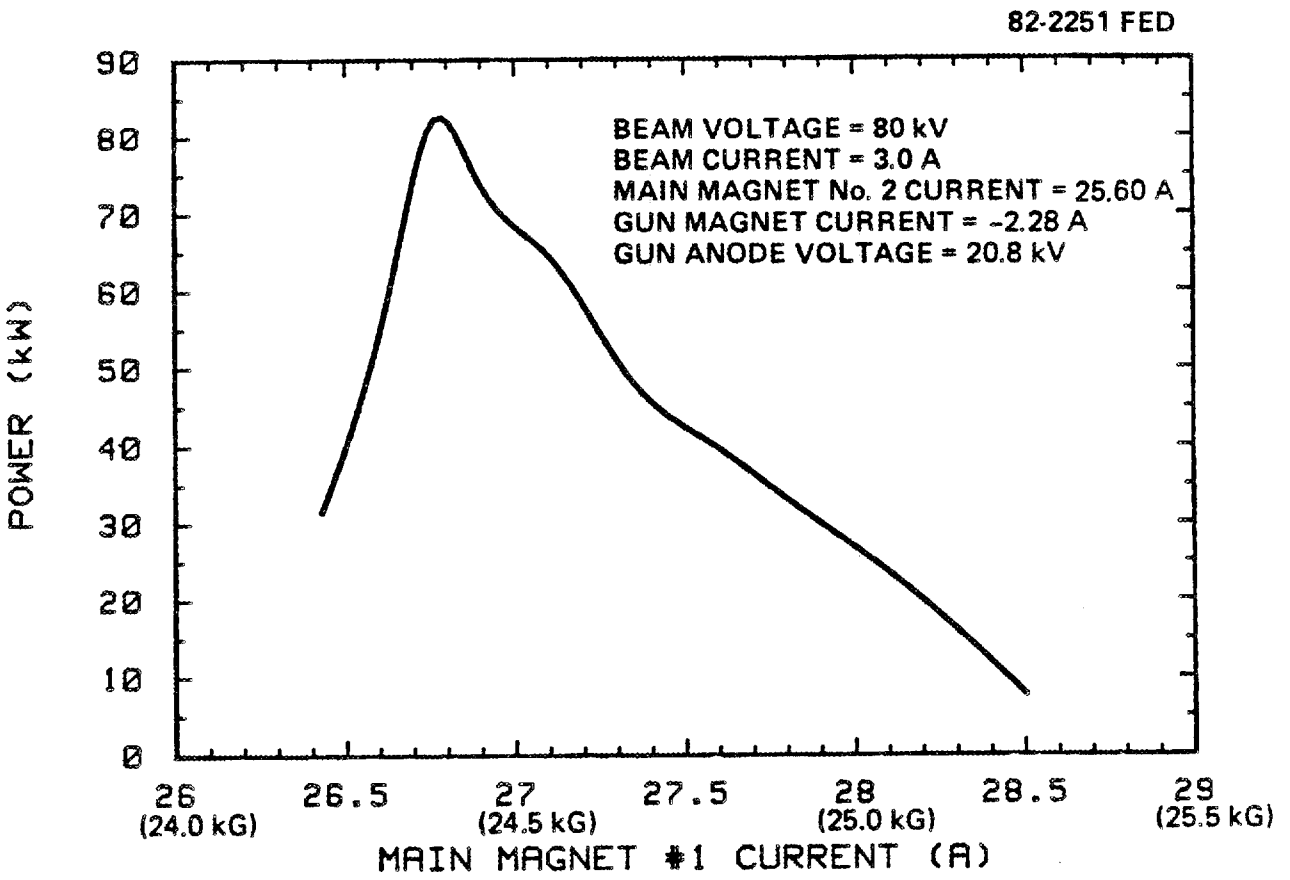

Figure 335. Output Power VS Main Magnet No. 1 Current for a Beam Current of 3.0A for the VGE-8006 S/N X-5 in CW Operation.

locking with variation of main magnet current would be necessary to determine the role the main magnet field plays.

Before removal of X-5 from the socket, tests were conducted to determine the mode pattern of the 50 GHz competing mode. Heat sensitive paper was placed in the output waveguide, then the tube was operated for a short amount of time in the 50 GHz modes. Results for modes at 50.68 GHz and 51.8 GHz are shown in Figure 336. They show definite radial structure, although no identification of the modes were made.

d. Tests with DC-200 RF Load

A cooling system was installed which made it possible to use a fluid other than water in the rf load. The fluid chosen was DC-200. Comparisons of the performance of X-5 with the waterload and the DC-200 rf load were made for similar CW operating parameters. Table 47 lists a comparison made for a beam current of 3.5 A. In general, rf load power levels using DC-200 (calculated using the conversion factor shown in Table 47) were lower than those for the waterload for similar operating conditions. Power lost in the window FC-75 fluid and body circuit were slightly higher for the DC-200 load than for the waterload. This phenomenon was not understood completely.

As the beam current was increased, the rf load was monitored for boiling, using an accelerometer fastened to the load. As the beam current was raised to 4.4 A, only minor boiling was detected in the load, as opposed to significant boiling in the waterload at 3.8 A. It should be noted here that each time the current was raised, the output power was optimized by varying gun anode voltage and magnetic field.

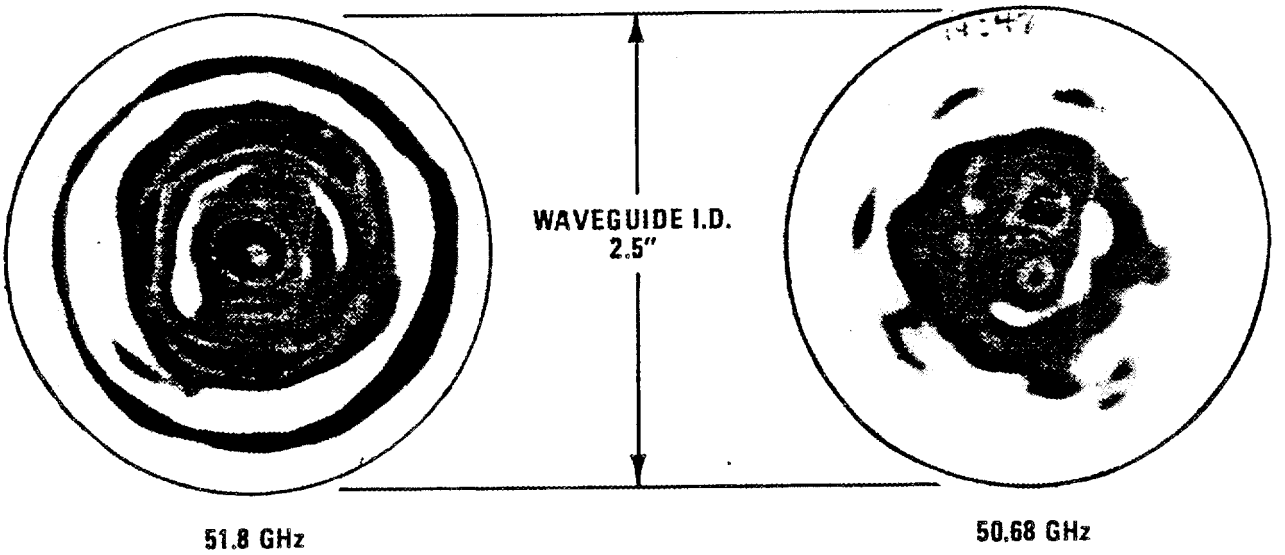

Figure 336. Mode Patterns of Competing Modes at 50.08 GHz Obtained Using Temperature-Sensitive Paper in the Output Waveguide of the VGE-8006, S/N X-5, in CW Operation

Table 47
Comparison of X-5 Performance into Water Load
and DC-200 RF Load
(CW Operation)

Water Load	DC-200 RF Load
Tube Parameters:	
Beam Voltage = 80.0 kV	Beam Voltage = 80.2 kV
Beam Current = 3.5 A	Beam Current = 3.5 A
Gun Anode Voltage = 20.6 kV	Gun Anode Voltage = 20.8 kV
Main Magnet #1 Current = 26.64 A	Main Magnet #1 Current = 26.64 A
Main Magnet #2 Current = 25.40 A	Main Magnet #2 Current = 25.47 A
Gun Magnet Current = 2.30 A	Gun Magnet Current = 2.31 A
Field at Cavity = 23.66 kG	Field at Cavity = 23.69 kG
Power Measurements:	
FC-75 (window) - 1.26 kW	FC-75 (window) - 1.75 kW
Body Circuit - 1.70 kW	Body Circuit - 1.87 kW
Window Water - 0.013 kW	Window Water - 0.046 kW
Waterload - 105 kW	*DC-200 RF Load - 94 kW

*Conversion factor = 0.097 kW/^{o}C-gpm was used to calculate DC-200 rf load power.

While operating at a beam current of 4.4 A, the inner ceramic on the double-disc window broke, filling the tube with FC-75. Operating parameters for the tube at the time of the window failure are shown in Table 48.

Table 48

Operating Parameters for X-5 at the Time of Window Failure

Beam Voltage = 80.2 kV
Beam Current = 4.4 A
Gun Anode Voltage = 20.9 kV
Main Magnet #1 Current = 26.56 A
Main Magnet #2 Current = 25.49 A
Gun Magnet Current = 2.29 A
Power Loss in FC-75 = 2.37 kW
Power Loss in Body = 2.68 kW
Power in DC-200 RF Load = 122 kW

e. Inspection of X-5 Following Window Failure

X-5's window had one crack that extended across its diameter. It was wider on one edge and narrowed to a point where it was practically invisible on the opposite side. The gap was wider on the vacuum face than on the FC-75 face at equal distances from the edge. This was due to the fact that after the crack was initiated, atmospheric pressure and the pressure from the FC-75 deflected the ceramic inward to the vacuum.

When the window was illuminated from behind, two concentric circular white zones were visible. These zones did not align with the calculated location of the electric field maxima in the TE_{02} mode. SEM analysis of the fractured surface found no evidence of melting in these regions. There was evidence of high temperature, but the ceramic melting temperature was not reached. For this reason, it is believed that the concentric rings were due to rewhitening of the ceramic after discoloration from x-rays, unless there was an rf-aided annealing mechanism. The white shade of alumina can be restored by firing at 900°C. The crack was believed to be initiated by high hoop stresses at the edge of the window.

A visual inspection of the collector revealed none of the damage or erosion observed on X-4. In addition, the drift tube section

which precedes the cavity was undamaged. These two observations indicate that the improved magnet and the addition of a collector coil have alleviated asymmetric beam propagation and deposition in the large collector. A detailed comparison of the transverse magnetic field of the magnet used on X-5, and the original magnet used on X-4, were shown in Figure 7.

2. Rebuild

a. Hi-Potting and Short Pulse Aging

The testing of VGE-8006A, S/N X-5R began on August 7, 1984. Hi-potting, 500 μs pulse aging, and pulsed characteristic curves went normally. The pulsed data were similar to VGE-8006A, S/N X-7 and typical of the step cavity which has been used in many 60 GHz gyrotrons.

b. Long Pulse Aging and Collector Profiles

The tube was aged to 20 ms pulse duration, both with and without rf, so that collector power density profiles could be made using the technique described in Section IX-K-2. Figures 337 and 338 show the results with no rf and with rf, respectively. The initial beam is landing about 6" farther into the collector than on VGE-8006A, S/N X-7 and only one collector coil was required to obtain the same peak power densities as X-7. These are 1.2 kW/cm^2 without rf and 1 kW/cm^2 with rf after correcting for the power balance between the measured data and actual tube parameters. This was considered acceptable based on the performance and examination of VGE-8006A, S/N X-7. The tube was then aged to 100 ms pulse duration before preparing for CW operation.

c. CW Operation

Prior to CW operation, the IR grid and waveguide attenuator were installed. Both the long wave and short wave IR cameras were mounted and aligned. The rf power was increased gradually by the same technique as used on VGE-8006A, S/N X-7. That is, gradually raising the beam current at

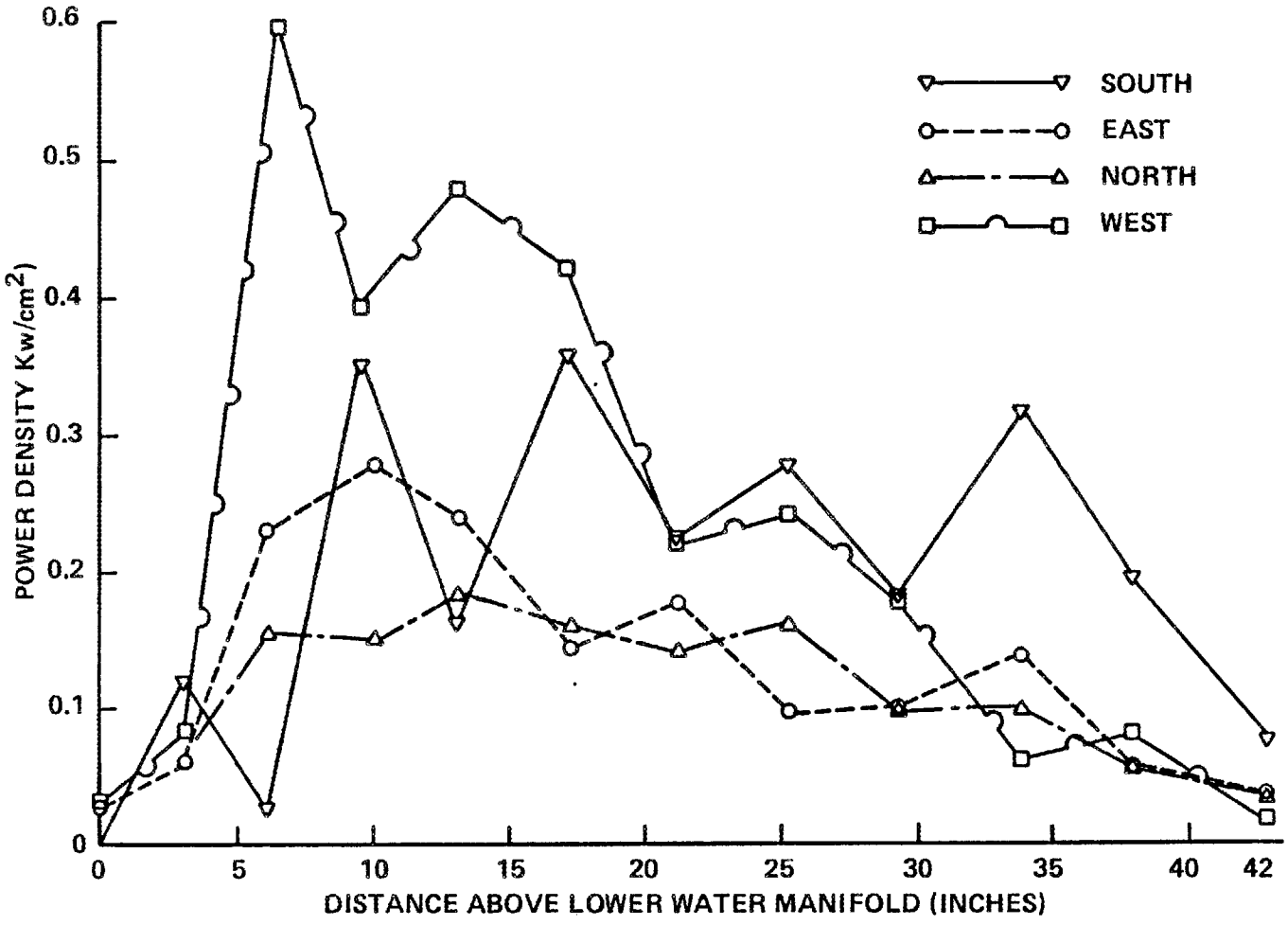

Figure 337. Collector power density distribution for VGE-8006A S/N X-5R with no rf and coil at 8 inches with 0.5A

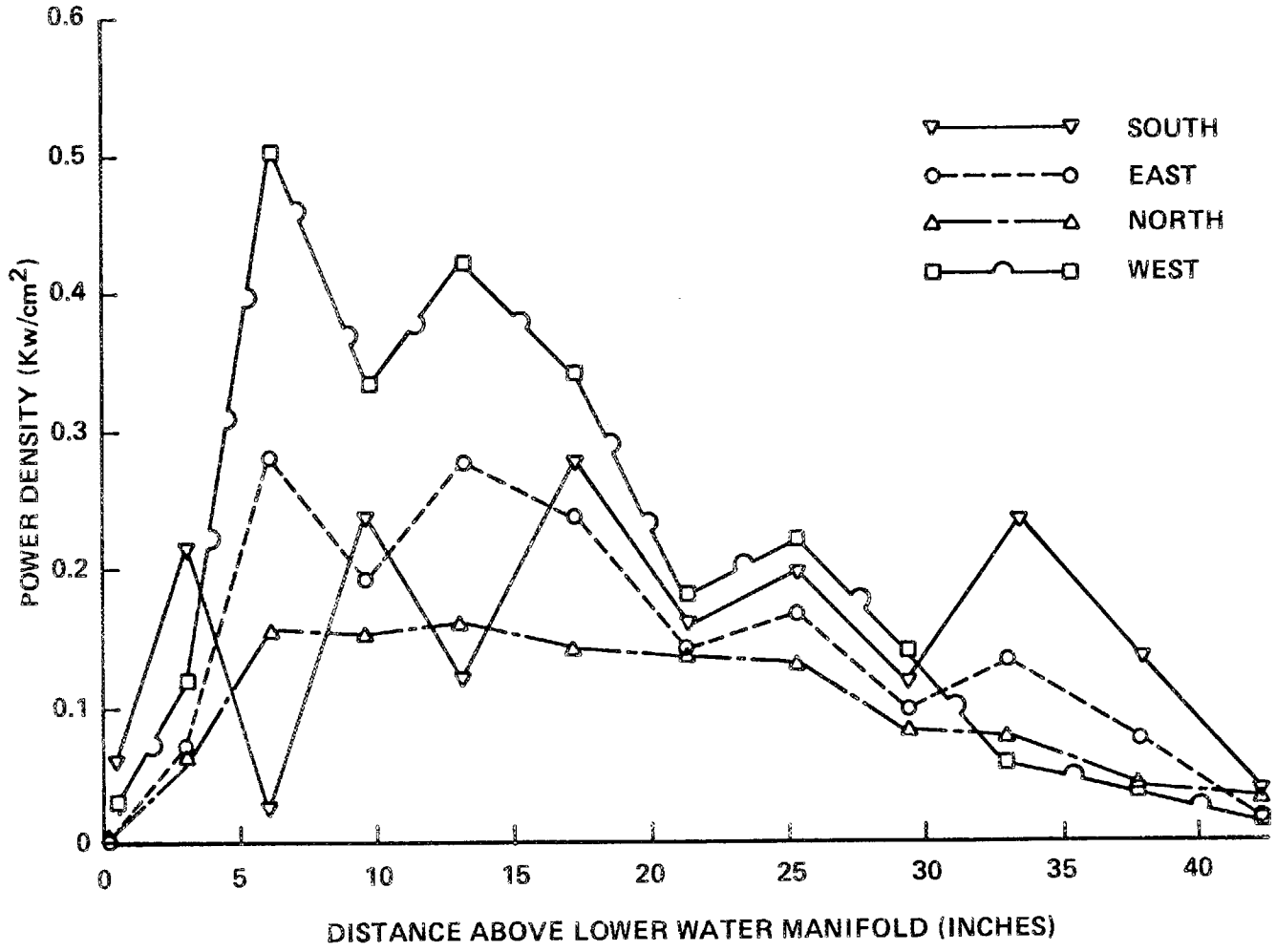

Figure 338. Collector power density for VGE-8006A S/N X-5R with rf and coil at 8 inches with 0.5A

a beam voltage of 80 kV. A maximum power of 108 kW was obtained at a beam voltage of 80 kV and a beam current of 4.0 amperes.

The window temperature at this level was 93°C with an FC-75 flow of 8.2 GPM and an FC-75 inlet temperature of 18.4°C. By contrast, the window temperature on VGE-8006A S/N X-7 at 110 kW was 63.5°C with an FC-75 inlet temperature of 14.7°C and the same FC-75 flow.

d. Superconducting Magnet and Collector Power Density Measurements

An area of some concern during these tests, was a phenomenon observed in the superconducting magnet S/N 1007 which had been in the Nike Zeus Test Set for some time, including during the VGE-8006A, S/N X-7 tests. The concern was that the required trim coil current had some dependence on the helium level. That is, when the magnet dewar was filled from, say 70% to 95%, the trim coil current had to be readjusted to minimize body current and obtain the same rf performance. It was thought that some mechanical shifting occurred in the dewar when it was filled which affected the transverse magnetic field.

Magnet S/N 1007 was replaced by magnet S/N 1002 before further CW or pulsed testing. Transverse magnetic field measurements were made on magnet S/N 1007 after it was removed from the test set. The initial results were inconclusive and further evaluation is needed to explain the erratic behavior of magnet S/N 1007. It should also be noted that this behavior has not been observed with magnet S/N 1002.

Figure 339 shows the collector density profile of VGE-8006A, S/N X-5R in magnet S/N 1002 with no rf and under the same collector coil conditions as VGE-8006A, S/N X-7. Although the greatest power density still favors the south and west sides, the distribution between sides is closer in magnitude than on X-7. This was also noted on a pulse tube tested in magnet S/N 1002. In fact, on the pulse tube the highest power densities were on the north side.

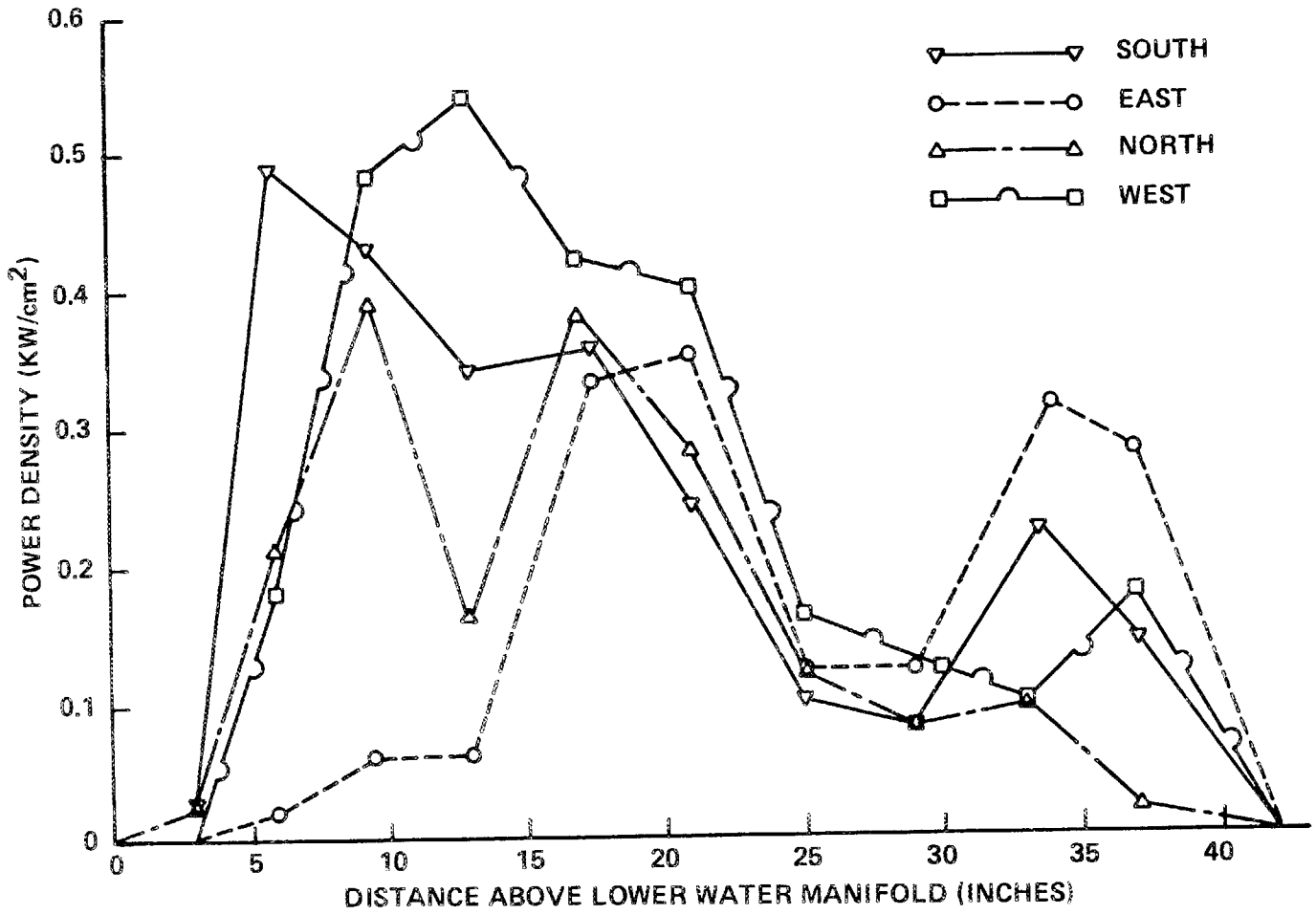

Figure 339. Collector power density distribution for VGE-8006A, S/N X-5R, in magnet No. 1002 with no rf and coil at 8 inches with 0.5A

Previously, the high south side and west side power densities were considered to be a direct result of the Nike Zeus Test Set environment. It now appears that it is a combination of environment, magnet and possibly even the tube. These measurements were continued on pulse tubes and CW tubes since knowledge of the collector power density in our environment and the customers' environment will be necessary to ensure reliable, long life operation.

e. Further Testing

After the collector density profiles were completed, the tube was prepared for further CW tests. Part of this preparation was to age the tube to a 100 ms pulse duration at 20% duty. During the tests, an rf characteristic was observed which, as yet, hasn't been completely understood. That is, at long pulse, output power appeared to be limited to 180 - 185 kW. When attempting to exceed this level by raising the gun anode voltage or lowering the gun magnetic field, the rf pulse would oscillate and the power supply would, with a modest amount of gun gas, "crowbar" before the pulse was complete. At first, this appeared to be a peak rf power problem. However, over 210 kW was obtained by raising the beam voltage or the beam current or both with no problem, albeit at a lower efficiency. The problem appeared when the ratio of transverse to axial velocity was increased above a certain value.

The only thing which would directly affect the gun would be mirroring of the electron beam. This same phenomenon had been observed during the short pulse testing of this tube and may have had some bearing on the problems with further CW testing.

Shortly after CW testing resumed, the new FC-75 chiller which had been purchased for the Super Power Test Set modification was installed in the Nike Zeus Test Set to obtain higher and cooler FC-75 flow. The highest CW rf power obtained when CW testing resumed with the new FC-75 chiller was 140 kW at a beam voltage of 80.1 kV and a beam current of 4.7 amps for an efficiency of 37%. The window temperature was 109°C with 10.85 GPM of FC-75 flow at an inlet temperature of 15.7°C. The other major

tube losses, such as power dissipation in the cavity and power dissipation in the FC-75, were close to those described in Section IX.K.4 for VGE-8006A, S/N X-7 at this power level.

The following day it was very difficult to get the tube over 100 kW without creating a lot of gun gas. This was true even at gun anode voltages below those described earlier as being a problem. Three days were spent trying to operate the tube stably at a high CW power level. At the CW rf power level of 100 kW, the window temperature was 75°C at an FC-75 flow of 10.85 GPM and an inlet temperature of 10.9°C.

Excessive gun gas and crowbarring frustrated any efforts to exceed or even operate at the 100 kW CW power level. The tests were terminated at this point.

F. VGE-8060 S/N P-1R3

Test results on the Princeton VGE-8060, P-1R3, are discussed here because an experiment originally scheduled for the CW development program was incorporated in P-1R3 to enable earlier evaluation. This was the selective resistive coating cavity originally built up for the sixth experimental tube, third CW tube, VGE-8006, S/N X-6. In this cavity, the addition of sputtered resistive coating in a selective area on the ID of the cavity resulted in a lowering of the measured Q of the TE_{22} mode from Q = 290 to Q = 200. This was accomplished with negligible effect on the Q of the TE_{02} mode.

Test results showed that this change had little effect on the operating range at the high efficiency magnetic field. This is shown in Figure 340 which is a plot of frequency versus gun-anode voltage for various values of magnetic field. However, at magnetic fields slightly higher than the maximum efficiency value, there was a noticeable departure from previous 60 GHz gyrotrons. This is indicated by the double line between I_1 = 25.0 a and 25.2 amperes. The dashed line represents the approximate separation between TE_{02} and non-circular modes in typical 60 GHz tubes.

ORNL – DWG-83-2134

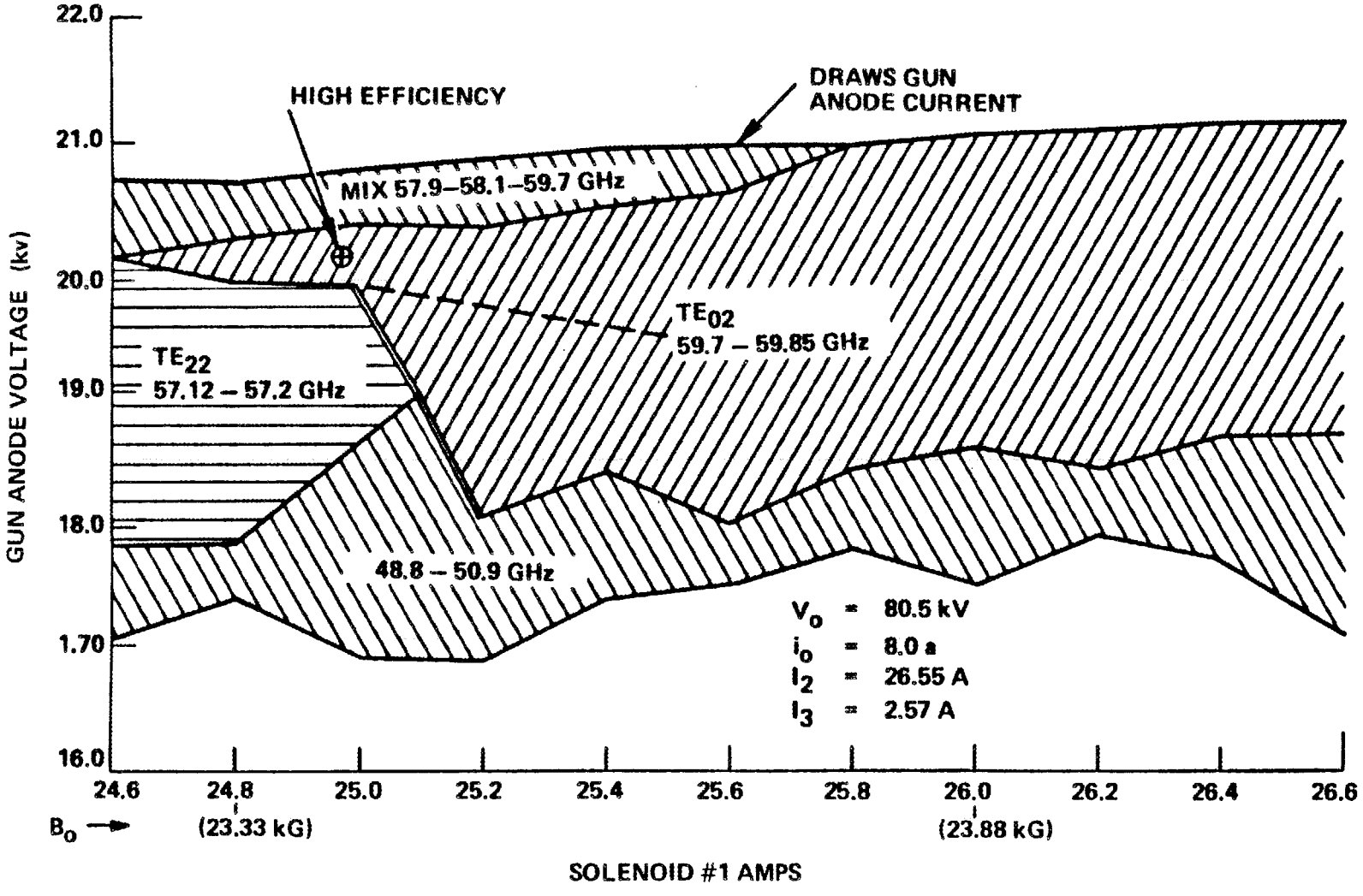

Figure 340. VGE-8060 (P-IR3) Oscillation Map

A line in parameter space can be found on which power can be varied with the gun anode voltage over a fairly wide range, i.e., 36 to 205 kw peak rf power, or 7.5 dB. Power versus gun anode voltage is shown in Figure 341 for magnet currents I_1 = 25.15 amperes and I_2 = 26.55 amperes which produce a magnetic field of approximately 23.49 kG at the cavity. Also shown is a more typical curve of rf power versus gun anode voltage showing interference by the presence of the TE_{22} mode with I_1 = 25.05 amperes and I_2 = 26.55 amperes corresponding to a magnet field of 23.45 kG.

The maximum rf power obtained from this tube was 240 kw at 37.5% efficiency, which is fairly typical of 60 GHz gyrotrons.

These tests on P-1R3 indicate that indeed, the tenacious TE_{22} mode is the primary limitation to obtaining a large dynamic range, that is, controlling the rf power output with the gun anode voltage alone. The resistive coating relieved this problem somewhat, but further design work would be required to give high efficiency, wide dynamic range performance. Although this resistive coating worked well in a relatively low duty, pulsed tube, there was some concern about using any lossy coating in very high duty or CW gyrotrons. Further studies would need to be made concerning the variation of loss with temperature.

G. SIXTH EXPERIMENTAL TUBE (THIRD CW TUBE)

1. Salient Features

X-6 was the third 60 GHz CW tube to be tested during the development program. It incorporated a new double-disc output window design which utilized thinner ceramics, improved ceramic surface qualities, and jetting of the FC-75 coolant between ceramic discs. A second new feature of X-6 was the use of a TE_{01}/TE_{02} step cavity to improve the tube's resistance to mode competition, primarily with the TE_{221} mode. The characteristics of the step cavity and the use of an iris on the output of the cavity have been discussed in Section VI.C and Reference 23.

ORNL – DWG-83-2135

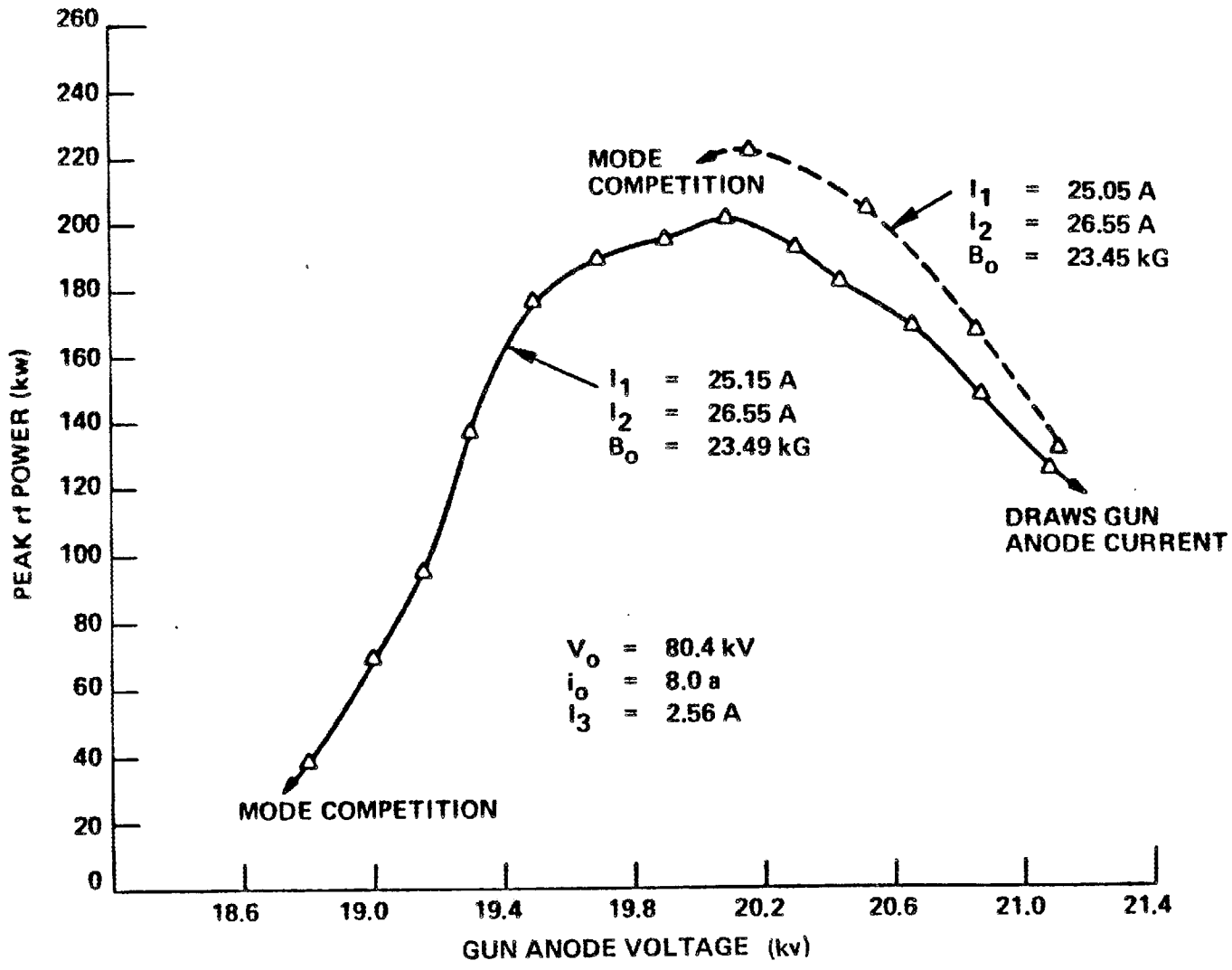

Figure 341. VGE-8060 S/N P-IR3 RF Power VS Gun Anode Voltage

2. Pulse Test Results

Following initial processing of the tube, pulsed data were taken on X-6 at duty factors of 1-2% (typically 0.5 ms pulse duration at 30 s^{-1} repetition rate). As indicated by theoretical analyses, the role of the magnetic taper on the efficiency of the step cavity was expected to be important. Because of this, data were taken for a wide range of magnetic tapers, in addition to the normal parameter variation curves. In the following, the values of magnetic tapers listed are percentages across the whole length of step cavity, and the magnetic fields quoted are those for the geometric center of the entire TE_{011}/TE_{021} cavity.

In Figure 342, the output power versus gun anode voltage for the case of a 2% magnetic taper is plotted. The output power varied smoothly from 0 to over 200 kW without mode competition or other disruptive instabilities.

The operating range of 2.5 kV in gun anode voltage may be contrasted to a range of 1 kV for X-5, as shown in Figure 328. The entire low gun-anode voltage side of the curve was missing for X-5 (TE_{221} mode competition) whereas the full curve was measured for X-6.

A plot is shown in Figure 343 of output power as a function of main magnet #1 current, again for a 2% taper. Since the taper changes slightly when main magnet #1 is varied, as noted in Figure 343, the coils were adjusted to provide the 2% taper at the peak power point. An oscillation map for X-6 with a 2% magnetic taper is shown in Figure 344. In contrast to the operation of all previous tubes, there is almost no mode competition from the TE_{221} mode. The maximum power region is centrally located in the TE_{02} portion of the map, giving rise to the dynamic range indicated by Figure 342. The 50 GHz mode, present on previous tubes, was still present, but did not appear to degrade the efficiency or stability of the tube. Since the 50 GHz mode cannot be attributed to a simple cavity mode, it is possible that it occurs in the output taper or collector, in which case it has no effect on the desired TE_{021} mode. The portion labeled 59.3 - 59.5 GHz is an oscillation that has a frequency similar to the TE_{02}

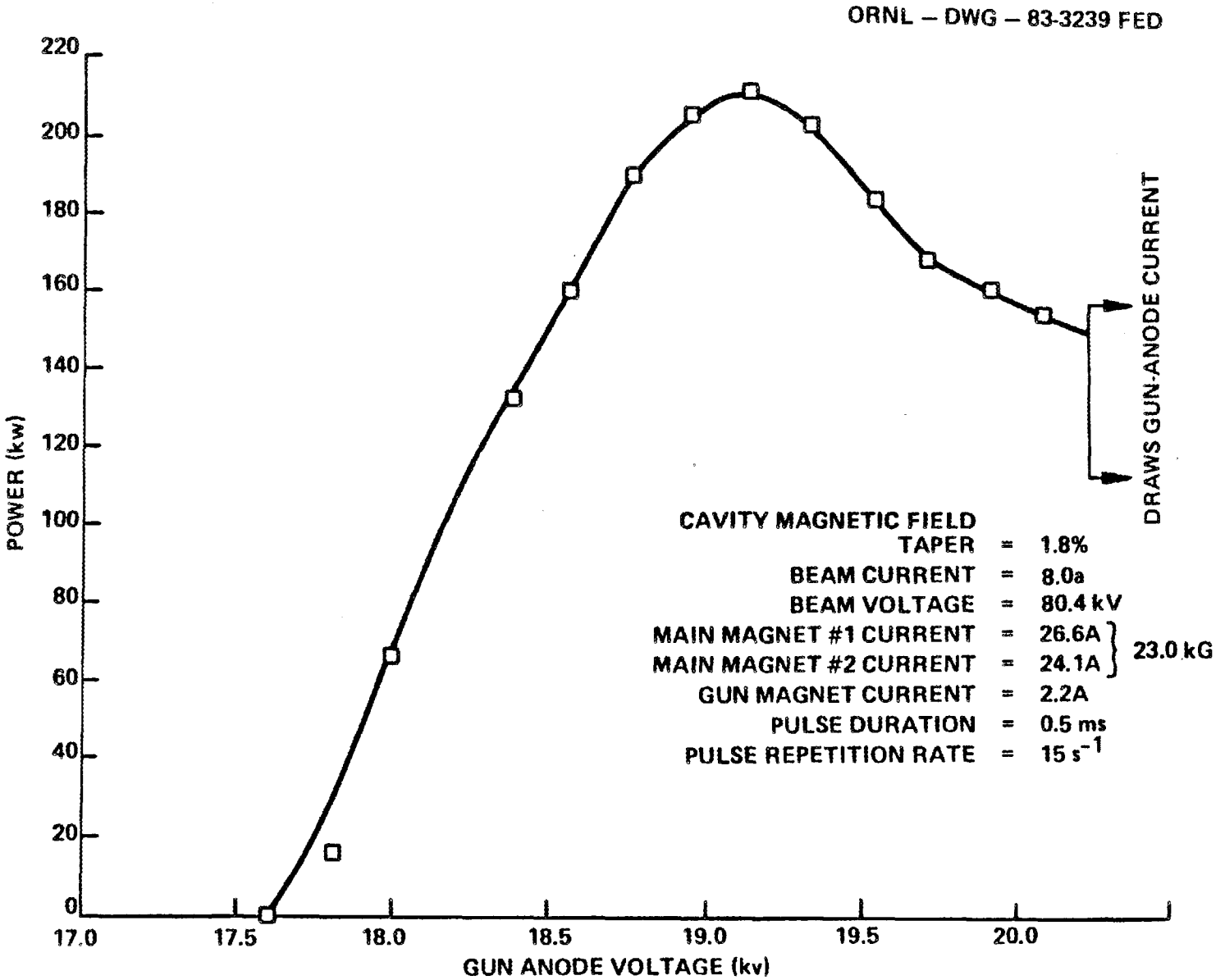

Figure 342. Output Power VS Gun Anode Voltage with a 2% Magnetic Taper Across the Cavity for the VGE-8006 S/N X-6

ORNL – DWG – 83-3241 FED

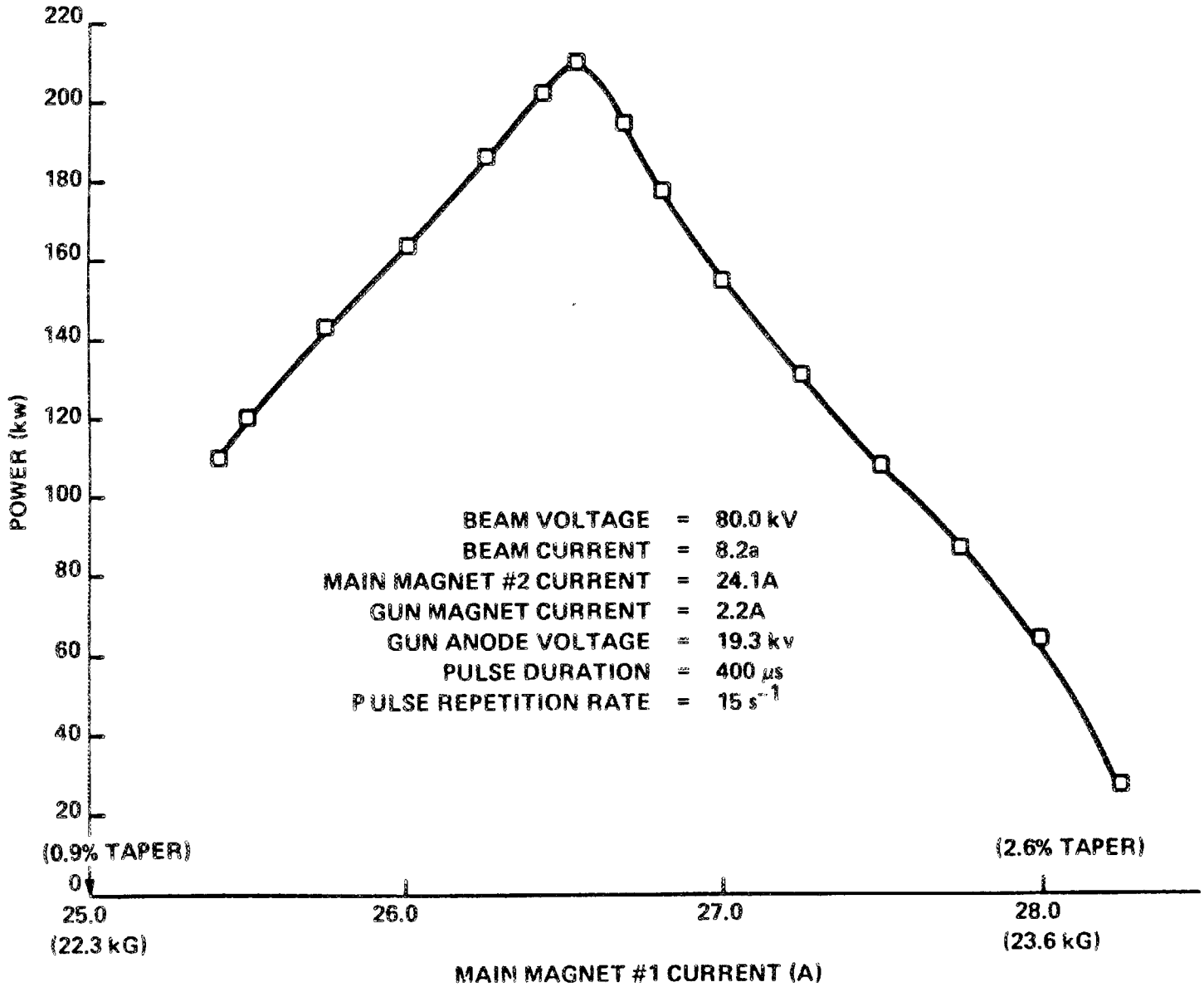

Figure 343. Output Power VS Main Magnet No. 1 Current with a 2% Magnetic Taper Across the Cavity for the VGE-8006 S/N X-6

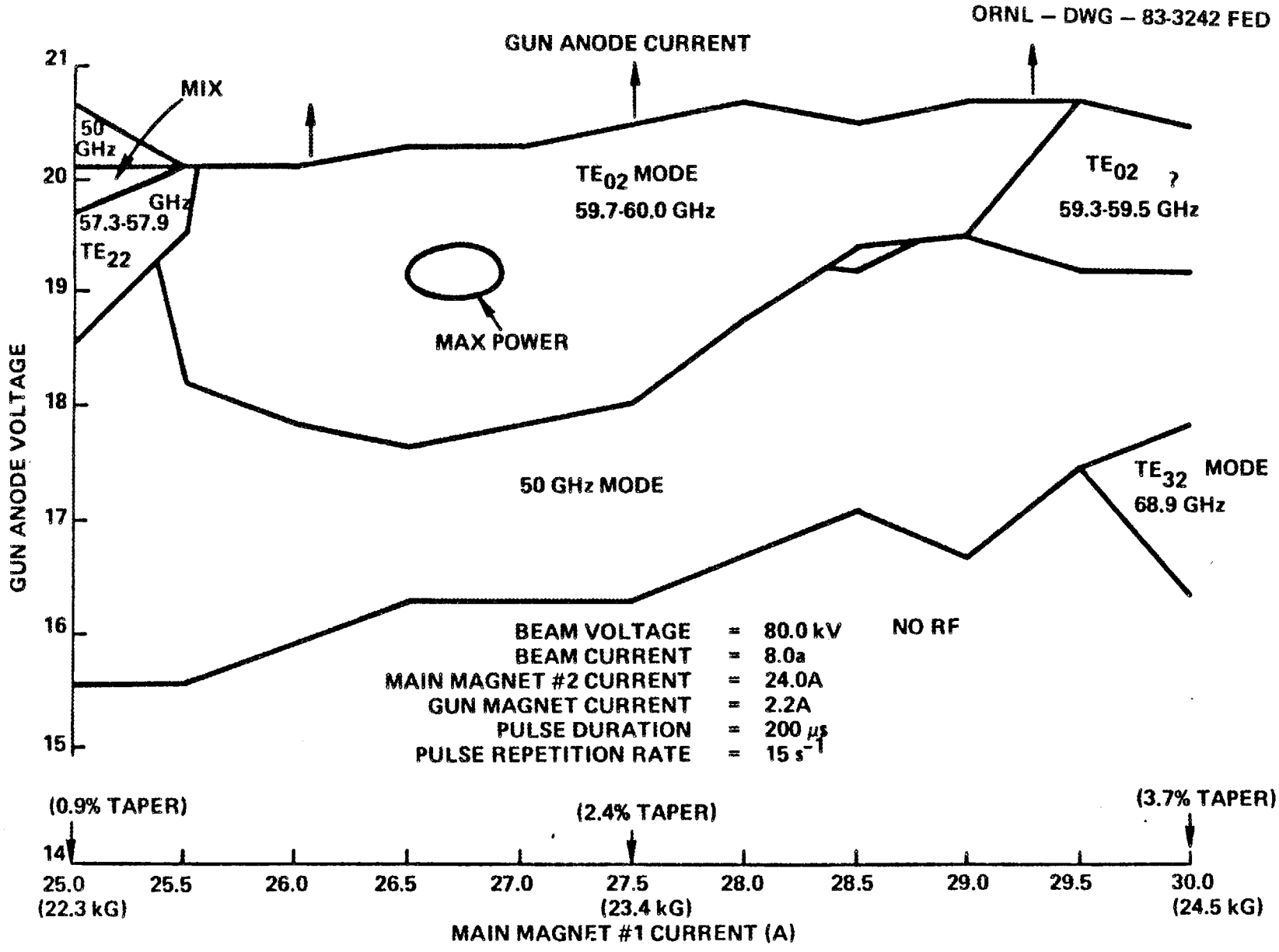

Figure 344. Oscillation Map with a 2% Magnetic Taper Across the Cavity for the VGE-8006 S/N X-6

mode, but it occurs at very high magnetic fields and is not of particular interest because its power output is very low.

Following the initial tests with a 2% magnetic taper, operation using different magnetic tapers across the cavity was investigated. In Figure 345 is plotted output power versus main magnet #1 current for different values of beam current, using a 3% magnetic taper. In this case, we were able to reach 230 kW at 8 a, up from 210 kW with a 2% taper. A plot of frequency versus main magnet #1 current for the 3% taper case is shown in Figure 346. In Figure 347, we show the results of increasing the magnetic taper to 6% in a plot of output power versus main magnet #1 current. The peak efficiencies were higher than those measured with the 3% taper for each of the three values of beam current tested. However, the dynamic range of operation was somewhat decreased with the 6% taper.

Output power versus main magnet #1 current for a 9% magnetic taper is shown in Figure 348. Efficiencies for 3 a and 5 a have continued to increase, while the 8 a case remained the same as with the 6% taper, 250 kw at 38.9% efficiency. Again, a decrease in the dynamic range over which the TE_{021} mode may be operated is seen. The oscillation map shown in Figure 349 illustrates this phenomenon readily. The peak power is now limited by gun anode interception in the presence of the drastic magnetic field taper. In addition, there were numerous parameter combinations which resulted in body current. These were due to either the enlarged beam size in the beam tunnel (for a positive magnetic taper the magnetic field is lower in the beam tunnel region) or to the mirroring of the electrons. In addition, modes at 64 GHz and 68 GHz supplanted the 50 GHz mode in some of the parameter space. The 64 GHz and 68 GHz modes may be identified with the TE_{611} and TE_{321} cavity modes, respectively. In Figures 350 and 351 output power is plotted versus gun anode voltage and beam current, respectively, for the 9% taper. These curves further indicate the role of gun anode interception in limiting tube power and range of operation. The appearance of gun anode current at low beam currents probably results from space charge effects in the gun.

To complete the investigation of the effects of the magnetic taper, output power versus main magnet #1 current for the case of no

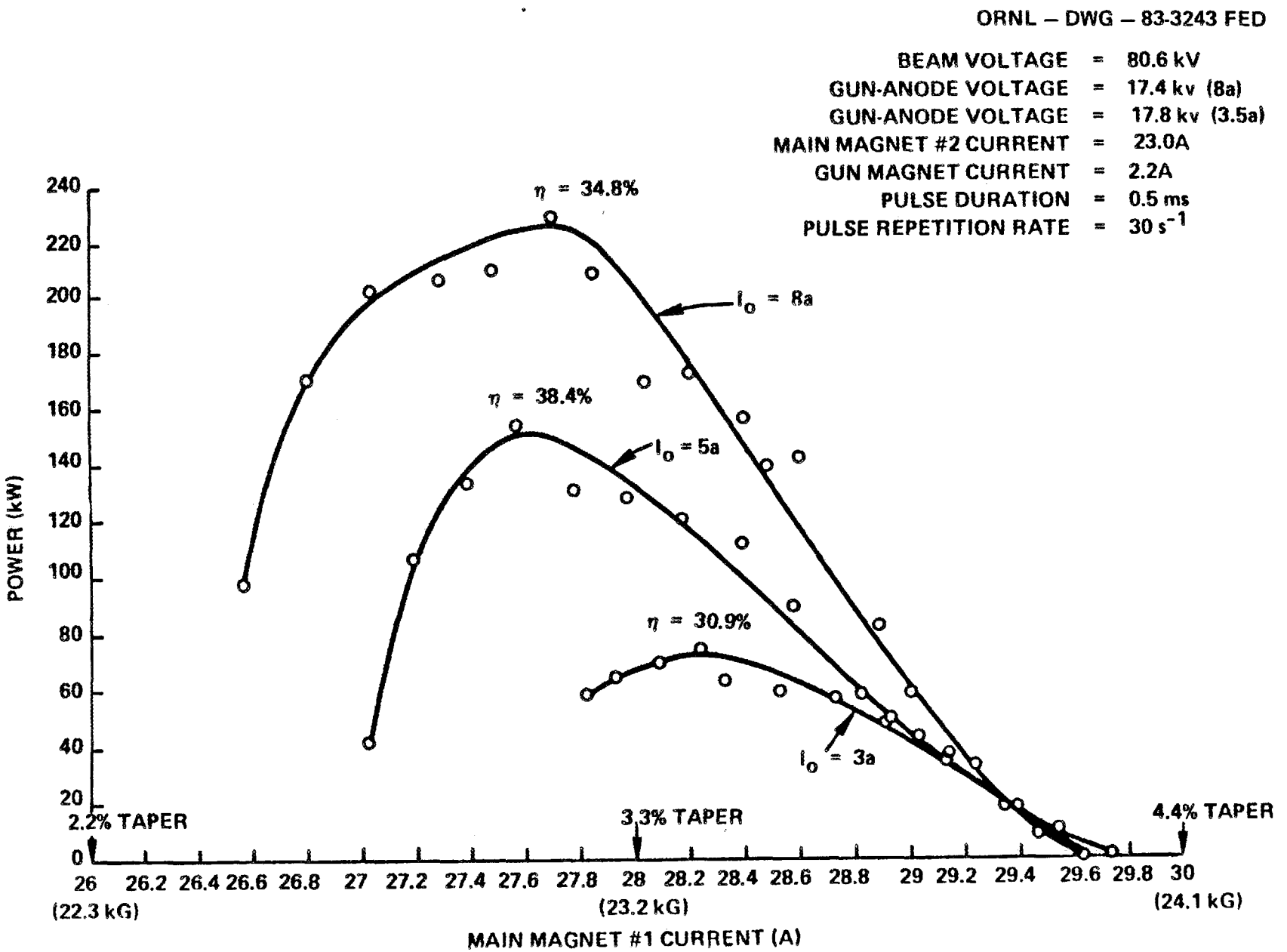

Figure 345. Output Power VS Main Magnet No. 1 Current with a 3% Magnetic Taper Across the Cavity for Three Values of Beam Current for the VGE-8006 S/N X-6

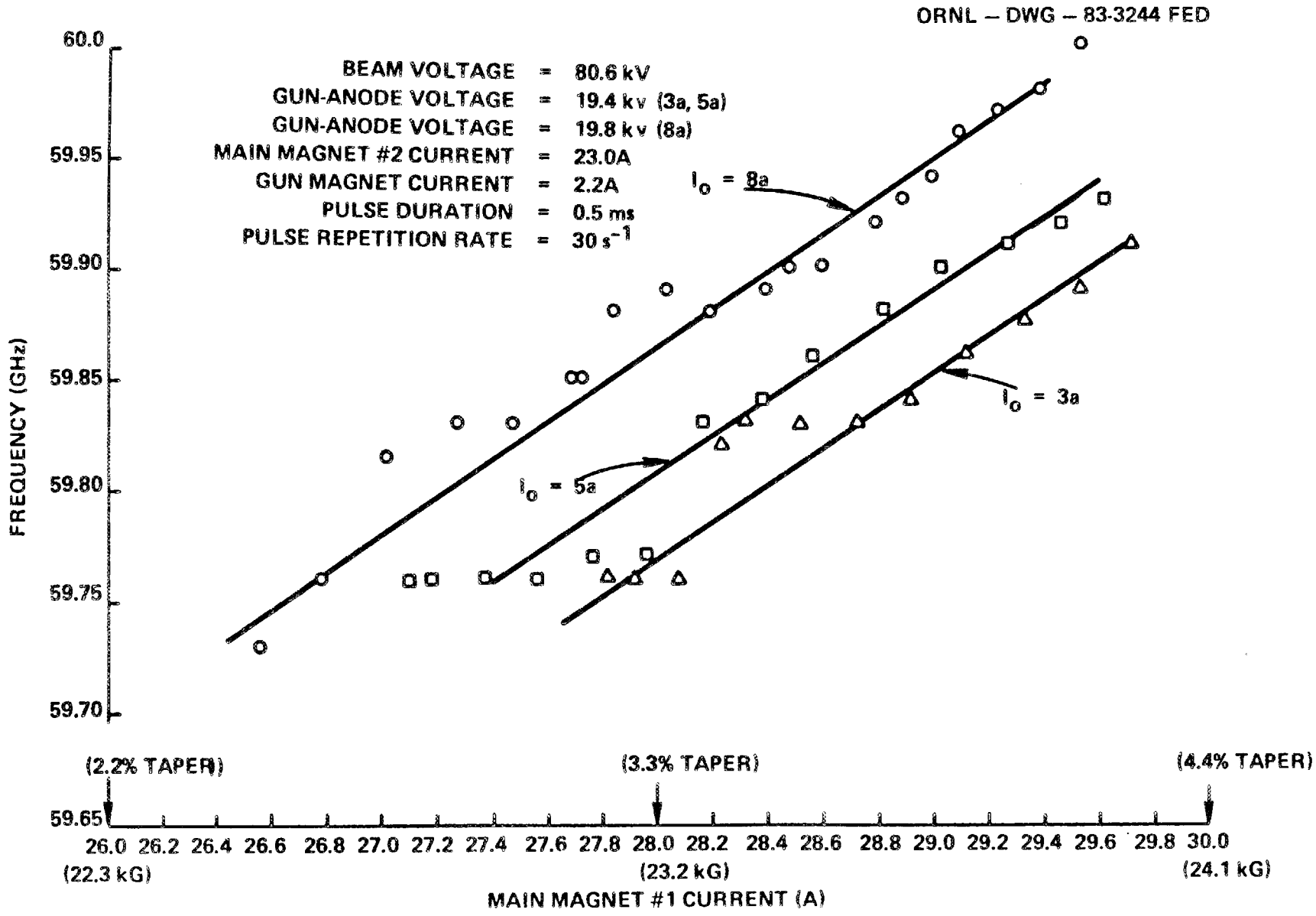

Figure 346. Frequency VS Main Magnet No. 1 Current with a 3% Magnetic Taper Across the Cavity for Three Different Beam Currents for the VGE-8006 S/N X-6

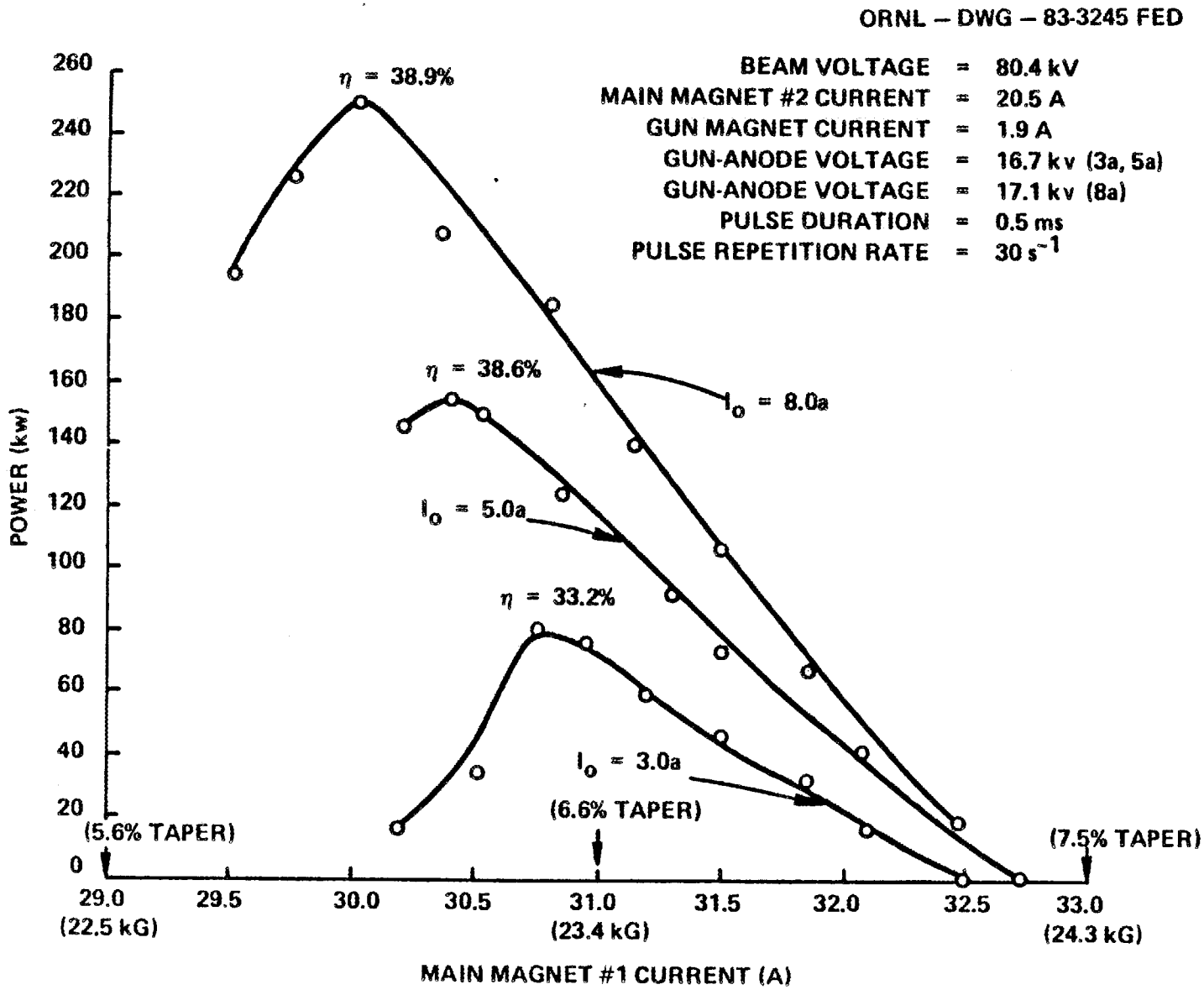

Figure 347. Output Power VS Main Magnet No. 1 Current with a 6% Magnetic Taper Across the Cavity for Three Different Beam Currents for the VGE-8006, S/N X-6

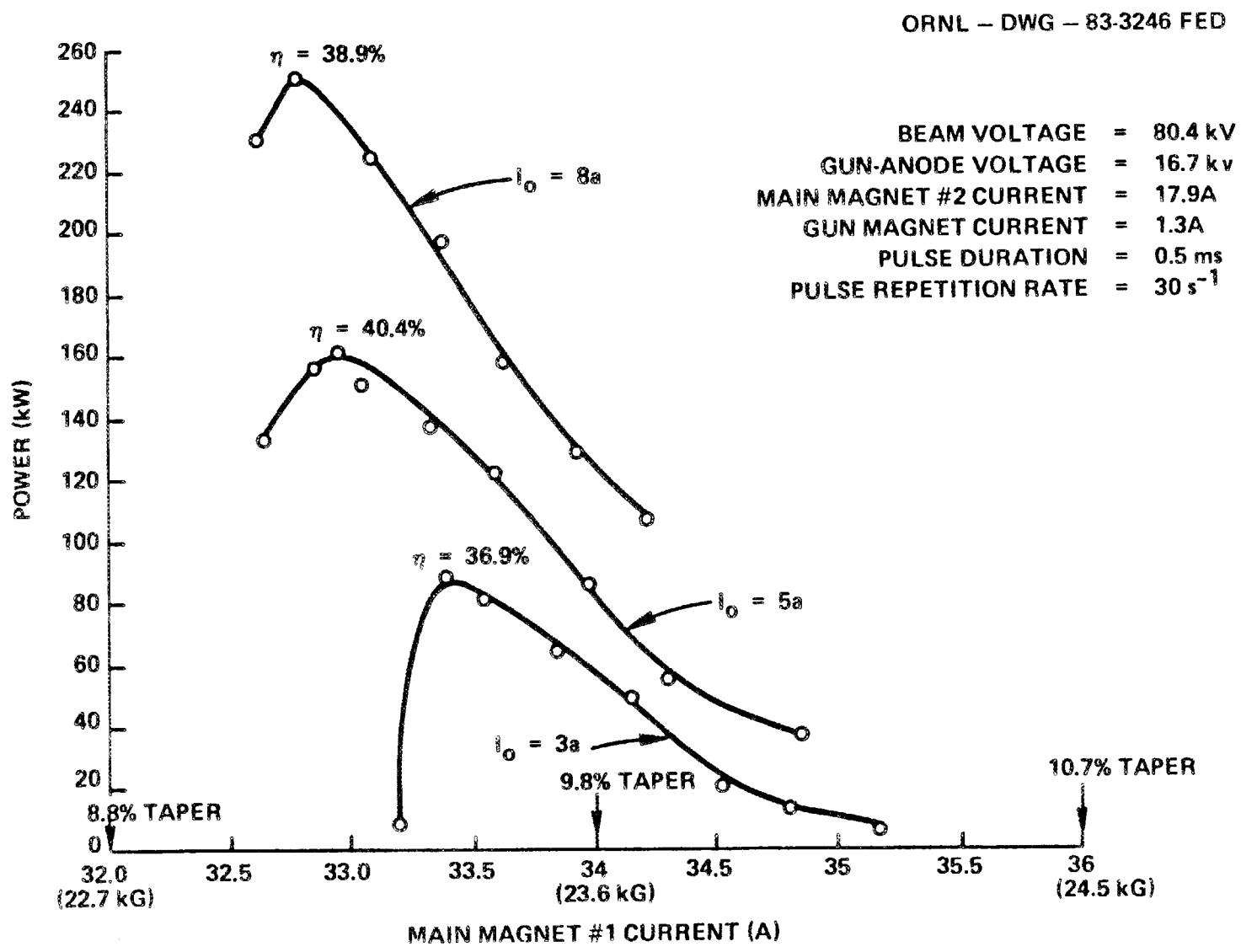

Figure 348. Output Power VS Main Magnet No. 1 Current with a 9% Magnetic Taper Across the Cavity for Three Values of Beam Current for the VGE-8006, S/N X-6

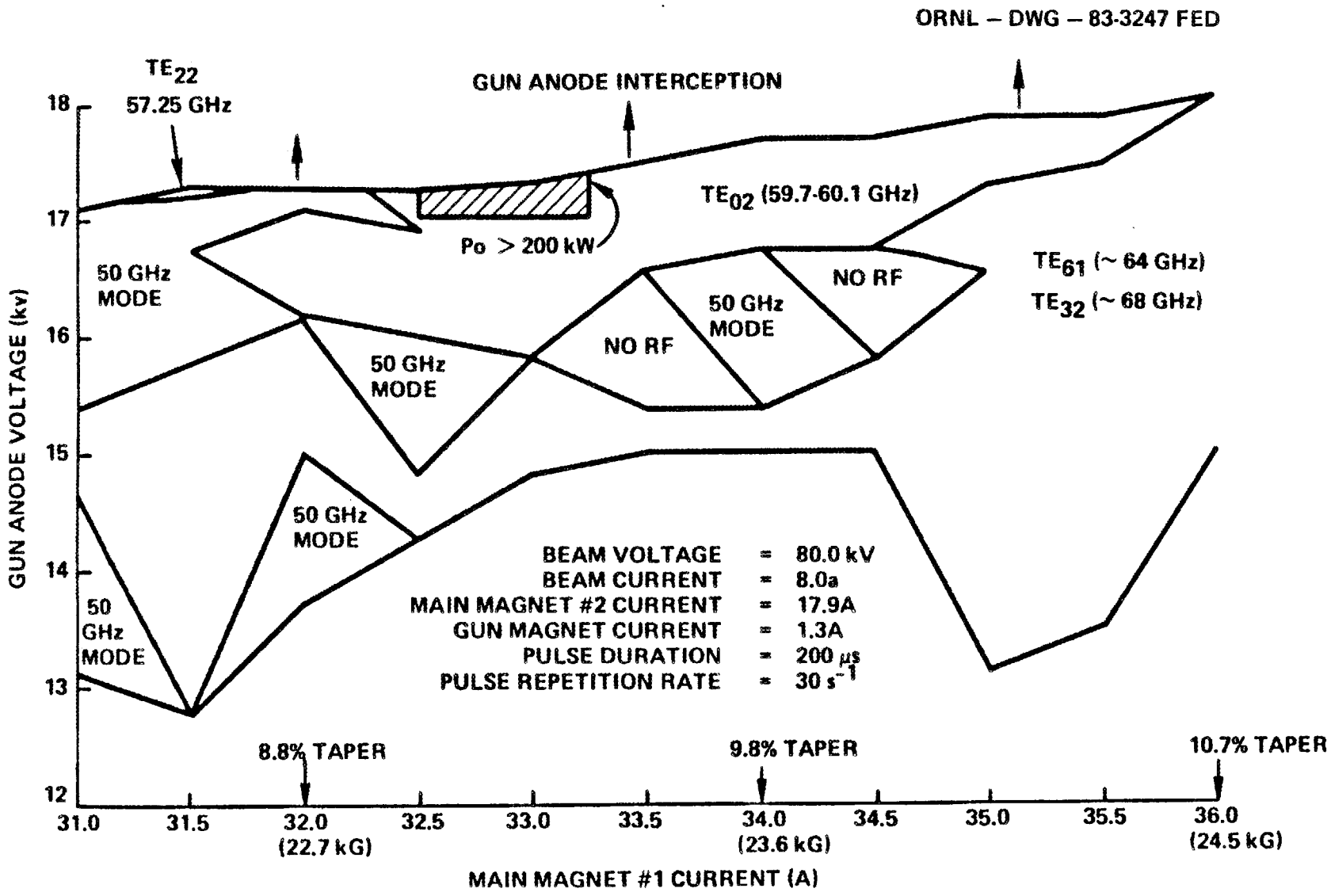

Figure 349. Oscillation Map with a 9% Magnetic Taper Across the Cavity for the VGE-8006, S/N X-6

ORNL – DWG – 83-3248 FED

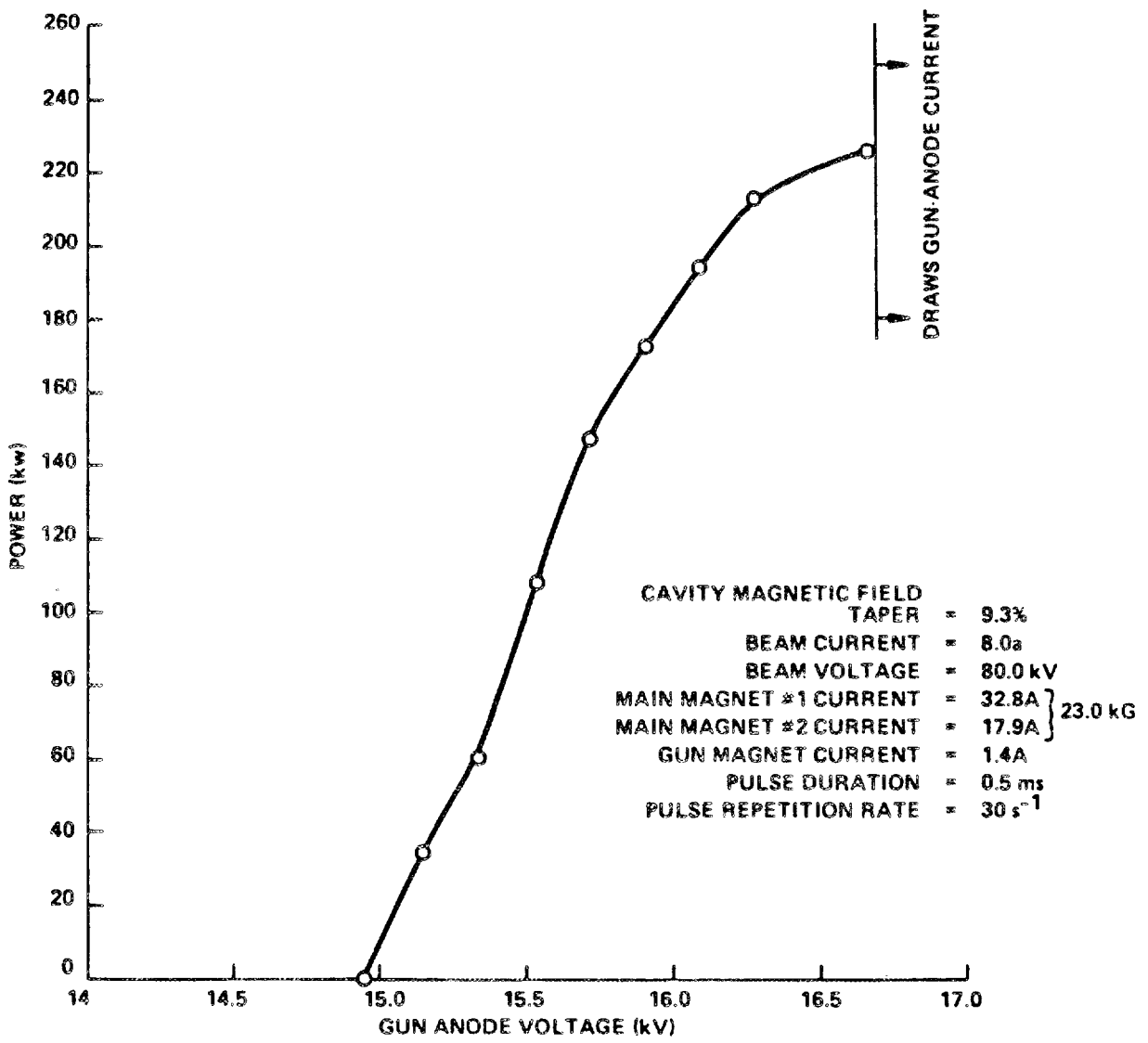

Figure 350. Output Power VS Gun Anode Voltage for 9% Magnetic Taper Across the Cavity for the VGE-8006, S/N X-6

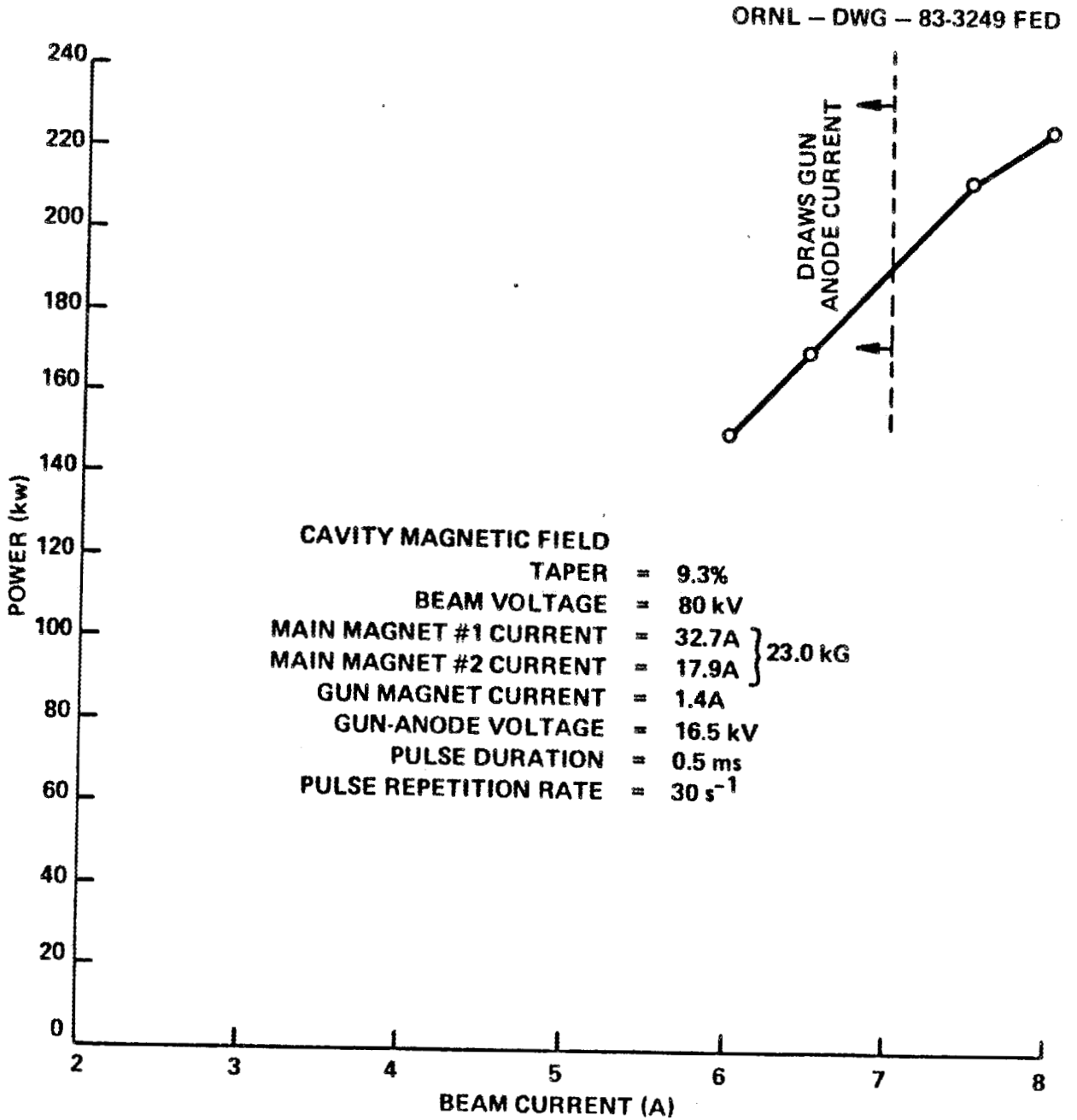

Figure 351. Output Power VS Beam Current for 9% Magnetic Taper Across the Cavity for the VGE-8006, S/N X-6

magnetic taper is plotted in Figure 352. Without any magnetic taper, efficiencies at all values of beam current fell drastically. Operation over a wide range of parameter space was still possible, but 200 kw could not be achieved with a beam current of 8 a under these conditions.

In summarizing the results of the pulse tests on X-6, the step cavity design successfully eliminated mode competition with the TE_{221} mode. Operation over a wide range of parameter space at power levels well over 200 kw was possible in the presence of 2-6% magnetic tapers. Such parametric control and overall tube stability was a marked improvement over previous tubes, which employed a standard gyrotron cavity (X-5, X-3R, etc.). Problems with gun anode interception and body current, encountered to some extent at 6-9% tapers, were anticipated due to the global effects of the magnetic taper on beam propagation in other parts of the tube. A schematic diagram of the magnet coil and cavity positions superimposed on a plot of the magnetic field profile is shown in Figure 353. Magnetic field profiles both with and without tapers across the cavity are included. For the tapered case (approximately 12%, as shown here), the effects of the taper are evident all the way back to the gun region, showing the possibility of beam degradation (velocity spread due to tapered field and lower transverse energy due to lower compression ratio at the cavity entrance) and beam interception on tube parts designed for a flat field profile. Finally, the above results for different magnetic tapers are compared with the theoretical predictions mentioned in Section VI.

Optimum efficiencies are shown in Figure 354 as a function of magnetic field taper for three different values of beam current for the above experiments and as predicted by large signal calculations. All of the large signal calculations were performed by following electron trajectories through the rf electromagnetic fields calculated by SUPERFISH for the step cavity design used on X-6, in the presence of various dc magnetic field tapers across the cavity. The efficiency is defined as the average loss in energy of the particles divided by their initial energies. All of the calculations were for electrons with an energy of 80 keV and an initial perpendicular to parallel velocity ratio of 2. The experimental points are based on the power measured in the output waterload and do not include

ORNL – DWG – 83-3250 FED

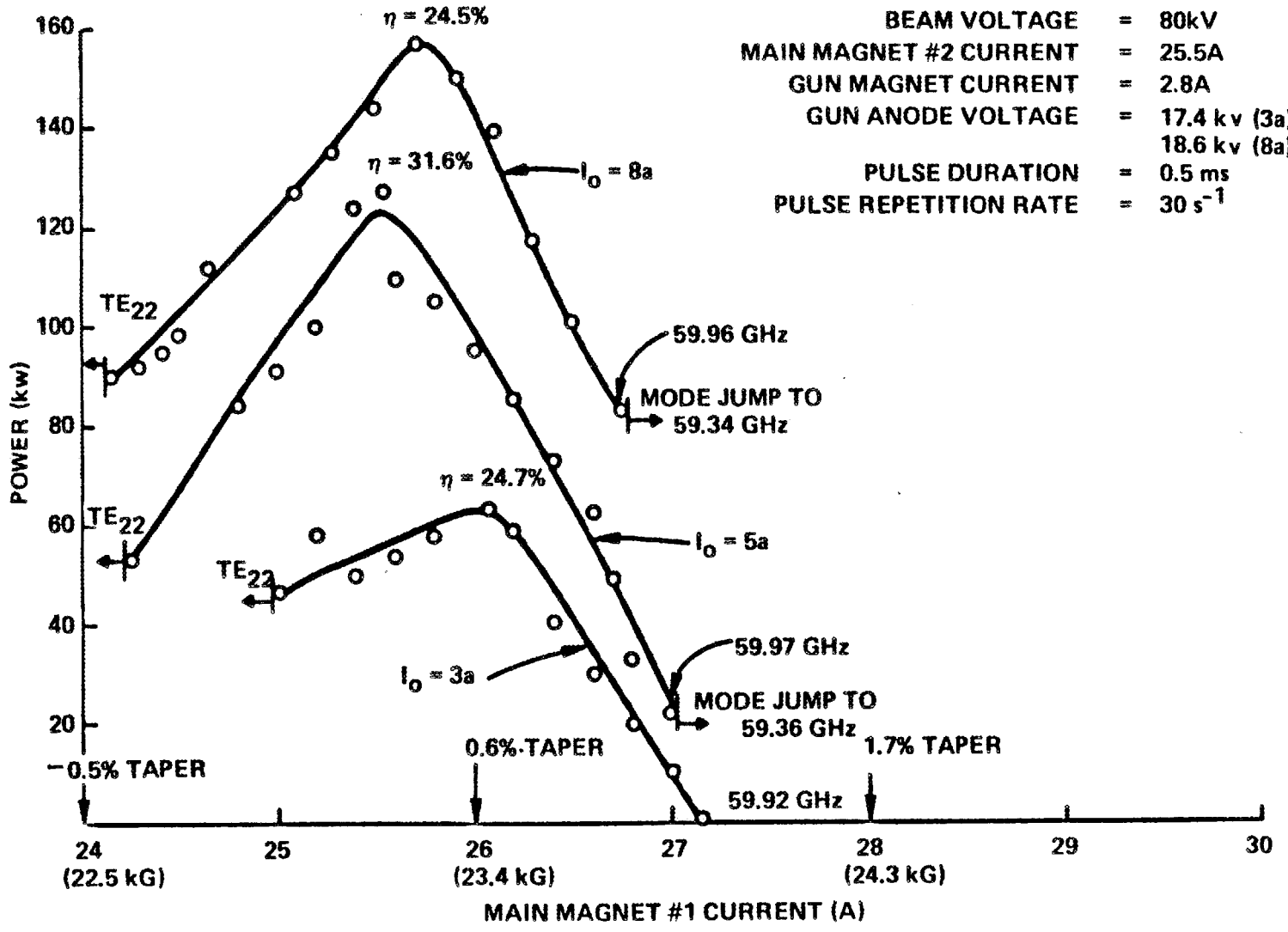

Figure 352. Output Power VS Main Magnet No. 1 Current with No Magnetic Taper Across the Cavity, for Three Values of Beam Current for the VGE-8006, S/N X-6

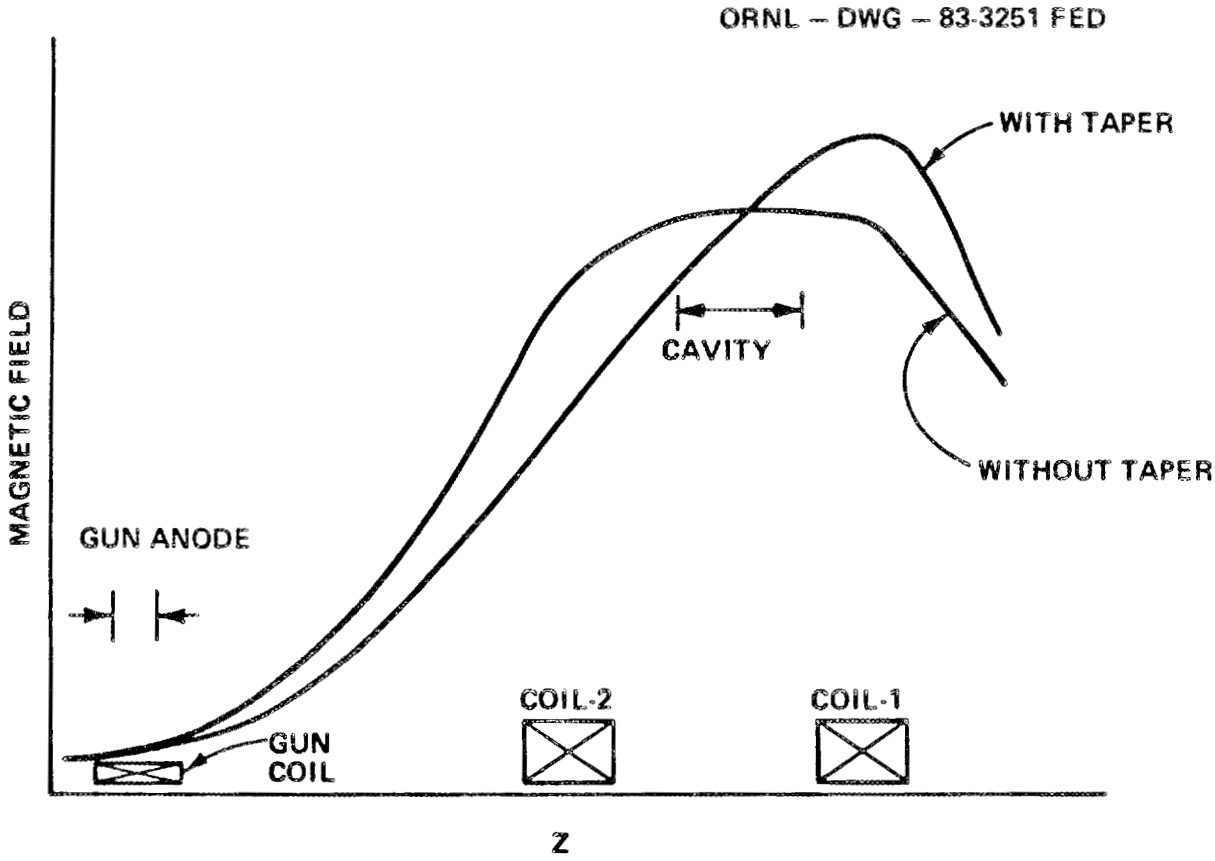

Figure 353. Schematic Diagram Showing the Relative Positions of the Three Magnet Coils and the Step Cavity for X-6, Tapered and Flat Magnetic Field Profiles are Plotted on the Same Axial Scale

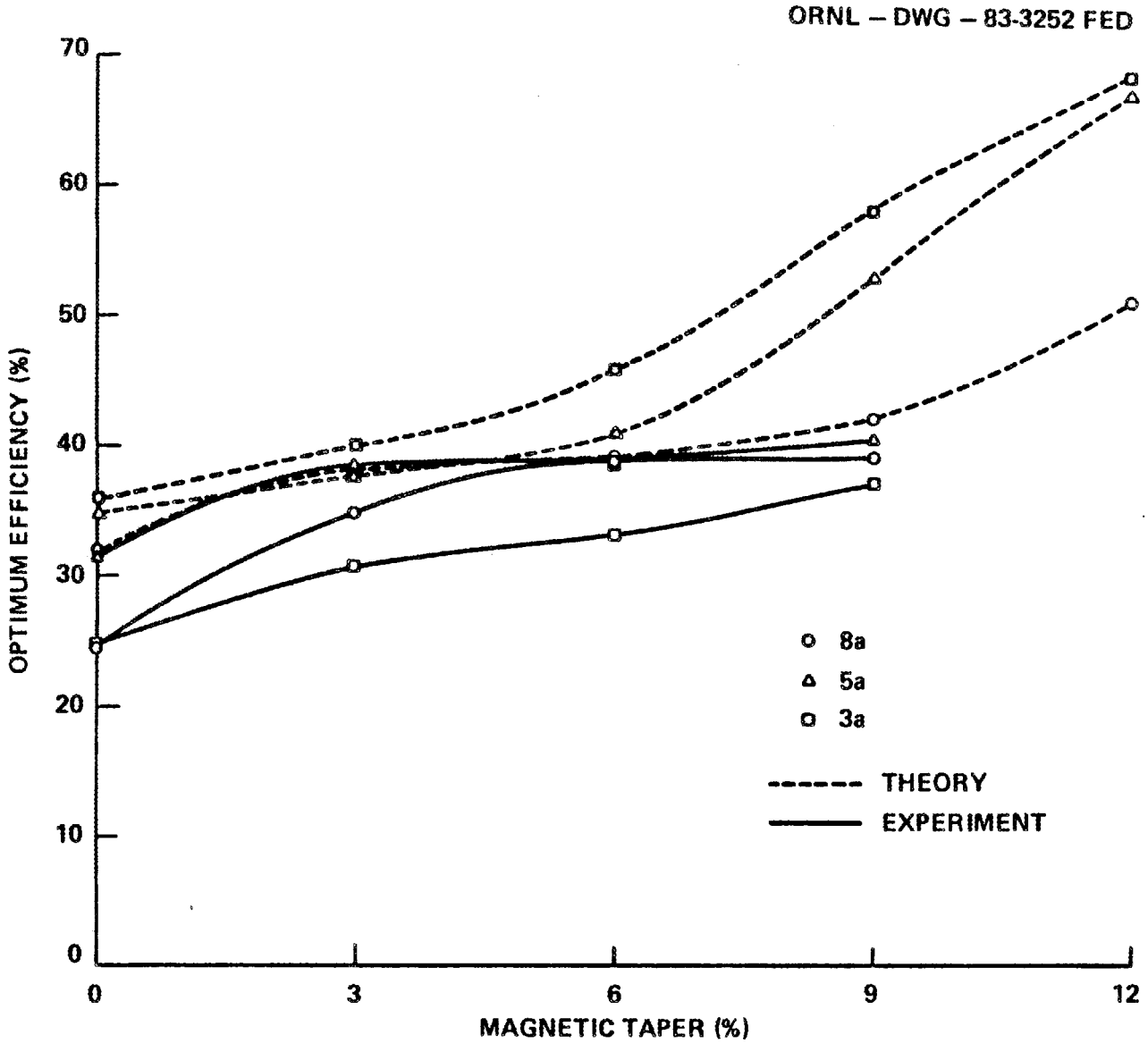

Figure 354. Comparison of Optimum Efficiencies as a Function of Magnetic Field Taper for Different Beam Currents, as Predicted by Theory and Observed on VGE-8006, S/N X-6. Efficiencies are Optimized with Respect to the Average Magnetic Field Across the Cavity.

cavity and window losses. If losses were included, experimental efficiencies would be increased by 2-4 percentage points. From Figure 354, we see that there is good agreement for a beam current of 8 a for all values of magnetic taper, while the 5 a case agrees for tapers up to 6%, but diverges at 9% magnetic taper. For 3 a, we observe a spread of about 10 - 12 percentage points between theory and experiment for 0-6% tapers and 20 percentage points for 9% taper. The discrepancies at the high values of magnetic taper can be attributed to the problems of beam propagation, beam quality, and reduced transverse energy as previously discussed. The disagreement at low beam current is less understood, but may be due to the effects of beam loading or window mismatch on the loaded Q of the cavity. However, the overall success of the analytic techniques in predicting the performance of X-6 gives confidence to our understanding of step, or complex, cavities.

3. Thermal Paper Mode Patterns

Before commencing CW operation of X-6, mode patterns were observed on thermal paper for short periods of operation. A typical exposure, while operating at 200 kw power levels for 0.5 ms pulses, was 3-5 pulses. Initial examination of the thermographs revealed peaks at the two TE_{02} maxima, as expected. In addition, a strong TE_{01} peak was observed, and a small radius inner ring which corresponded to a higher order TE_{0n} mode. By cutting out the center of the paper, longer exposures were feasible, allowing efforts to locate rings outside of the second TE_{02} maximum. No such outer maxima were found.

These measurements on the CW tube configuration demonstrated significant mode conversion, though quantitative estimates were not possible with this type of measurement. Measurements at various axial positions were made with the thermal paper to observe the kaleidoscopic patterns of the mode mixture. In addition, mode-specific directional couplers developed by GA Technologies were employed to quantify the mode mixture. Finally, further tests were made on pulse tubes with and without the step cavity which confirmed the large CW collector as the main source of the mode conversion.

4. CW Test Results

Following pulse tests of X-6, CW operation of the tube was begun. The IR camera system described in Section VIII.B was used to monitor the temperature of the output window. In addition, the waterload/pre-attenuator system described in Section V was used for CW operation.

The initial plan for the CW tests of X-6 was to slowly bring the tube up to higher and higher power levels while continually monitoring the window temperature. Tests were performed using 2-3% magnetic tapers across the cavity, because of the stable operation exhibited during pulse testing with these tapers. During CW testing, the temperature of the window was to be kept less than 100°C.

In Figure 355, output power is plotted versus main magnet #1 current for a 3% magnetic taper. These results are similar to those of Figure 345 for pulse operation except the efficiencies are higher than those observed during pulse testing. In Figure 356, output power versus gun anode voltage is plotted for the case of a 3% magnetic taper and a beam current of 4.9 A. A similar curve, but varying beam voltage instead of gun anode voltage, is shown in Figure 357. In Figure 358, the dependence of output power on beam current for a maximum current of 5 A is plotted. Figure 359 shows a plot of power detected in the body water circuit as a function of output power for a current of 3 A. Theory predicts between 2 to 3 kW of power loss in the cavity at 100 kW, so the measurements were in agreement. In all of these curves, it was possible to operate with window temperatures of less than 100°C. However, it was noticed that for different combinations of parameters (slightly different frequencies), the window temperature would vary markedly for similar output power levels. Because of this phenomenon, the output power level was very carefully increased by adjusting the gun anode voltage, main magnet #1 current, and beam current. Window temperatures were kept to less than 100°C.

Finally, at 4:05 pm on June 8, 1983, the beam current was raised to 7.2 A, enabling the power level to reach 206 kW while retaining a window

ORNL – DWG – 83-3253 FED

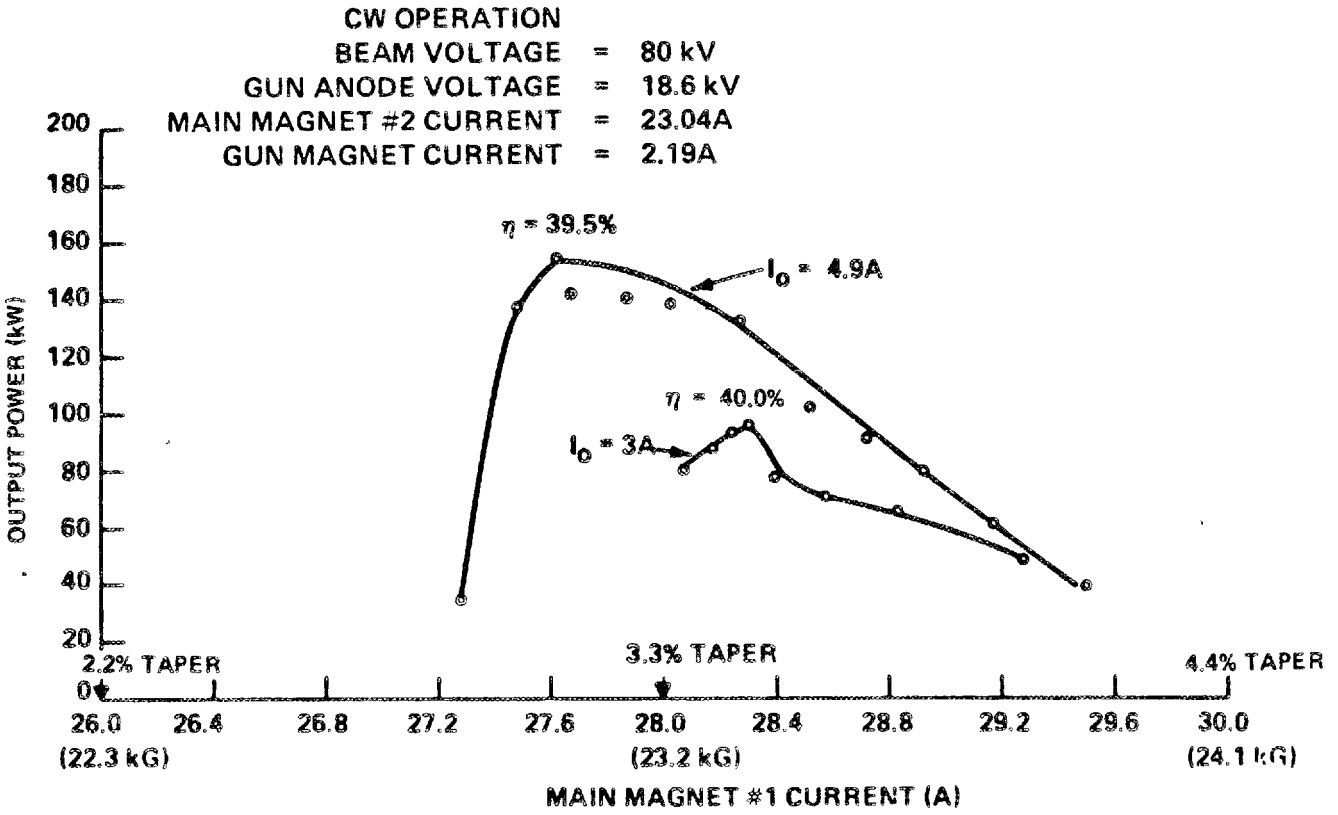

Figure 355. Output Power VS Main Magnet No. 1 Current with a 3% Magnetic Taper Across the Cavity for Two Values of Beam Current. The Tests Were Performed on the VGE-8006, S/N X-6 During CW Operation.

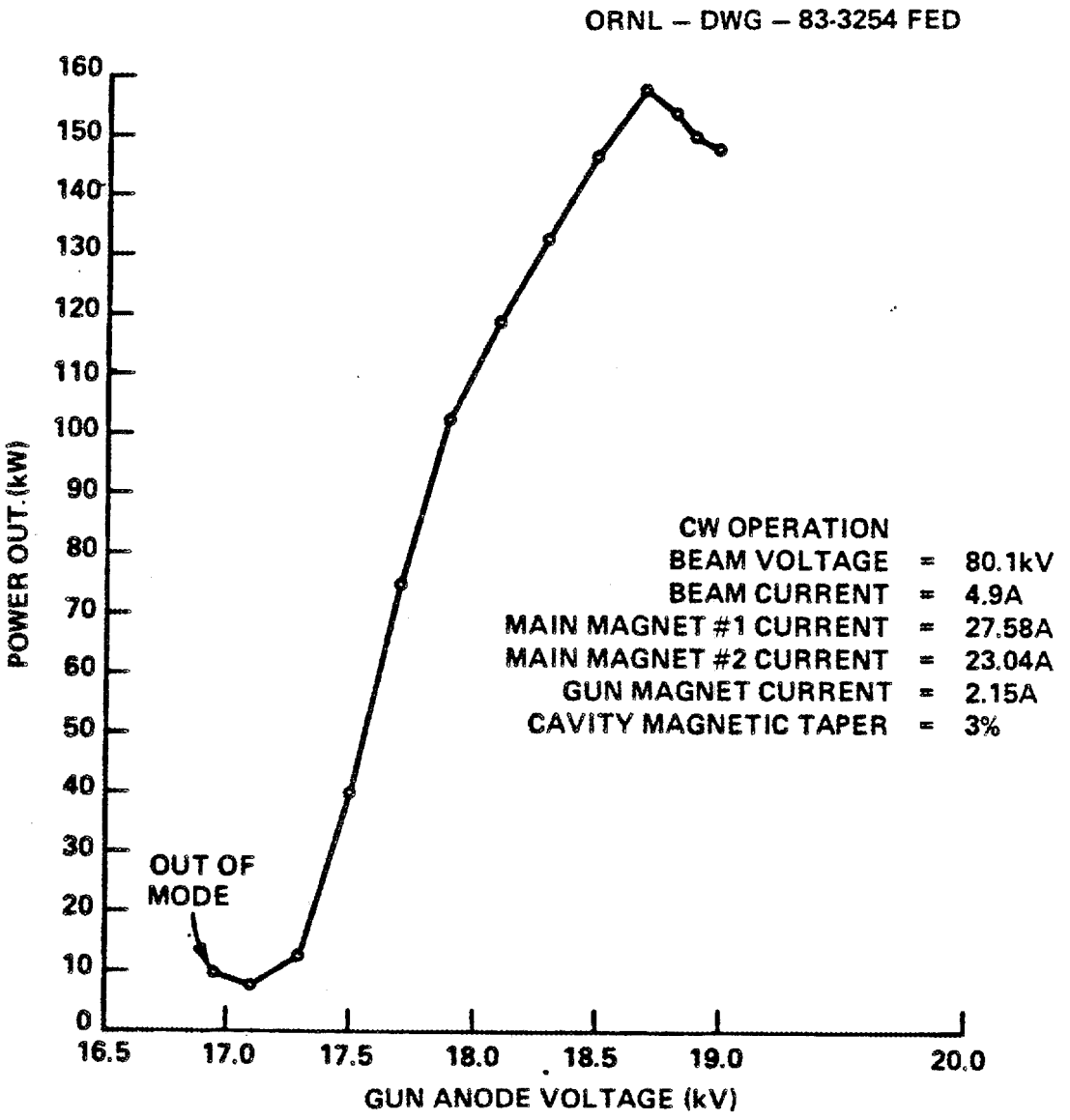

Figure 356. Output Power VS Gun Anode Voltage with a Magnetic Taper of 3% Across the Cavity for a Beam Current of 4.9A. The Tests were Performed on the VGE-8006, S/N X-6 During CW Operation.

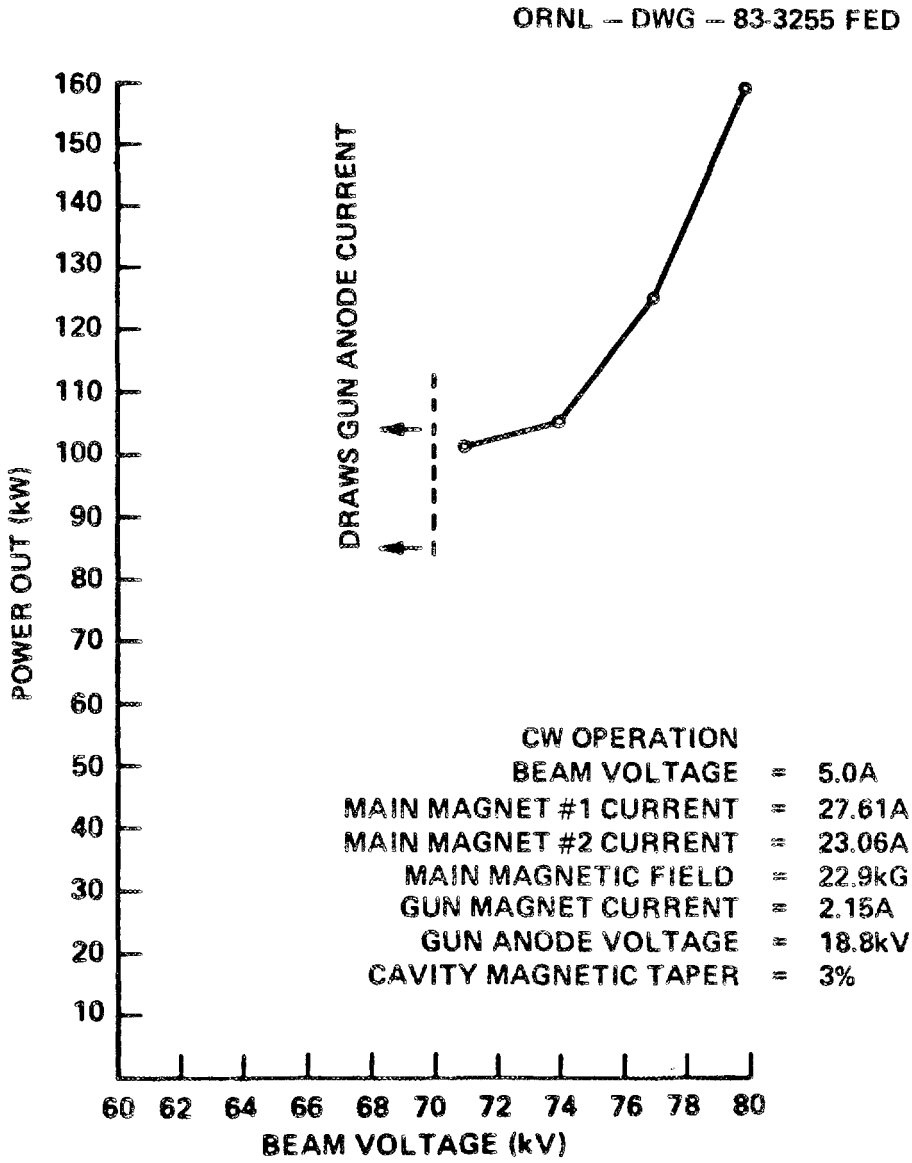

Figure 357. Output Power VS Beam Voltage with a Cavity Magnetic Taper of 3% for a Beam Current of 5A. The Tests were Performed on the VGE-8006, S/N S-6 During CW Operation.

ORNL – DWG – 83-3256 FED

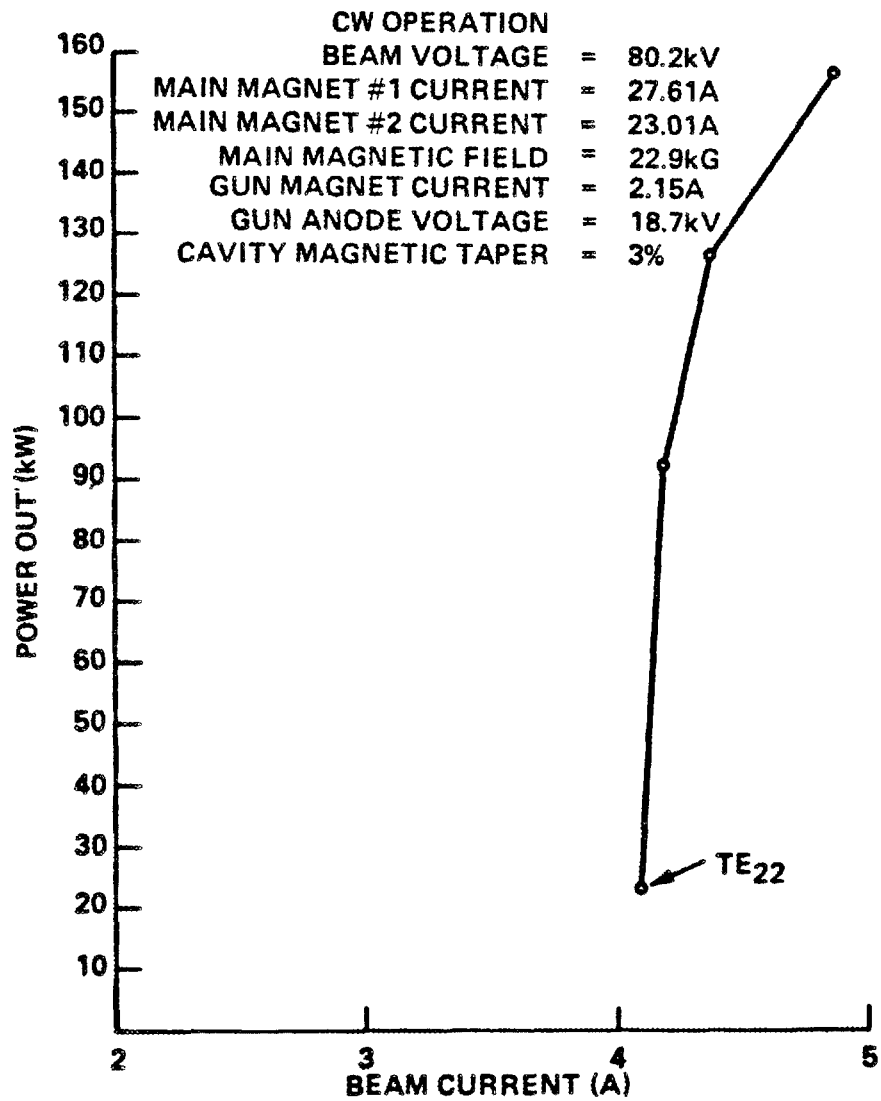

Figure 358. Output Power VS Beam Current with a 3% Magnetic Taper Across the Cavity for the VGE-8006, S/N X-6 in CW Operation

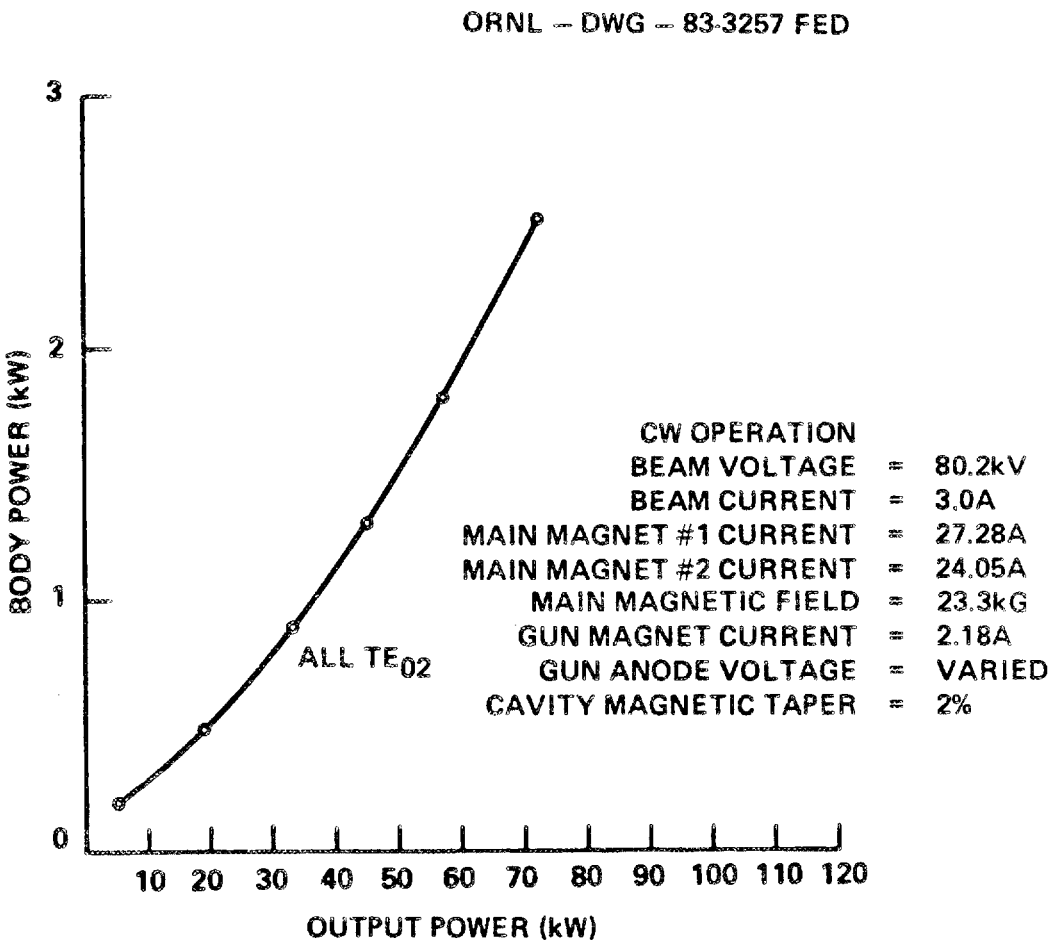

Figure 359. Body Power (Cavity and Beam Tunnel Losses) VS Output Power with a Magnetic Taper of 2% for a Beam Current of 3A. Power was Varied by Changing the Gun Anode Voltage on the VGE-8006, S/N X-6 During CW Operation.

temperature of between 95° - 100°C. The tube ran smoothly at a 200+ kW level for 25 minutes before a crowbar halted tube operation. The tube was quickly brought back to the 200 kW level where it remained for another 35 minutes before the tube was intentionally turned off. In all, one hour of operation at a power level in excess of 200 kW was achieved. Operating parameters for 200 kW operation are shown in Table 49.

Table 49
Operating Parameters for 200 kW CW
Operation of VGE-8006 S/N X-6

Output Power	=	206 kW
Frequency	=	59.82 GHz
Beam Voltage	=	80.3 kV
Gun Anode Voltage	=	18.6 kV
Beam Current	=	7.2 A
Main Magnet #1 Current	=	27.44 A
Main Magnet #2 Current	=	23.09 A
Gun Magnet Current	=	2.21 A
Efficiency	=	35.6%
Duty Factor	=	100% (CW)

FC-75 Power Loss = 2.14 kW
Peak Window Temperature = 100°C

Following the achievement of 200 kW CW, further investigations of the effects of parameter variation on window temperatures were carried out. A plot of the peak window temperature as a function of main magnet #1 current for an output power of 120 kW, was shown in Section VIII. The power was kept at 120 kW by varying the gun anode voltage. There was a drastic change in temperature (~20°C) for a relatively small change in magnetic field ($\lesssim$ 1%). Unfortunately, further testing of this phenomenon was delayed due to a failure in the IR camera system. The causes of this drastic change are believed to be due to changes in the relative phases of the output mode mixture due to changes in operating frequency. A change of 20-30 MHz in frequency was observed over the magnetic field range investigated. Further studies of the output mode purity and additional IR measurements helped explain this behavior.

A compilation of all window temperature measurements made on X-6 were plotted as a function of power in Section VIII. Variations in room

temperature and FC-75 temperature were pointed out. The FC-75 temperatures varied due to the installation of a chiller enabling use of FC-75 with a bulk temperature of ~ 10 - 20°C. A plot of FC-75 ΔT as a function of output power is shown in Figure 360. The line labeled 8.7 gpm denotes unchilled FC-75 and the 8.5 gpm line denotes chilled FC-75. The chiller caused an additional pressure drop which cut the flow rate by 0.2 gpm. Further discussion of the FC-75 chiller is included in Section VIII.

In summarizing the CW test results of X-6, operation at 200 kW CW represented the achievement of a major goal of the 60 GHz Development Program. In attaining 200 kW CW, the IR window monitoring system was found to be invaluable. The step cavity added a wide range of parametric flexibility to the performance of the tube, which allowed careful evaluation of the window temperature under a wide variety of operating conditions. In addition, the FC-75 chiller and the waterload/pre-attenuator were important in ultimately reaching 200 kW CW. In further tests on X-6, improved understanding of the output mode purity and the role of changes of operating parameters on the peak window temperature were the central areas of investigation.

5. Mode Content Measurements

Several methods were employed to make qualitative and quantitative measurements of the mode content of the microwave output of X-6. Initial tests were made by placing thermal sensitive paper in the 2.5-inch diameter output waveguide. 3M Infrared Copy Paper Type II was used. By limiting the tube to a few pulses, a mode pattern was obtained without burning the paper. However, in the presence of only a small amount of mode impurity (TE_{on} modes other than the TE_{02} mode), such mode patterns give relatively little information about the actual composition of the mode mixture. The relative phasing of the different modes drastically affected the apparent mode pattern at a given longitudinal plane. To obtain additional information, mode patterns were made simultaneously over a distance along the guide comparable to the beat wavelengths for the TE_{on} modes of interest. These measurements enabled identification of the modes comprising the microwave output of the tube. The mode patterns on the thermal paper indicated the

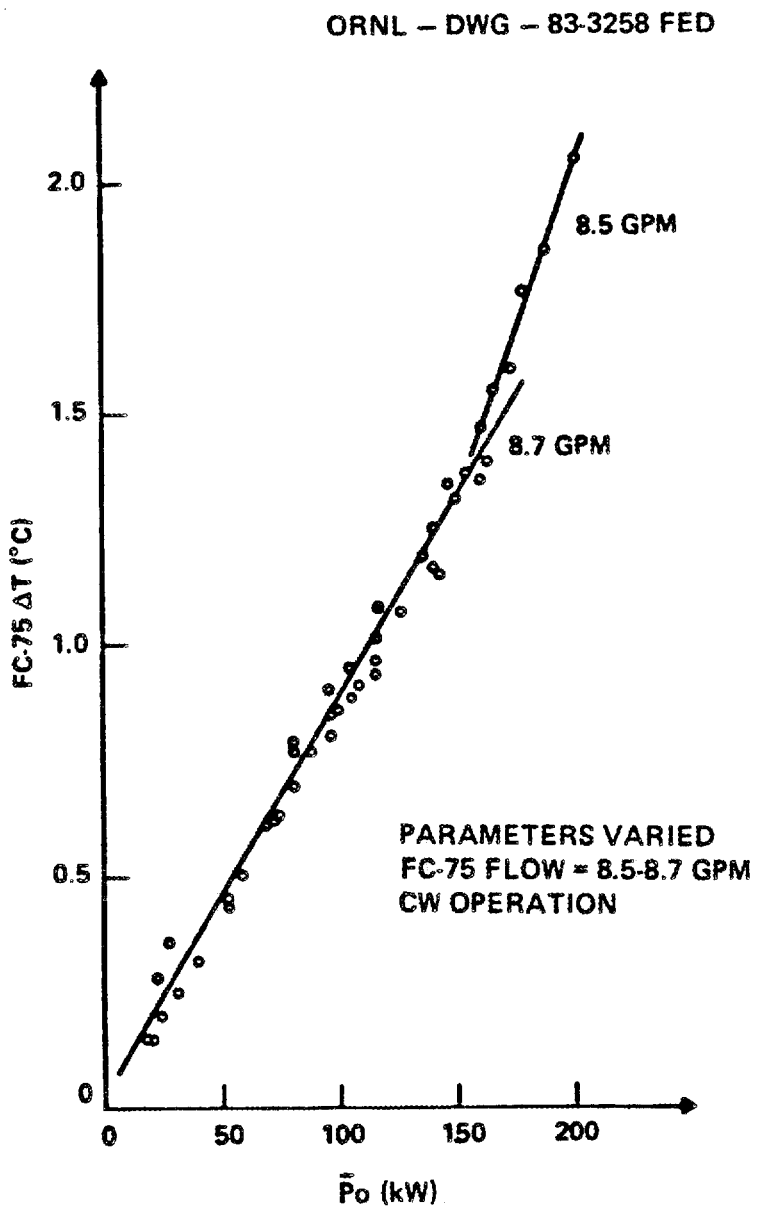

Figure 360. FC-75 ΔT (Outlet Temperature - Inlet Temperature) as a Function of Output Power for the VGE-8006, S/N X-6, During CW Operation. All Combinations of Tube Parameters are Included in the Plot.

presence of the TE_{01} and TE_{03} modes, as well as the TE_{02} mode. Unfortunately, quantitative measurements were not practical using this technique because of the limited gray scale of the thermal paper.

To gain quantitative information on the mode content of X-6, measurements were made using mode-selective directional couplers, designed and constructed by GA Technologies, to couple to different TE_{on} modes[46,47]. These couplers were loaned to Varian by GA Technologies. Relative calibrations of the couplers were obtained by GA Technologies by analyzing the calculable output of a step transition. Absolute calibrations were made using phase velocity transducers to the fundamental rectangular waveguide mode. The assistance of Dr. Charles Moeller of GA Technologies in furnishing the couplers and participating in the actual measurements on X-6 is gratefully acknowledged.

Figure 361 shows a schematic diagram of the experimental setup using the couplers to measure the mode content. The tapers and waveguide bend convert less than 3% of the incident mode. Measurements on X-6 indicated that as much as 86 - 88% of the output mode consisted of the TE_{01} and TE_{03} modes, while the TE_{02} mode represented about 12-14%. The TE_{04} mode contributed less than 1% to the mode mixture. The approximate contributions of the TE_{01} and TE_{03} modes were 38% and 48%, respectively. Measurements were taken for several different combinations of tube parameters. Relative variations in mode content of 30% were observed for different parametric combinations, though no specific trends were identified. (The percentages listed above represent average values.) To further isolate the cause of the mode conversion, tests were performed on a pulse tube. These measurements are discussed in Section VIII.

6. Additional CW Test Results

Following the mode measurements performed under pulse conditions, additional CW tests of X-6 were carried out to further characterize the tube during high power CW operation. Early in these tests, the outer window disc failed because of operation with an acoustic probe in the guide, previously discussed in the window section. The ceramic disc was quickly replaced and

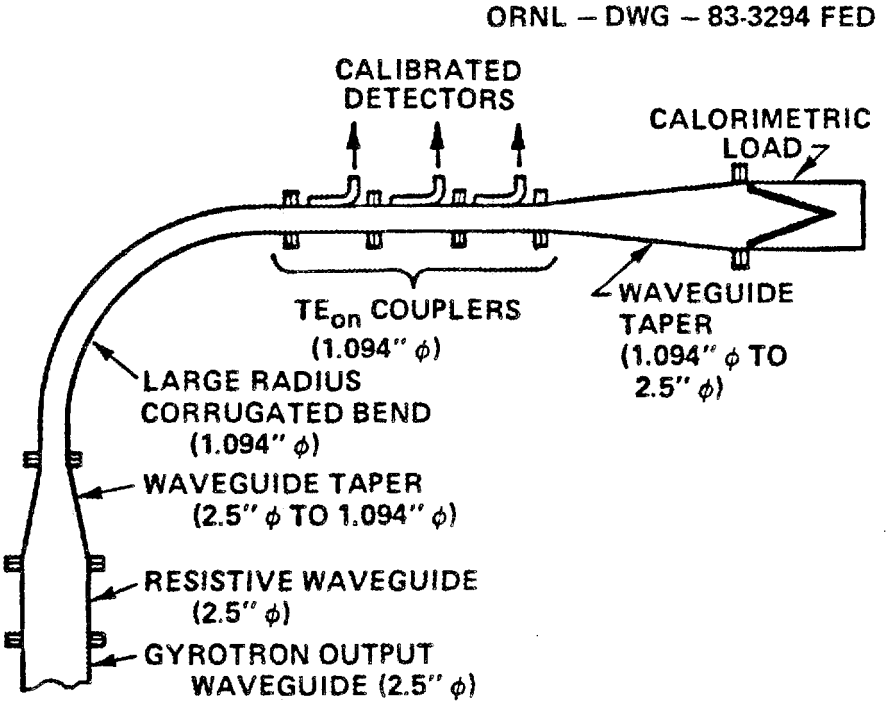

Figure 361. Schematic of Experimental Set-Up for Mode Content Measurements on X-6 Using Mode Selective Directional Couplers Furnished by GA Technologies

the tube was brought up to power in CW operation. In Figures 362 and 363, output power is plotted as a function of beam current and gun anode voltage, respectively. The curves are similar to those obtained during pulse operation. Following these tests, on August 12, 1983, the tube was operated continuously for one hour without interruption at a power level which varied between 210 kW and 214 kW CW. This concluded the tests on X-6.

H. VGE-8006A S/N 101

1. Salient Features

The measurements of the mode content of the output of X-6, reported in the previous section, indicated insufficient mode purity to satisfy the experimental requirements of the major gyrotron users. To improve this situation, it had to be determined if the mode conversion was being caused by the CW collector geometry, the step cavity, or a combination of the two.

Theoretical calculations reported in an earlier section indicated that the output of either the step cavity or the standard tapered cavity should be greater than 98% TE_{02}. The computations reported in the earlier collector section of this report strongly indicate that it is the CW collector geometry which caused the high levels of mode conversion measured on X-6.

To verify these conclusions, mode content measurements were made on a pulsed 60 GHz tube which incorporated the same step cavity as used on X-6. This tube was identical in all other respects to X-6, except for the collector and the output window. The effect of the output window on mode conversion is considered to be negligible, so this test provided a good indication of the relative mode purity of the two different collector designs. The X-6 collector consisted of a gaussian uptaper to a large diameter, followed by a gaussian downtaper to a 2.5-inch diameter waveguide. The pulsed tube collector consisted of a gradual linear taper to a 2.5-inch diameter waveguide.

ORNL – DWG – 83-3295 FED

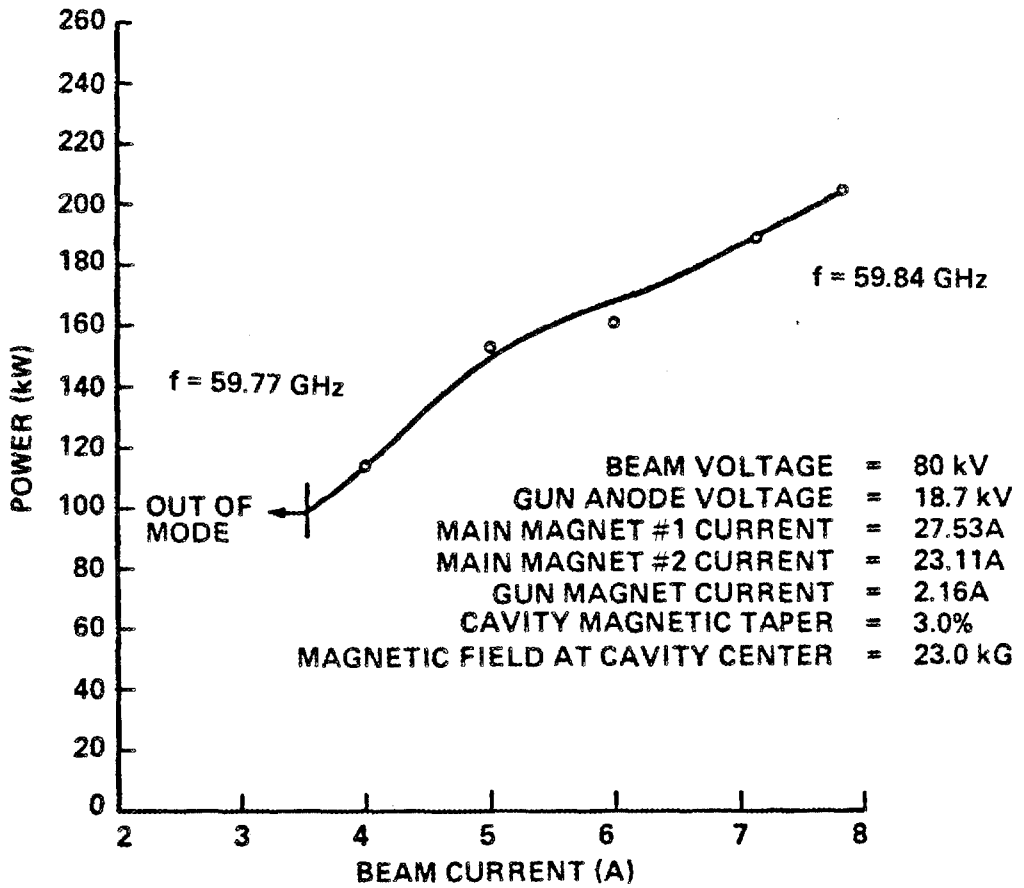

Figure 362. Power VS Beam Current for X-6 - CW Operation

ORNL – DWG – 83-3296 FED

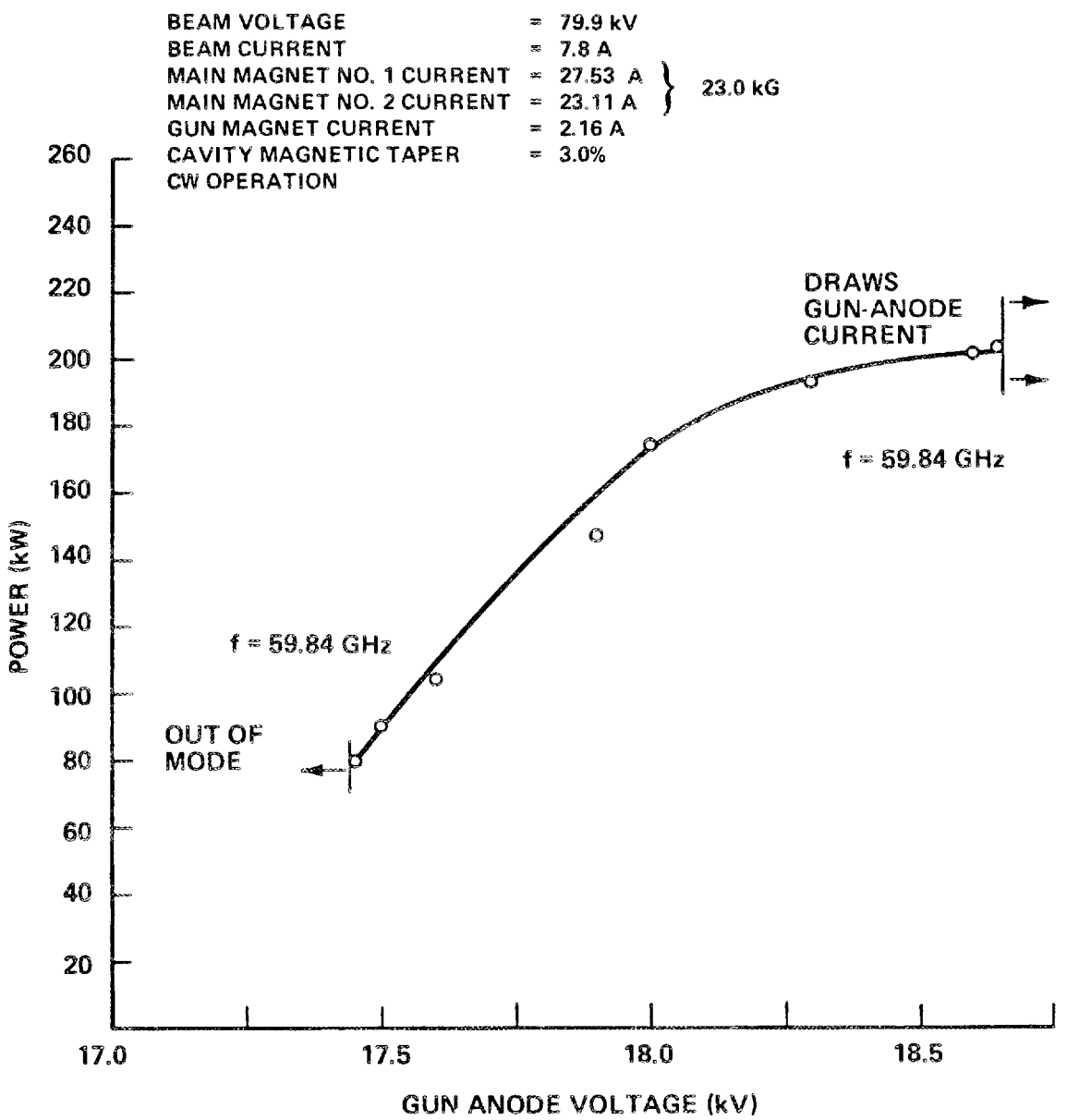

Figure 363. Power VS Gun-Anode Voltage for X-6 CW Operation

Using the directional coupler techniques described in the previous section, the mode content of the output of VGE-8060A, S/N 8 was measured with the help of Dr. Charles Moeller of GA Technologies. Using the TE_{01}, TE_{02} and TE_{03} couplers, the measurements indicated that 94% of the output was in the TE_{02} mode. Additional measurements were made using a TE_{02}, TE_{01} mode converter and a single TE_{01} coupler to eliminate the effect of variations in coupler calibration. These measurements indicated 90% of the output was in the TE_{02} mode. Both of these results agreed reasonably well with the theoretical value of 93%. Based upon these results, it was concluded that the large amount of mode conversion observed in the output of X-6 was due to the CW collector geometry, not the step cavity.

To arrive at a short term solution to this problem, VGE-8006A, S/N 101 was built identically to X-6 except that an extended length pulsed tube collector was substituted for the normal CW collector. Proper profiling and alignment of the collector magnetic field was investigated to reduce the power densities on the inside surface of the collector to a level which would allow reliable CW operation. To monitor the power densities on the inside surface, the transient temperature rise from a single beam pulse with no cooling water flow was measured.

2. Beam Distribution Measurements

Beam distribution in the collector was determined by measuring the temperature rise on the outside wall of the collector. This method required operation of the collector with the cooling water off. A single pulse was initiated and the temperature rise as a function of time was measured at various locations along the collector. The temperature increases were then compared to theoretical predictions to infer the incident heat flux. The major limitation of this technique was the transverse diffusion of the heat, ignored in the theory. The heat from a hot spot will diffuse to cooler areas of the collector. This smooths the measured power distribution and makes the hot spots seem cooler than they actually are. Despite this limitation, the technique is valuable in providing a relative indication of

the power density at the various points along the collector. This information is used to profile the collector magnetic field to obtain more uniform power distribution.

To illustrate the effect of the transverse diffusion of heat, an oscilloscope picture of ΔT versus time for two sensors is given in Figure 364. The bottom trace is of a relative hot spot on the collector. The temperature quickly rises to its peak value and then starts to decline as the heat diffuses away. The time constant of the temperature rise is 2 to 3 seconds which is in good agreement with the theoretical prediction. The upper trace represents a cooler area of the collector. The temperature rises gradually over the length of the oscilloscope trace (20 seconds total). This is caused by the heat from neighboring hot spots diffusing into the area monitored by this sensor.

The measurements on 101 were performed at a pulse duration of 5 ms. This pulse duration was chosen because it is long enough to give a measurable temperature rise and short enough to minimize the risk to the collector with the cooling water off. Three collector coils were installed to profile the collector magnetic field for an even beam distribution. The top coil in the stack was operated in reverse polarity to cancel out the fringe magnetic field in the upper collector region. This is to prevent damage to the top of the collector. The other two coils were positioned below the bucking coil and could be adjusted for maximum axial spreading of the beam.

The initial series of measurements indicated that the power densities near the bottom of the collector were too high for safe operation. The removal of the iron pole piece at the top of the magnet dewar and the use of the bottom collector coil as an aiding coil helped to reduce this power density to a safer level. A graph of power density versus aiding coil current for a sensor near the bottom of the collector is given in Figure 365. The power density in this area was reduced 40% by using the aiding coil.

ORNL-PHOTO-0098-83

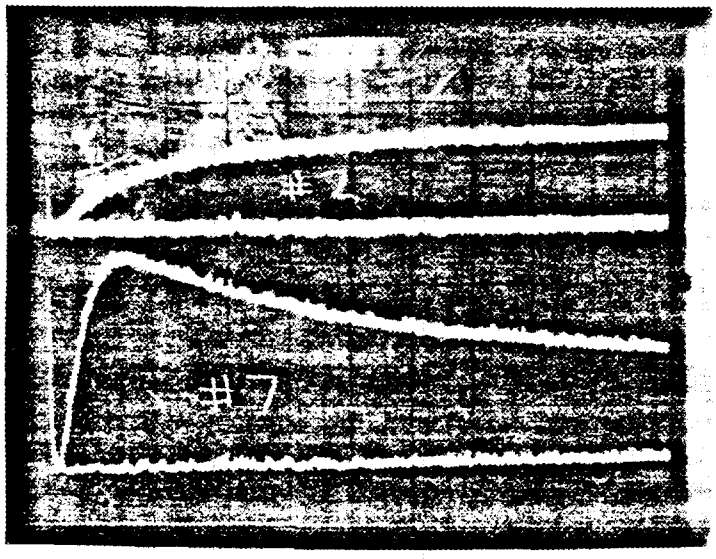

Figure 364. Temperature VS Time for Two Sensor Positions

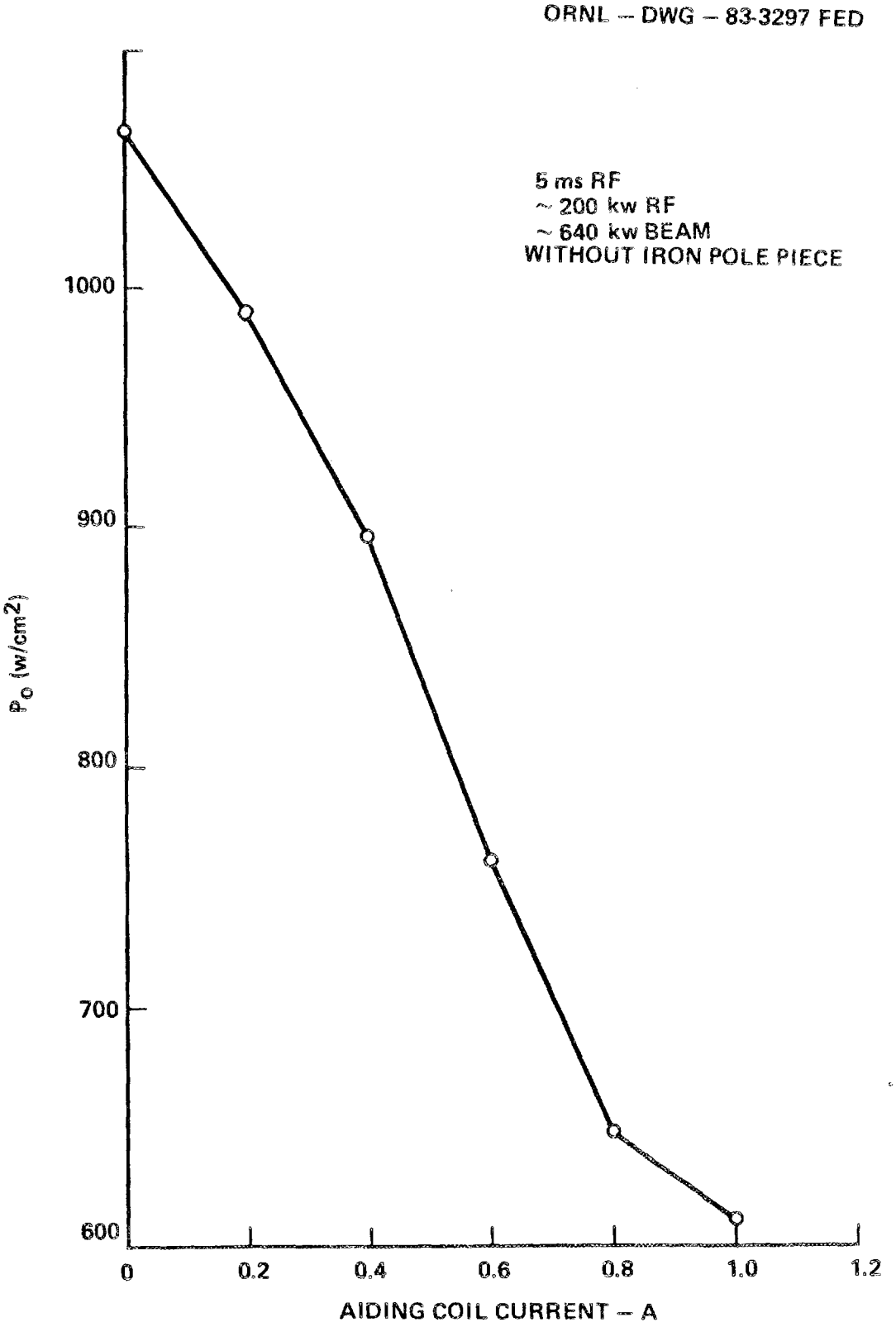

Figure 365. Peak Heat Flux VS Aiding Coil Current

The second major area of investigation was the asymmetric collection of the beam. It was expected that slight misalignment of the collector and magnetic field axes would cause azimuthal asymmetries in the collector power density. To check asymmetries, four sensors were placed around the bottom of the collector. A factor of four was observed in the indicated power density for two sensors 180° apart. To improve the alignment of the collector and magnetic field axes and reduce the asymmetrical collection, the tube was tilted using an adjustable support plate. The removal of a steel water fitting located near the collector also helped improve the symmetry of the beam collection. In the final configuration, the temperature difference between opposite sensors was reduced from a factor of 4 to a factor of 2.5, but complete symmetry could not be achieved.

In this configuration, an axial profile was made of collector power density in each of four directions. These data are given in Figures 366 and 367. The graph in Figure 366 shows the power density profile for 640 kw of beam power and 200 kw of rf output. Z = 0 corresponds to the support surface for the tube at the top of the magnet. Most of the beam is still being collected in the lower portion of the collector. A peak power density of 900 w/cm^2 is indicated. This value is within the cooling capacity of this collector geometry. However, there is significant concern that the true peak power density may actually be higher because of calibration problems and limited spatial resolution of the measurement technique. Figure 367 gives the same information as Figure 366 except that in this case there is no rf output power. The peak indicated power density in this case is 1.3 kw/cm^2.

To check the accuracy of the graphs, a numerical integration of the power density profile over the inside collector surface was performed. In both cases, the integrated power was exactly 26% below what would be expected from the actual operating conditions. This indicates a repeatable systematic type of error in the measurement technique. One possible way to compensate for this error is to multiply the power density by a constant to bring the integrated power density into agreement with the actual operating conditions. When this technique was followed, peak power densities of

ORNL – DWG – 83-3298 FED

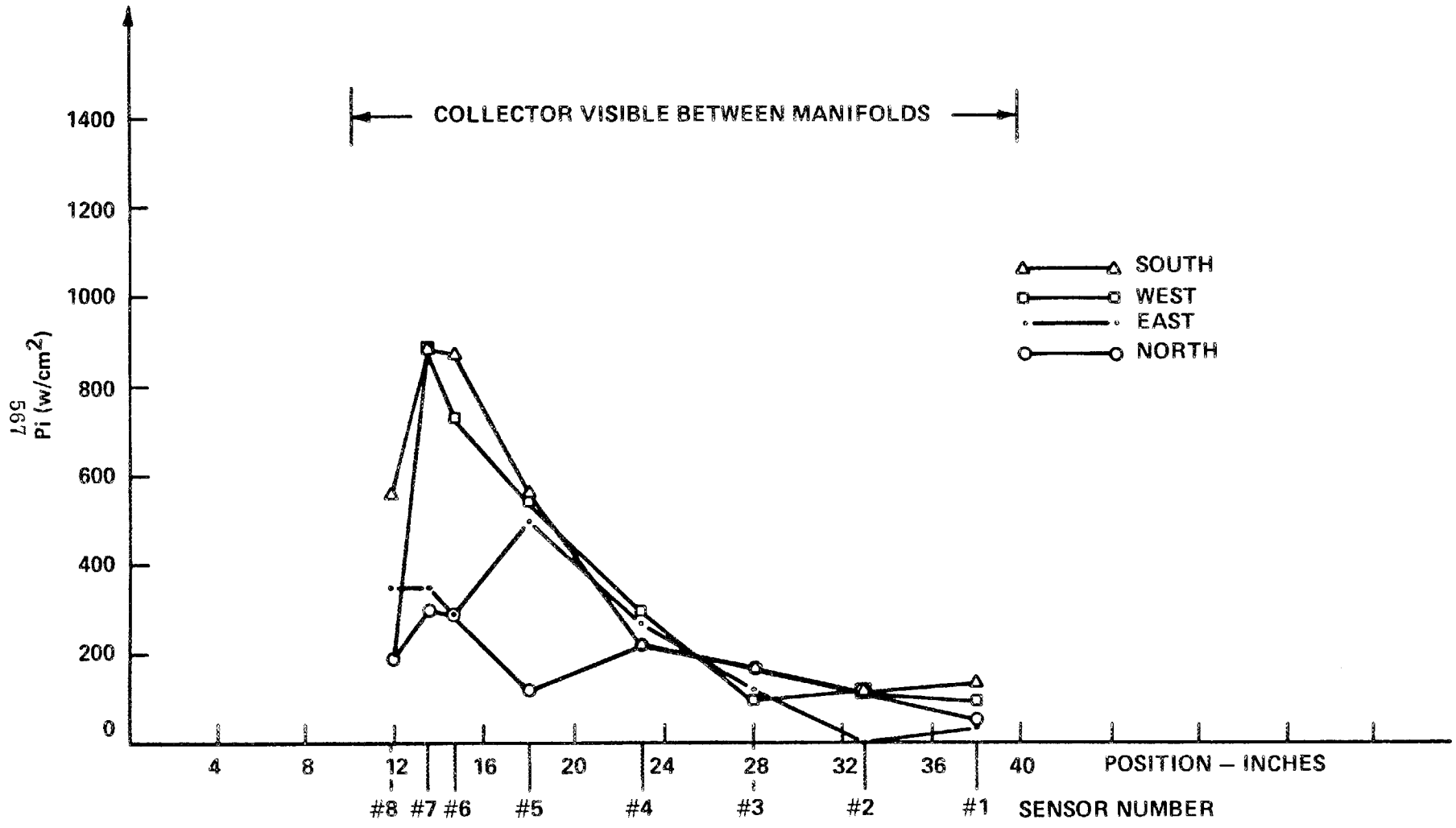

Figure 366. Incident Heat Flux VS Position VGE-8006A S/N 101, 5 ms RF Pulse, 640 kw Beam, 200 kw RF

ORNL – DWG – 83-3299 FED

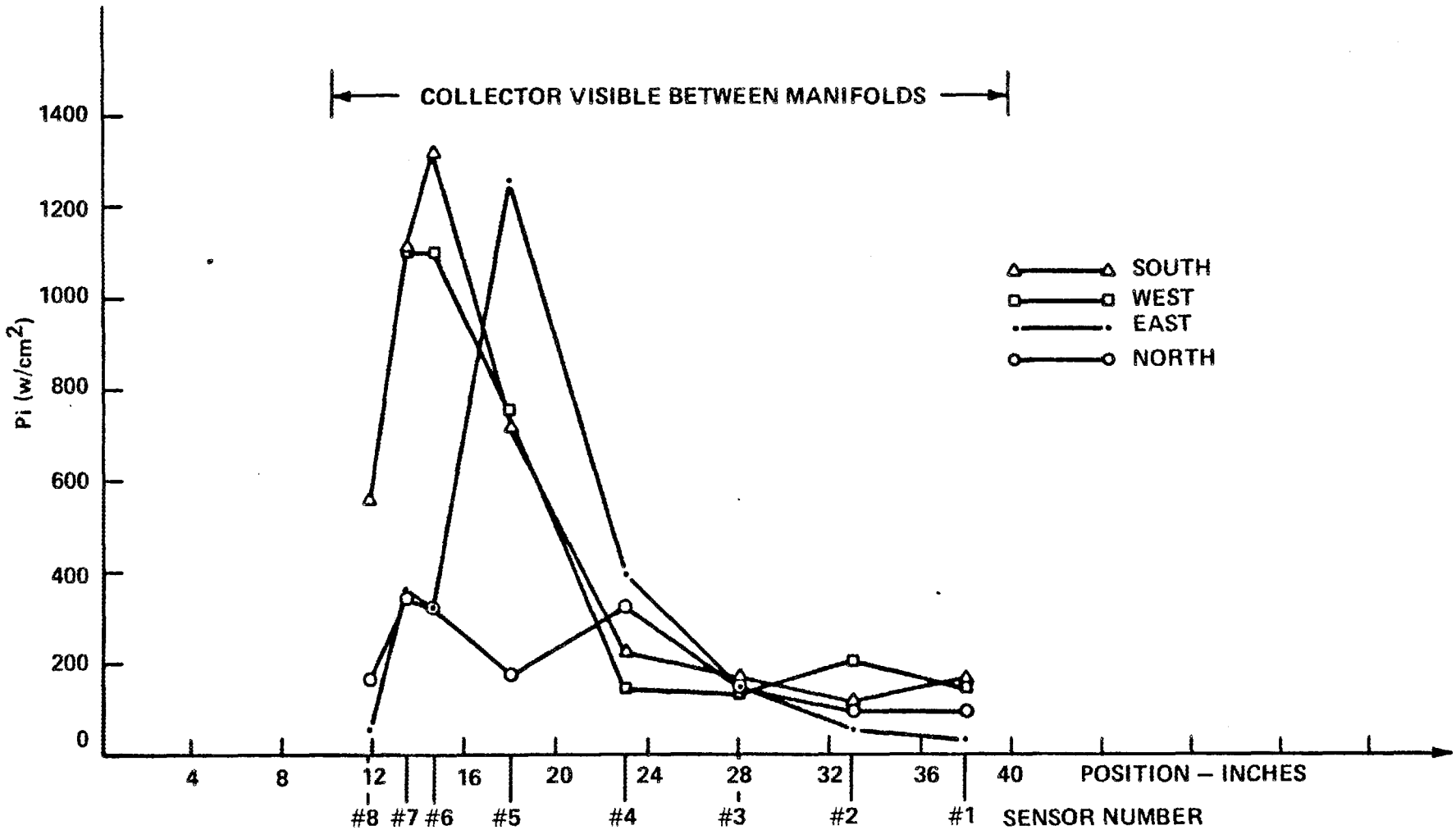

Figure 367. Incident Heat Flux VS Position VGE-8006A S/N 101, 5 ms Pulse, 640 kw Beam, no RF

1.2 kw/cm^2 for the rf case and 1.7 kw/cm^2 for the no rf case resulted. If these peak power densities actually existed, this arrangement of collector coils and collector geometry would be marginal for reliable CW operation.

There were two possibilities to bring the power densities down to a safe level. One was to lengthen the collector. This would allow the bucking coil to be moved higher up and still protect the upper portion of the collector. This, in turn, would allow more flexibility in adjusting the aiding field in the lower portion of the collector. The power density profile in this case would be more uniform and have a lower peak value. The other possibility was the alignment of the collector mechanical and magnetic axes. As can be seen in Figures 366 and 367, there were still some alignment problems. Various techniques to improve this situation were pursued. These included aligning the beam with respect to the beam tunnel and the installation of additional temperature sensors. The measurement technique was automated with a computerized data aquisition system. The loan of an Analog Devices MACSYM computer from Union Carbide Corporation Nuclear Division to get this work started is gratefully acknowledged. This allowed quick observation of the effects of any change in tube orientation on the collected power symmetry.

In summary, a technique was implemented on S/N 101 to measure the relative power densities at various positions along the collector. It was found that asymmetries and the need to protect the top of the collector were the major limitations to obtaining a uniform power density profile. Various measures were implemented to solve these problems and provide the low mode conversion and CW reliability required of this collector design.

3. Microwave Performance

The microwave performance of S/N 101 was very similar to X-6. The oscillation map is shown in Figure 368. Any TE_{22} modes are all at lower magnetic fields than those required for TE_{02} operation. As in X-6, the only competing modes are the 50 GHz modes, but they do not limit the dynamic range of the operating TE_{02} mode.

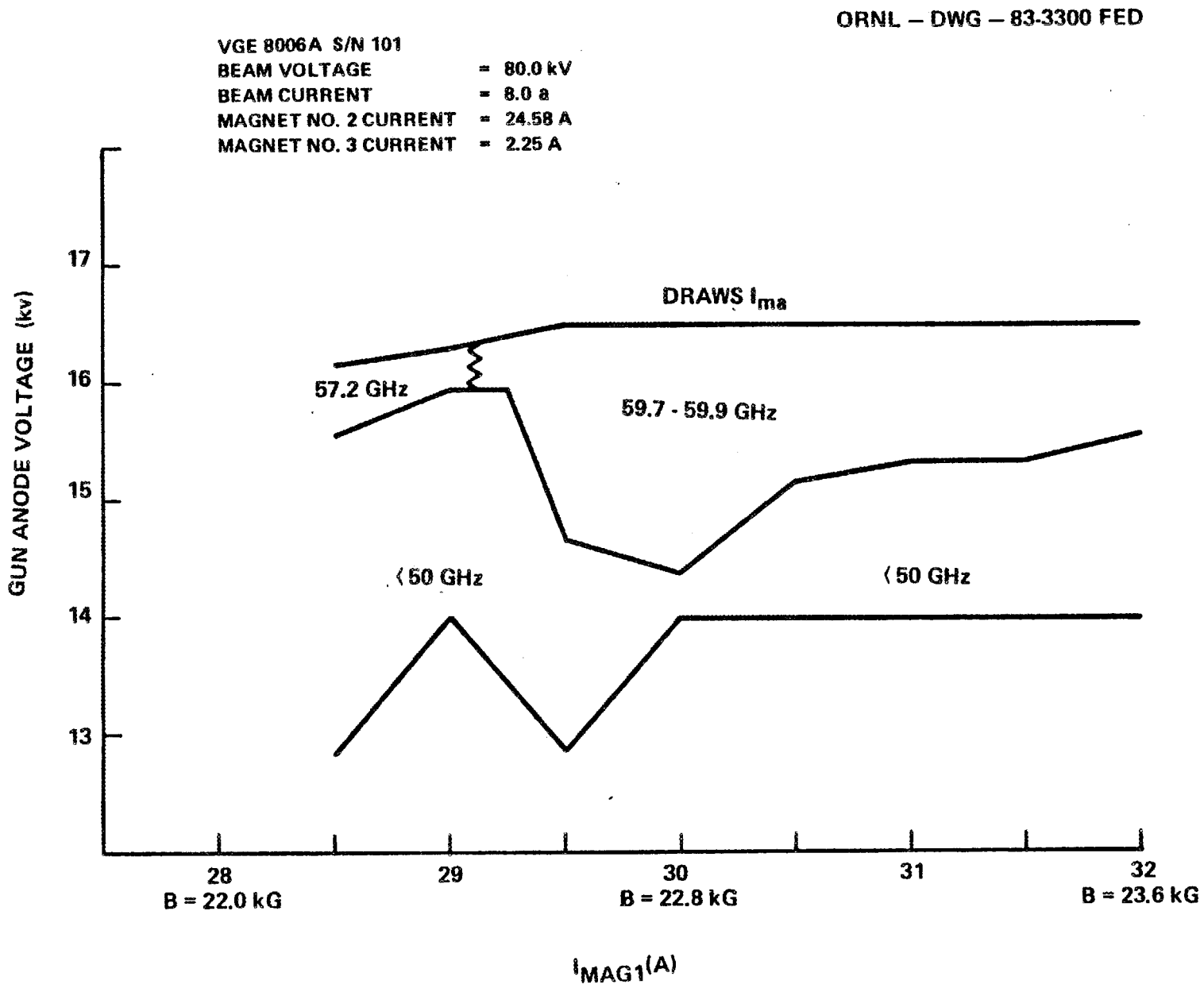

Figure 368. Oscillation Map

The maximum rf power obtained was 240 kw at an efficiency of 37.5%. This was with a magnetic field taper of 3%. At zero magnetic taper, the maximum rf power obtained was 190 kw at an efficiency of 29.7%. These results are similar to X-6 and are in good agreement with computer predictions.

Figure 369 shows the variation of power with gun anode voltage, and the large dynamic range exhibited by the step cavity. Figure 370 shows the variation of rf power with the gun magnet current. This follows the gun anode voltage curve very closely, as it should, since they should exhibit similar control over the transverse velocity. This is much more evident with the absence of the TE_{22} mode afforded by the step cavity.

Figures 371, 372 and 373 show the variation of rf power with Magnet No. 1 current, beam voltage and beam current, respectively. These curves are consistent between the conventional and step cavities.

The tube was initially aged in the long pulse mode to 5 msec. Several days were spent taking collector power density measurements. The tube was then taken to 500 msec pulse duration with rf. The single-pulse power measuring technique gave 205 kw at this pulse duration. The tube ran for over two hours with 500 ms pulsing without any crowbars. This was the pulse duration required by GA Technologies. S/N 101 was shipped to GA Technologies with two large collector coils.

I. VGE-8006A S/N 102

1. Salient Features

This was the second tube to be built and tested to solve the collector mode purity problem in a CW tube. The cavity used was step cavity #1, which exhibited excellent mode purity in previous measurements. The collector was the 2-1/2-inch diameter design with linear 2° tapers. The straight section of the collector was extended an additional 12 inches, giving an overall tube length of 103 inches, compared to 105 inches for X-5 and X-6.

ORNL – DWG – 83-3301 FED

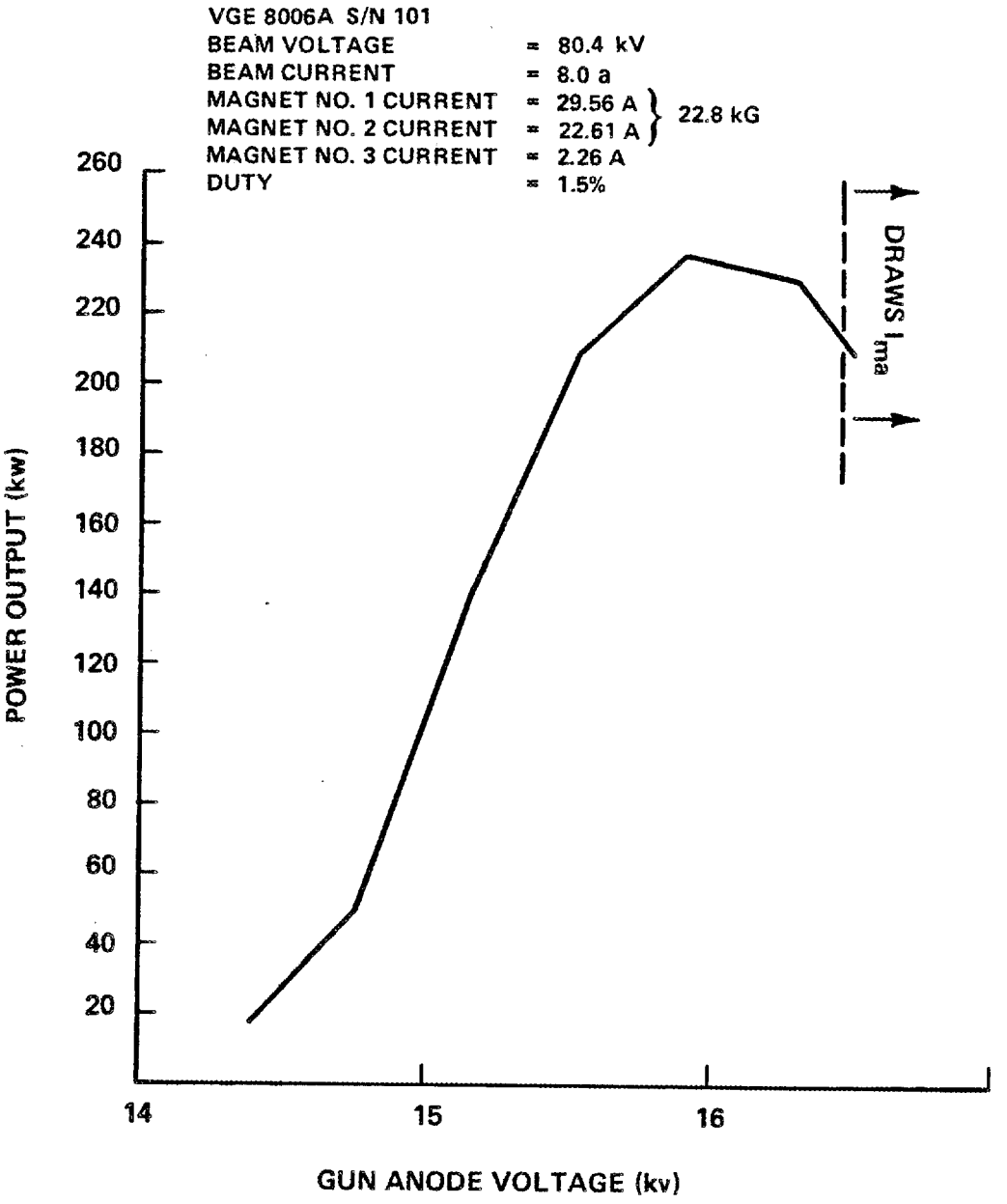

Figure 369. Peak Power Out VS Gun Anode Voltage

ORNL – DWG – 83-3302 FED

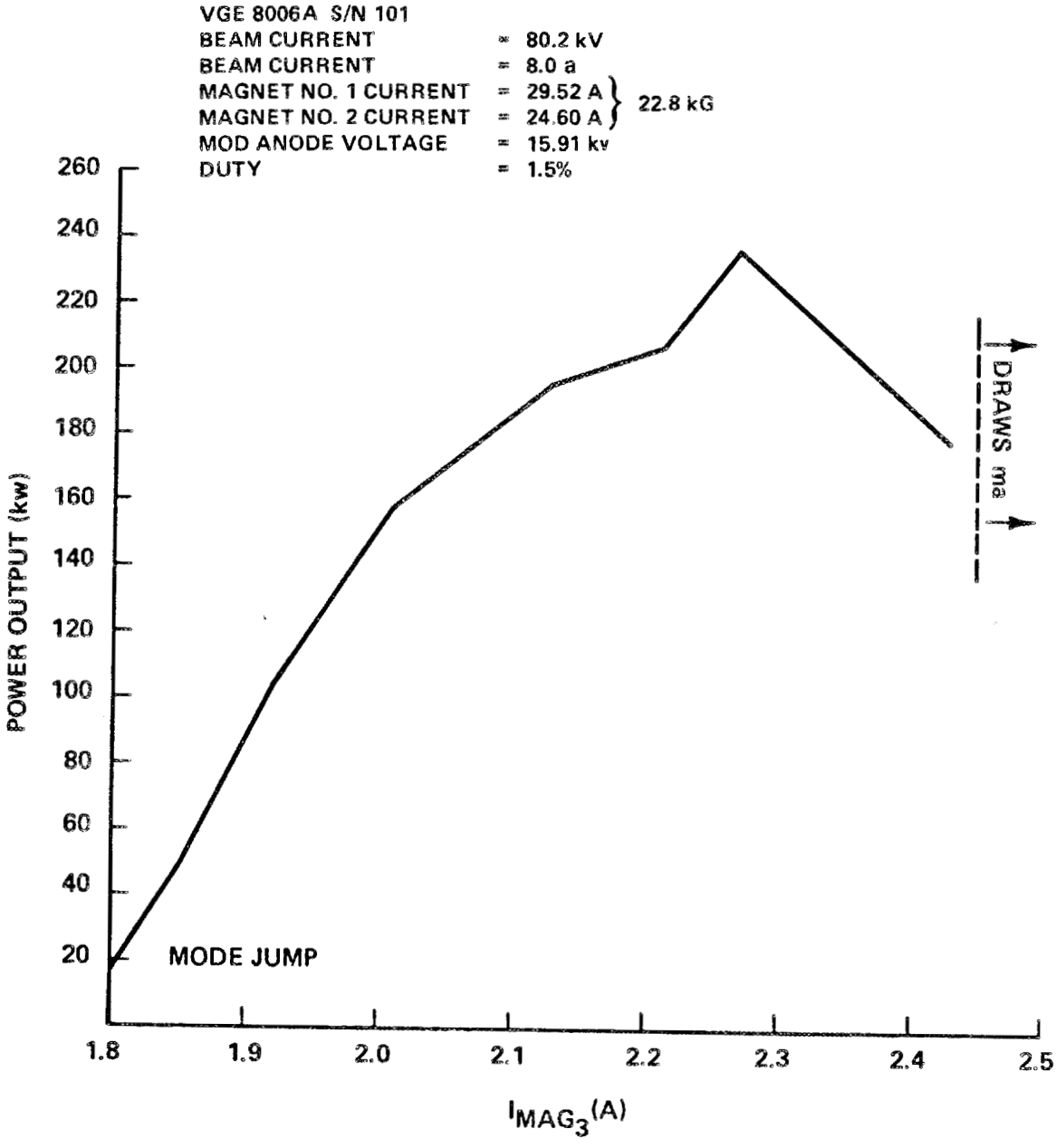

Figure 370. Peak Power Out VS Magnet No. 3 Current

ORNL – DWG – 83-3303 FED

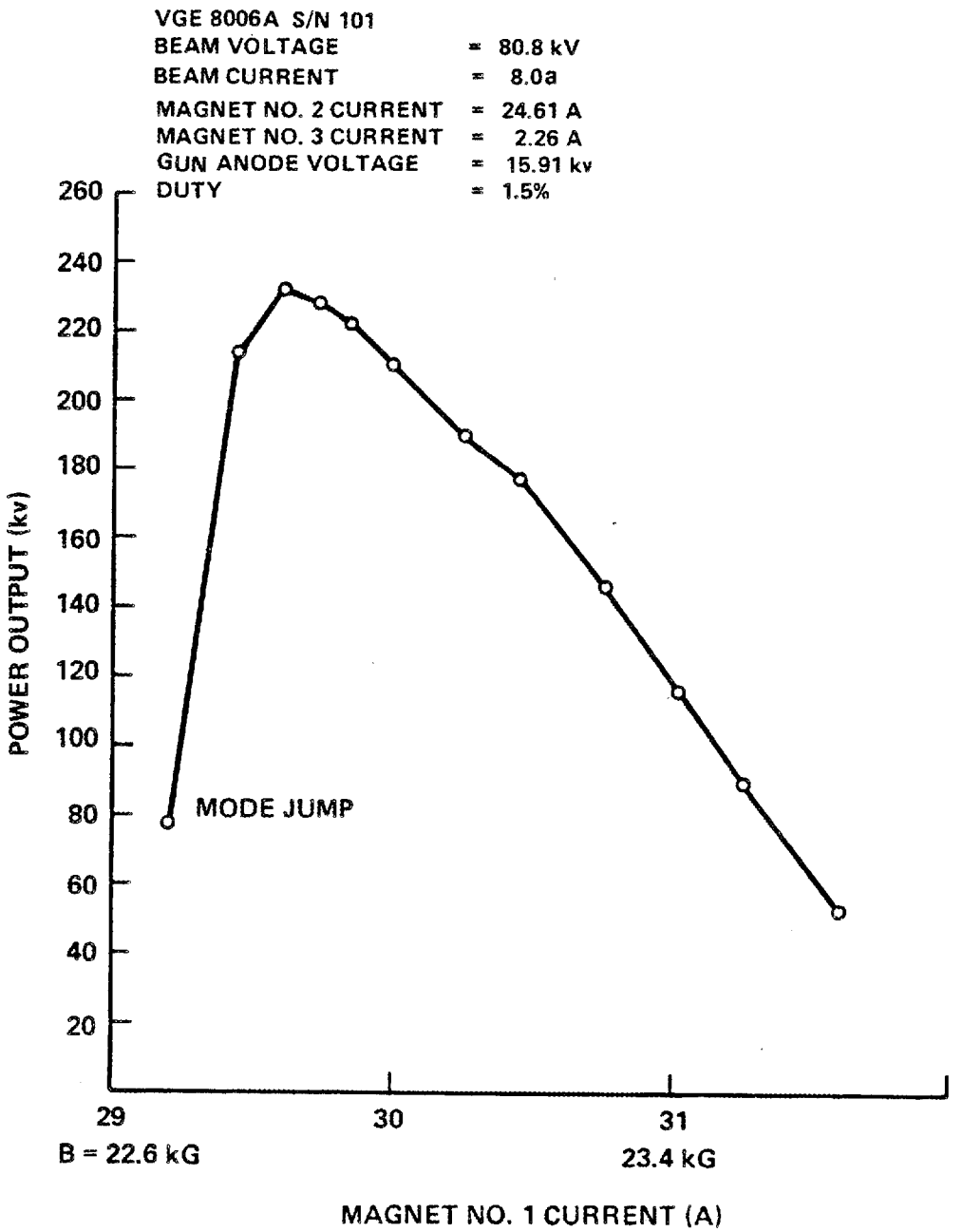

Figure 371. Peak Power Out VS Magnet No. 1 Current

ORNL – DWG – 83-3304 FED

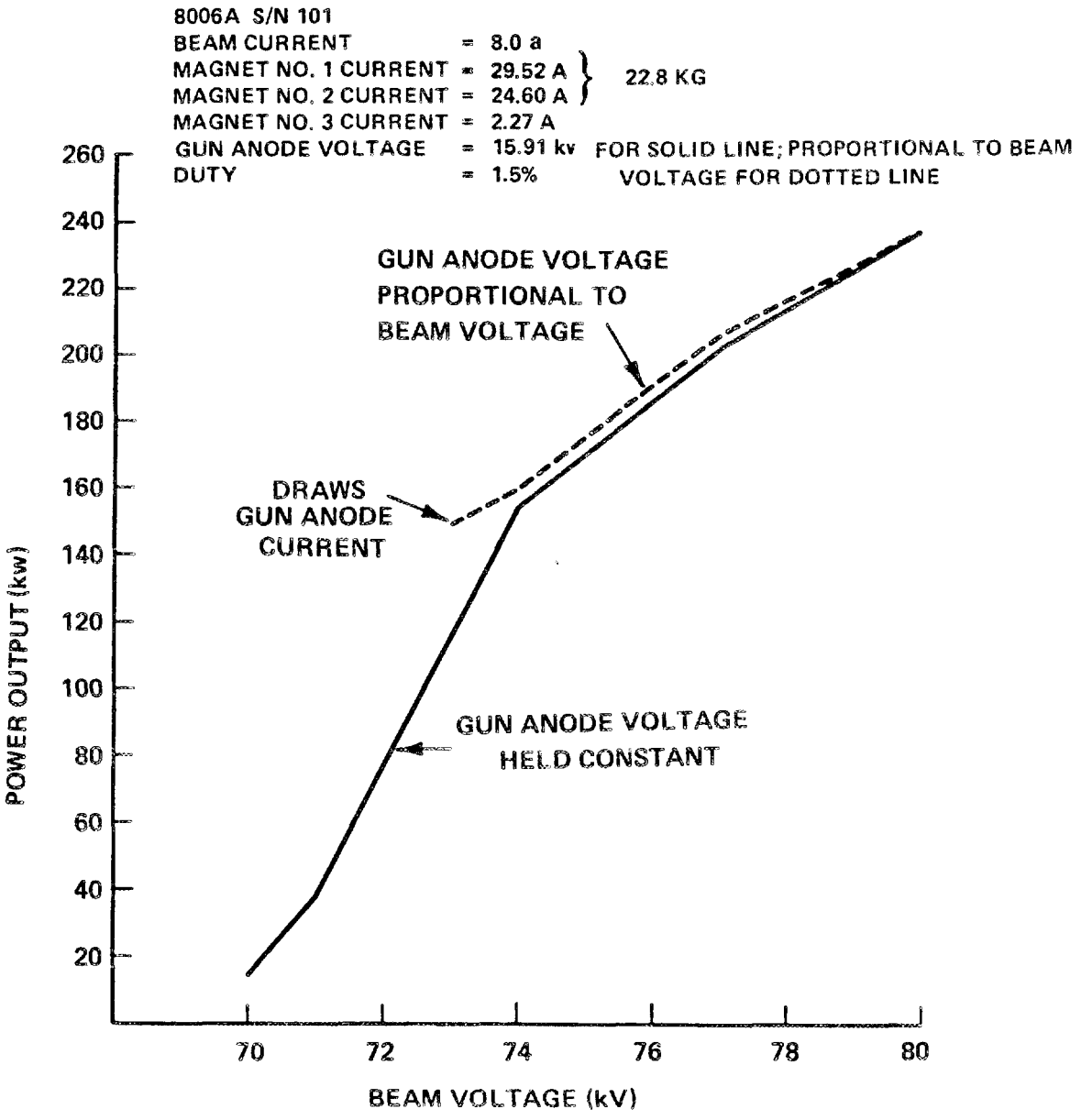

Figure 372. Peak Power Out VS Beam Voltage

ORNL – DWG – 83-3305 FED

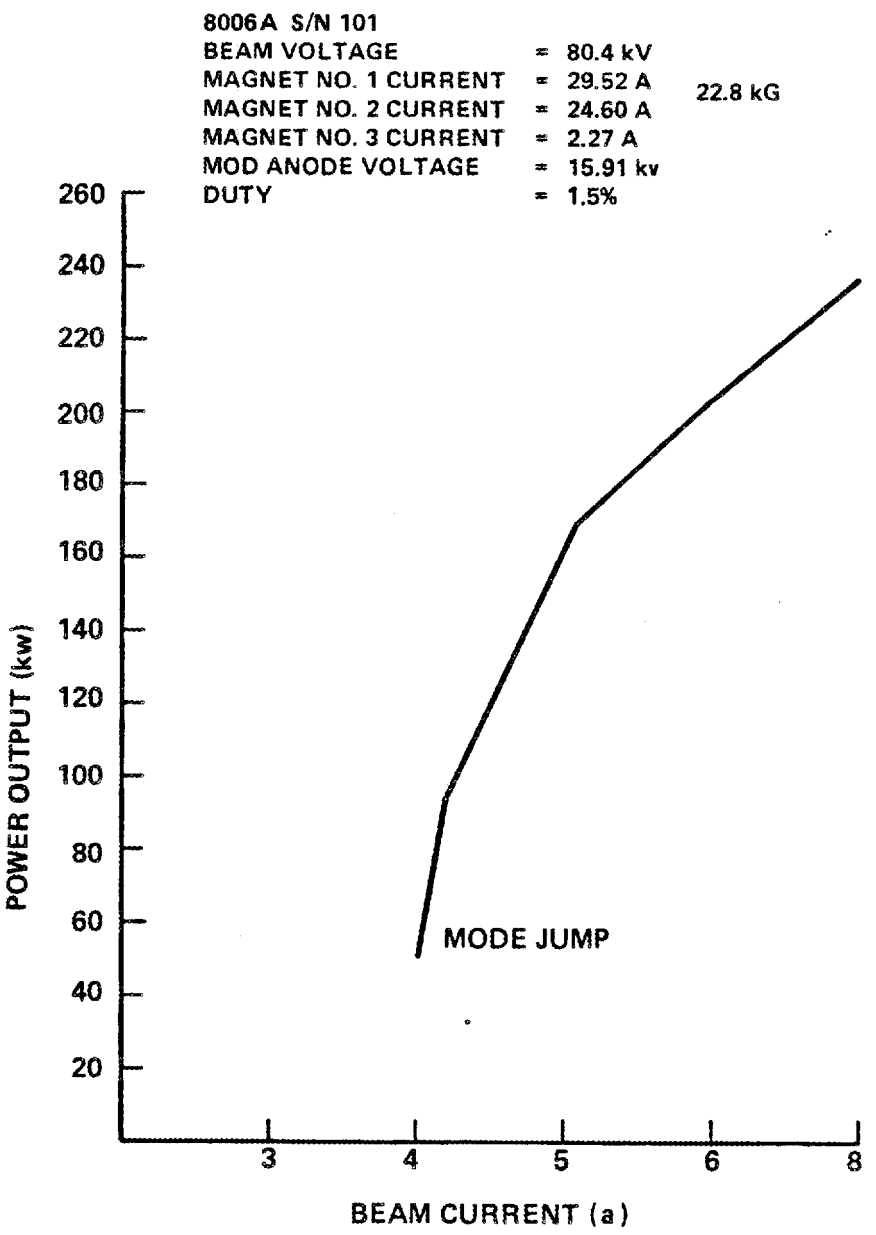

Figure 373. Peak Power Out VS Beam Current

2. Test Results

S/N 102 was first tested in the pulse mode to determine cavity characteristics and parameter variations. During this phase of the testing, mode purity measurements were made by C. Moeller of GAT (GA Technologies, Inc.) using the GAT couplers. Collector distribution measurements were taken which showed identical asymmetrical distribution on the same side as S/N 101. This strongly suggested an environmental or magnet problem rather than a tube alignment problem.

The best evidence of mode purity is shown in Figure 374. Plotted is the peak window temperature as measured by the IR camera as a function of main magnetic field. X-6 showed a 20°C change in window temperature, due principally to a combination of frequency shift and phasing of the various modes at the plane of the window. S/N 102, on the other hand, stayed nearly constant over the same excursion of magnetic field.

Figures 375 and 376 show the variation of power with gun anode voltage and gun coil current, respectively. In the absence of competition from the TE_{22} mode, the variation in power output is achievable with either gun anode voltage or gun coil current, as it should be.

S/N 102 was tested to 500 ms pulse duration. The emission cooling noted in S/N 101 was again seen in S/N 102 as a droop in cathode current of about 9% in 500 ms. Because of this, the cathode current at the leading edge of the pulse had to be increased to 8.4 a to average 200 kw across the pulse. To solve this problem, a heater pulser was developed which keeps the cathode current at a more constant level for long beam pulses.

3. CW Testing

S/N 102 was tested to 76 kW CW rf power at 80 kV and 2.5 A, at an efficiency of 38%. The window temperature at this level was 66°C. The test was terminated because of a very slowly increasing gas pressure. At that time, the only part of the tube that was appreciably hotter than ambient

ORNL-DWG 83-3329

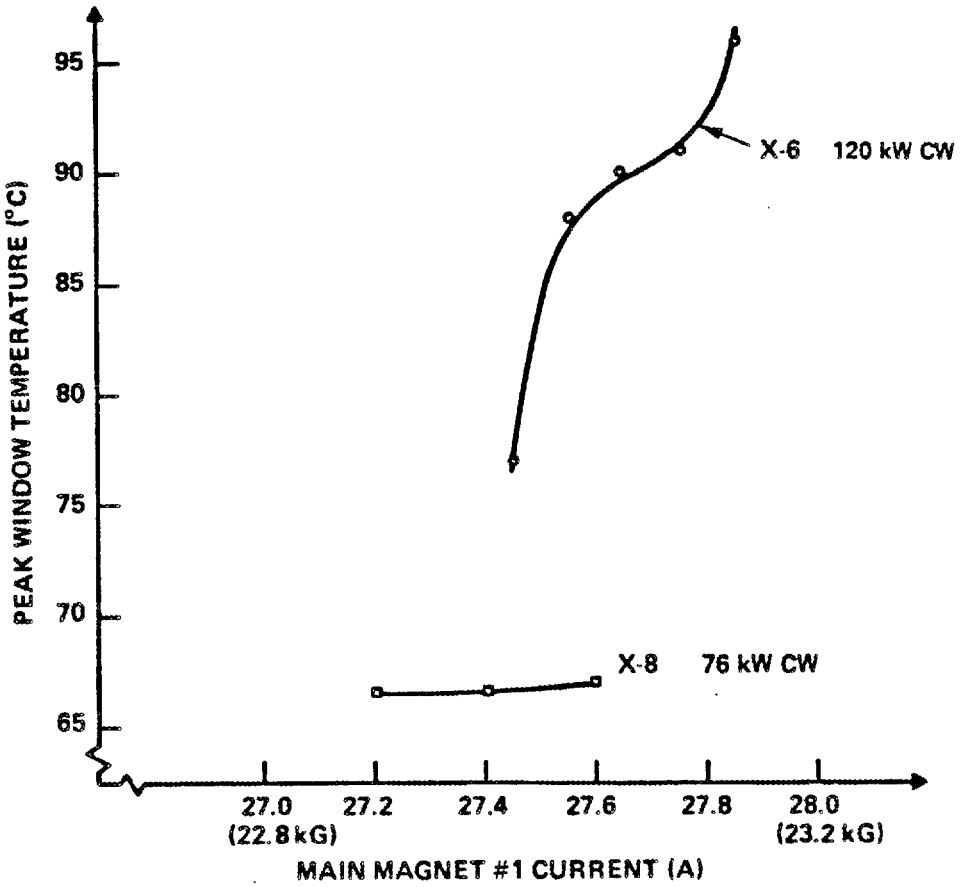

Figure 374. Peak Window Temperature VS Main Magnet No. 1 Current

ORNL-DWG 83-3330

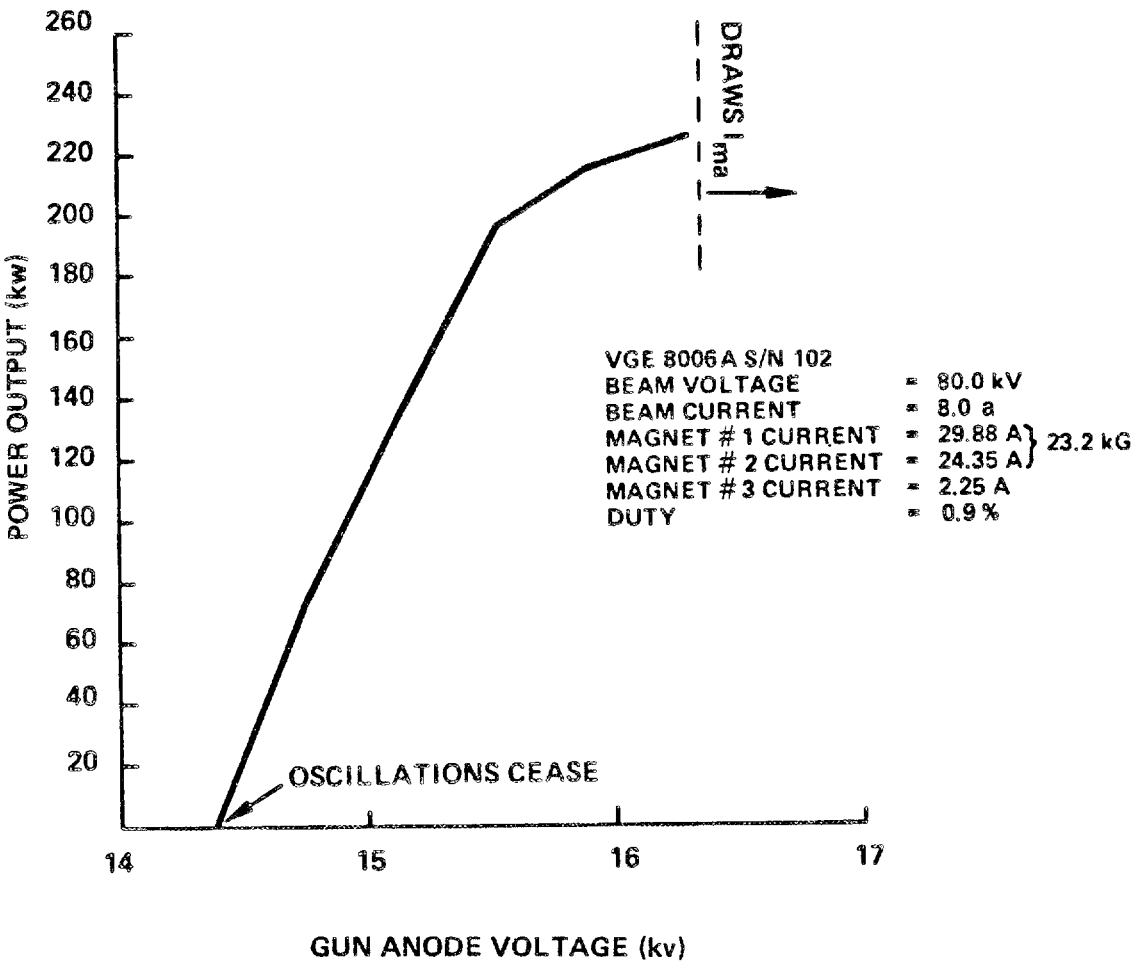

Figure 375. Peak Power Output VS Gun Anode Voltage for S/N 102

ORNL-DWG 83-3331

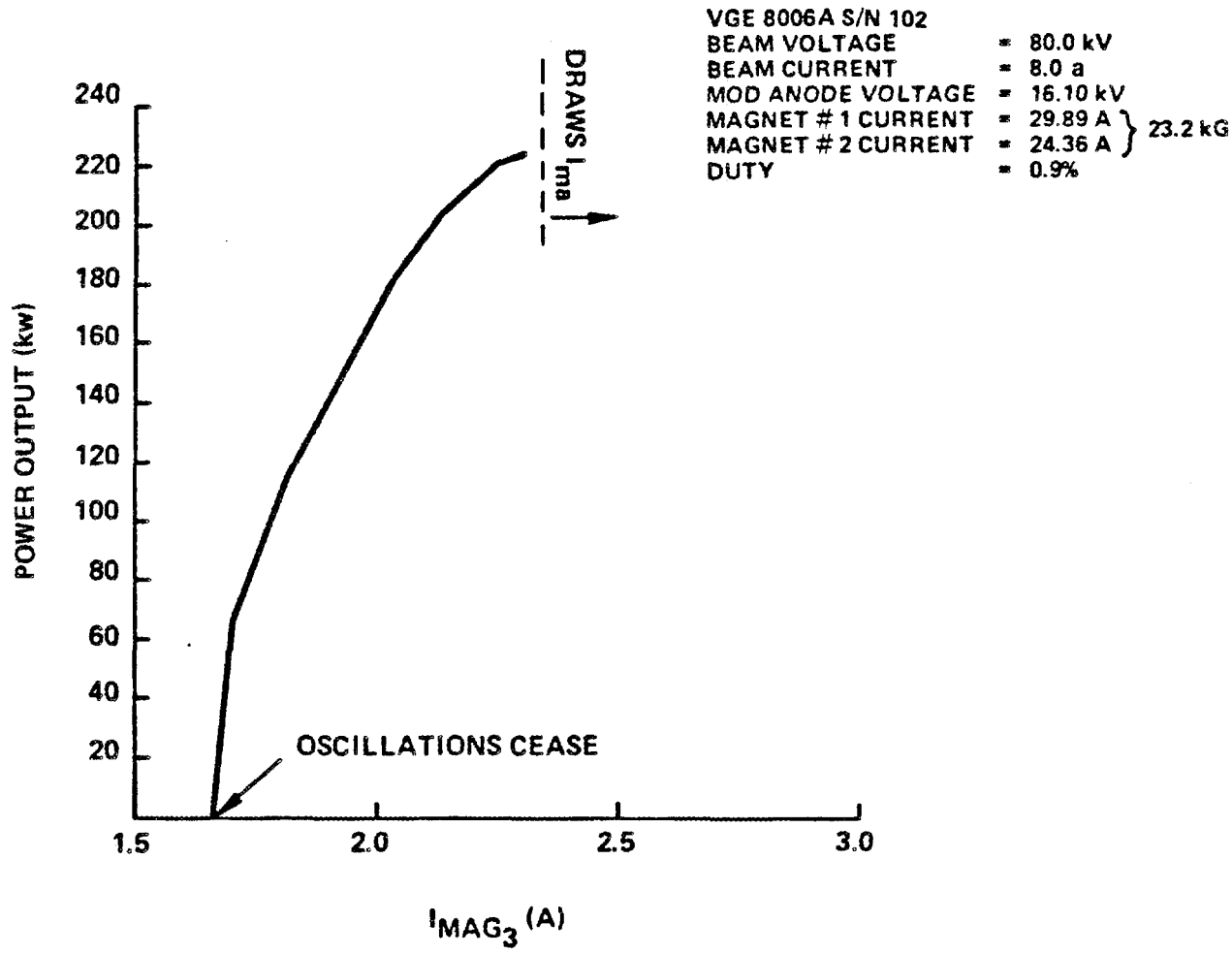

Figure 376. Peak Power Output VS Magnet No. 3 Current for S/N 102

temperature was the area around the lower collector seal. A temperature rise in that area was not seen in X-6; the seal temperature was not being monitored at the time of the X-6 measurements. Running the tube in a high-duty pulse mode to measure this temperature rise with RTD sensors was prevented by constant gas bursts and crowbarring.

The tube was subsequently cut open for inspection. No beam damage, which could have explained the heating, was noted at either the top of the taper or the bottom end of the collector. It was still not clear whether the heating was caused by beam or rf effects. Another CW tube would be tested to evaluate this seal heating more closely.

It was suspected that there might have been a leak in the body or taper section. Extensive leak testing was performed but nothing conclusive was found.

S/N 102 was rebuilt with a new gun. Immediately after exhaust, the cathode ion pump current rose to about 3-1/2 microamps. The fact that this was noted on the cathode pump and not the collector pump indicated that the problem was either in the body or taper section of the tube.

Extensive leak testing was again performed with no conclusive evidence of the location of a leak. However, there was a tentative indication of a leak in the taper assembly. This was never pinpointed exactly. S/N 102 was rebuilt with a new body section, tested to 500 ms and delivered to GAT.

J. SEVENTH EXPERIMENTAL TUBE

The following tests were performed on the seventh experimental tube, VGE-8006A, S/N X-7:

- Pulsed operation, including initial aging, characterizing the tube and mode-purity measurements

- Collector power density measurements using wrap-on coils

- 100 kW CW operation, where several output power sensitivity curves were taken

- 200 kW CW operation for 2 hours

- Cyclic fatigue, where 10,039 pulses were accumulated

- Emission cooling, or 30-second test

1. Pulse Operation

These tests started on June 1, 1984, and lasted for about 12 days. During initial aging, some erratic body current behavior was noted. This was cured by energizing one of the trim coils to 4.75 amperes. This setting was used on all the pulsed and CW tests.

Figure 377 shows the oscillation map taken during pulsed operation. As with all step cavity tubes, the 57.25 GHz, TE_{22} mode occupies very little area and does not interfere at all with the TE_{02} operation. The 40 - 50 GHz modes are observed on both CW and pulsed tubes. They do not produce a great amount of power. A maximum of 6 kW has been observed.

Figure 378 shows peak rf power out as a function of main magnet coil #1. Peak rf power at 200 kw was obtained at 500 μsec pulse duration. As can be seen, the rf power varies quite smoothly over this range of magnetic field. The frequency, on the other hand, stays constant at 59.80 GHz at power levels over 200 kw. Between 32.2 A and 32 A of coil #1 current there is a jump to 59.85 GHz and then a smooth variation to 59.95 GHz of 38 kw of output power.

The final short pulse tests measured the mode content of X-7, using the directional couplers on loan from GAT. The results of these tests are shown in Table 50. They are consistent with the mode content measurements made on the long pulse tubes delivered to GAT.

ORNL-DWG 84-2791

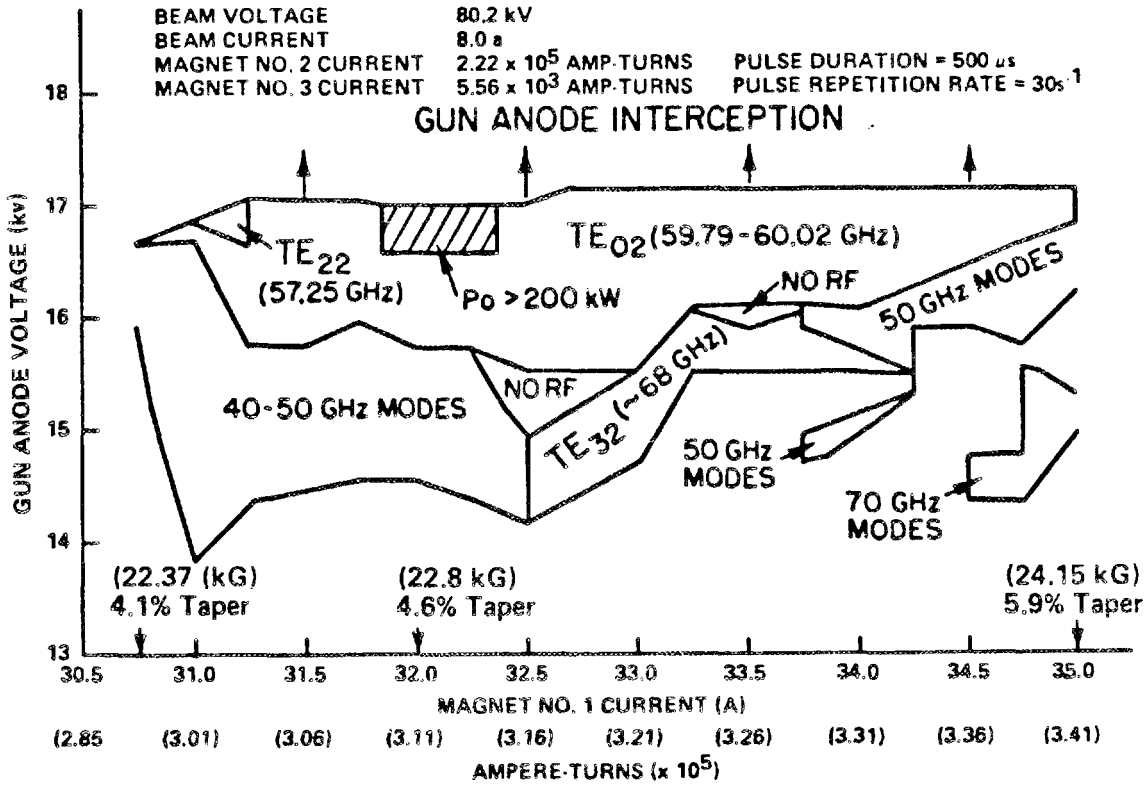

Figure 377. VGE-8006A S/N X-7 Oscillation Map

ORNL-DWG 84-2792

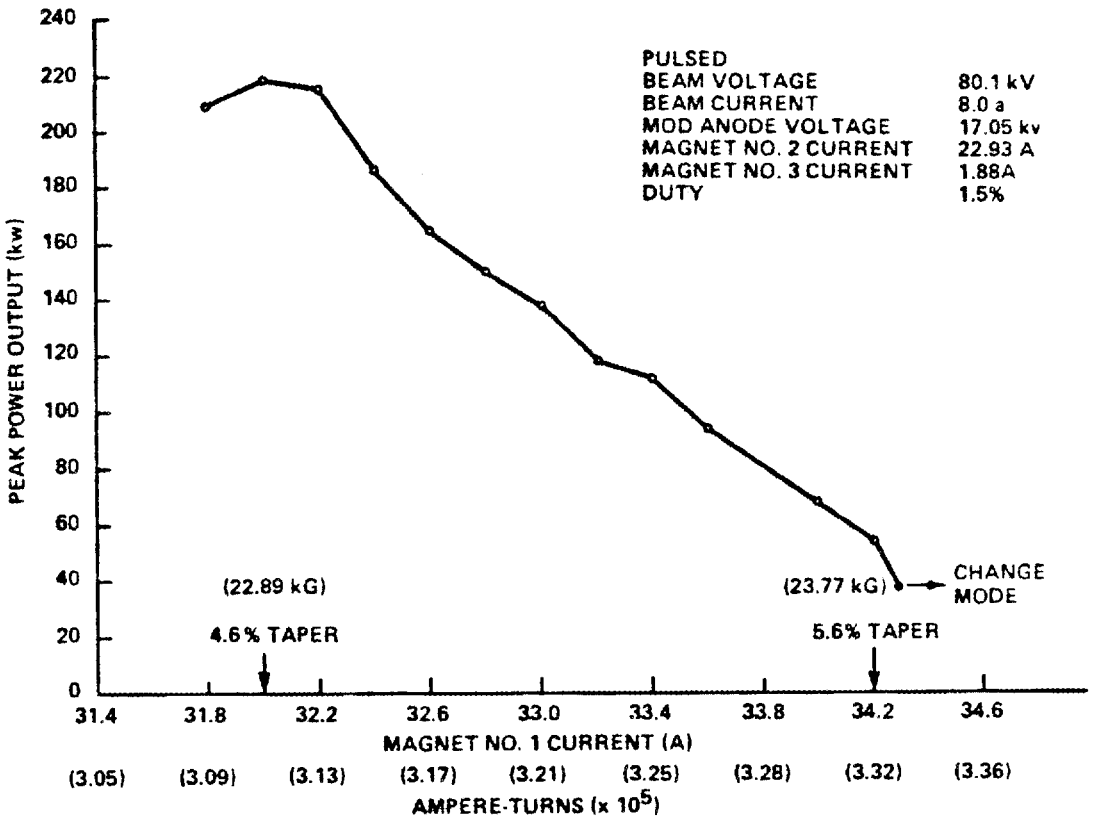

Figure 378. Peak Power Out VS Magnet No. 1 Current

Table 50
Mode Content Measurements
on X-7 (Pulsed)

TE_{01}	TE_{02}	TE_{03}
2.3 ± 2%	95.3% ± 1.6%	2.4 ± 0.5%

2. Collector Distribution Studies

The method investigated for optimizing the beam distribution on the collector used wrap-on coils which were first introduced on VGE-8006A, S/N 104, one of the tubes delivered to GAT. Previously, large coils, as used on the 28 GHz CW tubes were tried, but it was found that they were not effective in spreading the beam. They only moved it up and down. The small wrap-on coils provide greater $\partial B_z/\partial z$, give more control of the magnetic field profile, and more effectively spread the spent beam. Figure 379 shows the measured X-7 collector power density profile without any coils.

The arrangement ultimately used on X-7 included two coils. The density profile for this case is shown in Figure 380, without rf, and in Figure 381, with rf.

The integrated power in both magnetic field profiles is about 50% of the real power. Correcting for this gives a peak power density of 1.2 kW/cm^2, without rf, and 1.0 kW/cm^2, with rf.

There is still some concern about the asymmetries observed in the collector power density with operation of tubes in the Nike Zeus Test Set. The power density is always high in south and west and always low in north and east. GAT has performed the same type of measurements and found very little asymmetry. There are two possible explanations. First, the tube sits close to the middle of the tank at GAT, while in Nike Zeus, the tube is in the corner of the tank. Second, at GAT, the tubes are in a large gallery, while in the Nike Zeus Test Set the tube is in a lead house containing many magnetic fixtures.

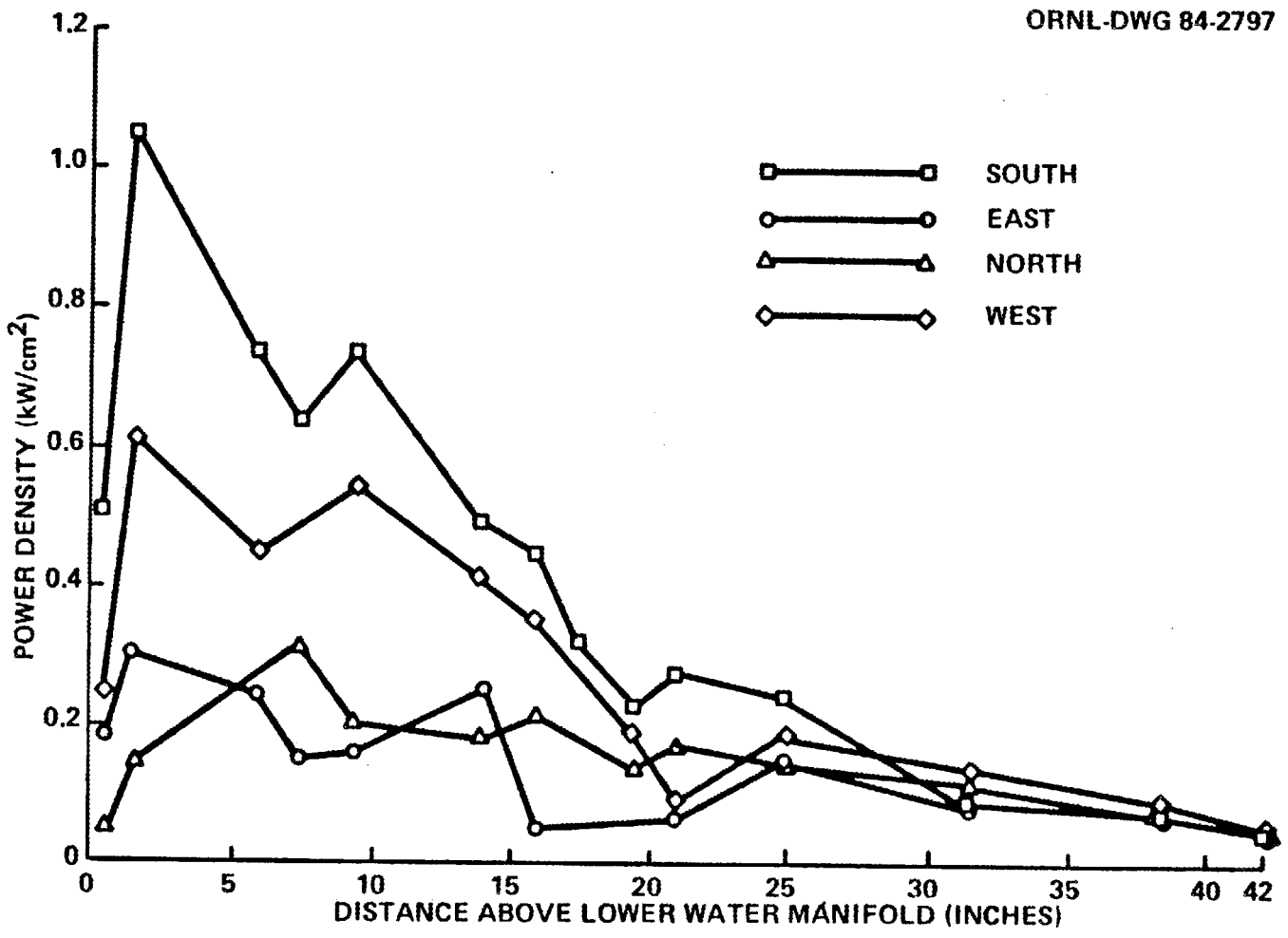

Figure 379. X-7, Collector Power Density, No Coils, Without RF

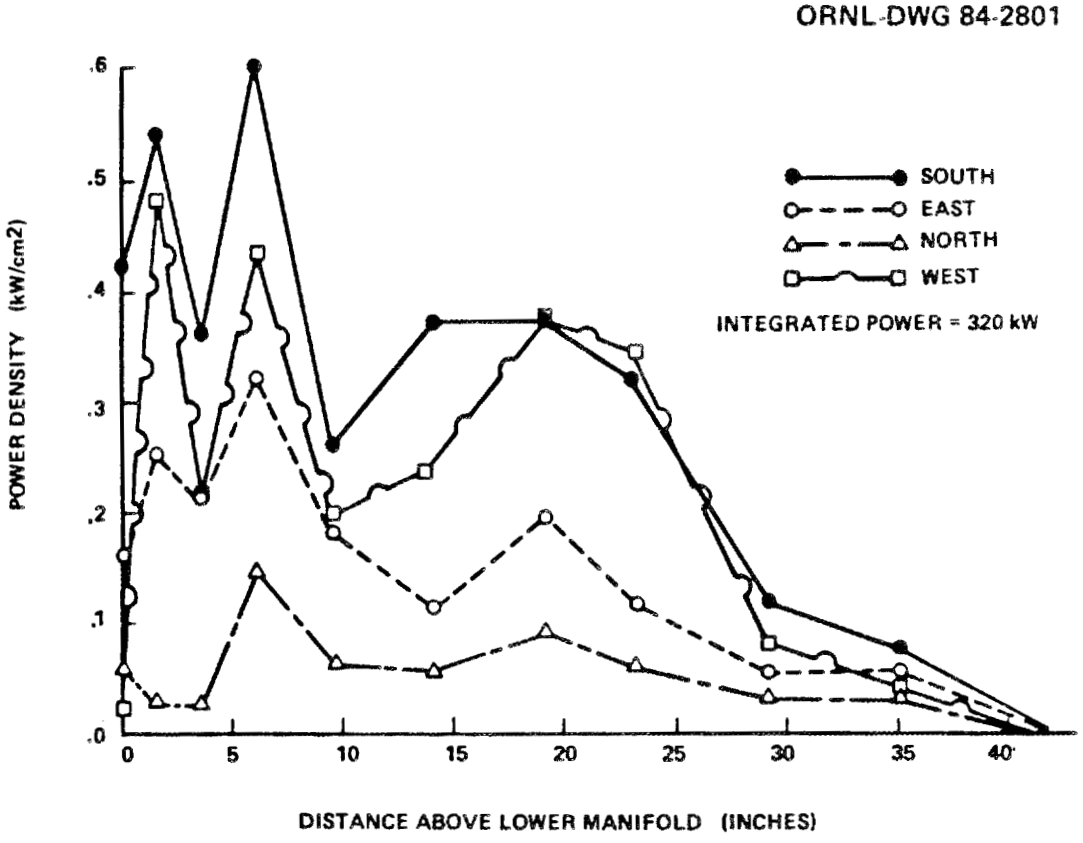

Figure 380. X-7 Collector Power Density, Two Aiding Coils at 0" and 8", One Amp in Each Coil Without RF

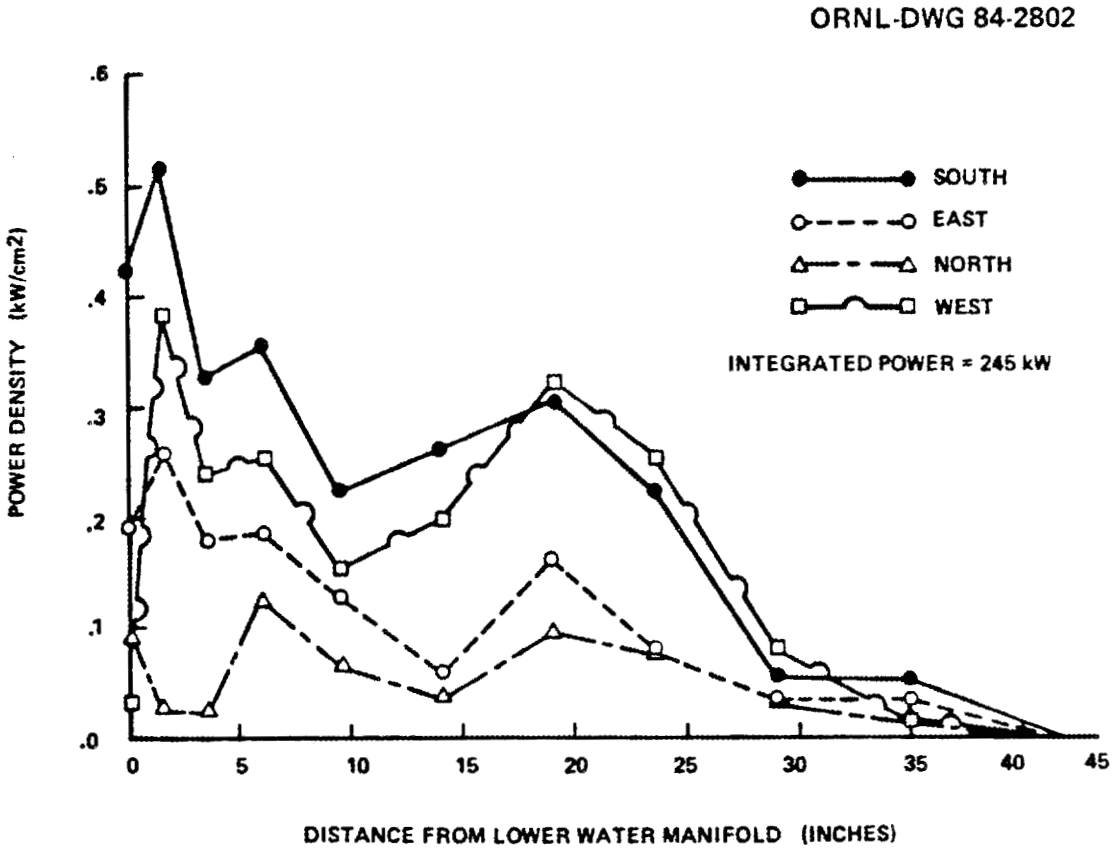

Figure 381. X-7 Collector Power Density, Two Aiding Coils at 0" and 8", One Amp in Each Coil With RF

3. 100 Kilowatt CW Operation

X-7 was CW-aged in the following manner: The beam voltage was set to 80 kV. The rf power was increased by raising the beam current slowly. By increasing the filament power, the onset of TE_{02} oscillation was at 2 amperes with 34 kW of rf power output.

The CW aging was interrupted at 3.35 amperes, or 104 kW of rf power, in order to take some CW sensitivity curves. Figure 382 shows rf output power as a function of main magnet current. As in the pulse case, the rf power varied smoothly with magnetic field. The frequency stayed constant at 59.77 GHz from 104 kW to 37 kW, and then jumped to 59.84 GHz at 30 kW and 59.87 GHz at 14 kW. Figure 383 shows the variation of rf power output with gun anode voltage, a smooth variation of power from 104 kW to 4 kW. Figure 384 shows the variation of rf output power with beam voltage, both, with the gun anode held constant with respect to the cathode, and with the gun anode proportional to the beam voltage.

4. 200 kW CW Operation

The beam current was brought up slowly from 3.35 amperes to 7.5 amperes where 207 kilowatts of rf power was obtained. The power was brought up in 10 kW steps and the following parameters were monitored and recorded at each level:

1. waterload flow and Δt
2. window temperature
3. FC-75 flow, temperature and Δt
4. cavity flow and Δt
5. taper flow and Δt
6. lower seal flow and Δt
7. upper seal flow and Δt

The collector water flow was held constant at 165 gpm, but the Δt was not monitored or recorded.

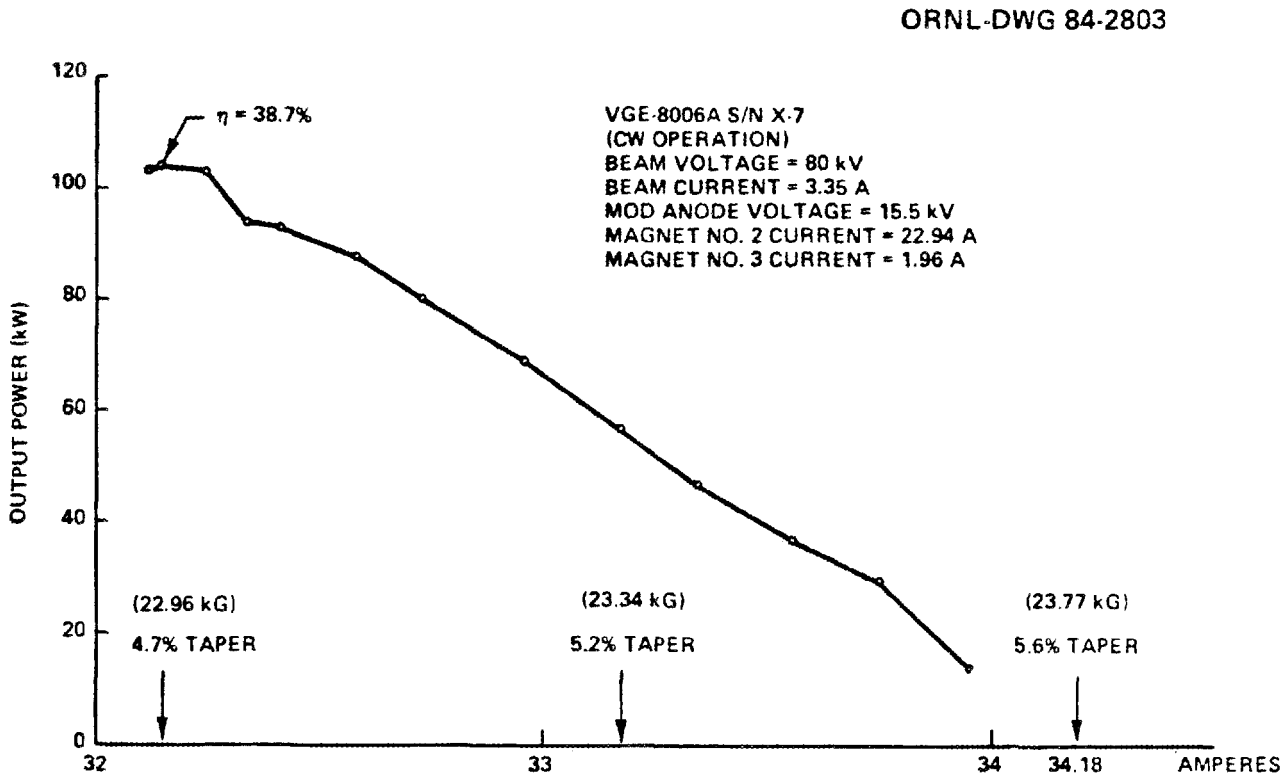

Figure 382. Output Power VS Main Magnet No. 1 Current

ORNL-DWG 84-2804

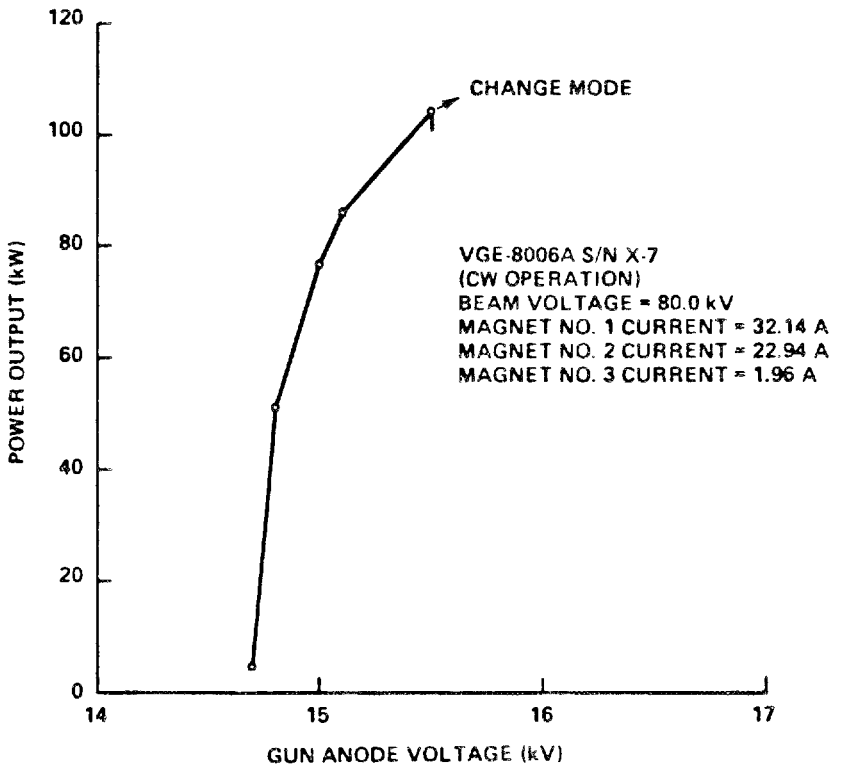

Figure 383. Power Out VS Gun Anode Voltage

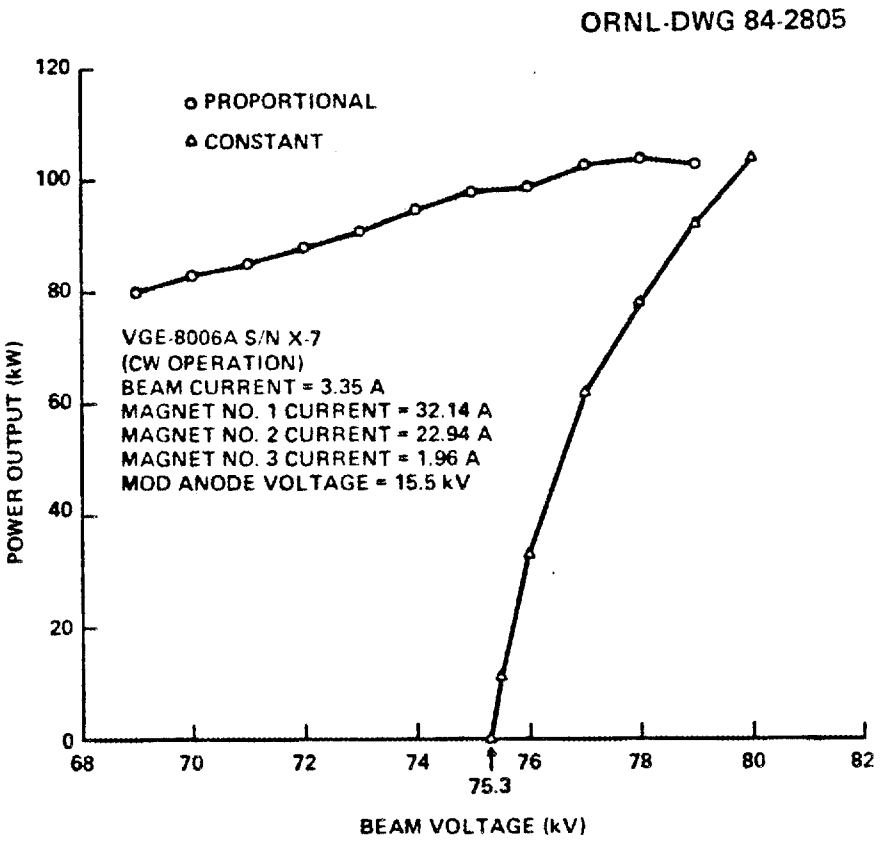

Figure 384. Power Out VS Beam Voltage

Table 51 shows the operating conditions for 207 kW of rf output power. The output efficiency at this power level was 34.4%. Factoring in the internal tube losses of 14.5 kW gave an interaction efficiency of 36.8%. The two largest factors in the internal tube losses were the rf interaction cavity and the window FC-75. These are plotted in Figures 385 and 386, respectively.

Table 51

Operating Conditions for 207 kW CW RF Output Power

Beam Voltage	80.0 kilovolts
Beam Current	7.5 amperes
Gun Anode Voltage	16.6 kilovolts
Heater Voltage	9.5 volts
Heater Current	3.92 amperes
Solenoid #1 Current	302,926 ampere turns
Solenoid #2 Current	224,595 ampere turns
Solenoid #3 Current	5,950 ampere turns
Solenoid #4 Current	2,345 ampere turns
Collector Coil Current (2)	1.0 ampere aiding in each coil
Duty	100%
Frequency	59.74 GHz
Gun Anode Current	<2.0 mA
Body Current	<5.0 mA
Collector Water Flow	165 gpm (US)
Body Water Flow	25 gpm (US)
Window FC-75 Flow	7.85 gpm (US)
FC-75 Temperature	$14.5 \pm 0.5^{\circ}C$

At the 207 kW level, the power in the lower collector seal was 60 watts, the power in the upper collector seal was 220 watts, and the power in the taper and beam shaver combined was 840 watts.

One of the big concerns, of course, was the ability of the window to transmit 200 kW of a 95% pure TE_{02} mode. 200 kW had already been

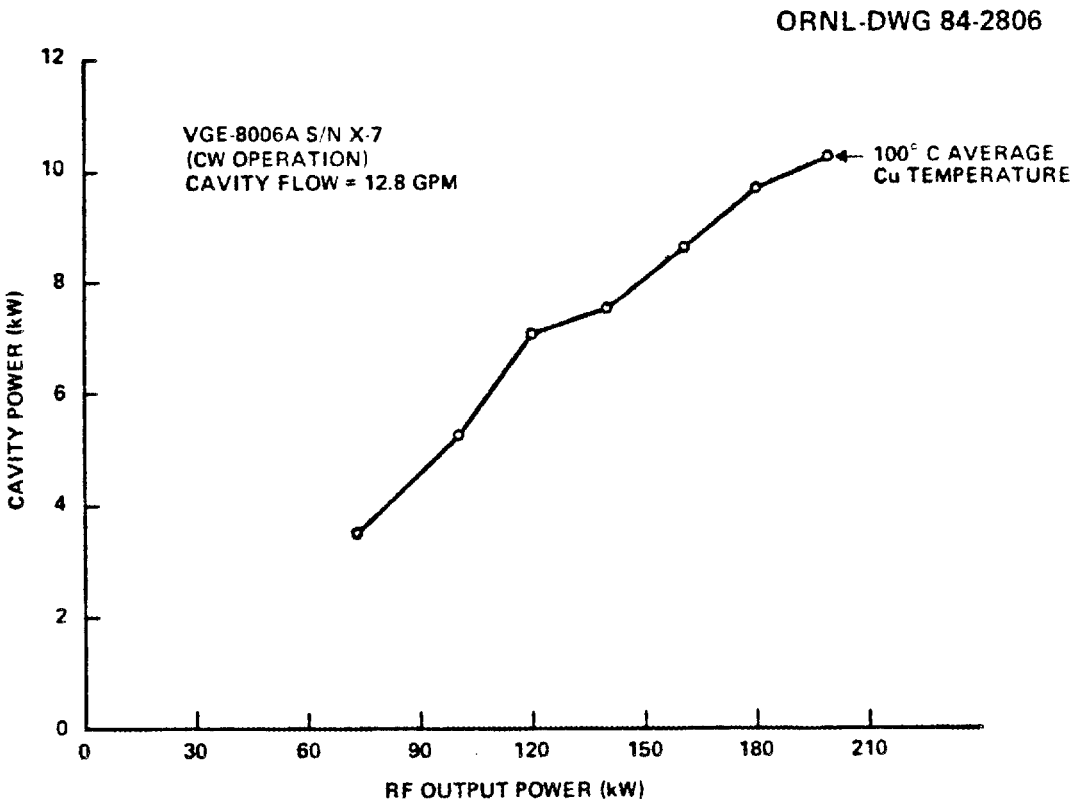

Figure 385. VGE-8006 A S/N X-7 Cavity Power VS Output Power (CW Operation)

ORNL-DWG 84-2807

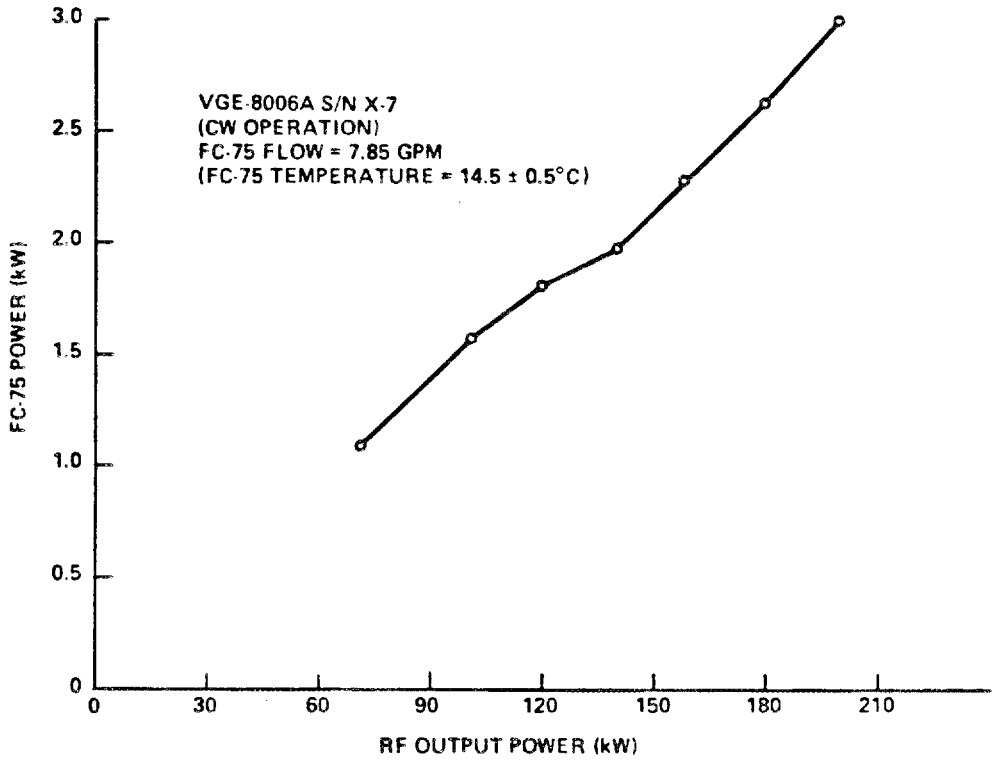

Figure 386. VGE-8006 A S/N X-7 FC-75 Power VS Output Power

demonstrated on VGE-8006, S/N X-6, but with highly mixed modes and with the magnetic field tuned in order to minimize the window temperature.

The effect of tuning magnetic fields was investigated on X-7 at the 100 kW level, and the window temperature was found to be insensitive to variations in magnetic field at a constant power level.

During all of the CW testing, the IR camera was used to minitor window temperature. This involved mounting the IR grid in the waveguide system, keeping the camera aligned, and constantly monitoring the FC-75 temperature, grid temperature, and IR system. Figure 387 shows maximum window temperature versus rf output power. The FC-75 temperature was held at $14.5 \pm 0.5^{\circ}C$ during the entire test. The difference between baffles was that the new baffle had a more jetting effect towards the center of the window, which was the area of maximum window temperature. Figure 387 shows a nonlinear peak window temperature variation with output power, particularly at the higher power levels where it tends to flatten out. Possible reasons for this variation are:

1. The mode mix changes.
2. The mode mix is constant, but the relative phasing of modes changes.
3. Nucleate boiling improves heat transfer at higher power levels.
4. Reflection "temperature" from the grid is not properly accounted for.

It is not clear at this point which of these explanations may apply. Further investigation is needed.

VGE-8006A, S/N X-7 was run for 2 hours at the 203 kW CW level without interruption from either the tube or the test equipment. All Δt's were monitored and recorded at the beginning of the test, after one hour, and at the conclusion of the test. The only change observed was a slight increase in cavity power during the first hour, with no further change during the second hour. The output frequency remained constant during the

ORNL-DWG 84-2808

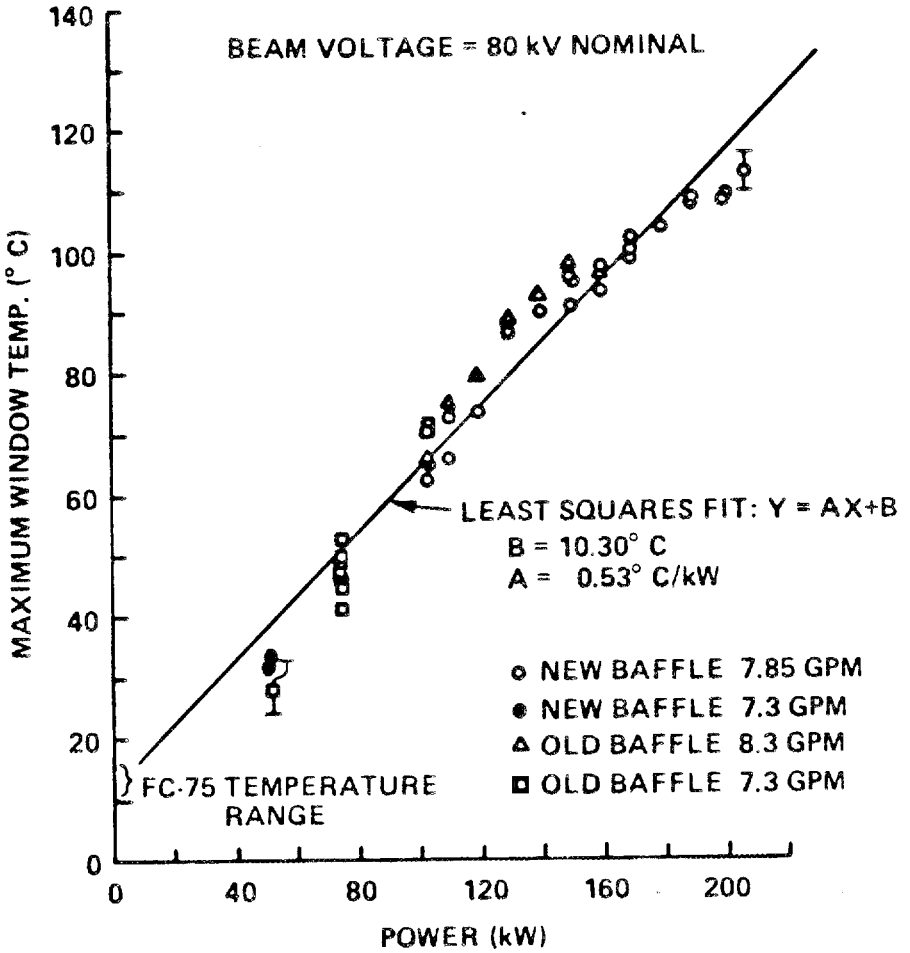

Figure 387. Maximum Window Temperature VS Output Power

two hour run. After the two hour run, a power down-power up curve was attempted. Smooth variation of power from 203 kW to 140 kW was achieved by varying only the gun anode. At the 140 kW level the tube began to crowbar. The reason is not clear, but one possibility is that the tube may have been on the verge of dropping into one of the 40 - 50 GHz modes. These proved to be the most difficult problem in CW operation. It was not possible to bring the tube up through these modes to operating level at a CW current greater than 3 amps without the collector gassing up and the tube arcing. Further processing might have eventually eliminated this difficulty. One possible reason for the difficulty with the 40 - 50 GHz modes is that at higher current levels up to 6 kW of output power were measured in pulsed operation. Since the window is not well matched at these frequencies, a lot of reflected power probably remains trapped in the tube.

5. Cyclic Fatigue

X-7 was the first gyrotron used for cyclic fatigue testing. The parameters were 80 kV, 8 A, 3 s pulse duration, 5.5 s between pulses (35.5% duty). The rf output power was 200 kW.

To compensate for emission cooling for this test and the 30-second test, a filament boost circuit was installed in the test set. This was designed to give 0 to 50% filament voltage boost, starting up to 30 seconds before the pulse or up to 30 seconds after the pulse. In the initial design, the starting time could be moved only as close as one second before the pulse or 2 seconds after the pulse. The pulser was later modified to have minimum times of 50 milliseconds in both the pre-pulse and post-pulse modes. The boost is shut off at the end of each pulse.

At 35.5% duty, the starting filament power before boost was 12.54 watts. This is about half the normal filament power for pulsed operation of 23.4 watts. The reason is that the cathode does not cool down in 5.5 seconds after the boost and, hence, needs less average filament power to maintain the cathode temperature.

The boost was to 40.18 watts and started one second before the pulse. During the initial phase of this test, the filament boost was not working properly. Consequently, the first 2000 pulses were run with a current of 9 amps at the beginning of the pulse, and 7 amps at the end of the pulse. The remainder of the 10,039 pulses were with 8 amps constant across the 3 second pulse using the filament boost.

During the cyclic testing, the only parameter which had a measurable change was the output frequency. During CW tests, it had measured constant at 59.83 GHz. With cyclic testing, the frequency got progressively higher, finally ending up at 59.97 GHz after 10,039 cycles.

The cyclic fatigue test was not terminated at this point because of any problem, but rather, to perform 30-second pulse tests. The plan was to complete the 35,000 pulses after the emission cooling or 30-second test was completed.

6. Emission Cooling

The purpose of this test was to determine if 200 kW of rf power could be maintained over a 30-second pulse by keeping the beam current constant within 2%. This required the heater boost circuit.

The tube aged readily to 30-second operation. The initial filament power for 8 amps beam current was 23.4 watts, normal for pulse operation. The filament boost required was to 39.77 watts and began one second before the pulse. Figure 388 shows the relationship between CW, 30-second boost, and pulsed filament power. The interpulse period was 38 seconds for 44% duty.

In general, the filament power determined the current amplitude, and the boost determined the slope. The amplitude of the boost was quite critical. A 1% change in boost resulted in 0.5 amps change in 30 seconds. The boost was started one second before the pulse, due to the limitation of the heater boost circuit at the time. It would have been better to start it closer to the beam pulse, perhaps synchronous with it.

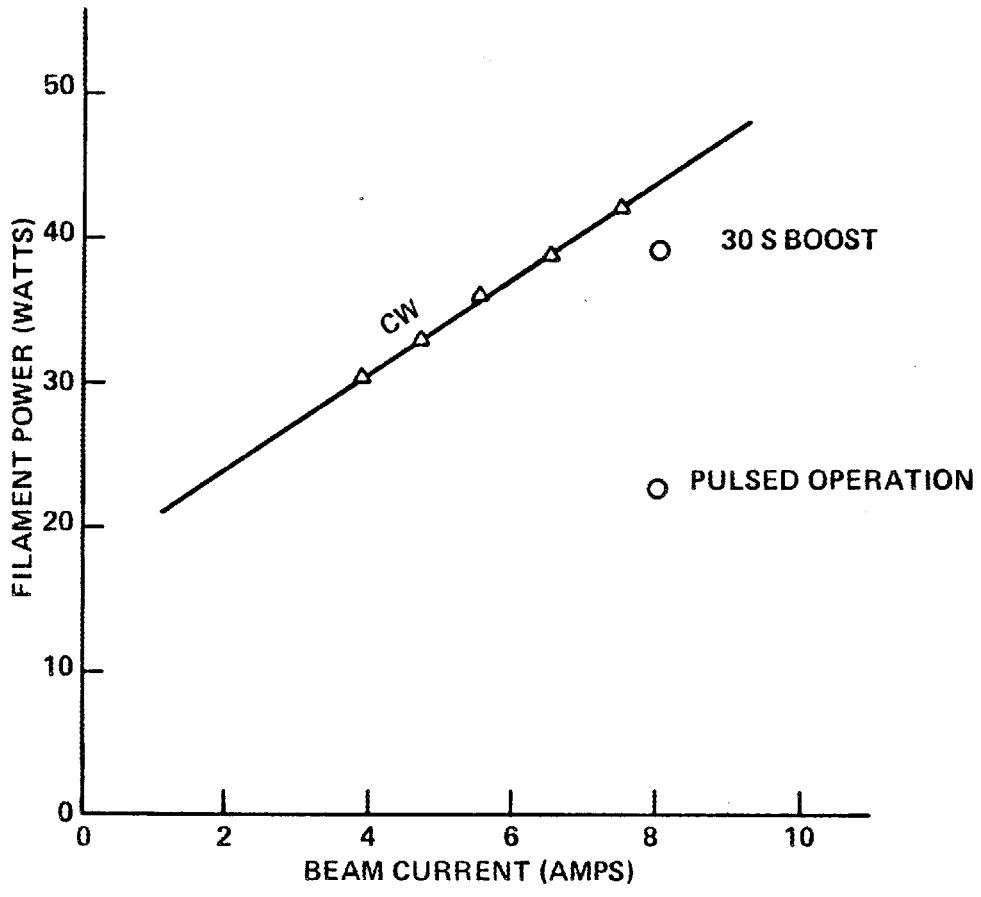

Figure 388. VGE-8006A S/N X-7 comparison of CW, pulsed, and 30 S boost filament power

Figure 389 shows the 30-second, 8 ampere pulse. The overshoot on the leading edge appears to be due to starting the boost too early. 154 kW of rf power, averaged over the pulse, was obtained in this operation. The rf pulse shape as shown in Figure 389 was not particularly flat, possibly indicating that one of the power supply parameters was not remaining sufficiently flat. The average power level of 154 kW may indicate that the power level at the beginning of the pulse was well above 200 kW. Before this situation could be adequately investigated, the vacuum-side window cracked, filling the tube with FC-75.

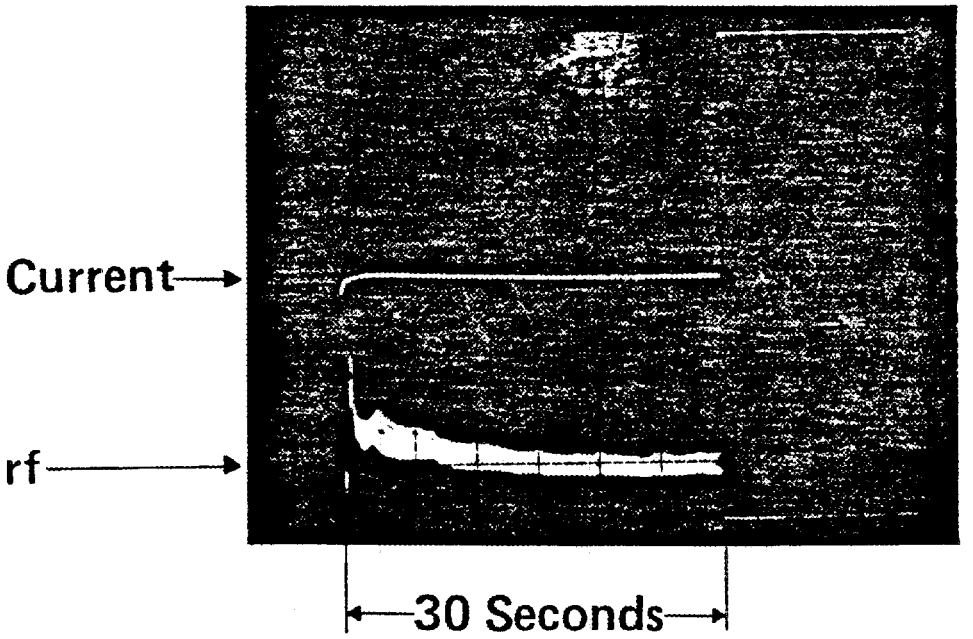

Figure 389. 30-Second Pulse

X. 56 GHz GYROTRON DEVELOPMENT

A separate task of the program was to develop a 200 kW CW 56 GHz gyrotron. Its development depended heavily on the basic success of the 60 GHz program. Modifications to the 60 GHz tube, X-3R, which improved tube stability, were incorporated into the 56 GHz design.

A. GUN

The gun assembly prints and piece part prints are the same as those of the 60 GHz tube[48].

B. ANODE SECTION

The lower magnetic field for the 56 GHz operation, as compared to 60 GHz operation, means that the electron beam will be larger at 56 GHz. This necessitates enlarging the drift tube diameter. The anode drift tube section from the 60 GHz tube was redesigned to allow for the larger 56 GHz beam size. The anode load cavity was also modified for larger beam size. Modifications on the X-3R anode load cavity were shown to eliminate body heating modes. These modifications were incorporated into the 56 GHz design.

C. CAVITY ASSEMBLY

The oscillator cavity was scaled from the 60 GHz design to 56 GHz. The cavity design also reflected the design of X-3R. The cavity diameter and output taper angle were changed to keep the same physical length and make some of the 56 GHz and 60 GHz parts interchangeable. The cavity was computer analyzed, and Figure 390 shows the calculated efficiency for various beam currents and cavity magnetic fields. The cavity was built and cold tested. Figure 391 shows that the Q of the TE_{02} mode is higher than that for the 60 GHz cavity design. Its Q was 11% higher than that for the 60 GHz cavity design, while the Q of the TE_{22} mode remained the same.

Dwg. 82-3608 FED

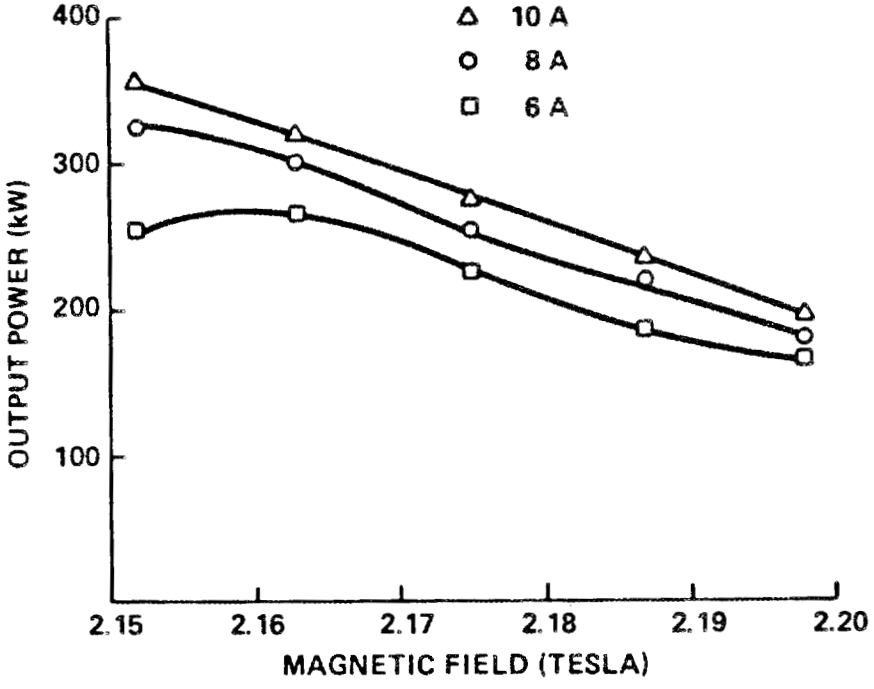

Figure 390. Calculated Output Power for the 56 GHz Cavity for Three Beam Currents at 80 kV

Dwg. 82-3609 FED

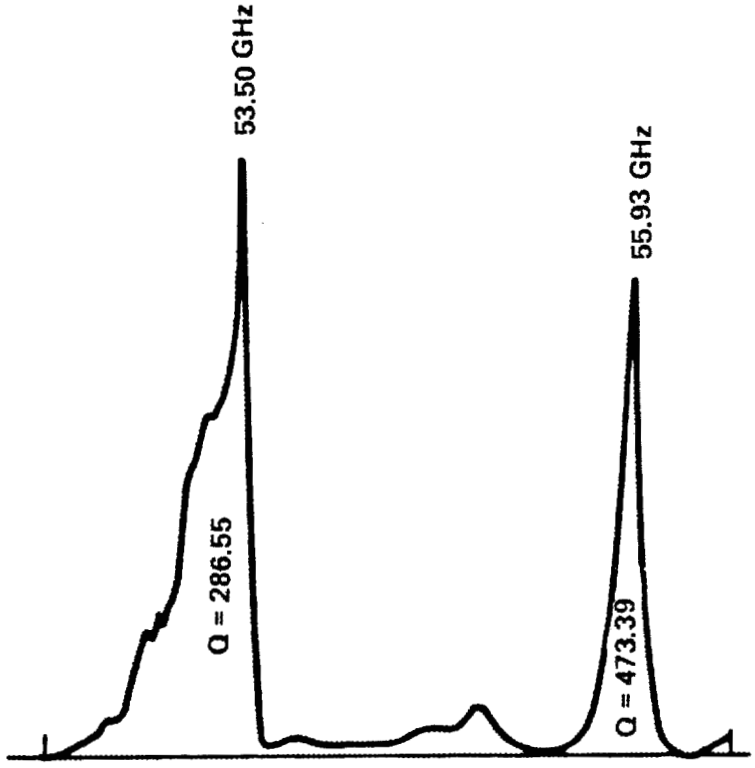

Figure 391. 56 GHz Cavity Measured Resonances

D. OUTPUT TAPER AND COLLECTOR

The output taper was designed to match the new cavity diameter and to incorporate the changes in the 60 GHz tube, X-3R. The collector and tapers are the same design as the 60 GHz CW tube, X-4.

E. WINDOW

The output window was designed to be electrically thinner than the original 60 GHz design. This lessened the mode competition difficulties observed in the 60 GHz CW tube. The bandwidth and VSWR for the 56 GHz design are shown in Figure 392. The thinner design was tried on the 60 GHz CW tube, X-5. The window worked well until it broke at the 120 kW CW output power level. The 56 GHz window was checked for cracks and flaws with a dye penetrant. There were no cracks or flaws detected on the window surfaces. One chip was found on the window edge. Since the chip was on the corner between the edge and surface and was well rounded, it was not considered likely to cause any stress concentration. Analysis of the broken window on the 60 GHz CW tube, X-5, showed that the break was due to ceramic overstress. Computer analysis of the window showed that the stresses on the vacuum side, due to rf losses and vacuum loading, were about 20 ksi at the edge, as shown in Figures 393 and 394. This was very close to the manufacturer's number for allowable ultimate tensile stress. For this reason tube testing was limited to less than 120 kW of output power.

F. TEST RESULTS

1. Pulse Testing

During pulse testing, the tube achieved 280 kw at 3.6% duty with 44% efficiency, as shown in Table 52. Figure 395 shows the tube performance for various beam currents over the same range of magnetic fields. The maximum efficiencies are all very close for quite a range of beam currents. Maximum efficiency with beam current agrees qualitatively with calculations. Figure 396 shows operation at peak power while varying the magnetic field. Figure 397 shows the output power versus the beam current. Figure 398 shows

Dwg. No. 82-2226 FED

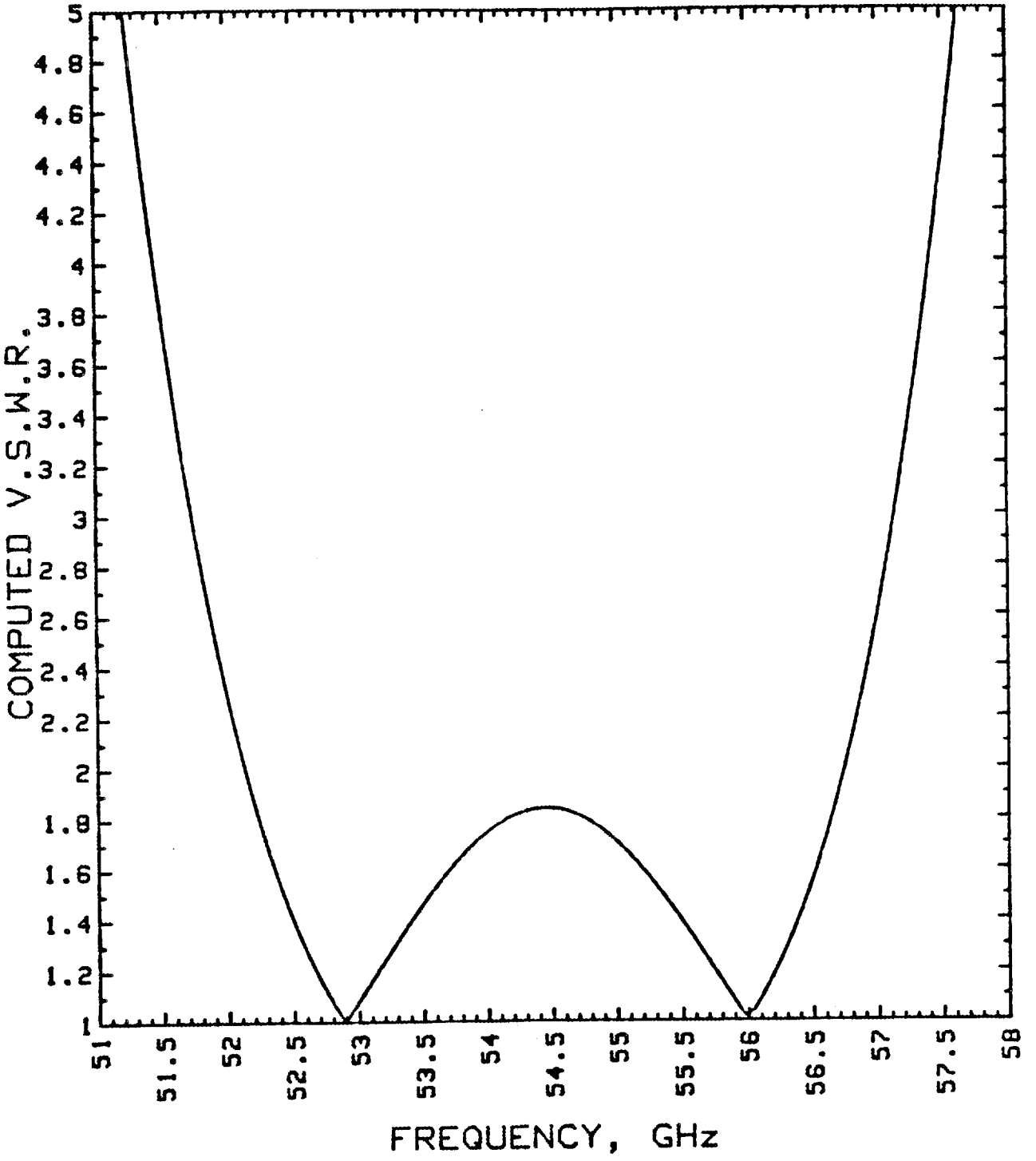

Figure 392. Computed VSWR for 56 GHz Double-Disc Window

ORNL – DWG-83-2136

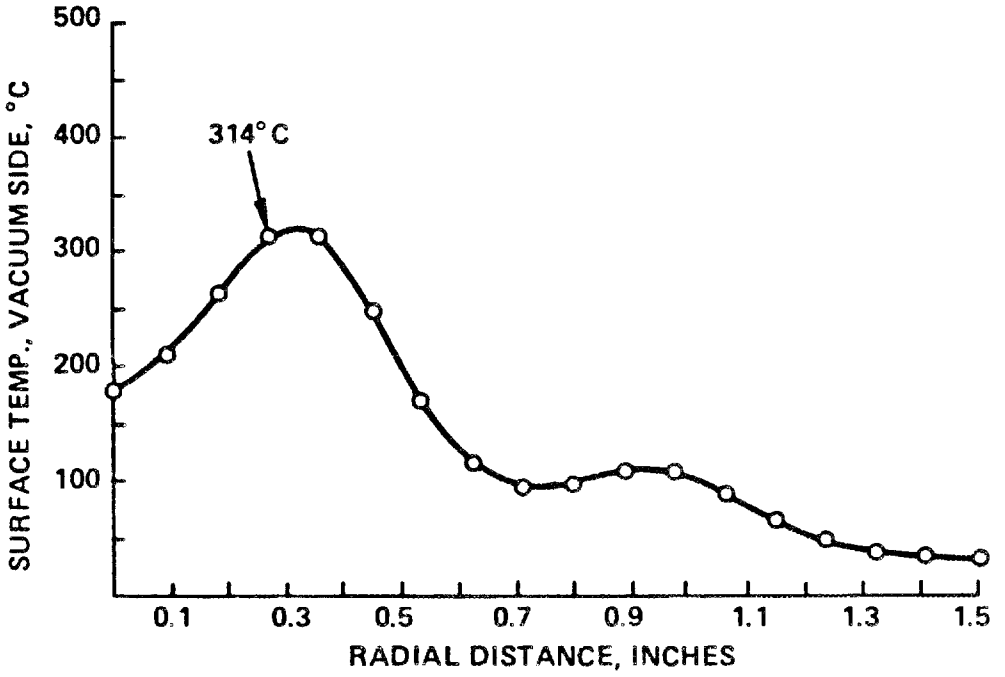

Figure 393. Temperature Distribution on Vacuum Side of 60 GHz Double-Disc Window 1.5 λ Thick, 120 kW, CW

ORNL – DWG-83-2137

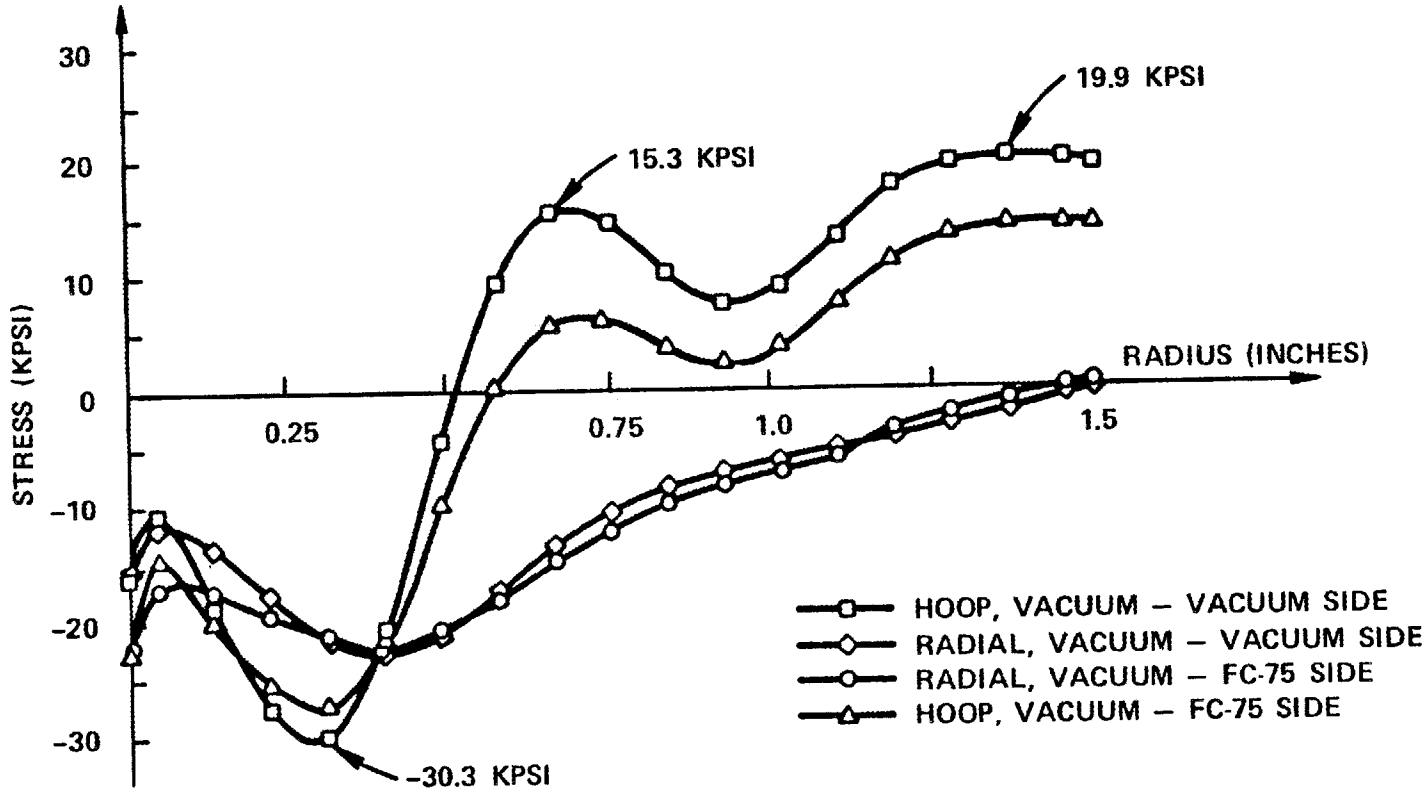

Figure 394. Thermal Stress Distribution for 60 GHz Double-Disc Window 1.5 λ Thick, 120 kW, CW

ORNL – DWG-83-2138

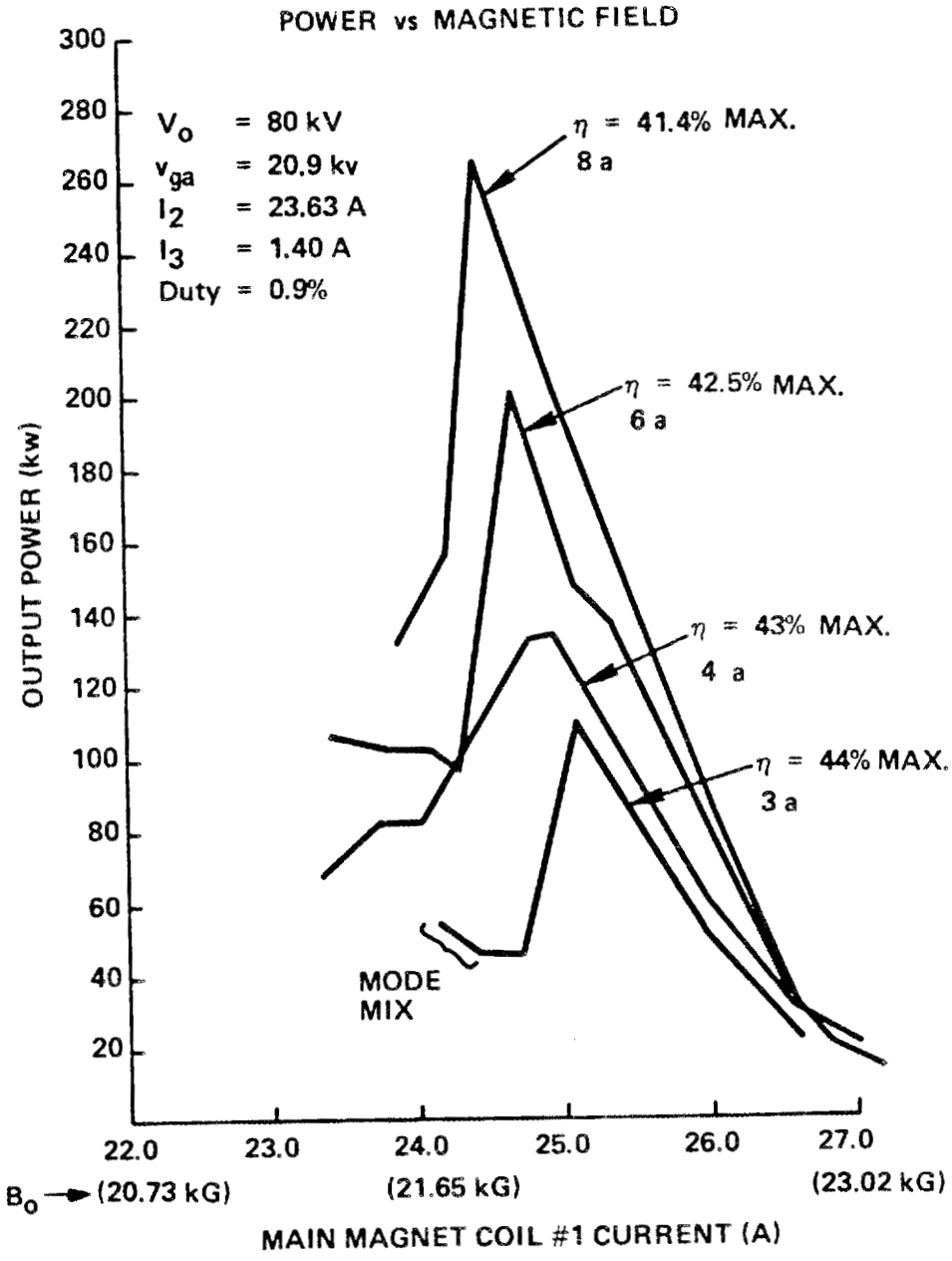

Figure 395. 56 GHz Pulsed Power vs Magnetic Field with Beam Current as a Parameter

ORNL – DWG-83-2139

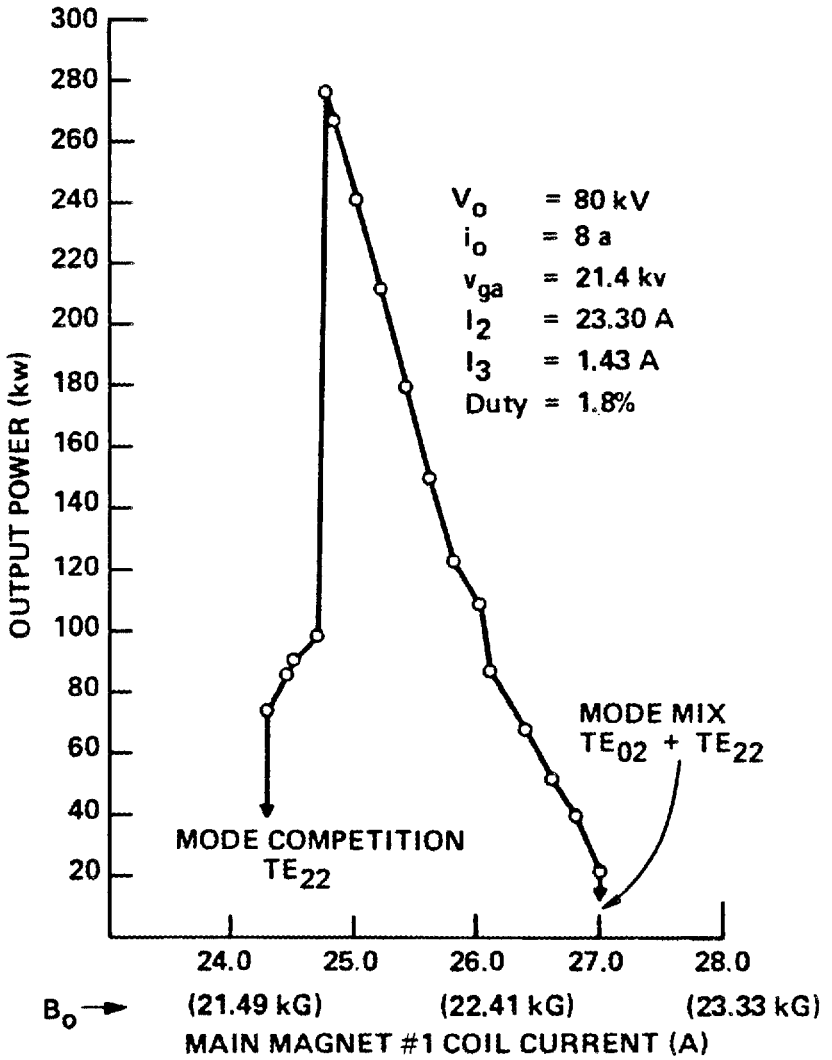

Figure 396. 56 GHz Peak Pulsed Power vs Magnetic Field

ORNL – DWG-83-2140

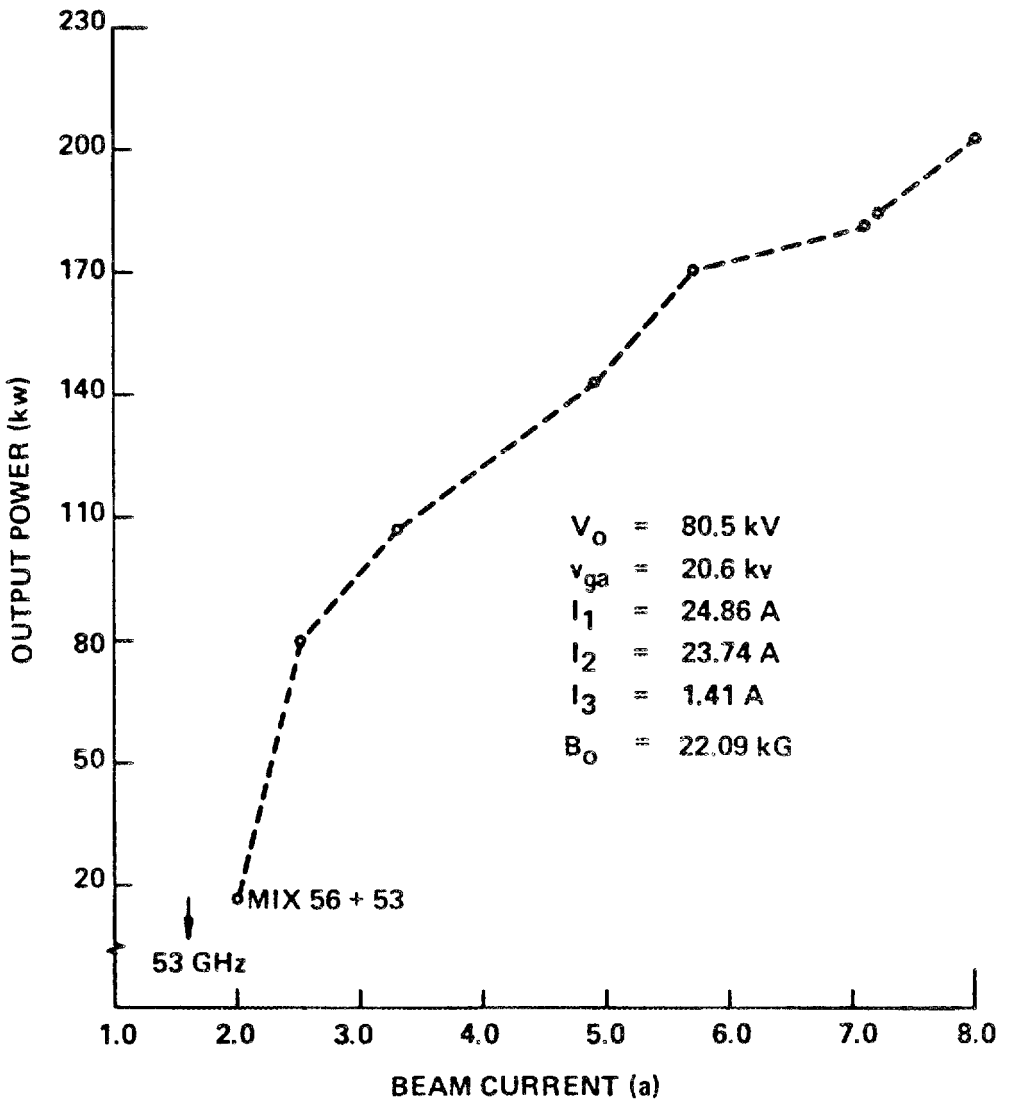

Figure 397. 56 GHz Pulsed Power vs Beam Current

ORNL – DWG-83-2141

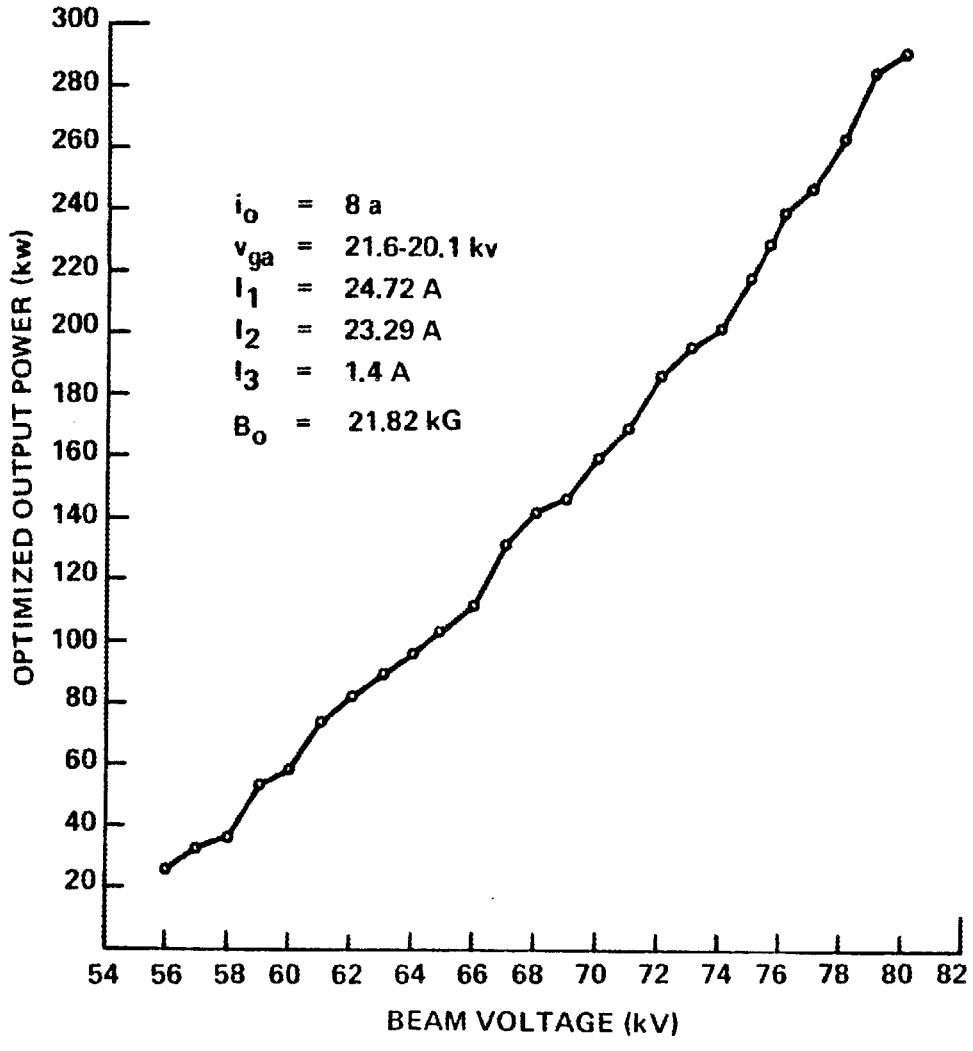

Figure 398. 56 GHz Optimized Pulsed Power vs Beam Voltage

the optimized output power when varying beam voltage. The power was optimized by varying the gun anode voltage within the range indicated. The next two figures, 399 and 400, show how the output power varies when the gun magnet current or gun anode voltage is varied. Figure 400 was obtained when the main magnet Section I was also varied slightly, as indicated. Figure 401 shows that if the magnetic field (I_1) is not adjusted, the range of gun anode voltage over which power is obtained is quite limited by mode competition. The oscillation maps for 8 amperes and 3 amperes beam current are shown in Figure 402 and 403, respectively. The maps for the two current levels are very similar.

Table 52

56 GHz Pulsed Data

Beam Voltage	80.2	Kilovolts
Beam Current	8.0	Amperes
Mode Anode Current	21.4	Kilovolts
Solenoid #1 Current	24.69	Amperes
Solenoid #2 Current	23.34	Amperes
Solenoid #3 Current	1.41	Amperes
Pulse Length	500	Microseconds
Duty	3.0	%
Output Power	285	Kilowatt
Efficiency	44	%
Frequency	55.96	GHz
Main Magnetic Field	21.83	kG

G. CW TESTING

The tube achieved 105 kW with 3 amperes of beam current for an efficiency of 43%. The CW testing was limited to 105 kW output because of the limitations of the window diagnostic system. This, therefore, limited operation to 3 amperes. If an IR system had been in place to monitor the window temperature, the tube could have been tested at higher levels.

ORNL – DWG-83-2142

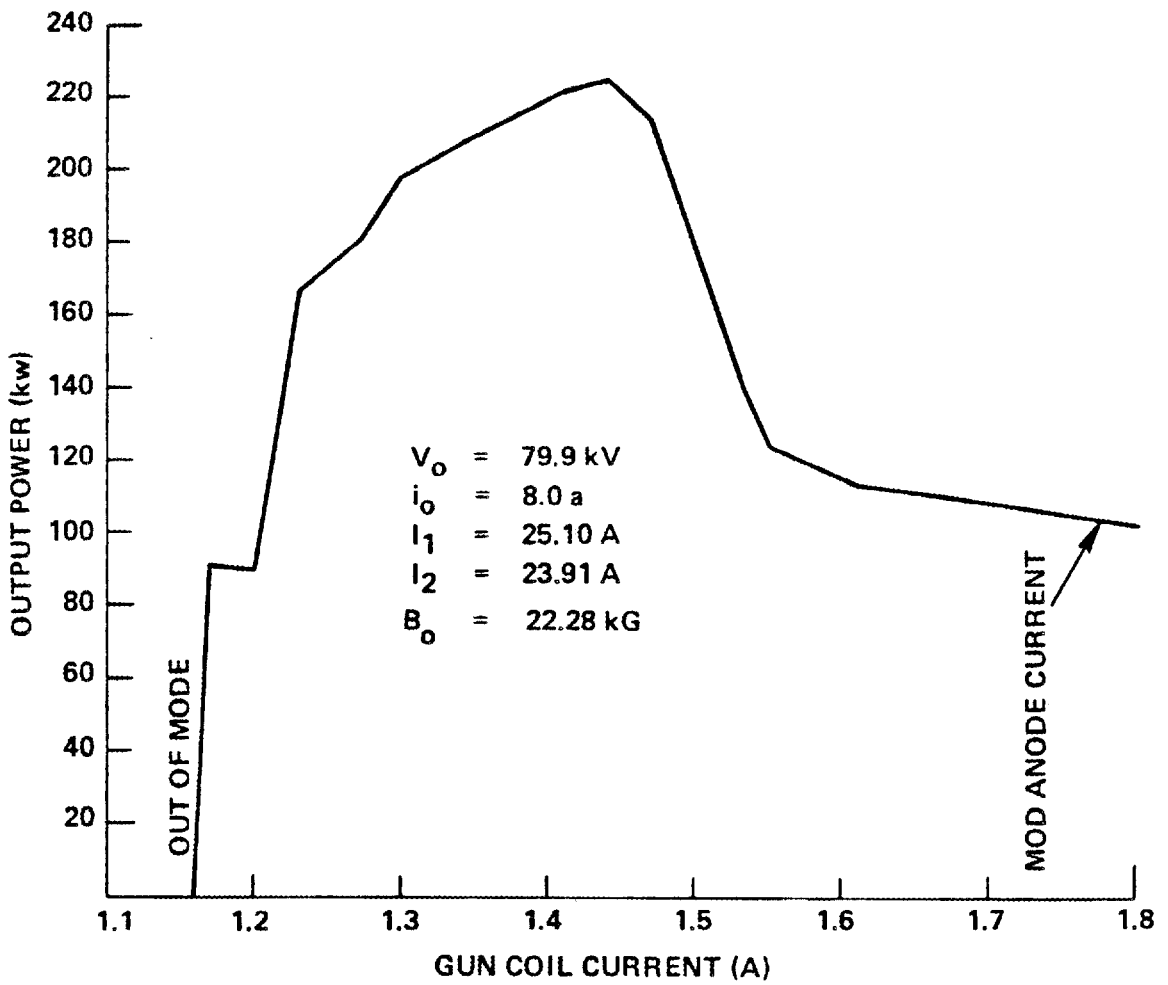

Figure 399. 56 GHz Pulsed Power vs Gun Coil Current

ORNL – DWG-83-2143

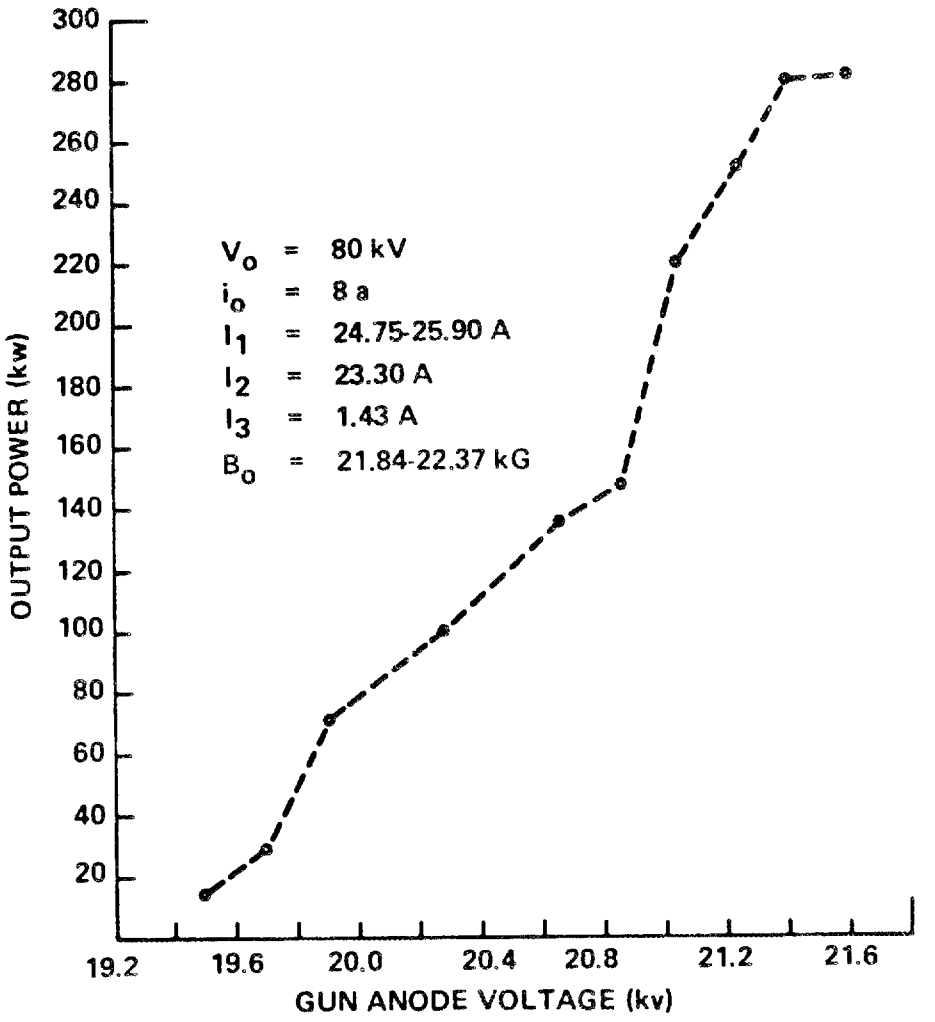

Figure 400. 56 GHz Pulsed Power vs Gun Anode Voltage (Optimized)

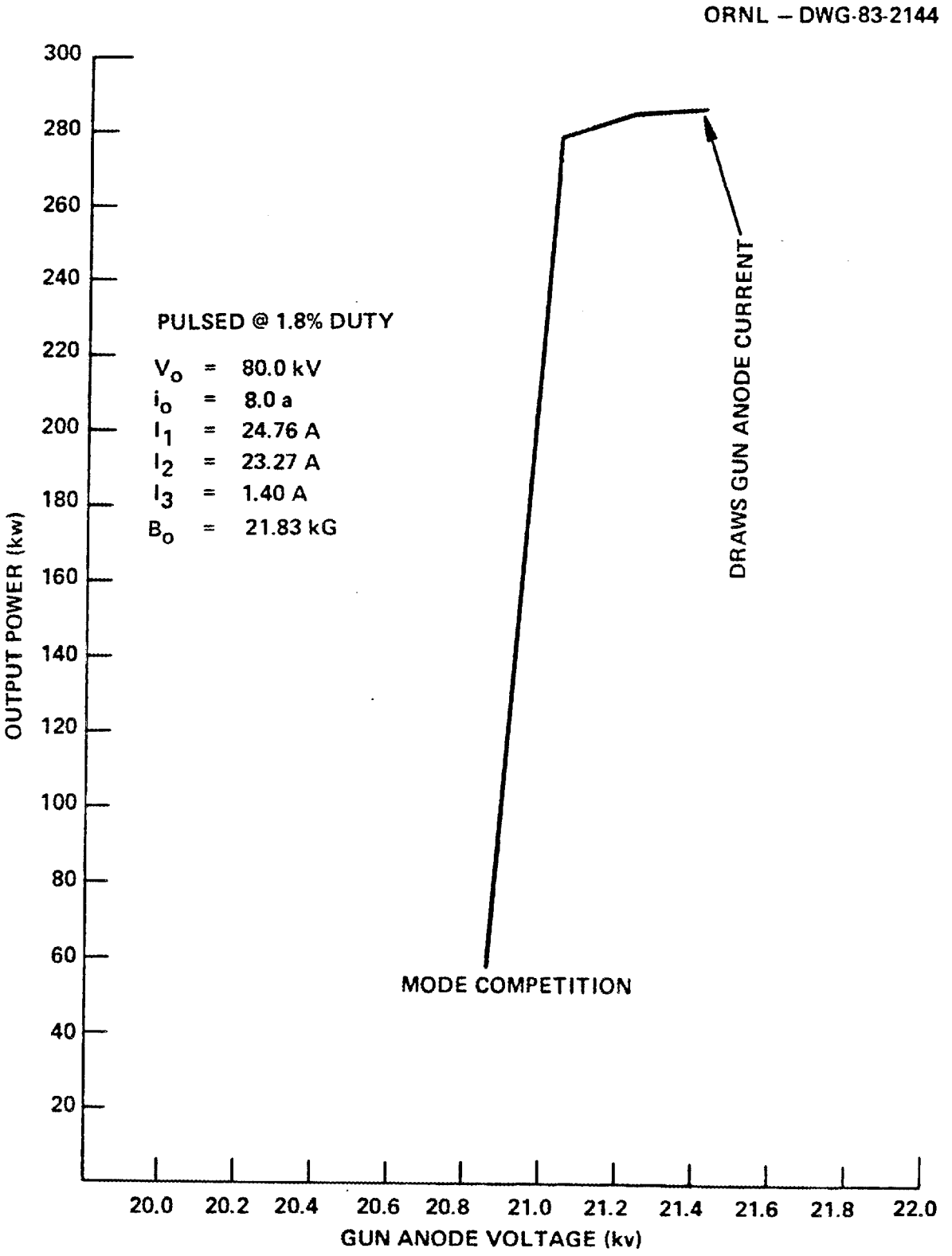

Figure 401. 56 Pulsed Power vs Gun Anode Voltage

ORNL – DWG-83-2145

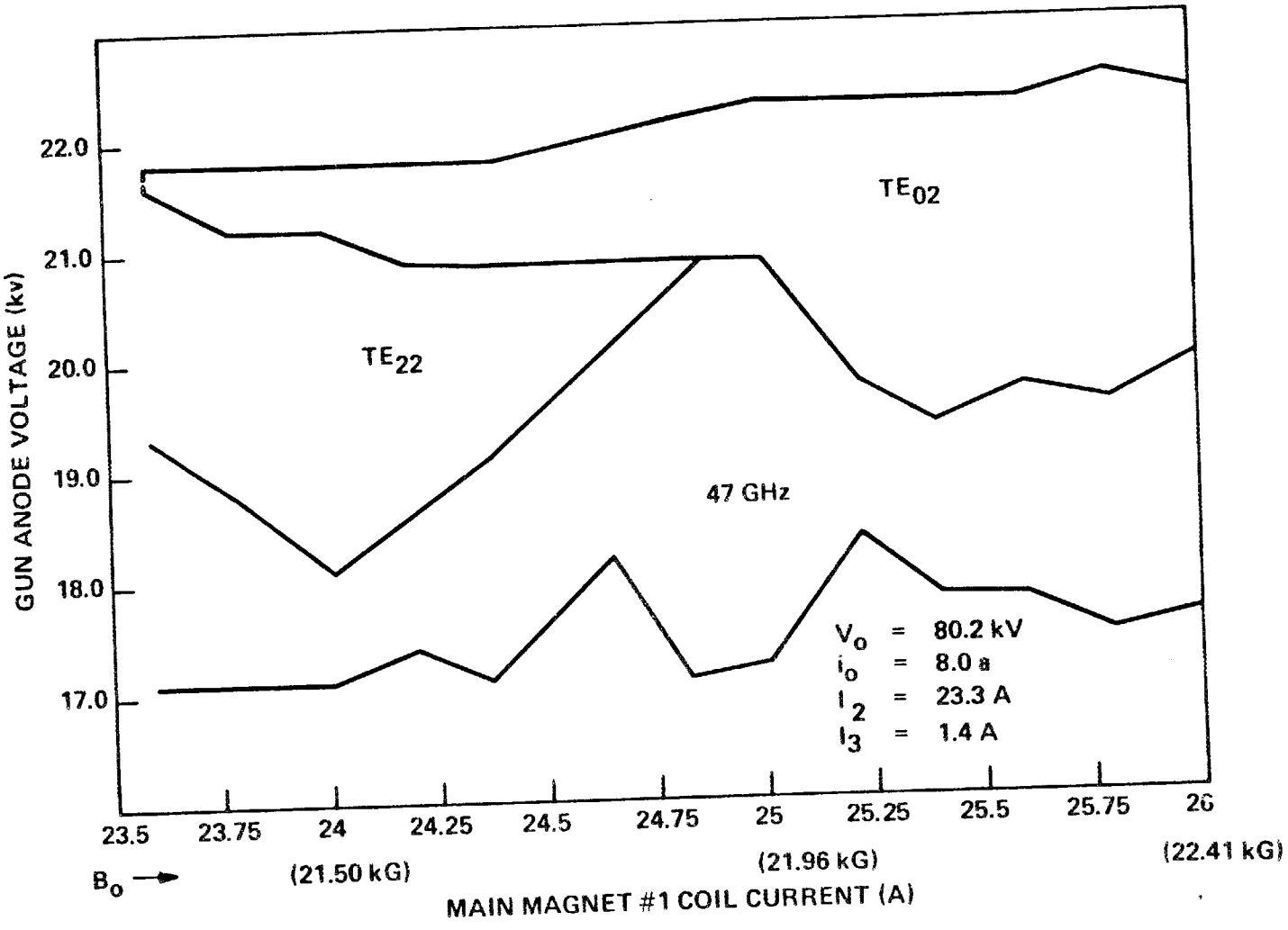

Figure 402. 56 GHz Pulsed 8 Amp Oscillation Map

ORNL – DWG-83-2146

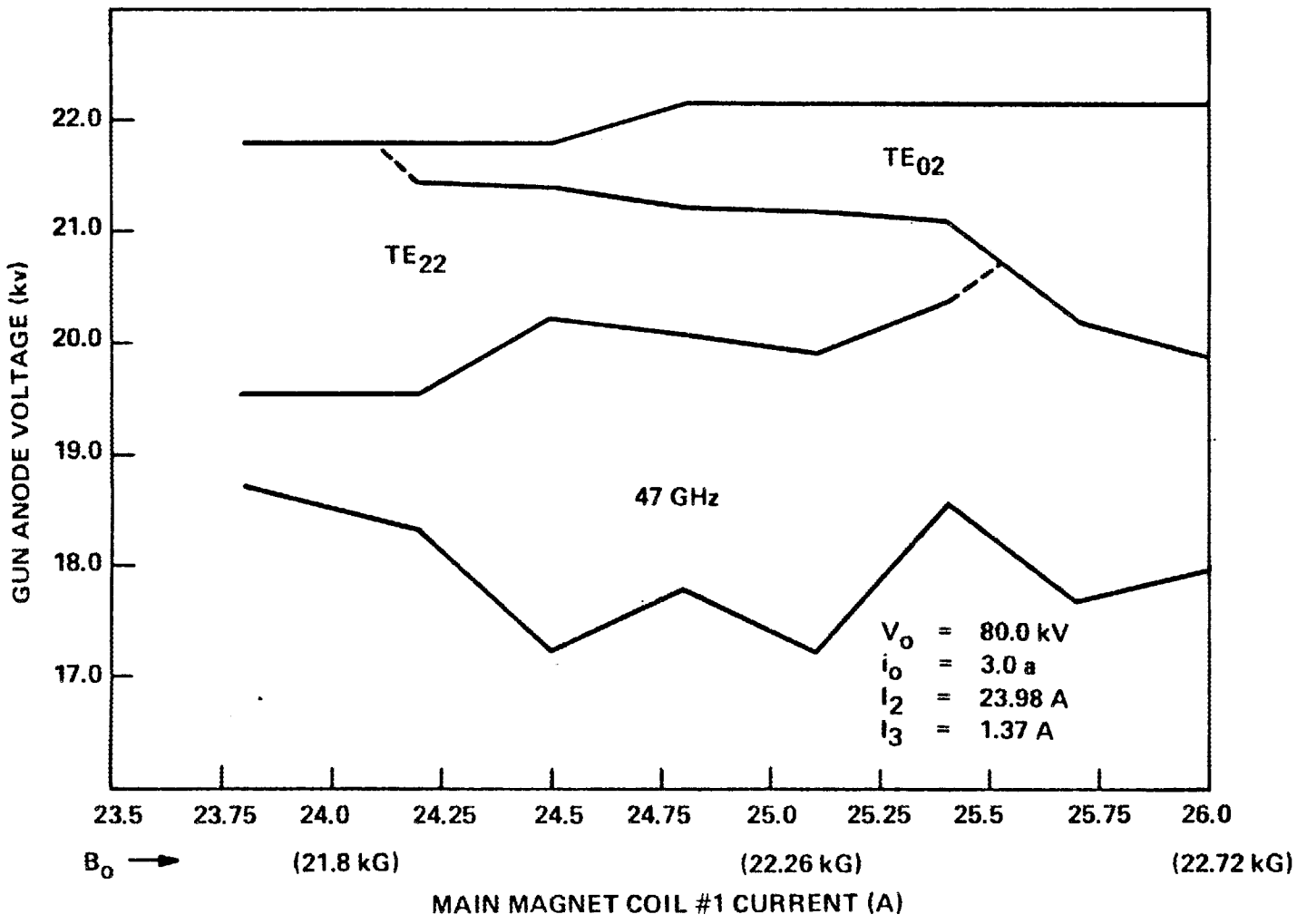

Figure 403. 56 GHz Pulsed 3 Amp Oscillation Map

Table 53 shows the 105 kW operation of the tube. Figures 404 through 407 show operation with tube parameters varied. The CW power versus magnetic field curve looks very similar to the pulsed power curve, except that the power is maximum at the point of switching to the TE_{22} mode. This is due to the fact that with operation at a low beam current, the region of TE_{02} operation is more limited than at higher currents, as seen in a typical starting current graph. By varying parameters at higher beam currents, the tube will probably have more dynamic range. A comparison of Figures 406 and 407 shows an increase in dynamic range when beam voltage and gun anode voltage are simultaneously varied. Again, these curves are at only 3 amperes. At 8 amperes they will be somewhat different. Figure 408 is the 3 ampere CW oscillation map. It is quite similar to the pulsed, 3 ampere oscillation map shown in Figure 403.

Table 53

56 GHz CW Operation

Beam Voltage	80.2	Kilovolts
Beam Current	3.0	Amperes
Gun Anode Voltage	22.0	Kilovolts
Solenoid #1 Current	24.85	Amperes
Solenoid #2 Current	23.62	Amperes
Solenoid #3 Current	1.41	Amperes
Output Power	105	Kilowatts
Efficiency	43	%
Frequency	55.89	GHz

The 56 GHz development program has verified frequency scaling of gyrotrons using a common gun, as predicted by Varian computer analysis. The program has also achieved 285 kw pulsed, with 44% efficiency, and 105 kW CW, with 43% efficiency. With new window designs developed during the 60 GHz development program, 200 kW could be achieved.

ORNL – DWG-83-2147

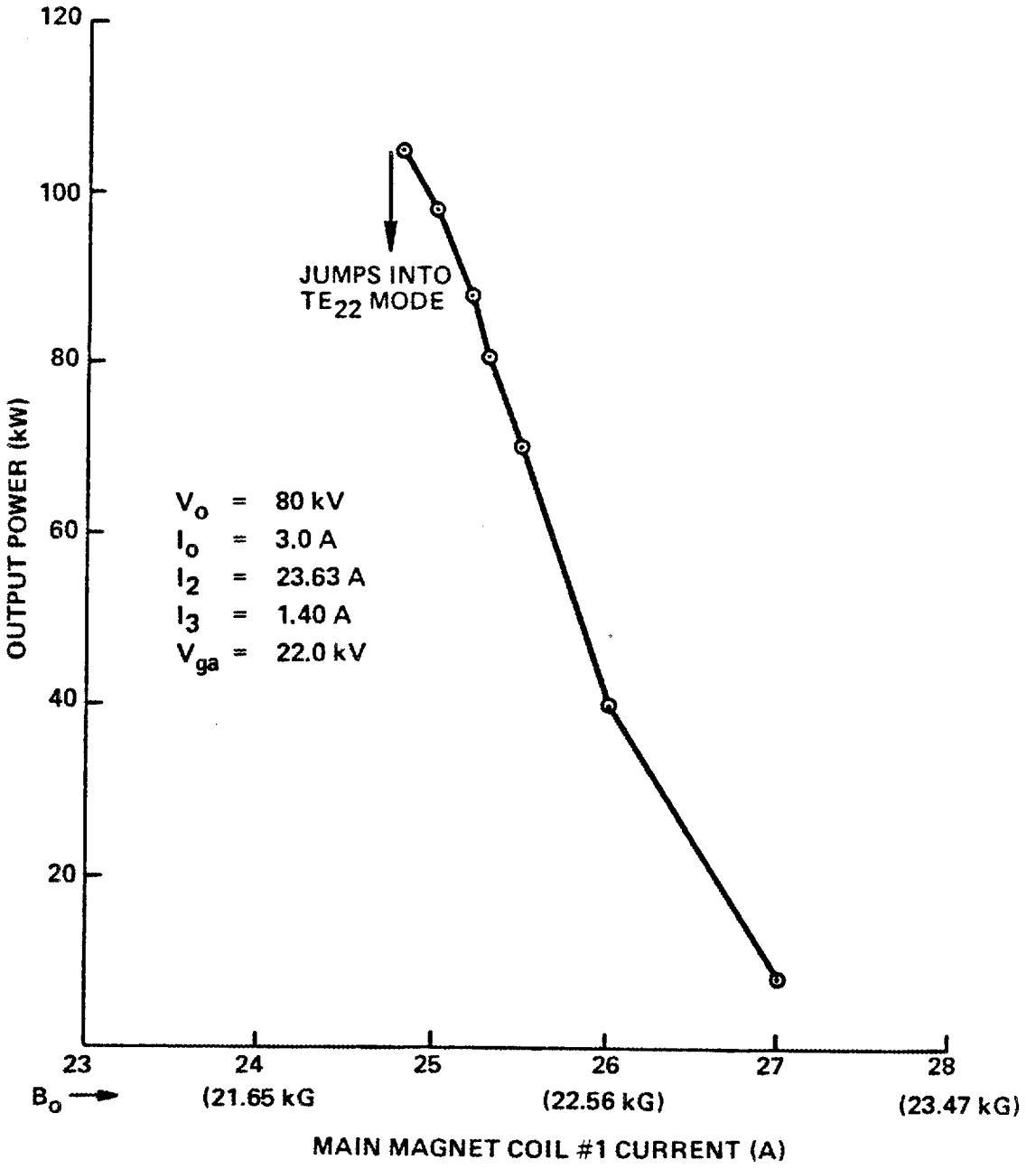

Figure 404. 56 GHz CW Power vs Magnet Current

ORNL – DWG-83-2148

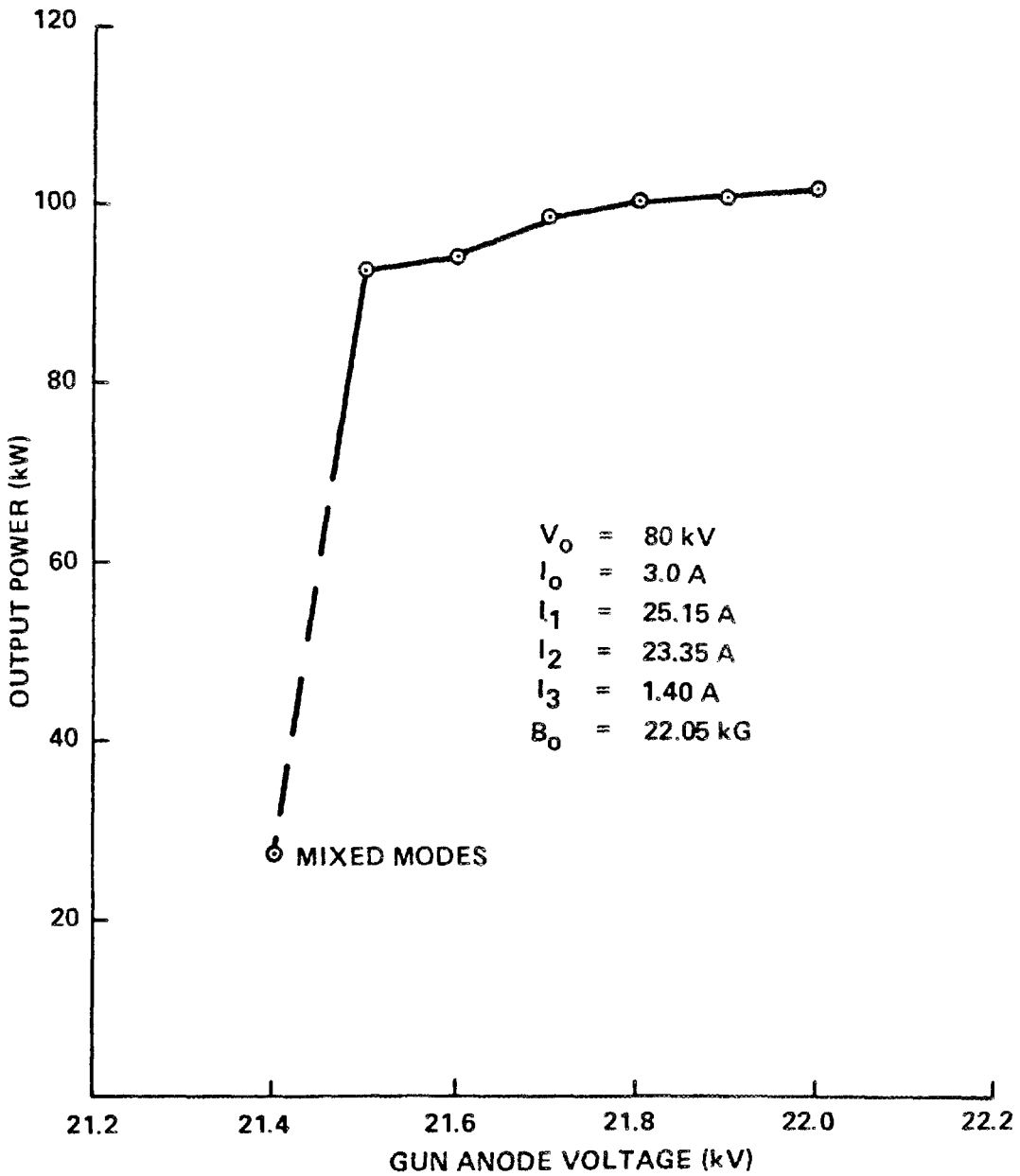

Figure 405. 56 GHz CW Power vs Gun Anode Voltage

ORNL – DWG-83-2149

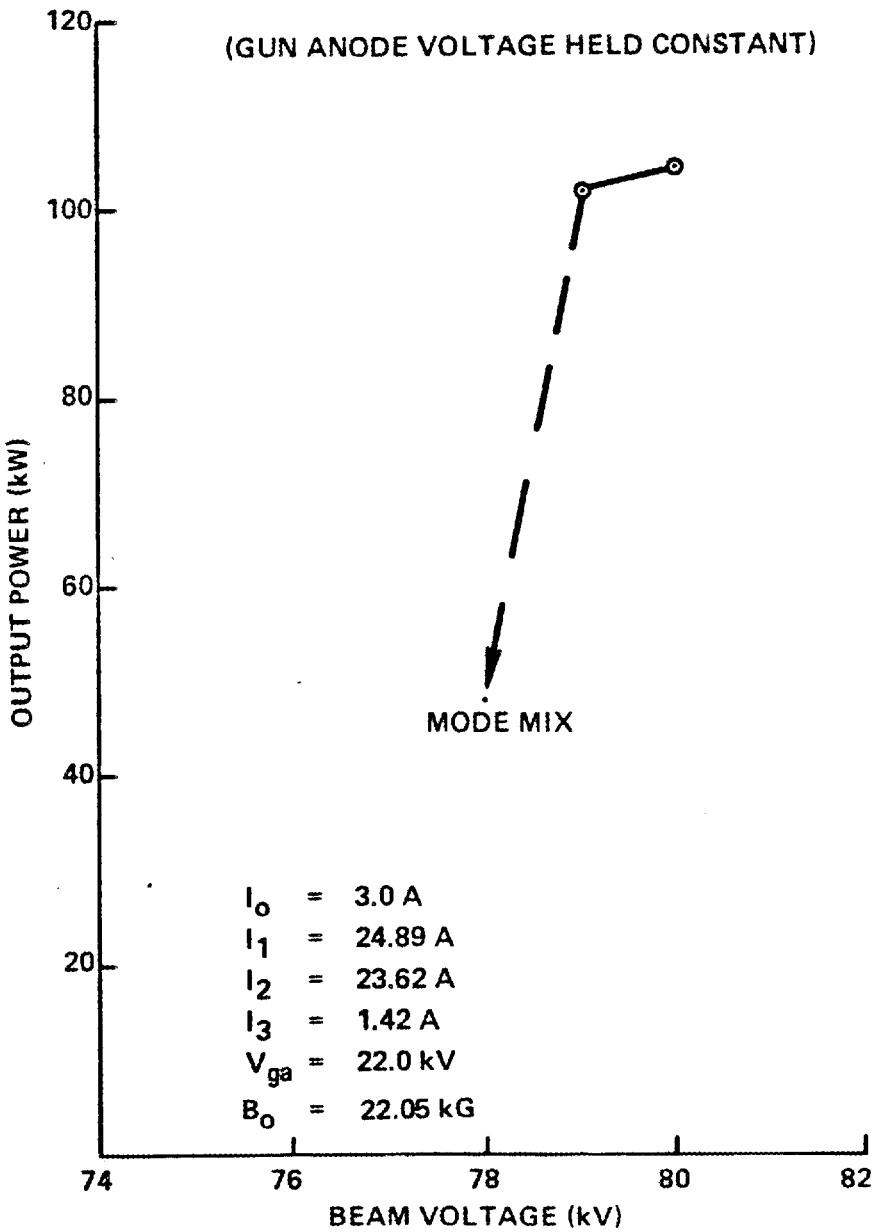

Figure 406. 56 GHz CW Power vs Beam Voltage

ORNL – DWG-83-2150

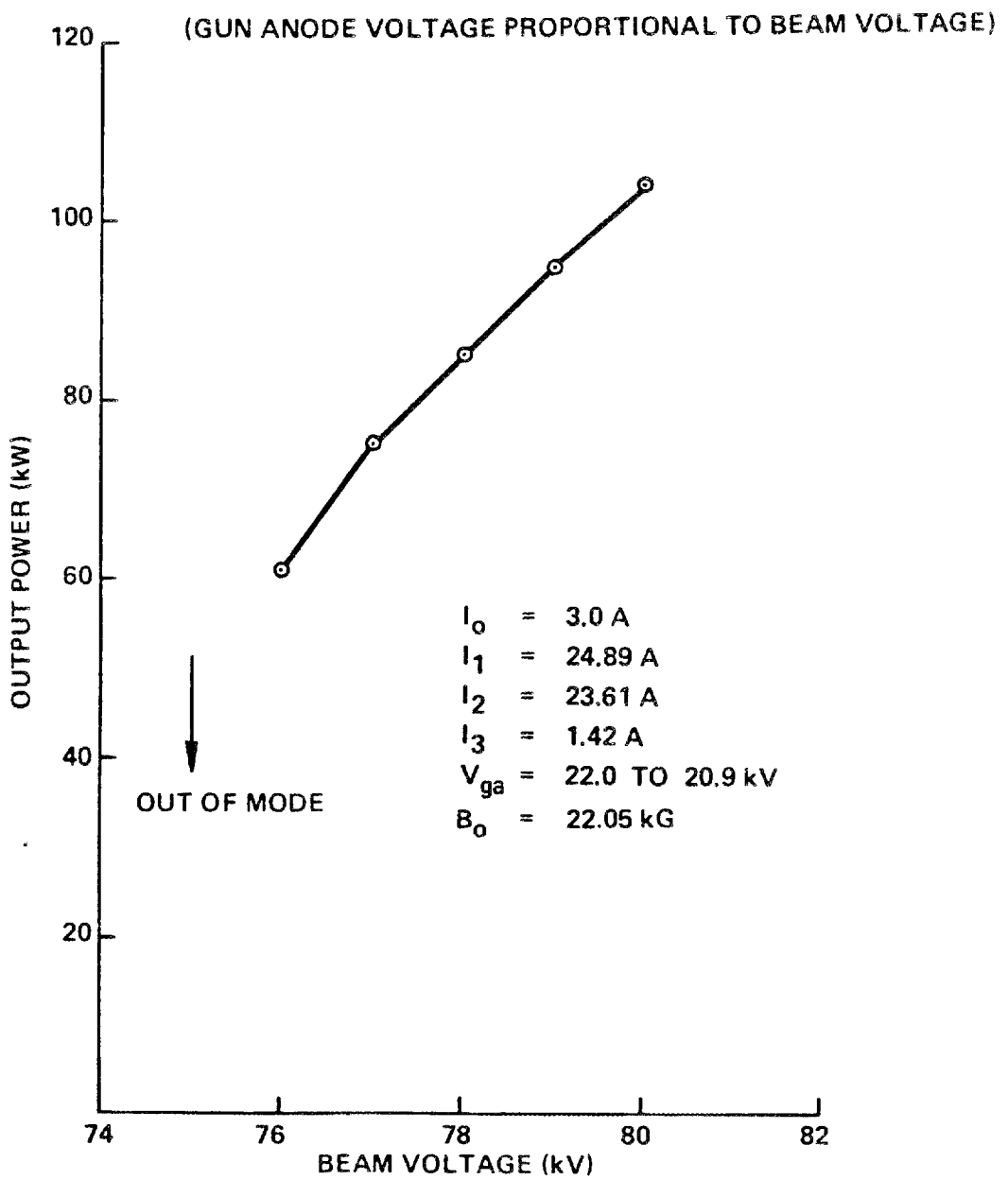

Figure 407. 56 GHz CW Power vs Beam Voltage

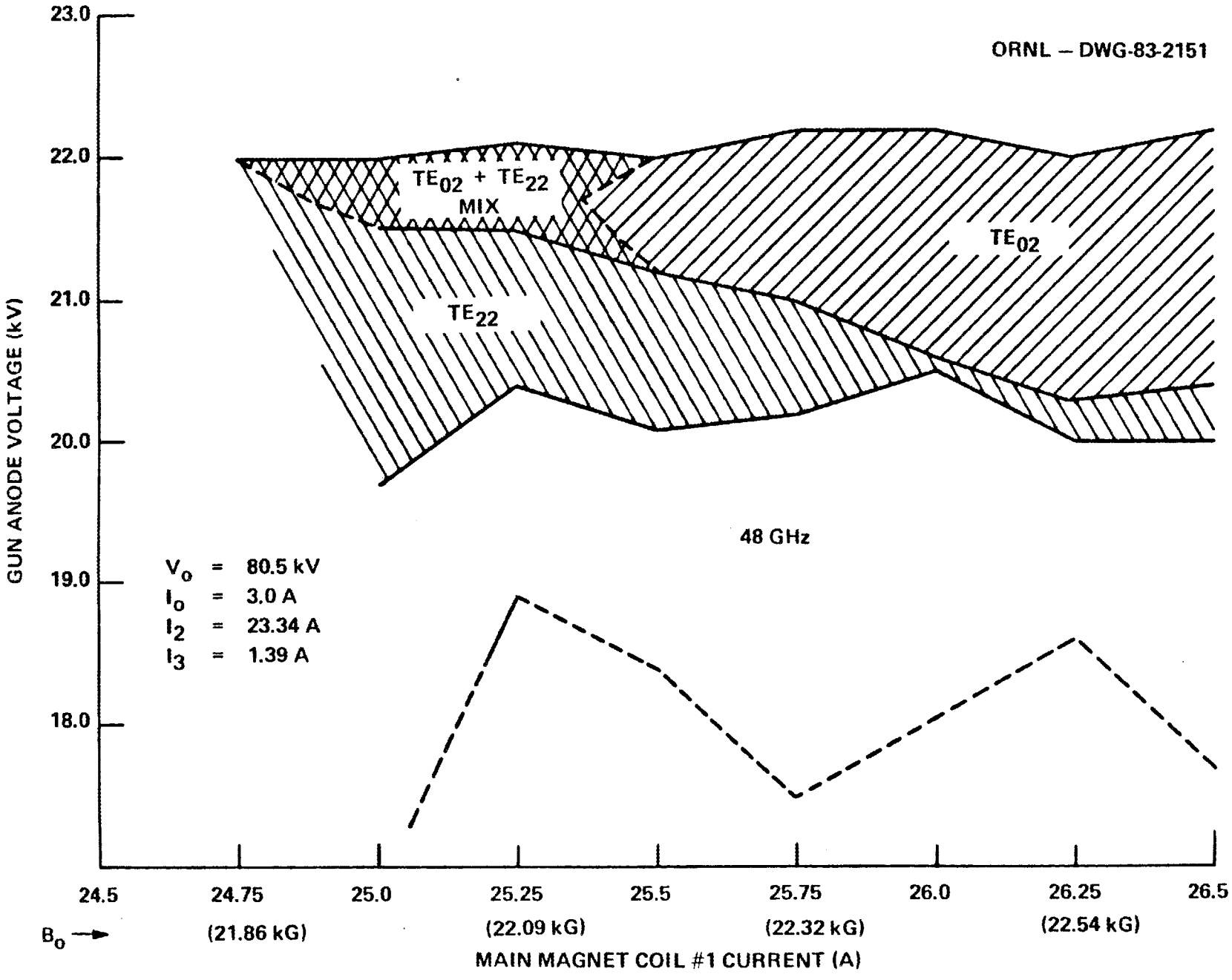

Figure 408. VGE-8005 Oscillation Map, CW, (3 A)

XI. SUMMARY

During the past five and one-half years, the Varian gyrotron development program has developed a 60 GHz, 200 kW CW gyrotron, studied gyrotron behavior using 28 GHz 200 kW CW tubes, studied frequency scaling, developed a 56 GHz gyrotron and studied design of a 100 GHz, 1 MW gyrotron[49]. This development program was funded by Oak Ridge National Laboratory, operated by Union Carbide Corporation and Martin Marietta Energy Systems, Inc., for the U.S. Department of Energy.

In April 1979, development of a 110 GHz, 200 kW CW gyrotron started. Six months later, the computer design of the gun, cavity, collector, window and superconducting solenoid magnet were completed.

In December 1979, the program was redirected to develop 60 GHz, 200 kW CW, 100 ms pulsed and 30 s pulsed gyrotrons. The original magnet design was retained. The computer designs of the collector and window were completed by February 1980. The following month, the computer design of the gun was completed. The cavity design was completed in May 1980.

In June 1980, the magnet purchase contract with Magnetic Corporation of America was signed. The first magnet was delivered six months later.

Assembly of the first gun was completed in December 1980, and the first experimental tube, X-1, was installed for test the following month. Tests of X-1, completed in March 1981, indicated 150-200 kw of peak output power at 100 ms pulse duration and identified a beam alignment problem in the magnet and a sensitivity problem to modulator pulse shape.

In April 1981, the Nike Zeus Test Set was shut down to intall the long pulse modulator. During the shut down, the second experimental tube, X-2, and third experimental tube, X-3, were assembled.

X-2 included a water-cooled anode and a change of length to shift the cathode position. X-3 was like X-2 except for a modified anode load cavity.

By August 1981, the Nike Zeus Test Set was operable for tube testing. Testing of X-1 demonstrated 86 kw of output power at 60 ms pulse duration at 12% duty and identified a body heating problem, before failing in test with a collector water-to-vacuum leak. Collector beam damage was observed.

X-3, in November 1981, demonstrated 200 kw of output power at 100 ms. Tests identified residual signs of a dynamic range problem, mode interference from the TE_{22} mode and body heating. The tube was destroyed when the modulator pulse repetition rate generator failed, taking the tube to >30% duty.

X-2 demonstrated 100 kw peak output power at 20% duty and confirmed the previously observed problem areas of limited dynamic range, TE_{22} mode interferences and body heating.

In December 1981, assembly of the fourth experimental tube, X-4, was completed. X-4 was a CW tube, like X-3 except for a five-inch inside diameter collector and a double-disc, face-cooled window.

X-4 demonstrated, in March 1983, 70 kW CW output power, 640 kW CW beam power and 32 s beam pulse duration at 50% duty. Testing was terminated because of deteriorating rf performance caused by melting in the collector downtaper.

A rebuild of X-3, X-3R, was also completed in March 1983. X-3R incorporated a new, shorter cavity with higher Q, and a modified drift tube to avoid body heating. X-3R demonstrated 230 kw peak output power with 36% efficiency, the elimination of body heating, improved dynamic range and extended operation with 200 kw at 100 ms pulse duration.

In May 1982, assembly of the fifth experimental tube, X-5, was completed. This tube was a CW version of X-3R. It demonstrated 123 kW CW output power before a vacuum-side window failure. Window failure of this tube led to an investigation and implementation of an infrared window observation system for later tubes.

The first step cavity was introduced in the sixth experimental tube, X-6, assembled in April 1983. On June 8, 1983, X-6 demonstrated 200 kW of CW output power. This represented a major milestone in gyrotron development. The tube also demonstrated improved stability and dynamic range and identified a multimode output problem. This same month, the infrared camera system, which measured the window temperature, was first demonstrated.

In July 1983, the program emphasis shifted to pure mode output. A 2.5-inch inside diameter collector was incorporated into the seventh experimental tube, X-7. Assembly was completed in May 1984. The next month, X-7 demonstrated 200 kW CW operation with 95% TE_{02} mode and cyclic fatigue performance.

A gyrotron behavior study started in December 1980 to investigate gyrotron arcing, the maximum power capability at 28 GHz, stability and parameter variation effects, and improved cavity designs.

In October 1981, the study concluded with the following results: Diagnostics for observing arcing were improved. Processing procedures reduced arcing. A 342 kW CW window limit was demonstrated at 28 GHz. Mode mapping gave insight and understanding to stability problems. Alternate cavity designs gave understanding, but not performance.

An alternate frequency study started in February 1981 to determine methods of scaling gyrotron designs $\pm 20\%$ in frequency. At the end of the six month study, scaling the 60 GHz tube to 52 and 56 GHz and the 28 GHz tube to 30 GHz appeared feasible. Gun scaling to 30 GHz was marginal.

A 56 GHz gyrotron development was started in January 1982, based on the design results of the alternate frequency study. In November of the same year, 285 kw of peak output power with 44% efficiency was demonstrated. CW output was intentionally limited to 105 kW because of the failure of the X-5 window.

In March 1983, a 100 GHz, 1 MW gyrotron design study began. During the six month program, detailed calculations were performed for TE_{0n1} and TE_{m11} cavities, guns, windows and output systems.

XII. REFERENCES

1. H. R. Jory, E. L. Lien, and R. S. Symons, Final report, "Millimeter Wave Study Program", Oak Ridge National Laboratory Order No. Y12 11Y-49438V, November 1975.

2. D. V. Kisel, G. S. Korablev, V. G. Navel'yev, M. I. Petelin and Sh. E. Tsimring, "An Experimental Study of a Gyrotron, Operating at the Second Harmonic of the Cyclotron Frequency, with Optimized Distribution of the High Frequency Field", Radio Engineering and Electronic Physics, Vol. 19, No. 4, 95-100, 1974.

3. S. Hegji, H. Jory, and J. Shively, "Development Program for a 200 kW CW, 28 GHz Gyroklystron Quarterly Report No. 6", Union Carbide Contract No. 53X01617C, Varian Associates, Inc., July through September 1977.

4. H. Jory, S. Evans, S. Hegji, J. Shively, R. Symons and N. Taylor, "Development Program for a 200 kW, CW, 28 GHz Gyroklystron Quarterly Report No. 9", Union Carbide Corporation Contract No. W-7405-eng-26, ORNL Sub-01617/9, Varian Associates, Inc., April through June 1978.

5. V. A. Flyagin et al, "The Gyrotron", IEEE Trans. MTT-25, No. 6 pp. 522-527, June 1977.

6. F. Friedlander, E. Galli, H. Jory, F. Kinney, K. Miller, J. Shively and R. Symons, "Development Program for a 200 kW CW 28 GHz Gyroklystron Quarterly Report No. 1", Union Carbide Corporation Contract No. 53X01617C, Varian Associates, Inc., July 1976.

7. F. Friedlander, E. Galli, H. Jory, K. Miller, J. Shively, and R. Symons, "Development Program for a 200 kW CW 28 GHz Gyroklystron Quarterly Report No. 2, "Union Carbide Corporation Contract No. 53X01617C, Varian Associates, Inc. October 1976.

8. V. M. Manilov and S. E. Tsimring, "Synthesis of Axially Symmetric Systems of the Formation of Helical Electron Beams", Radiotekhnika, Elektronika, vol. 23, No. 7, pp. 1486 - 1499 July 1978.

9. L. Solymar "Monotonic Multi-Section Tapers for Overmoded Circular Waveguides", I.E.E. paper #2839R pp. 121 - 128 January 1959.

10. K. Tomiyasu, "Mode Conversion in Short Conical and Asymmetrical-Rectangular Waveguide Tapers", IRE MTT pp. 197 - 199, 1968.

11. D. S. Stone, K. L. Felch and S. T. Spang, "Mode Specific Reflectometry in Multimode Waveguide", IEEE Trans. Microwave Theory Tech. Vol. MTT-31 No. 9 pp. 710 - 718, Sept 1983.

12. J. Dimeff and L. J. Fox, "Electromagnetic Radial Diverter Calorimetric Load, U.S. Pat. Off. Application Serial No. 517603, filed July 27, 1983.

13. H. R. Jory and A. W. Trivelpiece, J. Appl. Phys., 39, No. 7, 3053 (1968).

14. H. Derfler, T. Grant, D. S. Stone, Proceedings IEEE Intl. Conf. Plasma Science, Sante Fe, NM (May 1981) pg. 48.

15. S. V. Kolosov, A. A. Kurayeu, G. Ya. Slepyan, and F G. Sheuchenke Radiotekha Elektron, 20, No. 7 1440 (1975).

16. K. R. Chu - private communication.

17. G. S. Nusinovich - private communication.

18. G. S. Nusinovich and R. E. Erm, Elektron, Tekh., Ser. 1: Elektron UHF, No. 8 55-60 (1972).

19. K. R. Chu, M. E. Read, and A. K. Ganguly, IEEE Trans. Microwave Theory Tech., Vol. MTT-28, No. 4, 318 (1980).

20. K. E. Kreischer and R. J. Temkin, International Journal of Infrared and Millimeter Waves, Vol. 1, No. 2, 195 (1980).

21. K. R. Chu, Phys. Fluids 21, 2354 (1978).

22. Y. Carmel et al., IEEE International Conference on Plasma Science - Conference Record, p. 62 (May 1982).

23. R. S. Symons and S. J. Evans, "Multi-diameter Cavity for Reduced Mode Competition in Gyrotron Oscillator", U.S. Patent Application Serial Number 448,663.

24. Y. Carmel et al., "Realization and Stabilization of a Stable and Highly Efficient Gyrotron for Controlled Fusion Research," Physical Review Letters, Vol. 50, No. 2, pp. 112 - 116, 1983.

25. Carslaw and Jaeger, Conduction of Heat in Solids, Oxford Press, London 1959.

26. W. H. McAdams, Heat Transmission, McGraw-Hill, New York 1954, p. 389, S. Mirshak, W. S. Durant and R. H. Towell, "Heat Flux at Burnout", E.I. duPont de Nemours and Co., AEC Research and Development Report, February 1959.

27. M. L. Anthony, "Temperature Distributions in Composite Slabs due to a Suddenly Activated Plane Heat Source", Instn. Mech. Engrs., London and ASME, New York, 1951 pp. 236 - 249.

28. W. E. Mason, Jr., "TACO - a Finite Element Heat Transfer Code", Lawrence Livermore Laboratory, UCID-17980, February 1980.

29. W. H. McAdams, Heat Transmission, McGraw-Hill Book, Company, Inc., New York, 1954, Third Edition, p. 219.

30. Ibid, p. 393

31. Ibid, p. 392

32. R. C. Crosby and D. H. Desy, "Dispersion Strengthening in Copper-Alumina and Copper-Yttria Alloys", Bureau of Mines R1 7266, June 1969.

33. E. H. Schmidt, "Mechanical Property Data for Oxygen-Free High-Conductivity Copper and Boron Deoxidized Copper", NASA Tech Brief 66-10273 (North American Aviation, Inc.) Feb. 1966.

34. F. Pawlek and K. Reichel, "The Effect of Impurities on the Electrical Conductivity of Copper", Zeit Metallkunde, Vol. 47, 1956, p. 347.

35. AMAX Inc. specifications.

36. J. J. Esposito and R. F. Zabora, "Thrust Chamber Life Prediction Vol I Mechanical and Physical Properties of High Performance Rocket Nozzle Materials", NASA CR-134806, Mar. 1975.

37. Specifications, Glidden Metals Division of SCM Corp.

38. H. S. Carslaw and J. C. Jaeger Conduction of Heat in Solids, Second Edition, Oxford University Press, 1959, p. 112.

39. K. Liu, Oak Ridge National Laboratory, private communication.

40. H. G. Unger, "Circular Waveguide Taper of Improved Design", The Bell System Technical Journal, Vol. 37, July 1958, pp. 899 - 912.

41. C. H. Tang, "Optimization of Waveguide Tapers Capable of Multimode Propagation", IEEE Trans. on Microwave Theory and Techniques, pp. 442-452, September 1961.

42. W. Flugge, "Handbook of Engineering Mechanics, McGraw Hill, New York 1962, p. 34-39

43. Ibid, p. 44-48.

44. K. R. Chu, Phys. Fluids 21, 2354 (1978).

45. G. S. Nusinovich and R. E. Erm, Elektronnaya Tekhnika, Series 1, Elektronika UHF 1972, No. 8, pp 55-60.

46. C. Moeller, Int. J. Electronics, 53, No. 6 (1982) pp. 587-593.

47. S. E. Miller, Bell System Tech. J., 33 (1954) pp. 667-719.

48. S. J. Evans et al, "60 GHz Gyrotron Development Program Alternate Frequency Study", Report prepared by Varian Associates, Inc., under Subcontract Purchase Order No. 53Y-21453C for Oak Ridge National Laboratory operated by Union Carbide Corporation for the U.S. Department of Energy, Contract W-7405-eng-26, August 1981.

49. K. Felch, R. Bier, M. Caplan and H. Jory, "100 GHz, 1 MW, CW Gyrotron Study Program Final Report", prepared by Varian Associates, Inc., under Subcontract Purchase Order No. 53Y-21453C for Oak Ridge National Laboratory, operated by Union Carbide Corporation for the U.S. Department of Energy under Contract No. W-7405-eng-26, September 1983.

APPENDIX A

DIELECTRIC PROPERTIES OF WATER[1,2]

Water exhibits an anomalous dielectric dispersion at millimeter wavelengths. Debye first gave the theory of an ideal polar dielectric in an rf field in terms of a single relaxation time. It has been shown that the following expression holds generally for linear dielectrics:

$$e - e_o = \frac{e_s - e_o}{1 + j\omega t} \tag{1}$$

where t = relaxation time

e = complex dielectric constant

e_o = that part of the dielectric constant which is due to the atomic and electronic polarization, and is assumed to be real and independent of ω

ω = angular frequency

e_s = static dielectric constant.

And the following expression holds generally for optical constants:

$$n^2 - k^2 = e' = \frac{e_s - e_o}{1 + \omega^2 t^2} + e_o = \frac{e_s - e_o}{1 + [\lambda_s/\lambda]^2} + e_o \tag{2}$$

$$2nk = e'' = \frac{(e_s - e_o)\omega t}{1 + \omega^2 t^2} = \frac{(e_s - e_o)\lambda_s/\lambda}{1 + [\lambda_s/\lambda]^2}$$

where, n = real part of refractive index

k = absorption coefficient

e' = real part of e

e'' = imaginary part of e

λ_s = wavelength corresponding to $1/t$

λ = wavelength corresponding to ω

$$\tan \delta = \frac{e''}{e'} = \frac{(e_s - e_o)\ \lambda_s/\lambda}{e_s - e_o\ [\lambda_s/\lambda]^2}.$$

These equations represent the fall of dielectric constant from its static value, e_s, to its optical value, e_o. The fall is accompanied by a single broad absorption band in the neighborhood of the characteristic wavelength λ_s. λ_s is a function of temperature.

The constants used in this theory are shown in Table AI.

Table I

Constants for Dielectric Properties of Water

$e_o = 5.5$

Temperature [°C]	e_s	λ_s [cm]
0	88.2	3.34
10	84.2	2.39
20	80.36	1.80
30	76.7	1.39
40	73.1	1.12
50	69.8	0.912
60	66.6	0.760
75	62.1	0.608

Theory and measurements have been demonstrated to agree to within one percent up to 23.6 GHz and have been confirmed recently at 60 GHz.[3]

Calculated dielectric constants and loss tangents for several popular frequencies are given in Table II for temperatures from 0°C to 75°C. These data are plotted in various ways in Figures 1 through 4.

Table II
Dielectric Properties of Water

T °C	28 GHz e'	28 GHz tan δ	35 GHz e'	35 GHz tan δ	60 GHz e'	60 GHz tan δ	95 GHz e'	95 GHz tan δ	140 GHz e'	140 GHz tan δ
0	13.21	1.82	10.60	1.88	7.31	1.66	6.23	1.24	5.84	0.90
10	18.65	1.57	14.46	1.73	8.80	1.79	6.85	1.49	6.13	1.14
20	25.06	1.31	19.32	1.50	10.86	1.78	7.73	1.65	6.54	1.34
30	32.01	1.08	25.10	1.27	13.65	1.66	8.99	1.71	7.15	1.50
40	37.78	0.89	30.45	1.07	16.72	1.50	10.47	1.69	7.88	1.58
50	42.76	0.74	35.64	0.90	20.34	1.33	12.38	1.61	8.86	1.62
60	46.13	0.63	39.69	0.76	23.94	1.17	14.49	1.49	9.99	1.60
75	48.30	0.50	43.14	0.62	28.32	0.98	17.51	1.32	11.75	1.51

ORNL – DWG-83-2153

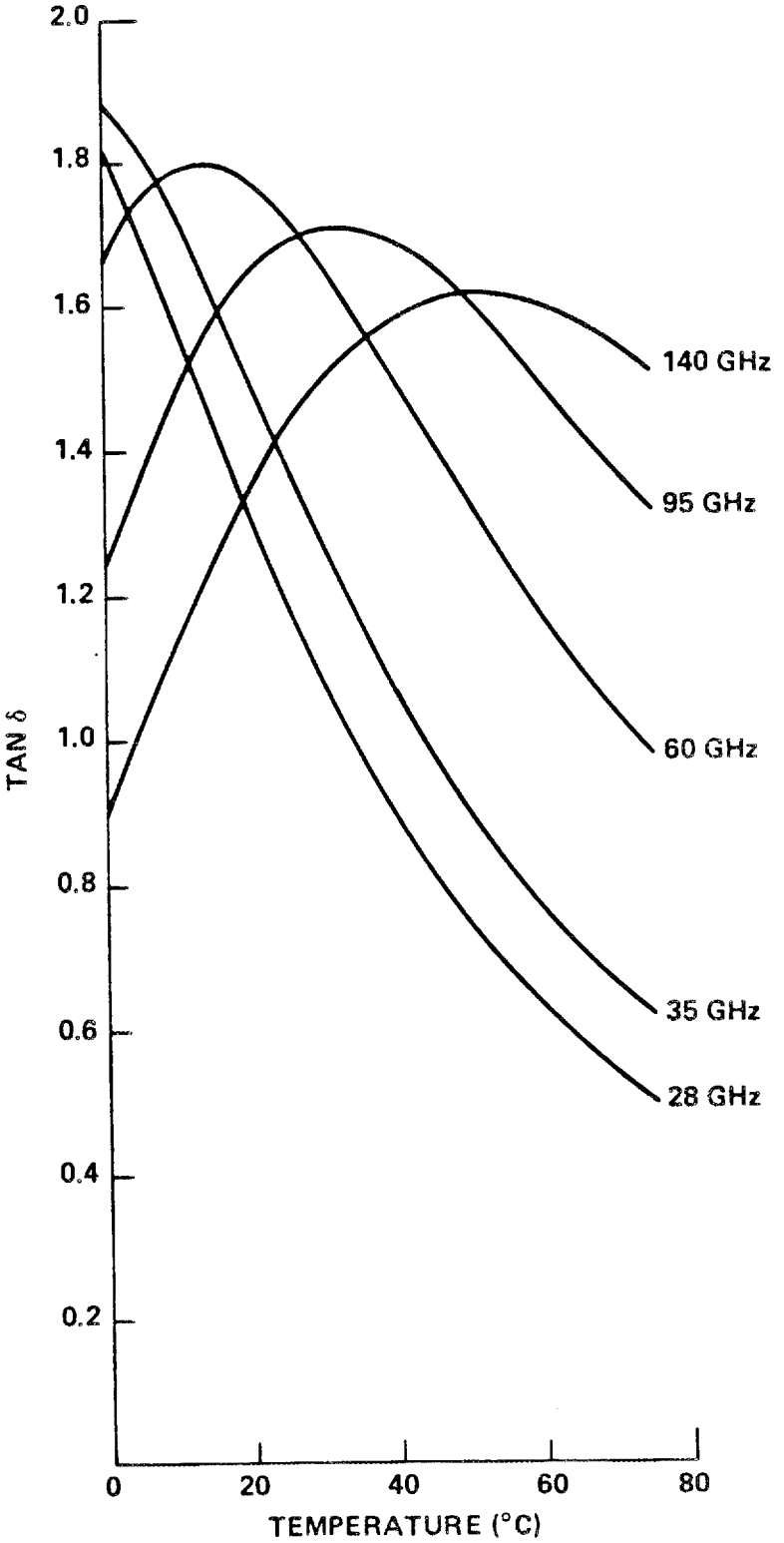

Figure 1. Temperature Dependence of the Loss Tangent of Water for Several Popular Frequencies

ORNL – DWG-83-2154

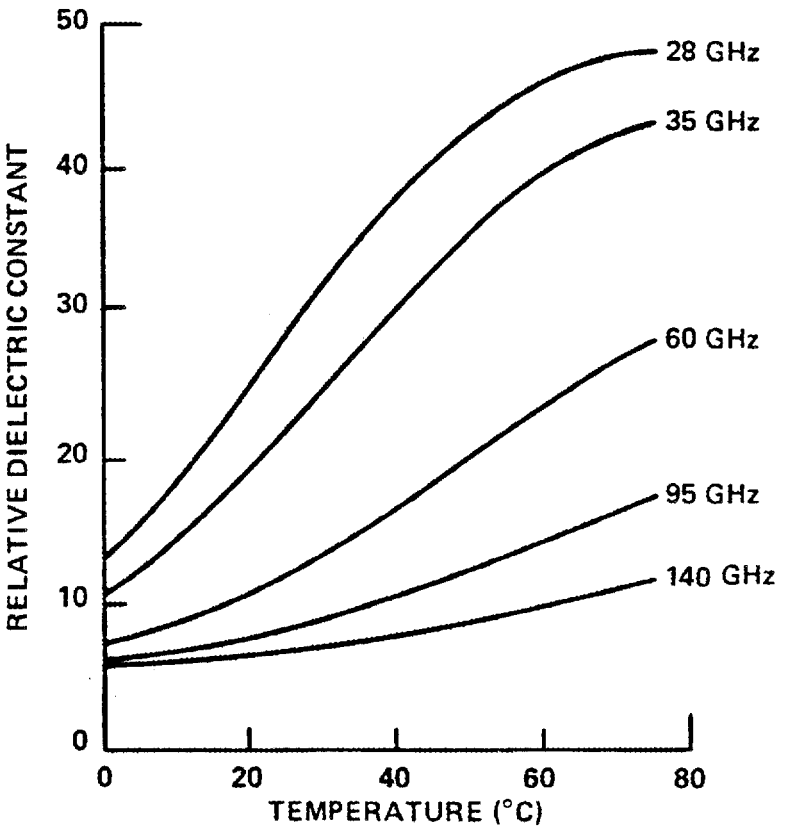

Figure 2. Temperature Dependence of the Relative Dielectric Constant of Water for Several Popular Frequencies

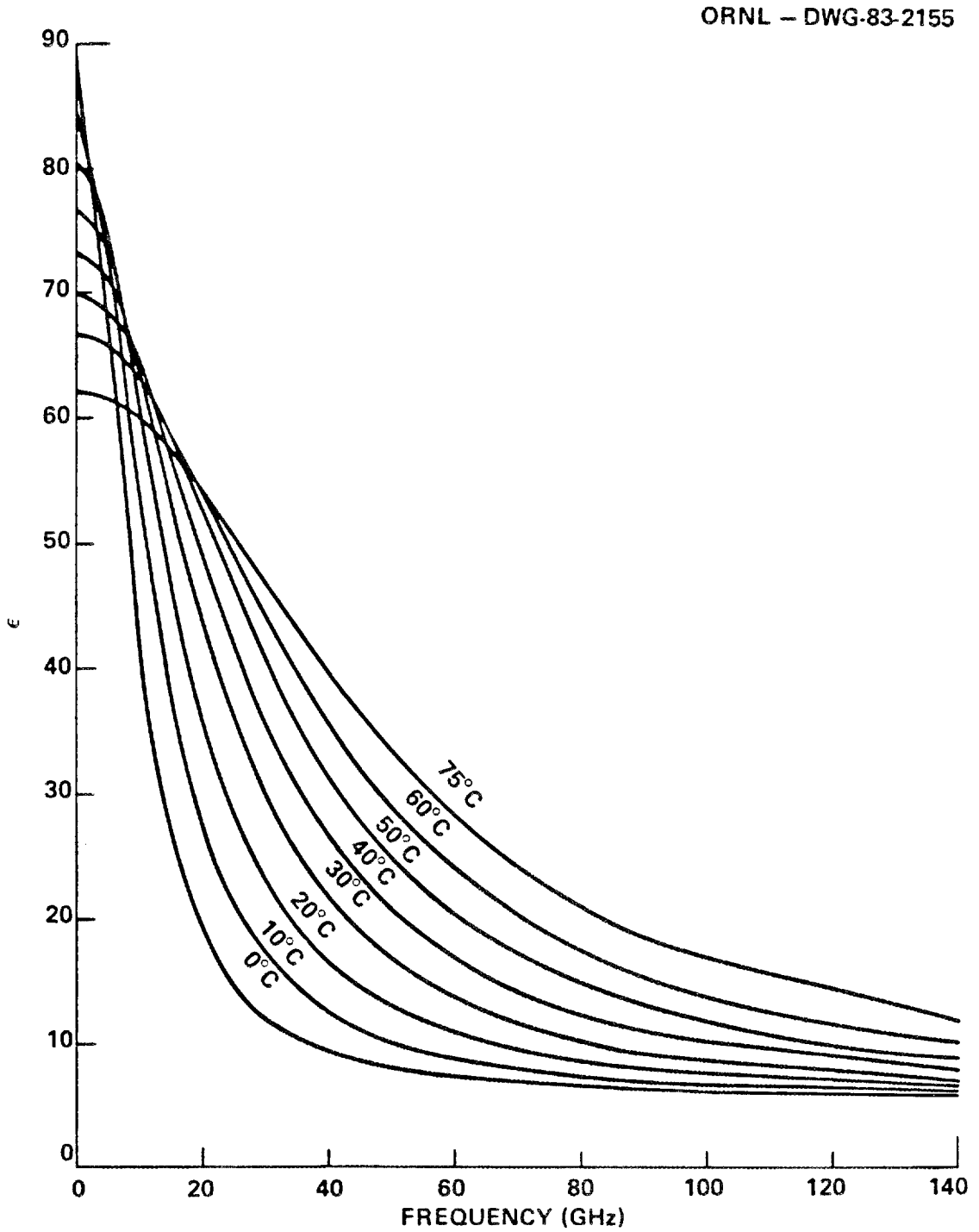

Figure 3. Frequency Dependence of the Dielectric Constant of Water for Several Temperatures

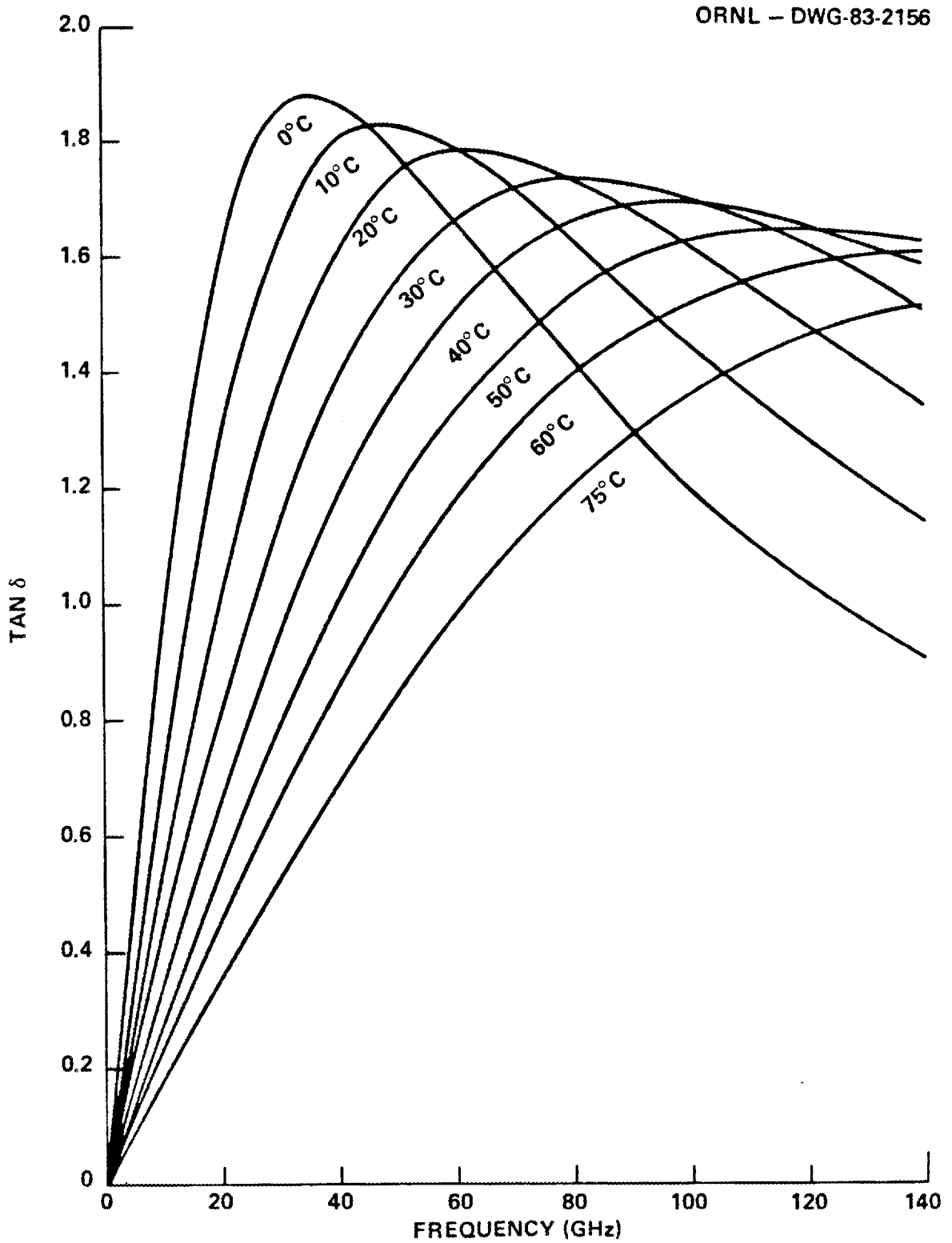

Figure 4. Frequency Dependence of the Loss Tangent of Water for Several Temperatures

REFERENCES

1. C. H. Collie, J. B. Hasted and D. M. Ritson, "The Dielectric Properties of Water and Heavy Water", Proc. Phys. Soc., 60 p. 145 (1948).

2. S. Ramo, J. R. Whinnery and T. Van Duzer, Fields and Waves in Communication Electronics, John Wiley & Sons, Inc., New York, 1965, p. 330.

3. M. N. Afsar and J. B. Hasted, "Submillimetre Wave Measurements of Optical Constants of Water at Various Temperatures", Infrared Physics, Vol. 18, pp. 835 - 841, Pergamon Press Ltd (1978).

APPENDIX B

MODE CONVERSION IN OVERMODED CIRCULAR WAVEGUIDES AT CONICAL CYLINDRICAL JUNCTIONS

A. DERIVATION OF WAVE FIELDS IN A CONICAL TAPER

The solution of Maxwell's equations in spherical coordinates gives for the wave electric field, assuming that only TE modes are propagating,[1]

$$E_r = E_\theta = 0; \; E_\phi = \frac{C_1}{\sqrt{r}} \; H^{(2)}_{p+1/2}(\beta r) \; \frac{d}{d\theta}\left[P_p(\cos\theta)\right] \tag{1}$$

where, C_1 is a constant, $\beta = 2\pi/\lambda$, $H^{(2)}_{p+1/2}$ is the Hankel function of the second kind of half integer order $(p + 1/2)$, P_p is the Legendre polynomial of integer order p, and the coordinate system (r, θ, ϕ) is shown in Figure 1.

In the limit of small angle: $\theta \ll 1$, and $r/\lambda \gg 1$, so we may write

$$E_\phi = \frac{C_1}{\beta r} \; J_1\left[(p + 1/2)\theta\right] \exp\left[-i\left\{\beta r + \sum_{\ell = 1}^{3} b_\ell \frac{(p + 1/2)^{2\ell}}{(\beta r)^{2\ell-1}}\right\}\right], \tag{2}$$

where the constants b_ℓ are: $b_1 = 1/2$, $b_2 = 1/24$, and $b_3 = 1/80$. Now we match the boundary conditions at $\theta = \theta_o$, namely, that $E_\phi(\theta_o) = 0$. So we require $(p + 1/2)\theta = X_{1n}$, where X_{1n} is the nth positive root of the equation $J_1(X) = 0$. The expression for E_ϕ becomes

$$E_\phi = \frac{e^{-i\beta r}}{\beta r} \sum_{n = 1}^{s} g_n J_1\left(X_{1n} \frac{\theta}{\theta_o}\right) \exp\left[-i \sum_{\ell = 1}^{3} \beta_\ell \frac{X_{1n}^{2\ell}}{(\beta r)^{2\ell-1}\theta_o^{2\ell}}\right], \tag{3}$$

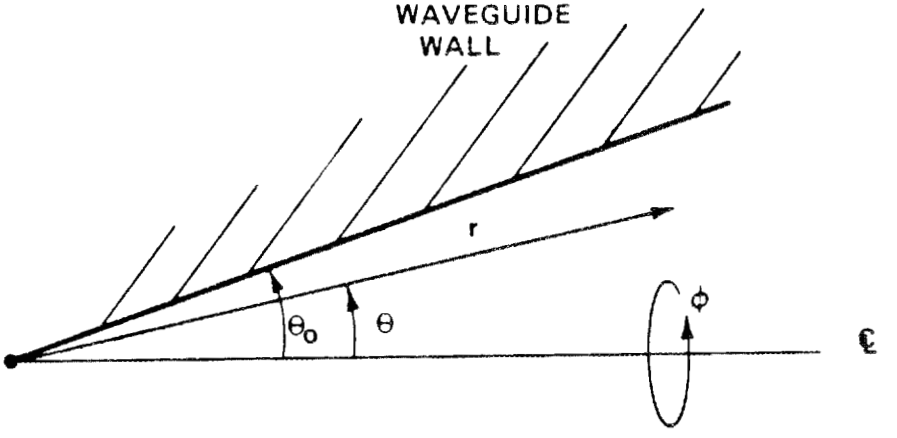

Figure 1. Spherical Coordinate System in Cone

where E_ϕ is now expressed as a linear combination of TE_{on} modes from the lowest order (TE_{01}) to the highest order which will propagate (TE_{os}). The order s beyond which modes are cut off is

$$s \cong \frac{2a}{\lambda} - \frac{1}{4} \qquad (s \gg 1) \quad . \tag{4}$$

B. MATCHING THE BOUNDARY CONDITIONS AT THE CONICAL-CYLINDRICAL JUNCTION

We now introduce a complication and allow the first taper (taper angle Θ_{10}) to be joined to a second taper (taper angle Θ_{20}). This geometry is shown in Figure 2. To simplify the mathematics of matching the wave electric fields at the boundary defined by the arc at r_2 through the angle Θ_2, we will express the coordinate system (r_1, Θ_1) in the first taper in terms of the coordinate system in the second taper (r_2, Θ_2). Then we will let the second taper angle Θ_{20} go to zero for the case of a conical-cylindrical junction. From Figure 2 we have

$$r_1^2 = r_2^2 + (r_2 - d)^2 - 2r_2(r_2 - d)\cos\Theta_2 \quad . \tag{5}$$

For small angles

$$r_1 = d\left[1 + \frac{a}{2d}(\Theta_{10} - \Theta_{20})\frac{\Theta_2^2}{\Theta_2^2}\right] \quad , \tag{6}$$

and also

$$\frac{\Theta_1}{\Theta_{10}} \simeq \frac{\Theta_2}{\Theta_{20}} \quad . \tag{7}$$

The second term in the brackets in Equation 6 is much less than unity so we can expand,

$$\left[1 + \frac{a}{2d}(\Theta_{10} - \Theta_{20})\frac{\Theta_2^2}{\Theta_{20}^2}\right]^{-(2\ell-1)} \simeq 1 - \frac{a}{2d}(\Theta_{10} - \Theta_{20})\frac{\Theta_2^2}{\Theta_{20}^2}(2\ell-1) \quad . \tag{8}$$

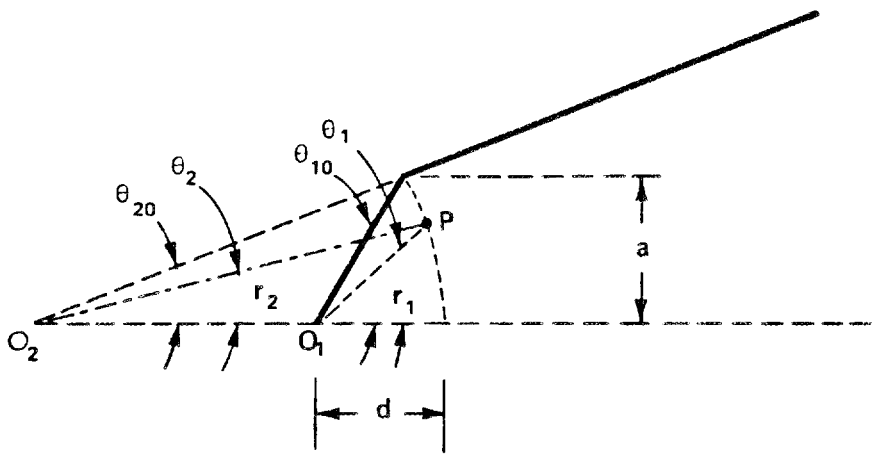

Figure 2. Junction of Two Conical Tapers of Different Angle

From Equation 3, the expression for the field intensity of a single incident TE_{on} mode in the first taper is

$$E_{\phi}^{(1)} = \frac{g_n^{(1)}}{\beta r_1} J_1\left(X_{1m} \frac{\theta_1}{\theta_{10}}\right) \exp\left[-i\left\{\beta r_1 + \sum_{\ell=1}^{3} b_\ell \frac{X_{1n}^{2\ell}}{(\beta r_1)^{2\ell-1} \theta_{10}^{2\ell}}\right\}\right] . \tag{9}$$

Substituting the coordinate system of the second taper through Equations 6 and 7, we have

$$E_{\phi}^{(1)} = C_2 J_1\left(X_{1n} \frac{\theta_2}{\theta_{20}}\right) \exp\left[-i\left(\frac{\beta a}{2}[\theta_{10} - \theta_{20}] \frac{\theta_2^2}{\theta_{20}^2}\right)\left(1 - \sum_{\ell=1}^{3} b_\ell (2\ell-1)\left(\frac{\lambda}{\lambda_{cn}}\right)^{2\ell}\right)\right] \tag{10}$$

where $\lambda_{cn} = 2\pi a/X_{1n}$ is the cutoff wavelength of the TE_{on} mode at the junction, and C_2 is another constant.

If we take Equation 10 in the limit $\theta_{20} \to 0$ then the second taper becomes a cylinder and the field intensity in the first taper may be expressed as

$$E_{\phi}^{(1)} = C_2 J_1\left(X_{1n} \frac{\theta_2}{\theta_{20}}\right) \exp\left[-i\left(\frac{\beta a}{2} \theta_{10} \frac{\theta_2^2}{\theta_{20}^2}\right)\left(1 - \sum_{\ell=1}^{3} b_\ell (2\ell-1)\left(\frac{\lambda}{\lambda_{cn}}\right)^{2\ell}\right)\right] . \tag{11a}$$

while the field intensity in the cylinder will be

$$E_{\phi}^{(2)} = \sum_{m=1}^{\infty} T_{mn} J_1\left(X_{1m} \frac{\theta_2}{\theta_{20}}\right) , \tag{12a}$$

or equivalently, by using Equation 7,

$$E_\phi^{(1)} = C_2 J_1\left(X_{1n}\frac{\Theta_1}{\Theta_{10}}\right)\exp\left[-i\left(\frac{\beta a}{2}\,\Theta_{10}\,\frac{\Theta_1^2}{\Theta_{10}^2}\right)\left(1 - \sum_{\ell=1}^{3} b_\ell(2\ell-1)\left(\frac{\lambda}{\lambda_{cn}}\right)^{2\ell}\right)\right], \tag{11b}$$

$$E_\phi^{(2)} = C_3 \sum_{m=1}^{\infty} T_{mn} J_1\left(X_{1m}\frac{\Theta_1}{\Theta_{10}}\right) \quad . \tag{12b}$$

The parameters C_2 and C_3 are constants.

Thus, we have eliminated the dummy variable Θ_2/Θ_{20} as expected for the case of a conical-cylindrical junction. The purpose of considering a second taper angle Θ_2 was to demonstrate that the expressions for the electric field in the conical taper and the cylinder are really special cases of a more general solution (Equation 3).

Now we require that $E_\phi^{(1)} = E_\phi^{(2)}$ at the boundary, define $t = \Theta_1/\Theta_{10}$, and write $\Theta_{10} \to \Theta_o$:

$$C_2 J_1\left(X_{1n}t\right)\exp\left[-i\left(\frac{\beta a\Theta_o}{2}\right)t^2\left[1 - \sum_{\ell=1}^{3} b_\ell(2\ell-1)\left(\frac{\lambda}{\lambda_{cn}}\right)^{2\ell}\right]\right] \tag{13}$$

$$= C_3 \sum_{m=1}^{\infty} T_{mn} J_1(X_{1m}t) \quad .$$

We are after an expression for the coefficients T_{mn}. Absorbing the constants C_2 and C_3 into the coefficients T_{mn}, multiplying both sides by $J_1(X_{1m'}t)t$ and integrating over the taper angle with $\int_0^1 dt$:

$$\int_0^1 tJ_1(X_{1n}t)J_1(X_{1m'}t)\exp\left[iKt^2\right]dt$$

$$= \sum_{m=1}^{\infty} T_{mn} \int_0^1 tJ_1(X_{1m}t)J_1(X_{1m'}t)dt \quad , \tag{14}$$

where

$$K \equiv \frac{-\pi a\theta_o}{\lambda}\left[1 - \sum_{\ell=1}^{3} b_\ell\,(2\ell - 1)\left(\frac{\lambda}{\lambda_{cn}}\right)^{2\ell}\right] \simeq \frac{-\pi a\theta_o}{\lambda} \quad \text{for } a/\lambda \gg 1 \quad . \tag{15}$$

The integral on the right-hand side of Equation 14 is:

$$\int_0^1 tJ_1(X_{1m}t)J_1(X_{1m'}t)dt = 0 \quad m' \neq m \quad ,$$

$$= \frac{J_o^2(X_{1m})}{2} \quad m' = m \quad . \tag{16}$$

Dropping the primes on the m's we solve Equation 14 for the complex coefficient T_{mn}:

$$T_{mn} = \frac{2}{J_o^2(X_{1m})} \int_0^1 te^{iKt^2} J_1(X_{1m}t)J_1(X_{1n}t)dt \quad . \tag{17}$$

C. POWER CONVERSION COEFFICIENT

1. Large taper angle $(\pi a\theta_o/\lambda > 1,\ \theta_o \ll 1)$.

The total power in the TE_{om} mode is given by $P_m \propto |T_{mn}|^2 J_o^2(X_{1m})$. Thus the ratio $P_m/P_n \equiv P_{mn}$, which is the power coversion from a pure TE_{on} mode at the junction to the TE_{om} mode is,

$$P_{mn} \equiv \frac{P_m}{P_n} = \frac{|T_{mn}|^2}{|T_{nn}|^2} \frac{J_o^2(X_{1m})}{J_o^2(X_{1n})} \quad . \tag{18}$$

Equations 17 and 18 represent the desired result in the limit of large taper angle.

2. Small taper angle $(\pi a\Theta_o/\lambda < 1,\ \Theta_o << 1)$.

In this case we can simplify the expression for T_{mn} by expanding the argument of the exponential in the integrand:

$$T_{mn} \simeq \frac{2}{J_o^2(X_{1m})} \left[\int_0^1 tJ_1(X_{1m}t)J_1(X_{1n}t)dt + iK \int_0^1 t^3 J_1(X_{1m}t)J_1(X_{1n}t)dt \right] \quad . \tag{19}$$

For m = n, the first integral is non-zero and is much greater than the second integral and we find

$$T_{nn} \simeq \frac{2}{J_o^2(X_{1m})} \left[\frac{J_o^2(X_{1m})}{2} \right] = 1 \quad . \tag{20}$$

For $m \neq n$, the first integral in Equation 19 is identically zero and we have,

$$T_{mn} \simeq \frac{2iK}{J_o^2(X_{1m})} \int_0^1 t^3 J_1(X_{1m}t)J_1(X_{1n}t)dt \quad . \tag{21}$$

This integral has been evaluated by Solymar[3] and the result gives

$$\left|T_{mn}\right| = 8K \frac{J_o(X_{1n})}{J_o\left(X_{1m}\right)} \frac{X_{1m}\ X_{1n}}{\left(X_{1m}^{\ 2} - X_{1n}^{\ 2}\right)^2} \quad . \tag{22}$$

Substituting into Equation 18 for P_{mn},

$$P_{mn} = \frac{a^2\ \Theta_o^{\ 2}}{\lambda^2} \cdot \frac{64\pi^2 X_{1m}^{\ 2}\ X_{1n}^{\ 2}}{\left(X_{1m}^{\ 2} - X_{1n}^{\ 2}\right)^4} \tag{23}$$

which is the desired result in the limit $\pi a\Theta_o/\lambda < 1$, $\Theta_o << 1$.

Mode power ratios, $P_{mn}(K)$, where the transductance parameter $K \equiv -\pi a\Theta_o/\lambda$, can be calculated for values of $K \gtrsim 1$. Here, the parameter, a, is the cylindrical waveguide radius, Θ_o is the taper angle, and λ is the free space wavelength. For a cylindrical-conical junction the sign of K is reversed. However, as we will see below, the sign of K affects only the phase of the transduced modes and does not affect the amplitudes of the mode power ratios. The ratio of power converted into the TE_{om} mode from a pure incident TE_{on} mode was previously found to be

$$P_{mn}(K) = \frac{64\ X_{1m}^2\ X_{1n}^2}{(X_{1m}^2 - X_{1n}^2)^4} K^2, \text{ for } \left|K\right| < 1. \tag{24}$$

where X_{1n} is the nth positive root of $J_1(X) = 0$. In order to generalize Equation 24 for $K > 1$ we use Equation 18,

$$P_{mn}(K) = \frac{J_o^2\ (X_{1m})}{J_o^2\ (X_{1n})} \frac{\left|T_{mn}\ (K)\right|^2}{\left|T_{nn}\ (K)\right|^2}, \text{ for } \left|K\right| \lesssim 2.5, \tag{25}$$

where

$$T_{mn}(K) = \frac{2}{J_o^2(X_{1m})} \int_0^1 te^{ikt^2} J_1(X_{1m}t)\, J_1(X_{1n}t)dt \qquad (26)$$

The integral in Equation 26 has been evaluated numerically for various (m, n) and K. The results are shown in Figures 3 - 8 where only the absolute values, $T_{mn}(K)$ vs K , as required by Equation 25 are given. The results agree with those quoted by Solymar[3] and those calculations have been extended to include m or n = 5, 6 and values of K in the range 2.5 - 10.

Using Equation 25 and the results for $|T_{mn}(K)|$, the mode conversion, $P_{mn}(K)$, has also been computed as shown in Figures 9 - 14. For values of $K \gtrsim 4$ these calculations yield physically meaningless results ($P_{mn} > 1$). Apparently, for $|K| \gtrsim 2.5$ the theoretical analysis of the problem is no longer correct. As the symptoms of this error in analysis are values of P_{mn} which exceed unity, one suspects that the boundary condition applied at the conical-cylindrical junction does not properly account for depletion of the pure incident TE_{on} wave during the mode conversion process. For this reason the region of validity of Equation 25 is limited to $|K| \lesssim 2.5$.

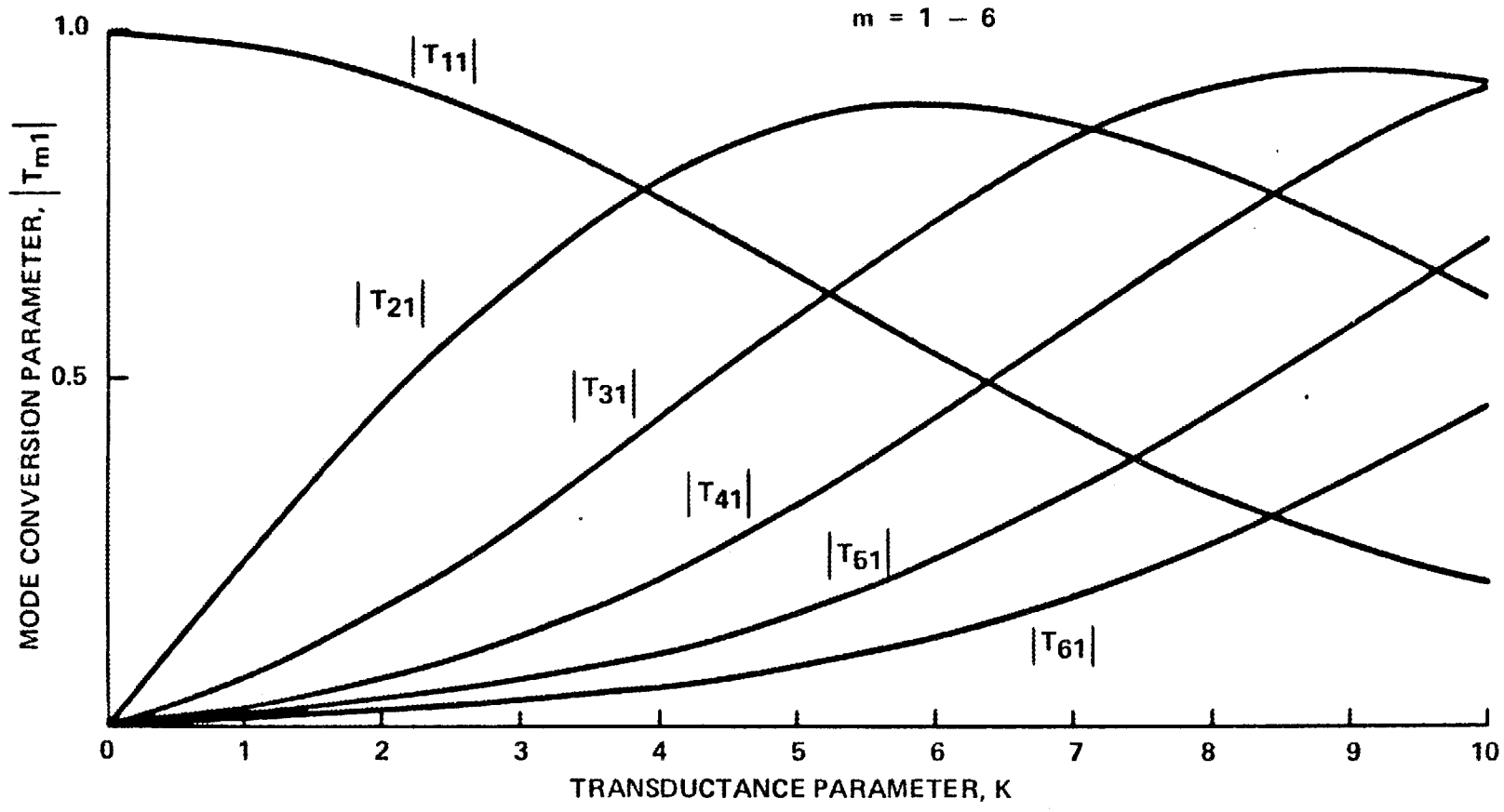

Figure 3. Variation of the Mode Conversion Parameter, $|T_{m1}|$, with the Transductance Parameter, K

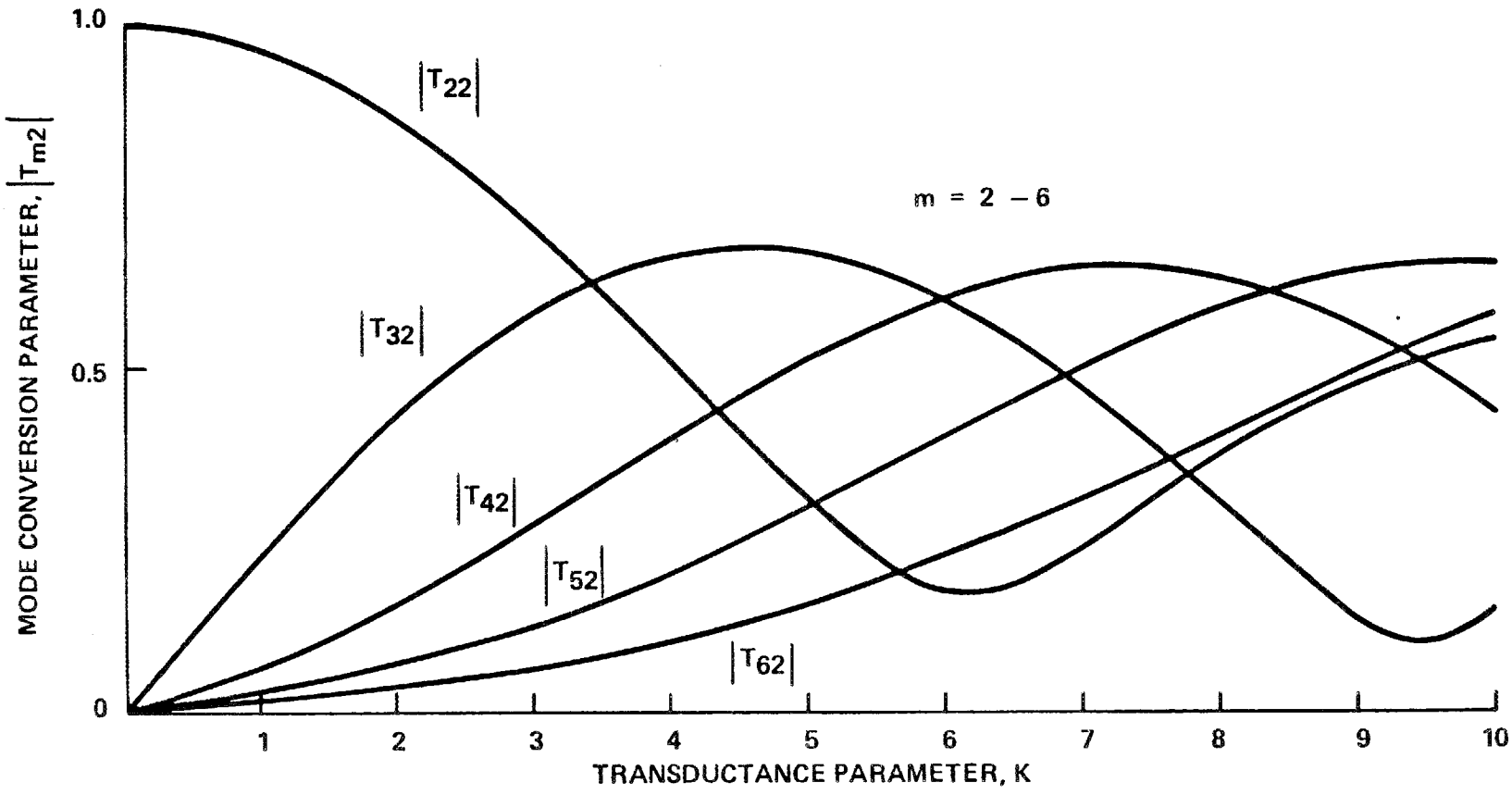

Figure 4. Variation of the Mode Conversion Parameter, $|T_{m2}|$, with the Transductance Parameter, K

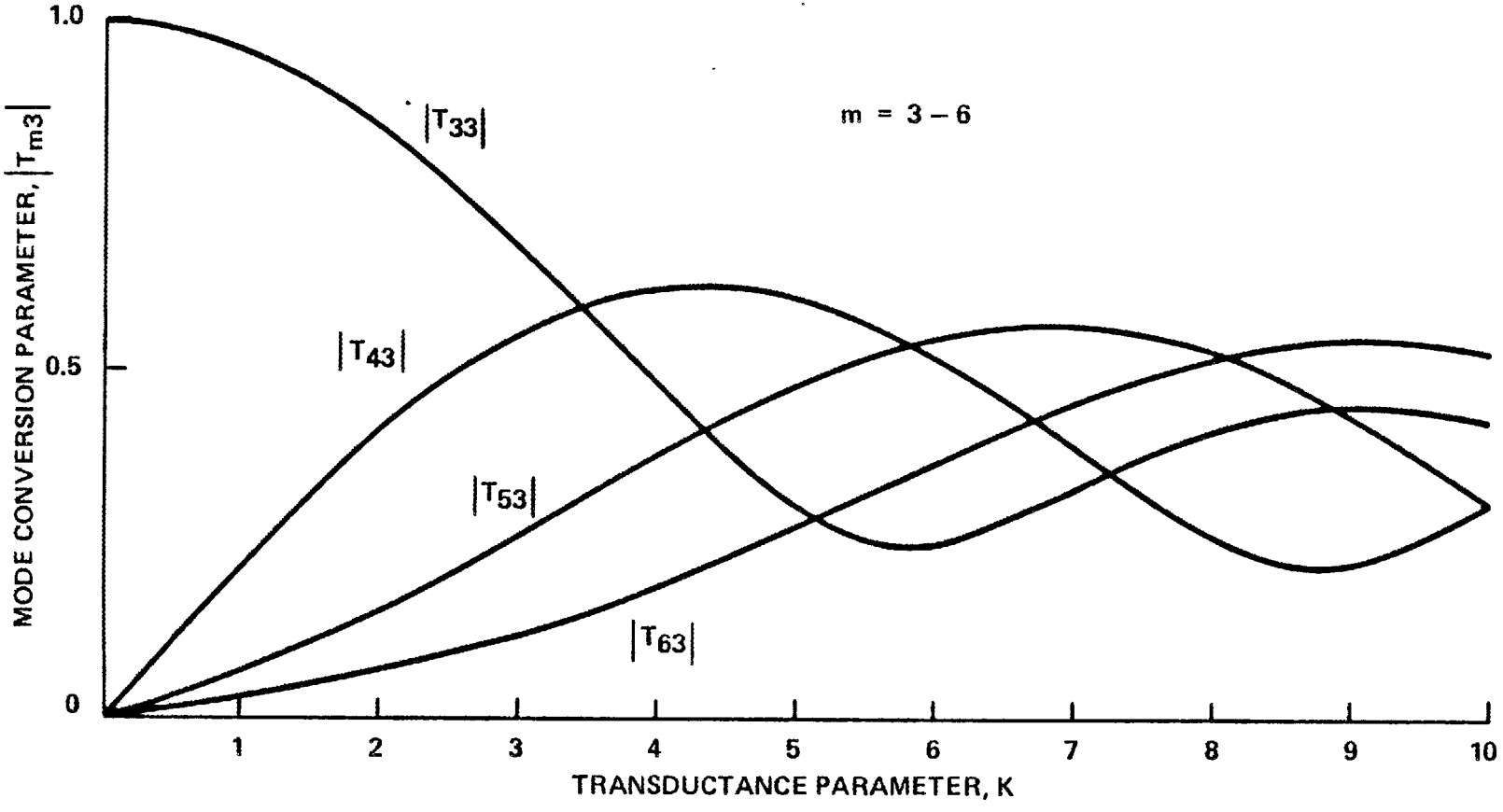

Figure 5. Variation of the Mode Conversion Parameter, $|T_{m3}|$, with the Transductance Parameter, K

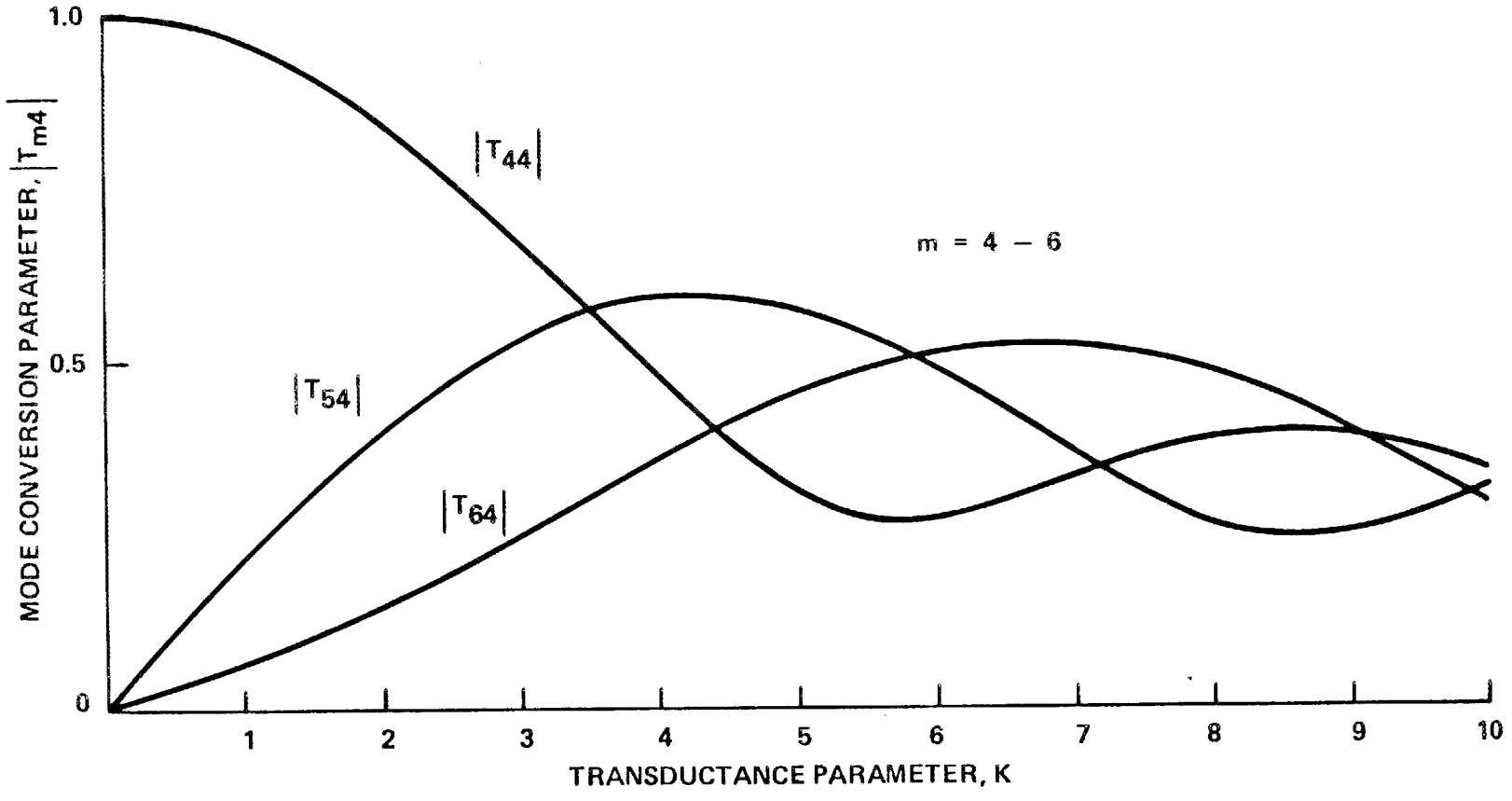

Figure 6. Variation of the Mode Conversion Parameter, $|T_{m4}|$, with the Transductance Parameter, K

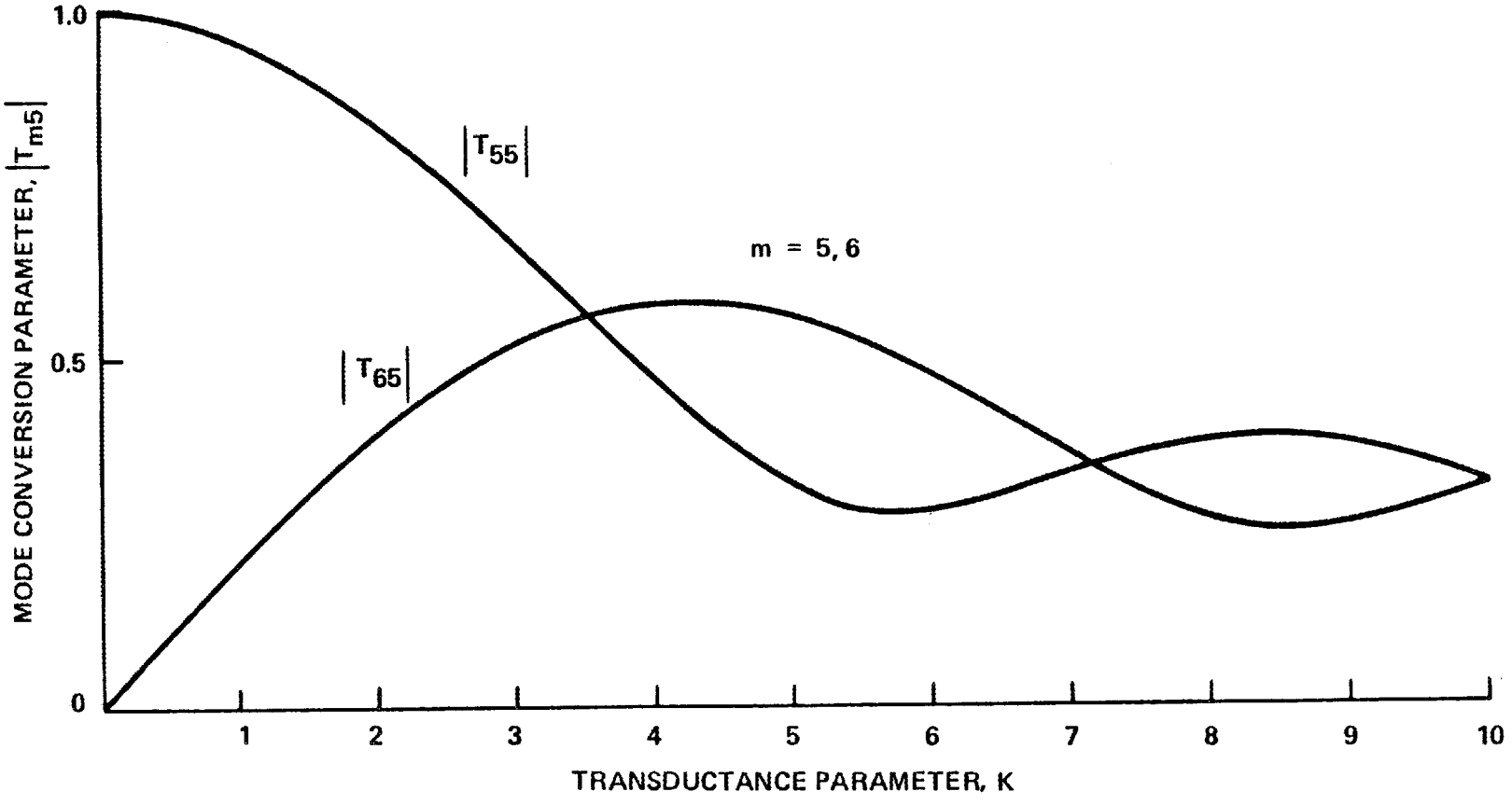

Figure 7. Variation of the Mode Conversion Parameter, $|T_{m5}|$, with the Transductance Parameter, K

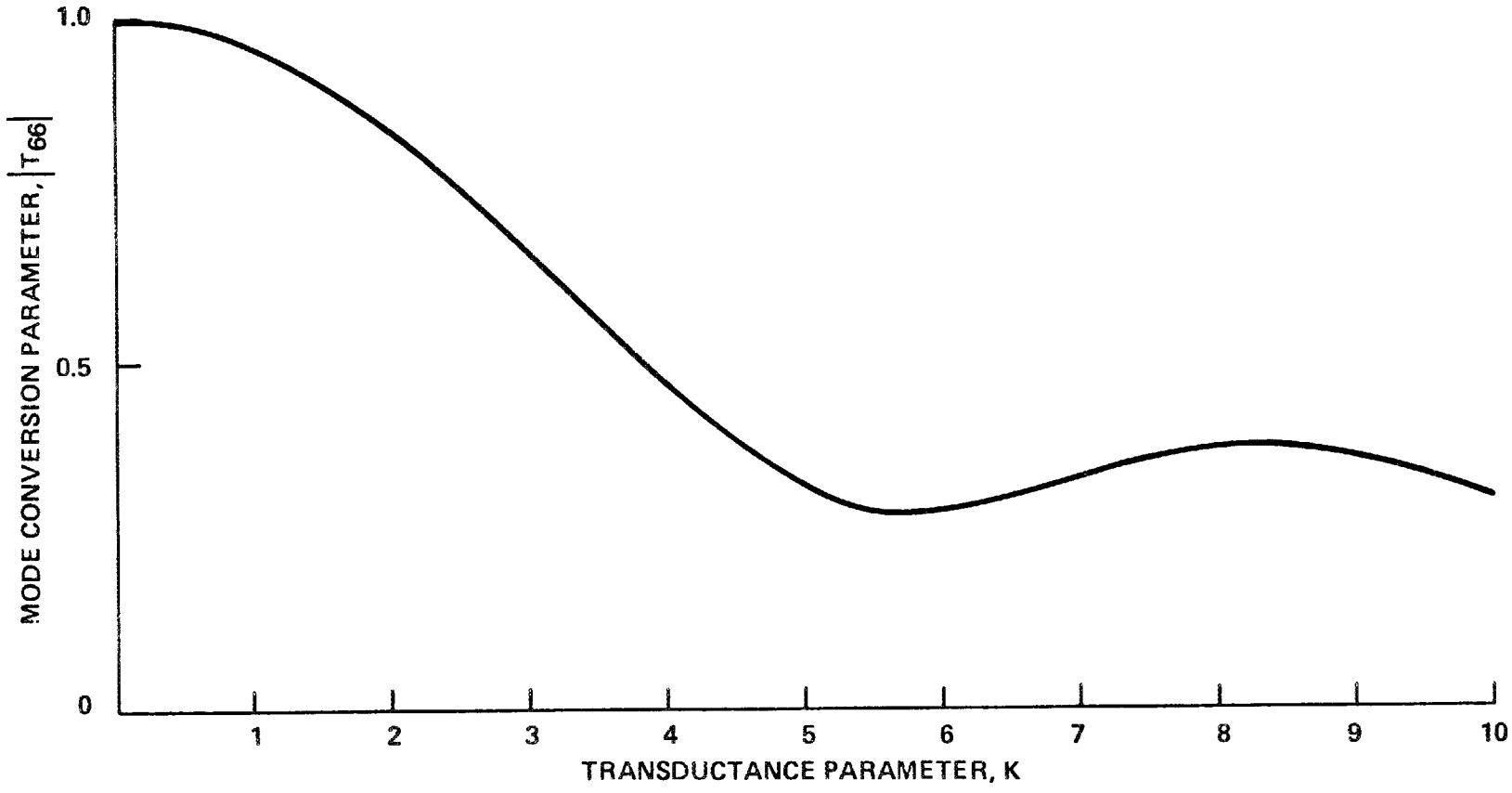

Figure 8. Variation of the Mode Conversion Parameter, $|T_{66}|$, with the Transductance Parameter, K

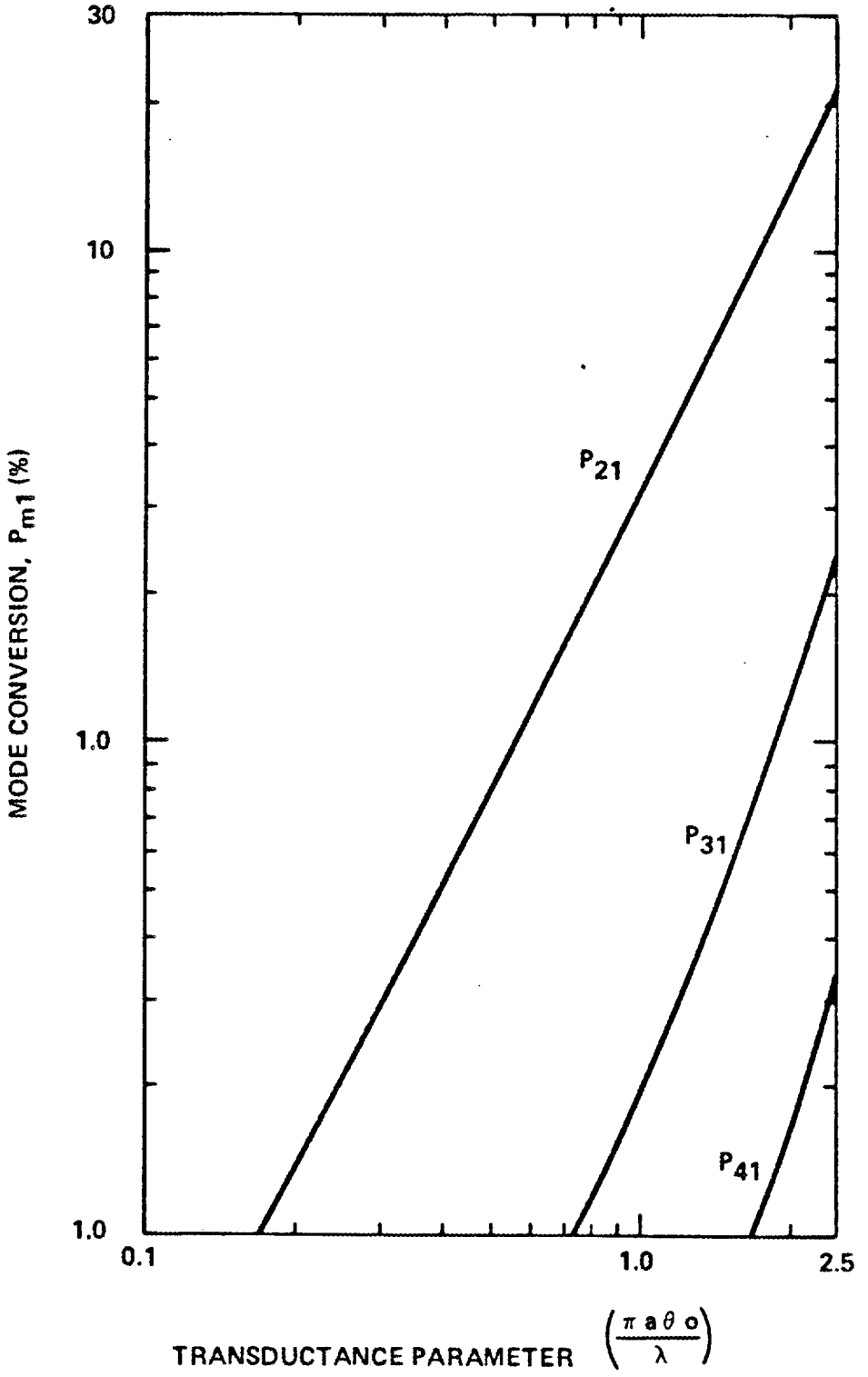

Figure 9. Mode Conversion, P_{m1}

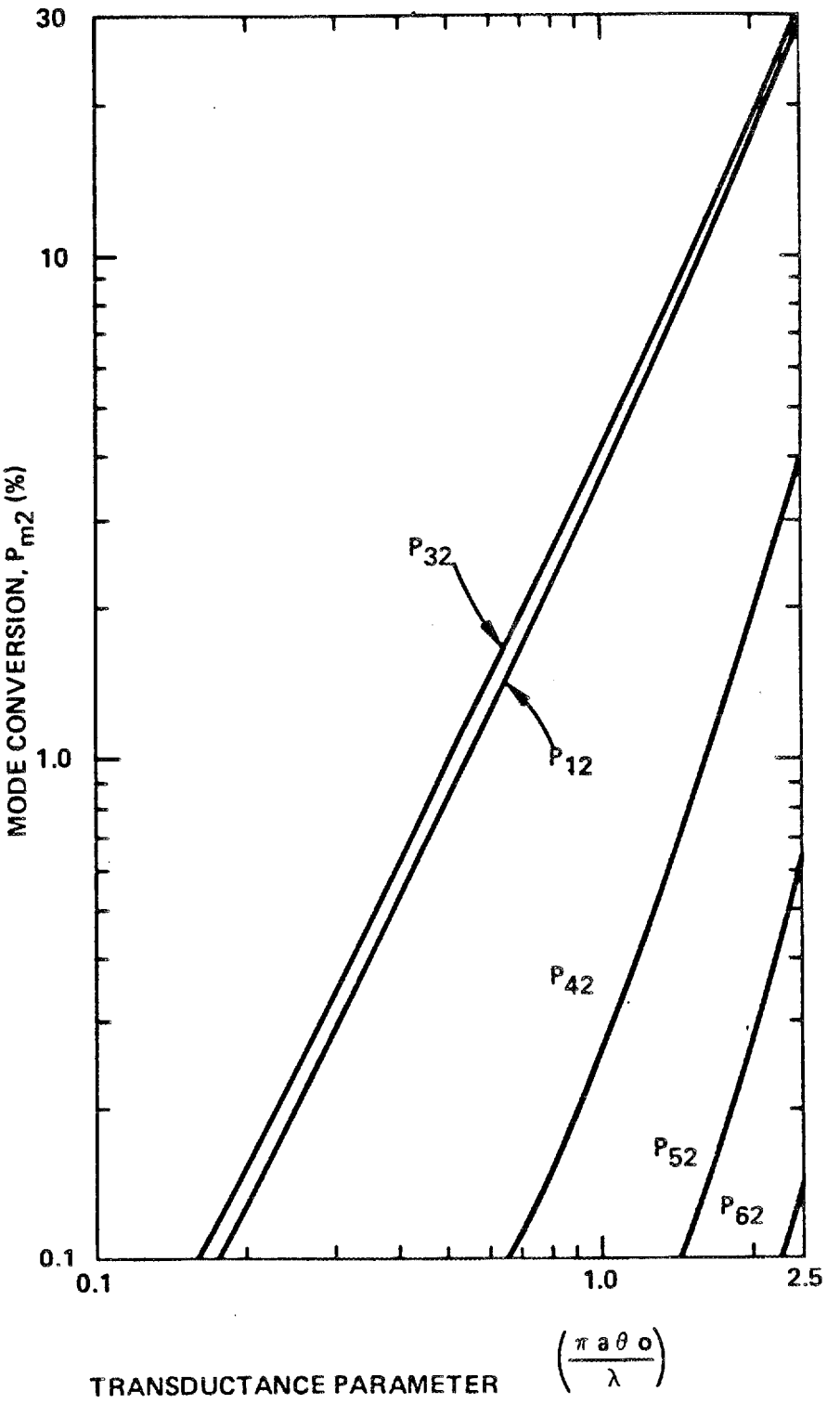

Figure 10. Mode Conversion, P_{m2}

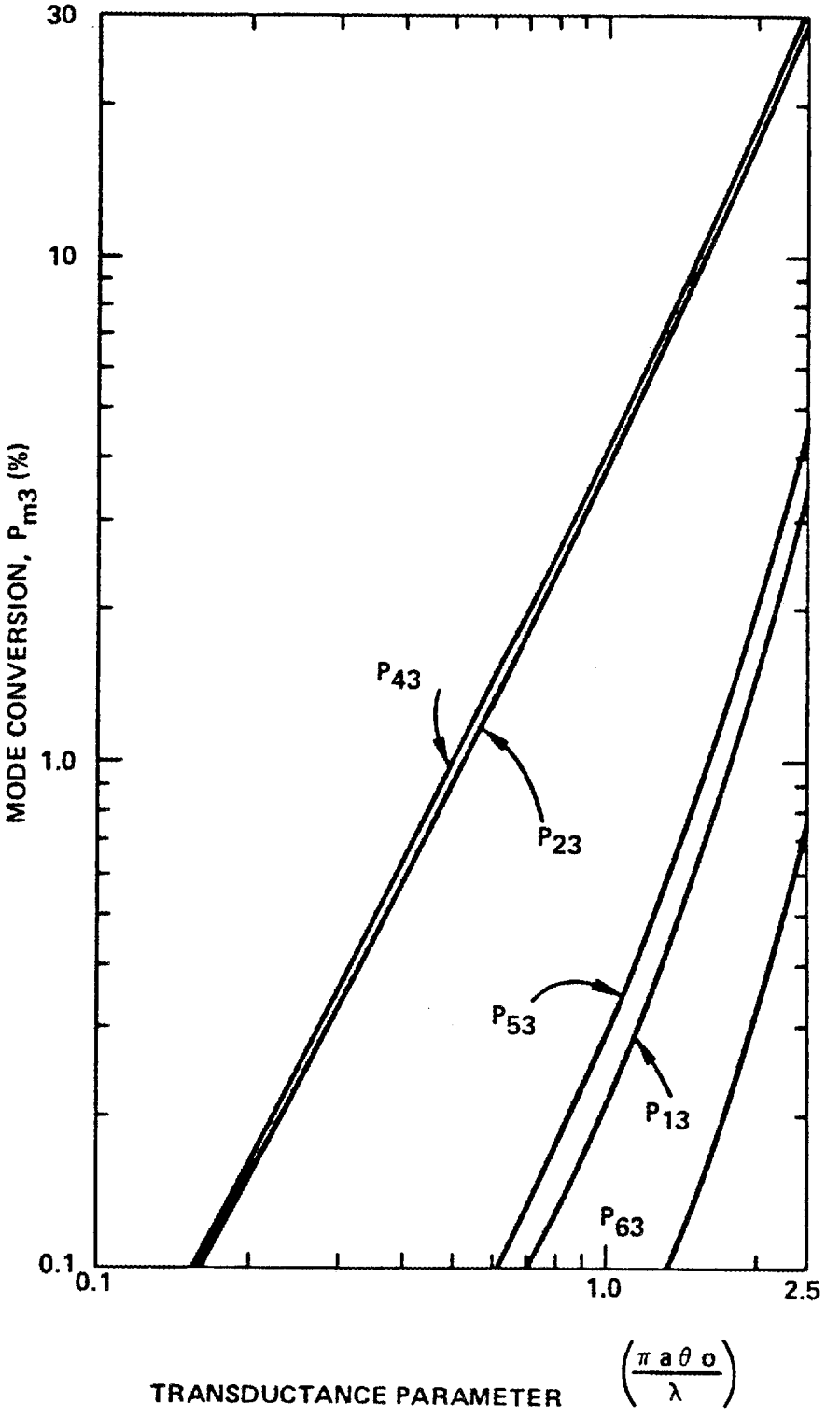

Figure 11. Mode Conversion, P_{m3}

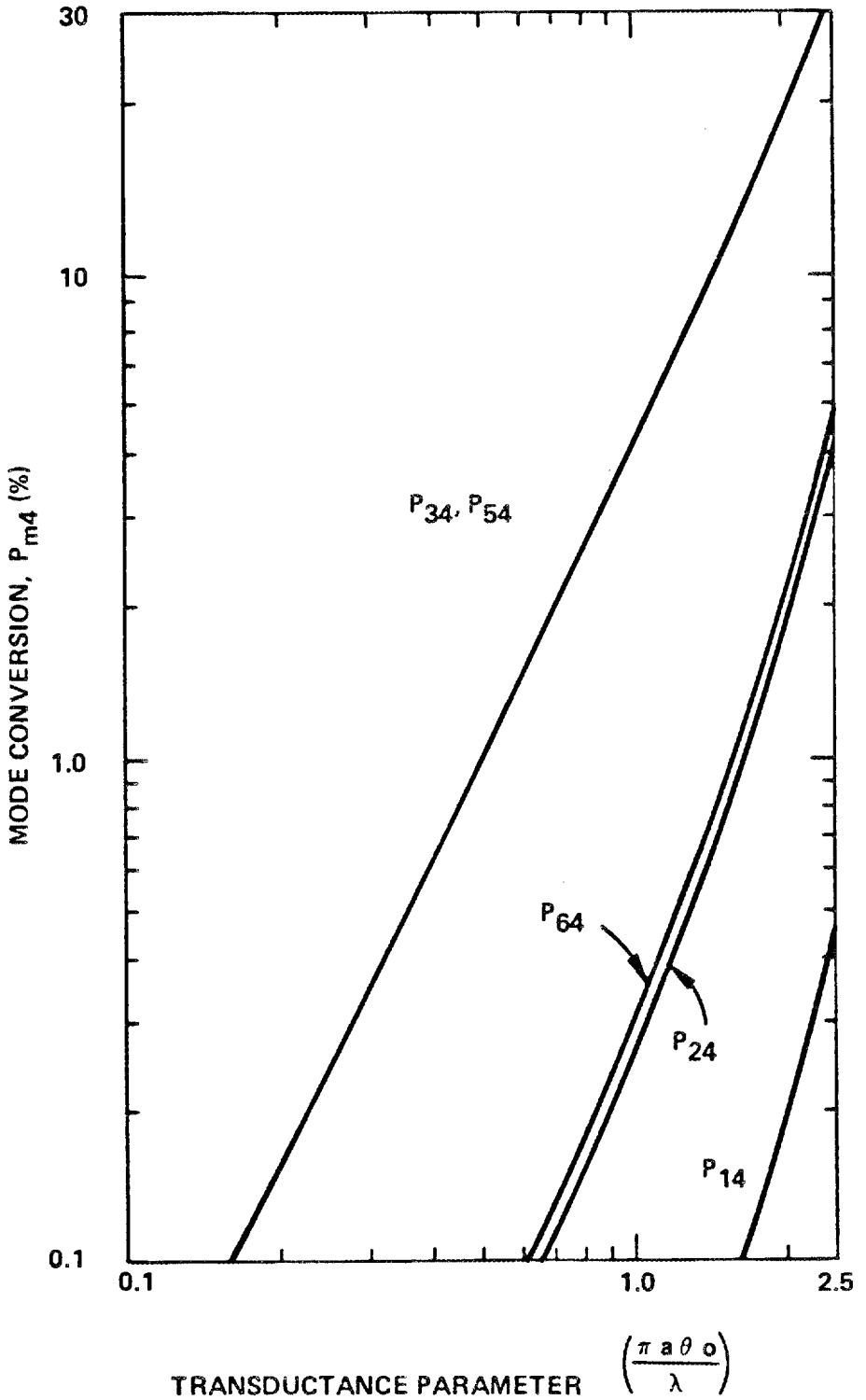

Figure 12. Mode Conversion, P_{m4}

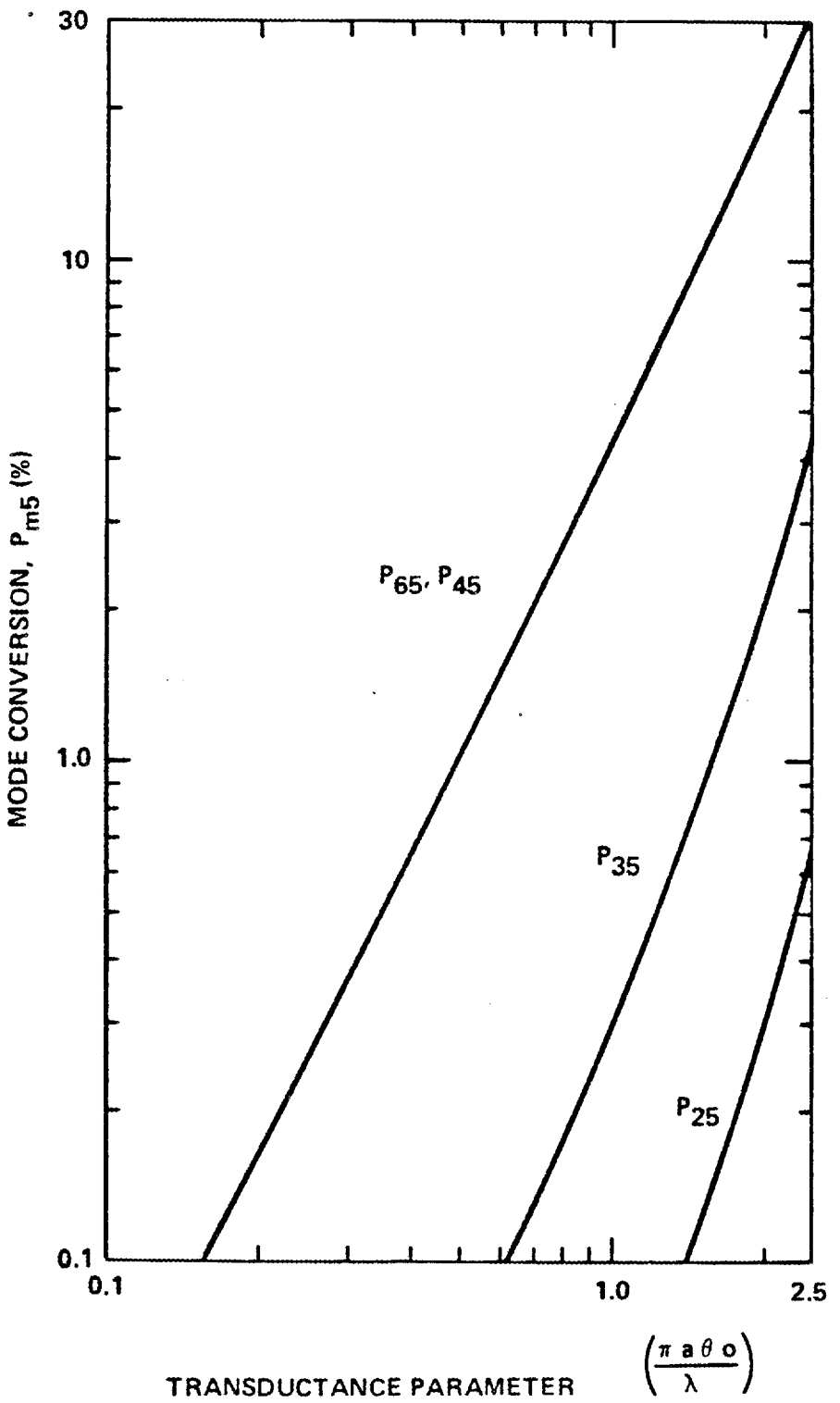

Figure 13. Mode Conversion, P_{m5}

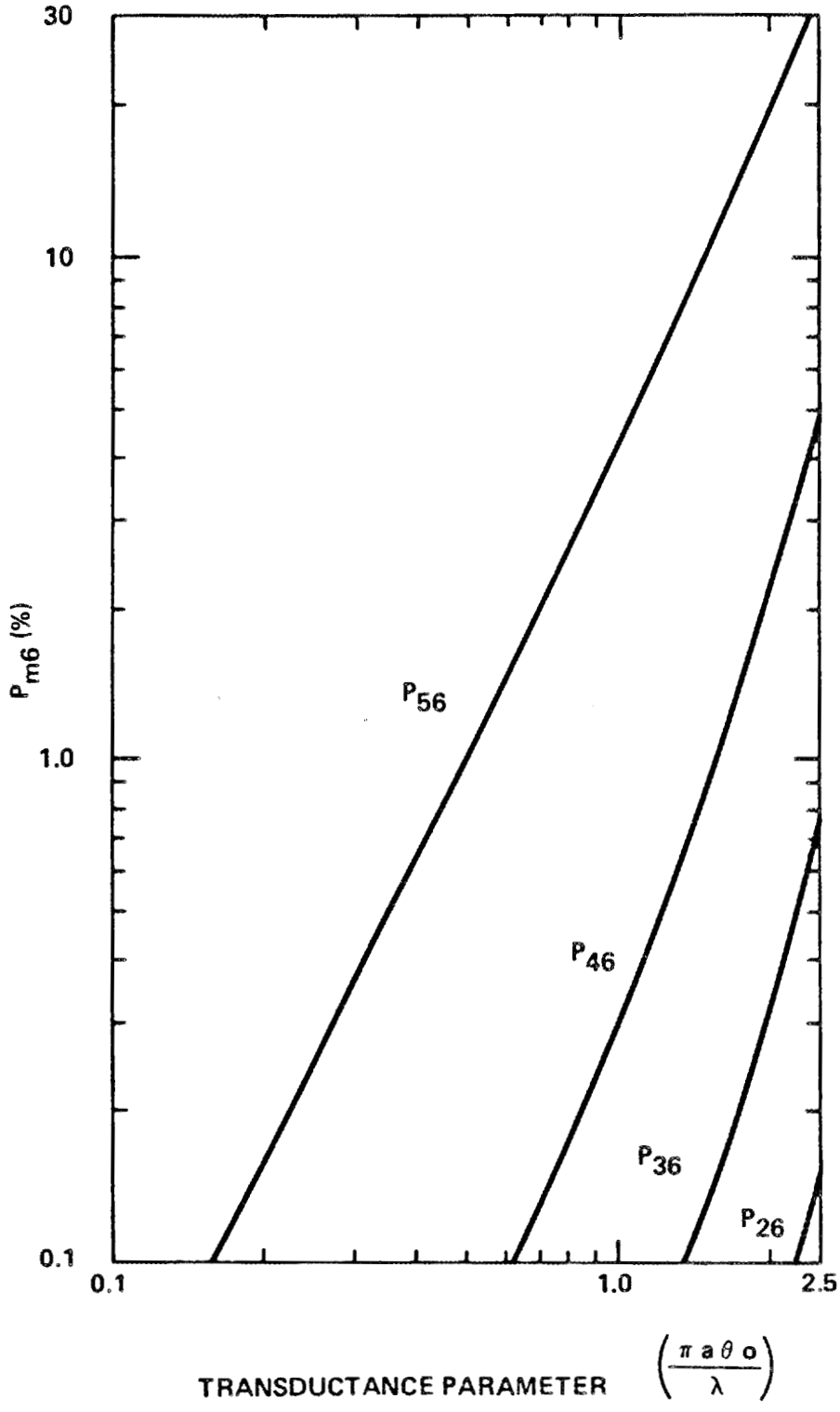

Figure 14. Mode Conversion, P_{m6}

REFERENCES

1. P. M. Morse and H. Feshback, Methods of Theoretical Physics, Part II, McGraw-Hilll, New York, 1953, p. 1462.

2. L. D. Landau and E. M. Lifshitz, Electrodynamics of Continuous Media, Pergamon Press, Oxford, 1960, p. 295.

3. L. Solymar, "Monotonic Multi-Section Tapers for Overmoded Circular Waveguide", IRE-MTT, 1959, p. 121.

APPENDIX C

VOLTAGE TRAVELING WAVE RATIO MEASUREMENTS*

A technique for measuring the mode content of the power flow in a multimode transmission line was developed. In this appendix the analysis behind the measurement technique[1] and some experimental considerations are discussed.

A. DEFINITION OF VTWR

The ratio of the maximum and minimum values of the beating wave electric fields of any two modes propagating in a multimode guide may, by analogy to the well established vernacular of the single mode waveguide, be denoted the voltage traveling wave ratio (VTWR) for the two modes in question. In general, the VTWR's will be a function of position in the plane normal to the direction of propagation in the guide. Measurements of the VTWR's can be easily related to the fractions of total power propagating in each waveguide mode. This information may be used to:

(1) characterize the operating mode output of a high power source with multimode output such as a gyrotron,

(2) analyze the mode conversion properties of overmoded waveguide components,

(3) determine the optimum locations along the line for lossy obstructions,

(4) allow transductance matching (induced destructive interference of one or more unwanted modes)[2].

* NOTICE OF IEEE COPYRIGHT: This section contains excerpts from a manuscript which has been accepted for publication in the IEEE Transactions on Microwave Theory and Techniques and is therefore subject to the standard IEEE copyright agreement. This notice is required by that agreement.

The voltage traveling wave ratio (VTWR) is defined in the following manner. Consider the superposition of the two plane waves with complex amplitudes A_n and A_m traveling in a multimode guide in the positive z direction. The resultant wave amplitude may be written as,

$$C(z) = \left|A_n\right| e^{ik_n z + i\phi_n} + \left|A_m\right| e^{ik_m z + i\phi_m} \tag{1}$$

$$\text{where } \phi_{n,m} \equiv \arctan \left\{ \frac{\text{Im} \langle A_{n,m} \rangle}{\text{Re} \langle A_{n,m} \rangle} \right\} \tag{2}$$

and $k_{n,m}$ are the propagation constants or wave numbers. Cases where such a resultant wave, or beat pattern, is measured by a detector sensitive to the quantity,

$$\left|C(z)\right|^2 = \left|A_n\right|^2 + \left|A_m\right|^2 + 2\left|A_n\right|\left|A_m\right| \cos \left\{(k_n - k_m)z + (\phi_n - \phi_m)\right\} \tag{3}$$

are of interest. The beat wave number is defined as $k_{nm} \equiv k_n - k_m /2$. The beat wavelength is $\lambda_{nm} \equiv 2\pi/K_{nm}$. The beat phase, $(\phi_n - \phi_m)$, may be eliminated by suitable choice of origin in z. Solving for the ratio of the maximum and minimum values of $C(z)$, we define the voltage traveling wave ratio,

$$\text{VTWR} \equiv \frac{\left|C(z)\right|_{max}}{\left|C(z)\right|_{min}} = \left| \frac{\left|A_n\right| + \left|A_m\right|}{\left|A_n\right| - \left|A_m\right|} \right| = \pm\left(\frac{\left|A_n\right| + \left|A_m\right|}{\left|A_n\right| - \left|A_m\right|}\right); \begin{cases} \text{Upper sign:} \\ \left|A_n\right| > \left|A_m\right| \\ \text{Lower sign:} \\ \left|A_n\right| < \left|A_m\right| \end{cases}, \tag{4}$$

where the value of the VTWR can range from unity to infinity. This equation can be solved for the ratio

$$\frac{\left|A_m\right|^2}{\left|A_n\right|^2} = \left(\frac{\text{VTWR} \mp 1}{\text{VTWR} \pm 1}\right)^2 \quad \begin{matrix} \text{Upper Sign} & \left|A_n\right| > \left|A_m\right| \\ \text{Lower Sign} & \left|A_n\right| < \left|A_m\right| \end{matrix} \quad . \tag{5}$$

Equation 5 relates a measurable quantity, the VTWR for modes n and m, to the ratio of traveling plane wave amplitudes.

B. VTWR'S IN CYLINDRICAL WAVEGUIDE

The fractions $|a_n|^2$ of the total transmission line power contained in each waveguide mode can be deduced from the measured beat wave pattern $|C(\vec{r},z)|^2$. The multimode transmission line is uniform in the direction of propagation but may have any arbitrary cross section. The measured resultant beat wave pattern arises from the superposition of many modes traveling in the positive z direction. This general case (arbitrary number of modes traveling in a waveguide of arbitrary cross section) has been analyzed and the exact treatment by which $|C(\vec{r},z)|^2$ may be decomposed into the constituent normal modes of the waveguide can be prescribed.

For the special case of two circular electric modes propagating in cylindrical waveguide, the general result may be simplified. Using the definition as expressed in Equation 4, the mode power ratio can be determined:

$$\frac{|a_m|^2}{|a_n|^2} = G_{nm}(r)\left(\frac{VTWR(r) \mp 1}{VTWR(r) \pm 1}\right)^2 \tag{6}$$

where the guide factor is defined according to:

$$G_{nm}(r) \equiv \frac{\left|J_o(x_m)\right|^2 \left|J_1\left(\frac{x_n r}{a}\right)\right|^2}{\left|J_o(x_n)\right|^2 \left|J_1\left(\frac{x_m r}{a}\right)\right|^2} \quad , \text{ with } G_{nm}(r) = G_{mn}^{-1}(r).$$

C. MODE BUNCHES

When VTWR measurements are performed on systems in which the transductance mismatches are not severe, the general analysis may be simplified. One such simplification, which is useful in gyrotron engineering, is that one need only consider transduction of a pure TE_{on} mode into the mode bunch ($TE_{o\,n-1}$, TE_{on}, $TE_{o\,n+1}$). This approximate treatment is often valid because mode conversion occurs preferentially into nearest

neighbor modes. (The exception to this occurs when a resonant structure is encountered, such as a waveguide segment close to a mode cutoff.) Thus, a pure TE_{on} circular electric mode will tend to diffuse under an envelope in k-space to form a bunch of modes centered at $k = k_n$, with the wings of the k-space envelope trailing to zero for other modes $m \neq n$. For example, in cylindrical waveguides the TE_{on} mode bunches are contained under the envelope:

$$P_k \propto \frac{X_{1n}^2 \quad X_{1m}^2}{\left(X_{1n}^2 - X_{1m}^2\right)^4} \tag{7}$$

where X_{1n} is the nth positive root of $J_1(X) = 0$. For $n \sim 1$, it can be seen from Equation 7 that since $P_k \sim m^{-6}$ the mode bunch is effectively limited to the three modes $m = n-1$, n, and $n+1$.

D. GUIDE FACTORS

The two-mode guide factor, G_{nm}, defined in Equation 6, has been computed for the mode bunches presently of interest in gyrotron research, as shown in Table I. The two-mode VTWR, Equation 6, can be used when considering bunches of three modes by performing the VTWR measurements at a radial position for which one of the three modes is identically zero. For example, to find the mode power fractions for the mode bunch (TE_{01}, TE_{02}, TE_{03}), the mode power ratios, $|a_2|^2/|a_1|^2$ and $|a_3|^2/|a_1|^2$ must be measured. [The ratio $a_3^2 \quad a_2^2$ in this unique example is not measured because the TE_{01} has no non-trivial nulls.] This requires the computation of G_{13} and G_{12}. There are often more than one radial null to choose from as shown in Table I. In this case, the values of $G_{13}(X_1 a/X_2) = 1.091$, $G_{12}(X_1 a/X_3) = 0.7961$, and $G_{12}(X_2 a/X_3) = 1.256$ are required.

The VTWR measurements must be performed over a longitudinal interval which is greater than or equal to one-half of the largest beat wavelength, λ_{nm}, of interest in the system. Table II lists all the half beat wavelengths for pairs of circular electric mode through the TE_{05} for the standard 2 1/2" diameter multimode guide at several frequencies. Table III lists the minimum VTWR measurement intervals for the first three circular

TABLE I

GUIDE FACTOR FOR CIRCULAR ELECTRIC MODE BUNCHES

RADIAL NULL POINTS (r/a)	RADIAL NULL POINTS (inches, in 2.5" DIAM. GUIDE)	MODE BUNCHES					
		TE_{01},	TE_{02}, TE_{03}	TE_{02},	TE_{03}, TE_{04}	TE_{03},	TE_{04}, TE_{05}
		GUIDE FACTOR		GUIDE FACTOR		GUIDE FACTOR	
NONE	—	G_{23}	—				
$\frac{X_1}{X_2}$ = 0.5462	0.683	G_{13}	1.091	G_{34}	15.04		
$\frac{X_1}{X_3}$ = 0.3766	0.471	G_{12}	0.7961	G_{24}	1.026	G_{45}	1.633
$\frac{X_2}{X_3}$ = 0.6896	0.862		1.256		1.024		0.8100
$\frac{X_1}{X_4}$ = 0.2876	0.360			G_{23}	1.709	G_{35}	1.011
$\frac{X_2}{X_4}$ = 0.5265	0.658				0.01832		1.542
$\frac{X_3}{X_4}$ = 0.7636	0.955				2.175		1.010
$\frac{X_1}{X_5}$ = 0.2326	0.291					G_{34}	2.344
$\frac{X_2}{X_5}$ = 0.4259	0.532						0.2382
$\frac{X_3}{X_5}$ = 0.6177	0.772						0.5072
$\frac{X_4}{X_5}$ = 0.8089	1.011						2.729

TABLE II

ONE-HALF BEAT WAVELENGTHS (INCHES)						
	FREQ. (GHz)	28	35	60	90	110
	FREE SPACE WAVELENGTH (in.)	0.422	0.337	0.197	0.131	0.107
MODE PAIR						
TE_{01}	TE_{02}	8.1	10.3	17.9	27.1	33.3
	TE_{03}	3.0	3.9	6.9	10.5	12.9
	TE_{04}	1.5	2.0	3.7	5.7	7.0
	TE_{05}	0.8	1.2	2.3	3.6	4.4
TE_{02}	TE_{03}	4.8	6.3	11.3	17.2	21.1
	TE_{04}	1.9	2.5	4.7	7.2	8.9
	TE_{05}	0.9	1.4	2.7	4.1	5.1
TE_{03}	TE_{04}	3.0	4.3	8.1	12.5	15.4
	TE_{05}	1.1	1.8	3.5	5.5	6.8
TE_{04}	TE_{05}	1.8	3.0	6.2	9.7	12.0

TABLE III

VTWR MEASUREMENT INTERVALS (inches)

FREQUENCY (GHz)	FREE SPACE WAVELENGTH (inches)	MODE BUNCH		
		TE_{01}, TE_{02}, TE_{03}	TE_{02}, TE_{03}, TE_{04}	TE_{03}, TE_{04}, TE_{05}
28	0.422	8.1	4.8	3.0
35	0.337	10.3	6.3	4.3
60	0.197	17.9	11.3	8.1
90	0.131	27.1	17.2	12.5
110	0.107	33.3	21.1	15.4

electric mode bunches. These intervals are on the order of 10" - 20" and are not too large for performing practical VTWR measurements. Although the present trend in gyrotron design is toward higher frequency (downward in Table III), this is accompanied by a trend in operating mode toward higher radial mode number (to the right in Table III). Thus, for present circular electric mode devices, or those under consideration, the relevant VTWR measurement intervals will remain in the practical range of 10" - 20".

REFERENCES

1. D. S. Stone, "Mode Analysis in Multimode Waveguides using Voltage Traveling Wave Ratios", IEEE Trans. Vol. MTT-29, No. 2, pp. 91-95, February 1981.

2. L. Solymer, "Monotonic Multi-Section Tapers for Overmoded Circular Waveguide", I.E.E. paper #2839R pp. 121-128, January 1959.

ORNL/Sub/79-21453/21
July 1984

INTERNAL DISTRIBUTION

1. P. F. Becher
2. L. A. Berry
3. T. S. Bigelow
4. G. M. Galyon
5. H. H. Haselton
6-8. G. R. Haste
9. H. D. Kimrey, Jr.
10. R. P. Jernigan
11. H. C. McCurdy
12. D. H. Metzler
13. O. B. Morgan, Jr.
14. J. Sheffield
15. T. L. White
16-17. Laboratory Records Department
18. Laboratory Records, ORNL-RC
19. Y-12 Document Reference Section
20-21. Central Research Library
22. Fusion Energy Division Library
23. Fusion Energy Division Publications Office
24. J. M. Spicer, ORNL Patent Office
25-26. Technical Information Center Oak Ridge, TN 37830

EXTERNAL DISTRIBUTION

27. M. N. Afsar, Francis Bitter National Magnet Laboratory, MIT, Cambridge, MA 02139
28. D. S. Beard, Component Branch, Office of Fusion (ETM), Department of ER-531, GTN, Washington, DC 20545
29. N. Bowen, Princeton University, Plasma Physics Laboratory, P. O. Box 451, Princeton, NJ 08540
30. R. A. Dandl, AMPC, Inc., 2210 Encinitas Blvd., Suite P, Encinitas, CA 92024
31. J. F. Decker, Office of Fusion Energy, Office of Energy Research, ER-1, GTN, Department of Energy, Washington, D. C. 20545
32. N. Dionne, Raytheon Company, Foundry Avenue, Waltham, MA 02254
33. W. Friz, AFAL/DHM, Wright-Patterson AFB, OH 45433
41. T. V. George, Office of Fusion Energy, Office of Research, ER-531, GTN, U. S. Department of Energy, Washington, DC 20545
42. T. Godlove, ER-20.2:GTN/OHENP, U. S. Department of Energy, Washington, DC 20545
43. V. L. Granatstein, Naval Research Laboratory, Code 6740, Washington, DC 20545
44. G. M. Haas, Office of Fusion Energy, Office of Research, ER-533, GTN, U. S. Department of , ER-531, GTN, Washington, DC 20545
45. J. L. Hirshfield, Yale University, Department of Engineering and Applied Science, P. O. Box 2159, Yale Station, New Haven, CT 06520
46. W. W. Ho, Rockwell International Science Center, 1049 CAmino dos Rios, Thousand Oaks, CA 91360
47. H. Hsuan, Plasma Physics Laboratory, Princeton University, P. O. Box 451, Princeton, NJ 08544
48. K. Krause, MFE Electronics Engineering Department, Lawrence Livermore National Laboratory, P. O. Box 551 (/L-634), Livermore, CA 94550
49. J. V. Lebacqz, Stanford Linear Accelerator Center, Stanford University, P. O. Box 4349, Bin 30, Stanford, CA 94305
50. C. M. Loring, EIMAC, Div. of Varian, 301 Industrial Way, San Carlos, CA 94070
51. C. Moeller, GA Technologies, Inc., Fusion and Advanced Technology, P. O. Box 85608, San Diego, CA 92138

52. Office of Assistant Manager for Research and Development, Oak Ridge Operations Office, Department of, Oak Ridge, TN 37830
53. R. Prater, GA Technologies, Inc., Fusion and Advanced Technology, P. O. Box 85608, San Diego, CA 92138
54. R. Profant, Office of Nuclear Materials Production, DP 13.2, GTN, U. S. Department of Energy, Washington, DC 20545
55. M. E. Read, Naval Research Laboratory, Code 6740, Washington, DC 20375
56. D. B. Remsen, GA Technologies, Inc., Fusion and Advanced Technology, P. O. Box 85608, San Diego, CA 92138
57. T. E. Roemesser, TRW, Defense & Space Systems, 1 Space Park, Bldg. R-1, Room 2044, Redondo Beach, CA 90278
58. G. Simonis, Harry Diamond Laboratory, 2800 Powder Mill Road, Adelphi, MD 20783
59. M. S. Sparks, Scientific Research Center, 9507 High Ridge Place, Beverly Hills, CA 90210
71. B. L. Stallard, Lawrence Livermore Laboratory, (L-437), P. O. Box 5511, Livermore, CA 94550
72. H. S. Staten, Office of Fusion, Office of Energy Research, ER-531, GTN, U. S. Department of Energy, Washington, DC 20545
73. M. A. Stroscio, AFOSR, Boiling Air Force Base, Washington, DC 20332
74. R. S. Symons, Litton Industries, Inc., Electron Tube Division, 960 Industrial Road, San Carlos, CA 94070
75. P. J. Tallerico, AT-5, Accelerator Technology Division, Los Alamos Scientific Laboratory, Mail Stop 821, P. O. Box 1663, Los Alamos, NM 87545
76. J. J. Tancredi, Electron Dynamics Division, Hughes Aircraft Company, 3100 W. Lomita Boulevard, Torrance, CA 90509
77. R. J. Temkin, Plasma Fusion Center, Mass. Institute of Technology, 170 Albany Street, NW16-254, Cambridge, MA 02139
78. Director, U. S. Army Ballistic Missle Defense Advance Technology, Attn: D. Schenk, ATC-R, P. O. Box 1500, Huntsville, AL 35807

VARIAN DISTRIBUTION

79.	R. Berry
80.	R. Bier
81-83.	J.E. Camp
84.	M. Caplan
85.	L.J. Craig
86.	K.L. Felch
87.	L.J. Fox
88-90.	C.R. Frazer
91.	H. Huey
92.	G. Huffman
93.	R.L. Ives
94.	H.R. Jory
95.	D. Latshaw
96.	E. Lien
97.	N. Lopez
98.	J.F. Moran
99.	J. Nielson
100.	D.R. Pirkle
101.	J.F. Shively
102.	S.T. Spang
103-104.	A. Staprans
105.	Technical Library